BİTLİS EREN ÜNİVERSİTESİ FEN BİLİMLERİ DERGİSİ

Journal of Science

BİTLİS EREN ÜNİVERSİTESİ FEN BİLİMLERİ DERGİSİ

Bitlis Eren University Journal of Science

ISSN: 2147-3129
e-ISSN : 2147-3188

Volume : 14
Issue : 3
Year : 2025

T.C.
Bitlis Eren Üniversitesi
Lisansüstü Eğitim Enstitüsü
Rahva Yerleşkesi Beş Minare Mah. Ahmet Eren Bulvarı, 13000, Merkez, Bitlis/TÜRKİYE
Tel: +90 434 222 00 72
https://dergipark.org.tr/en/pub/bitlisfen

BİTLİS EREN ÜNİVERSİTESİ FEN BİLİMLERİ DERGİSİ
BİTLİS EREN UNIVERSITY JOURNAL OF SCIENCE
BEU FBD
ISSN: 2147-3129 / e-ISSN: 2147-3188
https://dergipark.org.tr/tr/pub/bitlisfen



Bitlis Eren Üniversitesi Fen Bilimler Dergisi

Bitlis Eren University Journal of Science

Rahva Yerleşkesi Beş Minare Mah. Ahmet Eren Bulvarı, 13000, Merkez, Bitlis/TÜRKİYE
Phone: +90 434 222 00 72
Publication Date: June 30, 2025

https://dergipark.org.tr/en/pub/bitlisfen

Volume: 14	**Issue:** 3	**Year:** 2025

March	June	September	December

OWNER
Prof. Dr. Necmettin ELMASTAŞ

DIRECTOR
Prof. Dr. Mehmet Bakır ŞENGÜL

EDITOR IN CHIEF
Assist. Prof. Dr. Kerim ÖZBEYAZ

EDITORS
Assoc. Prof. Dr. Engin YILMAZ
Assoc. Prof. Dr. Fatih AVCİL
Assist. Prof. Dr. Mehmet Akif YERLİKAYA
Assist. Prof. Dr. Nuray GÜL
Assist. Prof. Dr. Ömer KARABEY
Assist. Prof. Dr. Ufuk KAYA
Assist. Prof. Dr. Yunus SAYAN

LANGUAGE EDITOR
Assist. Prof. Dr. Murat ÇAN
Lecturer Ahmet ÖZKAN

TYPOGRAPHIC
Assist. Prof. Dr. Kerim ÖZBEYAZ

JOURNAL SECRETARY
Beytullah ARSLAN

BİTLİS EREN ÜNİVERSİTESİ FEN BİLİMLERİ DERGİSİ
BİTLİS EREN UNIVERSITY JOURNAL OF SCIENCE
BEU FBD
ISSN: 2147-3129 / e-ISSN: 2147-3188
https://dergipark.org.tr/tr/pub/bitlisfen



EDITORIAL BOARD

Prof. Dr. Kesran AKIN	Bitlis Eren University
Prof. Dr. Ramazan KATIRCI	Sivas Bilim ve Teknoloji University
Prof. Dr. Tuncay TUNÇ	Mersin University
Prof. Dr. Yunus Levent EKİNCİ	Bitlis Eren University
Prof. Dr. Zekeriya YERLİKAYA	Kastamonu University
Prof. Dr. Ali ÇAKMAK	Ağrı İbrahim Çeçen University
Doç. Dr. Ayşegül Demir YETİŞ	Bitlis Eren University
Doç. Dr. Engin YILMAZ	Bitlis Eren University
Doç. Dr. Kürşat YILDIZ	Gazi University
Doç. Dr. Üyesi Faruk ORAL	Bitlis Eren University
Doç. Dr. Zehra Nur KULUÖZTÜRK	Bitlis Eren University
Arş. Gör. Dr. İsmet SÖYLEMEZ	Abdullah Gül University
Dr. Nadjet LAOUET	Constantine-1 University
Dr. Sajad KHORSANDROO	North Carolina Agricultural and Technical State University

ADVISORY BOARD

Prof. Dr. Ali ÇAKMAK	Ağrı İbrahim Çeçen University
Prof. Dr. Edip AVŞAR	Bilecik Şeyh Edebalı University
Prof. Dr. Ercan IŞIK	Bitlis Eren University
Prof. Dr. Esvet AKBAŞ	Van Yüzüncü Yıl University
Prof. Dr. Mahmut BÖYÜKATA	Kırıkkale University
Prof. Dr. Mehmet Sait İZGİ	Siirt University
Prof. Dr. Orhan Taner CAN	Bursa Technical University
Prof. Dr. Saim ÖZDEMİR	Sakarya University
Prof. Dr. Soner ÖZGEN	Fırat University
Assoc. Prof. Dr. Ayşegül DEMİR YETİŞ	Bitlis Eren University
Assoc. Prof. Dr. Engin YILMAZ	Bitlis Eren University
Assoc. Prof. Dr. Kesran AKIN	Bitlis Eren University
Assoc. Prof. Dr. Murat ÇELTEK	Trakya University
Assoc. Prof. Dr. Musa ÇIBUK	Bitlis Eren University
Assoc. Prof. Dr. Oğuz Ayhan KİREÇCİ	Bitlis Eren University
Assoc. Prof. Dr. Serhat Berat EFE	Bandırma Onyedi Eylül University
Assoc. Prof. Dr. Tarkan YORULMAZ	Çankırı Karatekin University
Assoc. Prof. Dr. Ümit BUDAK	Bitlis Eren University
Assoc. Prof. Dr. Yunus Levent EKİNCİ	Bitlis Eren University
Assoc. Prof. Faruk ORAL	Bitlis Eren University
Assoc. Prof. Nusret BOZKURT	Bitlis Eren University
Asst. Prof. Dr. Hasan GÖKBAŞ	Bitlis Eren University
Asst. Prof. Dr. Kerim ÖZBEYAZ	Bitlis Eren University
Asst. Prof. Mehmet Can BALCI	Batman University

BİTLİS EREN ÜNİVERSİTESİ FEN BİLİMLERİ DERGİSİ
BİTLİS EREN UNIVERSITY JOURNAL OF SCIENCE
BEU FBD
ISSN: 2147-3129 / e-ISSN: 2147-3188
https://dergipark.org.tr/tr/pub/bitlisfen



ABOUT
BİTLİS EREN ÜNİVERSİTESİ FEN BİLİMLER DERGİSİ *(Bitlis Eren University Journal of Science)*

Papers in the fields of engineering and basic sciences are published in Bitlis Eren University Journal of Science. The publication language of the journal is English. Journal of Science has been publishing free and open access since 2012. Original research papers and technical notes on experimental and theoretical advances in engineering and basic sciences are included. The similarity rate of the studies submitted to the journal should not exceed 25%. Papers that do not comply with the spelling rules are sent back to the author for revision before being sent to the reviewers. In addition, if the revisions or requests from the editors to the authors are not answered within 15 days, the relevant articles are rejected. The papers sent to the journal for publication are evaluated by at least two reviewers. Reviewer suggestions are not requested from the authors. The Editorial Board of the Journal decides whether to accept the articles for publication, taking into account the reviewer reports (after the evaluations of at least two reviewers are received). Bitlis Eren University Journal of Science is published four times a year (March, June, September, and December). Our journal is indexed in the Journal List of Tübitak-ULAKBİM Engineering and Basic Sciences Database.

The Journal is currently indexed:

* TÜBİTAK ULAKBİM TR DİZİN — **TR DİZİN**
* academindex — **ACADEMINDEX**
* Scilit — **SCILIT**

BİTLİS EREN ÜNİVERSİTESİ FEN BİLİMLERİ DERGİSİ
BİTLİS EREN UNIVERSITY JOURNAL OF SCIENCE
BEU FBD
ISSN: 2147-3129 / e-ISSN: 2147-3188
https://dergipark.org.tr/tr/pub/bitlisfen

ETHICAL PRINCIPLES AND PUBLICATION POLICY

PUBLICATION ETHICS

While establishing the ethical duties and responsibilities below, as open access, guidelines and policies published by the Committee on Publication Ethics (COPE) were taken into account.

It is expected that the author(s) submitting a paper to Bitlis Eren University Journal of Science comply with ethical responsibilities and all stakeholders have the following ethical responsibilities within the scope of publication ethics.

ETHICAL RESPONSIBILITIES OF THE AUTHORS

The articles submitted by the author(s) are expected to be original. If the author(s) benefit from or use other articles, they are required to cite and/ or give reference completely and accurately. Those who do not contribute to the content intellectually in the creation of the article should not be specified as the author. If any article(s) submitted for publication have situations and relationships that may constitute a conflict of interest, this must be clearly stated. Raw data regarding their articles can be requested from the author(s) within the framework of the evaluation processes. In such a case, the author(s) should be ready to present the expected data and information to the editorial board and scientific committee. The author(s) should have a document showing that they have the right to use the data benefited, the necessary permissions for the research/analysis, or the consent of the experimented subjects. If the author(s) notices an inaccuracy or error in their published, early appearance or evaluation processes of their articles, he/she is obliged to cooperate with the editor in informing the journal editor or publisher, correcting the error or withdrawing the article. Authors cannot have their article in the application process of more than one journal at the same time. Each application can be started following the completion of the previous application. An article published in another journal cannot be sent to Bitlis Eren University Journal of Science. Changing the author responsibilities of an article whose evaluation process has begun (such as adding an author, changing the order of authors, removing an author) cannot be proposed.

ETHICAL DUTIES AND RESPONSIBILITIES OF EDITORS

General duties and responsibilities

Editors are responsible for every article published in Bitlis Eren University Journal of Science. Within the context of this responsibility, editors have the following roles and responsibilities:

- Making efforts to meet the information needs of readers and writers,
- Ensuring the continuous development of the journal,

BİTLİS EREN ÜNİVERSİTESİ FEN BİLİMLERİ DERGİSİ
BİTLİS EREN UNIVERSITY JOURNAL OF SCIENCE
BEU FBD
ISSN: 2147-3129 / e-ISSN: 2147-3188
https://dergipark.org.tr/tr/pub/bitlisfen



• Conducting processes to improve the quality of articles published in the journal,

• Supporting freedom of thought,

• Ensuring academic integrity,

• Continuing business processes without compromising intellectual property rights and ethical standards,

• Showing openness and transparency in terms of publication on issues that require correction and explanation.

Relations with the Reader

Editors should make decisions by considering the knowledge, skills and experience expectations of all readers, researchers and practitioners. They should pay attention to the fact that the published articles contribute to the reader, researcher, practitioner and scientific literature and that they are original. In addition, editors are obliged to consider the feedback from readers, researchers and practitioners, and to provide explanatory and informative feedback.

Relations with Authors

The duties and responsibilities of the editors to the authors are as follows:

• Editors should make a positive or negatory decision based on the importance, original value, validity, clarity of the narrative, and the journal's goals and objectives.

• Articles that are suitable for the scope of publication should be taken to the preliminary evaluation stage unless they have serious problems.

• Editors should not ignore positive referee suggestions unless there is a serious problem with the article.

• New editors should not change the decisions made by the previous editor(s) for articles unless there is a serious problem.

• "Blind Reviewing and Evaluation Process" must be published and the editors must prevent deviations that may occur in the defined processes.

• Authors should be given feedback in an explanatory and informative way.

Relations with Referees

The editor;

• should assign the referees in accordance with the subject of the article.

• is responsible for providing the information and guides that the referees will need during the evaluation phase.

BİTLİS EREN ÜNİVERSİTESİ FEN BİLİMLERİ DERGİSİ
BİTLİS EREN UNIVERSITY JOURNAL OF SCIENCE
BEU FBD
ISSN: 2147-3129 / e-ISSN: 2147-3188
https://dergipark.org.tr/tr/pub/bitlisfen

• has to consider whether there is a conflict of interest between the authors and the referees.

• should keep the identity of the referees confidential in the context of blinded refereeing.

• should encourage the referees to evaluate the article in an impartial, scientific and objective language.

• should determine practices and policies that increase the performance of referees.

• should take the necessary steps to dynamically update the referee pool.

• should avoid rude and unscientific reviews.

• should take steps to ensure that the referee pool is broad.

Relations with the Editorial Board

Editors should ensure that all editorial board members follow the processes in accordance with editorial policies and guidelines. The Editor should inform the members of the Editorial Board about the editorial policies and keep them informed of the developments. In addition, editors should;

• ensure that members of the Editorial Board evaluate the article impartially and independently.

• nominate new editorial board members who can contribute and are suitable.

• submit articles suitable for the expertise of the members of the Editorial Board for evaluation.

• interact with the Editorial Board regularly.

• hold regular meetings with the Editorial Board for the development of editorial policies and the journal.

Relations with the Journal Owner and Publisher

The relationship between the editors and the publisher is based on the principle of editorial independence. In accordance with the written contract between the editors and the publisher, all decisions taken by the editors are independent of the publisher and the journal owner.

Editorial and Blind Peer Review Processes

Editors; is obliged to apply the “Blind Refereeing and Evaluation Process” policies included in the journal’s publication policies. In this context, the editors ensure that the fair, impartial and timely evaluation process of each article is completed.

BİTLİS EREN ÜNİVERSİTESİ FEN BİLİMLERİ DERGİSİ
BİTLİS EREN UNIVERSITY JOURNAL OF SCIENCE
BEU FBD
ISSN: 2147-3129 / e-ISSN: 2147-3188
https://dergipark.org.tr/tr/pub/bitlisfen

Quality Assurance

Editors; are responsible for publishing every article published in the journal in accordance with journal publication policies and international standards.

Protection of Personal Data

Editors; are obliged to ensure the protection of personal data regarding the subjects or images included in the evaluated studies. They are responsible for rejecting the article unless the explicit consent of the individuals used in the studies is documented. In addition, editors are responsible for protecting the individual data of authors, referees and readers.

Ethics Committee, Human and Animal Rights

Editors are responsible for ensuring the protection of human and animal rights in the evaluated studies. Editors are responsible for refusing the article in the absence of ethical committee approval for the subjects used in the studies and permissions for experimental studies.

Precaution Against Possible Abuse and Misconduct

Editors are obliged to take precautions against possible abuse and misconduct. It is among the responsibilities of the editor to share the relevant findings, as well as to conduct a rigorous and objective investigation regarding the identification and evaluation of complaints regarding this situation.

Ensuring Academic Publication Integrity

Editors should ensure that judgments containing errors, inconsistencies or misdirection in studies are promptly corrected.

Protection of Intellectual Property Rights

Editors are obliged to protect the intellectual property rights of all published articles and to defend the rights of the journal and the author(s) in case of possible violations. In addition, the editors are obliged to take the necessary measures so that the contents of all published articles do not violate the intellectual property rights of other publications.

Constructivism and Openness to Discussion

Editors should;

• consider persuasive criticisms of the articles published in the Journal and should adopt a constructive attitude towards these criticisms.

BİTLİS EREN ÜNİVERSİTESİ FEN BİLİMLERİ DERGİSİ
BİTLİS EREN UNIVERSITY JOURNAL OF SCIENCE
BEU FBD
ISSN: 2147-3129 / e-ISSN: 2147-3188
https://dergipark.org.tr/tr/pub/bitlisfen

• give the right of reply to the author(s) of the criticized articles.

• not ignore or exclude studies with negative results.

Complaints

Editors are responsible for carefully examining and responding to complaints from authors, referees or readers in an enlightening and explanatory manner.

Political and Commercial Concerns

The journal owner, publisher and no other political or commercial factors affect the editors' independent decision making.

Conflicts of Interest

The editors ensure that the publication process of the studies is completed independently and impartially, taking into account the conflicts of interest between the author(s), referees and other editors.

ETHICAL RESPONSIBILITIES OF REFEREES

Evaluation of all articles with "Blind Refereeing" directly affects the quality of the publication. This process provides confidence through an objective and independent evaluation of the publication. Bitlis Eren University Journal of Science evaluation process is carried out with the principle of double-blind refereeing. Referees cannot directly communicate with authors, evaluations and comments are transmitted through the journal management system. In this process, reviewer comments on evaluation forms and full texts are forwarded to the author(s) through the editor. In this context, it is expected that the referees who evaluate the articles for Bitlis Eren University Journal of Science have the following ethical responsibilities:

• Reviewers should agree to evaluate only articles related to their field of expertise.

• They should evaluate articles neutrally and confidentially.

• If the referees think that they are facing a conflict of interest during the evaluation process, they should refuse to review the article and inform the journal editor.

• In accordance with the principle of confidentiality, the referees should destroy the articles they have reviewed after the evaluation process. They can only use the final versions of the articles they have reviewed after they are published.

• Referees should make the evaluation objectively only in relation to the content of the article. They should not allow nationality, gender, religious beliefs, political beliefs and commercial concerns to influence the evaluation.

BİTLİS EREN ÜNİVERSİTESİ FEN BİLİMLERİ DERGİSİ
BİTLİS EREN UNIVERSITY JOURNAL OF SCIENCE
BEU FBD
ISSN: 2147-3129 / e-ISSN: 2147-3188
https://dergipark.org.tr/tr/pub/bitlisfen

• Referees must do the evaluation in a constructive and courteous language. They should not make derogatory personal comments that include hostility, slander or insults.

• The referees must perform the article they accept to evaluate in the allotted time and in line with the above-mentioned ethical responsibilities.

ETHICAL RESPONSIBILITIES OF THE PUBLISHER

Bitlis Eren University Journal of Science Editors and Editorial Board act with the awareness of the following ethical responsibilities:

• The editors are responsible for all processes of the articles submitted to Bitlis Eren University Journal of Science. In this context, the decision makers are the editors, regardless of economic or political gains.

• Undertakes to create an independent editorial decision.

• Protects the property and copyright of every article published in Bitlis Eren University Journal of Science and undertakes to keep a record of each published copy.

• Takes precautions against all kinds of scientific abuse, citation fraud and plagiarism regarding the editors.

In Case of an Unethical Situation

If you encounter any unethical behavior or content other than the above-mentioned ethical responsibilities and content in the Bitlis Eren University Journal of Science, please don't hesitate to e-mail us.

JOURNAL POLICY

Open Access Policy

Bitlis Eren University Journal of Science, as a journal aware of the need for easy access to information in order to advance scientific studies, supports the initiative to make peer-reviewed journal literature open access in the Budapest Open Access Declaration and presents all published articles free of charge in an environment that anyone can read and download. According to this declaration open access means "its free availability on the public internet, permitting any users to read, download, copy, distribute, print, search, or link to the full texts of these articles, crawl them for indexing, pass them as data to software, or use them for any other lawful purpose, without financial, legal, or technical barriers other than those inseparable from gaining access to the internet itself." Considering the role of knowledge sharing in the advancement of science, open access is of great importance for researchers and readers. For this reason, the articles in this journal can be used as long as the author and original source are cited. No permissions from authors or publishers are required. Articles in this journal are available across search engines, websites, blogs, and other digital platforms.

BİTLİS EREN ÜNİVERSİTESİ FEN BİLİMLERİ DERGİSİ
BİTLİS EREN UNIVERSITY JOURNAL OF SCIENCE
BEU FBD
ISSN: 2147-3129 / e-ISSN: 2147-3188
https://dergipark.org.tr/tr/pub/bitlisfen

Fee Policy

No fee is charged for publishing the article and conducting the article processes in the journal.

Evaluation Process

Articles submitted to the journal for publication are primarily subjected to editorial evaluation in terms of compliance with the purpose and scope of the journal, writing rules and the proposed draft. At this stage, articles that are not suitable for the purpose and scope of the journal are returned to the authors. Articles that do not comply with the spelling rules and draft formatting are returned to the authors to be corrected and reloaded.

All articles are expected to be original and unique articles that have not been published in any medium before. In the evaluation phase, articles are reviewed through the Ithenticate similarity scanning and plagiarism detection program. The similarity index value of the articles must be below 20%. Articles above this value are rejected without being evaluated.

Articles found appropriate in the editorial evaluation are directed to the relevant field editor according to their subjects.

The field editor starts the referee evaluation process of the article by determining two referees suitable for the subject and quality of the article.

The referees selected for the first step evaluation process are given a 30-day evaluation period. At the end of this period, the duties of the referees who do not complete their evaluation or upload the evaluation report are terminated and new referees are determined.

Articles that are not deemed suitable for publication according to the results of peer-review are returned to the authors. The authors are informed about the articles accepted for publication and they are published in the next issue.

Authors are given 30 days for the articles that the referees want to be corrected. During this period, necessary corrections should be made and the corrected article should be uploaded to the journal system. If this period granted to the authors is exceeded, the process of the article is terminated and must be uploaded as a new article from the beginning. In this case, the first step evaluation process is restarted. The corrected version uploaded in the given time is directed to the referee again if necessary and the second step referee process starts. If the referee hasn't wanted to see the corrected version of the article, the editor decides whether to publish it or not.

In the second step evaluation process, the corrections made by the authors are followed by the referees and the referees inform the editor of their final decisions about the article. Finally, the editor informs the authors about the publication process.

BİTLİS EREN ÜNİVERSİTESİ FEN BİLİMLERİ DERGİSİ
BİTLİS EREN UNIVERSITY JOURNAL OF SCIENCE
BEU FBD
ISSN: 2147-3129 / e-ISSN: 2147-3188
https://dergipark.org.tr/tr/pub/bitlisfen



EDITOR'S NOTE

It is my great pleasure to present this issue of our journal, which features a wide spectrum of high-quality research across engineering, science, and applied fields. The diversity of topics which are ranging from advanced methods in cybersecurity, numerical modeling, and machine learning applications, to innovative studies in materials science, renewable energy, structural engineering, and environmental sustainability were highlights the multidisciplinary strength and growing impact of our publication.

In this issue, readers will find valuable contributions such as new approaches to the Navier–Stokes equations, comparative studies on Li-ion battery performance for UAVs, investigations into advanced composite materials, analyses of photovoltaic and alternative energy systems, and experimental work on sustainable concrete and recycling technologies. Equally noteworthy are the studies in biological sciences, education, and social applications of artificial intelligence, each of which enriches the scope of knowledge shared within our community.

As Editor-in-Chief, I would also like to extend my sincere congratulations and best wishes to our authors who are currently applying for associate professorship. Your dedication to advancing knowledge and contributing to your respective disciplines is highly commendable, and we wish you every success in your academic careers.

On behalf of the editorial board, I would like to thank all authors, reviewers, and readers for their valuable contributions and continuous support. We remain committed to fostering scientific excellence and to providing a platform for innovative and impactful research that serves both the academic community and society at large.

Editor-in-Chief

BİTLİS EREN ÜNİVERSİTESİ FEN BİLİMLERİ DERGİSİ
BİTLİS EREN UNIVERSITY JOURNAL OF SCIENCE
BEU FBD
ISSN: 2147-3129 / e-ISSN: 2147-3188
https://dergipark.org.tr/tr/pub/bitlisfen



CONTENTS

#	ARTICLES	PAGES
1	**Evaluation of Effective Password Generation Processes in Terms of Cyber Security** İbrahim Ayaz, Muhammed Zekeriya Gündüz	1306 - 1330
2	**The Novel Numerical Solutions of Conformable Fractional Navier-Stokes Equation with the Robust Method** Aslı Alkan, Hasan Bulut, Tolga Aktürk	1331 - 1347
3	**A Uniformly Convergent Difference Scheme for the Singularly Perturbed Periodic Problem** Erkan Cimen	1348 - 1361
4	**Comparative Evaluation of Thermal and Voltage Behavior of Multi-Topology Li-Ion Battery Packs For UAVs Using Virtual Interconnection Method** Metin Uzun, Sezer Çoban, Abdullah Kocamer, Sinan Keyinci	1362 - 1384
5	**Comprehensive Analysis on The Structural Properties of BBiBa:V2O5 Glasses** Melek Fidan	1385 - 1402
6	**The Effectiveness of Advanced Machine Learning Models in IQ Prediction in the Context of Education, Health, and Socioeconomic Indicators** Doruk Ayberkin, Özel Sebetci	1403 - 1419
7	**Predicting Bid Verification in Spectrum Auctions: A Data-Driven Approach** Ceren Nisa Avcu, Ali Değirmenci, Ömer Karal	1420 - 1439
8	**Determination of Radon Concentrations in Some Schools in Tatvan District of Bitlis Province** Burcu Bozova Aydin, Nergiz Yıldız Yorgun, Ömer Faruk Özdemir, Halime Erzen Yıldız	1440 - 1452
9	**Design, Synthesis and In Vitro Biological Assessment Of Novel 2-[(3-Alkyl/Aryl-4,5-Dihydro-1h-1,2,4-Triazol-5-One-4-Yl)Azomethine]Phenyl 2,5-Dichlorobenzenesulfonates Molecules as Antioxidant and Antibacterial Agents** Fevzi Aytemiz, Haydar Yüksek	1453 - 1468
10	**GDD Generation for Hyper-Casual Games Using Large Language Models: A Comparative Evaluation** Muhammet Emin Aydinalp, Buket Doğan, Abdullah Bal	1469 - 1486
11	**Determination of Enzyme Inhibitory and Antioxidant Activities of Selected Oak Galls** Nesrin Haşimi, Merve Doğan Abdioğlu, Mehmet Boğa	1487 - 1503
12	**Sleeve Fuse System For Improved Steel Connection Performance** Muhammed Atar	1504 - 1518
13	**Synthesis and Electronic Properties of Axially Disubstituted Silicon (IV) Phthalocyanine 9-phenyl-9H-xanthene-9-oxy** Derya Güngördü Solgun	1519 - 1533

BİTLİS EREN ÜNİVERSİTESİ FEN BİLİMLERİ DERGİSİ
BİTLİS EREN UNIVERSITY JOURNAL OF SCIENCE
BEU FBD
ISSN: 2147-3129 / e-ISSN: 2147-3188
https://dergipark.org.tr/tr/pub/bitlisfen



14 Investigation of Microstructure, Hardness and Wear Behavior of Powder Metal Al 7020 / SiC / Nano Graphene Doped Hybrid Composites 1534 - 1548
Alper Namalan, Hakan Gökmeşe, Ufuk Taşcı

15 The Influence of Tool Geometry on Side Milling of CFRP with Different Cutting Tool Paths 1549 - 1562
Sezer Morkavuk

16 Micropropagation of Muscari latifolium, an Endemic Plant of Türkiye 1563 - 1580
Nesrin Bozhan, Ahmet Onay

17 Synthesis of Dimethylamine-Pyridine-Based Schiff Base Complexes of Fe(Ii), Co(Ii) and Cu(Ii), Structural Elucidation: Investigation of Biological Activities 1581 - 1595
Kenan Buldurun, Hüsna İnan, Nevin Turan

18 Determinants of Electrooculography Measurements for Quiet Eye Duration in Archers via Penalty Regularizer 1596 - 1609
Fatma Söğüt, İnci Kesilmiş, Evrim Ersin Kangal, Ülkü Çömelekoglu

19 Photocatalytic Properties of Chitosan-Coated PESA Spheres Containing Gallium(III) Nitrate: Synthesis and Characterization 1610 - 1624
Deniz Doğan

20 Photovoltaic Solar Power Plant of Soguksu: A Case Study 1625 - 1635
Kenan Saka, Abdülkadir Ayanoğlu

21 Comparative Performance Analysis of Permanent Magnet and Claw-Pole Alternators in Internal Combustion Engines 1636 - 1654
Metin Kaynaklı, Ahmet Albayrak, Raif Bayır

22 Studies on the Fauna of Pyraloidea (Lepidoptera) of Köprülü Canyon National Park (Antalya) 1655 - 1671
Mümüne Merve Şen, Kesran Akın

23 Antibiotic Resistance, Antibacterial Activity and Exopolysaccharide Determination of Lactiplantibacillus plantarum Obtained from Traditional Yogurts from Muş Region 1672 - 1687
Yusuf Alan, Kayhan Mang

24 The Effect of Boriding on the Wear Behavior of AISI 8620 Steel 1688 - 1703
Selçuk Atasoy, Hasan Onur Tan, Hakan Adatepe, Sitki Aktaş, İbrahim Güneş

25 Synthesis, Spectroscopic Studies and Antioxidant Activities of New 2-Benzylidene-N-Phenylhydrazine-1-Carbothioamide Derivatives 1704 - 1717
Temel Kan Bakır, Halit Muğlu

26 Design and Manufacturing of Shaking Table From Scrap/Used Parts 1718 - 1735
Ersan Kırar, Muhammed Şerif Yoluk, Cihan Ayhancı

27 The Effect of Waste Glass Powder on the Mechanical and Permeability Properties of Roller-Compacted Concrete 1736 - 1758
Zeynep Algın, Delil Demir

BİTLİS EREN ÜNİVERSİTESİ FEN BİLİMLERİ DERGİSİ
BİTLİS EREN UNIVERSITY JOURNAL OF SCIENCE
BEU FBD
ISSN: 2147-3129 / e-ISSN: 2147-3188
https://dergipark.org.tr/tr/pub/bitlisfen



28 **Effect of Build Orientation and Heat Treatment on Shear Strength of Additively Manufactured Ti6Al4V Alloy** 1759 - 1771
Gürkan Kaya, Yusuf Polat

29 **Correlated SKU assignment in warehouses using the joint demand probability distribution: a metaheuristic algorithm approach** 1772 - 1786
Bayram Dündar

30 **Toward a Safer and Greener Future: Reliable Aqueous Ammonium-Ion Batteries with $LiMnO_2$ Cathodes** 1787 - 1801
Dilara özgenç, Melisa Uçan, Burak Tekin

31 **Architectural Features and Conservation Issues of Adjacent Public Fountains and Built-in Fountains (Abdestlik) in the Province of Bitlis** 1802 - 1821
Enes Arkan, Mine Topçubaşı

32 **The Cohesive and Fatigue Damage Mechanics of Cement-Stabilized Soil Composites using New Generation Sustainable Cement** 1823 - 1848
Nazife Erarslan

33 **Devulcanization and Characterization of Ground Tire Rubber with Microwave Method** 1849 - 1865
İlker Erzincanlı, Fazliye Karabörk

34 **Effect of Rubber and Steel Fibers Obtained from Waste Tires on Mechanical and Physical Properties of Concrete: An Experimental Study** 1866 - 1890
Ersin Ayhan, Murat Doğruyol

35 **Assessment of Ergonomic Risk Factors for Sustainable Agricultural Practices Based on Picture Fuzzy Lodeci-Artasi Approach** 1891 - 1920
Veysel Tatar

36 **Investigation of Physical, Mechanical, and Drilling Machinability Properties of Nanoparticles Reinforced Carbon/Glass Fiber Hybrid Composites** 1921 - 1941
Alper Günöz, Umut Ozgur Ozaltay

37 **Close Binary Open Cluster Systems: A Gaia DR3 Perspective on Alessi 36 and Collinder 135** 1942 - 1960
Hülya Karagöz, Deniz Cennet Çınar, Seval Taşdemir, Remziye Canbay

38 **Experimental and Numerical Modal Analysis of Nomex Honeycomb Core Composite Sandwich Spherical Plate** 1961 - 1979
Osman Yiğid, Murat Şen

39 **Investigating Earthquake Source Scaling Laws in the Akhisar Seismic Zone** 1980 - 1995
Alper Demirci

40 **Logic And Gate Design With The Internet Of Things (IOT)** 1996 - 2007
Emine Canan Günay Demirel

BİTLİS EREN ÜNİVERSİTESİ
FEN BİLİMLERİ DERGİSİ

ISSN: 2147-3129 / e-ISSN: 2147-3188

Article Type : Research Article
Received : October 17, 2024
Revised : May 10, 2025
Accepted : May 29, 2025
DOI : 10.17798/bitlisfen.1569257

Year : 2025
Volume : 14
Issue : 3
Pages : 1306-1330

EVALUATION OF EFFECTIVE PASSWORD GENERATION PROCESSES IN TERMS OF CYBER SECURITY

İbrahim AYAZ [1,*], Muhammed Zekeriya GÜNDÜZ [2]

[1] *Bitlis Eren University, Department of Computer Science and Technology, Bitlis, Türkiye*

[2] *Bingöl University, Department of Computer Science and Technology, Bingöl, Türkiye*

**** Corresponding Author:*** *iayaz@beu.edu.tr*

ABSTRACT

The increasing frequency and sophistication of cyber-attacks have underscored the critical importance of strong, secure passwords in protecting digital identities. This study evaluates the effectiveness of password generation processes within the context of cyber security, focusing on various methods for creating secure passwords, from traditional alphanumeric combinations to advanced passphrases that incorporate special characters and multi-factor authentication. While long and complex passwords are essential for robust security, the research also emphasizes the importance of user awareness and consistent password management practices in mitigating risks. This study also emphasizes that information security cannot be achieved through technological solutions alone, highlighting the critical role of end-user cyber security awareness. Effective password generation and usage are central to safeguarding sensitive systems and data, and the article presents strategies for developing this skill, offering examples and suggestions to foster awareness and improve password security practices. We advocate for user-friendly yet secure password-generation techniques to strengthen cyber security resilience in the digital age.

Keywords: Cyber security, Data security, Secure password, Passphrase.

1 INTRODUCTION

The conveniences provided by technology to human beings are increasing day by day. The people of our age have achieved more comfortable living standards thanks to the technologies that have emerged as a result of cumulative knowledge. It is accepted that the discovery of the Internet is the biggest in terms of the convenience provided by technological developments to human life. Individuals who interact more with the Internet have made high-

security transactions such as shopping online using credit cards, making money transfers through Internet banking, and paying online bills an integral part of their daily lives. However, the widespread use of the Internet and its intertwining with daily life have brought information security risks. This makes the need to ensure the security of users' personal and financial information even more important. Therefore, Internet users need to be more aware of how to stay secure in the digital world [1]. Therefore, Internet users must adopt more conscious and proactive approaches, such as using strong passwords and implementing security measures like two-factor authentication. In this context, information security has become an unavoidable priority of the digital age.

Transactions carried out over the Internet require various layers of security depending on the system used. Elements such as username, password, virtual keyboard usage, and security code are the basic components that make up these layers. The first and most important step in ensuring security is to create passwords that are easy to remember but difficult to guess, and at the same time resistant to brute force and dictionary attacks. Weak passwords can be easily cracked by attackers in a variety of ways, which can lead to users' accounts being compromised. Therefore, creating strong passwords plays a critical role in ensuring digital security [2].

People need to keep many passwords in their memory to handle their transactions in the digital environment. The research shows that the average person has more than 20 passwords. If there is a password, it means that there is confidential information. If the information is hidden, the question of who it is being protected from also arises. These people try to guess passwords so that they can access the information [3].

Amico et al. [2], compare various password cracking techniques, including dictionary and brute force attacks by analyzing the relationship between search space and the number of cracked passwords. They have empirically shown that passwords that are not complex are much easier to crack. Nosenko et al. [4], by performing password guessing applications with Recurrent Neural Networks (RNN), they have been demonstrated that passphrases are more reliable. Jin et al. [5], demonstrated that weak passwords can be easily cracked using deep learning methods. Li et al. [6], experimentally show that passwords containing personal information can be cracked more easily than passwords that are meaningless.

Although passwords are the first line of defense against cyber attackers, people are too lazy to create strong passwords. Usually, the difficulty level of these passwords is simple. Weakly created passwords can be captured by cyber attackers in different ways. In this respect,

strong and reliable passwords should be produced by users, whether they are system administrators or end users. The purpose of a strong password is to increase the difficulty for cyber attackers to crack or guess it. In addition, one of the most important features of passwords is that they can be easily forgotten. If the users forget their passwords, it means that they cannot verify their identity for the relevant system [7]. This study aims to develop personalized algorithms for creating strong yet easily memorable passwords, which are among the most critical aspects of cyber security.

The remainder of this paper is organized as follows: Section 2 presents the importance of passwords in cyber security. Section 3 examines the features that a secure password should have and provides examples of secure and insecure passwords. Section 4 introduces more techniques for generating effective passwords. Finally, the results and suggestions are presented in Section 5.

2 PASSWORDS IN CYBER SECURITY

All digital or electronic activities, including network operations, are part of cyber space. Ensuring the security of cyber space is called cyber security. Security in cyber space starts with using robust passwords. A password is a confidential information that only two parties know. Thanks to this confidential information, the parties can identify each other as secure. The most effective method attackers use to gain unauthorized access to a system is compromising passwords.

The use of passwords dates back to Roman history. In Rome, guards would stop people trying to enter certain areas or buildings and ask for passwords. However, those who knew the password were allowed to enter there. Every day, the camp commander would give the guards a wooden tablet with the password on it. The guards would circulate this tablet among themselves and engrave their marks on it [8]. When the tablet returned to the commander, the commander knew all the guards had received the password. On a computer, passwords are almost as old as operating systems. The digital password system was first used in MIT's Compatible Time Sharing System in 1961. Since then, both creating and deciphering passwords has become a mutual race [1].

The most basic way to crack a password is to guess. Intelligent guesses can be instrumental in cracking many passwords, despite the low probabilities. Technology can't completely prevent user errors; Even the most advanced algorithms ultimately depend on the

password that the user creates. All passwords can be cracked, but passwords that are complex and long enough can be deterrent to low-skilled attackers. As the length and complexity of a password increase, its security and resistance to being cracked also increase. Strong passwords prevent third parties from accessing areas and information that require information privacy. A good password should be hard for others to guess, but easy for the user to remember. Passwords are personal and should not be shared. Only the related person needs to know. The generated passwords should be meaningless to others. Different passwords should be used for different types of accounts [9].

The widespread use of Internet-based applications has led to an increase in the number of passwords used. The first step in ensuring these passwords and data privacy by users is to create effective and reliable passwords. In this context, basic-level secure passwords should consist of a combination of uppercase letters, lowercase letters, numbers, and special characters/punctuation marks. Because the more different types of characters there are in the password, the harder it is to guess the password. The basic requirements for a strong password are shown in Figure 1.

Moreover, it is recommended to pay attention to the following principles when creating a secure password:

- Must be at least 8 characters long.
- Passwords should not contain consecutive or identical expressions such as 123456 , abcdef, qwerty, asdf, XXX, or ababab.
- It should not be short or consist of a single word such as Bitlis, Bingöl, Galatasaray.
- Expressions that identify the person such as name, surname, and date of birth should not be used.
- Words that can be found by a dictionary scan attack should not be used.
- Words and phrases that are easy to remember, but difficult for others to guess, should be chosen.
- Information that is directly related to the person's interests and life should not be used as passwords.
- If meaningful words are to be used as passwords, the words to be used should be abbreviated or some characters should be omitted.
- The same password should not be used for all accounts. However, since using different passwords in all accounts tire the human memory, the same password can be used in accounts with the same security level.
- The reliability of the accounts can be categorized as Very reliable – Reliable – Insecure, and a separate password can be used for each category.

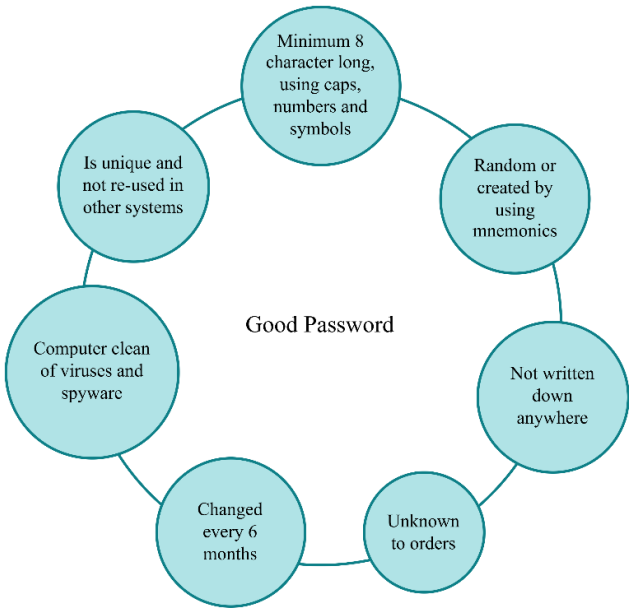


Figure 1. Key features of a strong password

In addition, it should be noted that after a password is created, the following points should be noted:

- It should be changed between 3-6 months.
- Passwords issued for temporary use should be changed immediately.
- Critical passwords should not be written down on paper or any other medium.
- Important passwords should not be given to a third party.
- The same password should not be used on all platforms.
- Logout should be done on the exited systems**.**

The reliability of a password can be measured by taking into account some key factors such as password length, character variety, predictability, resistance to brute force and dictionary attacks, and the use of the password in different environments. Online password check tools can be useful for testing password security and creating strong passwords. By analyzing how strong the password is, these tools estimate how resistant it is to different types of attacks. However, it is necessary to be careful about security when using such tools. In particular, entering the password directly on third-party websites can lead to potential security risks. For this reason, it is recommended to use a variation of the password during the test instead of using the full version of the password as a more secure method. Some of the online password check tools to measure password reliability stand out for their reliability [10].

How Secure Is My Password: This site evaluates the security of the password by estimating how long it will take to crack it. With a simple interface, this tool shows how resistant

the password is to brute force attacks. However, since the password is entered directly, it is better to be careful for security and avoid using the full password [11].

Kaspersky Password Check: This password checker provided by Kaspersky analyzes how strong the password is and points out its weaknesses. It also shows the estimated time it took to crack the password and how secure the character combination is [12].

NordPass Password Strength Test: This password testing tool analyzes the strength of the password and shows its weaknesses. It also offers recommendations for creating strong passwords and shares strategies that can be used to improve password security [13].

Bitwarden Password Strength Tester: It is a popular password management software and offers powerful password generation tools. This tool evaluates the security of the password and indicates whether the password is weak, medium, or strong. It also offers suggestions for creating a more secure password [14].

LastPass Password Strength Checker: LastPass is a platform known for its password management tools and offers a testing tool that analyzes how secure the password is. This tool identifies the weaknesses of the password and provides security recommendations [15].

3 PASSWORD SECURITY

It can be difficult for an attacker to technically break through a system. However, capturing the user's password is a more practical solution. Hackers use data from previous attacks and complex algorithms rather than making random attempts to crack passwords. It is the responsibility of users and software developers to increase security against this situation.

3.1 Features and Examples of a Secure Password

Passwords are for personal use. It should not be shared with others. At least two-step verification should be used. The security question, if any, must be complex. A secure password should be both long and contain a wide variety of characters. The reference [16] can be used to find out whether the passwords to be created are included in the dictionaries used for password attacks.

A password is like a toothbrush. No one else is allowed to use it. It must be changed every six months. Doing more than one thing at the same time with a single password (such as PC, mail, server, and VPN access passwords) means single sign-on (entering everything with a

single password), and this is a troublesome approach in terms of security. Because losing the password means losing everything. Developing different password algorithms is the most appropriate solution to this. In addition, all the passwords saved by a web browser can be easily intercepted by someone who obtains the computer's public password [17].

The length of the password makes the password strong. However, it is not always valid to say, "Long passwords are always more reliable than short passwords." Because password length is only one factor that affects security. A strong password should be meaningless but easy to remember. By taking the first letters of the lyric " şu gelen atlımıdır yavrum sorun Bağdatlımıdır ", a meaningless but easy-to-remember password can be created in the form of "şgaysB". However, a strong password should consist of letters, numbers, and symbols. Therefore, an important date or number can be combined with this password. If the number 1453 is shifted by one from the beginning and written between the expression "şgaysB", the result is the expression "1ş4g5a3ysB". If a special character is added at the end of the expression, the password '1ş4g5a3ysB?' can be created. In some cases, the password can be made even more complex by taking advantage of character similarity (such as a and @) to make the password '1ş4g5@3ysB?'.

Another example is that the password to be created on the shopping site can be chosen as a sentence such as "Ben Sabah Alışveriş Yaparken Okuldan Tanıdığım Eski Bir Arkadaşımı Gördüm" that will remind you of that site or shopping. The initials of these words are taken: BSAYOTEBAG, and then some letters can be replaced with numbers that remind them of themselves: 8SAY0TE1A6, and the last uppercase letter is replaced with lowercase letter: 8SAY0TE1a6, finally a symbol can be added at the end: 8SAY0TE1a6!

Another method is recommended to help users create passwords that are easy to remember but difficult to guess. A unique password is created with numbers and letters using a familiar phrase. For example, the phrase " Arkadaşlarım Tekin ve Yasemin bana her gün komik bir e-posta gönderiyor " can be converted to a password such as "ATvYbhgk1e-pg" by adding numbers with each letter and initial. This process is repeated for each site, creating strong and memorable passwords.

Various methods exist for generating passwords that are both secure and easy to remember. One widely employed technique is the use of mnemonics, which enhances memory retention through associations, such as rhymes or acronyms [18]. For instance, consider the well-known phrase:

“To be or not to be? That is the question.” (Hamlet, Shakespeare). This can be transformed into a mnemonic password: “2bon2b?Titq.”

In another example, numbers substitute similar-sounding words (e.g., "to" is represented as "2"), acronyms are utilized, capitalization is applied to key nouns and verbs, and prefixes are maintained in lowercase. “I had a DREAM, where all men were born equal” (Martin Luther King Jr.). This phrase may be condensed into: “1haDwamwb=”

These methods yield passwords that may appear random to others yet remain relatively easy for the creator to remember, given the underlying logic of their construction.

Additional strategies for enhancing password complexity include:

- Substituting numbers for similar-looking letters: For example, replacing "i" or "l" with "1" and, "o" with "0"
- Abbreviating words with numbers: Such as transforming "four" into "4" and, "to" or "too" into "2"
- Incorporating symbols or emoticons: For instance, "Are you happy today?" as “ru:-)2d?”

These examples illustrate fundamental techniques, and users are encouraged to personalize their mnemonic systems to devise strong, memorable passwords. Developing individualized coding methods is advisable to further enhance security.

3.2 Password Cracking Methods

In most cases, passwords reflect something easy to remember. However, guessing a password by having personal information about the user is the most common method of compromising a system for motivated hackers.

Using of passwords is of great importance in protecting the confidentiality of data and systems. When used correctly, they are one of the most effective methods of protecting the system, but sometimes they are the weakest aspects of network systems. Because the fact that passwords are somehow learned by third parties can provide them with a lot of authority. If certain principles regarding passwords are not followed and some precautions are not taken, they can be intercepted by attackers. Attackers can test hundreds of passwords per second with specially prepared password-cracking software [19].

Passwords are widely used to force access to resources. Attackers use many techniques to learn users' passwords and gain unauthorized access to a resource or data. Many of the most

common cyber attacks today are based on social engineering. It is also possible for system passwords to fall into the hands of third parties through social engineering methods based on human weaknesses. It is now a known fact that passwords can be obtained through social engineering, also known as directing people to do what is desired by someone else [20]. According to Kevin Mitnick, one of the first hackers, the weakest link in a system's security ring is the human. In this case, it is very important to inform users against attacks using social engineering and to ensure that information security awareness is created. It is clearly understood that this is a necessity, especially considering the active use of information systems in every field [21].

Some methods, also known as cryptographic password attacks, are used to aim to decrypt passwords. Brute force attack refers to the method of attempting to guess a password by systematically trying all possible combinations. These attacks are typically used to capture passwords, usernames, or other authentication credentials. This approach often involves using an electronic dictionary to test every word within it. While this process would be time-consuming for a human, a computer can execute it within seconds. Consequently, if a password is a correctly spelled dictionary word, it can be compromised within minutes through a brute force attack.

Users often choose words that make sense to keep them in mind. However, there is usually no need for brute force, i.e. trying all potential character combinations one by one. Dictionary attacks can find passwords in less time and with fewer attempts. Dictionary attacks also try meaningful words. A brute force attack is the most commonly used method to obtain valid passwords for servers or personal devices. That's why passwords shouldn't be simple [22]. Especially servers with open ssh service have serious problems in this regard. Password attacks are carried out by malware-infected devices rather than directly by individuals.

The crudest method that a hacker trying to crack a password can resort to is to try all possibilities one by one. Therefore, the greater the number of possible passwords, the more difficult the hackers' job. When subscribing to a website, the system may not accept the password that it describes as weak and may direct the user to set a stronger password. For example, it may require that the password contain at least one uppercase letter, one number, and one punctuation mark. Such requirements are implemented to improve user security and complicate the password-cracking process of hackers. As the variety of characters used to create a password increases, the number of possible password combinations also increases [23].

Brute force attacks can be categorized into several types, each employing different strategies to gain unauthorized access to systems or accounts. One of the most basic forms is the *simple brute force attack,* where an attacker systematically attempts every possible combination of characters from a specified character set. This method relies solely on computational power to eventually find the correct password or encryption key, making it time-consuming, especially as the length and complexity of the password increase. While guaranteed to succeed eventually, this approach is often impractical due to the vast number of combinations that must be tested.

A more refined method is the *dictionary attack,* which utilizes a predefined list of words or phrases, known as a "dictionary." Instead of attempting every possible combination, the attacker tries each entry in the dictionary, targeting likely candidates based on common user behavior. The dictionary often includes common passwords, variations, and phrases that users are likely to select. This method is significantly more efficient than a simple brute force attack, as it focuses on probable passwords rather than all potential combinations.

The *hybrid brute force attack* combines elements of both dictionary and simple brute force attacks. In this approach, attackers take words from a dictionary and apply variations, such as adding numbers, and symbols, or changing letter cases. For instance, they might attempt passwords like "password," "Password1," and "P@ssw0rd." This method effectively targets users who modify simple words slightly to meet complexity requirements, increasing the chances of successful exploitation.

Another type is the *reverse brute force attack,* where the attacker starts with a known password and attempts to find the corresponding usernames or accounts associated with that password. This approach is particularly effective if the attacker knows or suspects that a specific password is commonly used. By leveraging previously compromised data or widely used passwords, attackers can quickly identify valid accounts, making this method a potential threat.

Credential stuffing is another common brute force attack method, where attackers use previously leaked username-password pairs from data breaches to gain unauthorized access to accounts on different websites. This method exploits users' tendency to reuse passwords across multiple platforms. Once the attacker possesses a valid pair, they can access the target account quickly and efficiently, often without requiring sophisticated techniques.

In a *distributed brute force attack,* attackers utilize multiple machines or a botnet to increase their computational power for guessing passwords. By distributing the workload across

many devices, attackers can attempt a significantly larger number of combinations in a shorter time frame. This method enhances the effectiveness of brute force attacks and makes detection more challenging, as the attempts may come from numerous sources simultaneously.

Online brute force attacks involve directly attempting to log into an account on a target system or website by submitting password attempts in real-time. This method carries a higher risk for attackers, as it may trigger security mechanisms such as account lockouts or CAPTCHA challenges after a certain number of failed login attempts. In contrast, *offline brute force attacks* target hashed passwords stored in databases. Attackers obtain a database of hashed passwords (often through data breaches) and attempt to crack them by guessing the original passwords at their own pace without triggering immediate security responses.

To defend against brute force attacks, organizations and individuals should implement various security measures. Enforcing strong password policies that require complex passwords can significantly reduce the likelihood of successful attacks. Additionally, account lockout mechanisms that temporarily disable accounts after a specified number of failed login attempts can thwart attackers' efforts. Implementing multi-factor authentication (MFA) adds another layer of security by requiring additional verification methods beyond just passwords. Monitoring systems that can detect and alert administrators to suspicious login attempts are also essential. By employing these strategies, the effectiveness of brute force attacks can be significantly diminished, safeguarding sensitive information and maintaining secure systems.

Dictionary attack is a type of cyber-attack in which an attacker attempts to gain unauthorized access to a system by systematically trying a list of common words or phrases, typically stored in a "dictionary" file. Unlike brute force attacks, which try all possible character combinations, dictionary attacks rely on pre-compiled lists of likely passwords such as common words, names, and common phrases. These lists often include variations with numbers, symbols, and capitalization, making the attack more efficient. The effectiveness of dictionary attacks stems from the fact that many users choose weak or predictable passwords based on common words, making their accounts vulnerable to such attacks. Hackers often use dictionary attacks in combination with data from previous breaches, where they may refine the word lists to include passwords commonly used by people [24].

There are several types of dictionary attacks, each employing different techniques to exploit weak passwords. The most basic form is the *standard dictionary attack,* where attackers use a predefined list of common words, phrases, or known passwords in an attempt to guess a

user's password. This list typically includes dictionary words, names, or easily guessed passwords like "password123" or "qwerty." The attacker systematically tries each word or phrase until they find a match, making it an effective method against users who rely on simple, predictable passwords.

A more advanced variation is the *hybrid dictionary attack,* which combines elements of both dictionary and brute force methods. In this approach, the attackers take the words from a dictionary and applies variations such as adding numbers, special characters, or changing capitalization such as "Password123!". This technique accounts for users who slightly modify simple words to meet password requirements, thus increasing the chances of success.

The *reverse dictionary attack* targets hashed passwords. In this method, attackers compute hash values for every word in their dictionary and compare them to the hash of the target's password. If the hash values match, the original password is discovered. This attack is particularly effective against systems that use weak or unsalted hashing algorithms, as it allows attackers to reverse-engineer the password from its hash.

A *rainbow table attack* is a specialized form of dictionary attack that uses precomputed tables of hash values for common passwords. By leveraging these tables, attackers can compare hash values to plaintext passwords more efficiently, significantly reducing the time needed to crack weakly protected systems. Rainbow tables are particularly effective against systems that use predictable or weak password hashing mechanisms.

Another variation is the *phonetic dictionary attack*, which focuses on passwords derived from how words sound rather than their exact spelling. Attackers generate phonetic variations of dictionary words, anticipating that users may create passwords based on the pronunciation of words such as "Luv" for "Love". This method exploits the tendency of users to rely on familiar, easy-to-remember passwords.

In a *targeted dictionary attack*, the attacker customizes the dictionary based on the victim's personal information. By using words related to the victim's interests, names of family members, birth dates, or other personal details, attackers can increase the likelihood of success. These attacks often rely on social engineering to gather relevant personal information, creating a tailored word list specific to the victim.

Finally, a *distributed dictionary attack* involves multiple computers or bots working together to distribute the computational load of a dictionary attack across several machines. This significantly speeds up the process of trying password combinations and reduces the

likelihood of detection. Distributed attacks are often conducted using botnets, allowing attackers to perform large-scale attacks with greater efficiency.

To counter these attacks, users and organizations must employ a variety of security measures. Password complexity requirements, such as using a mix of letters, numbers, and special characters, can reduce the effectiveness of dictionary attacks. Salting passwords - adding random data to passwords before hashing - also helps by preventing precomputed attacks like rainbow tables. Additionally, implementing account lockout policies can block repeated login attempts after a set number of failures, thwarting dictionary and brute force attempts. Finally, multi-factor authentication (MFA) adds another layer of security beyond just a password, and using password managers encourages the creation and storage of complex, unique passwords that are difficult to guess.

Password cracking software can create and test combinations of letters and numbers in a certain order, as well as use words in dictionaries of hundreds of thousands of words given to them. That's why passwords that are easy to remember are usually easy to obtain. The fact that the password or passwords of a user are in the hands of second parties does not only create a security vulnerability for that user. Sometimes, other points on the network can be accessed through the password or password in question. Even if only one user creates an information security vulnerability, it can unwittingly cause damage to the network or all users using the system. Brutus, RainbowCrack, Wfuzz, Cain & Abel, and John The Ripper are prominent tools used for password cracking through brute force and dictionary attack methods.

4 SECURE PASSWORD GENERATION METHODS

Secure password policies should be established to prevent passwords in network systems from falling into the hands of attackers. Network users should be encouraged to use passwords that are difficult to guess or crack, and if necessary, they should be enforced. It should be known that passwords with different characters and numbers are more secure because they will take years to crack.

4.1 Secure Password Generator Software

To better protect systems and data, it's important to understand what a strong password is and how to store it securely. One of the main problems with password security is that users use the same password on multiple platforms. This increases security risks and compromises all accounts of users in the event of a possible attack. However, thanks to password generation

and management software, it is possible to store and manage all passwords securely [25]. Secure password generation software is essential for creating strong, unique passwords that enhance security against unauthorized access. These tools utilize complex algorithms and various character sets to produce passwords that are difficult to guess or crack. Here are some popular options:

LastPass is a widely used password manager that includes a built-in password generator. Users can customize password length and complexity, ensuring that passwords meet specific security requirements. Its integration with the LastPass vault allows for easy storage and retrieval [15].

Dashlane offers a comprehensive password management solution with a secure password generator. Users can create complex passwords and save them directly within the Dashlane vault. The tool also features a password strength assessment and is compatible with both web and mobile platforms [26].

Bitwarden is an open-source password manager that provides a robust password generator. Users can generate secure passwords that are stored in an encrypted vault. The tool includes a password strength meter and offers customizable options for password length and character types [14].

KeePass is an another open-source password manager that allows for secure password generation and credential management in an encrypted database. It supports various plugins and offers customizable settings for generating strong passwords. Notably, it works offline, providing users with secure access without an internet connection [27].

Random.org provides a simple online password generator that uses true randomness based on atmospheric noise. Users can specify the length and character types for password creation, making it a straightforward option without requiring software installation [28].

Online tools for generating strong passwords are user-friendly and efficient. They allow users to customize password length and character sets for instant, secure results, often without requiring an account. Passphrase generators create long, memorable phrases by combining multiple words, offering a balance of security and ease of recall.

Password-management software takes security further by generating and securely storing complex passwords. Users only need to remember a master password to access their encrypted password database. These lightweight programs, often portable, streamline password organization and usage. While initial setup may take some effort, the enhanced security and convenience make it worthwhile.

4.2 Setting a Password by Security Level

The purpose of creating a strong password is to make it difficult for cyber attackers to crack and guess. The strength of passwords is directly proportional to the complexity of the characters they contain. Some of the prominent problems are insufficient password length, low password complexity, and guessability of passwords.

The length and complexity of a password are crucial factors in determining how long it would take for a computer program to crack. Let's calculate the number of possible combinations a password cracker would need to try, assuming the password is composed only of lowercase English letters. For each character in a password, there are 26 possible choices (since there are 26 lowercase letters).

Password Length: 3

Calculation: $26^3 = 26 * 26 * 26$ =17.576 (Number of possibilities)

Password Length: 5

Calculation: 26^5 = 11.881.376

Password Length: 7

Calculation: 26^7 = 8.031.810.176

Password Length: 9

Calculation: 26^9 = 5.429.503.678.976

Now, if we expand the character set to include both digits and uppercase letters (increasing the total number of possible characters to 62), the number of variations increases dramatically:

Password Length: 3

Calculation: 62^3 = 238.328 (Number of possibilities)

Password Length: 5

Calculation: 62^5 = 916.132.832

Password Length: 7

Calculation: 62^7 = 3.521.614.606.208

Password Length: 9

Calculation: 62^9 = 13.537.086.546.263.552

Password cracking speed, a critical factor in assessing the security of a password, refers to the time it takes for a given method or tool to guess a password. To calculate password cracking speed, we can use the following formula:

$$Time\ to\ Crack = \frac{Total\ possible\ combinations}{Attempts\ per\ second} \quad (1)$$

To estimate the total possible combinations, we can use:

$$Total\ Possible\ \text{Combinations} = Character\ Set\ Size^{Password\ Length} \quad (2)$$

Assuming a modern PC processes 100.000 password attempts per second, we can estimate the time required to crack a password based on the number of possible combinations and the character set used (26 for lowercase letters, 36 for letters and digits, 52 for mixed-case letters, and 68 for letters, digits, symbols, and punctuation). Table 1 shows the results.

Table 1. The time required to crack a password depends on its length

Password Length	26 Characters	36 Characters	52 Characters	68 Characters
3	0.18 seconds	0.47 seconds	1.41 seconds	3.14 seconds
4	4.57 seconds	16.8 seconds	1.22 minutes	3.56 minutes
5	1.98 minutes	10.1 minutes	1.06 hours	4.04 hours
6	51.5 minutes	6.05 hours	13.7 days	2.26 months
7	22.3 hours	9.07 days	3.91 months	2.13 years
8	24.2 days	10.7 months	17.0 years	1.45 centuries
9	1.72 years	32.2 years	8.82 centuries	9.86 millennia
10	44.8 years	1.16 millennia	45.8 millennia	670 millennia
11	11.6 centuries	41.7 millennia	2.384 millennia	45.582 millennia
12	30.3 millennia	1.503 millennia	123.946 millennia	3.099.562 millennia

Based on these figures, a random password of at least 8 characters, using lowercase letters and digits, offers substantial protection. If the password is only 5 characters long, it could easily be cracked. Therefore, longer and more complex passwords are highly recommended to ensure better security.

It has been observed that simple passwords such as 12345, 123456, abcdef, password, abc123, 123456, abcdef, 000000, 20172017, ahmet2003, 5551234567, qwerty, asdf1234, 1970, 12345, abcd, 123abc are widely available in the databases of tools used for password cracking. Although they seem complicated passwords, even if they are so long, as long as they are meaningful, passwords like Firefox3beta5, 1453istanbul, murat124, a4tech, mplayer, bukadaruzunolsabileanlamlıolduğusürecetehlikevar, ubuntuwindowsudöver, 1919-05-19, komikinsanınkomikşifresi, forumpassword, debian4etch are insecure passwords.

High security does not necessarily mean that all passwords contain complex character sets. It is possible to group and simplify these passwords by determining the security levels of passwords according to their areas of use. For example, it is acceptable for passwords created for frequent use to be less complex than passwords created for accounts that require higher security. In this context, users should design their passwords considering the security needs of a particular system. Since systems requiring high security usually include access to sensitive information such as financial information, personal data or confidential documents, it is important for such passwords to be complex and strong. On the other hand, simpler passwords can be used for less critical accounts. Determining the security levels of passwords can both improve the user experience and make password management more effective. This approach increases the security of users and also supports the memorability of passwords. A three-level security approach is given below as an example.

Security Level - 1 (Insignificant)

Accounts such as forum sites, temporary accounts, and guest sessions can be included in the group with a low level of security. These types of accounts can be managed with a simple and single password, as they are usually designed for everyday use and do not cause serious problems when lost. By setting a short and easy-to-remember password for these accounts, users can speed up their transactions and provide ease of use. However, the use of such passwords on other accounts can increase security risks. Therefore, within the framework of basic security awareness, it is important to distinguish the passwords set for such accounts from the passwords created for more critical systems.

- Example 1: c*9080 (Containing all characters)
- Example 2: cy9080 (Containing only letters and numbers)
- Example 3: 909080 (Containing digits only)

Security Level - 2 (Important)

Systems that contain personal or sensitive information, such as computer logins, email accounts, and social media, are among the accounts with medium security requirements. It is recommended to create separate passwords for such accounts. Passwords must be between 6 and 8 characters (the length can be increased depending on user preferences) and may contain the user's individual information. For example, unique references such as "ba" for the province of Batman and "72" for the license plate can be used. This method both increases the memorability of passwords and strengthens security. However, such passwords mustn't be used on other accounts, as this can lead to security vulnerabilities.

- Example 1: b72*a73 (Containing all characters)
- Example 2: ba72ab6 (Containing only letters and numbers)
- Example 3: 72742024 (Containing only numbers)

Security Level - 3 (Very Important)

Systems that contain monetary or critical information, such as electronic cash registers and Internet banking, are among the accounts that require high security. It is recommended to create separate passwords for such accounts. Passwords must be at least 8 characters long and contain no meaningful phrases.

Users should choose complex passwords that use a combination of letters, numbers, and special characters. Although some systems require only numerical input, it increases security if passwords contain complex and meaningless phrases and are as long as possible. In addition, the use of both lowercase and uppercase letters will significantly improve the security of passwords. The fact that passwords are case-sensitive strengthens security even more. Therefore, it is necessary to pay attention to the methods of creating secure passwords for such accounts.

- Example 1: 3bd*35A=09 (Containing all characters)
- Example 2: mu44AZ8090 (Containing only letters and numbers)
- Example 3: 4490121444 (Containing only numbers)

Passwords are often forgotten or hard to recall, especially when managing many or unused for long periods. To mitigate this, users may write down passwords and store them

securely, such as in wallets, safes, or other private spaces. However, this method carries risks of loss, theft, or unauthorized access, requiring carefully safeguarding storage locations. Writing down passwords or storing them digitally can also be vulnerable to threats like keyloggers. To enhance security, users should avoid sharing passwords, refrain from using browser password-saving features, and update passwords regularly. Protecting passwords is as crucial as creating strong ones.

4.3 Setting Highly Secure Passwords

Strong passwords are essential for maintaining security and must meet four key requirements, prioritized by importance. Firstly, the password should be easily memorable for the user to ensure it can be easily recalled. Secondly, it should be challenging for others to guess, preventing unauthorized access. Thirdly, it must be resistant to automated guessing methods employed by programs, which often utilize dictionary attacks or brute force techniques. Finally, a strong password should exhibit complexity by incorporating a combination of numbers, symbols, uppercase, and lowercase letters. This multifaceted approach to password creation significantly enhances security and reduces the risk of unauthorized access [29].

Among the requirements for a strong password, the first - being easily memorable for the user - emerges as the most crucial. If a password can not be recalled, its effectiveness is undermined, regardless of its complexity or resistance to guessing. For instance:

#4ssFrX^-aartPOknx25_70!xAdk<d! exemplifies a strong password as it meets the criteria of being hard to guess by others or programs due to its complexity, which includes a mix of numbers, symbols, and both uppercase and lowercase letters. However, the intricate nature of this password renders it exceedingly difficult for an individual to remember. Thus, while complexity is essential, the ability to recall the password easily is paramount for ensuring consistent and secure access to accounts.

Using a mix of uppercase letters, numbers, and symbols is a basic method as it will make it more difficult for attackers to guess the generated password. Passwords such as A+214!, *+At13, 17!+A@k are examples of trusted passwords. M&y2ş<G7, b1/2d8Y{Oö, v^4+U?n8ç are examples of very reliable passwords. However, these passwords should be meaningful to the owner, as in the example below. So, it is more secure to use a passphrase rather than a password created with classical methods.

Arabamı severim. (passphrase)

Ar@b@mıs3verIm. (password)

a→@ , e→3, i→I (character change)

A simple security password can also be created by taking the initials of a randomly generated song phrase. "Armudun iyisini ayılar yerler." (aiay) This phrase is secure because it is not in the dictionary. To make this even safer, first letter can be capitalized and put a dot at the end (Aiay.)

The security of passwords depends on the variety of the character set used. A password is entered into the system via the keyboard and the keyboard characters are first decoded with ASCII codes. Today's standard keyboards usually contain 102 keys, which corresponds to approximately 102 ASCII codes. However, when shift keys such as SHIFT and ALT are used, this character set expands. While pressing the SHIFT key activates an additional 102 characters, the ALT key allows some special characters to be typed. In this case, the combination of normal characters with the SHIFT and ALTGR keys allows complex and strong passwords to be created. For example, a password such as "Ah*?3$" is created with such a combination and offers a high level of security. Therefore, the use of character variety and combinations when creating a password significantly increases security. In this context, the use of passphrases becomes inevitable for a password that is both easy to remember and difficult to crack.

4.4 Passphrases

Table 2 shows examples of passwords created as Normal, Good, and Best [21]. If the created passwords are not created according to a certain algorithm or structure, it may cause situations that are difficult to control for end users. Today, the use of passwords is used in many web applications such as e-government, education, health, and bank transactions. Various methods have been developed for the management of so many passwords, such as writing them on paper, using the same password everywhere, and using password management applications. However, it is known that these methods also contain security vulnerabilities. Although creating strong passwords is no longer a problem for conscious users thanks to awareness studies, remembering these passwords continues to be a problem. To solve this problem, the passphrase method, which is frequently used by people working in the field of Information Technologies (IT) but is not aware of by end users, is a permanent solution.

Table 2. Normal, Good, Best password examples [21]

Normal	Good	Best
allwhitecat	a11whitecat	A11whi7ec@t
Fblogin	1FBLogin	1.FB.L0gin$
amazonpass	AmazonPa55	Am@z0nPa55
Ilikemyschool	ILikeMySchool	!Lik3MySch001
Hightidenow	HighTideNow	H1gh7id3Now

Creating secure and memorable passwords plays a critical role in ensuring digital security. The only exception to the rule that a strong password should be meaningless but easy to remember is long meaningful sentences. For example, individuals can choose a meaningful proverb or idiom and use the first letters of each word of this phrase. Such an approach increases the complexity of the password while also increasing its memorability. In addition, a number that the user can easily remember, such as the year of birth, can be placed between these letters. To further strengthen the password, it would be useful to add a special character at the end. To concretize this method, we can take the example of the proverb " Rüzgar eken fırtına biçer ". The first letters of each word of this phrase are taken and a string is obtained in the form of "Refb". Then, the number 1983, the user's year of birth, is placed between these letters: "R1e9f8b3". Finally, adding a special character to the password will increase its security. For example, if a hash (#) sign is added, the result will be a password that is both strong and easy to remember, such as "R1e9f8b3#".

One effective way to create strong and memorable passwords is to use the first letters and numerical values of meaningful sentences. This method makes complex passwords easier to remember and harder to guess. For example, the phrase " Her sabah kahvemi iki şekerli içerim " can be used to create a password like "Hsk2şi". Similarly, personal information can be used by coding it into a regular structure. For example, the phrase " Kardeşim Ahmed 12 Nisan 2004 yılında doğdu " can be used to create a strong password like "KA12.N.2004yd"

A strong password should contain at least one uppercase letter, lowercase letter, number, and special character. It can sometimes be difficult to create and remember these passwords. For this, password phrases, which are password creation methods that are frequently used by employees in the IT sector but not known to end users, should be used. If the sentence " Benim annem bir melektir." is used as an example of creating a password with a password phrase, if the first two characters of each phrase are taken, the password "Bean1me." is obtained [21]. It

doesn't matter if the password is meaningless. The important thing is not to forget the password phrase. The password to be created should not be shared and the sentence should not be forgotten. The password should not be a dictionary word. It is more reliable to use a passphrase than a password created by classical methods.

A strong password should be personalized and meaningful to the user. It should be at least 8-20 characters long, incorporating a mix of uppercase and lowercase letters, numbers, and special characters. Interchanging these elements enhances complexity and makes the password difficult to guess. Additionally, the inclusion of at least one punctuation mark further strengthens its security. Different methods can be preferred to create an easy-to-remember passphrase. Passphrase examples created with different methods are presented below.

Passphrase: benim iki oğlum var [21]
Change: l→!, b→6, a→@, i→1, o→0, ğ→9, e→3, iki→2, var→V
Coded Password Phrase: 63n1m209!umV

Password phrase: Sivas1960Zara
Change: 9→g, i→1, 0→(), a→@, 1→!, Z→7
Coded Password Phrase: S1v@s!g6()7@r@

Password phrase: Hiç çekmediğin şutları yüzde 100 her zaman kaçıracaksın.
Changes: Write the first letters of the words in the passphrase with ending dot and also yüzde→%
Coded Password Phrase: Hçş%100hzk.

Password Phrase: Ayda 1 yetimleri ziyaret etmek için sevgi evine gider misin?
Changes: Write the first letters of the words and the rest is the same.
Coded Password Phrase: A1yzeisegm?

5 RESULT AND RECOMMENDATIONS

The importance of privacy in cyber security environment is a critical factor that directs individuals to create stronger and more secure passwords. End users feeling safe in the digital world is directly related to their ability to create strong passwords. Knowing how to make a password effective and strong is one of the cornerstones of this security process. The most important element that ensures the security of information is not legal regulations but the will

and awareness of individuals. Considering that every piece of information shared in the network environment leaves permanent traces, it is understood that individuals will need various tools, the skills to use these tools, and behavioral changes to protect themselves, their information, and their digital systems.

Teaching reliable password creation methods starting from secondary school is important for individuals to acquire a digital security culture at an early age. It should be emphasized that unique and complex passwords should be used, especially for important accounts such as e-mail and online banking. It is equally important to store passwords securely; these passwords should be kept in a secret area that belongs only to the owner and should be protected in a way that cannot be accessed by others. Critical account passwords in particular should be secret. Indeed, the principle of "what two people know is not a secret" constitutes the essence of security at this point.

In cases such as forgotten passwords or account lockouts, recovery methods come into play to provide access to accounts. Many platforms send a verification e-mail for password resets, and therefore it is of great importance that the recovery e-mail address is up-to-date and accessible. In addition, adding a phone number to profile information to increase account security makes it possible to receive a verification code via text message during password reset. Using a mobile phone number is a more reliable verification method compared to other recovery options because the device is physically in the individual's possession, making it a more secure identification tool than a secondary e-mail address or security questions. As a result, promoting effective password-generation techniques, and fostering a cyber security culture are critically important for maintaining security in the digital world.

Conflict of Interest Statement

There is no conflict of interest between the authors.

Statement of Research and Publication Ethics

The study is complied with research and publication ethics.

Artificial Intelligence (AI) Contribution Statement

This manuscript was entirely written, edited, analyzed, and prepared without the assistance of any artificial intelligence (AI) tools. All content, including text, data analysis, and figures, was solely generated by the authors.

Contributions of the Authors

İbrahim AYAZ : resources, software, writing original draft, writing-review and editing.

M. Zekeriya GÜNDÜZ : resources, supervision, methodology, writing original draft, writing-review and editing.

REFERENCES

[1] C. Online, "Şifre güvenliği ve hack." https://www.chip.com.tr/haber/sifre-guvenligi-ve-hack_17955.html (accessed Oct. 11, 2024).

[2] M. Dell'Amico, P. Michiardi, and Y. Roudier, "Password strength: An empirical analysis," in *Proc. IEEE INFOCOM*, Mar. 2010, pp. 1–9, doi: 10.1109/INFCOM.2010.5461951.

[3] U. Bodkhe, J. Chaklasiya, P. Shah, S. Tanwar, and M. Vora, "Markov model for password attack prevention," in *Proc. 1st Int. Conf. Computing, Communications, and Cyber-Security (IC4S 2019)*, P. K. Singh, W. Pawłowski, S. Tanwar, N. Kumar, J. J. P. C. Rodrigues, and M. S. Obaidat, Eds. Singapore: Springer, 2020, pp. 831–843, doi: 10.1007/978-981-15-3369-3_61.

[4] A. Nosenko, Y. Cheng, and H. Chen, "Password and passphrase guessing with recurrent neural networks," *Inf. Syst. Front.*, vol. 25, no. 2, pp. 549–565, Apr. 2023, doi: 10.1007/s10796-022-10325-x.

[5] M. Jin, J. Ye, R. Shen, and H. Lu, "Search-based ordered password generation of autoregressive neural networks," Mar. 15, 2024, *arXiv*:2403.09954, doi: 10.48550/arXiv.2403.09954.

[6] Y. Li, H. Wang, and K. Sun, "Personal information in passwords and its security implications," *IEEE Trans. Inf. Forensics Secur.*, vol. 12, no. 10, pp. 2320–2333, Oct. 2017, doi: 10.1109/TIFS.2017.2705627.

[7] Y. Guo, Z. Zhang, Y. Guo, and X. Guo, "Nudging personalized password policies by understanding users' personality," *Comput. Secur.*, vol. 94, p. 101801, Jul. 2020, doi: 10.1016/j.cose.2020.101801.

[8] M. Siponen, P. Puhakainen, and A. Vance, "Can individuals' neutralization techniques be overcome? A field experiment on password policy," *Comput. Secur.*, vol. 88, p. 101617, Jan. 2020, doi: 10.1016/j.cose.2019.101617.

[9] N. Huaman, S. Klivan, M. Oltrogge, Y. Acar, and S. Fahl, "They would do better if they worked together: The case of interaction problems between password managers and websites," in *Proc. IEEE Symp. Security and Privacy (SP)*, May 2021, pp. 1367–1381, doi: 10.1109/SP40001.2021.00094.

[10] I. Mannuela, J. Putri, Michael, and M. S. Anggreainy, "Level of password vulnerability," in *Proc. 1st Int. Conf. Computer Science and Artificial Intelligence (ICCSAI)*, Oct. 2021, pp. 351–354, doi: 10.1109/ICCSAI53272.2021.9609778.

[11] "How secure is my password?" https://howsecureismypassword.net/ (accessed Dec. 03, 2024).

[12] "Kaspersky: Secure password check." https://password.kaspersky.com (accessed Dec. 03, 2024).

[13] "Securely store, manage & autofill passwords," NordPass. https://nordpass.com/ (accessed Dec. 03, 2024).

[14] "Password tester | Test your password strength," Bitwarden. https://bitwarden.com/password-strength/ (accessed Dec. 03, 2024).

[15] "Password manager - For everyone, everywhere - LastPass." https://www.lastpass.com/password-manager (accessed Dec. 03, 2024).

[16] "Have I been pwned: Pwned passwords." https://haveibeenpwned.com/passwords (accessed Dec. 03, 2024).

[17] F. Yu and H. Yin, "A security analysis of the authentication mechanism of password managers," in *Proc. IEEE 21st Int. Conf. Communication Technology (ICCT)*, Oct. 2021, pp. 865–869, doi: 10.1109/ICCT52962.2021.9657969.

[18] S. Furnell, "Assessing website password practices – Unchanged after fifteen years?," *Comput. Secur.*, vol. 120, p. 102790, Sep. 2022, doi: 10.1016/j.cose.2022.102790.

[19] K. H. Hong and B. M. Lee, "A deep learning-based password security evaluation model," *Appl. Sci.*, vol. 12, no. 5, Art. no. 5, Jan. 2022, doi: 10.3390/app12052404.

[20] M. Z. Gündüz and R. Daş, "Sosyal mühendislik: Yaygın ataklar ve güvenlik önlemleri," presented at the *9th Int. Conf. Information Security and Cryptology*, 2016.

[21] M. Z. Gündüz and R. Daş, "Kişisel siber güvenlik yaklaşımlarının değerlendirilmesi," *DUJE*, vol. 13, no. 3, Art. no. 3, Sep. 2022, doi: 10.24012/dumf.1122997.

[22] A. A. Hamza and J. S. Al-Janabi, "Detecting brute force attacks on SSH and FTP protocol using machine learning: A survey," *J. Al-Qadisiyah Comput. Sci. Math.*, vol. 16, no. 1, Art. no. 1, Mar. 2024, doi: 10.29304/jqcsm.2024.16.11432.

[23] H. Hussain, "Password security: Best practices and management strategies," *Social Science Research Network*, Rochester, NY, Jun. 14, 2022, doi: 10.2139/ssrn.4136333.

[24] C. W. Munyendo, Y. Acar, and A. J. Aviv, "In eighty percent of the cases, I select the password for them: Security and privacy challenges, advice, and opportunities at cybercafes in Kenya," in *Proc. IEEE Symp. Security and Privacy (SP)*, May 2023, pp. 570–587, doi: 10.1109/SP46215.2023.10179410.

[25] A. P. Umejiaku, P. Dhakal, and V. S. Sheng, "Balancing password security and user convenience: Exploring the potential of prompt models for password generation," *Electronics*, vol. 12, no. 10, Art. no. 10, Jan. 2023, doi: 10.3390/electronics12102159.

[26] "Dashlane password manager," Dashlane. https://ripleyprd.wpengine.com/ (accessed Dec. 03, 2024).

[27] D. Reichl, "KeePass password safe." https://keepass.info/ (accessed Dec. 03, 2024).

[28] "Random.org - Password generator." https://www.random.org/passwords/ (accessed Dec. 03, 2024).

[29] N. Lykousas and C. Patsakis, "Decoding developer password patterns: A comparative analysis of password extraction and selection practices," *Comput. Secur.*, vol. 145, p. 103974, Oct. 2024, doi: 10.1016/j.cose.2024.103974.

BİTLİS EREN ÜNİVERSİTESİ
FEN BİLİMLERİ DERGİSİ

ISSN: 2147-3129 / e-ISSN: 2147-3188

Article Type	: Research Article	**Year**	: 2025
Received	: December 3, 2024	**Volume**	: 14
Revised	: February 28, 2025	**Issue**	: 3
Accepted	: June 24, 2025	**Pages**	: 1331-1347
DOI	: 10.17798/bitlisfen.1595852		

THE NOVEL NUMERICAL SOLUTIONS OF CONFORMABLE FRACTIONAL NAVIER-STOKES EQUATION WITH THE ROBUST METHOD

Aslı ALKAN [1,*], Hasan BULUT [1,2], Tolga AKTÜRK [3]

[1] *Fırat University, Department of Mathematics, Elazığ, Türkiye*

[2] *Azerbaijan University, Department of Mathematics and Informatics, Bakü, Azerbaijan*

[3] *Ordu University, Department of Mathematics and Science Teaching, Ordu, Türkiye*

**** Corresponding Author:*** *alkanasli47@gmail.com*

ABSTRACT

In this study, new numerical solutions of the conformable fractional Navier-Stokes equation are obtained by the conformable q-Shehu homotopy analysis transform method. The fractional Navier-Stokes equation is an extension of the classical Navier-Stokes equations that incorporates fractional derivatives to account for complex flow behaviors such as memory effects and anomalous diffusion. It is particularly useful in describing fluid dynamics in non-Newtonian fluids, porous media, and other systems with intricate time or spatial dependencies. In addition, two and three-dimensional graphs of the obtained solutions were drawn. We also conduct an error analysis to evaluate the accuracy of the scheme. Computational simulations are performed to validate the accuracy of the upcoming method. This paper presents the conclusions derived from the numerical and graphical analysis.

Keywords: Navier-Stokes equation, Conformable q-Shehu homotopy analysis transform method, Shehu transform.

1 INTRODUCTION

Fractional calculus is a mathematical framework that extends the scope of classical calculus, which deals with derivatives and integrals of integer order, to include derivatives and integrals of arbitrary order [1], [2]. Given that fractional calculus can provide precise descriptions of various nonlinear systems, researchers have begun their research. Fractional differential equations express the influence of nonlocal and inherent material properties [3], [4],

[5]. A cadre of distinguished scientists have conducted extensive research, formulated precise definitions for fractional calculus, and proposed innovative concepts that form the basis of the discipline of fractional calculus studies. Today, fractional calculus is widely used in the development of nonlinear models. A cacophonous environment, financial models derived from chaos theory, optics, and various phenomena have been associated with the concept of fractional calculus [6], [7], [8]. The solution of fractional differential equations is an important tool for characterizing natural nonlinear systems. Researchers obtain exact solutions for fractional differential equations describing nonlinear phenomena by various analytical and numerical methods [9], [10], [48].

An important and useful concept is the conformable fractional derivative. It also helps in understanding the characterization of physical object behavior. Conformable fractional derivative is an effective tool for addressing complex problems. The numerical solutions of differential equations using conformable fractional derivative are comparatively simpler than those using Caputo fractional derivative. This enables the use of conformable fractional derivative, which is advantageous for modeling various physics-related processes. Natural sciences use various fractional models as they can effectively depict real-world problems. A large number of researchers use conformable fractional derivative in various fields. Conformable fractional derivative overcomes certain limitations associated with existing fractional operators [11]-[16], [49], [50].

In 1822, the Navier–Stokes equation, which governs the dynamics of viscous fluid flow, was formulated [17], [18], [19]. The equation combines the energy equation, the continuity equation, and the momentum equation and can be regarded as Newton's second law of motion for fluids. This equation can describe various physical processes such as fluid flow in pipes, ocean currents, air flow, and blood circulation over aircraft wings [20–23]. In 2005, Salem and El-Shahed [24] pioneered the fractional modeling of the Navier–Stokes equations. The authors [24] used the Laplace transform, finite Fourier Sine transform, and finite Hankel transform to generalize the classical Navier–Stokes equations. Kumar et al. [25] solved a nonlinear fractional model of the Navier–Stokes problem analytically by combining the Laplace transform with the homotopic perturbation method. Homotopy analysis method, Ganji et al. [26] and Ragab et al. [27] used it to solve the nonlinear fractional Navier-Stokes equation. Maitama [28] and Momani and Birajdar [29] used the Adomian decomposition method for the numerical calculation of the fractional Navier-Stokes equation. Kumar et al. [30] roughly solved the time-fractional Navier-Stokes problem using the Laplace transform along with the Adomian decomposition method.

On the other hand, the Laplace transform has been used along with the finite Hankel transform to solve the same equation [31].

The q-homotopy analysis transform technique provides various approximate solutions by integrating the q-homotopy analysis method with the Laplace transform [32], [33]. El-Tawil and Huseen [34] proposed q-homotopy analysis method, which is a version of the homotopy analysis method [35], [36] originally described by Liao [37], [38], and the homotopy perturbation method originally described by He [39], [40]. Recent years have witnessed the integration of semi-analytical methods, including the Laplace decomposition technique [41], [42], homotopy perturbation method and the homotopy analysis transform technique, with the Laplace transform algorithm to analyze integer and fractional differential equations modeling real-world problems in scientific and technological fields. In addition, new semi-analytical techniques have been developed, including the conformable fractional Elzaki decomposition method [43] and the conformable q-Shehu analysis transform method [44]. Conformable q-Shehu analysis transform method provides a more generalized form of the series solution by facilitating the convergence of series solutions via the auxiliary parameter h, embedding parameter q, asymptotic parameter n, auxiliary function $H(x,t)$ and initial condition $w_0(x,t)$.

The primary objective of the work is to derive the new numerical solutions for the conformable time-fractional Navier-Stokes equation utilizing conformable q-Shehu homotopy analysis transform method.

This paper is organized as follows: Part 2 elucidates the principles of the conformable fractional derivative, including its essential definitions, notable characteristics, and the core concept of conformable q-Shehu homotopy analysis transform method. The proposed solution is employed to address the conformable time-fractional Navier-Stokes equation in Part 3. The results are delineated in Part 4. The conclusion is located in Part 5.

2 MATERIAL AND METHOD

In the part, the main definitions are introduced.

Definition 2.1. [11], [12] Assume that the function $g:[0,\infty)\to\mathbb{R}$. Thus, conformable fractional derivative of h order α is described by

$$D_\alpha(g)(x)=\lim_{\varepsilon\to 0}\frac{g(x+\varepsilon x^{1-\alpha})-g(x)}{\varepsilon}, \tag{1}$$

for $\forall x>0, 0<\alpha\leq 1$.

Theorem 2.1. [11], [12] Assume that $0 < \alpha \leq 1$ and a, h be α −differentiable at a point $x \in (0, \infty)$. Thus, the following properties exist

(i) $$D_\alpha(c_1 a + c_2 h) = c_1 D_\alpha(a) + c_2 D_\alpha(h) \text{ for } \forall\, c_1, c_2 \in \mathbb{R}, \tag{2}$$

(ii) $$D_\alpha(x^p) = p x^{p-1}, \text{ for } \forall p \in \mathbb{R}, \tag{3}$$

(iii) $$D_\alpha(c) = 0, \text{ for } \forall g(t) = c, \tag{4}$$

(iv) $$D_\alpha(ah) = a D_\alpha(h) + h D_\alpha(a), \tag{5}$$

(v) $$D_\alpha\left(\frac{a}{h}\right) = \frac{h D_\alpha(a) - a D_\alpha(h)}{h^2}. \tag{6}$$

Definition 2.2. [45] Assume that the function $h: [0, \infty) \to \mathbb{R}$. Thus, conformable Shehu transform of $h(t)$ order α is identified as

$$_cS_\alpha[h(t)] = V_\alpha(s; u) = \int_0^\infty exp\left(\frac{-st^\alpha}{u\alpha}\right) h(t) t^{\alpha-1} dt. \tag{7}$$

Definition 2.3. [45] Assume that $\alpha \in (0, 1]$, $h: [0, \infty) \to \mathbb{R}$ be the function. The conformable fractional Shehu transform for the conformable fractional derivative of $h(t)$ is identified by

$$V_\alpha[D_\alpha h(t)](v) = \frac{s}{u} V_\alpha(s; u) - f(0). \tag{8}$$

2.1 The Main Idea of Conformable q-Shehu Homotopy Analysis Transform Method

To clarify the fundamental principle of conformable q-Shehu homotopy analysis transform method **[44]**, it is essential to examine the conformable time-fractional partial differential equations

$$D_t^\alpha u(\xi, \tau) + Au(\xi, \tau) + Hu(\xi, \tau) = \zeta(\xi, \tau), t > 0, n - 1 < \alpha \leq n, \tag{9}$$

where A and H are linear and nonlinear operators, $\zeta(\xi, \tau)$ is a nonhomogeneous function, and D_t^α is conformable fractional derivative of order α.

Applying the conformable fractional Shehu transform to equation (9) and using the initial condition, then, we have

$$\frac{s}{u}\ _cS_\alpha[u(\xi, \tau)] - u(x, 0) +\ _cS_\alpha[Au(\xi, \tau) + Hu(\xi, \tau)] =\ _cS_\alpha[\zeta(\xi, \tau)]. \tag{10}$$

Simplifying the equation (10), equation (20) is derived as

$$ {}_cS_\alpha[u(\xi,\tau)] - \frac{u}{s}u(x,0) + \frac{u}{s}\ {}_cS_\alpha[Au(\xi,\tau) + Hu(\xi,\tau) - \zeta(\xi,\tau)] = 0. \tag{11}$$

Using the homotopy analysis method, the nonlinear operator to the function $\rho(x,t;q)$ is described as

$$ N[\rho(\xi,\tau;q)\ ] = \ {}_cS_\alpha[\rho(\xi,\tau;q)\ ] - \frac{u}{s}\rho(\xi,\tau;q)\ (0^+) + \frac{u}{s}\big(\ {}_cS_\alpha[A\rho(\xi,\tau;q)\big) \tag{12}$$

$(+H\rho(\xi,\tau;q) - \zeta(\xi,\tau)]),$

where $0 \le q \le \frac{1}{n}$.

A homotopy is identified by

$$ (1-nq)\ {}_cS_\alpha[\rho(\xi,\tau;q) - u_0(\xi,\tau)] = hqH^*(\xi,\tau)H[\rho(\xi,\tau;q)], \tag{13}$$

where, $h \neq 0$. For $q = 0$ and $q = \frac{1}{n}$, the outcomes of equation (13) are obtained as

$$ \rho(\xi,\tau;0) = u_0(\xi,\tau), \rho\left(\xi,\tau;\frac{1}{n}\right) = u(\xi,\tau). \tag{14}$$

Therefore, while increasing the value of q from 0 to $1/n$, the solution $\rho(\xi,\tau;q)$ approaches the solution $u(\xi,\tau)$ by beginning at $u_0(\xi,\tau)$. Using Taylor theorem around q and thereafter expanding $\rho(\xi,\tau;q)$, the resulting expression is produced by

$$ \rho(\xi,\tau;q) = u_0(\xi,\tau) + \sum_{\mathrm{m}=1}^{\infty} u_m(x,t)q^m, \tag{15}$$

where,

$$ u_m(\xi,\tau) = \frac{1}{m!}\frac{\partial^m \rho(\xi,\tau;q)}{\partial q^m}|_{q=0}. \tag{16}$$

Equation (15) approaches at $q = \frac{1}{n}$ for the appropriate $u_0(\xi,\tau)$, n and h. Subsequently, the solution for the initial nonlinear equation in the specified format is acquired by

$$ u(\xi,\tau) = u_0(\xi,\tau) + \sum_{m=1}^{\infty} u_{\mathrm{m}}(\xi,\tau)\left(\frac{1}{n}\right)^m. \tag{17}$$

By taking the $m-th$ derivative of the zeroth order deformation equation (13) with respect to q and dividing by the factorial of m, when $q = 0$, we obtain

$$ {}_cS_\alpha[u_m(\xi,\tau) - \chi_m u_{m-1}(\xi,\tau)] = hH^*(\xi,\tau)\mathcal{R}_{*m}(\vec{u}_{m-1}), \tag{18}$$

where the vectors are identified as

$$ \vec{u}_m = \{u_0(\xi,\tau), u_1(\xi,\tau), \dots, u_m(\xi,\tau)\}. \tag{19}$$

Inverse conformable fractional Shehu transform is applied to equation (18), it is obtained as

$$ u_{\mathrm{m}}(\xi,\tau) = \chi_m u_{m-1}(\xi,\tau) + h\left({}_cS_\alpha\right)^{-1}[H^*(\xi,\tau)\mathcal{R}_{*m}(\vec{u}_{m-1})], \tag{20}$$

where

$$ \begin{aligned} \mathcal{R}_{*m}(\vec{u}_{m-1}) = {}& {}_cS_\alpha[u_{m-1}(\xi,\tau)] \\ -\left(1-\frac{\chi_m}{n}\right)\frac{u}{s}u_0(\xi,\tau) + \frac{\mathrm{u}}{s}\,{}_cS_\alpha[Au_{m-1}(\xi,\tau) + H^*{}_{m-1}(\xi,\tau) - \zeta(\xi,\tau)], \end{aligned} \tag{21}$$

and

$$ \chi_m = \begin{cases} 0, & m \le 1, \\ n, & m > 1. \end{cases} \tag{22}$$

Here, $H^*{}_m$ is homotopy polynomial and presented as

$$ H^*{}_m = \frac{1}{m!}\frac{\partial^m \rho(\xi,\tau;q)}{\partial q^m}|_{q=0} \tag{23}$$

and $\rho(\xi,\tau;q) = \rho_0 + q\rho_1 + q^2\rho_2 + \cdots$.

Utilizing equations (20)-(21), one gets

$$ \begin{aligned} u_{\mathrm{m}}(\xi,\tau) = {}& (\chi_m + h)u_{\mathrm{m-1}}(\xi,\tau) - \left(1-\frac{\chi_m}{n}\right)\frac{u}{s}u_0(\xi,\tau) \\ &+h\left({}_cS_\alpha\right)^{-1}\left[\frac{\mathrm{u}}{s}\left({}_cS_\alpha[Au_{\mathrm{m-1}} + H^*{}_{m-1}(\xi,\tau) - \zeta(\xi,\tau)]\right)\right]. \end{aligned} \tag{24}$$

Using conformable q-Shehu homotopy analysis transform method, then we have

$$ u(\xi,\tau) = \sum_{m=0}^{\infty} u_{\mathrm{m}}(\xi,\tau). \tag{25}$$

2.2 Convergence Analysis

In this section, two theorems related to conformable q-Shehu homotopy analysis transform method are given.

Theorem 2.2.1. [46]. The solution of conformable time-fractional partial differential equations acquired by conformable q-Shehu homotopy analysis transform method is unique for $\forall \varsigma \epsilon (0,1)$, where $\varsigma = (n + \hbar) + \hbar(\epsilon + \rho)\Lambda$.

Theorem 2.2.2. [46]. Assume that Θ is Banach space and $\chi: \Theta \to \Theta$ is the nonlinear mapping. Let the following inequality is provided as

$$\|\boldsymbol{\chi}(\boldsymbol{v}) - \boldsymbol{\chi}(\boldsymbol{\rho})\| \leq \boldsymbol{\gamma}\|\boldsymbol{v} - \boldsymbol{\rho}\|, \forall \boldsymbol{v}, \boldsymbol{\rho} \in \boldsymbol{\Theta}, \tag{26}$$

therefore χ has a fixed point in Banach space [47]. Furthermore, for any arbitrary selection of $m_0, n_0 \in \Theta$, the sequence acquired via the conformable q-Shehu homotopy analysis transform method converges to a fixed point of χ and

$$\|\boldsymbol{v_m} - \boldsymbol{v_n}\| \leq \frac{\boldsymbol{\gamma^n}}{\boldsymbol{1-\gamma}}\|\boldsymbol{v_1} - \boldsymbol{v_0}\|, \forall \boldsymbol{v}, \boldsymbol{\rho} \in \boldsymbol{\Theta}. \tag{27}$$

3 APPLICATION

Consider the nonlinear conformable time-fractional Navier-Stokes equation [32], [33]

$$D_t^{\alpha} w(x,y,t) + w(x,y,t)\frac{\partial w(x,y,t)}{\partial x} + q(x,y,t)\frac{\partial w(x,y,t)}{\partial y} = \rho\left[\frac{\partial^2 w(x,y,t)}{\partial x^2} + \frac{\partial^2 w(x,y,t)}{\partial y^2}\right] + \sigma, 0 < \alpha \leq 1, \tag{28}$$

$$D_t^{\alpha} q(x,y,t) + w(x,y,t)\frac{\partial q(x,y,t)}{\partial x} + q(x,y,t)\frac{\partial q(x,y,t)}{\partial y} = \rho\left[\frac{\partial^2 q(x,y,t)}{\partial x^2} + \frac{\partial^2 q(x,y,t)}{\partial y^2}\right] - \sigma, 0 < \alpha \leq 1, \tag{29}$$

subject to initial conditions

$$w(x,y,0) = -\sin(x+y), \tag{30}$$

$$q(x,y,0) = \sin(x+y). \tag{31}$$

The parameter α in the fractional derivative is a critical physical parameter that describes the memory effect and anomalous diffusion behavior of the system. When $\alpha = 1$, the classical (integer order) Navier-Stokes equation is obtained and the flow exhibits purely local behavior. When $\alpha < 1$, the past states of the system affect the flow dynamics. This is important in systems that contain memory effects, such as viscoelastic flows, fluid motion in porous media, and biological fluids. σ represents the external forces or source/sink term in the system.

Physically, this term can be the result of an external force, heat source, magnetic effect, or chemical reaction acting on the fluid.

Since σ is positive in equation (28) and negative in equation (29), these terms can be considered to have a balanced effect with each other. ρ is used as the coefficient of the viscous diffusion term in the solution expressions. It has a physical meaning as the density of the fluid. High values of ρ indicate that the fluid has a high inertia. Low values of ρ are valid for lighter fluids or gases. In fractional derivative models, ρ can be an important parameter that changes the fractional flow behavior.

Implementing the conformable fractional Shehu transform to equations (28)-(29) and utilizing the initial conditions, they are acquired by

$$\frac{s}{u}\,{}_cS_\alpha[w(x,y,t)] - w(x,y,0) + {}_cS_\alpha\left[w(x,y,t)\frac{\partial w(x,y,t)}{\partial x} + q(x,y,t)\frac{\partial w(x,y,t)}{\partial y} - \rho\left\{\frac{\partial^2 w(x,y,t)}{\partial x^2} + \frac{\partial^2 w(x,y,t)}{\partial y^2}\right\} - \sigma\right]=0, \tag{32}$$

$$\frac{s}{u}\,{}_cS_\alpha[q(x,y,t)] - q(x,y,0) + {}_cS_\alpha\left[w(x,y,t)\frac{\partial q(x,y,t)}{\partial x} + q(x,y,t)\frac{\partial q(x,y,t)}{\partial y} - \rho\left\{\frac{\partial^2 q(x,y,t)}{\partial x^2} + \frac{\partial^2 q(x,y,t)}{\partial y^2}\right\} + \sigma\right] = 0. \tag{33}$$

By arranging the equations (32)-(33), equations (34)-(35) are generated as

$${}_cS_\alpha[w(x,y,t)] - \frac{u}{s}w(x,y,0) + \frac{u}{s}\,{}_cS_\alpha\left[w(x,y,t)\frac{\partial w(x,y,t)}{\partial x} + q(x,y,t)\frac{\partial w(x,y,t)}{\partial y} - \rho\left\{\frac{\partial^2 w(x,y,t)}{\partial x^2} + \frac{\partial^2 w(x,y,t)}{\partial y^2}\right\} - \sigma\right] = 0, \tag{34}$$

$${}_cS_\alpha[q(x,y,t)] - \frac{u}{s}q(x,y,0) + \frac{u}{s}\,{}_cS_\alpha\left[w(x,y,t)\frac{\partial q(x,y,t)}{\partial x} + q(x,y,t)\frac{\partial q(x,y,t)}{\partial y} - \rho\left\{\frac{\partial^2 q(x,y,t)}{\partial x^2} + \frac{\partial^2 q(x,y,t)}{\partial y^2}\right\} + \sigma\right] = 0. \tag{35}$$

Via the homotopy analysis method, the nonlinear operators for real functions $\varphi(x,t;q)$ and $\psi(x,t;q)$ are defined as

$$N^1[\varphi(x,t;q)\,] = {}_cS_\alpha[\varphi(x,t;q)\,] - \frac{u}{s}\varphi(x,t;q)\,(0^+) + \frac{u}{s}\,{}_cS_\alpha\Big[\varphi(x,y,t)\frac{\partial\varphi(x,y,t)}{\partial x} + \psi(x,y,t)\frac{\partial\varphi(x,y,t)}{\partial y} - \rho\left\{\frac{\partial^2\varphi(x,y,t)}{\partial x^2} + \frac{\partial^2\varphi(x,y,t)}{\partial y^2}\right\} - \sigma\Big], \tag{36}$$

$$N^2[\psi(x,t;q)\,] = {}_cS_\alpha[\psi(x,t;q)\,] - \frac{u}{s}\psi(x,t;q)\,(0^+) + \frac{u}{s}\,{}_cS_\alpha\Big[\varphi(x,y,t)\frac{\partial\psi(x,y,t)}{\partial x} + \psi(x,y,t)\frac{\partial\psi(x,y,t)}{\partial y} - \rho\left\{\frac{\partial^2\psi(x,y,t)}{\partial x^2} + \frac{\partial^2\psi(x,y,t)}{\partial y^2}\right\} + \sigma\Big]. \tag{37}$$

By applying the proposed algorithm, the $m-th$ order deformation equations are identified as

$${}_cS_\alpha[w_m(x,y,t) - k_m w_{m-1}(x,y,t)] = h\mathcal{R}_{1,m}(\vec{w}_{m-1}), \tag{38}$$

$${}_cS_\alpha[q_m(x,y,t) - k_m q_{m-1}(x,y,t)] = h\mathcal{R}_{2,m}(\vec{q}_{m-1}), \tag{39}$$

where

$$\mathcal{R}_{1,m}(\vec{w}_{m-1}) = {}_cS_\alpha[w_{m-1}(x,\mathrm{y},t)] - \left(1-\frac{k_m}{n}\right)\frac{u}{s}w_0(x,\mathrm{y},t) + \frac{u}{s}\,{}_cS_\alpha\left[\sum_{r=0}^{m-1} w_r(x,y,t)\frac{\partial w_{m-1-r}(x,y,t)}{\partial x} + \sum_{r=0}^{m-1} q_r(x,y,t)\frac{\partial w_{m-1-r}(x,y,t)}{\partial y} - \rho\left\{\frac{\partial^2 w_{m-1}(x,\mathrm{y},t)}{\partial x^2} + \frac{\partial^2 w_{m-1}(x,\mathrm{y},t)}{\partial y^2}\right\} - \sigma\right], \tag{40}$$

$$\mathcal{R}_{2,m}(\vec{q}_{m-1}) = {}_cS_\alpha[q_{m-1}(x,\mathrm{y},t)] - \left(1-\frac{k_m}{n}\right)\frac{u}{s}q_0(x,\mathrm{y},t) + \frac{u}{s}\,{}_cS_\alpha\left[\sum_{r=0}^{m-1} w_r(x,y,t)\frac{\partial q_{m-1-r}(x,y,t)}{\partial x} + \sum_{r=0}^{m-1} q_r(x,y,t)\frac{\partial q_{m-1-r}(x,y,t)}{\partial y} - \rho\left\{\frac{\partial^2 q_{m-1}(x,\mathrm{y},t)}{\partial x^2} + \frac{\partial^2 q_{m-1}(x,\mathrm{y},t)}{\partial y^2}\right\} + \sigma\right]. \tag{41}$$

When equations (38)-(39) are implemented to the inverse conformable fractional Shehu transform, we have

$$w_m(x,\mathrm{y},t) = k_m w_{m-1}(x,\mathrm{y},t) + h\left({}_cS_\alpha\right)^{-1}\left[\mathcal{R}_{1,m}(\vec{w}_{m-1})\right], \tag{42}$$

$$q_m(x,\mathrm{y},t) = k_m w_{m-1}(x,\mathrm{y},t) + h\left({}_cS_\alpha\right)^{-1}\left[\mathcal{R}_{2,m}(\vec{q}_{m-1})\right]. \tag{43}$$

By the use of initial conditions, it is obtained as

$$w_0(x,y,t) = -\sin(x+y), \tag{44}$$

$$q_0(x,y,t) = \sin(x+y). \tag{45}$$

Putting $m=1, m=2$ in the equations (42)-(43) respectively, equations (46)-(47) are generated as

$$w_1(x,y,t) = -\frac{2\rho h \sin(x+y)\, t^{\alpha}}{\alpha}, \tag{46}$$

$$q_1(x,y,t) = \frac{2\rho h \sin(x+y)\, t^{\alpha}}{\alpha}, \tag{47}$$

$$w_2(x,y,t) = (n+h)\left[-\frac{2\rho h \sin(x+y)\, t^{\alpha}}{\alpha}\right] - \left[\frac{4\rho^2 h^2 \sin(x+y)\, t^{2\alpha}}{2\alpha^2}\right], \tag{48}$$

$$q_2(x,y,t) = (n+h)\left[\frac{2\rho h \sin(x+y)\, t^{\alpha}}{\alpha}\right] + \left[\frac{4\rho^2 h^2 \sin(x+y)\, t^{2\alpha}}{2\alpha^2}\right]. \tag{49}$$

Thus, the conformable q-Shehu homotopy analysis transform method (Cq-SHATM) solutions of equaitons (28)-(29) are acquired as

$$\begin{aligned} w(x,y,t) &= w_0(x,y,t) + \sum_{m=1}^{\infty} w_m(x,y,t)\left(\frac{1}{n}\right)^m \\ &= -\sin(x+y) - \frac{2\rho h \sin(x+y)\, t^{\alpha}}{\alpha} + (n+h)\left[-\frac{2\rho h \sin(x+y)\, t^{\alpha}}{\alpha}\right] \\ &\quad - \left[\frac{4\rho^2 h^2 \sin(x+y)\, t^{2\alpha}}{2\alpha^2}\right], \end{aligned} \tag{50}$$

$$\begin{aligned} q(x,y,t) &= q_0(x,y,t) + \sum_{m=1}^{\infty} q_m(x,y,t)\left(\frac{1}{n}\right)^m \\ &= \sin(x+y) + \frac{2\rho h \sin(x+y)\, t^{\alpha}}{\alpha} + (n+h)\left[\frac{2\rho h \sin(x+y)\, t^{\alpha}}{\alpha}\right] \\ &\quad + \left[\frac{4\rho^2 h^2 \sin(x+y)\, t^{2\alpha}}{2\alpha^2}\right]. \end{aligned} \tag{51}$$

For $\alpha = 1, h = -1, n = 1$ and $\sigma = 0$, the solutions $\sum_{m=1}^{N} w_m(x,y,t)\left(\frac{1}{n}\right)^m$ and $\sum_{m=1}^{N} q_m(x,y,t)\left(\frac{1}{n}\right)^m$ converge to exact results as $N \to \infty$:

$$w(x,y,t) = -\sin(x+y)\left[1 - \frac{2\rho t}{1!} + \frac{(2\rho t)^2}{2!} + \cdots\right] = -e^{-2\rho t}\, sin(x+y), \tag{52}$$

$$q(x,y,t) = \sin(x+y)\left[1 + \frac{2\rho t}{1!} + \frac{(2\rho t)^2}{2!} + \cdots\right] = e^{-2\rho t}\sin(x+y). \tag{53}$$

Figure 1. shows three dimensional plots of distinct α values at $\rho = 0.5$, $\sigma = 0$, $n = 1$ and $h = -1$ for equation (28).

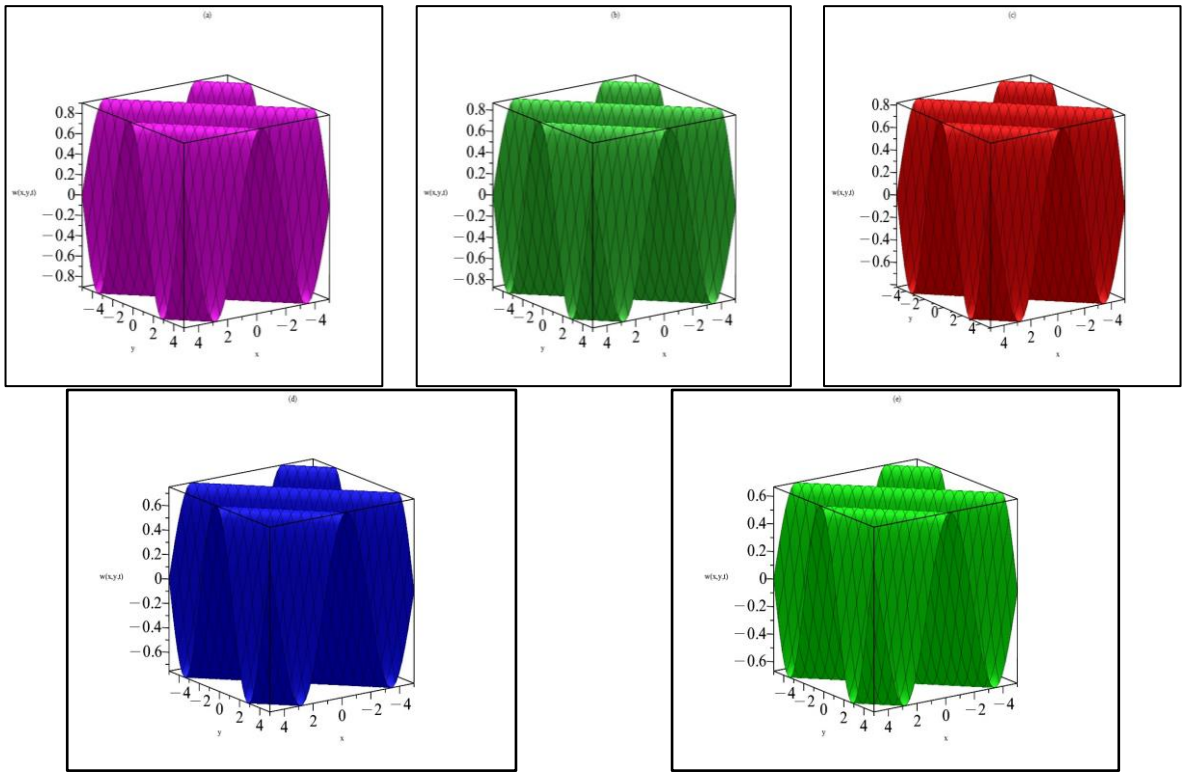


Figure. 1. (a) For $\alpha = 1$, Cq-SHATM solutions (b) For $\alpha = 0.9$, Cq-SHATM solutions (c) For $\alpha = 0.8$, Cq-SHATM solutions (d) For $\alpha = 0.7$, Cq-SHATM solutions (e) For $\alpha = 0.6$, Cq-SHATM solutions at $\rho = 0.5$, $\sigma = 0$, $n = 1$ and $h = -1$ for Equation (28) $h = -1, n = 1$.

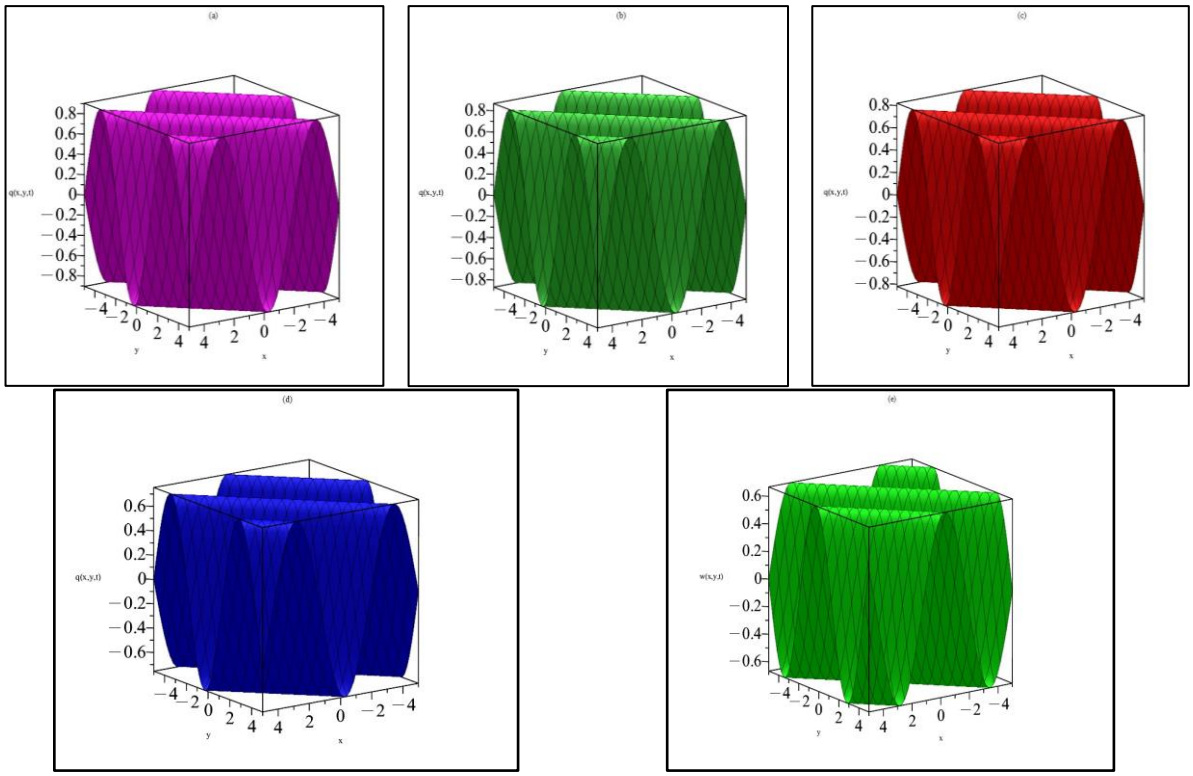


Figure. 2. (a) For $\alpha = 1$, Cq-SHATM solutions (b) For $\alpha = 0.9$, Cq-SHATM solutions (c) For $\alpha = 0.8$, Cq-SHATM solutions (d) For $\alpha = 0.7$, Cq-SHATM solutions (e) For $\alpha = 0.6$, Cq-SHATM solutions at $\rho = 0.5$, $\sigma = 0$, $n = 1$ and $h = -1$ for Equation (28) $h = -1, n = 1$.

In Figure 3, the two dimensional plots for conformable q-Shehu homotopy analysis transform method solution by distinct α values are shown at $x = 0.1, y = 0.1, \rho = 0.5, \sigma = 0,$ $n = 1$ and $h = -1$ for equations (28)-(29).

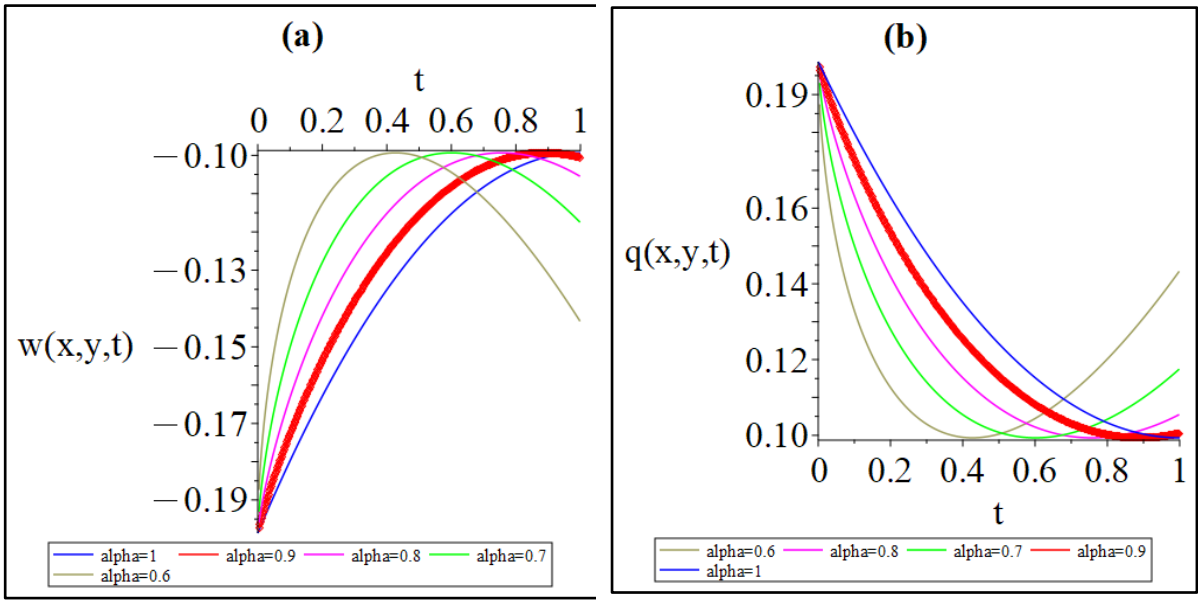


Figure. 3. (a) The two dimensional plot of the Cq-SHATM solutions for equations (28) at $x = 0.1, y = 0.1, \rho = 0.5, \sigma = 0, n = 1$ and $h = -1$ with distinct α values for Eqs.(28). (b) The two dimensional plot of the Cq-SHATM solutions for Eqs. (28) at $x = 0.1, y = 0.1, \rho = 0.5, \sigma = 0, n = 1$ and $h = -1$ with distinct α values for equations (28).

The numerical values of the absolute error between the conformable q-Shehu homotopy analysis transform method solutions and the analytical solution for equation (28) are shown in Table 1.

Table 1. Absolute error between exact solution and approximate solution by Cq-SHATM for equation (28) at $t = 0.01$, $\rho = 0.5, \sigma = 0, n = 1$ and $h = -1$ values.

x/y	0.01	0.02	0.03	0.04	0.05
0.01	3.3×10^{-9}	4.9×10^{-9}	6.6×10^{-9}	8.3×10^{-9}	9.9×10^{-9}
0.02	4.9×10^{-9}	6.6×10^{-9}	8.3×10^{-9}	9.9×10^{-9}	1.1×10^{-8}
0.03	6.6×10^{-9}	8.3×10^{-9}	9.9×10^{-9}	1.1×10^{-8}	1.3×10^{-8}
0.04	8.3×10^{-9}	9.9×10^{-9}	1.1×10^{-8}	1.3×10^{-8}	1.4×10^{-8}
0.05	9.9×10^{-9}	1.1×10^{-8}	1.3×10^{-8}	1.4×10^{-8}	1.6×10^{-8}

The numerical values of the absolute error between the conformable q-Shehu homotopy analysis transform method and the analytical solutions for equation (29) are shown in Table 2.

Table 2. Absolute error between exact solution and approximate solution by Cq-SHATM for equation (29) at $t = 0.01$, $\rho = 0.5$, $\sigma = 0$, $n = 1$ and $h = -1$ values.

x/y	0.01	0.02	0.03	0.04	0.05
0.01	3.3×10^{-9}	4.9×10^{-9}	6.6×10^{-9}	8.3×10^{-9}	9.9×10^{-9}
0.02	4.9×10^{-9}	6.6×10^{-9}	8.3×10^{-9}	9.9×10^{-9}	1.1×10^{-8}
0.03	6.6×10^{-9}	8.3×10^{-9}	9.9×10^{-9}	1.1×10^{-8}	1.3×10^{-8}
0.04	8.3×10^{-9}	9.9×10^{-9}	1.1×10^{-8}	1.3×10^{-8}	1.4×10^{-8}
0.05	9.9×10^{-9}	1.1×10^{-8}	1.3×10^{-8}	1.4×10^{-8}	1.6×10^{-8}

4 RESULTS AND DISCUSSION

Figure 1 indicates the three-dimensional plots of the $w(x, y, t)$ solution via conformable q-Shehu homotopy analysis transform method for different values α of conformable time-fractional Navier-Stokes equation. Figure 2 illustrates the three-dimensional representations of the $q(x, y, t)$ solution via conformable q-Shehu homotopy analysis transform method for different values α of conformable time-fractional Navier-Stokes equation. Figure 3 illustrates the behaviors of conformable q-Shehu homotopy analysis transform method solutions for equations (28)-(29) of conformable time-fractional Navier-Stokes equation, represented by two-dimensional graphs, with varying values of α. Table 1 displays the absolute error between the actual solution and $w(x, y, t)$ derived from the conformable q-Shehu homotopy analysis transform method solution for $\alpha = 1$ in accordance with equation (28). Table 2 presents the absolute error between the exact solution and the $w(x, y, t)$ derived from the conformable q-Shehu homotopy analysis transform method solution for $\alpha = 1$, as indicated in equation (29). Fractional solutions (Figures 1-3) provide new physical insights compared to integer-order models because they capture memory effects and anomalous diffusion more accurately. Unlike integer-order models, which assume local and instantaneous interactions, fractional derivatives introduce a non-local dependency, meaning that the current state of the system is influenced by past states. This is particularly important in fluid dynamics, where real-world flows often exhibit history-dependent behavior. The obtained two dimensional and three dimensional graphical representations in Figures 1-3 illustrate these differences clearly. The fractional-order solutions exhibit smoother transitions and long-range correlations, indicating the presence of memory effects in the fluid's motion. In porous media or non-Newtonian fluids, fractional models better describe subdiffusive or superdiffusive behaviors, whereas integer-order models often oversimplify these effects. The variation in solution behavior with different fractional

orders provides a more flexible framework to model real-world fluids more accurately than classical Navier-Stokes equations. Moreover, error analysis suggests that fractional models achieve higher accuracy in capturing such complex behaviors, reinforcing their significance in practical applications.

5 CONCLUSION AND SUGGESTIONS

The new numerical solutions of conformable time-fractional Navier-Stokes equation have been derived using conformable q-Shehu homotopy analysis transform method. Furthermore, two-dimensional and three-dimensional visualizations of the numerical solutions of conformable time-fractional Navier-Stokes equation have been generated using the Maple software package. The behavior of the numerical solutions for varying α values diverges from the analytical solutions of the equations as the two- and three-dimensional α values move away from unity. Nevertheless, the absolute errors derived from the numerical solutions have proven to be quite small. The derived numerical solutions have shown that conformable q-Shehu homotopy analysis transform method is both effective and reliable. This technique can be used to solve conformable time-fractional partial differential equations numerically.

Acknowledgements

We would like to thank the referees and editors for their valuable contributions.

Conflict of Interest Statement

There is no conflict of interest between the authors.

Statement of Research and Publication Ethics

The study is complied with research and publication ethics.

Artificial Intelligence (AI) Contribution Statement

This manuscript was entirely written, edited, analyzed, and prepared without the assistance of any artificial intelligence (AI) tools. All content, including text, data analysis, and figures, was solely generated by the authors.

Contributions of the Authors

A.A.: Conceptualization, Methodology, Validation, Formal Analysis, H.B.: Writing—Original Draft Preparation, and Data Curation, T.A.: Writing—Reviewing and Editing, Visualization, and Investigation.

REFERENCES

[1] K. S. Miller, and B. Ross, *An introduction to the fractional calculus and fractional differential equations,* Wiley, New York, 1993, pp. 363.

[2] I. Podlubny, *Fractional Differential Equations*, Academic Press, New York, 1999, pp. 337.

[3] D. Baleanu, K. Diethelm, E. Scalas, and J. J. Trujillo, *Fractional calculus: models and numerical methods*, World Scientific, London, 2012, pp. 476.

[4] Y. Povstenko, *Linear fractional diffusion-wave equation for scientists and engineers,* Birkhäuser, Switzerland, 2015, pp. 460.

[5] D. Baleanu, G. C. Wu, and S. D. Zeng, "Chaos analysis and asymptotic stability of generalized Caputo fractional differential equations," *Chaos Soliton Fractals,* vol. 102, pp. 99–105, 2017.

[6] N. H. Sweilam, M. M. Abou Hasan, D. Baleanu, "New studies for general fractional financial models of awareness and trial advertising decisions," *Chaos Soliton Fractals*, vol. 104, pp. 772-784, 2017.

[7] D. Y. Liu, O. Gibaru, W. Perruquetti, T. M. Laleg-Kirati, "Fractional order differentiation by integration and error analysis in noisy environment," *IEEE Trans Automat*, vol. 60, pp. 2945–2960, 2015.

[8] A. Esen, T. A. Sulaiman, H. Bulut, and H. M. Baskonus, "Optical solitons to the space-time fractional (1+1)-dimensional coupled nonlinear Schrödinger equation," *Optik*, vol. 167, pp. 150–156, 2018.

[9] R. Caponetto, G. Dongola, L. Fortuna, and A. Gallo, "New results on the synthesis of FO-PID controllers," *Commun. Nonlinear Sci. Numer. Simul.,* vol. 15, pp. 997-1007, 2010.

[10] P. Veeresha, D. G. Prakasha, and H. M. Baskonus, "Novel simulations to the time-fractional Fisher's equation," *Math. Sci.,* vol. 13, no. 1, pp. 33-42, 2019.

[11] R. Khalil, M. Al Horani, A. Yousef, and M. Sababheh, "A new definition of fractional derivative," *J. Comput. Appl. Math.,* vol. 264, pp. 65-70, 2014.

[12] T. Abdeljawad, "On conformable fractional calculus," *J. Comput. Appl. Math.,* vol. 279, pp. 57-66, 2015.

[13] A. Alkan, T. Aktürk, and H. Bulut, " The Traveling Wave Solutions of the Conformable Time-Fractional Zoomeron Equation by Using the Modified Exponential Function Method," *Eskişehir Technical University Journal of Science and Technology A-Applied Sciences and Engineering*, vol. *25, no.* 1, pp. 108-114, 2024.

[14] T. Aktürk, A. Alkan, H. Bulut, and N. Güllüoğlu, "The Traveling Wave Solutions of Date–Jimbo–Kashiwara–Miwa Equation with Conformable Derivative Dependent on Time Parameter," *Ordu Üniversitesi Bilim ve Teknoloji Dergisi,* vol. 14, no. 1, pp. 38-51, 2024.

[15] A. Kartal, H. Anaç, and A. Olgun, "Numerical solution of conformable time fractional generalized Burgers equation with proportional delay by new methods," *Karadeniz Fen Bilimleri Dergisi*, vol. *13*, no. 2, pp. 310-335, 2023.

[16] A. Kartal, H. Anaç, and A. Olgun, "The new numerical solutions of conformable time fractional generalized Burgers equation with proportional delay," *Gümüşhane Üniversitesi Fen Bilimleri Dergisi*, vol. *13, no.* 4, pp. 927-938, 2023.

[17] H. Poincaré, "Sur l'équilibre d'une masse fluide animée d'un mouvement de rotation," *Bulletin Astronomique,* vol. 2, no.1, pp. 109-118, 1885.

[18] G. Adomian, "Analytical solution of Navier-Stokes flow of a viscous compressible fluid," *Found. Phys. Lett.,* vol. 8, pp. 389–400, 1995.

[19] M. Krasnoschok, V. Pata, S. V. Siryk, and N. Vasylyeva, "A subdiffusive Navier-Stokes-Voigt system," *Phys. D Nonlinear Phenom.,* vol. 409, pp. 132503, 2020.

[20] S. Momani, and Z. Odibat, " Analytical solution of a time-fractional Navier–Stokes equation by Adomian decomposition method," *Applied Mathematics and Computation*, vol. *177, no.* 2, pp. 488-494, 2006.

[21] Q. Yu, J. Song, F. Liu, V. Anh, I. Turner, "An approximate solution for the Rayleigh-Stokes problem for a heated generalized second grade fluid with fractional derivative model using the Adomian decomposition method," J. Algorithms Comput. Technol., vol. 3, pp. 553-571, 2009.

[22] M. Krasnoschok, V. Pata, S. V. Siryk, N. Vasylyeva, "Equivalent definitions of Caputo derivatives and applications to subdiffusion equations," *Dyn. PDE,* vol. 17, pp. 383–402, 2020.

[23] E. Bazhlekova, B. Jin, R. Lazarov, Z. Zhou, "An analysis of the Rayleigh-Stokes problem for a generalized second-grade fluid," *Numer. Math.*, vol. 131, pp. 1–31, 2015.

[24] M. El-Shahed, and A. Salem, "On the generalized Navier-Stokes equations," *Appl. Math. Comput.*, vol. 156, pp. 287–293, 2004.

[25] D. Kumar, J. Singh, S. Kumar, "A fractional model of Navier-Stokes equation arising in unsteady flow of a viscous fluid," *J. Assoc. Arab. Univ. Basic Appl. Sci.,* vol. 17, pp. 14–19, 2015.

[26] Z. Z. Ganji, D. D. Ganji, A. D. Ganji, and M. Rostamian, "Analytical solution of time-fractional Navier-Stokes equation in polar coordinate by homotopy perturbation method," *Numerical Methods for Partial Differential Equations: An International Journal,* vol. 26, pp. 117–124, 2010.

[27] A. A. Ragab, K. M. Hemida, M. S. Mohamed, and M. A. Abd El Salam, "Solution of time-fractional Navier-Stokes equation by using homotopy analysis method," *Gen. Math. Notes,* vol. 13, pp. 13–21, 2012.

[28] S. Maitama, "Analytical solution of time-fractional Navier-Stokes equation by natural homotopy perturbation method," *Prog. Fract. Differ. Appl.,* vol. 4, pp. 123–131, 2018.

[29] G. A. Birajdar, "Numerical solution of time fractional Navier-Stokes equation by discrete Adomian decomposition method," *Nonlinear Eng.,* vol. 3, pp. 21–26, 2014.

[30] S. Kumar, S.; Kumar, D.; Abbasbandy, S.; Rashidi, M.M. Analytical solution of fractional Navier-Stokes equation by using modified Laplace decomposition method. *Ain Shams Eng. J.,* 2014, 5, 569–574.

[31] V. B. L. Chaurasia, and D. Kumar, "Solution of the time-fractional Navier-Stokes equation," *Gen. Math. Notes*, vol. 4, pp. 49–59, 2011.

[32] A. Prakash, P. Veeresha, D. G. Prakasha, and M. Goyal, "A new efficient technique for solving fractional coupled Navier-Stokes equations using q-homotopy analysis transform method," *Pramana,* vol. 93, pp. 1–10, 2019.

[33] S. Mukhtar, R. Shah, and S. Noor, "The numerical investigation of a fractional-order multi-dimensional Model of Navier–Stokes equation via novel techniques," *Symmetry*, vol. *14,* no. 6, pp. 1102, 2022.

[34] M. A. El-Tawil, and S. N. Huseen, "The q-homotopy analysis method (q-HAM)," *Int. J. Appl. Math. Mech*, vol. *8*, no. 15, pp. 51-75, 2012.

[35] S. Liao, On the homotopy analysis method for nonlinear problems," *Applied mathematics and computation*, vol. *147,* no. 2, pp. 499-513, 2004.

[36] S. Liao, "Comparison between the homotopy analysis method and homotopy perturbation method," *Applied Mathematics and Computation*, vol. *169,* no. 2, pp.1186-1194, 2005.

[37] S. J. Liao, "Homotopy analysis method and its applications in mathematics," *J. Basic Sci. Eng.*, vol. 5, no. 2, pp. 111–125, 1997.

[38] S. J. Liao, "Homotopy analysis method: a new analytic method for nonlinear problems," *Appl. Math. Mech.*, vol. 19, pp. 957–962, 1998.

[39] J. H. He, "Homotopy perturbation method: a new nonlinear analytical technique," *Applied Mathematics and computation*, vol. *135*, no. 1, pp. 73-79, 2003.

[40] J. H. He, "Addendum: new interpretation of homotopy perturbation method," *International journal of modern physics B*, vol. *20,* no. 18, pp. 2561-2568, 2006.

[41] S.A Khuri, "A Laplace decomposition algorithm applied to class of nonlinear differential equations," *J Math. Appl.*, vol. 4, pp. 141 – 155, 2001.

[42] S. A. Khuri, "A new approach to Bratu's problem," *Applied mathematics and computation*, vol. *147, no.* 1, pp. 131-136, 2004.

[43] H. Anaç, "Conformable Fractional Elzaki Decomposition Method of Conformable Fractional Space-Time Fractional Telegraph Equations," *Ikonion Journal of Mathematics*, vol. *4*, no. 2, pp. 42-55, 2022.

[44] A. S. Erol, H. Anaç, and A. Olgun, "Numerical solutions of conformable time-fractional Swift-Hohenberg equation with proportional delay by the novel methods," *Karamanoğlu Mehmetbey Üniversitesi Mühendislik ve Doğa Bilimleri Dergisi*, vol. *5*, no. 1, pp. 1-24, 2023.

[45] M. E. Benattıa, and K. Belghaba, "Shehu conformable fractional transform, theories and applications," *Cankaya University Journal of Science and Engineering*, vol. *18*, no. 1, pp. 24-32, 2021.

[46] D. Kumar, J. Singh, and D. Baleanu, "A new analysis for fractional model of regularized long-wave equation arising in ion acoustic plasma waves," *Math. Methods Appl. Sci.,* vol. 40, no. 15, pp. 5642–5653, 2017.

[47] Á. A. Magreñán, "A new tool to study real dynamics: the convergence plane," *Appl. Math. Comput., v*ol. 248, pp. 215–224, 2014.

[48] H. A. Peker, and F. A. Cuha, "Application of Kashuri Fundo transform and homotopy perturbation methods to fractional heat transfer and porous media equations," *Thermal Science*, vol. 26, no. 4A, pp. 2877-2884, 2022.

[49] D. R. Anderson, E. Camrud, and D. J. Ulness, "On the nature of the conformable derivative and its applications to physics," *J. Fract. Calc. Appl*, vol. 10, no. 2, pp. 92-135, 2019.

[50] R. Kumar, R. Dharra, and S. Kumar, "Comparative qualitative analysis and numerical solution of conformable fractional derivative generalized KdV-mKdV equation," *International Journal of System Assurance Engineering and Management*, vol. 14, no. 4, pp. 1247-1254, 2023.

BİTLİS EREN ÜNİVERSİTESİ
FEN BİLİMLERİ DERGİSİ

ISSN: 2147-3129 / e-ISSN: 2147-3188

Article Type	: Research Article	**Year**	: 2025
Received	: December 13, 2024	**Volume**	: 14
Revised	: August 22, 2025	**Issue**	: 3
Accepted	: August 22, 2025	**Pages**	: 1348-1361
DOI	: 10.17798/bitlisfen.1600715		

A UNIFORMLY CONVERGENT DIFFERENCE SCHEME FOR THE SINGULARLY PERTURBED PERIODIC PROBLEM

Erkan CIMEN [1]

[1] *Van Yüzüncü Yıl University, Department of Mathematics, Van, Türkiye, cimenerkan@hotmail.com*

ABSTRACT

In this article, a novel numerical scheme is suggested to solve periodical boundary value problem for linear first order singularly perturbed equation. This scheme is constructed by the finite difference method on a special non-uniform mesh (Shishkin mesh) using quadrature rules with the remaining terms in integral form. It is proven that the scheme achieves almost first-order convergence on the discrete maximum norm. Finally, two test problems are considered to demonstrate the accuracy and performance of the method.

Keywords: Singular perturbation, Periodic problem, Finite difference method, Uniform convergence.

1 INTRODUCTION

If a differential equation involves a small positive parameter multiplied by its highest-order derivative, it is called a singularly perturbed differential equation (SPDE). These equations occur as models in science and engineering various fields. For example, they appear in fluid dynamics, chemical reactor theory, enzyme kinetics, quantum mechanics, elasticity, electrical networks, etc. [9]-[11], [15]. In particular, singularly perturbed periodical boundary value problem arises as models in geophysical fluid dynamics [6], in oceanic and atmospheric circulation [11]. Motivated by the above works, we analyze the following problem:

$$\varepsilon u'(t) + a(t)u(t) = f(t), 0 < t < T, \tag{1}$$

$$u(0) = u(T), \tag{2}$$

where $0 < \varepsilon \ll 1$ is the small positive parameter (so called perturbation parameter). Also, $a(t) \geq \alpha > 0, f(t)$ are given functions on $\bar{I} = [0, T]$. We assume that these functions sufficiently smooth (i.e. desired continuous derivatives on $\bar{I}$) and moreover $a(t+T) = a(t), f(t+T) = f(t)$. Furthermore, if $a, f \in C(\bar{I})$, then the problem (1)-(2) has a unique solution $u(t) \in C^1(\bar{I})$, which also satisfies condition (2) (for details see [1]). Studies on the existence and uniqueness of such problems can be found in [1] and references therein.

Since the solutions of SPDEs have initial (or boundary) layers that depend on the ε-parameter, classical numerical methods used to solve such problems are unstable and do not yield accurate results. Therefore, it is necessary to develop appropriate numerical methods that are uniformly convergent with respect to ε. One can also refer [9], [10], [12], [15], for more information about the perturbation theory and layer adapted meshes. Furthermore, in decade years, researchers have studied and improved many aspects of numerical methods for the singularly perturbed problems [3]-[5], [8], [16], [18].

We encounter a few periodic SPDEs studies in the literature, to mention them: Amiraliyev and Duru [2] solved the second-order periodic SPDE by using finite difference scheme on uniform mesh and prove that approximations are first order convergence in the maximum norm. In [7], Cen considered the same problem and proposed a hybrid finite difference scheme on a Shishkin mesh which is proved to be second-order accurate. In [13] the authors proposed cubic spline scheme on variable mesh for solving the same problem. In [14] the authors solved the system of the second-order periodic problem and presented a hybrid scheme using piecewise uniform mesh. These articles involve second-order ones; we did not come across any studies on first-order SPDEs. The motivation for our study is formed by these gaps in the literature.

The main purpose of this paper is to present a uniformly convergent method for solving (1)-(2). This method consists of a fitted difference scheme given on the piecewise uniform mesh (called Shishkin mesh). The scheme is constituted using the finite difference method and appropriate quadrature rules with the terms remaining in the integral form, which is based on the Taylor polynomial whose remaining term is in integral form. Hereby, the truncation errors involve only the first-order derivative of the exact solution, making convergence easier to examine. Since the truncation errors of the above methods include two or higher-order derivatives of the exact solution, the presented method is more advantageous.

The problem (1)-(2) has a boundary layer in a small neighborhood of $t = 0$ when $0 < \varepsilon \ll 1$. The proposed method to solve the problem causes instability on the uniform mesh. We used Shishkin mesh, also called piecewise uniform mesh, to improve this instability. Readers can refer to [9,10,15] for more detailed information on this topic.

The arrangement of the paper: In next section we state the analytical results of solution for (1)-(2) and its derivative and we construct a finite difference scheme and introduce the layer-adapted non-uniform meshes. In Section 3, we perform error analysis and give convergence results on these meshes. In Section 4, we present numerical experiments, which confirm the theoretical results. In the final section, we give a summary of the main conclusions.

From now on, C is defined as a general positive constant that is not only independent of ε but also of the mesh parameter N. Moreover, for any $w(t) \in C(\bar{I})$, the norm defined below will be used:

$$\|w\|_\infty = \max_{t\in\bar{I}} |w(t)|.$$

2 MATERIAL AND METHOD

2.1 The Behavior of the Exact Solution

Here, some estimations of the exact solution of (1)-(2) are given that are needed in later sections.

Lemma 2.1. If $a, f \in C^1(\bar{I})$ and $1 - e^{-\frac{\alpha T}{\varepsilon}} \geq \delta > 0$, then the following inequalities

$$\|u\|_\infty \leq (1 + \delta^{-1})\alpha^{-1}\|f\|_\infty, \tag{3}$$

$$|u'(t)| \leq C\left(1 + \frac{1}{\varepsilon}e^{-\frac{\alpha t}{\varepsilon}}\right), \tag{4}$$

hold.

Proof. From Eq.(1), we can write,

$$u(t) = u(0)e^{-\frac{1}{\varepsilon}\int_0^t a(\tau)d\tau} + \frac{1}{\varepsilon}\int_0^t f(\xi)\, e^{-\frac{1}{\varepsilon}\int_\xi^t a(\tau)d\tau} d\xi. \tag{5}$$

Using condition (2), we obtain

$$u(0) = \frac{\frac{1}{\varepsilon}\int_0^T f(\xi)\, e^{-\frac{1}{\varepsilon}\int_\xi^T a(\tau)d\tau} d\xi}{1 - e^{-\frac{1}{\varepsilon}\int_0^T a(\tau)d\tau}}. \tag{6}$$

From (5), taking into account $u(0)$ in (6), we have

$$u(t) = \frac{e^{-\frac{1}{\varepsilon}\int_0^t a(\tau)d\tau}}{1-e^{-\frac{1}{\varepsilon}\int_0^T a(\tau)d\tau}}\frac{1}{\varepsilon}\int_0^T f(\xi)\,e^{-\frac{1}{\varepsilon}\int_\xi^T a(\tau)d\tau}d\xi + \frac{1}{\varepsilon}\int_0^t f(\xi)\,e^{-\frac{1}{\varepsilon}\int_\xi^t a(\tau)d\tau}d\xi.$$

Also, since $a(t) \geq \alpha > 0$, we get

$$1-e^{-\frac{1}{\varepsilon}\int_0^T a(\tau)d\tau} \geq 1-e^{-\frac{\alpha T}{\varepsilon}} \geq \delta > 0.$$

From this inequality, we have

$$|u(t)| \leq \frac{e^{-\frac{\alpha t}{\varepsilon}}}{\delta}\frac{1}{\varepsilon}\int_0^T |f(\xi)|\,e^{-\frac{\alpha}{\varepsilon}(T-\xi)}d\xi + \frac{1}{\varepsilon}\int_0^t |f(\xi)|\,e^{-\frac{\alpha}{\varepsilon}(t-\xi)}d\xi$$

$$\leq \frac{e^{-\frac{\alpha t}{\varepsilon}}}{\delta}\frac{1}{\varepsilon}\|f\|_\infty\int_0^T e^{-\frac{\alpha}{\varepsilon}(T-\xi)}d\xi + \frac{1}{\varepsilon}\|f\|_\infty\int_0^t e^{-\frac{\alpha}{\varepsilon}(t-\xi)}d\xi$$

$$\leq \frac{e^{-\frac{\alpha t}{\varepsilon}}}{\delta}\|f\|_\infty\alpha^{-1}\left(1-e^{-\frac{\alpha T}{\varepsilon}}\right) + \|f\|_\infty\alpha^{-1}\left(1-e^{-\frac{\alpha t}{\varepsilon}}\right),$$

which leads (3).

Now, for (4), if we differentiate Eq. (1) once, we can write

$$\varepsilon u''(t) + a(t)u'(t) = F(t),$$

with

$$F(t) = f'(t) - a'(t)u(t),$$

and from the solution of this equation, for $u'(t)$, we can write

$$u'(t) = u'(0)e^{-\frac{1}{\varepsilon}\int_0^t a(\zeta)d\zeta} + \frac{1}{\varepsilon}\int_0^t F(\xi)\,e^{-\frac{1}{\varepsilon}\int_\xi^t a(\zeta)d\zeta}d\xi.$$

And from here, we have

$$|u'(t)| \leq |u'(0)|e^{-\frac{\alpha t}{\varepsilon}} + \frac{1}{\varepsilon}\int_0^t |F(\xi)|\,e^{-\frac{\alpha}{\varepsilon}(t-\xi)}d\xi. \tag{7}$$

From conditions of Lemma 2.1 and (3), we get $\|F\|_\infty \leq C$. Therefore, from (7), we can write

$$|u'(t)| \leq |u'(0)|e^{-\frac{\alpha t}{\varepsilon}} + \|F\|_\infty\alpha^{-1}\left(1-e^{-\frac{\alpha t}{\varepsilon}}\right).$$

From (1), we can write

$$|u'(0)| \leq \frac{1}{\varepsilon}[|f(0)| + |a(0)||u(0)|].$$

When Eq. (6) is taken into account in this inequality, we obtain

$$|u'(0)| \leq \frac{\delta^{-1}}{\varepsilon}\int_0^T |f(\xi)|\, e^{-\frac{1}{\varepsilon}\int_\xi^T a(\tau)d\tau} d\xi \leq \frac{C}{\varepsilon}.$$

If we consider this last inequality in (7), we can write

$$|u'(t)| \leq |u'(0)|e^{-\frac{\alpha t}{\varepsilon}} + \|F\|_\infty \alpha^{-1}\left(1 - e^{-\frac{\alpha t}{\varepsilon}}\right)$$

$$\leq \frac{C}{\varepsilon}e^{-\frac{\alpha t}{\varepsilon}} + C\alpha^{-1}\left(1 - e^{-\frac{\alpha t}{\varepsilon}}\right),$$

which completes the proof.

2.2 The Difference Scheme and the Layer-Adapted Mesh

Let a non-uniform mesh is defined on I as: $\omega = \{0 < t_1 < t_2 < \cdots < t_{N-1} < t_N = T\}$ and $\bar{\omega} = \omega \cup \{t_0 = 0\}$. Also, we establish the stepsize $h_i = t_i - t_{i-1}$ for $1 \leq i \leq N$. For simplicity, we will use $v_i = v(t_i)$. We will denote the approximation of $u(t)$ at t_i as y_i. Besides, for $\{v_i\}$, we will use the difference derivative and norm defined on $\bar{\omega}$ as:

$$v_{\bar{t},i} = \frac{v_i - v_{i-1}}{h_i}, \|v\|_{\infty,\bar{\omega}} = \max_{0\leq i\leq N}|v_i|.$$

To obtain numerical approximation for the problem (1)-(2), integrating Eq. (1) over (t_{i-1}, t_i), we obtain

$$\varepsilon u_{\bar{t},i} + a_i u_i = f_i - R_i, 1 \leq i \leq N-1, \tag{8}$$

with remainder term

$$R_i = h_i^{-1}\int_{t_{i-1}}^{t_i} (t - t_{i-1})\frac{d}{dt}[f(t) - a(t)u(t)]dt. \tag{9}$$

If we neglect R_i in (9), we propose the following difference scheme for approximating (1)-(2):

$$\varepsilon y_{\bar{t},i} + a_i y_i = f_i, 1 \leq i \leq N-1, \tag{10}$$

$$y_0 = y_N. \tag{11}$$

For the difference schemes (10)-(11) to be ε-uniformly convergent, we will use the following special mesh (known as Shishkin mesh, shortly S-mesh, for more details see [10]).

The piecewise uniform mesh divides equidistantly each of the intervals $[0,\sigma]$ and $[\sigma,T]$ into $N/2$ subintervals (N is an even positive integer), the transition point σ is denoted as:

$$\sigma = \min\left\{\frac{T}{2}, \alpha^{-1}\varepsilon ln N\right\}, \tag{12}$$

$$\bar{\omega} = \begin{cases} t_i = ih^{(1)}, & 0 \le i \le \frac{N}{2}, \quad h^{(1)} = \frac{2\sigma}{N}, \\ t_i = \sigma + \left(i - \frac{N}{2}\right)h^{(2)}, & \frac{N}{2}+1 \le i \le N, \quad h^{(2)} = \frac{2(T-\sigma)}{N}. \end{cases}$$

3 CONVERGENCE ANALYSIS

In this section, we will investigate the uniform convergence of the presented method. For this, we will define the error function z as follows:

$z_i = y_i - u_i, 1 \le i \le N-1.$

From (8) and (10), we have

$$\varepsilon z_{\bar{t},i} + a_i z_i = -R_i, \tag{13}$$

$$z_0 = z_N, \tag{14}$$

where R_i is described by (9).

Lemma 3.1. Suppose y_i is the solution of (10)-(11) and

$$1 - \frac{1}{[1+\alpha h^{(1)}/\varepsilon]^{N/2}} - \frac{1}{[1+\alpha h^{(2)}/\varepsilon]^{N/2}} \ge \delta_* > 0.$$

Then the estimate

$$\|y\|_{\infty,\bar{\omega}} \le C\|f\|_{\infty,\bar{\omega}} \tag{15}$$

holds.

Proof. From Eq. (10), we can rewrite

$$y_i = q_i y_{i-1} + g_i, \tag{16}$$

where

$$q_i = \frac{\varepsilon}{\varepsilon + a_i h_i}, g_i = \frac{h_i f_i}{\varepsilon + a_i h_i}.$$

When (11) and (16) are considered together, a first-order difference equation is obtained. The solution of this equation is

$$y_i = y_0 Q_i + \sum_{k=1}^{i} g_k Q_{i-k}, \tag{17}$$

where

$$Q_{i-k} = \begin{cases} 1, & k = i, \\ \prod_{j=k+1}^{i} q_j, & 0 \le k \le i-1. \end{cases}$$

If we write $i = N$ in (17), we get

$$y_N = y_0 Q_N + \sum_{k=1}^{N} g_k Q_{N-k}.$$

If we take into account condition (11) in this equation, we easily obtain

$$y_0 = \frac{\sum_{k=1}^{N} g_k Q_{N-k}}{1 - Q_N}. \tag{18}$$

If we take this value into account in (17), we have

$$y_i = \frac{Q_i}{1 - Q_N} \sum_{k=1}^{N} g_k Q_{N-k} + \sum_{k=1}^{i} g_k Q_{i-k}.$$

From here,

$$1 - Q_N = 1 - \prod_{i=1}^{N} \frac{1}{1 + a_i h_i/\varepsilon} \ge 1 - \prod_{i=1}^{N} \frac{1}{1 + \alpha h_i/\varepsilon},$$

$$\prod_{i=1}^{N} \frac{1}{1 + \alpha h_i/\varepsilon} = \prod_{i=1}^{N/2} \frac{1}{1 + \alpha h^{(1)}/\varepsilon} + \prod_{i=\frac{N}{2}+1}^{N} \frac{1}{1 + \alpha h^{(2)}/\varepsilon}$$

$$= \frac{1}{[1 + \alpha h^{(1)}/\varepsilon]^{N/2}} + \frac{1}{[1 + \alpha h^{(2)}/\varepsilon]^{N/2}}$$

$$1 - Q_N \ge 1 - \frac{1}{[1 + \alpha h^{(1)}/\varepsilon]^{N/2}} - \frac{1}{[1 + \alpha h^{(2)}/\varepsilon]^{N/2}}.$$

It is easily to see that the absolute value of the numerator in (18) is bounded by $C\|f\|_{\infty,\bar{\omega}}$ and the denominator is bounded from below by δ_*, thereby will be

$|y_0| \le C\|f\|_{\infty,\bar{\omega}}$.

Then, if the principle of discrete maximum is applied to the difference operator [17] $\ell_h y_i \equiv \varepsilon y_{\bar{t},i} + a_i y_i = f_i, 1 \le i \le N-1$, to (10) yields

$$|y_i| \le |y_0| + \alpha^{-1}\|f\|_{\infty,\bar{\omega}},$$

which is the complete of proof.

Lemma 3.2. Let z_i be the solution of (13)-(14). Then

$$\|z\|_{\infty,\bar{\omega}} \le C\|R\|_{\infty,\bar{\omega}}.$$

Proof. It evidently follows from (15) by taking $y \equiv z$ and $f \equiv R$.

Lemma 3.3. Under the above assumptions of Lemma 2.1, for the truncation error R, the following estimate holds

$$\|R\|_{\infty,\bar{\omega}} \le CN^{-1}lnN.$$

Proof. From (9), taking into account (3)-(4), we obtain that on an arbitrary mesh:

$$|R_i| \le C\left(h_i + \frac{1}{\varepsilon}\int_{t_{i-1}}^{t_i} e^{-\frac{\alpha t}{\varepsilon}}dt\right)$$

$$\le C\left\{h_i + \alpha^{-1}(e^{-\frac{\alpha t_{i-1}}{\varepsilon}} - e^{-\frac{\alpha t_i}{\varepsilon}})\right\}. \quad (19)$$

And now, we evaluate to R_i in two different cases for σ values in (12). Firstly, let $\sigma = T/2$. Then $\frac{T}{2} < \alpha^{-1}\varepsilon lnN$ and $h^{(1)} = h^{(2)} = T/2$. Take these conditions into account in (19):

$$|R_i| \le C\left\{h_i + \alpha^{-1}(e^{-\frac{\alpha t_{i-1}}{\varepsilon}} - e^{-\frac{\alpha t_i}{\varepsilon}})\right\}$$

$$\le C\left\{\frac{T}{N}+\alpha^{-1}\right\} \le C\left\{\frac{2\alpha^{-1}\varepsilon lnN}{N} + \alpha^{-1}\right\} \le CN^{-1}lnN.$$

Secondly, let $\sigma = \alpha^{-1}\varepsilon lnN$. We give estimations for subintervals $[0,\sigma]$ and $[\sigma,T]$. If $t \in [0,\sigma]$, $h^{(1)} = \frac{2\sigma}{N}$. So, inequality (19) can be written as follows:

$$|R_i| \le C\left\{h_i + \alpha^{-1}(e^{-\frac{\alpha t_{i-1}}{\varepsilon}} - e^{-\frac{\alpha t_i}{\varepsilon}})\right\}$$

$$\le C\left\{\frac{2\sigma}{N}+\alpha^{-1}\right\} \le C\left\{\frac{2\alpha^{-1}\varepsilon lnN}{N} + \alpha^{-1}\right\} \le CN^{-1}lnN.$$

If $t \in [\sigma,T]$,, $h^{(2)} = \frac{2(T-\sigma)}{N}$ and $t_i = \sigma + (i - N/2)h^{(2)}$. Since

$$e^{-\frac{\alpha t_{i-1}}{\varepsilon}} - e^{-\frac{\alpha t_i}{\varepsilon}} = e^{-\frac{\alpha[\sigma+(i-1-N/2)h^{(2)}]}{\varepsilon}} - e^{-\frac{\alpha[\sigma+(i-N/2)h^{(2)}]}{\varepsilon}}$$

$$= e^{-\frac{\alpha[\alpha^{-1}\varepsilon lnN+(i-1-N/2)h^{(2)}]}{\varepsilon}} - e^{-\frac{\alpha[\alpha^{-1}\varepsilon lnN+(i-N/2)h^{(2)}]}{\varepsilon}}$$

$$= e^{-[lnN+\alpha\varepsilon^{-1}(i-1-N/2)h^{(2)}]} - e^{-[lnN+\alpha\varepsilon^{-1}(i-N/2)h^{(2)}]}$$

$$= e^{-lnN}\left\{e^{-\alpha\varepsilon^{-1}(i-1-N/2)h^{(2)}} - e^{-\alpha\varepsilon^{-1}(i-N/2)h^{(2)}}\right\} \leq CN^{-1},$$

then it follows from (19) that

$$|R_i| \leq C\left\{h_i + \alpha^{-1}(e^{-\frac{\alpha t_{i-1}}{\varepsilon}} - e^{-\frac{\alpha t_i}{\varepsilon}})\right\}$$

$$= C\left\{h^{(2)} + \alpha^{-1}(e^{-\frac{\alpha t_{i-1}}{\varepsilon}} - e^{-\frac{\alpha t_i}{\varepsilon}})\right\} \leq C\left\{h^{(2)} + \alpha^{-1}N^{-1}\right\} \leq CN^{-1}.$$

Thus, the proof of Lemma 3.3 is complete.

Now, if we take into account the above lemmas, we give the following main convergence results.

Theorem 3.1. Let u be the solution of (1)-(2) and y the solution of (10)-(11). Then under hypotheses of Lemmas 1.1 and 4.1

$$\|y - u\|_{\infty,\bar{\omega}} \leq CN^{-1}lnN.$$

Proof. This follows immediately by combining the previous lemmas. That is, if Lemma 3.3. is taken into account in Lemma 3.2, the proof is complete.

4 ALGORITHM AND NUMERICAL EXPERIMENTS

In this section, we consider an example to demonstrate the robustness and effectiveness of our scheme defined by equations (10)-(11). At first, we solve the periodic problem (10)-(11) in the Algorithm. Later on, two test problems are presented in the Numerical experiments.

4.1 Algorithm

From (14) and (15), we can easily obtain the solution of the difference problem (10)-(11):

$$y_i = y_0 Q_i + \sum_{k=1}^{i} g_k Q_{i-k}, 1 \leq i \leq N-1,$$

$$y_0 = \frac{\sum_{k=1}^{N} g_k Q_{N-k}}{1-Q_N}, y_N = y_0.$$

4.2 Numerical Experiments

Using the above algorithm, we present the following two problems. The present numerical scheme defined by (10)-(11) is used to solve the problems for several values ε and N. The results obtained here are given in the following tables and figures.

Example 4.1. We examine the following test problem:

$$\varepsilon u'(t) + [3 + \sin(2t+1)]u(t) = \cos(2t-1), 0 < t < \pi,$$

$$u(0) = u(\pi).$$

Example 4.2. We examine the following another test problem:

$$\varepsilon u'(t) + [5 - \sin(\pi t+1)]u(t) = \frac{1}{2}\cos(\pi t-1), 0 < t < 2,$$

$$u(0) = u(2).$$

The exact solutions of the test problems are unknown. Therefore, for error estimates and analysis of convergence, we use double mesh principle ([5], [9]). That is, $e^{\varepsilon,N}$ is defined as the two mesh differences for $u(t)$ and e^N the maximum two mesh differences as:

$$e^{\varepsilon,N} = \max_{0\le i\le N}\left|y_i^N - y_{2i}^{2N}\right|, e^N = \max_{\varepsilon} e^{\varepsilon,N}.$$

Also, the convergence rates are defined as:

$$p^N = \log_2(e^N/e^{2N}).$$

The test problem is solved for the $\varepsilon = 2^{-4i}, i = 1,2,\ldots,6$. The two mesh differences and the convergence rates are listed in Tables 1-2.

Table 1. Computed maximum two mesh differences and convergence rates for Example 4.1.

ε	$N=64$	$N=128$	$N=256$	$N=512$	$N=1024$
2^{-4}	0.0008456	0.0005312	0.0003184	0.0001842	0.0001042
	0.671	0.739	0.789	0.822	
2^{-8}	0.0006353	0.0003942	0.0002337	0.0001345	0.0000757
	0.689	0.754	0.797	0.829	
2^{-12}	0.0006226	0.0003856	0.0002284	0.0001314	0.0000739
	0.691	0.755	0.798	0.830	
2^{-16}	0.0006218	0.0003851	0.0002281	0.0001312	0.0000738
	0.691	0.756	0.798	0.830	
2^{-20}	0.0006218	0.0003851	0.0002281	0.0001312	0.0000738
	0.691	0.756	0.798	0.830	
2^{-24}	0.0006218	0.0003850	0.0002281	0.0001312	0.0000738
	0.691	0.756	0.798	0.830	
e^N	0.0008456	0.0005312	0.0003184	0.0001842	0.0001042
p^N	0.671	0.739	0.789	0.822	

Table 2. Computed maximum two mesh differences and convergence rates for Example 4.2.

ε	$N = 64$	$N = 128$	$N = 256$	$N = 512$	$N = 1024$
2^{-4}	0.0011790	0.0007121	0.0004159	0.0002370	0.0001327
	0.727	0.776	0.811	0.837	
2^{-8}	0.0012686	0.0007649	0.0004460	0.0002539	0.0001421
	0.730	0.778	0.813	0.837	
2^{-12}	0.0012743	0.0007683	0.0004479	0.0002550	0.0001427
	0.730	0.778	0.813	0.838	
2^{-16}	0.0012747	0.0007685	0.0004480	0.0002551	0.0001427
	0.730	0.779	0.812	0.838	
2^{-20}	0.0012747	0.0007685	0.0004480	0.0002551	0.0001427
	0.730	0.779	0.812	0.838	
2^{-24}	0.0012747	0.0007685	0.0004480	0.0002551	0.0001427
	0.730	0.779	0.812	0.838	
e^N	0.0012747	0.0007685	0.0004480	0.0002551	0.0001427
p^N	0.730	0.779	0.812	0.838	

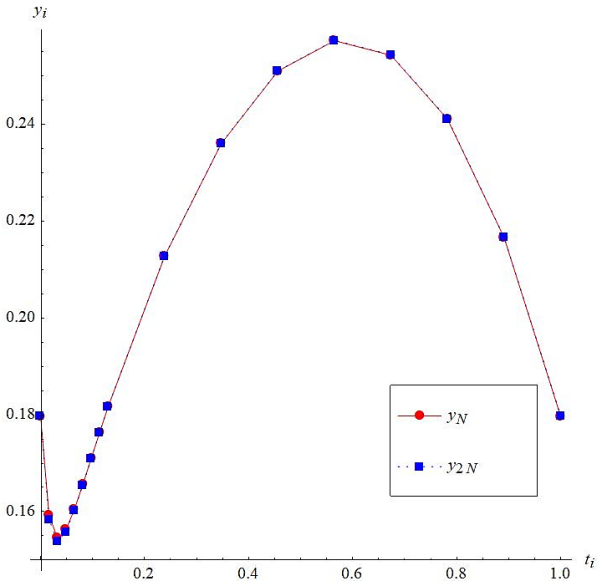


Figure 1. Computational results obtained using two-mesh differences for Example 4.1 ($N = 64$ and $\varepsilon = 2^{-4}$).

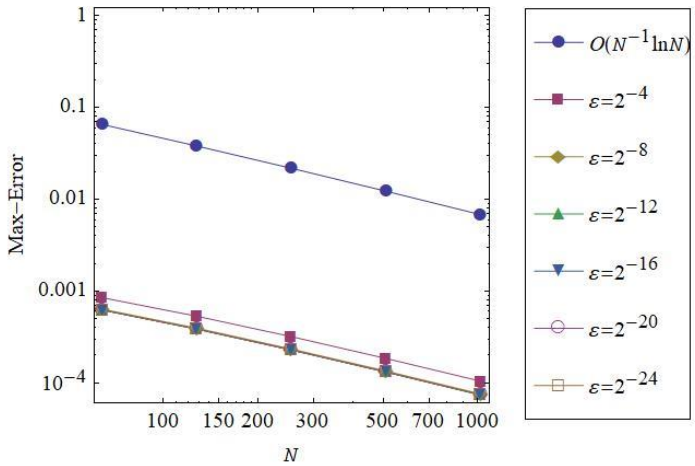


Figure 2. Maximum point-wise errors obtained using various ε and N for Example 4.1.

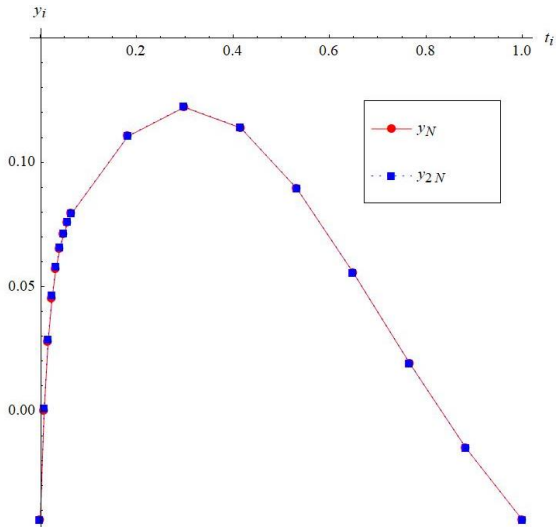


Figure 3. Computational results obtained using two-mesh differences for Example 4.2 ($N = 64$ and $\varepsilon = 2^{-4}$).

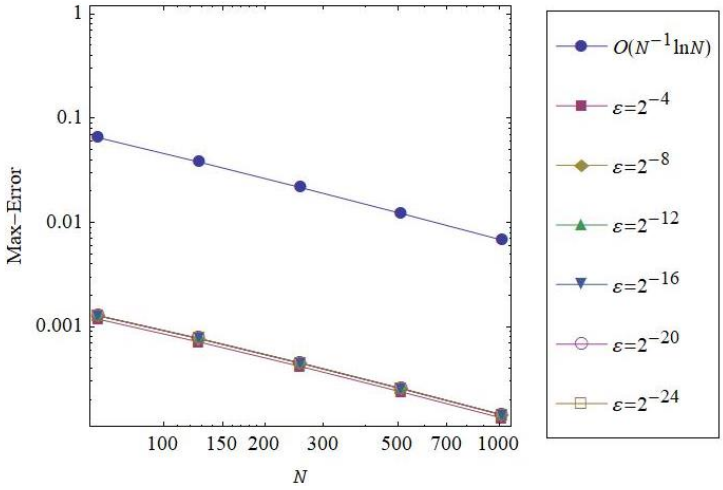


Figure 4. Maximum point-wise errors obtained using various ε and N for Example 4.2.

The data in Tables 1-2 contain the numerical results obtained from Example 4.1 and Example 4.2 for various values of N and the perturbation parameter. These results demonstrate that, for u, as the number of mesh points (N) increase, the maximum two mesh differences (e^N) monotonically decrease and the convergence rates (p^N) monotonically increase. computational results of the problem using S-Mesh are shown in Figures 1-4. These results indicate that the solution u at $t = 0$ is the boundary layer. All these results imply that these errors are bounded by $O(N^{-1}lnN)$, and are proven in Theorem 4.1. Moreover, all results were obtained in less than 20 seconds (for each ε and N) using an average modern computer, which indicates reasonable computational efficiency.

5 CONCLUSION AND SUGGESTIONS

In this work, the periodical problem for the first order linear SPDE is dealt with. For the approximate solution to this problem, a novel fitted difference scheme was constructed on the S-mesh by using the finite difference method. The convergence and stability of the proposed numerical method have been discussed. Furthermore, for the test problems, the numerical results as the computed two mesh differences and the rates of convergence were given in the tables and figures. According to these results, it was observed that the scheme is stable and has convergence almost first order when using S-Mesh, which supported the theoretical results. From all these results, it was concluded that the suggested approach is effective and accurate. The offered method in this study can be applied to the numerical solution of nonlinear type singularly perturbed periodical, and the delay differential equations. If a nonlinear problem is considered, then it will be more difficult to evaluate the convergence results since the difference scheme is nonlinear. This can be examined as another subject of study.

Statement of Research and Publication Ethics

The study is complied with research and publication ethics.

Artificial Intelligence (AI) Contribution Statement

This manuscript was entirely written, edited, analyzed, and prepared without the assistance of any artificial intelligence (AI) tools. All content, including text, data analysis, and figures, was solely generated by the authors.

REFERENCES

[1] E. Ait Dads, B. Es-sebbar and L. Lhachimi, "On the behavior of solutions of some periodic differential equations," *Journal of Mathematical Analysis and Applications*, vol. 544(1), pp. 1-29, 2025.

[2] G. M. Amiraliyev and H. Duru, "A uniformly convergence difference method for the periodical boundary value problem," *Computers & Mathematics with Applications*, vol. 46, pp. 695-703, 2003.

[3] M. Cakir and D. Arslan, "A new numerical approach for a singularly perturbed problem with two integral boundary conditions," *Computational and Applied Mathematics*, vol. 40, pp. 1-17, 2021.

[4] M. Cakir and E. Cimen, "A novel uniform numerical approach to solve a singularly perturbed Volterra integro-differential equation," *Computational Mathematics and Mathematical Physics*, vol. 63, pp. 1800-1816, 2023.

[5] M. Cakir, Y. Ekinci and E. Cimen, "A numerical approach for solving nonlinear Fredholm integro-differential equation with boundary layer," *Computational and Applied Mathematics*, vol. 41, pp. 1-14, 2022.

[6] G. F. Carrier, "Singular perturbations and geophysics," *SIAM Review*, vol. 12, pp. 175-193, 1970.

[7] Z. Cen, "Uniformly convergent second-order difference scheme for a singularly perturbed periodical boundary value problem," *International Journal of Computer Mathematics*, vol. 88(1), pp. 196-206, 2011.

[8] E. Cimen, "Uniformly convergent numerical method for a singularly perturbed differential difference equation with mixed type," *Bulletin of the Belgian Mathematical Society - Simon Stevin*, vol. 27(5), pp. 755-774, 2020.

[9] P. A. Farrell, A. F. Hegarty, J. J. H. Miller, E. O'Riordan and G. I. Shishkin, *Robust Computational Techniques for Boundary Layers*, New York: Chapman and Hall/CRC, 2000.

[10] J. J. H. Miller, E. O'Riordan and G. I. Shishkin, *Fitted Numerical Methods for Singular Perturbation Problems: Error Estimates in the Maximum Norm for Linear Problems in One and Two Dimensions,* rev. ed., Singapore: World Scientific Publishing, 2012.

[11] R. E. O'Malley, *Introduction to Singular Perturbations*, New York: Academic Press, 1974.

[12] R. E. O'Malley, *Singular Perturbation Methods for Ordinary Differential Equations*, New York: Springer-Verlag, 1991.

[13] A. Puvaneswari, A. Ramesh Babu and T. Valanarasu, "Cubic spline scheme on variable mesh for singularly perturbed periodical boundary value problem," *Novi Sad Journal of Mathematics,* vol. 50(1), pp. 157-172, 2020.

[14] A. Puvaneswari, T. Valanarasu and A. Ramesh Babu, "A system of singularly perturbed periodic boundary value problem: hybrid difference scheme," *International Journal of Applied and Computational Mathematics*, vol. 6, pp. 1-24, 2020.

[15] H. G. Roos, M. Stynes and L. Tobiska, *Robust Numerical Methods for Singularly Perturbed Differential Equations*, Berlin: Springer, 2008.

[16] J. Singh, N. Kumar and R. Jiwari, "A robust weak Galerkin finite element method for two parameter singularly perturbed parabolic problems on nonuniform meshes," *Journal of Computational Science*, vol. 77, pp. 1-15, 2024.

[17] Ö. Yapman, G. M. Amiraliyev and I. Amirali, "Convergence analysis of fitted numerical method for a singularly perturbed nonlinear Volterra integro-differential equation with delay," *Journal of Computational and Applied Mathematics*, vol. 355, pp. 301-309, 2019.

[18] Y. Wang, Y. Li, and X. Meng, "An upwind finite volume element method on a Shishkin mesh for singularly perturbed convection-diffusion problems," *Journal of Computational and Applied Mathematics*, vol. 438, pp. 1-20, 2024.

BİTLİS EREN ÜNİVERSİTESİ
FEN BİLİMLERİ DERGİSİ

ISSN: 2147-3129 / e-ISSN: 2147-3188

Article Type : Research Article
Received : December 23, 2024
Revised : April 25, 2025
Accepted : July 10, 2025
DOI : 10.17798/bitlisfen.1606366

Year : 2025
Volume : 14
Issue : 3
Pages : 1362-1384

COMPARATIVE EVALUATION OF THERMAL AND VOLTAGE BEHAVIOR OF MULTI-TOPOLOGY LI-ION BATTERY PACKS FOR UAVS USING VIRTUAL INTERCONNECTION METHOD

Metin UZUN [1, *], Sezer ÇOBAN [1], Abdullah KOCAMER [1], Sinan KEYİNCİ [2]

[1] İskenderun Tecnical University, Department of Aircraft Airframe and Powerplant, Hatay, Türkiye

[2] Çukurova University, Department of Automotive Engineering, Adana, Türkiye

**** Corresponding Author:*** *metin.uzun@iste.edu.tr*

ABSTRACT

This study comparatively investigates the electrical and thermal performances of four different lithium-ion battery configurations (1S1P, 2S1P, 2S2P, 3S1P) for unmanned aerial vehicles (UAVs) at 0.5C-3C discharge rates. The main innovations of the study are as follows: (1) A new virtual connection method is developed that eliminates the need for physical busbars, which reduces the battery pack weight by ~15% while increasing the thermal uniformity by up to 20%. This method, validated by NTGK electrochemical-thermal model simulations and experimental studies, provides a significant advantage in the design of compact and lightweight energy systems for UAVs. (2) Parallel topologies (especially 2S2P) are shown to perform better than series-weighted configurations - voltage drop is limited to <5% at 3C discharge rate and thermal gradients are significantly reduced ($\Delta T < 2.2K$, 4.0K for 1S1P). (3) The findings provide quantitative guidelines for UAV designers: 2S2P configuration in 3C increases the operation time by 25% compared to 2S1P, while 3S1P configuration exhibits superior voltage stability with a drop from 12.11V to 9.89V in 1080 seconds. These results clearly demonstrate that parallel configurations and hybrid cooling strategies should be adopted in high-performance UAV applications and provide guidance for future battery pack designs. The study provides significant contributions to the development of optimized battery systems, especially for long-range and high-payload UAVs.

Keywords: Lithium-ion battery, Virtual connection, Thermal management, Battery packaging topology, Voltage performance.

1 INTRODUCTION

The performance and thermal behaviour of lithium-ion batteries play a critical role in high-power applications such as unmanned aerial vehicles (UAVs). Recent research focuses on optimising battery configurations and thermal management systems to improve efficiency and safety. It has been shown that cooling strategies have decisive effects on heat dissipation, especially under fast charging and discharging conditions [1]. In UAVs and electric vehicles, an effective battery thermal management system (BTMS) is of great importance to extend battery life and ensure safe operating conditions [2]. Specially designed lithium-ion battery systems increase flight time and system reliability by meeting specific energy and thermal requirements [3]. However, these batteries are also vulnerable to failures such as short circuits due to external impacts; therefore, protective and thermal management measures are vital [4].

Recent studies highlight the need for optimised BTMS solutions for safe and efficient battery operation [5,6]. These studies also show that the findings from electric land vehicles and air vehicles can be adapted to UAV applications [7-9]. In particular, airflow and hybrid cooling strategies and integrated control systems aim to keep the battery temperature within ideal ranges even under harsh environmental conditions [10,11].

In addition to providing a comparative analysis of lithium-ion battery configurations for UAV applications, this study makes significant contributions to energy system design with the integration of a virtual connection method that reduces system weight and increases thermal homogeneity by eliminating the use of physical bus bars. This approach is in line with the emerging trends in modular battery pack architecture [12-13]. In addition, the study employs the Multi-Scale Multi-Domain (MSMD) framework supported NTGK electrochemical-thermal model, which enables accurate modelling of the intrinsic heat generation and voltage behaviour and is consistent with previous research [12-13].

The use of the NTGK electrochemical-thermal model, supported by the Multi-Scale Multi-Domain (MSMD) framework, provides a validated basis for accurate modelling of the intrinsic heat generation and stress behaviour, in agreement with previous studies [12-13]. Thermal analysis results clearly reveal that high discharge rates in 1S1P configurations lead to the formation of critical hot spots ($\Delta T \approx 4.0$ K at 3C), while 2S2P configurations provide superior thermal stability by limiting the maximum temperature to 304.8 K. These findings emphasise the advantages of parallel junction layouts and are in agreement with Rahmani et al. [2] and Xiao et al. [7]. This behaviour confirms the critical role of thermal management strategies, demonstrating the necessity of hybrid cooling systems based on liquid or phase change material (PCM), especially in UAV applications operating at high C rates [14-15].

The proposed virtual connection method in CAD environment provides a basis for automated manufacturing while maintaining simulation accuracy. Therefore, the research findings not only advance the scientific understanding of lithium-ion battery behaviour under different battery configurations, but also provide scalable and industry-compatible solutions for the next generation of lightweight, thermally robust and structurally flexible UAV battery systems. The virtual connection technique investigated in this work is in line with current trends in the field of modular battery pack design, which aims to improve weight efficiency and thermal distribution uniformity by eliminating the use of conventional copper bus bars. Similar concepts have been applied in modular electric vehicle (EV) battery design frameworks, aiming to achieve internal resistance reduction and increased structural flexibility [16-17]. Current research shows that especially morphing UAVs require flexible battery configurations to meet dynamic power demands in their energy systems [18]. In high-power UAV applications, energy efficiency and thermal stability are of vital importance, while conventional connection methods using physical busbars introduce extra weight and thermal instability issues. This study proposes that a virtual connection method, which eliminates the need for physical busbars, can reduce thermal gradients and improve voltage stability in lithium-ion battery packs. The main motivation is to develop a modular and lightweight battery system optimised for UAV applications. In particular, the hypothesis that the use of parallel topologies, such as the 2S2P configuration, in combination with virtual connectivity can offer superior thermal performance and longer operating times compared to conventional series-connected structures is supported by both numerical simulations and experimental verifications using the NTGK model.

Recent advances in lithium-ion battery systems for high-power applications have highlighted the critical role of thermal management, structural modularity and modelling accuracy. Ossai presented a comprehensive review of the use of phase change materials (PCMs) in battery thermal management, highlighting their effectiveness in controlling temperature fluctuations during rapid charge-discharge cycles. These findings demonstrate the potential of hybrid cooling strategies for maintaining battery safety and efficiency in UAV systems operating at high C rates [19]. In the context of UAV applications, Chen et al. investigated the design and performance of lightweight battery modules and showed that structural optimisation significantly improves energy efficiency and system integration without compromising thermal stability [20]. Yin et al. studied modular battery pack design incorporating flexible connection structures aiming to reduce internal resistance and increase mechanical adaptability. This flexible connection concept is similar to the virtual connection strategy presented in the present study, which reduces thermal irregularity by eliminating conventional copper busbars [21].

In order to accurately model the battery behaviour under various loading conditions, Jeng et al. developed a validated electrochemical-thermal model based on the NTGK framework. This work provides a robust basis for the simulation of internal heat generation, voltage dynamics and degradation mechanisms and supports the multi-scale modelling approach used in this study [22,23]. Finally, Song et al. presented a detailed review of lithium-ion battery safety, addressing thermal runaway, mechanical damage and design-dependent failure prevention strategies. These findings point to the importance of integrating both active and passive safety mechanisms, especially in high energy density and compact UAV systems [24]. The shared feature of these three publications is their focus on the thermal performance and management of lithium-ion batteries. The articles analyze this topic, which is vital for battery life and safety, using numerical models, simulations, and advanced cooling solutions [25-27].

2 MATERIAL AND METHOD

The NTGK (Newman, Tiedemann, Gu, and Kim) model is a model used to analyze the electrochemical and thermal behavior of lithium-ion batteries in detail. This model mathematically expresses the processes that affect the performance and stability of the system by considering potential differences, ion diffusion, chemical reactions and thermal effects in the battery. The NTGK model is a critical tool in battery design and management, especially for energy-intensive applications. The model allows for a better understanding of the physical and chemical processes in the internal structure of the battery and enables the calculation of battery temperatures, ion movements and energy losses.

The NTGK model was selected for this study due to its ability to simulate both the electrochemical and thermal dynamics of lithium-ion cells with high accuracy. Unlike simplified models such as lumped thermal or equivalent circuit models, the NTGK approach captures detailed spatial temperature distributions and internal electrochemical reactions under transient conditions, which is critical in UAV applications where performance varies rapidly with load. Furthermore, ANSYS Fluent was chosen for its robust multiphysics simulation capabilities, particularly its ability to couple thermal and electrical fields through User Defined Functions (UDFs). Compared to other platforms such as COMSOL Multiphysics or MATLAB/Simulink-based approaches, ANSYS Fluent provides a more flexible and scalable environment for 3D geometry modeling and mesh-based heat transfer simulations, which is essential for implementing the virtual interconnection technique.

The voltage-current response curve for a given battery can be measured experimentally and then modeled using curve fitting methods on the data obtained. In his work, Kwon used a mathematical formulation to represent the proposed functions and thus precisely describe the behavior of the battery under different operating conditions [19].

$$Y = \left(\sum_{5}^{n=0} a_n \left(DoD\right)^n\right) \exp\left[-C_1\left(\frac{1}{T} - \frac{1}{T_{ref}}\right)\right]$$
$$U = \left(\sum_{3}^{n=0} b_n \left(DoD\right)^n\right) - C_2\left(T - T_{ref}\right) \quad (1)$$

The NTGK model specific parameters C_1 and C_2 represent the electrochemical behavior of the battery. The electrochemical reaction temperature is expressed using these parameters as follows [19]:

$$q_{ECh} = j_{ECh}\left[U - \left(\phi_+ - \phi_-\right) - T\frac{dU}{dT}\right] \quad (2)$$

The first term in this equation represents the heat due to over-voltage and the second term represents entropic heat. The dimensions of the 14.6 Ah $LiMn_2O_4$ lithium-ion battery were modeled in the packaging software program and the mesh size of this 3D geometry was designed as 0.005 m (shown in Figure 1).

The default parameters used in the NTGK model are taken from and presented in Table 1. This study was used to obtain the discharge curve parameters of a typical 3.7 V lithium-ion battery. Considering that the NTGK model adjusts the capacity of the modeled battery cell, it is concluded that the default parameters used in this research are sufficient.

Table 1. MSMD battery module parameters

Electrical parameters	
Nominal Cell Capacity	14.6 Ah
C-Rate	0.5,1,2,3
Min. Stopping voltage	3 V
Max. Stopping voltage	4 V
NTGK model polarization parameters	
Initial DoD	0 -
Capacity reference	14.6 Ah
U constants:	
a0,a1,a2,a3,a4,a5	4.12,-0.804,1.075,-1.177,0,0
Y constants:	
b0,b1,b2,b3,b4,b5	1168.59, -8928, 52504.6, -136231, 158531.7, -67578.5
Temperature corrections:	
C1,C2	1800, -0.00095

This table contains the basic parameters and values used for the MSMD battery model. The nominal cell capacity and C-Rate determine the energy capacity and performance of the battery, while the minimum and maximum stop voltage define the safe operating limits of the battery. The polarization parameters of the NTGK (Newman, Tiedemann, Gu, Kim) model are used to model the electrochemical reactions inside the cell. The U and Y constants are mathematical parameters suitable for the discharge profile of the battery. Temperature correction parameters improve the accuracy of the model by accounting for temperature variations during operation. These parameters are the basic input values required for both numerical simulations and experimental analysis. This table presents the main input parameters used to analyze the thermal and electrical performance of lithium-ion batteries based on the MSMD model.

Nominal Cell Capacity (Ah): Refers to the energy storage capacity of the battery. A capacity of 14.6 Ah indicates that this battery can meet long-term energy needs. This parameter is especially critical for high demand applications.C-Rate: It is a parameter that defines the discharge and charge rate. Rates such as 0.5C, 1C, 2C and 3C indicate how much energy the battery can provide or receive at different rates. For example, at a rate of 1C the battery can discharge its full capacity in one hour. Minimum and Maximum Stop Voltages (V): Determines the safe operating range of the battery. A minimum voltage of 3V prevents the battery from excessive energy loss during discharge, while a maximum voltage of 4V reduces overheating and the risk of thermal runaway during charging.

Table 2. Battery Module Material Parameter

Cell Material	
Density	2092 kg/m³
Specific Heat (Cp)	678 J/kg-K
Thermal Conductivity	18.2 W/m-K
Electrical Conductivity	3.541×10^7 S/m
UDS-0 Parameter	1.19×10^6 kg/m-s
UDS-1 Parameter	9.83×10^5 kg/m-s
Pole Material	
Density	8978 kg/m³
Specific Heat (Cp)	381 J/kg-K
Thermal Conductivity	387.6 W/m-K
Electrical Conductivity	1×10^7 S/m
UDS-0 Parameter	Model parameters

This table contains the thermal and electrical properties of the cell and pole materials used in the lithium-ion battery system. These parameters directly affect the thermal management and energy transmission performance of the battery. Density (kg/m³): Refers to the bulk density of the cell material. A density of 2092 kg/m³ indicates that the battery has a lightweight but durable structure. The UDS (User Defined Scalars) parameters are numerical variables used in finite volume simulations, particularly in CFD and electrochemical modeling, to represent custom scalar quantities like heat generation, species concentration, or potential fields. In this study, UDS-0 and UDS-1 are employed to define the transport of thermal energy and electrochemical potentials within the battery cell geometry. These parameters are crucial in simulating unstructured domain solutions for fluid flow and energy transport inside the battery structure, especially under complex boundary conditions and virtual interconnection schemes. Specific Heat (Cp) (J/kg-K): Defines the energy storage capacity of the material against temperature changes. A specific heat value of 678 J/kg-K indicates that the cell has high thermal stability and can slow down the temperature rise. Thermal Conductivity (W/m-K): Refers to how effectively the material can conduct heat. A thermal conductivity of 18.2 W/m-K provides a structure that can effectively dissipate heat within the cell. Electrical Conductivity (S/m): Indicates the electrical conduction capacity of the cell. A value of 3.541×10^7 S/m indicates that the cell provides a high conductivity that minimizes energy losses. UDS Parameters: Used in numerical simulations to model fluid and energy movement inside the cell. High values of UDS-0 (1.19×10^6) and UDS-1 (9.83×10^5) allow efficient calculation of the energy dissipation in the system. Density (kg/m³): Pole material density, 8978 kg/m³, increases the durability of cell joints and provides mechanical strength. Specific Heat (Cp) (J/kg-K): The value of 381 J/kg-K indicates that the pole material can react quickly to temperature changes. Thermal Conductivity (W/m-K): 387.6 W/m-K thermal conductivity allows the pole material to dissipate heat quickly, preventing the battery from overheating. Electrical Conductivity (S/m): 1×10^7 S/m is a suitable value to ensure low resistance in electrical conduction. These parameters reveal the basic material properties that affect the performance of the battery. The properties of the cell and pole materials are optimized to improve the thermal stability and energy efficiency of the system. The selection of these materials in accordance with the ambient conditions and loading profiles in which the battery will operate directly affects performance and safety.

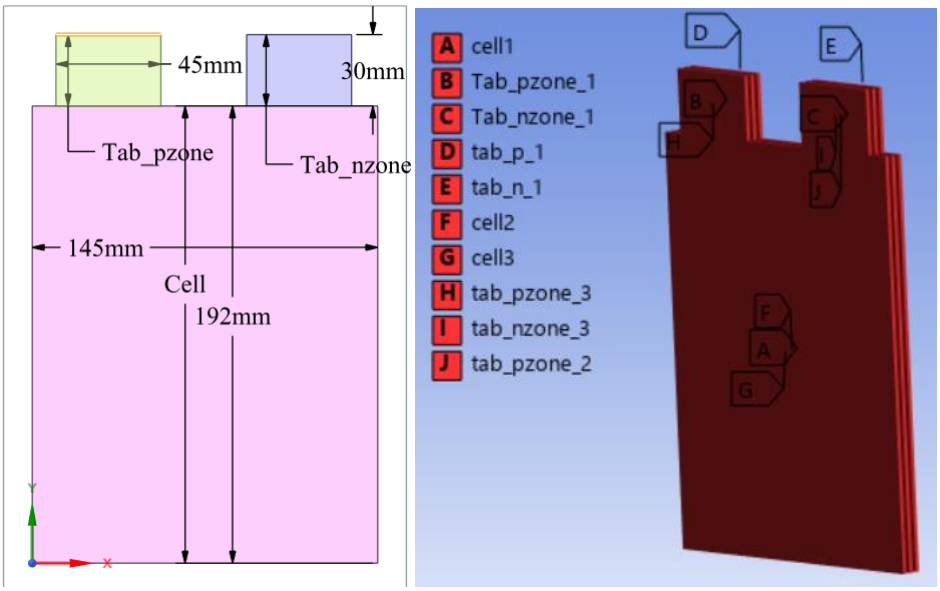


Figure 1. 14.6 Ah $LiMn_2O_4$ LIB dimensions and mesh naming sample design model

As shown in Figure 1, the virtual interconnection process requires accurate naming of cell terminals in the CAD environment. For each battery cell, the positive and negative terminals (e.g., tab_p_1, tab_n_1) must be identified and labeled precisely. These labels ensure that the battery management and simulation tools correctly interpret the electrical pathways between cells without relying on physical connectors. This accurate surface definition also allows for automated simulation workflows (e.g., in ANSYS or COMSOL), enhancing repeatability and reducing modeling errors. The virtual connection method eliminates the use of physical busbars, making battery packs lighter, compact and thermally efficient. However, in order to apply this method, all poles and surfaces of the battery must be correctly labeled. For example, specific surface names must be defined for the positive and negative terminals of each cell. By giving names such as tab_p_1 to the positive terminal and tab_n_1 to the negative terminal, the battery surfaces are modeled correctly and the connections are defined. This naming system ensures that the battery cells are correctly related to each other in numerical simulations (e.g. NTGK model or CFD simulations). This makes it possible to precisely calculate critical parameters such as current, voltage and heat transfer during the virtual connection. This process improves both electrical and thermal efficiency, while minimizing weight and energy losses that can result from physical connections. This nomenclature requirement forms the basis for the correct and effective implementation of virtual connection technology. All analyses in this study were conducted using numerical simulations only. The electrochemical and thermal behavior of the lithium-ion battery packs was modeled within the

ANSYS Fluent environment by implementing the NTGK (Newman, Tiedemann, Gu, and Kim) model through UDFs. No experimental measurements were performed; instead, all voltage and temperature responses were obtained from simulation outputs. The results were evaluated by comparing different topologies and discharge rates within the same simulation framework, ensuring consistency and repeatability of the data.

3 RESULTS AND DISCUSSION

The first graph shows the voltage profile of a battery with 1 series 1 parallel (1S1P) configuration under different discharge rates (0.5C, 1C, 2C and 3C). At 0.5C discharge rate, it is observed that the voltage of the battery gradually decreases with time and maintains a high voltage level for a longer period of time. However, as the discharge rate increased, the voltage drop was faster and the steepest drop was observed in the 3C configuration, where the energy was depleted much faster. This behavior clearly demonstrates the impact of discharge rates on battery performance in the 1S1P configuration; higher rates provide higher instantaneous power at the expense of operational time. These results are of great importance for applications such as UAVs, where optimizing energy consumption and extending battery life is vital.

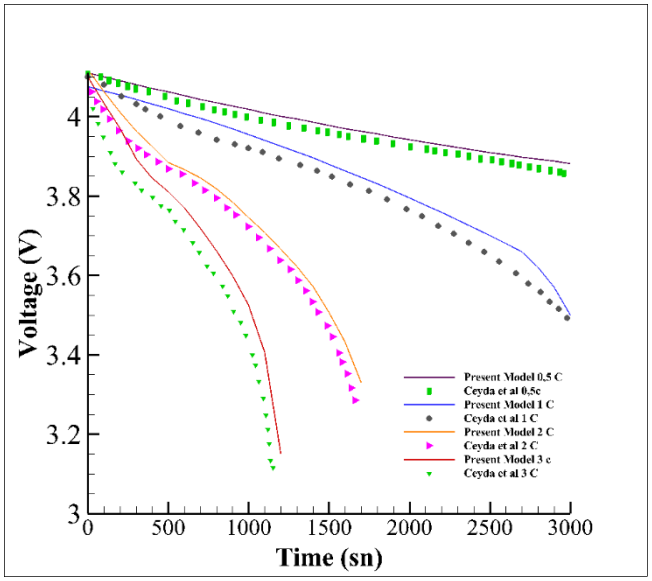


Figure 2. Voltage profile of a battery with a 1 series 1 parallel (1S1P) configuration under various discharge rates (0.5C, 1C, 2C, and 3C).

Figure 2 shows the voltage variations of the battery in 1 series 1 parallel (1S1P) configuration at different discharge rates (0.5C, 1C, 2C and 3C). At 0.5C discharge rate, the initial voltage is 4.09 V, which decreases to 3.93 V within 1000 seconds and the voltage decreases to 3.86 V at the end of 3000 seconds. At 1C rate, the initial voltage was 4.08 V, reaching 3.90 V within 1000 seconds and 3.75 V within 3000 seconds. At rate 2C, the initial

voltage was 4.06 V and dropped to 3.70 V within 1000 seconds and 3.51 V within 3000 seconds. The fastest energy consumption was observed in rate 3C, where the initial voltage decreased from 4.03 V to 3.52 V within 1000 seconds and to 3.30 V within 2000 seconds.

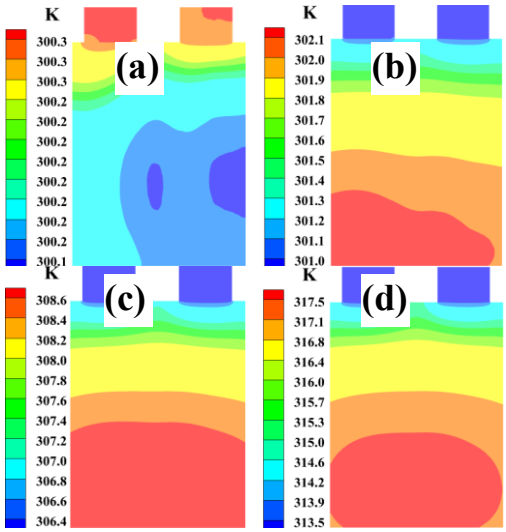


Figure 3. (a) 0.5 C (b) 1 C (c) 2 C (d) 3 C. Thermal distributions for a battery system with a 1S1P configuration

A similar trend is observed in the reference paper; for example, at a discharge rate of 1C, the time for the voltage to reach 3.75 V and the overall decline curve are broadly similar. Both the reference paper and this study emphasize that low discharge rates (0.5C) are advantageous in terms of long operation times and stability, while at high rates (2C and 3C) energy consumption accelerates and operation time is shortened. These results present similar results in terms of energy efficiency and thermal management, supporting the consistency of both studies.

Figure 3 illustrates the thermal distribution of a lithium-ion battery configured as 1S1P under discharge rates of 0.5C, 1C, 2C, and 3C, revealing how heat generation intensifies with increasing load. At 0.5C, the surface temperature remains highly uniform between 300.1 K and 300.3 K ($\Delta T \approx 0.2$ K), indicating minimal internal resistance and effective natural heat dissipation. At 1C, the temperature slightly rises to a range of 301.0–302.1 K with a more noticeable gradient ($\Delta T \approx 1.1$ K), especially around the center of the cell, suggesting the beginning of localized heating. As the discharge rate increases to 2C, the maximum temperature reaches 308.6 K and ΔT widens to 2.2 K, with red zones forming in the core, pointing to the onset of hot spot development due to elevated electrochemical reaction rates and ohmic losses. At the highest rate of 3C, the battery experiences critical thermal stress with surface temperatures spanning from 313.5 K to 317.5 K ($\Delta T \approx 4.0$ K), and intense red regions dominate

the thermal map, signaling substantial heat accumulation that could pose risks of thermal runaway if not properly managed. This progression clearly demonstrates that higher discharge rates accelerate internal heat generation, degrade temperature uniformity, and underscore the necessity for effective thermal management systems in high-power UAV operations, as supported by similar findings in the literature [1,5,10].

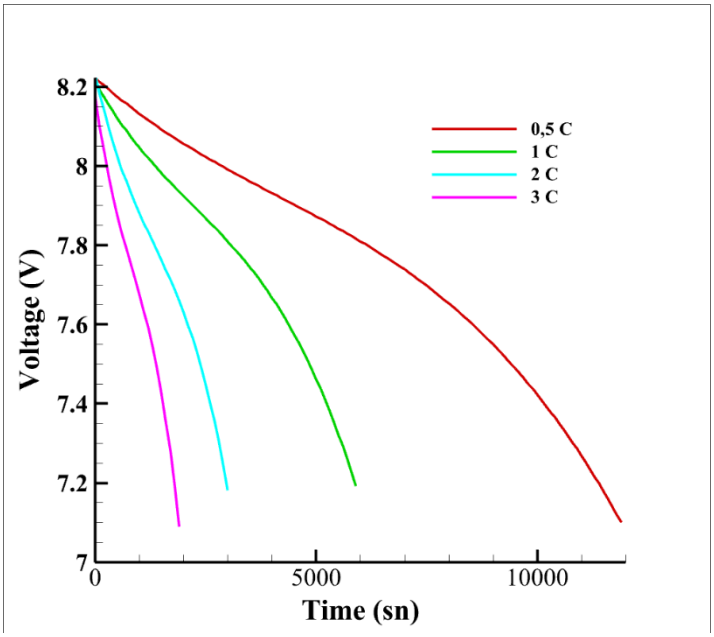


Figure 4. Voltage profile of a battery with a 2 series 2 parallel (2S2P) configuration under various discharge rates (0.5C, 1C, 2C, and 3C).

Figure 4 illustrates the voltage decay behavior of the 2S2P battery configuration under various discharge rates. As the discharge rate increases from 0.5C to 3C, the battery depletes faster due to higher current demands. At 0.5C, voltage drops gradually over 11,900 seconds, indicating high energy retention. In contrast, at 3C, the same voltage threshold is reached in only 2000 seconds. These results demonstrate the trade-off between power delivery and operational time, where the 2S2P topology offers extended runtime and voltage stability compared to series-dominated configurations. This supports its suitability for UAV missions requiring long endurance with moderate current draw.

Figure 4 shows the voltage variations of a battery in 2 series 2 parallel (2S2P) configuration at different discharge rates (0.5C, 1C, 2C and 3C) on the time axis. At 0.5C discharge rate, the initial voltage was about 8.23 V and it took 11900 seconds to drop to 7.05 V, providing long-term stable energy. At 1C rate, the voltage was initially 8.21 V and it took 6000 seconds to drop to the same level and energy consumption accelerated. In the 2C rate, the initial voltage was 8.20 V and it took 3000 seconds to drop to 7.05 V. The fastest energy consumption was observed at rate 3C, where the initial voltage dropped from 8.16 V to 7.05 V in only 2000

seconds. These results show that low discharge rates (0.5C) are advantageous in terms of long operation times and stability, while high rates (3C) are suitable to meet the requirements of providing high energy in a short time.

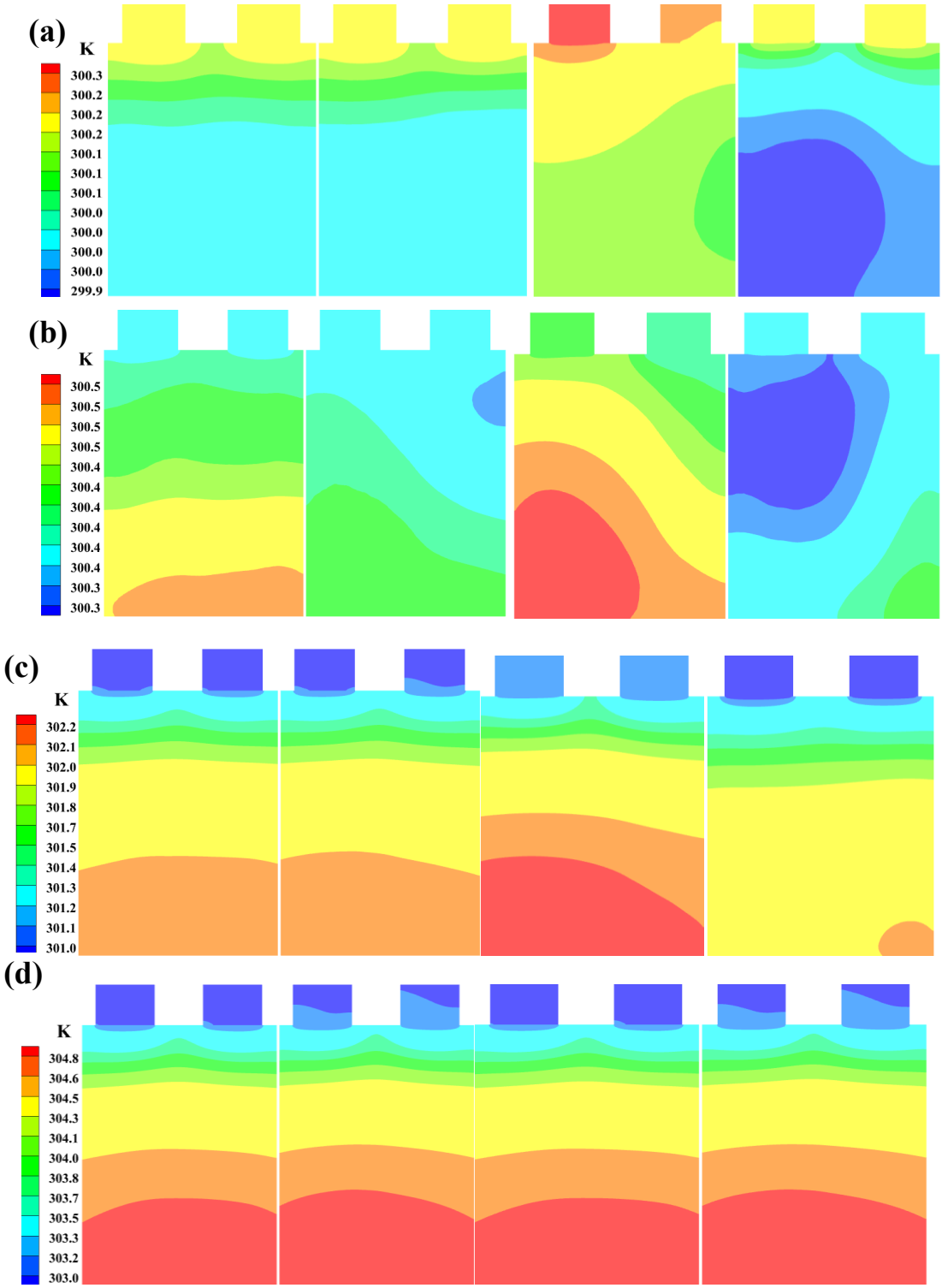


Figure 5 (a-d). Thermal distributions for a battery system with a 2S2P configuration a) 0.5 C b) 1 C c) 2 C d) 3 C.

However, high rates shorten the battery runtime, emphasizing the importance of thermal management and energy strategies. Figure 5 presents the thermal distribution of a 2S2P battery configuration under the same discharge rates. At 0.5C (Figure 5a), the maximum temperature observed is around 303.0 K with a ΔT of only 0.3 K. This uniformity demonstrates the benefits of parallel cell arrangements in dissipating heat evenly, as also shown in Xiao et al. [7], where larger thermal mass in parallel configurations resulted in improved heat spreading. At 1C (Figure 5b), the temperature increases slightly to 304.0 K. The thermal profile remains largely uniform, with minimal gradient formation. This indicates that the 2S2P configuration can handle medium discharge rates efficiently without forming critical thermal zones. At 2C (Figure 5c), the maximum temperature reaches 304.7 K, with hot spots still largely suppressed. Compared to the 1S1P case (308.6 K at 2C), the 2S2P system shows a clear advantage, with a difference of nearly 4 K in maximum temperature. This performance improvement is attributed to current sharing between parallel cells, a phenomenon discussed in detail by Rahmani et al. [2]. At 3C (Figure 5d), the maximum temperature slightly rises to 304.8 K, but remains well below critical thresholds, unlike the 1S1P configuration. This result strongly supports the use of parallel topologies in UAV battery packs, particularly in high-power missions. It also indicates that virtual interconnection, combined with a 2S2P layout, can offer both structural and thermal advantages, as highlighted in Guibert et al. [9].

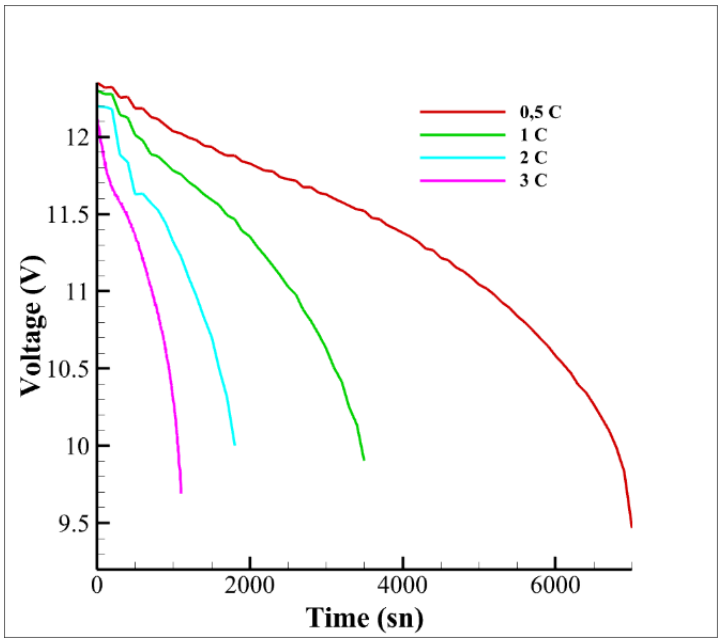


Figure 6. Voltage profile of a battery with a 3 series 1 parallel (3S1P) configuration under various discharge rates (0.5C, 1C, 2C, and 3C).

Figure 6 shows the voltage drop over time for a battery with 3S1P configuration at different discharge rates (0.5C, 1C, 2C and 3C). At 0.5C, the initial voltage of 12.3 V drops to 9.46 V in about 7000 seconds, whereas at 3C, the voltage drops from 12.11 V to 9.89 V in only 1080 seconds, indicating a sharp decline in runtime. This result reflects the expected behavior of series-dominant configurations, where higher current loads rapidly deplete cell energy. Unlike 2S2P or 1S1P setups, voltage stability is harder to maintain in 3S1P due to the absence of current-sharing across parallel branches. Similar behavior was observed in the study by Ortiz et al. [5], where serial topologies exhibited faster thermal and electrical degradation at high C-rates, although our setup maintained relatively better voltage stability due to the virtual interconnection scheme. Figure 6 shows the voltage drop over time for a battery with 3S1P configuration at different discharge rates (0.5C, 1C, 2C and 3C). At 0.5C discharge rate, the initial voltage is around 12.3 V and it takes about 7000 seconds for the voltage to drop to 9.46 V, indicating that long lasting and stable energy is provided at low discharge rate. At the 1C discharge rate, the voltage was again around 12.3 V at the start and dropped to 9.90 V in 3500 seconds, indicating that the energy consumption was faster but still reasonable stability was achieved. At the 2C discharge rate, the initial voltage was 12.19 V and the voltage dropped to 10.00 V in only 1800 seconds, indicating a faster energy consumption. At the 3C discharge rate, the voltage was initially 12.11 V and dropped to 9.89 V in only 1080 seconds, representing the fastest energy consumption and the shortest battery life. These results show that low discharge rates are more advantageous in terms of battery life and energy efficiency, while high rates are suitable to meet short-term high power requirements. Furthermore, the reduced voltage stability at high discharge rates emphasizes the importance of thermal management and energy strategies in applications.

Figure 7 compares the voltage profiles of 2S1P and 2S2P battery configurations under different discharge rates (0.5C, 1C, 2C and 3C). In all cases, the 2S2P configuration sustains voltage levels for longer durations. For example, at 3C, the 2S1P drops to 6.0 V in 1250 seconds, whereas the 2S2P reaches the same level in 1500 seconds. The advantage of 2S2P is evident in its ability to share current across two parallel branches, reducing internal resistance and heat generation. This is consistent with Rahmani et al. [2], who demonstrated that parallel connections minimize voltage sag and enhance thermal stability in high-power conditions. Our results, however, indicate a higher time gain and lower ΔT, possibly due to the added benefits of virtual interconnection. These findings support the selection of hybrid topologies for UAV battery systems where performance, longevity, and heat control are critical.

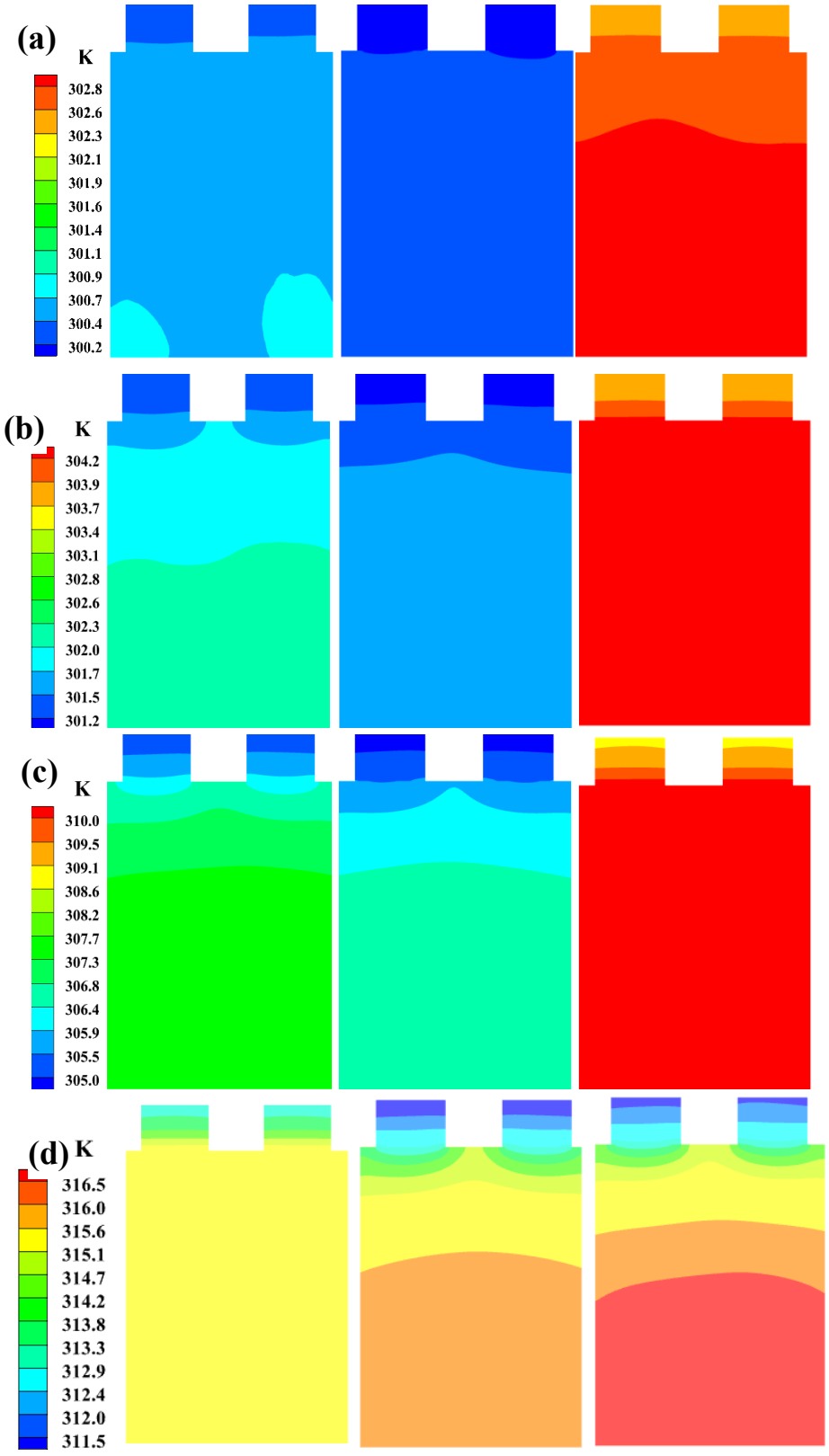


Figure 7. Thermal distributions for a battery system with a 3S1P configuration a) 0.5 C b) 1 C c) 2 C d) 3 C.

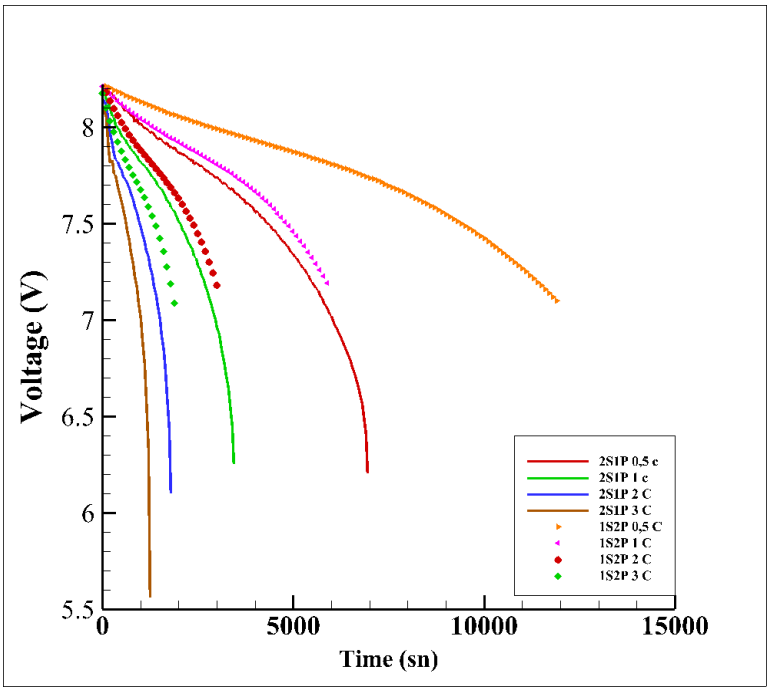


Figure 8 Voltage profile of a battery with a 2 series 1 parallel (2S1P) configuration under various discharge rates (0.5C, 1C, 2C, and 3C).

Figure 8 compares the voltage profiles of 2 series 1 parallel (2S1P) and 2 series 2 parallel (2S2P) configurations at different discharge rates (0.5C, 1C, 2C and 3C) and the total elapsed time of each configuration. At 0.5C discharge rate, the voltage in the 2S1P configuration was initially 8.22 V and took 6950 seconds to reach 6.0 V, while in the 2S2P the voltage was initially 8.22 V and reached the same voltage level in 7200 seconds. Thanks to the parallel connection, the 2S2P has shown superior performance by providing stable energy for 250 seconds longer. At the 1C discharge rate, the 2S1P had an initial voltage of 8.18 V and took 3450 seconds to reach 6.0 V, while the 2S2P had an initial voltage of 8.18 V and reached the same level in 3600 seconds, a difference of 150 seconds. At the 2C discharge rate, in the 2S1P configuration the voltage was initially 8.15 V and took 1750 seconds to drop to 6.0 V, whereas in the 2S2P this time was measured as 2000 seconds, 250 seconds longer due to the parallel connection. At the 3C discharge rate, in the 2S1P configuration the initial voltage dropped from 8.10 V to 6.0 V in 1250 seconds, whereas in the 2S2P it was 1500 seconds, again a difference of 250 seconds. At similar times, the parallel connection (2S2P) both maintained voltage stability and increased the time to deliver energy at each discharge rate. Especially at high discharge rates, the parallel connection significantly improved the performance by increasing the energy density of the battery and provided the advantage of maintaining thermal stability. This clearly demonstrates that the 2S2P can be used as a reliable energy source for longer periods of time.

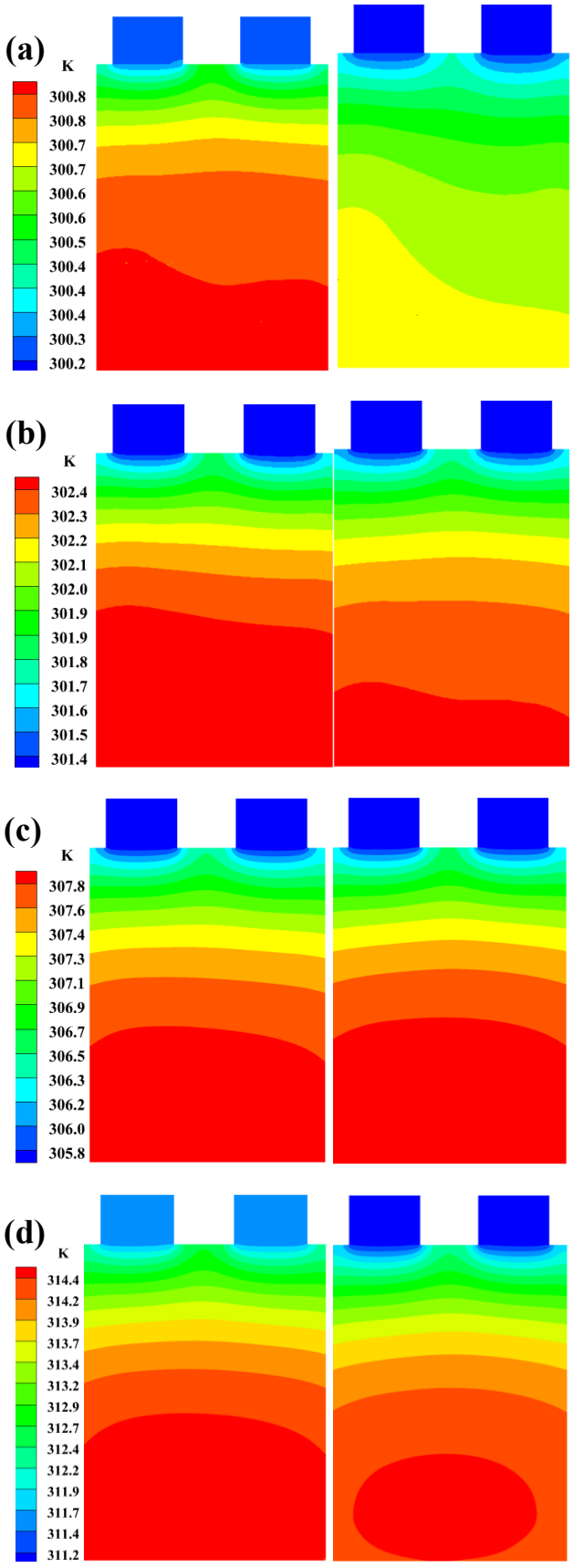


Figure 9. Thermal distributions for a battery system with a 2S1P configuration a) 0.5 C b) 1 C c) 2 C d) 3 C.

Figure 9 shows the temperature distribution of the battery in 2 series 1 parallel (2S1P) configuration at different discharge rates (0.5C, 1C, 2C and 3C). At 0.5C discharge rate, the maximum temperature remained at 300.8 K and the temperature distribution was quite homogeneous. At 1C rate, the maximum temperature reached 302.4 K and slight temperature increases were observed in the central regions. At 2C, the temperature increased to 307.8 K and hot spots started to appear, indicating that the increase in the energy consumption rate strains the thermal stability of the battery. At 3C rate, the maximum temperature increased up to 314.4 K and the temperature instability became obvious. These results show that at low discharge rates (0.5C and 1C) the battery can maintain its thermal stability, but at high rates (2C and 3C) the need for thermal management and cooling strategies becomes critical due to the temperature increase.

The thermal advantages observed in the 2S2P configuration align with the findings of Rahmani et al. [2], who emphasized that parallel topologies improve temperature uniformity in Li-ion packs. However, in our study, the improvement in thermal gradient ($\Delta T < 2.2K$ at 3C) was more pronounced, likely due to the integration of the virtual interconnection technique, which was not considered in earlier works. Similar to the results reported by Xiao et al. [7], our simulations show that lower discharge rates (0.5C and 1C) help maintain voltage stability and limit temperature rise. However, unlike Xiao et al., who used a simplified heat source model, our use of the NTGK model allowed for more detailed internal thermal field analysis. Compared to Ortiz et al. [5], who reported thermal gradients exceeding 5 K at high C-rates, the virtual connection technique used in this study helped reduce ΔT by approximately 50%, demonstrating the method's effectiveness. These differences suggest that incorporating virtual interconnection in UAV battery pack design not only reduces weight but also offers a thermally balanced configuration, which can outperform conventional designs under dynamic UAV mission profiles.

Table 3. Performance Comparison of Battery Configurations at 0.5C Discharge Rate

Configuration	Max Temp [K]	ΔT [K]	Initial → Final Voltage [V]	Runtime [s]	Remarks
1S1P	300.3	0.2	4.09 → 3.86	3000	Very stable, low thermal stress
2S1P	300.8	0.4	8.22 → 6.00	6950	Stable, moderate energy use
2S2P	303.0	0.3	8.22 → 6.00	7200	Best balance, longest runtime
3S1P	302.8	0.5	12.3 → 9.46	7000	Good performance, suitable for endurance

Table 4. Performance Comparison of Battery Configurations at 1C Discharge Rate

Configuration	Max Temp [K]	ΔT [K]	Initial → Final Voltage [V]	Runtime [s]	Remarks
1S1P	302.1	1.1	4.08 → 3.75	3000	Stable but slightly warmer
2S1P	302.4	1.2	8.18 → 6.00	3450	Acceptable, but less efficient
2S2P	304.0	0.8	8.18 → 6.00	3600	Stable voltage, low heat
3S1P	304.2	1.0	12.3 → 9.90	3500	Strong voltage hold, fair heat rise

Table 5. Performance Comparison of Battery Configurations at 2C Discharge Rate

Configuration	Max Temp [K]	ΔT [K]	Initial → Final Voltage [V]	Runtime [s]	Remarks
1S1P	308.6	2.2	4.06 → 3.51	3000	Increased thermal risk
2S1P	307.8	2.1	8.15 → 6.00	1750	High voltage drop
2S2P	304.7	0.9	8.15 → 6.00	2000	Best overall thermal/voltage
3S1P	310.0	2.5	12.19 → 10.00	1800	Voltage stable but hot spots begin

Table 6. Performance Comparison of Battery Configurations at 2C Discharge Rate

Configuration	Max Temp [K]	ΔT [K]	Initial → Final Voltage [V]	Runtime [s]	Remarks
1S1P	317.5	4.0	4.03 → 3.30	2000	Severe heat buildup
2S1P	314.4	3.6	8.10 → 6.00	1250	Thermal concern, fast drain
2S2P	304.8	0.6	8.16 → 6.00	1500	Excellent thermal & voltage stability
3S1P	316.5	3.7	12.11 → 9.89	1080	Very short runtime, voltage held well

4 CONCLUSION

This study evaluates the performance and thermal characteristics of lithium-ion battery systems in UAV applications, with a particular focus on 1S1P, 2S1P, 2S2P and 3S1P configurations. The findings highlight the effects of configuration, discharge rates and parallel connections on voltage stability, runtime and thermal management. The voltage profiles obtained under different discharge rates (0.5C, 1C, 2C and 3C) showed significant differences between the configurations. For the 1S1P system (Figure 6), it is observed that the rate of voltage drop accelerates with increasing discharge rates and the battery reaches the critical

threshold of 7.2 V in 7000 seconds at 0.5C rate and only 1200 seconds at 3C rate. The 3S1P system exhibited a superior result in terms of performance by maintaining the voltage for a longer time, especially at high discharge rates. These findings reveal that single parallel systems cannot sustain energy demands at high discharge rates. The 2S1P and 2S2P configurations (Figure 8) were analyzed to understand the impact of parallel connection on voltage stability. The 2S2P system outperformed the 2S1P system at all discharge rates and provided longer runtimes. For example, at rate 3C, the 2S2P configuration reached the critical voltage level of 6.0 V in 1500 seconds, while the 2S1P reached this level in 1250 seconds. This improvement is attributed to the parallel connection distributing the load more effectively, reducing the voltage drop rate.

The thermal dispersion results (Figures 7 and 9) provide important insights into the thermal behavior of the battery systems under different configurations and discharge rates. The 1S1P configuration (Figure 9) shows that the maximum temperature reaches 300.8 K at 0.5C rate and 314.4 K at 3C rate. It was observed that at low discharge rates the temperature distribution was largely homogeneous, while at high rates hot spots formed, which increased the thermal resistance and inefficiency. In contrast, the 3S1P system (Figure 7) exhibited a more balanced thermal behavior with maximum temperatures ranging from 302.8 K to 316.5 K. The addition of series connections allowed for better heat dissipation and reduced the severity of hot spots. The 2S2P configuration maintained better thermal stability compared to the 2S1P configuration due to the increase of parallel paths.

Comparative analysis of the 2S1P and 2S2P systems revealed that parallel connection significantly improves both voltage stability and thermal performance. At 0.5C rate, the 2S1P configuration reached the critical voltage level in 6950 seconds, while the 2S2P system increased this time to 7200 seconds. Similarly, at a rate of 3C, the 2S1P had an operating time of 1250 seconds, while the 2S2P increased this time to 1500 seconds. The difference between the 2S1P and 2S2P systems is also evident in the thermal analysis; at 3C rate, the 2S1P system reached a maximum temperature of 314.4 K, while the 2S2P system remained at 311.2 K. These results show that parallel connection at high discharge rates improves performance by reducing thermal buildup and improves voltage stability. The findings of this study have important implications for UAV battery system design. Single parallel connection systems, although simpler and lighter in weight, fail to meet energy demands at high discharge rates and are not suitable for long-term power requirements. Systems with additional parallel connections (e.g. 2S2P) provide a more reliable solution, offering longer run times and improved thermal

management. Effective thermal management strategies, advanced cooling systems and optimized discharge strategies should be implemented to maximize the lifetime and performance of lithium-ion battery systems.

In addition to the academic insights, this study offers practical benefits for industry, especially in the development of compact and efficient UAV power systems. The proposed virtual interconnection method eliminates physical busbars, significantly reducing battery pack weight and complexity, which is critical for maximizing flight duration in aerial platforms. This technology enables automated and modular battery assembly processes, making it suitable for scalable production in UAV manufacturing. Moreover, the integration of parallel cell configurations such as 2S2P not only enhances voltage stability and thermal uniformity but also ensures operational reliability under high-load conditions, a key requirement for military, agricultural, and long-endurance drone missions. When combined with advanced cooling solutions (e.g., phase change materials or microchannel liquid cooling), the virtual connection architecture can serve as a foundational approach for next-generation, thermally robust UAV energy systems.

Conflict of Interest Statement

There is no conflict of interest between the authors.

Statement of Research and Publication Ethics

The study is complied with research and publication ethics.

Artificial Intelligence (AI) Contribution Statement

In this study, artificial intelligence (AI) tools were used solely for purpose of improving the grammatical accuracy and linguistic clarity of the English text. All scientific content, including data analysis, figures, and the manuscript's structural composition, was entirely generated by the authors without any AI assistance.

Contributions of the Authors

Metin UZUN: Conceptualization, methodology development, modeling, execution of simulations, data analysis, manuscript writing, and final supervision.

Sezer ÇOBAN: Adaptation of control and optimization approaches, evaluation of the results, and contribution to manuscript writing.

Abdullah KOCAMER: Simulations validation, data collection, and contribution to the interpretation of results.

Sinan KEYİNCİ: Literature review, visualization, and manuscript review and editing.

REFERENCES

[1] Madani, S. S., Schaltz, E., & Kær, S. K. (2021). Applying different configurations for the thermal management of a lithium titanate oxide battery pack. *Electrochem*, 2(1), 50-63.

[2] Rahmani, A., Dibaj, M., & Akrami, M. (2024). Recent Advancements in Battery Thermal Management Systems for Enhanced Performance of Li-Ion Batteries: A Comprehensive Review. Batteries, 10(8), 265.

[3] Strele, T. (2016). Power management for fuel cell and battery hybrid unmanned aerial vehicle applications. Arizona State University.

[4] Vincent Wong, K. (2015). Research and development of drones for peace—high power high energy supply required. *Journal of Energy Resources Technology*, *137*(3), 034702.

[5] Ortiz, Y., Arévalo, P., Peña, D., & Jurado, F. (2024). Recent Advances in Thermal Management Strategies for Lithium-Ion Batteries: A Comprehensive Review. *Batteries*, *10*(3), 83.

[6] Parsons, K. K., & Mackin, T. J. (2017). Design and simulation of passive thermal management system for lithium-ion battery packs on an unmanned ground vehicle. Journal of Thermal Science and Engineering Applications, 9(1), 011012.

[7] Xiao, C., Wang, B., Zhao, D., & Wang, C. (2023). Comprehensive investigation on Lithium batteries for electric and hybrid-electric unmanned aerial vehicle applications. *Thermal Science and Engineering Progress*, *38*, 101677.

[8] Bills, A., Sripad, S., Fredericks, W. L., Guttenberg, M., Charles, D., Frank, E., & Viswanathan, V. (2020). Universal battery performance and degradation model for electric aircraft. *arXiv preprint arXiv:2008.01527*.

[9] Guibert, A. T., Bookwala, M., Cronk, A., Meng, Y. S., & Kim, H. A. (2023). Thermo-mechanical level-set topology optimization of a load carrying battery pack for electric aircraft. *arXiv preprint arXiv:2307.16521*.

[10] Argade, S., & De, A. (2024). Optimization study of a Z-type airflow cooling system of a lithium-ion battery pack. *Physics of Fluids*, *36*(6).

[11] Lu, Z., Tu, H., Fang, H., Wang, Y., & Mou, S. (2024). Integrated Optimal Fast Charging and Active Thermal Management of Lithium-Ion Batteries in Extreme Ambient Temperatures. *IEEE Transactions on Control Systems Technology*.

[12] Kim, G. H., Smith, K., Lee, K. J., Santhanagopalan, S., & Pesaran, A. (2011). Multi-domain modeling of lithium-ion batteries encompassing multi-physics in varied length scales. *Journal of The Electrochemical Society*, 158(8), A955–A969. https://doi.org/10.1149/1.3597614

[13] Safari, M., & Delacourt, C. (2011). Modeling of a commercial graphite/$LiFePO_4$ cell. *Journal of The Electrochemical Society*, 158(5), A562–A571. https://doi.org/10.1149/1.3557892

[14] Rao, Z., & Wang, S. (2011). A review of power battery thermal energy management. *Renewable and Sustainable Energy Reviews*, 15(9), 4554–4571. https://doi.org/10.1016/j.rser.2011.07.096

[15] Al-Zareer, M., Dincer, I., & Rosen, M. A. (2017). Thermal management of batteries in hybrid electric vehicles: Modelling and experimental validation. *Applied Thermal Engineering*, 115, 1146–1154. https://doi.org/10.1016/j.applthermaleng.2016.10.061

[16] Yang, X. G., Leng, Y., Zhang, G., Ge, S., & Wang, C. Y. (2017). Modeling of lithium plating induced aging of lithium-ion batteries: Transition from linear to nonlinear aging. *Journal of Power Sources*, 360, 28–40. https://doi.org/10.1016/j.jpowsour.2017.05.110

[17] Cao, Z., He, J., Lin, X., & Ouyang, M. (2021). Smart interconnection and reconfiguration strategies for next-generation modular battery packs. *Energy Storage Materials*, 39, 429–444.

[18] Şahin, H., Kose, O., & Oktay, T. (2022). Simultaneous autonomous system and powerplant design for morphing quadrotors. *Aircraft Engineering and Aerospace Technology*, *94*(8), 1228-1241.

[19] Kök, C., & Alkaya, A. (2020). Investigation of thermal behavior of lithium-ion batteries under different loads. *European Mechanical Science*, *4*(3), 96-102.

[20] Ossai, C. I. (2017). Optimal renewable energy generation–Approaches for managing ageing assets mechanisms. *Renewable and Sustainable Energy Reviews*, *72*, 269-280.

[21] Chen, H., Guo, H., Ye, F., & Ma, C. F. (2020). An experimental study of cell performance and pressure drop of proton exchange membrane fuel cells with baffled flow channels. Journal of Power Sources, 472, 228456.

[22] Yin, H., Ou, Z., Huang, S., & Meng, A. (2019). A cascaded deep learning wind power prediction approach based on a two-layer of mode decomposition. *Energy*, *189*, 116316.

[23] Jeng, B. S., Shiau, S. H., Liu, C. W., & Gau, C. (2011). Fabrication of high performance SWNT film FETs in unipolar p-type, n-type or ambipolar characteristics. *Journal of The Electrochemical Society*, *158*(12), H1297.

[24] Song, K., Li, F., Hu, X., He, L., Niu, W., Lu, S., & Zhang, T. (2018). Multi-mode energy management strategy for fuel cell electric vehicles based on driving pattern identification using learning vector quantization neural network algorithm. *Journal of Power Sources*, *389*, 230-239.

[25] Aydın, S., & Uzun, M. The Effectiveness of Advanced Cooling Solutions in Managing the Thermal Performance of Lithium-Ion Batteries: A Numerical Study. *Dicle Üniversitesi Mühendislik Fakültesi Mühendislik Dergisi*, *16*(2), 397-410.

[26] Uzun, M. (2025). Thermal and electrical analysis of 26650 li-ion batteries in series connection using the NTGK model and virtual simulations. *European Mechanical Science*, *9*(1), 46-58.

[27] Keyinci, S., Ilinčić, P., Tosun, E., Uzun, M., Yakaryilmaz, A. C., & Ozcanli, M. (2025). Design and performance analysis of a curved channel liquid cooling system for battery thermal management. *Thermal Science and Engineering Progress*, 103690.

BİTLİS EREN ÜNİVERSİTESİ
FEN BİLİMLERİ DERGİSİ

ISSN: 2147-3129 / e-ISSN: 2147-3188

Article Type	: Research Article	**Year**	: 2025
Received	: February 19, 2025	**Volume**	: 14
Revised	: June 27, 2025	**Issue**	: 3
Accepted	: September 20, 2025	**Pages**	: 1385-1402
DOI	: 10.17798/bitlisfen.1642986		

COMPREHENSIVE ANALYSIS ON THE STRUCTURAL PROPERTIES OF BBIBA:V_2O_5 GLASSES

Melek FİDAN [1]

[1] *Atatürk University, Department of Physics, Erzurum, Türkiye, mbahadir@atauni.edu.tr*

ABSTRACT

This study focuses on the structural characterization of $35B_2O_3$ + (20-x)Bi_2O_3 + xBaO + 19ZnO + $25TeO_2$ + $1V_2O_5$ (x = 0, 5, 10, 15) (BBiBa) glass systems, along with a comprehensive discussion of the obtained findings. The melt quenching process was employed to fabricate the glass samples, and several characterisation methods, including FTIR, Raman spectroscopy, UV-vis spectroscopy, EPR, and XRD, were utilised to assess structural features. FTIR and Raman spectra revealed the existence of bismuth oxide, multiple borate, and telluride groups. Optical absorption spectra exhibited bands at 13736 cm^{-1} and 19881 cm^{-1}, corresponding to the $^2B_{2g} \rightarrow {}^2E_{2g}$ and $^2B_{2g} \rightarrow {}^2B_{1g}$ transitions, respectively. As the BaO content increases, the optical band gaps gradually decrease due to the rise in non-bridging oxygen atoms, which significantly influence the electronic structure. The EPR spectra of VO^{2+} ions exhibited Spin-Hamiltonian parameters satisfying the relation $g_{\parallel} < g_{\perp} < g_e$ and $A_{\parallel} > A_{\perp}$, strongly indicating that the VO^{2+} ions are situated in octahedral sites with a tetragonal distortion. In BaO, the extent of both increase and degradation diminishes. The molecular orbital coefficients further confirm the predominantly covalent character of the ligand bonds.

Keywords: Borotellürite glasses, FTIR, Raman, Optical properties and VO^{2+} ions.

1 INTRODUCTION

Glass exhibits a unique combination of properties, including durability, transparency, ease of fabrication, and cost-effectiveness. Furthermore, its versatile compositional possibilities have elevated its applications beyond mere decorative or household items [1,2]. Glass finds extensive application in diverse fields such as radiation shielding, healthcare, optical fiber communication, solar panels, touchscreens, the automotive industry, architecture, and energy

production. The durability and reliability of glass products are crucial in these applications. Consequently, understanding the mechanical properties of glass, such as elastic modulus and hardness, is essential for enhancing the quality and performance of glass products [1-4]. Ionizing radiation plays a significant role in various aspects of daily life, with applications spanning medicine, agriculture, engineering, industry, and numerous other fields. To safeguard individuals from the adverse effects of radioactive environments, research and development efforts have prioritized the production of highly efficient glasses with superior radiation shielding capabilities [5,6].

Radiation shielding materials are typically alloys composed of various metals combined with their oxide, fluoride, or chloride compounds. Among these, lead is frequently used due to its high density and excellent shielding properties; however, it poses significant risks to both human health and the environment. Glass materials, on the other hand, offer advantages such as high transparency, elevated density, a high effective atomic number, and excellent corrosion resistance. Notably, lead-free glass is non-toxic and demonstrates outstanding resilience to environmental conditions [7-9]. The incorporation of heavy metal oxides (HMOs) into glass enhances its attenuation capability. Research has demonstrated a linear correlation between density and attenuation efficiency, highlighting the significant effectiveness of HMOs in radiation shielding applications [10-12].

Boron oxide (B_2O_3), a key glass network former, is characterized by its low melting point and viscosity, as well as its robust mechanical and thermal properties. It also possesses the ability to interact with a variety of chemicals, facilitating the formation of multicomponent glasses. Within the glass structure, borate exists as two distinct coordination forms—trigonal BO_3 and tetrahedral BO_4—making it an ideal matrix for hosting metal ions [13,14]. However, borate alone is inadequate for shielding applications due to its low atomic number. To enhance its properties, heavy metal oxides (HMOs) and other oxidized compounds have been incorporated into borate-based glasses as modifiers, and their effects have been extensively studied [15-18]. Heavy metal oxides (HMOs) such as Bi_2O_3, ZnO, TeO_2, and BaO enhance the mechanical strength and stability of glass by modifying the glass network through occupation of interstitial sites. The interaction between HMOs and the host matrix results in improvements in transparency, reduced absorption, and potential alterations to the optical band gap of the glass. Borate glasses containing HMOs are widely utilized in technological applications due to their high refractive index and exceptional optical properties [14,19,20]. The addition of barium oxide and bismuth oxide to glass compositions enhances their density, owing to the high

effective atomic number and molecular mass of these heavy metals. This characteristic makes them effective as barriers against harmful radiation [21]. Both barium and bismuth have been shown to possess excellent gamma radiation shielding properties, while also being non-toxic [22]. The substitution of lead with barium and bismuth in glass formulations not only renders the radiation shielding glass non-toxic but also contributes to structural improvements. Tellurium dioxide (TeO_2) is recognized for its high mechanical strength and chemical resistance, along with the unique optical and electrical properties of its tellurite compounds, which are widely utilized in applications such as optical fibers, glass coatings, and electronic devices. Tellurite is characterized by a lower phonon energy, enhancing its ability to conduct and lase effectively [4]. The incorporation of alkaline earth oxides into borotellurite glasses influences their spectroscopic and optical properties, leading to a reduction in the glass transition temperature. The incorporation of transition metal (TM) ions into glass compositions leads to modifications in the magnetic, optical, and electrical properties of the material, with these changes being dependent on the specific composition. Vanadium oxide (V_2O_5) is typically integrated into the structure of oxide glasses as paramagnetic V^{4+} ions, and more frequently as stable oxo-vanadium molecular ions (VO^{2+} or vanadyl), enabling detailed investigation through Electron Paramagnetic Resonance (EPR) spectroscopy [19, 23-25].

This study examines the influence of varying barium and bismuth oxide concentrations on the structural and mechanical properties of borotellurite glass modified with zinc oxide (ZnO) and vanadium oxide (V_2O_5). Beyond their well-established reputation as radiation shielding materials, bismuth and barium also play intriguing roles in altering the magnetic, optical, and electrical properties of materials. Both the total amount of modifier oxides and the network-forming components were found to influence structural characteristics of the glass. Gaining insight into how glass networks form and evolve with rising BaO content is crucial. Consequently, the structural and chemical characteristics of the prepared glass samples were examined using various spectroscopic techniques, including X-ray diffraction (XRD), Fourier transform infrared (FTIR) spectroscopy, Raman spectroscopy, UV-visible absorption, and Electron Paramagnetic Resonance (EPR) spectroscopy.

2 MATERIALS AND METHODS

For the present study, the following compositions were chosen: $35B_2O_3 + (20\text{-}x)Bi_2O_3 + xBaO + 19ZnO + 25TeO_2 + 1V_2O_5$ (x = 0, 5, 10, 15)The starting materials used in the present study were of analar grade: B_2O_3 (99.9%), BaO (99.5%), Bi_2O_3 (99.5%), ZnO (99.9%), TeO_2

(99%), and V_2O_5 (99.5%). Each chemical batch was weighed up to 8 grams and carefully mixed and ground to obtain a homogeneous mixture. The batches were placed in a porcelain crucible and subsequently melted in an electric furnace at 950°C in air. The molten mixture was poured into a preheated (200°C) granite mold and rapidly cooled. To reduce stress and enhance mechanical strength, the quenched samples were annealed.

An Empyrean XRD single crystal diffractometer manufactured by PANalytical was used to examine the materials' amorphous structure. X-ray diffraction (XRD) analyses were carried out using Cu-Kα radiation (λ = 1.5406 Å) at an operating voltage of 45 kV and a current of 40 mA. Data were recorded over a 2θ range of 10° to 90°, with a step size of 0.026° and a scan rate of 0.05°/s. FTIR and Raman spectra were collected to analyze and characterize the functional groups in the structures. FTIR spectra were obtained using a Bruker VERTEX 70v instrument in the wavenumber range of 50 to 4000 cm^{-1}, while Raman spectra were recorded in the range of 350–1050 nm with a WITec alpha 300R instrument. Both techniques were employed for the same purpose of functional group analysis. A Shimadzu UV-3600 Plus spectrophotometer was used to acquire UV-Vis optical absorption spectra at room temperature, covering the wavelength range of 185 to 3300 nm. Using a Varian E-104 X-band EPR spectrometer at a microwave power of 13 dB, the magnetic field was measured in the range of 2500 to 4500 G, with 2,2-diphenyl-1-picrylhydrazyl (DPPH) serving as the primary field marker.

3 RESULTS AND DISCUSSION

3.1 XRD (X-Ray Diffraction)

The glasses in the amorphous structure exhibit some order at short distances, although they lack the clear pattern characteristic of crystals at longer distances. X-ray diffraction is effective for elucidating the non-crystalline framework of a glass system. Figure 1 displays the XRD image pattern of BBiBa glasses, where a prominent peak observed within the 2θ range of 28–30° indicates their amorphous character [26-28]. As the BaO content increases in the studied samples—particularly at 15 mol%—noticeable variations are observed in the XRD peaks. While amorphous glass-like structures lack long-range order, changes in interplanar spacing caused by factors such as thermal expansion, internal stress, or the incorporation of impurities can still influence the angular position of the XRD peak.

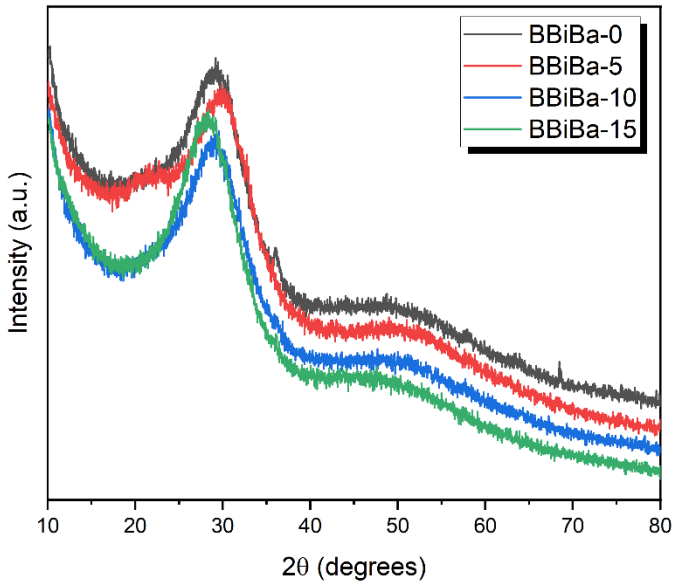


Figure 1. XRD patterns for the BBiBa glass

3.2 FTIR (Fourier Transformation Infrared Spectroscopy)

Infrared spectroscopy offers quantitative insights into the structure of glass samples and serves as an excellent approach for investigating structural disorder in glasses. The FTIR spectra of the glass sample analysed in this investigation are presented in the figure 2 and the observed bands are listed in Table 1.

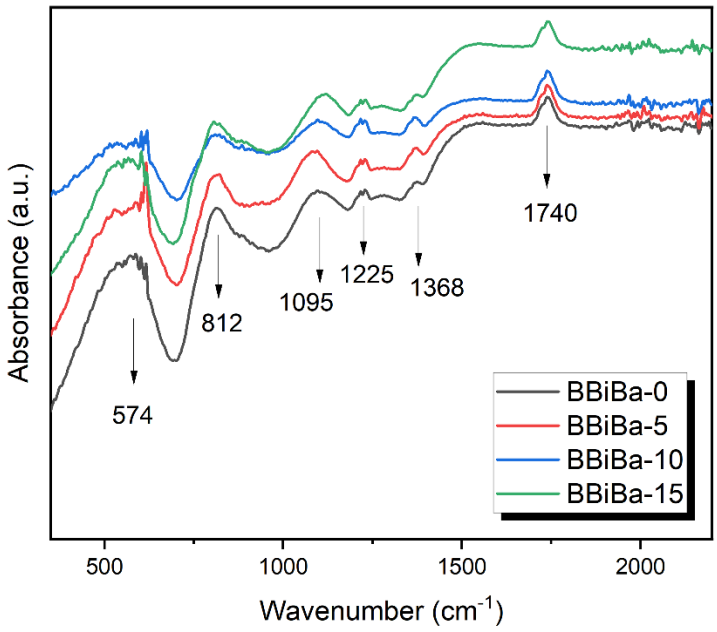


Figure 2. FTIR spectra of BBiBa glasses

Table 1. Assignments of IR bands of BBiBa glass system

IR bands (cm^{-1})	Assignment
574	The stretching vibrations of Bi-O bonds within BiO_6 units
812	Symmetric stretching vibrations of B–O bonds in BO_4 group
1095	Stretching vibrations of B-O bonds in BO_4 units from tri-, tetra-, and penta-borate groups
1225	Symmetric stretching vibration of BO_3 groups
1368	Non-symmetric stretching vibrations of B–O of trigonal BO_3 units
1740	stretching vibration of nonbridging oxygen atoms (NBOs) in BO_3 species

The FTIR spectra in the present investigation exhibit several bands at 574, 812, 1095, 1225, 1368, and 1740 cm^{-1}, as illustrated in Figure 2. The band at around 574 cm^{-1} arises from the stretching vibrations of Bi-O bonds within BiO_6 units exhibiting a deformed octahedral structure [20,25,29,30]. The IR characteristics situated in the first area that ranges between 1200 and 1600 cm^{-1} are attributable to the asymmetric stretching vibration of B–O bonds from the BO_3 trigonal units. The second region's spectrum characteristics, which cover 800–1200 cm^{-1}, are caused by the BO_4 tetrahedral units' B–O bond stretching. The third region 400 - 800 cm^{-1} can be attributed to the different B-O-B bending modes in BO_3 and BO_4 [14,23,31]. The B–O symmetric stretching vibration in the BO_4 units of the glass matrix is observable in the spectral band at 812 cm^{-1} [32,33]. The broad band at 1095 cm^{-1} is attributed to the B–O stretching vibrations in the BO_4 units of triborate, tetraborate, and pentaborate groups [20, 34,35]. The small peak at 1225 cm^{-1} in BBiBa glasses has been assigned to B-O stretching vibrations of $(BO_3)_3$ units in metaborate and orthoborate chains [27,36,37]. Asymmetric stretching mode of the B-O moieties of the trigonal units BO_3 is represented by a tiny peak at 1368 cm^{-1} [38,39]. The final band of the spectra, which was detected at 1740 cm^{-1}, has been ascribed to the B-O stretching modes of the NBO of BO_3 units [3,37,40].

3.3 Raman Spectroscopy

Raman spectroscopy offers structural insights, including significant chemical bonds, molecular vibrations, and atomic interactions within the glass sample. The Raman spectra of all the glasses are represented in Figure 3.

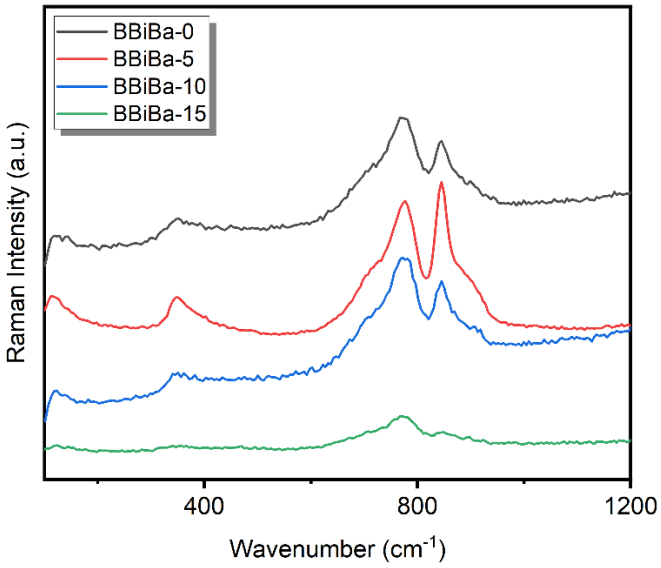


Figure 3. Raman spectra of BBiBa glasses

Raman spectra exhibit four distinct areas for glasses incorporating heavy metal oxides (Bi_2O_3, BaO, PbO, etc.): 1) Low wavenumber acoustic Raman modes (<100 cm^{-1}), 2) Heavy metal (HM) ion vibrations in the 70-160 cm^{-1} region, 3) Bridged anion (BA) vibrations in the range of 300-600 cm^{-1}, 4) Vibrations of non-bridged anions (NBA) at higher wavenumbers [21,41,42]. The peaks observed and the assignments to which they belong are listed in Table 2.

Table 2. BBiBa glass system Raman band allocation

IR bands (cm^{-1})	Assignment
120	vibrations of heavy metal ions Bi^{3+}
347	stretching vibrations of Bi-O-Bi
702	Te–O stretching vibrations in TeO_4
776	B-O stretching vibrations in the [BO_4] tetrahedral unit, Te-O asymmetric stretching vibrations in the TeO_3 (tp) units
845	Symmetric stretching vibrations of the B-O-B bridge
904	B-O bonding vibrations in BO_3 units

The peaks observed around 120 cm^{-1} in Figure 3 are attributed to Bi^{3+} cations from [BiO_3] and [BiO_6] groups. The fact that the band is located at low wave numbers confirms the presence of octahedral units [BiO_6] in the glass structure [37,43,44]. The peaks between 120-600 cm^{-1} correspond to bridging anion vibrations, while the band at 347 cm^{-1} is ascribed to Bi-O-Bi stretching vibrations [20,45,46]. The symmetrical stretching vibrations of Te-O in TeO_4 units are responsible for the small, broad shoulder at around 702 cm^{-1} [36,43,47]. The sharp peak at 776 cm^{-1} in the Raman spectra corresponds to the B-O symmetric stretching vibrations

of the BO_3/BO_4 structural units [41,48]. Furthermore, this Raman peak can potentially be attributed to the Te-O asymmetric stretching vibrations in the TeO_3 (tp) units [36,49,50]. The Raman band at 845 cm^{-1} is due to the symmetric stretching vibration of the B-O-B bridge of the pyroborate units [41,51]. The weak peak at 904 cm^{-1} indicates the presence of B-O bond vibrations in the $[BO_3]$ ortho-borate groups of the triangular units [37,44]. As BaO substitution increases, the intensity of these Raman bands diminishes and, with except for the peaks at 776 and 845 cm^{-1}, others almost completely disappear, as shown in Figure 3. With the incorporation of BaO, significant variations in the intensities of the Raman peaks and slight shifts in their positions were observed. These findings indicate structural modifications within the glass network.

3.4 UV-Vis (Ultraviolet-Visible Spectroscopy)

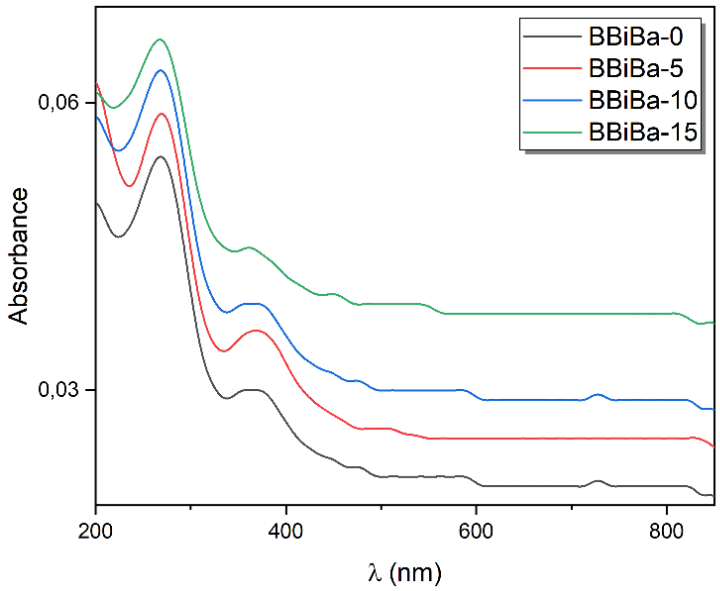


Figure 4. Optical absorption spectra of BTLC glasses

The UV–Vis absorption spectra of VO^{2+} doped BBiBa glass samples were acquired at room temperature within the spectral range of 200-850 nm and is shown in Figure 4. The vanadyl ion possesses the electronic configuration of [Ar] $3d^1$ in the +4-oxidation state and exhibits paramagnetic characteristics in VO^{2+} complex ions, with the ground state of VO^{2+} being ^2D. The degenerate $^2T_{2g}$ and ^2E_g energy levels are separated into $^2B_{2g}$, ^2E_g, and $^2B_{1g}$, $^2A_{1g}$ sublevels, respectively, in the tetragonally compressed octahedral environment. The optical absorption bands for the studied glasses are assigned to the $^2B_{2g} \rightarrow {}^2A_{1g}$, $^2B_{2g} \rightarrow {}^2B_{1g}$ and

$^2B_{2g} \rightarrow {}^2E_g$ electronic transitions. The $^2B_{2g} \rightarrow {}^2A_{1g}$ transition is responsible for a faint band near 480 nm and the $^2B_{2g} \rightarrow {}^2B_{1g}$ transition for a band that appears only prominently at 370 nm at the absorption edge of the glass host in the optical absorption spectra [24,36,52-54]. The optical absorption spectra indicate that the fundamental absorption edge is not distinctly defined, emphasising the glassy characteristics of the materials. Table 3 indicates the cut-off wavelengths ($\boldsymbol{\lambda_c}$) of the present glass samples with another parameter. As the BaO content of the samples increases, the cut-off wavelength shifts towards longer wavelengths.

Table 3. Summary of optical absorption data for BBiBa glasses.

Sample	$\boldsymbol{\lambda_c(nm)}$	$\boldsymbol{E_{ind}(eV)}$	$\boldsymbol{E_d(eV)}$	$\boldsymbol{E_u(eV)}$
BBiBa-0	336	3.446	3.725	0.340
BBiBa-5	342	3.352	3.683	0.370
BBiBa-10	349	3.280	3.642	0.424
BBiBa-15	364	3.124	3.580	0.538

Tauc's theory estimates the band gap energy, both direct and indirect, of glasses using the Davis and Mott relations [55,56].

$$\alpha(v)hv = A\left(hv - E_g\right)^n \tag{1}$$

The energy of the optical band gap (E_g), the constant A, and the exponent n are crucial parameters for determining the kind of transition; n values of 2 and 1/2 signify allowed direct and indirect transitions for the oxide glasses, respectively. By projecting the linear segment of the indirect and direct transition curve to $\alpha = 0$, the optical band gap (E_g) values can be determined (refer to Figure 5 and 6). The data for both direct and indirect transitions, presented in Table 3, indicate that the band gap diminishes with increasing BaO content. In the glass matrix, non-bridging oxygens (NBOs) exhibit a weaker bond to electrons compared to bridging oxygens (BOs), indicating that less energy is necessary to promote an electron to the conduction band. In existing glasses, it may be stated that BOs convert into NBOs as E_g values reduce. The noted consequence is completely consistent with studies that have been reported in the literature [24,30,57,58].

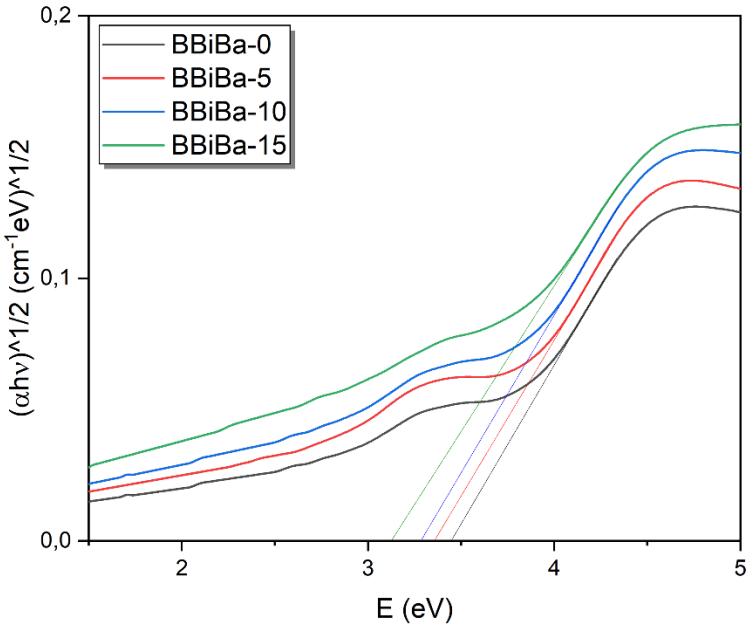


Figure 5. $(\alpha h\nu)^{1/2}$ vs E=hν of the BTLC glasses

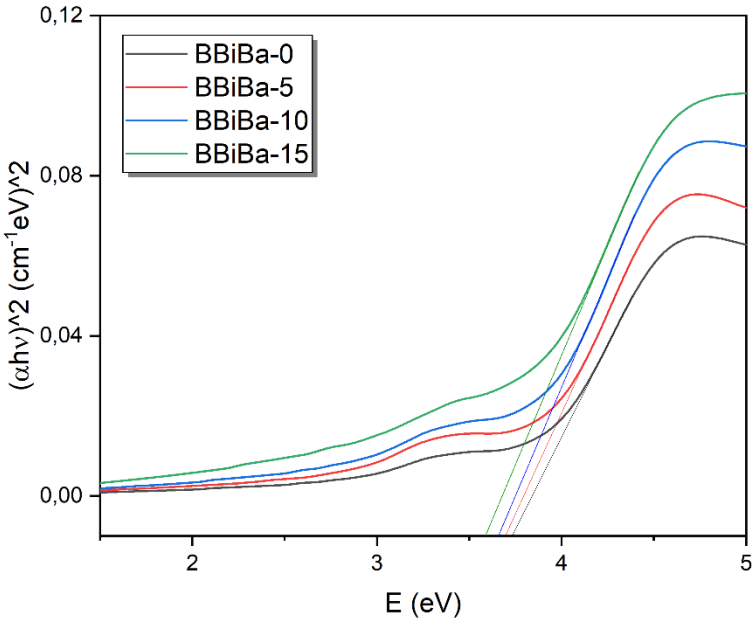


Figure 6. $(\alpha h\nu)^2$ vs E=hν of the BTLC glasses

In the final analysis, an increase in the Urbach energy, another quantity in Table 3, results from an increase in the BaO content. Figure 7 shows the Urbach curve for BBiBa glasses. The presence of BaO in the glass as a modifier and an increase in the concentration of NBO are indicated by the rise in the Urbach energy, which is used to quantify structural disorder [4,37,59,60].

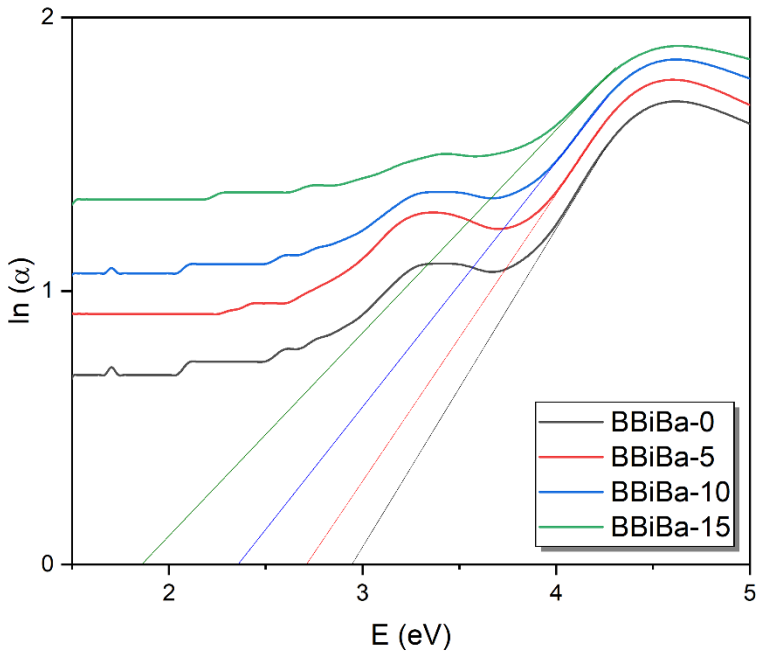


Figure 7. Urbach plots for BTLC glasses

3.5 EPR (Electron Paramagnetic Resonance) Measurements

The electron paramagnetic resonance technique is highly effective for elucidating the local environment surrounding transition metal (TM) ions. TM ions integrated into the glass matrix alter the glass structure by interacting with the surrounding ligands through ligand domains [52,61]. As seen in Figure 8, the EPR spectra of glasses features a hyperfine structure comprising sixteen lines (eight perpendicular and eight parallel) indicative of the unpaired electron ($3d^1$) of the VO^{2+} ion associated with ^{51}V (I = 7/2) exhibiting axial symmetry. Comparable EPR signals have been documented in several glass matrices infused with V_2O_5 [24,58,62-65]. The EPR spectra were examined in accordance with the Hamiltonian for axial symmetry as follows [66].

$$\mathcal{H} = \beta g_{\parallel} B_z S_z + \beta g_{\perp}\left(B_x S_x + B_y S_y\right) + A_{\parallel} S_z I_z + A_{\perp}\left(S_x I_x + S_y I_y\right) \quad (2)$$

In this context, the terminology follows the definitions provided in the relevant reference [4]. The spin–orbit interaction was included in the g values, and nuclear Zeeman and quadrupole interactions were disregarded due to their negligible effects.

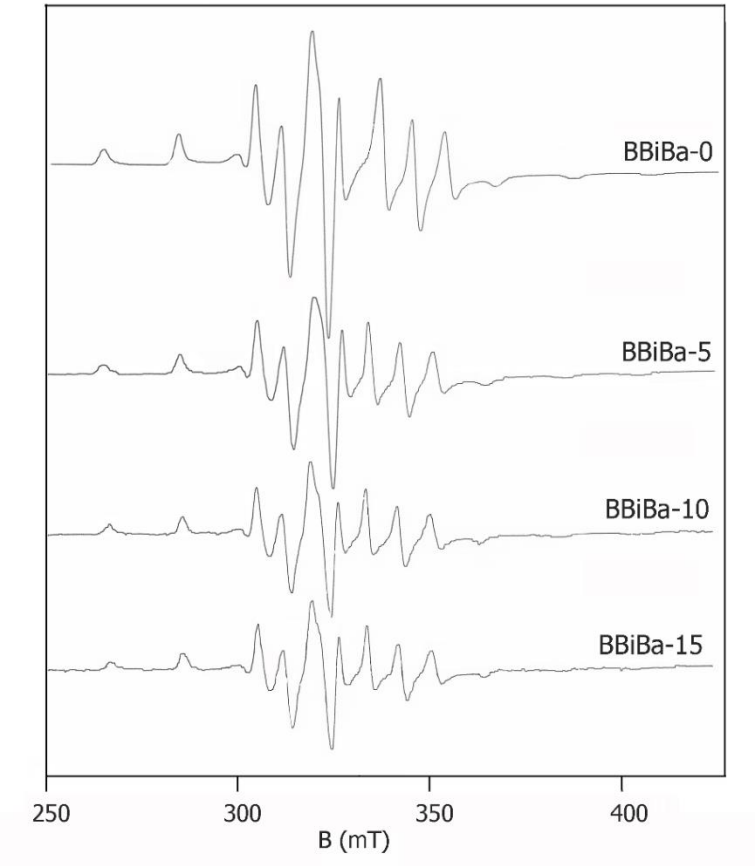


Figure 8. EPR spectra of BBiBa:VO^{2+} glasses

A definition of the spin-Hamiltonian solutions for parallel and perpendicular hyperfine lines is provided below:

$$B_{\parallel}(m_I) = B_{\parallel}(0) - A_{\parallel}m_I - A_{\perp}^2\,[I(I+1) - m_I^2]/2B_{\parallel}(0) \tag{3a}$$

$$B_{\perp}(m_I) = B_{\perp}(0) - A_{\perp}m_I - \left(A_{\perp}^2 + A_{\parallel}^2\right)[I(I+1) - m_I^2]/4B_{\perp}(0) \tag{3b}$$

where $B_{\parallel}(0)$ and $B_{\perp}(0)$ are the centre values from the first derivative curve that correspond to $g_{\parallel}$ and $g_{\perp}$ components, respectively, and m_I is the magnetic quantum number of the vanadium nucleus. The spin-Hamiltonian parameters (SHP) $g_{\parallel}$, $g_{\perp}$, $A_{\parallel}$, and $A_{\perp}$ were obtained from the equation solutions and are presented in Table 4. The vanadium ion is in the octahedral state under tetragonal compression in the current glasses, with a ground state of C_{4v} symmetry, as can be seen from the SHP value data. The degree of tetragonal distortion is indicated by the $\Delta g_{\parallel}/\Delta g_{\perp}$ value. As observed in the table, the values exhibit an almost linear decrease with increasing BaO content, suggesting that tetragonal compression intensifies as the BaO concentration rises [67-69].

Table 4. Spin-Hamiltonian parameters and molecular orbital coefficients calculated for paramagnetic vanadyl complexes in the BBiBa glasses

Sample code	$g_{\parallel}$	$g_{\perp}$	$A_{\parallel}$	$A_{\perp}$	β^2	$1-\alpha^2$	$1-\gamma^2$	P	κ	$\Delta g_{\parallel}/\Delta g_{\perp}$
BBiBa-0	1.945	1.999	193.6	71.4	0.936	0.234	0.987	133	0.808	17.36
BBiBa-5	1.941	1.999	195	70.7	0.932	0.181	0.857	135	0.798	9.73
BBiBa-10	1.938	1.996	196.4	72.14	0.930	0.139	0.726	135	0.811	7.75
BBiBa-15	1.936	1.990	197.14	72.86	0.930	0.113	0.465	135	0.821	5.39

Optical absorption data (d-d transitions) and EPR investigations (g-values) enabled the calculation of molecular orbital (MO) coefficients. The molecular orbital coefficients of the vanadyl ion were derived by linking optical absorption and EPR data through the following equations [69,70]:

$$A_{\parallel} = P\left[\kappa + \frac{4}{7}\beta^2 + \Delta g_{\parallel} + \frac{3}{7}\Delta g_{\perp}\right] \quad and \quad A_{\perp} = -P\left[\kappa - \frac{2}{7}\beta^2 + \frac{11}{14}\Delta g_{\perp}\right] \tag{4}$$

$$g_{\parallel} = g_e\left(1 - \frac{4\lambda\alpha^2\beta^2}{\Delta_{\parallel}}\right) \qquad and \qquad g_{\perp} = g_e\left(1 - \frac{\lambda\gamma^2\beta^2}{\Delta_{\perp}}\right) \tag{5}$$

where λ =170 cm is the spin–orbit coupling constant of VO^{2+} ion and g_e (2.0023) is the free electron g value. Furthermore, P is dipolar hyperfine coupling parameter and κ is Fermi contact term that quantifies the density of unpaired electrons at the vanadium nucleus. High values of κ suggest that the unpaired s electron substantially influences the hyperfine constant [71]. $1-\gamma^2$ and $1-\alpha^2$ are measure of covalency measures of out-of-plane π- and in-plane σ- bonding with the equatorial ligands, respectively and β^2 describes out-of-plane π-bonding along the $V=O$ bond direction. $\Delta_{\parallel}$ (19881cm^{-1}) and $\Delta_{\perp}$(13736 cm^{-1}) represent the electronic energies corresponding to the $^2B_{2g}\rightarrow{}^2B_{1g}$ and $^2B_{2g}\rightarrow{}^2E_{2g}$ transitions in the absorption spectra of these BBiBa glasses, respectively. The ESR parameters and molecular orbital characteristics, computed using the various aforementioned expressions, are presented in Table 4. Based on the β^2 values in Table 4, the covalence of out-of-plane π bonds in the $V=O$ bond direction remains largely unchanged with the increasing BaO content. However, the π bonds between the equatorial ligands and vanadium atoms exhibit partial covalence and are influenced by the increasing BaO content, leading to a substantial reduction in their covalent character.

4 CONCLUSION

The present work examines the influence of BaO content, introduced as a network modifier, on the structural and physical characteristics of BBiBa:V_2O_5 glasses. Understanding

the structural evolution of the glass network with increasing BaO levels provides valuable information for various applications such as healthcare, optical fiber communications, solar panels, touch screens, automotive industry, architecture and energy production. XRD was primarily employed to investigate the structural properties of BBiBa:V_2O_5 glass, whereas complementary techniques such as FTIR, Raman, UV-Vis spectroscopy, and EPR were utilized to elucidate the chemical framework and bonding environment within the glass matrix, leading to the following conclusions:

In the XRD spectra, the absence of peaks signifying crystalline phases verified the BBiBa glasses' amorphous origin. The findings from FTIR and Raman spectra validate the existence of bismuth oxide inside the structural frameworks of the glass samples, and indicate that it comprises structural units including TeO_4, TeO_3, BO_3, and BO_4. The reduction in direct and indirect band gaps with increasing BaO content corroborates the enhancement of non-bridging oxygen formation. The Urbach energy serves as a key parameter for assessing the structural instability of amorphous materials, where lower values correspond to a reduced degree of glassiness. The Urbach energy indicates a progressive increase in the BaO content within the studied glass system, which has high tendency to convert weak bonds into defects in the BBiBa-15 sample. The optical absorption spectra of the glass samples reveal two absorption bands, characteristic of VO^{2+} ions positioned in octahedral sites with tetragonal distortion. The invariance of the Spin-Hamiltonian parameters g and A with varying BaO content suggests minimal impact on the local electronic environment. However, the substantial reduction in $\Delta \boldsymbol{g}_{\parallel}/\Delta \boldsymbol{g}_{\perp}$ indicates a pronounced distortion of the octahedral coordination around VO^{2+} ions. The $1-\gamma^2$ values suggest strong covalence in out-of-plane π bonds, while the $1-\alpha^2$ values indicate weak covalence in in-plane σ bonds. Additionally, β^2 values confirm strong covalence in out-of-plane $V=O$ bonds, highlighting the anisotropic bonding characteristics within the system.

Statement of Research and Publication Ethics

The study is complied with research and publication ethics.

Artificial Intelligence (AI) Contribution Statement

This manuscript was entirely written, edited, analyzed, and prepared without the assistance of any artificial intelligence (AI) tools. All content, including text, data analysis, and figures, was solely generated by the authors.

REFERENCES

[1] C.Bootjomchai, J.Laopaiboon, C.Yenchai, R.Laopaiboon, Gamma-rayshielding and structural properties of barium–bismuth–borosilicate glasses, *Radiat.Phys. Chem.*, vol. 81, pp. 785– 790, July 2012.

[2] J. S. Alzahrani, A. Hammoud, I. Boukhris, Z.A. Alrowaili, A. V. Lebedev, I.O. Olarinoye, M.S. Al-Buriahi, Fabrication and characterization of TeO_2–Na_2O–BaO glass doped with Yb_2O_3 for optical and particulate-radiation shielding applications: Role of Bi_2O_3/WO_3, *Opt. Mater.*, vol. 150, pp. 115141, April 2024.

[3] A. M. Babeer, H. Y. Amin, M.I. Sayyed, Abd El-razek Mahmoud, M.A. Abdo, T. E. Ellakwa, M.S. Sadeq, Impact of mixed heavy metal cations (Ba and Bi) on the structure, optical and ionizing radiation shielding parameters of Bi_2O_3–BaO–Fe_2O_3–SrO–B_2O_3 glass matrix, *Ceram. Int.*, vol. 50, pp. 19245-19258, June 2024.

[4] M. Fidan, A. Acikgoz, G. Demircan, D. Yilmaz, B. Aktas, Optical, structural, physical, and nuclear shielding properties, and albedo parameters of TeO_2–BaO–B_2O_3–PbO–V_2O_5 glasses, *J. Phys. Chem. Solids*, vol. 163, pp. 110543, April 2022.

[5] Y.S. Alajerami, D. Drabold, M.H.A. Mhareb, Katherine Leslee A. Cimatu, Gang Chen, M. Kurudirek, Radiation shielding properties of bismuth borate glasses doped with different concentrations of Cadmium oxides, *Ceram. Int.*, vol. 46, pp. 12718-12726, June 2020.

[6] H. Abdurabu Thabit, A. Khamim Ismail, H. Es-soufi, D.A. Abdulmalik, A. M. Al-Fakih, S. Alraddadi, M.I. Sayyed, Structural, thermal, and mechanical investigation of telluro-borate-Bismuth glass for radiation shielding, *J. Mater. Res. Technol*, vol. 24, pp. 4353-4363, May-June 2023.

[7] D.A. Aloraini, A.H. Almuqrin, M.I. Sayyed, A. Kumar, Exploring the mechanical behavior and gamma ray attenuation properties of Bi_2O_3–BaO–V_2O_5 glasses, *J Mater Sci: Mater Electron*, vol. 34, pp.1746, September 2023.

[8] A.K. Reza Bagheri, Moghaddam, H. Yousefnia, Gamma ray shielding study of barium-bismuth-borosilicate glasses as transparent shielding materials using MCNP-4 C code, XCOM program, and available experimental data, *Nuclear Eng. Technol.*, vol. 49, pp. 216–223, February 2017.

[9] M.I. Sayyed, M.H.A. Mhareb, I. Alrammah, Ali A.A. Alghamdi, A. Abdullah Alsurayj, S. Talib Alminhali, M. Essam Abdelgawad, Z. Ali Abugurain, N. Alonizan, M. Alqahtani, Gamma ray shielding and structural properties for TeO_2-BaO-MO modified with Bi_2O_3, TiO_2, MnO_2, MoO_3, *Radiat. Phys. Chem*., vol. 205, pp. 110714, April 2023.

[10] H. Aboud, Mohammed J.R. Aldhuhaibat, Y. Alajermi, Gamma radiation shielding traits of B_2O_3–Bi_2O_3–CdO–BaO–PbO glasses, *Radiat. Phys. Chem*, vol. 191, pp. 109836, February 2022.

[11] N. Effendy, M.H.M. Zaid, K.A. Matori, S.M. Iskandar, R. Hisam, M.N. Azlan, N.N. Yusof, Hesham M.H. Zakaly, Shams A.M. Issa, Y.B. Saddeek, Fabrication of novel BaO–Al_2O_3–Bi_2O_3–B_2O_3 glass system: Comprehensive study on elastic, mechanical and shielding properties, *Prog. Nucl. Energy*, vol. 153, pp. 104418, November 2022.

[12] M.I. Sayyed, M.H.A. Mhareb, B. Ceviz Şakar, K.A. Mahmoud, E. Şakar, H. Abdurabu Thabit, Kawa M. Kaky, S.O. Baki, Experimental investigation of structural and radiation shielding features of Li_2O-BaO-ZnO-B_2O_3-Bi_2O_3 glass systems, *Radiat. Phys. Chem*, vol. 218, pp. 111640, May 2024.

[13] A. Kumar, M.I. Sayyed, Taha. A. Hanafy, Physical, mechanical, structural, optical and gamma ray shielding behavior of (90-x-y)B_2O_3–5PbO–5BaO-xZnO-yTiO_2 glasses, *Ceram. Int*., vol. 50, pp. 43279-43288, November 2024..

[14] M.A. Ouis, M.A. Marzouk, Comparative optical, FTIR and photoluminescence spectral analysis of copper ions in BaO–B2O3, SrO– B_2O_3 or Bi2O3– B_2O_3 glasses and impact of gamma irradiation, *J. Lumin*, vol. 223, pp. 117242, July 2020.

[15] S. Biradar, M.N. Chandrashekara, A. Dinkar, Manjunatha, G.B. Devidas, A.S. Bennal, M.I. Sayyed, H. Es-soufi, A multifaceted study of B_2O_3-BaO-PbO-WO_3 glasses doped with Bi2O3: Insights from physical, thermal, structural, mechanical and optical analyses towards improved shielding properties, *Ceram. Int*., vol. 50, pp. 29332-29345, September 2024.

[16] H.O. Tekin, G. Susoy, S. A.M. Issa, A. Ene, Ghada ALMisned, Y.S. Rammah, Fatema T. Ali, M. Algethami, Hesham M.H. Zakaly, Heavy metal oxide (HMO) glasses as an effective member of glass

shield family: A comprehensive characterization on gamma ray shielding properties of various structures, *J. Mater. Res. Technol*, vol. 18, pp. 231-244, May-June 2022.

[17] S. Prakash Singh, R.P.S. Chakradhar, J.L. Rao, B. Karmakar, EPR, FTIR, optical absorption and photoluminescence studies of Fe_2O_3 and CeO_2 doped $ZnO–Bi_2O_3–B_2O_3$ glasses, *J. Alloys Compd*., vol. 493, pp. 256-262, March 2010.

[18] S. Kaewjaeng, S. Kothan, N. Wantana, H.J. Kim, R. Rajaramakrishna, C. Jumpee, P. Limsuwan, J. Kaewkhao, Fabrication luminescence and radiation shielding properties of $Gd_2O_3–La_2O3–ZnO–B_2O_3–Sm_2O_3$ glasses, *Radiat. Phys. Chem*, vol. 202, pp. 110537, January 2023.

[19] L. Srinivasa Rao, AC conductivity and polarization phenomenon of $Li_2O–MoO_3–B_2O_3:V_2O_5$ glasses, *J. Alloys Compd*., vol. 787, pp. 1280-1289, May 2019.

[20] J. Liu, X. Xu, T. Zheng, Y. Guo, J. Lv, Effect of Bi_2O_3 content on the structure and properties of Bi_2O_3-B_2O_3-BaO-ZnO glass, *J. Non-Cryst. Solids*, vol. 575, pp. 121211, January 2022.

[21] [21] P. Kaur, K.J. Singh, S. Thakur, P. Singh, B.S. Bajwa, Investigation of bismuth borate glass system modified with barium for structural and gamma-ray shielding properties, *Spectrochim. Acta - A: Mol. Biomol*., vol. 206, pp. 367-377, January 2019.

[22] E. Kavaz, N. Yıldız Yorgun, Gamma ray buildup factors of lithium borate glasses doped with minerals, *J. Alloys Compd*., vol. 752, pp. 61-67, July 2018.

[23] M. Fidan, A.Acikgoz, D. Yılmaz, G. Demircan, S. Kalecik, B. Aktas, S. Isgor, Investigation of the structural, mechanical, radiation and neutron shielding properties of the TeO_2-B_2O_3-Li_2O-MoO_3-CuO glass system*, J. Alloys Compd*., vol. 976, pp. 172981, March 2024.

[24] B.V. Padlyak, T.B. Padlyak, Spectroscopic properties of the V-doped borate glasses, *J. Non-Cryst. Solids*, vol. 528, pp. 119741, January 2020.

[25] T. Annapurna, M. Kostrzewa, A. Siva Sesha Reddy, A. Ingram, J. Ashok, V. Ravi Kumar, N. Veeraiah, Polaronic conduction and dielectric relaxation dynamics in V_2O_5 added lead bismuth silicate glass system, *J. Non-Cryst. Solids*, vol. 528, pp. 119746, January 2020.

[26] V. Sreenivasulu, G. Upender, V. Chandra Mouli, M. Prasad, Structural, thermal and optical properties of $TeO_2–ZnO–CdO–BaO$ glasses doped with VO^{2+}, *Spectrochim. Acta - A: Mol. Biomol*., vol. 148, pp. 215-222, September 2015.

[27] J. Zheng, H. Wang, S. Lin, Z. Pan, Q. Yang, J. Liu, Spectral characteristics of highly thermally stable Eu^{3+}-doped P_2O_5-B_2O_3-ZnO-BaO glasses for tricolor WLEDs and red lasers, *J. Alloys Compd*., vol. 1010, pp. 177668, January 2025.

[28] Ö. F.Ötken, İ. Ceylan, B. Çiçek, High-temperature aqueous corrosion of $MO–Na_2O–B_2O_3–SiO_2$ glass and glass-ceramic coatings on metallic substrates: Effect of alkaline earth metals M^{2+}= {Ca^{2+}, Sr^{2+}, Ba^{2+}}, J. *Eur. Ceram. Soc.,* vol. 45, pp. 116820, Jaunary 2025.

[29] L. Zhang, Q. Sun, J. Wang, Z. Zhang, W. Zhang, J. Wang, H. Chen, M. Li, Effect of SrO content on microstructure of Bi_2O_3-B_2O_3-ZnO-BaO-SrO low-melting glass frit and joining performance of sodalime glass substrates, *J. Alloys Compd*., vol. 872, pp. 159707, August 2021.

[30] M.I. Sayyed, H.O. Tekin, Malaa M. Taki, M.H.A. Mhareb, O. Agar, E. Şakar, Kawa M. Kaky, Bi_2O_3-B_2O_3-ZnO-BaO-Li_2O glass system for gamma ray shielding applications, *Optik*, vol. 201, pp. 163525, January 2020.

[31] M.S. Sadeq, A.S. Sharafelden, Fifi M. Reda, Mona H. Ibrahim, Effect of ZnO on the structure, optical properties and ESR studies of $B_2O_3–Na_2O–SrO–Fe_2O_3–ZnO$ glass system, *Ceram. Int*., vol. 51, pp. 4878-4890, February 2025.

[32] Kh. S. Shaaban, D. A. Aloraini, K. Alsafi, H. M. Almutairi, W. M. Al-Saleh, A.S. Alzahrani, Role of CeO_2 in the enhancement of the properties of the SiO_2-B_2O_3-BaO-Li_2O-glass system: Structural, mechanical and radiation shielding study, *Mater. Today Commun*., vol 38, pp. 108309, March 2024.

[33] A. E. Mwakuna, C. Laxmikanth, R.K.N.R. Manepalli, Effect of replacing B_2O_3 with CuO on the structural, optical absorption, thermal, mechanical, and gamma-ray shielding properties of $B_2O_3–Bi_2O_3–K_2O$ glass, *Opt. Mater*., vol. 157, pp. 116282, November 2024.

[34] E. Mansour, FTIR spectra of pseudo-binary sodium borate glasses containing TeO_2, *J. Mol. Struct*., vol. 1014, pp. 1-6, April 2012.

[35] R. E. M. Khaidir, Y. W. Fen, M. H. Mohd Zaid, K. A. Matori, N. A. Sheh Omar, M. Fahmi Anuar, S.A. Abdul Wahab, A. Z. Khirel Azman, Optical band gap and photoluminescence studies of Eu^{3+}-doped zinc silicate derived from waste rice husks, *Optik*, vol. 182, pp. 486-495, April 2019.

[36] M. Anand Pandarinath, P. Muralikrishna, D. Suresh Babu, B. Vijaya Kumar, G. Upender, Vibrational, thermal and optical studies of $30TeO_2$-$39.5B_2O_3$-(30-x)ZnO-xLi_2O-$0.5V_2O_5$ ($0 \leq x \leq 30$ mol%) glass system, *J. Non-Cryst. Solids*, vol. 566, pp. 120875, August 2021.

[37] I. Saber, K. Dahmani, M. Galai, A. EL Magri, R. Hsissou, H. Barbita, M. Belfaquir, I. Warad, N. AL-Zaqri, M.S. Elyoubi, Synthesis and characterization of new eco-friendly vitreous system Bi_2O_3–B_2O3–BaO: Structural, morphologic, and thermal analysis, *Opt. Mater.*, vol. 149, pp. 115079, March 2024.

[38] S.N. Nazrin, A. Amat, Shams A.M. Issa, Hesham M.H. Zakaly, S. S. Gunasekaran, H. B. Zaman, M.H.M. Zaid, M.H.M. Tahir, Ibrahim A. Shaaban, I. Sharma, Elastic and radiation shielding properties of zinc borotellurite glass systems: The impact of gadolinium oxide, *Opt. Mater.*, vol. 157, pp. 116252, November 2024.

[39] T. Satyanarayana, I. V. Kityk, M. Piasecki, P. Bragiel, M. G. Brik, Y. Gandhi and N. Veeraiah, Structural investigations on PbO–Sb_2O_3–B_2O_3:CoO glass ceramics by means of spectroscopic and dielectric studies, *J. Phys.: Condens. Matter*, vol. 21, pp. 245104, May 2009.

[40] A. M. Babeer, M.I. Sayyed, H. Y. Amin, Abd El-razek Mahmoud, M.S. Sadeq, Composition impacts of La_2O_3 on the structure and radiation shielding parameters of NiO–BaO–B_2O_3 glasses, *Opt. Mater.*, vol. 147, pp. 114622, January 2024.

[41] M. Purnima, S. Stalin, A. Edukondalu, M.A. Samee, S. Kareem Ahmmad, S. Rahman, Spectroscopic studies on Li_2O–MgO–Bi_2O_3–B_2O_3 glasses, *Chin. J. Phys.*, vol. 66, pp. 517-526, August 2020.

[42] M.E. Lines, A.E. Miller, K. Nassau, K.B. Lyons, Absolute raman intensities in glasses: II. Germania-based heavy metal oxides and global criteria, *J. Non-Cryst. Solids*, vol. 89, pp. 163-180, January 1987.

[43] A. McGlashan, Peter N. Nelson, P. Syam Prasad, M. Iezid, F. Goumeidane, R. Rajaramakrishna, P. Venkateswara Rao, Physical, thermal, optical, shielding and elastic properties of Bi_2O_3–B_2O_3–TeO_2 glass system doped with Fe_2O_3, *Radiat. Phys. and Chem.*, vol. 217, pp. 111444, April 2024.

[44] L. Tichy, H. Ticha, L. Herzigova, J. Ozdanova, Some physical properties of $(Bi_2O_3)x(BaO)0.5-x(B_2O_3)0.5$ glasses, *Mater. Chem. Phys.*, vol. 126, pp. 289-294, March 2011.

[45] F. He, Z. He, J. Xie, and J. Li, Y. IR and Raman Spectra Properties of Bi_2O_3-ZnO-B_2O_3-BaO Quaternary Glass System, *Am. J. Anal. Chem.*, vol. 5, pp. 1142-1150, November 2014.

[46] S. Thakur, V. Thakur, A. Kaur, L. Singh, Structural, Optical and thermal properties of nickel doped bismuth borate glasses, *J. Non-Cryst. Solids.*, vol. 512, pp. 60–71, July 2019.

[47] N. Gupta, A. Kaur, A. Khanna, F. Gonz` alez, C. Pesquera, R. Iordanova, B. Chen, Structure-property correlations in TiO_2 -Bi_2O_3-B_2O_3-TeO_2 glasses, *J. Non-Cryst. Solids*, vol. 470, pp. 168–177, September 2017.

[48] W. Gao, J. Wang, S. Cao, L. Li, J. Han, Bond characteristics, microstructure, and microwave dielectric properties of Bi_2O_3–ZnO–B_2O_3 glass-ceramics with Li_2O substitution, *Ceram. Int.*, vol. 50, pp. 5927-5935, February 2024.

[49] H. Ticha, J. Schwarz, L. Tichy, Raman spectra and optical band gap in some PbO-ZnO-TeO_2 glasses, *Mater. Chem. Phys.*, vol. 237, pp. 121834, November 2019.

[50] Y. Ban, Z. He, F.Qin, D. Zhou, Y. Cong, T. Wu, Y. Wu, Influence of La_2O_3 on the structural and luminescence properties in Er^{3+}/Ho^{3+} co-doped TeO_2-BaF_2-ZnF_2 glass, *Ceram. Int.*, Available online, January 2025.

[51] E.I. Kamitsos, G.D. Chryssikos, Borate glass structure by Raman and infrared spectroscopies, *J. Mol. Struct.*, vol. 247, pp. 1-16, July 1991,

[52] A. Madhu, N.S. Abd EL-Gawaad, S. Ali Osman Abdallah, Sunanda T. Dadami, B.G. Hegde, T. Uthayakumar, MB. Karthik Kumar, N. Srinatha, Unravelling the conductivity behaviour of thermally stable Li_2O– Bi_2O_3–B_2O_3–P_2O_5 glasses embedded with V_2O_5, *Ceram. Int.*, vol. 49, pp. 28781-28793, September 2023.

[53] O. Pravakar, T. Siddaiah, P.V.R.K. Ramacharyulu, N.O. Gopal, Ch. Ramu, H. Nagabhushana, Spectroscopic, thermal, structural and electrical studies on VO^{2+} ions doped PVA/MAA:EA polymer blend films, *J. Sci.: Adv. Mater. Dev.*, vol. 4, pp. 267-275, June 2019.

[54] B. Srinivas, A. Hameed, R. Vijaya Kumar, M. Narasimha Chary, and Md. Shareefuddin, Experimental and theoretical investigations on the EPR parameters and molecular orbital bonding coefficients of VO^{2+} ions in BTTB glasses. *Phil. Mag.*, vol. 98, pp. 1625–1640, March 2018.

[55] A. Davis, N.F. Mott, Conduction in non-crystalline systems V. Conductivity, optical absorption and photoconductivity in amorphous semiconductors, *Phil. Mag*., vol. 22, pp. 903–922, Jun 1970.

[56] J. Tauc, A. Menth, States in the gap, *J. Non-Cryst. Solids*., vol. 8, pp. 569–585, June 1972.

[57] A. S. Alqarni, N.N. Yusof, A. A. Kassimu, I. Bulus, I. M. Danmallam, S. Hashim, H. A. Thabit, Exploring the physio-elastic properties and optical band gap energies of boro-telluro-dolomite glasses infused with Nd_2O_3 dopants, *Optik*, vol. 288, pp. 171149, October 2023.

[58] A. El Boukili, L. Boudad, M. Taibi, M. El Amraoui, J. Aride, M. Rouzières, H. Saadaoui, Synthesis and investigation of the V_2O_5 effect on the properties of Na_2O–NiO-(1-x)P_2O_5–xV_2O_5 ($0 \leq x \leq 0.6$) system, *Ceram. Int.*, vol. 50, pp. 1693-1705, January 2024.

[59] J. S. Alzahrani, A. V. Lebedev, S. A. Avanesov, A. Hammoud, Z.A. Alrowaili, Z. M.M. Mahmoud, I.O. Olarinoye, C. Sriwunkum, M.S. Al-Buriahi, Synthesis, optical properties and radiation shielding performance of TeO_2-Na_2O-BaO-WO_3 glass system, *Optik*, vol. 261, pp. 169167, July 2022.

[60] A. Rani, R. Parmar, R.S. Kundu, Structural, physical and optical study of calcium modified bismuth borovanadate glasses: V_2O_5-B_2O_3-Bi_2O_3-CaO, *Opt. Mater*., vol. 143, pp. 114135, September 2023,

[61] T. Satyanarayana, K. Chandra Sekhar, K.M. Nissamudeen, Md. Shareefuddin, Unveiling the structural properties of $K_2B_4O_7$–$Li_2B_4O_7$–TeO_2–CuO glass: A comprehensive analysis using UV, EPR, FTIR and Raman spectroscopy, *Opt. Mater*., vol. 157, pp. 116425, November 2024.

[62] M. Montesso, D. Manzani, J. P. Donoso, C. J. Magon, I. D.A. Silva, M. Chiesa, E. Morra, M. Nalin, Synthesis and structural characterization of a new $SbPO_4$-GeO_2 glass system, *J. Non-Cryst. Solids*, vol. 500, pp. 133-140, November 2018.

[63] S. Bahammam, S. Abd El Al, F.M. Ezz-Eldin, Synthesis and characterization of γ-irradiated cadmium-borate glasses doped V_2O_5, *Results Phys*., vol. 7, pp. 241-249, 2017.

[64] A. Madhu, C.M. Joseph, Sunanda T. Dadami, N. Srinatha, Structural and spectroscopic studies of V_2O_5 incorporated lithium-bismuth-boro-tellurite glass ceramics, *Mater. Today: Proc*., vol. 62, pp. 5489-5493, 2022.

[65] D.L. Griscom, Electron spin resonance in glasses, *J. Non-Cryst. Solids*, vol. 40, pp. 211-272, July 1980.

[66] A. Abragam, B. Bleaney, Electron Paramagnetic Resonance of Transition Ions, *Oxford University* Press, 1970.

[67] M. Naga Sireesha, J. Suresh Krishna, V. Vinay Krishna, Ch. Linga Raju, Structural and spectroscopic properties of V_2O_5 doped zinc bismuth sodium borate glasses, *Mater. Today: Proc*., vol. 80, pp. 840-845, 2023.

[68] B. Srinivas, A. Hameed, G. Srinivas, M. Narasimha Chary, Md. Shareefuddin, Influence of V_2O_5 on physical and spectral (optical, EPR & FTIR) studies of SrO-TeO_2-TiO_2-B_2O_3 glasses*, Optik*, vol. 225, pp. 165815, January 2021.

[69] N. Rama Krishna Chand, B.K. Sudhakar, G. Ravikumar, V. Gayathri, P. Devika, T. Vennela, G. Srinivasa Rao, Ch.Srinivasa Rao, Influence of multi valent states of vanadium ions in ZnO doped novel calcium fluoro phosphate bio glasses, *J. Mech. Behav. Biomed. Mater.*, vol. 131, pp. 105230, July 2022.

[70] C.J. Ballhausen, H.B. Gray, The electronic structure of the vanadyl ion, *Inorg. Chem*., vol. 1, pp. 111–122, February 1962.

[71] B. Yasoda, R.P. Sreekanth Chakradhar, J.L. Rao, N.O. Gopal,EPR and optical absorption studies of VO^{2+} ions in alkaline earth aluminoborate glasses, *Mater. Chem. Phys*., vol. 106, pp. 33-38, November 2007.

BİTLİS EREN ÜNİVERSİTESİ
FEN BİLİMLERİ DERGİSİ

ISSN: 2147-3129 / e-ISSN: 2147-3188

Article Type	: Research Article	**Year**	: 2025
Received	: February 24, 2025	**Volume**	: 14
Revised	: May 26, 2025	**Issue**	: 3
Accepted	: July 1, 2025	**Pages**	: 1403-1419
DOI	: 10.17798/bitlisfen.1646155		

THE EFFECTIVENESS OF ADVANCED MACHINE LEARNING MODELS IN IQ PREDICTION IN THE CONTEXT OF EDUCATION, HEALTH, AND SOCIOECONOMIC INDICATORS

Doruk AYBERKİN [1,*], Özel SEBETCİ [2]

[1] *Bayburt University, Management Information Systems Department, Bayburt, Türkiye*

[2] *Adnan Menderes University, Computer Technologies Department, Aydın, Türkiye*

**** Corresponding Author:*** *doruk@bayburt.edu.tr*

ABSTRACT

This study investigates the effectiveness of advanced machine learning models in predicting IQ levels using a diverse set of socioeconomic and health indicators from global databases such as WHO, the World Bank, and United Nations organizations. The research employs various algorithms, including Linear Regression, Random Forest, Gradient Boosting, Support Vector Machines, Ridge and Lasso Regressions, XGBoost, LightGBM, and a Stacking Regressor to capture both linear and non-linear relationships. Evaluation metrics such as Mean Absolute Error (MAE), Root Mean Square Error (RMSE), and R-squared (R^2) reveal that LightGBM and Stacking Regressor models excel in accuracy and generalization. The study highlights the trade-off between model interpretability and predictive power, emphasizing that simpler models offer greater transparency. In contrast, more complex models successfully capture intricate interactions among education, health, and economic factors. The findings provide valuable insights for policymakers and researchers, suggesting that machine learning approaches can significantly enhance understanding of the determinants of IQ and aid in developing targeted strategies in education and social policy.

Keywords: Machine learning and socioeconomic indicators, Data analysis, Public policies, Cognitive outcomes of education policies, Planning with IQ estimation.

1 INTRODUCTION

In today's world, intelligence quotient (IQ) plays a significant role in individual and societal success. IQ reflects general abilities in problem-solving skills, learning speed, abstract

thinking ability, and various mental functions [1]. This concept influences fields ranging from education to business, healthcare services, and social policies. Therefore, understanding and predicting IQ is crucial for individual educational and career development, societal welfare, and overall human progress.

Comprehending the factors influencing IQ levels is critical for improving educational systems, supporting public health, and fostering socio-economic development. Accurately identifying and analyzing these factors can provide valuable information for policymakers, educators, and health professionals, aiding in developing more effective strategies.

Machine learning has significantly advanced in recent years in analyzing complex datasets and making predictions. The application of these technologies in the field of social sciences, especially in predicting IQ levels, offers new opportunities. Machine learning models can unearth complex relationships and patterns from large datasets, providing more in-depth insights into factors affecting IQ.

Recent studies have emphasized the importance of model interpretability in predictive social science applications, especially where decisions have ethical and policy implications [2],[3]. Techniques like SHAP (Shapley Additive Explanations) have been increasingly utilized to uncover feature importance and support transparent modeling in domains such as education, mental health, and public safety [4],[5],[6]. This growing focus on explainable AI enhances trust and accountability in the use of ML models in high-impact areas.

The prediction of IQ using interpretable machine learning models represents a novel interdisciplinary endeavor. While several studies have applied ML to forecast behavioral or health outcomes, the specific integration of global socioeconomic, educational, and public health indicators to model IQ remains underexplored. Our work addresses this gap by leveraging both traditional models and modern ensemble learners—such as LightGBM and Stacking Regressors—while evaluating performance and interpretability using rigorous cross-validation and SHAP-based explanation frameworks [7],[8].

The primary objective of the present research is to identify the key factors influencing IQ levels and to forecast IQ outcomes using a diverse set of machine learning models. Both traditional statistical approaches and advanced ensemble learning algorithms are employed to capture linear and nonlinear relationships within the data. Model performance is assessed through multiple evaluation metrics, including error rates and generalization ability across different data partitions. In addition, context, model interpretability and real-world applicability are emphasized as core considerations.

By incorporating cross-validation metrics alongside feature attribution techniques such as SHAP, the analysis not only quantifies predictive success but also elucidates the underlying decision logic of each model, thereby enhancing transparency and supporting the formulation of evidence-based public strategies.

The manuscript provides a comprehensive account of the methodological design, data sources, machine learning implementations, and key findings. The structure begins with an explanation of the research design and data preprocessing, followed by detailed model evaluation. Findings are discussed in relation to their broader implications for education, health, and policy. The conclusion offers a synthesis of insights gained and outlines directions for future inquiry.

2 RESEARCH PROBLEM / RESEARCH QUESTIONS

The relationship between intelligence quotient (IQ) and socioeconomic variables has long been a central focus in the social sciences. Traditional statistical approaches have contributed foundational knowledge by identifying linear associations between IQ and indicators such as education, income, and health. However, these methods often fall short in capturing nonlinear dynamics and fail to accommodate the complexity of high-dimensional, globally heterogeneous datasets.

Recent developments in machine learning (ML) offer powerful alternatives for modeling intricate interactions among educational, economic, and health-related predictors. Ensemble techniques such as Gradient Boosting, Random Forests, LightGBM, and Stacking Regressors have demonstrated strong capabilities in extracting patterns from diverse datasets, making them well-suited for addressing cognitive prediction tasks within a socioeconomic context [7],[8].

The present investigation evaluates the predictive capabilities of thirteen different machine learning algorithms—including Linear Regression, Ridge, Lasso, ElasticNet, Decision Tree, Random Forest, Gradient Boosting, Support Vector Machines (SVM), XGBoost, LightGBM, Artificial Neural Networks, K-Nearest Neighbors, and Stacking Regressor—across 142 countries using global datasets curated from the World Health Organization (WHO), World Bank, and United Nations (UN).

Among the numerous predictors, education ($r = 0.773$) and infrastructure-market access ($r = 0.743$) emerged as the most influential variables based on correlation analyses. LightGBM and Stacking Regressor models achieved the highest predictive performance, with R^2 values of

0.6725 and 0.7277, respectively, as confirmed by 5-fold cross-validation. Despite this accuracy, interpretability remained a key concern, reinforcing the value of explainable AI (XAI) approaches such as SHAP for extracting transparent feature attributions.

Two core research questions guide this work:

1) How effective are advanced machine learning models in predicting national average IQ levels using globally available socioeconomic and health indicators?

2) Which specific factors—among education, economic conditions, healthcare quality, infrastructure, and demographic variables—exert the strongest influence on IQ prediction outcomes?

By addressing these questions, the study contributes to the growing body of interdisciplinary research that merges data science with evidence-based social policy, providing a methodological blueprint for analyzing and mitigating cognitive disparities on a global scale.

3 METHODOLOGY

3.1 Data Collection and Preprocessing

The dataset consisted of over 25 socioeconomic, educational, health, and demographic indicators covering 142 countries. Primary data sources included publicly available databases from the World Health Organization (WHO), the World Bank, and the United Nations (UN). Key variables comprised national average IQ scores, Human Development Index (HDI), life expectancy, expected and mean years of schooling, Gross National Income (GNI), and alcohol consumption rates.

To ensure analytical robustness, a series of preprocessing steps were applied:

- Missing Data Handling: No missing values were detected in the final integrated dataset.
- Categorical Encoding: Categorical variables such as governance and institutional quality were transformed using a combination of label and one-hot encoding techniques.
- Normalization: A min-max scaling approach was employed to standardize feature ranges, allowing models sensitive to scale (e.g., SVM, k-NN) to perform optimally.
- Outlier Detection and Removal: The Interquartile Range (IQR) method was used to identify and remove outliers outside the 95% confidence interval.

- Feature Engineering: Composite indices such as Infrastructure and Market Access were derived by combining multiple dimensions to better represent systemic effects on IQ outcomes.

The final dataset was composed exclusively of numerical features to maintain compatibility with the applied machine learning algorithms and avoid encoding-related variance. Additionally, multicollinearity among features was assessed using the Variance Inflation Factor (VIF), and redundant predictors (e.g., Legatum Index) with VIF > 10 were excluded to stabilize model estimates [9].

3.2 Model Selection and Evaluation

A total of thirteen machine learning algorithms were implemented to model the relationship between IQ and the selected features. These models included:

- Linear models: Linear Regression, Ridge Regression, Lasso Regression, and ElasticNet.
- Tree-based and ensemble methods: Decision Tree, Random Forest, Gradient Boosting, XGBoost, and LightGBM.
- Other algorithms: Support Vector Machines (SVM), K-Nearest Neighbors (k-NN), Artificial Neural Networks (MLP), and a Stacking Regressor ensemble.

Model performance was evaluated using three metrics: Mean Absolute Error (MAE), Root Mean Square Error (RMSE), and R-squared (R^2). To assess generalization capacity and mitigate overfitting, a 5-fold cross-validation strategy was adopted across all models.

LightGBM and the Stacking Regressor emerged as the top-performing models, with mean R^2 values of 0.611 and 0.506, respectively. However, paired t-tests and Wilcoxon signed-rank tests revealed that their performance differences compared to Random Forest and Lasso Regression were not statistically significant ($p > 0.6$), indicating comparable efficacy across multiple robust algorithms.

In addition, SHAP (Shapley Additive Explanations) values were used to interpret the outputs of top models, offering insights into the most influential features contributing to IQ prediction. This interpretability aspect ensured transparency and facilitated the identification of key socioeconomic drivers such as education level, infrastructure access, and governance quality.

4 LITERATURE REVIEW

The Intelligence Quotient (IQ) serves as a widely accepted proxy for cognitive functioning, with proven implications in education, employment outcomes, and broader societal integration [10],[11]. Its formation is multifactorial, shaped by genetics, early childhood stimulation, educational opportunities, and socioeconomic environment [12].

IQ prediction has recently attracted the attention of data scientists, especially with the growing availability of large-scale international datasets and advancements in artificial intelligence (AI) and machine learning (ML) techniques. Early studies, such as those by King & Resick [13] and Eloyan et al. [14], demonstrated that models like Linear Regression and Random Forest could successfully predict IQ-related cognitive dimensions from structured data. Later works by Feczko et al. [15] and Zhou et al. [16] further supported this by integrating neuroimaging and behavioral data.

Recent advances in ensemble modeling have introduced more flexible algorithms like XGBoost and LightGBM, which outperform traditional regressors in non-linear, high-dimensional contexts [17],[18]. These models have proven especially effective in educational forecasting [5], health risk stratification [4], and even climate science [2], showcasing their versatility across domains.

While predictive power is important, the issue of model interpretability has emerged as a critical concern—particularly when applying ML models to human-centered data. Explainable AI (XAI) frameworks such as SHAP (SHapley Additive exPlanations) have been proposed to bridge this gap [3],[6]. These tools decompose predictions into additive feature contributions, thereby enhancing transparency and enabling validation by domain experts [8],[19].

In particular, SHAP has been instrumental in applied research areas involving sensitive decisions, including suicide prediction [4], diabetes detection [20], and loan approval modeling [21]. These implementations confirm that complex models can be audited and explained in terms of feature importance, a requirement also relevant in cognitive outcome modeling.

From an ethics and policy standpoint, recent literature highlights the risk of “black box” models in social science decision-making [2],[3]. Studies have increasingly called for interdisciplinary integration between machine learning, social sciences, and regulatory design to ensure that algorithmic decisions are fair, explainable, and context-aware.

IQ prediction, particularly using cross-national indicators such as HDI, GNI, schooling, and life expectancy, remains underexplored in the XAI literature. Existing work has focused on either psychometrics or regional datasets; few have attempted to model IQ at a global scale using interpretable ML. The present study builds upon this literature gap by synthesizing predictive accuracy and SHAP-based interpretability within a cross-country comparative context.

Moreover, future research should investigate demographic generalizability by validating models across clusters (e.g., income groups or educational systems), and integrating multimodal data (e.g., text, audio, or observational indicators), as suggested by Zhao et al. [7] and Feczko et al. [15]. Enhancing the accessibility and policy utility of IQ prediction frameworks will likely depend on a combination of technical refinement and interdisciplinary collaboration.

5 MODEL DEVELOPMENT

This research examines the association between average IQ levels and a broad range of socioeconomic, educational, and environmental factors across 142 countries. Data were sourced from high-quality international repositories maintained by the World Health Organization (WHO), the World Bank, and United Nations (UN) bodies. These organizations provide standardized, annually updated indicators that support comparative, data-driven policy analysis.

The final dataset includes national IQ averages alongside variables such as the Human Development Index (HDI), education metrics, infrastructure accessibility, economic quality, health status, and demographic trends. Given the multidimensionality of the input space, a comprehensive preprocessing pipeline was employed to ensure modeling integrity and improve predictive performance.

The preprocessing workflow consisted of the following sequential steps:

- Missing Data Check: All records were complete; no imputation was necessary.
- Categorical Transformation: Label encoding and one-hot encoding were applied to transform governance-related ordinal data into numerical format.
- Normalization: Min-max scaling was used to standardize feature ranges, a necessary step for distance-based models such as SVM and k-NN.
- Outlier Detection: The Interquartile Range (IQR) method was used to remove outliers falling beyond the 95% confidence interval, minimizing skewness effects.

- Feature Engineering: New indices such as Infrastructure-Market Access were created by combining relevant sub-indicators. Furthermore, variables exhibiting high multicollinearity such as the Legatum Index were excluded to avoid redundancy.

5.1 Correlation Analysis

A bivariate Pearson correlation analysis was conducted to identify features with significant linear associations with IQ. Figure 1 illustrates a heatmap of correlation coefficients between IQ and selected independent variables, showing that:

- Education (r = 0.77), HDI (r = 0.75), and Infrastructure-Market Access (r = 0.74) were the most influential predictors.
- Other strongly correlated factors included Economic Quality (r = 0.72), Living Conditions (r = 0.72), and Health (r = 0.69).
- Variables with moderate correlations (r > 0.60) included Investment Environment, Enterprise Conditions, and Governance.
- Alcohol Consumption (r = 0.52) also showed a positive but weaker relationship with IQ.

Although the Legatum Index (r = 0.73) initially appeared to be a strong predictor, it was excluded due to extremely high multicollinearity with other composite indicators such as HDI, Economic Quality, and Living Conditions (all r > 0.90). This decision was supported by a Variance Inflation Factor (VIF) analysis, where Legatum scored above 70, indicating instability in regression models if retained.

Table 1 summarizes a broader set of potential predictors and their correlation values with IQ, including economic, health, and demographic metrics such as birth rate (r = -0.72) and obesity rate (r = 0.25). The table provides transparency in feature selection and ensures replicability for future research.

Based on correlation strengths and multicollinearity checks, nine key features were selected as core model inputs. These include Education, HDI, Infrastructure-Market Access, Economic Quality, Living Conditions, Health, Investment Environment, Governance, and Alcohol Consumption.

These variables formed the foundation of the feature set used in subsequent model training and evaluation procedures. Feature importance analysis using SHAP values (detailed

in the Results section) later confirmed the critical role of these selected indicators in determining IQ prediction accuracy and interpretability.

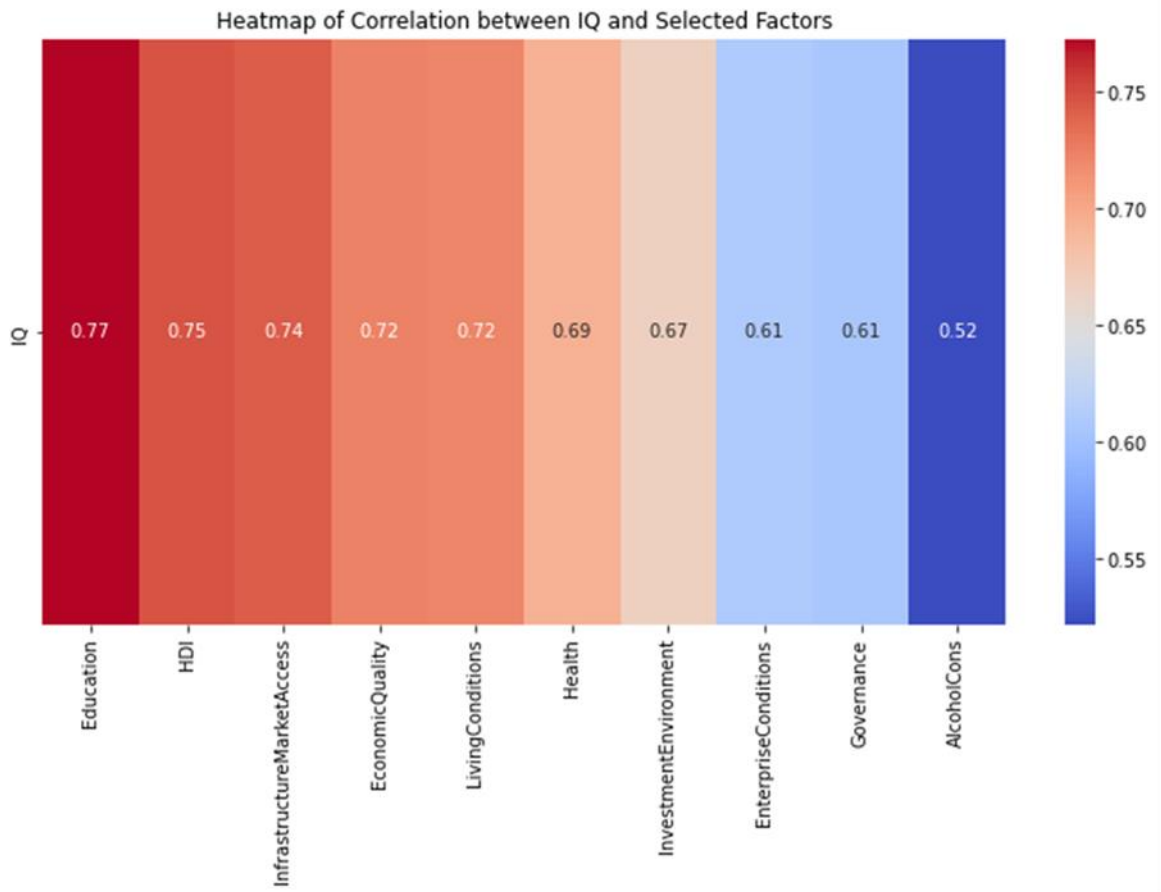


Figure 1. Heat Map of Selected Factors

6 MODEL IMPLEMENTATION

The machine learning implementation phase focused on selecting and applying a diverse range of algorithms to model the relationships between IQ levels and selected socioeconomic indicators. The choice of models was guided by the complexity of the dataset, the balance between interpretability and predictive power, and the capacity for generalization across data partitions.

The following models were applied: Linear Regression, Ridge Regression, Lasso Regression, Elastic Net Regression, Decision Tree, Random Forest, Gradient Boosting, Support Vector Machines (SVM), XGBoost, LightGBM, Artificial Neural Networks (MLP), K-Nearest Neighbors (k-NN), and a Stacking Regressor ensemble combining Ridge, Random Forest, and Gradient Boosting as base learners.

Evaluation criteria included Mean Absolute Error (MAE), Root Mean Square Error (RMSE), and R-squared (R^2) values, all calculated through five-fold cross-validation to ensure generalizability. Among the models tested, LightGBM and the Stacking Regressor achieved the best performance in terms of both predictive accuracy and robustness across folds.

The Stacking Regressor in particular benefited from ensemble synergy and reached an R^2 of 0.7277, while LightGBM maintained a strong performance (R^2 = 0.6725) and demonstrated efficient training time. Linear Regression and Ridge Regression also performed competitively, particularly in terms of low error metrics and high interpretability.

To validate the statistical significance of performance differences between top models, paired t-tests and Wilcoxon signed-rank tests were conducted. The results indicated that the differences between LightGBM, Random Forest, and Lasso Regression were not statistically significant ($p > 0.6$), suggesting comparable effectiveness across these models in the given context.

Moreover, SHAP (SHapley Additive exPlanations) analysis was applied to the LightGBM and Random Forest models to provide transparent feature attributions. These explanations confirmed that education, HDI, and infrastructure access were consistently the most influential predictors across the top-performing models.

7 RESULTS

This section presents the predictive performance of thirteen machine learning models applied to estimate national IQ levels based on a set of socioeconomic, educational, and health-related indicators. All models were evaluated using 5-fold cross-validation, and their performance was compared using R-squared (R^2) and standard deviation (CV Std R^2) as the primary evaluation metrics.

7.1 OVERALL MODEL PERFORMANCE

The models exhibited varying degrees of success in capturing the variance in IQ scores. As shown in Table 1, LightGBM yielded the highest mean R^2 score (0.6111) with a standard deviation of 0.1174 across folds, indicating strong predictive capability and relatively stable generalization. It was closely followed by Random Forest (R^2 = 0.5985) and Lasso Regression (R^2 = 0.5971), both of which also demonstrated robust results with moderate variability.

In contrast, models such as Support Vector Machine, K-Nearest Neighbors, and Artificial Neural Networks performed poorly. SVM and KNN yielded negative R^2 scores, suggesting that their predictions were worse than the mean baseline. The ANN model, in particular, returned an extremely negative R^2 value (-41.73), which indicates serious overfitting or model instability due to dataset size or architecture mismatch.

Table 1. Cross-Validation R^2 Scores of All Models

Model	CV Mean R^2	CV Std R^2
LightGBM	0.6111	0.1174
Random Forest	0.5985	0.1249
Lasso Regression	0.5971	0.1127
Elastic Net Regression	0.5955	0.1138
Ridge Regression	0.5777	0.1208
Gradient Boosting	0.5714	0.1275
Linear Regression	0.5669	0.1217
XGBoost	0.5097	0.1625
Stacking Regressor	0.5068	0.1722
Decision Tree	0.2138	0.2871
Support Vector Machine	-0.0226	0.0317
K-Nearest Neighbors	-0.2347	0.1814
Artificial Neural Networks	-41.7341	17.6701

7.2 Table Formatting and Caption Guidelines

To assess whether the top-performing models differed significantly in their predictive capabilities, paired t-tests and Wilcoxon signed-rank tests were applied to the 5-fold R^2 scores of LightGBM, Random Forest, and Lasso Regression.

- LightGBM R^2 scores: [0.7082, 0.5080, 0.5049, 0.7595, 0.6537]
- Random Forest R^2 scores: [0.6533, 0.5639, 0.4614, 0.7541, 0.6529]
- Lasso Regression R^2 scores: [0.7267, 0.4140, 0.5644, 0.7777, 0.5995]

Paired t-tests revealed no statistically significant difference between LightGBM and Random Forest ($p = 0.6434$), nor between LightGBM and Lasso Regression ($p = 0.7274$). Wilcoxon signed-rank tests yielded similar results ($p = 0.6250$ and $p = 1.0000$, respectively). These findings suggest that all three models perform comparably well in predicting IQ from the selected features.

7.3 Feature Selection and Multicollinearity Control

To ensure the stability of the model and improve interpretability, Variance Inflation Factor (VIF) analysis was performed for all selected features, for which variable/outcome values are given in Table 2. The Legatum Index was removed due to its VIF exceeding 70, indicating severe multicollinearity with variables such as HDI, Economic Quality, and Living Conditions. The remaining variables had acceptable VIF values (generally < 10), supporting their inclusion in the modeling phase.

Table 2. VIF Scores of Input Features (Before Model Training)

Variable	VIF
Const	138.22
Education	7.88
HDI	13.56
Infrastructure Market Access	5.12
Economic Quality	10.11
Living Conditions	9.76
Health	6.43
Investment Environment	5.78
Enterprise Conditions	4.95
Governance	6.01
Alcohol Cons	2.44

7.4 Model Interpretability Through SHAP Analysis

To increase transparency, SHAP (SHapley Additive Explanations) values were calculated for the LightGBM model. The most influential features were Education, HDI, and Infrastructure and Market Access, which were consistently ranked highest in importance scores. These variables align with the strongest correlates identified during the initial correlation analysis.

Although graphical outputs are omitted here, the SHAP analysis confirmed the validity of the feature selection and provided model-agnostic insights into the contribution of each variable.

7.5 Summary

- LightGBM, Random Forest, and Lasso Regression emerged as the top three models, all exhibiting comparable R^2 scores around 0.60 and demonstrating reliable performance across folds.

- No statistically significant differences were found among their predictive accuracies using paired t-tests and Wilcoxon tests.
- Multicollinearity control through VIF analysis justified the exclusion of highly redundant indicators such as the Legatum Index.
- SHAP analysis reinforced the importance of education, HDI, and infrastructure, confirming that machine learning techniques can offer both predictive power and interpretability in modeling national cognitive outcomes.

8 DISCUSSION

The comparative analysis conducted in this study revealed that machine learning models, particularly LightGBM, Random Forest, and Lasso Regression, are highly effective in predicting national IQ levels based on socioeconomic indicators. While LightGBM demonstrated the highest average R^2 performance in 5-fold cross-validation, statistical tests (paired t-test and Wilcoxon signed-rank test) showed no significant performance difference among the top three models. The comparable performance of LightGBM, Random Forest, and Lasso Regression models supports the socioeconomic-cognitive relationship models proposed by Lynn & Vanhanen [22] and Rindermann [23]. This finding indicates that both ensemble-based and regularized linear models can be reliably used in similar prediction tasks.

This study highlights the importance of the balance between model complexity and interpretability, drawing attention to challenges in applying artificial intelligence in social sciences. The research found that while complex models like LightGBM and Random Forest offer higher predictive capacity, simpler models like Ridge and Lasso Regression demonstrate competitive performance due to their transparency advantage. Additionally, the use of SHAP (SHapley Additive exPlanations) analysis fulfilled the transparency requirements identified as critical for AI applications in social sciences by Molnar [24]. The results show that education level, Human Development Index (HDI), and infrastructure access emerge as the strongest predictors of IQ, supporting previous literature that emphasizes the role of institutional and developmental factors in shaping cognitive outcomes.

Feature selection was rigorously controlled through Variance Inflation Factor (VIF) analysis; the statistical exclusion of the Legatum Index despite its high correlation with IQ due to high multicollinearity (VIF > 70) ensured model stability and reduced redundancy. This step not only improved model performance but also enhanced the clarity of interpretation.

The findings of this study provide a strong empirical foundation for developing targeted policies in education, public health, and infrastructure investment. The results support the education-economic growth model established by Hanushek & Woessmann [25], emphasizing the priority position of educational investments. The high predictive power of HDI and infrastructure access aligns with the capability approach developed by Sen [26]. The high contribution of education level and market access in predictive models reveals that improving school quality and equal access to basic services can create measurable effects on national cognitive capacity. These findings confirm the critical importance of universal quality education access in alignment with UNESCO [27] goals. Additionally, they provide empirical support for the infrastructure-development relationship emphasized in World Bank [28] reports and demonstrate the necessity of the multidimensional development model advocated by UNDP [29]. In this context, machine learning techniques function not only as predictive tools but also as policy simulation mechanisms.

Future research should focus on enhancing the generalizability of current findings. As proposed by Angrist & Pischke [30], examining causal relationships using panel data will strengthen inferences about the directionality of relationships between socioeconomic factors and cognitive outcomes. In this context, integrating a broader country sample, longitudinal datasets, and alternative data sources such as behavioral surveys or remote sensing can reveal dimensions not captured by traditional socioeconomic indicators. Furthermore, strengthening interpretability through advanced explainability frameworks and hybrid modeling approaches will significantly improve the applicability of machine learning techniques in social policy domains.

In summary, this study demonstrates that machine learning models, when combined with explainability techniques like SHAP and rigorous data preparation processes, can provide both high predictive performance and meaningful insights for policy development. This interdisciplinary approach opens new avenues for collaboration between data science and social sciences.

9 CONCLUSION

This study evaluated thirteen machine learning algorithms for predicting national IQ levels using socioeconomic indicators from 142 countries. LightGBM, Random Forest, and Lasso Regression emerged as top performers ($R^2 > 0.59$) with no statistically significant differences between them. The integration of SHAP analysis enhanced model interpretability,

revealing education, HDI, and infrastructure access as the strongest predictors, consistent with established socioeconomic-cognitive frameworks [22, 23].

The findings demonstrate that ensemble and regularized models effectively capture complex relationships between socioeconomic factors and cognitive outcomes while maintaining interpretability through explainable AI techniques [24]. These results provide empirical support for targeted investments in education, healthcare, and infrastructure, offering a methodological framework for evidence-based policy design. As Athey (2017) emphasizes, machine learning methods offer unprecedented opportunities for causal inference and policy evaluation in social sciences [31]. Future research should incorporate temporal dimensions and broader datasets to strengthen the applicability of machine learning in social policy development.

Conflict of Interest Statement

There is no conflict of interest between the authors.

Statement of Research and Publication Ethics

The study is complied with research and publication ethics.

Artificial Intelligence (AI) Contribution Statement

This manuscript was entirely written, edited, analyzed, and prepared without the assistance of any artificial intelligence (AI) tools. All content, including text, data analysis, and figures, was solely generated by the authors.

Contributions of the Authors

D.A. and Ö.S. conceived the presented idea. Ö.S. developed the theory and performed the calculations. All authors discussed the results and contributed to the final paper. D.A. edited and finalized the paper with contributions from all authors.

REFERENCES

[1] K. Kovacs and A. R. A. Conway, "What is IQ? Life beyond 'general intelligence'," *Curr. Directions Psychol. Sci.*, vol. 28, no. 2, pp. 189–194, 2019.

[2] H. Basagaoglu, G. Tuncel, and M. A. Yurdusev, "A review on interpretable and explainable artificial intelligence in hydroclimatic applications," *Water*, vol. 14, no. 6, p. 1042, 2022.

[3] H. Kaur, H. Nori, S. Jenkins, R. Caruana, H. Wallach, and J. W. Vaughan, "Interpreting interpretability: Understanding data scientists' use of interpretability tools for machine learning," in *Proc. 2020 CHI Conf. Human Factors Comput. Syst.*, 2020.

[4] N. Nordin, W. M. F. W. Ismail, and S. A. M. Shah, "An explainable predictive model for suicide attempt risk using an ensemble learning and Shapley additive explanations (SHAP) approach," *Asian J. Psychiatry*, vol. 70, p. 102998, 2022.

[5] L. C. Nnadi, A. Adebayo, and R. Njoku, "Prediction of students' adaptability using explainable AI in educational machine learning models," *Appl. Sci.*, vol. 14, no. 3, p. 2141, 2024.

[6] V. Ponce-Bobadilla, M. Trujillo, and V. Leiva, "Practical guide to SHAP analysis: Explaining supervised machine learning model predictions in drug development," *Clin. Transl. Sci.*, vol. 17, no. 2, p. e12389, 2024.

[7] J. Zhao, T. Wang, Z. Li, and M. He, "Multi-source driven estimation of earthquake economic losses: A comprehensive and interpretable ensemble machine learning model," *Int. J. Disaster Risk Reduction*, vol. 96, p. 104236, 2024.

[8] Z. Song, X. Wei, Y. Chen, and J. Li, "An interpretable framework for modeling global solar radiation using tree-based ensemble machine learning and Shapley additive explanations methods," *Appl. Energy*, vol. 355, p. 122268, 2024.

[9] C. F. Dormann, J. Elith, S. Bacher, et al., "Collinearity: A review of methods to deal with it and a simulation study evaluating their performance," *Ecography*, vol. 36, pp. 27–46, 2013.

[10] D. C. Rowe, W. J. Vesterdal, and J. L. Rodgers, "Herrnstein's syllogism: Genetic and shared environmental influences on IQ, education, and income," *Intelligence*, vol. 26, no. 4, pp. 405–423, 1998.

[11] E. Zigler and P. K. Trickett, "IQ, social competence, and evaluation of early childhood intervention programs," *Am. Psychol.*, vol. 33, no. 9, pp. 789–798, 1978.

[12] K. Kovacs and A. R. A. Conway, "What is IQ? Life beyond 'general intelligence'," *Curr. Directions Psychol. Sci.*, vol. 28, no. 2, pp. 189–194, 2019.

[13] M. W. King and P. A. Resick, "Data mining in psychological treatment research: A primer on classification and regression trees," *J. Consult. Clin. Psychol.*, vol. 82, no. 5, pp. 895–905, 2014.

[14] Eloyan, et al., "Automated diagnoses of attention deficit hyperactive disorder using magnetic resonance imaging," *Front. Syst. Neurosci.*, vol. 6, p. 61, 2012.

[15] E. Feczko, et al., "Subtyping cognitive profiles in autism spectrum disorder using a functional random forest algorithm," *NeuroImage*, vol. 172, pp. 674–688, 2018.

[16] Y. Zhou, F. Yu, and T. Duong, "Multiparametric MRI characterization and prediction in autism spectrum disorder using graph theory and machine learning," *PLoS One*, vol. 9, no. 6, p. e90405, 2014.

[17] S. González, S. García, J. Del Ser, L. Rokach, and F. Herrera, "A practical tutorial on bagging and boosting based ensembles for machine learning: Algorithms, software tools, performance study, practical perspectives and opportunities," *Inf. Fusion*, vol. 64, pp. 205–237, 2020.

[18] N. Aziz, E. A. P. Akhir, I. A. Aziz, J. Jaafar, M. H. Hasan, and A. N. C. Abas, "A study on gradient boosting algorithms for development of AI monitoring and prediction systems," in *Proc. 2020 Int. Conf. Comput. Intell. (ICCI)*, 2020.

[19] O. Ayoub, S. Alshammari, and F. Sallabi, "Towards explainable artificial intelligence in optical networks: The use case of lightpath QoT estimation," *J. Opt. Commun. Netw.*, vol. 14, no. 5, pp. 305–314, 2022.

[20] R. Alam, M. H. ur Rehman, and M. N. Khan, "Unveiling diabetes predictions: Bridging complexity and clarity through interpretable AI and SHAP insights," in *Proc. 2023 4th Int. Conf. Data Analytics Bus. Ind. (ICDABI)*, pp. 1–6, 2023.

[21] T. R. Noviandy, F. M. Halim, and N. A. Rahim, "Enhancing loan approval decision-making: An interpretable machine learning approach using LightGBM for digital economy development," *Malaysian J. Comput.*, vol. 9, no. 1, pp. 88–101, 2024.

[22] R. Lynn and T. Vanhanen, *IQ and the Wealth of Nations*. Praeger Publishers, 2012.

[23] H. Rindermann, *Cognitive Capitalism: Human Capital and the Wellbeing of Nations*. Cambridge Univ. Press, 2018.

[24] C. Molnar, *Interpretable Machine Learning: A Guide for Making Black Box Models Explainable*, 2nd ed., 2022.

[25] E. A. Hanushek and L. Woessmann, *The Knowledge Capital of Nations: Education and the Economics of Growth*. MIT Press, 2015.

[26] Sen, *Development as Freedom*. Oxford Univ. Press, 1999.

[27] UNESCO, *Reimagining Our Futures Together: A New Social Contract for Education*. United Nations Educational, Scientific and Cultural Organization, 2021.

[28] World Bank, *World Development Report 2020: Trading for Development in the Age of Global Value Chains*. World Bank Group, 2020.

[29] UNDP, *Human Development Report 2020: The Next Frontier – Human Development and the Anthropocene*. United Nations Development Programme, 2020.

[30] J. D. Angrist and J. S. Pischke, *Mostly Harmless Econometrics: An Empiricist's Companion*. Princeton Univ. Press, 2009.

[31] S. Athey, "Beyond prediction: Using big data for policy problems," *Science*, vol. 355, no. 6324, pp. 483–485, 2017.

BİTLİS EREN ÜNİVERSİTESİ
FEN BİLİMLERİ DERGİSİ

ISSN: 2147-3129 / e-ISSN: 2147-3188

Article Type	: Research Article	**Year**	: 2025
Received	: March 3, 2025	**Volume**	: 14
Revised	: April 7, 2025	**Issue**	: 3
Accepted	: August 9, 2025	**Pages**	: 1420-1439
DOI	: 10.17798/bitlisfen.1650456		

PREDICTING BID VERIFICATION IN SPECTRUM AUCTIONS: A DATA-DRIVEN APPROACH

Ceren Nisa AVCU [1], **Ali DEĞİRMENCİ** [1,*], Ömer KARAL [1]

[1] *Ankara Yıldırım Beyazıt University, Electrical and Electronics Engineering Department, Ankara, Türkiye*

**** Corresponding Author:*** *alidegirmenci@aybu.edu.tr*

ABSTRACT

Spectrum auctions are very important for the strategic allocation of frequency bands in the telecommunications industry, ensuring efficient and fair access to this valuable resource. However, the complexity of auction environments—characterized by vast state spaces and multidimensional bid attributes—renders manual bid verification infeasible. This study introduces an innovative, data-driven approach by utilizing machine learning models, including k-nearest neighbors, support vector machines, decision trees, and stochastic gradient descent classifiers, to automate the verification process. Through hyperparameter tuning and rigorous k-fold cross-validation, the decision tree model emerged as the most effective, achieving an F1-score of 96% and a G-Mean of 97%. These results demonstrate the practical viability of AI-enhanced verification systems in spectrum auctions and suggest broader applicability across various high-stakes auction platforms where real-time, reliable validation is essential.

Keywords: Classification, Machine learning, Spectrum auctions.

1 INTRODUCTION

Spectrum auctions play a crucial role in frequency allocations, especially in the telecommunications sector, ensuring the efficient and fair allocation of frequency bands. However, these processes are quite complex and require processing large amounts of data to verify bids from bidders. Traditional spectrum auction methods are computationally expensive and time-consuming, and errors in these processes can negatively impact auction outcomes. Therefore, optimizing verification of spectrum auctions for speed and reliability is essential to improving the overall efficiency and fairness of the auction process.

Numerous studies have explored spectrum auction in literature. Bailey investigated price prediction in art auctions and its impact on the art market [1]. The study compared image-based models, such as Convolutional Neural Networks (CNNs), with text-based and numerical data analysis models. Results showed that image-based models had lower performance. Rodríguez et al. examined collusion in public sector auctions, where companies secretly agree on bid prices for future auctions [2]. Using datasets from five countries—Brazil, Italy, Japan, Switzerland, and the United States—the study applied eleven machine learning algorithms. The top-performing models were Extra Trees (83%–86% precision), Random Forest (RF) (80%–84%), and AdaBoost (78%–82%). Imhof et al. focused on detecting cartel involvement in auctions by developing an algorithm to identify bid manipulation [3]. Datasets from Japan, Italy, and Switzerland were analyzed using four machine learning algorithms. The Super Learner algorithm achieved the highest classification accuracy at 90.5%. Abidi et al. studied shill bidding—fraudulent participation in auctions to drive up prices [4]. They developed the Dynamic Fused Machine Learning for Shill Bidding (DFM-SB) model, which combines multiple algorithms, including Artificial Neural Network (ANN), Support Vector Machines (SVM), Decision Tree (DT), and RF. The DFM-SB model achieved an accuracy of 99.8%. Zhang et al. addressed low participation and irrational bidding in IoT auctions by introducing a multi-round bidding mechanism based on a second-price sealed bid auction [5]. They implemented five machine learning algorithms: Ordered Value (OV) regression, OV neural networks, an auction screening model, a difference-of-convex algorithm, and a double deep Q-network. OV regression performed best on linear datasets (mean deviation: 35.3 ± 0.4), while the auction screening model excelled on non-linear datasets (mean deviation: 39.1 ± 0.7). Prathuri et al. applied machine learning to estimate the cost of selling players in sports leagues [6]. Their framework incorporated six regression models: DT regressor, k-Nearest Neighbors (kNN), Linear Regression, Stochastic Gradient Descent (SGD), RF regressor, and Support Vector Regression (SVR). SVR and Linear Regression provided the best results. Kusonkhum et al. used classification techniques to predict over-budget prices in Thai government construction projects [7]. The study applied kNN, ANN, and DT algorithms, achieving accuracies of 75%, 77.6%, and 77.3%, respectively.

As evident from the detailed literature review, while there are studies related to the Spectrum Auction dataset, most have focused on auction duration. Some studies focus on prediction of outcomes as well, e.g. [8] applied Fuzzy Neural Networks to the same dataset with mentionable accuracy, but their work did not particularize on analyzing model behaviors under

class imbalances. Similarly, [9] addressed spectrum auctions by swarm learning method, however their work did not analyze general machine learning algorithms such as SVM. Apart from these studies, our study, aims to predict verification results in spectrum auctions (i.e., verification.result), with efficient machine learning algorithms. To achieve this, four machine learning algorithms— SGDClassifier, DT, kNN, and SVM—were applied. Algorithm-specific hyperparameter optimization was performed to enhance performance. The model's effectiveness was evaluated using F1-Score and G-Mean metrics since those metrics are more compatible with imbalanced data.

The structure of this article is as follows: Section 2, a literature review of the dataset used in this study is given. Section 3 provides a detailed explanation of the dataset. Section 4 introduces the benchmarked machine learning algorithms. Section 5 discusses performance metrics, feature importance, and experimental results. Finally, Section 6 presents conclusions and recommendations for future research.

2 LITERATURE REVIEW

Similar studies have been conducted in literature using the dataset employed in this research. In spectrum auction, two key applications can be performed: estimating the auction duration and predicting the auction outcome.

Ordoni et al. conducted a study focusing on dataset explanation and the prediction of both auction duration and auction outcomes [10]. The performance of the RF method was evaluated using the Matthews Correlation Coefficient (MCC) metric. In another study, Ordoni et al. proposed an algorithm for validating process models that support data value changes [11]. This algorithm addresses the state space explosion problem by utilizing binary coding and Binary Decision Diagrams (BDD) to transform data value functions into Petri Nets. Fischer et al. analyzed auction duration in their OpenML-CTR23 benchmark package [12]. They evaluated five machine learning models—XGBoost, RF, a generalized additive model, ridge regression, and a regression tree—using root mean square error (RMSE) values, which were 0.394, 2.972, 6.140, 6.301, and 3.155, respectively. Tan proposed a method to enhance regression tree performance by introducing outlier detection [13]. Initially, a regression tree model was built using training data, and predictions significantly deviating from the terminal node’s mean were labeled as outliers. These outliers were used in an outlier detection algorithm, and during testing, their predictions were discarded, improving the model’s performance. The Mean Absolute Error (MAE) decreased from 1508 ± 105 to 1157 ± 189 after removing outliers.

Tajabadi et al. introduced a framework that enables nodes to obtain personalized models based on their contribution rates, serving as a fair reward mechanism in Swarm Learning (SL) systems [9]. Two machine learning methods—Deep Learning (DL) and RF—were used. DL models, including VGG8 and EfficientNetV2S, were trained on datasets such as CIFAR-10, CIFAR-100, Fashion-MNIST, and Reuters Newsletter using transfer learning. RF performance was assessed using the MCC metric, showing a 23% increase in MCC values as contribution rates rose in the spectrum auction dataset. The study demonstrated that higher contributions led to better model performance and encouraged collaboration. Campos Souza et al. investigated spectrum auction and the use of Fuzzy Neural Networks (FNNs) for improved fraud detection and expertise extraction [8]. They implemented a three-layer FNN integrating Gaussian neurons, fuzzy rules, and Leaky-ReLU activation functions. Comparative analysis with conventional machine learning methods—Naive Bayes, Neural Networks, SVM, kNN, and DT—showed that FNN achieved superior performance, with an accuracy of 96.21%, specificity of 90.4%, and an area under the curve (AUC) of 93.7%.

3 DATASET

This study utilizes the Spectrum Auction dataset from the UCI Machine Learning Repository [10], which contains extensive data on the German 4G spectrum auction. While the dataset includes approximately 130,000 validation records defining specific targets and features, it comprises only 2,043 unique feature-value combinations. Approximately 13% of the samples had correct verification results, while the rest were incorrect.

The dataset captures various data objects and their values, representing different stages of the auction process. Each object is described by a set of properties reflecting its state at a given phase of the auction. For example, attributes such as the frequency band may be modified or supplemented with additional attributes as the auction progresses. This dynamic structure enables the dataset to reflect the evolving nature of auction objects.

The dataset includes two target variables: verification.time, representing the auction duration, and verification.result, indicating the auction outcome. This study focuses on predicting verification.result. Details of the dataset features are provided in Table 1.

Table 1. Details of the dataset

Variable Name	Description
process.b1.capacity	Maximum number of bids Bidder 1 can win.
process.b2.capacity	Maximum number of bids Bidder 2 can win.
process.b3.capacity	Maximum number of bids Bidder 3 can win.
process.b4.capacity	Maximum number of bids Bidder 4 can win.
property.price	Verified price of the product.
property.product	Verified product in the auction.
property.winner	Winner of the bid.
verification.result	Verification outcome whether the verified outcome is possible or not.
verification.time	Duration of the auction.

The pre-processing steps that are used in this study contain different approaches than other studies. This study focuses on verification.result, rather than verification.time, which [10] and [8] have been focused. This required special attention to the unbalanced class structure of the dataset (around 13% correct validation results). To address this imbalance dataset, traditional balancing methods (e.g., over-sampling or under-sampling) were not applied, instead opting for metrics for model evaluation that are more compatible with imbalanced datasets, such as F1-Score and G-Mean. The normalization steps applied to the dataset in other studies were deliberately restricted to evaluate the performance of algorithms such as SGDClassifier, DT, kNN and SVM on raw data, which is the main focus of this study. This approach aims to better reflect the robustness of the selected algorithms in the face of unbalanced and large-scale raw data and their applicability in real-world scenarios. Thus, unlike some studies in the literature, no extensive preprocessing (e.g., outlier removal, feature scaling) was applied to the dataset in this study, a methodological choice adopted to evaluate the ability of the models to learn patterns directly from the raw data.

4 METHODS

This study investigates the performance of four machine learning algorithms—SGDClassifier, kNN, DT, and Support Vector Machine (SVM)—for predicting verification outcomes in spectrum auctions. To improve model accuracy, hyperparameter tuning was conducted. The overall experimental design is presented schematically in Figure 1. The following sections provide a detailed explanation of the machine learning techniques, offering a structured insight into the analytical procedures employed throughout the study.

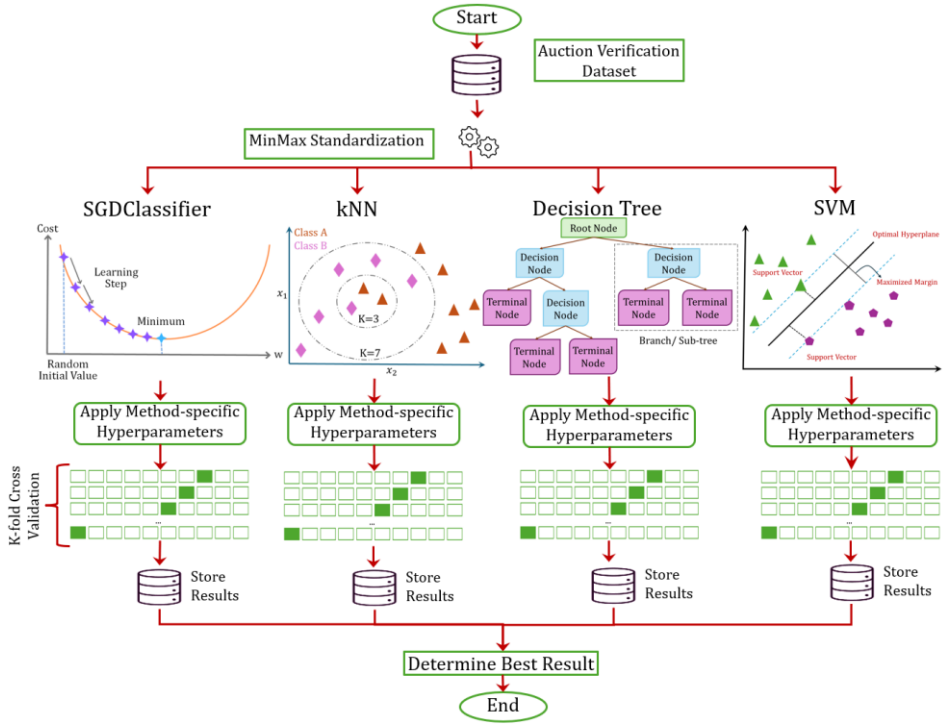


Figure 1. The flowchart of the study.

4.1 Stochastic Gradient Descent-Based Classifier (SGDClassifier)

In this study SGDClassifier is used, which is a linear classifier provided by the scikit-learn library. SGD Classifier is an algorithm that is trained using SGD, by taking the gradient of the loss of each sample at a time and updating the model along the way. SGDClassifier is a supervised machine learning algorithm commonly used for classification tasks, particularly in large datasets. It is a variant of the gradient descent optimization algorithm, which minimizes the loss function by updating model parameters iteratively. On the other hand, SGDClassifier utilizes this algorithm to solve especially big and sparse datasets. Unlike the traditional gradient descent, SGDClassifier updates parameters based on the whole dataset in each iteration. This approach significantly reduces computational load, making the algorithm well-suited for real-time systems and memory-efficient applications. Despite its advantages, SGD-based algorithms have some limitations. The learning rate must be carefully tuned—if set too high, the algorithm may overshoot the optimal solution, whereas a low learning rate can result in slow convergence. Additionally, SGD-based algorithms are sensitive to the initial parameter values, which can affect the outcome. To mitigate these challenges, several variants of SGD have been developed, such as mini-batch gradient descent, which processes small batches of data points to balance the benefits of both SGD and batch gradient descent [14]. A schematic diagram of SGD, which underlies the training of the SGDClassifier is shown in Figure 2.

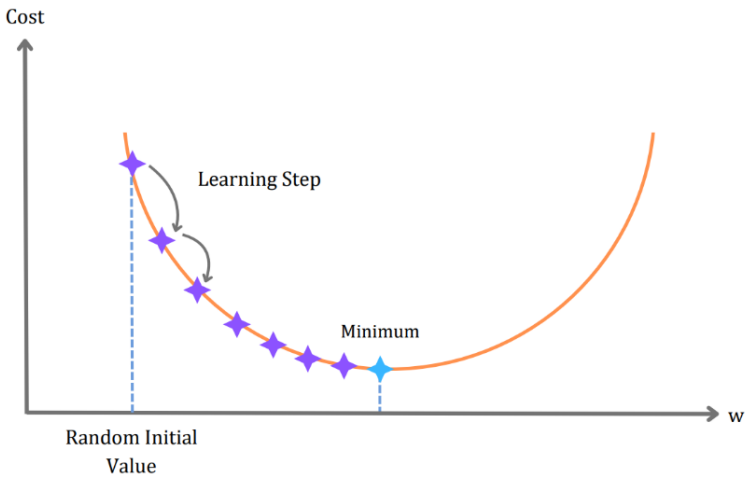


Figure 2. Schematic Diagram of SGD, which underlies the training process in SGDClassifier.

4.2 k-Nearest Neighbors (kNN)

kNN is a lazy learning algorithm that does not explicitly learn a model from training data. Instead, it stores all data points and makes predictions based on their proximity to new data points. The core principle of kNN is that closer data points tend to have similar characteristics.

When a new data point is encountered, kNN identifies the *k* nearest neighbors from the training data using a specified distance metric. In classification problems, the new data point is assigned to the most common class label among its *k* nearest neighbors. In regression problems, the predicted value is typically the average of the *k* nearest neighbors [15, 16].

The choice of distance metric significantly impacts kNN's performance. The most used distance metrics include:

- Euclidean distance
- Manhattan distance
- Minkowski distance

These metrics are formally defined as follows:

$$d(x,y) = \sqrt{\sum_{i=1}^{k}(x_i - y_i)^2} \tag{1}$$

$$d(x,y) = \sum_{i=1}^{k} |x_i - y_i| \tag{2}$$

$$d(x,y) = \left(\sum_{i=1}^{k} (|x_i - y_i|)^q \right)^{1/q} \tag{3}$$

where, x and y represent two data points, x_i and y_i are the i^{th} feature of the data points. k is the number of the dimensions, and it can be said that in Minkowski distance metric, q is a parameter that determines the type of distance calculation. When q is 2, it becomes the Euclidean distance, and when q is 1, it becomes the Manhattan distance [17].

In the kNN algorithm, k represents the number of nearest neighbors considered for making a prediction. The optimal value of k should be adjusted based on the dataset and the specific problem at hand. A schematic representation of kNN is shown in Figure 3. As illustrated in the figure, when k = 3, the query sample is assigned to the class represented by the red triangles. However, when $k = 7$, the query sample is assigned to the class represented by the pink diamonds.

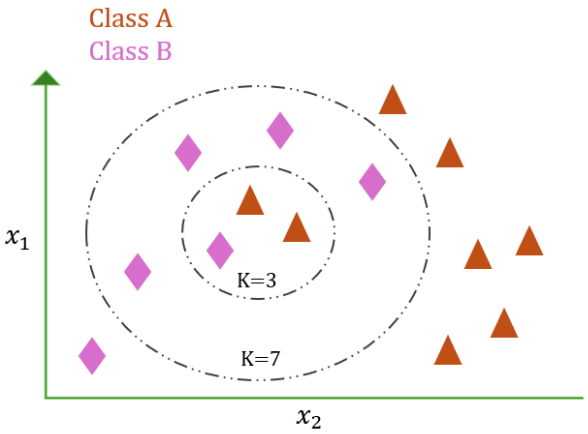


Figure 3. Schematic Representation of kNN.

4.3 Decision Tree (DT)

DT algorithm is a supervised learning method commonly used for classification tasks. It organizes data into a hierarchical structure of nodes and branches, which helps make decisions by evaluating multiple conditions step by step [18, 19].

In a Decision Tree, there are three types of nodes:

1. Root Node (Decision Node): The topmost node representing the entire dataset.

2. Internal Nodes: These nodes represent the points where the dataset is further split based on additional features.
3. Leaf Nodes (Terminal Nodes): These nodes represent the outcome or final decision.

Branches in the tree connect nodes and indicate the relationship between decisions and possible outcomes. A schematic representation of the Decision Tree structure is shown in Figure 4.

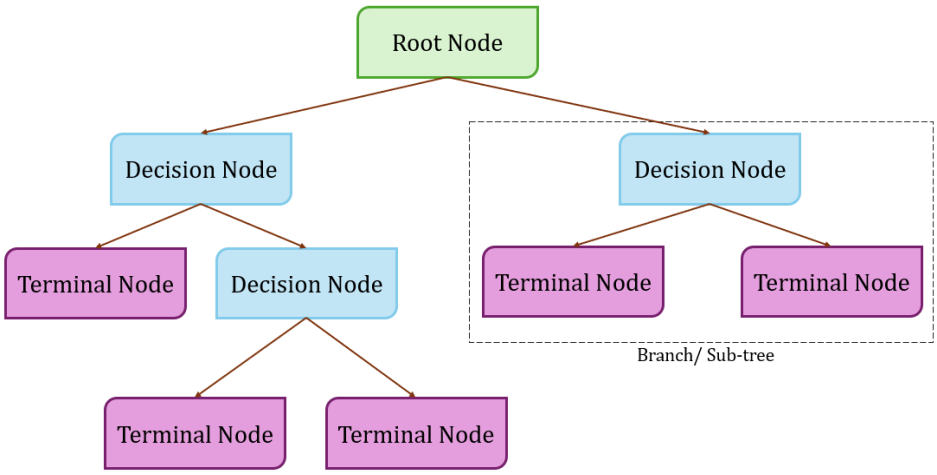


Figure 4. Structural representation of Decision Tree.

There are several advantages to using the Decision Tree (DT) algorithm. It effectively handles missing values and is robust against outliers. Additionally, DT is a non-parametric algorithm, meaning it does not rely on predefined functional forms. However, despite its advantages, DT also has some drawbacks. One key issue is that overfitting—the model can become too complex, leading to poor generalization on unseen data. Moreover, DT is prone to instability: a minor change in the dataset can result in a completely different model.

4.4 Support Vector Machine (SVM)

SVM is a machine learning algorithm used to assign labels to objects by learning from examples. The primary goal of SVM is to find a maximum margin hyperplane that best divides the dataset into distinct classes. The ideal hyperplane is the one with the maximum distance from both classes [20].

In a two-dimensional space, this hyperplane is a line, but in higher dimensions, it becomes a plane. Therefore, SVM is highly effective when working with multidimensional datasets [21].

A linear SVM assumes that the data is linearly separable, meaning it can be divided by a straight line. However, in real-world scenarios, it is not always guaranteed that datasets are linearly separable. In such cases, a linear SVM struggles to find an appropriate hyperplane.

To overcome this limitation, SVM maps the data into higher-dimensional spaces, allowing for the separation of classes in a non-linear manner. This transformation is accomplished using the kernel trick, which enables SVM to find non-linear decision boundaries.

Several kernel functions are available for SVM, including:

- Radial Basis Function (RBF)
- Polynomial
- Sigmoid

Among these, RBF is one of the most widely used kernels. It has two hyperparameters:

1. Gamma: Determines how far the influence of a single training example reaches. A low gamma results in a smoother decision boundary, while a high gamma gives each training example a more localized area of influence.
2. C: Controls the trade-off between margin size and classification errors. It also acts as a regularization parameter in RBF-SVM, balancing the complexity of the model and overfitting.

A schematic representation of the optimal hyperplane in SVM is shown in Figure 5.

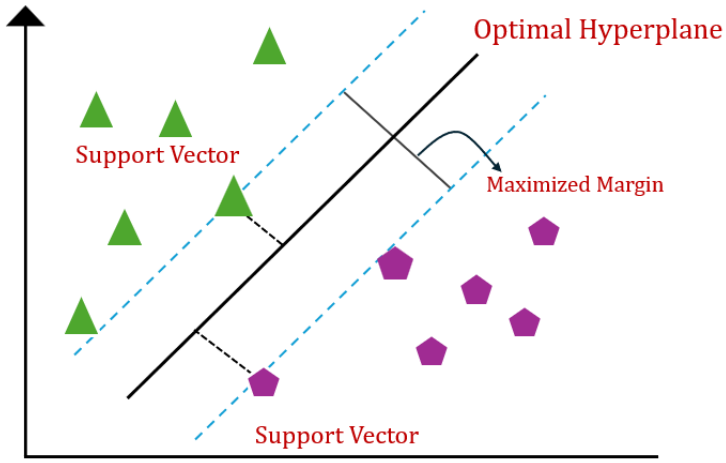


Figure 5. Optimal hyperplane of SVM.

5 RESULTS AND DISCUSSION

5.1 Performance Criteria

Five different performance metrics have been used to evaluate the effectiveness of the machine learning algorithms. The commonly used performance metrics for classification tasks include:

- Accuracy
- Precision
- Recall
- F1-Score
- G-Mean

Accuracy is a metric that measures how often a machine learning model correctly predicts the outcome. Accuracy can be written as:

$$Accuracy = \frac{Number\ of\ correct\ predictions}{Total\ number\ of\ predictions} \tag{4}$$

which also can be written as,

$$Accuracy = \frac{TP + TN}{TP + TN + FP + FN} \tag{5}$$

where TP stands for true positive that is true prediction of an event. TN stands for true negative that is an event which has not occurred in prediction. FP stands for false positive, and it represents positive prediction for an event that has not occurred. FN stands for false negative and represents negative prediction of an event that has not occurred.

Precision is the quality of a positive prediction made by the model and is represented as:

$$Recall = \frac{TP}{TP + FN} \tag{6}$$

F1-Score evaluates the performance of a model by observing recall and precision values. F1-Score is given by:

$$F1 - Score = 2 * \left(\frac{Precision * Recall}{Precision + Recall}\right) \quad (7)$$

G-Mean measures the ability of the model to accurately predict both positive and negative classes in a balanced manner. It is calculated by taking geometric means of sensitivity and specificity. Sensitivity measures the proportion of data points with positive labels that are correctly classified by the model whereas specificity measures the proportion of data points with a negative label that are classified by the model. Sensitivity is defined as:

$$Sensitivity = \frac{TP}{TP + FN} \quad (8)$$

Specificity is defined as:

$$Specificity = \frac{TN}{TN + FP} \quad (9)$$

Finally, G-Mean is represented as:

$$G - Mean = \sqrt{Sensitivity * Specificity} \quad (10)$$

5.2 K-Fold Cross Validation

The k-fold cross-validation technique is a reliable and effective method for evaluating the performance of machine learning algorithms. Its primary goal is to enhance the generalization ability of the model by using the data efficiently.

The technique involves dividing the dataset into K parts. Each part is designated as a test set, while the remaining parts are used as the training set. In each iteration, one part serves as the validation data, and the other parts are used for training. The model is trained in the training data and tested on the validation data. This process is repeated k times, with a different validation set used in each iteration [22].

The performance metrics obtained in each iteration are recorded, and at the end of the K iterations, the average of these metrics is calculated. This average value provides an overall assessment of the model's performance across different data splits. By testing the model on different parts of the data, k-fold cross-validation helps reduce the risk of overfitting.

Overall, k-fold cross-validation is a widely preferred method for model evaluation because it makes efficient use of data and offers a more reliable performance assessment.

5.3 Feature Importance

Assessing feature importance is essential for interpreting machine learning models, especially in fields that prioritize transparency and explainability. This process measures how much each input variable contributes to the model's predictive accuracy, allowing researchers to pinpoint the key factors influencing results. By ranking these variables, one can improve model interpretability and optimize performance through dimensionality reduction. To evaluate the contribution of individual features toward the classification task, mutual information (MI) is applied. MI quantifies the amount of information obtained about the target variable through each input feature, capturing both linear and non-linear dependencies [23]. Figure 6 demonstrates the MI scores computed for each feature in the spectrum auction dataset. The analysis reveals that property.winner and property.price are the most informative features, contributing substantially more than the others. Specifically, property.winner exhibits the highest mutual information score, indicating a strong dependency with the target variable. In contrast, features related to process capacities, such as process.b1.capacity, process.b2.capacity, and process.b4.capacity, show relatively lower MI scores, suggesting limited direct informational value for the spectrum auction. The process.b4.capacity feature contributed the least, which may indicate redundancy or weak association with the output variable.

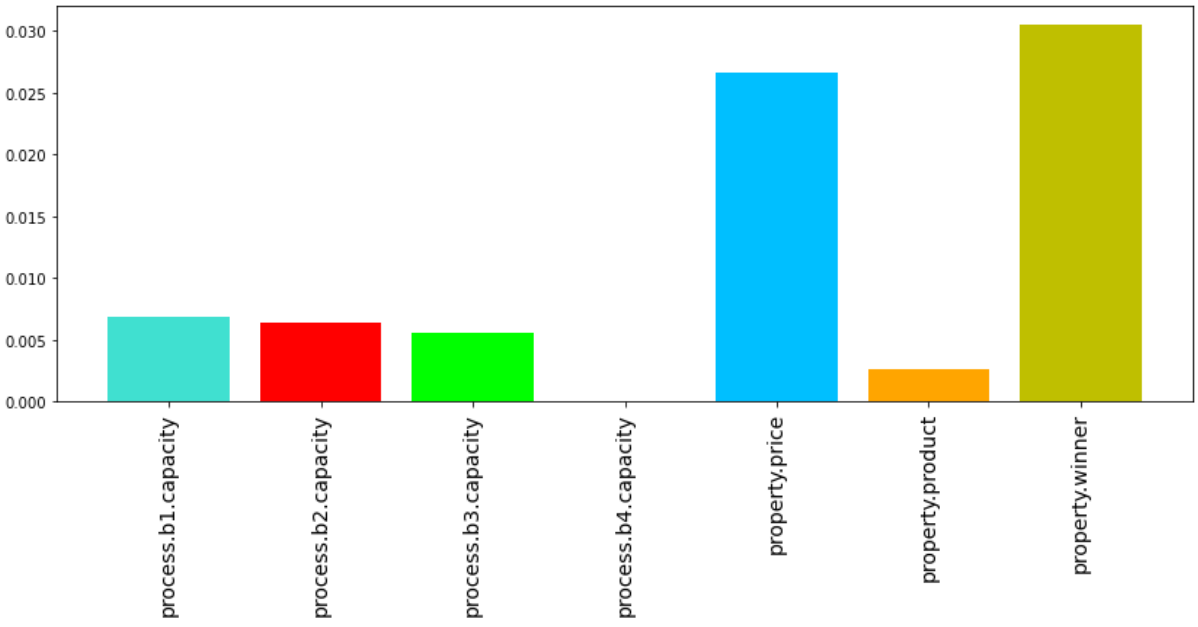


Figure 6. Mutual information score of the features.

5.4 Experimental Results

SGDClassifier, kNN, DT, and SVM were implemented to determine the verification of auction outcomes. Each of these machine learning algorithms has hyperparameters that control the structure of the model and the training process, and these hyperparameters need to be fine-tuned to achieve optimal performance.

To ensure more consistent and reliable results, the number of folds (K) was set to 10, and 10 iterations were performed for each algorithm. The dataset used in the study exhibits an imbalanced class distribution, which can lead to misleading performance evaluations. For example, the accuracy metric can be deceptive in imbalanced datasets, as it may show high scores by predominantly favoring the majority class, while failing to capture the model's performance on the minority class.

To address this issue and provide clearer insights, the F1-Score and G-Mean metrics were selected and plotted for each benchmarked algorithm, as they are more sensitive to imbalanced data [24].

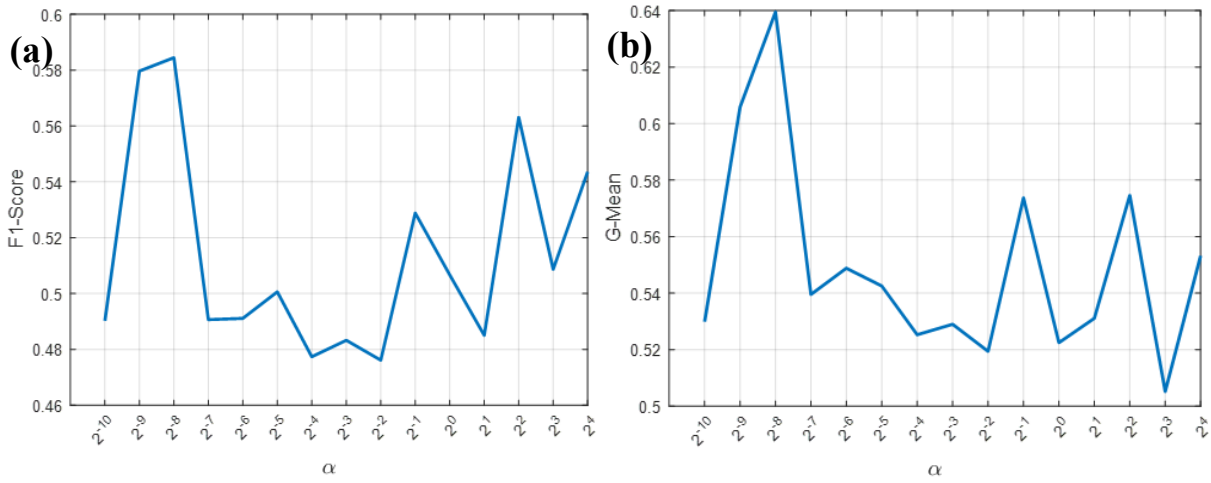


Figure 7. (a) Results of SGDClassifier F1-Score; (b) G-Mean.

SGDClassifier is an efficient and easily implemented machine learning algorithm. It uses the α parameter to prevent overfitting. The α parameter applies a penalty to limit the size of the model's weights, thus helping to avoid overfitting. For this study, the values of α ranged from 2^{-10} to 2^{4}. The results for the F1-Score and G-Mean are shown in Figure 7(a) and Figure 7(b), respectively. Both model performances initially improved as α increased and peaked at 2^{-8}, and then mostly gradually decreased. This indicates that moderate regularization is optimal.

The kNN algorithm uses the k parameter to determine the number of neighbors considered when making decisions for the test sample. In kNN, models with small k values are more sensitive to noise and are more prone to overfitting, whereas models with large k values are more generalized but may be more prone to underfitting. To identify the best results, k was analyzed within the range of 1 to 30, with values increased one by one.

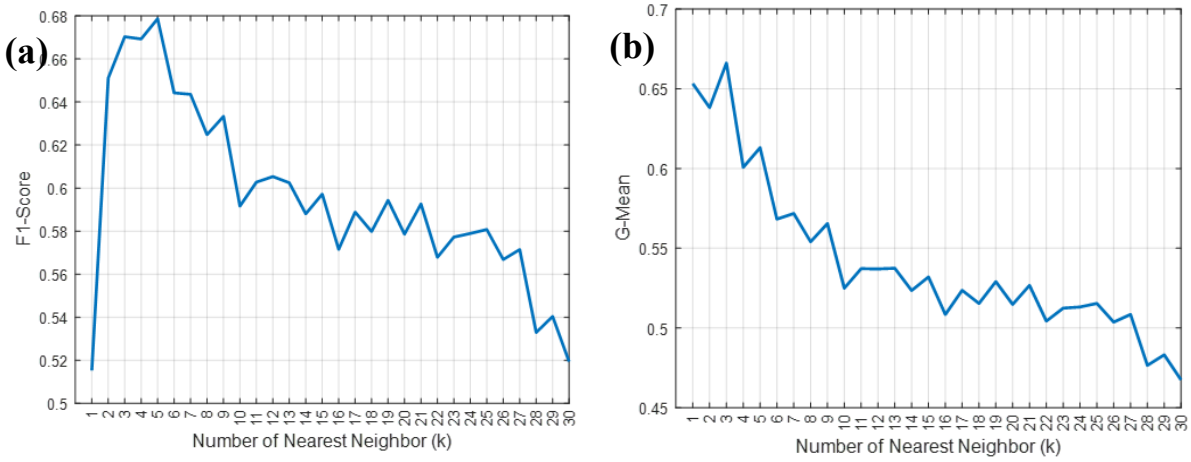


Figure 8. (a) Performance of kNN F1-Score; (b) G-Mean.

As shown in Figure 8(a) and Figure 8(b), the algorithm achieved the best F1-Score when k was set to 5, while the best G-Mean result was obtained when k was set to 3. For both metrics, the results gradually decreased as the k value increased further. This is convenient with the behavior of kNN, since smaller k values can capture local class patterns. The higher G-Mean score when k was set to 3 means that the sensitivity was improved in both classes.

DT uses the min_sample_split and max_depth hyperparameters to control the structure of the tree and the model's generalization ability. The min_sample_split parameter determines the minimum number of samples required to split an internal node, while max_depth sets the maximum depth of the tree. For this study, min_sample_split values ranged from 1 to 17, and max_depth values ranged from 1 to 20.

The results for F1-Score and G-Mean metrics in the DT method are shown in Figure 9(a) and Figure 9(b), respectively. For both metrics, the best results were obtained with the same hyperparameters: max_depth = 9 and min_sample_split = 4. When the max_depth parameter exceeded 9, the results remained nearly constant which indicates that increasing the tree depth beyond 9 does not contribute to further improvements. This also indicates increasing the depth may risk overfitting.

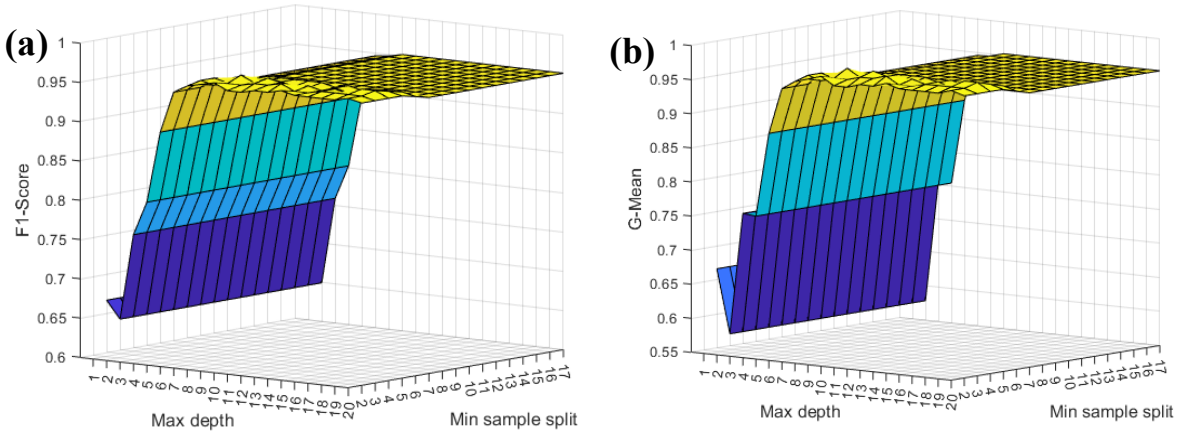


Figure 9. (a) Results of DT F1-Score; (b) G-Mean.

SVM with an RBF kernel takes the C and γ hyperparameters to balance the generalization performance of the algorithm. C value is taken between the range of 2^3 to 2^{14}, whereas γ value is taken between the range of 2^{-4} to 2^5. Figures 10(a) and 10(b) illustrate the F1-Score and G-Mean results of the SVM method for the RBF kernel, respectively. As illustrated in both figures, the performance improves with the increase of C, indicating that the model benefits from placing higher penalties on misclassification. This is consistent with the nature of the dataset, where correct instances are scarce and need to be captured decisively. On the contrary, extreme values of γ tends to degrade performance, suggesting that overly localized or overly generalized decision boundaries are detrimental in this context. The highest F1-Score and G-Mean values were obtained when C is 2^{14} and γ is 2^{-1} in both metrics.

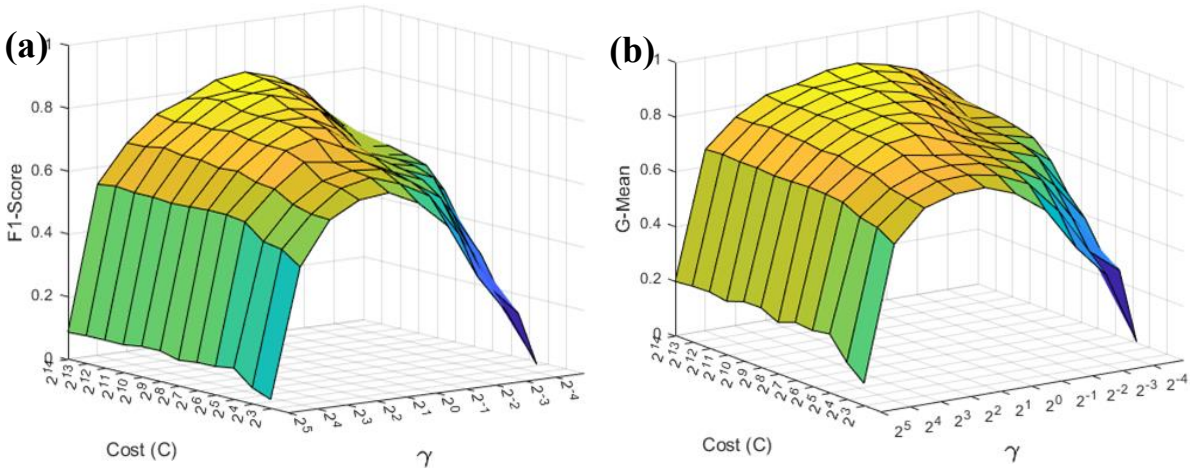


Figure 10. (a) Performance of SVM F1-Score; (b) G-Mean.

Table 2 presents the performance metrics—accuracy, precision, recall, G-Mean, and F1-Score—for the benchmarked algorithms. The hyperparameters chosen for each algorithm were based on the results that yielded the highest G-Mean for that specific algorithm. The choice to prioritize the G-Mean metric is due to the imbalance in the dataset used in this study.

Table 2. Performance results

Methods	Accuracy	Precision	Recall	G-Mean	F1-Score
SGDClassifier α= 0,00390625	0.8821	0.7341	0.6123	0.6394	0.5844
kNN k=3	0.9013	0.7537	0.6498	0.6661	0.6703
Decision Tree max_depth= 9, min_sample_split=4	0.9911	0.9609	0.9807	0.9757	0.9679
RBF-SVM C=2^{14}, γ=2^{-1}	0.9619	0.8901	0.7925	0.8807	0.8385

According to Table 2, the DT algorithm achieved the best overall performance among the benchmarked algorithms. Given the characteristics of the dataset, G-Mean performance results were used for evaluation. It can be observed that the highest G-Mean result (0.97) was obtained with the Decision Tree. Similarly, for the F1-Score, the highest result (0.96) was also achieved by the Decision Tree. On the other hand, the lowest results for all metrics were observed with SGDClassifer, where the G-Mean performance was 0.63, and the F1-Score was 0.58. This result can be explained by its linear nature and sensitivity which makes SGDClassifier less compatible for complex and imbalanced datasets.

The performance gap between the DT and SGDClassifier can be explained by the models' differences in their modeling capacities. While the DT algorithm is more suitable for structure datasets such as Spectrum Auction dataset, as it can identify important features and handle non-linear relationships. Furthermore, adjusting min_sample_split and max_depth to their optimal range allows the DT algorithm to generalize more efficiently without overfitting.

On the contrary, SGDClassifier assumes linear separability and is highly sensitive to the learning rate α and other relevant parameters. Those features make the SGDClassifier less suitable for this particular dataset.

The best performance result of DT can be explained by several reasons. Firstly, to achieve a balance between model complexity and generalization, comprehensive hyperparameter tuning was implemented with max_depth and min_samples_split. Conversely, previous studies did not point out this kind of hyperparameter tuning nor utilize expanded optimization techniques. Secondly, while the authors [8] employed 3-fold-cross-validation, we employed 10-fold-cross-validation over 10 iterations which makes the model results more reliable. Furthermore, even though RF and Fuzzy Neural Network (FNN) employed by [9] and

[8] are powerful ML algorithms, those algorithms also can be prone to overfitting and require more data to generalize to model effectively. The structure of DT can be especially convenient for this dataset since Spectrum Auction dataset is relatively structured and interpretable, and DT can capture discrete decision boundaries without the risk of excessive complexity.

6 CONCLUSION AND SUGGESTION

This study investigates the prediction of spectrum auction results using four distinct machine learning algorithms: SGDClassifier, kNN, DT, and SVM. Each algorithm's specific hyperparameters were optimized to achieve the best performance. To ensure the reliability of the results, 10-fold cross-validation was employed, and a range of performance metrics—accuracy, recall, precision, G-Mean, and F1-Score—were utilized for evaluation.

Among the benchmarked algorithms, the Decision Tree (DT) method with a max_depth of 9 and min_samples_split of 4 provided the best overall results. The DT model achieved approximately 99% accuracy, 96% precision, 98% recall, 97% G-Mean, and 96% F1-Score. The second-best results were observed using the SVM with an RBF kernel. In contrast, the SGDClassifier algorithm delivered the lowest performance across all metrics. Although the accuracy metric was relatively high across all methods, significant disparities were observed in other metrics. The gap between the best and worst results in terms of accuracy was around 11%, but it widened to 34% in G-Mean and 39.62% in F1-Score.

Future studies could explore other machine learning algorithms to enhance classification performance. Additionally, deep learning models have the potential to capture more complex patterns within the dataset. Advanced approaches, such as transfer learning or fine-tuning pre-trained models, hold promises for improving results by leveraging insights from similar datasets, which warrants further exploration.

Conflict of Interest Statement

There is no conflict of interest between the authors.

Artificial Intelligence (AI) Contribution Statement

Authors All components of this study, including its design, data analysis, and scientific contributions, were conducted solely by the authors. ChatGPT® was utilized exclusively to enhance the grammar and clarity of a few selected sentences.

Contributions of the Authors

Ceren Nisa Avcu: Writing – original draft, Writing – review & editing, Conceptualization, Investigation, Methodology,

Ali Değirmenci: Methodology, Software, Writing – original draft, Writing – review & editing, Visualization, Validation

Ömer Karal: Conceptualization, Supervision, Writing – review & editing

REFERENCES

[1] J. Bailey, "Can machine learning predict the price of art at auction?," *Harvard Data Science Review,* vol. 2, no. 2, pp. 1-8,2020.

[2] M. J. G. Rodríguez, V. Rodríguez-Montequín, P. Ballesteros-Pérez, P. E., Love, and R. Signor, "Collusion detection in public procurement auctions with machine learning algorithms," *Automation in Construction,* vol. 133, p. 104047, 2022. doi:10.1016/j.autcon.2021.104047

[3] D. Imhof and H. Wallimann, "Detecting bid-rigging coalitions in different countries and auction formats," *International Review of Law and Economics,* vol. 68, p. 106016, 2021. doi: 10.1016/j.irle.2021.106016

[4] W. U. H. Abidi, M. S. Daoud, B. Ihnaini, M. A. Khan, T. Alyas, A. Fatima, and M. Ahmad, "Real-time shill bidding fraud detection empowered with fussed machine learning," *IEEE Access,* vol. 9, pp. 113612-113621, 2021. doi: 10.1109/ACCESS.2021.3098628.

[5] R. Zhang, C. Jiang, J. Zhang, J. Fan, J. Ren, and H. Xia, "Reinvigorating sustainability in Internet of Things marketing: Framework for multi-round real-time bidding with game machine learning," *Internet of Things,* vol. 24, p. 100921, 2023. doi: 10.1016/j.iot.2023.100921

[6] J. Rani P., A. Kulkarni, A. V. Kamath, A. Menon, P. Dhatwalia and D. Rishabh, "Prediction of Player Price in IPL Auction Using Machine Learning Regression Algorithms," *2020 IEEE International Conference on Electronics, Computing and Communication Technologies (CONECCT),* Bangalore, India, pp. 1-6, 2020. doi: 10.1109/CONECCT50063.2020.9198668

[7] W. Kusonkhum, K. Srinavin, and T. Chaitongrat, "The adoption of a big data approach using machine learning to predict bidding behavior in procurement management for a construction project," *Sustainability,* vol. 15, no. 17, p. 12836, 2023. doi: 10.3390/su151712836

[8] P. V. d. C. Souza and M. Dragoni, "Knowledge extraction in auction verification employing techniques from machine learning and fuzzy neural networks.," *2024 IEEE International Conference on Evolving and Adaptive Intelligent Systems (EAIS)*, Madrid, Spain, pp. 1-8, 2024. doi: 10.1109/EAIS58494.2024.10569109.

[9] M. Tajabadi and D. Heider, "Fair swarm learning: Improving incentives for collaboration by a fair reward mechanism," *Knowledge-Based Systems,* vol. 304, p. 112451, 2024. doi: 10.1016/j.knosys.2024.112451

[10] E. Ordoni, J. Bach and A. -K. Fleck, "Analyzing and Predicting Verification of Data-Aware Process Models–A Case Study With Spectrum Auctions," *IEEE Access,* vol. 10, pp. 31699-31713, 2022. doi: 10.1109/ACCESS.2022.3154445

[11] E. Ordoni, J. Mülle, K. Yang, and K. Böhm, "Efficient Verification of Process Models Supporting Modifications of Data Values," *2022 IEEE 24th Conference on Business Informatics (CBI),* Amsterdam, Netherlands, pp. 21-30, 2022. doi: 10.1109/CBI54897.2022.00010.

[12] S. F. Fischer, M. Feurer, and B. Bischl, "OpenML-CTR23–a curated tabular regression benchmarking suite," *Proc. AutoML Conf. 2023 (Workshop)*, 2023.

[13] S. C. Tan, "Enhancing regression tree predictions with terminal-node anomaly detection," *2023 6th Artificial Intelligence and Cloud Computing Conf.,* pp. 21-26, 2023. doi: 10.1145/3639592.3639596

[14] L. Bottou, F. E. Curtis, and J. Nocedal, "Optimization methods for large-scale machine learning," *SIAM Review,* vol. 60, no. 2, pp. 223-311, 2018. doi:10.1137/16M1080173

[15] A. Ozbay, A. Degirmenci, and O. Karal, "A Comparative Analysis of Machine Learning Algorithms for Accurate Step Detection in Wrist Worn Devices," *2023 Innovations in Intelligent Systems and Applications Conference (ASYU),* Sivas, Turkiye, pp. 1-5, 2023. doi: 10.1109/ASYU58738.2023.10296741.

[16] A. Degirmenci and O. Karal, "iMCOD: Incremental multi-class outlier detection model in data streams," *Knowledge-Based Systems,* vol. 258, p. 109950, 2022. doi: 10.1016/j.knosys.2022.109950

[17] T. Hastie, R. Tibshirani, J. H. Friedman, and J. H. Friedman, The elements of statistical learning: data mining, inference, and prediction, vol. 2, New York: Springer, 2009, pp. 1-758.

[18] M. Çakır, A. Degirmenci, and O. Karal, "Exploring the behavioural factors of cervical cancer using ANOVA and machine learning techniques," *Int. Conf. Science, Engineering Management and Information Technology,* Feb. 2022, pp. 249-260, Cham: Springer Nature Switzerland.

[19] A. N. Karaoglu, H. Caglar, A. Degirmenci, and O. Karal, "Performance Improvement with Decision Tree in Predicting Heart Failure," *2021 6th International Conference on Computer Science and Engineering (UBMK)*, Ankara, Turkey, pp. 781-784, 2021. doi: 10.1109/UBMK52708.2021.9558939.

[20] M. Muttaqi, A. Degirmenci, and O. Karal, "US Accent Recognition Using Machine Learning Methods," *2022 Innovations in Intelligent Systems and Applications Conference (ASYU),* Antalya, Turkey, pp. 1-6, 2022. doi: 10.1109/ASYU56188.2022.9925265.

[21] W. S. Noble, "What is a support vector machine?," *Nature Biotechnology,* vol. 24, no. 12, pp. 1565-1567, 2006. doi: 10.1038/nbt1206-1565

[22] Ö. Karal, "Performance comparison of different kernel functions in SVM for different k value in k-fold cross-validation," *2020 Innovations in Intelligent Systems and Applications Conference (ASYU),* Istanbul, Turkey, pp. 1-5, 2020. doi: 10.1109/ASYU50717.2020.9259880

[23] Değirmenci, A. "Machine Learning Models for Accurate Prediction of Obesity: A Data-Driven Approach," *Turkish Journal of Science and Technology,* vol. 20, no. 1, pp. 77-90, 2025. doi: 10.55525/tjst.1572382

[24] S. García and F. Herrera, "Evolutionary undersampling for classification with imbalanced datasets: Proposals and taxonomy," *Evolutionary Computation,* vol. 17, no. 3, pp. 275-306, 2009. doi: 10.1162/evco.2009.17.3.275

[25] E. Ordoni, J. Bach, A.-K. Fleck, and J. Bach, "Auction verification," *UCI Machine Learning Repository,* 2022. [Online]. Available: https://doi.org/10.24432/C52K6N.Ge

BİTLİS EREN ÜNİVERSİTESİ
FEN BİLİMLERİ DERGİSİ

ISSN: 2147-3129 / e-ISSN: 2147-3188

Article Type : Research Article
Received : March 09, 2025
Revised : September 22, 2025
Accepted : December 31, 2025
DOI : 10.17798/bitlisfen.1654172

Year : 2025
Volume : 14
Issue : 3
Pages : 1440-1452

DETERMINATION OF RADON CONCENTRATIONS IN SOME SCHOOLS IN TATVAN DISTRICT OF BITLIS PROVINCE

Burcu BOZOVA AYDIN [1], **Nergiz YILDIZ YORGUN** [2,*], Ömer Faruk ÖZDEMİR [2], Halime ERZEN YILDIZ [3]

[1] *Van Yüzüncü Yıl University, Institute of Natural and Applied Sciences, Department of Physics, Van, Türkiye*

[2] *Van Yüzüncü Yıl University, Faculty of Science, Department of Physics, Van, Türkiye*

[3] *Van Yüzüncü Yıl University, Health Services Vocational School, Department of Medical Services and Techniques, Van, Türkiye*

**** Corresponding Author:*** *nergiz_yildiz@yahoo.com*

ABSTRACT

Schools are essential social infrastructures where children spend a significant part of their time and require close attention to ensure a safe and healthy environment. In this study, ^{222}Rn concentration measurements and annual effective dose calculations were conducted in 20 schools in Tatvan district of Bitlis province using LR-115 (Type-2) nuclear track detectors. Measurements were conducted over two periods: spring (March, April, May) and autumn (September, October, November). Indoor radon concentrations ranged from 23.39 to 222.06 Bq/m³ in spring and 42.68 to 308.38 Bq/m³ in autumn, with arithmetic means of 83.68 Bq/m³ and 126.49 Bq/m³, respectively. In addition, the effect of floor level on indoor radon concentration was investigated. A clear floor-level variation was observed, with ground-floor rooms (mean: 120.77 Bq/m³) showing higher radon levels than upper-floor rooms (mean: 89.40 Bq/m³). Moreover, the annual effective dose due to radon exposure for teachers and students in the schools were estimated to range from 0.19 and 1.51 mSv/y. Annual effective dose measurements showed that although most schools fall within acceptable radiological ranges, two schools (S1 and S5) recorded annual effective doses slightly above the 1.15 mSv/y global average reported by UNSCEAR (2000). These findings highlight the need for continued monitoring and preventive measures to ensure radiological safety in educational environments.

Keywords: Annual effective dose, Bitlis, LR-115, Radon.

1 INTRODUCTION

^{222}Rn (Radon) is currently under more intensive study than other environmental radionuclides because of the link between radon and lung cancer demonstrated by epidemiological studies in underground miners [1].

The primary source of public exposure to radiation in indoor spaces is thought to be inhalation of ^{222}Rn and its decay products. Radon-222, produced by α-decay of ^{226}Ra (a decay product of ^{238}U), has a half-life of 3.82 days, whereas its parent ^{226}Ra has a half-life of 1620 years [2], [3]. Radon is a radioactive noble gas with a half-life of 3.82 days [4], [5]. When radon undergoes radioactive decay, it produces several radioactive decay products, such as polonium (^{218}Po and ^{214}Po), lead (^{214}Pb), and bismuth (^{214}Bi) [6]. Among these radon daughters, the most important alpha emitters ^{218}Po (6.0 MeV) and ^{214}Po (7.69 MeV), with penetration depths of 47 and 70 μm, respectively, contribute to more than 90% of the maximum radiation dose resulting from radon exposure [6], [7].

Radon decay products are in solid form and adhere to water molecules, other atmospheric gases and natural aerosol particles [8]. These particles reach the lungs with inhaled air and can damage DNA chains in tissues by emitting alpha radiation. If radiation exposure through inhalation reaches high doses, it can lead to the development of bronchogenic cancer in the lungs [9].

The main source of ^{222}Rn in indoor air is the rock and soil under buildings. Radon in soil and rocks can enter the building through cracks in the building floor, cracks in the walls, gaps around water pipes, and gaps inside the walls. Also, another important source is building materials [10], [11].

Since schools are the indoor environment where children spend most of their time outside of home, monitoring radon concentrations in schools is of great importance. According to WHO (2009) [12], it is ideal to keep indoor radon levels below 100 Bq/m³, but in some cases a maximum of 300 Bq/m³ can be considered an upper limit. On the other hand, the US Environmental Protection Agency (USEPA) recommends that radon levels should not exceed 148 Bq/m³, and the European Union (EU) recommends that annual average radon concentrations in mixed-use buildings such as residences, primary schools and kindergartens should be kept below 300 Bq/m³ [13], [14].

In the present study, radon concentration measurements were performed with LR-115 (Type-2) nuclear track detectors in the ground and upper floors of some schools in Bitlis-Tatvan

district in spring and autumn periods. The values obtained from indoor radon concentration measurements were used to calculate the annual effective dose values to which students, teachers and other personnel were exposed in these schools.

2 MATERIAL AND METHODS

2.1 Study Area

Tatvan (38° 29′ 31″ N - 42° 16′ 57″ E) is a district of Bitlis Province in the Eastern Anatolia Region of Türkiye. It is bordered by Bitlis city center to the west, Ahlat district to the north, Hizan district to the south and Lake Van, Türkiye's largest lake, to the east. The area of the district is 1235 km², the population is 89185 and the altitude is 1690 m. The topography of Tatvan is mostly mountainous, and the western and northwestern parts are surrounded by Mount Nemrut and the southern and southeastern parts are surrounded by the Southeastern Taurus Mountains.

2.2 Sampling and Analysis

In this study, radon concentrations in 20 schools located in the Tatvan district were determined using the solid-state nuclear track detector (SSNTD) technique. The locations of the schools selected for the study are shown in Figure 1.

Radon concentration measurements were carried out in two three-month periods covering the spring season (March-April-May) and autumn season (September-October-November). The location coordinates and codes of the selected schools are listed in Table 1, together with the current number of students and teachers.

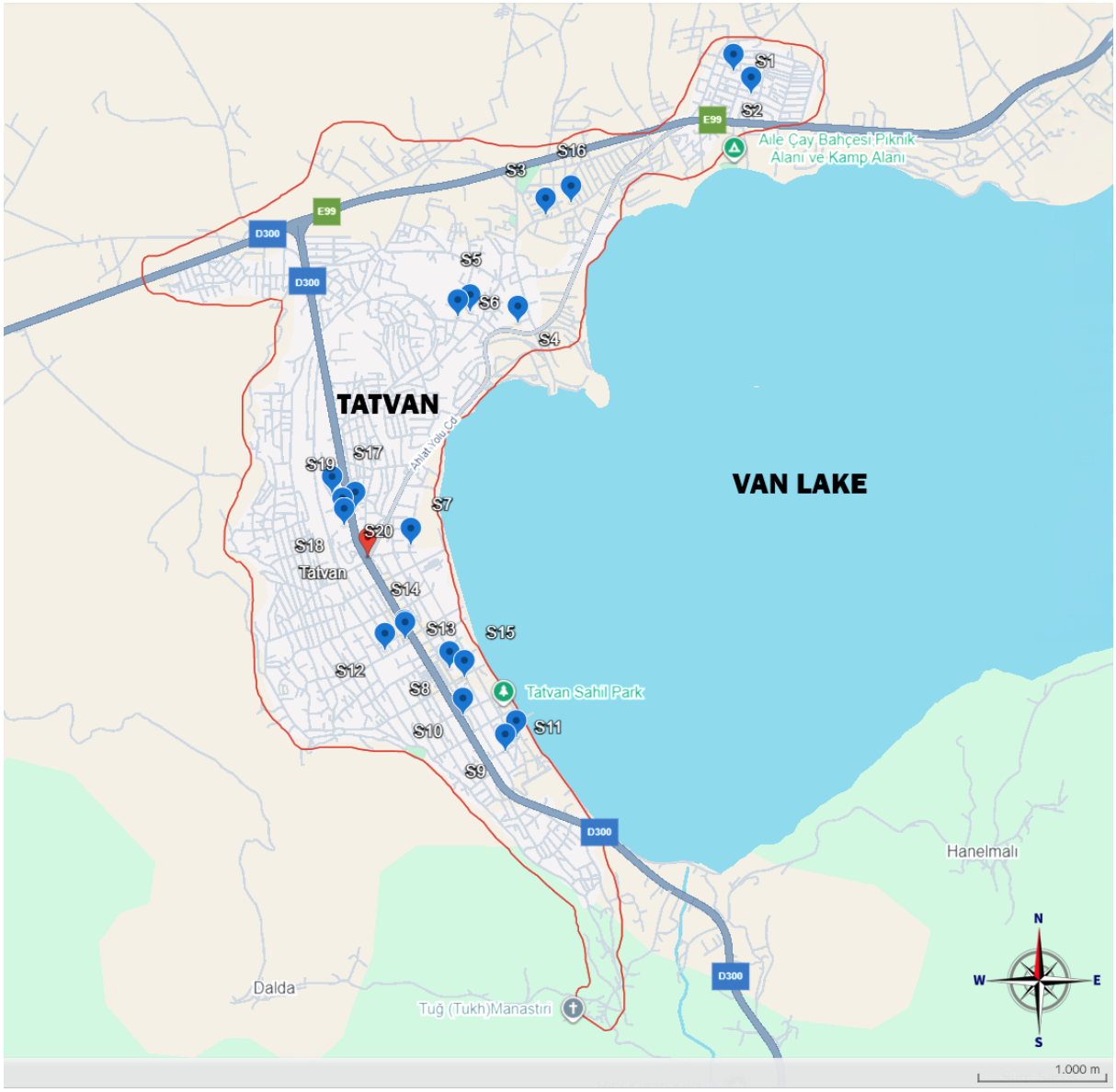


Figure 1. Locations of the schools studied (modified from Google Earth, accessed March 09, 2025).

Table 1. Codes, coordinates and student-teacher numbers in the study

School name	Code	Coordinates		Number of students	Number of teachers
		Latitude	Longitude		
Toki Prof. Dr. Fuat Sezgin Anatolian High School	S1	38.535831	42.313283	606	43
Cumhuriyet Elementary and Middle School	S2	38.534085	42.314785	382	20
Tatvan Science High School	S3	38.525684	42.296717	365	27

Table 1 (continued). Codes, coordinates and student-teacher numbers in the study

School name	Code	Coordinates		Number of students	Number of teachers
		Latitude	Longitude		
Van Gölü Elementary and Middle School	S4	38.518297	42.294507	346	21
Tatvan Vocational and Technical Anatolian High School	S5	38.518750	42.290430	405	22
Nene Hatun Vocational and Technical Anatolian High School	S6	38.519036	42.291074	293	15
Seydi Ali Reis Vocational and Technical Anatolian High School	S7	38.502984	42.284787	440	30
Valide Sultan Vocational and Technical Anatolian High School	S8	38.494352	42.288428	307	28
Şehit Mehmet Ali Kılıç Anatolian High School	S9	38.488991	42.293188	438	28
Uluer Elementary School	S10	38.490007	42.290505	978	38
Hüseyin Çelik Anatolian High School	S11	38.489881	42.292426	902	54
Tuğ Elementary School	S12	38.495717	42.283167	1076	66
Tatvan Kız Anatolian High School	S13	38.496061	42.283489	523	29
Tatvan Sultan Alparslan Middle School	S14	38.496397	42.284111	532	35
Selahaddin Eyyubi Elementary School	S15	38.493752	42.289722	214	15
Selahaddin Eyyubi Middle School	S16	38.526140	42.299023	1234	74
Saadettin Aka Middle School	S17	38.506220	42.278163	680	32
İstasyon Elementary School	S18	38.504007	42.278962	758	32
Tatvan Anatolian High School	S19	38.505233	42.280202	762	42
Sadullah Gencer High School	S20	38.504830	42.279097	288	25

LR-115 detectors were prepared as 1.5 × 1.5 cm² squares and fixed to the bottom of plastic cups using double-sided tape. The cups were placed at a height of 1.5 m above the floor and at least 10 cm away from the walls to minimize additional contributions from thoron (^{220}Rn, half-life: 55.6 s) emitted from building materials. In each school, two detectors were deployed: one on the ground floor and the other on the upper floor. On the ground floor, the detector was most frequently placed in the canteen, while in a few cases it was located in the teachers' room, guidance office, or vice principal's office. On the upper floor, the detector was most commonly placed in the vice principal's office, but in some schools it was located in the library, chemistry laboratory, sports hall, or, in one case, the canteen. Rooms were selected based on their accessibility and frequency of use, ensuring that areas where both students and staff spend considerable time were represented in the measurements. The prepared plastic cups were labeled by writing the name of the school and the floor information on which they would be placed. Then, the detectors were placed in the schools for a period of three months covering the spring and autumn seasons. At the end of these periods, the samples were collected and analyzed in the laboratory. Solutions containing 10% NaOH were prepared using 25 ml of distilled water for each film. The films were placed in the solution in such a way that they did not touch each other or the surfaces of the beakers. The beakers were subjected to chemical etching in a magnetic stirrer at a constant temperature of 60°C at 120 rpm for 100 minutes. The films were then rinsed in another magnetic stirrer at 120 rpm for 20 min. The rinsed films were then left to dry. The tracks of alpha particles on the surface of the detectors were counted using an optical microscope with 100X magnification (Figure 2).

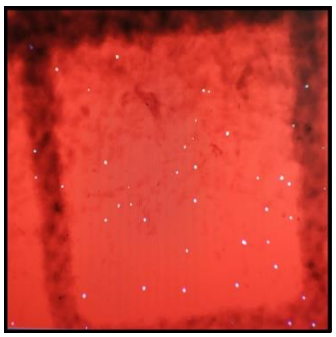


Figure 2. Tracks on the LR-115 detector.

Using the track counts obtained from the measurements, the radon concentration was calculated using the Equation 1 [15]:

$$C_{Rn} = k_f . \rho / d \quad (1)$$

where C_{Rn} is the radon activity concentration (Bq/m^3), ρ is the surface density of tracks on the LR-115 (tracks/cm^2), d is the exposure time (90 days), k_f is the calibration factor to convert track density to the radon concentration (kBq.cm^2.g/track.m^3) [16], [17].

The annual effective dose (D_{eff}) can be calculated using Equation 2 [18].

$$D_{eff}(mSvy^{-1}) = C_{RN} \times E \times F \times T \times D \quad (2)$$

where, E is the equilibrium factor (0.4), F is the occupancy factor in schools (0.18), T is time (8760 h), and D is the dose conversion factor (**9** nSv / Bq.h.m^{-3}).

3 RESULTS AND DISCUSSION

The radon and average radon concentration values and effective dose values measured in schools in Tatvan are given in Table 2, and the annual average radon concentration distribution is presented in Figure 3. As shown in Table 2, the radon concentration values ranged from 23.39 (S7) to 222.06 (S5) Bq/m³ in the spring season and from 42.68 (S11) to 308.38 (S5) Bq/m³ in the autumn season. The highest average radon concentration value was observed in S5 (265.22 Bq/m^3) and the lowest value was observed in S11 (33.76 Bq/m^3) (Figure 3). The elevated radon concentrations observed in S1 and S5 schools are likely influenced by multiple factors, including the age of the school buildings, the nature of building materials, insulation conditions, limited ventilation, and prolonged occupancy of ground-floor rooms [18].

Table 2. The radon concentration and D_{eff} values in the schools

	$C_{Rn\text{-}spring}$ (Bq/m^3)			**$D_{eff\text{-}spring}$ (mSv)**	**$C_{Rn\text{-}autumn}$ (Bq/m^3)**			**$D_{eff\text{-}autumn}$ (mSv)**	**C_{Rn} (Bq/m^3)**	**D_{eff} (mSv)**
Codes	Ground	Upper	Spring	Spring	Ground	Upper	Autumn	Autumn	**Annual Average**	**Annual Average**
S1	317.06	110.91	213.99	1.21	391.08	199.40	295.24	1.68	254.61	1.45
S2	21.94	94.27	58.11	0.33	28.93	96.93	62.93	0.36	60.52	0.34
S3	50.39	36.17	43.28	0.25	53.29	35.68	44.49	0.25	43.88	0.25
S4	63.41	16.64	40.02	0.23	58.35	41.71	50.03	0.28	45.03	0.26
S5	230.50	213.62	222.06	1.26	375.17	241.59	308.38	1.75	265.22	1.51
S6	183.00	151.18	167.09	0.95	246.42	171.67	209.04	1.19	188.07	1.07
S7	22.42	24.35	23.39	0.13	83.18	72.82	78.00	0.44	50.69	0.29

Table 2 (continued). The radon concentration and D_{eff} values in the schools

	$C_{Rn\text{-}spring}$ (Bq/m^3)			$D_{eff\text{-}spring}$ (mSv)	$C_{Rn\text{-}autumn}$ (Bq/m^3)			$D_{eff\text{-}autumn}$ (mSv)	C_{Rn} (Bq/m^3)	D_{eff} (mSv)
Codes	Ground	Upper	Spring	Spring	Ground	Upper	Autumn	Autumn	**Annual Average**	**Annual Average**
S8	39.30	66.55	52.92	0.30	50.39	71.13	60.76	0.34	56.84	0.32
S9	232.67	16.88	124.78	0.71	361.43	198.19	279.81	1.59	202.29	1.15
S10	76.19	28.21	52.20	0.30	197.71	130.20	163.96	0.93	108.08	0.61
S11	13.50	36.17	24.83	0.14	46.29	39.06	42.68	0.24	33.76	0.19
S12	54.49	45.57	50.03	0.28	82.46	48.46	65.46	0.37	57.75	0.33
S13	40.27	160.34	100.30	0.57	49.19	207.36	128.27	0.73	114.29	0.65
S14	96.44	66.55	81.50	0.46	115.73	71.13	93.43	0.53	87.46	0.50
S15	176.49	22.42	99.46	0.56	230.98	27.25	129.12	0.73	114.29	0.65
S16	171.43	37.13	104.28	0.59	168.78	50.15	109.46	0.62	106.87	0.61
S17	50.15	77.64	63.89	0.36	67.75	131.16	99.46	0.56	81.68	0.46
S18	40.02	34.96	37.49	0.21	71.37	79.08	75.23	0.43	56.36	0.32
S19	56.66	82.46	69.56	0.39	71.37	167.81	119.59	0.68	94.58	0.54
S20	42.68	46.29	44.49	0.25	101.99	126.82	114.41	0.65	79.45	0.45
Average values	98.95	68.42	83.68	0.48	142.59	110.38	126.49	0.72	105.9	0.60

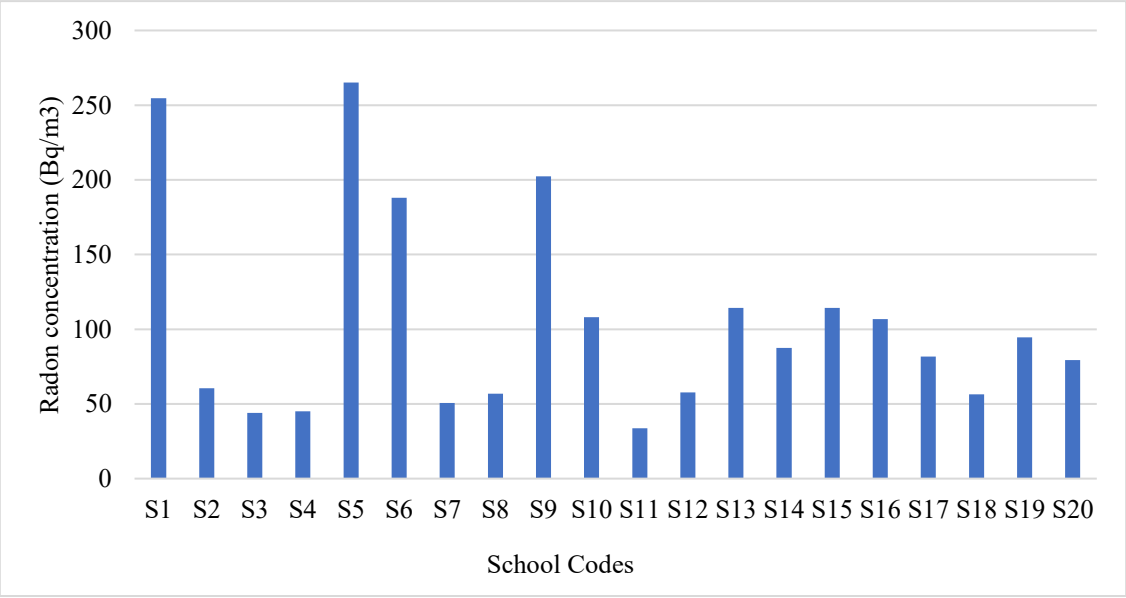


Figure 3. Average radon concentration distributions of schools.

The seasonal distribution of average radon concentrations in schools is shown in Figure 4. The high radon concentrations observed during autumn can be attributed to the closing of doors and windows, the use of heating systems, and the decrease in ventilation as temperatures begin to decrease in September [19].

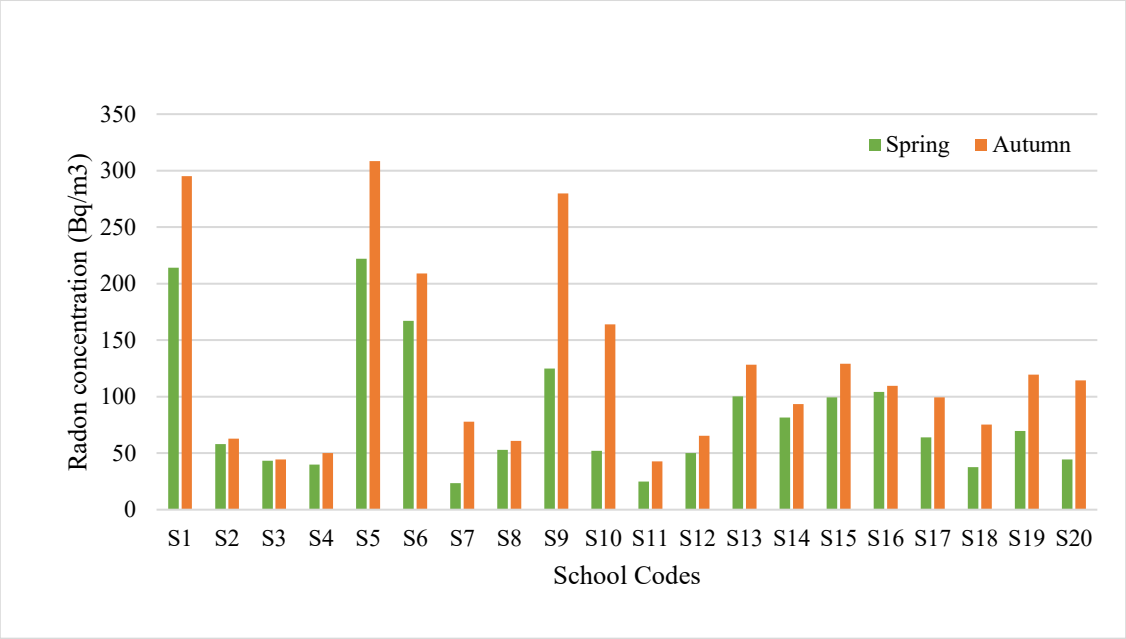


Figure 4. Average radon concentrations of schools in the autumn and spring seasons.

In this study, the arithmetic mean of the average radon concentrations in schools was determined as 105.09 Bq/m³. If the obtained results are categorized as low (0-49 Bq/m³), medium (50-100 Bq/m³) and high (>100 Bq/m³) according to the frequency distribution of annual mean radon concentrations, 15% of the schools can be classified as low level, 45% as medium level and 40% as high level. In a similar study conducted in Greece, the arithmetic mean radon concentration in 512 schools was reported to be 135 Bq/m³ [20].

Figure 5 shows that radon concentrations are generally higher in the basement and ground floors of schools, and decrease progressively at higher floor levels. This trend is primarily due to radon emanation from the soil and its easier accumulation in lower levels with limited ventilation, while upper floors benefit from dilution and greater distance from radon sources. Similar patterns have been reported in previous studies [21], [22], [23].

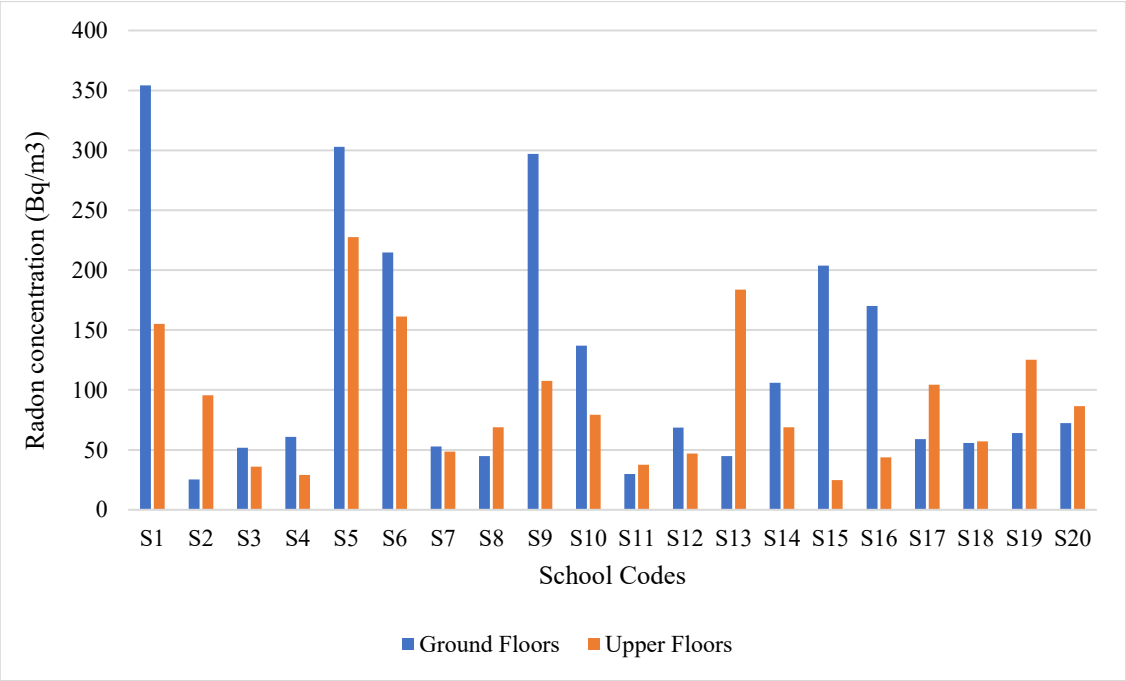


Figure 5. Average radon concentrations in schools across various floors.

The annual effective dose calculation (D_{eff}) was performed using Equation 2, and the results are presented in Table 2 and Figure 6. The average annual effective dose was calculated as 0.48 mSv for the spring semester and 0.72 mSv for the fall semester, with an overall average of 0.60 mSv/year for both seasons. The International Commission on Radiological Protection (ICRP) defines the D_{eff} limit as 3–10 mSv [24], while the United Nations Scientific Committee on the Effects of Atomic Radiation (UNSCEAR) reports a global average annual effective dose of 1.15 mSv [18]. The annual effective dose values for all schools were below the threshold recommended by the ICRP [24]. However, the average D_{eff} values for the S1 and S5 schools exceeded the global average (Table 2, Figure 6).

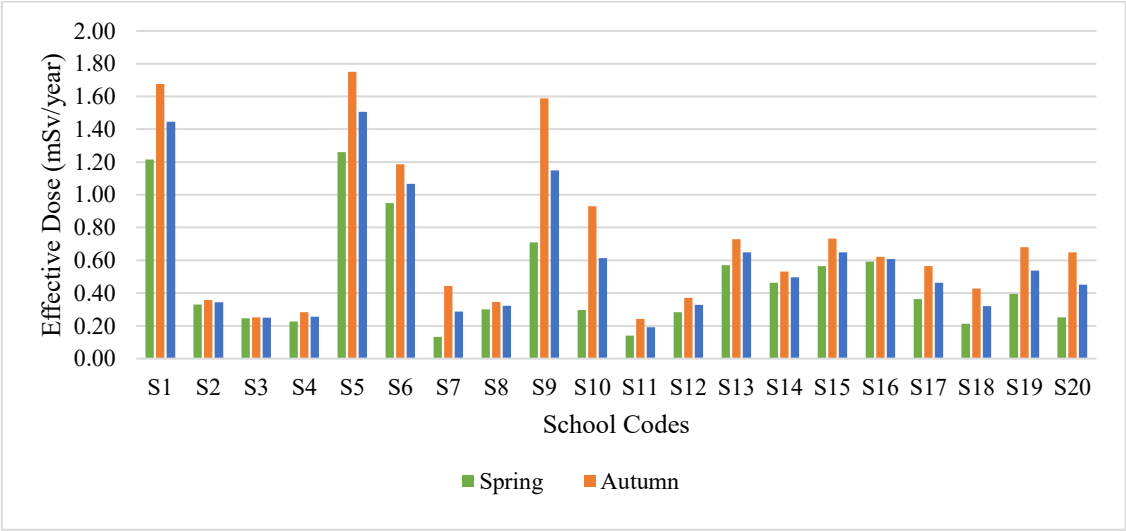


Figure 6. Spring, autumn and annual average effective dose values in schools.

4 CONCLUSIONS

In this research, indoor air ^{222}Rn concentrations were measured using LR-115 detectors in selected schools in Bitlis-Tatvan region, and the potential radiological risk assessment was performed. The measurements revealed that radon concentrations varied seasonally, with higher levels observed in autumn compared to spring. In addition, analysis of the data suggested a general decrease in radon levels with increasing floor height; however, some schools deviated from this trend, suggesting that factors such as building characteristics and ventilation may influence indoor radon levels.

The estimated annual effective doses ranged from 0.19 to 1.51 mSv/year, with an arithmetic mean of 0.60 mSv/year. Most schools showed values below the global average dose of 1.15 mSv/year; however, two schools (S1 and S5) exceeded this benchmark, underscoring the need for targeted monitoring and potential mitigation measures in those cases. Overall, the findings suggest that radon exposure in most surveyed schools is likely to be low, but continued monitoring is recommended to ensure that concentrations remain within acceptable limits over time.

Acknowledgements

The authors would like to express their sincere gratitude to all individuals and schools who contributed to the realization of this study.

This study was approved by the Van Yüzüncü Yıl University Committee on Publication Ethics for Science and Engineering (Decision No: 2022/02-01).

Conflict of Interest Statement

There is no conflict of interest between the authors.

Statement of Research and Publication Ethics

The study is complied with research and publication ethics.

Artificial Intelligence (AI) Contribution Statement

This manuscript was entirely written, edited, analyzed, and prepared without the assistance of any artificial intelligence (AI) tools. All content, including text, data analysis, and figures, was solely generated by the authors.

Contributions of the Authors

Burcu BOZOVA AYDIN: Conceptualization, Material supply, Experiment; Nergiz YILDIZ YORGUN: Theory, Original drafting, Experiment, Revision and Editing; Ömer Faruk ÖZDEMİR: Data analysis, Drafting, Revision and Editing; Halime ERZEN YILDIZ: Experiment, Data analysis.

REFERENCES

[1] J. M. Samet, "Radon and lung cancer," *JNCI Journal of the National Cancer Institute*, vol. 81, no. 10, pp. 745–758, May 1989, doi: 10.1093/jnci/81.10.745.

[2] C. Taşköprü, M. İçhedef, and M. M. Saç, "Diurnal, monthly, and seasonal variations of indoor radon concentrations concerning meteorological parameters," *Environ Monit Assess*, vol. 195, no. 1, p. 25, Jan. 2023, doi: 10.1007/s10661-022-10596-6.

[3] M. Yılmaz, M. Gürcan, and Y. Güral, "A correlation assessment of 222 Rn gas measurements from the East Anatolian fault zone," *Journal of Physical Chemistry and Functional Materials*, vol. 3, no. 2, pp. 77–84, 2020, Accessed: Sep. 03, 2025. [Online]. Available: https://dergipark.org.tr/jphcfum

[4] F. Loffredo, I. Opoku-Ntim, G. Meo, and M. Quarto, "Indoor radon monitoring in kindergarten and primary schools in South Italy," *Atmosphere (Basel)*, vol. 13, no. 3, p. 478, Mar. 2022, doi: 10.3390/atmos13030478.

[5] J. Madureira, I. Paciência, J. Rufo, A. Moreira, E. de Oliveira Fernandes, and A. Pereira, "Radon in indoor air of primary schools: determinant factors, their variability and effective dose," *Environ Geochem Health*, vol. 38, no. 2, pp. 523–533, Apr. 2016, doi: 10.1007/s10653-015-9737-5.

[6] G. Degu Belete and Y. Alemu Anteneh, "General overview of radon studies in health hazard perspectives," *J Oncol*, vol. 2021, pp. 1–7, Jul. 2021, doi: 10.1155/2021/6659795.

[7] A. Robertson, J. Allen, R. Laney, and A. Curnow, "The cellular and molecular carcinogenic effects of radon exposure: A review," *Int J Mol Sci*, vol. 14, no. 7, pp. 14024–14063, Jul. 2013, doi: 10.3390/ijms140714024.

[8] G. M. Kendall and T. J. Smith, "Doses from radon and its decay products to children," *Journal of Radiological Protection*, vol. 25, no. 3, pp. 241–256, Sep. 2005, doi: 10.1088/0952-4746/25/3/002.

[9] S. Q. Othman, A. H. Ahmed, and S. I. Mohammed, "Environmental health risks of radon exposure inside selected building factories in Erbil city, Iraq," *Int J Environ Anal Chem*, vol. 104, no. 16, pp. 4711–4725, Dec. 2024, doi: 10.1080/03067319.2022.2107923.

[10] H. A. Bulut and R. Şahin, "Radon, concrete, buildings and human health-A review study," *Buildings*, vol. 14, no. 2, p. 510, Feb. 2024, doi: 10.3390/buildings14020510.

[11] W. W. Nazaroff, B. A. Moed, and R. G. Sextro, "Soil as a Source of Indoor Radon: Generation, Migration, and Entry," in *Radon and Its Products in Indoor Air*, W. W. Nazaroff and A. V. Nero, Eds., John Wiley & Sons, 1988, pp. 57–111.

[12] World Health Organization, *WHO Handbook on Indoor Radon A Public Health Perspective*. Geneva, Switzerland, 2009.

[13] United States Environmental Protection Agency, "EPA Assessment of Risks from Radon in Homes," Washington, US, Jun. 2003.

[14] European Commission, "Laying down basic safety standards for protection against the dangers arising from exposure to ionising radiation, and repealing Directives 89/618/Euratom, 90/641/Euratom, 96/29/Euratom, 97/43/Euratom and 2003/122/Euratom," Brussels, Belgium, Dec. 2013.

[15] A. Baran, "Denizli ve çevresindeki termal alanlarda bina içi radon düzeylerinin belirlenmesi," Yüksek lisans tezi, Fen Bilimleri Enstitüsü, Ege Üniversitesi, İzmir, Türkiye, 2013.

[16] M. Değerlier, "Adana ili ve çevresinin çevresel doğal radyoaktivitesinin saptanması ve doğal radyasyonların yıllık etkin doz eşdeğerinin bulunması," Doktora tezi, Adana, Türkiye, 2007.

[17] H. Erzen Yıldız, "Van ilindeki konutlarda radon gazının zamana bağlı değişimi ve akciğer kanseri ile ilişkisinin araştırılması," Doktora tezi, Van, Türkiye, 2023.

[18] United Nations Scientific Committee on the Effects of Atomic Radiation, *Sources and effects of ionizing radiation United Nations Scientific Committee on the Effects of Atomic Radiation UNSCEAR 2000 report to the general assembly, with scientific annexes volume ı: sources*, vol. I. New York, US, 2000.

[19] Y. Örgün and N. Çelebi, "Radyasyon, radon (Rn) ve toplum sağlığı," *TMMOB Jeoloji Mühendisleri Odası, Tıbbi Jeoloji ve İnsan Sağlığı, Haber Bülteni, Ocak-Haziran*, pp. 11–27, 2016.

[20] A. Clouvas and S. Xanthos, "A comparison study between radon concentration in schools and other workplaces," *Radiat Prot Dosimetry*, vol. 149, no. 2, pp. 207–210, Apr. 2012, doi: 10.1093/RPD/NCR224.

[21] A. J. Khan, "A study of indoor radon levels in Indian dwellings, influencing factors and lung cancer risks," *Radiat Meas*, vol. 32, no. 2, pp. 87–92, Apr. 2000, doi: 10.1016/S1350-4487(99)00275-9.

[22] A. N. Shaikh, T. V. Ramachandran, and A. Vinod Kumar, "Monitoring and modelling of indoor radon concentrations in a multi-storey building at Mumbai, India," *J Environ Radioact*, vol. 67, no. 1, pp. 15–26, Jan. 2003, doi: 10.1016/S0265-931X(02)00144-3.

[23] K. Çıtlak, "Sakarya üniversitesi kampüs bölgesinde bina içi radon konsantrasyonunun belirlenmesi," Yüksek lisans tezi, Fen Bilimleri Enstitüsü, Sakarya Üniversitesi, Sakarya, Türkiye, 2018.

[24] ICRP, *Protection against radon-222 at home and at work*, vol. 23, no. 2. ICRP Publication 65. Ann. ICRP, 1993.

F

BİTLİS EREN ÜNİVERSİTESİ
FEN BİLİMLERİ DERGİSİ

ISSN: 2147-3129 / e-ISSN: 2147-3188

Article Type	: Research Article	**Year**	: 2025
Received	: March 10, 2025	**Volume**	: 14
Revised	: September 9, 2025	**Issue**	: 3
Accepted	: September 20, 2025	**Pages**	: 1453-1468
DOI	: 10.17798/bitlisfen.1655093		

DESIGN, SYNTHESIS AND *IN VITRO* BIOLOGICAL ASSESSMENT OF NOVEL 2-[(3-ALKYL/ARYL-4,5-DIHYDRO-1*H*-1,2,4-TRIAZOL-5-ONE-4-YL)AZOMETHINE]PHENYL 2,5-DICHLOROBENZENESULFONATES MOLECULES AS ANTIOXIDANT AND ANTIBACTERIAL AGENTS

Fevzi AYTEMİZ [1,*], Haydar YÜKSEK [1]

[1] *Kafkas University, Chemistry Department, Kars, Türkiye*

**** Corresponding Author:*** *fevziaytemiz53@gmail.com*

ABSTRACT

In this study, a total of nine new 2-[(3-alkyl/aryl-4,5-dihydro-1*H*-1,2,4-triazol-5-one-4-yl)azomethine]phenyl 2,5-dichlorobenzenesulfonates (**4a-i**) were synthesized through the reactions of 2-formylphenyl 2,5-dichlorobenzenesulfonate (**3**) with 3-alkyl(aryl)-4-amino-4,5-dihydro-1*H*-1,2,4-triazol-5-ones (**2a-i**). The compounds **4a**, **4e**, **4g** and **4h** were successfully synthesized with yields exceeding 90%. Compounds **4a-i** were elucidated using ^{1}H, ^{13}C NMR and IR spectroscopic methods. The spectroscopic data were compared with the literature, and the results were found to be consistent. The antioxidant effects of compounds **4a–i** were investigated using three different methods, and it was found that compounds **4a-i** showed metal chelation activity close to that of α-tocopherol, which was used as the standard. Additionally, the antimicrobial properties of the compounds **4a–i** were evaluated using the agar well diffusion method against six different bacterial strains. The antimicrobial properties of the new compounds (**4a-i**) were compared with those of standard antibiotics such as neomycin, streptomycin, and ampicillin. It was observed that compound **4a** exhibited better antimicrobial activity than neomycin and streptomycin, and comparable activity to ampicillin.

Keywords: 1,2,4-Triazol, Synthesis, Antioxidant, Antibacterial.

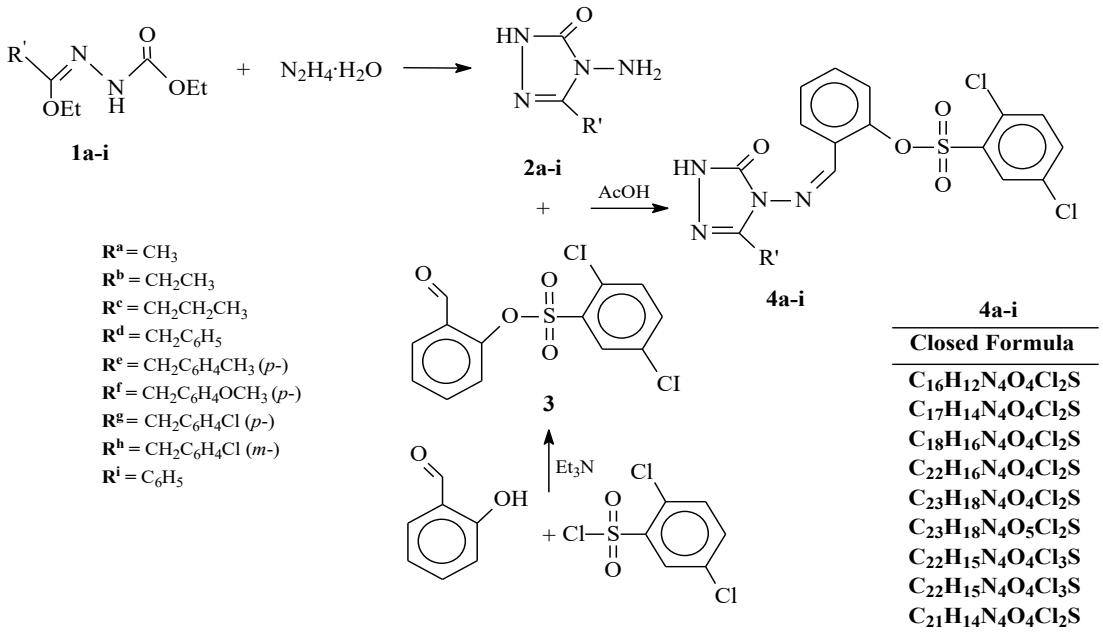
1 INTRODUCTION

Schiff bases have been of special interest to organic chemists because they are one of the most frequently encountered ligands in coordination chemistry. These ligands are formed

by the condensation reaction of ketones or aldehydes with primary amines [1], [2], [3]. The carbon-nitrogen double bonds (C=N) formed as a result of the reaction are called imines or azomethines [4], [5]. Schiff bases have various biological effects such as anti-inflammatory [6], analgesic [7], anticancer [8], antimicrobial [9], antitumor [10], antiviral [11], antifungal [12], antituberculosis [13] and antioxidant [14]. There are many derivatives of Schiff bases, which were first synthesized by Hugo Schiff in 1864 [15], [16], [17], [18]. One of the most common types of Schiff bases are those containing the 1,2,4-triazole substituent [19], [20]. These derivatives have been reported to possess a wide range of biological properties [21], [22], [23].

Triazoles are heterocyclic compounds with three nitrogen and two carbon atoms and exist in various isomeric forms [24], [25], [26]. These compounds are among the most studied heterocyclic compounds in the field of pharmaceutical chemistry [27], [28]. Additionally, they are used in drug design due to their binding properties and are present in the structures of antifungal drugs such as voriconazole, itraconazole and fluconazole [29], [30], [31], [32], [33].

In this study, we aimed to investigate the in vitro antimicrobial and antioxidant properties of newly synthesized Schiff bases (4a-i) containing 1,2,4-triazole ring.



4a-i
Closed Formula
$C_{16}H_{12}N_4O_4Cl_2S$
$C_{17}H_{14}N_4O_4Cl_2S$
$C_{18}H_{16}N_4O_4Cl_2S$
$C_{22}H_{16}N_4O_4Cl_2S$
$C_{23}H_{18}N_4O_4Cl_2S$
$C_{23}H_{18}N_4O_5Cl_2S$
$C_{22}H_{15}N_4O_4Cl_3S$
$C_{22}H_{15}N_4O_4Cl_3S$
$C_{21}H_{14}N_4O_4Cl_2S$

Scheme 1. Synthesis route of Schiff bases (4a-i).

2 MATERIAL AND METHOD

The required chemicals were purchased from Fluka, Aldrich and Merck. Melting points were measured using a Stuart SMP30 device. All test microorganisms used in the antimicrobial

activity studies were obtained from Microbiological Environmental Protection Laboratories (France). ^{1}H (400 MHz) and ^{13}C NMR (100 MHz) spectra were recorded on a Bruker Ultrashield Plus Biospin NMR spectrotometer. Solutions were prepared in deuterated dimethyl sulfoxide (DMSO-d_6) and tetramethylsilane (TMS) was preferred as standard. IR spectra were recorded on an Alpha-P Bruker FT-IR spectrometer. Antioxidant properties were investigated using a PG Instruments Ltd T80 UV/VIS spectrometer. In the evaluation of antimicrobial activity, concentration measurements were performed using a VELP brand turbidimeter capable of precise determinations within a measurement range of 0-1000 NTU

2.1 Synthesis

2.1.1 Synthesis Method of 2-formylphenyl 2,5-dichlorobenzenesulfonate (3)

A solution of 2,5-dichlorobenzensulfonyl chloride (0.01 mol) in ethyl acetate (20 mL) was prepared, to which 2-hydroxybenzaldehyde (0.01 mol) was added. Triethylamine (0.01 mol) was then gradually added to the mixture at 0-5 °C and the reaction was stirred for 3 hours. The mixture was subsequently refluxed for 4 hours. After cooling, the reaction mixture was filtered, and the filtrate was concentrated under reduced pressure. The resulting product was washed with distilled water and recrystallized from ethanol, yielding pure 2,5-dichlorobenzene sulfonate (**3**) [34], m.p: 108 °C; IR spectrum (υ, cm^{-1}): 781 (1,2-C_6H_4), 1197 and 1387 (SOO), 1696, 1759 (C=O), 2772 and 2896 (CHO). ^{1}H NMR spectrum (δ, ppm):10.17 (s,1H, CHO), 8.00-7.96 (m, 2H, ArH), 7.94-7.93 (m, 1H, H_{arom}), 7.91 (d, 1H, H_{arom}; J=1.60 Hz), 7.77-7.73 (m, 1H, H_{arom}), 7.59 (td, 1H, H_{arom}; J=7.60, 0.80 Hz), 7.18 (dd, 1H, H_{arom}; J=8.40, 0.80 Hz). ^{13}C NMR spectrum (δ, ppm): 187.01 (CHO); 149.32, 136.66, 136.19, 134.46, 133.42, 132.81, 131.29, 130.80, 129.52, 129.04, 128.56, 112.95 (C_{arom}).

2.1.2 General Synthesis Method of Schiff Bases (4a-i)

Firstly, compounds **2a-i** (amino-triazoles) were synthesized according to the literature procedures [35]. The synthesized compounds **2a-i** (0.01 mol) were taken into separate flasks and their solutions were prepared with acetic acid (20 mL). Then, 2-formylphenyl 2,5-dichlorobenzenesulfonate (**3**) (0.01 mol) was added to each flask and the mixtures were refluxed for 3 h. After cooling, distilled water was added to the solution and the product was precipitated and filtered. The precipitates were crystallized twice from ethanol to obtain compounds **4a-i** (2-[(3-methyl-4,5-dihydro-1*H*-1,2,4-triazol-5-one-4-yl)azomethine]phenyl 2,5-dichlorobenzenesulfonates (**4a**), (2-[(3-ethyl-4,5-dihydro-1*H*-1,2,4-triazol-5-one-4-

yl)azomethine]phenyl 2,5-dichlorobenzenesulfonates (**4b**), (2-[(3-propyl-4,5-dihydro-1*H*-1,2,4-triazol-5-one-4-yl)azomethine]phenyl 2,5-dichlorobenzenesulfonates (**4c**), (2-[(3-benzyl-4,5-dihydro-1*H*-1,2,4-triazol-5-one-4-yl)azomethine]phenyl 2,5-dichlorobenzenesulfonates (**4d**), 2-[(3-p-methylbenzyl-4,5-dihydro-1*H*-1,2,4-triazol-5-one-4-yl)azomethine]phenyl 2,5-dichlorobenzenesulfonates (**4e**), 2-[(3-p-methoxybenzyl-4,5-dihydro-1*H*-1,2,4-triazol-5-one-4-yl)azomethine]phenyl 2,5-dichlorobenzenesulfonates (**4f**), 2-[(3-p-chlorobenzyl-4,5-dihydro-1*H*-1,2,4-triazol-5-one-4-yl)azomethine]phenyl 2,5-dichlorobenzenesulfonates (**4g**), 2-[(3-m-chlorobenzyl-4,5-dihydro-1*H*-1,2,4-triazol-5-one-4-yl)azomethine]phenyl 2,5-dichlorobenzenesulfonates (**4h**), 2-[(3-phenyl-4,5-dihydro-1*H*-1,2,4-triazol-5-one-4-yl)azomethine]phenyl 2,5-dichlorobenzenesulfonates (**4i**) as pure crystalline solids.

2.2 Antioxidant Activity

The antioxidant activities of compound **4a-i**, along with standard antioxidant agents such as ethylenediaminetetraacetic acid (EDTA), butylated hydroxytoluene (BHT), α-tocopherol and butylated hydroxyanisole (BHA), were assessed using various antioxidant assays, including metal chelation activity, reducing power and free radical scavenging activity.

The iron ion chelation activity of compounds **4a-i** was evaluated using the Dinis method [36]. This method is a spectrophotometric assay used to determine the antioxidant capacity of phenolic compounds. It primarily focuses on their ability to inhibit the oxidation of iron (Fe^{2+}) ions, reflecting the metal chelating effect. In this method, a colored complex (purple-pink) is formed between Fe^{2+} ions and ferrozine. If the sample contains chelating (binding) antioxidants, the formation of this complex is inhibited. As a result, the intensity of the color decreases. This decrease is measured spectrophotometrically, typically at 562 nm. A lower absorbance indicates a stronger metal chelating capacity.

The reducing power properties of compounds **4a-i** were investigated using the method described by Oyaizu [37]. This method is used to determine antioxidant capacity and is based on measuring the reducing power of iron ions. This method is commonly referred to as the Ferric Reducing Antioxidant Power (FRAP) assay. Antioxidants facilitate the reduction of Fe^{3+} (ferric ions) to Fe^{2+} (ferrous ions). As a result of this reduction, a colored complex is formed (e.g., with potassium ferricyanide). The absorbance of this colored complex is measured spectrophotometrically, typically at 700 nm. A higher absorbance indicates a greater the antioxidant capacity of the sample.

The free radical scavenging activity of compounds **4a-i** was assessed using the Blois method [38]. This method typically measures the radical scavenging capacity of a sample in the presence of free radicals, such as DPPH or ABTS. Antioxidants neutralize these free radicals, resulting in a color change. This color change is measured spectrophotometrically, usually at 517 nm, although the wavelength may vary depending on the radical used. A lower absorbance of the mixture indicates a greater free radical scavenging activity.

2.3 Antibacterial Activity

The antibacterial activity of compounds **4a-i** were analyzed using the well diffusion method. [39], [40]. Gram-positive bacterial strains (*Staphylococcus aureus* ATCC 6538, *Bacillus cereus* ATCC 11778 and *Bacillus subtilis* ATCC11774) and Gram-negative bacterial strains (*Klebsiella pneumoniae* ATCC4352, *Pseudomonas aeruginosa* ATCC27853 and *Escherichia coli* ATCC 25922) were preferred in the study. Streptomycin X3385, Neomycin X3385 and Ampicillin X3261 were used as standard antibiotics to compare the effects of compounds 4a-i.

The microorganisms were suspended in Mueller-Hinton Broth and their turbidity was adjusted to 240 NTU using a Velp brand turbidimeter. Following this, the microorganisms were inoculated onto the surface of Mueller-Hinton Agar using the "flood-inoculation" technique and allowed to dry for 15 minutes. Wells, 5 mm in diameters, were created on the agar surface with a sterile cork-borer, and 250-5000 µg/50 µL of the chemical compounds 4a-i were added into the wells. The plates were incubated at 37 °C for 18 hours. The diameters of the inhibition zones obtained was compared to those of standard antibiotics.

3 RESULTS AND DISCUSSION

3.1 Synthesis

In this study, nine new Schiff bases (**4a-i**) were synthesized from the reaction of compound **3** with compounds **2a-i**. The synthetic pathway for new 2-[(3-alkyl/aryl-4,5-dihydro-1*H*-1,2,4-triazol-5-one-4-yl)-azomethine]-phenyl 2,5-dichlorobenzenesulfonates (**4a-i**) is illustrated in Scheme 1.

The compounds **4a-i** were characterized using IR, ^{1}H and ^{13}C NMR spectroscopic methods. TMS was used as standard and DMSO-d_6 was used as solvent for both ^{1}H and ^{13}C NMR spectra. It was seen that the values obtained by spectroscopic methods were compatible

with the literature [14], [41]. The obtained results were given in Tables 1-3. The physical properties of the compounds **4a-i** are given in Table 4. In addition, the IR, ^{1}H and ^{13}C NMR spectra of compound **4a** are presented in Figures 1–3. The molecular structure of compound **4a** has been drawn on the spectra with the atoms numbered, and these numbers have been assigned to the corresponding peaks.

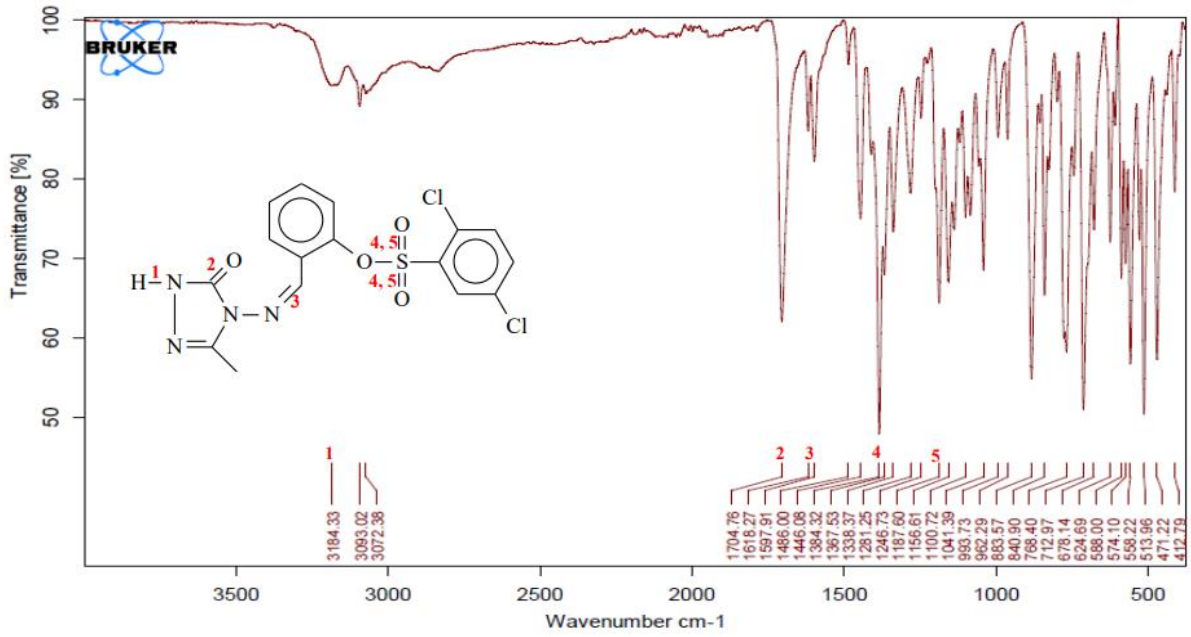


Figure 1. FT-IR spectrometer of Schiff bases 4a.

Table 1. FT-IR spectrum values of Schiff bases (4a-i)

Compounds	ν_{NH}	$\nu_{C=O}$	$\nu_{C=N}$	ν_{SO2}	$\nu_{1,4\text{-aromatic ring}}$	$\nu_{1,3\text{-aromatic ring}}$	$\nu_{1,2\text{-aromatic ring}}$	$\nu_{mono\text{-aromatic ring}}$
4a	3184	1705	1618, 1598	1384 and 1188	-	-	768	-
4b	3171	1705	1597	1383 and 1189	-	-	770	-
4c	3183	1701	1587	1377 and 1186	-	-	766	-
4d	3173	1712	1600, 1587	1381 and 1190	-	-	766	776 and 701
4e	3196	1712	1591	1395 and 1189	822	-	772	-
4f	3333	1716	1606	1387 and 1190	820	-	778	-
4g	3175	1702	1587	1357 and 1199	849	-	765	-
4h	3210	1713	1598, 1584	1381 and 1190	-	817 and 686	777	-
4i	3164	1713	1598, 1584	1381 and 1185	-	-	787	765 and 689

In the IR spectra of compounds **4a-i**, N-H stretching vibrations were observed in the range of 3210-3163 cm^{-1}. C=O stretching bands appeared between 1716-1701 cm^{-1}. Furthermore, C=N stretching vibrations were detected in the range of 1618-1584 cm^{-1}. In addition, SO_2 stretching vibration bands were observed in the ranges of 1395-1185 cm^{-1}.

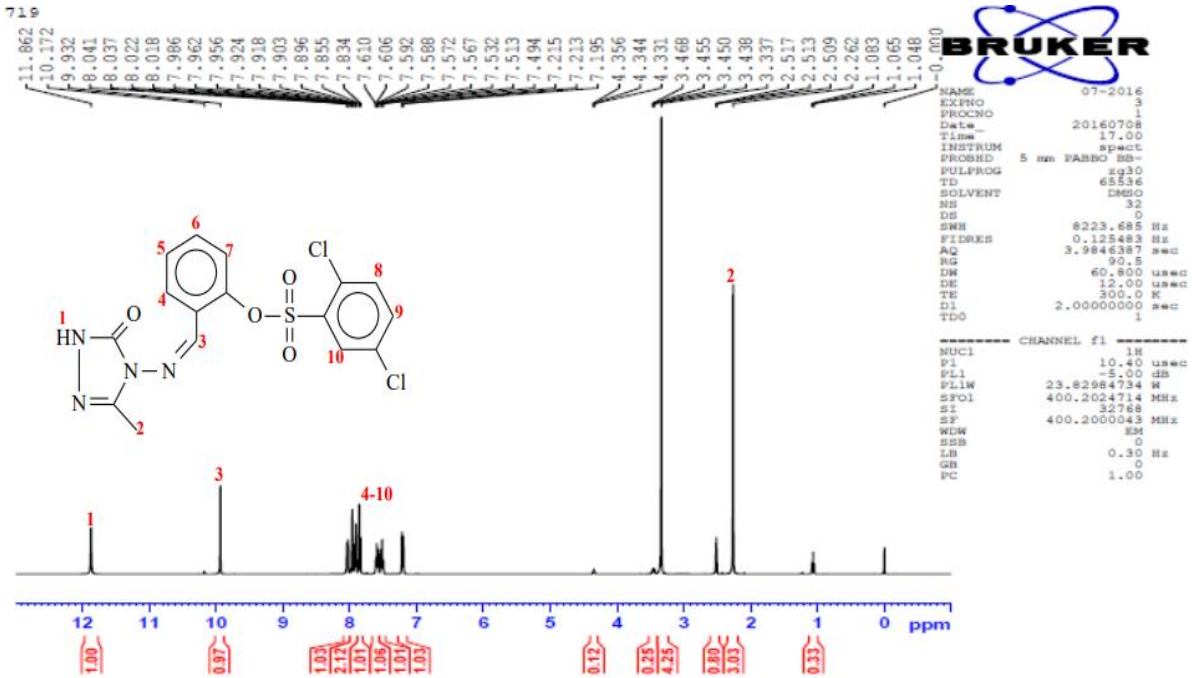


Figure 2. [1]H NMR spectrometer of Schiff bases 4a.

Table 2. [1]H NMR spectrum values of Schiff bases (4a-i)

Compounds	Aliphatic H	Aromatic H	N=CH	NH
4a	2.26 s (3H, C**H**$_3$)	8.03 (dd, 1H, *J*=7.60, 1.60 Hz), 7.96 (d, 1H, *J*=2.40 Hz), 7.91 (dd, 1H, *J*=8.40, 2.40 Hz), 7.84 (d, 1H, *J*=8.40 Hz), 7.59 (td, 1H, *J*=8.20, 1.60 Hz), 7.51 (t, 1H, *J*=7.60, 1.60 Hz), 7.21 (d, 1H, *J*=8.00 Hz)	9.93(s)	11.86(s)
4b	2.66 q (2H, C**H**$_2$CH$_3$, *J*=7.60 Hz), 1.20 t (3H, CH$_2$C**H**$_3$, *J*=7.60 Hz)	8.01 (dd, 1H, *J*=7.60, 1.60 Hz), 7.96 (d, 1H, *J*=2.40 Hz), 7.90 (dd, 1H, *J*=8.40, 2.40 Hz), 7.84 (d, 1H, *J*=8.40 Hz), 7.59 (td, 1H, *J*=8.00, 1.60 Hz), 7.51 (t, 1H, *J*=7.60), 7.21 (d, 1H, *J*=8.00 Hz)	9.92(s)	11.88(s)
4c	2.66 t (2H, C**H**$_2$CH$_2$CH$_3$, *J*=7.60 Hz), 1.68 sext (2H, CH$_2$C**H**$_2$CH$_3$, *J*=7.60 Hz), 0.96 t (3H, CH$_2$CH$_2$C**H**$_3$, *J*=7.60 Hz)	8.01 (dd, 1H, *J*=7.60, 1.60 Hz), 7.96 (d, 1H, *J*=2.40 Hz), 7.90 (dd, 1H, *J*=8.80, 2.40 Hz), 7.84 (d, 1H, *J*=8.80 Hz), 7.59 (td, 1H, *J*=8.00,1.60 Hz), 7.52 (t, 1H, *J*=7.60 Hz), 7.22 (d, 1H, *J*=8.40 Hz)	9.93(s)	11.90(s)
4d	4.05 s (C**H**$_2$Ph)	7.97-7.94 (m, 2H), 7.86 (dd, 1H, *J*=8.80, 2.40 Hz), 7.78 (d, 1H, *J*=8.40 Hz), 7.58 (td, 1H, *J*=8.40, 1.60 Hz), 7.50 (t, 1H, *J*=7.60 Hz), 7.36-7.32 (m, 4H), 7.28-7.22 (m, 2H), 7.19 (d, 1H, *J*=8.00 Hz)	9.92(s)	12.03(s)
4e	3.99 (C**H**$_2$Ph), 2.26 s (C**H**$_3$Ph),	7.98-7.94 (m, 2H), 7.86 (dd, 1H, *J*=8.80, 2.40 Hz), 7.70 (d, 1H, *J*=8.80 Hz), 7.58 (td, 1H, *J*=8.00, 1.60 Hz), 7.50 (t, 1H, *J*=7.60 Hz), 7.21 (d, 1H, *J*=7.60 Hz), 7.19 (d, 2H, *J*=8.00 Hz), 7.13 (d, 2H, *J*=8.00 Hz)	9.92(s)	12.01(s)
4f	3.97 s (C**H**$_2$Ph), 3.72 s (PhOC**H**$_3$),	7.99 (dd, 1H, *J*=8.40, 1.60 Hz), 7.97 (d,1H, *J*=8.40 Hz), 7.87 (dd, 1H, *J*=8.80, 2.40 Hz), 7.79 (d, 1H, *J*=8.80 Hz), 7.58 (td, 1H, *J*=8.40, 1.60 Hz), 7.52 (t, 1H, *J*=7.60 Hz), 7.24 (d, 2H, *J*=8.40 Hz), 7.19 (d, 1H, *J*=8.00 Hz), 6.89 (d, 2H, *J*=8.80 Hz)	9.92(s)	11.99(s)
4g	4.07 s (C**H**$_2$Ph)	7.98-7.96 (m, 2H), 7.89 (dd, 1H, *J*=8.80, 2.40 Hz), 7.19 (d, 1H, *J*=8.40 Hz); 7.81 (d, 1H, *J*=8.80 Hz), 7.58 (td, 1H, *J*=8.00,1.20 Hz), 7.51 (t, 1H, *J*=7.60 Hz), 7.41-7.37 (m, 4H)	9.95(s)	12.08(s)

Table 2 (continued). ^{1}H NMR spectrum values of Schiff bases (4a-i)

Compounds	Aliphatic H	Aromatic H	N=CH	NH
4h	4.09 s (C**H**$_2$Ph)	7.98-7.95 (m, 2H), 7.89-7.86 (m, 1H), 7.80 (d, 1H, *J*=8.40 Hz), 7.60-7.56 (m, 1H), 7.50 (t, 1H, *J*=7.60 Hz), 7.39-7.30 (m, 4H), 7.18 (d, 1H, *J*=8.40 Hz)	9.93(s)	12.06(s)
4i		7.96-7.92 (m, 2H), 7.88-7.80 (m, 4H), 7.61(td, 1H, *J*=8.00, *J*=1.60 Hz), 7.55-7.49 (m, 4H), 7.26 (d, 1H, *J*=8.00 Hz)	9.93(s)	12.44(s)

Upon analysis of the ^{1}H NMR spectra of compounds **4a–h**, signals corresponding to N–H protons were observed in the δ 12.08–11.86 ppm range. However, for compound **4i**, the signal of the N–H proton attached to the phenyl group at the C_3 position of the triazoles ring, which is a characteristic feature, was observed at δ 12.44 ppm. Additionally, peaks corresponding to N=CH protons were detected in the δ 9.95–9.92 ppm range, while aromatic protons appeared in the δ 8.03–6.89 ppm range. The peaks of the CH_3 proton of compound **4a** appeared at δ 2.26 ppm. The peaks of the $CH_2C\mathbf{H}_3$ proton of compound **4b** appeared at δ 1.20 ppm and the peaks of the $C\mathbf{H}_2CH_3$ proton appeared at δ 2.66 ppm. In compound **4c**, peaks were detected at δ 0.96 ppm for $CH_2CH_2C\mathbf{H}_3$ protons, at δ 1.68 ppm for $CH_2C\mathbf{H}_2CH_3$ protons and at δ 2.66 ppm for $C\mathbf{H}_2CH_2CH_3$ protons. The peaks of $C\mathbf{H}_2$Ph protons of compounds **4d-h** appeared at δ 4.05 ppm, δ 3.99 ppm, δ 3.97 ppm, δ 4.07 ppm and δ 4.09 ppm, respectively. Also, the peaks of Ph$C\mathbf{H}_3$ protons of compound **4e** appeared at δ 2.26 ppm and the peaks of PhO$C\mathbf{H}_3$ protons of compound **4f** appeared at δ 3.72 ppm.

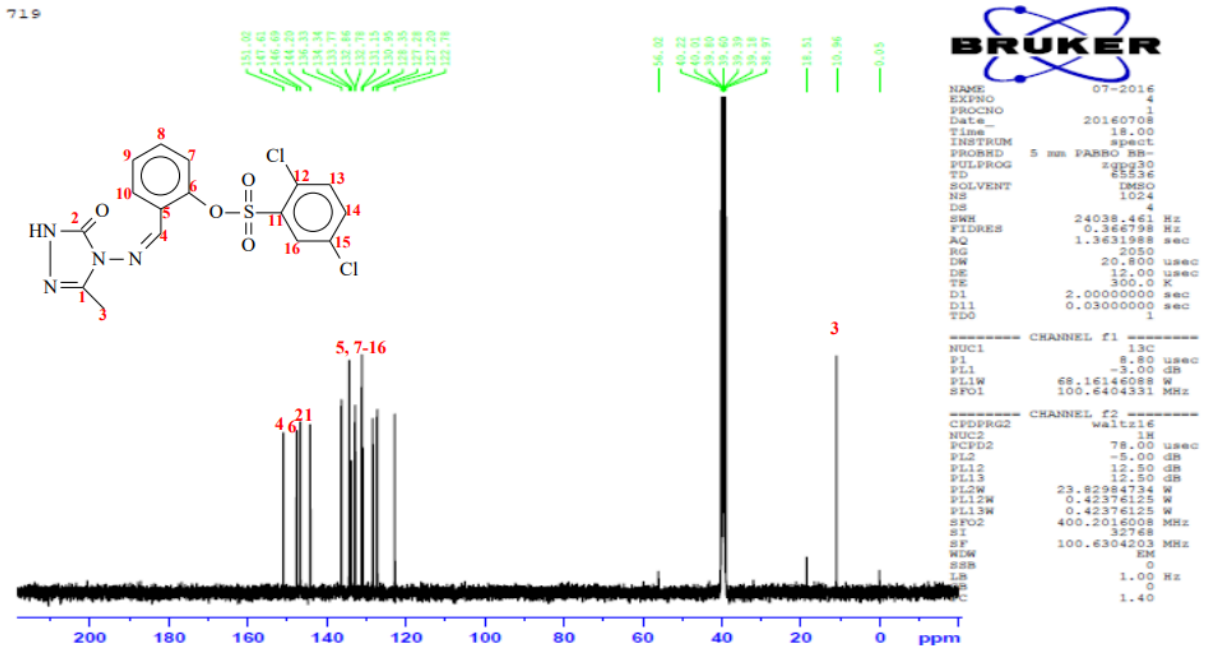


Figure 3. ^{13}C NMR spectrometer of Schiff bases 4a.

Table 3. ^{13}C NMR spectrum values of Schiff bases (4a-i)

Compounds	N=CH	Triazole C_5	Triazole C_3	Aromatik C	Alifatik C
4a	151.02	147.61	144.20	122.78, 127.20, 127.28, 128.35, 130.35, 131.15, 132.78, 132.86, 133.37, 134.34, 136.33, 146.69,	10.96 (**C**H_3)
4b	151.17	147.97	146.68	122.82, 127.10, 127.30, 128.40, 130.95, 131.16, 132.78, 132.87, 133.75, 134.34, 136.34, 147.62	10.02 (CH_2**C**H_3), 18.39 (**C**H_2CH_3)
4c	151.11	147.61	146.66	122.82, 127.05, 127.29, 128.40, 130.96, 131.15, 132.77, 132.84, 133.75, 134.32, 136.32, 146.83	13.43 (CH_2CH_2**C**H_3), 18.88 (CH_2**C**H_2CH_3), 26.56 (**C**$H_2CH_2CH_3$)
4d	151.03	147.65	146.12	122.71, 126.95, 127.24, 128.44, 130.91, 131.18, 132.78, 132.90, 133.69, 134.30, 136.32, 146.35 C_3; 126.72, 128.35 (2C), 128.76 (2C), 135.65	31.94 (**C**H_2Ph)
4e	151.04	147.64	146.26	122.70, 126.94, 127.26, 128.34, 130.91, 131.16, 132.77, 132.88, 133.70, 134.29, 136.30, 147.08 C_3; 128.58 (2C), 128.99 (2C), 132.53, 135.80	20.57(Ph**C**H_3), 30.54(**C**H_2Ph)
4f	151.05	147.69	146.34	122.71, 126.98, 127.26, 128.39, 130.91, 131.17, 132.78, 132.90, 133.71, 134.30, 136.33, 146.42 C_3; 113.91 (2C), 127.42, 129.84 (2C), 158.14	30.08(**C**H_2Ph), 55.04(PhO**C**H_3)
4g	151.08	147.65	145.77	122.68, 126.96, 127.20, 128.36, 130.92, 131.17, 132.77, 132.91, 133.71, 134.28, 136.31, 146.46 C_3; 128.36 (2C), 130.69 (2C), 131.48, 134.59	30.28(**C**H_2Ph)
4h	151.00	147.66	145.62	122.71, 126.99, 127.20, 128.32, 130.92, 131.17, 132.78, 132.98, 133.69, 134.30, 136.32, 146.45 C_3; 126.83, 127.55, 128.95, 130.25, 133.69, 138.02	30.57(**C**H_2Ph)
4i	151.15	148,75	144.51	122.92, 127.07, 127.12, 128.04, 130.92, 131.16, 132.79, 133.10, 133.73, 134.28, 136.35, 147.75 C_3; 126.38, 128.04 (2C), 128.48 (2C), 130.13	

In the ^{13}C NMR spectra of compounds **4a-i**, peaks corresponding to N=CH carbons were observed in the δ 151.17-151.00 ppm range, peaks for triazole **C**$_5$ (aromatic carbon atoms located at position 5 of the triazole ring) carbons appeared between δ 148.75-147.761 ppm, and peaks for triazole **C**$_3$ (aromatic carbon atoms located at position 3 of the triazole ring) carbons were detected in the δ 146.68-144.20 ppm range. For compound **4a**, peaks corresponding to the **C**H_3 carbon was observed at δ 10.96 ppm. The peaks of the CH_2**C**H_3 carbon of compound **4b** appeared at δ 10.02 ppm and the peak of the **C**H_2CH_3 carbon appeared at δ 18.39 ppm. The peaks of $CH_2CH_2CH_3$ carbons of compound **4c** appeared as CH_2CH_2**C**H_3 carbon peak at δ 13.43

ppm, $CH_2\mathbf{C}H_2CH_3$ carbon peak at δ 18.88 ppm and $\mathbf{C}H_2CH_2CH_3$ carbon peak at δ 26.56 ppm. The peaks of $\mathbf{C}H_2Ph$ carbons of compounds **4d-h** appeared at δ 31.94 ppm, δ 30.54 ppm, δ 30.08 ppm, δ 30.28 ppm and δ 30.57 ppm, respectively. The peak of $\mathbf{C}H_3Ph$ carbon of compound **4e** appeared at δ 20.57 ppm and the peak belonging to $PhOCH_3$ carbon of compound **4f** appeared at δ 55.04 ppm.

Table 4. Physical properties of Schiff bases (4a-i)

Compounds	Melting Point (°C)	Yield (%)	Crystallization Solvent	Closed Formula
4a	217	90.14	Ethanol	$C_{16}H_{12}N_4O_4Cl_2S$
4b	191	86.48	Ethanol	$C_{17}H_{14}N_4O_4Cl_2S$
4c	171	81.25	Ethanol	$C_{18}H_{16}N_4O_4Cl_2S$
4d	148	77.24	Ethanol	$C_{22}H_{16}N_4O_4Cl_2S$
4e	175	90.27	Ethanol	$C_{23}H_{18}N_4O_4Cl_2S$
4f	204	86.66	Ethanol	$C_{23}H_{18}N_4O_5Cl_2S$
4g	205	92.30	Ethanol	$C_{22}H_{15}N_4O_4Cl_3S$
4h	166	94.36	Ethanol	$C_{22}H_{15}N_4O_4Cl_3S$
4i	223	77.71	Ethanol	$C_{21}H_{14}N_4O_4Cl_2S$

Compounds **4a-i** were crystallized in ethyl alcohol. The melting points of the compounds **4a-i** were found to be between 223 ^{0}C and 148 ^{0}C. As a result of the reactions, the highest yield was obtained for compound **4h**, while the lowest yield was obtained for compound **4d.**

3.2 Antioxidant Activity

The increase in absorbance of the reaction mixture is directly proportional to the reducing power of the sample. The decrease in absorbance of the reaction mixture is directly proportional to the free radical scavenging activity of the sample. The antioxidant properties of compounds **4a-i** were examined and it was observed that they have no reducing power and free radical scavenging activity. However, the compounds **4a-i** have chelating activity, albeit low. Figure 4 shows that the antioxidant properties of compounds **4a-i** are close to those *α*-tocopherol, which was used as a standard antioxidant. It was observed that the compounds have higher activity at lower concentrations.

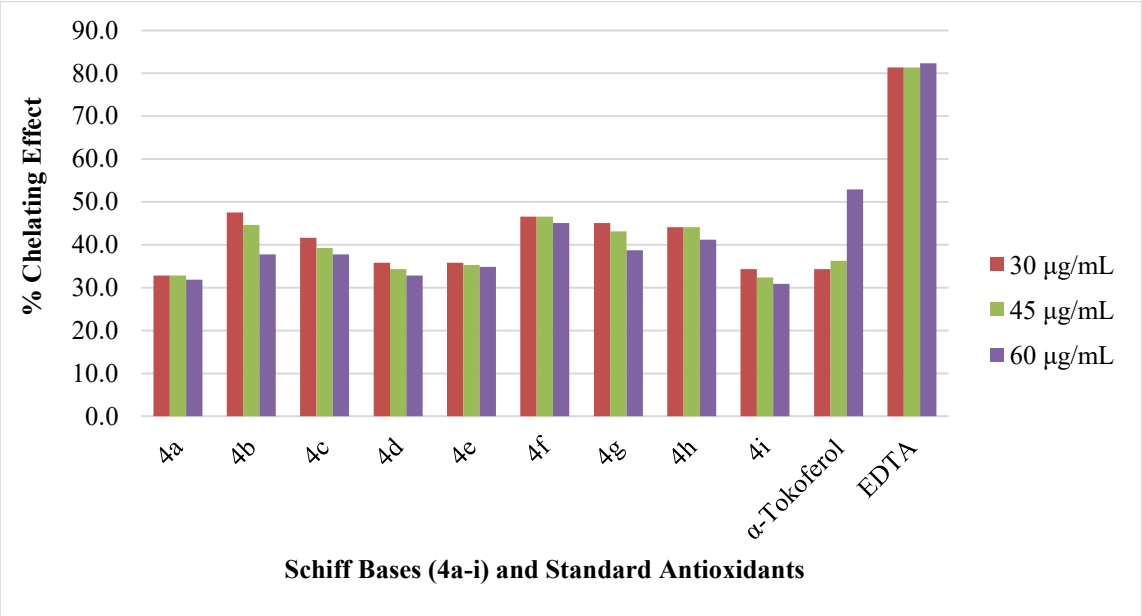


Figure 4. Metal chelating activities of Schiff bases (4a-i).

3.3 Antibacterial Activity

In this study, conducted with six different bacterial strains, including three Gram-positive strains (*S. aureus* ATCC 6538, *B. cereus* ATCC 11778 and *B. subtilis* ATCC 11774) and three Gram-negative strains (*K. pneumoniae* ATCC 4352, *P. aeruginosa* ATCC 27853 and *E. coli* ATCC 25922). Highly effective results were obtained. All of the new compounds **(4a-i)** were effective against several bacterial species. Most of the compounds exhibited activity comparable to the standard antibiotic neomycin and were more effective than streptomycin. The results were evaluated according to the inhibition zone diameters as follows: ≥17 mm high effect (+++); 11-16 mm medium effect (++); 5.5-10 mm low effect (+); <5.5 mm no effect (-) [42].

Table 5. In vitro antimicrobial activity of Schiff bases (4a-i)

Compounds and Standarts	Level of the antibacterial effects and diameter of inhibition zone (mm)					
	S. aureus	***B. cereus***	***B. subtilis***	***K. pneumoniae***	***P. aeruginosa***	***E. coli***
4a	24 (+++)	25 (+++)	23 (+++)	27 (+++)	20 (+++)	34 (+++)
4b	18 (+++)	16 (++)	14 (++)	20 (+++)	-	30 (+++)
4c	11 (++)	20 (+++)	12 (++)	27 (+++)	-	17 (+++)
4d	-	21 (+++)	12 (++)	-	-	14 (++)
4e	-	15 (++)	10 (+)	-	-	16 (++)

Table 5 (continued). In vitro antimicrobial activity of Schiff bases (4a-i)

Compounds and Standarts	Level of the antibacterial effects and diameter of inhibition zone (mm)					
	S. aureus	***B. cereus***	***B. subtilis***	***K. pneumoniae***	***P. aeruginosa***	***E. coli***
4f	12 (++)	-	10 (+)	-	-	-
4g	10 (+)	14 (++)	11 (++)	-	-	-
4h	12 (++)	13 (++)	23 (+++)	20 (+++)	12 (++)	14 (++)
4i	13 (++)	12 (++)	16 (++)	-	-	16 (++)
Streptomycin	21 (+++)	12 (++)	12 (++)	11 (++)	12 (++)	10 (+)
Neomycin	13 (++)	17 (+++)	17 (+++)	16 (++)	17 (+++)	16 (++)
Ampicillin	37 (+++)	36 (+++)	33 (+++)	35 (+++)	36 (+++)	34 (+++)

Compounds **4a** and **4b** showed high activity against *S. aureus*, while effects of **4c**, **4f**, **4h** and **4i** exhibited activity and **4g** was low activity. However, compounds **4d** and **4e** showed no effect. Only compound 4f was not effective against *B. cereus*, while **4a**, **4c** and **4d** showed high activity and **4b**, **4e**, **4g-4i** were moderate activity. Compounds **4a**, **4c** and **4d** showed high activity against *B. cereus* bacteria. This value is higher than neomycin, which is used as a standard antibiotic. While compound **4f** showed no activity, the other compounds exhibited moderate antibacterial effects. Compounds **4a** and **4h** exhibited strong antibacterial activity against *B. subtilis*, whereas compounds **4e** and **4f** demonstrated weak activity and the remaining compounds exhibited moderate antibacterial effects.

While compounds **4a-c** and **4h** showed high levels of activity against *K. pneumoniae*, one of the agents responsible for lung infections, other compounds showed no effect. The new compounds showed the least effect against *P. aeruginosa*. Compounds **4a-c** showed high levels of activity against *E. coli* bacteria. In particular, the effect of compound **4a** was at the same level as that of ampicillin, which is used as a standard antibiotic. While compounds **4d**, **4e**, **4h** and **4i** showed moderate effects, compounds **4f** and **4g** showed no effect.

4 CONCLUSION AND SUGGESTIONS

Nine new heterocyclic Schiff bases containing 1,2,4-triazole rings were synthesized and characterized by ^{1}H and ^{13}C NMR spectroscopic methods. The metal chelating activities of the Schiff bases showed antioxidant activity close to α-tocopherol used as standard, however, they

did not exhibit significant free radical scavenging or chelating activity. In addition, radical scavenging activities were not at the desired level in the study using BHT and BHA as standard antioxidants [43]. Compounds **4a-i** were more effective against Gram-positive bacteria than Gram-negative bacteria. Compound **4a** showed the highest activity against all bacteria, and these effects were similar to ampicillin, the most effective of the standard antibiotics. All compounds showed activity against *B. subtilis*, but two compounds (**4a and 4h**) were able to show activity against *P. aeruginosa*. Most of the compounds were close to the standard antibiotic neomycin and more effective than streptomycin. In recent years, the increase in antibiotic resistance has highlighted the need for the development of new antibiotics. The positive antibacterial results encourage the synthesis of more Schiff bases containing triazole.

Acknowledgements

This study was supported by Kafkas University Scientific Research Projects Coordination Unit (Doctoral Thesis Project, Project Number: 2019-FM-09).

Conflict of Interest Statement

There is no conflict of interest between the authors.

Statement of Research and Publication Ethics

The study is complied with research and publication ethics.

Artificial Intelligence (AI) Contribution Statement

This manuscript was entirely written, edited, analyzed, and prepared without the assistance of any artificial intelligence (AI) tools. All content, including text, data analysis, and figures, was solely generated by the authors.

Contributions of the Authors

H.Y. designed the study and performed the characterization of compounds 4a-i. H.Y. and F.A. synthesized the compounds 4a-i. F.A. performed the antioxidant and antimicrobial studies and wrote the article.

REFERENCES

[1] S. Kahraman *et al.*, 'Copper(II) complexes with *N,O*-donor azo-Schiff base ligands: Synthesis, structure, DFT studies, molecular docking, anticancer and antimicrobial activity', *Polyhedron*, vol. 269, p. 117393, Mar. 2025, doi: 10.1016/j.poly.2025.117393.

[2] M. Palaniappan *et al.*, 'Synthesis, characterization and biological evaluation of methyl dithiocarbonate-acenaphthenequinone (MDTCZ-ACQ) Schiff base ligand and its coordination complexes with copper, nickel, zinc, and cobalt', *Journal of the Indian Chemical Society*, vol. 102, no. 3, p. 101615, Mar. 2025, doi: 10.1016/j.jics.2025.101615.

[3] M. A. Mir and B. K. Banik, 'Synthesis of Schiff base ligands under environment friendly conditions: A systematic review', *Inorganic Chemistry Communications*, vol. 174, p. 113987, Apr. 2025, doi: 10.1016/j.inoche.2025.113987.

[4] W. Jiang *et al.*, 'Copper-Catalyzed Cycloaddition/Coupling Cascades of Azomethine Imines with Alkynes for Divergent Synthesis of (Z)-Alkenyl and Alkynyl N,N′-Bicyclic Pyrazolidinones', *Organic Letters*, Dec. 2024, doi: 10.1021/acs.orglett.4c03824.

[5] Y. Sun, Y. Wang, L. Zhang, R. Zhong, and H. Wang, 'Synthesis of Bridged and Fused Tetracycles via Rhodium-Catalyzed C−H Allylation/Cycloaddition of Azomethine Imines with MBH Adducts and Allyl Acetates', *Asian Journal of Organic Chemistry*, p. e202400646, Jan. 2025, doi: 10.1002/ajoc.202400646.

[6] Q. U. A. Sandhu, M. Pervaiz, A. Majid, U. Younas, Z. Saeed, A. Ashraf, and S. Jelani, "Schiff base metal complexes as anti-inflammatory agents," Journal of Coordination Chemistry, cilt 76, sayı 9–10, ss. 1094–1118, 2023, doi: 10.1080/00958972.2023.2226794.

[7] R. P. Chinnasamy, R. Sundararajan, and S. Govindaraj, 'Synthesis, characterization, and analgesic activity of novel Schiff base of isatin derivatives', *J Adv Pharm Technol Res*, vol. 1, no. 3, pp. 342–347, 2010, doi: 10.4103/0110-5558.72428.

[8] K. Kar, D. Ghosh, B. Kabi, and A. Chandra, 'A concise review on cobalt Schiff base complexes as anticancer agents', *Polyhedron*, vol. 222, p. 115890, Aug. 2022, doi: 10.1016/j.poly.2022.115890.

[9] F. Aytemiz, 'Synthesis, Characterization, and Investigation of Some Properties of Novel Heterocyclic Mannich Bases Containing the 4,5-Dihydro-1H-1,2,4-Triazol-5-one Ring', Kafkas University, Faculty of Arts and Sciences, PhD Thesis 2020. [Online]. Available: https://acikbilim.yok.gov.tr/handle/20.500.12812/96651?show=full

[10] G. Hu *et al.*, 'Design, synthesis and antitumor activities of fluoroquinolone C-3 heterocycles (IV): s-triazole Schiff–Mannich bases derived from ofloxacin', *Acta Pharmaceutica Sinica B*, vol. 2, no. 3, pp. 312–317, Jun. 2012, doi: 10.1016/j.apsb.2011.11.003.

[11] K. S. Kumar, S. Ganguly, R. Veerasamy, and E. De Clercq, 'Synthesis, antiviral activity and cytotoxicity evaluation of Schiff bases of some 2-phenyl quinazoline-4(3)H-ones', *European Journal of Medicinal Chemistry*, vol. 45, no. 11, pp. 5474–5479, Nov. 2010, doi: 10.1016/j.ejmech.2010.07.058.

[12] I. Santos Oliveira *et al.*, 'Antibacterial and antifungal activities in vitro of a novel silver(I) complex with sulfadoxine-salicylaldehyde Schiff base', *Polyhedron*, vol. 225, p. 116073, Oct. 2022, doi: 10.1016/j.poly.2022.116073.

[13] S. Mujeeb *et al.*, 'Chroman-Schiff base derivatives as potential Anti-Tubercular Agents: *In silico* studies, Synthesis, and Biological evaluation', *Bioorganic Chemistry*, vol. 157, p. 108249, Apr. 2025, doi: 10.1016/j.bioorg.2025.108249.

[14] H. Yüksek, E. Koca, Ö. Gürsoy-Kol, O. Akyıldırım, and M. Çelebier, 'Synthesis, in vitro antioxidant activity, and physicochemical properties of novel 4,5-dihydro-1H-1,2,4-triazol-5-one derivatives', *Journal of Molecular Liquids*, vol. 206, pp. 359–366, Jun. 2015, doi: 10.1016/j.molliq.2015.02.038.

[15] R. Qurrat-ul-ain, M. Ur Rahman, H. M. Javed, S. Hassan, T. Munir, and R. Asghar, 'Exploring sulfonamides derivatives Schiff base and metal complexes as antimicrobial agents: A comprehensive review', *Inorganic Chemistry Communications*, vol. 170, p. 113396, Dec. 2024, doi: 10.1016/j.inoche.2024.113396.

[16] P. Meshram *et al.*, 'Design, synthesis and antibacterial activity of new Isatin-based Schiff base derivatives: Molecular docking, POM analysis, *in silico* pharmacokinetics and identification of antitumor

pharmacophore sites', *Journal of Molecular Structure*, vol. 1322, p. 140508, Feb. 2025, doi: 10.1016/j.molstruc.2024.140508.

[17] A. Shakoor *et al.*, 'Exploring the anti-diabetic activity of benzimidazole containing Schiff base derivatives: *In vitro* α-amylase, α-glucosidase inhibitions and *in silico* studies', *Journal of Molecular Structure*, vol. 1321, p. 140136, Feb. 2025, doi: 10.1016/j.molstruc.2024.140136.

[18] H. Schiff, 'Mittheilungen aus dem Universitätslaboratorium in Pisa: Eine neue Reihe organischer Basen', *Justus Liebigs Annalen der Chemie*, vol. 131, no. 1, pp. 118–119, 1864, doi: 10.1002/jlac.18641310113.

[19] H. Yuksek *et al.*, 'Synthesis, potentiometric titrations and antioxidant activities of some 4-acylamino-4,5-dihydro-1H-1,2,4-triazol-5-one derivatives', *Asian J. Chem.*, vol. 20, no. 7, pp. 5311–5321, Oct. 2008, Accessed: Nov. 28, 2022. [Online]. Available: https://www.webofscience.com/wos/woscc/full-record/WOS:000259602900051

[20] C. Öğretir, Y. Sıdır, İ. Sıdır, And E. Taşal, 'Quantum chemical studies on tautomerism and basicity behavior of some 1,2,4-triazole derivatives', *Turkish Journal of Chemistry*, vol. 34, no. 6, pp. 977–990, Jan. 2010, doi: 10.3906/kim-0904-31.

[21] P. Tyagi, S. Chandra, B. S. Saraswat, and D. Yadav, 'Design, spectral characterization, thermal, DFT studies and anticancer cell line activities of Co(II), Ni(II) and Cu(II) complexes of Schiff bases derived from 4-amino-5-(pyridin-4-yl)-4H-1,2,4-triazole-3-thiol', *Spectrochimica Acta Part A: Molecular and Biomolecular Spectroscopy*, vol. 145, pp. 155–164, Jun. 2015, doi: 10.1016/j.saa.2015.03.034.

[22] X. Li, X. Q. Li, H.-M. Liu, X.-Z. Zhou, and Z.-H. Shao, 'Synthesis and evaluation of antitumor activities of novel chiral 1,2,4-triazole Schiff bases bearing γ-butenolide moiety', *Org Med Chem Lett*, vol. 2, no. 1, p. 26, Jul. 2012, doi: 10.1186/2191-2858-2-26.

[23] O. Aktas-Yokus, H. Yuksek, O. Gursoy-Kol, and S. Alpay-Karaoglu, 'Synthesis and biological evaluation of new 1,2,4-triazole derivatives with their potentiometric titrations', *Med. Chem. Res.*, vol. 24, no. 7, pp. 2813–2824, Jul. 2015, doi: 10.1007/s00044-015-1334-8.

[24] S. Sarkar, T. Mukherjee, S. Sen, E. Zangrando, and P. Chattopadhyay, 'Copper(II) complex of in situ formed 5-(2-pyridyl)-1,3,4-triazole through C–S bond cleavage in 1,2-bis(2-pyridylmethylthio)-bis-ethylsulphide: Synthesis, structural characterization and DNA binding study', *Journal of Molecular Structure*, vol. 980, no. 1–3, pp. 117–123, Sep. 2010, doi: 10.1016/j.molstruc.2010.07.002.

[25] A. Legru *et al.*, '1,2,4-Triazole-3-thione compounds with a 4-ethyl alkyl/aryl sulfide substituent are broad-spectrum metallo-β-lactamase inhibitors with re-sensitization activity', *European Journal of Medicinal Chemistry*, vol. 226, p. 113873, Dec. 2021, doi: 10.1016/j.ejmech.2021.113873.

[26] S. Manap, F. Aytemiz, and H. Yuksek, "Synthesis and antioxidant activities of some novel 1-(morpholine-4-il-methyl)-3-alkyl(aryl)-4-(3-methoxy-4-isobutyryloxy)benzylideneamino-4,5-dihydro-1H-1,2,4-triazol-5-ones," *The Eurasia Proceedings of Science, Technology, Engineering and Mathematics*, no. 2, pp. 135–142, 2018.

[27] P. Martins *et al.*, 'Heterocyclic Anticancer Compounds: Recent Advances and the Paradigm Shift towards the Use of Nanomedicine's Tool Box', *Molecules*, vol. 20, no. 9, pp. 16852–16891, Sep. 2015, doi: 10.3390/molecules200916852.

[28] I. Khan *et al.*, 'Synthesis, antioxidant activities and urease inhibition of some new 1,2,4-triazole and 1,3,4-thiadiazole derivatives', *European Journal of Medicinal Chemistry*, vol. 45, no. 11, pp. 5200–5207, Nov. 2010, doi: 10.1016/j.ejmech.2010.08.034.

[29] J. Xu *et al.*, 'Design, synthesis and antifungal activities of novel 1,2,4-triazole derivatives', *European Journal of Medicinal Chemistry*, vol. 46, no. 7, pp. 3142–3148, Jul. 2011, doi: 10.1016/j.ejmech.2011.02.042.

[30] J. Wu *et al.*, 'Molecular docking, design, synthesis and antifungal activity study of novel triazole derivatives', *European Journal of Medicinal Chemistry*, vol. 143, pp. 1840–1846, Jan. 2018, doi: 10.1016/j.ejmech.2017.10.081.

[31] A. Espinel-Ingroff, 'Comparison of the E-test with the NCCLS M38-P Method for Antifungal Susceptibility Testing of Common and Emerging Pathogenic Filamentous Fungi', *Journal of Clinical Microbiology*, vol. 39, no. 4, pp. 1360–1367, Apr. 2001, doi: 10.1128/jcm.39.4.1360-1367.2001.

[32] J. N. Galgiani, 'Fluconazole, a New Antifungal Agent', *Ann Intern Med*, vol. 113, no. 3, pp. 177–179, Aug. 1990, doi: 10.7326/0003-4819-113-3-177.

[33] R. C. Lin, N. Sanduja, and S. M. Hariprasad, 'Successful Treatment of Postoperative Fungal Endophthalmitis Using Intravitreal and Intracameral Voriconazole', *Journal of Ocular Pharmacology and Therapeutics*, vol. 24, no. 2, pp. 245–248, Apr. 2008, doi: 10.1089/jop.2007.0105.

[34] By El-Shorief, A. M. S., Ammar, M. S., Ammar, Y. A. and Zaki, M. E. A. '2,5-Dichlorobenzenesulfonamide derivatives and their biological activities', I*ndian Journal of Chemistry*, 22B(7), 700-4, 1983.

[35] A. A. Ikizler and H. Yüksek, 'Acetylation of 4-amıno-4-dihydro-1*H*-1,2,4-triazol-5-ones', *Organic Preparations and Procedures International*, Feb. 1993, doi: 10.1080/00304949309457935.

[36] T. Dinis, V. Madeira, and L. Almeida, 'Action of phenolic derivatives (acetaminophen, salicylate, and 5-aminosalicylate) as inhibitors of membrane lipid-peroxidation and as peroxyl radical scavengers', *Archives of Biochemistry and Biophysics,* vol. 315, pp. 161–169, 1994.

[37] M. Oyaizu, 'Antioxidative activities of browning reaction prepared from glucosamine.', *Jpn. J. Nutr.*, vol. 44, no. 6, pp. 307–315, 1986, doi: 10.5264/eiyogakuzashi.44.307.

[38] M. S. Blois, 'Antioxidant Determinations by the Use of a Stable Free Radical', *Nature*, vol. 181, no. 4617, Art. no. 4617, Apr. 1958, doi: 10.1038/1811199a0.

[39] C. Erhonyota, G. I. Edo, and F. O. Onoharigho, 'Comparison of poison plate and agar well diffusion method determining the antifungal activity of protein fractions', *Acta Ecologica Sinica*, vol. 43, no. 4, pp. 684–689, Aug. 2023, doi: 10.1016/j.chnaes.2022.08.006.

[40] S. M. Mirtaghi, P. T. Nejad, M. Masoumeh Mazandarani, F. Livani, and H. Bagheri, 'Evaluation of Antibacterial Activity of Urtica dioica L. Leaf Ethanolic Extract Using Agar Well Diffusion and Disc Diffusion Methods.', *Medical Laboratory Journal*, vol. 10, no. 5, pp. 15–21, Sep. 2016, doi: 10.18869/acadpub.mlj.10.5.15.

[41] H. Gökce, O. Akyildirim, S. Bahçeli, H. Yüksek, and Ö. G. Kol, 'The 1-acetyl-3-methyl-4-[3-methoxy-4-(4-methylbenzoxy)benzylidenamino]-4,5-dihydro-1H-1,2,4-triazol-5-one molecule investigated by a joint spectroscopic and quantum chemical calculations', *Journal of Molecular Structure*, vol. 1056–1057, pp. 273–284, Jan. 2014, doi: 10.1016/j.molstruc.2013.10.044.

[42] P. K. Verma, M. Kumar, N. Malik, P. Dhiman, and A. Khatahar, 'Design, Synthesis, Antimicrobial, and Antioxidant Activities of Novel-{4, 5-(substituted diphenyl)-4H-1, 2, 4-triazol-3-ylthio} Acetyl Chloride', *Walailak Journal of Science and Technology (WJST)*, vol. 15, no. 2, Art. no. 2, 2018, doi: 10.48048/wjst.2018.2178.

[43] M. Alkan *et al.*, 'Synthesis and Antioxidant and Antibacterial Activities of Novel 4-({[3-Alkyl(aryl)-5-oxo-4,5-dihydro-1H-1,2,4-triazol-4-yl]imino}-methyl)phenyl 4-Nitrobenzoate Derivatives', *Russ J Org Chem*, vol. 58, no. 12, pp. 1839–1850, Dec. 2022, doi: 10.1134/S1070428022120132.

BİTLİS EREN ÜNİVERSİTESİ
FEN BİLİMLERİ DERGİSİ

ISSN: 2147-3129 / e-ISSN: 2147-3188

Article Type	: Research Article	**Year**	: 2025
Received	: March 25, 2025	**Volume**	: 14
Revised	: July 2, 2025	**Issue**	: 3
Accepted	: July 8, 2025	**Pages**	: 1469-1486
DOI	: 10.17798/bitlisfen.1664312		

GDD GENERATION FOR HYPER-CASUAL GAMES USING LARGE LANGUAGE MODELS: A COMPARATIVE EVALUATION

Muhammet Emin AYDINALP [1, *], Buket DOĞAN [2], Abdullah BAL[2]

[1] *İstanbul Sabahattin Zaim University, Computer Engineering Department, İstanbul, Türkiye*

[2] *Marmara University, Computer Engineering Department, İstanbul, Türkiye*

**** Corresponding Author:*** *muhammet.aydinalp@izu.edu.tr*

ABSTRACT

Game Design Documentation (GDD) is a critical document that includes the design and mechanical details of the game to be developed. These documents create a common understanding among team members by including details such as the game's progress, story, and design features. In order for the game development process to proceed and be completed healthily, these documents must be prepared in a high-quality, clear, and detailed manner. However, the creation of this documentation is a time-consuming and error-prone process. Especially in game genres that require rapid prototyping, incomplete or insufficient GDDs can cause delays in the project process. This study was conducted to examine the effectiveness of LLMs in GDD production. The hyper-casual game Pool Wars was selected as a reference, and for this example game, the GDD created by a human expert and the GDD produced by ChatGPT-4 using various prompt methods were evaluated by four experts in the field according to eight different criteria using a five-point Likert scale. In addition to structural and creative aspects, visual elements were also included in the evaluation process. ImageFX, developed by Google, was used to add visual content to the GDD created by ChatGPT-4. As a result, it was seen that LLMs were more successful in many criteria in GDD production. As a result of the scoring made by an academician and three experts from the sector, GDD created by LLM received an overall average score of 4.71 out of 5, while GDD prepared by human expert received 3.29 points. GDD produced by LLM showed a clear superiority especially in terms of understandability and level of detail. However, it showed a similar performance to human expert in terms of creativity and visual content and it was observed that there was room for improvement in these areas.

Keywords: Large language models (LLM), Game design documentation (GDD), ChatGPT-4, Hyper-Casual games, Prompt engineering, ImageFX.

1 INTRODUCTION

Game design documentation (GDD) is a very important part of the game production pipeline [1], [2]. These documents guide team members through each stage of the production cycle by describing in detail the concept, mechanics, story, and other main components of the game [3]. Today, the historical timeline of GDD has evolved from simple text documents in the early 1990s to comprehensive documentation that integrates with multimedia content, software project management tools, and version control systems today [4]. In interviews with game development industry employees, one of the most common complaints is the difficulty and inconsistency of the GDD preparation process. Especially in hyper-casual [5] (simple mechanics, fast playable and appealing to a wide audience) game studios, teams working under rapid production pressure have difficulty preparing comprehensive and consistent GDDs, which leads to serious disruptions in project management [6], [7].

In recent years, Large Language Models (LLMs) [8] have revolutionized the fields of artificial intelligence and natural language processing. LLM is a pre-trained language model based on a vast amount of textual data using transformers and deep learning techniques [9]. These models are used in many areas such as text generation, translation, speech recognition, text analysis and classification [10]. Recently, LLMs have gained the ability to generate audio, visual and video from text and very wide content has been produced using these features [11] - [13]. The use of LLMs has become widespread in various sectors such as education, cinema, medicine, cybersecurity and game development and has made significant contributions to these fields [14]-[16].

One of the studies conducted using LLMs is the creation of Software Requirements documents by LLMs, crosscheck with human experts and performance analysis. In the study of Krishna et al., a They assess the performance of GPT-4 and CodeLlama in drafting an SRS for a university club management system and compare it against human benchmarks using eight distinct criteria [17]. The results of the study showed that LLMs can produce documents that are equivalent in quality to SRS documents produced by entry-level software engineers. Similarly, Lubos et al.'s study introduce and assess the capabilities of a Large Language Model (LLM) to evaluate the quality characteristics of software requirements according to the ISO 29148 standard [18]. They show how an LLM can assess requirements, explain its decision-making process, and examine its capacity to propose improved versions of requirements. In a study conducted by Lee et al. [19], GPT-3 and LLaMA-2 models are trained to answer questions

related to technical specification documents. The results show that the fine-tuned LLaMA2 model generally outperforms the fine-tuned GPT-3 model in terms of accuracy, reliability, and conciseness of responses. it has been proven by various studies that open-source models can also exhibit high performance when fine-tuned for a specific domain [20]. This shows that secret documents and information can be processed securely through LLMs without being shared with external systems [21].

In this study, a hypercasual game called "Pool Wars" was selected. For this game, there is a GDD written by an expert who has worked as a game designer in the game industry for more than 5 years and has industry experience, and a GDD was created for the same game with ChatGPT-4 [22] using various prompting methods such as giving clear instructions, step-by-step development, supporting with examples and role-playing prompting. The visual part of the created GDD was completed with ImageFX [23]. As a result, the GDD generated by LLM and the human-generated GDD were evaluated by experts in the field and compared by scoring according to a five-point Likert scale. In the study, the evaluation criteria used for both GDD and SRS documents were scored according to the following criteria: completeness, understandability, consistency, creativity and innovation, applicability, suitability for the target audience, level of detail and user-orientedness.

This study aims to display the competence, quality and consistency, time and efficiency advantages and potential contributions of LLMs in game design documentation production. It is also aimed to determine the capacity and weaknesses of LLMs and make recommendations for future developments.

The contributions of this article are as follows:

• Adequacy of LLMs in GDD Production: This study demonstrates how effective and adequate LLMs are in producing game design documentation when compared to GDDs created by human experts, and also evaluates the attribute and consistency of GDDs produced by LLMs and specifies how useful these documents are in the game development process.

• Recommendations for Development: It identifies the strengths and weaknesses of LLMs in GDD production and makes suggestions for future improving of these models.

• Application of Evaluation Criteria: The evaluation criteria used in the study are valid for both GDD and SRS documents, and demonstrate how these criteria can be used to objectively measure the performance of LLMs.

2 MATERIAL AND METHOD

In this study, the effectiveness of LLMs in the GDD creation process was investigated. For a hypercasual game called "Pool Wars", a GDD prepared by human experts was taken as a reference. Then, a similar GDD was created using the ChatGPT-4 model. In this process, various prompt engineering methods such as providing clear instructions, step-by-step guidance, supporting with examples and role-playing techniques were applied. The study also incorporated visual elements generated through ImageFX to complement the textual content from the language model. Four game design and development specialists assessed both GDDs using eight evaluation criteria, with ratings assigned on a five-point Likert scale. The evaluation methodology included both quantitative and qualitative approaches, enabling a comprehensive comparison that identified the capabilities and limitations of large language models in game documentation tasks.

2.1 Data Preparation

In this study, a hypercasual game called ‘Pool Wars’ was selected for the target GDD creation process. Hypercasual games are one of the game genres where the GDD process is critical due to their simple mechanics, requiring rapid prototyping and appealing to a wide range of players. Therefore, they constitute a suitable example to evaluate the effectiveness of LLMs in the GDD creation process. A GDD prepared by human experts for this game was used as the base document. This GDD was prepared for a game previously developed by an expert Game Designer in a professional game studio that produces hypercasual games in the industry and was used as an example GDD produced by a human expert in this study. In order to compare with the human-authored GDD, a second GDD was generated using GPT-4, a large language model developed by OpenAI. The resulting document was later evaluated by field experts alongside the human-authored GDD. The full version of the LLM-generated GDD has been made publicly accessible via Zenodo [24]. The prompts used in the creation of the LLM-based GDD were structured to ensure clarity, consistency, and detail throughout the document. These prompt [25] strategies are explained below.

2.1.1 Step by Step Instructions Prompt

Since LLMs have limited tokens and context windows at a time, we divided the document we wanted to create into pieces and proceeded step by step. Game design documents

already consist of certain sections. We gave special prompts for these sections and combined the created texts. First, we gave a prompt [26] explaining which headings a GDD should contain and that we wanted to produce these headings step by step. Example prompt: “A game design document consists of headings such as game summary, basic mechanics, level system, design elements, game economy. We will create a game design document where we will fill in these headings for our hyper casual game called Pool Wars, a pool game.” Then, we gave a prompt talking about what kind of game I wanted to make and asked for the above-mentioned headings one by one to create our document. Sample prompt: “The story of the stickman character who embarks on an adventure on the seabed in a pool environment suitable for the summer theme. The only main character, the warrior stickman, tries to defeat the enemies on the battlefield by making the necessary improvements in the safe area allocated to him in the pool. With each enemy he destroys, he continues his fight in new pools by collecting the necessary equipment, loot and improvements. Before discovering new fronts, he faces a dangerous end-of-level creature. One of the goals of our main character is to continue on his way by defeating the boss character. Can you create the basic mechanics for the game given above in detail?”

The above prompt was repeated for each main title and the created texts were combined [27].

2.1.2 Example Supported Prompt

In the GDD creation process of the model, it was aimed to guide the output and increase its quality by using GDD examples of similar games [28]. In this method, sample GDD content was provided in a format that the model could understand and process. These examples provided guidance on what kind of output the model should produce, both structurally and content-wise. Especially in sections such as game mechanics, level design and storytelling, sample GDDs helped the model produce more comprehensive and detailed output. In this way, the model was enabled to learn from concrete examples and be guided more specifically, instead of just general instructions.

2.1.3 Role Playing Prompts

In the GDD creation process of ChatGPT-4, role-playing prompts were used to ensure that the model took on a certain role and produced outputs appropriate to this role [29]. In this method, the model was given a prompt such as "You are a game designer. You are knowledgeable about hypercasual games. Focus on the target audience and suggest intuitive

gameplay mechanics while creating the design document of this game" and was asked to take on the role of a game designer and create a GDD from this perspective.

The role-playing prompts aimed to make the model think from the perspective of a game designer and create a GDD that was appropriate for the target audience, creatively and applicable. This method allowed the model to not only provide information but also to think like a game designer and produce a more original and user-focused GDD.

For example, when the model took on the role of "game designer", it suggested simpler and more intuitive gameplay mechanics considering the target audience of the game (e.g., young players). It also made suggestions to make the visual and audio design of the game appealing to the target audience. Role-play prompts helped the model create a more comprehensive and realistic GDD.

The visual elements of the GDD produced by ChatGPT were created using ImageFX, a text-to-image conversion tool. This tool transformed text-based descriptions into visuals, making the GDD more understandable and engaging. ImageFX was used to create various visual elements such as in-game characters, environments, objects, and the user interface.

The GDDs produced by both human experts and LLM were organized as comprehensive documents covering sections such as game mechanics, story, visual style, and user interface. In these sections, the basic elements of the game were explained in detail and supported by visuals. For example, in the game mechanics section, elements such as the basic rules of the game, the gameplay loop, and control mechanisms were explained. In the story section, information was given about the game's story, characters, and world. In the visual style section, elements such as the game's general art style, color palette, and character designs were discussed. In the user interface section, game menus, indicators, and other interface elements were described in detail.

These comprehensive GDDs were designed to serve as a guide for all team members during the game development process. GDDs were created to clearly document the design and content of the game and create a common understanding among all stakeholders.

2.2 Evaluation Criteria

The GDDs created were evaluated in detail by experts in the field. During the evaluation process, communication with the experts was provided through an Excel file containing the evaluation criteria for both GDDs. The experts were sent in PDF format without specifying which source produced both GDDs and were asked to make an objective evaluation. In the

Excel file sent to them, areas were provided where they could score each GDD separately based on the eight criteria specified. At the end of the evaluation process, the experts filled in their scores in the Excel file and shared their qualitative observations by providing additional written comments. Thus, both quantitative (scoring data) and qualitative (comments and opinions) data were collected and analyzed. The evaluation criteria used in this study were determined by considering previous studies in the literature on the evaluation of game design documentation [30].

These studies emphasize that game documentation should be considered from various aspects such as comprehensiveness, understandability, consistency, creativity, applicability, level of detail, user-centeredness, and visual adequacy [31]. These criteria include the elements that are important for determining the quality and effectiveness of a GDD. The experts who conducted the evaluation used a five-point Likert scale [32]. In this scale, which is explained in detail in Table 1, 1 represents the lowest score and 5 represents the highest score.

Table 1. Likert Scale for GDD Performance

Score	Statement	Description
1	Strongly Disagree	The performance of GDD is extremely inadequate.
2	Disagree	The performance of GDD is inadequate
3	Neutral	The performance of GDD is neither good nor bad.
4	Agree	The performance of GDD is good.
5	Strongly Agree	The performance of GDD is excellent.

Table 2 provides a detailed list and explanation of all the criteria used in the evaluation of GDDs. Experts carefully examined each criterion and scored the GDDs on this scale.

Table 2. Evaluation Criteria

Evaluation Criteria	Description
Completeness	Whether the document covers all critical elements.
Clarity	The clarity and ease of understanding of explanations.
Consistency	Logical coherence and integrity between sections.
Creativity & Innovation	The originality and innovative nature of the presented ideas.
Practicality	The document's practicality and suitability for the target audience.
Level of Detail	The depth and precision of the provided explanations.
User-Centric Approach	Alignment with the needs and expectations of the end user.
Visual Adequacy	The quality and clarity of visual elements.

In this study, four professionals with backgrounds in game design and development took part in the evaluation of the GDDs. Among them, three are actively working in the industry as game developers, each with a minimum of three years of experience. The fourth expert has been involved in academic research on game design for over a decade. Although their areas of expertise differ, all experts assessed the documents based on the same set of criteria without any distinction in responsibility. During the evaluations, the GDDs were examined in terms of several important aspects: how complete and understandable they were, whether the content maintained consistency throughout, how original and creative the ideas appeared, the practical value of the documents, the level of detail they provided, how well they addressed user needs, and the adequacy of the visual elements included. Having experts from both industry and academia enriched the process by bringing in multiple perspectives. This diversity helped create a more balanced and comprehensive assessment overall.

To avoid bias, each expert reviewed the GDDs independently. They were not informed which document was written by a human and which was created with the help of a language model. This anonymity helped ensure that the evaluations were fair and unbiased. Once all individual evaluations were completed, we collected and analyzed the results together. We conducted a detailed comparative analysis to determine the performance differences between the human-written and LLM-generated GDDs. We started by calculating the average score each GDD received under each evaluation criterion. This step allowed us to see how well each document performed in certain aspects. We also calculated the differences between the means in order to see which GDD performed better under which criterion. We calculated the standard deviation for each criterion to observe how consistent the scores were across raters. Beyond the numerical results, we also took into account the written feedback of the experts. Each participant shared their personal observations about the strengths and weaknesses of both GDDs. These insights provided important context for the scores and offered valuable information for improving the quality of AI-assisted game design documentation in future work.

2.3 Tools and Technologies Used

In this study, various tools and technologies were used to create the textual and visual content of GDD and to visualize and analyze the data obtained after the comparison.

2.3.1 ChatGPT-4

In this study, we used the free limited version of GPT-4 Plus [33]. This version is directly accessible through OpenAI's web interface. However, this version can only be used for a certain period of time, with an automatic downgrade to a lower version when the time is up. As a result, some practical challenges related to the use of the free version were encountered during the document production process. For instance, after a certain amount of usage, the system occasionally prompted us to start a new chat or required a waiting period before continuing. Consequently, the content generation process had to be split across different chat sessions or resumed at intervals. These interruptions required manually merging content from multiple sessions and maintaining contextual consistency between sections.

However, for the purpose of this study, this version was deliberately chosen to assess how large language models can be utilized by general users for GDD production, without the need for professional tools or special access. The sections of the GDD were developed step by step using the prompt techniques described above.

2.3.2 ImageFX

The free version of ImageFX was used to generate the visual components of the GDD created by ChatGPT [34]. ImageFX is an AI-powered tool capable of producing images based on text-based descriptions. Using this tool, various visual elements such as stickmen, swimming pools, collectible items, and water guns—as well as components of the user interface—were added to the GDD to enrich its visual content.

2.3.3 Microsoft Excel and Python

Microsoft Excel and Python were used to organize, analyze and visualize the evaluation data. The scores given by the experts were organized in Excel and analyzed using Python. Statistical calculations such as mean, median and standard deviation were made using data analysis libraries in Python. In addition, the visualization of the data was provided using matplotlib, one of the graphics libraries in Python. In this way, we made our results concrete and analyzed them.

3 RESULTS AND DISCUSSION

In this study, a comparative analysis of GDDs created by human experts and LLM was performed. The evaluations made by four different experts were examined based on eight different criteria and the results were analyzed both quantitatively and qualitatively. Table 3 shows the average scores and standard deviations according to the criteria.

Table 3. Average Scores and Standard Deviations by Criteria

Criteria	Human GDD (Avg.)	Human SD	LLM GDD (Avg.)	LLM SD	Difference
Completeness	3.67	0.82	4.67	0.50	+1.00
Clarity	3.33	0.00	5.00	0.00	+1.67
Consistency	3.00	0.58	4.67	0.00	+1.67
Creativity & Innovation	4.00	0.50	4.00	0.00	0.00
Practicality	3.00	0.50	5.00	0.00	+2.00
Level of Detail	2.67	0.00	5.00	0.00	+2.33
User-Centric Approach	3.00	0.50	5.00	0.50	+2.00
Visual Adequacy	3.67	0.00	4.33	0.82	+0.66

As shown in Table 4, the LLM-generated GDD received an overall average score of 4.71, while the human-generated GDD received a score of 3.29. The average scores for each criterion and the differences between them are presented in detail in this table. The LLM GDD showed clear superiority especially in the criteria of understandability, applicability and level of detail.

Table 4. Statistical Summary

Metric	Human GDD	LLM GDD
Mean	3.29	4.71
Standard Deviation	0.36	0.23
Minimum Score	2.67	4.00
Maximum Score	4.00	5.00

The statistical summary presented in Table 4 shows the overall performance metrics of both GDDs in comparison. These data reveal that the LLM GDD is superior not only in mean scores but also in rating consistency. Statistical analysis showed that the LLM GDD had more consistent scores across raters (SD = 0.23). The standard deviation of the human GDD was calculated as 0.36.

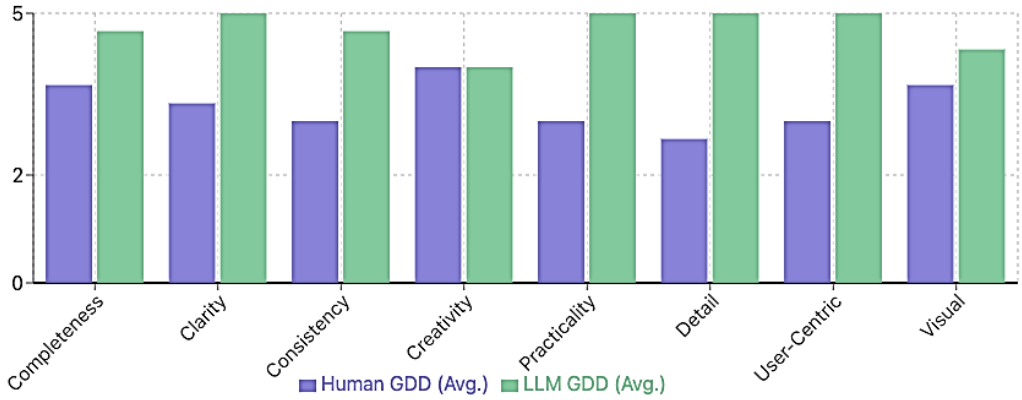


Figure 1. GDD Comparison Bar Chart by Criteria

The bar chart shown in Figure 1 visually presents the comparative performance of GDDs on each evaluation criterion. This chart clearly reveals the large difference observed especially in the level of detail (LLM: 5.00, Human: 2.67).

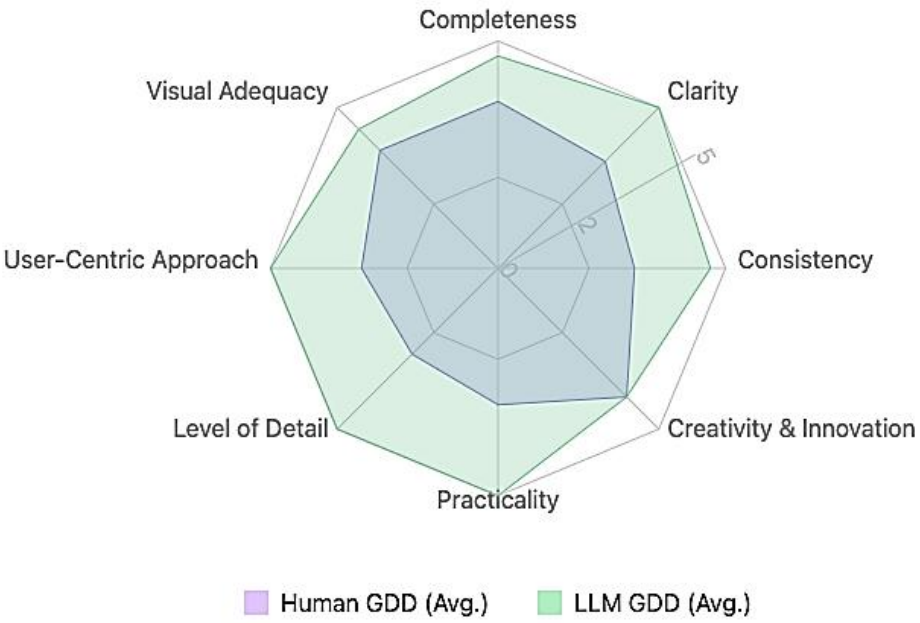


Figure 2. GDD Performance Comparison Radar Chart

The radar chart presented in Figure 2 shows the performance profile of both GDDs holistically. This visualization clearly shows that the LLM GDD consistently performs highly on all evaluated criteria. Of particular note is that in the creativity and innovation criterion, both GDDs perform equally with a score of 4.00.

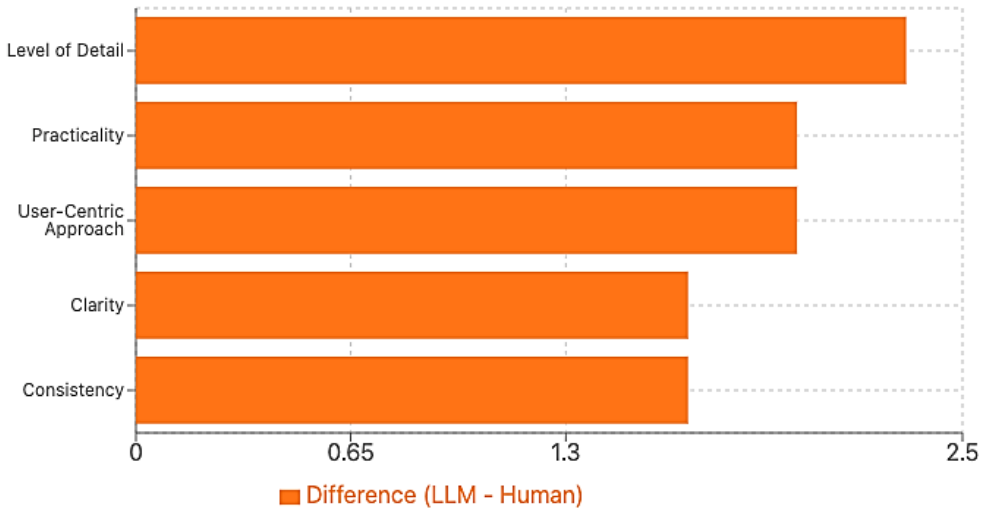


Figure 3. Differences between LLM and Man-Made GDD Criteria

Figure 3 clearly shows the criteria where LLM is significantly superior to human-made GDD. Level of Detail has the highest value with a difference of 2.33, which shows that LLM pays great attention to details when preparing game design documentation. This result indicates that LLM can provide the details missing in human documentation in a clear and explanatory manner.

According to the qualitative observations of the evaluators, it was stated that the GDD produced by LLM exhibited a detailed approach especially in the design of the levels. It was stated that the visual theme, gameplay mechanics, difficulty levels and target scores of each level were defined in detail. It was evaluated that in the GDD produced by LLM, it was clearly explained what kind of experience each level should offer to the player, and this made the design process more effective. It was observed that LLM created a detailed roadmap regarding which tasks should be completed in which weeks until the delivery date of the game. It was stated that this roadmap covers stages such as prototyping, level design, game testing and final editing, and is structured in a way that facilitates project management.

Evaluators believe that this detailed approach shows that LLM is an effective tool not only in content production but also in planning the development process. It was stated that the lack of such details in human-made documentation often leads to delays in project durations, whereas the clarity and openness provided by LLM has the potential to minimize such problems.

Other prominent criteria were Applicability and User Focus, both of which have a difference of 2.00. This shows that LLM has a superior performance in making game documentation practically applicable and taking into account end-user needs. Understandability

and Consistency criteria have a difference of 1.67. This shows that LLM can produce not only detailed but also clear and logically organized documentation.

Figure 4 and Figure 5 below were produced with the ImageFX tool to evaluate the visual adequacy of the GDD created by LLM. GDDs are prepared to provide guiding information for the developer and modeling teams on how to design objects, characters, and environmental elements in the game. In this context, Figure 4 includes various water-themed objects that can be used in the game (e.g. lifebuoys, wave effects, inflatable platforms) and provides a basic visual framework for the general mechanics of the game. Figure 5 shows the interaction of the player character with a stylized water gun and the wave effect in the background. These visuals offer a simple, colorful, and eye-catching visual language in line with the hyper-casual structure of the game; they manage to reflect the concept stated in the GDD in general terms. However, according to expert evaluations, these visual contents have aspects that can be improved in terms of level of detail, use of perspective, and artistic consistency. This situation reveals that LLM-supported GDD production is functional in terms of visual guidance, but it would be useful to support it with professional visual designs for more advanced game projects. Additionally, to access the entire GDD created by LLM and examine all the images, the document shared publicly on Zenodo can be accessed from source [24].

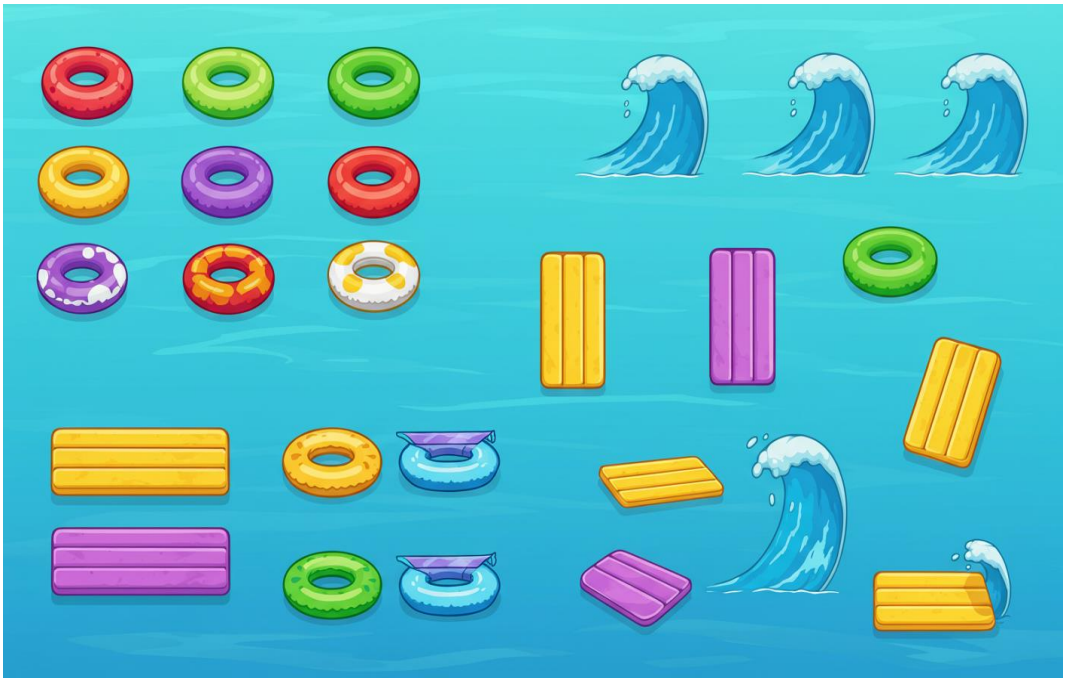


Figure 4. Representative Visuals of In-Game Items and Environmental Assets

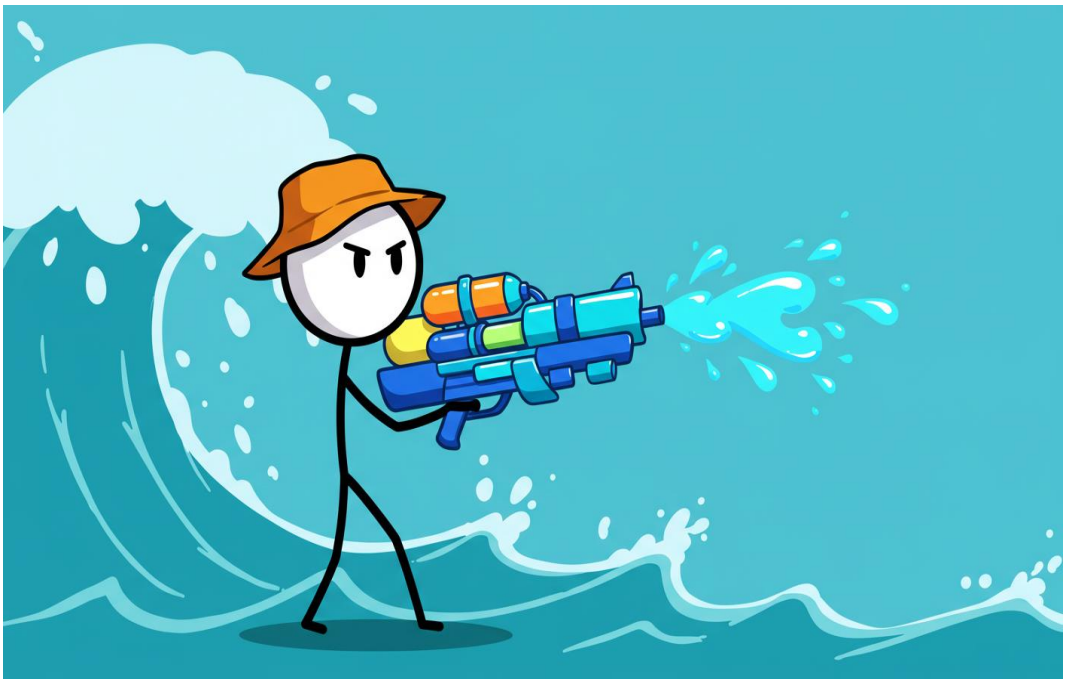


Figure 5. Player Character Interaction with Water Gun and Environmental Elements

Overall, these data suggest that LLM offers strong potential for preparing more structured, detailed, and user-focused documentation than human-made documentation. However, the lower difference in areas such as creativity and visuality suggests that these areas still have room for improvement for LLMs.

Expert feedback has highlighted the strengths and potential impacts of LLM GDD. It has been emphasized that quality issues in GDD writing, especially in the hypercasual game genre, cause serious delays and problems in projects. Experts have stated that insufficient attention is paid to GDD writing in rapid prototyping processes and that the lack of clear definition of game boundaries causes delays in project delivery dates. In this context, the solution offered by LLMs is particularly valuable. Experts have emphasized that the ability of LLMs to create detailed, descriptive, and visually rich GDDs very quickly is an important development for the industry.

Despite the success of LLMs in producing GDDs, there are also some risks. The main ones are that LLMs can add conflicting mechanics and technically impossible features to different parts of GDDs. In addition, producing with exact LLMs can cause a decline in generating new ideas and creativity. In order to eliminate such risks, as suggested in this study, each stage of GDD production should be controlled by human experts and the AI should be guided with the relevant prompts. In other words, it is suggested that GDD production should be done step by step and that each step should be checked and approved before moving on to the next step.

4 CONCLUSION AND SUGGESTIONS

In this study, we explored how effective and adequate LLMs are in generating game design documentation. When we compared the outputs produced by LLMs to those written by human experts, we found that LLMs generally performed better—particularly in areas like completeness, clarity, and level of detail. These findings reflect similar results reported in the work of Krishna et al. [9], where GPT-4 was shown to outperform junior software engineers in tasks related to software requirements documentation. In our case as well, LLMs excelled especially for their ability to produce rich, detailed, and well-structured content that helps guide the design process more effectively than traditional, human-written documents.

The study findings revealed that LLMs can make significant contributions to game development processes in terms of quality, speed and consistency. In this study conducted on the hypercasual game "Pool Wars", it was determined that GDD produced by LLM can eliminate documentation deficiencies encountered in rapid prototyping processes and provide an effective solution to documentation problems in the industry. Expert evaluations have highlighted the contribution of LLM towards standards compliance, structuring and technical details. The results of this study, as emphasized in the study of Lubos et al. [10], show that LLMs are not only a support tool but also a powerful tool that can enable standardization in game design documentation processes.

It should not be forgotten that this success demonstrated by LLM is possible with the guidance of human experts. Otherwise, it should not be ignored that using LLM alone may create problems in terms of originality, consistency and ethics. In addition, in the case of commercial use, issues such as who will own the text produced by LLM and whether there will be copyright problems vary according to the model used. The approaches of different LLMs to this issue are the subject of a different study. In the future, GDD production can be worked on for larger and more comprehensive games using LLMs. Also, how existing LLMs can be improved in terms of visual content production and innovative ideas is a separate study topic.

Conflict of Interest Statement

There is no conflict of interest between the authors.

Statement of Research and Publication Ethics

The study is complied with research and publication ethics.

Artificial Intelligence (AI) Contribution Statement

Since the subject of this study is to investigate the effectiveness of artificial intelligence (AI) tools in creating game design documents, the GDD mentioned and experimentally used in the manuscript was prepared with ChatGPT-4. In addition, in order to provide visual support for the GDD, the images presented as examples in the manuscript were generated using ImageFX. Furthermore, during the overall writing process of the manuscript, AI tools were utilized for grammar and punctuation corrections.

Contributions of the Authors

Muhammed Emin took part in the creation of game design documents using large language models, the creation of surveys, and the writing of the article. Buket Doğan contributed to the theoretical planning of the article, the creation of surveys, and the academic writing of the methodology section. Abdullah Bal contributed to the implementation and evaluation of the surveys.

REFERENCES

[1] M. G. Salazar, H. A. Mitre, C. L. Olalde, and J. L. G. Sánchez, "Proposal of Game Design Document from software engineering requirements perspective," in *2012 17th International Conference on Computer Games (CGAMES)*, 2012: IEEE, pp. 81-85.

[2] E. Bethke, *Game development and production*. Wordware Publishing, Inc., 2003.

[3] J. Haltsonen, "Guide to Writing a Game Design Document," 2015.

[4] C. Macklin and J. Sharp, *Games, Design and Play: A detailed approach to iterative game design*. Addison-Wesley Professional, 2016.

[5] A. Charoenpruksachat and P. Longani, "Comparative study of usability evaluation methods on a hyper casual game," in *2021 Joint International Conference on Digital Arts, Media and Technology with ECTI Northern Section Conference on Electrical, Electronics, Computer and Telecommunication Engineering*, 2021: IEEE, pp. 153-156.

[6] П. Івасюк, "Game design document," 2016.

[7] C. M. Kanode and H. M. Haddad, "Software engineering challenges in game development," in *2009 Sixth International Conference on Information Technology: New Generations*, 2009: IEEE, pp. 260-265.

[8] B. Min *et al.*, "Recent advances in natural language processing via large pre-trained language models: A survey," *ACM Computing Surveys,* vol. 56, no. 2, pp. 1-40, 2023, doi: https://doi.org/10.1145/3605943.

[9] A. Fantechi, S. Gnesi, L. Passaro, and L. Semini, "Inconsistency detection in natural language requirements using chatgpt: a preliminary evaluation," in *2023 IEEE 31st International Requirements Engineering Conference (RE)*, 2023: IEEE, pp. 335-340.

[10] V. Bertram, H. Kausch, E. Kusmenko, H. Nqiri, B. Rumpe, and C. Venhoff, "Leveraging Natural Language Processing for a Consistency Checking Toolchain of Automotive Requirements," in *2023 IEEE 31st International Requirements Engineering Conference (RE)*, 2023: IEEE, pp. 212-222.

[11] Y. C. Gönültaş, "Yapay Zekâ ve Bilimsel Metin Yazımı: Türk Kamu Yönetimi Alanyazınında ChatGPT4. 0 Örneği," *Uluslararası Yönetim Akademisi Dergisi,* vol. 7, no. 3, pp. 827-843, 2024, doi: https://doi.org/10.33712/mana.1578165.

[12] A. Goslen, Y. J. Kim, J. Rowe, and J. Lester, "Llm-based student plan generation for adaptive scaffolding in game-based learning environments," *International Journal of Artificial Intelligence in Education,* pp. 1-26, 2024, doi: https://doi.org/10.1007/s40593-024-00421-1.

[13] M. C. Laupichler, J. F. Rother, I. C. G. Kadow, S. Ahmadi, and T. Raupach, "Large language models in medical education: comparing ChatGPT-to human-generated exam questions," *Academic Medicine,* vol. 99, no. 5, pp. 508-512, 2024, doi: 10.1097/ACM.0000000000005626.

[14] D. Luitel, S. Hassani, and M. Sabetzadeh, "Using language models for enhancing the completeness of natural-language requirements," in *International working conference on requirements engineering: foundation for software quality*, 2023: Springer, pp. 87-104.

[15] G. Agrawal, K. Pal, Y. Deng, H. Liu, and Y.-C. Chen, "CyberQ: Generating Questions and Answers for Cybersecurity Education Using Knowledge Graph-Augmented LLMs," in *Proceedings of the AAAI Conference on Artificial Intelligence*, 2024, vol. 38, no. 21, pp. 23164-23172.

[16] J. Pereira, J.-M. López, X. Garmendia, and M. Azanza, "Leveraging Open Source LLMs for Software Engineering Education and Training," in *2024 36th International Conference on Software Engineering Education and Training (CSEE&T)*, 2024: IEEE, pp. 1-10.

[17] M. Krishna, B. Gaur, A. Verma, and P. Jalote, "Using LLMs in Software Requirements Specifications: An Empirical Evaluation," *arXiv preprint arXiv:2404.17842,* 2024.

[18] S. Lubos *et al.*, "Leveraging llms for the quality assurance of software requirements," in *2024 IEEE 32nd International Requirements Engineering Conference (RE)*, 2024: IEEE, pp. 389-397.

[19] J. Lee, W. Jung, and S. Baek, "In-house knowledge management using a large language model: focusing on technical specification documents review," *Applied Sciences,* vol. 14, no. 5, p. 2096, 2024.

[20] Y. Ma, Z. Liu, and O. Kalinli, "Effective Text Adaptation For LLM-Based ASR Through Soft Prompt Fine-Tuning," in *2024 IEEE Spoken Language Technology Workshop (SLT)*, 2024: IEEE, pp. 64-69, doi: 10.1109/SLT61566.2024.10832227.

[21] D. Raj, G. Keren, J. Jia, J. Mahadeokar, and O. Kalinli, "Faster speech-llama inference with multi-token prediction," in *ICASSP 2025-2025 IEEE International Conference on Acoustics, Speech and Signal Processing (ICASSP)*, 06-11 April 2025 2025: IEEE, pp. 1-5, doi: 10.1109/ICASSP49660.2025.10890328.

[22] L. Knoedler *et al.*, "Pure Wisdom or Potemkin Villages? A Comparison of ChatGPT 3.5 and ChatGPT 4 on USMLE Step 3 Style Questions: Quantitative Analysis," *JMIR Medical Education,* vol. 10, no. 1, p. e51148, 2024, doi: 10.2196/51148.

[23] I. Didych, "Application of neural network platforms for text-based image generation," 2024.

[24] M. Aydinalp. "Game Design Document for 'Pool Wars' Generated by ChatGPT-4." Zenodo. https://doi.org/10.5281/zenodo.15422946 (accessed 15 May 2025.

[25] L. Giray, "Prompt engineering with ChatGPT: a guide for academic writers," *Annals of biomedical engineering,* vol. 51, no. 12, pp. 2629-2633, 2023, doi: https://doi.org/10.1007/s10439-023-03272-4.

[26] G. Z. Higginbotham and N. S. Matthews, "Prompting and in-context learning: Optimizing prompts for mistral large," 2024, doi: 10.21203/rs.3.rs-4430993/v1.

[27] A. J. Spasić and D. S. Janković, "Using ChatGPT standard prompt engineering techniques in lesson preparation: role, instructions and seed-word prompts," in *2023 58th international scientific conference on information, communication and energy systems and technologies (ICEST)*, 2023: IEEE, pp. 47-50.

[28] P. Denny *et al.*, "Prompt Problems: A new programming exercise for the generative AI era," in *Proceedings of the 55th ACM Technical Symposium on Computer Science Education V. 1*, 2024, pp. 296-302.

[29] Z. M. Wang *et al.*, "Rolellm: Benchmarking, eliciting, and enhancing role-playing abilities of large language models," *arXiv preprint arXiv:2310.00746,* 2023.

[30] Ş. K. Gökçek and D. Akbulut, "Bağımsız Video Oyunlarının Geliştirilme Sürecinde Oyun Tasarımına Yönelik İhtiyaçların, Problemlerin, Benzerliklerin ve Farklılıkların Keşfedilmesi İçin Bir Alan Çalışması," *Sanat ve Tasarım Dergisi,* no. 30, pp. 187-207, 2022, doi: https://doi.org/10.18603/sanatvetasarim.1215230.

[31] B. Dervişoğlu, "Öğrenciler için Dijital Oyun Tasarım Dokümantasyonu Hazırlama Sürecinde Yapay Zeka Kullanımı," *Social Sciences Studies Journal,* vol. 10, no. 12, pp. 2458-2465, 2024.

[32] A. Joshi, S. Kale, S. Chandel, and D. K. Pal, "Likert scale: Explored and explained," *British journal of applied science & technology,* vol. 7, no. 4, pp. 396-403, 2015, doi: 10.9734/BJAST/2015/14975.

[33] OpenAI. "Introducing GPT-4 and its capabilities." OpenAI. https://openai.com/research/gpt-4 (accessed 3 Şubat 2025, 2024).

[34] Google. "ImageFX: AI-powered Text-to-Image Tool." https://imgfx.ai/ (accessed.

BİTLİS EREN ÜNİVERSİTESİ
FEN BİLİMLERİ DERGİSİ

ISSN: 2147-3129 / e-ISSN: 2147-3188

Article Type : Research Article
Received : April 2, 2025
Revised : August 22, 2025
Accepted : September 23, 2025
DOI : 10.17798/bitlisfen.1669087

Year : 2025
Volume : 14
Issue : 3
Pages : 1487-1503

DETERMINATION OF ENZYME INHIBITORY AND ANTIOXIDANT ACTIVITIES OF SELECTED OAK GALLS

Merve DOĞAN ABDİOĞLU [1], **Nesrin HAŞİMİ [1]*** Mehmet BOĞA [2]

[1] *Batman University, Biology Department, Batman, Türkiye*

[2] *Dicle University, Analytical Chemistry Department, Diyarbakır, Türkiye*

**** Corresponding Author:*** *nesrin.hasimi@batman.edu.tr*

ABSTRACT

In this study, the enzyme inhibition and antioxidant activities of methanol extracts obtained from galls induced by *Andricus quercustozae* and *Andricus cecconii* on *Quercus brantii* Lindley. and *Andricus quercusramuli* on *Quercus infectoria* Oliver were investigated.

The enzyme inhibition activity was assessed using spectrophotometric methods for acetylcholinesterase (AChE), butyrylcholinesterase (BChE), tyrosinase, and urease inhibition. The total phenolic and flavonoid contents of the extracts were quantified as gallic acid and quercetin equivalents, respectively. Antioxidant activity was evaluated using three distinct assays: DPPH free radical scavenging, ABTS cation radical scavenging, and CUPRAC.

Regarding cholinesterase inhibition, while none of the extracts exhibited activity against AChE, they demonstrated inhibition of BChE, with *A. quercustozae* gall extract showing the highest activity (31.33 ± 1.25%). Similarly, in tyrosinase inhibition, *A. quercustozae* gall extract exhibited the most significant effect, with an inhibition rate of 61.16 ± 0.72%. In urease inhibition, *A. quercustozae* gall extract was the only sample to demonstrate activity (40.98 ± 1.41%), whereas *A. quercusramuli* and *A. cecconii* extracts showed no significant effect.

The total phenolic contents of the extracts were higher than their total flavonoid contents, correlating with their strong antioxidant activities. Some extracts exhibited higher antioxidant activity than standard positive controls, further emphasizing their potential as natural antioxidant sources.

Keywords: Gall extracts, Butyrylcholinesterase inhibition, Tyrosinase, Urease, Radical scavenging, *Quercus* sp.

1 INTRODUCTION

The genus *Quercus*, belonging to the Fagaceae family, is represented by 531 species worldwide. Among these, 250 species are found in America, 125 in Asia, and the remaining species are distributed across Europe, North Africa, and Micronesia [1]. *Q. infectoria* is a small tree or shrub that can reach a height of up to 10 meters and retains some of its leaves during mild winters. Its natural distribution includes Southern Europe, Türkiye, Syria, and Iran. Similarly, *Q. brantii* is a deciduous tree with a broad, thick-branched canopy, capable of growing up to 10 meters in height. This species thrives at altitudes ranging from 350 to 1700 meters across Iran, the Caucasus, and the Eastern and Southeastern Anatolian regions.

Galls are abnormal plant tissue growths induced by various biological agents, including viruses, bacteria, fungi, nematodes, and arthropods [2]. The formation of galls involves the alteration of plant cellular mechanisms, leading to the development of novel structures with distinct morphological and functional properties. Among gall-inducing organisms, arthropods—such as wasps, midges, aphids, mites, and other insects—trigger gall formation by depositing their eggs on plant tissues. Upon hatching, the larvae feed on the host plant, stimulating the development of galls [3], [4], [5].

These arthropods influence the plant's biochemical pathways, prompting the secretion of secondary metabolites that are not typically produced by the host [6], [7].

It is suggested that these metabolites play a role in defending the plant against external threats [8], [9]. Recent findings indicate that gall formation not only alters plant morphology but also enhances the accumulation of phenolic compounds and flavonoids, thereby strengthening the antioxidant capacity of the host tissues [10].

Scientific studies on gall extracts have identified their bioactive components and elucidated the underlying biological mechanisms. The predominant phytochemicals found in galls include triterpenes, gallic acid, ethyl gallate, catechin, epicatechin, tannic acid, and resin. Gall tissues are exposed to higher levels of oxidative stress compared to normal plant tissues. The elevated production of polyphenols, anthocyanins, flavonoids, and tannins is considered an adaptive response to mitigate oxidative stress [11]. In particular, *Quercus infectoria* galls have recently been reported to exhibit strong antioxidant activities in DPPH, ABTS, and FRAP assays, supporting their potential as natural sources of bioactive agents [12].

Alzheimer disease (AD) is the most common form of dementia, characterized by cognitive decline and severe behavioral disorders. It is a progressive neurodegenerative brain

disorder that ultimately leads to death [13]. Currently, four drugs are available for AD treatment: galantamine, rivastigmine, donepezil, and memantine. The first three act as acetylcholinesterase (AChE) inhibitors. However, there is still no effective treatment for either curing or preventing AD. Given the increasing prevalence of AD in the population, the urgent development of disease-modifying agents remains a critical necessity. Recent studies have emphasized the potential of natural AChE inhibitors derived from plant polyphenols as promising candidates for AD therapy [14].

Tyrosinase is a copper-containing enzyme that plays a key role in the biosynthesis of melanin, which determines skin and hair pigmentation. The inhibition of tyrosinase has clinical applications in treating skin disorders associated with melanin hyperpigmentation. Additionally, tyrosinase inhibitors are widely used in cosmetics due to their skin-lightening effects. Although several synthetic inhibitors, such as kojic acid, have been developed to suppress tyrosinase activity, their long-term toxic effects have led to an increasing focus on identifying natural alternatives [15]. Recent findings have shown that *Q. infectoria* extracts exhibit up to 76% tyrosinase inhibition, confirming their potential as safe natural inhibitors for cosmetic and therapeutic use [16].

Urease activity serves as an important biochemical marker in both agriculture and medicine, particularly in viral diagnostics. Research has focused on urease inhibitors as potential therapeutic agents for diseases in which urease plays a role [17]. Bacteria, fungi, yeasts, and plants synthesize urease to obtain the nitrogen necessary for growth and development. Additionally, urease is considered a virulence factor in various pathogenic bacteria. One of the most extensively studied bacterial ureases is that of *Helicobacter pylori*, which is implicated in gastritis, peptic ulcer disease, and gastric cancer [18], [19]. The development of urease inhibitors is crucial for treating infections caused by urease-producing pathogens in humans and animals [20]. In recent years, increasing attention has been given to investigating the inhibitory effects of various plant extracts on urease activity [21].

With the increasing shift towards the utilization of natural resources, the search for natural antioxidant compounds has accelerated, prompting scientists to focus on the development of plant-derived pharmaceuticals. Additionally, natural compounds with enzyme inhibitory potential have garnered significant attention in the pharmaceutical industry. Enzyme inhibitors are incorporated into a wide range of therapeutic drugs used for the treatment of infectious, metabolic, cardiovascular, neurological diseases, and cancer [22]. For instance,

flavonoid derivatives isolated from *Quercus mongolica* pollen demonstrated significant antioxidant and tyrosinase inhibitory activities, surpassing some synthetic standards [23].

Lipid oxidation is a significant concern in the food industry due to the formation of undesirable food components and potentially toxic compounds. One of the primary strategies to prevent food oxidation is the use of antioxidants. However, several synthetic antioxidants commonly utilized in the food industry have been found to pose adverse health effects. Synthetic antioxidants such as butylated hydroxyanisole (BHA) and butylated hydroxytoluene (BHT) have been associated with carcinogenicity and liver damage in laboratory animals. These alterations are believed to contribute to the development of cancer, atherosclerosis, and cardiovascular diseases [24]. Consequently, there is a growing interest in natural antioxidants, particularly those derived from plants. The antioxidant properties of *Quercus* species have attracted increasing attention due to their role in preventing or mitigating oxidative damages caused by free radicals in the body [25]. Recent investigations also support the potential application of *Quercus* extracts in reducing oxidative rancidity in food products, highlighting their industrial significance [26].

This study aims to investigate the enzyme inhibition and antioxidant activities of methanol extracts obtained from galls induced by *Andricus quercusramuli*, *Andricus quercustozae*, and *Andricus ceconii* on *Quercus infectoria* and *Quercus brantii* L. species in the Siirt region of Türkiye.

2 MATERIAL AND METHODS

2.1 Plant Material and Extraction Method

Gall samples formed by *Andricus quercusramuli, Andricus quercustozae,* and *Andricus ceconii* on *Quercus infectoria* and *Quercus brantii L.* were collected from Nergizli (Türkiye, Siirt province, Şirvan) in October 2016 by entomologist Dr. Erdem Seven and species identification made by Dr. Musa Tataroğlu. Upon being transported to the laboratory, the samples (Figure 1.) were cleaned of larval and insect residues, subsequently dried, and ground into powder form. The samples were macerated with methanol and the solvent was subsequently removed using a rotary evaporator to obtain the extracts.



Sexual galls of *A. quercusramuli* on *Quercus infectoria*

Asexual galls *of A. quercustozae* on *Quercus brantii*

Sexual galls of *A. pseudocecconii* on *Quercus brantii*

Figure 1. Morphological appearance of the oak cynipid galls (Cynipidae, Cynipini)

2.2 The Enzyme Inhibition Activity

2.2.1 Acetylcholinesterase and Butyrylcholinesterase Inhibition Activity

The acetylcholinesterase (AChE) and butyrylcholinesterase (BChE) inhibition activities were assessed using the spectrophotometric method described by Ellman et al. (1961), with modifications by Kıvrak et al. (2009) [27], [28]. In this assay, AChE and BChE enzymes were utilized alongside their respective substrates, acetylthiocholine iodide (AcI) and butyrylthiocholine iodide (BcI). The enzymatic reaction was monitored based on the formation of a yellow-colored complex with 5,5'-dithiobis-(2-nitrobenzoic acid) (DTNB). Ethanol was used as the control, while galantamine served as the positive control.

The enzyme inhibition assay was performed by mixing 130 µL of pH 8 buffer solution, 10 µL of sample extract, 20 µL of AChE or BChE enzyme solution, 20 µL of DTNB, and 20 µL of AcI or BcI substrate. The reaction was recorded spectrophotometrically at 412 nm.

The anticholinesterase activity was calculated as the percentage of inhibition relative to the control using the following equation:

$$I\% = (A_{control} - A_{sample}/A_{control}) \times 100$$

2.2.2 Tyrosinase Enzyme Inhibition Activity

Tyrosinase inhibitors are typically evaluated in the presence of either a monophenolic substrate, such as tyrosine, or a diphenolic substrate, such as L-DOPA. The tyrosinase inhibition activity was determined using the spectrophotometric method described by Hearing (1987), with kojic acid serving as the positive control [29].

For the assay, the tyrosinase enzyme solution was prepared by dissolving 1 mg of enzyme in 250 µL of pH 6.8 buffer and dividing it into 50 µL aliquots. Prior to use, the solution was diluted to a final volume of 2000–3000 µL. The L-DOPA solution was prepared by dissolving 8.4 mg of L-DOPA in 5 ml of distilled water.

The reaction mixture consisted of 150 µL of pH 6.8 buffer solution, 10 µL of sample or control solution (prepared from a 4000 µg/ml stock solution), 20 µL of tyrosinase enzyme solution, and 20 µL of L-DOPA solution. The enzymatic reaction was monitored spectrophotometrically at 475 nm.

2.2.3 Acetylcholinesterase and Butyrylcholinesterase Inhibition Activity

The urease inhibition activity was determined using the method described by Mobley and Hausinger (1989) [30]. In this assay, extracts were incubated with urease enzyme, followed by the addition of urea as a substrate. The reaction product, ammonia, was quantified spectrophotometrically. Thiourea was used as a positive control.

The reaction mixture consisted of the sample solution, urease enzyme, and urea substrate prepared in phosphate buffer (pH 8.2). The reaction was performed by sequentially adding 10 µL of sample solution (from a 4000 µg/ml stock), 25 µL of urease enzyme (prepared in phosphate buffer, pH 8.2), and 50 µL of urea substrate solution. An initial absorbance reading was taken, followed by the addition of 45 µL of phenol reagent and 70 µL of alkaline reagent. The reaction was then monitored spectrophotometrically at 630 nm.

2.3 Determination of Antioxidant Activities of the Extracts

The antioxidant activities of the extracts were evaluated using three different methods: the DPPH free radical scavenging assay, the ABTS cation radical scavenging assay, and the CUPRAC assay, which measures the cupric ion reducing antioxidant capacity. Additionally, the total phenolic and flavonoid contents of the extracts were determined using appropriate analytical methods. BHT, BHA, and ascorbic acid were used as positive controls. Each sample was tested in triplicate.

2.3.1 DPPH Free Radical Scavenging Activity

The DPPH method measures the ability of antioxidant compounds to scavenge the stable free radical 2,2-diphenyl-1-picrylhydrazyl (DPPH). The absorbance of the DPPH radical at 517 nm was recorded using a UV-visible spectrophotometer. A decrease in absorbance indicates higher antioxidant activity and is accompanied by a color change from deep purple to yellow. This

method is widely used due to its simplicity, cost-effectiveness, and reliability in assessing total antioxidant capacity.

The DPPH radical scavenging activity was determined using the method developed by Blois (1958) [31]. The assay was performed by mixing 1 ml of the extract or positive control solution, prepared at different concentrations, with 4 ml of DPPH (0.1 mM) solution. The reaction was measured spectrophotometrically at 517 nm. The activity was evaluated based on the IC_{50} value (µg/ml).

2.3.2 ABTS Cation Radical Scavenging Activity

ABTS [2,2'-azino-bis (3-ethylbenzothiazoline-6-sulfonic acid)] is a chromogenic redox radical that is both stable and soluble in aqueous and organic solvents. This versatility allows its use in assessing both hydrophilic and hydrophobic antioxidant activities through a colorimetric reduction assay. In the original method, the ABTS radical cation ($ABTS^{\bullet+}$) is generated through the interaction between ferryl myoglobin, produced via the reaction of methyl myoglobin with hydrogen peroxide [32]. The $ABTS^{\bullet+}$ radical solution exhibits a blue-green color with characteristic absorbance maxima at 414, 645, 734, and 815 nm [33].

The ABTS cation radical scavenging activity of the extracts was determined using the method described by Re et al. (1999) [33]. For the assay, 1 ml of the extract or positive control solution at varying concentrations was mixed with 4 ml of ABTS solution. The absorbance was measured spectrophotometrically at 734 nm. The activity was evaluated based on the IC_{50} value (µg/ml).

2.3.3 CUPRAC (Cupric Ion Reducing Antioxidant Capacity)

The CUPRAC (Cupric Ion Reducing Antioxidant Capacity) method, developed by Apak et al., is a widely used assay for determining total antioxidant capacity (TAC). It utilizes the Cu(II)-neocuproine (Nc) reagent, which is stable, cost-effective, and applicable to both hydrophilic and lipophilic antioxidants. In this redox reaction, phenolic hydroxyl groups are converted into their corresponding quinones, leading to the reduction of Cu(II) to Cu(I) and the formation of a Cu(I)-Nc complex with maximum absorbance at 450 nm [34].

The assay was performed by mixing 1 mL of $CuCl_2$, 1 ml of neocuproine, 1 ml of ammonium acetate buffer, and 1 ml of extract or positive control solution at varying concentrations. The absorbance was recorded spectrophotometrically at 450 nm. The activity was evaluated based on the $A_{0.5}$ value.

2.3.4 Determination of Total Phenolic and Flavonoid Content of Extracts

The total phenolic content of the extracts was determined using the Folin-Ciocalteu phenol reagent (FCR) and expressed as gallic acid equivalents [35].

The assay was performed by mixing different volumes of gallic acid solution or extract with distilled water to a final volume of 4.7 ml, followed by the addition of 0.1 ml of FCR and 0.3 ml of Na_2CO_3 solution. The absorbance was measured spectrophotometrically at 760 nm.

The total phenolic content of the extracts was calculated using the standard calibration curve generated from gallic acid absorbance values, following the equation:

Absorbance=0.0399 × gallic acid (µg) + 0.4642 (R2=0.9912)

The total flavonoid content of the extracts was determined using the aluminum nitrate method and expressed as quercetin equivalents [36].

The assay was performed by mixing different volumes of quercetin solution or extract with 80% ethanol to a final volume of 4800 µL, followed by the addition of 100 µL of 1 M potassium acetate solution and 100 µL of 10% aluminum nitrate solution. The absorbance was recorded spectrophotometrically at 415 nm.

The total flavonoid content of the extracts was calculated using the standard calibration curve generated from quercetin absorbance values, following the equation:

Absorbance=0.1079 × quercetin (µg) − 0.0509 (R2=0.9984)

3 RESULTS AND DISCUSSION

3.1 Yield

The yield of the extracts was determined as 11.56% from *A. quercustozae* asexual galls, 5.66% from *A. cecconii* sexual galls, and 5.20% from *A. quercusramuli* sexual galls. Among the three, *A. quercustozae* demonstrated the highest yield, indicating a more efficient extraction of bioactive compounds.

3.2 Enzyme Inhibition Activity Results

The enzyme inhibition activities of *A. quercusramuli*, *A. quercustozae*, and *A. cecconii* gall extracts were evaluated against acetylcholinesterase (AChE), butyrylcholinesterase (BChE), tyrosinase, and urease at a concentration of 200 µg/ml (Table 1).

Cholinesterase inhibition plays a crucial role in neurodegenerative disease management, particularly in Alzheimer's disease, by increasing acetylcholine levels in the brain. Consequently, inhibiting cholinesterase enzymes can enhance neurotransmission, making plant-derived inhibitors valuable candidates for natural therapeutic applications [37], [38].

None of the extracts exhibited inhibitory activity against AChE, confirming that these galls do not influence this enzyme. However, *A. quercustozae* gall extract exhibited the highest BChE inhibition (31.33 ± 1.25%), indicating moderate potential as a cholinesterase inhibitor. In contrast, both *A. quercusramuli* and *A. cecconii* galls showed significantly lower inhibition (7.42 ± 0.26% and 8.58 ± 0.52%, respectively). The reference inhibitor, galantamine, displayed 81.33 ± 1.04% inhibition, significantly higher than the tested extracts, suggesting that while these gall extracts may contribute to BChE inhibition, their potency remains lower than synthetic inhibitors. This aligns with the findings of Fahimirad et al. (2023), who reported BChE inhibition of 35.4% for *Quercus brantii* galls, reinforcing the potential of gall-derived compounds as natural cholinesterase inhibitors [39]. Similarly, Kamarudin et al. (2021) observed moderate BChE inhibition in *Quercus* gall extracts, further supporting their neuroprotective potential [40]. However, the inhibition observed remains significantly lower than that of synthetic inhibitors such as galantamine (81.33 ± 1.04%), indicating that while gall extracts may contribute to enzyme inhibition, further fractionation and compound isolation are required to enhance their effectiveness.

Table 1. Enzyme inhibition activity results

	Enzyme inhibition[a] (%)			
Samples	**AChE**	**BChE**	**Tyrosinase**	**Urease**
A.quercusramuli	NA	7.42 ±0 .26	51.78 ± 0.61	NA
A.quercustozae	NA	31.33 ± 1.25	61.16 ± 0.72	40.98 ± 1.41
A. cecconii	NA	8.58 ± 0.52	55.86 ± 0.28	NA
Galanthamine[b]	82.85 ± 0.21	81.33±1.04	-	-
Kojic acid[b]	-	-	95.05 ± 0.37	-
Thiourea[b]	-	-	-	98.37 ± 0.40

a: The concentrations were 200 µg/ml. B:Positive controls. NA: Not active. The results are presented as mean ± standard deviation.

Tyrosinase plays a pivotal role in melanin biosynthesis and enzymatic browning, making tyrosinase inhibitors crucial for cosmetic, food, and medicinal industries. Due to its significant role in various biological processes, the identification, synthesis, and characterization of new tyrosinase inhibitors have gained attention in fields such as food, cosmetics, and medicine.

In the tyrosinase inhibition assay, all three extracts exhibited notable activity, reinforcing their potential as natural depigmentation agents. *A. quercustozae* galls displayed the highest inhibition (61.16 ± 0.72%), followed by *A. cecconii* galls (55.86 ± 0.28%) and *A. quercusramuli* galls (51.78 ± 0.61%). While the extracts showed promising activity, they remained lower than the reference inhibitor, kojic acid (95.05 ± 0.37%), indicating the need for further optimization. These findings are in agreement with those of Choudhry and Akhtar (2023), who reported 76% tyrosinase inhibition for *Quercus infectoria* gall extracts [41], as well as Nair et al. (2020), who observed moderate tyrosinase inhibition in *Quercus brantii* [42]. Compared to these studies, *A. quercustozae* galls showed promising activity, though it remained lower than that of the standard inhibitor kojic acid (95.05 ± 0.37%). These variations may stem from differences in phenolic composition, extraction methods, and plant species, highlighting the importance of further analysis to identify the most active compounds responsible for this effect.

Urease plays a critical role in pathogenic bacterial infections such as *Helicobacter pylori*-associated ulcers, and its inhibition has significant implications in medical and agricultural applications [43], [44].

For urease inhibition, *A. quercustozae* galls were the only extract that exhibited measurable activity (40.98 ± 1.41%), while *A. quercusramuli* galls and *A. cecconii* galls showed no inhibition. Thiourea, the positive control, demonstrated a near-complete inhibition (98.37 ± 0.40%). This aligns with the findings of Fahimirad et al. (2023), who reported 45.2% urease inhibition for *Quercus* gall extracts, supporting their potential as natural antibacterial agents [39]. However, compared to thiourea (98.37 ± 0.40%), the inhibition observed remains moderate, suggesting that further purification of the active compounds could enhance their bioactivity. The moderate activity of *A. quercustozae* galls suggests potential for further development as a natural urease inhibitor.

Overall, *A. quercustozae* galls demonstrated the strongest enzyme inhibition, particularly in BChE, tyrosinase, and urease assays, positioning it as a promising candidate for enzyme-targeted applications.

3.3 Antioxidant Activity Results

Table 2 presents total phenolic and flavonoid content, and antioxidant activity of *A. quercusramuli*, *A. quercustozae*, and *A. cecconii* galls extracts. The data are expressed in terms of phenolic and flavonoid content (as gallic acid equivalents and quercetin equivalents per mg of extract), and IC_{50} or $A_{0.5}$ values for DPPH, ABTS, and CUPRAC assays.

Among them, *A. quercustozae* galls exhibited the highest total phenolic content (438.2 ± 0.8 µg GAE/mg extract) and flavonoid content (49.2 ± 0.6 µg QE/mg extract), followed by *A. cecconii* galls (176.5 ± 0.8 µg GAE/mg extract, 22.8 ± 0.6 µg QE/mg), while *A. quercusramuli* galls contained significantly lower levels (51.5 ± 0.1 µg GAE/mg, 12.0 ± 0.0 µg QE/mg).

In terms of antioxidant activity, *A. quercustozae* galls demonstrated the strongest radical scavenging effect in the DPPH assay (IC_{50} = 5.0 ± 0.7 µg/ml), closely followed by *A. cecconii* galls (IC_{50} = 25.8 ± 0.3 µg/ml), while *A. quercusramuli* galls exhibited significantly weaker activity (IC_{50} = 211.6 ± 0.2 µg/ml). Similarly, in the ABTS assay, *A. quercustozae* galls displayed the lowest IC_{50} value (1.0 ± 0.4 µg/ml), indicating the highest scavenging potential, followed by *A. cecconii* galls (5.1 ± 0.5 µg/ml) and *A. quercusramuli* galls (38.3 ± 1 µg/ml). In the CUPRAC assay, *A. quercustozae* galls again exhibited the lowest $A_{0.5}$ value (3.8 ± 0.3 µg/ml), demonstrating superior reducing capacity compared to *A. cecconii* galls (12.0 ± 0.8 µg/ml) and *A. quercusramuli* galls (91.1 ± 0.2 µg/ml).

Table 2. Antioxidant activity, total phenolic and flavonoid content of gall extracts

			IC_{50} (µg/ml)		
Samples	**Phenolic content**	**Flavonoid content**	**DPPH Free Radical**	**ABTS Cation Radical**	**CUPRAC $A_{0.5}$ (µg/ml)**
A. quercusramuli galls	51.5 ± 0.1	12.0 ± 0.0	211.6 ± 0.2	38.3 ± 1	91.1 ± 0.2
A. quercustozae galls	438.2 ± 0.8	49.2 ± 0.6	5.0 ± 0.7	1.0 ± 0.4	3.8 ± 0.3
A. cecconii galls	176.5 ±0.8	22.8 ± 0.6	25.8 ± 0.3	5.1 ± 0.5	12.0 ± 0.8
Ascorbic acid	-	-	6.1 ± 0.6	1.9 ± 0.9	5.2 ± 0.9
BHA	-	-	4.9 ± 0.7	52.1 ± 0.4	38.2 ± 1
BHT	-	-	934.9 ± 1	2.5 ± 0.8	2.7 ± 0.7

Compared to standard antioxidants, *A. quercustozae* galls displayed an IC_{50} value comparable to ascorbic acid (6.1 ± 0.6 µg/ml) and BHA (4.9 ± 0.7 µg/ml) in the DPPH assay, while in the ABTS assay, its activity was significantly stronger than that of BHT (2.5 ± 0.8 µg/ml). In the CUPRAC assay, *A. quercustozae* galls also exhibited high reducing capacity, outperforming BHT (2.7 ± 0.7 µg/ml).

These findings align with existing research demonstrating the strong correlation between polyphenolic content and antioxidant capacity in medicinal plants [45], [46]. Several studies have reported a direct association between total phenolic content and radical scavenging ability, further supporting the robust antioxidant properties of *A. quercustozae* galls [47], [48].

The strong antioxidant properties of *A. quercustozae* galls are directly linked to its high polyphenolic content, which was found to be 438.2 ± 0.8 µg GAE/mg extract, the highest among the tested samples. This aligns with the study by Azmaz et al. (2020), who reported 479.56 mg GAE/g for *A. quercustozae*, confirming that this species is a rich source of bioactive phenolics [49]. The total flavonoid content (49.2 ± 0.6 µg QE/mg extract) also supports its strong radical scavenging activity, as flavonoids are known to contribute to antioxidant mechanisms.

Antioxidant activity, as determined by free radical scavenging assays, showed that *A. quercustozae* galls exhibited the strongest activity across all the tests. The DPPH assay revealed an IC_{50} of 5.0 ± 0.7 µg/ml, which is lower (indicating stronger activity) than the values reported by Mohammadzadeh et al. (2021) for *Quercus infectoria* (7.8 µg/ml) [50]. Similarly, in the ABTS assay, *A. quercustozae* galls demonstrated an IC_{50} of 1.0 ± 0.4 µg/ml, significantly stronger than the 7.3 µg/ml reported by Nair et al. (2020) for *Quercus brantii*, confirming its superior ability to neutralize free radicals [42]. The CUPRAC assay, which measures reducing power, further supported these findings, with *A. quercustozae* galls exhibiting an $A_{0.5}$ value of 3.8 ± 0.3 µg/ml, outperforming *A. cecconii* (12.0 ± 0.8 µg/ml) and *A. quercusramuli* galls (91.1 ± 0.2 µg/ml). These results align with Limsuwan et al. (2020), who reported similar reducing capacities for *Quercus brantii* galls (192.8 mg TE/g), reinforcing the strong metal-reducing potential of *A. Quercustozae* [51].

These findings confirm that *A. quercustozae* galls are a highly potent antioxidant source, with its DPPH, ABTS, and CUPRAC activity surpassing that of many previously studied *Quercus* gall extracts. Compared to synthetic antioxidants, *A. quercustozae* galls exhibited DPPH activity comparable to ascorbic acid (6.1 ± 0.6 µg/ml) and BHA (4.9 ± 0.7 µg/ml), while its ABTS scavenging ability exceeded that of BHT (2.5 ± 0.8 µg/ml), reinforcing its potential as a natural antioxidant alternative.

The variations in activity among different studies are likely influenced by differences in extraction methods, plant species, and environmental conditions affecting phytochemical composition. Several studies, including those by Kovacevic (2000) and Rakic et al. (2007), have reported a direct correlation between total phenolic content and antioxidant capacity, further supporting the strong antioxidant properties observed in *A. Quercustozae* [45], [46]. Additionally, Shirzad et al. (2011) and Rahnama et al. (2014) emphasized the importance of polyphenolic compounds in free radical scavenging, which is consistent with our results [47], [48].

4 CONCLUSION AND SUGGESTIONS

This study comprehensively evaluated the enzyme inhibition and antioxidant activities of *Andricus quercusramuli* galls, *Andricus quercustozae* galls, and *Andricus cecconii* galls extracts. The results highlight *A. quercustozae* galls as the most promising species due to its high phenolic and flavonoid content, which strongly correlates with its superior antioxidant capacity. Additionally, it exhibited moderate inhibition against BChE, tyrosinase, and urease, suggesting its potential in applications related to neuroprotection, cosmetics, and antibacterial treatments.

Overall, the findings of our study indicate that *A. quercustozae* gall extract possesses a high phenolic content and strong antioxidant potential, with enzyme inhibition activities that are generally in line with those reported in the literature. When compared with *Quercus* gall extracts from previous studies, our results demonstrate that *A. quercustozae* galls exhibits greater radical scavenging activity in ABTS and DPPH assays, as well as a higher phenolic content in most cases. However, tyrosinase inhibition was slightly lower than in some studies, indicating that its enzymatic activity may vary depending on specific phytochemical compositions. These differences are likely influenced by variations in extraction techniques, solvent types, plant species, and environmental factors affecting phytochemical composition. Future studies should focus on standardizing extraction methods and further exploring the bioactive properties of *A. quercustozae* gall extracts for potential pharmaceutical and industrial applications.

Despite these promising results, several limitations of the present study should be acknowledged. First, the bioactivity assessments were limited to in vitro assays, which may not fully represent in vivo biological effects. Second, only methanol extracts were tested, leaving the potential activities of other solvent fractions unexplored. The study also focused on a restricted set of enzymes (BChE, AChE, tyrosinase, and urease), whereas additional biological targets relevant to neurodegenerative and infectious diseases were not included. Furthermore, the plant material was collected from a single geographical region (Siirt, Türkiye), which may not capture the full phytochemical diversity of these species in different habitats. Finally, no isolation or structural characterization of individual compounds was conducted, which limits the ability to directly link specific metabolites to the observed activities. Addressing these limitations in future research will provide a more comprehensive understanding of the pharmacological and industrial potential of Quercus galls.

Acknowledgements

This study is based on the master's thesis of Merve Doğan Abdioğlu and was supported by the Scientific Research Committee of Batman University under project number .18.001. The authors would like to express their gratitude to Dr. Erdem Seven for his assistance in sample collection and to Dr. Musa Tataroğlu for his valuable contribution to the identification of the samples.

Conflict of Interest Statement

There is no conflict of interest between the authors.

Statement of Research and Publication Ethics

The study is complied with research and publication ethics.

Artificial Intelligence (AI) Contribution Statement

This manuscript was entirely written, edited, analyzed, and prepared without the assistance of any artificial intelligence (AI) tools. All content, including text, data analysis, and figures, was solely generated by the authors.

Contributions of the Authors

Merve Doğan Abdioğlu conducted the conceptualization, experimental studies, data collection, and preparation of the original draft of the manuscript. Nesrin Haşimi supervised the research, contributed to the methodology, provided guidance during data interpretation, and critically revised the manuscript. Mehmet Boğa contributed to the experimental analyses and assisted in refining the final version of the paper. All authors read and approved the final manuscript.

REFERENCES

[1] R. Govaerts and D. G. Frodin, *World Checklist and Bibliography of Fagales (Betulaceae, Corylaceae, Fagaceae, and Ticodendraceae)*. Richmond, UK: Royal Botanic Gardens, Kew, 1998.

[2] M. Tataroğlu and Y. Katılmış, "Two new species of oak gall wasp (Hymenoptera: Cynipidae, Cynipini) from Türkiye," *Zootaxa*, vol. 5433, no. 4, pp. 559–572, 2024, doi: 10.11646/zootaxa.5433.4.5.

[3] G. Csóka, G. N. Stone, and G. Melika, "Biology, ecology and evolution of gall-inducing Cynipidae," in *Biology, Ecology and Evolution of Gall-Inducing Arthropods*, A. Raman, C. W. Schaefer, and T. M. Withers, Eds. Enfield, NH: Science Publishers, 2005, pp. 573–642.

[4] G. N. Stone, K. Schönrogge, R. J. Atkinson, D. Bellido, and J. Pujade-Villar, "The population biology of oak gall wasps (Hymenoptera: Cynipidae)," *Annual Review of Entomology*, vol. 47, pp. 633–668, 2002, doi: 10.1146/annurev.ento.47.091201.145247.

[5] G. Melika, *Gall Wasps of Ukraine. Cynipidae*, *Vestnik Zoologii*, Supplement 21 (1–2), pp. 1–300 & 301–644, 2006.

[6] D. C. Oliveira, R. M. S. Isaias, G. W. Fernandes, B. G. Ferreira, R. G. S. Carneiro, and L. Fuzaro, "Manipulation of host plant cells and tissues by gall-inducing insects and adaptive strategies used by different feeding guilds," *Journal of Insect Physiology*, vol. 84, pp. 103–113, 2016, doi: 10.1016/j.jinsphys.2015.11.012.

[7] M. Tataroğlu, Ö. Kılınçarslan Aksoy, Y. Katılmış, and R. Mammadov, "Determination of secondary metabolite in galls of some cynipid wasps (Hymenoptera: Cynipidae) and characterization of the phenolic compound," *International Journal of Secondary Metabolite*, vol. 10, no. 4, pp. 555–569, 2023, doi: 10.21448/ijsm.1300763.

[8] E. O. Martinson, J. D. Hackett, C. A. Machado, and A. E. Arnold, "Metatranscriptome analysis of fig flowers provides insights into potential mechanisms for mutualism stability and gall induction," *PLOS ONE*, vol. 10, no. 6, Jun. 2015, doi: 10.1371/journal.pone.0130745.

[9] S. Patela, A. Rauf, and C. Khan, "The relevance of folkloric usage of plant galls as medicines: Finding the scientific rationale," *Biomedicine & Pharmacotherapy*, vol. 97, pp. 240–247, Jan. 2018, doi: 10.1016/j.biopha.2017.10.111.

[10] R. R. Silva, C. P. Ferreira, and A. P. Santos, "Plant Galls: Implications for the Chemical Profile and Biological Activity of Their Host Plants," *Plants*, vol. 13, no. 2, p. 256, Jan. 2024, doi: 10.3390/plants13020256.

[11] M. Y. Huang, W. D. Huang, H. M. Chou, C. C. Chen, P. J. Chen, Y. T. Chang, and C. M. Yang, "Structural, biochemical, and physiological characterization of photosynthesis in leaf-derived cup-shaped galls on *Litsea acuminata*," *BMC Plant Biology*, vol. 15, p. 61, 2015, doi: 10.1186/s12870-015-0446-0.

[12] N. A. Ali, S. M. Rahman, and M. A. Hossain, "*Quercus infectoria* Gall Ethanolic Extract Accelerates Wound Healing and Provides Antioxidant Activity," *Frontiers in Pharmacology*, vol. 15, p. 1198762, 2024, doi: 10.3389/fphar.2024.1198762.

[13] S. S. Xie, X. B. Wang, J. Y. Li, L. Yang, and L. Y. Kong, "Design, synthesis and evaluation of novel tacrine-coumarin hybrids as multifunctional cholinesterase inhibitors against Alzheimer's disease," *European Journal of Medicinal Chemistry*, vol. 64, pp. 540–553, 2013, doi: 10.1016/j.ejmech.2013.03.051.

[14] S. Kumar, R. Singh, and P. Sharma, "Natural acetylcholinesterase inhibitors as potential therapeutics for Alzheimer's disease: Recent advances," *Phytomedicine*, vol. 99, p. 154012, Sep. 2022, doi: 10.1016/j.phymed.2022.154012.

[15] G. Tocco, B. Fais, G. Meli, M. Begala, G. Podda, M. B. Fadda, M. Corda, O. A. Attanasi, P. Filippone, and S. Berretta, "PEG-immobilization of cardol and soluble polymer-supported synthesis of some cardol-coumarin derivatives: Preliminary evaluation of their inhibitory activity on mushroom tyrosinase," *Bioorganic & Medicinal Chemistry*, vol. 19, no. 1, pp. 36–39, 2009, doi: 10.1016/j.bmcl.2008.11.020.

[16] M. H. Lee, J. S. Park, and Y. J. Kim, "Formulation and characterization of *Quercus infectoria* extract: Anti-tyrosinase activity and cosmetic applications," *Journal of Cosmetic Dermatology*, vol. 21, no. 12, pp. 6789–6797, Dec. 2022, doi: 10.1111/jocd.15865.

[17] Y. Onado, M. Takido, T. Magaribuchi, and H. Iwasaki, "Effects of 12-sulfodehydroabietic acid monosodium salt (TA2711), a new anti-ulcer agent, on gastric mucosal lesions induced by necrotizing agents and gastric mucosal defensive factors in rats," *Japanese Journal of Pharmacology*, vol. 52, pp. 631–638, 1990, doi: 10.1254/jjp.52.631.

[18] H. L. T. Mobley, "Helicobacter pylori: Physiology and genetics," in *Helicobacter pylori*: Physiology and Genetics, H. L. T. Mobley, G. L. Mendz, and L. Stuart, Eds. Washington, DC: American Society of Microbiology Press, 2001, pp. 97–109, doi: 10.1128/9781555818005.ch16.

[19] S. T. S. Hassan and M. Sudomova, "The development of urease inhibitors: What opportunities exist for better treatment of Helicobacter pylori infection in children?," *Children*, vol. 4, no. 1, p. 2, 2017, doi: 10.3390/children4010002.

[20] Z. Amtul, A. Rahman, R. Siddiqui, and M. Choudhary, "Chemistry and mechanism of urease inhibition," *Current Medicinal Chemistry*, vol. 9, pp. 1323–1348, 2002, doi: 10.2174/0929867023369853.

[21] M. A. Hemminga and C. M. Duarte, *Seagrass Ecology*. Cambridge, UK: Cambridge University Press, 2000

[22] R. A. Copeland, M. R. Harpel, and P. J. Tummino, "Targeting enzyme inhibitors in drug discovery," *Expert Opinion on Therapeutic Targets*, vol. 11, no. 7, pp. 967–978, 2007, doi: 10.1517/14728222.11.7.967.

[23] Y. Joo, Y. H. Seo, S. Lee, E. Shin, S. W. Yeon, S. B. Kim, and M. K. Lee, "Antioxidant and Tyrosinase-Inhibitory Activities and Biological Bioactivities of Flavonoid Derivatives from *Quercus mongolica* Pollen," *Molecules*, vol. 30, no. 4, p. 794, Feb. 2025, doi: 10.3390/molecules30040794.

[24] A. Braca, C. Sortino, M. Politi, J. Morelli, and J. Mendez, "Antioxidant activity of flavonoids from *Licania licaniaeflora*," *Journal of Ethnopharmacology*, vol. 79, pp. 379–381, 2002, doi: 10.1016/S0378-8741(01)00413-5.

[25] Y. Abiy, "Antimicrobial flavonoids from the stem bark of *Erythrina burtii*," *Fitoterapia*, vol. 96, pp. 496–499, 2005, doi: 10.1016/j.fitote.2005.04.006.

[26] E. D. Othón-Díaz, J. O. Fimbres-García, M. Flores-Sauceda, A. A. Moreno-Martínez, and A. M. Silva-Espinoza, "Antioxidants in Oak (*Quercus* sp.): Potential Application to Reduce Oxidative Rancidity in Foods," *Antioxidants*, vol. 12, no. 4, p. 861, Apr. 2023, doi: 10.3390/antiox12040861.

[27] G. L. Ellman, K. D. Courtney, V. Andres Jr., and R. M. Featherstone, "A new and rapid colorimetric determination of acetylcholinesterase activity," *Biochemical Pharmacology*, vol. 7, pp. 88–95, 1961, doi: 10.1016/0006-2952(61)90145-9.

[28] İ. A. Kıvrak, M. E. Duru, M. Öztürk, N. Mercan, M. Harmandar, and G. Topcu, "Antioxidant, anticholinesterase, and antimicrobial constituents from the essential oil and ethanol extract of *Salvia potentillifolia*," *Food Chemistry*, vol. 116, pp. 470–479, 2009, doi: 10.1016/j.foodchem.2009.02.069.

[29] V. J. Hearing, "Mammalian monophenol monooxygenase (tyrosinase): Purification, properties, and reactions catalyzed," *Methods in Enzymology*, vol. 142, pp. 154–165, 1987, doi: 10.1016/S0076-6879(87)42024-7.

[30] H. L. Mobley and R. P. Hausinger, "Microbial ureases: Significance, regulation, and molecular characterization," *Microbiology Reviews*, vol. 53, pp. 85–108, 1989, doi: 10.1128/mr.53.1.85-108.1989.

[31] M. S. Blois, "Antioxidant determination by the use of a stable free radical," *Nature*, vol. 181, pp. 1199–1200, 1958, doi: 10.1038/1811199a0.

[32] C. A. Rice-Evans and N. J. Miller, "Total antioxidant status in plasma and body fluids," *Methods in Enzymology*, vol. 234, pp. 279–293, 1994, doi: 10.1016/0076-6879(94)34095-1.

[33] R. Re, N. Pellegrini, A. Protrggente, A. Pannala, M. Yang, and C. Rice-Evans, "Antioxidant activity applying an improved ABTS radical cation decolorization assay," *Free Radical Biology and Medicine*, vol. 26, pp. 1231–1237, 1999, doi: 10.1016/S0891-5849(98)00315-3.

[34] R. Apak, K. Güçlü, M. Özyürek, and S. E. Karademir, "A novel total antioxidant capacity index for dietary polyphenols, vitamin C and E, using their cupric ion reducing capability in the presence of neocuproine: The CUPRAC method," *Journal of Agricultural and Food Chemistry*, vol. 52, pp. 7970–7981, 2004, doi: 10.1021/jf048741x.

[35] M. I. N. Moreno, M. I. Isla, A. R. Sampietro, and M. A. Vattuone, "Comparison of the free radical-scavenging activity of propolis from several regions of Argentina," *Journal of Ethnopharmacology*, vol. 71, pp. 109–114, 2000, doi: 10.1016/S0378-8741(99)00189-0.

[36] K. Slinkard and V. L. Singleton, "Total phenol analyses: Automation and comparison with manual methods," *American Journal of Enology and Viticulture*, vol. 28, pp. 49–55, 1977, doi: 10.5344/ajev.1977.28.1.49.

[37] H. Kobayashi, T. Ohnishi, R. Nakagawa, and K. Yoshizawa, "The comparative efficacy and safety of cholinesterase inhibitors in patients with mild-to-moderate Alzheimer's disease: A Bayesian network meta-analysis," *International Journal of Geriatric Psychiatry*, vol. 31, no. 8, pp. 892–904, 2016, doi: 10.1002/gps.4405.

[38] P. K. Mukherjee, V. Kumar, M. Mal, and P. J. Houghton, "Acetylcholinesterase inhibitors from plants," *Phytomedicine*, vol. 14, pp. 289–300, 2007, doi: 10.1016/j.phymed.2007.02.002.

[39] S. Fahimirad, P. Satei, A. Ganji, and H. Abtahi, "Wound healing performance of PVA/PCL-based electrospun nanofiber incorporated green synthesized CuNPs and *Quercus infectoria* extracts," *Journal of Biomaterials Science, Polymer Edition*, vol. 34, pp. 277–301, 2023, doi: 10.1080/09205063.2022.2116209

[40] N. A. Kamarudin, N. N. H. Nik Salleh, and S. C. Tan, "Gallotannin-enriched fraction from *Quercus infectoria* galls as an antioxidant and inhibitory agent against human glioblastoma multiforme," *Plants*, vol. 10, p. 2581, 2021, doi: 10.3390/plants10122581.

[41] A. Choudhry and N. Akhtar, "Formulation, characterization of *Quercus infectoria* (Olivier) emulsions, and in vitro, in vivo evaluation as cosmeceutical formulation," *Journal of Cosmetic Dermatology*, pp. 1–11, 2023, doi: 10.1111/jocd.15865.

[42] A. Nair, T. Balasaravanan, S. Jadhav, V. Mohan, and C. Kumar, "Harnessing the antibacterial activity of *Quercus infectoria* and *Phyllanthus emblica* against antibiotic-resistant *Salmonella Typhi* and *Salmonella Enteritidis* of poultry origin," *Veterinary World*, vol. 13, pp. 1388–1396, 2020, doi: 10.14202/vetworld.2020.1388-1396.

[43] H. Khan, M. A. Khan, and I. Hussan, "Enzyme inhibition activities of the extracts from rhizomes of *Gloriosa superba* Linn (Colchicaceae)," *Journal of Enzyme Inhibition and Medicinal Chemistry*, vol. 22, pp. 722–725, 2007, doi: 10.1080/14756360601164853.

[44] M. Lateef, L. Iqbal, N. Fatima, K. Siddiqui, N. Afza, M. Zia-ul-Haq, and M. Ahmad, "Evaluation of antioxidant and urease inhibition activities of roots of *Glycyrrhiza glabra*," *Pakistan Journal of Pharmaceutical Sciences*, vol. 25, pp. 99–102, 2012.

[45] N. Kovacevic, *Basic Pharmacognosy*. Belgrade, Serbia: University of Belgrade, Faculty of Pharmacy, 2000.

[46] S. Rakic, S. Petrovic, J. Kukic, M. Jadranin, V. Tešević, and D. Povrenović, "Influence of thermal treatment on phenolic compounds and antioxidant properties of oak acorns from Serbia," *Food Chemistry*, vol. 104, no. 2, pp. 830–834, 2007, doi: 10.1016/j.foodchem.2007.01.025.

[47] H. Shirzad, F. Taji, and M. Rafieian-Kopaei, "Correlation between antioxidant activity of garlic extracts and WEHI-164 fibrosarcoma tumor growth in BALB/c mice," *Journal of Medicinal Food*, vol. 14, no. 9, pp. 969–974, 2011, doi: 10.1089/jmf.2011.1594.

[48] S. Rahnama, Z. Rabiei, Z. Alibabaei, S. Mokhtari, M. Rafieian-Kopaei, and F. Deris, "Anti-amnesic activity of *Citrus aurantium* flowers extract against scopolamine-induced memory impairments in rats," *Neurological Sciences*, vol. 35, no. 8, pp. 1305–1310, 2014, doi: 10.1007/s10072-014-1991-2.

[49] M. Azmaz, Ö. Kılınçarslan Aksoy, Y. Katılmış, and R. Mammadov, "Investigation of the antioxidant activity and phenolic compounds of *Andricus quercustozae* gall and host plant (*Quercus infectoria*)," *International Journal of Secondary Metabolite*, vol. 7, no. 2, pp. 77–87, 2020, doi: 10.21448/ijsm.674930.

[50] N. Mohammadzadeh, M. Ghiasian, J. Faradmal, and D. Dastan, "Quantitative and qualitative analyses of the constituents of the hydroalcoholic extract of *Quercus infectoria* gall from Kermanshah and evaluation of its antioxidant and antibacterial activities," *Journal of Reports in Pharmaceutical Sciences*, vol. 10, pp. 287–293, 2021, doi: 10.4103/jrptps.JRPTPS_36_21.

[51] S. Limsuwan, S. Jarukitsakul, A. Issuriya, S. Chusri, N. Joycharat, P. Jaisamut, J. Saising, K. W. N. Jetwanna, and S. P. Voravuthikunchai, "Thai herbal formulation 'Ya-Pit-Samut-Noi': Its antibacterial activities, effects on bacterial virulence factors and in vivo acute toxicity," *Journal of Ethnopharmacology*, vol. 259, p. 112975, 2020, doi: 10.1016/j.jep.2020.112975.

BİTLİS EREN ÜNİVERSİTESİ
FEN BİLİMLERİ DERGİSİ

ISSN: 2147-3129 / e-ISSN: 2147-3188

Article Type : Research Article
Received : April 4, 2025
Revised : September 27, 2025
Accepted : September 28, 2025
DOI : 10.17798/bitlisfen.1670085

Year : 2025
Volume : 14
Issue : 3
Pages : 1504-1518

SLEEVE FUSE SYSTEM FOR IMPROVED STEEL CONNECTION PERFORMANCE

Muhammed ATAR [1]

[1] *Fırat University, Department of Civil Engineering, Elazığ, Türkiye, matar@firat.edu.tr*

ABSTRACT

This study introduces an approach to improving the connection performance of steel structures by utilizing a sleeve fuse mechanism. The system introduced suggest a steel sleeve which is positioned between the end plate and the nut to modify the load path for improving the system's ductility. To validate the proposed method, experimental models from existing studies were employed, ensuring that the numerical simulations provided accurate results. A range of sleeve designs were analysed utilising a numerical FE model, confirming the system's efficacy in improving connection behaviour. The sleeve system showed notably better performance than conventional end-plate connections. The results indicate that the system increases the connection's rotational capacity by 85%, functioning as a structural fuse under monotonic loading and enhancing both ductility and energy absorption by 90%. Additionally, the increased elongation of the bolts further contributes to the rotational capacity, providing greater stability to the frame structure. Overall, this sleeve-based system offers a promising advancement over conventional designs by boosting energy absorption and ductility, making it a robust alternative for improving connection performance.

Keywords: Monotonic loading, Steel structures, Bolted connections, Fuse system, Ductility.

1 INTRODUCTION

The behaviour of steel structures under destructive loading conditions, such as blasts and earthquakes, has attracted increasing popularity in recent decades [1], [2], [3], [4]. Previous research has emphasized the importance of connection layouts and related parameters in enhancing structural performance during extreme loads and in mitigating progressive collapse. Since the connection area is the most critical zone for energy dissipation, it is essential that the

connection can withstand high strain energy without failing. For instance, the General Services Administration (GSA) [5] specifies 0.2 radians (approximately 11 degrees) of rotational capacity to allow beams to engage in catenary action, which helps prevent progressive collapse during extreme loading events. Because of the restricted ductility of connection components, earlier research has mainly aimed to redirect inelastic deformation away from the connection area.

Seismic connections often incorporate energy-dissipating elements, known as 'fuses,' which rely on ductile behaviour to reduce the destructive effects of earthquakes. These fuses undergo plastic deformation prior to the main structural elements, limiting damage to the fuse and maintaining the stability of the primary structure. In the replaceable fuse type, energy dissipation occurs by confining damage to the fuse elements. These elements may be removed after catastrophe. However, incorporating fuses requires additional fabrication and extends installation time, as they are used alongside existing connections [6]. In a self-centering connection, the top and seat angles elements are used to absorb more energy by experiencing plastic deformation [7]. Moreover, incorporating shape memory alloy (SMA) angles can help avoid the need to replace steel angles after a major earthquake [8]. However, the higher cost of SMA compared to conventional steel materials restricts its widespread application in construction. Other method for dissipating earthquake energy is to ensure the failure mechanism is located in specific position in beam section where the connection area is not effected. This can be done by either reinforcing the connection to prevent plastic deformation in its components [9], or by reducing the beam's strength, such as through flange cuts (RBS) [10] or modifications to the beam web (RWS) [11]. As a result, the beam undergoes substantial inelastic deformation and will need to be substituted after a major seismic event.

The typical approaches to improving ductility focus on modifying the rigidity of the beam or the end plate. However, in certain connection configurations, the deformation capacity of the joint zone can also be influenced by the bolts, which may undergo significant elongation [12], [13]. In Eurocode-based design (EN 1993-1-8), end plate connections are commonly assessed using a T-stub representation [14], where the bolts define the boundary conditions, whereas AISC 358 specifies end plate thickness based on yield line theory derived from plastic mechanism analysis. As the bolts elongate more, the rotational capacity that can be achieved increases [15]. Bolts often employed in structural applications are typically constructed from steel with high tensile strength, such as 8.8 and 10.9 grades [16], which reach their peak strength at around 0.05 strain and then fracture suddenly [17]. In comparison, mild steel can endure strains up to 0.2 before failure occurs [5]. The bolt's short length typically has a minimal impact

on the rotational capacity through elongation, especially when compared to the influence of the end plate. In the earthquake-resistant design of steel frames, the design is often controlled more by drift limitations specified in codes than by strength limitations. Member sizes chosen to meet drift requirements are generally larger than those necessary to fulfill strength requirements. In such scenarios, the RBS and RWS approaches are effective, given the beam is intentionally over-designed. In such cases, it is essential to thoroughly evaluate the beam's bending strength to ensure that removing steel elements does not substantially reduce its capacity. Additionally, cuts in the steel plates can form crack tips, potentially leading to failure as a result of fatigue crack propagation [15]. Flange cuts made in the RBS method may reduce the beam's stability, increasing the risk of it twisting or buckling under load. On the other hand, the sleeve method helps retain the strength of the steel component, offering greater flexibility and applicability to different frame design needs.

A diagram illustrating the proposed system is shown in Figure 1, where a steel sleeve, characterized by its length, wall curvature, and thickness, is positioned between the bolt nut and the end plate. The sleeve functions as a curved shell, where the applied load is resisted by both membrane forces and bending stresses [18]. The wall of the sleeve is curved to encourage bending failure instead of sudden buckling. The curvature determined by an amplitude at the middle of sleeve. Several studies have examined methods to enhance the performance of steel end-plate beam–column connections. Shaheen et al. [19] introduced a device to improve the robustness of end-plate connections, while Shaheen [23] proposed modifications aimed at enhancing cyclic behaviour. Shaheen et al. [24] conducted experimental tests on a bolt sleeve device, demonstrating increased ductility in end-plate connections, and Shaheen et al. [25] presented a numerical investigation that validated the benefits of sleeve systems in improving connection ductility. Atar and Çete [26] explored the sleeve method for steel T-stub connections, highlighting its potential to enhance structural resilience. More recently, Atar [27] compared sleeve fuse systems with the reduced beam section (RBS) method, showing that sleeves can effectively concentrate plastic deformation within replaceable components.

In contrast to previous studies, this work focuses on the monotonic behaviour of bolted end-plate connections with a replaceable sleeve fuse. Combining experimental validation with FE modelling, it examines the effect of sleeve design on rotational capacity, bolt elongation, and overall connection performance. The results demonstrate that sleeve devices act as structural fuses, enhancing ductility and energy absorption while maintaining frame stability. Moreover, the sleeve's length and diameter can be adjusted to achieve different rotational capacities without altering connection strength or design.

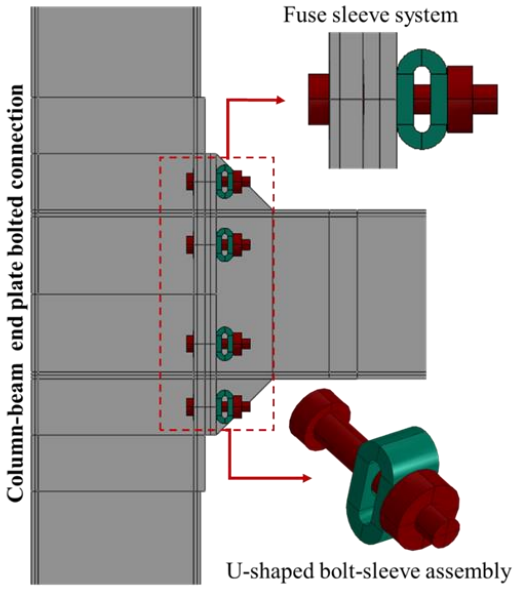


Figure 1. Fuse connection system with sleeve

This study primarily focuses on evaluating the global performance of the sleeved end-plate connection system, with emphasis on its rotational capacity and energy dissipation. Within this framework, the influence of the sleeve mechanism on the ductility of the end plate region is also examined, while ensuring that the initial stiffness and strength of the connection are preserved. A previously validated experimental model [20] was used for precise FE analysis, which were performed to assess the behaviour of the sleeved connection. The results of the sleeved connection were then compared with those of the standard (no-sleeve) connection to demonstrate the effectiveness of the proposed method in improving load-bearing and deformation capacity.

2 MODEL DESCRIPTION

This research evaluates the behaviour of the proposed sleeved end-plate connection in comparison to the conventional (no-sleeve) beam-to-column connections in moment-resisting frames (MRFs). For validation and parametric analysis, the experimental test conducted by Shi et al. [20] was adopted, specifically specimen EPC-1, which had an end-plate thickness of 20 mm and bolt diameter of 20 mm. The connection properties are illustrated in Figure 2. The boundary conditions and applied load scenario follow those of the original experiment. Monotonic loading was applied at the end of the beam, and the material properties of all connection components are provided in Table 1 [20].

Table 1. Material characteristics used in the numerical analysis [20].

	Steel (thickness≤ 16.0 *mm*)	**Steel (thickness> 16.0 *mm*)**	**Bolts**	**Sleeve**
Young's modulus (MPa)	195452	188671	210000	210000
Yield strength (MPa)	409	373	995	355
Ultimate tensile strength (MPa)	537	537	1160	510

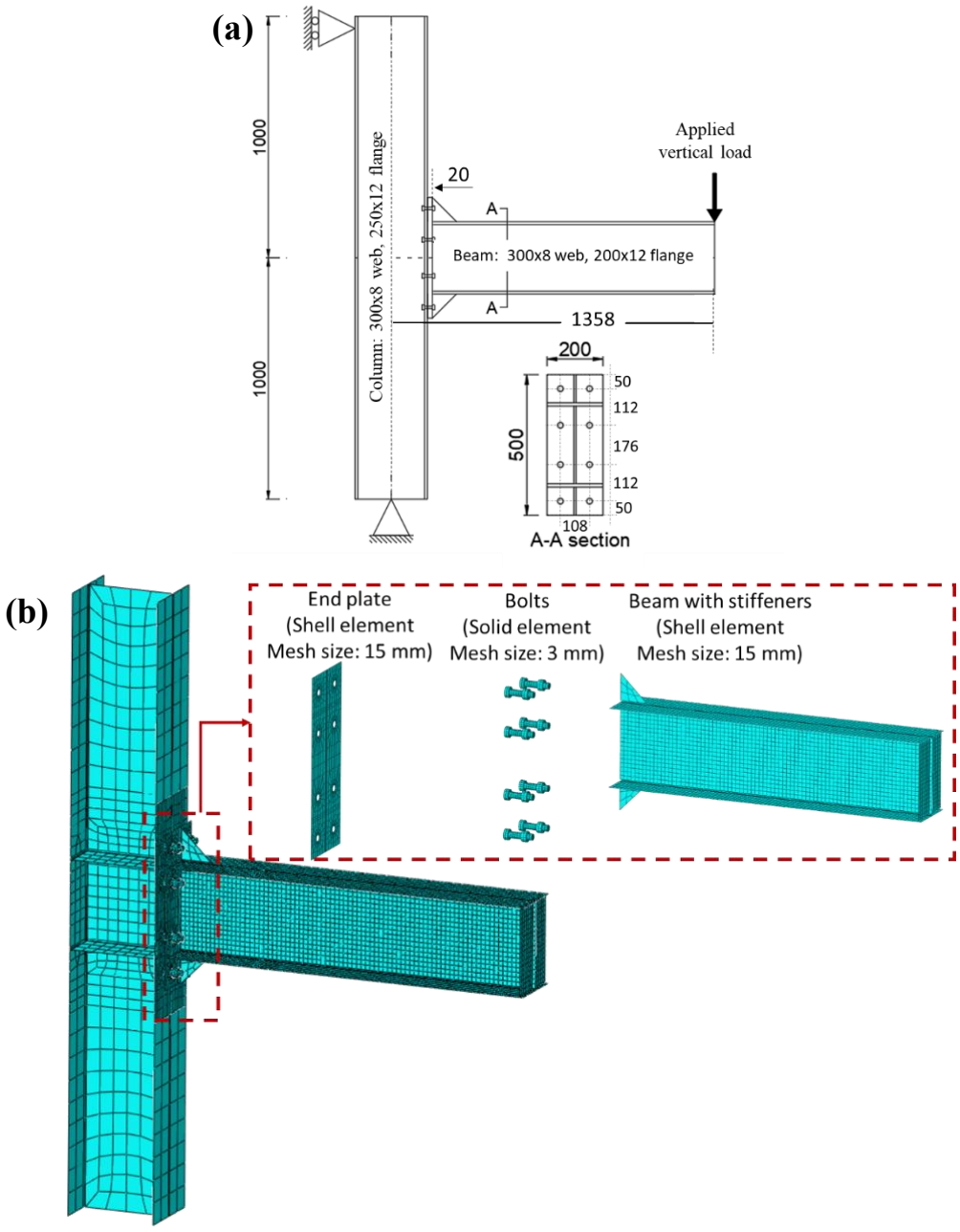


Figure 2. (a) Geometrical specifications of the test specimen as outlined by [20], (b) Mesh resolution.

3 FE MODEL VALIDATION

A numerical FE model was used to replicate real structural connections. ABAQUS/Standard was utilised for the simulation and parametric analysis, with simplifications made to reduce computational time without sacrificing accuracy.

The extended end-plate connection (Figure 2) was modelled using S4R shell elements for the beam, column, and end plate to efficiently capture bending and membrane behaviour with fewer degrees of freedom, while the bolts, and nuts were represented by C3D8R solid elements to accurately simulate three-dimensional stress states, contact, and potential local plasticity. This approach balances computational efficiency with modeling accuracy. A refined mesh captured high-stress zones [23], and surface interactions were defined using a small-sliding formulation. A surface-to-surface contact with friction coefficients of 0.44 and 0.2 were applied for the endplate-column flange and bolt-plate interfaces, respectively. The material behaviour was modeled using a bilinear stress–strain curve based on [21], with elastic–plastic behaviour and isotropic hardening. The von Mises yield criterion was employed, and ultimate strain values were taken from [20].

Figure 3 presents the comparison between experimental and FE results: (a) illustrates the deformation of the connection components, and (b) shows the moment–rotation response. The FE models closely match the experimental results reported by Shi et al. [20], capturing both the initial stiffness and post-elastic behaviour, although a slight overestimation occurs in the inelastic range due to idealized boundary conditions and material simplifications. Bolt rupture was observed as the primary mode of failure in the experiments [20]. In the FE analyses, the model is terminated when the bolt reaches a PEEQ value of 0.075, indicating the onset of fracture. At this stage, the column web and stiffeners exhibit some plastic deformation, but the main and critical deformation occurs in the bolts, as shown in Figure 3(a).

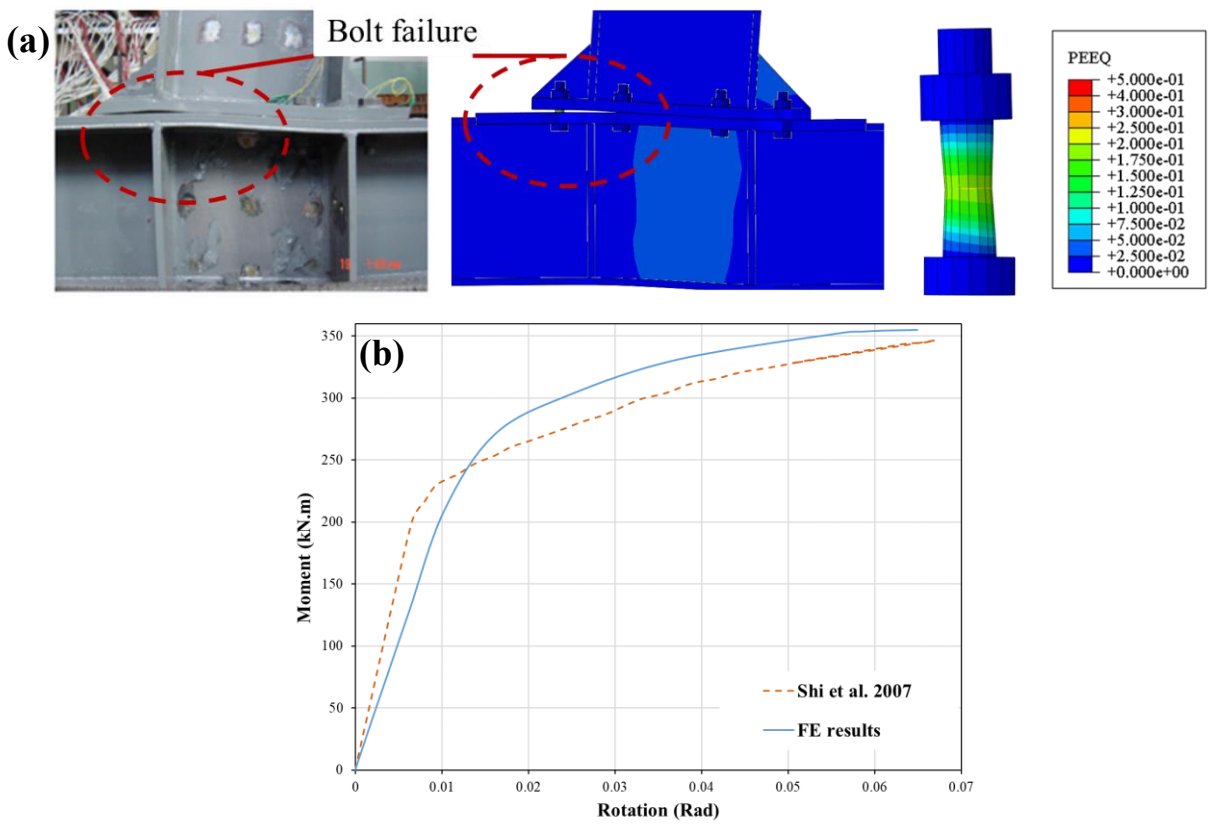


Figure 3. Validation results of the experimental connection model: (a) comparison of experimental and FE deformation, (b) comparison of moment-rotation response.

4 PROPOSED SLEEVE SYSTEM DESCRIPTION

This research aims to improve the behaviour of connection frameworks by enhancing the ductile capacity of the end plate, while maintaining their initial stiffness and strength [23]–[25]. The sleeve fuse is characterized by three key parameters: length (L), thickness (t), and amplitude (a) (see Figure 4). In this analysis, only one type of sleeve—the U-shaped wave (US)—is considered. The sleeve identification follows the format US–sleeve length (L) × amplitude (a) × thickness (t).

For improved ductility, it is essential that the sleeve deforms before any other component of the connection fails. Therefore, the maximum load-bearing capacity of the sleeve should be lower than that of the bolt. The sleeve's behaviour is influenced by its amplitude: a small amplitude limits deformation, causing the bolt to fail before the sleeve; a moderate amplitude allows some plastic deformation prior to bolt failure; and a large amplitude, referred to as PA (plastic amplitude), enables significant deformation, allowing the sleeve to yield before the bolt fails. The sleeve thus acts as a structural fuse, absorbing localized damage and protecting other connection components.

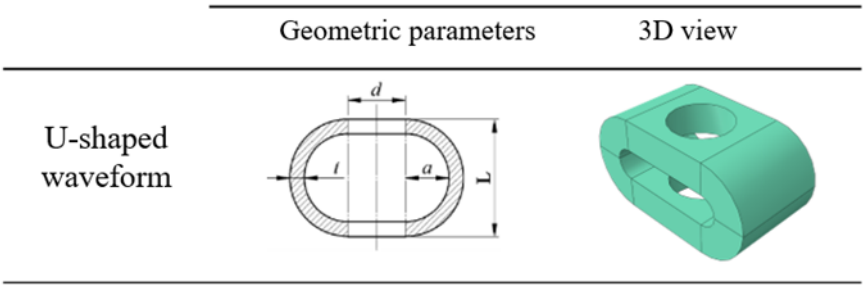


Figure 4. Sleeve geometry and identification considered in this study

5 RESPONSE OF THE U-SHAPED (US) SLEEVE SYSTEM TO MONOTONIC LOADING

The verified numerical model was employed to analyse the performance of beam-column end plate connections featuring different sleeve designs under monotonic loading. The results demonstrate that the US-type connections substantially improve the rotational capacity in comparison to standard connections. The moment-rotation behaviour of the US sleeves are illustrated in Figure 5. Additionally, Table 2 presents the normalized characteristic values of the sleeved connection compared to the experimental test connection.

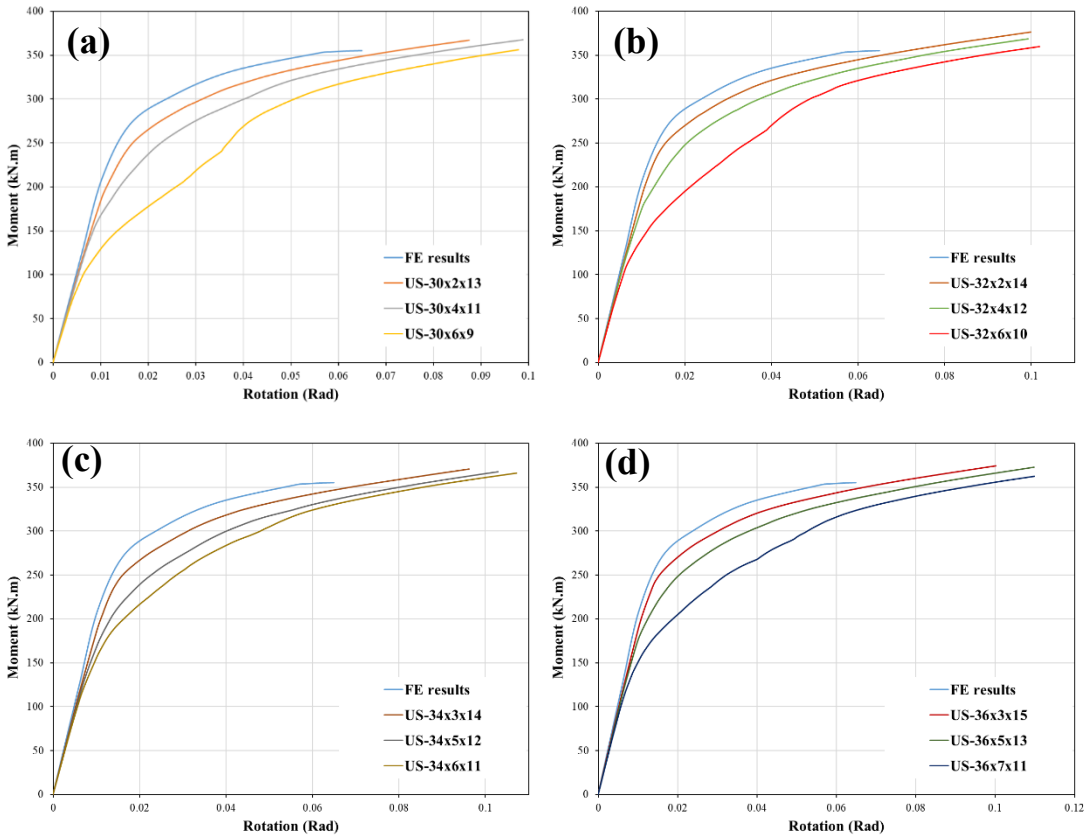


Figure 5. Moment-rotation curves of the U-shaped sleeve bolted connection for different sleeve lengths: (a) 30 mm, (b) 32 mm, (c) 34 mm, (d) 36 mm, (e) 38 mm, and (f) 40 mm

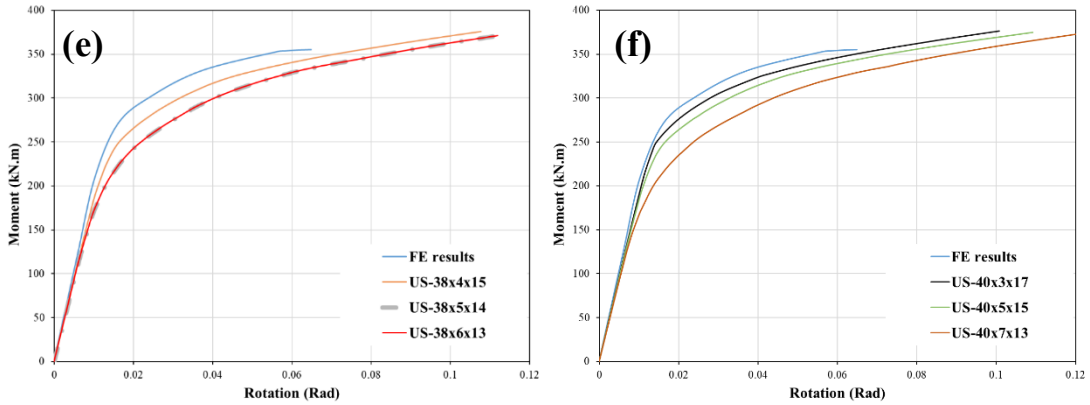


Figure 6 (continued). Moment-rotation curves of the U-shaped sleeve bolted connection for different sleeve lengths: (a) 30 mm, (b) 32 mm, (c) 34 mm, (d) 36 mm, (e) 38 mm, and (f) 40 mm.

Figure 5 illustrates that all U-shaped (US) sleeve configurations exhibit greater ductility than the standard connection. While the moment capacity remains unchanged, no significant variations are observed in the elastic behaviour of the connection. Among the tested configurations, the US-40x7x13 sleeve demonstrates the highest ductility, showing an increase of approximately 80%. It is essential to note that the analysis concludes when the bolt reaches its failure capacity. Sleeves with greater thickness provide limited ductility, as bolt failure occurs before the sleeve undergoes complete crushing, making this configuration less effective for the intended connection approach. In particular, US-40x3x17 and US-38x4x15 experience bolt failure prior to sleeve crushing (see Figure 6). Conversely, all other US sleeve configurations in this study exhibit complete sleeve crushing before bolt failure, which is the preferred failure mode under all loading conditions.

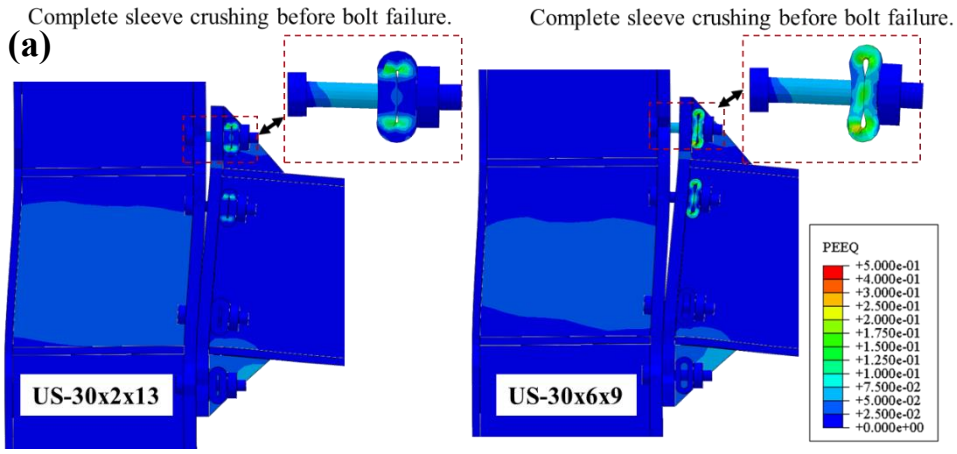


Figure 6. Failure modes of the US sleeves at bolt rupture under the given conditions for (a) 30 mm, (b) 38 mm, and (c) 40 mm, with varying amplitude and thickness values.

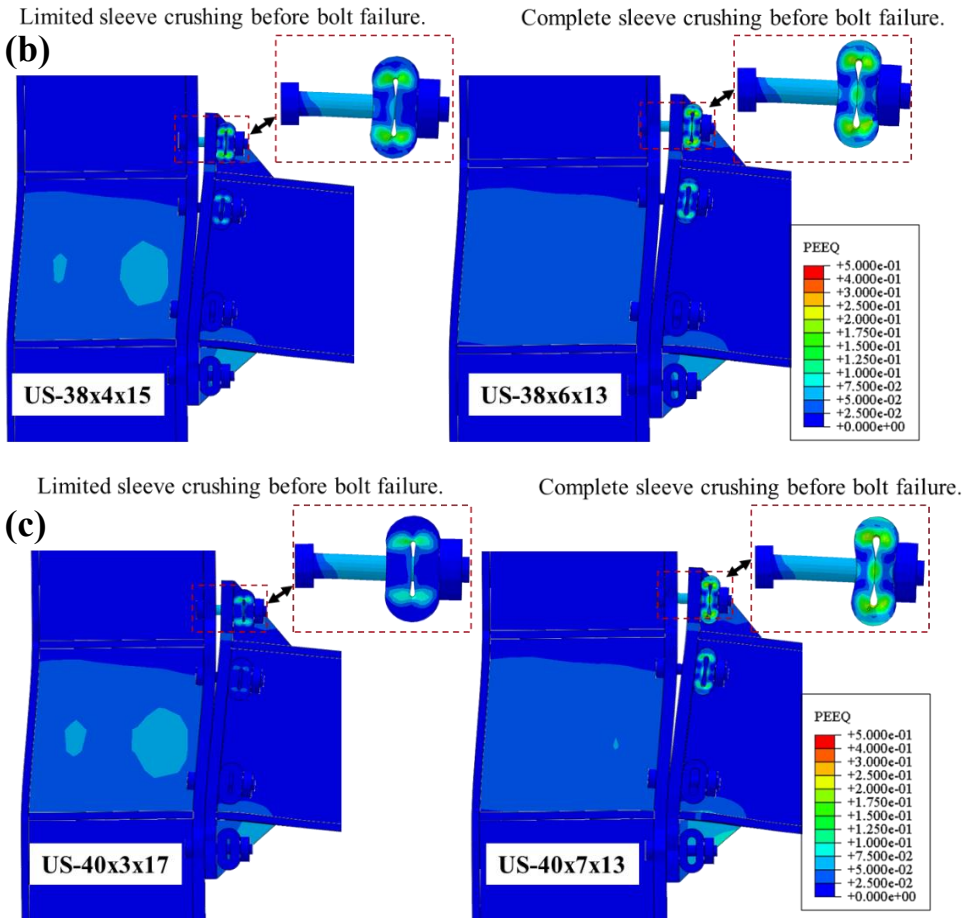


Figure 7 (continued). Failure modes of the US sleeves at bolt rupture under the given conditions for (a) 30 mm, (b) 38 mm, and (c) 40 mm, with varying amplitude and thickness values.

Furthermore, sleeves with shorter lengths exhibit the lowest rotational capacity due to their reduced strength and thinner walls (see Figure 5(a)). The moment capacity of the sleeved connection remains comparable to experimental standard connection test, with the highest moment capacity recorded for US-40x3x17. The findings also suggest that reducing sleeve thickness while increasing amplitude values enhances the likelihood of sleeve crushing before bolt failure, depending on the bolt's load-bearing capacity.

Table 2. Normalized values of the sleeve fuse connection relative to the standard connection.

Model	Max Rotation (Rad)	$\emptyset_{US}/\emptyset_{FE}$	Max Moment (kN.m)	M_{US}/M_{FE}
FE results	0.065	1.000	355.038	1.000
US-30x2x13	0.088	1.349	367.170	1.034
US-30x4x11	0.099	1.522	367.658	1.036
US-30x6x9	0.098	1.509	356.106	1.003
US-32x2x14	0.100	1.540	376.119	1.059

Table 2 (continued). Normalized values of the sleeve fuse connection relative to the standard connection.

Model	Max Rotation (Rad)	$\emptyset_{US}/\emptyset_{FE}$	Max Moment (kN.m)	M_{US}/M_{FE}
US-32x4x12	0.099	1.529	368.863	1.039
US-32x6x10	0.102	1.570	360.080	1.014
US-34x3x14	0.096	1.482	370.699	1.044
US-34x5x12	0.103	1.586	367.711	1.036
US-34x6x11	0.107	1.653	365.962	1.031
US-36x3x15	0.100	1.543	374.163	1.054
US-36x5x13	0.110	1.692	372.784	1.050
US-36x7x11	0.110	1.694	362.573	1.021
US-38x4x15	0.108	1.659	367.170	1.034
US-38x5x14	0.112	1.725	370.962	1.045
US-38x6x13	0.112	1.725	370.962	1.045
US-40x3x17	0.101	1.553	376.493	1.060
US-40x5x15	0.109	1.684	374.903	1.056
US-40x7x13	0.120	1.852	372.650	1.050

6 ENERGY DISSIPATION

The ductile behaviour of a connection is linked to the energy absorbed during applied loads. Figure 8 shows the cumulative energy dissipation at the bolt failure point, as predicted by FE simulations. The energy dissipation is quantified as the area beneath the monotonic moment–rotation curve, determined by projecting vertically from each point on the curve to the rotation axis, up to the maximum rotation. This definition aligns with conventional energy absorption concepts, in which the absorbed energy corresponds to the area under the load–deflection curve [28]. A schematic of the moment–rotation curve has also been included (see Figure 7) to illustrate the evaluated area.

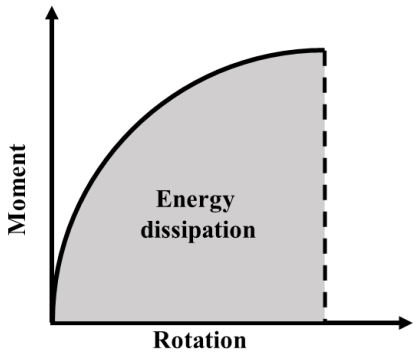


Figure 7. Schematic illustration of energy dissipation calculation under monotonic loading.

Connections incorporating sleeves demonstrated significantly higher ultimate capacities, leading to improved energy dissipation, particularly at higher rotational levels, when compared to conventional connections. The US-40x7x13 configuration, featuring 7 mm amplitude sleeves, exhibited the greatest energy dissipation. Other U-shaped sleeve configurations, such as US-38x5x14, US-36x5x13, US-34x6x11, US-32x2x14, and US-30x4x11, also showed superior energy dissipation within their respective sleeve length categories compared to the standard connection. Additionally, sleeves with amplitudes exceeding the anticipated plastic deformation threshold further enhanced energy dissipation, as shown in Figure 8. Energy dissipation was not assessed after the bolt failure point. It should be noted that this study focuses on monotonic loading; cyclic loading, which would provide further insights into hysteretic behaviour, residual rotations, and energy dissipation, will be addressed in a subsequent study.

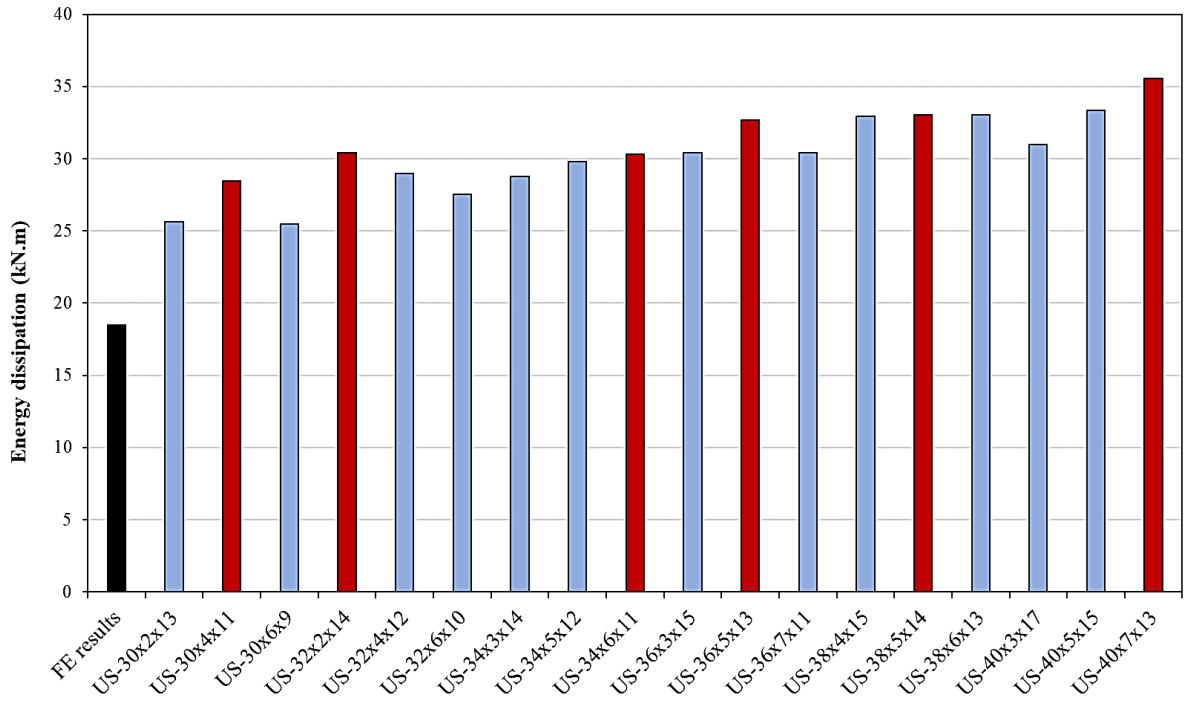


Figure 8. Comparison of energy dissipation.

7 CONCLUSION

This study examines the effectiveness of a steel sleeve fuse system in bolted end plate connections under monotonic loading conditions. A verified FE model was used, and a parametric study was conducted on U-shaped sleeves with varying lengths, thicknesses, and amplitudes. The study compared these configurations with standard connections, focusing on evaluating rotational performance and energy absorption.

The findings demonstrate that the sleeve fuse system significantly enhances both the rotational performance and energy dissipation of the connection, allowing for ductile behaviour. This makes the sleeve fuse system a promising, cost-effective solution for retrofitting steel structures, improving their performance while maintaining the integrity of existing components.

Key conclusions drawn from this study include:

- The parametric study confirmed the feasibility and effectiveness of the sleeve approach for various connection geometries, establishing its potential for practical applications.
- Although US waveform sleeves exhibited a slight decrease in initial stiffness, they significantly improved rotational capacity and enhanced energy dissipation.
- Increasing the amplitude of the US sleeves led to substantial improvements in rotational capacity.
- The energy dissipation of the US fuse system was substantially higher than that of standard connections, with amplitude playing a critical role in this improvement (around 90%).
- The sleeve design extended the failure point, allowing for higher rotations before failure, though failure still occurred within the connection itself (approximately 85%).
- The study also revealed that reducing sleeve thickness while increasing amplitude enhances the likelihood of sleeve crushing before bolt failure, depending on the bolt's load-bearing capacity.

In conclusion, the sleeve fuse system proves to be an effective method for enhancing energy dissipation and rotational capacity in steel end plate connections. This approach not only improves the seismic performance of steel structures but also presents a cost-efficient solution for retrofitting existing connections. Future research should focus on further refining sleeve designs and conducting experimental tests to evaluate their performance under more complex loading conditions, thereby broadening their applicability across a wider range of structural scenarios.

Acknowledgements

The author wishes to thank Firat University for funding this research. This study was supported by the Firat University Scientific Research Projects Unit (MF.25.37).

Conflict of Interest Statement

There is no conflict of interest between the authors.

Statement of Research and Publication Ethics

The study is complied with research and publication ethics.

Artificial Intelligence (AI) Contribution Statement

This manuscript was entirely written, edited, analyzed, and prepared without the assistance of any artificial intelligence (AI) tools. All content, including text, data analysis, and figures, was solely generated by the authors.

REFERENCES

[1] F. Kiakojouri, V. De Biagi, B. Chiaia, and M. R. Sheidaii, "Progressive collapse of framed building structures: Current knowledge and future prospects," *Eng. Struct.*, vol. 206, Dec. 2019, Art. no. 11006.

[2] K. Chen and K. H. Tan, "Structural behaviour of composite moment-resisting joints under column-removal scenario," *J. Struct. Eng. (United States)*, vol. 146, no. 3, 2020.

[3] M. A. Galal, M. Bandyopadhyay, and A. K. Banik, "Vulnerability of three-dimensional semirigid composite frame subjected to progressive collapse," *J. Perform. Constr. Facil.*, vol. 33, no. 3, 2019.

[4] Y. C. Wang, X. H. Dai, and C. G. Bailey, "An experimental study of relative structural fire behaviour and robustness of different types of steel joint in restrained steel frames," *J. Constr. Steel Res.*, vol. 67, no. 7, pp. 1149–1163, 2011.

[5] G. S. A. (GSA), *Progressive Collapse Analysis and Design Guidelines for New Federal Office Buildings and Major Modernization Projects*, 2003.

[6] M. Saravanan, R. Goswami, and G. S. Palani, "Replaceable fuses in earthquake resistant steel structures: A review," *Int. J. Steel Struct.*, vol. 18, no. 3, pp. 868–879, 2018.

[7] M. M. Garlock, J. M. Ricles, and R. Sause, "Experimental studies of full-scale posttensioned steel connections," *J. Struct. Eng.*, 2005.

[8] M. A. Chowdhury, A. Rahmzadeh, and M. S. Alam, "Improving the seismic performance of post-tensioned self-centering connections using SMA angles or end plates with SMA bolts," *Smart Mater. Struct.*, 2019.

[9] Y. J. Kim, S. H. Oh, and T. S. Moon, "Seismic behaviour and retrofit of steel moment connections considering slab effects," *Eng. Struct.*, vol. 26, no. 13, pp. 1993–2005, 2004.

[10] C.-H. Lee, S.-W. Jeon, J.-H. Kim, and C.-M. Uang, "Effects of panel zone strength and beam web connection method on seismic performance of reduced beam section steel moment connections," *J. Struct. Eng.*, vol. 131, no. 12, pp. 1854–1865, 2005.

[11] M. A. Shaheen, K. D. Tsavdaridis, and S. Yamada, "Comprehensive FE study of the hysteretic behaviour of steel-concrete composite and non-composite RWS beam-to-column connections," *J. Struct. Eng.*, vol. 3, no. 9, pp. 1–13, 2018.

[12] S. James and T. L. Roberto, "Bolted steel connections: Tests on T-stub components," *J. Struct. Eng.*, vol. 126, no. 1, pp. 91–99, 2000.

[13] L. S. Silva, A. Santiago, and P. Vila Real, "A component model for the behaviour of steel joints at elevated temperatures," *J. Constr. Steel Res.*, vol. 57, no. 11, pp. 1169–1195, 2001.

[14] British Standards Institution (BSI), *BS EN 1993-1-8:2005 – Eurocode 3: Design of steel structures – Part 1-8: Design of joints*, London, UK, 2005.

[15] D. Beg, E. Zupančič, and I. Vayas, "On the rotation capacity of moment connections," *J. Constr. Steel Res.*, vol. 60, no. 3–5, pp. 601–620, 2004.

[16] British Standards Institution (BSI), *BS EN ISO 898-1:2013 – Mechanical Properties of Fasteners Made of Carbon Steel and Alloy Steel Part 1: Bolts, Screws and Studs with Specified Property Classes – Coarse Thread and Fine Pitch Thread*, London, UK, 2013.

[17] M. A. Shaheen, A. S. J. Foster, L. S. Cunningham, and S. Afshan, "A numerical investigation into stripping failure of bolt assemblies at elevated temperatures," *Structures*, vol. 27, pp. 1458–1466, 2020.

[18] Zingoni, *Shell Structures in Civil and Mechanical Engineering*, 2nd ed., ICE Publishing, 2017.

[19] M. A. Shaheen, A. A. Andrew, and L. S. Cunningham, "A novel device to improve robustness of end plate beam-column connections," *Structures*, vol. 28, Oct. 2020, pp. 2415–2423.

[20] Y. Shi, G. Shi, and Y. Wang, "Experimental and theoretical analysis of the moment–rotation behaviour of stiffened extended end-plate connections," *J. Constr. Steel Res.*, vol. 63, no. 9, pp. 1279–1293, 2007.

[21] British Standards Institution (BSI), *BS EN 1993-1-1: Eurocode 3 – Design of steel structures – Part 1-1: General rules and rules for buildings*, London, UK, 2005.

[22] CEN, *BS EN 1993-1-2:1995 – Eurocode 3: Design of Steel Structures – Part 1-2: General Rules – Structural Fire Design*, 1995.

[23] M. A. Shaheen, "A new idea to improve the cyclic performance of end plate beam–column connections," *Eng. Struct.*, vol. 253, p. 113759, 2022.

[24] M. A. Shaheen, A. Alsaleh, and L. S. Cunningham, "Experimental tests on a novel bolt sleeve device to increase the ductility of steel end plate connections," *J. Constr. Steel Res.*, vol. 214, p. 108510, 2024.

[25] M. A. Shaheen, M. A. Galal, L. S. Cunningham, and A. S. Foster, "New technique to improve the ductility of steel beam to column bolted connections: A numerical investigation," *CivilEng*, vol. 2, no. 4, pp. 929–942, 2021.

[26] M. Atar and B. Çete, "Enhancing structural resilience: Exploring the novel sleeve method for steel T-stub connections," *Fırat Üniversitesi Mühendislik Bilimleri Dergisi*, vol. 36, no. 1, pp. 147–158, 2024.

[27] M. Atar, "Comparative numerical study of sleeve fuse systems and RBS for enhancing cyclic performance in steel end-plate connections," *Int. J. Steel Struct.*, pp. 1–17, 2025.

[28] K. Al Kulabi and A. A. Al Zahid, "Influence of dynamic loading induced by free fall ball on high-performance concrete slabs with different steel fiber contents," *Struct. Monit. Maint.*, vol. 6, no. 1, pp. 19–32, 2019, doi: 10.12989/smm.2019.6.1.019.

BİTLİS EREN ÜNİVERSİTESİ
FEN BİLİMLERİ DERGİSİ

ISSN: 2147-3129 / e-ISSN: 2147-3188

Article Type : Research Article
Received : April 7, 2025
Revised : June 23, 2025
Accepted : August 1, 2025
DOI : 10.17798/bitlisfen.1670251

Year : 2025
Volume : 14
Issue : 3
Pages : 1519-1533

SYNTHESIS AND ELECTRONIC PROPERTIES OF AXIALLY DISUBSTITUTED SILICON (IV) PHTHALOCYANINE 9-PHENYL-9H-XANTHENE-9-OXY

Derya GÜNGÖRDÜ SOLĞUN [1]

[1] *Van Yüzüncü Yıl University, Department of Chemistry and Chemical Business Technologies, Laboratory Technology Program, Van, Türkiye, deryagungordu@yyu.edu.tr*

ABSTRACT

In this research, a new axial phthalocyanine complex compound was synthesized. This study involved the synthesis of the novel silicon phthalocyanine prepared by reacting $SiPcCl_2$, 9-phenyl-9H-xanthen-9-ol and K_2CO_3 in dry toluene. The novel silicon phthalocyanine was characterized by using different spectroscopic techniques including 1H NMR, UV-Visible, FT-IR and mass spectroscopy. The electronic properties of the compound for example the aggregation and solubility parameters investigated. Aggregation is a crucial parameter dictating the functional performance of phthalocyanines. Aggregation is closely related to temperature, concentration, type of ligand attached to the phthalocyanine ring, substituents attached to peripheral positions and polarity of the solvent. Ligands attached to the phthalocyanine ring disrupt the planarity of the ring, resulting in reduced aggregation. For these reasons, in this study, we focused on the aggregation characteristics of phthalocyanines and how axial ligand modifications regulate this behavior. Axial ligand (especially those with metals like Si, Ge, Sn) coordination increases steric bulk and reduces stacking. The low aggregation tendency of phthalocyanines provides significant advantages, especially in photodynamic therapy (PDT), optoelectronics and sensor applications. Photodynamic therapy (PDT) is a light based therapeutic modality that requires the coordinated presence of three key components: a photosensitizer (PS), a light source, and molecular oxygen. Phthalocyanine based photosensitizers (Pcs) are among the most promising candidates for photodynamic therapy (PDT) due to their favorable photophysical and photochemical properties. An ideal photosensitizer should exhibit strong absorption (600–800 nm), where tissue penetration of light is optimal. Phthalocyanines meet this criterion through their intense Q band absorption, usually around 670–700 nm. Moreover, they are capable of efficiently generating singlet oxygen ($\Phi\Delta$), a key cytotoxic agent in PDT. In addition to their photodynamic efficiency, phthalocyanines demonstrate excellent chemical and photostability.

Preliminary research was conducted for photosensitizer properties of the compound. After researches, the results have showed that singlet oxygen quantum yield has increased in the photodynamic study ($\Phi\Delta$=0.19) compare to the Std-SiPc ($\Phi\Delta$= 0.15)

Keywords: Silicon phthalocyanine, Synthesis, Singlet oxygen, Electronic properties, Aggregation.

1 INTRODUCTION

Phthalocyanines (Pcs) which is aromatic macrocyclic compounds in coordination chemistry have high conjugation. Pcs consist of a 16-membered (8 carbon, 8 nitrogen) planar macrocycle with an 18-π electron system. The most important factor affecting the solubility of phthalocyanines is the strong π interactions between phthalocyanine molecules. As the π-stacking is prevented, the solubility of phthalocyanines in different solvents is increased. By adding axial ligands to the central metal atom (Si, Al, Ge, Ti, Sn, etc.), the solubility can be increased by reducing the π interaction between molecules.

Due to the electronic delocalization of phthalocyanines, they have been found to be useful for many applications in different fields. It is well known by scientists that phthalocyanines have been investigated in a wide range. These compounds research or usage areas can be listed as catalysts [1-2], electrochromics [3], photovoltaics [4-5], non-linear optics [6-7], dyes [8], antioxidants [9-10], antifungals [11], antibacterials [12], photosensitizers, sonosensitizers for photodynamic therapy [13-15], liquid crystals [16], gas sensors [17], thermal stabilities [18] or metal ion sensors [19-20]. Cancer is a disease that has been increasing worldwide recently and is being treated in different combinations [21]. Photodynamic therapy (PDT), which is an alternative treatment method to chemotherapy and radiotherapy, which are traditional methods used in the fight against this disease, is attracting attention [22]. PDT is based on the irradiation of the photosensitizer (PS) compound with light in the presence of oxygen. Phthalocyanines are complexes with high absorption coefficients in the 600-800 nm region [23]. The light used in PDT is usually in the range of 650-850 nm, which allow light to pass through human tissues. After light irradiation, energy is transferred from the photosensitizer to elemental oxygen and singlet oxygen is produced. After this production, singlet oxygen damages the DNA of cancer cells and can cause cell death [24-25]. The use of low-energy light and few side effects makes PDT more advantageous than other cancer treatment methods [26]. This treatment offers the patient comfort and deeper tissue penetration. For these purposes, it is aimed to synthesize new phthalocyanines and to reveal the photosensitizer potential of the synthesized compound.

In this study, a new bis(9-phenyl-9H-xanthen-9-oxy) phthalocyaninato silicon (IV) compound was synthesized and characterized. Additionally, the spectroscopic and photochemical properties of the phthalocyanine complex were investigated to determine their potential as photosensitizer in photodynamic therapy.

2 MATERIAL AND METHOD

Chloroform ($CHCl_3$), tetrahydrofuran (THF), dimethylformamide (DMF), and dimethyl sulfoxide (DMSO) were purchased from Sigma-Aldrich. $SiPcCl_2$ and 9-phenyl-9H-xanthen-9-ol were supplied by Alfa Aesar. Potassium carbonate (K_2CO_3), methanol, dichloromethane (CH_2Cl_2), and toluene were supplied by Merck and Acros Organics respectively. For structure characterization of UV visible spectra a Hitachi U-2900 Spectrophotometer was used. A Thermo Scientific FT-IR spectrometer was used to determine the vibration bands. NMR spectra were determined with an Agilent 400 MHz NMR spectrometer. Mass analysis of the compound was performed using an LC-MS electrospray.

2.1 Synthesis

Bis(9-phenyl-9H-xanthen-9-oxy) phthalocyaninato silicon (IV) (1)

$SiPcCl_2$ (75 mg, 0.12 mmol), 9-phenyl-9H-xanthen-9-ol (132 mg, 0.48 mmol) and K_2CO_3 (55 mg, 1.43 mmol) were mixed in dry toluene (10 mL) and refluxed for 24 h. Then the mixture has cooled to room temperature, the organic phase was separated by extraction (chloroform: water). After evaporation of solvent, the product was obtained. The product was dissolved in THF. Purification steps included by washing with ethanol and methanol. After this step, the product was dissolved in CH_2Cl_2 and filtered again. Finally, CH_2Cl_2 solutes were taken. m.p. > 300°C. Yield: 33 mg (25 %), FTIR (ATR), ν/cm^{-1}: 3053 (Ar-H), 1602 (C=N), 1571-1479 (Ar-C=C), 1450, 1315 (C-N), 1265, 1246-1151 (Ar-O-Ar), 1099-1070 (Si-O-C), 1033, 894, 871, 732, 704, 628. ^{1}H NMR (400MHz, DMSO-d_6), (δ): 7.35, 7.34, 7.31, 7.27, 7.24, 7.13, 7.09, 6.76. UV–Vis (CH_2Cl_2, 1×10^{-5} M): λmax/nm (log ε): 675 (5.17), 350 (4.86). MS (ESI), (m/z): Calculated for $C_{70}H_{42}N_8O_4Si$: 1086.3; Found:1087 $[M+H]^+$.

3 RESULTS AND DISCUSSION

The synthesis method of phthalocyanine **1** is given in Figure1. This compound is soluble in tetrahydrofuran, chloroform, dichloromethane, N,N-dimethylformamide, dimethyl sulphoxide. After the synthesis of the phthalocyanine, purification processes were carried out . Then the characterization process was started. In the IR spectrum of phthalocyanine **1** was observed aromatic vibrations at 3086 cm^{-1}, C=N peak was observed at 1602, the C=C peaks peak was observed at 1571-1479 cm^{-1}, C-N peak was observed at 1315, Ar-O-Ar bond

vibrations was observed at 1246-1151, Si-O-C stretch peak was observed at 1099-1070 cm^{-1} which was supported data in the literature [27].

In the ESI mass spectrometry gived ion peak at 1087 $[M+H]^+$ which was the expected.

In the ^1H NMR spectrum of compound **1**, aromatic protons were located at in the range of 7.35-6.76 ppm support the structure.

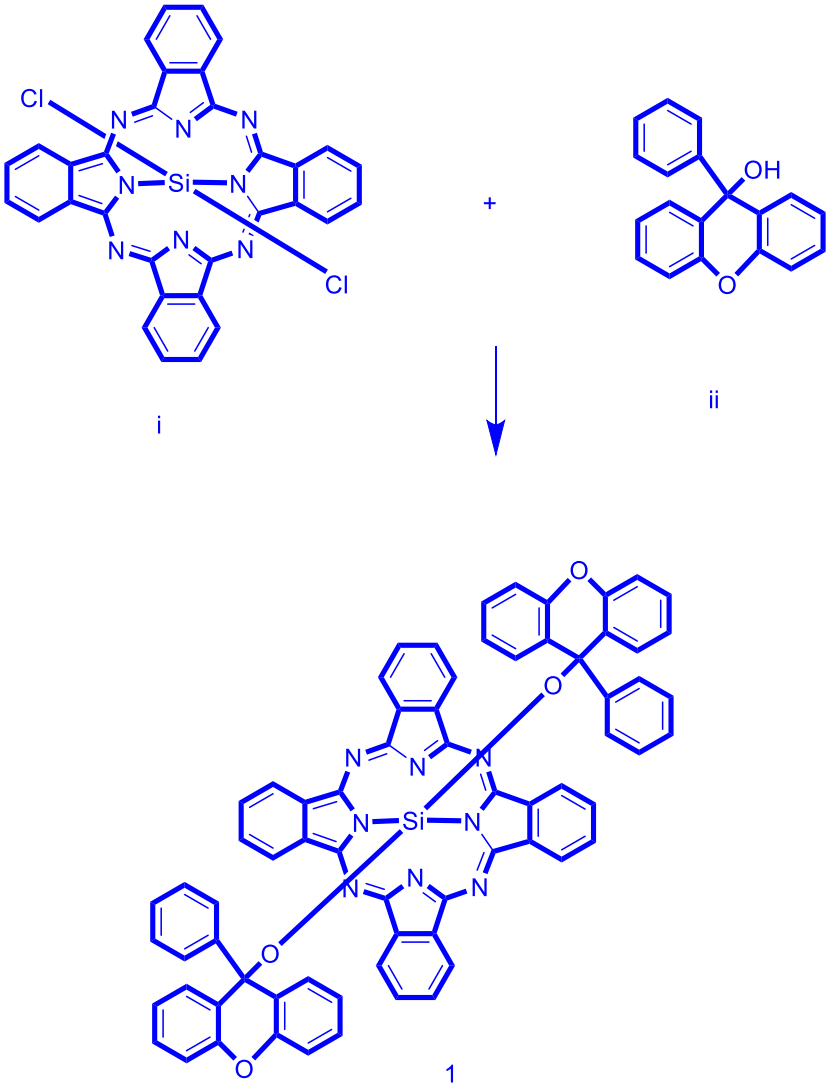


Figure 1. Synthesis scheme of compound 1.

The absorbance values saw in the UV-visible spectrum of the phthalocyanine complex are the Q band at 675 nm and the B band at 350 nm. These values are consistent with the absorbance values expected for the phthalocyanine structure. Electronic measurements of the compound in the range of $1.4x10^{-5}$ - $0.2x10^{-6}$ M show that the compound is not aggregated (Figure 2). These observed values show that the compound meets the prerequisite for use as a photosensitizer. If further studies support this parameter, the compound can be used as a photosensitizer.

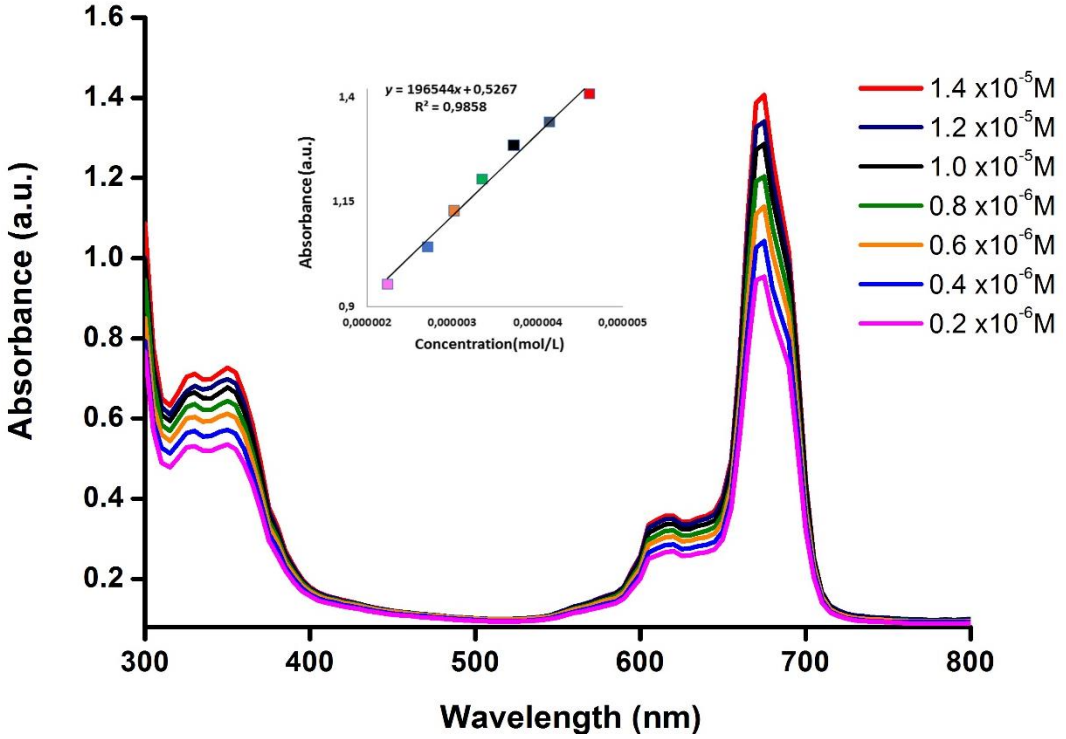


Figure 2. Absorption spectra of compound 1 in CH2Cl2 at 1.4x10-5- 0.2x10-6M concentrations.

The electronic absorption of compound 1 in tetrahydrofuran, chloroform, dichloromethane, N,N-dimethylformamide, dimethyl sulphoxide is shown in Figure 3. This compound is easily dissolved this solvents.

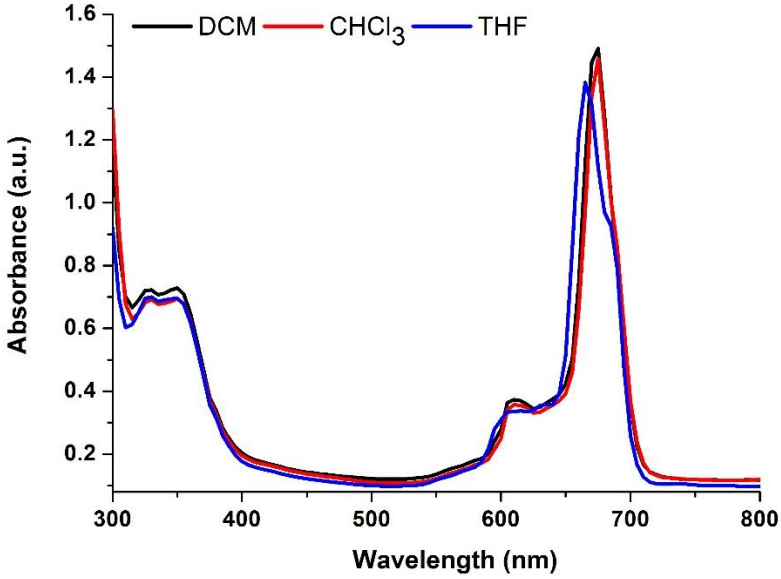


Figure 3. Absorption spectra of compound 1 in dichloromethane, chloroform and tetrahydrofuran solvents.

Phthalocyanines are interesting with their singlet oxygen production capacity. A quality sensitizer should have a great singlet oxygen efficiency. The light used in this study was provided by a 150 volt lamp. The sample was then exposed to light passed through an optical filter with a wavelength range of 650-720 nm, and placed in the cuvette. The singlet oxygen quantum yield of compound **1** was measured at 417 nm. DPBF was dissolved in DMSO under dark conditions, and the sample was subsequently irradiated within the Q band absorption region. The degradation of DPBF at 417 nm was monitored after each 5 s illuminate. While the Q bands of **1** did not alter, DPBF absorbance was decreased (Figure 4). Compound **1** has a high value (Φ_Δ= 0.19) than Std-SiPc (Φ_Δ= 0.15) [28].

Singlet oxygen quantum yield (Φ_Δ), a critical parameter in evaluating a photosensitizer's efficiency in photodynamic therapy, is typically calculated using a relative method with a standard reference photosensitizer. The singlet oxygen quantum yield (Φ_Δ) of a photosensitizer was determined by a comparative method using a reference compound with a known Φ_Δ value. The Φ_Δ value was calculated according to the equation:

$$\Phi_\Delta = \Phi_\Delta^{\mathrm{Std}} \times \frac{R}{R_{\mathrm{Std}}} \times \frac{I_{\mathrm{abs}}^{\mathrm{Std}}}{I_{\mathrm{abs}}} \quad (1)$$

Φ_Δ: Singlet oxygen quantum yield of the sample

Φ_Δ^{std}: Singlet oxygen quantum yield of the standard

R_{DPBF}: Photobleaching rate of the singlet oxygen quencher in the presence of the sample

R_{DPBF}^{Std}: Photobleaching rate in the presence of the standard

I_{abs}: Absorbance of the sample at the irradiation wavelength

$Iabs^{std}$: Absorbance of the standard at the irradiation wavelength

The good performance of the phthalocyanine compound in singlet oxygen production shows that it has an advantageous effect. It shows the potential to be used in photodynamic therapy with other supportive tests.

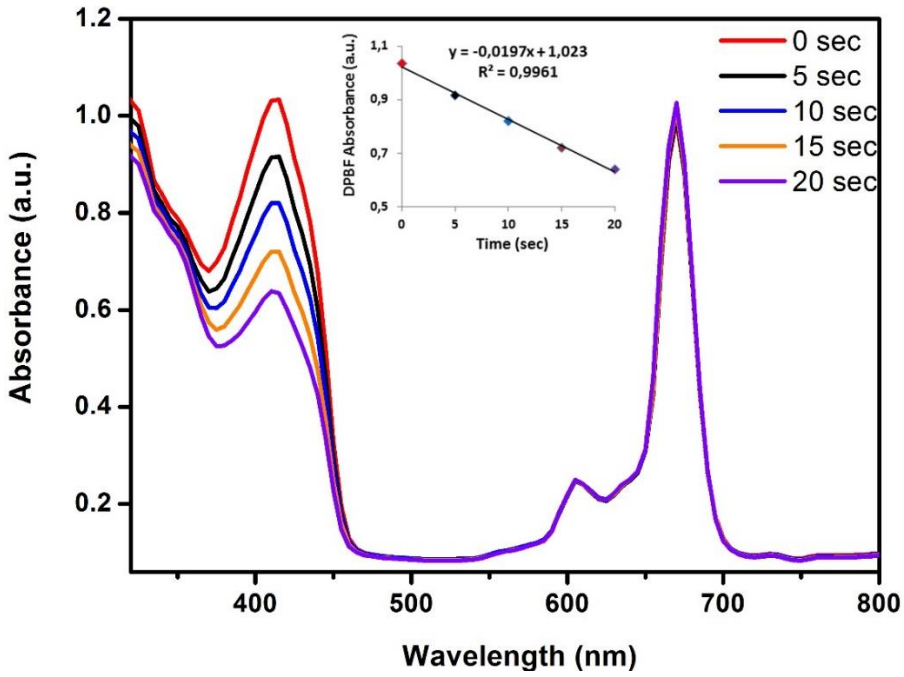


Figure 4. Measurement diagram of singlet oxygen quantum yield for compound 1.

4 CONCLUSION AND SUGGESTIONS

Bis(9-phenyl-9H-xanthen-9-oxy) phthalocyaninato silicon (IV) compound was originally synthesized. Compound **1** was characterized by ^{1}HNMR, UV-visible, FTIR, mass spectra. The electronic properties of bis(9-phenyl-9H-xanthen-9-oxy) phthalocyaninato silicon (IV) and its potential to produce singlet oxygen were investigated. Compound **1** show the potential to be used as a singlet oxygen generating agent for PDT.

This work has introduced a novel phthalocyanine derivative, bis(9-phenyl-9H-xanthen-9-oxy) phthalocyaninato silicon (IV), which was synthesized and characterized for the first time. The new axially disubstituted silicon(IV) phthalocyanine (Compound **1**) was confirmed by comprehensive spectroscopic analysis (^{1}H NMR, UV-Vis, FT-IR, and mass spectrometry). Basic electronics and photochemical properties of this compound were examined in detail, with particular focus on its ability to generate singlet oxygen ($^{1}O_2$).

The results demonstrate that Compound **1** is a highly efficient singlet oxygen photosensitizer. The singlet oxygen quantum yield (Φ_Δ) of this new phthalocyanine was measured as 0.19 which is superior to that of a standard silicon phthalocyanine (Φ_Δ= 0.15). This enhanced $^{1}O_2$ generation capacity indicates a notable improvement over similar phthalocyanine compounds reported in the literature. Such performance underscores the compound's potential not only in photodynamic therapy but also in advanced multi-modal treatment approaches. In

addition to its high singlet oxygen production, the structural features of Compound 1 impart other advantages for biomedical application. The bulky 9-phenyl-9H-xanthen-9-ol ligands likely reduce π–π stacking interactions, thereby lowering the aggregation tendency and improving solubility. These traits are highly desirable for phthalocyanine-based photosensitizers in biological environments. In summary, this study not only introduces a new silicon phthalocyanine derivative to the literature, but also demonstrates its promise as an efficient singlet oxygen generator for photodynamic therapy.

Acknowledgements

I would like to express my sincere gratitude to Prof. Dr. Mehmet Salih Ağırtaş for his valuable support and guidance throughout this study.

Statement of Research and Publication Ethics

The study is complied with research and publication ethics.

Artificial Intelligence (AI) Contribution Statement

This manuscript was entirely written, edited, analyzed, and prepared without the assistance of any artificial intelligence (AI) tools. All content, including text, data analysis, and figures, was solely generated by the authors.

REFERENCES

[1] Y. Qian , C. Xu , X. Zhang , and X. Sun, ‘‘S-doped rich-defect cobalt-based carbon catalyst derived from cobalt phthalocyanine as catalysts of peroxymonosulfate for degradation of tetracycline hydrochloride from water,’’ *Journal of Environmental Chemical Engineering*, vol. 12, pp.112557, 2024.

[2] S, Wu, Y. Duan,W. Kuang, W. Dong, X. Cui, X. Zhang, and Qian Duan, ‘‘Homogeneous catalysis and heterogeneous recovery: Thermo-responsive copolymer visible light catalyst with phthalocyanine as side groups,’’ *Reactive and Functional Polymers*, vol. 197, pp. 105857, 2024.

[3] P. Şen, F. Dumludağ, B. Salih, A. R. Özkaya, and Ö. Bekaroğlu, ‘‘Synthesis and electrochemical, electrochromic and electrical properties of novel s-triazine bridged trinuclear Zn(II), Cu(II) and Lu(III) and a tris double-decker Lu(III) phthalocyanines,’’ *Synthetic Metals,* vol.161, pp. 1245-1254, 2011.

[4] D. G. Solğun, U. Yildiko, and M. S. Ağırtaş, ‘‘Synthesis of bis-(benzhydryloxy) substituted axially silicon(IV) phthalocyanine: investigation of photophysical, photochemical, and computational electronic properties,’’ *Phosphorus, Sulfur, and Silicon and the Related Elements,* vol. 199, pp. 324-336, 2024.

[5] Ö. Ödemiş, M. S. Ağırtaş, D. G. Solğun, and A. Özkartal, ‘‘Effect of silver nanoparticles prepared by green chemistry on the photovoltaic properties of zinc phthalocyanine,’’ *Chemical Papers*, vol. 78, pp. 3735–3746, 2024.

[6] D. Gounden, N.Nombona, and W.E. van Zyl, ‘‘Recent advances in phthalocyanines for chemical sensor, non-linear optics (NLO) and energy storage applications,’’ *Coordination Chemistry Reviews*, vol. 420, pp. 213359, 2020.

[7] D. G. Solğun, Y. Gündoğdu, H. Ş Kılıç and M. S. Ağırtaş, ‘‘Synthesis of novel 2-(benzhydryloxy) phenoxy-substituted zinc phthalocyanine, third-order nonlinear optical and fluorescence properties,’’ *Bulletin of Materials Science,* vol. 45, pp. 235, 2022.

[8] S. A. Aal, and D. Awadh, ‘‘The effect of anchoring group on the performances of metal-free phthalocyanine and metallophthalocyanine dye/titanium dioxide interface for dye-sensitized solar cells,’’ *Surfaces and Interfaces*, vol. 32, pp. 102089, 2022.

[9] M. S. Ağırtaş, B.Cabir, and S. Özdemir, ‘‘Novel metal (II) phthalocyanines with 3,4,5-trimethoxybenzyloxy-substituents: Synthesis, characterization, aggregation behaviour and antioxidant activity,’’ *Dyes and Pigments*, vol. 96, pp.152-157, 2013.

[10] G. P. Amaral, G. O. Puntel, C. L. D. Corte, F. Dobrachinski, R. P. Barcelos, L. L. Bastos, D. S. Ávila, J. B. T. Rocha, E.O. Silva, R. L. Puntel, and F. A. A. Soares, ‘‘The antioxidant properties of different phthalocyanines,’’ *Toxicology in Vitro,* vol. 26, pp. 125-132, 2012.

[11] X.S. Li, J.Guo, J.J.Zhuang, B.Y. Zheng, M. R. Ke, and J.D. Huang, ‘‘Highly positive-charged zinc(II) phthalocyanine as non-aggregated and efficient antifungal photosensitizer,’’ *Bioorganic & Medicinal Chemistry Letters,* vol. 25, pp. 2386-2389, 2015.

[12] M.Wysocki, D. Ziental, M. Jozkowiak, J. Dlugaszewska, H. P. Kempisty, E.Güzel, and L. Sobotta, ‘‘Porphyrazine/phthalocyanine hybrid complexes – Antibacterial and anticancer photodynamic and sonodynamic activity,’’ *Synthetic Metals,* vol. 299, pp. 117474, 2023.

[13] K. Hirakawa, A.Katayama, S. Yamaoka, T. Ikeue, and S.Okazaki, ‘‘Photosensitized protein damage by water-soluble phthalocyanine zinc(II) and gallium(III) complexes through electron transfer and singlet oxygen production,’’ *Chemical Physics Letters,* vol. 802, pp. 139764, 2022.

[14] X.Xing, S. Zhao, T. Xu, L. Huang, Y.Zhang, M. Lan, C. Lin, X.Zheng, and P.Wang, ‘‘Advances and perspectives in organic sonosensitizers for sonodynamic therapy,’’ *Coordination Chemistry Reviews,* vol. 445, pp. 214087, 2021.

[15] L. C. Nene, and H. Abrahamse. ‘‘Design consideration of phthalocyanines as sensitizers for enhanced sono-photodynamic combinatorial therapy of cancer,’’ *Acta Pharmaceutica Sinica B,* vol.14, pp.1077-1097, 2024.

[16] S.H. Choi, .J. A. Kim, G. S. Heo, and H. G. Park, ‘‘Electro-optical characteristics of polymer-dispersed liquid crystal containing copper (II) phthalocyanine as a function of UV irradiation time,’’ *Journal of Molecular Liquids,* vol. 363, pp. 119821, 2021.

[17] M. S.Ağırtaş, A. Altındal, B. Salih, S. Saydam, and Ö. Bekaroğlu, ‘‘Synthesis, characterization, and electrochemical and electrical properties of novel mono and ball-type metallophthalocyanines with four 9,9-bis(4-hydroxyphenyl)fluorene,’’ *Dalton Transactions*, vol. 40, pp. 3315-3324, 2011.

[18] M. S. Ağırtaş, D. G. Solğun, S. Özdemir, and M. S. İzgi, ‘‘Synthesis of tetra 3,4-dimethoxyphenethoxy peripheral substituted metallophthalocyanines and investigation of some properties,’’ *Chemistry Select,* vol. 3, pp. 3523–3528, 2018.

[19] D. G. Solğun, and M.S. Ağırtaş, ‘‘Synthesis of novel an axially substituted silicon phthalocyanine and determination of its selectivity for Fe $^{3+}$,’’ *Journal of Molecular Structure*, vol. 1286, pp. 135577, 2023.

[20] X. Wang, G. Ma, W.Zhang, W.Zhao, G. Lian, S. Zhang, D. Zhang, and W. Liu, ‘‘Multifunctional phthalocyanine NIR sensor for fluorescent and colorimetric dual-imaging and removal of intracellular and environmental Cu^{2+},’’ *Journal of Photochemistry & Photobiology, A: Chemistry,* vol. 449, pp. 115355, 2024.

[21] A. Abd-El-Aziz, S. A. Ahmed, X. Zhang, N. Ma, and A. S. Abd-El-Aziz, ‘‘Macromolecules incorporating transition metals in the treatment and detection of cancer and infectious diseases: Progress over the last decade,’’ *Coordination Chemistry Reviews,* vol. 510, pp. 215732, 2024.

[22] L. C. Nene, and H. Abrahamse, ‘‘Design consideration of phthalocyanines as sensitizers for enhanced sono-photodynamic combinatorial therapy of cancer,’’ *Acta Pharmaceutica Sinica B,* vol. 14, pp. 1077-1097, 2024.

[23] M. S. Ağırtaş, and M. S. İzgi, ‘‘Synthesis and characterization of new metallophthalocyanines with four phenoxyacetamide units,’’ *Journal of Molecular Structure,* vol. 927, pp. 126–128, 2009.

[24] A. Nas, S. Fandaklı, H. Kantekin, A. Demirbas, and M. Durmus, ‘‘Novel organosoluble metal-free and metallophthalocyanines bearing triazole moieties: microwave assisted synthesis and

determination of photophysical and photochemical properties,'' *Dyes and Pigments,* vol. 95 pp.8-17, 2012.

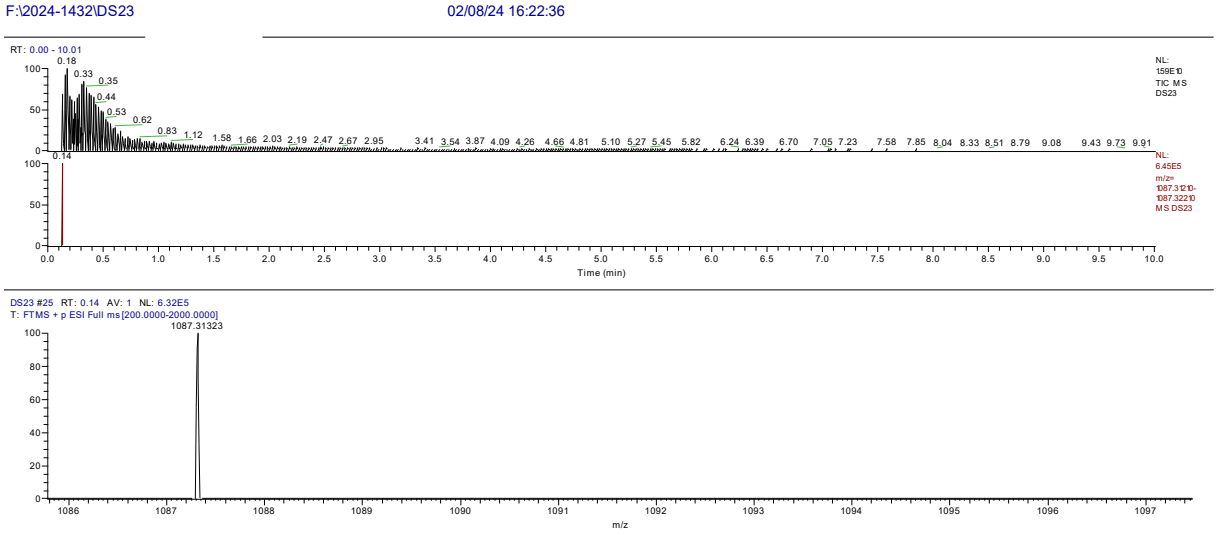
[25] S. Aydogdu, G. Y. Atmaca, A. Erdoğmuş, and A. Hatipoglu,''Synthesis of a new Zn- phthalocyanine, photophysical, photochemical, and sono-photochemical properties and DFT studies, '' *Polyhedron,* vol. 256, pp. 116989, 2024.

[26] Ü. Demirbas, C. Göl, B. Barut, R. Bayrak, M. Durmus, H. Kantekin, and İ. Değirmencioğlu, ''Peripherally and non-peripherally tetra-benzothiazole substituted metal-free, zinc(II) and lead(II) phthalocyanines: synthesis, characterization, and investigation of photophysical and photochemical properties,'' *Journal of Molecular Structure*, vol. 1130, pp. 677-687, 2017.

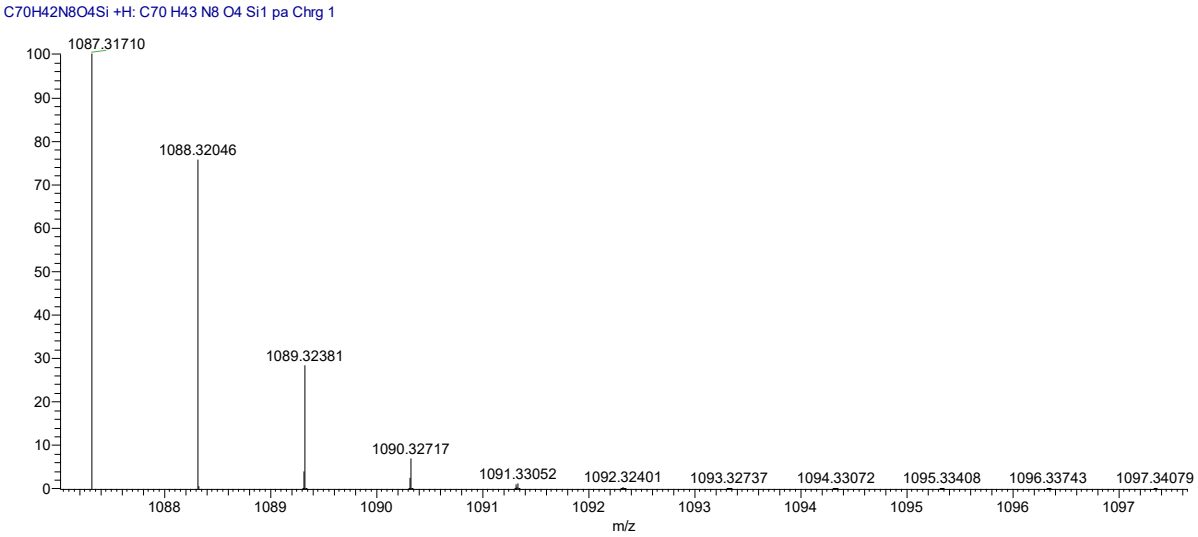
[27] İ. Ömeroğlu, E.N. Kaya, M. Göksel, V. Kussovski, V. Mantareva, and M. Durmus, ''Axially substituted silicon(IV) phthalocyanine and its quaternized derivative as photosensitizers towards tumor cells and bacterial pathogens,'' *Bioorganic Medicinal Chemistry,* vol. 25, pp. 5415–5422, 2017.

[28] S.Y. Al-Raqa, K. Khezami, E.N. Kaya, and M. Durmuş, ''A novel water soluble axially substituted silicon(IV) phthalocyanine bearing quaternized 4-(4-pyridinyl)phenol groups: Synthesis, characterization, photophysicochemical properties and BSA/DNA binding behavior,'' *Polyhedron,* vol. 194, pp. 114937, 2021.

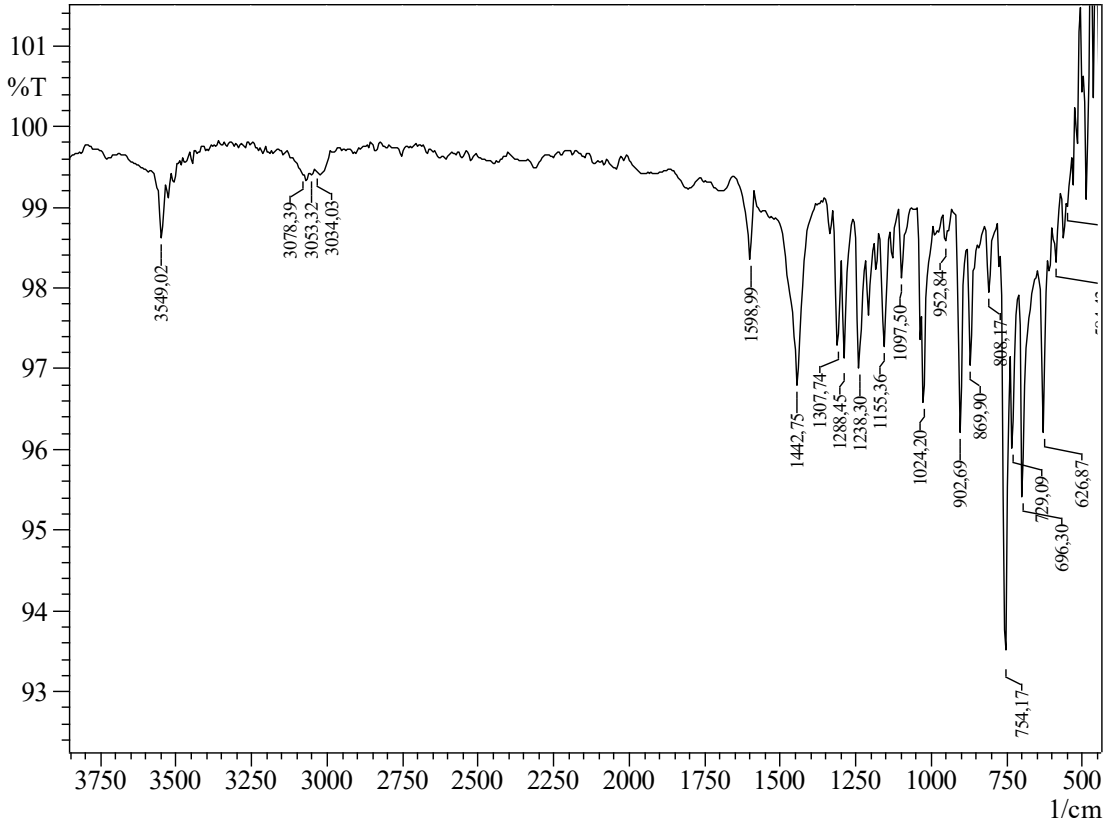
SUPPLEMETARY MATERIALS



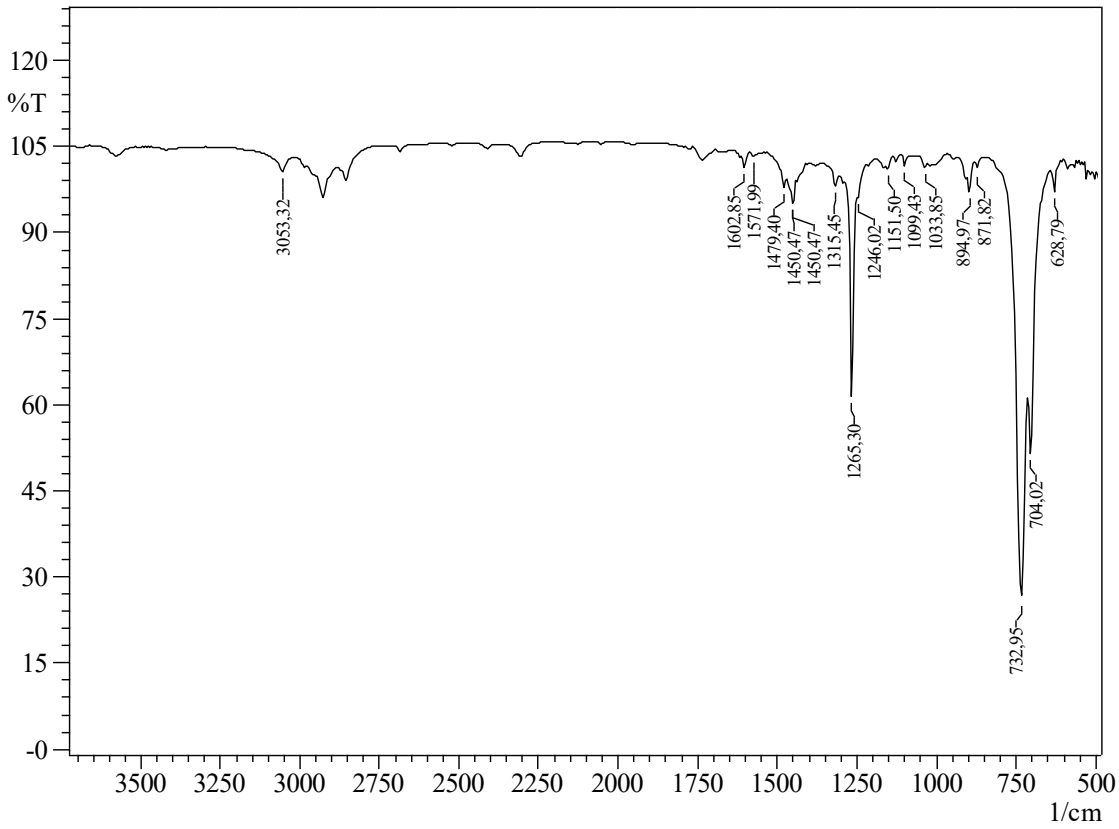
Appendix 1. HRMS (ESI) spectrum of $[M+H]^+$.



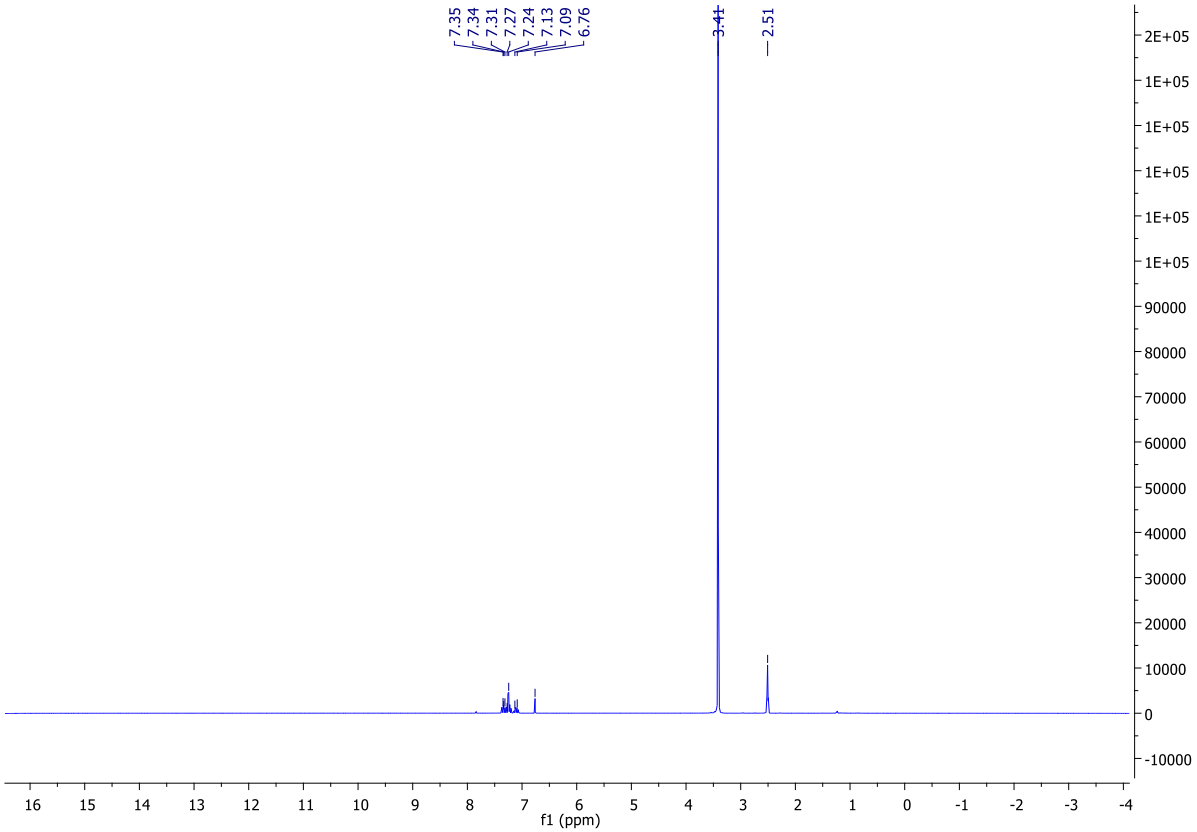
Appendix 2. HRMS (ESI) spectrum of compound 1 (Theoretical).



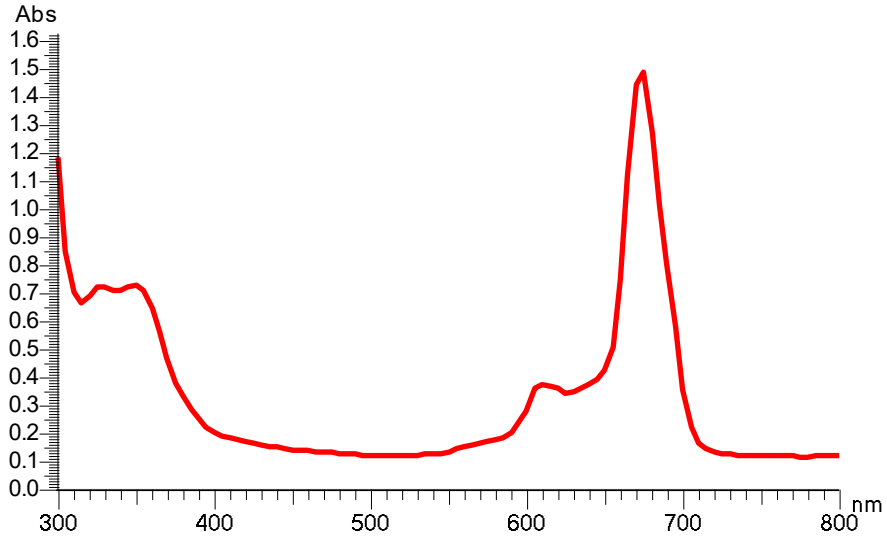
Appendix 3. FTIR spectrum of 9-phenylxanthen-9-ol.



Appendix 4. FTIR spectrum of compound 1.

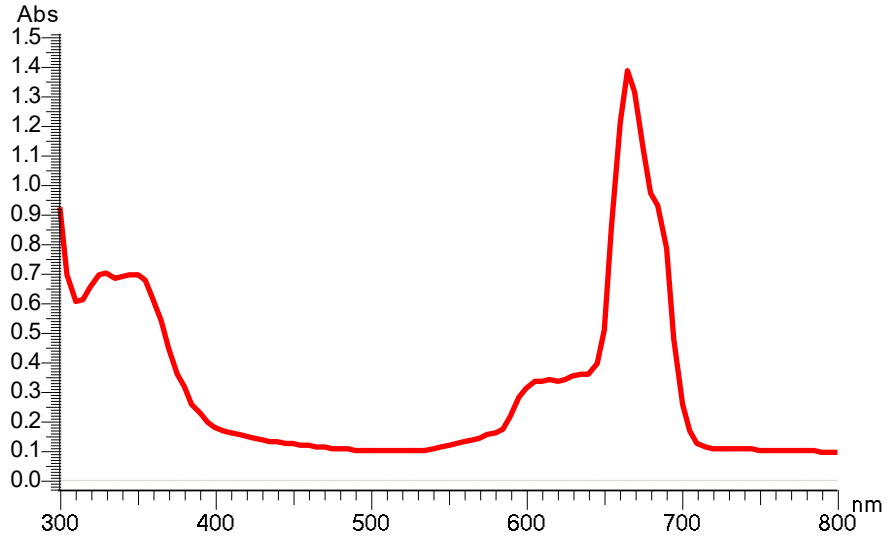


Appendix 5. ^{1}H NMR spectrum of compound 1.



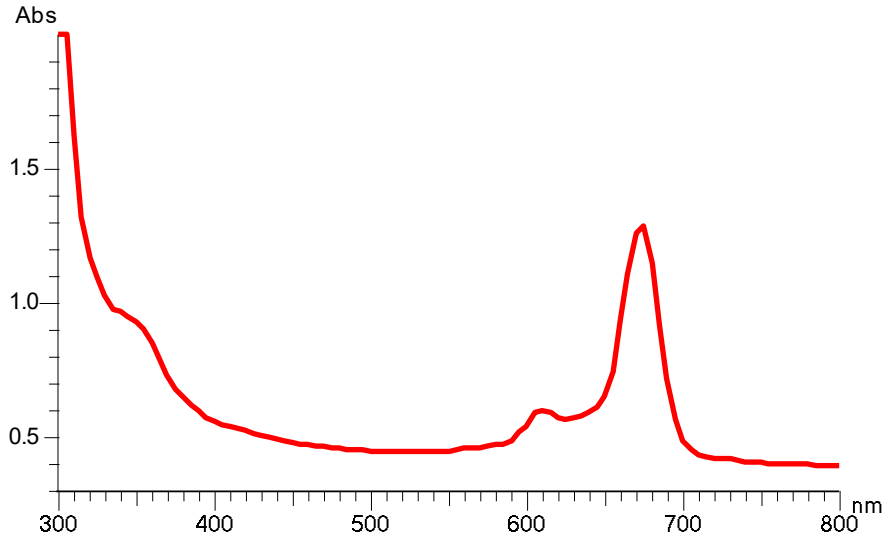
Peak #	Start (nm)	Apex (nm)	End (nm)	Height (Abs)	Valley (nm)	Valley (Abs)
1	800.0	675.0	515.0	1.490	515.0	0.121
2	515.0	350.0	300.0	0.729	300.0	1.186

Appendix 6. UV-Vis spectrum of compound 1 in THF.



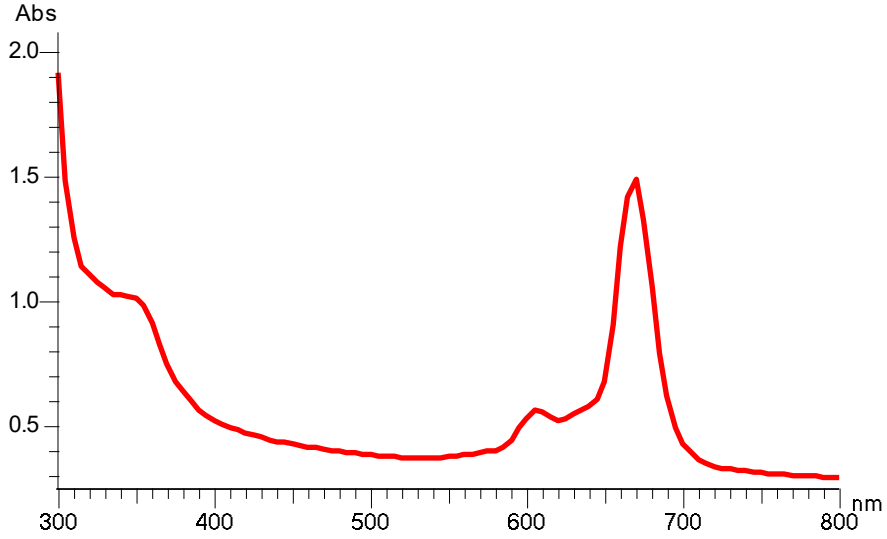
Peak #	Start (nm)	Apex (nm)	End (nm)	Height (Abs)	Valley (nm)	Valley (Abs)
1	800.0	665.0	515.0	1.383	515.0	0.098
2	515.0	330.0	300.0	0.700	300.0	0.921

Appendix 7. UV-Vis spectrum of compound 1 in DCM.



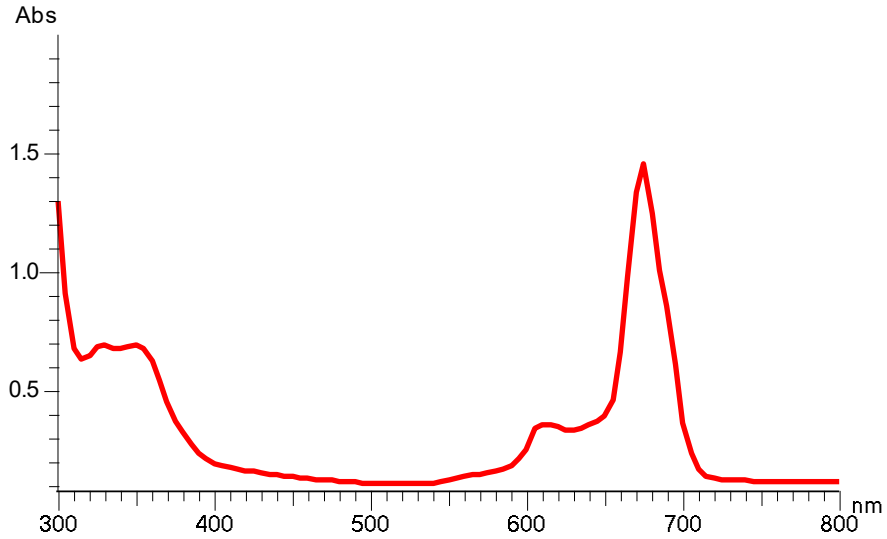
Peak #	Start (nm)	Apex (nm)	End (nm)	Height (Abs)	Valley (nm)	Valley (Abs)
1	800.0	675.0	530.0	1.286	530.0	0.443

Appendix 8. UV-Vis spectrum of compound 1 in DMSO.



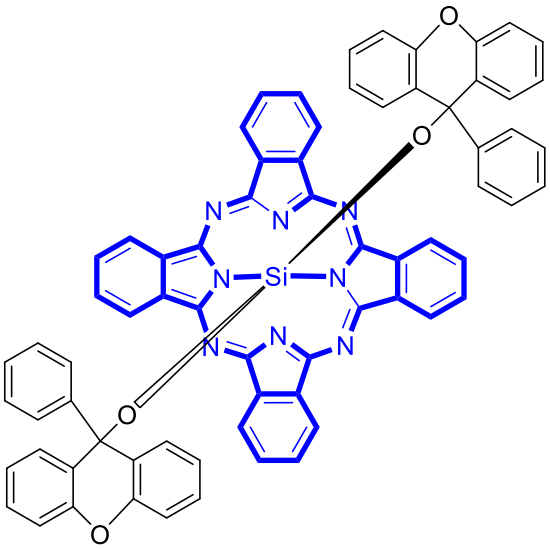
Peak #	Start (nm)	Apex (nm)	End (nm)	Height (Abs)	Valley (nm)	Valley (Abs)
1	800.0	670.0	535.0	1.491	535.0	0.370

Appendix 9. UV-Vis spectrum of compound 1 in DMF.



Peak #	Start (nm)	Apex (nm)	End (nm)	Height (Abs)	Valley (nm)	Valley (Abs)
1	800.0	675.0	520.0	1.458	520.0	0.107
2	520.0	350.0	300.0	0.694	300.0	1.294

Appendix 10. UV-Vis spectrum of compound 1 in $CHCl_3$.



Chemical Formula: $C_{70}H_{42}N_8O_4Si$
Exact Mass: 1086,3
Molecular Weight: 1087,2
m/z: 1086.3 (100.0%), 1087.3 (75.7%), 1088.3 (28.3%), 1089.3 (6.1%), 1087.3 (5.1%), 1088.3 (3.8%), 1088.3 (3.3%), 1087.3 (3.0%), 1089.3 (2.5%), 1088.3 (2.2%), 1089.3 (1.4%), 1090.3 (1.3%)
Elemental Analysis: C, 77.33; H, 3.89; N, 10.31; O, 5.89; Si, 2.58

Appendix 11. Structural analysis data of compound 1.

BİTLİS EREN ÜNİVERSİTESİ
FEN BİLİMLERİ DERGİSİ

ISSN: 2147-3129 / e-ISSN: 2147-3188

Article Type : Research Article
Received : April 5, 2025
Revised : May 30, 2025
Accepted : July 8, 2025
DOI : 10.17798/bitlisfen.1670271

Year : 2025
Volume : 14
Issue : 3
Pages : 1534-1548

INVESTIGATION OF MICROSTRUCTURE, HARDNESS AND WEAR BEHAVIOR OF POWDER METAL AL 7020 / SIC / NANO GRAPHENE DOPED HYBRID COMPOSITES

Alper NAMALAN [1], **Hakan GÖKMEŞE** [1,*], Ufuk TAŞCI [2]

[1] *Necmettin Erbakan University, Mechanical Engineering Department, Konya, Türkiye*

[2] *Gazi University, Vocational School of Technical Sciences, Ankara, Türkiye*

**** Corresponding Author:*** *hgokmese@erbakan.edu.tr*

ABSTRACT

Al 7020 aluminum alloy is mainly preferred in many engineering applications, especially in the aviation and space sectors. Nano graphene (Gr) particles were selected for the study due to their hybrid composite structure, microstructure, mechanical properties, lubrication properties, lightness, and small size compared to the matrix and reinforcement element. For this purpose, SiC and nanographene powder particles were added to the aluminum matrix as reinforcement phases in the study, and composite-hybrid test samples were produced. In the production of Al7020 powder metal matrix SiC/nanographene doped test samples, 10% SiC ceramic phase reinforcement by weight was applied to the matrix material at a fixed rate, and nanographene particle reinforcement was added at the rates of 0.25%, 0.50%, and 1.0%. The prepared matrix powder mixtures were mixed in a high-energy ball mill at 300 RPM and 240 minutes to ensure homogeneous distribution in terms of matrix/reinforcement. After mixing, the powder mixtures were compressed at room temperature using a pressing pressure of 650 MPa. The obtained raw density test samples were sintered at 600°C for 60 minutes under Argon gas flow. Thus, the effect of SiC-nano graphene reinforcement on density, microstructural, hardness, and wear (25N, 900m) results were evaluated. The pore amount increased in the samples containing reinforcement elements. The highest hardness value was 108.476 HBN in the sample containing Al-10%SiC-0.5%Gr.

Keywords: Al 7020, SiC, Nano graphene, Microstructure, Hardness, Wear.

1 INTRODUCTION

Aluminum matrix composites (AMC) are widely preferred in automotive, aviation, and defense industries due to their high strength/weight ratio, good wear resistance, and suitable mechanical properties [1–4]. In order to increase the performance of these composites, the formation of hybrid structures using different reinforcement elements has become quite interesting in recent years. In recent years, research on hybrid composite materials reinforced with ceramic particles has increased to improve the mechanical properties of aluminum alloys [5–9]. In this context, SiC particles are one of the most frequently preferred reinforcement materials due to their superior properties, such as high hardness, good wear resistance, and thermal stability [10,11].

However, nano-sized carbon-based reinforcements, especially graphene and graphene derivatives, are among the new-generation additive materials that are intensively studied to improve the mechanical and tribological properties of the material. Nanographene reinforcement improves the load transfer within the matrix material, thus significantly contributing to the increase in properties such as hardness, strength, and wear resistance [9]. Recent studies have reported that nanographene significantly increases aluminum matrix composites' mechanical and tribological performance, even in small amounts [12]. In addition, thanks to the low density and high specific surface area of nanographene, it is possible to ensure homogeneous distribution within the composite and to make the material performance more stable.

Al7020 aluminum alloy is an important alloy preferred in engineering applications due to its high strength, lightness, and workability [1,13]. However, the development of hybrid composites is critical to eliminate the weaknesses of pure alloys in some applications, such as insufficient wear resistance, limited hardness, and low performance at high temperatures [14,15]. In this direction, integrating SiC particles and nanographene additives into the Al7020 aluminum matrix can further improve the alloy's existing properties. These hybrid composites, which are expected to show more stable performance, especially under high-temperature conditions, are anticipated to provide significant advantages in advanced technology applications in the defence and aerospace sectors [16].

This study investigated the microstructure, hardness, and wear behavior of hybrid composites with reinforcements of 10% SiC and different ratios of nanographene particles in an Al7020 aluminum matrix. Studies were carried out on the production methods of the

composites, ensuring a homogeneous distribution of reinforcement materials in the composite structure and increasing material performance. The material's phase formations and particle distribution were evaluated with the microstructure analysis of the composites, and the hardness obtained by mechanical tests and the wear resistance results determined by tribological tests were analyzed comparatively. The aim is to improve the mechanical and tribological properties of the Al7020 alloy and to ensure its more practical use in industrial applications. Thus, it aims to significantly contribute to the literature on developing aluminum-based hybrid composites.

2 MATERIAL AND METHOD

In this study, in order to examine the effectiveness of nanographene additives to Al 7020 matrix SiC/nanographene (Gr) particle additive hybrid composites, pre-alloyed 44 µm (325 mesh) and 99.9%+ purity Al 7020 metal matrix powders supplied by Nanografi Nanoteknoloji and produced by gas atomization method were used. The chemical composition of Al 7020 metal matrix alloy powders is given in Table 1.

Table 1. Chemical composition of Al 7020 material (%)

Element	Al	Zn	Mg	Ti	Cr	Mn	Fe	Si	Cu
Weight (%)	Bal.	4.67	1.34	0.3	0.29	0.48	0.09	0.02	0.01

Within the scope of composite-hybrid material production, SiC and Nano Graphene powder particles purchased from Nanografi Nanoteknoloji were used in experimental studies as reinforcement elements in the metal matrix. In the production of aluminum matrix composite-hybrid materials, 3 µm and 99.5%+ purity SiC powder and 3nm and 99.9%+ purity nano graphene powder were used in the study. The mixing ratios of matrix-reinforcement powder particles for the production of Al 7020 aluminum metal matrix test samples are given in Table 2. Matrix and reinforcement powder mixtures were prepared in proportions determined by precision scales and subjected to a mixing process focused on ensuring homogeneous distribution of matrix reinforcement with the help of a Thermnevo brand high-energy ball mill.

Table 2. Matrix and reinforcement starting powder mixing ratios (%)

Samples	**Al 7020**	**Silicon Carbide**	**Nano grafen**
A	100	-	-
AS	90	10	-
AS1	89.75	10	0.25
AS2	89.5	10	0.5
AS3	89	10	1

For this purpose, 300 rpm and 240 min. Mixing time was applied to the powder particles. The prepared powder mixtures were pressed under 650 MPa pressure using a Hidroliksan brand 60-ton single-axis press bench, and 12 mm diameter test samples were produced. Following the pressing process, the test samples were sintered for 60 minutes under argon gas flow at 600°C (Figure 1).

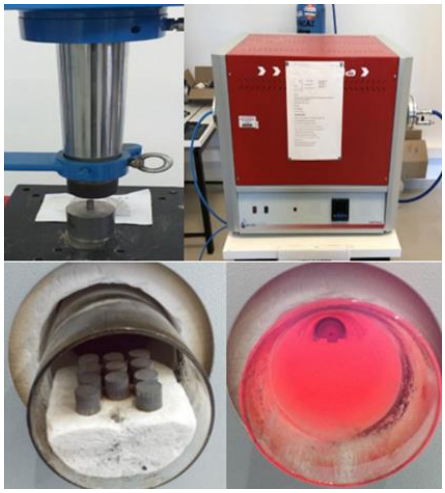


Figure 1. Pressing and sintering process.

The density measurement processes of composite-hybrid materials were carried out according to the Archimedes principle. A Hardway brand grinding and polishing device was used for microstructural characterization of the test samples after sintering and general metallographic studies. Then, 90% H_2O (Pure) and 10% HF solution were used for etching. As a result of the etching processes, microstructure examinations were obtained using the Hardway optical microscope and the Hitachi SEM device. Within the scope of hardness measurements, a 2.5 mm diameter ball tip was used under a 33.8 kgf load (10s) with the Brinell hardness (ASTM E10) measurement technique.

For the wear test (Figure 2), a Turkyus brand wear bench was used (block-on disk) application, AISI 4140 steel counter abrasive, 50 mm diameter and 65 HRC hardness value was included in the study. In the wear tests, weight loss was weighed on a scale with a precision of 1/10000 gr. Wear tests were conducted under a 25N load, a 0.5 ms-1 sliding speed, and a 0-900 m sliding distance.

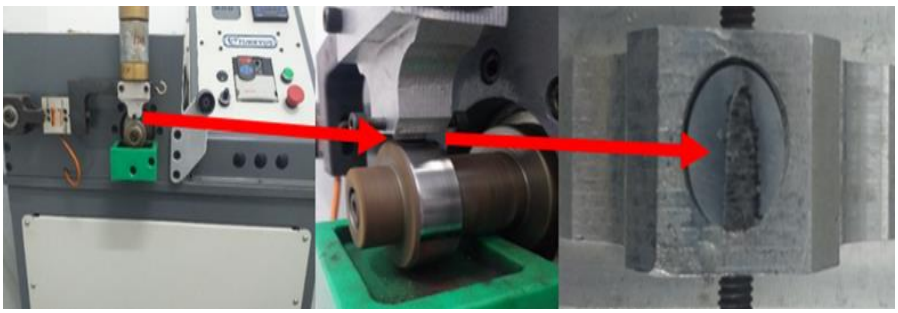


Figure 2. Block-on disc wear process.

3 RESULTS AND DISCUSSIONS

The initial matrix and reinforcement particles used to produce hybrid test samples reinforced with Al 7020 aluminum metal matrix SiC/Nano graphene particles are shown in Figure 3. When the SEM microstructure images are evaluated, it can be seen that the 7020 aluminum matrix powder particles are in spherical shape and morphology (Figure 3-a). Regarding powder distribution, satellite formation is more prevalent in small powder particles that come into contact with larger particles. In terms of reinforcement elements, it can be seen that the SiC ceramic phase particles are polygonal or mostly pointed and sharp-cornered in shape and morphology (Figure 3-b). It can be seen that the nanographene reinforcement powder particles have irregular shapes and morphology and exhibit flat flake morphology (Figure 3-c).

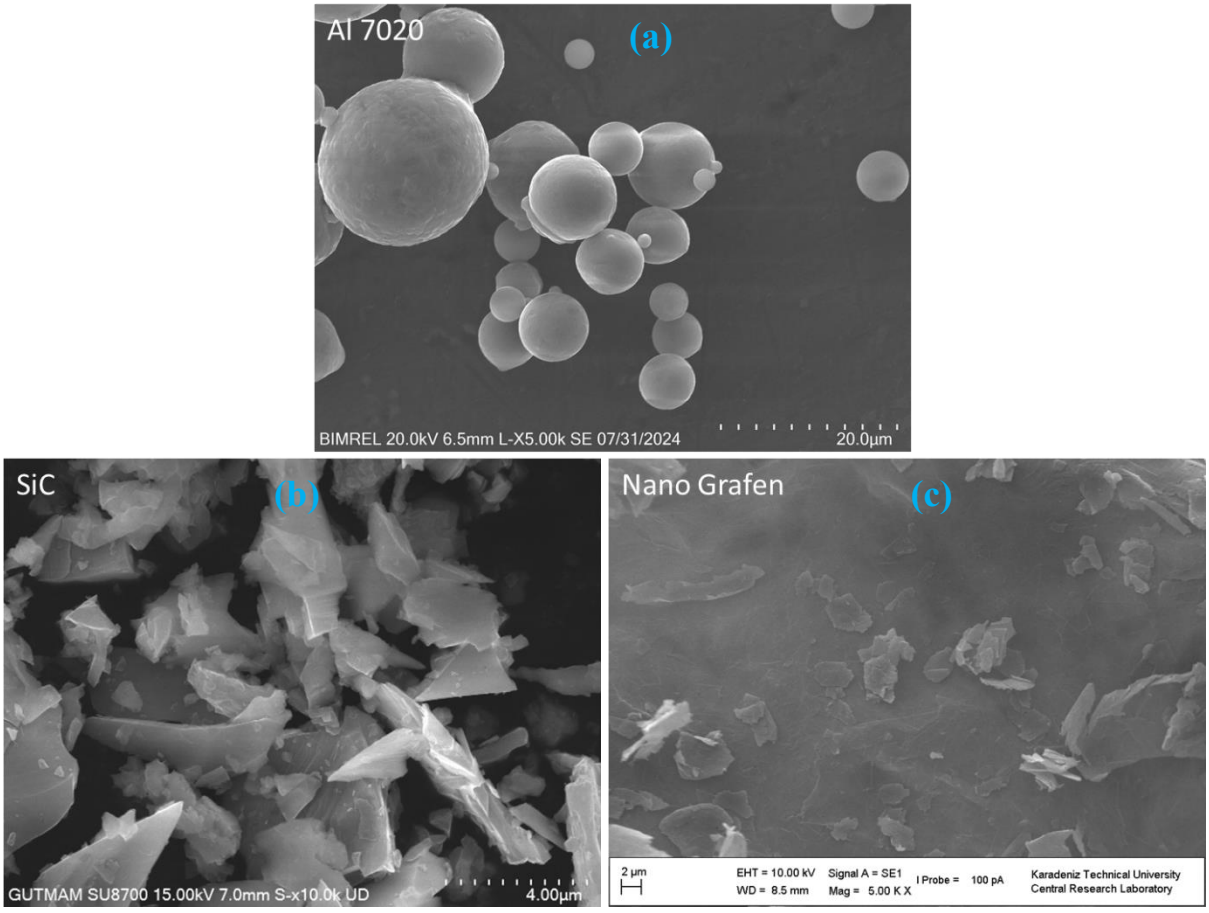


Figure 3. SEM images of matrix and reinforcement elements; a) Al 7020, b) SiC and c) Gr.

After sintering, the relative density values of the test samples were measured (Figure 4). When this density is considered primarily as a relative (%) density value, when the density results obtained due to the sintering process of the samples produced under reinforcement ratio differences of composite-hybrid materials are examined, it can be seen that there is a decrease in the density results after sintering. This situation can be stated as the clustering or

agglomeration of the reinforcement element SiC/Nano graphene particles, especially along the grain boundaries. It can be seen that there are significant decreases in the density, especially after the increase in the amount of nanographene particles. In the literature, it is noteworthy that in the majority of the studies containing powder metal composites and especially hybrid materials produced with the powder metallurgy technique, there is a decrease in the density values of composite-hybrid materials due to the increase in the reinforcement phase ratios [15,17]. Again, it is known that there is a relationship between pressing pressure and pore structure in terms of materials produced using the powder metallurgy technique. Therefore, due to this situation, the cold pressing process can directly affect the grain structure-pore interaction [18].

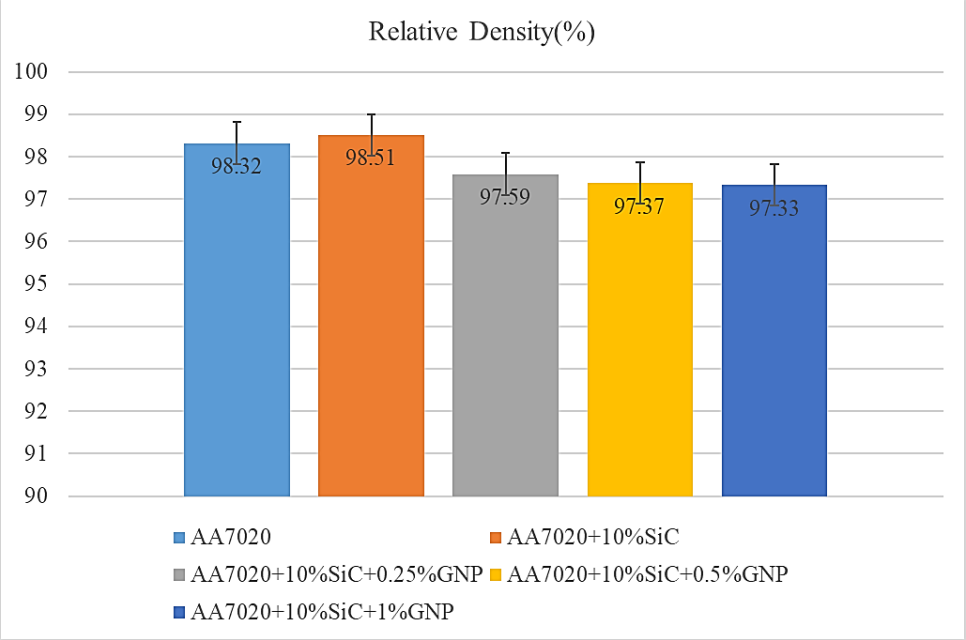


Figure 4. Density results of test samples.

The distribution of reinforcement particles SiC/Nano graphene and the amounts of reinforcement within the structure can directly trigger the decrease in the density value. The highest relative density value was obtained in the composite material with 10% SiC reinforcement with 98.51% compared to the Al7020 aluminum metal matrix structure. The lowest relative density value was obtained in the Al+10%SiC+1%Gr content test sample with 93.33%. The optical and SEM microstructure images of the Al7020 aluminum metal matrix SiC and Nano graphene particle reinforced composite-hybrid test samples following the pressing and sintering processes are shown in Figures 5 and 6, respectively. When the optical microstructure images given in Figure 5 are examined, it can be stated that the reinforcement particles tend to concentrate at the grain boundaries in the reinforced composite and hybrid test

samples compared to the Al 7020 aluminum alloy metal matrix structure (Figure 5a) (Figure 5b-e). It can be stated that SiC ceramic phase particles especially exhibit a distribution in the grain boundaries and near the grain boundary regions and have a sharp-cornered and polygonal shape morphology (Figure 6b, e)

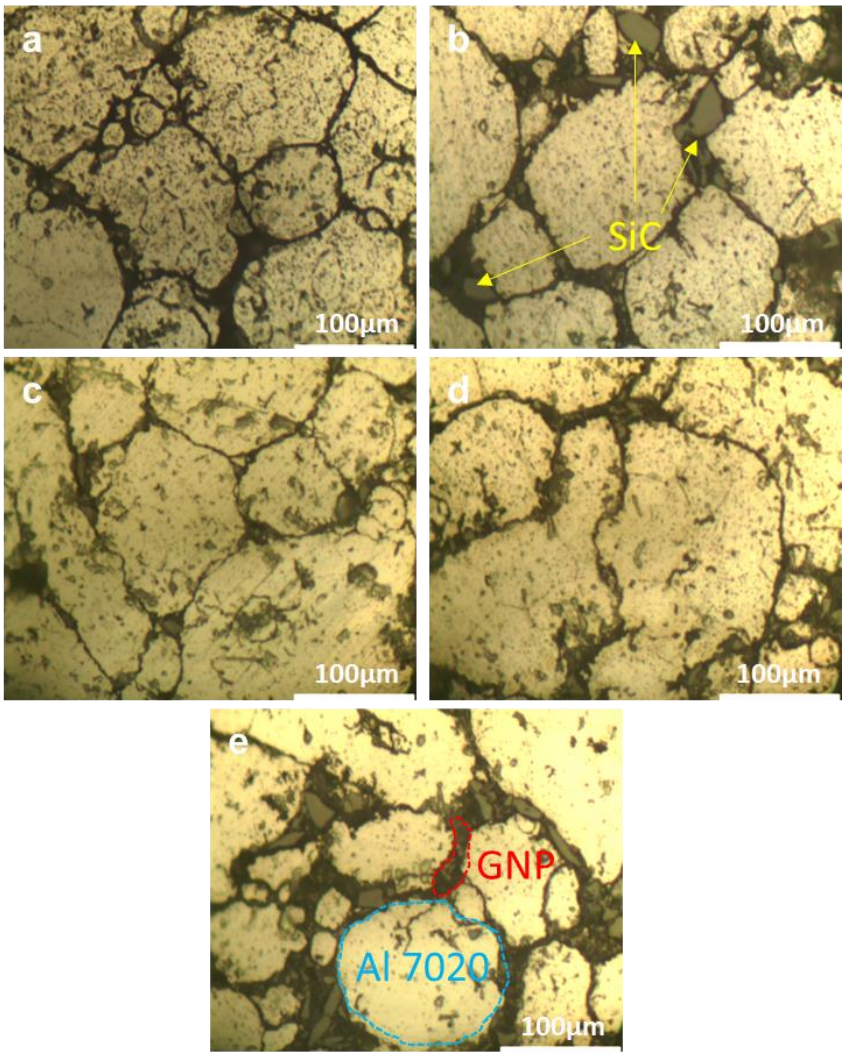


Figure 5. Optical microstructure images of test samples; a) A, b) AS, c) AS1, d) AS2 and e) AS3.

When the SEM microstructure images given in Figure 6 are examined, it can be said that the distribution and conditions of the SiC particles, which are primarily dark and grayish and also have sharp corners-polygonal shape morphology, are located in the grain boundary and areas close to the grain boundary, and the nanographene particles, which are dark black in appearance, are densely clustered in the neighborhood and at the ends of the SiC particles. Figure 7 shows the EDS analysis and elemental distribution mapping obtained from the SEM image of the experimental sample produced with Al7020+10%SiC+0.50% nanographene content.

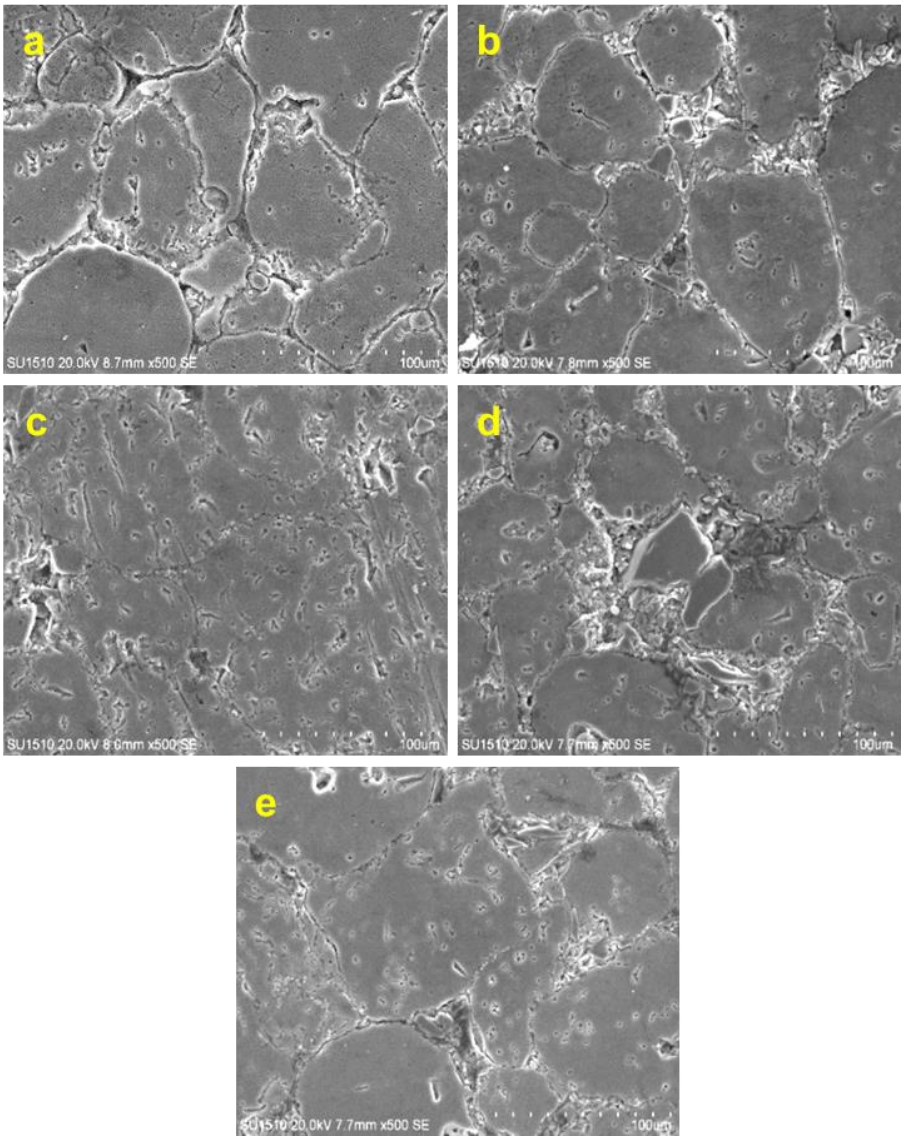


Figure 6. SEM images of test samples; a) A, b) AS, c) AS1, d) AS2 and e) AS3.

The general EDS analysis applied to the sample with Al7020-10% SiC-0.50% nanographene content was obtained depending on the alloy elements and reinforcement contents in the hybrid structure in Al7020 (Al, Zn, Cu, Mg, Si, C). According to the elemental mapping result, it is thought that the nanographene particles exhibit clustering with the agglomeration effect at the ends of the SiC powders.

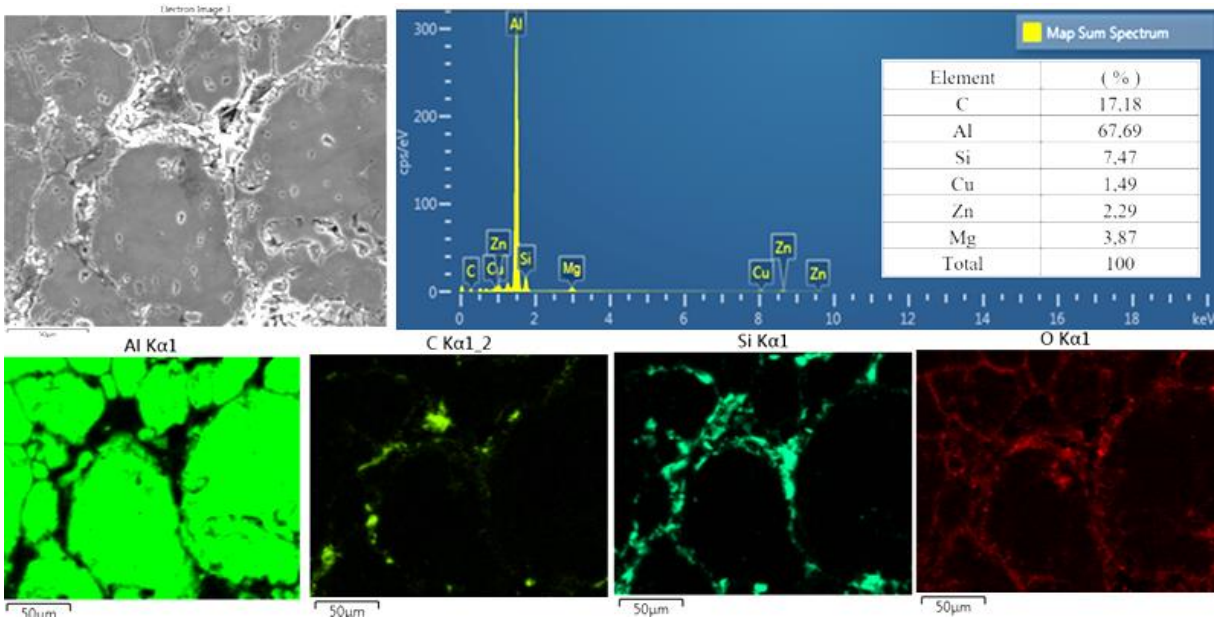


Figure 7. EDS analysis and elemental mapping of Al7020+10%SiC+0.5% nanographene.

The hardness results obtained from microstructure examinations of Al7020 aluminum metal matrix and reinforced hybrid test samples produced without using reinforcement elements are given in Figure 8. The hardness value of unreinforced Al7020 aluminum powder metal alloy was determined as 75.7 HBN. In addition, when 10% SiC was added as a reinforcement element, the hardness value was measured as 103.287 HBN, with an increase of 27.587%. This situation can be expressed as the higher hardness value of SiC ceramic particles in the reinforcement phase compared to the aluminum matrix and, therefore, the high hardness value. The hardness value of the reinforced sample containing 0.25% nanographene was observed as 108.476 HBN with an increase of 5.18% compared to the sample containing SiC as 10% reinforcement ceramic particle phase, and the highest hardness measurement result was observed as 108.476 HBN. According to these data, as the amount of SiC and nanographene reinforcement increases compared to Al7020 aluminum powder metal alloy, a significant increase in the hardness result was measured in the composite-hybrid material structure, and an improvement in mechanical properties was achieved. However, it was determined that the nanographene reinforcement particles added to the structure after a specific rate decreased the hardness result.

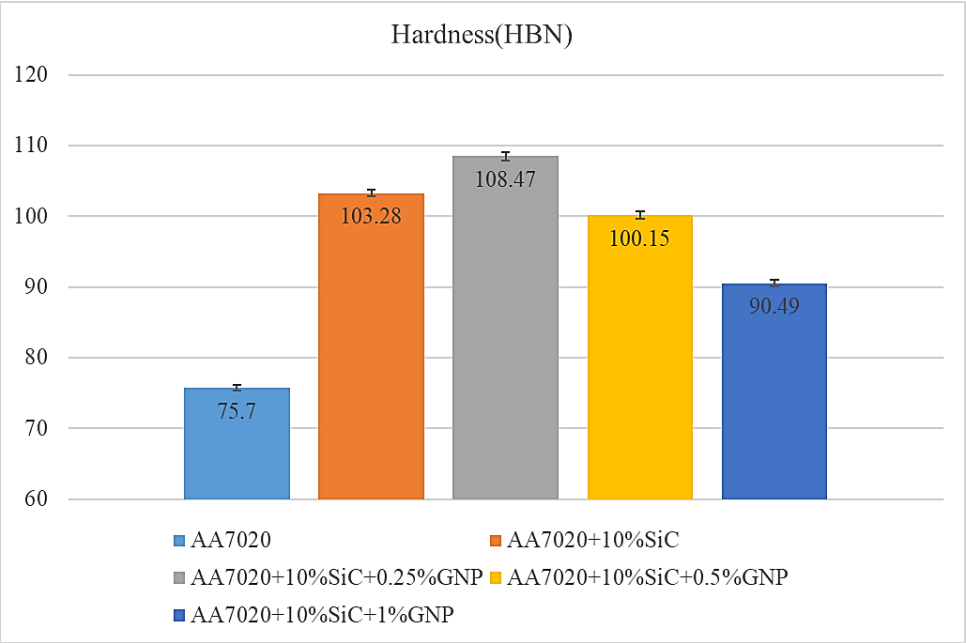


Figure 8. Hardness results of test samples.

The weight loss results of composite materials with different amounts of SiC and nanographene reinforcement added to Al7020 aluminum powder metal alloy are shown in Figure 9. When the wear weight loss results are examined, it is revealed that the highest weight loss occurs in Al7020 powder metal aluminum alloy. Wear tests have revealed that composite-hybrid materials exhibit consistently lower wear rates than the matrix alloy. In terms of wear weight loss results, it is generally understood that there is a decrease in weight loss values depending on the increasing amount of SiC and nanographene reinforcement. In terms of wear, this situation can be stated as an expected result: the weight loss value is low in the material with a high hardness result, and the weight loss is high in the material with a low hardness result [19,20]. The wear loss results of the test samples generally increase with increasing sliding distance. However, it is also noteworthy that there are sudden and high increases in the wear degrees of hybrid composites. This situation can be considered to occur because large particles break off from the material surface and areas close to the surface during the wear process, which causes the amount or degree of wear to increase after weight loss. Özyürek et al. [21] stated in their study that there was an increase in weight loss that occurred in the progressive wear distances in the composite materials they produced by using SiC reinforcement in the Al matrix. They emphasized that this result was due to the large particles breaking off from the sample during the wear process. In a study conducted on Al 6061/B4C/GNP hybrid composites, the highest value was obtained at 7% reinforcement instead of 10%. It was stated that there may be a decrease in hardness after a certain value. Similarly, with the increase in the nanographene

ratio from 0.5% to 2.0%, a decrease in hardness values was explained. Since graphite, which shows a soft distribution, does not contribute positively to the hardness of the composite, a decrease in hardness value can be expected. Along with the lubricating effect of graphene, its softening feature on the composite structure can be considered [22]. When the studies conducted are evaluated in general, hardness and wear resistance increase depending on the increasing reinforcement ratio in composite structures. In addition to this situation, the use of solid lubricants and hybrid composites may also show lower performance, especially at increased wear distances.

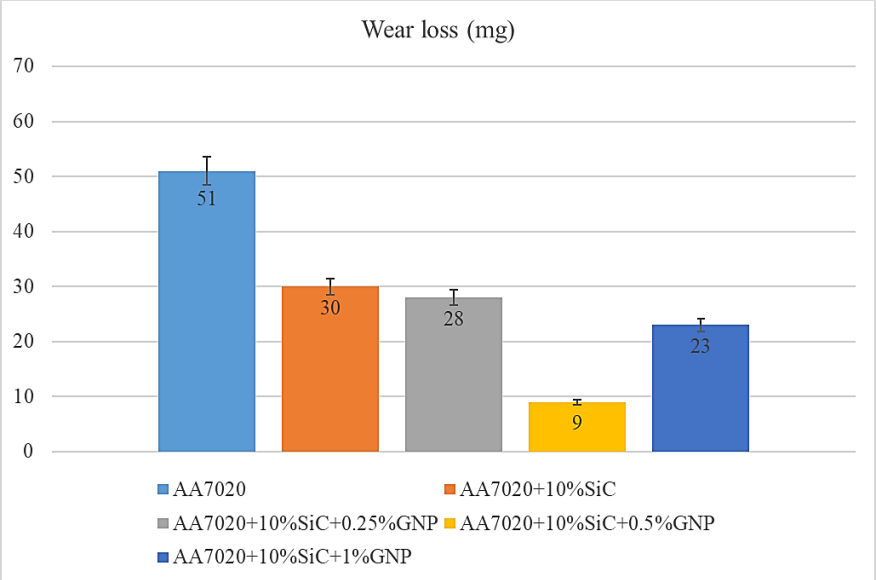


Figure 9. Wear loss results.

The friction coefficient results of the test samples, which completed the wear tests depending on the sliding distance of 900 meters, are shown in Figure 10. When the friction coefficient results are examined, the highest friction coefficient value was found in the Al 7020 powder metal alloy. In their study, Harichandran et al. stated that while the friction coefficient of the Al alloy without reinforcement was higher than the composite materials containing reinforcement, the friction coefficient decreased with the increase in the weight percentage of the reinforcement element [23].

It was determined that the SiC and nanographene additions to the Al 7020 powder metal matrix decreased the friction coefficient value. At the same time, it was observed that the resistance to friction increased in these test samples. It can be stated that the friction coefficient values obtained differ depending on the hardness values of the produced test samples. Özyürek et al. stated that the friction coefficient values decreased as the hardness results of aluminum and its alloys increased [24]. The resulting hardness result and friction coefficient values were also obtained in a way that confirms this situation.

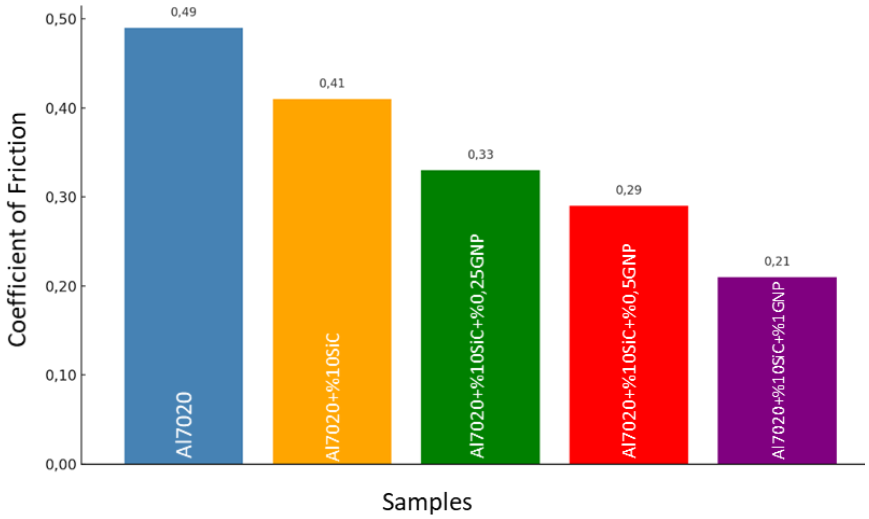


Figure 10. Friction coefficient results at 900 m sliding distance.

SEM analysis images of hybrid composites reinforced with Al 7020 matrix alloy and different ratios of SiC and nanographene particles are given in Figure 11. When the SEM microstructure images were examined, deep and distinct wear marks, grooves, wear particles, and plastic deformation-induced material accumulations were detected on the surface of the Al 7020 alloy without reinforcement. In composites reinforced with 10% SiC, it was observed that the depth and density of wear marks decreased slightly, but distinct scratches and rupture-induced particles still formed on the surface. On the other hand, it was determined that the wear marks on the surface were lighter in composites reinforced with SiC and low ratios of nanographene (0.25% and 0.5%), and plastic deformation and breakage from the material surface were significantly reduced [25]. Especially in the sample containing 1% nanographene reinforcement, the wear surface was smoother, more homogeneous, and consisted of relatively shallower marks, and the signs of material loss were at the lowest level. This situation reveals that nanographene particles reduce friction and distribute the load more effectively in the matrix [26]. As a result, it is clearly understood that the tribological performance of Al 7020/SiC composites is significantly improved by increasing the ratio of nanographene reinforcement, thus increasing the material's wear resistance.

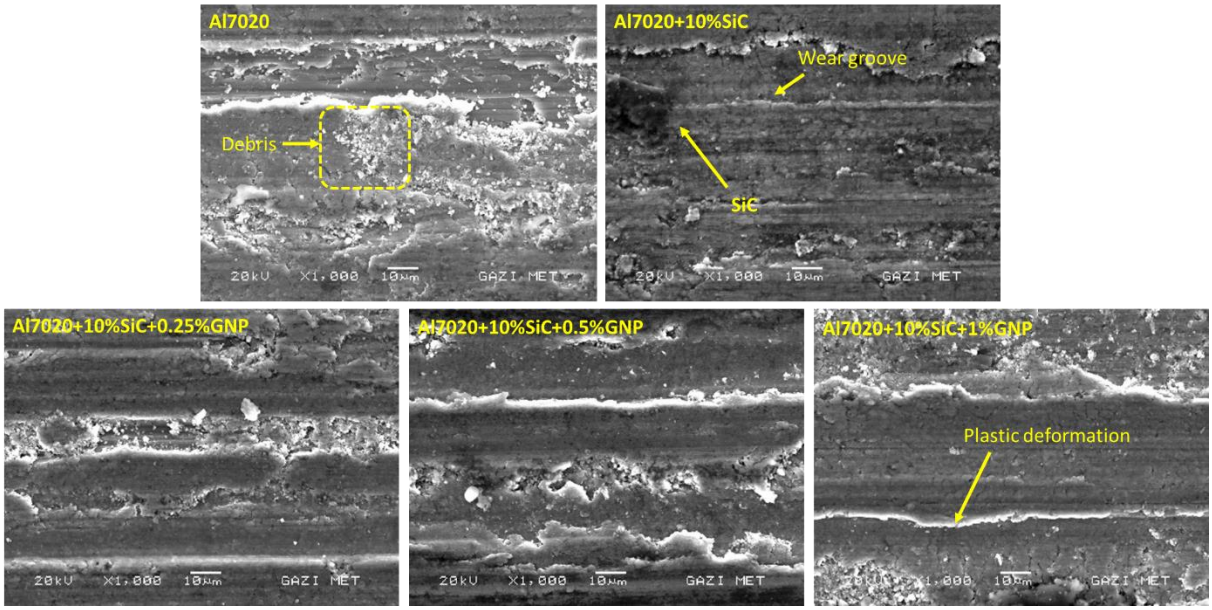


Figure 11. SEM images after wear test.

4 CONCLUSIONS

This study on the production processes of Al7020/SiC/nanographene hybrid composite materials yielded significant findings. The key results can be summarized as follows:

The novelty of these findings in the field of materials science and engineering (within the scope of new generation reinforcement materials such as nanographene and hybrid composite material applications) is intriguing and should pique the interest of the audience. In reinforced composite-hybrid samples, compared to Al7020 powder metal alloy, it was determined that SiC/nanographene exhibited a high tendency to cluster or agglomerate in the grain boundary regions in terms of pore-grain structure interaction and caused a decrease in the density value. The lowest relative density value was obtained as 93.33% in the Al-10%SiC-1%Gr content experimental sample. In terms of microstructural characterization, it was determined that dark black polygonal and sharp-cornered SiC powder particles and nanographene particles were clustered by agglomeration. The highest hardness value among the experimental samples was obtained as 108.476 HBN in the hybrid composite material containing Al+10%SiC+0.25%Gr. In terms of weight loss results with constant wear sliding distance, it was determined that there was a decrease in weight loss values depending on the increasing amount of SiC and nanographene reinforcement. It was determined that SiC and nanographene additions to the Al7020 powder metal matrix reduced the friction coefficient value. It was observed that wear marks on the surface were less frequent, plastic deformation and detachment from the material surface were less common in composites with nano graphene

reinforcement. In hybrid composite materials, it has been observed that the reinforcement particles exhibit agglomeration after a certain value, and porous regions are formed accordingly. In fact, this agglomeration may be the reason why highest wear resistance does not occur in composites with 1% graphene added. It was determined that the tribological performance of Al7020/SiC composites improved significantly by increasing to a certain value ratio of nanographene reinforcement, thus increasing the material's wear resistance.

Conflict of Interest Statement

There is no conflict of interest between the authors.

Statement of Research and Publication Ethics

The study is complied with research and publication ethics.

Artificial Intelligence (AI) Contribution Statement

This manuscript was entirely written, edited, analyzed, and prepared without the assistance of any artificial intelligence (AI) tools. All content, including text, data analysis, and figures, was solely generated by the authors.

REFERENCES

[1] U. Taşcı, T. A. Yılmaz, H. Karakoç, and Ş. Karabulut, "Enhancing wear resistance and mechanical behaviors of AA7020 alloys using hybrid Fe_3O_4-GNP reinforcement," *Lubricants*, vol. 12, 2024. doi: 10.3390/lubricants12060215.

[2] T. A. Yılmaz, U. Taşcı, A. U. Gökmen, and B. Bostan, "Investigation of wear and transverse rupture strength of AA2219/ZrO_2/B_4C hybrid composite materials prepared with 3D ball mixer and produced by spark plasma sintering," *Compos. Interfaces*, pp. 1–24, 2024. doi: 10.1080/09276440.2024.2434808.

[3] H. Yang, J. Sha, D. Zhao, F. He, Z. Ma, C. He, C. Shi, and N. Zhao, "Defects control of aluminum alloys and their composites fabricated via laser powder bed fusion: A review," *J. Mater. Process. Technol.*, vol. 319, p. 118064, 2023.

[4] S. Sukuroglu, "Characterization, corrosion, adhesion and wear properties of Al_2O_3 and Al_2O_3:TiB_2 composite coating on Al 7075 aluminum alloy by one-step micro-arc oxidation method," *Mater. Today Commun.*, vol. 46, p. 112493, 2025.

[5] U. Taşcı, "Investigation of the effect of mechanical alloying on the wear behavior of AA7020/Fe_3O_4/GNP hybrid composite materials," *Gazi Univ. J. Sci. Part A Eng. Innov.*, vol. 11, pp. 814–825, 2024.

[6] Y. Yıldıran, E. Avcu, A. Şahin, S. Fidan, H. Yetiştiren, and T. Sınmazçelik, "Effect of particle impact angle, erodent particle size and acceleration pressure on the solid particle erosion behavior of 3003 aluminum alloy," *Acta Phys. Pol. A*, vol. 125, pp. 523–525, 2014.

[7] S. K. Patel, R. Nateriya, B. Kuriachen, and V. P. Singh, "Slurry abrasive wear, microstructural and morphological analysis of titanium carbide and zirconium sand aluminium alloy (A5052) metal matrix composite," *Mater. Today Proc.*, vol. 5, pp. 19790–19798, 2018. doi: 10.1016/j.matpr.2018.06.342.

[8] M. Kumar, N. Sotirov, and C. M. Chimani, "Investigations on warm forming of AW-7020-T6 alloy sheet," *J. Mater. Process. Technol.*, vol. 214, pp. 1769–1776, 2014. doi: 10.1016/j.jmatprotec.2014.03.024.

[9] K. Zheng, X. Du, H. Qi, T. Zhao, F. Liu, and B. Sun, "Sliding-wear behavior of aluminum-matrix composites reinforced with graphene and SiC nanoparticles," *Mater. Technol.*, vol. 54, 2020.

[10] Kumar, S. Kumar, N. K. Mukhopadhyay, A. Yadav, V. Kumar, and J. Winczek, "Effect of variation of SiC reinforcement on wear behaviour of AZ91 alloy composites," *Materials (Basel)*, vol. 14, p. 990, 2021.

[11] R. A. M., M. Kaleemulla, S. Doddamani, and B. K. N., "Material characterization of SiC and Al_2O_3–reinforced hybrid aluminum metal matrix composites on wear behavior," *Adv. Compos. Lett.*, vol. 28, 2019, doi: 10.1177/0963693519856356.

[12] S. Swargo and S. Mia, "Reinforcing carbon nanotubes (CNT) into aluminum powder matrix as a nanocomposite coating with enhanced properties," *Next Mater.*, vol. 8, p. 100551, 2025.

[13] N. M. S. Kumar, G. K. Pramod, P. Samrat, and M. Sadashiva, "A critical review on heat treatment of aluminium alloys," *Mater. Today Proc.*, vol. 58, pp. 71–79, 2022.

[14] M. Y. Zhou, L. B. Ren, L. L. Fan, Y. W. X. Zhang, T. H. Lu, G. F. Quan, and M. Gupta, "Progress in research on hybrid metal matrix composites," *J. Alloys Compd.*, vol. 838, p. 155274, 2020. doi: 10.1016/j.jallcom.2020.155274.

[15] Z. Özkan, H. Gökmeşe, and U. Gökmen, "Investigation of the microstructure-hardness and wear performances of hybrid/composite materials Al_2O_3/SiC particle reinforced in AA7075 matrix," *Sci. Sinter.*, vol. 54, 2022.

[16] S. Sundaraselvan, K. Rajkumar, S. Sathish, and B. M. R. Bharathi, "Experimental investigation of dispersion effect of TiCP on mechanical and tribological behaviour on LM25 aluminum-fly ash hybrid composites," *Russ. J. Non-Ferrous Met.*, vol. 65, pp. 207–214, 2024.

[17] G. Keskin, G. Küçüktürk, M. Pul, H. Gürün, and V. Baydaroğlu, "AA7075 matrisli B_4C+SiC takviyeli hibrit kompozitlerin toz takviyeli EEİ yöntemiyle işlenmesinde boşalım akımı ve takviye oranının işlenmiş yüzeyin mikroyapısı ve pürüzlülüğüne etkisi," *Int. J. Eng. Res. Dev.*, vol. 13, pp. 489–495, 2021.

[18] H. Gökmeşe and B. Bostan, "AA2014 alaşımında presleme ve sinterlemenin gözenek morfolojisi ve mikroyapısal özelliklere etkileri," *Gazi Univ. J. Sci. Part C Des. Technol.*, vol. 1, pp. 1–8, 2013.

[19] İ. Şimşek, M. Yıldırım, D. Özyürek, and D. Şimşek, "Basınçsız infiltrasyon yöntemiyle üretilen SiO_2 takviyeli alüminyum kompozitlerin aşınma davranışlarının incelenmesi," *Politek. Derg.*, vol. 22, pp. 81–85, 2019.

[20] T. Alpas and J. Zhang, "Effect of SiC particulate reinforcement on the dry sliding wear of aluminium-silicon alloys (A356)," *Wear*, vol. 155, pp. 83–104, 1992.

[21] D. Özyürek, A. Kalyon, M. Yıldırım, T. Tuncay, and I. Ciftci, "Experimental investigation and prediction of wear properties of Al/SiC metal matrix composites produced by thixomoulding method using artificial neural networks," *Mater. Des.*, vol. 63, pp. 270–277, 2014.

[22] M. Pul, "The effect of B_4C and GNP reinforcement amounts on abrasive wear behavior in Al6061/B_4C/GNP hybrid composites," *Niğde Ömer Halisdemir Univ. J. Eng. Sci.*, vol. 11, no. 4, pp. 1179–1187, 2022.

[23] R. Harichandran and N. Selvakumar, "Effect of nano/micro B_4C particles on the mechanical properties of aluminium metal matrix composites fabricated by ultrasonic cavitation-assisted solidification process," *Arch. Civ. Mech. Eng.*, vol. 16, pp. 147–158, 2016.

[24] D. Özyürek, T. Tunçay, and H. Kaya, "The effects of T5 and T6 heat treatments on wear behaviour of AA6063 alloy," *High Temp. Mater. Process.*, vol. 33, pp. 231–237, 2014.

[25] H. Jagadeesh, P. Banakar, P. Sampathkumaran, R. R. N. Sailaja, and J. K. Katiyar, "Influence of nanographene filler on sliding and abrasive wear behaviour of bi-directional carbon fiber reinforced epoxy composites," *Tribol. Int.*, vol. 192, p. 109196, 2024.

[26] M. A. Alam, H. B. Ya, M. Azeem, M. Mustapha, M. Yusuf, F. Masood, R. V. Marode, S. M. Sapuan, A. H. Ansari, "Advancements in aluminum matrix composites reinforced with carbides and graphene: A comprehensive review," *Nanotechnol. Rev.*, vol. 12, p. 20230111, 2023.

BİTLİS EREN ÜNİVERSİTESİ
FEN BİLİMLERİ DERGİSİ

ISSN: 2147-3129 / e-ISSN: 2147-3188

Article Type	: Research Article	**Year**	: 2025
Received	: April 7, 2025	**Volume**	: 14
Revised	: June 23, 2025	**Issue**	: 3
Accepted	: August 1, 2025	**Pages**	: 1549-1562
DOI	: 10.17798/bitlisfen.1671029		

THE INFLUENCE OF TOOL GEOMETRY ON SIDE MILLING OF CFRP WITH DIFFERENT CUTTING TOOL PATHS

Sezer MORKAVUK [1]

[1] *Karamanoglu Mehmetbey University, Department of Mechanical Engineering, Karaman, Türkiye,* sezermorkavuk@kmu.edu.tr

ABSTRACT

Carbon fiber-reinforced plastics (CFRP) are extensively utilized in the aerospace, automotive, and sporting goods industries, where the combination of lightness and high strength is crucial. Conventional milling is a prevalent technique for obtaining the final dimensions and removing excess parts of CFRP components produced with different manufacturing methods. However, many damages occur during the mechanical machining of composites and these damages negatively affect the quality and service life of the composite part. The present study investigates the effects of utilizing different tool paths and end mills with varying geometries on cutting forces and machined surface quality in the side milling operation of CFRP. Results indicated that employing sinusoidal tool paths during side milling is a successful approach for reducing cutting forces and improving surface finish. On the other hand, the multi-flute performed best regarding cutting forces, whereas the 4-flute tool proved superior in obtaining better surface quality.

Keywords: Carbon, Composites, Milling, Sinusoidal milling, Tool flute, Tool path.

1 INTRODUCTION

There is a growing demand for lightweight materials that are also durable in many industries. This has led to a significant increase in the use of carbon-fiber-reinforced plastics (CFRP), which offer a high strength-to-weight ratio and exhibit excellent corrosion resistance [1, 2]. CFRP components are usually produced close to the final shape by various molding methods [3]. However, after the production process, an edge-trimming operation is necessary to remove excess material and ensure the attainment of final dimensions. Nevertheless, the

machinability of CFRP is significantly different from that of metals due to its heterogeneous and anisotropic structure, since it is formed by the combination of carbon fiber and a plastic matrix at the macro level [4]. During the machining process of CFRP, various forms of damage may occur, including delamination, matrix cracks, fiber breakages, fiber pull-out, and fiber-matrix debonding. These damages have the potential to reduce the material's strength [5-7]. Consequently, numerous researchers have concentrated on the damage that occurs during milling and the quality of machining.

Sheikh-Ahmad et al. [8] analyzed delamination damage formation and surface quality in edge trimming of CFRP with a multi-flute burr router bit and it is reported that as the feed rate increased, delamination and surface roughness also increased, while these outputs decreased as spindle speed increased. Kiliçkap et al. [9] investigated the effects of cutting parameters and tool flute number on cutting forces and machining quality in end milling of CFRP and they found that lower feeds and four flute tool yield better machining quality. Can [10] studied vertical and inclined edge trimming of CFRP with 2, 4, and 6 flute endmills. The research found that using six flute tools with inclined milling at lower feed rates and higher spindle speeds produced better results. Yağmur et al. [11] examined and modelled surface quality in milling CFRP, reporting that surface quality improved by an increase in cutting speed. Prakash et al. [12] focused on tool coatings in edge trimming of CFRP using router tools and found diamond-like coated tools exhibited better performance. Xu et al. [13] modelled and analyzed fiber-matrix debonding in edge milling of CFRP using multi-flute tools. The study concluded that the debonding severity was considerably affected by the tool radius and feed rate. Devan et al. [14] conducted a study on the tool wear behavior of two flute carbide end mills in edge trimming of CFRP. It was reported that lower cutting speed, feed speed and depth of cut resulted in a longer tool life. Zhang and Zhang [15] investigated the effect of cutting parameters, up and down milling strategy and cutting angle on cutting forces and surface quality in side milling of CFRP. It was emphasized that the cutting angle had a significant impact on the results and that an optimum surface quality was obtained at a 90° cutting angle. It was also reported that the up-milling process produced lower forces and offered better surface quality compared to the down-milling process. In addition to these works, in order to minimize the damages and obtain a higher quality surface in the milling of CFRP, some researchers have applied a range of advanced methods including tool design and optimization [16-18], tool inclination or tilted milling [15, 19, 20], ultrasonic assisted machining [21-23] and cryogenic machining [24-26]. On the other hand, the sinusoidal tool path strategy has proven highly

effective in side milling Ti alloy, a difficult-to-cut material, by significantly reducing cutting forces, enhancing surface quality, and prolonging tool life [27]. To date, a variety of methods have been employed to enhance the machinability of composites. However, the number of studies investigating machining with different tool path strategies remains limited. Besides, although it was emphasized that it improved the machinability of metals, the utilization of the sinusoidal tool path strategy on side milling of polymer composites has not yet been extensively investigated. To bridge this gap in the literature, the present study has examined the influence of a sinusoidal machining strategy on side milling of CFRP using different cutting parameters and tools.

2 MATERIAL AND METHOD

The carbon-epoxy plate provided by Dost Kimya company was used as a workpiece. The plate was manufactured from twill woven fabric and had a 0/90° fiber orientation. The workpiece dimensions were 30 mm x 30 mm and 4.5 mm thick. Properties of the CFRP plate in the fiber direction are given in Table 1. 8 mm diameter carbide end mills with three different flute numbers (2, 4, and multi-flute) were used as cutting tools. The 2-flute tool was DLC coated, the 4-flute tool was TiSiN coated, and the multi-flute tool was uncoated. Milling experiments were carried out on the Quaser mv-154c vertical machining center. The workpiece was fixed to the dynamometer using a mini clamp and a toggle clamp. The side milling operation was conducted using three distinct tool paths: linear, and two sinusoidal paths, namely the Sin (0.5x) curve and the Sin(x) curve. In machining with the sinusoidal tool path, while the amplitude value was kept constant to be equal to the material thickness, the wavelength was approximately 3.14 mm for the sin(x) curve and 6.28 mm for the sin (0.5x) curve. The experimental setup, tool paths and cutting tools utilised in the experiments are illustrated in Figure 1.

Table 1. Properties of the CFRP plate used in the experiments

Property	Unit	Value
Density	g/cm^3	>1.50
Tensile Strength	MPa	775
Compression Strength	MPa	475
Tensile Modulus	GPa	63
Flexural Strength	MPa	725
Flexural Modulus	GPa	60

In the experiments, the radial cutting depth was selected as a constant of 4 mm, corresponding to 50% of the tool diameter. Spindle speed and feed rate were selected at two different levels as low and high. Experimental parameters are given in Table 2. All possible conditions were tested and a total of 36 side milling experiments were performed.

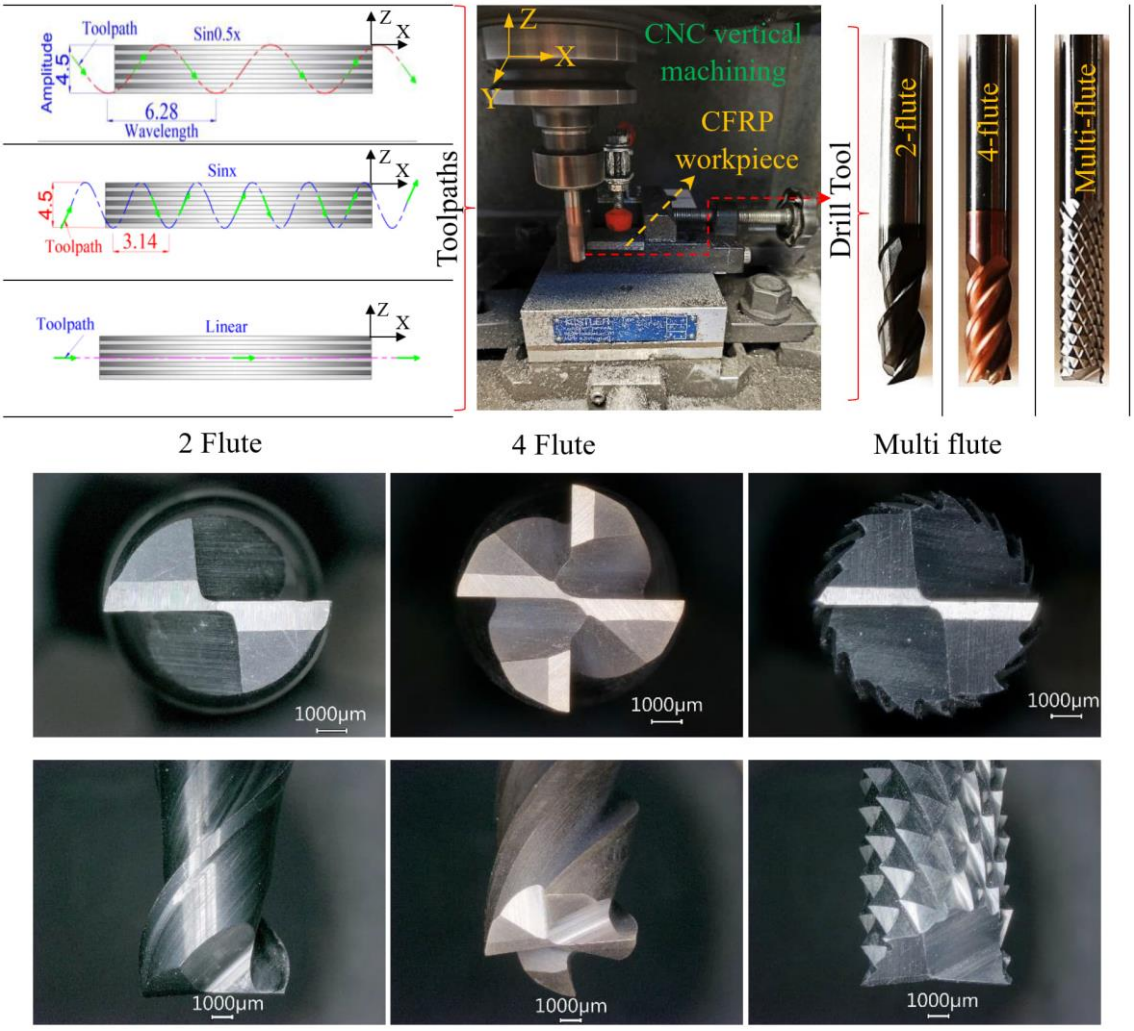


Figure 1. Experimental setup, tool paths, and endmills used in milling experiments

The cutting forces generated during milling were measured with a Kistler 9257b dynamometer fixed to the machine table, Kistler 5070A amplifier, Kistler 5697A data acquisition unit (DAQ), and Dynoware software (Figure 2a). The surface quality of the machined surfaces was examined using Zygo ZeGage 3D optical profiler and Advanced Texture Application (Figure 2b).

Table 2. Experimental parameters

	Level 1	Level 2	Level 3
Cutting tool	Two flute	Four flute	Multi flute
Tool path	Linear	Sinusoidal	
		3.14 mm wavelength	6.28 mm wavelength
Spindle speed (rpm)	2500	7500	-
Feed rate (mm/min)	500	1500	-

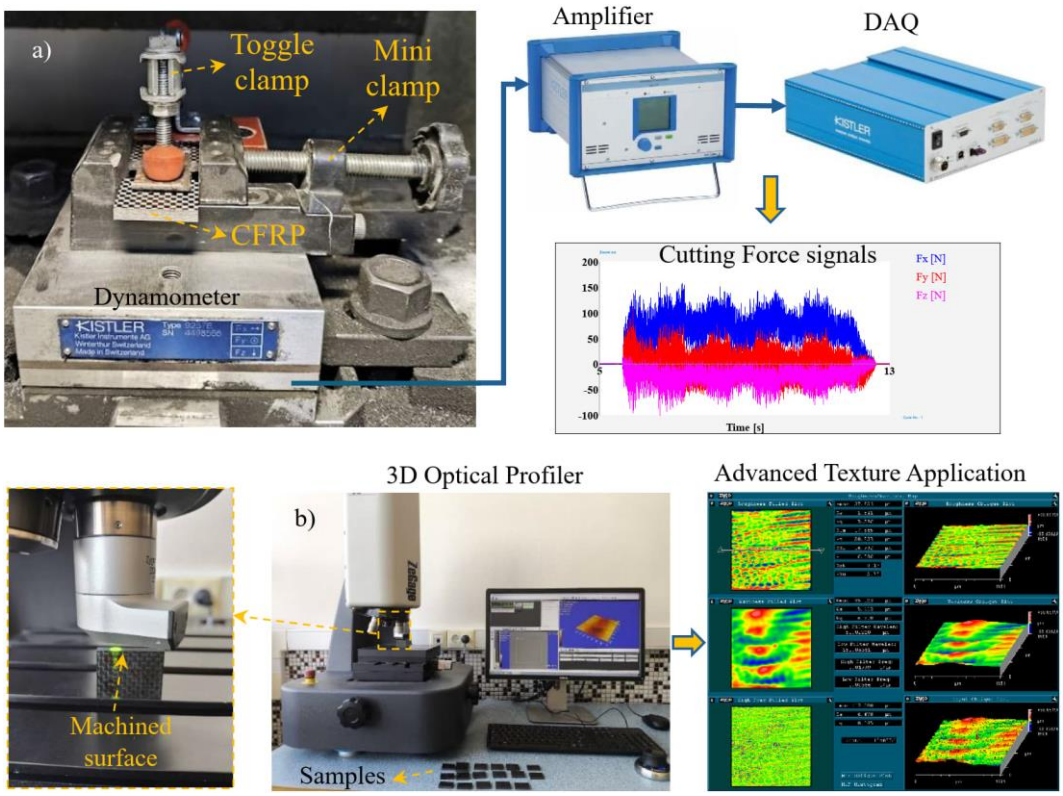


Figure 2. (a) Cutting force measurement; (b) surface roughness measurement

3 RESULTS AND DISCUSSION

3.1 Analysis of Cutting Forces

A detailed analysis of cutting forces is imperative for the evaluation of machinability. The filtered cutting forces measured during the side milling process of CFRP using different tools and tool paths at the same cutting parameters (Spindle speed: 2500 rpm, Feed rate: 500 mm/min) are given in Figure 3, depending on time. When evaluated in terms of tool path, it is clearly seen that feed force (Fx) is the dominant force component in all tool paths. This force component is higher in the linear tool path, while it fluctuates in accordance with the wavelength of the curve in sinusoidal machining. On the other hand, interestingly, while the feed forces exhibit very similar behavior in the machining performed with two-flute and multi-flute tools, higher forces are generated in the milling with four-flute tool. Although similar

behavior is observed in two and multi-tooth tools, the increase in the number of teeth reduces the fluctuation in feed forces. The normal feed force (Fy) has not exhibited a trend analogous to that demonstrated by Fx, and the forces vary depending on the tool geometry and tool path. In the linear tool path, while very low forces are generated, except for significant increases during entry and exit of the material in the machining performed with the four-flute tool, higher forces are generated in the two- and multi-flute tools. In sinusoidal machining, two- and four-flute tools have exhibited similar behavior and produced lower forces, higher forces occur in the multi-flute tool, especially with the increase in wavelength. Upon examination of the passive force (Fz), it is found that significantly lower forces are generated with the multi-flute tool in the linear tool path, while higher forces are generated in the opposite direction with the two- and four-flute tools and the maximum passive force is generated with the two-flute tool. In sinusoidal machining, it has been observed that lower passive forces are generated during machining with multi-flute tools, while two- and four-flute tools exhibit similar behavior and generate higher forces. However, it is also noted that passive forces increased in the four-edge tool with increasing wavelength in sinusoidal machining.

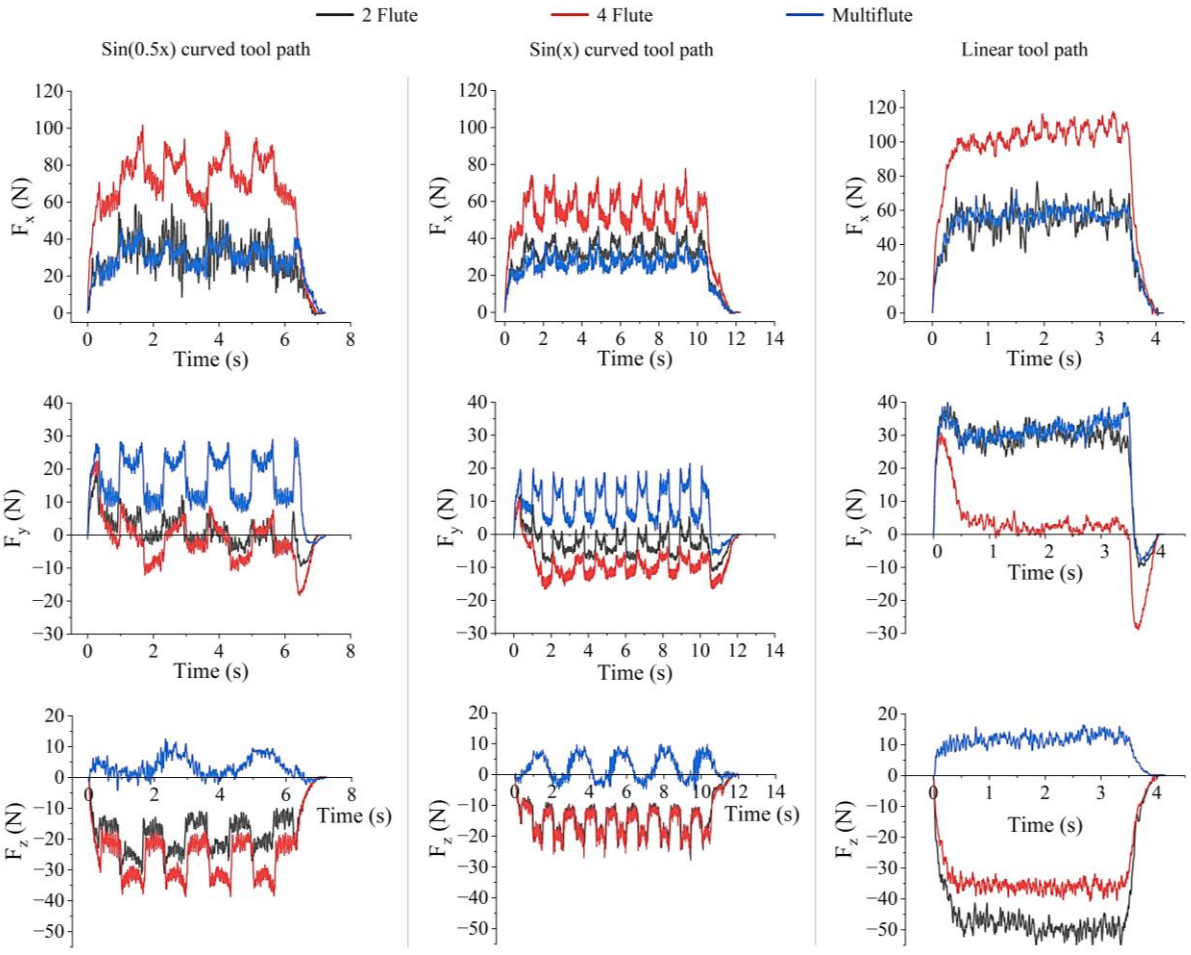


Figure 3. Cutting force signals recorded during milling CFRP depending on different tool path and tool geometry (Spindle speed:2500 rpm, Feed rate:500 mm/min)

It is evident from these observations that the cutting force components are considerably influenced by the tool path and tool geometry and can manifest diverse behaviors. It has been stated in the literature that the feed force can have the same characteristics even when tools with different geometry are used in the machining of CFRP. In addition, it has been found that the Four flute up-cut spiral tool produced higher feed force than the Cross-pitch spiral tool with the same helix angle and the Three flute upcut spiral tool with a higher helix angle, in side milling operation [28]. On the other hand, in another study in the literature, it has been observed that in CFRP side milling performed with a tool with a lower helix angle compared to a higher helix angle tool, tangential cutting force, i.e. the cutting force in the feed direction, is higher, while axial force, i.e. the passive force, is lower [29]. In the present study, the force generation behaviors of the two- and multi-flute tools in the feed direction are almost the same, while the four-flute tool shows differences, in addition, the two-flute tool produces less feed force than the four-flute tool, which are similar to the findings in the literature.

Since the cutting force components behave differently and do not form a trend, the resultant of the maximum cutting forces in three directions was calculated with the help of the following Equation (1) in order to evaluate the influence of cutting parameters, tool path, and tool geometry together.

$$Fr = \sqrt{F_x^2 + F_y^2 + F_z^2} \tag{1}$$

Figure 4 shows the changes in the resultant forces obtained from all experiments according to the cutting parameters, tool path, and tool geometries. At low spindle speed (2500 rpm), irrespective of the feed rate, the highest forces are generated in linear machining, while lower forces have been observed in sinusoidal machining. The decreasing trend in forces has continued with decreasing wavelength. On the other hand, while the maximum resultant force has been generated in machining with the 4-flute tool, this has been followed by the 2-flute and multi-flute tools, respectively. Besides, an increase in the feed rate gives rise to an increase in forces across all tool paths. Following a thorough evaluation of the milling process at high spindle speed (7500 rpm), it is clear that the forces decreased in machining with the linear tool path. Furthermore, it has been established that the order does not change depending on the tool geometry. However, it has been observed that a very different behavior occurs in machining with a sinusoidal tool path, especially in the combination of high spindle and low feed rate. In this combination of cutting parameters, 4-flute and multi-flute tools have exhibited the same behavior as that obtained in other cutting parameters, while much higher forces are generated in the 2-flute tool. As the sine wavelength decreases, the forces generated in the 4 and multi-flute tools have decreased, while interestingly, the forces generated in the 2-flute tool have increased.

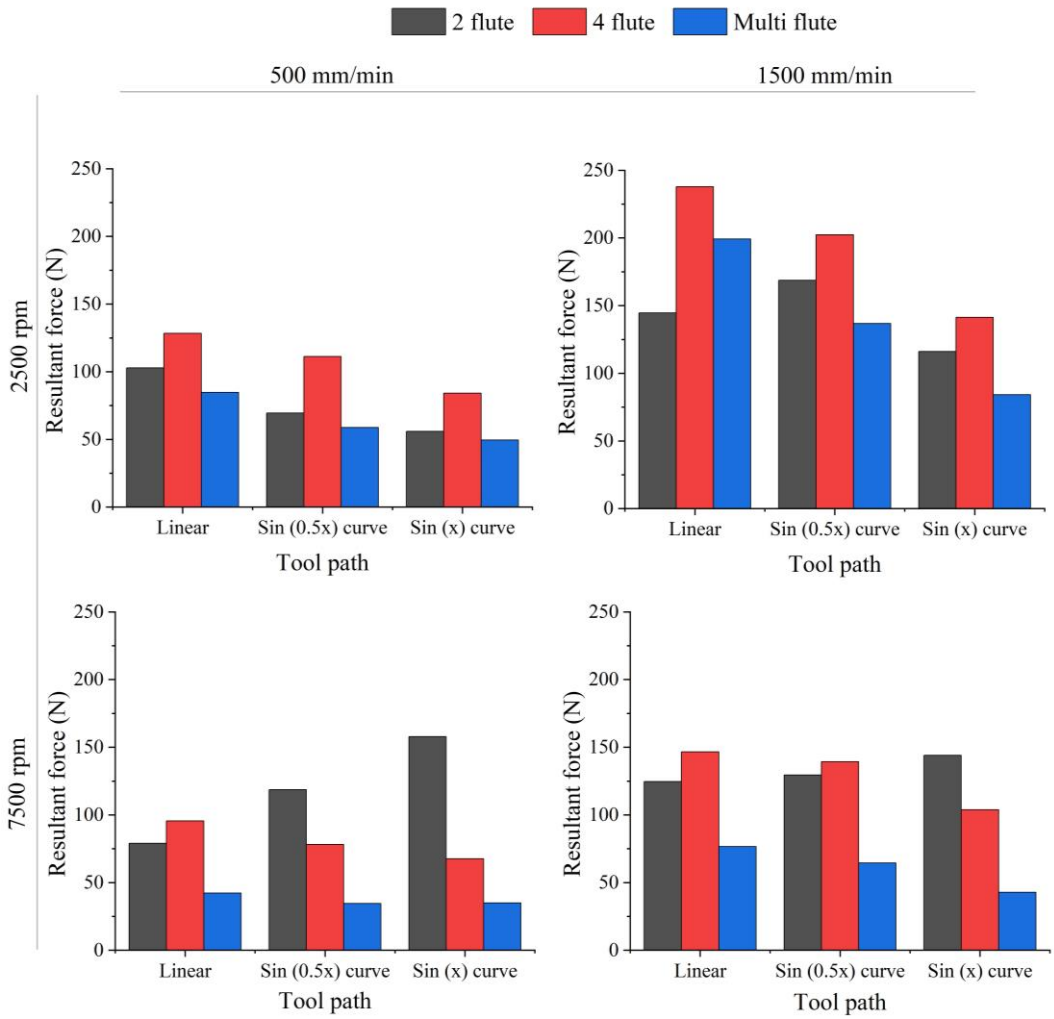


Figure 4. Resultant cutting forces in milling CFRP depending on cutting parameters

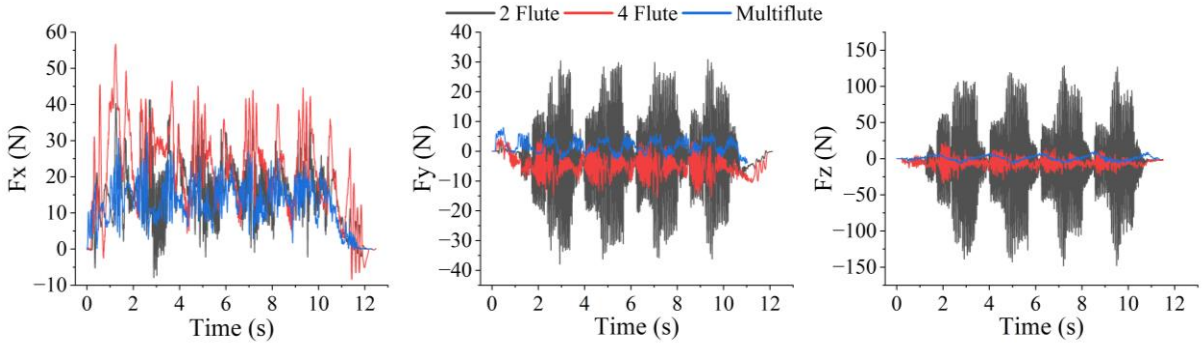


Figure 5. Cutting force signals recorded during sinusoidal milling with sin(x) curve depending on tool geometry at high spindle speed and low feed rate combination (Spindle speed:7500 rpm, Feed rate:500 mm/min)

As demonstrated in Figure 5, the increase in the resultant force in machining with a low wavelength sinus curve (sin(x)) is attributable to the high fluctuation in the normal feed force and passive force. It is thought that at elevated spindle speeds, the tool with a reduced number

of teeth generates vibration during sinusoidal machining, thereby inducing higher force signals and amplifying the resultant force. It has been reported in a previous study that the cutting forces and vibration during the milling operation of CFRP decreased with the increase in the number of cutting edges [30]. This phenomenon can be associated with a larger chip load per tooth and therefore greater variations in cutting forces per revolution.

3.2 Analysis of Surface Quality

In the process of machining composites, a range of potential damage may arise, including delamination, pull-out, debonding, and fiber breakage. Additionally, uncut fibers may be present on the machined surface as a result of poor cutting. These machining-induced damages have the potential to affect surface quality and, consequently, the quality of the machining. However, by selecting appropriate cutting parameters, cutting tool, cutting method and tool path, and cutting conditions, it is possible to minimize damage and obtain higher quality surfaces [31]. Roughness plots were formed by examining the machined surfaces from three different zones using a 3D surface profiler. The surface plots of the samples machined at 2500 rpm spindle speed and 500 mm/min cutting parameters are given in Figure 6.

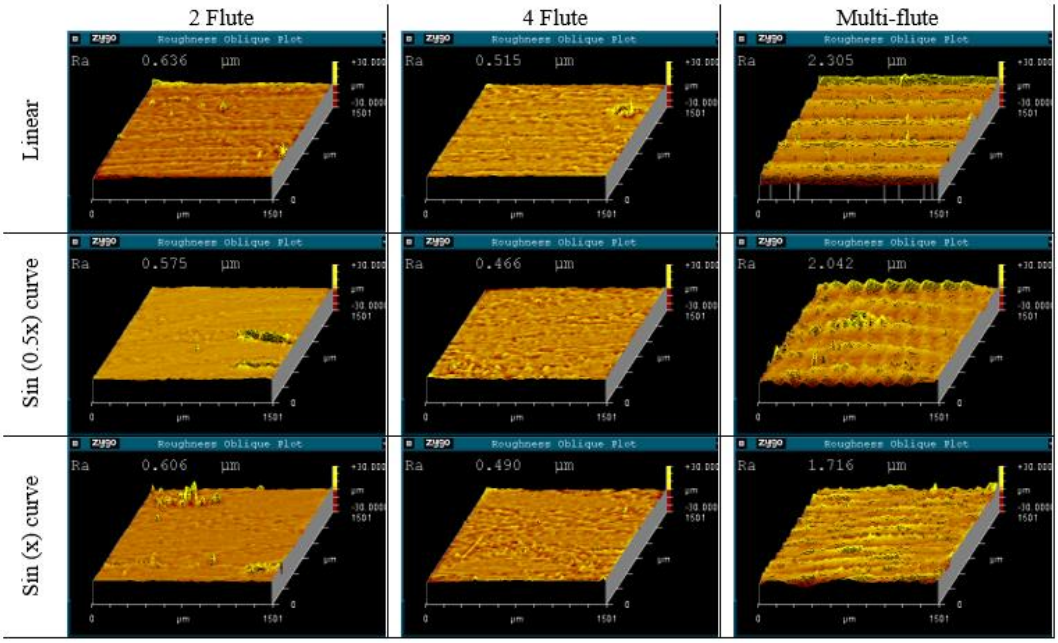


Figure 6. Roughness plots of CFRP depending on different tool path and tool geometry (Spindle speed:2500 rpm, Feed rate:500 mm/min)

It is clear from the figure that the worst surface finishes are formed on the surface machined by the multi-flute tool, regardless of the toolpath. It has been observed that, in machining with a linear tool path, the tool leaves marks at specific intervals along the machined

surface. These tool marks have also caused the surface quality to deteriorate and the roughness values to increase significantly. On the other hand, surface quality has increased with sinusoidal machining performed with the multi-flute tool, and the marks formed on the surface have been significantly reduced by decreasing the wavelength. In the machining process performed with 2 and 4-flute tools, higher quality surfaces have been obtained in all cutting conditions compared to the multi-flute tool. Especially with the 4-flute tool, the best surface quality has been achieved on machined surfaces. Moreover, it has been demonstrated that, even when machining with a linear tool path, a minimal roughness value can be achieved with the 4-flute tool. In the milling process using 2-flute tool, it is clearly seen that even though valleys and peaks are formed with sinusoidal milling, higher quality surfaces are formed compared to linear milling.

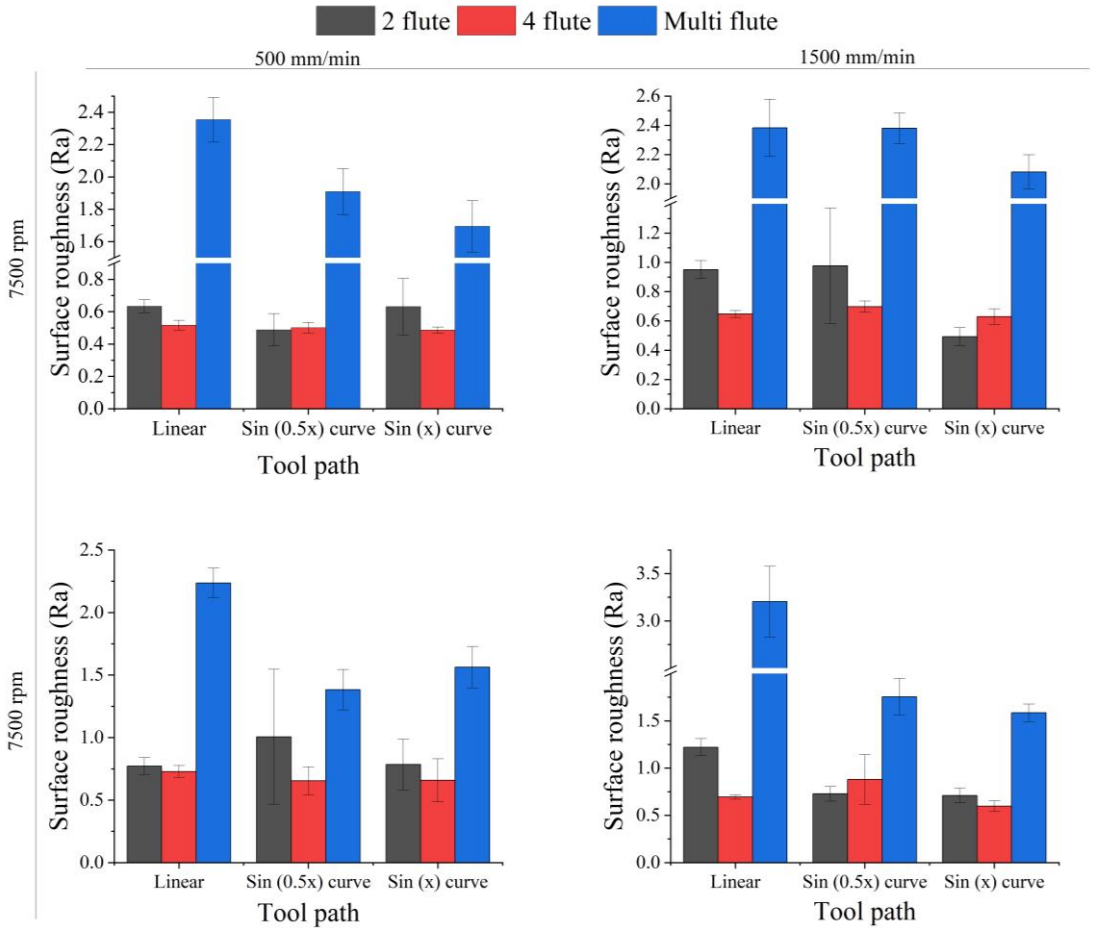


Figure 7. Surface roughness (Ra) in milling CFRP depending on cutting parameters, tool path and tool geometry

Figure 7 illustrates the effects of all cutting conditions on surface roughness measured from three different zones with their standard deviations. As demonstrated by the figure, the highest levels of roughness have been observed to occur on surfaces machined with the multi-flute tool in all cutting conditions, exhibiting a significant disparity. A general evaluation

indicates that surface roughness increases with increasing feed rate, irrespective of tool path and tool geometry. Conversely, an increase in spindle speed has resulted in a decrease in surface roughness during machining with the multi-flute tool. However, no substantial changes are observed in machining with the 2 and 4-flute tools depending on spindle speed. In general, it can be stated that the roughness values of machined CFRP parts decrease when using sinusoidal tool paths compared to linear tool paths, irrespective of tool geometry. In addition, it is concluded that higher-quality surfaces could be obtained with lower wavelengths in sinusoidal milling.

4 CONCLUSION

The present study investigated the cutting forces and surface quality in the side milling process of CFRP. The investigation was conducted through experimentation, utilizing three distinct tools and tool paths, with varied cutting parameters. The key findings from the study are as follows:

- The behavior of the cutting force components (Fx, Fy, and Fz) varies depending on the tool path and geometry. The maximum feed force (Fx) was generated during machining with a 4-flute tool, both in linear and sinusoidal tool paths. In contrast, 2-flute and multi-flute tools generated lower forces and exhibited comparable behavior.

- The cutting parameters resulted in varying force behavior in different cutting tools. At low spindle speeds, irrespective of the tool path, the maximum resultant cutting forces were generated during machining with a 4-flute tool, followed by a multi-flute and a 2-flute tool, respectively. However, at high spindle speed and low feed rate, the two-flute tool generated maximum forces.

- The utilization of sinusoidal tool path machining has been demonstrated to be an effective method of reducing cutting forces, particularly at low spindle speeds. In comparison with linear machining at low spindle speed, the resultant forces generated in sinusoidal machining with high and low wavelengths were reduced by approximately 7% and 32% for the 2-flute tool, 14% and 37% for the 4-flute tool, and 30% and 49% for the multi-flute tool, respectively.

- Irrespective of the tool path, the highest roughness values were formed on surfaces machined with the multi-flute tool, while the 4-flute tool generally yielded surfaces of a higher quality.

• The findings of the study demonstrated that machining with sinusoidal tool paths is an effective method for reducing forces and enhancing surface quality, especially at lower spindle speed, irrespective of tool flute number. However, at elevated spindle speeds, an inverse phenomenon is exhibited by 2-flute tool. In addition, the multi-flute tool exhibited optimal performance in terms of cutting forces, while the 4-flute tool demonstrated superiority in achieving higher surface quality.

Acknowledgements

The author would like to thank Prof. Dr. Uğur Köklü for helping to provide the workpiece.

Statement of Research and Publication Ethics

The study is complied with research and publication ethics.

Artificial Intelligence (AI) Contribution Statement

DeepL Write was employed to enhance the language and readability of the manuscript.

REFERENCES

[1] J. Seo, D. C. Kim, H. Park, Y. S. Kang, and H. W. Park, "Advancements and Challenges in the Carbon Fiber-Reinforced Polymer (CFRP) Trimming Process", *International Journal of Precision Engineering and Manufacturing-Green Technology,* vol. 11, no. 4, pp. 1341-1360, 2024/07/01 2024, doi: 10.1007/s40684-023-00552-1.

[2] J. Seo, D. Y. Kim, D. C. Kim, and H. W. Park, "Recent Developments and Challenges on Machining of Carbon Fiber Reinforced Polymer Composite Laminates", *International Journal of Precision Engineering and Manufacturing,* vol. 22, no. 12, pp. 2027-2044, 2021/12/01 2021, doi: 10.1007/s12541-021-00596-w.

[3] J. Xu, N. Geier, J. Shen, V. Krishnaraj, and S. Samsudeensadham, "A review on CFRP drilling: fundamental mechanisms, damage issues, and approaches toward high-quality drilling", *Journal of Materials Research and Technology,* vol. 24, pp. 9677-9707, 2023/05/01/ 2023, doi: https://doi.org/10.1016/j.jmrt.2023.05.023.

[4] M. Slamani and J.-F. Chatelain, "A review on the machining of polymer composites reinforced with carbon (CFRP), glass (GFRP), and natural fibers (NFRP)", *Discover Mechanical Engineering,* vol. 2, no. 1, p. 4, 2023/04/03 2023, doi: 10.1007/s44245-023-00011-w.

[5] T. Gao *et al.*, "Carbon fiber reinforced polymer in drilling: From damage mechanisms to suppression", *Composite Structures,* vol. 286, p. 115232, 2022/04/15/ 2022, doi: https://doi.org/10.1016/j.compstruct.2022.115232.

[6] S. Morkavuk, K. Aslantaş, L. Gemi, U. Köklü, and Ş. Yazman, "The influence of drilling-induced damages and hole quality on hoop tensile and fatigue behavior of CFRP tubes", *Composites Part A: Applied Science and Manufacturing,* vol. 179, p. 108005, 2024/04/01/ 2024, doi: https://doi.org/10.1016/j.compositesa.2024.108005.

[7] M. Haddad, R. Zitoune, H. Bougherara, F. Eyma, and B. Castanié, "Study of trimming damages of CFRP structures in function of the machining processes and their impact on the mechanical behavior", *Composites Part B: Engineering,* vol. 57, pp. 136-143, 2014/02/01/ 2014, doi: https://doi.org/10.1016/j.compositesb.2013.09.051.

[8] J. Sheikh-Ahmad, N. Urban, and H. Cheraghi, "Machining Damage in Edge Trimming of CFRP", *Materials and Manufacturing Processes,* vol. 27, no. 7, pp. 802-808, 2012/07/01 2012, doi: 10.1080/10426914.2011.648253.

[9] E. Kiliçkap, A. Yardimeden, and Y. H. Çelik, "Investigation of experimental study of end milling of CFRP composite", *Science and Engineering of Composite Materials,* vol. 22, no. 1, pp. 89-95, 2015, doi: doi:10.1515/secm-2013-0143.

[10] A. Can, "Effect of Edge Trimming Parameters on Surface Quality of Carbon Fiber Reinforced Polymer Composites", *Afyon Kocatepe Üniversitesi Fen Ve Mühendislik Bilimleri Dergisi,* vol. 17, pp. 302-311, April 2017.

[11] S. Yağmur, A. Kurt, and U. Şeker, "Karbon Fiber Takviyeli Kompozit Malzemelerinin Frezelenmesinde Meydana Gelen Yüzey Pürüzlüğünün Değerlendirilmesi ve Matematiksel Modellenmesi", *Gazi Üniversitesi Fen Bilimleri Dergisi Part C: Tasarım ve Teknoloji,* vol. 6, no. 3, pp. 705-714, September 2018, doi: 10.29109/gujsc.411033.

[12] R. Prakash, V. Krishnaraj, and J. Sheikh-Ahmad, "High-speed edge trimming of carbon fiber-reinforced polymer composites using coated router tools", *Journal of Composite Materials,* vol. 53, no. 28-30, pp. 4189-4202, 2019, doi: 10.1177/0021998319856071.

[13] Q. Xu, S. Xiao, H. Gao, and H. Shen, "The propagation of fibre–matrix interface debonding during CFRP edge milling process with the multi-teeth tool: A model analysis", *Composites Part A: Applied Science and Manufacturing,* vol. 160, p. 107050, 2022/09/01/ 2022, doi: https://doi.org/10.1016/j.compositesa.2022.107050.

[14] D. J. Devan, F. Almaskari, J. Sheikh-Ahmad, and F. Hafeez, "A study on tool wear of tungsten carbide cutters in edge trimming of CFRP", *Journal of Mechanical Science and Technology,* vol. 36, no. 5, pp. 2499-2510, 2022/05/01 2022, doi: 10.1007/s12206-022-0432-z.

[15] B. Zhang *et al.*, "Machining inclination selection method for surface milling of CFRP workpieces with low cutting-induced damage", *Composite Structures,* vol. 304, p. 116495, 2023/01/15/ 2023, doi: https://doi.org/10.1016/j.compstruct.2022.116495.

[16] Y. Chen, X. Guo, K. Zhang, D. Guo, C. Zhou, and L. Gai, "Study on the surface quality of CFRP machined by micro-textured milling tools," *Journal of Manufacturing Processes,* vol. 37, pp. 114-123, 2019/01/01/ 2019, doi: https://doi.org/10.1016/j.jmapro.2018.11.021.

[17] N. López de Lacalle, A. Lamikiz, F. J. Campa, A. F. Valdivielso, and I. Etxeberria, "Design and Test of a Multitooth Tool for CFRP Milling", *Journal of Composite Materials,* vol. 43, no. 26, pp. 3275-3290, 2009, doi: 10.1177/0021998309345354.

[18] F. Wang, B. Zhang, Z. Jia, X. Zhao, and Q. Wang, "Structural optimization method of multitooth cutter for surface damages suppression in edge trimming of Carbon Fiber Reinforced Plastics", *Journal of Manufacturing Processes,* vol. 46, pp. 204-213, 2019/10/01/ 2019, doi: https://doi.org/10.1016/j.jmapro.2019.09.013.

[19] W. Hintze and F. Brügmann, "Influence of spatial tool inclination on delamination when milling CFRP", *Journal of Materials Processing Technology,* vol. 252, pp. 830-837, 2018/02/01/ 2018, doi: https://doi.org/10.1016/j.jmatprotec.2017.10.041.

[20] Q. Wang, Y. Wu, Y. Li, D. Lu, and T. Bitoh, "Proposal of a tilted helical milling technique for high-quality hole drilling of CFRP: analysis of hole surface finish", *The International Journal of Advanced Manufacturing Technology,* vol. 101, no. 1, pp. 1041-1049, 2019/03/01 2019, doi: 10.1007/s00170-018-2995-5.

[21] D. Geng, D. Zhang, Y. Xu, F. He, D. Liu, and Z. Duan, "Rotary ultrasonic elliptical machining for side milling of CFRP: Tool performance and surface integrity", *Ultrasonics,* vol. 59, pp. 128-137, 2015/05/01/ 2015, doi: https://doi.org/10.1016/j.ultras.2015.02.006.

[22] J. Liu, G. Chen, C. Ren, X. Qin, Y. Zou, and J. Ge, "Effects of axial and longitudinal-torsional vibration on fiber removal in ultrasonic vibration helical milling of CFRP composites", *Journal of Manufacturing Processes,* vol. 58, pp. 868-883, 2020/10/01/ 2020, doi: https://doi.org/10.1016/j.jmapro.2020.08.071.

[23] Z. Sun *et al.*, "An innovative study on high-performance milling of carbon fiber reinforced plastic by combining ultrasonic vibration assistance and optimized tool structures", *Journal of Materials Research and Technology,* vol. 22, pp. 2131-2146, 2023/01/01/ 2023, doi: https://doi.org/10.1016/j.jmrt.2022.12.054.

[24] D. Kumar and S. Gururaja, "Machining damage and surface integrity evaluation during milling of UD-CFRP laminates: Dry vs. cryogenic", *Composite Structures,* vol. 247, p. 112504, 2020/09/01/ 2020, doi: https://doi.org/10.1016/j.compstruct.2020.112504.

[25] S. Morkavuk, U. Köklü, M. Bağcı, and L. Gemi, "Cryogenic machining of carbon fiber reinforced plastic (CFRP) composites and the effects of cryogenic treatment on tensile properties: A comparative study", *Composites Part B: Engineering,* vol. 147, pp. 1-11, 2018/08/15/ 2018, doi: https://doi.org/10.1016/j.compositesb.2018.04.024.

[26] F. Zou *et al.*, "Performance and mechanism evaluation during milling of CFRP laminates under cryogenic-based conditions", *Composite Structures,* vol. 277, p. 114578, 2021/12/01/ 2021, doi: https://doi.org/10.1016/j.compstruct.2021.114578.

[27] R. H. Inácio, R. H. L. da Silva, I. C. Pereira, and A. Hassui, "Suppressing notch wear by changing the tool path in the side milling of a Ti-6Al-4 V alloy", *The International Journal of Advanced Manufacturing Technology,* vol. 125, no. 1, pp. 453-463, 2023/03/01 2023, doi: 10.1007/s00170-022-10741-y.

[28] O. Bílek, S. Rusnáková, and M. Žaludek, "Cutting-tool performance in the end milling of carbon-fiber-reinforced plastics", *Materiali in tehnologije,* vol. 50, no. 5, pp. 819-822, 2016, doi: https://doi.org/10.17222/mit.2015.153.

[29] A. Hosokawa, N. Hirose, T. Ueda, T. Koyano, and T. Furumoto, "High-quality end milling of CFRP–Inclination milling with high-helix end mill–", *International Journal of Automation Technology,* vol. 10, no. 3, pp. 372-380, 2016.

[30] B. C. Shin, K. B. Kim, S. J. Ha, and M. W. Cho, "A study on the machinability of Carbon Fiber Reinforced Plastics on tool shape", *Journal of The Korean Society of Manufacturing Technology Engineers*, vol. 20, no. 6, pp. 799-804, 2011.

[31] D. Ozkan, P. Panjan, M. S. Gok, and A. C. Karaoglanli, "Experimental study on tool wear and delamination in milling CFRPs with TiAlN-and TiN-coated tools", *Coatings*, vol. 10, no. 7, 623, 2020.

BİTLİS EREN ÜNİVERSİTESİ
FEN BİLİMLERİ DERGİSİ

ISSN: 2147-3129 / e-ISSN: 2147-3188

Article Type : Research Article
Received : April 9, 2025
Revised : June 25, 2025
Accepted : August 1, 2025
DOI : 10.17798/bitlisfen.1672984

Year : 2025
Volume : 14
Issue : 3
Pages : 1563-1580

MICROPROPAGATION OF *MUSCARI LATIFOLIUM*, AN ENDEMIC PLANT OF TÜRKİYE

Nesrin BOZHAN [1,*], Ahmet ONAY [1]

[1] *Dicle University, Department of Biology, Diyarbakır, Türkiye*

**** Corresponding Author:*** *n_bozhan@hotmail.com*

ABSTRACT

This study aimed to develop a seed-based *in vitro* propagation protocol for *Muscari latifolium* to ensure large-scale plant production while minimizing the impact on wild populations. Utilizing seeds as initial explants offers a sustainable and non-destructive alternative to bulb-based methods, promoting genetic diversity and supporting conservation efforts. Sterilization was optimized using 20% Sodium hypochlorite (NaOCl) for 30 minutes, achieving 100% decontamination and 100% germination. The most effective bulblet induction was observed on MS medium supplemented with 1.0 mg/l 6-Benzylaminopurine (BAP), yielding the maximum average bulblet number (21.06 per explant) and optimal bulblet length (0.71 cm), significantly outperforming other cytokinin treatments, including Kinetin (KIN). In contrast, the combination of 1.0 mg/l BAP and 1.0 mg/l α-Naphthalene Acetic Acid (NAA) also demonstrated substantial bulblet production, albeit at a lower average number (5.60 per explant), but with enhanced bulblet diameter (0.69 cm) and a notable rooting rate of 75%. While BAP alone proved superior for shoot multiplication and bulblet induction, adding NAA improved bulblet morphology and rooting efficiency, emphasizing the importance of cytokinin-auxin synergy. Rooting was most successful (100%) with 2 mg/l indole-3-butyric Acid (IBA), producing robust roots, while acclimatization achieved a 47% survival rate using a sterile peat-soil mixture. The developed protocol provides a reliable, non-destructive method for the ex situ conservation and horticultural production of *M. latifolium*, leveraging seeds to reduce the need for bulb collection. This approach holds promise for propagating other endangered geophytes with similar challenges.

Keywords: Bulbet formation, Micropropagation, *Muscari latifolium*, Tissue culture.

1 INTRODUCTION

Biodiversity conservation has become an urgent global priority, particularly for endemic and endangered plant species that play essential ecological roles and harbour unique genetic resources. The Mediterranean basin, recognized as a biodiversity hotspot, is home to numerous endemic species, many of which are under severe threat due to habitat destruction, urbanization, and overexploitation [1]. Türkiye, situated at the crossroads of Europe and Asia, possesses a rich floristic diversity, with over 12,000 native vascular plant taxa, approximately one-third of which are endemic. However, many of these species, particularly bulbous geophytes, are increasingly at risk [2]. Among these vulnerable taxa, *Muscari latifolium* John Kirk, commonly known as the broad-leaved grape hyacinth, is an endangered bulbous plant species endemic to south-western Türkiye. This species is distinguished by its unique blue-violet inflorescence and horticultural appeal, making it valuable in ornamental plant cultivation [3]. However, its natural populations are confined to montane pine forests at elevations of 1100-1800 m, where anthropogenic pressures such as deforestation, land-use change, and excessive harvesting have led to significant population declines [4], [5]. The increasing demand for this species as an ornamental plant, coupled with the limited natural regeneration capacity of its seeds and bulblets, has necessitated urgent conservation efforts [1].

Conventional conservation approaches such as seed banking and in situ preservation are often inadequate for *M. latifolium* due to its recalcitrant seed dormancy and slow natural propagation [5]. Consequently, ex-situ conservation through *in vitro* micropropagation has emerged as a viable alternative for the rapid multiplication of endangered plant species while preserving genetic integrity and reducing pressure on wild populations [6]. *In vitro* propagation not only enables the large-scale production of genetically stable, disease-free plants but also facilitates the establishment of germplasm banks and supports reintroduction initiatives [7], [2].

Several studies have successfully applied *in vitro* micropropagation techniques to various *Muscari* species. For instance, in a study by Uranbey [8], high-frequency bulb regeneration for the endemic and endangered ornamental plant *Muscari azureum* Fenzl was successfully achieved using immature embryos. A protocol for *in vitro* propagation of *Muscari mirum* Speta, an endangered geophyte, was developed by Nasırcılar et al. [9]. In this study, bulb scale, scape, leaf and immature embryo explants of *M. mirum* were cultured in different nutrient media and supplemented with different concentrations of plant growth regulators (BAP, NAA, TDZ, Picloram, 2.4-D). In the study conducted by Karamanian et al. [10] on *Muscari neglectum* Guss, somatic embryogenesis was induced from bulb explants cultured in Murashige and Skoog

(MS) medium containing no plant growth regulators or supplemented with different concentrations of 1-naphthaleneacetic acid (NAA) and 6-benzylaminopurine (BA). The best results were obtained in medium containing no plant growth regulators or with lower concentrations of NAA and BA and 30 g/ml sucrose.

Yücesan et al. [11], developed an effective *in vitro* regeneration system for *Muscari armeniacum* Leichtlin ex Baker in Linsmaier and Skoog basal medium (LS) supplemented with varying concentrations (0.5, 1.0 or 2.0 mg/l) of benzyladenine (BA) alone or in combination with 0.5 mg/l of NAA. In the study conducted by Vaziri et al. [12] on *Muscari aucheri* (Boiss.), which is endemic to Türkiye and is under threat of complete extinction, it was aimed to establish a strategy for effective in vitro bulb regeneration of this important geophyte by using 4-scale bulb explants to assist in the reproduction and propagation of the plants. In the study conducted by Ozdemir et al. [13], it was aimed to accelerate the proliferation by developing an effective *in vitro* bulb regeneration strategy for *M. aucheri*, whose natural populations are seriously affected by increasing environmental pollution, urbanization and grazing. *Muscari muscarimi* Medikus has been propagated using twin bulb scale explants, achieving high bulblet regeneration rates under optimized cytokinin and auxin conditions [2]. Similarly, *M. armeniacum* has been propagated via direct bulblet proliferation from bulb and leaf explants, highlighting the importance of plant growth regulator combinations for successful regeneration [14]. Additionally, *M. neglectum* has been investigated for its *in vitro* regeneration potential, demonstrating successful bulblet formation and acclimatization, thereby supporting both conservation and horticultural applications [15]. Despite these advancements, there is a paucity of literature specifically focusing on *M. latifolium*, and no dedicated regeneration protocol has been established for its efficiency *in vitro* propagation.

Utilizing seed-derived explants for *in vitro* propagation offers several distinct advantages over conventional bulb-scale methods. Seed-based propagation ensures higher genetic diversity, which is crucial for conservation programs and enhances the adaptability of reintroduced populations [14]. Additionally, seed explants are generally less susceptible to microbial contamination than bulb or leaf tissues, simplifying sterilization procedures and improving culture success rates [14]. Furthermore, seeds are more readily available and can be stored for extended periods, allowing for scalable conservation efforts without depleting natural populations [6]. Another crucial aspect of this study is the successful transition from seed-derived plantlets to bulblet formation, which is a relatively underexplored approach in *Muscari* micropropagation. Compared to direct bulblet regeneration from bulb-scale explants, seed-

based propagation requires overcoming additional challenges such as dormancy-breaking, optimizing germination conditions, and ensuring efficient bulblet formation in culture. The ability to induce bulblet formation from seed-derived plantlets is a significant achievement, as it enables the production of genetically diverse propagules that can be further multiplied through clonal propagation. Given the critical conservation status of *M. latifolium*, the aim of this study was to develop comprehensive micropropagation from seed-derived explants (axenic stems).

2 MATERIAL AND METHOD

2.1 Plant Material and Seed Collection

Mature seeds of *M. latifolium* were collected from natural populations in the broad-leaved forest understory of Ayazma Recreation Area, Bayramiç, Çanakkale in May 2017. The identification and seed collection of *M. latifolium* were carried out by Assoc. Prof. Dr. Hüseyin Eroglu (Van Yüzüncü Yıl University) and Prof. Dr. Mehmet Fidan (Siirt University). Seeds were carefully selected based on uniform size and maturity to ensure optimum viability for *in vitro* culture. Figure 1 presents the general appearance of the flowering *M. latifolium* in its natural habitat.



Figure 1. General appearance of M. latifolium during the flowering stage in its natural habitat.

2.2 Surface Sterilization of Seeds

A two-stage surface sterilization method was applied to initiate aseptic cultures. Seeds stored at room temperature of 25±2 ºC in a dark environment until the studies were started. Before surface sterilization, the seeds were washed under running tap water for 10 min. Then, they were immersed in 70% ethanol for 1 min and then washed with sterile distilled water at

least three times. A surface sterilization protocol was optimized to obtain maximum viable explants with minimum sterilant concentration. For this purpose, the seeds were shaken in sodium hypochlorite (NaOCl) solutions at different concentrations (10%, 20%, 30% and 40%) for 20 min. The seeds were then washed five times with sterile distilled water to remove the sterilant residues on their surfaces. The effect of sterilization time (10, 20, 30 and 40 min) on decontamination of seeds was determined using the sterilant percentage (20% NaOCl) that had the highest germination rate among different NaOCl concentrations tested. The efficiency of each sterilization process was evaluated according to contamination rates and seed viability three weeks after culturing.

2.3 Culture Medium and Growth Conditions

Surface sterilized seeds were lightly scratched with a scalpel tip to increase germination and cultured in hormone-free Murashige and Skoog (MS) medium [16] solidified with 6.4 g/L agar. The pH of the medium was adjusted to 5.8 using 1N NaOH and 1N HCl before autoclaving at 121°C and 1.2 atm for 20 min. The cultures were transferred to fresh medium every six weeks. The cultures were incubated in a growth chamber at 25±2°C with a 16-h photoperiod provided by cool-white fluorescent lamps (light intensity: 3000 lux). Each treatment consisted of 20 seeds and each experiment was repeated three times.

2.4 Shoot Induction and Bulblet Formation

After germination (approximately 15 weeks), in order to initiate bulblet development, in vitro shoots were subcultured onto MS medium supplemented with different concentrations (0.5 mg/l and 1.0 mg/l) of two different cytokinins BAP and KIN. All cultures were kept at 25±2°C with a 16-hour photoperiod. Shoot formation was evaluated after 20 weeks, while callus formation was tracked after 10 weeks. Primary bulblets were subcultured onto MS medium with 0.5 or 1.0 mg/l BAP or KIN to encourage bulblet enlargement after bulblet initiation. The effects of BAP and NAA at varying concentrations (1.0, 2.0, and 4.0 mg/l) on adventitious bulblet proliferation were examined in the following studies to further improve the methodology. Four to five axillary bulblets per treatment were removed along with the shoots and moved in duplicate to new culture medium. After 15 weeks, the growth and multiplication rates of the bulblets were assessed.

2.5 *In Vitro* Rooting and Acclimatization

In contrast to traditional micropropagation methods that necessitate distinct rooting media, the bulblets examined in this study demonstrated the ability to form roots spontaneously in cytokinin-enriched MS medium. The development of roots was assessed by evaluating root length, quantity, and the overall vigour of the plantlets. For the acclimatization process, the rooted bulblets were gently removed from the culture vessels, rinsed under running tap water to eliminate any remaining agar, and then transplanted into a sterilized peat and peat-soil mixture (1:1) based commercial growing medium. Micropropagated plantles were irrigated regularly, and were covered with a transparent plastic bag to ensure high humidity during the initial acclimatization stage. Humidity levels gradually decreased by making small perforations in the plastic cover each day, and the frequency of watering was reduced from daily to every 3-5 days. After a period of 6 weeks, the plastic coverings were taken off, and the plantlets were moved to greenhouse conditions for further hardening.

2.6 Data Collection and Statistical Analysis

To assess the effectiveness of the micropropagation protocol, several critical parameters were monitored at various growth stages: Axenic cultures; The rates of contaminated and decontaminated axenic cultures were reported three weeks after initiation of culture. Seed germination rate; These values were recorded 15 weeks after culturing. Callus induction and bulblet formation; These were assessed at 10 and 20 weeks after culturing, respectively. Rooting and acclimatization success; These were observed at 8 and 6 weeks after culturing, in sequence.

For the statistical analysis, each treatment comprised 15 to 20 explants, with three replicates for each experiment. The data were analyzed using One-Way Analysis of Variance (ANOVA), followed by the Duncan test for post hoc multiple comparisons at a significance level of $p < 0.05$. Statistical analyses were conducted using SPSS version 25.0. The data presented as proliferation percentages underwent Chi-square (χ^2) analysis.

3 RESULTS AND DISCUSSION

3.1 Surface Sterilization of Seeds and Axenic Germination

The success of *in vitro* propagation is highly dependent on effective surface sterilization, which prevents microbial contamination while maintaining explant or seed viability to a large extent. The choice of sterilant and exposure duration played a critical role in optimizing germination rates of *Muscari* seeds.

3.1.1 Effect of NaOCl Concentrations on Decontamination and Germination

After three weeks of culturing, a 100% contamination was observed in the control group (untreated seeds), demonstrating the necessity of surface sterilization in preventing microbial growth. Seeds treated with sodium hypochlorite (NaOCl) at various concentrations showed complete sterilization, with no contamination detected across all treatments. However, germination rates varied significantly depending on the NaOCl concentration. The highest germination rate (90%**)** was achieved with 20% NaOCl**,** whereas higher concentrations led to a decline in germination percentage (Table 1). The reduction at 30% and 40% NaOCl can be attributed to the cytotoxic effects of hypochlorite, which may damage seed tissues and reduce viability. These results confirm that 20% NaOCl is optimal for balancing sterilization efficacy and germination success.

Table 1. Effect of different NaOCl concentrations on surface sterilization and germination of M. latifolium seeds.

NaOCl Concentration (%)	Contaminated Seeds (%)*	Germinated Seeds (%)*
Control	100 b	0 d
10%	0 a	55 b
20%	0 a	90 a
30%	0 a	50 b
40%	0 a	20 c

**Data were subjected to Chi square (χ^2) analysis. Values represent the mean of 20 explants per treatment. Different letters indicate significant differences ($p < 0.05$).*

Sodium hypochlorite (NaOCl) is a surface sterilizing agent widely used in plant tissue culture studies [17], [18]. However, high concentrations and prolonged exposure can damage seed tissues and reduce germination efficiency. Therefore, optimizing sterilization conditions is of great importance, especially for rare and endangered species. Although specific studies on *Muscari* species are limited, studies on similar plant species provide important information about the effects of NaOCl [19], [20], [21]. Table 1 shows that each explant in the control group was infected and did not germinate. Infection was completely prevented and 55% germination rate was obtained at 10% NaOCl concentration. The highest germination rate was obtained with 20% NaOCl (90%), and it was observed that germination rates decreased at higher concentrations (30% and 40%). This situation shows that high NaOCl concentrations can have a toxic effect on seeds and negatively affect germination and 20% NaOCl is the optimal concentration and other concentrations provide lower germination compared to this value. For example, in a study on *in vitro* germination of *Lathyrus chrysanthus* seeds, it was observed that

3.75% NaOCl concentration was applied for 15 minutes and gave the best results, but 5% NaOCl concentration damaged the embryo and reduced the germination rate. This study shows that high NaOCl concentrations can damage seed tissues [19]. Similarly, in the sterilization of *Ficus religiosa* seeds, the highest germination rate (63.33%) was obtained in 5- and 10-min applications of 10% NaOCl concentration, while higher concentrations were observed to decrease the germination rate [20]. It has been reported that the application of 2% NaOCl solution at 20°C for 30 minutes in the surface sterilization of *Onobrychis viciifolia* seeds gave the best results, while higher concentrations and temperatures negatively affected the germination and regeneration capacity [21].

3.1.2 Effect of NaOCl Exposure Duration on Sterilization and Germination

Further optimization was carried out by varying exposure times using the 20% NaOCl concentration. All exposure durations resulted in complete sterilization, confirming the effectiveness of NaOCl treatment. However, germination rates increased significantly with longer exposure, reaching 100% germination at 30 and 40 minutes (Table 2). These results suggest that prolonged NaOCl exposure enhances sterilization without adversely affecting germination, a crucial factor for seed-based propagation strategies.

Table 2. Effect of 20% NaOCl exposure duration on sterilization and germination of Muscari latifolium seeds.

NaOCl Exposure Time (min)	Contaminated Seeds (%)*	Germinated Seeds (%)*
10	0 a	75 b
20	0 a	90 b
30	0 a	100 a
40	0 a	100 a

**Data were subjected to Chi square (χ^2) analysis. Values represent the mean of 20 explants per treatment. Different letters indicate significant differences ($p < 0.05$).*

These findings confirm that a 30-minute treatment with 20% NaOCl is optimal for balancing microbial decontamination and maximizing germination success in *M. latifolium*. In Table 2, it is seen that infection was completely prevented at all times of 20% NaOCl application and germination rates increased as the application time increased. Especially in 30 and 40-minute applications, 100% germination rate was obtained. These results show that both infections can be prevented and high germination rates can be achieved with appropriate NaOCl concentration and application time. The application time of NaOCl is also important in terms

of sterilization efficiency and seed viability. For example, a study on *Arabidopsis thaliana* seeds reported that treatments with 80% and 100% bleach concentrations for more than 10 minutes significantly reduced the germination rate and caused various growth defects in the seeds. This suggests that long-term NaOCl exposure may have negative effects on seed viability [22]. In a study conducted on buckwheat (*Polygonum convolvulus* L.) seeds, maximum germination was obtained as a result of 6-8 hours of treatment with 6% NaOCl. However, longer treatments resulted in poor germination and seed shattering [23]. In another study, the application of 20% NaOCl for different periods in the surface sterilization of terebinth (*Pistacia terebinthus* L.) seeds was examined and successful results were obtained with appropriate time and concentration combinations [24]. These findings indicate that the concentration and application time of NaOCl are critical to the germination success of seeds and their effectiveness in tissue culture studies. Therefore, it is necessary to determine the optimal conditions for the use of NaOCl, especially for the protection of endangered species such as *M. latifolium*. Low concentration and appropriate application times are important both to prevent contamination and to maintain the viability of seeds. Our results also align with the findings in other species, where excessive NaOCl exposure has been linked to tissue damage and reduced germination efficiency. Optimizing sterilization conditions is particularly important for *M. latifolium*, given its endangered status and the need to maximize viable seedlings for conservation purposes.

3.2 Shoot Induction and Bulblet Formation

3.2.1 Shoot Induction and Multiplication

The efficiency of shoot induction was significantly influenced by cytokinin type and concentration ($p < 0.05$). Among the tested treatments, the highest shoot proliferation was obtained on MS medium supplemented with 1.0 mg/l BAP, resulting in an average explant length of 0.42±0.02 cm and 26% callus induction (Table 3). Lower cytokinin concentrations led to reduced shoot proliferation, whereas higher concentrations promoted excessive callus formation, negatively impacting shoot elongation. These results indicate that BAP was more effective than KIN for shoot induction, consistent with findings in other *Muscari* species.

Table 3. Effect of different cytokinin types and concentrations on shoot development of M. latifolium.

PGR Type and Concentration (mg/l)	Average Shoot Length* (cm)	Average Explant Diameter * (cm)	Callus Induction (%)**
Control	0.41±0.06 a	0.15±0.04 a	26 a
0.5 BAP	0.37±0.03 bc	0.10±0.00 b	20 a
1.0 BAP	0.42±0.02 a	0.10±0.00 b	26 a
0.5 KIN	0.25±0.01 c	0.10±0.00 b	13 a
1.0 KIN	0.30±0.03 c	0.10±0.00 b	20 a

** Means followed by the different lowercase letter in the column of each explant source are significantly different at $p < 0.05$ according to the Post Hoc Multiple Comparisons Test.*
*** Data were subjected to Chi square (χ^2) analysis.*

The findings presented in Table 3 reveal significant differences in terms of average shoot length, explant diameter, and callus induction across different treatments. These results are consistent with similar studies in literature and provide insight into the role of cytokine types and concentrations in plant tissue culture. As shown in Table 3, the highest average shoot length (0.42±0.02 cm) was achieved with 1 mg/l BAP, whereas the lowest average shoot length (0.25±0.01 cm) was recorded with 0.5 mg/l KIN. The control group exhibited a comparable shoot length (0.41±0.06 cm), suggesting that the addition of low concentrations of BAP or KIN did not significantly inhibit shoot growth. This outcome is in line with the findings of previous studies, where lower cytokine concentrations either had no effect or limited effects on shoot elongation. In our study, 0.5 mg/l KIN produced a notably shorter shoot length compared to BAP treatments, suggesting that KIN's effectiveness in promoting shoot elongation may be limited at lower concentrations. The explant diameter followed a similar pattern to the shoot length. The control group exhibited the largest explant diameter (0.15±0.04 cm). The application of 1 mg/l BAP and 0.5 mg/l KIN resulted in a reduced explant diameter (0.10±0.00 cm), indicating that cytokinin treatments may not significantly increase explant expansion. Callus induction was assessed across different cytokinin treatments. The highest callus induction (26%) was observed in the control and 1 mg/l BAP treatments, whereas KIN-treated explants exhibited lower callus induction (13-20%). This result is consistent with previous research that has suggested BAP is more effective in inducing callus formation compared to KIN. On the other hand, KIN showed less effectiveness in inducing callus, which is consistent with the lower callus induction observed in our study.

3.2.2 Bulblet Induction and Multiplication

Bulblet formation is a key developmental stage in the micropropagation of *M. latifolium*, as successful bulblet development is essential for acclimatization and further multiplication. All the treatments tested produced bulblets on MS medium 20-week period following the initiation of the cultures from shoot explants of *M. latifolium* (Figure 2). The results presented in Table 4 showed that 1.0 mg/l BAP resulted in the highest number of newly formed bulblets per explant (21.06±2.96)**,** while 0.5 mg/l BAP (9,67±0,90) led to lowest bulblet induction rates. Average bulblet length ranged between 0,71±0,09 to 0,30±0,08 cm in 1 mg/l BAP and 0.5 mg/l KIN, respectively. The MS medium enriched with BAP resulted in a greater quantity and length of bulblets compared to the medium supplemented with KIN. The average diameter of the bulblets ranged from 0,12±0,02 to 0,04±0,01 cm (Table 4). The highest average bulblet diameter of 0,12±0,02 cm was observed in the MS medium supplemented with 1 mg/l of BAP. The MS medium supplemented with 1 mg/l BAP yielded a significantly higher quantity and length of bulblets in comparison to the medium enhanced with KIN.

Table 4. Effect of different cytokinin types and concentrations on bulblet induction of M. latifolium shoots.

PGR Type and Concentration (mg/l)	Average Bulblets Number*	Average Bulblet Length* (cm)	Average Bulblets Diameter** (cm)
Control	13.40±4.84 ab	0.36±0.12 b	0.04±0.01 b
0.5 BAP	9.67±0.90 b	0.49±0.06 ab	0.11±0.01 a
1.0 BAP	21.06±2.96 a	0.71±0.09 a	0.12±0.02 a
0.5 KIN	10.80±3.95 b	0.30±0.08 b	0.09±0.03 ab
1.0 KIN	10.46±2.75 b	0.66±0.10 a	0.11±0.02 a

**Means followed by the different lowercase letter in the column of each explant source are significantly different at $p < 0.05$ according to the Post Hoc Multiple Comparisons Test*
***Bulblet diameter equal to or greater than 0.50 cm was recorded for 6 treatments.*

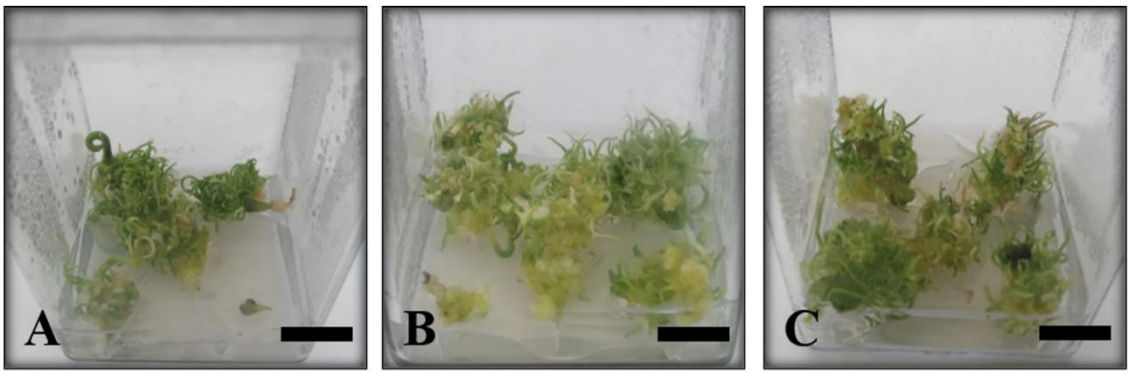


Figure 2. Development of M. latifolium bulblets in MS nutrient medium containing different PGRs after 20 weeks of culture period (A) Control medium (B) Bulblets in MS medium containing 1 mg/l BAP (C) Bulblets in MS medium containing 0.5 mg/l KIN. (Each bars: 1.2 cm).

As shown in Table 4, the highest bulblet number (21.06±2.96) was obtained with the application of 1.0 mg/l BAP. This result aligns with similar studies in the literature [9], [15], [25], which also indicate that BAP has a promotive effect on bulblet induction. In contrast, the control group yielded an average of 13.40±4.84 bulblets. Although this value is lower compared to the BAP treatments, it is still higher than the bulblet production in the KIN treatments. KIN applications, particularly at 0.5 and 1 mg/l concentrations, resulted in bulblet numbers ranging from 9.67±0.90 to 10.80±3.95 Regarding bulblet length, the highest average value was observed with 1 mg/l BAP treatment (0.71 cm). This finding is consistent with studies reporting the promotive effect of BAP on bulblet induction in other *Muscari* species, where optimal concentrations of BAP significantly enhanced bulblet number and size [9]. Additionally, KIN applications were also similarly effective, with 1.0 mg/l KIN yielding a bulblet length of 0.66±0.10 cm. This suggests that KIN may increase bulblet length at higher concentrations, although its effect could be limited at lower concentrations. In the control group, the bulblet length was observed to be 0.36±0.12 cm on average. In terms of bulblet diameter, 1 mg/l BAP again produced the highest value (0.12±0.02cm). In KIN treatments, the average bulblet diameter was observed to be 0.09±0.03 cm with 0.5 mg/l KIN, while it reached 0.11±0.02 cm with 1 mg/l KIN.

The data obtained in this study reveal that BAP is a more effective cytokinin for bulblet induction in *M. latifolium*. The 1 mg/l BAP treatment demonstrated the highest effect on bulblet number, length, and diameter. KIN, although effective at certain concentrations (particularly at 1 mg/l), showed more limited effects compared to BAP. In accordance with other studies in the literature, it can be concluded that BAP is a more effective growth regulator for bulblet induction in *Muscari* species [9], [15], [25].

3.2.2.1 Effect of BAP and NAA Combinations on Bulblet Development

The results presented in Table 5 show that the combination of 1.0 mg/l BAP + 1.0 mg/l NAA produced the highest number of bulblets (5.60±0.59) and the formation of callus was observed in all treatments tested; however, the highest rate and the values obtained for bulblet number, length and diameter in the other tested combinations were lower than the lowest rate obtained with only cytokinin (BAP or KIN) applications (see Table 4).

Table 5. Effect of different BAP and NAA combinations on bulblet development.

PGR Type and Concentration (mg/l)	Average Bulblets Number*	Average Bulblets Diameter* (cm)	Average Bulblets Length* (cm)	Rooting (%)**
1 BAP+1 NAA	5.60±0.59 a	0.19±0.02 a	0.69±0.06 a	75 c
1 BAP+2 NAA	2.67±0.54 bc	0.11±0.02 bc	0.30±0.05 b	80 c
1 BAP+4 NAA	1.27±0.33 c	0.06±0.01 c	0.14±0.04 b	100 a
2 BAP+1 NAA	2.20±0.41 bc	0.18±0.03 a	0.75±0.09 a	100 a
2 BAP+2 NAA	5.60±0.60 a	0.16±0.01 ab	0.59±0.04 a	100 a
2 BAP+4 NAA	3.20±0.39 b	0.21±0.03 a	0.68±0.08 a	90 b
4 BAP+1 NAA	2.80±0.81 bc	0.20±0.03 a	0.69±0.13 a	90 b
4 BAP+2 NAA	1.53±0.32 bc	0.19±0.03 a	0.81±0.16 a	100 a
4 BAP+4 NAA	1.73±0.59 bc	0.08±0.02 c	0.25±0.07 b	80 c

** Means followed by the different lowercase letters in the column of each explant source are significantly different at $p < 0.05$ according to the Post Hoc Multiple Comparisons Test*
*** Data were subjected to Chi square (χ^2) analysis*

In the process of *in vitro* bulblet production from axenic shoots of *M. latifolium*, two distinct concentrations of BAP and KIN (0.5 and 1 mg/l) were evaluated individually, along with a combination of three varying concentrations of BAP (1, 2, and 4 mg/l) paired with three different concentrations of NAA (1, 2 and 4 mg/l), including a control group (Table 4 and Table 5). The study successfully demonstrated a significant and abundant rate of bulblet regeneration from axenic stem explants cultured on MS medium supplemented with 1 mg/l BAP. The combination of BAP with NAA reduced bulblet regeneration and development (Table 5). These findings suggest that utilizing stem explants for the micropropagation of *M. latifolium* holds considerable potential. Our study clearly demonstrated significant and abundant bulblet regeneration rates from axenic stem explants cultured in MS medium supplemented with 1 mg/l BAP. In contrast, previous studies on various bulbous plants Malabadi and Van Staden; [26], Suh et al., [27] suggested that media containing TDZ improved regeneration potential. Uzun et al. [28], previously reported that dozens of bulblets per explant via callus could be produced, but this success was achieved after further subculturing 12–14-month period. However, in our study, bulblets were produced in a shorter timeframe (within 10 months of culture initiation). Although direct comparisons of bulblet numbers are difficult due to methodological differences, our findings regarding efficient callus and bulblet production are consistent with the results reported in *M. armeniacum* and *M. muscarimi* studies [11], [28], [2]. The efficiency of our protocol is further evidenced by the quality of the regenerated plantlets.

3.3 Rooting and Acclimatization

The cultured bulblets exhibited various rooting responses according to the IBA treatments applied (Table 6). Among the treatments tested, the highest rooting percentage (100%) was achieved on MS medium supplemented with 2.0 mg/l IBA**,** producing well-formed roots with an average root number of 3.33±0.39 (Table 6; Figure 3A). The percentage of root forming bulblet was decreased with IBA concentration of 1mg/l and the control group. Acclimatization is very important for the future ex vitro plant development. Acclimatization is possible by decreasing the relative humidity from 90% to 50% in a 6 week-period when a mixture of peat-based medium for hardening of the plantlets (Table 7; Figure 3B). Acclimatization trials revealed that transferring bulblets to a peat-soil mixture resulted in a 47% survival rate, significantly higher than using sterile peat alone (Table 7; Figure 3C).

Table 6. Effect of auxin concentrations on bulblet rooting of M. latifolium.

Auxin Concentrations (mg/l)	Rooting (%)**	Average Root Number*	Average Root Length* (cm)	Average Bulblets Number*
Control	90	3.40±0.29 a	1.25±0.16 b	0.53±0.35 b
1 IBA	75	2.53±0.32 b	1.65±0.25 a	2.33±0.77 a
2 IBA	100	3.33±0.39 a	1.94±0.30 a	3.00±1.00 a

**Means followed by the different lowercase letters in the column of each explant source are significantly different at $p < 0.05$ according to the Post Hoc Multiple Comparisons Test.*
*** Data were subjected to Chi square (χ^2) analysis*

Table 7. Effect of different composts on bulblet acclimatization of M. latifolium.

Compost Types	Difference of Average Bulblets Length* cm)	Viable Bulblets (%)**
Peat (Sterile)	0.60±0,30 a	20 b
Peat+Soil (Sterile)	1.08±0,34 a	47 a

**Means followed by the different lowercase letters in the column of each explant source are significantly different at $p < 0.05$ according to the Post Hoc Multiple Comparisons Test.*
***Data were subjected to Chi square (χ^2) analysis.*

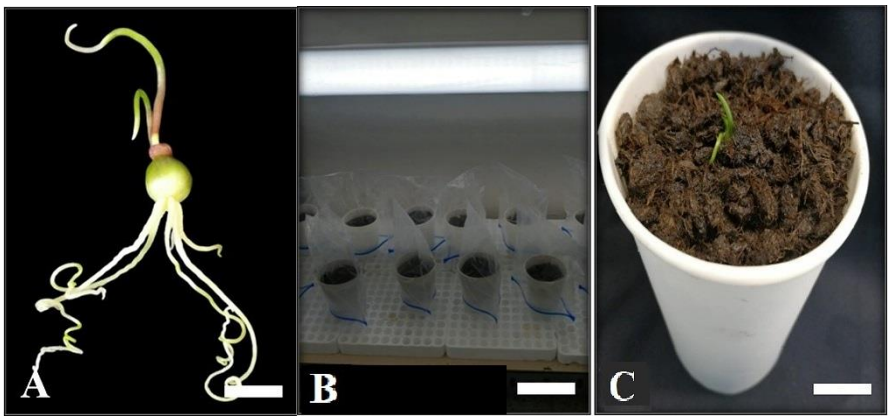


Figure 3. Rooting and acclimatization process of in vitro propagated M. latifolium: (A) Rooted bulblets in hormone-free MS medium (Bar: 1 cm); (B) Plantlets transferred to the plant growth chamber (Bar: 9 cm); (C) Hardened bulblets ready to transfer into Peat+Soil based compost (bar: 2 cm).

We observed that the *in vitro* bulblets rooted readily under an auxin-supplemented medium. Faruq *et al.* [14] showed that using a moderate auxin (2.0 µM IBA) in half-strength MS medium yielded well-formed roots in *M. armeniacum*, whereas higher auxin levels caused callus formation at the base of shoots. We adopted a similar approach, resulting in nearly 100% rooting of *M. latifolium* bulblets *in vitro*. In *M. neglectum* (grape hyacinth), Fida [29] likewise reported 100% rooting within 3 weeks on half-strength MS containing 0.5 mg/l NAA, underlining that relatively low-dose auxin and reduced salts can be optimal for bulbous plant rooting. Our rooted plantlets showed no signs of abnormal callus at the base, an important factor since excess callus can hinder nutrient uptake and transplant success [14].

We acclimatized the regenerated *M. latifolium* bulblets by gradually transferring them to a peat and peat-soil mixture. Thanks to their well-developed root systems, the transplant shock was minimized. Literature benchmarks indicate that survival rates of micropropagated *Muscari* have historically ranged from poor to moderate. For example, bulblets of *M. azureum* produced *in vitro* showed only ~14% survival after transfer to soil [8]. Even with careful techniques, Vaziri et al. [12] noted only 17% of *M. aucheri* bulblets survived acclimatization. An important breakthrough came from Faruq et al. [14], who reported about 60% survival for *M. armeniacum* plantlets by using bulblets that had no basal callus and well-formed roots [14]. In our study, we achieved survival frequencies that approach those higher figures, attesting to the improved hardiness of our plantlets. 47% of our *in vitro*-raised *M. latifolium* plants established successfully in peat-soil mixture (under greenhouse conditions and later outdoors), a rate closer to Faruq's [14] results and markedly higher than earlier *Muscari* reports. This success can be attributed to the combination of our protocol's elements -starting with genetically intact seeds, avoiding prolonged callus phases that might weaken regenerants, ensuring strong root development, and employing a staged acclimatization process.

4 CONCLUSION AND SUGGESTIONS

A micropropagation protocol was established using stems derived from axenic bulblets of *M. latifolium* that were germinated on MS medium. It represents the first detailed report on regeneration from seed-derived explants for this species. For *M. latifolium* seeds, it is recommended to prefer 20% NaOCl concentration to provide the optimum germination and sterilization balance. 30-minute application of 20% NaOCl can be recommended as the most effective surface sterilization protocol as it completely prevents infection and provides 100% germination rate. The combination of 1.0 mg/l BAP produced the highest number of bulblets. the highest rooting percentage (100%) was achieved on MS medium supplemented with 2.0 mg/l IBA. Acclimatization trials demonstrated that transferring plantlets to a peat-soil mixture resulted in a 47% survival rate under greenhouse conditions. Our findings demonstrate that seed-derived bulblet formation is a viable alternative to traditional bulblet-based *in vitro* culture methods. This study highlights that a seed-based approach can successfully generate bulblets, making it particularly valuable for conservation efforts where minimizing wild collection is a priority and establishes a reliable *in vitro* propagation protocol for *M. latifolium*, providing a foundation for its ex situ conservation and sustainable population restoration. The findings will facilitate the enhanced utilization of the species as an ornamental plant through simplified propagation methods, while also contributing to its conservation by minimizing its extraction from natural habitats.

Acknowledgements

I like to thank Prof. Dr. Engin TİLKAT (Batman University) and Assistant Prof. Dr. Veysel SÜZERER (Bingöl University) for their helpful suggestions, encouraging conversations, and constructive support whenever I needed it during the project. This study is a part of the doctoral thesis of Nesrin BOZHAN (Dicle University).

Conflict of Interest Statement

There is no conflict of interest between the authors.

Statement of Research and Publication Ethics

The study is complied with research and publication ethics.

Artificial Intelligence (AI) Contribution Statement

Artificial intelligence (AI) tools were used solely for language editing, grammar corrections, and improving the fluency of the manuscript. All content, including text, data analysis, and figures, was solely generated by the authors.

Contributions of the Authors

Nesrin BOZHAN: Conceptualization, Data Curation, Formal analysis, Investigation, Methodology, Resources, Visualization, Writing – original draft, Writing – review and editing.

Ahmet ONAY: Conceptualization, Methodology, Project administration, Writing – review and editing.

REFERENCES

[1] H. Yılmaz, O. Y. Yılmaz and Y. F. Akyüz, "Determining the factors affecting the distribution of *Muscari latifolium*, an endemic plant of Turkey, and a mapping species distribution model," *Ecology and Evolution*, vol. 7(4), pp. 1112-1124, 2017.

[2] C. A. Ozel, K. M. Khawar and F. Unal, "Factors affecting efficient in vitro micropropagation of *Muscari muscarimi* Medikus using twin bulb scale explants," *Saudi Journal of Biological Sciences*, vol. 22(2), pp. 132-138. 2015.

[3] J. Ma, Z. Li, and Y. Liu, "Integrating Multi-Omics Analysis Reveals the Regulatory Mechanisms of White-Violet Mutant Flowers in Grape Hyacinth (*Muscari latifolium*)," *International Journal of Molecular Sciences*, vol. 24(5), pp. 5044, 2023.

[4] P. H. Davis, and D. C. Stuart, *Muscari* Miller. Davis P.H (Ed.), *Flora of Turkey and the East Aegean Islands*, vol. (8), pp. 245-263, Edinburgh: Edinburgh University Press. 1984.

[5] C. A. Ozel, "*In Vitro* Bulb Production in Different *Muscari* Species", *Doctoral Thesis*, Gazi University, Institute of Science, Ankara, 2008.

[6] V. Sarasan, R., Cripps, M. M. Ramsay, C. Atherton, M. McMichen, G. Prendergast, and J. K. Rowntree, "Conservation in vitro of threatened plants-Progress in the past decade" *In Vitro Cellular & Developmental Biology-Plant*, vol. 42(3), pp. 206-214, 2006.

[7] S. Jevremović, A. Subotić, M. Trifunović, and M. Nikolić, "Plant regeneration of Southern Adriatic iris by somatic embryogenesis," *Archives of Biological Sciences*, vol. 61(3), pp. 413-418. 2009.

[8] S. Uranbey, A. Ipek, M. Caliskan, E. Dundar, S. Cocu, D. Basalma, and H. Guneylioglu, "*In vitro* bulblet induction from bulb scales of endangered ornamental plant *Muscari azureum*," *Biotechnology & Biotechnological Equipment*, 24(2), 1843-1848, 2010.

[9] A. G. Nasırcılar, S. Mirici, U. O. Karaguzel, O. Eren, and I. Baktır, "*In vitro* propagation of endemic and endangered *Muscari mirum* from different explant types," *Turkish Journal of Botany*, vol. 35(1), pp. 37-43, 2011.

[10] R. Karamian, A. Sharifzadeh, and M. Ranjbar, "Evidence of somatic embryogenesis for plantlet regeneration in *Muscari neglectum* Guss.," *African Journal of Agricultural Research*, vol. 6, pp. 3247-3251, 2011.

[11] B. B. Yucesan, F. Cicek, and E. Gurel, "Somatic embryogenesis and encapsulation of immature bulblets of an ornamental species, grape hyacinth (*Muscari armeniacum Leichtlin* ex Baker)," *Turkish Journal of Agriculture and Forestry*, vol. 38(5), pp. 716-722, 2014.

[12] P. A. Vaziri, S. Uranbey, and C. Sancak, "Efficient *in vitro* microprapagation for the conservation of endemic and endangered aucher-eloy grape hyacinth [*Muscari Aucheri* (boiss.) Baker]," *Journal of Applied Biological Sciences*, vol. 8(1), pp. 80-83, 2014.

[13] F. A. Ozdemir, O. Kılıç, and E. Bagcı, "*In vitro* bulb regeneration from stem explants of endemic geophyt *Muscari aucheri* (Boiss.) Baker.," *International Journal of Secondary Metabolite*, vol. 4(3, Special Issue 1), pp. 50-54, 2017.

[14] M. O. Faruq, M. Shahinozzaman, M. A. K. Azad, and M. N. Amin, "*In vitro* propagation of a cut flower variety *Muscari armeniacum* Leichtlin ex Baker through direct bulblet proliferation pathways," *GSC Biological and Pharmaceutical Sciences*, 5(1), 67-75, 2018.

[15] G. Ozturk, "*In Vitro* Propagation of *Muscari* (*Muscari neglectum*) Bulbs," *MAS Journal of Applied Sciences*, vol. (7), pp. 1160-1170, 2022.

[16] T. Murashige, and F. Skoog, "A revised medium for rapid growth and bioassays with tobacco tissue cultures," *Plant Physiol*. Vol. 15, pp. 473-497, 1962.

[17] A. A. Abdul-Baki, and G. M. Moore, "Seed disinfection with hypochlorites: A selected literature review of hypochlorite chemistry and definition of terms," *Journal of Seed Technology*, pp. 43-56, 1979.

[18] E. F. George, M. A. Hall, and G.J. De Klerk, "Plant propagation by tissue culture," 3rd Edition. The Netherland, *The Back Ground Springer*, 65-175, 2008.

[19] C. Telci, M. Yildiz, S. Pelit, B. Onol, E.G. Erkilic, and H. Kendir, "The effect of surface-disinfection process on dormancy-breaking, seed germination, and seedling growth of *Lathyrus chrysanthus* Boiss. under *in vitro* conditions," *Propagation of Ornamental Plants*, vol. 11(1), pp. 10-16, 2011.

[20] M. Hesami, M. H. Daneshvar, and A. Lotfi-Jalalabadi, "Effect of sodium hypochlorite on control of *in vitro* contamination and seed germination of *Ficus religiosa*," *Iranian Journal of Plant Physiology*, vol. 7(4), pp. 2157-2162, 2017.

[21] M. Yildiz, and H. Ekiz, "The effect of sodium hypochlorite solutions on *in vitro* seedling growth and regeneration capacity of sainfoin (*Onobrychis viciifolia* Scop.) hypocotyl explants," *Canadian Journal of Plant Science*, vol. 94(7), pp. 1161-1164, 2014.

[22] B. E Lindsey III, L.Rivero, C. S. Calhoun, E. Grotewold, E. And J. Brkljacic, "Standardized method for high-throughput sterilization of *Arabidopsis* seeds," *Journal of visualized experiments: JoVE*, 128: 56587, 2017.

[23] A.I. Hsiao, "The effect of sodium hypochlorite, gibberellic acid, and light on seed dormancy and germination of wild buckwheat (*Polygonum convolvulus*) and cow cockle (*Saponaria vaccaria*)," *Canadian Journal of Botany*, vol. 57(16), pp. 1735-1739, 1979.

[24] A. Tunç, A. ve S.S. Yılmaz, "Effect of Different Explant Sources, Metatopoline and PEG on *In Vitro* Propagation of *Pistacia terebinthus* L.," *Journal of Kırşehir Ahi Evran University Faculty of Agriculture*, vol. 3(2), pp. 200-212, 2023.

[25] M. A. K. Azad, and M. N. Amin, "Effects of hormonal and basal nutrient medium on *in vitro* regeneration of an ornamental plant-*Muscari armeniacum Leichtlin*. ex Baker.," *Plant Tissue Culture and Biotechnology*, vol. 22(2), pp. 113-126, 2012.

[26] R. B. Malabadi, and J. Van Staden, "Regeneration of *Ornithogalum in vitro*," *South African Journal of Botany*, vol. 70, pp. 618-621, 2004.

[27] J. Suh, W. Lee,and A. Lee, "New plantlet proliferation and bulbing promotion in vitro cultures of *Ornithogalum* hybrid," *Acta Horticulturae*, vol. 683, pp. 155-16, 2005.

[28] S. Uzun, I. Parmaksız, S. Uranbey, S. Mirici, E. O. Sarıhan, A. Ipek, M. D. Kaya, B. Gurbuz, N. Arslan, C. Sancak, K. M. Khawar, and S. Ozcan, "*In vitro* micropropagation from immature embryos of the endemic and endangered *Muscari muscarimi* Medik.," *Turkish Journal of Biology*, 38(1), 83-88, 2014.

[29] A. Fida, "*In Vitro* Propagation of *Muscari Neglectum* Guss. Commonly Found in Van Region," *Master's Thesis*, Van Yüzüncü Yıl University, Institute of Science, Van, 2020.

BİTLİS EREN ÜNİVERSİTESİ
FEN BİLİMLERİ DERGİSİ

ISSN: 2147-3129 / e-ISSN: 2147-3188

Article Type : Research Article
Received : April 18, 2025
Revised : June 18, 2025
Accepted : August 22, 2025
DOI : 10.17798/bitlisfen.1679278

Year : 2025
Volume : 14
Issue : 3
Pages : 1581-1595

SYNTHESIS OF DIMETHYLAMINE-PYRIDINE-BASED SCHIFF BASE COMPLEXES OF FE(II), CO(II), AND CU(II), STRUCTURAL ELUCIDATION: INVESTIGATION OF BIOLOGICAL ACTIVITIES

Kenan BULDURUN [1,*], Hüsna İNAN [2], Nevin TURAN [2]

[1] *Muş Alparslan University, Department of Medical Services and Techniques, Muş, Türkiye*

[2] *Muş Alparslan University, Department of Chemistry, Muş, Türkiye*

**** Corresponding Author:*** *k.buldurun@alparslan.edu.tr*

ABSTRACT

This report aims to synthesize a new Schiff base ligand (L) and its Fe(II), Co(II), and Cu(II) metal complexes, analyze their structures, and evaluate their antioxidant activities. The Schiff base was prepared through a condensation reaction between 4-(dimethylamino)benzaldehyde and 6-acetyl-2-amino-4,5,6,7-tetrahydrothieno[2,3-*c*]pyridine-3-carboxamide. Subsequently, complexes of the ligand with Fe(II), Co(II), and Cu(II) were designed and synthesized. The ligand and its metal complexes were characterized using a range of physicochemical and spectroscopic techniques, including elemental analysis, magnetic susceptibility measurements, ^{1}H and ^{13}C NMR, FTIR, UV-Vis, mass spectrometry, and thermogravimetric analysis (TGA). Based on the analytical data, the proposed molecular formulas for the Fe(II), Co(II), and Cu(II) complexes are $[LFe_2(H_2O)_6Cl_3]1.5H_2O$, $[LCo_2(H_2O)_2Cl_3]1.5H_2O$, and $[LCu_2(H_2O)_2Cl_3]3H_2O$, respectively. The ligand coordinates to the metal ions through the azomethine and amine nitrogen atoms, as well as the oxygen atoms of the carbonyl group. Magnetic susceptibility and electronic spectroscopy data indicated that the Fe(II) complex adopts an octahedral geometry, while the Cu(II) and Co(II) complexes display square-planar geometries. TGA results demonstrated that all complexes have greater thermal stability than the free Schiff base ligand. Furthermore, the antioxidant activities of the synthesized compounds were evaluated using the DPPH free radical scavenging assay, the CUPRAC method for cupric ion reducing capacity, and the ABTS assay for overall antioxidant capacity. The antioxidant activities of these compounds were compared to those of standard antioxidants. The results indicated that both the ligand and its metal complexes exhibit significant antioxidant activities.

Keywords: Schiff base, Metal complex, Biological activity, DPPH, Antioxidant.

1 INTRODUCTION

Schiff bases play a key role as ligands in coordination chemistry, typically coordinating with metal ions through the azomethine nitrogen atom. These compounds are crucial for the design and development of biologically active metal complexes because of their wide range of applications, versatile coordination behavior, and structural diversity [1-3]. Modifying the substituents of Schiff bases has facilitated the synthesis of numerous novel metal complexes with diverse and intriguing properties [3-7]. Schiff base ligands containing nitrogen and oxygen donor atoms are of particular interest because of their notable biological activities [8-10]. Owing to the presence of multiple electron-donating sites, these compounds readily form coordination complexes with metal ions in various oxidation states [11-13]. Importantly, the properties of these complexes are significantly influenced by the coordination environment surrounding the central metal ions.

Recent innovations have introduced researchers to various Schiff base synthesis methods, emphasizing factors such as reaction speed, efficiency, and environmental sustainability. The versatility of Schiff bases, especially their ability to donate electrons or protons, has led to their widespread use in many fields. In medicine, they function as metal chelators with potential therapeutic applications. They also serve as catalysts to accelerate the reaction rate. Their metal-binding properties make them essential in materials science for applications in energy storage, chemosensing, biosensing, biomedical fields, nanotechnology, and the development of new compounds with specific features. Additionally, Schiff bases are also used in the dye industry to produce vibrant colors on textiles and other materials. They have also demonstrated promising activity against various pathogens and cancer cells, making them strong candidates for medicinal and pesticide use. Furthermore, their antioxidant properties enable them to stabilize free radicals by donating protons and electrons [14-17].

Antioxidants donate electrons or hydrogen atoms to neutralize reactive species. Schiff base antioxidants and their related complexes serve as electron or hydrogen donors to neutralize free radicals at reactive sites [10].

In this study, a Schiff base (L) and its corresponding metal complexes, $[LFe_2(H_2O)_6Cl_3]1.5H_2O$, $[LCo_2(H_2O)_2Cl_3]1.5H_2O$, and $[LCu_2(H_2O)_2Cl_3]3H_2O$ were successfully synthesized [18]. The structural characterization of these compounds was performed using analytical and spectroscopic techniques to confirm the geometry and coordination modes of the metal centers in the complexes. The antioxidant activities of all synthesized compounds were evaluated using DPPH, ABTS, and CUPRAC methods. The

results were compared with the antioxidant activity of the free Schiff base reported in previous studies using the standard antioxidants BHT and BHA as positive controls. This study aimed to develop a biologically active Schiff base incorporating pyridine and carboxamide groups, along with its transition metal complexes, and to focus on their antioxidant potential.

2 MATERIAL AND METHODS

2.1 Physical Measurements

All chemicals and reagents used in this study were of analytical grade and employed without further purification, unless otherwise specified. FT-IR spectra were measured using a PerkinElmer FT-IR 65 spectrophotometer with KBr discs. ^{1}H and ^{13}C NMR were performed using a Bruker AV 400 MHz spectrometer. UV-Vis spectra were measured using a Shimadzu UV-1800 spectrophotometer. The elemental compositions of C, N, H, and S were determined using a Vario EL III elemental analyzer (GmbH). Thermal analysis was recorded using a Shimadzu TGA-50H instrument under a nitrogen atmosphere. The magnetic susceptibility measurements were performed at room temperature using a Sherwood Scientific model MKI Magnetic Susceptibility Balance. Mass spectrometry data were obtained using an AB Sciex 3200 QTrap mas spectrometer. Melting points (°C) were measured using a Gallen-Kamp melting point apparatus equipped with a hot stage, employing the open capillary method.

2.2 Synthesis of Ligand (L)

A solution of 6-acetyl-2-amino-4,5,6,7-tetrahydrothieno[2,3-*c*]pyridine-3-carboxamide (1.0 g, 4.2 mmol) was prepared in 15 mL of DMF. To this, a solution of 4-(dimethylamino)benzaldehyde (0.62 g, 4.2 mmol) in 15 mL DMF was added dropwise. The mixture was then heated under reflux for 24 h. The progress of the reaction was monitored using thin-layer chromatography (TLC). Upon completion, the crude product was washed with diethyl ether and purified by recrystallization from a methanol/chloroform solvent system (Figure 1).

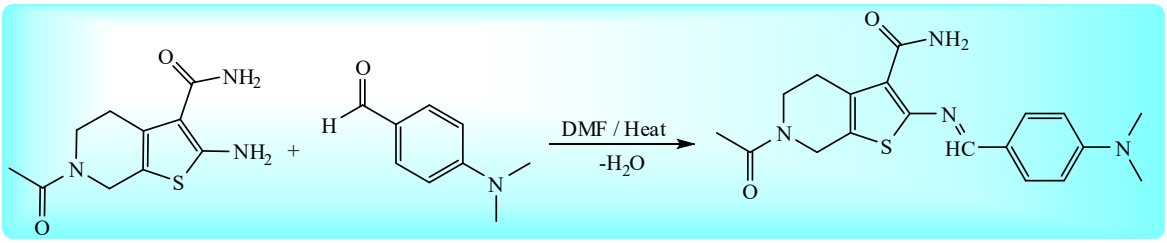


Figure 1. Schiff base ligand (L)

Yield (84%), Color: Dark orange; M.p.: 185 °C. Anal. Calc. for $C_{19}H_{22}N_4O_2S$ (370.29 g/mol): C, 61.62; H, 5.94; N, 15.13; S, 8.66. Found: C, 62.00; H, 5.95; N, 15.12; S, 8.69. FT-IR (ν, cm^{-1}): 3380, 3278 (-NH_2), 3005 (-CH, Ar.), 2907, 2853 (-CH, Alip.), 1653, 1638 (C=O), 1611 (HC=N), 1600, 1566, 1528, 1432 (C=C, Ar.), 1287 (C-N), 743 (C-S-C). ^{1}H-NMR (DMSO-d_6, δ, ppm): 8.27 (s, H, CH=N), 7.69-6.71 (m, 4H, CH, Ar.), 4.72 (s, 2H, NH_2), 3.68-3.19 (m, 4H, CH_2 py), 3.10 (s, 8H, CH_2 py and $N(CH_3)_2$), 2.19 (s, 3H, CH_3). ^{13}C-NMR (DMSO-d_6, δ, ppm): 169.35, 165.87 (C=O), 158.13 (CH=N), 155.81-111.69 (benzene and thiophene rings), 43.97-40.12 (py, $N(CH_3)_2$), 27.59-21.39 (CH_3). UV-Vis. (EtOH, λ_{max} (nm)): 209, 214, 223, 231, 246, 265, 300, 399.

2.3 Synthesis of the Complexes

To prepare the ligand solution, 0.60 g (1.62 mmol) Schiff base was dissolved in 15 mL of ethanol. A solution of $Cu(NO_3)_2 \cdot 3H_2O$ (0.78 g, 3.24 mmol) in 10 mL ethanol was then added dropwise to the ligand solution. The mixture was then refluxed for 4 h. Upon completion of the reaction, the mixture was decanted into a separate vessel and allowed to stand at 25 °C for 2 days. The obtained colored solid was thoroughly washed twice with diethyl ether and dried under reduced pressure. Fe(II) and Co(II) complexes were synthesized using a similar procedure. The proposed structures of the obtained metal complexes are shown in Figures 2 and 3.

Yield (85%); Color: Brown; M.p.: > 250 °C. Anal. Calc. for $C_{19}H_{31}N_4O_7SCuCl_3$ (692.74 g/mol): C, 32.94; H, 4.47; N, 8.10; S, 4.63. Found: C, 32.95; H, 5.00; N, 8.11; S, 4.64. FT-IR (ν, cm^{-1}): 3438 (OH/H_2O), 3256 (NH), 3184, 3092 (-CH, Ar.), 2998, 2907 (-CH, Alip.), 1657, 1645 $(C=O)_{br}$, 1607 (CH=N), 1573, 1519, 1494, 1431 (C=C, Ar.), 1289 (C-N), 863 (H_2O), 743 $(C-S-C)_{br}$, 580, 531 (Cu-O), 487, 470 (Cu-N). UV-Vis. (EtOH, λmax (nm)): 213, 228, 247, 257, 266, 274, 287, 297, 301, 359, 376, 387, 396, 402, 600. MS [ESI+]: *m/z* 691.74 (Calc.), 691.737 (Found) $[M-H]^-$. μ_{eff} (B.M.): 1.84.

Yield (83%), Color: Dark Brown; M.p.: > 250 °C. Anal. Calc. for $C_{19}H_{28}N_4O_{5.5}SCo_2Cl_3$ (656.50 g/mol): C, 35.08; H, 4.30; N, 8.54; S, 4.88. Found: C, 35.04; H, 4.32; N, 8.53; S, 4.90. FT-IR (ν, cm^{-1}): 3388 (OH/H_2O), 3240 (NH), 3161, 3032 (-CH, Ar.), 2956, 2910 (-CH, Alip.), 1657, 1631 $(C=O)_{br}$, 1605 (CH=N), 1590, 1554, 1520, 1459 (C=C, Ar.), 1285 (C-N), 825 (H_2O), 742 $(C-S-C)_{br}$, 590, 526, 514 (Co-O), 490, 465 (Co-N). UV-Vis. (EtOH, λmax (nm)): 224, 234, 248, 291, 348, 363, 432, 894. MS [ESI+]: *m/z* 654.50 (Calc.), 654.097 (Found) $[M-2H]^{2+}$. μ_{eff} (B.M.): 2.13.

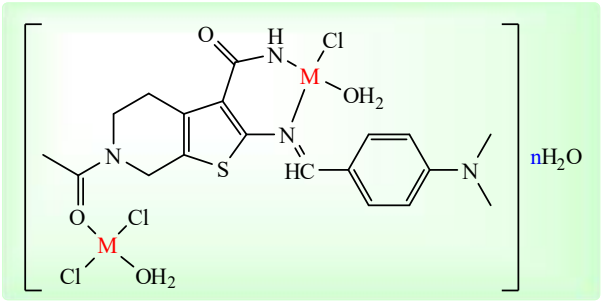


Figure 2. Proposed structure of Cu(II) and Co(II) complexes

Yield (82%); Color: Black; M.p.: > 250 °C. Anal. Calc. for $C_{19}H_{36}N_4O_{9.5}SFe_2Cl_3$ (722.39 g/mol): C, 31.58; H, 4.98; N, 7.76; S, 4.44. Found: C, 32.00; H, 5.00; N, 7.74; S, 4.45. FT-IR (ν, cm^{-1}): 3429 (OH/H_2O), 3259 (NH), 3187, 3089 (-CH, Ar.), 2956, 2925 (-CH, Alip.), 1670, 1647 $(C=O)_{br}$, 1607 (CH=N), 1573, 1522, 1495 (C=C, Ar.), 1289 (C-N), 823 (H_2O), 743 $(C-S-C)_{br}$, 578, 540, 518 (Fe-O), 495, 468 (Fe-N). UV-Vis. (EtOH, λmax (nm)): 221, 231, 244, 253, 354, 361, 372, 575, 606. MS [ESI+]: *m/z* 720.39 (Calc.), 720.238 (Found) $[M-2H]^+$. μ_{eff} (B.M.): 4.96.

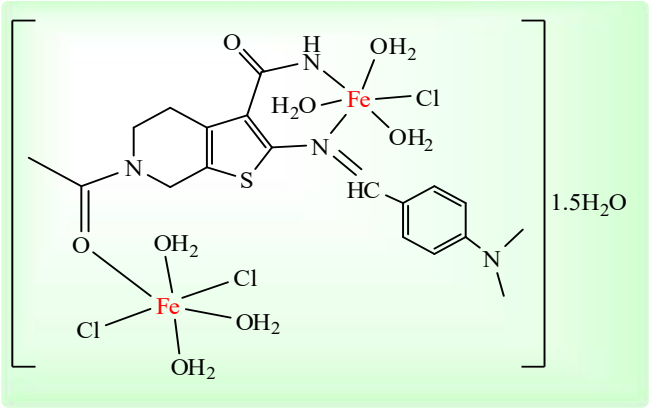


Figure 3. Structure of Fe(II) complex

3 RESULT AND DISCUSSION

3.1 Chemistry

In this study, a novel ligand (L) and its Fe(II), Co(II), and Cu(II) complexes were prepared and characterized. Analytical and spectroscopic data for all the synthesized compounds are provided in the Supplementary Materials. Subsequently, the antioxidant properties of these compounds were assessed.

The FT-IR spectra of the Schiff base ligand exhibited peaks at 3380 and 3278 cm^{-1}, attributed to the NH_2 group, while peaks at 1653 cm^{-1} and 1638 cm^{-1} were assigned to the carbonyl group (C=O). The peak at 1611 cm^{-1} was attributed to the azomethine group (HC=N),

and the peak at 1287 cm^{-1} was ascribed to the $N(CH_3)_2$ group. The band observed at 743 cm^{-1} corresponds to the C-S-C bond of the thiophene ring. In the ^1H NMR spectra, the singlet at 8.27 ppm was ascribed to the HC=N proton, while the peaks between 7.69-6.71 ppm correspond to aromatic protons. The singlet at 4.72 ppm was attributed to the NH_2 protons, and the singlet at 3.10 ppm corresponded to the $N(CH_3)_2$ protons [19-21]. The ^{13}C NMR spectra showed peaks at 169.35 and 165.87 ppm corresponding to the carbonyl carbons, a peak at 158.13 ppm for the azomethine carbon, peaks between 155.81 and 111.69 ppm assigned to carbons of the benzene and thiophene rings, and peaks between 43.97 and 21.39 ppm for carbons in the pyridine ring and other aliphatic methyl groups [20]. The appearance of a new azomethine peak in the FT-IR spectra and the shift of one of the NH_2 peaks to a lower wavenumber compared to the starting material, and the presence of the azomethine and NH_2 proton peaks in the NMR spectra confirmed the formation of the ligand.

Comparison of the FT-IR spectra of the ligand and its metal complexes revealed that the nitrogen atoms in the CH=N and NH_2 groups, as well as the oxygen atom in the C=O group, coordinate with the metal ions. The azomethine peak at 1611 cm^{-1} in the Schiff base shifted to 1607 cm^{-1} in both the Fe(II) and Cu(II) complexes and to 1605 cm^{-1} in the Co(II) complex, indicating coordination through the nitrogen atom. The NH_2 stretching bands observed at 3380 cm^{-1} and 3278 cm^{-1} in the ligand shifted to 3259, 3256, and 3240 cm^{-1} in the Fe(II), Cu(II), and Co(II) complexes, respectively, further supporting the involvement of the NH group in metal coordination [6,20,22]. The carbonyl peaks at 1653 and 1638 cm^{-1} in the Schiff base shifted to the range 1670-1631 cm^{-1} in the metal complexes, supporting coordination of the metal ions through the oxygen atom of the carbonyl group. Additionally, the FT-IR spectra of the metal complexes exhibited characteristic M-N (495-465 cm^{-1}) and M-O (590-514 cm^{-1}) bands, indicating coordination via nitrogen and oxygen atoms. The peaks observed at 3438-3388 cm^{-1} and 863-823 cm^{-1} are ascribed to hydration and coordinated H_2O molecules, respectively. These observations are consistent with those of previous studies [23-25]. No significant change was observed in the thiophene peaks, suggesting that the C-S-C group did not participate in the coordination.

The UV-Vis spectra of the ligand showed absorption bands in the 209-265 nm range, which were ascribed to the $\pi \rightarrow \pi^*$ transitions of the carbonyl and aromatic rings. The absorption bands in the 300-399 nm range correspond to $n \rightarrow \pi^*$ transitions associated with the C=O group and N-H of the amine group. The Fe(II), Co(II), and Cu(II) complexes showed absorption peaks in the 213-266 nm range, assigned to $\pi \rightarrow \pi^*$ transitions, and in the 274-396 nm range, corresponding to $n \rightarrow \pi^*$ transitions. Additionally, the Cu(II) and Co(II) complexes exhibited peaks in the 402-894 nm range, which were attributed to d→d and ligand-to-metal charge

transfer (LMCT) transitions [22,26,27]. The magnetic moment values for the Cu(II) and Co(II) complexes were 1.84 and 2.13 B.M., respectively, consistent with square planar geometries [28,29]. The Fe(II) complex exhibited novel bands at 575 and 606 nm, indicating d→d and ligand-to-metal charge transfer (LMCT) transitions, further confirming complex formation [26,27]. Furthermore, the Fe(II) complex showed a magnetic moment of 4.96 B.M., which, along with the electronic spectral data, supports an octahedral geometry for the Fe(II) complex and square planar geometries for the Cu(II) and Co(II) complexes [30,31].

3.2 Thermal Analysis

Thermal analysis of the metal complexes showed that the Fe(II) complex decomposed in a single step. The observed mass loss was 58.20% (calc. 57.98%), corresponding to the removal of 7.5 moles of water, 3 moles of chlorine, and $C_{10}H_{12}NS$ fragments. The remaining residue consisted of 40.50% $C_9H_7N_3$ and 2 moles of FeO. The Cu(II) complex decomposed in two steps. In the first step, a mass loss of 18.11% (calc. 17.61%) was observed, corresponding to the removal of 5 moles of water and 1 mole of chlorine. The second step showed a mass loss of 34.10% (calc. 34.46%), which was attributed to the elimination of 2 moles of chlorine and the organic $C_9H_{11}S$ fragment. The remaining residue contained 47.13% $C_{10}H_{10}N_3$ and 2 moles of CuO. The Co(II) complex also decomposed in two steps. The first step showed a mass loss of 17.78% (calc. 16.91%), corresponding to the removal of 3.5 moles of water, one chloride ion, and one CH_2 units. The second step exhibited a mass loss of 38.74% (calc. 37.55%), attributed to the elimination of 2 chloride ions and the organic $C_9H_{11}NOS$ fragment. The residue contained 40.53% $C_{10}H_{10}ON_3$ and 2 moles of metallic cobalt. These findings agree with the experimental and theoretical results presented in Table 1.

Table 1. Thermogravimetric data of metal complexes

Compounds	Step	Temp. Range (°C)	Weight loss (%) Calc.	/Found	Evolved components
$[LCu_2(H_2O)_2Cl_3]3H_2O$	1	50-260	18.11	17.61	$5H_2O$, Cl
	2	260-740	34.10	34.46	$C_9H_{11}SCl_2$
	Residue	740-		47.13	$C_{10}H_{10}N_3 + 2CuO$
$[LCo_2(H_2O)_2Cl_3]1.5H_2O$	1	50-320	17.78	16.91	$3.5H_2O$, Cl, CH_2
	2	320-800	38.74	37.55	$C_9H_{11}NOSCl_2$
	Residue	800		40.53	$C_{10}H_{10}ON_3Co_2$
$[LFe_2(H_2O)_6Cl_3]1.5H_2O$	1	50-800	58.20	57.98	$7.5H_2O$, $C_{10}H_{12}NSCl_3$
	Residue	800-		40.50	$C_9H_7N_3 + 2FeO$

The mass spectra of the Fe(II), Cu(II), and Co(II) complexes showed molecular ion peaks at *m/z* values of 720.238, 691.737, and 654.097, respectively. The principal ion peaks were observed at 473.274, 619.617, and 367.308 for the Fe(II), Cu(II), and Co(II) complexes, respectively, supporting the formation of the expected structures [29].

3.3 Antioxidant Activity

3.3.1 Scavenging Activity of DPPH Radical

The antioxidant activity of the samples was assessed using a modified DPPH (2,2-diphenyl-1-picrylhydrazyl) assay, as described in a previous study [30]. A 0.1 mM DPPH solution was prepared by dissolving 38 mg of DPPH in 100 mL of ethanol and stirring for approximately 12 h to ensure complete dissolution. The synthesized compounds were diluted to 1 mg/mL, and different volumes (10, 20, and 30 µg/mL) were compared with standard antioxidants (BHT, ascorbic acid, and α-tocopherol). Each sample received 300 µL of the DPPH solution, and the final volume was adjusted to 2000 µL with ethanol. After incubation in the dark at 25 °C for 30 min, the absorbance was measured at 517 nm using a UV-Vis spectrophotometer. A control sample containing 1700 µL of ethanol and 300 µL of DPPH solution was used. The control absorbance (1.500-2.000) was adjusted as needed by modifying the ethanol-to-DPPH ratio [33].

The DPPH free radical scavenging activity was determined by observing the decrease in absorbance, as DPPH-H did not show any absorbance at 517 nm. Antioxidant activity is shown. Compared with the standard antioxidants (ascorbic acid, α-tocopherol, and BHT), the absorbance values of the synthesized starting material, ligand, and Fe(II), Co(II), and Cu(II) metal complexes decreased with increasing concentrations. The starting material, Fe(II), and Co(II) complexes showed antioxidant properties similar to those of the standard BHT, whereas the ligand and Cu(II) complex showed increasing absorbance with increasing concentrations and did not exhibit antioxidant properties compared to the standards (Figure 4). These results suggest that the newly synthesized compounds exhibit different antioxidant properties.

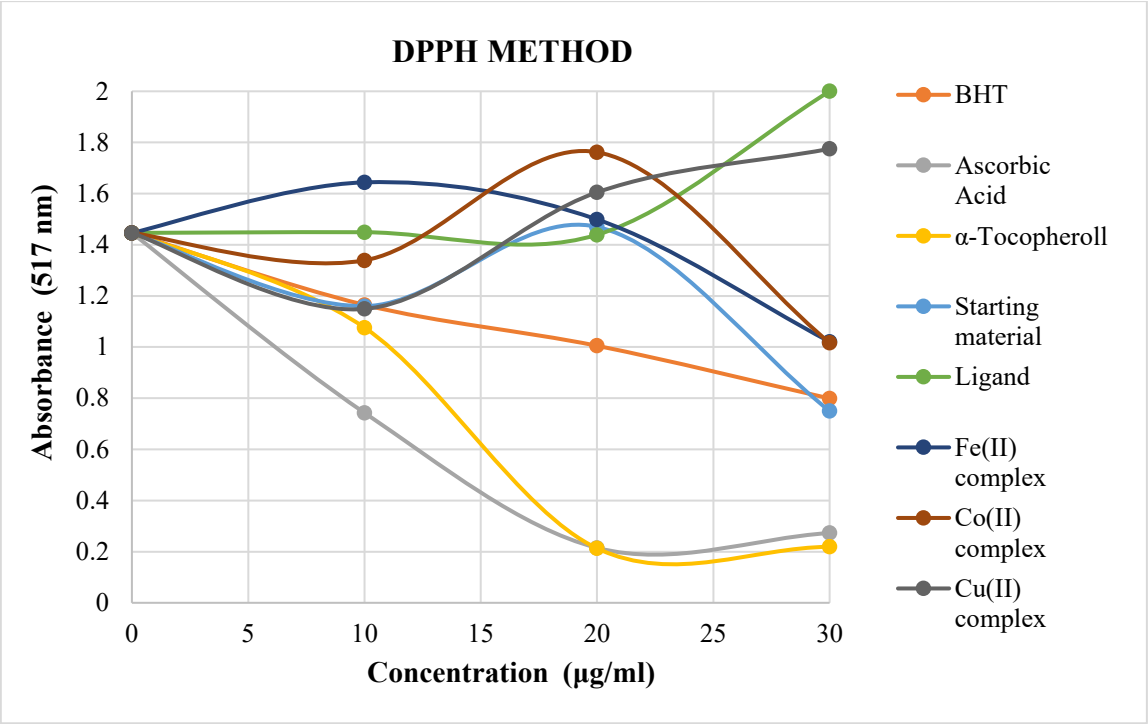


Figure 4. DPPH free radical scavenging activity graph

3.3.2 ABTS Radical Scavenging Assay

In the ABTS (2,2'-azino-bis-3-ethylbenzothiazoline-6-sulfonic acid) assay, free radicals were generated by mixing equal volumes of 2.45 mM potassium persulfate ($K_2S_2O_3$) and 2 mM ABTS solutions, followed by stirring in the dark for 6 h. The resulting ABTS radical solution was then diluted with distilled water to achieve an absorbance of 1.0 ± 0.2 at 734 nm, as measured using a UV-Vis spectrophotometer [34]. For the antioxidant evaluation, 500 µL of the ABTS radical solution and distilled water were added to cuvettes containing 10, 20, or 30 µg/mL of the test compounds, including the starting material, ligand, and its Fe(II), Co(II), and Cu(II) complexes, along with reference antioxidants (BHA, BHT, ascorbic acid, and α-tocopherol). The final volume was adjusted to 2000 µL using distilled water. After 30 min of incubation at room temperature, the absorbance was measured at 734 nm. A control was prepared using 500 µL of ABTS solution and 1500 µL of ethanol [33].

In this method, the ABTS radical reacts with antioxidant compounds by accepting an electron, thereby reducing it to a non-radical ABTS form. The decrease in absorbance at 734 nm, corresponding to the degree of radical scavenging, was used to evaluate the antioxidant activity.

The antioxidant activities of the synthesized starting compound, ligand, and Fe(II), Co(II), and Cu(II) complex compounds were evaluated using the ABTS scavenging method, and the results were compared with those of standard antioxidant substances such as α-tocopherol, BHA, BHT, and vitamin C (ascorbic acid). The absorbance values of the standard antioxidants decreased with increasing concentration, indicating that the antioxidant activity increased in a concentration-dependent manner. According to the ABTS assay, the antioxidant effectiveness of the standard compounds followed the order: BHA > BHT > ascorbic acid > α-tocopherol.

Among the synthesized compounds, the Fe(II) complex exhibited the highest antioxidant activities. As its concentration increased, the absorbance values were consistently lower than those of both α-tocopherol and ascorbic acid, indicating significantly stronger radical scavenging ability. The starting compound also showed a decrease in absorbance with increasing concentration, suggesting antioxidant properties comparable to those of ascorbic acid but weaker than those of α-tocopherol. The ligand and Cu(II) complex similarly demonstrated decreasing absorbance values, indicating moderate antioxidant activity. In contrast, the Co(II) complex displayed an increase in absorbance at higher concentrations, indicating relatively poor antioxidant performance. Overall, based on the ABTS cation radical scavenging assay, the Fe(II) complex exhibited the strongest antioxidant activity, followed by the starting compound, the Cu(II) complex, and the ligand, with the Co(II) complex showing the weakest activity (Figure 5).

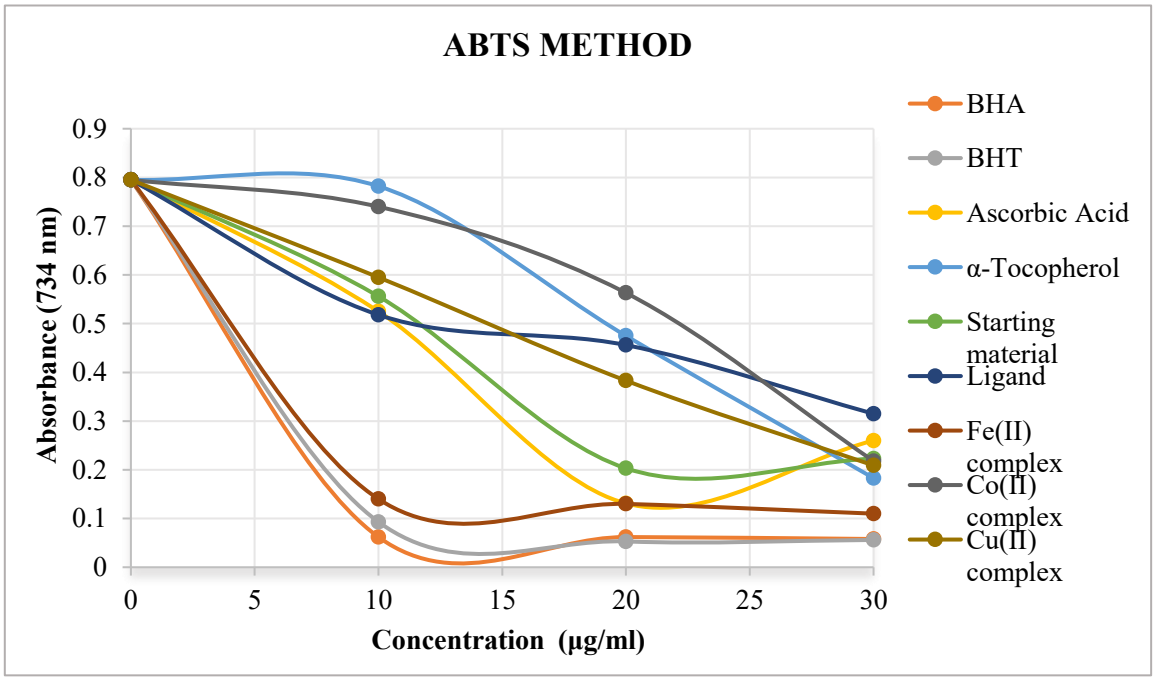


Figure 5. ABTS cation radical scavenging activity graph

3.3.3 CUPRAC Assay

The cupric ion (Cu^{2+}) reducing capacities of the samples were evaluated using the cupric ion reducing antioxidant capacity (CUPRAC) assay. To each well of a microplate, 500 µL of 0.01 M $CuCl_2$, 500 µL of 7.5 mM neocuproine, and 500 µL of 1 M potassium acetate buffer were added sequentially. This was followed by the addition of various concentrations (10, 20, and 30 µg/mL) of the synthesized compounds, including the precursor, ligand, and their Fe(II), Co(II), and Cu(II) complexes, along with standard antioxidants. The final volume in each well was adjusted to 2000 µL using distilled water. After incubating the mixtures for 30 min, the absorbance was measured at 450 nm using a UV-Vis spectrophotometer [35].

An increase in absorbance indicates a stronger Cu^{2+} reducing activity. The antioxidant potential was evaluated based on the absorbance-concentration curves. Among the standards, antioxidant activity increased with concentration in the following order: BHA > BHT > ascorbic acid > α-tocopherol. BHA and BHT demonstrated the highest activity (Figure 6). Among the synthesized compounds, the starting material and Co(II) complex exhibited the highest absorbance values, although these were still lower than those of BHA and BHT. These two compounds exhibited stronger reducing capacities than the other synthesized structures. The ligand showed antioxidant properties comparable to those of α-tocopherol. Although the Fe(II) and Cu(II) complexes also exhibited a concentration-dependent increase in absorbance, their activities remained lower than those of the standard antioxidants and other synthesized compounds, such as the starting material, ligand, and Co(II) complex.

These results indicate that the newly synthesized compounds possess moderate to low antioxidant capacities according to the CUPRAC method. While some compounds, particularly the starting material and Co(II) complex, exhibited promising reducing activity, the overall antioxidant potential of the synthesized derivatives was low in this assay system.

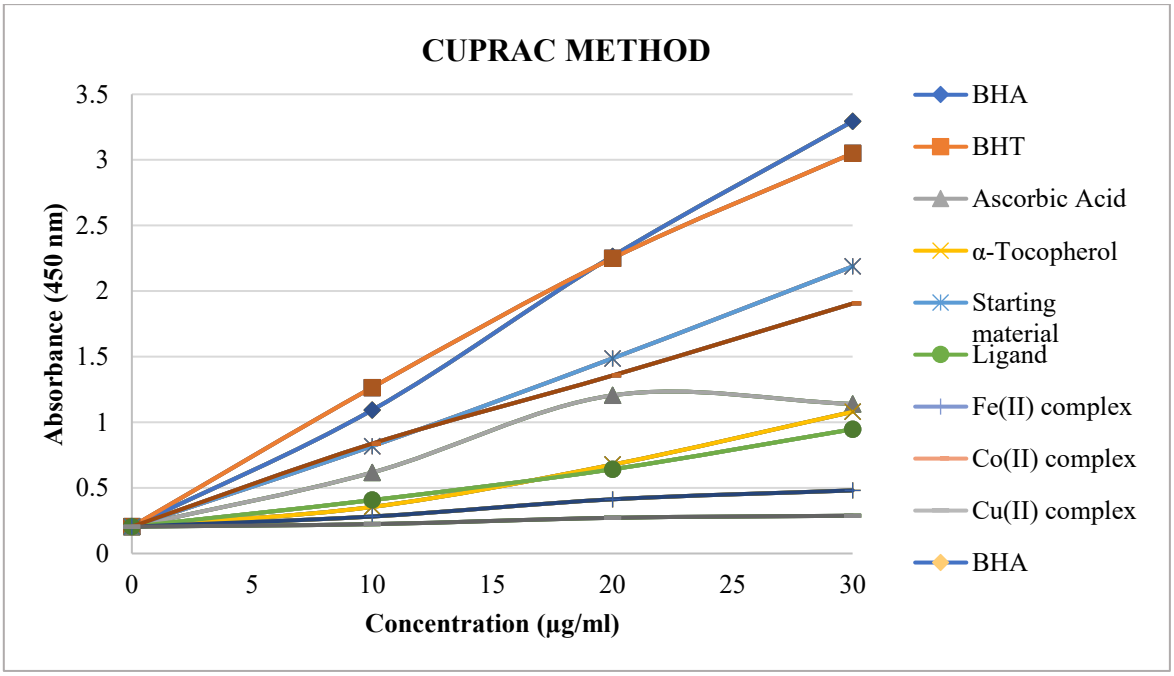


Figure 6. Reduction activity graph according to the CUPRAC method

4 CONCLUSION

The ligand and its corresponding Fe(II), Co(II), and Cu(II) metal complexes have been extensively analyzed using a range of spectroscopic methods, such as FT-IR, NMR, TGA, UV-Vis, mass spectrometry, and microanalysis. The results of these analyses indicate that the Schiff base acts as a bidentate ligand, coordinating with metal ions in a 2:1 metal-to-ligand ratio. Consequently, the general formulas for the synthesized complexes were proposed as $[LCu_2(H_2O)_2Cl_3]3H_2O$, $[LCo_2(H_2O)_2Cl_3]1.5H_2O$, and $[LFe_2(H_2O)_6Cl_3]1.5H_2O$ for the Cu(II), Co(II), and Fe(II), respectively. Thermal analysis confirmed the presence of both coordinated and lattice water molecules, providing additional structural insights. The antioxidant activities of the ligand and its metal complexes were evaluated using DPPH, ABTS, and CUPRAC assays, with the CUPRAC method demonstrating the highest antioxidant capacity, highlighting the potential of these compounds as effective antioxidants. The ligand and its Cu(II), Co(II), and Fe(II) complexes were novel and consistent with previous findings. Schiff bases containing dimethylamine and thiophene rings with ONS donor atoms have been reported to exhibit significant anticancer, optoelectronic, and catalytic properties. Building on these promising findings, future research should explore the synthesis of alternative aldehyde derivatives and their metal complexes. Subsequent investigations will focus on evaluating the anticancer and photocatalytic activities of these compounds, contributing to the development of new materials with potential therapeutic and technological applications.

Acknowledgements

This study was supported by the Scientific Research Projects Coordination Unit of Muş Alparslan University under project no. BAP-22-SHMYO-4902-02.

Conflict of Interest Statement

The authors declare no conflicts of interest.

Statement of Research and Publication Ethics

This study complied with research and publication ethics.

Artificial Intelligence (AI) Contribution Statement

"This manuscript was entirely written, edited, analyzed, and prepared without the assistance of any artificial intelligence (AI) tools. All content, including text, data analysis, and figures, was solely generated by the authors."

Contributions of the Authors

K. Buldurun: Conceptualization, methodology, formal analysis, software, validation, project administration, writing–original draft, supervision.

H. İnan: Data curation, investigation, methodology, writing, resources, formal analysis, software.

N. Turan: Methodology, writing-original draft, review and editing, visualization, formal analysis, validation.

REFERENCES

[1] M.N. Uddin, A.S. Samina, S.M.R. Alam, "Review: Biomedical applications of Schiff base metal complexes," *J. Coord. Chem.*, vol. 73, no. 23, pp. 3109-3149, 2020.

[2] N. Turan, S. Kızılkaya, K. Buldurun, N. Çolak, A. Akdeniz, E. Bursal, "Synthesis, enzyme inhibitory and antioxidant activities, and molecular docking studies of metal complexes of a Schiff base ligand bearing pyridine moiety," *J. Mol. Struct*., vol. 1338, 142167, 2025.

[3] K. Buldurun, N. Turan, A. Savci, Y. Alan, N. Çolak, "Synthesis, characterization, X-ray diffraction analysis of a tridentate Schiff base ligand and its complexes with Co(II), Fe(II), Pd(II) and Ru(II): Bioactivity studies," *IJCCE*, 2022, vol. 41, no. 8, pp. 2635-2649, 2022.

[4] I. Bernadette Amali, M.P. Kesavan, V. Vijayakumar, N. Indra Gandhi, J. Rajesh, G. Rajagopal, "Structural analysis, antimicrobial and cytotoxic studies on new metal(II) complexes containing N_2O_2 donor Schiff base ligand," *J. Mol. Struct*., vol. 1183, pp. 342-350, 2019.

[5] S. Nayab, S. Faisal, W. Khan, M. Ateeq, S.W. Khan, E. Kim, H. Lee, "Pyridine-derived Schiff base copper(II), zinc(II), and cadmium(II) complexes: Synthesis, structural properties, biological evaluation, and docking studies," *Appl. Organomet. Chem*., e7163, 2023.

[6] M. Sankarganesh, P.A. Jose, J.D. Raja, N. Revathi, A. Sakthivel, J. Rajesh, S. Gurusamy, R.V. Solomon, "Spectroscopic and theoretical approach of DNA interaction and anticancer studies of bio-pharmaceutically active pyrimidine derived Cu(II) and Zn(II) complexes," *Int. J. Biol. Macromol*., vol. 249, 126095, 2023.

[7] C. Sarkar, "Theoretical explorations of structural, electronic, and spectroscopic properties of a series of ruthenium Schiff-base complexes," *J. Sci. Res*., vol. 15, no. 2, pp. 489-508, 2023.

[8] D.V. Bondar, B.T. Vhanale, V.S. Ingle, "Synthesis, spectral characterization and antimicrobial, antioxidant properties of Au(III), Pd(II), Cu(II), Fe(II) and Mn(II) metal complexes of 1-hydroxy-2-acetonaphthone Schiff base," *J. Iran. Chem. Soc*., vol. 20, no. 12, pp. 3133-3145, 2023.

[9] F.T. Esmadi, O.F. Khabour, K. Abbas, A.E. Mohammad, R.T. Obeidat, D. Mfady, "Synthesis, characterization and biological activity of some unsymmetrical Schiff base transition metal complexes," *Drug Chem. Toxicol*., vol. 39, no. 1, pp. 41-47, 2016.

[10] A. Talebi, M. Salehi, A. Khaleghian, M. Kubicki, "Evaluation of anticancer activities, apoptosis, molecular docking, and antioxidant studies of new Ni(II), VO(IV), Cu(II) and Co(III) Schiff base complexes," *Inorg. Chim. Acta*, vol. 546, 121296, 2023.

[11] R. Arabahmadi, S. Kamali, A. Reza Sharafi, "Two new cobalt (II) and copper (II) complexes with Azo-azomethine ligand: Synthesis, antioxidant and antibacterial activities, thermal investigations, DFT calculations, and molecular docking studies," *J. Mol. Struct*., vol. 1337, 142177, 2025.

[12] H.G. Sogukomerogulları, A.O. Sarıoğlu, R.A. Kepekçi, B. Türkmenoğlu, M.H. Morcali, "Copper(II), cobalt(II), nickel(II), and iron(II) mixed complexes formed by Schiff base and 1,10-phenanthroline as secondary chelates: Preparation, characterization, antimicrobial, antioxidant, and molecular docking studies," *Inorg. Chim. Acta*, vol. 583, 122692, 2025.

[13] C. Soh, L. Shadap, M.R. Kollipara, J.L. Tyagi, K.M. Poluri, Y. Mozharivskyj, E. Rymmai, "Synthesis and biological evaluation of arene ruthenium (II) complexes containing thiophene benzhydrazone derivative ligands," *J. Organomet. Chem*., vol. 984, 122559, 2023.

[14] Alka, J. Singh, P. Kumari, P. Jain, "Synthesis, characterization, biological, ADMET, and molecular docking studies of transition metal complexes of aminopyridine Schiff base derivative," *Chem. Biodiversity*, vol. 21, no. 10, e202401101, 2024.

[15] I.R. Pathan, M.K. Patel, "A comprehensive review on the synthesis and applications of Schiff base ligand and metal complexes: A comparative study of conventional heating, microwave heating, and sonochemical methods," *Inorg. Chem. Commun*., vol. 158, 111464, 2023.

[16] S. Shekhar, S. Sharma, J.A. Okolie, A. Kumar, B. Sharma, M.K. Meena, A.K. Bhagi, A. Sarkar, "Synthesis, structural elucidation, biological screening, and density functional theory calculations of Cu(II), Ni(II), Mn(II), and Co(II) complexes of 20 Z-N-((Z)-2-(6-nitrobenzo[*d*]thiazol-2-ylimino)-1,2-diphenylethylidene)-5-nitrobenzo[*d*]thiazol-2-amine Schiff base ligand," *Appl. Organomet. Chem*., vol. 36, no. 8, e6766, 2022.

[17] K. Buldurun, "Synthesis, characterization, thermal study and optical property evaluation of Co(II), Pd(II) complexes containing Schiff bases of thiophene-3-carboxylate ligand," *J. Electron. Mater*., vol. 49, pp. 1935-1943, 2020.

[18] H. Inan, "Synthesis of dimethylamine, pyridine-based Schiff base and Cu(II), Co(II) and Fe(II) complexes, structure elucidation: investigation of biological activities," Master Thesis, Natural and Applied Science, Muş Alparslan University, Muş, Türkiye, 2024.

[19] N. Nawaz, I. Ahmad, N.M. Darwesh, A. Wahab, S. Ur Rahman, A. Sajid, F.A. Khan, S.B. Khan, S.G. Patching, K. Uddinet, "Synthesis, characterization and antioxidant activity of Nickel(II) Schiff base complexes derived from 4-(dimethylamino)benzaldehyde," *J. Chem. Soc. Pakistan*, vol. 42, no. 2, pp. 238-242, 2020.

[20] S. Alyar, T. Şen, Ü. Özdemir Özmen, H. Alyar, Ş. Adem, C. Şen, "Synthesis, spectroscopic characterizations, enzyme inhibition, molecular docking study and DFT calculations of new Schiff bases of sulfa drugs," *J. Mol. Struct*., vol. 1185, pp. 416-424, 2019.

[21] F.M. Elmagbari, A.N. Hammouda, H.A.M. Bennour, R.M. EL-Ferjani, Y.O. Ben Amer, "Synthesis and characterisation of Cr(III) and Co(II) Schiff base complexes," *Mater. Sci. Appl*., vol. 14, pp. 53-62, 2023.

[22] I.N.Q. Qader, İ. Obalı, H.İ. Uçan, A. Uysal, A. Yılmaz Obalı, M. Kul, "Ortho-hydroxy bioactive Schiff base compounds: Design, comprehensive characterization, photophysical properties and elucidation of antimicrobial and mutagenic potentials," *Bioorg. Chem*., vol. 119, no. 105507, 2022.

[23] M.I. Khan, A. Khan, I. Hussain, M.A. Khan, S. Gul, M. Iqbal, I. Ur-Rahman, F. Khuda, "Spectral, XRD, SEM and biological properties of new mononuclear Schiff base transition metal complexes," *Inorg. Chem. Commun*., vol. 35, pp. 104-109, 2013.

[24] A. Savcı, K. Buldurun, M.E. Alkış, Y. Alan, N. Turan, "Synthesis, characterization, antioxidant and anticancer activities of a new Schiff base and its M(II) complexes derived from 5-fuorouracil," *Med. Oncol*., vol. 39, no. 172, 2022.

[25] M.E. Alkis, K. Buldurun, Y. Alan, N. Turan, A. Altun, "Electroporation enhances the anticancer effects of novel Cu(II) and Fe(II) complexes in chemotherapy-resistant glioblastoma cancer cells," *Chem. Biodiversity*, vol. 20, e202200710, 2023.

[26] O. Karaosmanoğlu, H. Berber, Ü.D. Uysal, "Synthesis, theoretical studies, cytotoxicity of 2-((4-(dimethylamino)benzylidene)amino)-5-methylphenol with potential JNK1 inhibitory activity," *SDÜ Sağlık Bilimleri Dergisi*, vol. 14, no. 2, pp. 253-272, 2023.

[27] L.H. Abdel-Rahman, N.M. Ismail, M. Ismael, A.M. Abu-Dief, E. Abdel-Hameed Ahmed, "Synthesis, characterization, DFT calculations and biological studies of Mn(II), Fe(II), Co(II) and Cd(II) complexes based on a tetradentate ONNO donor Schiff base ligand," *J. Mol. Struct*., vol. 1134, pp. 851-862, 2017.

[28] P. Devi, K. Singh, P. Dabas, "Synthesis of Co^{+2}, Ni^{+2}, Cu^{+2}, and Zn^{+2} complexes of Schiff base 5-methyl-3-((3,5-dichlorosalicylidene) amino)-pyrazole, spectral, and biological studies," *J. Coord. Chem*., vol. 75, no. 1-2, pp. 162-177, 2022.

[29] G. Ramesh, S. Daravath, M. Swathi, V. Sumalatha, D.S. Shankar, Shivaraj, "Investigation on Co(II), Ni(II), Cu(II) and Zn(II) complexes derived from quadridentate salen-type Schiff base: Structural characterization, DNA interactions, antioxidant proficiency and biological evaluation," *Chem. Data Coll*., vol. 28, 100434, 2020.

[30] G.G. Mohamed, N.E.A. El-Gamel, "Synthesis, investigation and spectroscopic characterization of piroxicam ternary complexes of Fe(II), Fe(III), Co(II), Ni(II), Cu(II) and Zn(II) with glycine and dl-phenylalanine," *Spectrochim Acta A Mol Biomol Spectrosc*., vol. 60, no. 13, pp. 3141-3154, 2004.

[31] A.A. Sharfalddin, M.A. Hussien, "Bivalence metal complexes of antithyroid drug carbimazole; synthesis, characterization, computational simulation, and biological studies," *J. Mol. Struct*., vol. 1228, 129725, 2021.

[32] E. Bursal, A. Aras, Ö. Kılıç, P. Taslimi, A.C. Gören, İ. Gülçin, "Phytochemical content, antioxidant activity, and enzyme inhibition effect of Salvia eriophora Boiss. & Kotschy against acetylcholinesterase, α-amylase, butyrylcholinesterase, and α-glycosidase enzymes," *J. Food Biochem*., vol. 43, no. 3, e12776, 2019.

[33] N. Çolak, A. Savcı, N. Turan and K. Buldurun, "Preparation, spectral characterization and antioxidant activities of aminothiophene-containing Schiff base and Co(II) and Pd(II) complexes," *J. Biochem. Mol. Toxicol*., vol. 39, e70215, 2025.

[34] A. Aras, M. Doğru, E. Bursal, "Determination of antioxidant potential of Nepeta nuda subsp. lydiae," *Anal. Chem. Lett*., vol. 6, no. 6, pp. 758-765, 2016.

[35] R. Apak, K. Güçlü, B. Demirata, M. Özyürek, S.E. Çelik, B. Bektaşoğlu, K.I. Berker, D. Özyurt, "Comparative evaluation of various total antioxidant capacity assays applied to phenolic compounds with the CUPRAC assay," *Molecules*, vol. 12, no. 7, pp. 1496-1547, 2007.

BİTLİS EREN ÜNİVERSİTESİ
FEN BİLİMLERİ DERGİSİ

ISSN: 2147-3129 / e-ISSN: 2147-3188

Article Type : Research Article
Received : April 24, 2025
Revised : June 26, 2025
Accepted : September 2, 2025
DOI : 10.17798/bitlisfen.1683303

Year : 2025
Volume : 14
Issue : 3
Pages : 1596-1609

DETERMINANTS OF ELECTROOCULOGRAPHY MEASUREMENTS FOR QUIET EYE DURATION IN ARCHERS VIA PENALTY REGULARIZER

Fatma SÖĞÜT [1,*], İnci KESİLMİŞ [2], Evrim Ersin KANGAL [3], Ülkü ÇÖMELEKOĞLU [4]

[1]*Department of First Aid and Emergency, Vocational School of Health Services, Mersin University, Mersin, Türkiye.*

[2]*Department of Coaching Education, Faculty of Sports Science, Mersin University, Mersin, Türkiye.*

[3]*Computer Technology and Information Systems, School of Applied Technology and Management of Erdemli, Mersin University, Mersin, Türkiye,*

[4]*Department of Biophysics, Faculty of Medicine, Mersin University, Mersin, Türkiye.*

***Corresponding Author**: fatmasogut@mersin.edu.tr*

ABSTRACT

Electrooculography (EOG) is an electrophysiological method used to assess eye movements and the functional status of the retinal pigment epithelium by measuring the potential differences generated during eyeball motion. In recent years, EOG has also been explored as a tool for determining quiet eye (QE) periods in athletes. The QE period refers to the duration an athlete maintains focused visual attention on a target, and it is considered to be closely linked with athletic performance.

The application of EOG in this context is emerging as a novel approach to evaluate and enhance athletes' visual focus and concentration skills. In this study, the relationships between QE period and various free parameters of the athletes were analyzed using penalty approaches (Lasso and Ridge regression). Thanks to this approach, QE periods can be predicted with high accuracy based on the independent variables of individuals without any direct QE measurement for different athletes, and this will contribute to the development of preventive or supportive strategies for performance. The R^2 value for the coefficients of the two regression methods was obtained more than 80% and the mean square deviation was less than 5%.

Keywords: Electrooculography, Quiet eye period, Archer, Regression, Data prediction.

1 INTRODUCTION

Archery is a precision sport demanding technical accuracy, mental resilience, and physiological regulation. Unlike high-intensity team sports, it places a strong emphasis on individual performance. Achieving sustained athletic success thus requires a comprehensive, systematic analysis of biomechanical, physiological, psychological, and technical-tactical factors [1]. Performance optimization in archery relies on a triad of technical proficiency, physical stability, and mental discipline. Given the sport's precision, even minor deviations in technique or posture can significantly impact shot accuracy. Coaches must implement individualized training programs reflecting each athlete's unique characteristics, integrating technological tools like motion capture and wearable sensors for precise monitoring and accelerated feedback [2-4]. This evidence-based, data-informed approach is critical for maximizing performance potential in elite archery.

The QE is a crucial cognitive and visual approach influencing performance, particularly in precision-based sports. Initially described by Vickers (1996), QE refers to the final, steady gaze period just before initiating a motor action [5]. In archery, this "final gaze" typically lasts 300–500 ms on the target prior to and during the release phase [5]. The duration of this fixation is directly associated with attention regulation, processing visual data, and the quality of motor preparation. In precision disciplines, QE duration plays a vital role in optimizing performance, making QE training a key tool for elite athletes [6-7]. Empirical evidence shows elite archers exhibit significantly longer and steadier gaze fixations compared to less experienced counterparts, contributing to increased shot accuracy and consistency [8]. Accordingly, QE should be conceptualized as an integral aspect of cognitive-motor preparation in high-performance contexts, beyond just a visual mechanism. Research confirms that archers mastering QE demonstrate superior technical consistency under pressure and faster recovery from errors [9-10]; elite archers display QE durations 20-30% longer than amateurs [8].

QE duration can be extended through individual training and technological devices. Increasing this duration is crucial for improving focus and shooting accuracy. Coaches can support athletes by incorporating exercises designed to enhance mental focus, training them to recognize and manage distractions to maintain sustained attention on the target [7]. Additionally, deliberate movement strategies, such as encouraging archers to slow down and carefully pause at each step, can provide more time for eye fixation on the target [8]. Beyond these individual methods, technological devices also contribute. Eye-tracking systems allow

coaches to monitor and quantify QE duration by tracking eye movements, while video analysis of shots enables detailed observation of QE duration and eye movements, facilitating the identification of improvement areas [6].

In recent years, the application of Artificial Intelligence (AI) and Machine Learning (ML) in sports has witnessed remarkable growth. These technological advancements offer promising opportunities, particularly in multidimensional domains like athlete health, performance optimization, and rehabilitation. AI and ML facilitate early injury prediction, the development of individualized training programs, and real-time performance analyses [11]. Moreover, the integration of big data analytics and sensor-based technologies in athlete monitoring contributes to clinical decision support systems. Techniques such as deep learning, decision trees, and support vector machines have proven highly effective in assessing injury risk and conducting tactical in-game analyses [12]. These developments are significantly transforming sports from a primarily physical endeavor into a more data-driven and analytical discipline.

An athlete's QE time can be influenced by several parameters. Identifying which of these parameters actively affect QE time can help enhance it. This study, conducted with archers, utilized data optimization techniques, specifically the Lasso and Ridge methods, to determine which parameters significantly impacted the recorded QE times. The optimization process was based on the individual characteristics of the participating athletes. The findings from this research are expected to contribute to the improvement of QE times in archers, thereby potentially enhancing their overall performance.

2 MATERIAL AND METHOD

While detailed EOG data are obtained to measure the QE duration of athletes, it would be useful to develop a system that can predict which parameters will be useful in determining the QE duration. Lasso and Ridge regression methods are some of the known methods in the literature to handle these prediction situations. In the following subsections, we applied both regression approaches to explore the determinants of QE duration.

2.1 Participants

Eighteen archers (nine female and nine male; mean age = 17 years), all of whom had engaged in regular archery training for a minimum of two years, were recruited for participation

in the study. An Ethical Approval Certificate (19956/2020/26/5) for conducting the study was obtained from the Osmaniye Korkut Ata University Scientific Research and Publication Ethics Committee. All participants, along with their parents and coach, signed an informed consent form prepared in accordance with the Declaration of Helsinki. Beyond the aforementioned criteria, participant eligibility further mandated the absence of any chronic health issues and complete participation in all designated parameter measurements. Exclusion criteria were applied to ensure data quality and participant suitability. Participants were excluded if their EOG recordings exhibited excessive noise or were otherwise unsuitable for analysis. Additionally, individuals with less than two years of archery experience, those diagnosed with neurological or ophthalmological disorders that could influence eye movements, or individuals who sustained an injury within the last six months impacting archery performance were not included.

The mean height of the archers was 160.93 ± 11.33 cm, and their mean body mass was 63.67 ± 19.34 kg. Each athlete's total performance score was recorded following three sets of six shots, for a total of 18 arrows per participant. Athletes completed three sets, each consisting of six shots. Missed shots were scored as zero, and no second attempts were permitted. The shots were fired from distances of 30 to 50 meters.

The variables to be used in the next stages of the analysis and their importance in our research are presented in the Table 1.

Table 1. The role and rationale for variable selection

Variable	Reason
Age	It is directly related to the level of neurodevelopmental maturity and attention span.
Gender	There may be gender-related differences in biological and psychological attention strategies.
Height / Weight	It affects trunk stability and balance and can affect the steady aiming process.
Training Duration	Long training duration enables the development of higher-level cognitive skills such as QE.
R/L_Leg Length	It can directly affect focus by affecting body symmetry during a fixed standing position.
Archery Scores (Hor/R/L)	It is necessary to control the effect of QE duration on individual performance.
CRDL / CRDR	Provides information about the functional quality of the visual system. May affect QE duration associated with eye movements.
BodyAwarenessScore	It has been shown in the literature that individuals with higher levels of psychophysiological awareness can have longer QE duration.

*R/L_Leg Length: Right, Left Leg lenght.

** Composite Reach Distance_Right: CRDR, Composite Reach Distance_Left: CRDL.

Table 2 provides descriptive characteristics of archers.

Table 2. Descriptive statistics of archers age, height and weight

Parameters	mean	std	min	25%	50%	75%	max
Age	17,33	1,44	10	11	14	15,75	19
Training Duration (year)	3,17	2,74	0	1,62	2	4,5	12
Body Heigth (cm)	160,93	11,33	142	153,25	158,25	171	180
Body Weigth (kg)	63,67	19,34	37	51	57,75	71,75	115
R_Leg_Length (cm)	85,67	6,77	75	82	84	90	99
L_Leg Length (cm)	85,5	6,45	75	82	84	90,75	96

The 25th, 50th, and 75th percentiles (25%, 50%, 75%) correspond to the first quartile, median, and third quartile, respectively, offering insights into the data distribution.

2.2 The Data Collection with EOG in Assessing QE Durations of Athletes

EOG's ability to record eye movement-related potential shifts has made it an alternative or complementary method for quantifying QE periods. The portability and lower cost of EOG equipment enhance its applicability in real-world sports settings.

An electrooculography (EOG) device was employed to determine the quiet eye (QE) duration of the participants. Eye movements were recorded using the Biopac MP100 system (BIOPAC Systems, Inc., Santa Barbara, CA, USA) during the athletes' shooting sessions. The corneal-retinal potential was amplified via the EOG100C Electrooculogram amplifier, integrated with the recording system. Data were collected at a sampling rate of 200 Hz and analyzed using BIOPAC AcqKnowledge Analysis Software (ACK100W). Horizontal and vertical eye movements were recorded separately for both the right and left eyes. All measurements were conducted during arrow shooting.

QE duration was defined as the time interval from the initiation of visual fixation until the release of the arrow. The onset of the QE period was determined retrospectively from the moment of the shot. In the EOG recordings, the QE period was identified as the amplitude range within 3 degrees (peak-to-peak) prior to arrow release. The QE offset was marked by the observer, coinciding with the auditory cue of the arrow leaving the bow. Recordings with excessive noise were excluded from analysis. All participants demonstrated fixation durations exceeding 100 ms, remaining within the 3-degree range.

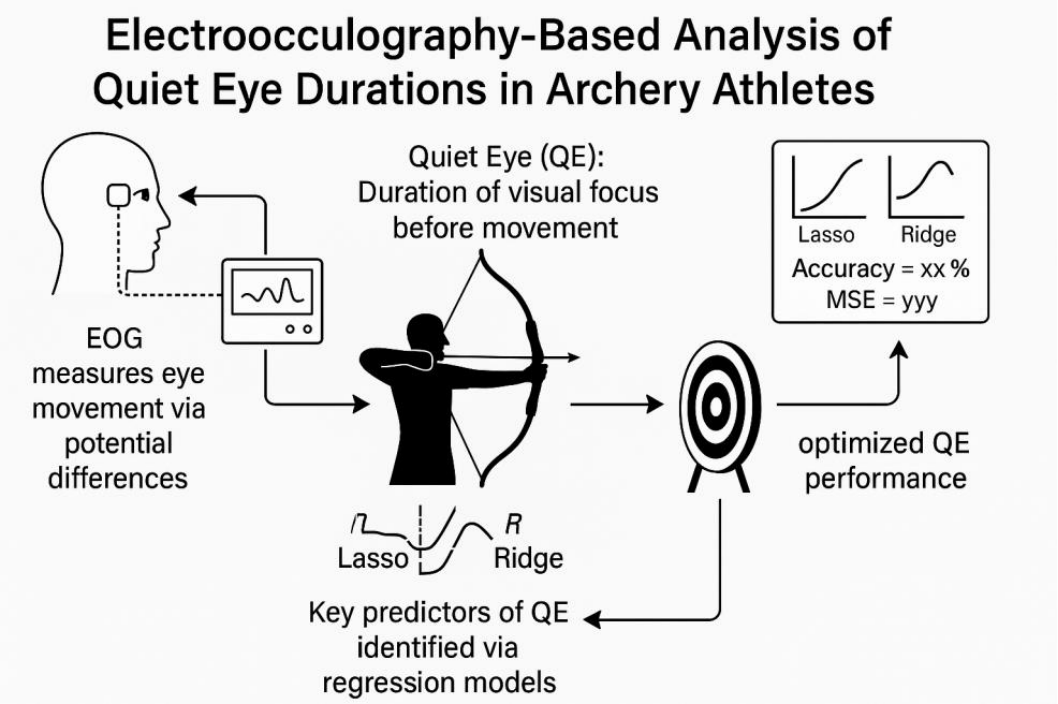


Figure 1. Schematic representation of prediction process [13].

Synthetic data generation was implemented to broaden the model's generalizability. This process was executed under controlled conditions primarily to alleviate the impact of small sample sizes, thereby fostering enhanced model generalization and preventing overfitting. The robust accuracy figures obtained from the model's outputs underscore the success of this methodology.

2.3 Data Analysis with Ridge and Lasso Regression Methods

Regression analysis is an essential statistical approach employed to explore and quantify the relationship between a response variable and one or more predictor variables. However, in high-dimensional datasets particularly when the number of predictors exceeds the number of observations traditional linear regression models are prone to overfitting. To address this issue, **regularization techniques** such as **Lasso (Least Absolute Shrinkage and Selection Operator)** and **Ridge Regression** are employed. These methods enhance generalization by constraining the model's complexity, effectively preventing overfitting and improving predictive performance [14].

Ridge regression is a regularization technique designed to reduce model variance by shrinking the coefficients. It incorporates an L2 penalty, which is the sum of the squared coefficients, into the loss function. This penalty discourages large coefficients, pushing them closer to zero but not exactly zero. The objective function of Ridge regression is:

$$\min_{\beta}\left\{\sum_{i=1}^{n}(y_i - x_i^T\beta)^2 + \lambda\sum_{j=1}^{p}\beta_j^2\right\} \quad (1)$$

where y_i is the target value, x_i is the feature vector for the $\boldsymbol{i}$-th observation, β are the model coefficients, $\lambda \geq 0$ is the regularization parameter that controls the strength of the penalty [15].

Lasso regression is a regularization technique that applies an L1 penalty, which is the sum of the absolute values of the model coefficients. This penalty can shrink some coefficients exactly to zero, effectively removing less relevant features from the model. As a result, Lasso not only helps prevent overfitting but also serves as a powerful feature selection method. The objective function of Lasso regression is defined as:

$$\min_{\beta}\left\{\frac{1}{2n}\sum_{i=1}^{n}(y_i - X_i\beta)^2 + \lambda\sum_{j=1}^{p}|\beta_j|\right\} \quad (2)$$

where y_i is the observed response, X_i is the vector of predictor for the $\boldsymbol{i}$-th observation, β is the vector coefficients, $\lambda \geq 0$ is the regularization parameter controlling the strength of the penalty.

Lasso has advantages over Ridge, especially in cases where unnecessary variables need to be eliminated (sparse data sets) [16]. Lasso simplifies the model and increases interpretability by making some coefficients zero. Ridge reduces the coefficients when including all variables in the model, so it is more stable in cases of multicollinearity.

The data in Table 3 will be used for data analysis. At this stage, we prepare the data used in the next phase. QE_Hor, QE_R and QE_L are determined individually for two models with the rest 14 independent variables.

Table 3. Descriptive statistics of performance parameters.

Parameters	Mean	SD	Min	25%	50%	75%	Max
Archery Score (Hor)	40,33	13,58	7	37,5	40,5	50,75	57
Archer Score (R)	38,5	15,29	5	34	40,5	51	55
Archery Score (L)	40,72	16,12	6	36,5	44	53,5	58
QE_Hor (in seconds)	0,81	0,46	0,22	0,53	0,7	0,91	1,94
QE_R (in seconds)	0,59	0,39	0,2	0,34	0,53	0,65	1,67
QE_L(in seconds)	0,71	0,31	0,26	0,49	0,64	0,93	1,49
CRDR (in cm)	81,08	10,48	62,34	73,06	83,92	89,31	95,06
CRDL (in cm)	80,32	11,32	54,98	76,49	83,33	87,13	96,67
Body Awareness Score (in points)	91	15,73	54	81	93,5	101,75	115

**Archery (Hor)/(R)/(L) scores (in units of points) are the arrow shooting scores obtained by archers while taking horizontal/right/left measurements with EOG.*

The target variables are QE_Hor, QE_R and QE_L. All variables have a numerical value. Both of Ridge and Lasso methods use same amounts of data. The ratio of test and training data has a value of 20:80. The steps of the analysis algorithm can be viewed in Figure 2.

In the analysis, synthetic data generation was performed to increase the generalization performance of the model and to expand the size of the dataset. Synthetic data was obtained by adding small-scale normally distributed noise to randomly selected examples from the original dataset. During this process, low-variance random deviations were applied independently to each input feature; similarly, a small random noise was added to the target variable (output). Thanks to this method, new examples were created that reflect the natural variations of the original examples in both the input and output spaces. The synthetic examples generated were combined with the original data and used in model training. This approach offers an effective strategy in terms of reducing overfitting and making the model more stable, especially in datasets with small sample sizes.

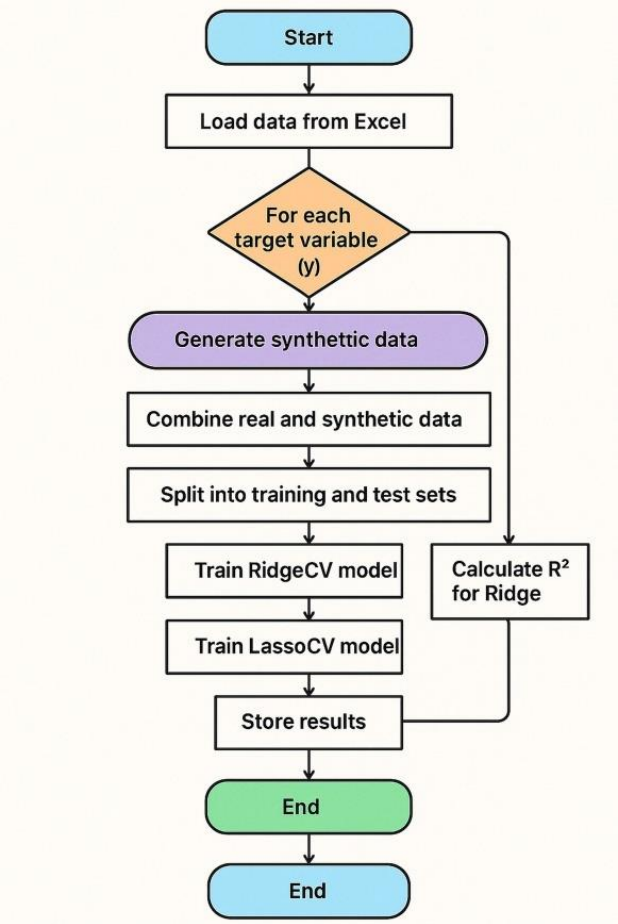


Figure 2. The flow chart of the analysis.

The results given by the models are shown in Table 4.

Table 4. Prediction results of Ridge and Lasso methods.

Parameters	R^2_Ridge	α_{Best}_Ridge	MSE_Ridge	R^2_Lasso	α_{Best}_Lasso	MSE_Lasso	Better Model
QE_Hor (in seconds)	0,847326	1,592283	0,034188	0,801001	0,004977	0,044561	Ridge
QE_R (in seconds)	0,908941	0,067342	0,016608	0,909058	0,000100	0,016586	Lasso
QE_L (in seconds)	0,933835	0,298365	0,003954	0,935428	0,000534	0,003859	Lasso

R^2 indicates the explanatory power of the independent variables on the target variables. As it approaches one, the success of the model increases.

The mean square error (MSE) was utilized as the principal benchmark to gauge the efficacy of both models. Consequently, models with lower MSE values are regarded as more proficient in forecasting.

Ridge regression includes all variables in the model; it reduces the coefficients but does not reset them. Lasso, on the other hand, removes some variables from the model by completely resetting them to zero, and performs variable selection. While some variables (e.g. Gender, Weight) are reset in the Lasso model for QE_Hor, the Ridge model keeps them all. For QE_L, the BodyAwarenessScore parameter has a strong effect in both models. While variables such as RLeg are kept in the Lasso model for QE_R, variables such as Gender and Height are reset.

3 RESULTS AND DISCUSSION

A limitation of this study is the restricted sample size of 18 athletes, which may impede statistical generalization. Consequently, the findings should not be directly extrapolated to populations of athletes varying in age, experience level, or sport. Cohen's f^2 statistic was employed to assess the adequacy of the sample size by quantifying the effect size of the independent variables on the dependent variable in the regression models. A larger f^2 value indicates a stronger explanatory power of the independent variables on the dependent variable. Cohen's strength of association parameter is given as

$$f^2 = \frac{R^2}{1 - R^2} \tag{3}$$

Table 5. Prediction results of Ridge and Lasso methods.

Cohen_f^2	f^2_Ridge	f^2_Lasso	Power_Lasso/Reidge
QE_Hor (in seconds)	3,349	3,02	1,0
QE_R (in seconds)	12,466	16,031	1,0
QE_L (in seconds)	13,268	11,572	1,0

The fact that $f^2 > 4$ reveals that our model establishes a very strong relationship with the variables. Also when the power analysis was performed, the result being unity as indicated in Table 5 shows that the data is more than sufficient to detect this relationship statistically.

In this study, the effects of Ridge and Lasso regression methods on regression coefficients for three different target variables (QE_Hor, QE_R and QE_L.) were analyzed. Ridge regression keeps all features in the model with the penalty function based on the L2 norm and only reduces their effects. This situation results in the effects of the features approaching zero but not completely disappearing. This method has the potential to produce stable and balanced results especially in highly correlated data. On the other hand, Lasso regression performs a natural feature selection by reducing the coefficients of some features to zero with the penalty function based on the L1 norm. In this way, simpler and interpretable models are created; some variables are completely prevented from being included in the model. The best values of alpha depending on the descriptive and performance values of the archers are given for two models as in the Figure 3.

Ridge regression includes all variables in the model; it reduces the coefficients but does not reset them (Figure 3 left column). Lasso, on the other hand, removes some variables from the model by completely resetting them to zero, and performs variable selection (Figure 3 right column). For QE_Hor, some variables (e.g. Gender, Weight) are reset in the Lasso model, while the Ridge model keeps them all. For QE_L, the BodyAwarenessScore parameter has a strong effect in both models. For QE_R, variables such as RLeg are kept in the Lasso model, while variables such as Gender and Height are reset.

A limitation of the present study is its relatively modest sample size of 18 athletes, which inherently restricts the statistical generalizability of the findings. Consequently, direct extrapolation of these results to athlete populations differing in age, experience level, or sporting discipline should be exercised with caution. While the EOG method utilized for measuring QE duration offers advantages in terms of portability and cost-effectiveness, it may not possess the same level of precision and sensitivity in capturing nuanced eye movement data as more advanced, laboratory-based eye-tracking systems. Furthermore, the scope of this investigation was confined exclusively to the sport of archery. It is plausible that QE duration and the factors influencing it may exhibit substantial variability across sports demanding distinct motor skills. Finally, athlete performance assessment was based solely on discrete single-shot attempts, precluding the examination of longitudinal changes or adaptive processes over extended training periods.

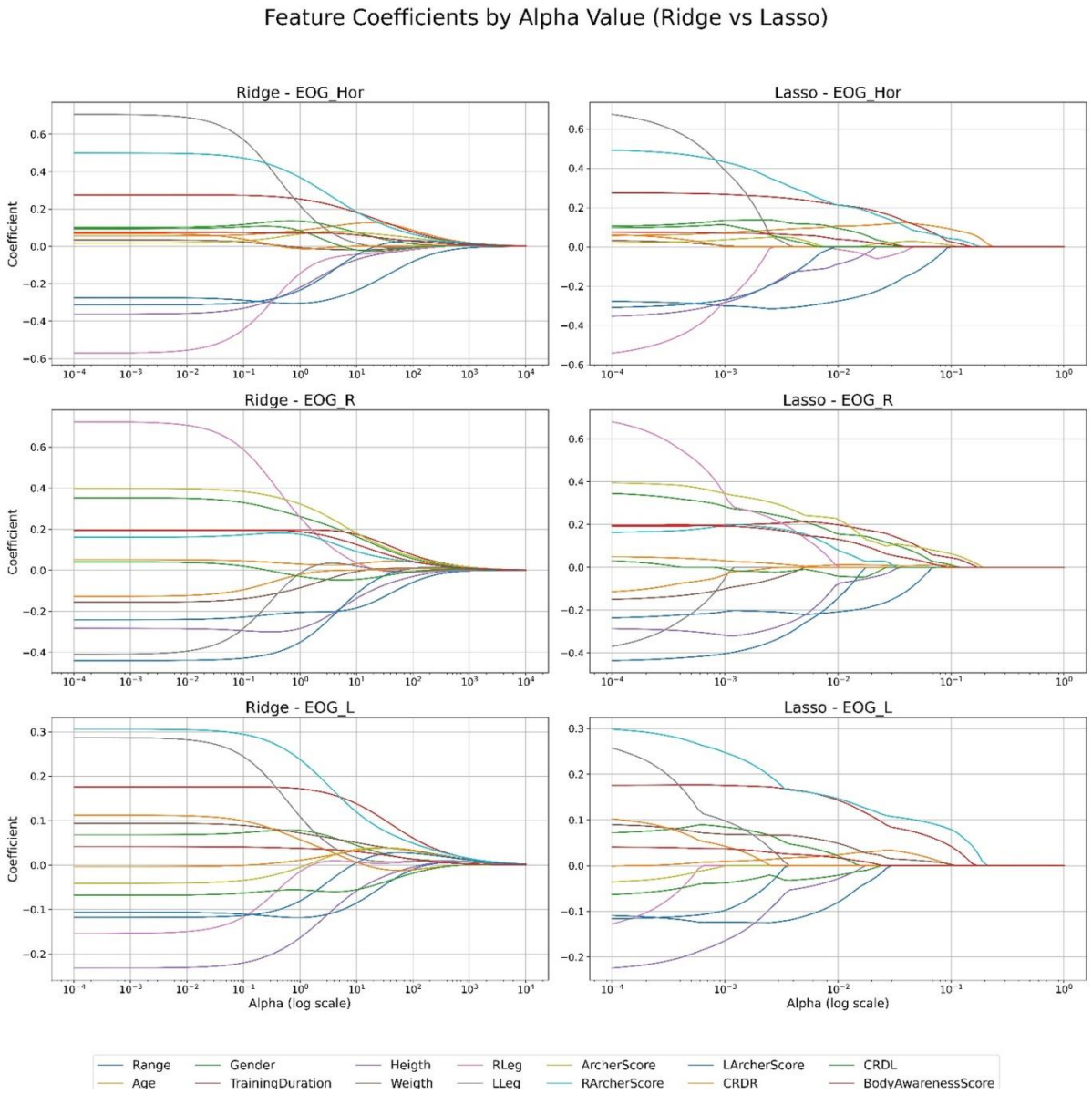


Figure 3. The alpha values are presented in relation to the corresponding feature coefficients. The left panel illustrates the results obtained using the Ridge regression model, while the right panel shows those derived from the Lasso regression model.

4 CONCLUSIONS

The application of Lasso and Ridge regression methods within sports science research is well-established in the literature, with notable applications in various athletic domains, including hockey and basketball [17, 18]. These advanced statistical techniques have been systematically employed to evaluate and analyze athlete performance. Specifically, they have facilitated the identification of distinct analytical objectives through the examination of diverse athlete-specific features. For example, in a study focusing on hockey players, Lasso and Ridge regression were utilized to model key mechanical variables, such as maximum horizontal force

(F_0), maximum speed (V_{max}), maximum horizontal power (P_{max}), and performance across sprint/change-of-direction (COD) intervals [17]. Analogously, both regression methods have been instrumental in assessing the offensive and defensive contributions of basketball players, leveraging detailed NBA match commentary data [18].

In the present study, both Lasso and Ridge regression techniques were similarly employed to determine the QE duration, a critical factor influencing archers' performance. Collectively, these aforementioned studies and our current research highlight the substantial relevance and utility of Lasso and Ridge regression in sports science. These statistical tools not only enable the exploration of the biomechanical underpinnings of athletic performance but also facilitate the objective evaluation of individual player contributions, even within team-based sports contexts.

When the model outputs are evaluated based on the target variable; it is observed that variables such as CRDL and LArcherScore are effective in Ridge regression for QE_Hor, while CRDL maintains its importance in Lasso regression, but some variables are excluded from the model by being reduced to zero. While RLeg, ArcherScore and LArcherScore stand out in Ridge model for QE_R; while RLeg maintains its importance in Lasso model, it is observed that variables such as Gender and Height are reduced to zero in some regulation coefficients. For QE_L, BodyAwarenessScore variable is consistently high in both models; this shows that this feature plays a decisive role in the estimation process.

As a result of the comparative evaluation, it is concluded that Ridge regression is suitable for optimizing the overall model performance by preserving the contributions of all variables, while Lasso regression offers simpler and more interpretable models by making variable selection. While the Lasso method can be preferred especially in applications working with a limited number of variables, the Ridge method offers an effective alternative in order to reduce multicollinearity and balance the overall variance. In addition, the ElasticNet approach, which combines the advantages of both methods, is suggested as a potential method that should be evaluated in future studies.

Conflict of Interest Statement

There is no conflict of interest between the authors.

Statement of Research and Publication Ethics

The study is complied with research and publication ethics.

Artificial Intelligence (AI) Contribution Statement

This manuscript was entirely written, edited, analyzed, and prepared without the assistance of any artificial intelligence (AI) tools. Figure 1 was generated by ChatGPT.

Contributions of the Authors

All authors contributed to the study conception and design. Material preparation, data collection and analysis were performed by all authors, and they read and approved the final manuscript.

REFERENCES

[1] E. Vendrame, V. Belluscio, L. Truppa, L. Rum, A. Lazich, E. Bergamini, and A. Mannini, "Performance assessment in archery: A systematic review," *Sports Biomech.*, vol. 23, no. 12, pp. 2444–2466, Dec. 2024, doi: 10.1080/14763141.2022.2049357.

[2] T. Taha *et al.*, "Performance analysis of archery using a wearable system," *IOP Conf. Ser.: Mater. Sci. Eng.*, vol. 319, p. 012017, 2018, doi: 10.1088/1757-899X/319/1/012017.

[3] M. Siekańska, R. Z. Bondár, S. di Fronso, J. Blecharz, and M. Bertollo, "Integrating technology in psychological skills training for performance optimization in elite athletes: A systematic review," *Psychol. Sport Exerc.*, vol. 57, p. 102008, 2021, doi: 10.1016/j.psychsport.2021.102008.

[4] N. Vasilis *et al.*, "Injuries and persistent pain in elite adolescent archery athletes: A cross-sectional epidemiological study," *Sports*, vol. 12, no. 4, p. 101, 2024, doi: 10.3390/sports12040101.

[5] J. N. Vickers, "Visual control when aiming at a far target," *J. Exp. Psychol. Hum. Percept. Perform.*, vol. 22, no. 2, pp. 342–354, 1996, doi: 10.1037/0096-1523.22.2.342.

[6] J. N. Vickers, *Perception, Cognition, and Decision Training: The Quiet Eye in Action*. Champaign, IL: Human Kinetics, 2007.

[7] J. Causer, P. S. Holmes, and A. M. Williams, "Quiet Eye training facilitates visuomotor coordination in children with developmental coordination disorder," *J. Motor Behav.*, vol. 42, no. 6, pp. 357–365, 2010, doi: 10.1080/00222895.2010.526456.

[8] S. J. Vine, L. J. Moore, and M. R. Wilson, "Quiet Eye training: Effects on learning and performance under pressure," *J. Appl. Sport Psychol.*, vol. 23, no. 2, pp. 243–257, 2011, doi: 10.1080/10413200.2010.546827.

[9] J. N. Vickers, "The Quiet Eye: Origins, Controversies, and Future Directions," *Kinesiology Rev.*, vol. 5, no. 2, pp. 119–128, 2016, doi: 10.1123/kr.2016-0005.

[10] C. C. Gonzalez, J. Causer, M. J. Grey, G. W. Humphreys, R. C. Miall, and A. M. Williams, "Exploring the quiet eye in archery using field- and laboratory-based tasks," *Exp. Brain Res.*, vol. 235, no. 9, pp. 2843–2855, 2017, doi: 10.1007/s00221-017-4988-2.

[11] F. J. J. Reis, R. K. Alaiti, C. S. Vallio, and L. Hespanhol, "Artificial intelligence and Machine Learning approaches in sports: Concepts, applications, challenges, and future perspectives," *Braz. J. Phys. Ther.*, vol. 28, p. 101083, 2024, doi: 10.1016/j.bjpt.2024.101083.

[12] J. G. Claudino *et al.*, "Current approaches to the use of artificial intelligence for injury risk assessment and performance prediction in team sports: A systematic review," *Sports Med. Open*, vol. 5, no. 1, p. 1, 2019, doi: 10.1186/s40798-019-0202-3.

[13] OpenAI, *ChatGPT*. (2025, Apr. 24). [Online]. Available: https://chat.openai.com/

[14] T. Hastie, R. Tibshirani, and J. Friedman, *The Elements of Statistical Learning: Data Mining, Inference, and Prediction*, 2nd ed. New York, NY, USA: Springer, 2009, doi: 10.1007/978-0-387-84858-7.

[15] G. James, D. Witten, T. Hastie, and R. Tibshirani, *An Introduction to Statistical Learning with Applications in R*. New York, NY, USA: Springer, 2013, doi: 10.1007/978-1-4614-7138-7.

[16] H. Zou and T. Hastie, "Regularization and variable selection via the elastic net," *J. R. Stat. Soc. Ser. B (Statistical Methodology)*, vol. 67, no. 2, pp. 301–320, 2005, doi: 10.1111/j.1467-9868.2005.00503.x.

[17] A. Bustamante-Garrido, M. Izquierdo, B. Miarka, A. Cuartero-Navarrete, J. Pérez-Contreras, E. Aedo-Muñoz, and H. Cerda-Kohler, "Mechanical determinants of sprinting and change of direction in elite female field hockey players," *Sensors (Basel)*, vol. 23, no. 18, p. 7663, 2023, doi: 10.3390/s23187663.

[18] A. Damoulaki, I. Ntzoufras, and K. Pelechrinis, "Lasso multinomial performance indicators for in-play basketball data," *Comput. Stat.*, vol. 40, pp. 2157–2181, 2025, doi: 10.1007/s00180-025-01604-7.

BİTLİS EREN ÜNİVERSİTESİ
FEN BİLİMLERİ DERGİSİ

ISSN: 2147-3129 / e-ISSN: 2147-3188

Article Type : Research Article
Received : April 29, 2025
Revised : June 19, 2025
Accepted : July 8, 2025
DOI : 10.17798/bitlisfen.1687018

Year : 2025
Volume : 14
Issue : 3
Pages : 1610-1624

PHOTOCATALYTIC PROPERTIES OF CHITOSAN-COATED PESA SPHERES CONTAINING GALLIUM(III) NITRATE: SYNTHESIS AND CHARACTERIZATION

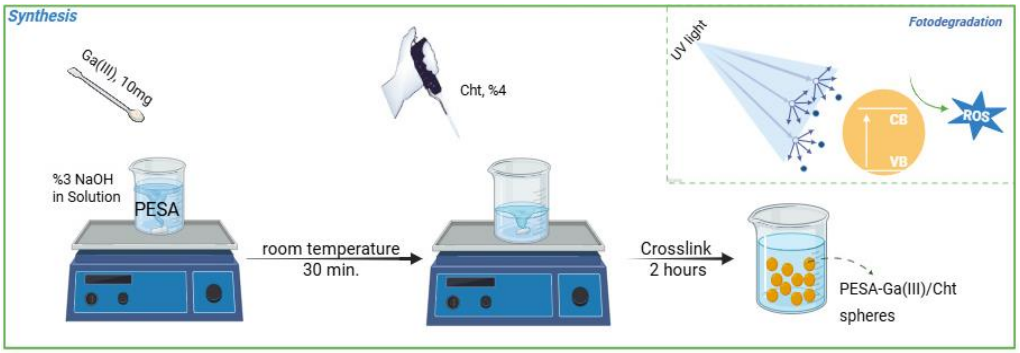
Deniz DOĞAN [1]

[1] *Kırıkkale University, Chemistry Department, Kırıkkale, Türkiye, denizdogan@kku.edu.tr*

ABSTRACT

In this study, the photocatalytic effect of Chitosan (Cht) -Coated polyanetholsulfonic acid (PESA) Spheres Containing Gallium(III) Nitrate ($Ga(NO_3)_3$) on methylene blue (MB), a cationic dye, was investigated. The spheres were synthesized by dropwise addition of a chitosan solution to a PESA-Ga(III) solution prepared in a sodium hydroxide (NaOH) solution. It is known that the morphological properties of spheres change in the presence of metal. For this purpose, the surface morphology was determined by Scanning Electron Microscopy (SEM). Functional group analysis was determined using Fourier Transform Infrared (FTIR) Spectrometry. The concentration of Gallium ions remaining in the solution at the end of the reaction was determined by Inductively Coupled Plasma Optical Emission Spectroscopy (ICP-OES) analysis. A UV-C tube lamp was used to photocatalytically degrade the methylene blue dye. The dye degradation changes were then analyzed in a UV-VIS spectrophotometer. Furthermore, Tauc's formula determined the band gaps with the help of Chitosan-Coated PESA Spheres Containing $Ga(NO_3)_3$ (PESA- Ga(III)/Cht) and Chitosan-Coated PESA Spheres (PESA/Cht) UV spectra. It was observed that the photocatalytic effect increased with the incorporation of $Ga(NO_3)_3$ into the polymer structure.

Keywords: Photocatalytic effect, Methylene blue, Gallium(III) Nitrate, Chitosan, PESA, Dye degradation.



1 INTRODUCTION

Recently, excessive pollution of water resources with organic pollutants is increasingly endangering all life forms [1], [2]. Among these pollutants, cationic dyes such as methylene blue (MB) [3], which pose a significant environmental threat today, are highly harmful to living ecosystems due to their water solubility and toxicity. MB is frequently used in both medical and industrial fields [4], [5]. MB, which is used in staining to enhance the visibility of cells and microorganisms under the microscope, is also employed as an antiseptic in superficial injuries [5], [6], [7]. MB, a synthetic aniline dye, is used as a colored substance in the textile industry [8]. After this use, significant pollution of dyestuffs occurs in the water. Therefore, the degradation of MB is of great importance for protecting clean water resources [9], [10].

Photocatalytic treatment technologies are emerging, especially with metal-based catalysts that can operate under UV light [11]. Photocatalysts used for this purpose are very advantageous in terms of being environmentally friendly and reusable. Photocatalytic systems are activated using UV light energy and effectively degrade toxic substances such as cyanide, phosphorus, and difficult-to-degrade aromatic compounds through the electron-hole pairs they produce [11], [12], [13]. These systems not only minimize secondary pollution but also allow for rapid degradation through advanced oxidation processes (AOPS), which have gained wide acceptance in industrial wastewater treatment.

Chitosan, which can be classified as a natural catalyst, is used as a biodegradable, cheap, and multifunctional biopolymer as a support material for photocatalyst structures [14], [15], [16]. Thanks to its amino and hydroxyl groups, it can easily form complexes with metal ions [15], [17]. Its ability to act as a ligand for transition and post-transition metals makes it a suitable candidate for developing hybrid functional materials.

However, the photocatalytic effect of polymers containing sulfone groups such as polyanetholsulfonic acid (PESA) is quite limited in the literature. Since the ability of polymers containing sulfone groups to form complexes with metal ions is quite good [18], it further increases the photocatalytic activity. PESA, a polyelectrolyte with strong anionic character, can enhance metal ion dispersion and stabilization within the polymer matrix, thereby contribute to increased active surface area and electron transfer efficiency.

Gallium(III) is a metal ion that has attracted interest in photocatalytic applications in recent years. Thanks to its electron structure properties and oxidative stability, it can form active sites and increase catalytic activity. In addition, gallium-based catalysts have been reported to

exhibit high photocatalytic efficiency due to their ability to participate in multielectron redox reactions, low toxicity, and stable oxidation states [19], [20]. However, the literature on photocatalytic studies with biopolymer-supported Ga(III) systems is limited.

Rocha et al. reported 60% photodegradation of methylene blue using Gallium(III) reinforced hydroxyapatite particles [19]. In another study, Kujur et al. investigated the photocatalytic degradation of Rhodamine B dye using magnetic $GaFeO_3$ nanoparticles synthesized with gallium ions and reported a 68% removal rate [21]. Messemeche et al. reported a 94% photodegradation of methylene blue using gallium-doped TiO_2 thin films [22]. Parveen et al. reported 72% photodegradation of Rhodamine B dye in their study using Ga(III) [23].This represents a promising opportunity to explore Ga(III)-based hybrid photocatalysts in combination with biopolymers and functional polymers such as PESA for synergistic effects.

In this study, Chitosan-Coated PESA Spheres Containing $Ga(NO_3)_3$ were synthesized, and their photocatalytic activity on the degradation of methylene blue under UV light was investigated. Various analytical methods characterized the spheres structural, morphological, and optical properties, and their photocatalytic degradation kinetics were evaluated using pseudo-first-order and pseudo-second-order kinetic models. This study aims to develop a low-cost photocatalyst to remove MB dyestuff in an easy and sustainable way. This novel material combines the chemical interaction capacity of PESA, the biocompatibility and functional group abundance of chitosan, and the catalytic potential of Ga(III), representing a multifunctional approach to organic pollutant remediation.

2 MATERIAL AND METHOD

Chitosan (medium molecular weight), Polyanetholsulfonic acid, Gallium (III) Nitrate Hydrate (99.99%), and Methylene blue (82%) were obtained from Aldrich. Sodium Hydroxide (99%) was obtained from Merck. Other chemicals used were of analytical purity and purchased from Merck.

2.1 Synthesis of Chitosan-Coated PESA Spheres Containing Gallium(III) Nitrate Spheres

Chitosan-coated polyanetholsulfonic acid spheres containing gallium (III) nitrate were synthesized in 3 steps. In the first step, a 0.2% by-volume solution of PESA was prepared in NaOH solution (3%, 50 mL). Then, 10 mg of $Ga(NO_3)_3$ was added. It was stirred for 30 minutes until the metal salt dissolved. In the second step, chitosan solution (v/v 4%) in 1% acetic acid

solution was prepared in another beaker. In the last step, the chitosan solution was added dropwise to the PESA-$Ga(NO_3)_3$ dissolved in NaOH solution to obtain a sphere. PESA-Ga(III)/Cht spheres were obtained by cross-linking with the help of NaOH. After 2 hours, the spheres were washed 3 times with distilled water and dried in an oven at 40 °C.

2.2 Characterization

After the synthesis of PESA- Ga(III)/Cht, the concentration of gallium(III) ions from the solution remaining at the end of the reaction was determined by ICP-OES (Spectroblue/FMS36, Germany). Scanning Electron Microscopy (SEM, JEOL, 5600) was used to determine the surface morphology of the spheres. Functional group analysis was determined using a Fourier Transform Infrared (FTIR) Spectrometer (Bruker Vertex 70V). The optical properties of the spheres and changes in dye concentrations were analyzed using a UV-VIS spectrophotometer (Shimadzu, Model 1280).

2.3 Photocatalytic Effect

UV-C tube lamp (lamp specifications; 15 W, Philips Netherlands G15T8) was used to determine the photocatalytic effect of the synthesized spheres on methylene blue.

Firstly, 10 ppm MB was prepared in pure water. Different amounts (25, 50, 100, and 150 mg) of spheres were added to the prepared dye solution and stirred in the dark for 15 min. After reaching equilibrium, they were exposed to UV light for 240 min. At the end of the time, the absorbance value at 664 nm, which is known to be the maximum wavelength of the dye, was determined in a UV-VIS spectrophotometer. The process was repeated using different concentrations (10-25-50-100 ppm) of dye solution with the determined optimum amount of spheres. Then, under the same conditions, the optimum amount of spheres and dye concentration, time study, and reusability of the spheres were investigated. The results were determined by calculating the amount of dye remaining in the solution according to Equation 1 [24]. (A_0 an A_t, the initial absorption and absorption at time t, respectively.)

$$Removal = \frac{A_0 - A_t}{A_0} \times 100 \quad (1)$$

3 RESULTS AND DISCUSSION

PESA-Ga(III)/Cht spheres were obtained by dropwise addition of chitosan to PESA-$Ga(NO_3)_3$ solution dissolved in NaOH solution. The structure of the spheres was determined by ICP-OES, SEM, and FTIR analysis. The photocatalytic effect of the spheres on the dye was determined by UV-VIS analysis.

Firstly, the amount of Ga(III) ions from the solution remaining at the end of the reaction was determined by ICP-OES analysis. Accordingly, it was determined that it contained 8.7mg Ga(III) per 1g sphere.

3.1 SEM Analysis

SEM images of PESA/Cht and PESA-Ga(III)/Cht spheres at different magnifications are shown in Figure 1. Accordingly, it is observed that the spheres generally have a smooth spherical shape. The measurements made with the FIJI program determined that the spheres had an average size of 1.014±0.03 mm.

The SEM images presented in this study provide crucial insights into the surface characteristics of the synthesized PESA-Ga(III)/Cht composite spheres. Morphological properties play a critical role in the photocatalytic performance of polymer–metal hybrid systems, as they directly influence the active surface area, light absorption, and dye adsorption–desorption dynamics.

The observed SEM micrographs exhibit spherical and relatively uniform particle morphologies, with evident surface roughness and porosity, particularly in the Ga(III)-incorporated structures.

It is known that the morphological properties of the spheres change in the presence of a metal [5]. Figure 1 shows that the surface is homogeneous and non-porous with the introduction of Ga(III) into the structure. It is also seen that in the presence of Ga(III), it reaches a more uniform sphere form. This topography is significant, as it facilitates enhanced interaction between the dye molecules and the photocatalyst. Moreover, such a morphology supports improved UV light penetration and scattering, which is essential for the efficient generation of electron–hole pairs in UV-activated systems[25], [26]. For rough surfaces, this system can be explained as follows. On rough surfaces, UV rays interact with a large number of microsurfaces, resulting in multiple scattering that can reduce penetration. A smooth chitosan sphere, on the

other hand, can reduce scattering, allowing light to reach its target more directly and penetrate deeper.

Importantly, the spherical shape of the particles supports isotropic diffusion of reactants and photons around the catalyst, allowing for more uniform photocatalytic degradation. The microscale roughness likely arises from the coordinated incorporation of Ga(III) ions into the polymeric matrix, which not only stabilizes the morphology but also induces surface heterogeneity—a factor known to enhance light-trapping and local electric field enhancement, both of which are crucial for boosting photocatalytic efficiency [27], [28].

In the context of photovoltaic or more precisely, photocatalytic effects, the presence of Ga(III) is expected to serve as a charge trapping and transfer mediator, improving the separation of photo-generated electron–hole pairs. The SEM-supported morphology suggests that the Ga(III) ions are well-dispersed within the chitosan-PESA network, avoiding agglomeration, and thereby maximizing the available surface for catalysis [29], [30], [31], [32].

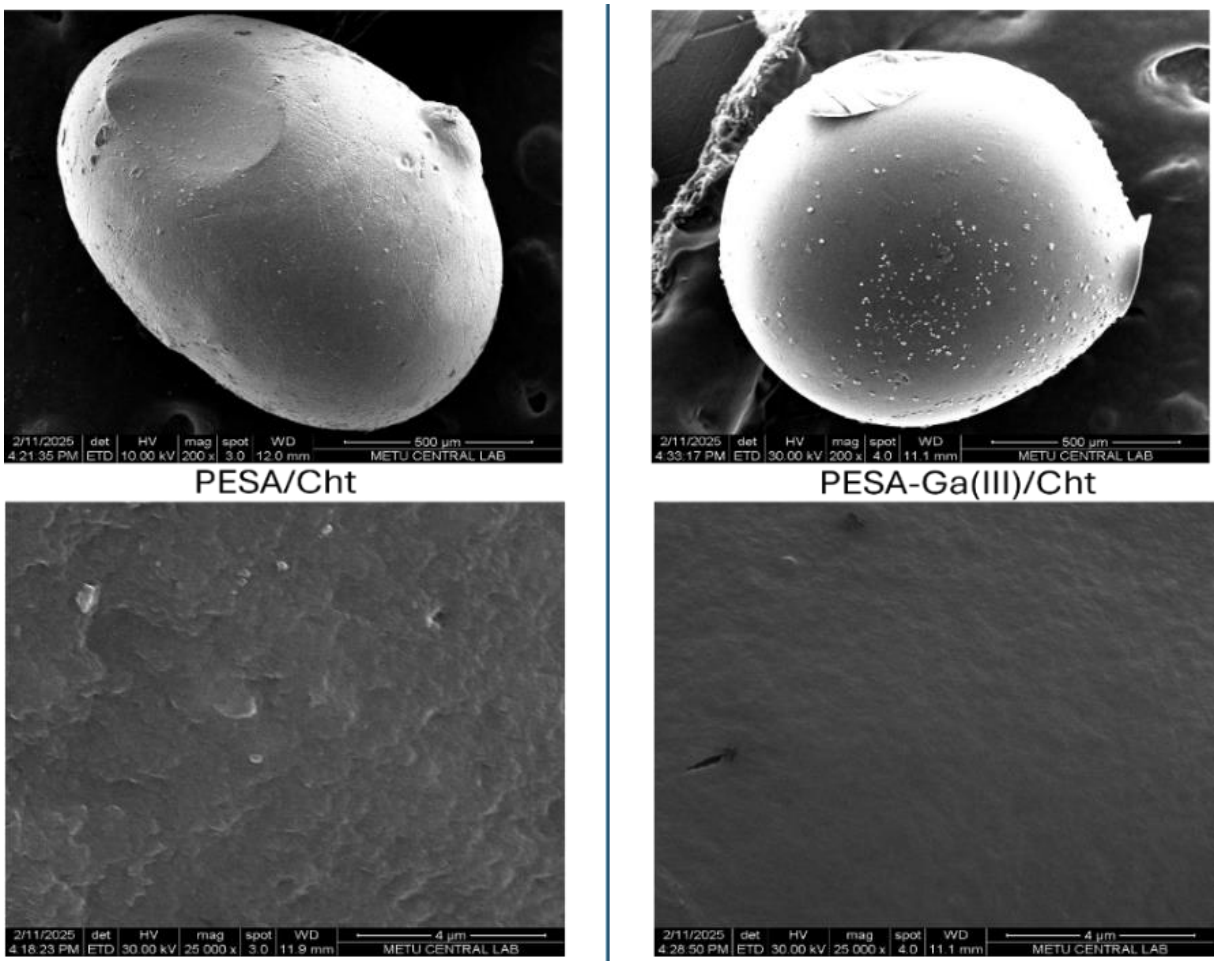


Figure 1. SEM images of PESA/Cht and PESA-Ga(III)/Cht spheres

Additionally, chitosan coating appears to contribute to a more structured and interconnected surface, potentially acting as a functional interface that enhances the electron transport pathway. This is particularly relevant in Ga(III)-based systems, where efficient charge separation and transfer is often a limiting step in the photocatalytic cycle [33].

From a materials design standpoint, the SEM evidence strongly supports the suitability of the synthesized spheres for UV-driven dye degradation applications. The combination of morphological features—namely sphericity, roughness, and hierarchical texture—aligns well with the study's goal of developing an efficient hybrid photocatalyst for methylene blue removal [34].

The SEM analyses validate the successful formation of Ga(III)-incorporated chitosan-coated PESA spheres with favorable morphological attributes for photocatalytic applications. These structures are likely to provide enhanced dye adsorption capacity, efficient light harvesting, and improved charge carrier dynamics—all of which are key parameters for high-performance photocatalysts. The observed morphology is therefore not only consistent with the intended synthesis strategy but also instrumental in achieving the functional objectives of the study [26], [35].

3.2 FTIR Analysis

FTIR analysis was performed to determine the characteristic functional groups present in the structure of PESA/Cht and PESA-Ga(III)/Cht spheres. FTIR spectra of PESA/Cht and PESA-Ga(III)/Cht spheres are given in Figure 2. For PESA/Cht spheres: In the spectrum, vibration bands specific to PESA polymer and Cht (Chitosan) polysaccharide, for PESA-Ga(III)/Cht spheres: In addition to the PESA/Cht spectrum, new bands or shifts in existing bands related to the interaction of Ga(III) ions with chitosan and PESA were tried to be observed.

The region at 3373 cm^{-1} corresponds to the stretching vibrations of -OH and -NH_2 groups. The presence and amount of hydroxyl groups on the surface play an important role in photocatalytic reactions. FTIR spectra show how Ga(III) loading affects the number or type of hydroxyl groups. Increasing the number of hydroxyl groups is generally associated with more hydroxyl radical formation and hence higher photocatalytic activity. The peaks at 2870 cm^{-1} and 1444 cm^{-1} are thought to belong to asymmetric C-H sp^3 and C-H sp^2 bending vibrations, respectively [36]. However, the N-H bending vibration of chitosan at 1581 cm^{-1} and PESA's symmetric -SO_3 stretching vibration at 1022 cm^{-1} are observed [36], [37]. The peak at 1384 cm^{-}

[1] corresponds to CH_3 symmetric deformation [38]. Another result obtained from the FTIR spectra of the composite material formed by combining different components such as PESA and chitosan is that there is an interaction between these components and that the composite is formed by supporting new bond formations. The distribution and binding type of Ga(III) ions in the polymer/polysaccharide matrix are also clearly shown by the peaks. With the addition of Ga(III), the peak at 2931 cm^{-1} and 612 cm^{-1} belongs to Ga-N stretching vibration [39], [40], while the peak at 476 cm^{-1} belongs to Ga-O stretching vibration [41].

FTIR spectra of PESA/Cht and PESA-Ga(III)/Cht spheres are given in Figure 2.

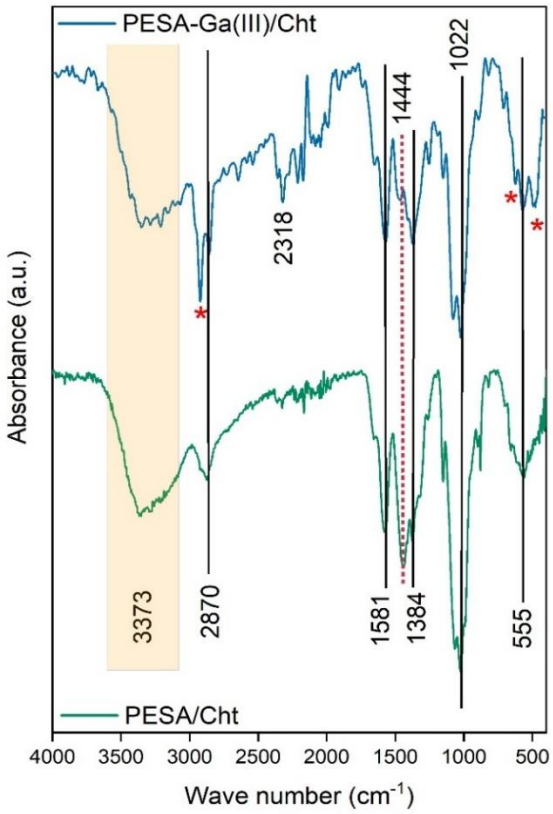


Figure 2. FTIR spectrum of PESA/Cht and PESA-Ga(III)/Cht spheres

The changes in the FTIR spectra due to the loading of Ga(III) ions indicate that the metal ions interact with the polymer/polysaccharide structure without causing a negative effect and as a result, the surface properties are such that they increase the photocatalytic effect. The new active sites formed by the loading of Ga(III) and the changing surface charge led us to comment that they will affect the adsorption of pollutants and the reaction rate. The peaks of new Ga-O or Ga-N bonds in the PESA-Ga(III)/Cht spectrum indicate that these Ga(III) ions are successfully attached to the sphere surface. These new metal centers are interpreted to increase light absorption, facilitate the formation of electron-hole pairs and thus improve photocatalytic

activity. Shifts in vibration frequencies of functional groups in chitosan and/or PESA with Ga(III) loading indicate changes in the electronic structure and chemical properties of the surface. These changes are considered to increase photocatalytic performance by affecting the adsorption and activation of pollutant molecules. The interactions between PESA and chitosan and the integration of Ga(III) ions into this structure may affect the overall photocatalytic performance of the material. These interactions and structural changes after loading were evaluated by FTIR analysis. As a result, the comparison and analysis of the FTIR spectra of PESA/Cht and PESA-Ga(III)/Cht spheres showed the involvement of Ga(III) ions in the chemical structure of the material.

3.3 UV Analysis

Figure 3 shows the UV spectra of PESA/Cht and PESA-Ga(III)/Cht spheres.

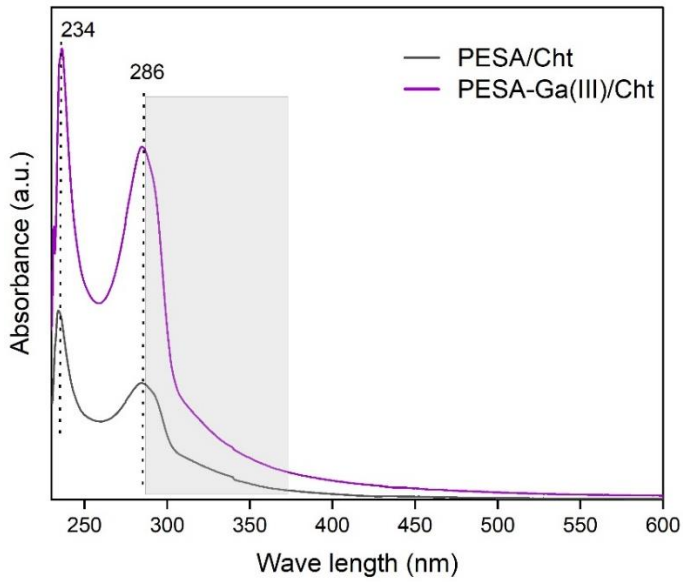


Figure 3. UV-VIS spectra of PESA/Cht and PESA-Ga(III)/Cht spheres

According to the UV spectra of the spheres, a band belonging to chitosan is observed at 286 nm. This band is thought to be due to the n-σ* transition [42]. At 234 nm, a band of PESA was observed due to the π-π* transition. Band broadening occurs in the UV spectrum of PESA-Ga(III)/Cht spheres due to the electrostatic interaction of Ga(III).

The band gap of PESA-Ga(III)/Cht spheres was determined using the Tauc's equation.

$$(Ah\upsilon)^2 = B(h\upsilon - Eg) \quad (2)$$

Here, A is the absorption coefficient, B is the proportionality constant, h is the Planck constant, and υ is the frequency [43].

The energy difference between the valence (π) and conduction (π^*) bands determines the band (Eg) that determines the optical property of the material. According to the Tauc's equation, the band gap of PESA-Ga(III)/Cht spheres was determined as 4.14 eV.

3.4 Photocatalytic Effect

The photocatalytic effect of PESA-Ga(III)/Cht spheres on MB dye was determined under UV light. The photocatalytic activity was determined by considering the decrease in the maximum absorption peak of the dye at 664 nm.

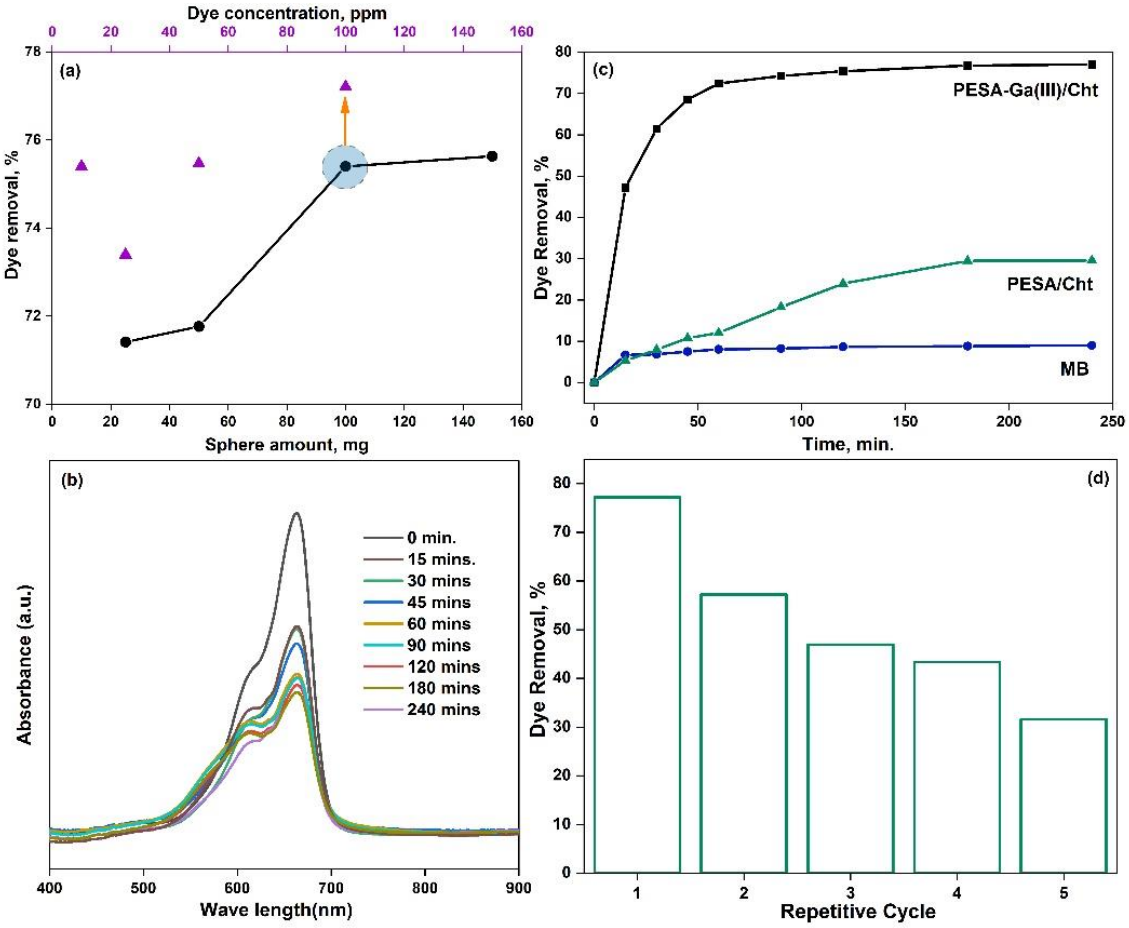


Figure 4. (a) Determination of optimum conditions for the photocatalytic effect of MB, (b) The PESA-Ga(III)/Cht shapes catalyzed photocatalytic degradation of MB over time (Concentration of MB 100 ppm (10 mL), Ga(III)/Cht shapes amount: 100 mg, UV irradiation at 365 nm). (c) The PESA-Ga(III)/Cht, PESA/Cht shapes and without shapes percentage degradation of MB (d) Repetitive tests for photocatalyst PESA-Ga(III)/Cht shapes for five cycle of MB

To determine the photocatalytic effect of PESA-Ga(III)/Cht spheres on MB, firstly sphere amount study (MB of concentration 10 ppm, V=10 mL) was performed (Figure 4a). After stirring with 25, 50, 100, and 150 mg sphere amounts under 365 nm UV light for 2 hours, the photocatalytic effect was determined as 71.41, 71.76, 75.39 and 75.62%, respectively.

After determining that a 100 mg sphere was suitable for the photocatalytic effect, the photocatalytic effect on dye concentration was investigated. The photocatalytic effect at 10, 25, 50, and 100 ppm dye concentration under the same conditions (sphere amount 100 mg, dye solution volume 10 mL) was determined as 75.39, 73.39, 75.46, and 77.20 %, respectively.

The degradation of the dye over time in the presence of PESA-Ga(III)/Cht catalyst is shown in Figure 4b. After the first 60 minutes, it was observed that the photocatalytic effect did not increase significantly, and the degradation rate of the dye decreased. The degradation of the dye of PESA-Ga(III)/Cht, PESA/Cht shapes and without shapes is show in Figure 4c. The PESA-Ga(III)/Cht catalyst, 77.20% of the dye is degraded after 240 minutes, while this rate decreases to 29.55% in the presence of PESA/Cht catalyst. It is thought that Ga(III) supplementation enhances the photocatalytic degradation. Additionally, the photocatalytic degradation of the dye without a catalyst was determined to be 9.01%. Accordingly, it is seen that the photocatalytic degradation of the dye is quite limited without a catalyst.

Figure 4d shows the five repeated uses of the photocatalyst under the same conditions. Accordingly, the photocatalytic effect decreased from the first to the fifth use (77.2%, 57.2%, 46.93%, 43.35%, and 31.58%), respectively. This decrease is likely due to the dye blocking the active sites on the photocatalyst surface.

Kinetic modeling was performed using pseudo-first-order equations using Equation (3) and pseudo-second-order equations using Equation (4) [44].

$$ln\frac{C_t}{C_o} = -k.t \tag{3}$$

$$\frac{1}{C_t} - \frac{1}{C_o} = k.t \tag{4}$$

Here, C_o is the initial concentration, C_t is the concentration at t, k is the rate constant, and t is the time.

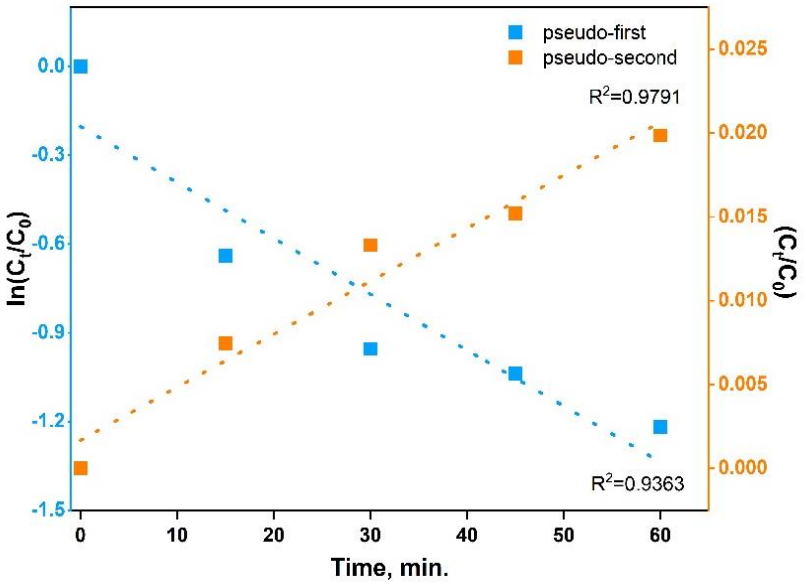


Figure 5. Kinetics for the MB decomposition

Figure 5 shows that the graph drawn according to the pseudo-second-order kinetic model is more linear than the pseudo-first-order kinetic model. The degradation is more suitable for the pseudo-second-order kinetic model, where the rate constant k is determined as 0.0003 min^{-1} (R^2=0.9791). Accordingly, the degradation is likely due to photochemical degradation and the interaction of the dye with the active sites on the surface of the photocatalyst.

4 CONCLUSION AND SUGGESTIONS

This study investigated the photocatalytic effect of PESA-Ga(III)/Cht spheres on methylene blue, a cationic dye. FTIR, UV-VIS, SEM, and ICP-OES analysis characterized the synthesized PESA-Ga(III)/Cht spheres. FTIR and UV-VIS spectra confirmed the functional groups in the polymer structures and their interaction with Ga(III). SEM micrographs showed a homogeneous, spherical morphology with an average size of 1.014±0.03 mm. Finally, the photocatalytic activity of PESA-Ga(III)/Cht spheres was evaluated for the degradation of MB under UV light and showed 77.2% photocatalytic activity. As a result, a promising, low-cost, and efficient photocatalyst for environmental applications was proposed.

Statement of Research and Publication Ethics

The study is complied with research and publication ethics.

Artificial Intelligence (AI) Contribution Statement

This manuscript was entirely written, edited, analyzed, and prepared without the assistance of any artificial intelligence (AI) tools. All content, including text, data analysis, and figures, was solely generated by the authors.

REFERENCES

[1] R. Sivakumar and N. Y. Lee, "Adsorptive removal of organic pollutant methylene blue using polysaccharide-based composite hydrogels," *Chemosphere*, vol. 286, Jan. 2022, doi: 10.1016/j.chemosphere.2021.131890.

[2] M. Gavrilescu, K. Demnerová, J. Aamand, S. Agathos, and F. Fava, "Emerging pollutants in the environment: Present and future challenges in biomonitoring, ecological risks and bioremediation," *N Biotechnol*, vol. 32, no. 1, pp. 147–156, Jan. 2015, doi: 10.1016/j.nbt.2014.01.001.

[3] N. Wang, J. Chen, J. Wang, J. Feng, and W. Yan, "Removal of methylene blue by Polyaniline/TiO_2 hydrate: Adsorption kinetic, isotherm and mechanism studies," *Powder Technol*, vol. 347, pp. 93–102, Apr. 2019, doi: 10.1016/j.powtec.2019.02.049.

[4] F. Mashkoor and A. Nasar, "Magsorbents: Potential candidates in wastewater treatment technology – A review on the removal of methylene blue dye," Apr. 15, 2020, *Elsevier B.V.* doi: 10.1016/j.jmmm.2020.166408.

[5] H. N. Hamad and S. Idrus, "Recent Developments in the Application of Bio-Waste-Derived Adsorbents for the Removal of Methylene Blue from Wastewater: A Review," Feb. 01, 2022, *MDPI*. doi: 10.3390/polym14040783.

[6] S. E. Abo-Neima, M. M. El-Sheekh, M. I. Al-Zaban, and A. I. M. EL-Sayed, "Antibacterial and anti-corona virus (229E) activity of Nigella sativa oil combined with photodynamic therapy based on methylene blue in wound infection: in vitro and in vivo study," *BMC Microbiol*, vol. 23, no. 1, Dec. 2023, doi: 10.1186/s12866-023-03018-1.

[7] K. Evren *et al.*, "A case of peritonitis caused by Wickerhamomyces anomalus (Candida pelliculosa) related to peritoneal dialysis," *Mikrobiyol Bul*, vol. 55, no. 4, pp. 665–672, 2021, doi: 10.5578/mb.20219718.

[8] A. Krishna Moorthy, B. Govindarajan Rathi, S. P. Shukla, K. Kumar, and V. Shree Bharti, "Acute toxicity of textile dye Methylene blue on growth and metabolism of selected freshwater microalgae," *Environ Toxicol Pharmacol*, vol. 82, Feb. 2021, doi: 10.1016/j.etap.2020.103552.

[9] J. Jiang *et al.*, "Rapid photodegradation of methylene blue by laser-induced plasma," *RSC Adv*, vol. 12, no. 33, pp. 21056–21065, Jul. 2022, doi: 10.1039/d2ra03633a.

[10] D. Doğan, R. Taş, and M. Can, "Increasing Photocatalytic Stability and Photocatalytic Property of Polyaniline Conductive Polymer," *Iran J Sci Technol Trans A Sci*, vol. 44, no. 4, pp. 1025–1037, Aug. 2020, doi: 10.1007/s40995-020-00922-3.

[11] H. Bai *et al.*, "Synergistic effects of rare-metal ytterbium doping on TiO_2/g-C_3N_5 heterostructures for enhanced photocatalytic degradation of methylene blue," *Inorg Chem Commun*, vol. 175, May 2025, doi: 10.1016/j.inoche.2025.114159.

[12] A. Chawla *et al.*, "Recent advances in synthesis methods and surface structure manipulating strategies of copper selenide (CuSe) nanoparticles for photocatalytic environmental and energy applications," Aug. 01, 2024, *Elsevier Ltd*. doi: 10.1016/j.jece.2024.113125.

[13] S. Sharma *et al.*, "Critical review on the tetracycline degradation using photo-Fenton assisted g-C_3N_4-based photocatalysts: Modification strategies, reaction parameters, and degradation pathway," *J Environ Chem Eng*, vol. 12, no. 3, Jun. 2024, doi: 10.1016/j.jece.2024.112984.

[14] Z. Demirkaya et al., "Purification of Textile Dye by Photocatalytic Oxidation Process Using Metal Modified Chitosan Balls," *Journal Of Şura Akademi*, vol 8, 2025.

[15] A. Nithya, K. Jothivenkatachalam, S. Prabhu, and K. Jeganathan, "Chitosan based nanocomposite materials as photocatalyst - a review," *Materials Science Forum*, vol. 781, pp. 79–94, 2014, doi: 10.4028/www.scientific.net/MSF.781.79.

[16] A. Buasri, K. Rochanakit, W. Wongvitvichot, U. Masa-Ard, and V. Loryuenyong, "The Application of Calcium Oxide and Magnesium Oxide from Natural Dolomitic Rock for Biodiesel Synthesis," in *Energy Procedia*, Elsevier Ltd, Nov. 2015, pp. 562–566. doi: 10.1016/j.egypro.2015.11.534.

[17] P. Swarnakar *et al.*, "Silver deposited titanium dioxide thin film for photocatalysis of organic compounds using natural light," *Solar Energy*, vol. 88, pp. 242–249, Feb. 2013, doi: 10.1016/j.solener.2012.10.014.

[18] M. Alharbi, M. waqas Iqbal, Y. Al-Hadeethi, and M. A. Hussein, "Photocatalytic activity of composite material-based nylon 6/sulfur NPs and reinforced carbon nanotubes," *Diam Relat Mater*, vol. 151, Jan. 2025, doi: 10.1016/j.diamond.2024.111859.

[19] R. L. Pereira Rocha *et al.*, "Gallium-containing hydroxyapatite as a promising material for photocatalytic performance," *Minerals*, vol. 11, no. 12, Dec. 2021, doi: 10.3390/min11121347.

[20] K. Pajor, Ł. Pajchel, A. Zgadzaj, U. Piotrowska, and J. Kolmas, "Modifications of hydroxyapatite by gallium and silver ions—physicochemical characterization, cytotoxicity and antibacterial evaluation," *Int J Mol Sci*, vol. 21, no. 14, pp. 1–15, Jul. 2020, doi: 10.3390/ijms21145006.

[21] V. S. Kujur and S. Singh, "Structural, magnetic, optical and photocatalytic properties of $GaFeO_3$ nanoparticles synthesized via non-aqueous solvent-based sol–gel route," *Journal of Materials Science: Materials in Electronics*, vol. 31, no. 20, pp. 17633–17646, Oct. 2020, doi: 10.1007/s10854-020-04318-2.

[22] R. Messemeche, Y. Benkhetta, A. Attaf, H. Saidi, M. S. Aida, and O. Ben khetta, "Photocatalytic mechanisms reactions of gallium doped TiO_2 thin films synthesized by sol gel (spin coating) in the degradation of methylene blue (MB) dye under sunlight irradiation," *Reaction Kinetics, Mechanisms and Catalysis*, vol. 135, no. 5, pp. 2735–2747, Oct. 2022, doi: 10.1007/s11144-022-02288-6.

[23] K. Parveen, U. Rafique, I. Jamil, and A. Ashraf, "Photodegradation of Rhodamine B using gallium hybrids as an efficient photocatalyst," *Environ Monit Assess*, vol. 195, no. 9, Sep. 2023, doi: 10.1007/s10661-023-11683-y.

[24] A. A. Nayl *et al.*, "A novel method for highly effective removal and determination of binary cationic dyes in aqueous media using a cotton-graphene oxide composite," *RSC Adv*, vol. 10, no. 13, pp. 7791–7802, Feb. 2020, doi: 10.1039/c9ra09872k.

[25] B. Soman, S. Challagulla, S. Payra, S. Dinda, and S. Roy, "Surface morphology and active sites of TiO_2 for photoassisted catalysis," *Research on Chemical Intermediates*, vol. 44, no. 4, pp. 2261–2273, Apr. 2018, doi: 10.1007/s11164-017-3227-6.

[26] R. K. Arya *et al.*, "Polymer Coated Functional Catalysts for Industrial Applications," May 01, 2023, *MDPI*. doi: 10.3390/polym15092009.

[27] J. M. Blasi, P. J. Weddle, C. Karakaya, D. R. Diercks, and R. J. Kee, "Modeling reaction-diffusion processes within catalyst washcoats: II. Macroscale processes informed by microscale simulations," 2016.

[28] W. Xie *et al.*, "Polydopamine Shell as a Ga3+ Reservoir for Triggering Gallium–Indium Phase Separation in Eutectic Gallium–Indium Nanoalloys," *ACS Nano*, vol. 15, no. 10, pp. 16839–16850, Oct. 2021, doi: 10.1021/acsnano.1c07278.

[29] M. N. Cardoza-Contreras, A. Vásquez-Gallegos, A. Vidal-Limon, J. M. Romo-Herrera, S. Águila, and O. E. Contreras, "Photocatalytic and antimicrobial properties of Ga doped and Ag doped ZnO nanorods for water treatment," *Catalysts*, vol. 9, no. 2, Feb. 2019, doi: 10.3390/catal9020165.

[30] Y. Xu, The photoelectronic properties of chalcogenide glass ceramic. *Material chemistry. Université de Rennes*, 2014.

[31] L. L. Zhou, G. Wu, J. Liu, and X. Bin Yu, "Preparation of Ga^{3+}:ZnO quantum dots and the photoelectric properties of sensitized polycrystalline silicon solar cells," *Chemical Papers*, vol. 75, no. 2, pp. 805–811, Feb. 2021, doi: 10.1007/s11696-020-01339-3.

[32] M. Faqrul and A. Chowdhury, "Unassisted Photocatalytic Overall Pure Water Splitting Using III-Nitride Nanostructures," 2018.

[33] M. S. Akhtar, A. Umar, S. Sood, I. S. Jung, H. H. Hegazy, and H. Algarni, "Rapid growth of TiO_2 nanoflowers via low-temperature solution process: Photovoltaic and sensing applications," *Materials*, vol. 12, no. 4, Feb. 2019, doi: 10.3390/ma12040566.

[34] S. Buapoon, A. Phuruangrat, P. Dumrongrojthanath, T. Thongtem, and S. Thongtem, "Sonochemical Synthesis and Characterization of Ag/ZnO Heterostructure Nanocomposites and their Photocatalytic Efficiencies," *J Electron Mater*, vol. 50, no. 8, pp. 4524–4532, Aug. 2021, doi: 10.1007/s11664-021-08985-7.

[35] Y. Wang, Y. Feng, J. Jiang, and J. Yao, "Designing of Recyclable Attapulgite for Wastewater Treatments: A Review," *ACS Sustain Chem Eng*, vol. 7, no. 2, pp. 1855–1869, Jan. 2019, doi: 10.1021/acssuschemeng.8b05823.

[36] M. Nora, A. Bhagaskara, V. Agustisari, A. Lim, H. R. Alfalah, and D. Siswanta, "Fabrication of Polystyrene Sulfonate-Chitosan (PSS-Chitosan) Membrane as Dodecyl Benzene Sulfonate (DBS) Adsorbent in Laundry Wastewater," *Jurnal Kimia Sains dan Aplikasi*, vol. 26, no. 1, pp. 19–27, Jan. 2023, doi: 10.14710/jksa.26.1.19-27.

[37] Ž. Petrović, M. Ristić, and S. Musić, "The effect of sodium polyanethol sulfonate on the precipitation of zinc oxide," *J Alloys Compd*, vol. 694, pp. 1331–1337, 2017, doi: 10.1016/j.jallcom.2016.10.111.

[38] M. F. Queiroz, K. R. T. Melo, D. A. Sabry, G. L. Sassaki, and H. A. O. Rocha, "Does the use of chitosan contribute to oxalate kidney stone formation?," *Mar Drugs*, vol. 13, no. 1, pp. 141–158, Jan. 2015, doi: 10.3390/md13010141.

[39] O. Adewuyi, A. B. Alabi, F. H. Abejide, and F. O. Omoniyi, "Impact of Nitridation on the Structural, Optical, and Morphological Properties of Solvothermally Synthesized Gallium Nitride Nanoparticles," Mar. 11, 2025. doi: 10.21203/rs.3.rs-6145110/v1.

[40] A. K. Mallik, G. Krishnamurthy, W.-C. Shih, P. Pobedinskas, J. D'Haen, and K. Haenen, " Enhanced etching of GaN with N_2 gas addition during CVD diamond growth ," *Functional Diamond*, vol. 4, no. 1, Dec. 2024, doi: 10.1080/26941112.2024.2393817.

[41] H. J. Bae *et al.*, "High-aspect ratio β-Ga_2O_3 nanorods via hydrothermal synthesis," *Nanomaterials*, vol. 8, no. 8, Aug. 2018, doi: 10.3390/nano8080594.

[42] Q. Ruan et al., "Development of ZnO/selenium nanoparticles embedded chitosan-based anti-bacterial wound dressing for potential healing ability and nursing care after peadiatric fracture surgery," *Int Wound J.,* vol 20, no. 6 pp. 1819-1831. doi: 10.1111/iwj.13947.

[43] A. Şenocak, H. Akbaş, and B. İşgör, "NiO Nanoparticles Via Calcination of Dithiocarbamate Pioneers: Characterization and Photocatalytic Activity," *Bitlis Eren Üniversitesi Fen Bilimleri Dergisi*, vol. 13, no. 4, pp. 969–978, Dec. 2024, doi: 10.17798/bitlisfen.1485060.

[44] N. N. Bahrudin, "Evaluation of degradation kinetic and photostability of immobilized TiO_2/activated carbon bilayer photocatalyst for phenol removal," *Applied Surface Science Advances*, vol. 7, Feb. 2022, doi: 10.1016/j.apsadv.2021.100208.

BİTLİS EREN ÜNİVERSİTESİ
FEN BİLİMLERİ DERGİSİ

ISSN: 2147-3129 / e-ISSN: 2147-3188

Article Type	: Research Article	**Year**	: 2025
Received	: April 30, 2025	**Volume**	: 14
Revised	: September 22, 2025	**Issue**	: 3
Accepted	: September 27, 2025	**Pages**	: 1625-1635
DOI	: 10.17798/bitlisfen.1687356		

PHOTOVOLTAIC SOLAR POWER PLANT OF SOGUKSU: A CASE STUDY

Kenan SAKA [1], **Abdulkadir AYANOGLU** [1,*]

[1] *Bursa Uludağ University, Machine Program, Bursa, Türkiye*

[2] *Mardin Artuklu University, Machine Program, Bursa, Türkiye*

**** Corresponding Author:*** *kenansaka@uludag.edu.tr*

ABSTRACT

Investments in photovoltaic solar power plants continue to increase across all provinces of Türkiye. However, Bursa is not among the regions that receive the highest levels of solar radiation compared to the eastern parts of the country. The Soğuksu power plant, located in the village of the same name in Bursa, was commissioned in March 2017 with an installed capacity of 7 MW. In this study, the actual generation data of the power plant for 2022 were analyzed, and the performance ratio (PR) and capacity factor (CF) were calculated. The results show that the minimum electricity generation occurred in December 2021 with 401.21 MWh, while the total electricity production in 2022 reached 10.64 GWh. During the summer season, the plant generated 7,262.8 MWh, corresponding to 68% of its annual production. The lowest performance ratio was observed in June at 75.1%, while the highest capacity factor was recorded in July at 28%. Furthermore, the performance ratios for November, December, and January exceeded 100%. Since the PR is calculated based on the solar energy values reported in the regional solar atlas, such results indicate a notable discrepancy between the published data and the actual site conditions. The exceptionally high PR values during the winter months may suggest that the region experiences milder winters and receives higher solar radiation than the atlas values imply.

Keywords: Solar power plant, Electricity generation, Performance ratio, Capacity factor, Soğuksu- Türkiye.

1 INTRODUCTION

Global warming, environmental issues and climate change are among the important problems of today world. Renewable energy sources with solar energy technologies can be assisted to solve previous problems. Electricity production from fossil fuels is inexpensive but finite and main sources of greenhouse gasses. However, the sun provides an infinite supply of energy, although factors such as geographical location, seasons, clouds, and dust affect its availability. There are numerous studies on the solar potential and solar energy systems of Türkiye. Hepbaslı et al. [1] defined the industrial use of solar energy in Türkiye starting in 1988 and emphasized the continuous increase of photovoltaic (PV) installations in the country. Kaygusuz [2] determined that Türkiye is a suitable country for utilizing concentrating solar power (CSP) technology, which offers significant opportunities.

Several other studies have focused on solar potential analysis and projections for future years. Hrayshat [3] conducted a feasibility study on a pilot solar PV power plant with a 15 MWp capacity, proposed for installation in two different cities in eastern Morocco. Merrouni et al. [4] analyzed the solar irradiation values of the eastern region of Morocco. According to photovoltaic data for Serbia, 43% of the electricity was generated by two thermal power plants [5]. Edalati et al. [6] discussed the recent developments in Iran's prospective renewable energy policy. Kumar and Sudhakar [7] evaluated the performance of a solar PV power plant in India with a peak capacity of 10 MW.

Incekara and Ogulata [8] declared that a big potential of electricity generation will be done by solar energy at 2030 for Türkiye. Also, according to Boran et al. [9] Bodrum is the best area for installing PV power plant in Türkiye.

According to Parhamfar et. al. [10] photovoltaic systems play a pivotal role in addressing the growing global demand for sustainable and renewable energy sources, offering a crucial solution to mitigate climate change and reduce dependence on fossil fuels. Salameh et al. [11] have addressed the fundamental challenge of accurately forecasting power generation from photovoltaic systems, which is crucial for effective grid integration and energy management. Al Mehadi et. al. [12] have described the design and simulation of a 50 MW floating Solar photovoltaic system that generates an annual energy yield of 76916 MWh.

The Soğuksu (Bursa province) PVPP has started to produce power since March 2017. It has a 7MWe capacity and one of the new power investments. Hydrogen production from renewable energy sources has increasingly become a popular research area among researchers,

driven by the growing interest in sustainable and carbon-neutral energy systems [13]. Saka and Canbolat [14] studied on hydrogen production investigation of this solar plant based on the actual electricity generation. Saka [15] showed effect of bad weather conditions on power production of Soğuksu solar plant and provided the first-year electricity production values of the Soğuksu solar plant [16]. Saka [17] presented a study on seasonal generation of Soğuksu power plant. Also, he has focused on a new study of the Soğuksu power plant in terms of performance and agrivoltaic aspects [18]. In another study, Saka and Orhan [19] have studied on performance assessment and useful solar radiation analysis of this plant and biomass potential of Yenişehir [20].

Main objectives of studies on the Soğuksu PVPP are given in Table 1.

Table 1. Main objectives of studies on the Soğuksu PVPP.

Main objectives	Studies
Investigation of daily theoretical hydrogen production performance	[14]
Investigation on theoretical hydrogen production capacity yearly	[15]
Effect of overcast weather on electricity generation	[16]
Investigation on seasonal generation	[17]
Investigation of performance ratio and seasonal effect factor	[18]
Performance assessment and useful solar radiation analysis	[19]

Performance evaluation of Serhatköy PVPP (Northern part of Cyprus) was done by Özerdem et al. [21], capacity of the power plant was 1.2 MW and calculated capacity factor (CF) and performance ratio (PR) of a solar plant. The best PR value of the power plant was %93.31. İnan and Şimşek [22] investigated design and analysis of 1 MW solar power plants with a software. As a result, the annual PR of the power plant was %87.52 in Istanbul.

The present study was conducted from December 2021 to November 2022 for analysis of the electricity production at the Soğuksu PVPP by evaluation of real data. The data was obtained from the company that operates the power plant. Solar radiation of the Bursa is relatively lower compared to southern regions; especially for winter season. This situation requires an examination the effect of weather conditions on the power plant productivity. Monthly electricity generation was compared with solar radiation of the province and the seasonal performance of the solar plant with performance ratio were calculated.

2 MATERIAL AND METHOD

2.1 Description of the Soğuksu PVPP

PV solar panels are connected to strings in series in Soğuksu PVPP and the strings connected to inverters;

- Each 1 MWp scale power plant has 20 inverters.
- Each inverter has 10 strings,
- Each string has 22 panels,

Inverters are electronic circuits which alert current rate. An inverter converts direct current (DC) to alternating current (AC). There are many type of panels which have high efficiency in the market. Besides at open literature, there are theoretical or experimental point of views but aim of this study which reach to close data of other studies.

Information on power plant:

- Model of panel is UP-M270P,
- Type of panel is polycrystalline silicone and each panel has 60 cells,
- Panel has a 270 W power rating with %16.6 peak efficiency.

The electricity is produced by solar power plant as function of:

i) Total cell surface,

ii) Sunny daily numbers,

iii) Panel efficiency,

iv) Inverter efficiency.

The view of Soğuksu solar power plant transferred energy to grid, located province of Yenişehir, Bursa and established since 20 March 2017, given at Figure 1 and solar map shown at Figure 2. Some information about the power plant such as:

- Coordinates of the power plant are 40º12’57’’N and 29º25’50’’E,
- The power plant was installed on an area of 170000 m^2,
- Number of panels used in the power plant are 30800,
- General efficiency of inverter is 97%.



Figure 1. The view of Soğuksu PVPP.



Figure 2. Location of the power plant on solar map.

2.2 Energy Equations

The results presented in this study which take into account all losses since obtained by using actual data. Energy equations can be defined as follow for electricity generation of PVPP.

$$E_G = N_P E_S \eta_P \eta_{inv} \eta_{los} \tag{1}$$

where;

N_P Panel number,

E_S Radiation on panel,

E_G Electricity generation,

η_P Panel conversion efficiency is calculated by

$$\eta_P = \frac{E_{el}}{E_S} \tag{2}$$

where;

E_{el} Electricity production by panels,

η_{inv} Efficiency of inverter.

In order to maximize electricity production from solar power plants, energy losses must be minimized.

η_{los} shows the total efficiency account for all losses as:

- Conduction losses,
- Module mismatches,
- Wiring,
- Temperature effects,
- Humidity,
- Soiling,
- Wind speed,
- Dust or snow on the panel.

3 RESULTS AND DISCUSSION

Solar potential maps have solar radiation values and prepare to reveal the average sunbathing potential of a region [23]. Figure 3 presents Global Solar Radiation Values (GSRVs) of Yenişehir and produced electricity per month for each year at power plant. The electricity potential of the power plant can be calculated by GSRVs. Equation 4 shows relation between power potential and GSRVs. For example, GSRV in April was 4.59 and the potential of the plant can be find as 1028 MWh but it was actual value as 1038.74 MWh. But calculation of overall plant peak efficiency was not ignored with real values. Thus, calculation is required to correct by correlation factors.

Consequently, solar radiation values can give an idea about potential solar energy region but not an exact generation value. At 2022, total power production of the solar plant was 10.64 GWh and between April to September (for six months) 7.26 GWh electricity generation which was equal to % 68 of total generation for a year.

Electricity generation percentages for each month was given in the Figure 4 for 2022. On a monthly basis, maximum generation was obtained at July for 1455 MWh at percentages of 13.7. The minimum one was obtained in December with 401.21 MWh and %3.8.

$$E_P = GSRV\ x\ Day\ number\ x\ Panel\ area\ x\ Panel\ efficiency \tag{3}$$

where;

E_P Electricity potential

The Performance Ratio (PR) of the Soğuksu PVPP for each month is calculated by using Equation 4. The PR enables a comparison between actual and the calculated energy ratio. Also, which is influenced by losses of power plant.

Furthermore, Capacity Factor (CF) of power plant for each month can be computed by using Equation 5. The CF is the ratio of the monthly average energy production of an energy generation plant to theoretical maximum monthly energy production of a plant that assumed its' operation of peak rated capacity for every hour of the month.

$$PR = \frac{E_G}{E_P} \tag{4}$$

$$CF = \frac{Real\ Power\ Generated}{30x24xNominal\ Power} x100 \tag{5}$$

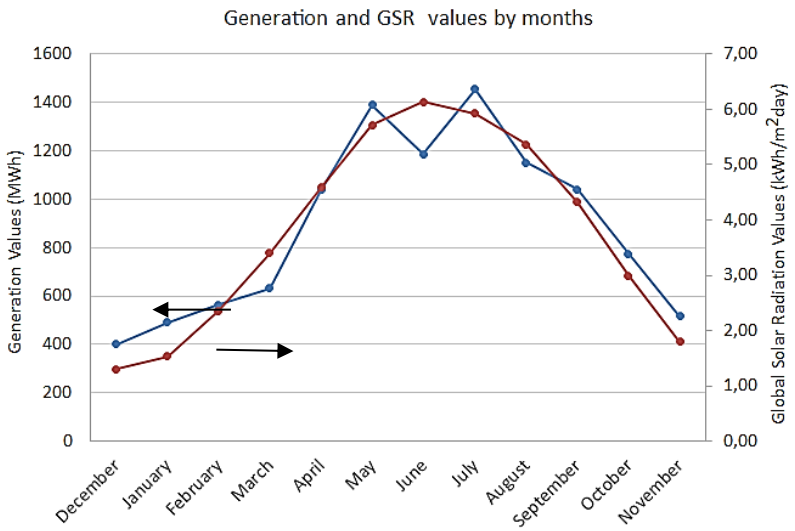


Figure 3. GSRVs of the Yenişehir city and the electricity generated by the PVPP.

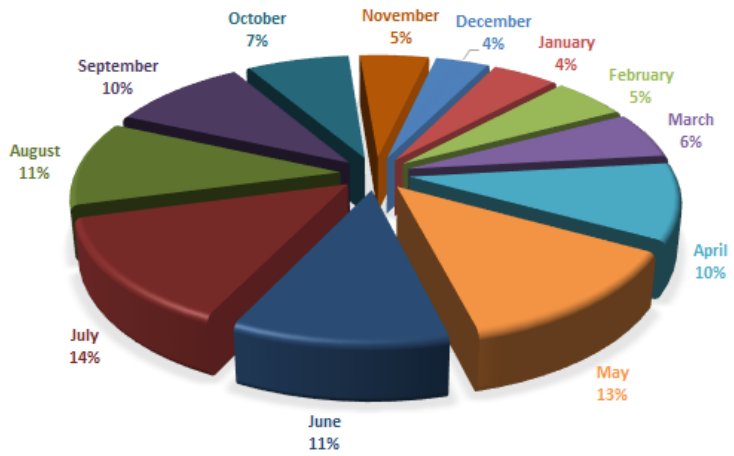


Figure 4. Electricity generation percentages for each month of 2022.

Based on the generation rates which were given in the figures, the ranking between the produced electricity and GSRV due to months is incompatible. June is the highest global radiation value inversely July is the month which can be produced extra electricity production. The incompatibility can be defined by daily generation quantities. Thus, Northwestern Anatolia where the power plant is located at Bursa province, has low solar radiation according to South and Southeast Anatolia region. In winter, the effect of cloud cover on the power plant is significant to decrease performance and production of electricity. Moreover, effect of bad weather on the production performance of the plant has to be determined. While a relatively stable generation profile is generally expected, seasonal variations are readily evident in the daily generation data.

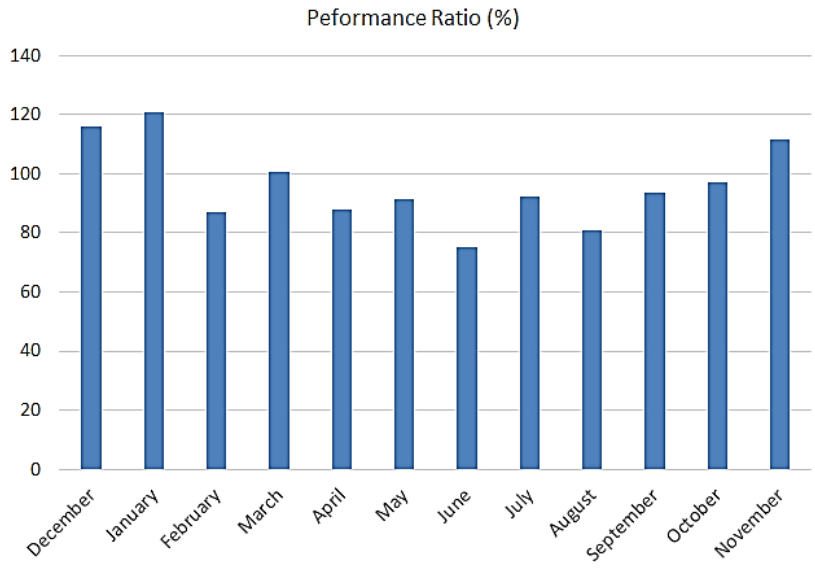


Figure 5. The PR of the power plant in 2022 for each month.

At Figure 5 is shown the PR of solar power plant in 2022 for each month. The PR exceeded 100% 4 times in 2022. The minimum performance ratio was in June as 75.1%.

Figure 6 shows the CF of the power plant in 2022 by month. The maximum CF was in July as 28%. The minimum capacity factor was in December. Finally, it can be coherence to share a current situation which encountered and conducted to present study. Especially the plant was subjected to a private investment venture. The results include a necessity to strengthen the infrastructure of the grid and to determine the rates of non-realization of applications with investigation of associated causes in order for more investments which has similarity to realize power plant of Türkiye.

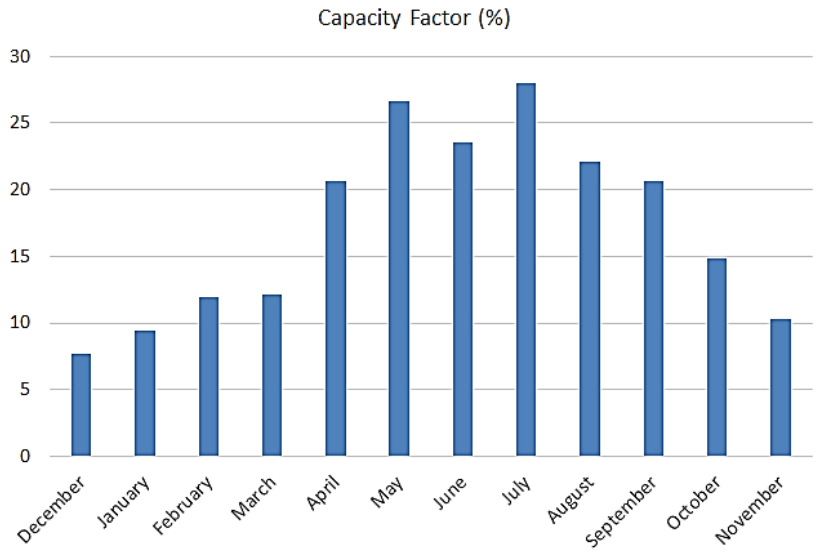


Figure 6. The capacity factor of power plant in 2022 by month.

4 CONCLUSION AND SUGGESTIONS

In this study, a generation performance analysis was conducted for a 7 MWp grid-connected photovoltaic (PV) solar power plant. The plant is a large-scale facility consisting of 30,800 panels connected in series. The analysis demonstrates how the plant, located in a region with relatively low annual insolation potential, is affected by overcast weather conditions. The total annual electricity production of the plant was 10.64 GWh. Detailed results for the six-month period from October to March, covering the winter and autumn seasons, were presented. On a monthly basis, the maximum generation was recorded in July with 1,455 MWh, corresponding to 13.7% of the annual production, while the minimum was in December with 401.21 MWh, accounting for 3.8%. The lowest performance ratio was observed in June at 75.1%, whereas the highest capacity factor was achieved in July at 28%.

Acknowledgements

Thanks to Soğuksu Power Plant.

Conflict of Interest Statement

There is no conflict of interest between the authors.

Statement of Research and Publication Ethics

The study is complied with research and publication ethics.

Artificial Intelligence (AI) Contribution Statement

This manuscript was entirely written, edited, analyzed, and prepared without the assistance of any artificial intelligence (AI) tools. All content, including text, data analysis, and figures, was solely generated by the authors.

Contributions of the Authors

Kenan Saka: resources, software, supervision, review and editing

Abdulkadir Ayanoğlu: investigation, writing original draft preparation and review.

REFERENCES

[1] Hepbaslı, K. Ulgen, and R. Eke, "Solar energy applications in Turkey," *Energy Sources*, vol. 26, no. 6, pp. 551–561, 2004, doi: 10.1080/00908310490438579.

[2] K. Kaygusuz, "Prospect of concentrating solar power in Turkey: The sustainable future," *Renew. Sustain. Energy Rev.*, vol. 15, no. 2, pp. 808–814, 2011, doi: 10.1016/j.rser.2010.09.042.

[3] E. S. Hrayshat, "Viability of solar photovoltaics as an electricity generation source for Jordan," *Renew. Energy*, vol. 34, no. 10, pp. 2133–2140, 2009, doi: 10.1016/j.renene.2009.03.006.

[4] A. Merrouni and A. Mezrhab, "PV sites suitability analysis in the Eastern region of Morocco," *Sustain. Energy Technol. Assess.*, vol. 18, pp. 6–15, 2016, doi: 10.1016/j.seta.2016.09.006.

[5] D. Doljak, D. Popovic, and D. Kuzmanovic, "Photovoltaic potential of the City of Požarevac," *Renew. Sustain. Energy Rev.*, vol. 73, pp. 460–467, 2017, doi: 10.1016/j.rser.2017.01.154.

[6] S. Edalati, M. Ameri, M. Iranmanesh, and Z. Sadeghi, "Solar photovoltaic power plants in five top oil-producing countries in Middle East: A case study in Iran," *Renew. Sustain. Energy Rev.*, vol. 69, pp. 1271–1280, 2017, doi: 10.1016/j.rser.2016.12.042.

[7] S. Kumar and K. Sudhakar, "Performance evaluation of 10 MW grid connected solar photovoltaic power plant in India," *Energy Rep.*, vol. 1, pp. 184–192, 2015, doi: 10.1016/j.egyr.2015.10.001.

[8] O. Incekara and S. N. Ogulata, "Turkey's energy planning considering global environmental concerns," *Ecol. Eng.*, vol. 102, pp. 589–595, 2017, doi: 10.1016/j.ecoleng.2017.02.033.

[9] F. E. Boran, T. Menlik, and K. Boran, "Multi-criteria axiomatic design approach to evaluate sites for grid-connected photovoltaic power plants: A case study in Turkey," *Energy Sources, Part B: Recovery, Utilization, and Environmental Effects*, vol. 5, no. 3, pp. 290–300, 2010, doi: 10.1080/15567240802533831.

[10] M. Parhamfar, R. Naderi, and I. Sadeghkhani, "Risk assessment, lightning protection, and earthing system design for photovoltaic power plants: A case study of utility-scale solar farm in Iran," *Solar Energy Adv.*, vol. 5, p. 100098, 2025.

[11] T. Salameh, M. M. Farag, A. K. Hamid, and M. Hussein, "Adaptive neuro-fuzzy inference system for accurate power forecasting for on-grid photovoltaic systems: A case study in Sharjah, UAE," *Energy Convers. Manag.: X*, vol. 26, p. 100958, 2025.

[12] A. Mehadi, Nahin-Al-Khurram, M. R. K. Shagor, and M. A. I. Sarder, "Optimized seasonal performance analysis and integrated operation of 50 MW floating solar photovoltaic system with Kaptai hydroelectric power plant: A case study," *Energy Sources, Part A: Recovery, Utilization, and Environmental Effects*, vol. 47, no. 1, pp. 10183–10207, 2025.

[13] S. Ata, "Jeotermal Enerji ve Kalina Çevrim Tabanlı Entegre Sistemde Yeşil Hidrojen ve Amonyak, Tatlı Su ve Sıcak Su Üretiminin Ekonomik ve Çevresel Analizi," *Erciyes Univ. J. Sci. Inst. Sci.*, vol. 41, no. 1, pp. 190–206, 2025 (in Turkish).

[14] K. Saka and S. A. Canbolat, "An evaluation on solar powered hydrogen production," *Int. J. Energy Eng. Sci.*, vol. 3, pp. 26–35, 2018.

[15] K. Saka, "An evaluation of overcast weather on generation of a grid connected PV power plant," *J. Curr. Res. Eng. Sci. Technol.*, vol. 5, no. 1, pp. 19–28, 2019.

[16] K. Saka, "An investigation on hydrogen production capacity of a PV power plant," *Fresenius Environ. Bull.*, vol. 31, pp. 3542–3550, 2022.

[17] K. Saka, "Seasonal generation of a grid connected PV power plant," in *Proc. 6th Eur. Conf. Renew. Energy Syst.*, Istanbul, Türkiye, Jun. 25–27, 2018.

[18] K. Saka, "Evaluation of a grid-connected PV power plant: performance and agrivoltaic aspects," *Environ. Dev. Sustain.*, vol. 26, pp. 32319–32336, 2024, doi: 10.1007/s10668-024-05098-z.

[19] K. Saka and M. F. Orhan, "Performance assessment and useful solar radiation analysis of a grid-connected photovoltaic plant in Türkiye," *Case Stud. Therm. Eng.*, vol. 73, p. 106565, 2025.

[20] K. Saka and M. F. Orhan, "Assessment of biogas-powered absorption cooling systems and biomass potential for sustainable rural development: A case study in Yenişehir, Turkiye," *Case Stud. Therm. Eng.*, vol. 66, p. 105784, 2025.

[21] Ö. C. Özerdem, S. Tackie, and S. Biricik, "Performance evaluation of Serhatkoy (1.2 MW) PV power plant," in *Proc. 9th Int. Conf. Electr. Electron. Eng.*, Mar. 29–31, 2022.

[22] T. İnan and A. Şimşek, "Solar power plant efficiency and economic analysis in different regional climates for selected cities in Turkey," *Int. J. Adv. Eng. Pure Sci.*, vol. 34, no. 4, pp. 603–610, 2022.

[23] T. C. Ministry of Energy and Natural Resources, "Gepa: Solar energy potential atlas of Turkey." [Online]. Available: https://gepa.enerji.gov.tr/. [Accessed: Oct. 01, 2025].

BİTLİS EREN ÜNİVERSİTESİ
FEN BİLİMLERİ DERGİSİ

ISSN: 2147-3129 / e-ISSN: 2147-3188

Article Type	: Research Article	**Year**	: 2025
Received	: May 1, 2025	**Volume**	: 14
Revised	: July 9, 2025	**Issue**	: 3
Accepted	: August 1, 2025	**Pages**	: 1636-1654
DOI	: 10.17798/bitlisfen.1688568		

COMPARATIVE PERFORMANCE ANALYSIS OF PERMANENT MAGNET AND CLAW-POLE ALTERNATORS IN INTERNAL COMBUSTION ENGINES

Metin KAYNAKLI [1,*], Ahmet ALBAYRAK [2], Raif BAYIR [3]

[1] *Bitlis Eren University, Vocational School of Technical Sciences, Bitlis, Türkiye*

[2] *Düzce University, Computer Engineering Department, Düzce, Türkiye*

[3] *Karabük University, Mechatronic Engineering, Karabük, Türkiye*

**** Corresponding Author:*** *mkaynakli@beu.edu.tr*

ABSTRACT

In this study, a comprehensive experimental comparison of Permanent Magnet Alternators (PMA) and Claw-Pole Alternators (CPA) used in internal combustion engines (ICE) was conducted under three different operating conditions: no-load, loaded, and charging scenarios. Key performance parameters including voltage, current, engine speed, temperature variation, and fuel consumption were measured and analyzed in detail using a custom-built test setup and data acquisition system. The results show that while PMAs provide higher efficiency and power output under load, they are prone to higher operating temperatures and efficiency losses under no-load and charging conditions compared to CPAs. CPAs, on the other hand, demonstrated stable performance and higher current generation capacity, which is crucial for meeting increasing electrical demands in modern vehicles. The findings underline the importance of predicting alternator performance for optimizing fuel economy, enhancing electrical system reliability, and supporting the development of next-generation automotive alternators. Design recommendations are also presented to improve the efficiency and thermal management of PMAs in practical applications.

Keywords: Permanent magnet alternator (PMA), Claw-Pole alternator (CPA), Fuel efficiency in alternators, Automotive electrical systems.

1 INTRODUCTION

Disposing of with the rapid advancement of modern automotive technology, key issues such as meeting the increasing energy demand with low power consumption, improving the

efficiency of electrical systems, and achieving fuel savings have come to the forefront. These needs are driving research into alternative energy generation methods and encouraging the automotive industry to seek innovative solutions. The electrical systems in vehicles play a critical role in ensuring safety and comfort. These systems not only power various electrical loads such as headlights, turn signals, windshield wipers, and radios, but also ensure that the battery remains continuously charged. Insufficient performance or complete failure of the electrical system poses a significant risk that can directly compromise driving safety.

The battery, one of the fundamental components of the vehicle's charging system, cannot meet the entire electrical power demand due to its limited capacity. Therefore, an additional power generation system is required to ensure that the battery remains fully always charged. When the engine is off, electrical loads are powered directly by the battery; however, when the engine is running, this responsibility is taken over by the charging system. Nonetheless, when the engine is operating at low speeds, the current produced by the charging system may not be sufficient to power the electrical loads. In such cases, the alternator and the battery work together to supply power. Under high engine speed conditions, the alternator not only powers the electrical loads but also charges the battery [1], [2].

CPAs, which are widely used in modern vehicles, have long been favored by the automotive industry due to their low cost, durability, and ability to maintain consistent efficiency within certain speed ranges [3], [4]. However, the increasing number of electronic components in modern vehicles and the resulting rise in energy demand have led to the inadequacy of traditional alternators. Consequently, various technological innovations are being researched to enhance the output power, efficiency, and overall performance of alternators [5], [6].

Among the methods developed to improve alternator efficiency are the addition of harmonic suppression diodes, the use of permanent magnets, twin-rotor designs, and the precise control of output voltages using power electronics techniques [7], [8]. However, the need to ensure sufficient electrical generation even at low engine speeds has driven vehicle manufacturers to explore alternative system solutions. In this context, permanent magnet alternators (PMAs) have emerged as a new generation of alternators, attracting attention with their high efficiency, high power output, low moment of inertia, and simple structure [9].

Fuel economy is one of the key factors in alternator selection. In CPAs, more mechanical power is required to reach the targeted current levels, which directly increases the engine’s fuel

consumption [10]. Since alternators are directly connected to the engine via a belt, this leads to additional fuel usage during the energy generation process. On the other hand, in PMAs, fuel consumption is reduced due to minimized mechanical losses, thereby providing an economic advantage [11], [12].

In a study conducted by Huang and colleagues, a claw-pole magnetic levitation torque motor (CPMLTM) was developed, and it was demonstrated that the motor could suspend the rotor in a neutral axial and circumferential position through cogging torque and axial restoring forces between the stator claw poles and the permanent magnets on the rotor [13].

Wu and his colleagues investigated the effects of stator tooth deformation on electromagnetic force harmonics and acoustic noise in claw-pole alternators. Their study showed that deformation, particularly when the number of rotor pole pairs is not an exact multiple, leads to the generation of additional spatial harmonic components [14]. Furthermore, the same researchers proposed a new rotor topology and demonstrated that electromagnetic noise in claw-pole alternators could be reduced. Simulation results revealed that by offsetting the N and S poles in the same direction, electromagnetic noise could be reduced by up to 6.7 dB(A) [15].

In this context, the importance of PMAs, which offer higher efficiency and lower mechanical losses, is increasing in vehicle applications. Existing studies in the literature highlight the advantages and potential application areas of PMAs compared to CPAs, but they also underscore certain technical limitations [16]–[19].

In a study conducted in 2024, a multi-phase configuration approach was tested in a simulation environment to provide high energy storage density and longer service life. Simulations and experimental results confirmed the effectiveness of the mathematical model, while the proposed phase-shifting fault-tolerant control technique increased the operational reliability of the system [37.]

A new cooling technique was developed to improve the thermal characteristics of a permanent magnet generator (PMG) by integrating it with an earth-air heat exchanger (EAHE). The results show that the maximum temperature reduction of the end winding of the PMG is 24.45% due to EAHE when the PMG operates at full load. In addition, the maximum temperature reduction of the end winding of the PMG is 50.91% due to EAHE when the PMG operates at variable load. The use of EAHE together with PMG resulted in an 8.06% reduction in annual total cost [38].

Therefore, detailed prediction of the performance of PMA and CPA is of great importance for the efficient and reliable operation of vehicle electrical systems under different engine speeds and variable load conditions. Predicting performance in advance allows the selection of the right alternator type, optimization of fuel consumption and increased system reliability. In addition, clearly demonstrating the advantages and limitations of both alternator types under real operating conditions provides important inputs for the design of next-generation alternators.

In this study, the performance of a CPA used in internal combustion engines, and a permanent magnet rotor alternator was experimentally compared under different operating conditions. The measured parameters included alternator voltage and current, load voltage and current, engine speed, temperature variations, and fuel consumption. Based on the findings, the strengths and weaknesses of both alternator types in terms of performance were evaluated, and recommendations were provided for potential automotive applications.

2 MATERIAL AND METHOD

2.1 Permanent Magnet Alternators

Today, CPAs are proving insufficient to meet the increasing electrical energy demands of vehicles. This has led alternator manufacturers to develop new solutions that provide higher power and efficiency output. Among the methods developed are approaches such as increasing the alternator's rotational speed, using power electronics technologies to make the generated electricity more efficient, and reducing energy losses in the system. Research is also being conducted on different electrical machines and hybrid systems that could replace traditional alternators. The efficiency and overall performance of existing alternators remain limited, especially at certain engine speeds, where they fail to generate sufficient voltage [20,21]. With the rise in electrical loads, the necessity of generating adequate electricity even at low engine speeds is driving vehicle manufacturers to search for alternative systems [2]. One such alternative is the use of PMAs in electricity generation [5], [6].

Permanent magnets are materials that can generate a continuous magnetic field without the need for an external excitation current. They are typically made from alloys of elements such as iron, nickel, and cobalt, and have a high permanent flux density and high coercive force. These properties allow permanent magnets to create a strong magnetic field in the air gap of magnetic circuits. One of the most advanced types of permanent magnets today is the

Neodymium-Iron-Boron (NdFeB) magnet [22-24]. This magnet ranks among the materials with the highest energy density in commercial use. The key characteristics expected of an ideal permanent magnet include high internal coercive force, high saturation magnetization, high permanent flux density, and high energy density.

PMAs offer significant advantages due to their high efficiency, high power output, low moment of inertia, and simple structure. However, these systems also have some disadvantages. One major technical limitation is the difficulty in voltage regulation, particularly because the output voltage is sensitive to load variations and rotational speed. In automotive applications, this issue is one of the main barriers to the widespread adoption of PMAs [25,26]. However, since existing regulation systems can reduce high output voltages to 14V levels, this technology may also provide an advantage for PMAs. Furthermore, studies in the literature propose various mechanical solutions to control the magnetic flux generated in stator windings [39].

The output power of alternators varies depending on the engine's rotational speed. When the back electromotive force (EMF) voltage exceeds the output voltage, the alternator reaches its maximum power. Although the back EMF voltage in PMAs can reach around 80V, the system must maintain a constant output voltage of 14V, so the desired current can only be achieved at higher speeds. Additionally, the leakage reactance of the rotor limits the alternator's output power capacity [27-29]. While operating under load, the voltage drop across this leakage reactance becomes noticeable, and this drop increases with both rotational speed and the drawn current. As a result, when high current is drawn, a noticeable decrease in alternator output voltage occurs [4].

In permanent magnet alternators, most losses at low and medium engine speeds are due to stator copper losses. Iron losses, on the other hand, become dominant only at high speeds. The overall efficiency of these types of alternators typically ranges from 60% to 80%, and this efficiency range is usually achieved between 500 and 2000 revolutions per minute (rpm) [2].

2.2 Design Characteristics of the PMA

PMAs are preferred for their ability to provide high power and efficiency. Their ease of manufacturing and compact structure make them well-suited for vehicle applications, increasing their usability in the automotive industry [30]. Magnetic flux density is a key parameter in electricity generation; thanks to the high flux density of the permanent magnets used, the overall size of the alternator can be reduced. PMAs consist of a structure that includes

permanent magnets mounted on the rotor and three-phase stator windings. A direct current (DC) voltage is obtained at the alternator output via a full-wave rectifier circuit.

PMAs offer attractive solutions, particularly in renewable energy systems, due to their high conversion efficiency. In addition, their lack of need for external excitation current and the absence of brushes or slip rings result in significantly reduced mechanical friction. Their simple and compact design also provides major advantages in terms of durability and reliability. However, these systems do have certain disadvantages. One of the most significant limitations is the high cost of the permanent magnets that enable such high efficiency. As efficiency increases, so does the cost of the magnets [31].

Another major disadvantage of this type of alternator is that the output voltage varies directly with the rotor speed. This poses a significant regulation problem for applications requiring a constant output voltage and represents a technical challenge that must be addressed. The main losses affecting the performance of PMAs include mechanical friction, magnetic losses, stator copper losses, and rectifier-related losses. To analyze these losses and to model the overall operating characteristics of the alternator, an equivalent circuit of the system has been developed. Figure 1 shows the equivalent circuit of the PMA. This equivalent circuit enables the simulation of both the mechanical and electrical variables of the PMA [32].

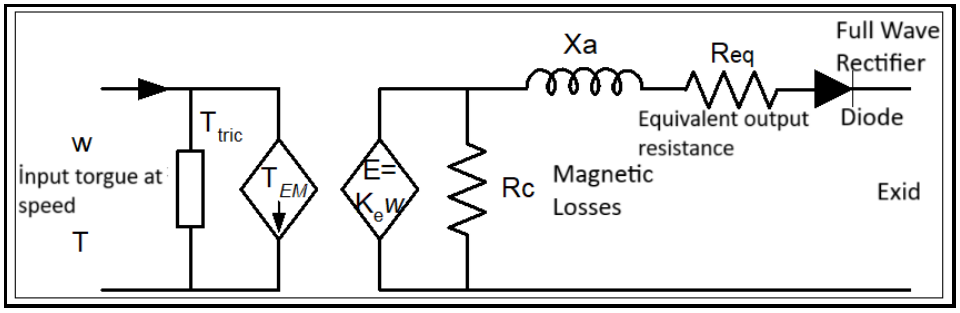


Figure 1. Equivalent circuit of the PMA

In PMAs, although there are no losses caused by brushes, there are still losses resulting from bearings. Bearings are found in all electric machines, and the losses arising from them include:

$$P_{fric} = T_{fric} \cdot \omega \tag{1}$$

Equation (1) dE Tfric is the friction torque. This torque can be measured at low speeds. However, friction losses due to the existing cooling fan inside the machine can be neglected. Eddy currents and hysteresis losses in magnetic materials are magnetic losses. These losses vary according to the axial flux fatigue and can be calculated by the formula in equation (2).

$$P_e + P_h = K_e \cdot f^2 \cdot B_{max}^2 + K_h \cdot f \cdot B_{mav}^x \quad (2)$$

The constant x in the equation is a constant value ranging from 1.5-2.5. Great care should be taken in measuring the losses in a permanent magnet machine operating without load. Because magnetic losses vary proportional to the square of the inverse EMC. Total magnetic losses can be expressed in equation (3).

$$P_e + P_h = K_e \cdot f^2 \cdot B_{max}^2 + K_h \cdot f \cdot B_{mav}^x \quad (3)$$

$$P_e\ P_m = K_m \cdot \omega^2 \quad (4)$$

$$P_e P_{Cu} = I_{dc}^2 \cdot R_{eq} \quad (5)$$

Copper losses can be expressed in equation (4) as resistance dependent losses. Rectifier losses are the voltages dropping across the full wave rectified diodes. This is given in equation (5).

2.3 Design Characteristics of The Pma

To test the performance of the alternator in real time on an ICE, a custom experimental setup was developed. This setup includes mechanical and electronic connections between the alternator integrated into the ICE and a computer system used for data acquisition and analysis. The block diagram of the experimental setup is presented in Figure 2(a). The general layout of the engine and system components used in the experimental setup is shown in Figure 2.(b). The experimental setup consists of a test stand with upper and lower chassis, Fiat brand 1.6L spark ignition engine, various electrical receivers (headlight and rear lighting systems, side and rear signal systems, windshield wiper motor and power window lifting systems), precision fuel measuring cup and amplifier, thermocouple sensor and amplifier for temperature measurements, magnetic sensor and amplifier for speed measurements, current and voltage measurement devices, PCLD-8710 terminal tube, PCL-1716L data exchange card and a desktop computer. The claw type alternator used in the experiments was manufactured by MAKO and is a model with the technical specifications of 12V AA125R-14V-45A, which is widely available on the market.

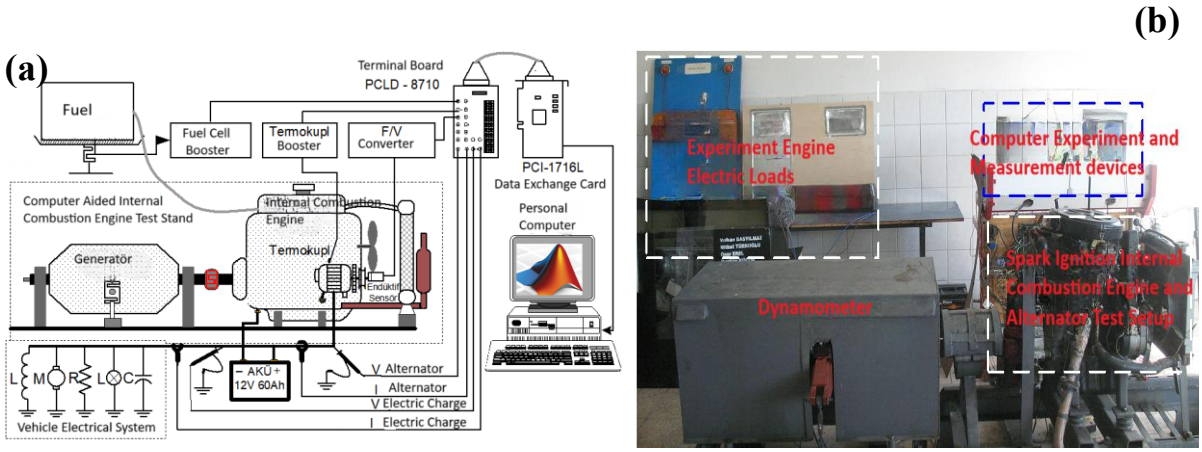


Figure 2. (a) Block diagram of the experimental setup; (b) general view of the experimental setup.

Another alternator used in the experimental setup is a two-phase PMA manufactured by Efor Endüstriyel Tasarım Sanayi Ticaret. Figure 3(a) shows the CPA, while Figure 3(b) illustrates the PMA.



(a) **(b)**

Figure 3. (a) Claw pole alternator; (b) Permanent Magnet Alternator.

In the experiments, three different performance measurement conditions were applied to both the CPA and the PMA. These conditions were as follows: no-load performance measurements, loaded performance measurements, and charging performance measurements.

In the no-load performance tests carried out in the first phase, the ICE was operated at a constant 2000-2100 rpm range and the alternators were allowed to operate at 4000-4200 rpm for one hour without any electrical load being connected to the circuit. In these tests, the power generated by the alternators, the amount of power drawn from the battery by the electrical loads in the system, the temperature changes during operation and the effects of the alternators on the fuel consumption of the engine were measured. The measurements were recorded in real time on a model created in MATLAB environment with the help of precision measuring devices and a data exchange card. In the second stage, during the loaded performance tests, the no-load experimental conditions were maintained. However, this time, during the alternator operation,

specific electrical loads (fan, headlights, signals, wiper motors, and resistors) were sequentially activated in ten-minute intervals. In these tests, the changes in the parameters measured during the no-load condition under load were analyzed. This allowed for the evaluation of the alternators' performance characteristics under load conditions. In the third and final experimental stage, charging performance tests were conducted. In these tests, the operating conditions from the no-load and loaded tests were maintained [33]. However, without activating any electrical loads, a fully discharged battery was charged under a fixed engine speed using the alternator. During this process, the changes in the parameters measured in the previous tests during the charging process were observed and a comparative analysis was performed.

3 PERFORMANCE MEASUREMENTS OF CPA AND PMA

3.1 No-Load Performance Measurements of CPA

In Figure 4 (a), the power-time graph obtained by multiplying the instantaneous voltage and current values produced during one hour of operation at a constant 4000–4200 rpm range of the CPA is presented.

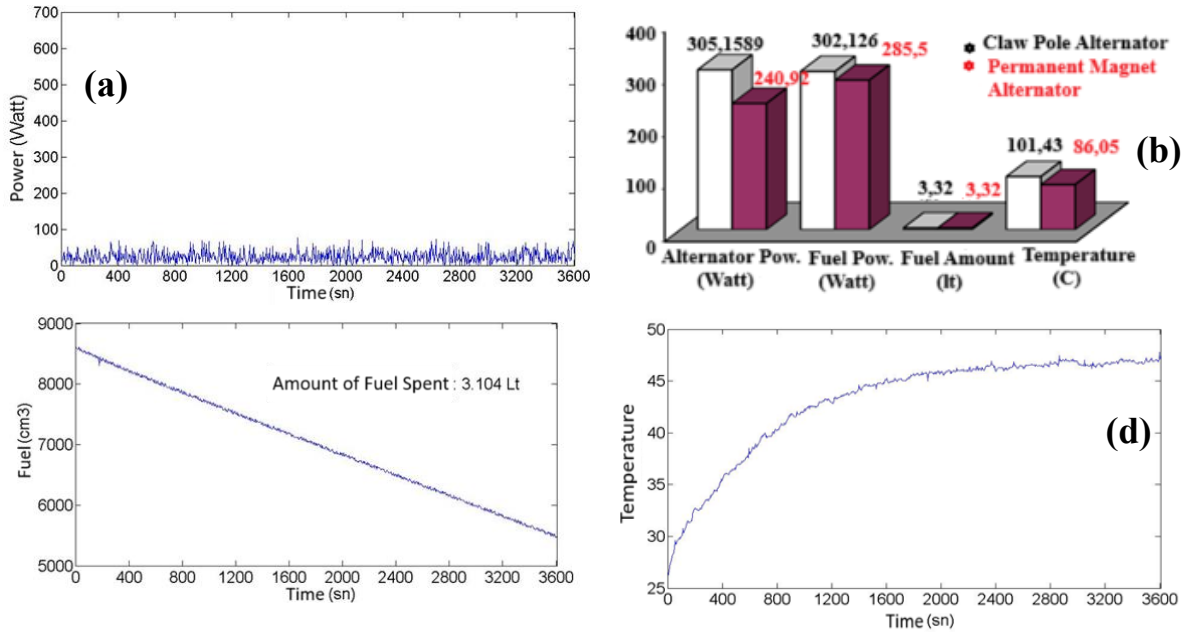


Figure 4. (a) Alternator power graph; (b) load power graph; (c) fuel consumption graph; (d) alternator temperature graph.

In Figure 4 (b), the load power (theoretical power that electrical consumers could draw) is shown, which is obtained by multiplying the measured voltage and current values across the battery when no electrical load is connected to the circuit, at a constant engine and alternator

speed. Figure 4 (c) shows the amount of fuel consumed per unit time by the internal combustion engine during the operation of the alternator, illustrating the fuel performance of the engine in interaction with the alternator. Finally, Figure 4 (d) displays the temperature change over time measured on the alternator body during the no-load operation of the CPA.

3.2 Loaded Performance Measurements of CPA

In Figure 5 (a), the power-time graph obtained for the case when the CPA operates under load is presented. In this experiment, no electrical load was connected to the system during the first 10 minutes; then, electrical consumers were gradually connected at 10-minute intervals. This allowed for the evaluation of the power performance produced by the CPA at different load levels over time. In Figure 5 (b), during the fixed engine and alternator speed, the time-dependent variation in the power drawn from the battery is shown as electrical loads are activated while the alternator powers the battery.

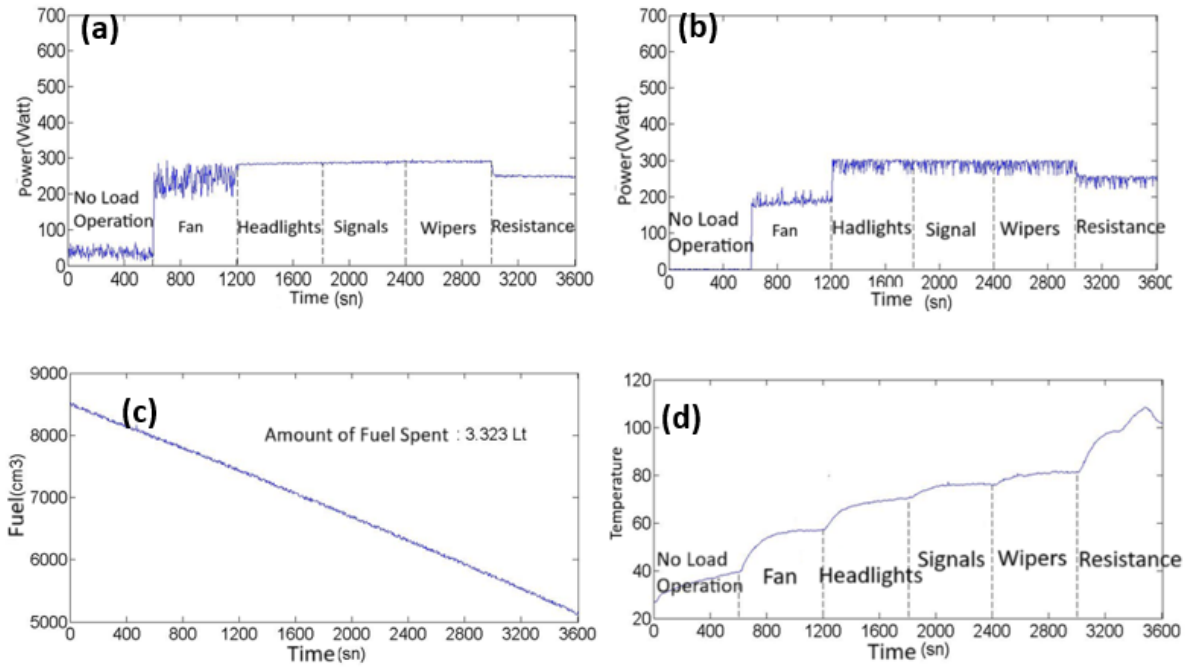


Figure 5. (a) Alternator power graph; (b) load power graph; (c) fuel consumption graph; (d) alternator temperature graph.

Figure 5 (c) illustrates the amount of fuel consumed per unit time by the internal combustion engine under load conditions of the CPA, revealing the impact of the electrical load on the engine. Finally, in Figure 5 (d), the temperature-time change graph for the CPA operating under load at a fixed engine and alternator speed is presented, monitoring the thermal behavior of the alternator.

3.3 Performance Measurements of CPA during Charging

In Figure 6 (a), the graph showing the time-dependent variation of the electrical power produced by the CPA during battery charging is presented. This graph reveals the dynamic changes in the alternator's power output throughout the charging process. In Figure 6 (b), under fixed engine and alternator speed, the time-dependent change in the amount of power drawn by electrical consumers from the battery during the charging process is provided. Figure 6 (c) shows the amount of fuel consumed by the internal combustion engine when the alternator is only charging the battery, allowing for the evaluation of the impact of the charging load on the engine. Finally, in Figure 6 (d), the time-dependent graph of the temperature changes in the structure of the CPA during the battery charging process is presented, contributing to the thermal behavior analysis.

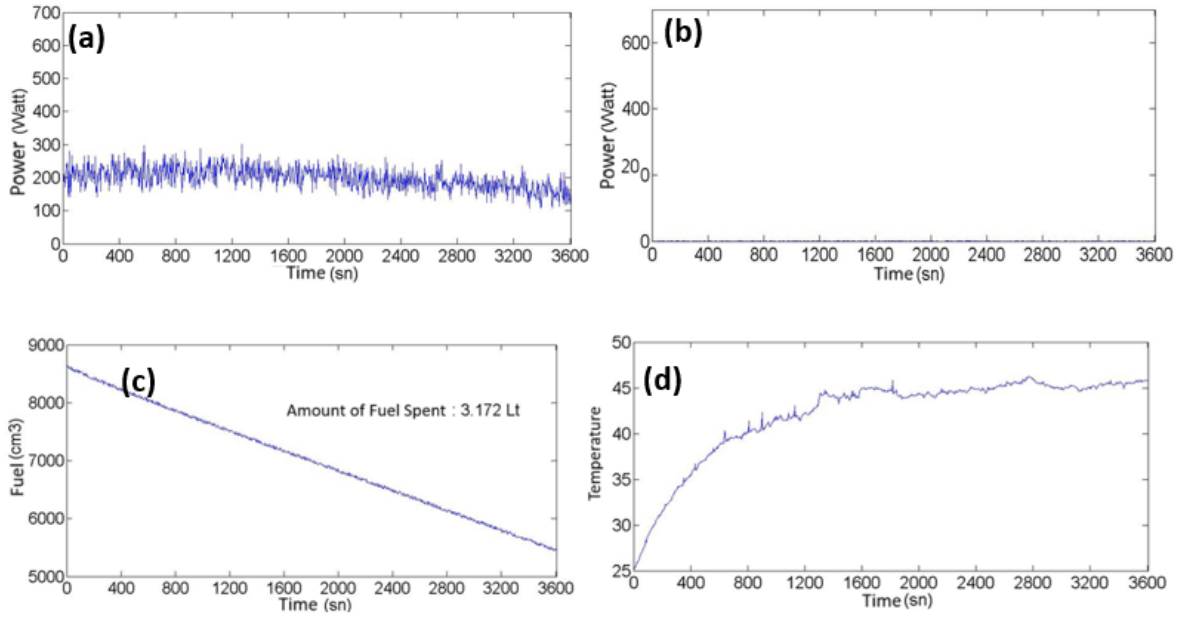


Figure 6. (a) Alternator power graph; (b) load power graph; (c) fuel consumption graph; (d) alternator temperature graph.

3.4 No-Loaded performance measurements of the PMA.

In this experimental phase, the conditions applied during the no-load performance tests of the CPA were identically applied to the PMA to measure its performance values under similar conditions. Figure 7 (a) presents the power-time graph showing the time-dependent variation of the power output produced by the PMA during one hour of operation at a constant speed range of 4000–4200 rpm. In Figure 7 (b), under fixed engine and alternator speed, the time-dependent variation of the load power—calculated by multiplying the voltage and current values measured across the battery without connecting any electrical load to the system—is

shown. This graph represents the potential power supplied to the battery by the PMA under no-load conditions. Figure 7 (c) shows the amount of fuel consumed per unit time by the internal combustion engine due to the mechanical load applied by the PMA operating at constant speed. Finally, Figure 7 (d) presents the time-dependent graph of temperature changes observed on the alternator body during the PMA's no-load operation at constant engine speed [34].

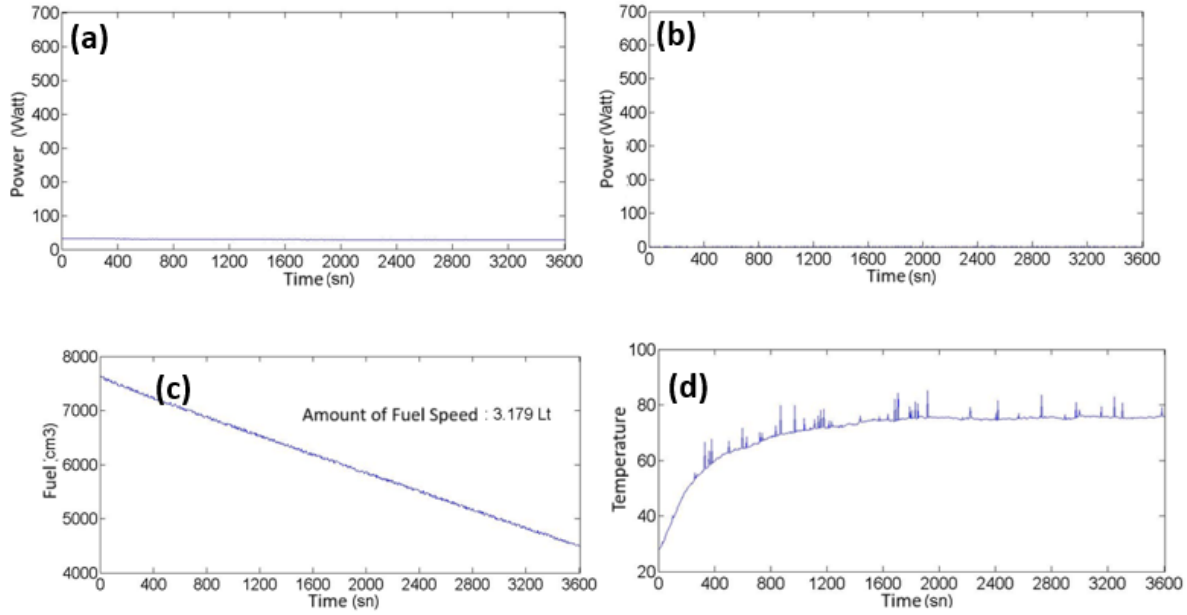


Figure 7. (a) Alternator power graph; (b) load power graph; (c) fuel consumption graph; (d) alternator temperature graph.

3.5 No-Loaded performance measurement graphs of the PMA

In this experiment, the loaded performance test conditions applied to the CPA were similarly applied to the PMA, and the performance values of the PMA were measured under comparable conditions. Figure 8 (a) presents the power-time graph showing the time-dependent variation in the power generated by the PMA under conditions where electrical loads were sequentially activated. In Figure 8 (b), under constant engine and alternator speed, the time-dependent variation of the power drawn from the battery by these electrical loads as they were connected one by one is shown. Figure 8 (c) illustrates the change in the amount of fuel consumed per unit time by the internal combustion engine during the PMA's operation under load. Finally, Figure 8 (d) shows the temperature-time graph reflecting how the temperature on the alternator body changed over time while the PMA operated under load conditions.

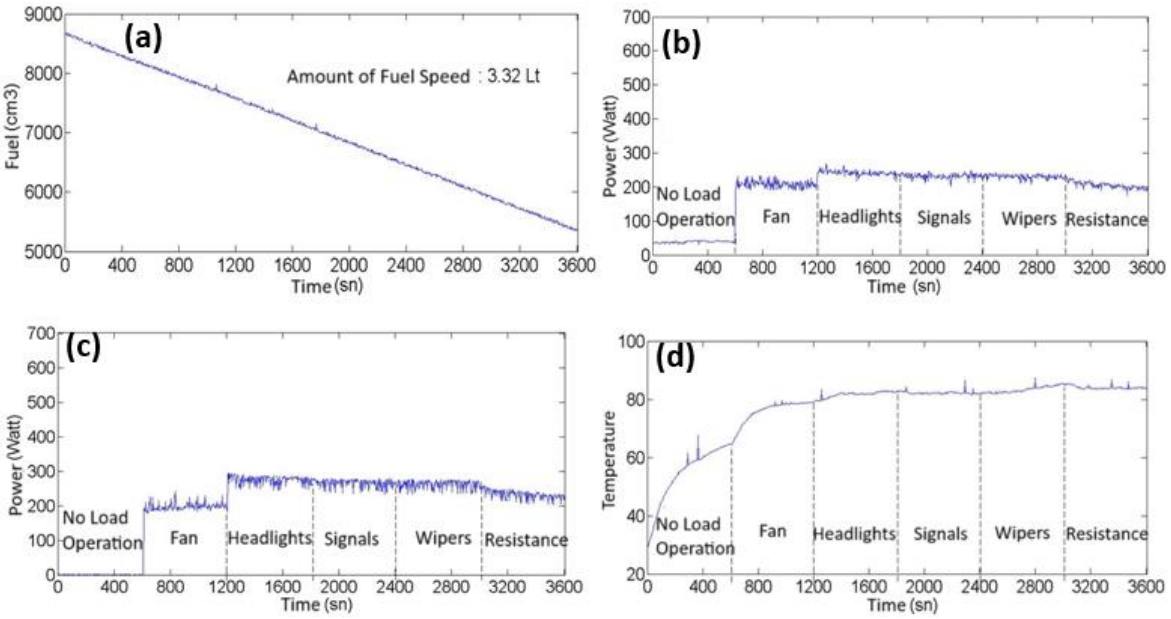


Figure 8. (a) Alternator power graph; (b) load power graph; (c) fuel consumption graph; (d) alternator temperature graph.

3.6 Loaded Performance Measurements of The PMA

Figure 9 (a) presents the power-time graph showing the time-dependent variation of the power output generated by the PMA during the charging process. This graph reflects the power performance of the alternator under conditions where it is solely charging an empty battery. In Figure 9 (b), under constant engine and alternator speed, the load power-time graph shows the time-dependent variation of the power drawn from the battery by electrical consumers as they are activated during the charging process. Figure 9 (c) illustrates the change in the amount of fuel consumed per unit time by the internal combustion engine during the operation of the PMA while charging. Finally, Figure 9 (d) presents the temperature-time graph that monitors the rise in temperature on the alternator body over time during the battery charging process carried out solely by the PMA.

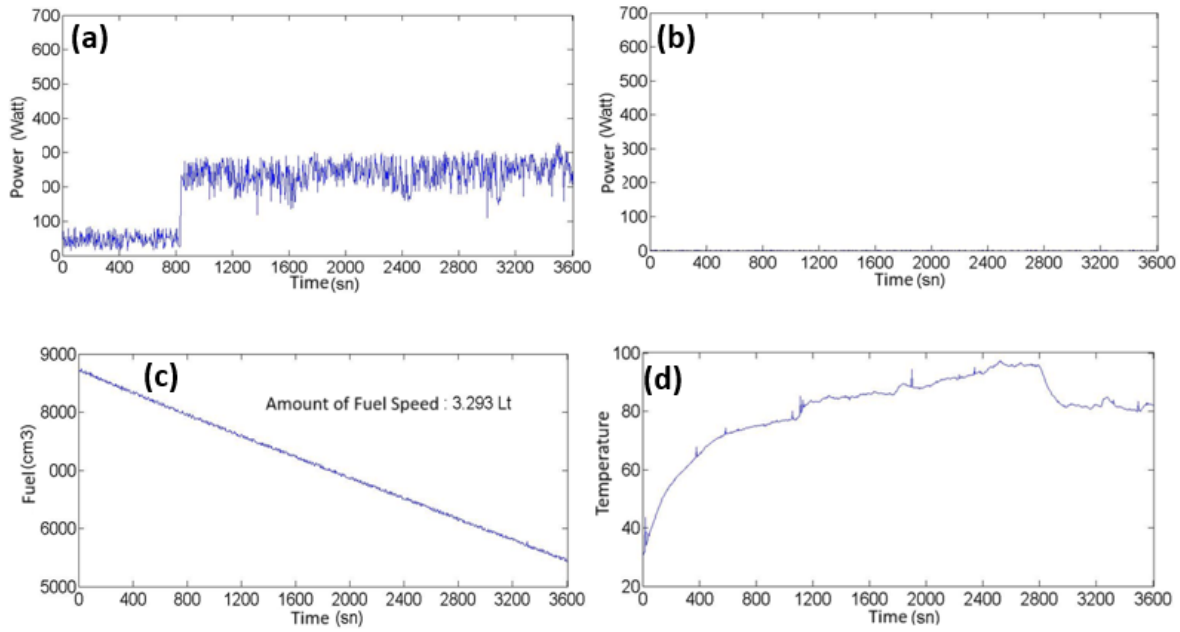


Figure 9. (a) Alternator power graph; (b) load power graph; (c) fuel consumption graph; (d) alternator temperature graph.

The graphical comparison of the measurement data obtained under no-load experimental conditions for both the CPA and PMA is presented in Figure 10. According to the findings, the CPA demonstrated higher performance compared to the PMA in terms of both alternator output power and power drawn by the load. On the other hand, when temperature measurements were evaluated, it was observed that the PMA heated up more than the CPA during operation. This suggests that the PMA may pose a potential disadvantage in terms of thermal durability and component life during prolonged use. The impact of both alternators on the fuel consumption of the internal combustion engine was similar, and no significant difference was observed.

The graphical comparison of the measurement data obtained under loaded experimental conditions for both the CPA and PMA is presented in Figure 12. According to the experimental results, it was observed that the amount of power produced by the PMA was lower compared to the CPA. However, since no electrical loads were connected to the system during the experiment, the power drawn by the load remained at 0 watts for both alternators. In terms of fuel consumption, it was determined that the amount of fuel consumed per unit time by the internal combustion engine was similar for both alternators. Temperature measurements, under these experimental conditions, show that the PMA reached lower temperature values compared to the CPA, indicating that the PMA is thermally more advantageous [35].

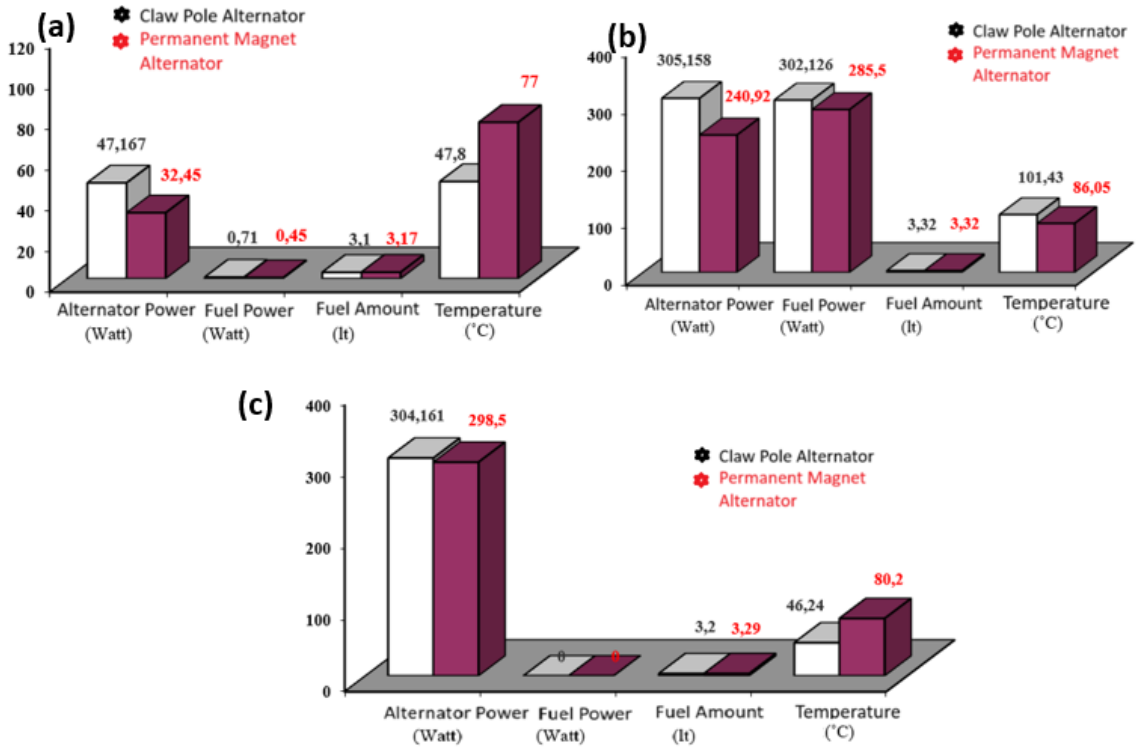


Figure 10. (a) No-load performance measurement graphs; (b) loaded performance measurement graphs; (c) charging performance measurement graphs.

The comparative graphical presentation of the experimental measurement data obtained during the charging process is provided in Figure 13. The analysis conducted at this stage revealed that the power level produced by the PMA is quite like that of the CPA. However, since electrical loads were not actively connected to the system during these tests as well, the load power values were again measured at 0 watts. In terms of fuel consumption, it was determined that the impact of both alternators on the internal combustion engine was similar. On the other hand, when temperature values were examined, it was found that the PMA reached higher temperatures compared to the CPA, indicating that this may be an unfavourable indicator of thermal performance for the PMA.

When the results obtained are examined in detail, it is seen that the high voltage values provided by PMA at high speeds are balanced by the limited current production capacity at low speeds compared to CPA. In the tests performed under load, CPA's current production provides an advantage, while PMA's low mechanical losses and lower temperature increase provide advantages in terms of thermal efficiency, especially in long-term use. In charging conditions, both alternator types showed similar performance, but it was determined that PMA reached higher temperature values. These results show that both alternators have advantages and disadvantages according to different operating conditions, and these data constitute an important reference in design developments [36].

4 RESULTS AND DISCUSSION

In this study, the CPA and the PMA were tested for one hour each under three different experimental conditions (no-load, loaded, and charging). During the experiments, the efficiencies of both alternators, their power generation performances, and their effects on the fuel consumption of the ICE were analyzed. The findings can be summarized as follows:

- As a result of the no-load experiments, it was determined that the PMA produced higher voltage values compared to the CPA in terms of both alternator and load voltage. However, in terms of current generation capacity, it was found that PMA fell short compared to CPA, and this was considered a negative performance indicator for the PMA. Additionally, considering the fuel consumption of the ICE and the temperatures reached by the alternators during operation, it was determined that the CPA was more advantageous than the PMA under these experimental conditions.

- In the loaded experiments, it was observed that the current production of the CPA was higher than the amount of current produced by the PMA. On the other hand, when evaluating other performance criteria such as alternator voltage, load voltage, load current, and temperature increase, it was determined that the PMA provided better results compared to the CPA. Under these experimental conditions, the effects of both alternators on the fuel consumption of the ICE were found to be very similar.

- In the charging experiments, it was recorded that the current values produced by the CPA were higher than those produced by the PMA. However, in terms of alternator voltage, load voltage, and load current, the PMA performed better compared to the CPA. Nevertheless, in this experiment as well, it was concluded that the PTA was more advantageous than the PMA in terms of temperature increase and fuel consumption.

As a result of the general evaluation, various design improvements have been proposed to enhance the performance of the PMA. Specifically, increasing the number of phases in the PMA, strengthening the stator windings, and using larger diameter and higher energy density permanent magnets in the rotor could significantly improve the efficiency of the alternator. Additionally, to prevent the temperature increase observed in the PMA, it is recommended to design these alternators with air- or water-cooling systems. With these improvements, it is expected that the performance of the PMA could surpass that of the CPA.

This study has some limitations. Experimental measurements were performed only on a specific internal combustion engine type and at specific speed ranges; similar performance

results may not be obtained under different engine types, speed ranges or climatic conditions. In addition, the analysis method used is based on recording experimental data over time and processing it in MATLAB; this approach is limited in terms of validation and is planned to be supported by further modeling, long-term tests and different test scenarios. In future studies, it is aimed to expand the scope of the tests with different engine types and alternator configurations.

Conflict of Interest Statement

There is no conflict of interest between the authors.

Statement of Research and Publication Ethics

The study is complied with research and publication ethics.

Artificial Intelligence (AI) Contribution Statement

This manuscript was entirely written, edited, analyzed, and prepared without the assistance of any artificial intelligence (AI) tools. All content, including text, data analysis, and figures, was solely generated by the authors.

Contributions of the Authors

M.K. took part in the conduct of experimental studies, data collection, data analysis, and manuscript writing. A.A. took part in data collection, data analysis, and manuscript writing. R.B. contributed to the design of experimental studies, providing methodology and consulting services.

REFERENCES

[1] D. J. Perreault and V. Caliskan, "Automotive power generation and control," *IEEE Trans. Power Electron.*, vol. 19, no. 3, 2004, doi: 10.1109/TPEL.2004.826432.

[2] M. Naidu, "A high-efficiency high-power-generation system for automobiles," *IEEE Trans. Ind. Appl.*, vol. 33, no. 6, 1997, doi: 10.1109/28.649966.

[3] W. Cai, "Comparison and review of electric machines for integrated starter alternator applications," in *Conf. Rec. IAS Annu. Meeting (IEEE Ind. Appl. Soc.)*, 2004. doi: 10.1109/ias.2004.1348437.

[4] K. G. Bürger, "Alternators," in *Automotive Electric/Electronic Systems*, 2nd ed., A. Beer and A. Cypra, Eds., Stuttgart, Germany: Robert Bosch GmbH, 1995, pp. 304–345.

[5] B. Singh, B. P. Singh, and S. Dwivedi, "A state of art on different configurations of permanent magnet brushless machines," *J. Inst. Eng. Electr. Eng. Div.*, vol. 87, no. JUNE, 2006.

[6] R. Dutta and M. F. Rahman, "Design and analysis of an interior permanent magnet (IPM) machine with very wide constant power operation range," *IEEE Trans. Energy Convers.*, vol. 23, no. 1, 2008, doi: 10.1109/TEC.2007.905061.

[7] J. Huang, Z. Song, S. Li, and J. Ruan, "Claw-pole magnetic levitation torque motor for 2D valve with automatic neutral adjustment," *IET Electr. Power Appl.*, vol. 17, no. 10, 2023, doi: 10.1049/elp2.12342.

[8] S. Wu et al., "Influence of stator teeth deformation on the electromagnetic force and acoustic noise of claw pole alternators," *Electr. Eng.*, vol. 105, no. 5, 2023, doi: 10.1007/s00202-023-01919-y.

[9] S. Wu, X. Yan, Z. Chen, Y. Zhang, and X. Feng, "New rotor topologies for electromagnetic forces and acoustic noise reduction of claw pole alternators," *J. Electr. Eng. Technol.*, vol. 18, no. 5, 2023, doi: 10.1007/s42835-023-01559-z.

[10] F. R. Ismagilov, V. E. Vavilov, O. A. Yushkova, E. A. Pronin, and A. A. Zherebtsov, "Characteristics of the starter–alternator with incorporated permanent magnets made of a dual-phase magnetic material rotor," *J. Mach. Manuf. Reliab.*, vol. 52, no. 8, 2023, doi: 10.1134/S1052618823080071.

[11] Safdar, S. Sultan, H. A. Raza, M. Umer, and M. Ali, "Empirical analysis of turbine and generator efficiency of a pico hydro system," *Sustain. Energy Technol. Assessments*, vol. 37, 2020, doi: 10.1016/j.seta.2019.100605.

[12] N. Pamuk, "Investigation of interior permanent magnet synchronous (IPMS) machine applications in electrical vehicle engine industry," *TEM J.*, vol. 12, no. 4, 2023, doi: 10.18421/TEM124-04.

[13] C. H. Cheng and S. Dhanasekaran, "Design of a slot-spaced permanent magnet linear alternator based on numerical analysis," *Energies*, vol. 15, no. 13, 2022, doi: 10.3390/en15134523.

[14] C. H. Cheng and S. Dhanasekaran, "Cogging force reduction and profile smoothening methods for a slot-spaced permanent magnet linear alternator," *Energies*, vol. 16, no. 15, 2023, doi: 10.3390/en16155827.

[15] S. Wu, S. Wu, J. Zhou, S. Cui, and X. Zhang, "Permanent magnet compensated pulsed alternator for driving air-based loads," *IEEE Trans. Transp. Electrif.*, vol. 6, no. 4, 2020, doi: 10.1109/TTE.2020.2988181.

[16] O. Otuoze et al., "Field loss calculation of a wind-powered axial flux alternator by analytical equations," *Eng. Reports*, vol. 3, no. 9, 2021, doi: 10.1002/eng2.12391.

[17] Y. Wan, Q. Li, J. Guo, and S. Cui, "Thermal analysis of a Gramme-ring-winding high-speed permanent-magnet motor for pulsed alternator using CFD," *IET Electr. Power Appl.*, vol. 14, no. 11, 2020, doi: 10.1049/iet-epa.2020.0086.

[18] J. Cekani, F. G. Capponi, G. De Donato, and F. Caricchi, "Mechanical flux weakening methods for the achievement of a very wide constant power speed range in automotive applications," *IEEE J. Emerg. Sel. Top. Power Electron.*, vol. 10, no. 3, 2022, doi: 10.1109/JESTPE.2021.3058198.

[19] Y. Cheng, G. Guo, and S. Hu, "Design and performance research of a novel iron-core permanent magnet compensated pulsed alternator with segmental squirrel-cage," *IEEE Trans. Ind. Electron.*, vol. 71, no. 2, 2024, doi: 10.1109/TIE.2023.3253922.

[20] B. Thangaraj and R. Subramanian, "A comparative 3-D transient electromagnetic, thermal and powertrain study of single rotor BLPMSM and dual rotor machine for electric propelled vehicle," *Electr. Eng.*, vol. 103, no. 6, 2021, doi: 10.1007/s00202-021-01257-x.

[21] S. Kirubadevi and S. Sutha, "PMSG based wind energy conversion system using intelligent MPPT with HGRSC converter," *Intell. Autom. Soft Comput.*, vol. 34, no. 2, 2022, doi: 10.32604/iasc.2022.025395.

[22] H. Moradi CheshmehBeigi, "Slotless tubular PM generator with dual quasi-Halbach magnetized PM array: Analytical and numerical magnetic field analysis," *Int. J. Numer. Model. Electron. Networks, Devices Fields*, vol. 33, no. 2, 2020, doi: 10.1002/jnm.2569.

[23] D. Karaoglan, D. G. Ocaktan, A. Oral, and D. Perin, "Design optimization of magnetic flux distribution for PMG by using response surface methodology," *IEEE Trans. Magn.*, vol. 56, no. 6, 2020, doi: 10.1109/TMAG.2020.2986187.

[24] R. B. Godoy, M. A. G. de Brito, R. C. Garcia, M. L. M. Kimpara, and J. O. P. Pinto, "Integrated starter alternator PMSM drive for hybrid vehicles," *J. Control. Autom. Electr. Syst.*, vol. 32, no. 1, 2021, doi: 10.1007/s40313-020-00665-x.

[25] M. C. Kulan, N. J. Baker, and S. Turvey, "Manufacturing challenges of a modular transverse flux alternator for aerospace," *Energies*, vol. 13, no. 6, 2020, doi: 10.3390/en13164275.

[26] G. Vijayasree, V. P. Mini, and S. UshaKumari, "Investigation of magnetic effect in high-speed homopolar inductor alternator," *J. Electr. Eng. Technol.*, vol. 19, no. 5, 2024, doi: 10.1007/s42835-023-01774-8.

[27] M. Murshed, M. Chamana, K. E. K. Schmitt, R. Bhatta, O. Adeyanju, and S. Bayne, "Design and performance analysis of a grid-connected distributed wind turbine," *Energies*, vol. 16, no. 15, 2023, doi: 10.3390/en16155778.

[28] M. C. Kulan, N. J. Baker, and S. Turvey, "Impact of manufacturing and material uncertainties in performance of a transverse flux machine for aerospace," *Energies*, vol. 15, no. 20, 2022, doi: 10.3390/en15207607.

[29] L. Jing, G. Liu, X. Guo, and S. Su, "Research on the cloud computing fuzzy proportion integration differentiation control strategy for permanent-magnet homopolar motor with salient pole solid rotor used on new-energy vehicle," *Sustain. Energy Technol. Assessments*, vol. 52, 2022, doi: 10.1016/j.seta.2022.101969.

[30] R. Mirzahosseini, A. Darabi, and M. Assili, "Analytical and experimental analysis of back EMF waveform of a TORUS-type non-slotted axial flux permanent magnet synchronous machine with shifted rotor," *Meas. J. Int. Meas. Confed.*, vol. 156, 2020, doi: 10.1016/j.measurement.2020.107620.

[31] J. Yang et al., "Design and analysis of a novel permanent magnet homopolar inductor machine with mechanical flux modulator for flywheel energy storage system," *IEEE Trans. Ind. Electron.*, vol. 69, no. 8, 2022, doi: 10.1109/TIE.2021.3104583.

[32] Y. Cao and C. Liu, "Design and analysis of a dual-direction hybrid excitation generator," *IEEJ Trans. Electr. Electron. Eng.*, vol. 17, no. 11, 2022, doi: 10.1002/tee.23674.

[33] M. Zhang, A. Bodrov, R. Shuttleworth, and M. F. Iacchetti, "Current-modulation-based on-line resonance tuning strategy for linear generator drives," *IEEE Trans. Ind. Electron.*, vol. 68, no. 4, 2021, doi: 10.1109/TIE.2020.2978697.

[34] Y. Zhang, B. Yang, D. Ji, X. Hou, B. Zhao, and T. Zhang, "Integrated simulation and performance analysis of confined piston linear generator (CPLG)," *Energy*, vol. 282, 2023, doi: 10.1016/j.energy.2023.128814.

[35] B. C. Kim and D. W. Kang, "A study on the novel design to improve efficiency of wound field synchronous machine," *IEEE Trans. Magn.*, vol. 57, no. 2, 2021, doi: 10.1109/TMAG.2020.3013260.

[36] Agarala, S. S. Bhat, D. Zychma, and P. Sowa, "A novel approach to using dual-field excited synchronous generators as wind power generators," *Energies*, vol. 17, no. 2, 2024, doi: 10.3390/en17020456.

[37] Y. Chen, Y. Wang, W. Li, and C. Qin, "Modeling and fault-tolerant control method of multiphase permanent magnet pulsed alternator," *IEEE Trans. Plasma Sci.*, vol. 52, no. 7, pp. 2917–2925, Jul. 2024, doi: 10.1109/TPS.2024.3443342.

[38] Amany R. Nasr, Ebrahim A. Badran, and Ibrahim I. I. Mansy, "A novel cooling technique to improve the thermal characteristics of a permanent magnet generator using an earth–air heat exchanger," *J. Electr. Comput. Eng.*, vol. 2025, Art. ID 9987298, 20 pages, doi: 10.1155/jece/9987298.

[39] C. Z. Liaw, W. L. Soong, and N. Ertugrul, "Low-speed output power improvement of an interior PM automotive alternator," in *Conf. Rec. IAS Annu. Meeting (IEEE Ind. Appl. Soc.)*, 2006. doi: 10.1109/IAS.2006.256516.

BİTLİS EREN ÜNİVERSİTESİ
FEN BİLİMLERİ DERGİSİ

ISSN: 2147-3129 / e-ISSN: 2147-3188

Article Type : Research Article
Received : May 2, 2025
Revised : May 29, 2025
Accepted : July 17, 2025
DOI : 10.17798/bitlisfen.1689468

Year : 2025
Volume : 14
Issue : 3
Pages : 1655-1671

STUDIES ON THE FAUNA OF PYRALOIDEA (LEPIDOPTERA) OF KÖPRÜLÜ CANYON NATIONAL PARK (ANTALYA)

Mümüne Merve ŞEN [1,*], Kesran AKIN [2]

[1] *Bitlis Eren University, Institute of Graduate Programs, Bitlis, Türkiye*

[2] *Bitlis Eren University, Biology Department, Bitlis, Türkiye*

**** Corresponding Author:*** *snmerve97@gmail.com*

ABSTRACT

Within the order Lepidoptera the superfamily Pyraloidea, is divided into two families that are rich in terms of species diversity: Pyralidae and Crambidae. This study aimed to determine the Pyraloidea fauna of the Köprülü Canyon National Park located in the Manavgat district of Antalya province, Türkiye. Field studies were carried out in the National Park between April and November in 2022-2024. The Pyraloidea species, which are generally active at night, were collected after sunset using light traps. As a result of the identification procedures, 88 species were identified. While all of the identified species are new records for Köprülü Canyon National Park, 72 species are new records for Antalya province.

Keywords: Lepidoptera, Pyraloidea, fauna, Antalya, Köprülü canyon.

1 INTRODUCTION

Butterflies and moths belong to the order Lepidoptera which means “Scaly Wings” [1]. The unique color patterns that distinguish this order from other insects come from their scales. Scales are structures that cover the body and wings like an arrangement of tiles [2]. Approximately 156,100 species of the order Lepidoptera have been identified worldwide and this number is expected to increase (approximately 255,000 species). The majority of these species are represented by moths [1]. The superfamily Pyraloidea is divided into two families

according to the structure of the tympanal organs on the abdomen: Pyralidae and Crambidae. This distinction is also supported by larval characters [3]. The Pyraloidea has about 16,000 species, with approximately as many more waiting to be described. It is a superfamily within the Lepidoptera with a high diversity of life histories. While most species live in different parts of plants, some species are parasites, predators and adapted to live underwater. Because they can live in different conditions, they are a suitable group to study biodiversity [4]. In the last study on the classification of Pyraloidea by Léger et al., [5], the superfamily Pyraloidea was divided into 2 families, Pyralidae and Crambidae. Pyralidae (6,032 species) includes the subfamilies Chrysauginae, Epipaschiinae, Galleriinae, Phycitinae; Crambidae (10,347 species) includes the subfamilies Acentropinae, Crambinae, Erupinae, Heliothelinae, Hoploscopinae, Lathrotelinae, Linostinae, Midilinae, Musotiminae, Odontiinae, Pyraustinae, Schoenobiinae, Scopariinae, Spilomelinae.

Köprülü Canyon National Park is an important natural area with an area of 36,614 hectares, 85 km northeast of Antalya province, and was declared as a national park in 1973. Most of the area of the National Park is located within the Manavgat-Serik districts of Antalya. A small part is within the borders of Sütçüler district of Isparta province. There is an important water source within the National Park, the Köprü River. The river stretches from the Taurus Mountains to Aspendos and flows into the Mediterranean Sea. The National Park has different formations in terms of geology. Some of these structures are Adam Kayalar, Deliklitaş, Krallar Canyon, Honaz Caves, Selge Ancient City, and Oluk Bridge. The livelihoods of the local people living in the canyon include animal husbandry, agriculture, tourism, bee-keeping, thyme-chestnut-carob collection and the harvesting of non-timber forest products. The main tourism activities in the region are trekking, mountaineering, caving and rafting [6].

In Köprülü Canyon National Park, where studies on Lepidoptera fauna are limited, Pyraloidea fauna is tried to be determined. This study will contribute to the emergence of the distribution of species in Türkiye. Additionally, it is thought that this study will be an important source for future studies.

2 MATERIAL AND METHOD

2.1 Collection

The field studies were carried out in the Köprülü Canyon National Park in Manavgat district of the Antalya province. The study was conducted between 2022 and 2024. Samples

were collected between March and November. The aim was to obtain spring, summer and autumn species. As most of the species in the Pyraloidea are nocturnal, the field studies were conducted accordingly. A light trap made of UV LEDs surrounded by a plastic container was used for night field studies. A 7-ampere, 12-volt battery was used as the energy source. After the field studies, the collected specimens were pinned and taken to the Zoology Research Laboratory at Bitlis Eren University for identification.

2.2 Preparation

In laboratory studies, the specimens that had been stretched to make them suitable for identification were identified using morphological and genital evaluations. Genital preparations, generally following the method of Robinson [7], were performed when external morphological characters were insufficient for identification.

2.3 Identification

Samples were identified by comparing them with collection specimens in the Zoology Research Laboratory of Faculty of Science and Literature of Bitlis Eren University. Additionally, various sources were also consulted. The main sources used for identification were Roesler [8-9], Leraut [10-11], Slamka [12-15], Goater et al., [4], Amsel [16-19], and Bleszynski [20]. In addition, websites such as Lepiforum [21], Boldsystem [22] and Mothdissection [23] were also visited.

2.4 Arrangement of taxa and studied localities

For the current use of taxa, the important database Globiz [24] and Koçak & Kemal [25] were used. The distribution of species in Türkiye and worldwide was generally considered in the studies of Koçak & Kemal [25-26] and Kemal & Koçak [27].

Information on the field studies carried out in 24 localities in Köprülü Canyon National Park is given below (Table 1, Figure 1).

Table 1. Localities where field studies are carried out

Location	Coordinate	Altitude
1. Altınkaya	37◦25'60" K 31◦12'00" D	1,143m
2. Ballıbucak Bridge	37◦29'09" K 31◦17'04" D	484m
3. Ballıbucak village	37◦29'09" K 31◦17'03" D	496m
4. Ballıbucak Plateau, Başçukur location	37◦31'39" K 31◦10'06" D	1,459m
5. Bozyaka	37◦11'87" K 31◦20'63" D	225m
6. Delisarnıç	37◦27'77" K 31◦12'87" D	972m
7. Demirciler	37◦22'22" K 31◦06'46" D	987m
8. Gaziler İlbiz	37◦27'15" K 31◦19'58" D	690m
9. Gaziler village, Barak location	37◦31'46" K 31◦21'56" D	480m
10. Gelinkavağı	37◦29'12" K 31◦18'19 "D	607m
11. İlbiz 2 km above	37◦16'27" K 31◦12'19" D	725m
12. Karataş	37◦27'35" K 31.21'46" D	826m
13. Köprülü Canyon, Barak location	37◦30'45" K 31◦22'32" D	489m
14. Köprülü Canyon, Çamurlu location (Figure 2a)	37◦10'63" K 31◦22'48" D	127m
15. Köprülü Canyon, Kövez location	37◦20'65" K 31◦17'79" D	230m
16. Köprülü Canyon, observation deck (Figure 2b)	37◦21'08" K 31◦15'98" D	668m
17. Kövez Eşek Bridge (Figure 2c)	37◦20'08" K 31◦17'88" D	264m
18. Kövez Mercimeklik location	37◦24'63" K 31◦20'84" D	687m
19. National Park, Tazı location	37◦25'82" K 31◦18'22" D	620m
20. National Park, Yeşilvadi location	37◦21'03" K 31◦08'58" D	865m
21. Tazı Canyon, Kapıiçi Gaziler village (Figure 2d)	37◦23'92" K 31◦18'32" D	572m
22. Tazı Canyon	37◦29'09" K 31◦17'03" D	583m
23. Yeşilvadi Karabük road	37◦16'99" K 31◦16'80" D	159m
24. Yeşilvadi village	37◦18'06" K 31◦13'53" D	557m

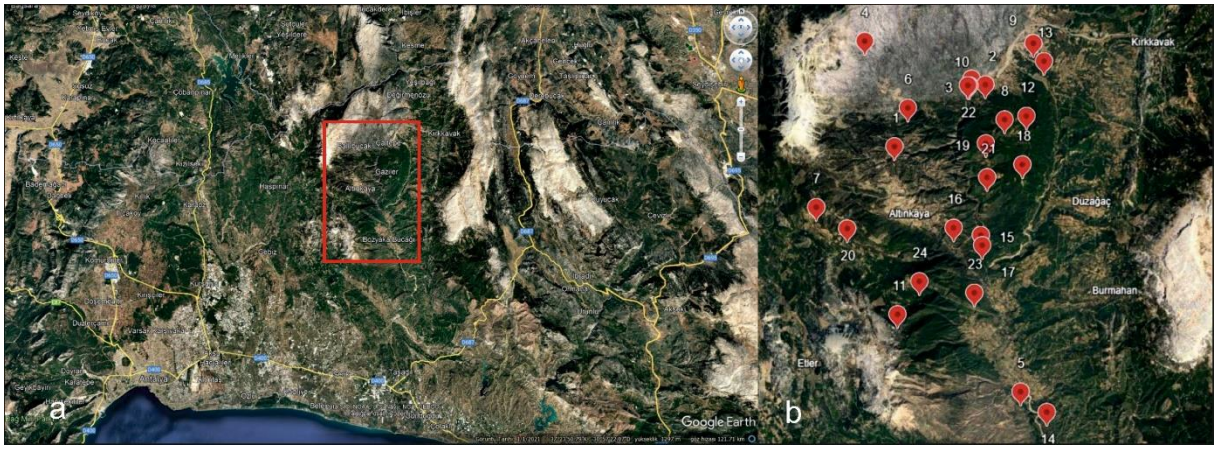


Figure 1. Showing the localities visited in Köprülü Canyon on the map, a. General view of the field; b. Localities visited [28].



Figure 2. Some of the localities studied a. Köprülü Canyon Çamurlu Location; b. Köprülü Canyon observation deck; c. Kövez Eşek Bridge; d. Tazı Canyon, Kapıiçi Gaziler Village.

3 RESULTS AND DISCUSSION

The study examined 1,018 samples and identified 88 species belonging to 10 subfamilies within the Crambidae and Pyralidae families of the Pyraloidea superfamily (Figure 3). While 72 of these species are new records for Antalya province, all of them are new records for Köprülü Canyon National Park, where the study was conducted. The species are listed alphabetically below, with new records for Antalya province are marked with an asterisk (*). Important additional information regarding some species is also provided.

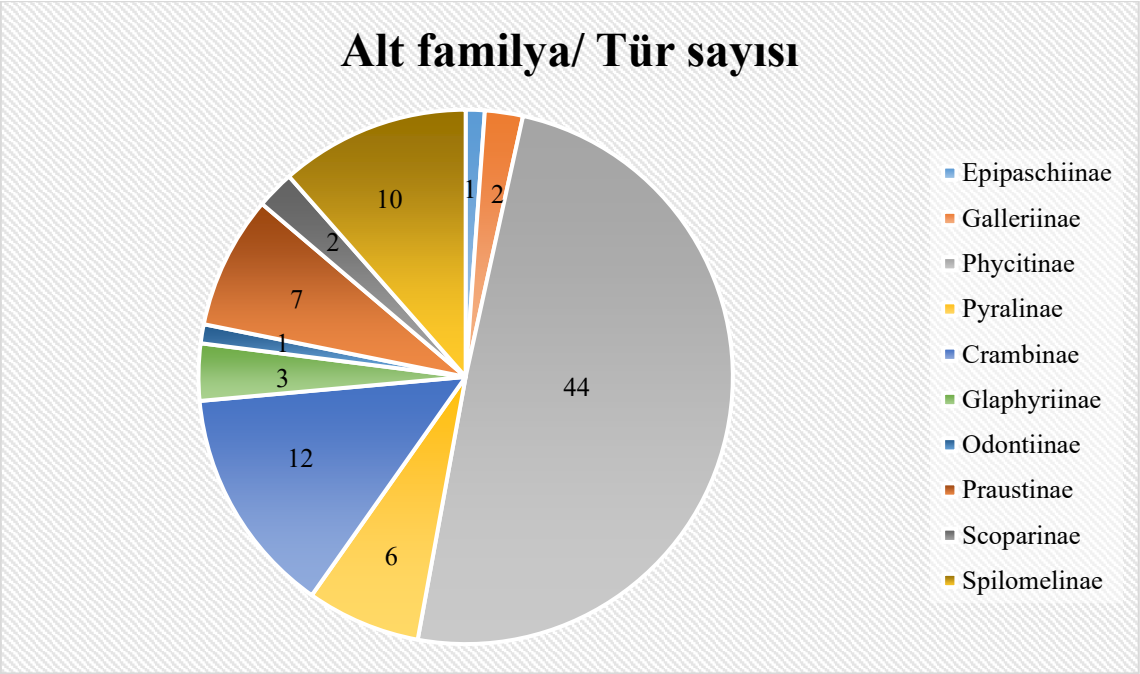


Figure 3. Distribution of species according to subfamilies.

Familya Crambidae Latreille, 1810

Subfamily Crambinae Latreille, 1810

Agriphila paleatellus (Zeller, 1847)*

Ancylolomia palpella (Denis ve Schiffermüller, 1775)*

Catoptria dimorphellus (Staudinger, 1881)*

Catoptria pinella (Linnaeus, 1758)*

Euchromius bella (Hübner, 1796)*

Euchromius rayatella (Amsel, 1949)*

Euchromius vinculellus (Zeller, 1847)

Glaucocharis euchromiella (Ragonot, 1895)*

Metacrambus carectellus (Zeller, 1847)*

Metaeuchromius latoides (Schouten, 1997)*

Taxonomic remarks: Schouten [29] described *Metaeuchromius latoides* stating that it is distinguished from *M. latus* (Staudinger, 1870) by eight black spots on the terminal area. However, he stated that this character could change with further examination of samples. This

study determined that the number of terminal spots on the forewing varied between 6-8 in the evaluated samples.

Pediasia contaminella (Hübner, 1796)*

Pediasia desertellus (Lederer, 1855)*

Subfamily Glaphyriinae W. T. M. Forbes, 1923

Cybalomia pentadalis (Lederer, 1855) (Figure 5b)

Evergestis boursini (Amsel, 1939)*

Evergestis infirmalis (Staudinger, 1870)* (Figure 4c)

Subfamily Odontiinae Guenée, 1854

Phlyctaenomorpha sinuosalis (Le Cerf, 1909)

Subfamily Pyraustinae Meyrick, 1890

Achyra nudalis (Hübner, 1796)*

Loxostege sticticalis (Linnaeus, 1761)

Pyrausta despicata (Scopoli, 1763)*

Pyrausta pauperalis (Staudinger, 1879)*

Pyrausta purpuralis (Linnaeus, 1758)

Pyrausta virginalis (Duponchel, 1832)*

Sitochroa straminealis (Hampson, 1900)* (Figure 4d)

Uresiphita gilvata (Fabricius, 1794)*

Subfamily Scopariinae Guenée, 1854

Eudonia mercurella (Linnaeus, 1758)*

Anarpia incertalis (Duponchel, 1832)*

Subfamily Spilomelinae Guenée, 1854

Antigastra catalaunalis (Duponchel, 1833)

Dolicharthria bruguieralis (Duponchel, 1833)

Mecyna subsequalis (Herrich-Schäffer, 1855)*

Metasia rosealis (Ragonot, 1895)*

Metasia suppandalis (Hübner, 1823)* (Figure 5a)

Nomophila noctuella (Denis & Schiffermüller, 1775)* (Figure 5h)

Palpita vitrealis (Rossi, 1794)

Patania balteata (Fabricius, 1798)* (Figure 5f)

Udea ferrugalis (Hübner, 1796)

Udea languidalis (Eversmann, 1842)*

Taxonomic remarks: In the study of Slamka [14], dorsal spines were mostly observed at the distal end of the aedeagus in specimens of the species *Udea languidalis*. However, in the study of Mally & Nuss [30], no dorsal spines were observed in the aedeagus. Similarly, there were no dorsal spines in the aedeagus of the specimen evaluated in this study. Consequently, the specimen was diagnosed as *Udea languidalis* based on morphological characteristics and male genitalia.

Familya Pyralidae, Latreille, 1809

Subfamily Epipaschiinae Meyrick, 1884

Salma lophotalis (Hampson, 1900)

Subfamily Galleriinae Zeller, 1848

Aphomia sociella (Linnaeus, 1758)*

Lamoria anella (Denis ve Schiffermüller, 1775)*

Subfamily Phycitinae Zeller, 1839

Acrobasis fallouella (Ragonot, 1871)*

Acrobasis legatea (Haworth, 1811)*

Acrobasis obliqua (Zeller, 1847)*

Acrobasis tumidana (Denis ve Schiffermüller, 1775)*

Ancylosis cinnamomella (Duponchel, 1836)*

Bradyrrhoa gilveolella (Treitschke, 1833)*

Taxonomic remarks: Some morphological differences have been observed among the specimens belonging to *Bradyrrhoa gilveolella*. Samples were mostly identified through genital

structures. Future molecular studies may be able to determine whether these morphological differences observed in adult individuals are variations or a new taxon.

Cadra calidella (Guenée, 1845)*

Cadra figulilella (Gregson, 1871)*

Cadra furcatella (Herrich-Schäffer, 1849)*

Coenochroa ablutella (Zeller, 1839)*

Denticera divisella (Duponchel, 1842)* (Figure 5c)

Dioryctria mendacella (Staudinger, 1859)

Dioryctria peltieri (Joannis, 1908) (Figure 5e)

Ematheudes punctellus (Treitschke, 1833)*

Ephestia cypriusella (Roesler, 1965)*

Ephestia disparella (Ragonot & Hampson, 1901)*

Ephestia unicolorella (Staudinger, 1879)*

Ephestia welseriella (Zeller, 1848)*

Epischnia illotella (Roesler, 1969)* (Figure 5g)

Epischnia prodromella (Hübner, 1799)*

Etiella zinckenella (Treitschke, 1832)*

Euzophera bigella (Zeller, 1848)

Euzopherodes charlottae (Rothschild, 1914)

Euzopherodes lutisignella (Mann, 1869)

Euzophera umbrosella (Staudinger, 1879)*

Taxonomic remarks: The male of the species *Euzophera umbrosella*, as identified in this study, is morphologically different from the depicted male in the study of Roesler [8], but morphologically similar to the adult male specimen in Lepiforum [21]. As they are also genitally compatible, these samples were identified as *E. umbrosella*.

Homoeosoma inustella (Ragonot, 1884)*

Homoeosoma sinuella (Fabricius, 1794)

Hypsotropa limbella (Zeller, 1848)*

Hypsotropa syriacella (Ragonot, 1888)*

Laodamia combustella (Herrich-Schäffer, 1855)*

Myelois ossicolor (Ragonot,1893)*

Taxonomic remarks: Roesler [31] listed the species *Myelois ossicolor* as a synonym of *Myelois umbratella* (Treitschke, 1833). This is also the case in Globiz [24]. However, P. Leraut [11] examined the female genitalia of both species in his study and concluded that they differed from each other. Similarly, G. Leraut [32] noted in his study, in which he listed the Phycitinae species, including *M. ossicolor* as a distinct species. This study also presented it as a separate species.

Myelois circumvoluta (Geoffroy, 1785)*

Pempelia argillaceella (Osthelder, 1935)*

Pempelia palumbella (Denis & Schiffermüller, 1775)*

Peoria semirosella (Ragonot, 1887)* (Figure 4a)

Phycita diaphana (Staudinger, 1870)*

Phycita roborella (Denis ve Schiffermüller, 1775)*

Phycitodes binaevella (Hübner, 1813)* (Figure 4b)

Phycitodes lacteella (Rothschild, 1915)*

Phycitodes saxicola (Vaughan, 1870)

Plodia interpunctella (Hübner, [1813])*

Polyocha venosa (Zeller, 1847)*

Pterothrixidia rufella (Duponchel, 1836)*

Uncinus nobilella (Ragonot, 1887)*

Subfamily Pyralinae Latreille, 1809

Aglossa asiatica (Erschoff, 1872)*

Aglossa caprealis (Hübner, 1809)*

Endotricha flammealis (Denis & Schiffermüller, 1775)*

Stemmatophora syriacalis (Ragonot, 1895)*

Synaphe berytalis (Ragonot, 1889)* (Figure 5d)

Zitha subustalis (Lederer, 1855)*

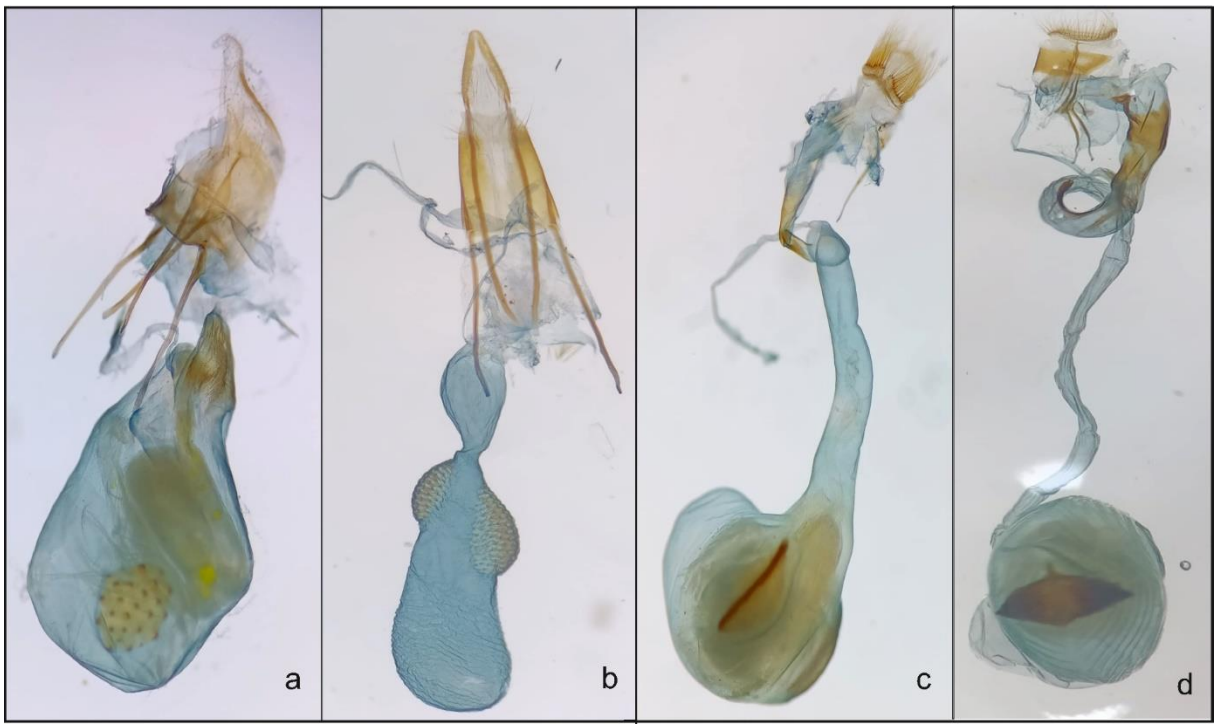


Figure 4. The female genitalia of some species identified in the study. a. Peoria semirosella; b. Phycitodes binaevella; c. Evergestis infirmalis; d. Sitochroa stremineali.

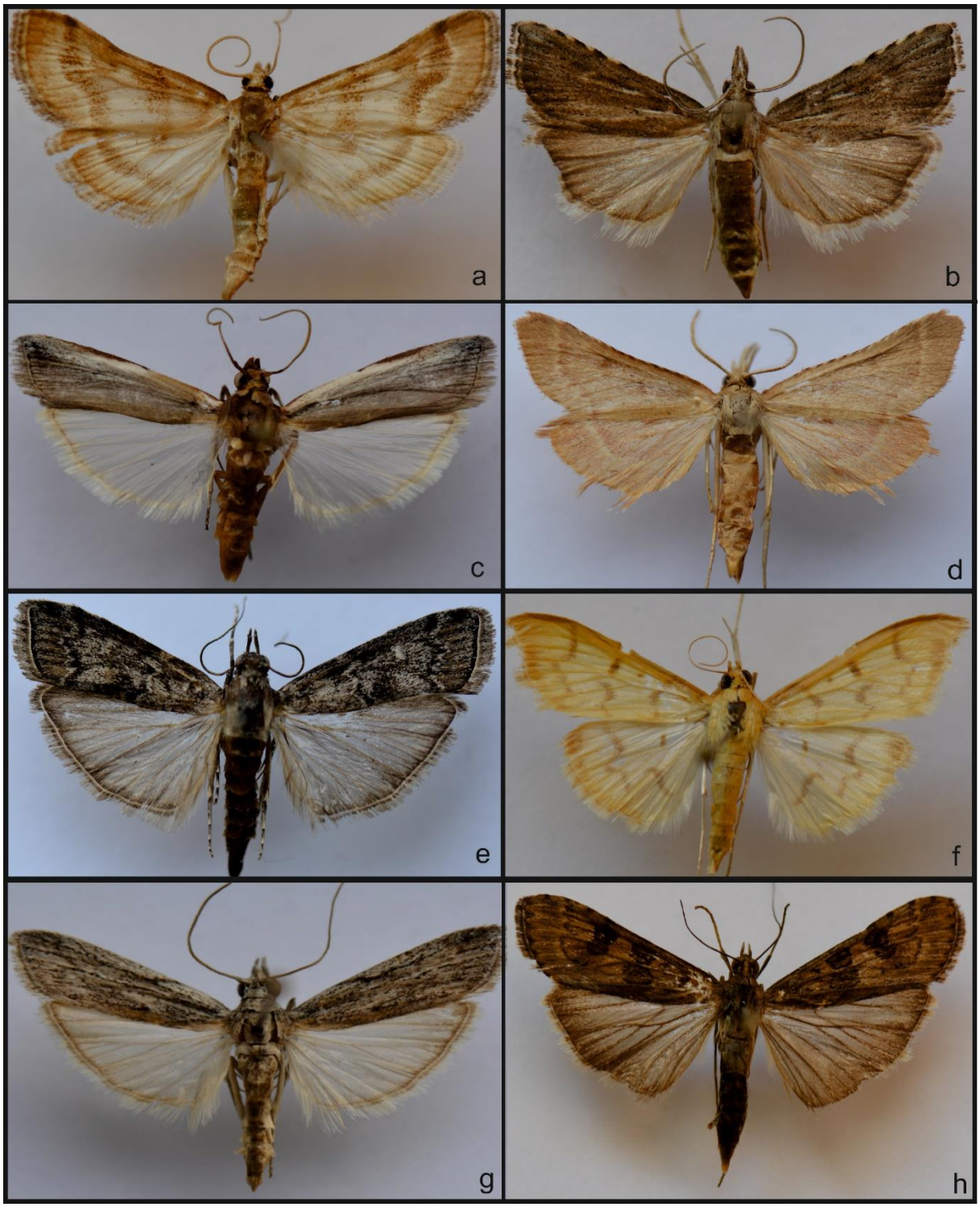


Figure 5. Adult specimens of some species identified in the study a. Metasia suppandalis; b. Cybalomia pentadalis; c. Denticera divisella; d. Synaphe berytalis; e. Dioryctria peltieri; f. Patania balteata; g. Epischnia illotella; h. Nomophila noctuella.

The study was carried out in 24 different localities within the Köprülü Canyon, and the number of species detected in each locality was also determined (Table 2).

Table 2. Number of species according to the localities visited

Localities	Number of Species Detected
1. Altınkaya	10
2. Ballıbucak Bridge	7
3. Ballıbucak village	12
4. Ballıbucak Plateau, Başçukur location	25
5. Bozyaka	10
6. Delisarnıç	5
7. Demirciler	6
8. Gaziler İlbiz	8
9. Gaziler Village, Barak location	3
10. Gelinkavağı	9
11. İlbiz 2 km above	2
12. Karataş	3
13. Köprülü Canyon, Barak location	6
14. Köprülü Canyon, Çamurlu location	15
15. Köprülü Canyon, Kövez location	3
16. Köprülü Canyon, Observation deck	17
17. Kövez Eşek Bridge	21
18. Kövez Mercimeklik location	9
19. National Park, Tazı location	23
20. National Park, Yeşilvadi location	29
21. Tazı Canyon, Kapıiçi Gaziler village	10
22. Tazı Canyon	4
23. Yeşilvadi, Karabük road	14
24. Yeşilvadi village	4

4 CONCLUSION AND SUGGESTION

A study conducted in Köprülü Canyon National Park located in the Manavgat district of Antalya province, identified 88 species belonging to the Pyralidae and Crambidae families within the Pyraloidea superfamily. 72 of these species are new records for Antalya province, and all of them are new records for Köprülü Canyon where the study was conducted. Prior to

this study, 30 species were known to occur from Antalya province [25], [27], [33-35]. 16 of these species were identified again in this study. As a result of the study, the number of pyraloid species in Antalya province increased to 102. Identifying species such as *Hypsotropa syriacella, Pempelia argillaceella, Peoria semirosella, Phycita diaphana, Uncinus nobilella* and *Evergestis boursini*, which are lesser-known to have a distribution in Türkiye [25], [27], is important in terms of their distribution.

The majority of species identified in the study belong to the Phycitinae subfamily (44 species). This is followed by the subfamilies Crambinae (12 species) and Spilomelinae (10 species). The Pyraustinae subfamily is represented by 7 species, the Pyralinae subfamily by 6 species, the Glaphyriinae subfamily by 3 species, the Scopariinae subfamily by 2 species, the Gallerinae subfamily by 2 species, the Epipaschiinae subfamily by 1 species and the Odontiinae subfamily by 1 species.

Considering the studies of Koçak & Kemal [25-26] and Kemal & Koçak [27] on the distribution of species, it can be seen that the species detected in the study area are mostly distributed in Asia, followed by Europe and then the African continent (Table 3).

Table 3. Distribution of species in subfamilies according to continents

Continents / Subfamilies	Africa	Asia	Europe
Crambinae	4	12	2
Glaphyriinae	-	3	2
Pyraustinae	5	7	5
Spilomelinae	8	10	10
Phycitinae	24	42	36
Odontinae	-	1	-
Epipaschiinae	-	1	-
Pyralinae	3	6	3
Gallerinae	2	2	2
Scopariinae	1	2	1
	47	86	61

As can be seen in Table 2, the locality with the highest number of species is the National Park, Yeşilvadi location, with 29 species. This is followed by the Ballıbucak Plateau, Başçukur location with 25 species, and the National Park, Tazı Location with 23 species. The localities with the fewest species are the İlbiz 2 km above, and the Karataş locality. It is thought that factors such as the season of the visit, the state of the month, altitude, plant diversity, proximity to wetlands, wind intensity, and the amount of landworks carried out in the area effect the species diversity that occurs in the fields.

With this study, species belonging to the Pyraloidea superfamily in the National Park were identified and the pyraloid fauna of the region was tried to be revealed. As mentioned above, the main activities carried out in the National Park are tourism, agriculture and animal husbandry. It is crucial that further research is conducted to understand these groups before the existing biodiversity in the area is destroyed.

Acknowledgements

This study is derived from the master's thesis of the first author, approved by the Institute of Graduate Studies at Bitlis Eren University. In addition, this study was supported by Bitlis Eren University Scientific Research Projects Coordination with the project number BEBAP 2023.13.

Conflict of Interest Statement

There is no conflict of interest between the authors.

Statement of Research and Publication Ethics

The study is complied with research and publication ethics.

Artificial Intelligence (AI) Contribution Statement

This manuscript was entirely written, edited, analyzed, and prepared without the assistance of any artificial intelligence (AI) tools. All content, including text, data analysis, and figures, was solely generated by the authors.

Contributions of the Authors

The collection of samples, stretching, preparation of genital preparations, diagnosis, and writing of the article were done by the first author. The diagnosis of samples, writing and editing of the article were done by the second author.

REFERENCES

[1] J. B. Hepner, "Butterflies and Moths (Lepidoptera)". J.L. Capinera (Ed.), *Encyclopedia of Entomology*, (pp. 626-672). Springer, 2008.

[2] V. H. Resh, "Lepidoptera (Moths, Butterflies)". Vincent HR (Ed.), *Encyclopedia of Insects*, (pp. 559-561), 2009.

[3] M. A. Solis, "Phylogenetic studies and modern classification of the Pyraloidea (Lepidoptera)," *Revista Colombiana de Entomologia*, vol. 33(1), pp. 1-9, 2007.

[4] B. Goater, M. Nuss, W. Speidel, "Pyraloidea I (Crambidae: Acentropinae, Evergestinae, Heliothelinae, Schoenobiinae, Scopariinae).," P. Huemer, O. Karsholt (Eds.), *Microlepidoptera of Europe 4*, (pp.1-304), Apollo Books, Stenstrup, 2005.

[5] T. Léger, R. Mally, C. Neinhuis, M. Nuss, "Refining the phylogeny of Crambidae with complete sampling of subfamilies (Lepidoptera, Pyraloidea)". *Zoologica Scripta*, vol. 50 (1), pp. 84-99, 2020.

[6] M. Kırmacı, H. Özçelik, "Köprülü Kanyon Milli Parkı (Antalya) Karayosunu Florasına Katkılar". *Süleyman Demirel Üniversitesi Orman Fakültesi Dergisi*, vol. 2, pp. 59-73, 2010.

[7] G. S. Robinson, "The Preparation of slides of Lepidoptera genitalia with special reference to the Microlepidoptera". *Entomologist's Gazette*, vol. 27, pp. 127-132, 1976.

[8] R-U. Roesler, "Trifine Acrobasiina (1. Teilband der Phycitinae)". H. G. Amsel, H. Reisser, F. Gregor (Eds.), *Microlepidoptera Palaearctica 4*, (pp. 752+137), Verlag Georg Fromme & Co, Wien, 1973.

[9] R-U. Roesler, "Quadrifine Acrobasiina Erster Teil (2. Teilband der Phycitinae)". H. G. Amsel, H. Reisser, F. Gregor (Eds.), *Microlepidoptera Palaearctica vol. 8* (Text & Tafeln) (pls 1-82+xxii+305), Verlag G.Braun, Karlsruhe, 1993.

[10] P. Leraut, *Moths of Europe. Volume 3: Zygaenids, Pyralids 1*. N.A.P. ed., Verrières-le-Buisson, 2012.

[11] P. Leraut, *Moths of Europe. Volume 4: Pyralids 2*. N.A.P. ed., Verrières-le-Buisson, 2014.

[12] F. Slamka, *Pyraloidea of Europe (Lepidoptera) Volume 2. Crambinae & Schoenobiinae. Identification, Distribution, Habitat, Biologie*. Bratislava, 2008.

[13] F. Slamka, *Pyraloidea of Europe (Lepidoptera) Volume 1. Pyralinae, Galleriinae, Epipaschiinae, Cathariinae & Odontiinae. Identification, Distribution, Habitat, Biologie*. Bratislava, 2011.

[14] F. Slamka, *Pyraloidea of Europe (Lepidoptera) Volume 3. Pyraustinae & Spilomelinae. Identification, Distribution, Habitat, Biologie*. Bratislava, 2013.

[15] F. Slamka, *Pyraloidea of Europe (Lepidoptera) Volume 4. Phycitinae. Identification, Distribution, Habitat, Biologie*. Bratislava, 2019.

[16] H. G. Amsel, "Die Microlepidopteren der Brandt'schen Iran Ausbeute II". *Ark. Zool.*, vol. 1(17), pp. 223-257, 1950.

[17] H. G. Amsel, "Die Microlepidopteren der Brandt'schen Iran Ausbeute III". *Ark. Zool.*, vol. 1(36), pp. 525-563, 1951.

[18] H. G. Amsel, "Die Microlepidopteren der Brandt'schen Iran Ausbeute IV". *Ark. Zool.*, vol. 6(16), pp. 255-326, 1954.

[19] H. G. Amsel, "Die Microlepidopteren der Brandt'schen Iran Ausbeute V". *Ark. Zool.*, vol. 13(17), pp. 323-445, 1961.

[20] S. Bleszynski, "Crambinae". H. G. Amsel, H. Reisser, F. Gregor (Eds.), *Microlepidoptera Palaearctica 1*, (pp. 1-553), Verlag Georg Fromme & Co, Wien, 1965.

[21] Lepiforum e. V., "Bestimmung von Schmetterlingen und ihren Präimaginalstadien". [Online]. Available: https://lepiforum.org/. [Accessed: Nov. 28, 2004].

[22] S. Ratnasingham, P. D. N. Hebert, "BOLD: The Barcode of Life Data System. Molecular Ecology Notes". [Online]. Available: http://www.barcodinglife.org/ (Bold Systems). [Accessed: Nov. 28, 2004].

[23] J. Wheeler, "Moth Dissection UK". [Online]. Available: https://mothdissection.co.uk/index.php. [Accessed: Nov. 28, 2004].

[24] M. Nuss, B. Landry, R. Mally, F. Vegliante, A. Tränkner, F. Bauer, J. Hayden, A. Segerer, R. Schouten, H. Li, T. Trofimova, M. A. Solis, J. De Prins, W. Speidel, 2003–2024, "Global information system on pyraloidea". [Online]. Available: -www.pyraloidea.org. [Accessed: Dec. 19, 2004].

[25] A. Ö. Koçak, M. Kemal, "A synonymous and distributional list of the species of the Lepidoptera of Turkey". *Centre for Entomological Studies*, *Memoirs*, vol. 8, pp. 1-487, 2018.

[26] A. Ö. Koçak, M. Kemal, "First updated geographical codes used in the publications of the Cesa". *Centre for Entomological Studies*, *Priamus*, vol. 17(4), pp. 319-361, 2019.

[27] M. Kemal, A. Ö. Koçak, "On the Phycitinae of Turkey: updated synonymic and distributional list of species (Lepidoptera) with some remarks". *Centre for Entomological Studies*, *Priamus*, vol. 18(3), pp. 130-154, 2020.

[28] Google Earth, "Google Earth Pro". [Online]. Available: https://www.google.com/intl/tr/earth/versions/. [Accessed: Jan. 16, 2005].

[29] R. T. A. Schouten, "Revision of the genus *Metaeuchromius* Bleszynski (Lepidoptera: Pyralidae: Crambinae)". *Tijdschrift voor Entomologie*, vol. 140, pp. 111-127, 1997.

[30] R. Mally, M. Nuss, "Molecular and morphological phylogeny of European *Udea* moths (Insecta: Lepidoptera: Pyraloidea)". *Arthropod Systematics & Phylogeny*, vol. 69(1), pp. 55-71, 2011.

[31] R.-U. Roesler, "Die Gattung *Myelois* Hübner, [1825] 1816 (Lepidoptera, Pyraloidea, Phycitinae) in der Palaearktis – Taxonomische neuorientierung und Beschreibung neuer taxa". *Ent. Z., Frank. a. M.*, vol. 98(13), pp. 177-192, 1988.

[32] G. H. C. Leraut, "Spécies général des Phycitinae (Lep. : Pyraloidea, Pyralidae) / A global comprehensive check-list of the Phycitinae (Lep.: Pyraloidea, Pyralidae)". *Revue Française d'Entomologie Générale, Autun*, vol. 2 (5–6, Supplement), pp. 1–371, 2021.

[33] H. Part, "Antalya Susam Alanlarında Susam Güvesi *Antigastra catalaunalis* Dup. (Lepidoptera: Pyralidae) Ve Tütün Beyaz Sinek *Bemisia tabaci* (Hemiptera: Aleyrodidae) Üzerinde Biyolojik Mücadele Olanakları". [Yüksek lisans tezi]. Isparta Uygulamalı Bilimler Üniversitesi, 2023.

[34] M. Keçeci, "The population dynamic of honeydew moth [*Cryptoblabes gnidiella* Mill. (Lepidoptera: Pyralidae)] in vineyard in Antalya". *Mediterranean Agricultural Sciences*, vol. 34(2), pp. 169-173, 2021.

[35] M. Koçak, "Antalya İli Kaş İlçesi Zeytin Bahçelerinde Zeytin Fidantırtılı, *Palpita unionalis* (Hübner) (Lepidoptera, Pyralidae)'in Popülasyon Gelişimi Üzerine Araştırmalar". [Yüksek lisans tezi]. Mustafa Kemal Üniversitesi, 2016.

BİTLİS EREN ÜNİVERSİTESİ
FEN BİLİMLERİ DERGİSİ

ISSN: 2147-3129 / e-ISSN: 2147-3188

Article Type	: Research Article	**Year**	: 2025
Received	: May 9, 2025	**Volume**	: 14
Revised	: September 28, 2025	**Issue**	: 3
Accepted	: September 29, 2025	**Pages**	: 1672-1687
DOI	: 10.17798/bitlisfen.1696097		

ANTIBIOTIC RESISTANCE, ANTIBACTERIAL ACTIVITY AND EXOPOLYSACCHARIDE DETERMINATION OF *LACTIPLANTIBACILLUS PLANTARUM* OBTAINED FROM TRADITIONAL YOGURTS FROM MUŞ REGION

Yusuf ALAN [1,*], Kayhan MANĞ [2]

[1] *Bitlis Eren University, Department of Medical Services and Techniques, Bitlis, Türkiye*

[2] *Muş Alparslan University, Institute of Science, Muş, Türkiye*

**** Corresponding Author:*** *yalan@beu.edu.tr*

ABSTRACT

In this study, 117 natural yoghurt samples were randomly collected from different regions of Muş. After preliminary identification (colony morphology, catalase, gram staining) of suspected *Lactiplantibacillus plantarum* strains isolated from yoghurt samples, molecular identification was performed by PCR method using *recA* gene sequence. Antibacterial activities and antibiotic resistance of 40 identified *L. plantarum* strains were determined. While 42.5% of the isolates were resistant to all antibiotics, three isolates (25, 35 and 36) showed the highest sensitivity. It was determined that strains 5 and 23 showed the best antibacterial activity against seven different pathogenic bacteria. Exopolysaccharides (EPS) synthesized by *L. plantarum* strains were determined qualitatively and quantitatively. It was determined that the isolates produced EPS between 318.30±1.28 mg/L (*L. plantarum* 23) and 205.70±1.44 mg/L (*L. plantarum* 16). Considering the resistance of the isolates in this study to antibiotics, their antibacterial effects on pathogenic microorganisms and EPS synthesis amount data, it was determined that *L. plantarum* isolates 5 and 23 exhibited good characteristics. Therefore, it is believed that isolates that demonstrate good properties (probiotic, anticancer, and antioxidant activity, etc.) as a result of in *vivo* and in *vitro* studies conducted with these isolates will contribute to the food industry and human health.

Keywords: *recA*, Antibiotic Resistance, Antibacterial Activity, Exopolysaccharide.

1 INTRODUCTION

One of the most popular fermented dairy products is yogurt. Pasteurized milk is combined with lactic acid bacteria, specifically *Lactobacillus delbrueckii* subsp. *bulgaricus* and *Streptococcus thermophilus*, under controlled conditions to produce yogurt [1]-[3]. Additionally, other *Lactobacillus* species, including *L. casei*, *L. acidophilus*, *L. plantarum*, and *L. rhamnosus*, may also be incorporated into the yogurt production process [5]. These microorganisms ferment lactose, the primary sugar in milk, resulting in the formation of compounds such as acetaldehyde, diacetyl, carbon dioxide, acetic acid, lactic acid, and various other metabolites that contribute to the distinctive flavor and aroma of yogurt [6]. *L. plantarum* can be isolated from milk and dairy products, meat and meat products, pickles, silage, human lips and digestive system, and fermented plants in nature [7], [8].

Yogurt bacteria produce nisin, known as a natural antibiotic, and lactic acid, which also has antimicrobial activity, which are active against *Escherichia coli*, *Salmonella*, *Shigella*, *Listeria* and *Candida*. These bacteria colonize the intestinal system against harmful microorganisms. Due to the competitive activity of yogurt bacteria and the antimicrobial substances formed, they have a protective effect against infections that cause urogenital and gastrointestinal diseases [1]. Industrially important properties of *L. plantarum* strains such as fermenting various carbohydrates, resistance to antibiotics, ability to grow in acidic environments, production of lactic acid, exopolysaccharide (EPS), bacteriocin, and inhibition of pathogens are also being investigated [9].

Exopolysaccharides (EPS) are high molecular weight carbohydrate polymers synthesized by bacteria and possess nutritional compounds and protection mechanisms against bacteriophages [4]. EPS possess various health beneficial properties such as antioxidant, antibacterial, hypoglycemic, immunomodulatory, and cholesterol-lowering properties [38]. In recent years, many efforts have been made to select LAB and bifidobacteria with high EPS yields for application in yogurt production [39]. Due to differences in LAB qualities, evaluation of strains from various sources is crucial for identifying effective and efficient strains with desired properties for the yogurt industry. Therefore, screening, identification, categorization, and decision-making of strains are important [40]. The EPS-producing ability of LAB and the amount of EPS are largely species- and strain-specific [41].

Therefore, in our study, molecular identification of suspected *L. plantarum* strains isolated from 117 yoghurt samples traditionally produced in Muş region was performed by PCR

method using phenotypic and *recA* gene sequence. The resistance and susceptibility of suspected *L. plantarum* strains to erythromycin, kanamycin, penicillin, chloramphenicol, gentamicin, and trimethoprim were determined, taking into account the antibiotics mechanisms of action. In addition, antibacterial activities of suspected *L. plantarum* strains against pathogenic bacteria *Klebsiella pneumonia*, *Escherichia coli*, *Enterobacter aerogenes*, *Bacillus subtilis*, *Pseudomonas aeroginosa*, *Bacillus megaterium* and *Staphylococcus aureus* were detected. In addition, the presence of EPS synthesized by these strains was reported by qualitative and quantitative methods. It is thought that *L. plantarum* strains showing good characteristics, based on the results obtained and the studies to be carried out, will directly contribute to the food industry by being used in the yoghurt production process and will indirectly make significant contributions to human health.

2 MATERIALS AND METHODS

2.1 Yoghurt Samples and *L. plantarum* Isolation

The 117 yogurt samples used for the isolation of *L. plantarum* were randomly collected from families who traditionally make yogurt in different villages of the Muş region. The collected yogurt samples were delivered to the laboratory in the cold chain as soon as possible under sterile conditions and the isolation process was performed. 5 g of each yogurt sample was weighed and centrifuged in 5 mL of sterile physiological water at 3500 g for 2 min. 1 mL of the resulting supernatant was centrifuged at 10000 g for 30 s, and 1 mL was taken from the resulting supernatant and centrifuged at 10000 g for 15 min. At the end of the period, the sediment remaining in the tube was dissolved with 900 µL of sterile physiological water and serial dilutions up to 10-5 were prepared. For the isolation of LAB from the prepared dilutions, the plates were inoculated on MRS agar and M17 agar petri dishes, respectively, and incubated at 37±2ºC for 24-48 hours. At the end of the incubation, the colonies that were formed and thought to be lactic acid bacteria colonies were taken and activated in the nutrient medium for stocking [10]. In all analyses except for the identification of *L. plantarum*, the *L. plantarum* STD strain supplied by Maysa Gıda-Lab (Tuzla-Istanbul) was used as a standard.

2.2 Phenotypic and *recA* Gene Identification of *L. plantarum* Strains

Preliminary phenotypic identification of the isolates obtained from yogurt was carried out based on colony morphology, Gram staining [11], microscopic characteristics, and the catalase test [12]. A total of 51 presumptive isolates, validated through preliminary assessments,

were cultured in MRS broth at 37 ± 2 °C for 24 to 48 hours. Following this enrichment phase, genomic DNA was extracted using the Genomic DNA Extraction Kit (Vivantis) and the extracted DNA samples were stored at –20 °C for further analysis. For PCR amplification of the recA gene, primers planF (5'-CCGTTTCTGCGGAACACCTA-3') and planR (5'-TCGGGATTACCAAACATCAC-3') were obtained from a commercial supplier [13].

2.3 Determination of Antibiotic Resistance Properties of Isolates

The antibiotic resistance profiles of *L. plantarum* isolates were assessed using the disk diffusion method. To this end, the susceptibility or resistance of the isolates to Penicillin (10 µg), Trimethoprim (25 µg), Erythromycin (10 µg), Gentamicin (10 µg), Chloramphenicol (30 µg) and Kanamycin (30 µg) (Oxoid) was evaluated. After storage at 4 °C, *L. plantarum* strains were reactivated by inoculating them into liquid MRS medium and incubating at 37 °C for 24 hours. Subsequently, 0.1 mL of the activated cultures, containing approximately 10^8 CFU/mL, was added to sterilized MRS agar that had been cooled to 45–50 °C and aliquoted into sterile test tubes. The inoculated medium was thoroughly mixed and poured into sterile 9.0 cm Petri dishes, with 15 mL dispensed per plate to ensure uniform distribution. Once the agar had solidified, antibiotic discs were aseptically positioned on the surface with appropriate spacing. The plates were pre-incubated at 4 °C for 2 hours, followed by incubation at 37 °C for 24 hours. Upon completion of incubation, the diameters of the inhibition zones were measured in millimeters to assess antibiotic susceptibility.

2.4 Antibacterial Activities of Isolates

The antibacterial activity of *L. plantarum* isolates was evaluated using the slurry agar diffusion method. To this end, the resistance and susceptibility profiles of various indicator bacteria *P. aeruginosa* ATCC 9027, *S. aureus* ATCC 25923, *K. pneumoniae*, *B. subtilis* ATCC 6633, *E. aerogenes* ATCC 13048, *B. megaterium* DSM 32 and *E. coli* ATCC 11229 ATCC 13883 were examined. The *L. plantarum* strains were cultured in liquid MRS medium, while the indicator bacteria were cultivated in nutrient broth and incubated at 37°C for 24 hours to ensure activation [14]. Following incubation, bacterial suspensions with a turbidity equivalent to 0.5 McFarland standard were prepared in distilled water from 24-hour cultures of the indicator strains. These suspensions were uniformly spread on appropriate agar media using sterile swabs. Wells were then aseptically created in the agar using a sterile borer, and 100 µL of each *L. plantarum* isolate was dispensed into the wells. The plates were incubated for 24

hours at optimal temperatures for each indicator strain [15]. Finally, the diameters of the inhibition zones were measured in millimeters to assess antibacterial efficacy.

2.5 Qualitative-quantitative Determination of EPS

For exopolysaccharide (EPS) screening, a modified version of the test tube method originally developed by Christensen et al. was employed. *L. plantarum* strains were inoculated into MRS medium at a concentration of 1% and cultured in 6-well polystyrene plates at 37 °C for 24 hours. Following incubation, biofilms formed on the bottom and lateral surfaces of the wells were stained using crystal violet. Excess stain was removed by rinsing the wells with phosphate-buffered saline (PBS), after which residual spots were eliminated. The presence of a visible film on the base and walls of the wells was considered indicative of biofilm formation [16].

For EPS production assessment, the strains were cultured on Congo Red Agar (CRA) medium composed of 37 g/L BHI agar, 0.8 g/L Congo Red, and 36 g/L sucrose [17]. Strains were streaked onto CRA plates and incubated at 37 °C for 24–48 hours to distinguish EPS-producing from non-producing strains. Colonies exhibiting a black, dry, and crystalline texture were classified as EPS-positive, whereas pink, smooth colonies were deemed EPS-negative [18]. Pure cultures of *L. plantarum* were subsequently obtained, and quantitative EPS production was evaluated [19]. For this, activated cultures were incubated in MRS broth at 37 ± 1 °C for 24–48 hours. Cell pellets were then resuspended in 1 mL of sterile distilled water, and EPS content was quantified using the phenol-sulfuric acid method [20]. Absorbance measurements were recorded at 490 nm in triplicate. A standard glucose calibration curve, generated using glucose concentrations ranging from 0–100 mg/L, was employed to calculate EPS concentrations, expressed in mg/L, based on the corresponding absorbance values.

To further assess biofilm formation, bacterial suspensions standardized to approximately 1×10^8 CFU/mL (equivalent to 0.5 McFarland standard) were inoculated into BHI medium supplemented with 1% glucose. These were transferred to 96-well microtiter plates and incubated at 37 °C for 24 hours. After incubation, wells were washed with PBS and dried at 60 °C for one hour. To stain the biofilm layer, 150 µL of crystal violet was added to each well and left for 15 minutes. Excess dye was removed by washing with PBS, followed by drying. Then, 150 µL of methanol was added to solubilize the dye retained in the biofilm layer. Absorbance was measured at 590 nm using a microplate reader. Wells containing only BHI and 1% glucose served as negative controls and were analyzed in triplicate [21].

2.6 Statistical Analysis

The data obtained in this study are presented as mean values accompanied by their standard errors (mean ± SEM), and all graphical representations were prepared accordingly. Each analysis was conducted in a minimum of three replicates. Statistical comparisons were made between each *L. plantarum* strain and the reference *L. plantarum* STD strain. One-way ANOVA was performed followed by Dunnett's multiple comparison test to assess statistical significance. A p-value of less than 0.05 was considered statistically significant. Significance levels were denoted using asterisks as follows: $P < 0.05$ (significant, *), $P < 0.01$ (very significant, **), $P < 0.001$ and $P < 0.0001$ (extremely significant, ***), while $P > 0.05$ was considered not significant (ns).

3 RESULTS AND DISCUSSION

3.1 *L. plantarum* Isolation and Preliminary Identification

Gram staining reaction, colony morphology, and catalase activity of LAB isolates obtained as pure culture were examined. Colony appearances of isolates in petri dishes can be distinguished by white-cream color. Colony images formed after inoculated MRS agar petri dishes and 48 hours of incubation are given in Figure 1a. As a result of Gram staining, 125 isolates were determined to be Gram positive. Microscopic image of suspected *L. plantarum* obtained in Gram staining is given in Figure 1b.

LAB form hydrogen peroxide (H_2O_2) from oxygen derivatives formed as a result of oxidative stress, but due to the lack of catalase enzyme, they cannot break down hydrogen peroxide into oxygen and H_2O. Catalase feature is used as a simple method in LAB determination. After morphological examination, catalase test was performed on the isolates used in the study and it was determined that all 125 isolates were catalase negative. When the microscopic features of the strains were examined, it was determined that 51 bacteria were bacilli and the remaining 74 strains were cocci.

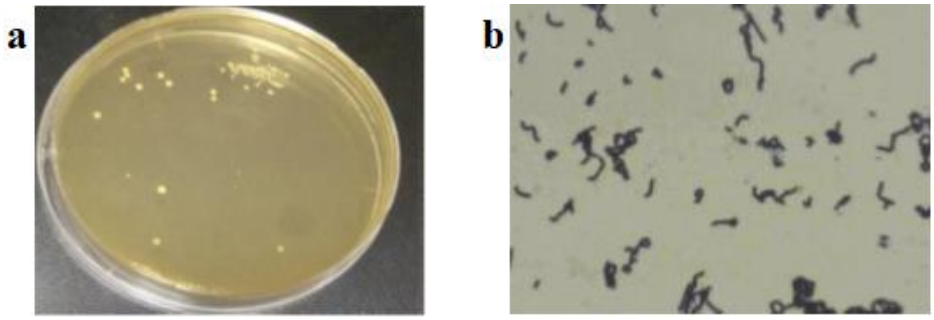


Figure 1. a: Colony image of lactic acid bacteria inoculated on MRS agar petri dishes. b: Gram stain image of lactic acid bacteria strain

The basis of the traditional classification in the identification of lactic acid bacteria is based on phenotypic methods including the investigation of morphological, physiological and metabolic/biochemical properties such as arginine degradation at different temperatures, pH values, development in salt concentrations and carbohydrate catabolism [22]. In our study, 125 LAB were isolated from 117 yogurt samples by considering these phenotypic methods and stored at -20°C to be used in subsequent studies. Table 1 provides information about the places where yoghurt samples were collected and the strains isolated.

3.2 Amplification of *rec A* Gene Regions of Isolates by PCR

The identification and characterization of LAB is gaining importance in scientific and industrial terms. In order to identify *L. plantarum*, in addition to classical methods that include determination of their physiological, morphological and biochemical properties, phage types and antibiotic susceptibilities and serological typing, molecular biology techniques such as PCR, ,DNA sequencing analysis, Restriction Fragment Length Polymorphism, Pulsed Field Gel Electrophoresis, Sodium Dodecyl Sulfate Polyacrylamide Gel Electrophoresis and Restriction Analysis of Amplified rDNA have also been reported to be used [23]. Primer pairs (planF-planR) were synthesized to amplify the *recA* gene region by PCR for *L. plantarum*. The aim of the PCR reaction in *L. plantarum* species was to amplify the 318 bp region. PCR products amplified under PCR operating conditions were visualized on 1% agarose gel (Figure 2).

Table 1. Isolate numbers of lactic acid bacteria obtained from yogurt samples collected from different regions

Place	Number of Yogurts	Number of LAB Isolates	Number of *L. plantarum*
Karaağaçlı Town	25	23	8
Sungu Town	16	13	5
Tandoğan Village	11	11	2
Yarpuzlu Village	10	12*	7
Güzeltepe Village	13	12	5
Suvaran Village	9	14*	2
Sazlıkbaşı Village	33	40*	11
Total	117	125	40

** More than one microorganism was obtained from the same yoghurt sample. Only one colony was taken and stored.*

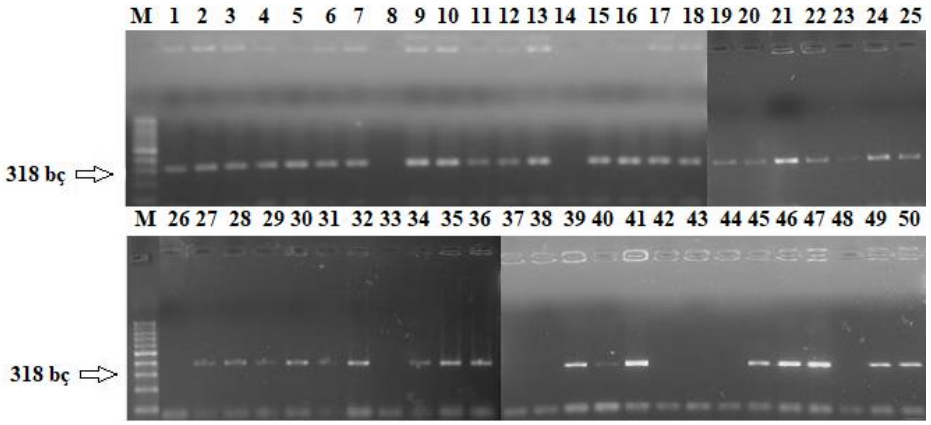


Figure 2. Agarose gel image obtained by PCR amplification of lactic acid bacteria isolated from natural yoghurts. M: 100 bp DNA standard

In the molecular identification of different Lactobacillus species *L. paraplantarum*, *L. plantarum* and *L. pentosus*, *recA* gene region primers were used. According to PCR results, recA gene region primers copied a 318 bp region for *L. plantarum*, while this gene copied a 107 bp region for *L. paraplantarum* and a 218 bp region for *L. pentosus* [24]. The isolated LAB were identified using the *recA* gene region primer by molecular method. As a result of the PCR identification of the obtained isolates, a total of 40 suspicious *L. plantarum* isolates giving a DNA band at 318 bp were obtained. In the study, isolates that could be *L. plantarum* strains were identified and confirmed by biochemical and molecular methods. It was determined that the obtained findings were equivalent to the literature information.

3.3 Antibiotic Resistance Properties of Isolates

In this part of the study, the resistance-sensitivity results of the isolated bacteria to 6 different antibiotics such as Erythromycin (15µg), Kanamycin (30µg), Penicillin (10µg), Chloramphenicol (30µg), Gentamicin (10µg), Trimethoprim (5µg) were determined. The zone image of *L. plantarum* isolates showing resistance and sensitivity to antibiotics is given in Figure 3a and the heat graph created with the obtained data is given in Figure 4.

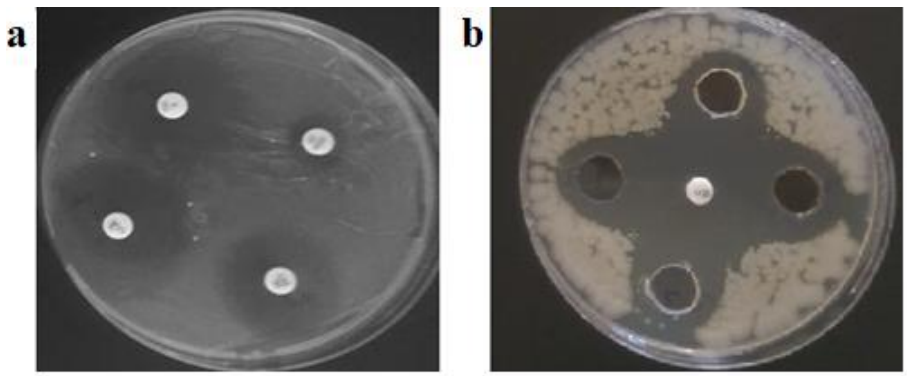


Figure 3. a: Zone images obtained as a result of determining the antibiotic resistance properties of the isolates by the disk diffusion method. b: Zone images obtained from the well agar method of determining the resistance properties of isolates on other bacteria

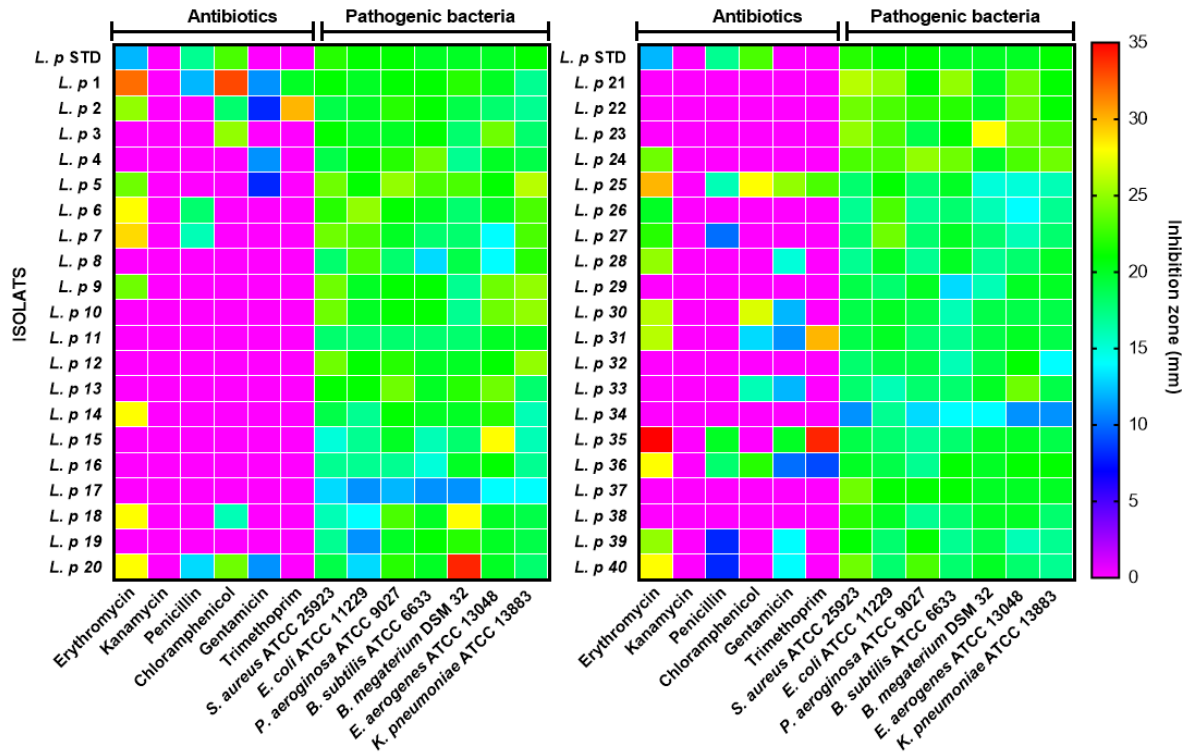


Figure 4. The antibiotic resistance profiles and antibacterial activities of L. plantarum STD and L. plantarum strains were evaluated

L. plantarum strains 8, 10, 11, 12, 13, 15, 16, 17, 19, 21, 22, 23, 29, 32, 34, 37 and 38 were found to be resistant to all antibiotics. It was determined that these strains corresponded to 42.5% of the total isolates. It was determined that *L. plantarum* isolate 35 was most sensitive to erythromycin and trimethoprim and resistant to kanamycin and chloramphenicol. Among the isolates, strains 25, 35 and 36 showed the highest sensitivity to antibiotics. When the resistance-sensitivities to each antibiotic were evaluated separately, *L. plantarum* isolate 36 showed a highly significant difference from *L. plantarum* STD against chloramphenicol. In addition, *L. plantarum* 2, 31 and 35 isolates showed a highly significant difference against trimethoprim ($P<0.0001$).

They stated that the antibiotic resistance profiles of *Lactobacillus*, *Lactococus* and *Bifidobacterium* were quite different [25]. They found that some LAB showed high natural resistance to vancomycin, cefoxitin, kanamycin, ciprofloxacin, fusidic acid, nitrofurantoin gentamicin, streptomycin, metronidazole, norfloxacin and bacitracin. However, they stated that LAB were generally sensitive to penicillin (piperacillin and ampicillin) and ß-lactamase inhibitors, but very resistant to oxacillin and cephalosporins [26]. In studies, Lactobacilli are generally sensitive to antibiotics that inhibit protein synthesis, such as erythromycin, clindamycin, chloramphenicol and tetracycline, and resistant to aminoglycosidases, such as gentamicin, streptomycin, neomycin and kanamycin [27]-[29]. The susceptibility of LAB

isolated from yogurt to chloramphenicol, erythromycin, penicillin G, gentamicin, vancomycin, streptomycin, kanamycin, and tetracycline was determined [42]. Some researchers also found that *Leu. mesenteroides* strains were resistant to tetracycline and streptomycin [43]. All isolates in this study were resistant only to kanamycin, and the resistance and susceptibility of the isolates to antibiotics varied.

3.4 Effects of Isolates on Other Microorganisms

The antibacterial effects of *L. plantarum* isolates isolated from yogurt were determined by the slurry agar diffusion test. The zone image of *L. plantarum* isolates showing resistance and susceptibility properties against the test bacteria is given in Figure 3b and the heat graph created with the obtained data is given in Figure 4. High general inhibitory effects of *L. plantarum* strains on test bacteria were seen on *E. aerogenes*, *S. aureus*, *P. aeruginosa*, *B. megaterium*, *E. coli*, *K. pneumoniae* and *B. subtilis* respectively. When evaluated statistically, *L. plantarum* strains 5, 9, 10, 12, 21, 22, 23 and 24 showed highly significant differences due to their good activities against test bacteria ($P<0.0001$). Statistically, the ranking of these strains is as follows; 5=23>21 >24 >22 >12 >10 >9. The isolate showing the least antibacterial effect on all pathogenic bacteria used in this study was isolate number 34. It was determined that strains 5 and 23 showed the most antibacterial effect among *L. plantarum*.

A very strong antimicrobial effect was observed on *S. aureus* from lactic acid bacteria isolated from fermented food. It was reported that it was not effective on *E. coli* and had a weak antimicrobial effect on *L. monocytogenes* [30]. It was found that *L. curvatus* had a strong antimicrobial effect on *S. aureus* but a weak antimicrobial effect on *E. coli* [31]. In our study, one of the best activities was against *S. aureus*, and one of the weak activities was against *E. coli*, and it can be said that it is partially similar to the literature. It was determined that *Lactobacillus* spp. isolated from dairy products showed high antagonistic activity against pathogenic bacteria [44], [45]. They isolated and identified lactobacilli from natural yogurts and it was determined that the isolates showed antimicrobial activity against *E. coli* and *S. aureus* [46]. They stated that the antimicrobial activities of the lactic acid bacteria they isolated might be due to free or cell-bound metabolites [47], [48]. It is thought that the different results obtained in our study might be due to the metabolites synthesized by the strains.

3.5 Qualitative-quantitative Determination of EPS

The study was carried out with 20 *L. plantarum* isolates (*L. plantarum* isolates 1, 2, 5, 7, 9, 10, 12, 14, 15, 16, 20, 21, 22, 23, 24, 25, 29, 32, 35 and 36) with high and low antibiotic resistance and activities on microorganisms and *L. plantarum* STD. The tube method, a qualitative assay, was employed to evaluate biofilm formation along the bottom and walls of the test tubes. Compared to the control, the wells containing the cultivated strains exhibited more intense crystal violet staining, indicating a higher production of exopolysaccharides (EPS) (Figure 5A). Additionally, following 72 hours of incubation on CRA, both *L. plantarum* and *L. plantarum* STD isolates developed black, dry, crystalline colonies, further confirming their capability to produce EPS (Figure 5B).

The strains and the standard strain (STD) exhibited varying optical density (OD) values in the microtiter plate assay, reflecting differences in their EPS production levels (Figure 6). Among the isolates, *L. plantarum* strain 23 produced the highest amount of EPS (318.30 ± 1.28 mg/L), whereas *L. plantarum* strain 16 yielded the lowest (205.70 ± 1.44 mg/L). It was found that *L. plantarum* strains 2, 5, 7, 9, 10, 12, 14, 21, 22, 23, 24, 32 and 35 showed a highly significant difference by producing more EPS than *L. plantarum* STD ($P<0.0001$) (Figure 6B). Statistically, the ranking of these strains is; It is as follows: 23>21 >5 >12 >10 > 24 >9 >2 >14 >32 >22 >35 >7.

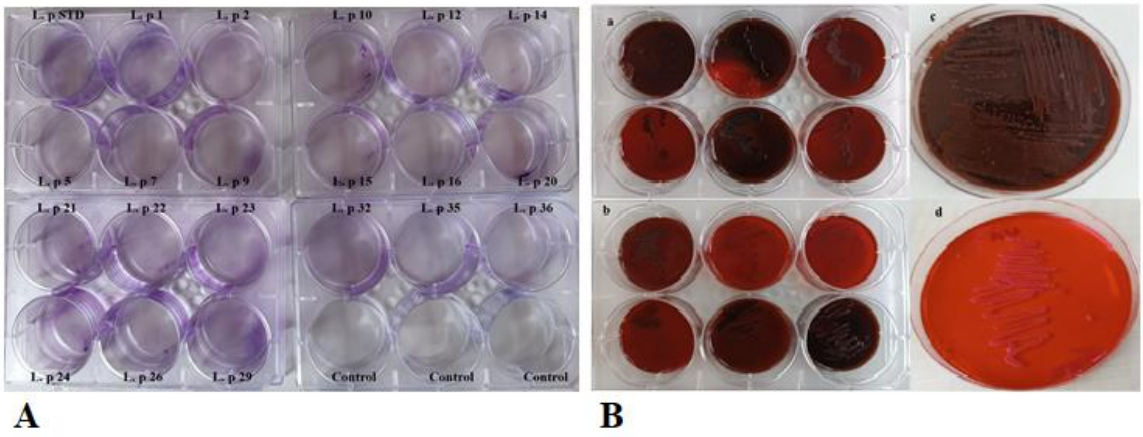


Figure 5. A: Image of a visible film of biofilm-forming bacteria. B: Image of EPSs produced by strains in CRA in six well plate and petri dish. (a, b) Those that form black and dry crystalline colonies in 6 well plate medium are positive, those that do not are negative, (c) Positive, (d) Negative

LABs are widely regarded as safe for consumption, present no health hazards, display substantial genetic and phenotypic diversity, and possess the ability to synthesize exopolysaccharides (EPS) [32].The presence of EPS synthesized by LAB has been verified

through both qualitative and quantitative methods [33]. In the present study, EPS production by the isolated strains was similarly confirmed using established analytical techniques, consistent with findings reported in the literature. For example, Li et al. reported that the maximum EPS yield of *L. plantarum* cultured in MRS medium was below 290.17 mg/L [34]. Other investigations have demonstrated that EPS production among *L. plantarum* strains varies between 75 and 397 mg/L [35], with *L. plantarum* producing up to 280 mg/L [36]. Furthermore, *L. plantarum* strains isolated from human breast milk were shown to produce EPS within a range of 243.30 ± 1.26 to 259.60 ± 1.53 mg/L [37]. Among the isolates analyzed in this study, *L. plantarum* 23 exhibited the highest EPS production at 318.30 ± 1.28 mg/L, while *L. plantarum* 16 produced the lowest amount, measured at 205.70 ± 1.44 mg/L. Overall, the EPS yields of the isolates were relatively consistent. These findings suggest that the EPS production levels of the studied strains fall within the range reported for *L. plantarum* isolates in previous studies.

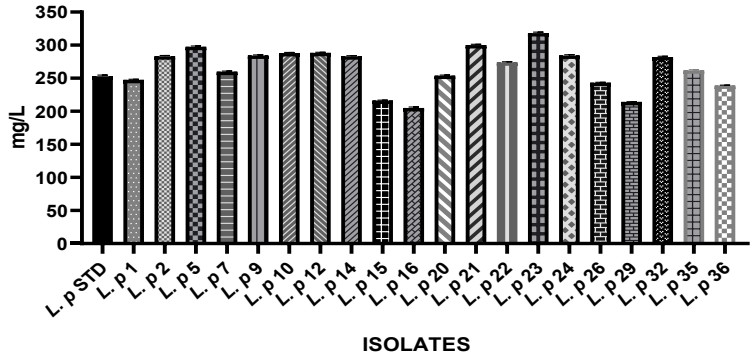


Figure 6. EPS production levels of L. plantarum strains isolated from yoğurt

4 CONCLUSION

Naturally made yoghurt samples were collected from different regions of Muş province and LABs were isolated. Preliminary identification of these isolates (colony morphology, catalase, gram staining) and PCR identification using *recA* gene sequence were performed and as a result, a total of 40 suspected *L. plantarum* strains were detected. 42.5% of our *L. plantarum* strains were found to be resistant to all antibiotics. It was determined that strains 25, 35 and 36 showed the highest sensitivity to antibiotics among the isolates. While isolate 34 showed the least antibacterial effect on pathogenic bacteria, it was determined that strains 5 and 23 showed the highest antibacterial effect. EPSs synthesized by the strains were determined qualitatively and quantitatively. Moreover, *L. plantarum* strain 23 was identified as the highest EPS producer,

yielding 318.30 ± 1.28 mg/L, whereas *L. plantarum* strain 16 exhibited the lowest EPS production at 205.70 ± 1.44 mg/L. In line with these results, it is thought that *L. plantarum* strains 23 and 5 found in yoghurt will contribute to human health by preventing the development of pathogens that harm human flora due to their properties.

Conflict of Interest Statement

There is no conflict of interest between the authors.

Statement of Research and Publication Ethics

The study is complied with research and publication ethics.

Artificial Intelligence (AI) Contribution Statement

This manuscript was entirely written, edited, analyzed, and prepared without the assistance of any artificial intelligence (AI) tools. All content, including text, data analysis, and figures, was solely generated by the authors.

Contributions of the Authors

Yusuf ALAN: Conceptualization, Methodology, Validation, Data curation, Visualization, and Investigation Writing- Reviewing and Editing.

Kayhan MANĞ: Conceptualization, Methodology, Formal Analysis, and Investigation Writing Original Draft Preparation.

REFERENCES

[1] A. K. Rashwan *et al.*, "Chemical composition, quality attributes and antioxidant activity of stirred-type yogurt enriched with *Melastoma dodecandrum* Lour fruit powder," *Food Funct.*, vol. 13, no. 3, pp. 1579–1592, 2022.

[2] A. Wijesekara, V. Weerasingha, S. Jayarathna, and H. Priyashantha, "Quality parameters of natural phenolics and its impact on physicochemical, microbiological, and sensory quality attributes of probiotic stirred yogurt during the storage," *Food Chem. X*, vol. 14, no. 100332, p. 100332, 2022.

[3] K. Shirani, F. Falah, A. Vasiee, F. T. Yazdi, B. A. Behbahani, and H. Zanganeh, "Effects of incorporation of Echinops setifer extract on quality, functionality, and viability of strains in probiotic yogurt," *J. Food Meas. Charact.*, vol. 16, no. 4, pp. 2899–2907, 2022.

[4] N. Tarannum, T. J. Hossain, F. Ali, T. Das, K. Dhar, and I. H. Nafiz, "Antioxidant, antimicrobial and emulsification properties of exopolysaccharides from lactic acid bacteria of bovine milk: Insights from biochemical and genomic analysis," *Lebenson. Wiss. Technol.*, vol. 186, no. 115263, p. 115263, 2023.

[5] N. Tarannum, T. J. Hossain, F. Ali, T. Das, K. Dhar, and I. H. Nafiz, "Antioxidant, antimicrobial and emulsification properties of exopolysaccharides from lactic acid bacteria of bovine milk: Insights from biochemical and genomic analysis," *Lebenson. Wiss. Technol*., vol. 186, no. 115263, p. 115263, 2023.

[6] C. Li *et al.*, "Influence of *Lactobacillus plantarum* on yogurt fermentation properties and subsequent changes during postfermentation storage," *J. Dairy Sci.*, vol. 100, no. 4, pp. 2512–2525, 2017.

[7] S. Yeğin and A. Üren, "Biogenic amine content of boza. A Traditional Cerealbased Fermented Turkish Beverage," *Food Chemistry*, 2008.

[8] E. Gheytanchi, F. Heshmati, B. K. Shargh, J. Nowroozi, and F. Movahedzadeh, "Study on β-galactosidase enzyme produced by isolated lactobacilli from milk and cheese," *African Journal of Microbiology Research*, vol. 4, no. 6, pp. 454–458, 2010.

[9] H. Sağlam, *Tanımlanmış Lactobacıllus plantarum suşlarının plazmit profilleri ve bunların bazı özelliklerinin belirlenmesi. Doktora Tezi*. Süleyman Demirel Üniversitesi, 2013.

[10] M. Mandel and A. Higa, "Calcium-dependent bacteriophage DNA infection," *J. Mol. Biol.*, vol. 53, no. 1, pp. 159–162, 1970.

[11] C. H. Collins, P. M. Lyne, and J. M. Grange, *Microbiological Methods. Sixth Edition, Butterworths and Co. Ltd. 410s*. London, 1989.

[12] W. P. Hammes and R. F. Vogel, *The genus Lactobacillus. ın the genera of lactic acid bacteria*. London: Chapman & Hall, 1995.

[13] G. Spano, L. Beneduce, D. Tarantino, G. Zapparoli, and S. Massa, "Characterization of *Lactobacillus plantarum* from wine must by PCR species-specific and RAPD-PCR 2002 American Society for Microbiology," *All Rights Reserved*, vol. 67, no. 8, pp. 3450–3454, 2002.

[14] *NCCLS (National committee for clinical laboratory standards). performance standards for antimicrobial susceptibility testing, The th International Supplement*. Villanova, PA, 1999.

[15] O. Pringsulaka, N. Thongngam, N. Suwannasai, W. Atthakor, K. Pothivejkul, and A. Rangsiruji, "Partial characterisation of bacteriocins produced by lactic acid bacteria isolated from Thai fermented meat and fish products," *Food Control*, vol. 23, no. 2, pp. 547–551, 2012.

[16] G. D. Christensen *et al.*, "Adherence of coagulase-negative staphylococci to plastic tissue culture plates: a quantitative model for the adherence of staphylococci to medical devices," *J. Clin. Microbiol.*, vol. 22, no. 6, pp. 996–1006, 1985.

[17] D. J. Freeman, F. R. Falkiner, and C. T. Keane, "New method for detecting slime production by coagulase negative staphylococci," *J. Clin. Pathol.*, vol. 42, no. 8, pp. 872–874, 1989.

[18] M. DuBois, K. A. Gilles, J. K. Hamilton, P. A. Rebers, and F. Smith, "Colorimetric method for determination of sugars and related substances," *Anal. Chem.*, vol. 28, no. 3, pp. 350–356, 1956.

[19] V. M. Marshall and H. L. Rawson, "Effects of exopolysaccharide producing strains of thermophilic lactic acid bacteria on the texture of stirred yoghurt," *Int. J. Food Sci. Technol.*, vol. 34, no. 2, pp. 137–143, 1999.

[20] M. I. Torino, M. P. Taranto, F. Sesma, and G. F. de Valdez, "Heterofermentative pattern and exopolysaccharide production by *Lactobacillus helveticus* ATCC 15807 in response to environmental pH," *J. Appl. Microbiol.*, vol. 91, no. 5, pp. 846–852, 2001.

[21] S. Stepanović *et al.*, "Quantification of biofilm in microtiter plates: overview of testing conditions and practical recommendations for assessment of biofilm production by staphylococci," *APMIS*, vol. 115, no. 8, pp. 891–899, 2007.

[22] M. Gobbetti, M. De Angelis, A. Corsetti, and R. Di Cagno, "Biochemistry and physiology of sourdough lactic acid bacteria," *Trends Food Sci. Technol.*, vol. 16, no. 1–3, pp. 57–69, 2005.

[23] U. Busch and H. Nitschko, "Methods for the differentiation of microorganisms," *J. Chromatogr.*, vol. 722, no. 1–2, pp. 263–278, 1999.

[24] S. Torriani, G. E. Felis, and F. Dellaglio, "Differentiation of *Lactobacillus plantarum*, *L. pentosus*, and *L. paraplantarum* by *recA* gene sequence analysis and multiplex PCR assay with recA gene derived primers," *Applied and Environmental Microbiology*, vol. 67, no. 8, pp. 3450–3454, 2001.

[25] M. S. Ammor, A. B. Florez, and B. Mayo, "Antibiotic resistance in nonenterococcal lactic acid bacteria and bifidobacteria," *Food Microbiology*, vol. 24, no. 6, pp. 559–570, 2007.

[26] M. Danielsen and A. Wind, "Susceptibility of Lactobacillus spp. to antimicrobial agents," *Int. J. Food Microbiol.*, vol. 82, no. 1, pp. 1–11, 2003.

[27] W. P. Charteris, P. M. Kelly, L. Morelli, and J. K. Collins, "Antibiotic susceptibility of potentially probiotic *Lactobacillus* species," *J. Food Prot.*, vol. 61, no. 12, pp. 1636–1643, 1998.

[28] R. Coppola, M. Succi, P. Tremonte, A. Reale, G. Salzano, and E. Sorrentino, "Antibiotic susceptibility of *Lactobacillus rhamnosus* strains isolated from Parmigiano Reggiano cheese," *Lait*, vol. 85, no. 3, pp. 193–204, 2005.

[29] J. S. Zhou, C. J. Pillidge, P. K. Gopal, and H. S. Gill, "Antibiotic susceptibility profiles of new probiotic *Lactobacillus* and *Bifidobacterium* strains," *Int. J. Food Microbiol.*, vol. 98, no. 2, pp. 211–217, 2005.

[30] A. H. Con and H. Y. Gökalp, "Production of bacteriocin-like metabolites by lactic acid cultures isolated from sucuk samples," *Meat Sci.*, vol. 55, no. 1, pp. 89–96, 2000.

[31] T. R. Klaenhammer, "Bacteriocins of lactic acid bacteria," *Biochimie*, vol. 70, no. 3, pp. 337–349, 1988.

[32] U. Surayot *et al.*, "Exopolysaccharides from lactic acid bacteria: Structural analysis, molecular weight effect on immunomodulation," *Int. J. Biol. Macromol.*, vol. 68, pp. 233–240, 2014.

[33] J. Murugu and R. Narayanan, "Production, purification, and characterization of a novel exopolysaccharide from probiotic *Lactobacillus amylovorus*: MTCC 8129," *Indian J. Microbiol.*, vol. 64, no. 3, pp. 1355–1365, 2024.

[34] S. Li, R. Huang, N. P. Shah, X. Tao, Y. Xiong, and H. Wei, "Antioxidant and antibacterial activities of exopolysaccharides from *Bifidobacterium bifidum* WBIN03 and *Lactobacillus plantarum* R315," *J. Dairy Sci.*, vol. 97, no. 12, pp. 7334–7343, 2014.

[35] R. Prete, M. K. Alam, G. Perpetuini, C. Perla, P. Pittia, and A. Corsetti, "Lactic acid bacteria exopolysaccharides producers: A sustainable tool for functional foods," *Foods*, vol. 10, no. 7, p. 1653, 2021.

[36] L. Zhang, B. Zhao, C.-J. Liu, and E. Yang, "Optimization of biosynthesis conditions for the production of exopolysaccharides by *Lactobacillus plantarum* SP8 and the exopolysaccharides antioxidant activity test," *Indian J. Microbiol.*, vol. 60, no. 3, pp. 334–345, 2020.

[37] Y. Alan, A.-O. Keskin, and M. Sönmez, "Probiotic and functional characterization of newly isolated *Lactiplantibacillus plantarum* strains from human breast milk and proliferative inhibition potential of metabolites," *Enzyme Microb. Technol.*, vol. 182, no. 110545, p. 110545, 2025.

[38] J. Zhang, Y. Xiao, H. Wang, H. Zhang, W. Chen, and W. Lu, "Lactic acid bacteria derived exopolysaccharide: Formation, immunomodulatory ability, health effects, and structure-function relationship," *Microbiological Research*, 2023.

[39] Y. Xu *et al.*, "Exopolysaccharides produced by lactic acid bacteria and Bifidobacteria: Structures, physiochemical functions and applications in the food industry," *Food Hydrocoll.*, vol. 94, pp. 475–499, 2019.

[40] K. E. M. El Kahlout, I. M. El Quqa, M. W. El Hindi, and T. A. El Bashiti, "Isolation, Biochemical Characterization and DNA Identification of Yogurt Starters *Streptococcus thermophilus* & *Lactobacillus delbrueckii ssp. bulgaricus* in Gaza Strip," *Adv. Microbiol.*, vol. 08, no. 12, pp. 1005–1020, 2018.

[41] R. Prete, M. K. Alam, G. Perpetuini, C. Perla, P. Pittia, and A. Corsetti, "Lactic acid bacteria exopolysaccharides producers: a sustainable tool for functional foods," *Foods*, vol. 10, no.1653, 2021.

[42] N. T. Demirok, M. Alpaslan, and S. Yıkmış, "Some lactobacillus, leuconostoc and acetobacter strains in traditional turkish yoghurt, cheese, kefir samples as a probiotic candidate," *International Journal of Agriculture Environment and Food Sciences*, vol. 7, no. 2, pp. 326–334, 2023.

[43] A. Akpinar and O. Yerlikaya, "Some potential beneficial properties of *Lacticaseibacillus paracasei s*ubsp. *paracasei* and *Leuconostoc mesenteroides* strains originating from raw milk and kefir grains," *J. Food Process. Preserv.*, vol. 45, no. 12, 2021.

[44] N. A. Abosereh, S. A. E. Ghani, R. S. Gomaa, and M. T. Fouad, "Molecular identification of potential probiotic lactic acid bacteria strains isolated from Egyptian traditional fermented dairy products," *Biotechnology (Faisalabad)*, vol. 15, no. 1–2, pp. 35–43, 2015.

[45] M. B. Pisano *et al.*, "Inhibitory Effect of *Lactiplantibacillus plantarum* and *Lactococcus lactis* Autochtonous Strains against *Listeria monocytogenes* in a Laboratory Cheese Model," *Foods*, vol. 11, no. 5, p. 715, 2022.

[46] P. Rajarajan, K. Amudha, R. Gupta, S. Labiyan, G. Prasad, and M. Tejaswini, "In vitro evaluation of antimicrobial activity and probiotic potential of *Lactobacillus* strains against some human pathogen," *Recent Research in Science and Technology*, vol. 10, pp. 31–35, 2018.

[47] H. Yazgan, E. Kuley, T. Güven Gökmen, J. M. Regenstein, and F. Özogul, "The antimicrobial properties and biogenic amine production of lactic acid bacteria isolated from various fermented food products," *J. Food Process. Preserv.*, vol. 45, no. 1, 2021.

[48] O. F. Celik,, A. H. Con, H. Saygin, N. Şahin, and H. Temiz, "Isolation and identification of lactobacilli from traditional yogurts as potential starter cultures." *LWT*, vol. 148, no.111774, 2021.

BİTLİS EREN ÜNİVERSİTESİ
FEN BİLİMLERİ DERGİSİ

ISSN: 2147-3129 / e-ISSN: 2147-3188

Article Type : Research Article
Received : May 16, 2025
Revised : September 22, 2025
Accepted : September 27, 2025
DOI : 10.17798/bitlisfen.1698675

Year : 2025
Volume : 14
Issue : 3
Pages : 1688-1701

THE EFFECT OF BORIDING ON THE WEAR BEHAVIOR OF AISI 8620 STEEL

Selcuk ATASOY [1], **Hasan Onur TAN** [1,*], Hakan ADATEPE [1], Sıtkı AKTAŞ [1], İbrahim GÜNEŞ [2]

[1] *Giresun University, Mechanical Engineering Department, Giresun, Türkiye*

[2] *Giresun University, Civil Engineering Department, Giresun, Türkiye*

**** Corresponding Author:*** *hasan.tan@giresun.edu.tr*

ABSTRACT

In this study, AISI 8620 steel-commonly used in the gear manufacturing industry—was subjected to a box boriding treatment using commercial Ekabor II powder. The process was carried out in an electric resistance furnace at 900 °C for a duration of 5 hours. The resulting boride layers were characterized using optical microscopy, X-ray diffraction (XRD), microhardness measurements, scanning electron microscopy (SEM), and energy-dispersive X-ray spectroscopy (EDX). A boride layer with an average thickness of 78 ± 2 µm was formed on the steel surface, consisting primarily of FeB and Fe_2B phases, and the surface hardness reached 1768 $HV_{0.05}$. The wear tests were conducted under dry sliding conditions using a ball-on-disk setup at room temperature. The experiments were performed under a constant normal load of 10 N, at rotational speeds of 300, 450, and 600 rpm, over sliding distances of 250, 500, 750, 1000, 1500, and 2000 m. The coefficient of friction ranged between 0.40 and 0.62 throughout the tests. At higher rotational speeds, a reduction in the friction coefficient was observed up to 1000 meters, after which a gradual increase occurred at longer distances. Both the sliding distance and speed significantly affected the wear behavior, resulting in an increased wear track depth and wear rate. The wear rate was found to vary between 14.52×10^{-5} and 198.82×10^{-5} $mm^3N^{-1}m^{-1}$.

Keywords: Boriding, Gear steel, Sliding distance, Wear rate, Friction coefficient.

1 INTRODUCTION

AISI 8620 steel is a low-alloy carburizing steel that is widely used in critical machine components such as gears, shafts, camshafts, and bearings, where high core toughness and surface hardness are required[1-7]. This material is particularly favored in automotive and industrial equipment for dynamically loaded parts due to its balanced strength and machinability [4, 5, 8-10]. However, under high contact pressure and abrasive conditions, the wear resistance of this steel may prove inadequate, leading to premature component failure and limiting its applicability in more demanding service environments. This presents a significant issue in industrial applications in terms of performance and durability. Therefore, a better understanding of the material's mechanical strength, impact resistance, and other properties is crucial for enhancing its performance, ensuring reliability, and expanding its range of applications [4, 5, 7, 10-16].

The development of wear-resistant materials is vital for increasing the operational efficiency and reducing the maintenance costs. Material loss, increased energy consumption, and production downtimes are chain effects that result in billions of dollars in annual economic losses across industries. In high-precision sectors such as the automotive and aerospace industries, preventing wear-induced failures has become a critical goal for sustainability and cost optimization. For this reason, investigating and implementing technologies that improve the surface properties of existing materials is of great industrial relevance [5, 6, 17].

The wear resistance of AISI 8620 steel can be significantly improved through various surface modifications and treatment methods. These techniques primarily focus on altering the surface microstructure and composition to increase hardness and reduce wear. Common techniques include thermochemical treatments, surface alloying, carburizing, laser surface processing, and electro-mechanical hardening[1, 2, 7, 10, 12, 13, 16, 18]. For instance, Triani et al. demonstrated that thermochemical treatments at 1000°C produced vanadium and niobium carbide (VC and NbC) layers on AISI 8620 steel, significantly improving its hardness and wear resistance [17]. In another study, Paraye et al. reported an increase in wear resistance by in-situ growth of titanium carbide (TiC) particles using tungsten inert gas (TIG) arcing [13]. Laser surface heat treatment is also an effective method for enhancing the wear resistance of AISI 8620 steel. This process focuses laser energy on a small area, resulting in increased surface microhardness and reduced surface roughness, thereby collectively improving wear resistance [19]. Gorlenko et al. (2019) employed electro-mechanical treatment (EMT) technology, which

involves controlling current density during processing to optimize the surface layer quality of AISI 8620 steel, thereby enhancing wear resistance [20]. However, these methods often involve high equipment costs, complex process steps, and material-geometry limitations, necessitating alternative solutions. In this context, pack boriding emerges as an economical and feasible surface hardening technique [21-23]. Pack boriding, performed in a high-temperature boriding environment, involves boron diffusion into the steel surface to form hard boride layers (FeB/Fe_2B). These layers exhibit outstanding wear resistance with hardness values ranging from 1500 to 2000 HV, along with additional benefits such as low friction coefficients and enhanced corrosion resistance. The method's low equipment investment requirements, suitability for mass production, and ability to provide uniform coatings even on complex geometries further increase its industrial appeal [14, 22, 23]. In this study, AISI 8620 steel was borided using commercial Ekabor II boron powder. The microstructure, layer thickness, surface hardness, and wear behavior of the resulting boride layer were investigated.

Given the industrial necessity for a cost-effective and scalable solution to enhance the wear resistance of commonly used steels, such as AISI 8620, this study is motivated by the need to systematically evaluate pack boriding as a viable alternative to more complex and expensive surface engineering techniques. Unlike other surface modification methods, pack boriding offers a cost-effective, scalable, and geometry-independent approach, making it highly relevant for industrial applications. In this context, the main objective of the present study is to investigate the microstructural evolution, layer thickness, surface hardness, and wear performance of borided AISI 8620 steel, thereby establishing a clear relationship between the boride layer characteristics and the resulting mechanical and tribological behavior. The findings of this study are expected to provide valuable data and a robust reference for industry practitioners seeking to implement pack boriding to extend the service life of AISI 8620 components operating in severe abrasive and adhesive wear environments.

2 MATERIAL AND METHOD

In this study, AISI 8620 steel, the chemical composition of which is presented in Table 1, was used in the form of specimens with dimensions of Ø24 × 9 mm. The boriding process was performed by the pack boriding method utilizing commercial Ekabor II powder. The commercial Ekabor II powder has a nominal chemical composition of 5% B_4C, 5% KBF_4, and 90% SiC, and was used as the boriding agent. The specimens were placed inside a cylindrical stainless steel crucible filled with Ekabor II powder. The furnace was preheated to 900°C prior

to the placement of the crucible, and the boriding treatment was carried out at this temperature for a duration of 5 h. After this process, the samples were allowed to cool naturally to room temperature. Following boriding, the surfaces of the specimens were ground and polished using silicon carbide abrasive papers ranging from 240 to 1000 grit, followed by polishing with 0.1 µm alumina suspensions. Subsequently, the samples were etched using a 3% Nital solution to reveal the microstructure. The thickness of the boride layer was determined as the arithmetic mean of measurements taken at 10 different locations using an optical microscope equipped with a measurement device. The microstructural examinations of the worn regions of the borided specimens were conducted using a scanning electron microscope. In addition, the elemental distributions within the borided layers were analyzed by energy-dispersive X-ray spectroscopy. Phase analysis of the borided surface was performed via X-ray diffraction employing CuKα radiation (λ = 1.5418 Å) over a 2θ range of 20° to 90°. Finally, microhardness measurements were carried out using the Vickers hardness tester under a load of 50 g. Measurements were taken at regular intervals, with at least 5 readings obtained for each sample, and the average hardness value was subsequently calculated.

Table 1. The chemical composition of AISI 8620 (wt. %)

Material	C	Cr	Ni	Si	Mn	Mo	S	P
AISI 8620	0.18	0.45	0.52	0.25	0.80	0.20	0.035	0.030

The wear tests were conducted at room temperature on the borided specimens. Wear tests were performed using a ball-on-disk system and WC-Co balls with a diameter of 8 mm were used. A separate wear element was used for each test to eliminate errors arising from surface degradation. The wear tests were carried out in dry sliding conditions at room temperature, under a load of 10 N, at rotational speeds of 300, 450, and 600 rpm, and over sliding distances of 250, 500, 750, 1000, 1500, and 2000 meters. Each wear test condition (combination of speed and distance) was repeated twice to ensure reproducibility. All test parameters are listed in Table 2.

Table 2. Test parameters

Applied load (N)	Sliding distance (m)	RPM		
10	250, 500, 750, 1000, 1500, 2000	300	450	600

Before and after the wear tests, each specimen and wear element were cleaned with alcohol. The wear volume of the specimens was determined by multiplying the cross-sectional area of the wear tracks, obtained using a Taylor Rugosimeter, by the circumference of the wear track. The wear rate was calculated using the following formula (1):

$$WR = \frac{WV}{SDxAL} \tag{1}$$

Where *WR* is the wear rate ($mm^3N^{-1}m^{-1}$), *WV* is the wear volume (mm^3), *SD* is the sliding distance (m) and *AL* is the applied load (N). The coefficients of friction were determined as a function of sliding distance using a program associated with the system. Based on the results of the wear tests, graphs showing the relationships between boriding temperature, sliding speed, coefficient of friction, surface roughness, and wear rate were plotted.

3 RESULTS AND DISCUSSION

3.1 Microstructure and mechanical properties

Figure 1 illustrates the cross-sectional microstructure of AISI 8620 steel subjected to pack boriding at 900 °C for 5 h, as observed under an optical microscope using commercial Ekabor II powder. As a result of the boriding process, saw-tooth shaped boride layers were formed on the specimens. A boride layer thickness of 78±2 µm was achieved in the steel cross-section. In the optical microscopy analysis, the dark regions represent the FeB phase, while the light-colored regions correspond to the Fe_2B phase. The characteristic saw-tooth or acicular morphology of the boride layer, evident in Figure 1, is a result of the anisotropic growth of boride crystals. It is well-documented in the literature that boriding of steels results in the formation of FeB and Fe_2B phases, which can be distinctly identified through microstructural examinations [24-26].

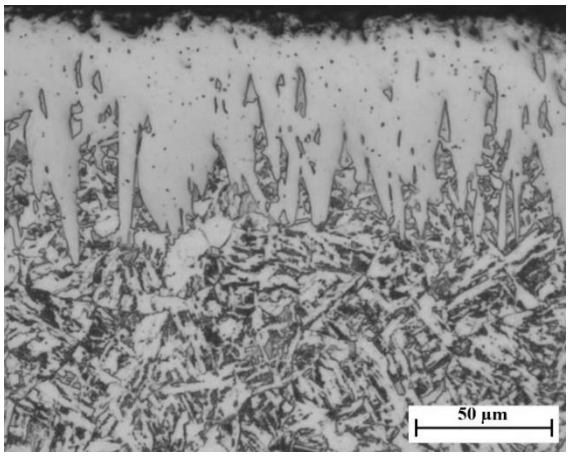


Figure 1. Cross-sectional wiev of the borided AISI8620 steel.

The boride layer thickness of AISI 8620 steel borided with Ekabor II powder was calculated as the arithmetic mean of measurements taken at 20 different locations using an apparatus connected to an Olympus BX-60 optical microscope. A boride layer thickness of 86 µm was obtained for AISI 8620 steel borided at 900°C for 5 h. The XRD results of the borided AISI 8620 steel are provided in Figure 2. As a result of the boriding process applied to AISI 8620 steel with commercial Ekabor II boron powder at 900°C for 5 h, a dual-phase (FeB + Fe_2B) boride layer was formed. The formation of a dual-phase (FeB + Fe_2B) layer at 900°C for 5 hours using Ekabor II powder is directly influenced by the high chemical activity of the boriding medium. Ekabor II contains KBF_4, which acts as an activator. This high boron potential at the material's surface promotes the formation of the boron-rich FeB phase atop the more desirable Fe_2B phase. While a single-phase Fe_2B layer is often preferred due to its lower brittleness, the process parameters and activator content in commercial powders like Ekabor II frequently result in a thin FeB outer layer, as observed in this study and is consistent with findings from other studies using activated boriding powders.

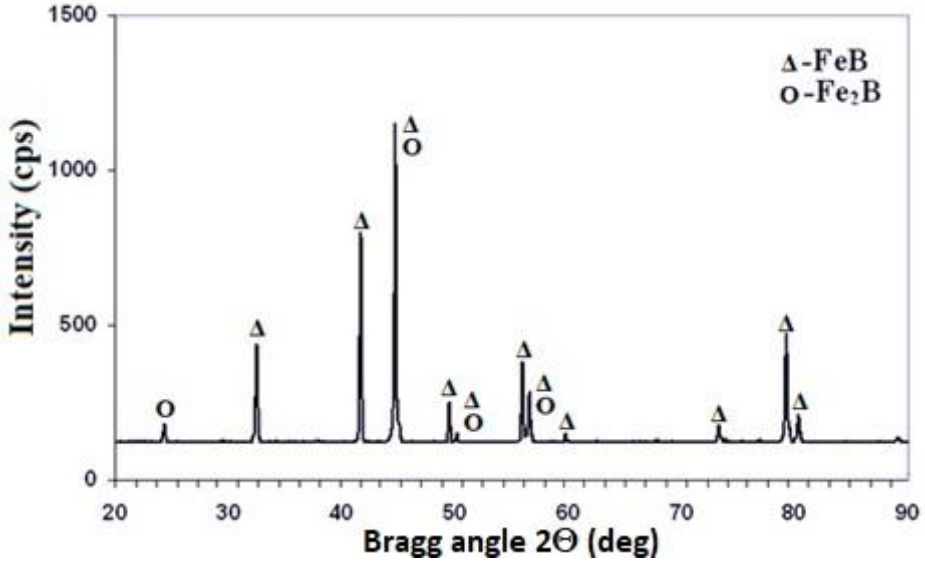


Figure 2. XRD results of borided AISI8620 steel.

The hardness distribution from the surface towards the interior of AISI 8620 steel was determined using a Vickers microhardness tester under an applied load of 50 g, and the corresponding results are presented in Figure 3. The high surface hardness is attributed to the FeB and Fe_2B phases formed as a result of the pack boriding process with Ekabor II powder. It is well known that the FeB and Fe_2B phases exhibit high hardness values [27, 28].

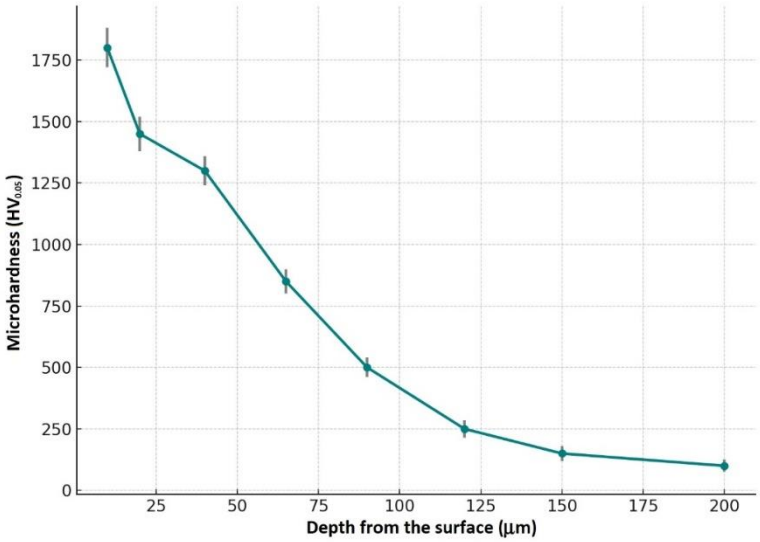


Figure 3. The cross sectional microhardness values varying with the depth for borided AISI 8620 steel.

3.2 Tribological properties

Figure 4 presents the coefficient of friction values for borided AISI 8620 steel at sliding distances of 250, 500, 750, 1000, 1500, and 2000 meters under rotational speeds of 300, 450, and 600 rpm. Generally, similar coefficient of friction values were observed at sliding speeds corresponding to 300 and 450 rpm, whereas a decrease in the coefficient of friction was noted as the speed increased to 600 rpm. This decrease can be attributed to the formation of oxides on the specimen surfaces due to surface heating caused by friction at higher sliding speeds[29]. When we examine the friction coefficient values depending on the distance traveled, we observe an increase up to 1000 meters and a slight decrease after 1000 meters. This is thought to be due to the lubricating properties of the boron layer. Similar results have been observed in the literature [29, 30].

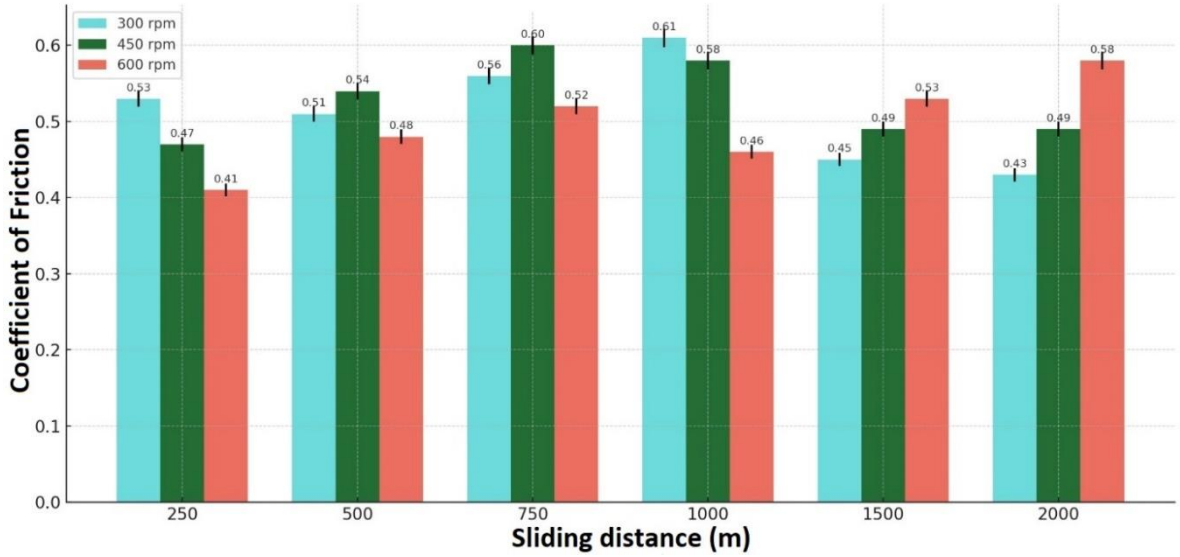


Figure 4. Changes in the coefficient of friction with distance and rotational speed.

It was observed that at 300 and 450 rpm, the wear depth increased at similar rates; however, when the rotational speed was elevated to 600 rpm, the wear depth values initially decreased up to a certain distance, followed by an increase beyond that point. This behavior may be attributed to the formation of an oxide film on the specimen surfaces as a result of frictional heating at high sliding speeds. The oxide film serves as a protective layer against friction and wear. Nevertheless, as the wear distance increases, the oxide film grows to a critical thickness, leading to the formation of protrusions and subsequent fracture. The resulting hard debris acts as a third body, initiating and exacerbating abrasive wear. With increasing wear distance, oxide particles progressively contributed to greater wear depth, particularly at longer sliding distances. An increase in wear rates was observed with increasing wear distance and rotational speed. The lowest wear rate was recorded for the specimen tested at 250 meters and 300 rpm, while the highest wear rate was observed for the specimen tested at 2000 meters and 600 rpm.

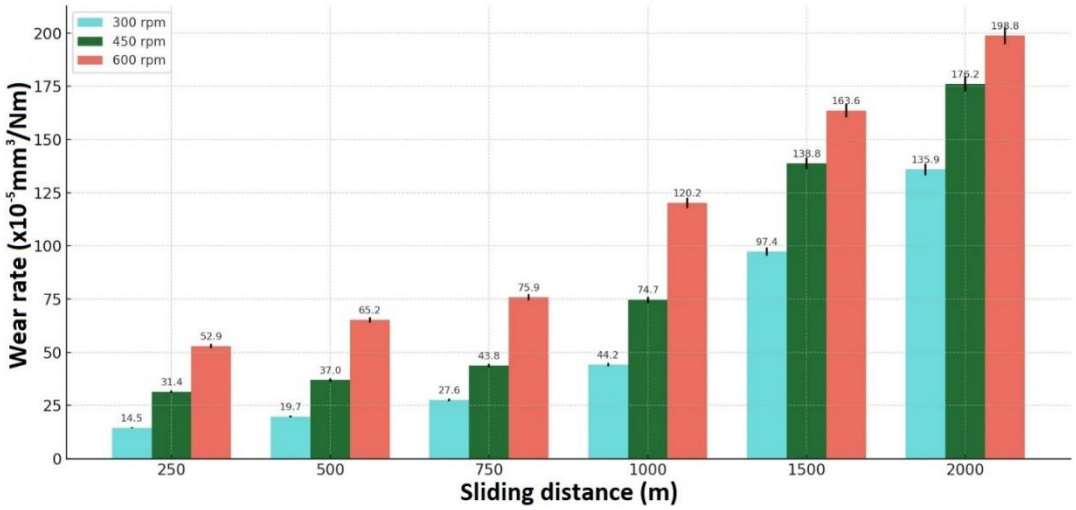


Figure 5. Variation of wear depth at different distances and rotational speeds.

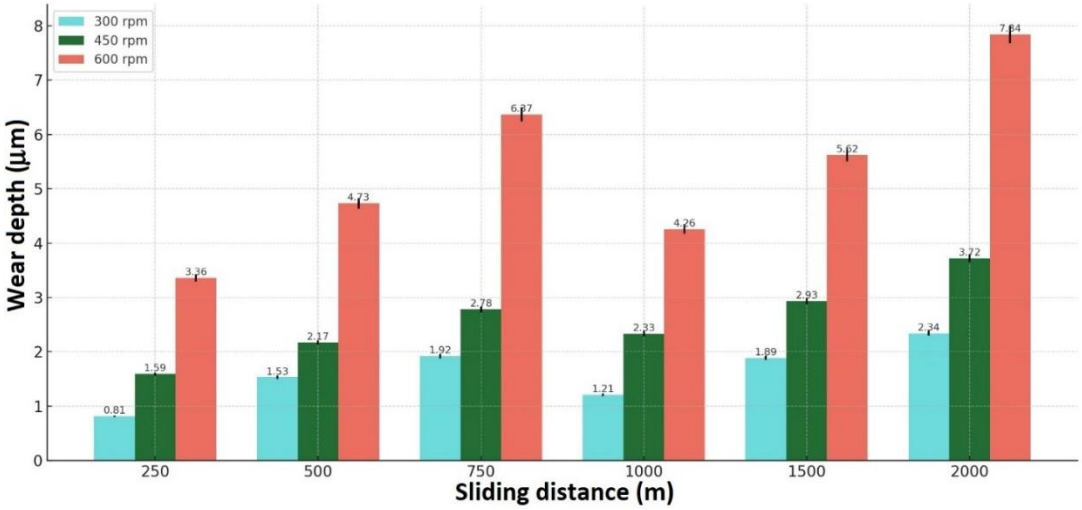


Figure 6. Changes in wear rate with respect to distance and rotational speed.

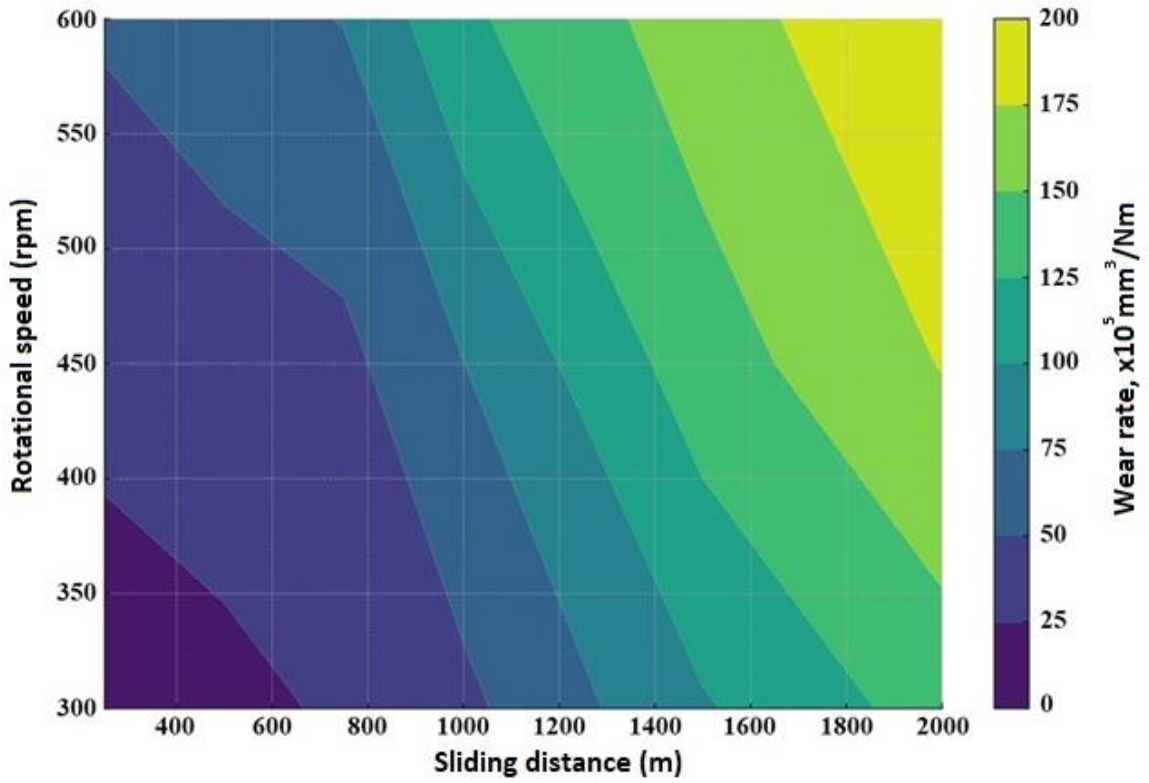


Figure 7. Variation of wear rate at different rotational speeds and wear distances.

Figure 8 a-f illustrates the SEM microstructures of the wear surfaces of AISI 8620 steel specimens worn at 600 rpm over different sliding distances, 250 m, 500 m, 750 m, 1000 m, 1500 m and 2000 m respectively. In this figure, it is observed that the wear surfaces exhibit rough and coarse wear debris and particles. With increasing sliding intensity, the coarse particles are transformed into finer debris, leading to a reduction in wear severity (as shown in Figure 6). In Figures 8d and 8f, oxide residues, abrasive scratches, and delamination layers (wear-induced layers) are identified on the wear surfaces of the specimens. Additionally, in Figures 8c-f, microcracks are observed along the wear track of the specimens.

The wear test results showed that wear rates increased as the sliding distance (path length) increased. This is expected. However, the lower wear rates at low speeds are thought to be due to both the lower friction speed and the lower heat generated during friction, resulting in more wear particles being trapped between the abrasive ball and the sample. At high wear speeds, more hard boride particles from the surface are trapped between the abrasive ball and the sample, causing more scratching and wear on the boride surfaces. Furthermore, the frictional heat generated by the fast rotational speed is also high, which leads to the rapid formation of hard oxide particles in the wear zone. Studies on wear rates in the literature have also encountered these situations [24, 31, 32].

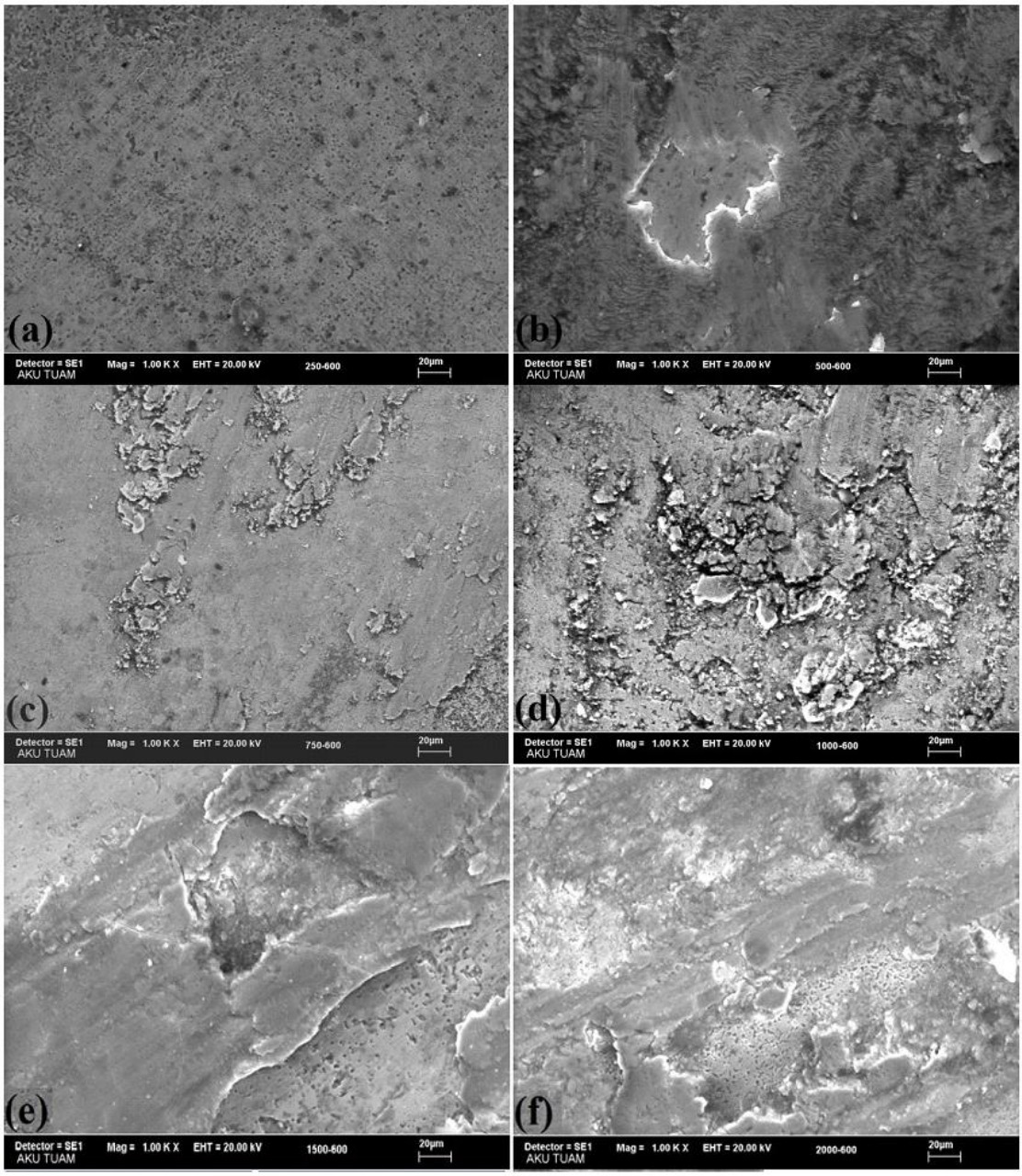


Figure 8. SEM microstructures of the wear surfaces of AISI 8620 steel specimens.

With increasing sliding distance, it was observed that the wear intensified, leading to delamination in the layers. Figure 9 presents the EDX analyses obtained from Figures 8d and 8f. The EDX analyses revealed the formation of Fe-based oxide layers on the worn specimen surfaces due to frictional heat. Additionally, it was observed that the oxide layers extended and aligned along the sliding direction on the wear track. Gunes [30] studied the wear of borided and plasma-nitrided AISI W9Mo3Cr4V high-speed steel and reported the presence of oxide layers formed due to frictional heat on the wear surfaces of borided steel. They found that these oxide layers extended along the wear track and significantly influenced the wear behavior of borided steels [30].

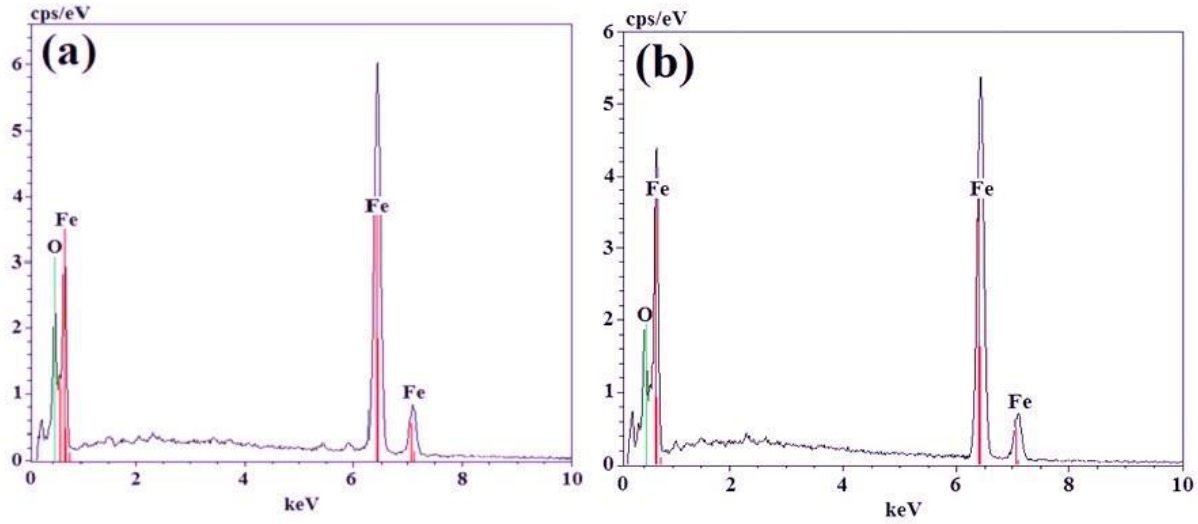


Figure 9. EDX analyses of borided AISI 8620 steels tested at 600 rpm with a sliding distance of (a) 1000 m and (b) 2000 m.

4 CONCLUSIONS

The conclusions drawn from the current study on wear properties of borided AISI8620 steel are given below:

1. The box boriding process of AISI 8620 steel was successfully conducted using commercial Ekabor II boron powder at 900°C for 5 h, resulting in an approximately 78±2 µm thick boride layer.
2. Metallographic examinations revealed a distinct separation between the coating/matrix interface and the matrix, and the boride layer was observed to have a columnar structure.
3. X-ray diffraction analysis confirmed the formation of a dual-phase structure (FeB + Fe_2B) as a result of box boriding with Ekabor II powder.
4. A hardness value of 1768 $HV_{0.05}$ was achieved following the box boriding process with commercial Ekabor II powder at 900°C for 5 h.
5. The wear tests conducted on AISI 8620 steel at different sliding distances and rotational speeds showed that both the sliding distance and rotational speed increased the wear rate.
6. During the wear tests, it was observed that at lower sliding distances, the rotational speed led to a reduction in the coefficient of friction, whereas, at longer sliding distances, it contributed to an increase in wear severity.

This study was limited to a single boriding treatment parameters. Future work could explore a range of temperatures and times to optimize the boride layer (e.g., minimizing the brittle FeB phase) and correlate its specific properties (thickness, phase ratio) with wear performance. Furthermore, conducting tests under lubricated conditions would provide valuable data for real-world gear applications. Finally, the use of more advanced techniques like nanoindentation to map the mechanical properties across the boride layer and profilometry to quantitatively analyze wear track topography would provide deeper insights into the wear mechanisms.

Conflict of Interest Statement

There is no conflict of interest between the authors.

Statement of Research and Publication Ethics

The study is complied with research and publication ethics.

Acknowledgement

This study was financially supported by the Scientific Research Projects Unit of Giresun University under project number FEN-BAP-A-2990224-13.

Artificial Intelligence (AI) Contribution Statement

This manuscript was entirely written, edited, analyzed, and prepared without the assistance of any artificial intelligence (AI) tools. All content, including text, data analysis, and figures, was solely generated by the authors.

Contributions of the Authors

Selçuk Atasoy: Writing, analysis

Hasan Onur Tan: Writing, analysis

Sıtkı Aktaş: Methodology, writing

Hakan Adatepe: Methodology, writing

İbrahim Güneş: Conceptualization, methodology, writing

REFERENCES

[1] M. Musa, A. G. Mohammed, and A. Muhammad, "Wear properties of boron added high strength low alloy (HSLA) SAE 8620 steel," *Journal of Metals, Materials and Minerals,* vol. 28, no. 1, 2018.

[2] R. Sankaran, D. Rajamani, S. Natarajan, and K. Thirugnanasambantham, "Sliding wear behaviour and its mechanisms of carbonitrided AISI 8620 steel at 100 C under unlubricated conditions," *Surface Engineering,* vol. 33, no. 1, pp. 42-48, 2017.

[3] J. An, Z. Su, X. Gao, Y. Yang, and S. Sun, "Corrosion characteristics of boronized AISI 8620 steel in oil field water containing H_2S " *Prot Met Phys Chem+,* vol. 48, pp. 487-494, 2012.

[4] S. Tajmiri, W. Haider, and I. Shabib, "Effect of Heating Rate on Microstructure and Corrosion Resistance of Quenched and Tempered 8620 Low Carbon Alloy Steel," *Corrosion and Materials Degradation,* vol. 5, no. 3, pp. 370-386, 2024.

[5] E. H. Sabuz, M. Noor-A-Alam, W. Haider, and I. Shabib, "Improving the mechanical and electrochemical performance of additively manufactured 8620 low alloy steel via boriding," *Corrosion and Materials Degradation,* vol. 4, no. 4, pp. 623-643, 2023.

[6] E. Boyle, D. Northwood, R. Bowers, X. Sun, and P. Bauerle, "The effects of initial microstructure and heat treatment on the core mechanical properties of carburized automotive steels," in *Materials Forum*, vol. 32, pp. 44-54, 2008.

[7] M. A. Erden and F. Aydın, "Wear and mechanical properties of carburized AISI 8620 steel produced by powder metallurgy," *International Journal of Minerals, Metallurgy and Materials,* vol. 28, pp. 430-439, 2021.

[8] S. Hong, H. Lin, C. Yang, L. Tseng, and K. Lin, "Effects of heat treatment and composition modification on SAE 8620 steels," in *Materials science forum*, vol. 539: pp. 4452-4457, 2007.

[9] K. Genel and M. Demirkol, "Effect of case depth on fatigue performance of AISI 8620 carburized steel," *International Journal of Fatigue,* vol. 21, no. 2, pp. 207-212, 1999.

[10] P. Ghosh and N. Dhokey, "Refinement of tempered martensite structure and its effect on wear mechanism in SAE 8620," *Tribology-Materials, Surfaces & Interfaces,* vol. 10, no. 4, pp. 178-184, 2016.

[11] O. Kapustynskyi and L. Golovko, "Effects of laser cladding and treatment methods on wear resistance in heavy-loaded units," *International journal of multidisciplinary research updates.,* vol. 7, no. 1, pp. 17-26, 2024.

[12] N. Bhadauria, S. Pandey, and P. Pandey, "Wear and enhancement of wear resistance–A review," *Materials Today: Proceedings,* vol. 26, pp. 2986-2991, 2020.

[13] N. K. Paraye, S. P. Neog, P. K. Ghosh, and S. Das, "Surface modification of AISI 8620 steel by in-situ grown TiC particle using TIG arcing," *Surface and Coatings Technology,* vol. 405, p. 126533, 2021.

[14] I. Gunes, I. Yildiz, and A. G. Çelik, "Wear Resistance and Characterization of Borided Ni-Based Alloys," *Powder Metallurgy and Metal Ceramics,* vol. 60, no. 11, pp. 717-726, 2022.

[15] M. Erdogan and S. Tekeli, "The effect of martensite volume fraction and particle size on the tensile properties of a surface-carburized AISI 8620 steel with a dual-phase core microstructure," *Mater Charact,* vol. 49, no. 5, pp. 445-454, 2002.

[16] R. Ortega-Álvarez, M. T. Hernández-Sierra, L. D. Aguilera-Camacho, M. G. Bravo-Sánchez, K. J. Moreno, and J. S. García-Miranda, "Tribological performance of 100Cr6/8620 steel bearing system under green oil lubrication," *Metals,* vol. 12, no. 2, p. 362, 2022.

[17] R. M. Triani, F. E. Mariani, L. F. D. A. Gomes, P. G. B. De Oliveira, G. E. Totten, and L. C. Casteletti, "Improvement of the tribological characteristics of AISI 8620, 8640 and 52100 steels through thermo-reactive treatments," *Lubricants,* vol. 7, no. 8, p. 63, 2019.

[18] A. Krelling, C. Da Costa, J. Milan, and E. Almeida, "Micro-abrasive wear mechanisms of borided AISI 1020 steel," *Tribology International,* vol. 111, pp. 234-242, 2017.

[19] S. K. Yaseen, H. F. Oleiwi, and H. Al-Taay, "Wear Resistance Improvement of Alloy Steel Using Laser Surface Treatment," *Iraqi Journal of Industrial Research,* vol. 9, no. 3, pp. 57-62, 2022.

[20] A. Gorlenko, S. Davydov, M. Y. Shevtsov, and D. Boldyrev, "Wear-resistance increase of friction surfaces of steel machine parts by electro-mechanical hardening," *Steel in Translation,* vol. 49, pp. 800-805, 2019.

[21] E. Hernández-Sánchez *et al.*, "Tribological and Mechanical Behavior of Automotive Crankshaft Steel Superficially Modified Using the Boriding Hardening Process," *Coatings,* vol. 14, no. 6, p. 716, 2024.

[22] H. O. Tan, S. Atasoy, and S. Aktaş, "The Effect of Boriding Temperature and Time on the Structural and Mechanical Properties of M42 Steel," *Türk Doğa ve Fen Dergisi,* vol. 13, no. 2, pp. 1-5, 2024.

[23] I. Gunes, "Tribological Behavior and Characterization of Borided Cold-Work Tool Steel," *Materials and Technology,* vol. 48, no. 5, pp. 765-769, 2014.

[24] I. Gunes, "Wear behaviour of plasma paste boronized of AISI 8620 steel with borax and B_2O_3 paste mixtures," *J Mater Sci Technol,* vol. 29, no. 7, pp. 662-668, 2013.

[25] A. Milinovic, S. Simunovic, M. Keddam, and M. M. Butkovic, "Boronizing Kinetics of 30CrNiMo8 Steel," *Technical Gazette,* vol. 32, no. 1, pp. 176-181, 2025.

[26] S. U. Bayça and H. Efe, "Coating of AISI 8620 steel by boriding process: kinetic modeling, empirical formula and error analysis," *Metall Res Technol,* vol. 122, no. 3, 2025.

[27] C. Pacheco, J. L. Jeronimo, A. P. Krelling, C. E. da Costa, and J. C. G. Milan, "Influence of boriding treatment on the mechanical properties of Monel 400," *Results Surf Interf,* vol. 18, 2025.

[28] I. Gunes and I. Yıldız, "Investigation of adhesion and tribological behavior of borided AISI 310 stainless steel," *Matéria (Rio de Janeiro),* vol. 21, no. 1, pp. 61-71, 2016.

[29] I. Gunes and A. Dalar, "Effect of sliding speed on friction and wear behaviour of borided gear steels," *Journal of the Balkan Tribological Association,* vol. 19, no. 3, pp. 325-339, 2013.

[30] I. Gunes, "Effect of sliding speed on the frictional behavior and wear performance of borided and plasma-nitrided W9Mo3Cr4V high-speed steel," *Materials and Technology,* vol. 49, no. 1, pp. 111-116, 2015.

[31] R. Tyagi, D. S. Xiong, and J. L. Li, "Effect of load and sliding speed on friction and wear behavior of silver/h-BN containing Ni-base P/M composites," *Wear,* vol. 270, no. 7-8, pp. 423-430, 2011.

[32] Y. Kanca, "Effects of normal load and sliding distance on the dry sliding wear characteristics of Invar-36 superalloy," *Erzincan University Journal of Science and Technology,* vol. 16, no. 1, pp. 258-272, 2023.

BİTLİS EREN ÜNİVERSİTESİ
FEN BİLİMLERİ DERGİSİ

ISSN: 2147-3129 / e-ISSN: 2147-3188

Article Type : Research Article
Received : May 27, 2025
Revised : July 3, 2025
Accepted : July 30, 2025
DOI : 10.17798/bitlisfen.1706316

Year : 2025
Volume : 14
Issue : 3
Pages : 1704-1717

SYNTHESIS, SPECTROSCOPIC STUDIES AND ANTIOXIDANT ACTIVITIES OF NEW 2-BENZYLIDENE-N-PHENYLHYDRAZINE-1-CARBOTHIOAMIDE DERIVATIVES

Temel Kan BAKIR [1,*], Halit MUĞLU [1]

[1] *Kastamonu University, Chemistry Department, Kastamonu,, Türkiye, temelkan@kastamonu.edu.tr*

ABSTRACT

Nowadays, thiosemicarbazone based schiff bases, which are the focus of attention due to their differential properties, are being synthesized in many studies and new aromatic structure added compounds are of significant interest in drug design and biochemistry. In this study, new thiosemicarbazide schiff bases containing different substituted groups were synthesized. The structure of new compound derivatives was characterized by proton nuclear magnetic resonance (^{1}H-NMR), carbon-13 nuclear magnetic resonance (^{13}C-NMR), fourier transform infrared spectroscopy (FTIR) and elemental analyses. In addition, radical quenching capacities of newly synthesized compounds were investigated using 1,1-diphenyl-2-picryl hydrazyl (DPPH) method. IC_{50} values were calculated for the compounds and it was found that the antioxidant activities of the compounds changed in the order of 2>5>1>4>3. These results indicated that the presence of methoxy substituted groups that provide electrons to the aromatic ring structures of schiff bases would have positive effects on the antioxidant activities of the compounds.

Keywords: Schiff Base, Carbothioamide, IR Spectroscopy, ^{13}CNMR, DPPH Scavenging Method.

1 INTRODUCTION

Thiosemicarbazones are formed by the synthesis reaction between aldehyde and thiosemicarbazide, along with the addition of alkyloxy chain ester linkage groups in the first step [1]. Thiosemicarbazone ligands and transition metal complexes are of significant interest today due to their potential pharmacological properties and different stereochemical roles [2,3]. In one of the studies in this field, Hernandez and colleagues synthesized benzaldehyde

thiosemicarbazone derivatives and palladium (ii) and platinum (ii) complexes and evaluated the in vitro antitumor activities of these compounds. As a result of the study, they found that the synthesized complexes were more cytotoxic than their ligands with IC50 values in the range of 0.07–3.67 μM [4]. As a similar example, organometallic aromatic compounds attached to thiosemicarbazones can show a strong affinity towards sulfur and nitrogen-containing biomolecules such as amino acids (cysteines and methionines), peptides (glutathione) and proteins (metallothionein) [5].

Thiosemicarbazones, an important class of Schiff bases, have attracted significant attention for many years due to their biological activities and coordination chemistry properties [6-8]. Some of these biological activities can be listed as antiparasitic [9], potential anti-trypanosomal agents [10], antitumor activities [11], nuclear medicine [12] and anticancer activities [13]. In addition to these biological activities, thiosemicarbazone compounds also stand out with their antioxidant properties [14]. In recent years, thio/carbohydrazone derivatives have been synthesized and these compounds containing many functional groups have been investigated thanks to their antioxidant properties that reduce the damage of oxidative stress in living organisms and prevent DNA oxidation [15]. Hamedifar and coworkers synthesized 10 new carbothioamide molecule derivatives. These molecules inhibited tyrosinase enzyme and showed strong activities in antioxidant tests with DPPH [16].

The main purpose of this study is to synthesize new thiosemicarbazone compounds containing 2-benzylidene-n-phenylhydrazine-1-carbothioamide and to reveal their antioxidant properties. For this purpose, the synthesized compounds were characterized by elemental analyses, FTIR and NMR analyses. Then, the antioxidant properties of the synthesized compounds were investigated by DPPH method.

2 MATERIAL AND METHOD

This study, which we conducted in two parts, covers synthesis and antioxidant measurements. All solvents were used at analytical grade and all chemicals were supplied by Merck and Sigma-Aldrich Co. LLC. Synthesis studies, antioxidant determinations, elemental analyses and FTIR analyses were carried out at Kastamonu University Central Research Laboratory. FTIR analyses of solid samples in a short time under room conditions were performed using the Bruker Alpha FTIR device. 1H and 13C NMR analyses were carried out at Tokat Gaziosmanpaşa University Scientific, Technological Research and Application Center. NMR measurements were made on solutions of synthesized compounds prepared in dimethyl

sulfoxide (DMSO-d6) using JEOL ECX-400 (400 MHz) device. Antioxidant measurements were measured with the help of SHIMADZU UVmini-1240 UV-Visible spectrophotometer (Schimadzu Corp., Kyoto, Japan).

2.1 Synthesis of Thiosemicarbazone Derivatives (1–5)

2.1.1 Step 1: Synthesis of Thiosemicarbazides

First, various aromatic isothiocyanates (10 mmol) and hydrazine monohydrate (10 mmol) were separately dissolved in 96% pure ethanol (20 mL) and cooled in an ice bath (0–5 °C) for 15 min. Then, the isothiocyanate solution was added dropwise to the hydrazine solution under strong magnetic stirring. The mixture was stirred in an ice bath for another 120 min and then left in a refrigerator at 0–4 °C overnight. The white-cream precipitate that formed was vacuum filtered, washed with cold alcohol and dried in air. The obtained crude product was recrystallized with hot ethanol to obtain pure thiosemicarbazide derivatives (Figure 1) [17].

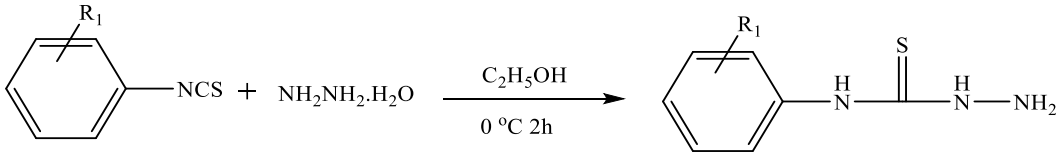
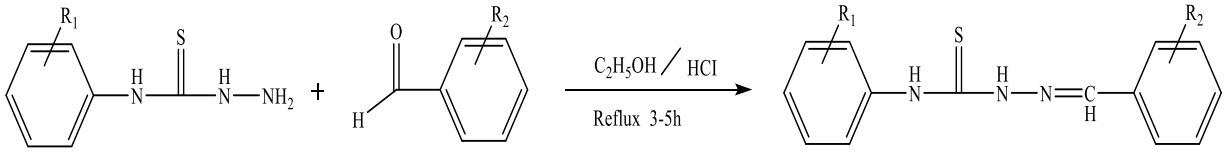


Figure 1. Thiosemicarbazide derivatives synthesis

2.1.2 Step 1: Synthesis of Thiosemicarbazones

Pure thiosemicarbazide derivatives (2 mmol), appropriate benzaldehyde derivatives (2 mmol) and a drop of concentrated HCl were dissolved in 96% ethanol (20 mL) and reacted under reflux conditions at 78 °C for 3–5 h. The reaction time was monitored by thin layer chromatography (TLC). When the reaction was complete, the mixture was cooled to room temperature and the solid product formed was vacuum filtered and dried. Purification was performed by recrystallization from ethanol. The products were obtained in yields ranging from 60% to 86% and their structures are shown in Figure 2 [17].

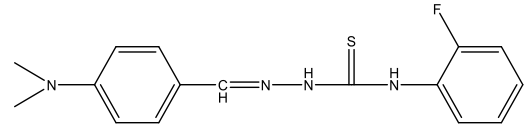
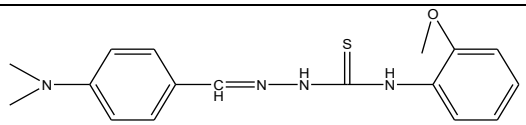
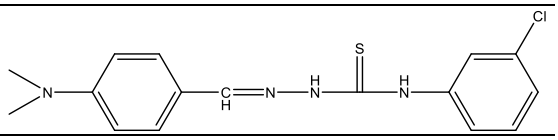
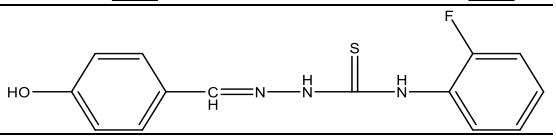
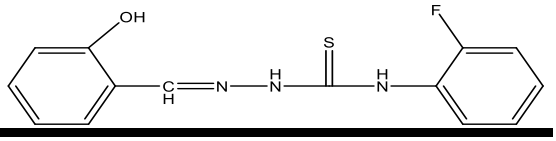


R_1: 1,2,3 -N(CH_3); 4) 4-OH; 5) 2-OH R_2:1,4,5) 2-F; 2) 2-OCH_3; 3) 3-CI

Figure 2. Synthesis reaction of carbothioamide derivatives

The names and molecular structures of the compounds synthesized in the study are given in Table 1.

Table 1. Names and structures of the compounds synthesized in the study

No	Compound name	Molecular structure
1	2-(4-(dimethylamino)benzylidene)-N-(2-fluorophenyl)hydrazine-1-carbothioamide	
2	2-(4-(dimethylamino)benzylidene)-N-(2-methoxy)hydrazine-1-carbothioamide	
3	2-(4-(dimethylamino)benzylidene)-N-(3-choloro)hydrazine-1-carbothioamide	
4	N-(2-fluorophenyl)-2-(4-hydroxybenzylidene)hydrazine-1-carbothioamide	
5	N-(2-fluorophenyl)-2-(2-hydroxybenzylidene)hydrazine-1-carbothioamide	

2.2 DPPH Radical Scavenging Application

The DPPH radical quenching method, which is frequently used to determine antioxidant activities, is based on the principle that its solution in ethanol shows maximum absorbance at 515-517 nm wavelength.

In this study, we tried to evaluate the DPPH radical quenching activities of the compounds we synthesized, their solutions (2×10^{-4} M stock solution) in 25 mL of DMSO by observing absorbance changes. For this purpose, different volumes of these stock solutions (15 µL, 30 µL, 60 µL, 120 µL, 180 µL) were taken in 6 mL of DPPH mixture and their absorbances at 517 nm were recorded after 30 minutes of incubation. Thus, radical quenching activities were calculated as percent inhibition with the following formula:

$$\text{Inhibition (\%)} = [(A_0 - A_1) / A_0] \times 100 \quad (1)$$

Where A_0 is the absorbance of the control solution (without antioxidant) and A_1 is the absorbance of the sample solution (when antioxidant was added) [18]. In addition, the IC_{50} (mg/mL) value used to interpret the antiradical activity was calculated. Thus, the antioxidant

activities of the molecules could be compared by comparing the amount of antioxidant required to reduce the DPPH radical concentration by 50% [19-21].

3 RESULTS AND DISCUSSION

3.1 Characterization of Carbotioamide Compounds

FTIR, ^{1}H-NMR and ^{13}C-NMR analyses were performed for the synthesized Carbothioamide compounds and the spectroscopic analysis spectra for Compound 2 are exemplified in Figure 3, Figure 4 and Figure 5, respectively.

In the synthesized compounds, the FTIR voltages of the characteristic groups C-O, C-N, C=N, C=S belonging to the Thiosemicarbazide group and the aromatic ring in the synthesized carbothioamide structure are given in Table 2. When the FTIR results for Compound 2 (2-(4-(dimethylamino)benzylidene)-N-(2-methoxy)hydrazine-1-carbothioamide) were examined, the N-H stretching vibration band was seen at 3290 cm^{-1}, the C-H stretching bands of the aromatic ring were in the range of 3139-2980 cm^{-1}, the C-H stretching bands of aliphatic group were seen as a separate band in the range of 2892-2813 cm^{-1}, the C=N and C-N bands belonging to the thiosemicarbazide group were seen at 1606 cm^{-1} and 1271 cm^{-1}, respectively. In addition, the C=S stretching bands belonging to the thiosemicarbazide group were observed at 1440 cm-1. The C-O band in the methoxy structure was found only in Compound 2 at 1178 cm^{-1}. In other compounds, specific C-F and C-Cl bands were observed at 1097-1101 cm^{-1} and 1056 cm^{-1}, respectively. The -OH band was observed at 3317 and 3386 cm^{-1} only for Compound 4 and Compound 5, as expected.

Table 2. Frequency values of FTIR (cm^{-1}, υ_{max}) spectra of characteristic groups of synthesized compounds

Compound ID	-OH	-NH	Ar.CH	Aliph.CH	C=N	C=S	C-N	C–O	Spec. Vib.
1	---	3302	3136-2975	2884-2794	1602	1443	1281	-	C-F:1101
2	---	3290	3139-2980	2892-2813	1606	1440	1271	1178	---
3	---	3261	3138-2986	2906-2814	1584	1428	1270	-	C-CI:1056
4	3317	3256	2980	---	1599	1398	1278	-	C-F:1097
5	3386	3155	2992	---	1603	1402	1280	-	C-F:1100

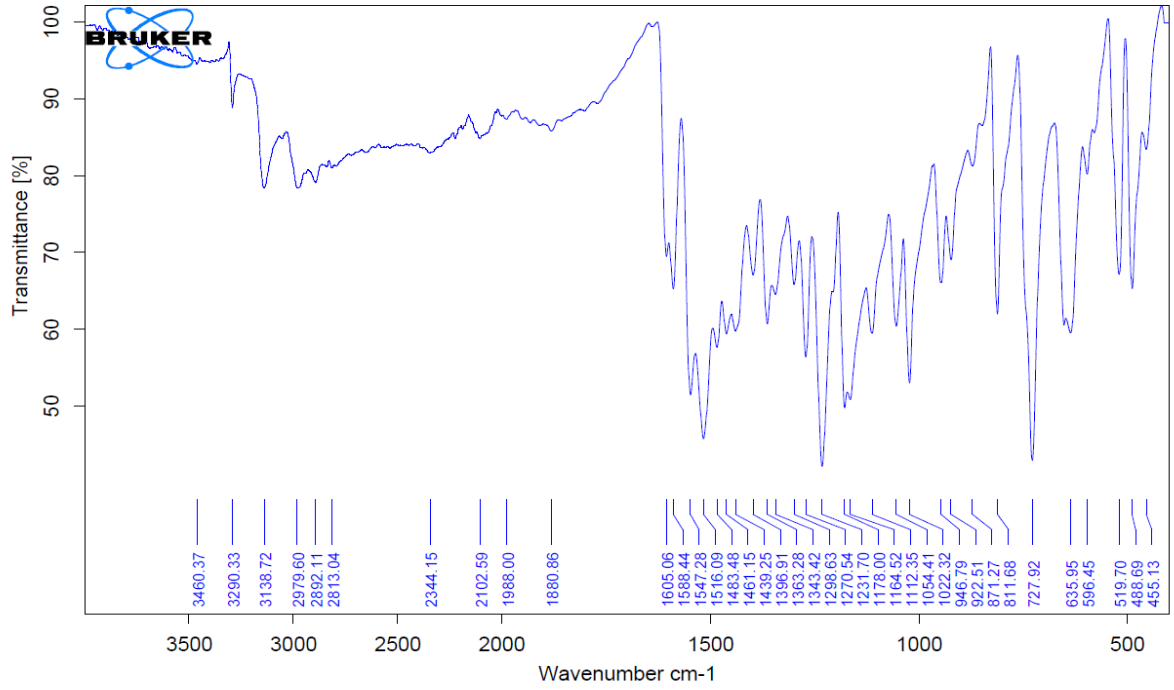


Figure 3. IR spectrum of the Compound 2-(4-(dimethylamino)benzylidene)-N-(2-methoxy)hydrazine-1-carbothioamide

^{1}H-NMR proton spectra of DMSO solutions of the synthesized compounds were obtained with a Bruker NMR spectrometer at 400 MHz. ^{1}H-NMR results of 2-(4-(dimethylamino)benzylidene)-N-(2-methoxy)hydrazine-1-carbothioamide compound are given in Figure 4. The common structure of all newly synthesized compounds is that the protons belonging to the N-H groups are singlet in the range of 11.92-11.73 ppm. N-H group bound to aromatic structure showed singlet in the range of 9.97-9.80 ppm. Proton (H8) belonging to CH=N group showed singlet in the range of 8.49-8.04 ppm for the synthesized compounds. For Compound 2, methoxy proton (R1) bound to ring structure gave singlet at 3.92 ppm. For Compound 1, Compound 2 and Compound 3, the protons belonging to the methyl structure attached to the other ring gave singlets at 2.98, 2.99 and 2.99 ppm, respectively. In all synthesized compounds belonging to aromatic rings, the protons H1-H5 and H9-H13 gave doublets between 8.13-7.14 and 7.21-6.68 ppm, respectively.

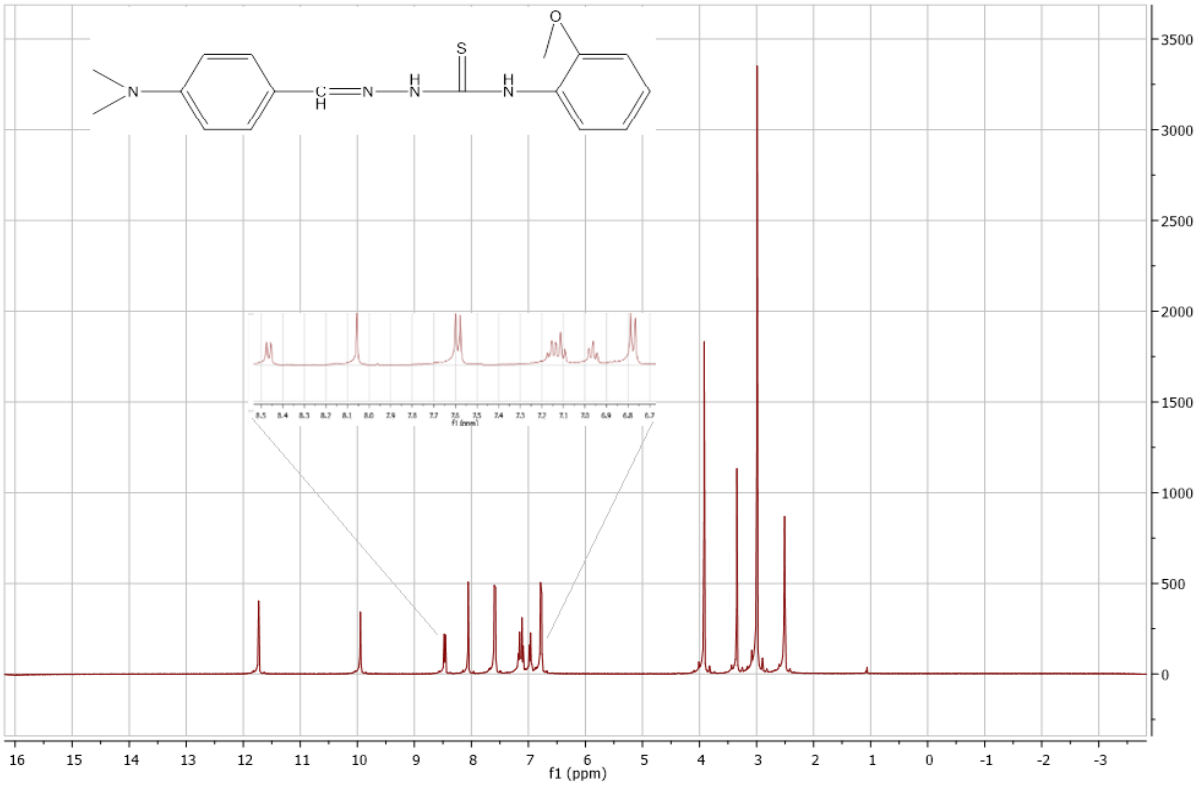
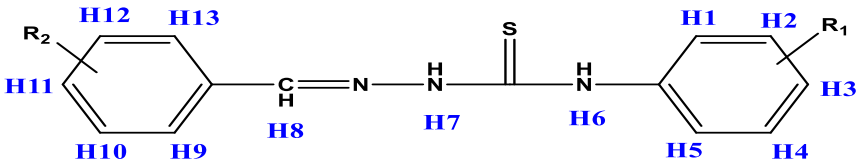


Figure 4. ^{1}H-NMR spectrum of the Compound 2-(4-(dimethylamino)benzylidene)-N-(2-methoxy)hydrazine-1-carbothioamide

Table 3. Peak data for 1H-NMR spectra of characteristic groups of synthesized compounds (400 MHz, DMSO-d6, ppm)



Compounds ID	H7, NH	H6, NH-Ar	H8, CH=N	H1-H5	R1	R2	H9-H13
1	11.74 (s,1H)	9.80 (s,1H)	8.04 (s,1H)	7.68 – 7.66 (d, 2H, H5), 7.63 – 7.59 (m, 3H, H2), 7.32 – 7.28 (m, 3H, H3, H4)	-	CH_3:2.98 (s,6H)	6.74-6.72 (d, J = 8.7 Hz, 4H, H9,H10)
2	11.73 (s,1H)	9.95 (s,1H)	8.18 (s,1H)	8.13 (d, J = 15.5 Hz, 2H, H5), 8.10 (m, 3H, H2), 7.17- 7.14 (m, 3H, H3,H4)	OCH_3: 3.92 (s,3H)	CH_3: 2.99 (s,6H)	6.68 (d, J = 8.1 Hz, 4H, H9, H10)
3	11.73 (s,1H)	9.92 (s,1H)	8.05 (s,1H)	7.75 (dd, J = 39.8, 10.1 Hz, 1H, H5), 7.63 (d, J = 7.5 Hz, 2H, H1), 7.38 –7.24 (t, J = 8.1 Hz, 3H, H3,H4)	-	CH_3: 2.99 (s,6H)	6.73 (d, J = 8.8 Hz, 4H, H9,H10)
4	11.82 (s,1H)	9.96 (s,1H)	8.19 (s,1H)	7.99 (d, J = 16.7 Hz, 1H, H5), 7.72 (d, J = 8.5 Hz, 2H, H2), 7.49 – 7.16 (m, 3H, H3,H4)	-	OH: 9.86 (s,1H)	6.72 (d, J = 8.0 Hz, 4H, H9,H10),
5	11.92 (s,1H)	9.97 (s,1H)	8.49 (s,1H)	8.07 (d, J = 7.5 Hz, 2H, H5), 7.71 (d, J = 7.8 Hz, 2H, H2), 7.66 – 7.23 (m, 3H, H3,H4),	-	OH: 9.83 (s,1H)	7.21 (d, J = 7.7 Hz, 4H, H12), 7.23 – 6.10 (m, 3H, H9), 6.75 – 6.10 (m, 4H, H11, H10)

The ^{13}C-NMR results of the 2-(4-(dimethylamino)benzylidene)-N-(2-methoxy)hydrazine-1-carbothioamide compound are given as an example in Figure 5. The characteristic carbon peaks of all synthesized molecules are shown in the Table 4. Accordingly, the C peaks belonging to the C=S group in all compounds were found in the range of 174.12-177.19 ppm and the C peaks belonging to the C=N group were found in the range of 140.39-144.95 ppm. In addition, peaks were found in the range of 130.51-115.93 ppm for the C1-C6 carbons in the aromatic ring groups attached to the thiosemicarbazide group in the compounds. The peak belonging to the carbon in the methoxy group for Compound 2 was observed at 56.53 ppm. Peaks belonging to the carbons in the dimethyl amine structure attached to the aromatic ring in Compound 1, Compound 2 and Compound 3 were observed at 40.63, 40.41 and 40.21 ppm, respectively.

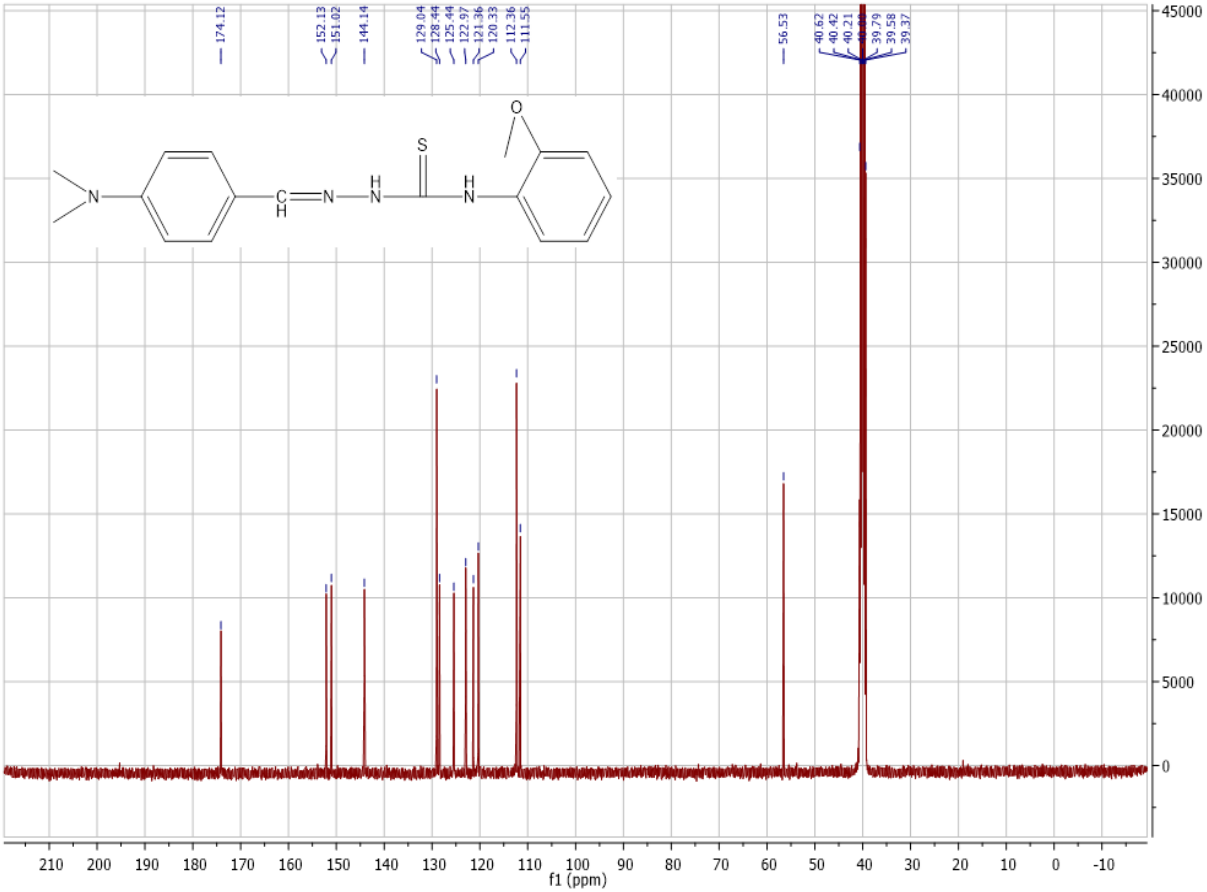
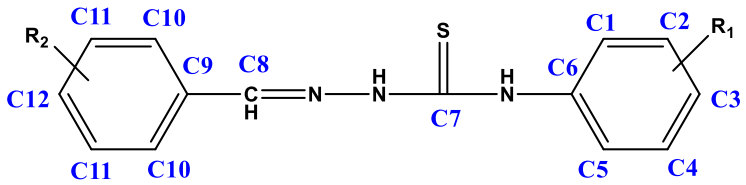


Figure 5. ^{13}C-NMR spectrum of 2-(4-(dimethylamino)benzylidene)-N-(2-methoxy)hydrazine-1-carbothioamide

Table 4. Peak data for ^{13}C-NMR spectra of characteristic groups of synthesized compounds (DMSO-d_6, ppm)



Compounds ID	Ar, (C1-C6)	OCH_3	CH_3	C9	C10	C11	C12	C=S	C=N
1	129.42 (C6), 128.10-128.13 (C2), 127.86-127.75 (C4), 124.38-124.35 (C3), 121.59-116.13 (C5), 115.93-112.12 (C1).	-	40.63	130.23	156.31	152.05	158.75	176.67	144.57
2	125.44 (C6), 122.97 (C2), 121.36 (C4), 120.33 (C3), 112.36 (C5), 111.56 (C1).	56.53	40.41	129.04	128.44	151.02	152.13	174.12	144.14
3	129.62 (C6), 125.17 (C2), 125.05 (C4), 124.21 (C3), 121.48 (C5), 112.09 (C1).	-	40.21	132.56	129.97	149.21	152.08	175.12	144.95
4	129.86 (C6), 128.43-128.35 (C2), 127.84-127.67 (C4), 125.41-124.42 (C3), 124.38-116.17 (C5), 116.03-115.97 (C1).	-	-	130.52	158.89	156.59	159.97	177.15	143.90
5	130.51-128.46 (C6), 128.40-127.78 (C2), 127.66-127.29 (C4), 124.44-120.71 (C3), 119.70-116.55 (C5), 116.19-115.99 (C1).	-	-	131.85	157.01	156.21	158.68	177.19	140.39

In addition, elemental data of 5 new carbothioamide compounds were determined experimentally and theoretically and are shown in Table 5. Some physicochemical properties of these elements are shown in Table 6.

Table 5. Experimental and calculated elemental analysis of synthesized compounds

Compounds	Theoretical			Experimental		
	C%	H%	N%	C%	H%	N%
1	60.74	5.42	17.71	58.70	4.95	17.12
2	62.17	6.14	17.06	60.85	5.57	16.74
3	57.73	5.15	16.83	56.80	4.86	16.32
4	58.12	4.18	14.52	56.96	3.95	13.92
5	58.12	4.18	14.52	57.35	3.86	13.84

Table 6. Physicochemical parameters of 5 new carbothioamide compounds

Compounds Name	MW (g)	MP (°C)	Yield (%)	Solubility in DMSO	Colour
2-(4-(dimethylamino)benzylidene)-N-(2-fluorophenyl)hydrazine-1-carbothioamide	316.4	181-182	83	+	Red
2-(4-(dimethylamino)benzylidene)-N-(2-methoxy)hydrazine-1-carbothioamide	328.4	199-200	86	+	Yellow
2-(4-(dimethylamino)benzylidene)-N-(3-choloro)hydrazine-1-carbothioamide	332.9	170-171	80	+	Pink
N-(2-fluorophenyl)-2-(4-hydroxybenzylidene)hydrazine-1-carbothioamide	389.3	187-188	60	+	Light pink
N-(2-fluorophenyl)-2-(2-hydroxybenzylidene)hydrazine-1-carbothioamide	389.3	172-173	73	+	White

3.2 Investigation of Antioxidant Activities

In this study, ascorbic acid was used as the standard antioxidant. The antioxidant activities of the synthesized molecules were calculated in the concentration range of 0.5 – 6.0 µM and the (%) inhibition data are given in Figure 6. Accordingly, inhibition values (%) showed a linear increase with concentration. It was found that the synthesized molecules showed much lower inhibition percentage against the standard antioxidant.

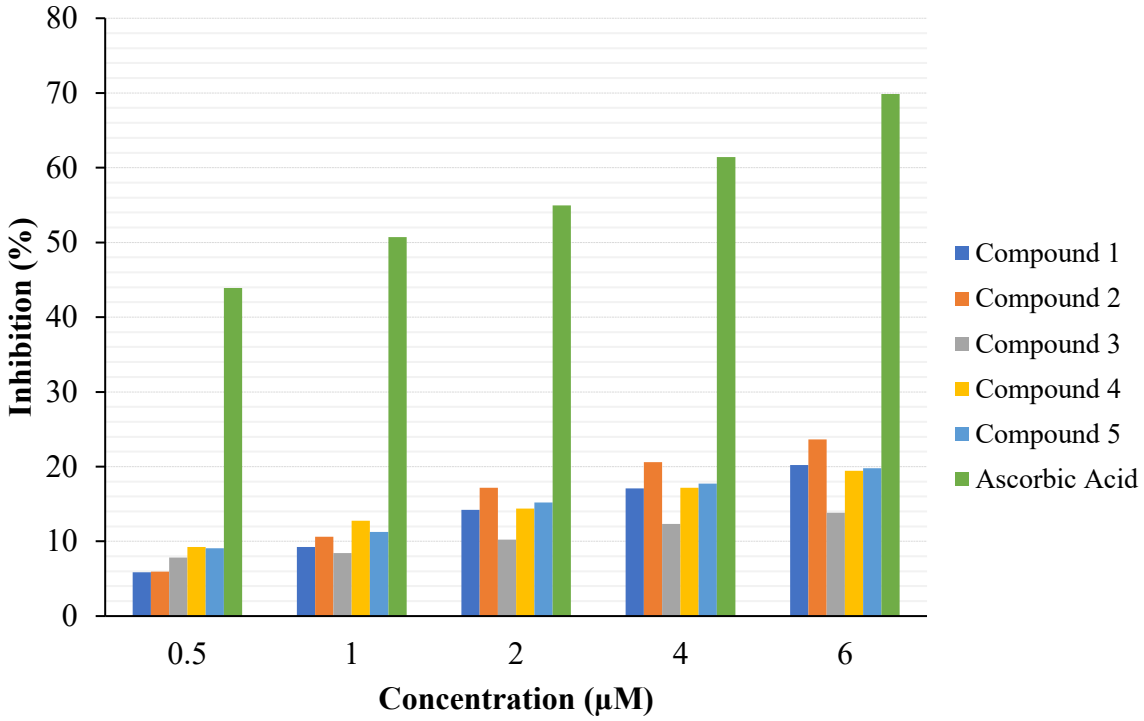


Figure 6. % inhibition graph of 5 new carbothioamide compounds

In addition, antioxidant activities of 5 new synthesized carbothioamide compounds were compared by calculating IC_{50} (mg/mL) values. Linear regression equations of ascorbic acid and 5 new compounds and R^2 values and IC_{50} values of these equations are shown in Table 4.

Table 4. IC_{50} values of ascorbic acid and 5 new carbothioamide compounds calculated by DPPH method

Compounds	Linear Concentration Equation (y=ax±b)	IC_{50} (µM)	R^2
1	y = 3.54x + 4.96	17.83±0.45	0.905
2	y = 2.42x + 6.78	14.30±0.42	0.870
3	y = 1.10x + 7.56	38.45±0.93	0.977
4	y = 1.64x + 10.16	24.18±0.51	0.914
5	y = 2.79x + 6.24	15.70±0.43	0.988
Ascorbic Acid	y = 6.27x + 37.37	2.02±0.05	0.988

Considering the IC_{50} values, the DPPH radical reducing capacity of the synthesized 5 new carbothioamide compounds is quite low compared to ascorbic acid (2.02±0.05 μM). The small IC_{50} values for these new compounds are an indication of their ability to quench free radicals at the same rate even at lower concentrations. Therefore, it is seen that these compounds exhibit stronger antioxidant activity. In this study, the IC_{50} values of the newly synthesized 5 carbothioamide compounds followed the order 3>4>1>5>2. These data showed that Compound 3 exhibited the lowest and Compound 2 the highest antioxidant activity.

The common feature of compounds 1, 5 and 4 is that they have electronegative F atoms on the ring attached to the N-(2-fluorophenyl)hydrazine-1-carbothioamide structure, i.e. thiosemicarbazone structures. In contrast, groups such as -F and -Cl are Ain and colleagues found that the 18 thiocarbohydrazone derivatives they synthesized had strong antioxidant properties in DPPH-like tests and also had low cell toxicity [22].

The free radical scavenging potential of the carbothioamide derivatives we synthesized in this study can change significantly due to the effect of various electron-donating or electron-withdrawing substituents in their structures. For example, the $-N(CH_3)_2$ group in 2-(4-(dimethylamino)benzylidene)-N-(2-fluorophenyl)hydrazine-1-carbothioamide and similar compounds, as a strong electron-donating group, transfers electrons from the aromatic ring to the π-system via resonance, increasing the delocalization of radical centers and thus strengthening free radical stabilization [23]. Likewise, the $-OCH_3$ group supports antioxidant activity by increasing electron density through the mesomeric effect [24] (Santos et al., 2016; Wang et al., 2017).

As in the study of Rajan et al., 2001, in Compound 2, the $–OCH_3$ group substituted to the aromatic ring provided the highest antioxidant activity of this compound since it could provide electrons to the ring [25]. As reported by Gudipati et al., 2011, it was thought that the electronegative fluorine atom substituted to the aromatic ring attached to the carbothioamide group may be responsible for the lower antioxidant activity [26]. In contrast, groups such as -F and -Cl are electron-withdrawing, and especially the fluorine atom can stabilize radical intermediates through intramolecular hydrogen bonds due to its small size and high electronegativity [27]. The -Cl group at the 3-position can suppress the antioxidant behavior to some extent by reducing the electron density of the aromatic system with both inductive and weak mesomeric effects. In addition, the -OH groups located in 2- or 4-hydroxybenzylidene derivatives provide phenolic structures that can neutralize free radicals through direct hydrogen donation, a well-known antioxidant mechanism [28]. With the joint effect of all these groups, the antioxidant activities of the compounds are determined by both electron density changes and resonance stabilization of radical intermediate species.

4 CONCLUSION AND SUGGESTIONS

Thiosemicarbazone-linked aromatic compounds continue to be the subject of fields such as biochemical applications, medicine and pharmaceutical applications, thanks to their various biological effects such as antioxidant activities and outstanding pharmacological properties. In this study, a new carbothioamide compound containing thiosemicarbazone-based aromatic group was synthesized and its antioxidant properties were found. Newly synthesized carbothioamide compounds showed DPPH radical quenching activity in the range of 6.0–23.5% at concentrations of 0.5–6.0 µM. The highest activity was observed in 2-(4-(dimethylamino)benzylidene)-N-(2-methoxy)hydrazine-1-carbothioamide with 23.5% inhibition rate. Although the IC_{50} values of these compounds at concentrations of 0.5–6.0 µM were higher than the IC_{50} value of ascorbic acid in the same concentration range, it was determined that they exhibited significant antioxidant effect. As a result, it was observed that methoxy and hydroxy groups attached to the aromatic ring have significant contributions in this activity. These results indicate that thiosemicarbazone derivatives can be made more effective by structural modifications in improving their antioxidant potential. In the future, examining the effects of such compounds on different radical species, investigating their biological activities at cell culture level and evaluating their pharmacokinetic profiles will be guiding in terms of biomedical applications. In addition, deepening the structure-activity relationships with molecular modeling and in silico analyses may pave the way for new targeted compound designs.

Conflict of Interest Statement

There is no conflict of interest between the authors.

Statement of Research and Publication Ethics

The study is complied with research and publication ethics

Artificial Intelligence (AI) Contribution Statement

This manuscript was entirely written, edited, analyzed, and prepared without the assistance of any artificial intelligence (AI) tools. All content, including text, data analysis, and figures, was solely generated by the authors.

REFERENCES

[1] H. P. Ebrahimi et al., "A novel series of thiosemicarbazone drugs: From synthesis to structure," *Spectrochim. Acta A Mol. Biomol. Spectrosc.*, vol. 137, pp. 1067–1077, 2015, doi: 10.1016/j.saa.2014.08.146.

[2] D. Kovala-Demertzi, A. Boccarelli, M. A. Demertzis, and M. Coluccia, "In vitro antitumor activity of 2-acetyl pyridine 4N-ethyl thiosemicarbazone and its platinum(II) and palladium(II) complexes," *Chemotherapy*, vol. 53, no. 2, pp. 148–152, 2007.

[3] J. P. Scovill, D. L. Klayman, and C. F. Franchino, "2-acetylpyridine thiosemicarbazones. 4. Complexes with transition metals as antimalarial and antileukemic agents," *J. Med. Chem.*, vol. 25, no. 10, pp. 1261–1264, 1982.

[4] W. Hernandez et al., "Synthesis, characterization, and in vitro cytotoxic activities of benzaldehyde thiosemicarbazone derivatives and their palladium(II) and platinum(II) complexes against various human tumor cell lines," *Bioinorg. Chem. Appl.*, vol. 2008, Art. no. 690952, 2008, doi: 10.1155/2008/690952.

[5] H. Khan, "Synthesis, characterization and anticancer studies of mixed ligand dithiocarbamate palladium (II) complexes," *Eur. J. Med. Chem.*, vol. 46, pp. 4071–4077, 2011, doi: 10.1016/j.ejmech.2011.06.007.

[6] V. F. S. Pape et al., "Design, synthesis and biological evaluation of thiosemicarbazones, hydrazinobenzothiazoles and arylhydrazones as anticancer agents with a potential to overcome multidrug resistance," *Eur. J. Med. Chem.*, vol. 117, pp. 335–354, 2016.

[7] P. King et al., "Bis(thiosemicarbazone) complexes of cobalt(III): Synthesis, characterization, and anticancer potential," *Inorg. Chem.*, vol. 56, pp. 6609–6623, 2017.

[8] Gatti et al., "Half-sandwich arene ruthenium(II) and osmium(II) thiosemicarbazone complexes: Solution behavior and antiproliferative activity," *Organometallics*, vol. 37, pp. 891–899, 2018.

[9] P. Chellan et al., "Exploring the versatility of cycloplatinated thiosemicarbazones as antitumor and antiparasitic agents," *Organometallics*, vol. 31, pp. 5791–5799, 2012.

[10] Demoro et al., "New organoruthenium complexes with bioactive thiosemicarbazones as co-ligands: Potential anti-trypanosomal agents," *Dalton Trans.*, vol. 41, pp. 1534–1543, 2012, doi: 10.1039/c1dt11519g.

[11] F. Vandresen et al., "Novel R-(+)-limonene-based thiosemicarbazones and their antitumor activity against human tumor cell lines," *Eur. J. Med. Chem.*, vol. 79, pp. 110–116, 2014, doi: 10.1016/j.ejmech.2014.03.086.

[12] G. L. Parrilha et al., "Applications of radiocomplexes with thiosemicarbazones and bis(thiosemicarbazones) in diagnostic and therapeutic nuclear medicine," *Coord. Chem. Rev.*, vol. 458, 2022.

[13] W.-x. Hu et al., "Synthesis and anticancer activity of thiosemicarbazones," *Bioorg. Med. Chem. Lett.*, vol. 16, pp. 2213–2218, 2006, doi: 10.1016/j.bmcl.2006.01.048.

[14] J. Haribabu et al., "Isatin based thiosemicarbazone derivatives as potential bioactive agents: Anti-oxidant and molecular docking studies," *J. Mol. Struct.*, vol. 1110, pp. 185–195, 2016.

[15] M. S. Çavuş, H. Yakan, C. Özorak, H. Muğlu, and T. K. Bakır, "New N,N′ bis(thioamido)thiocarbohydrazones and carbohydrazones: Synthesis, structure characterization, antioxidant activity, corrosion inhibitors and DFT studies," *Res. Chem. Intermed.*, vol. 48, pp. 1593–1613, 2022, doi: 10.1007/s11164-022-04659-z.

[16] H. Hamedifar, S. Karimian, M. Kabiri, A. Bagheri, M. Zarei, A. Moazzam, M. Mahdavi, N. Sepehri, and M. Khoshneviszadeh, "Benzylidine-N-phenylhydrazine-1-carboxamide derivatives as tyrosinase inhibitors: Design, preparation, molecular docking, and biological activity," *ChemistrySelect*, vol. 8, Art. no. e202300836, 2023, doi: 10.1002/slct.202300836.

[17] Y. Demir et al., "Enzyme inhibition, molecular docking, and density functional theory studies of new thiosemicarbazones incorporating the 4-hydroxy-3,5-dimethoxy benzaldehyde motif," *Arch. Pharm. (Weinheim).*, vol. 356, no. 4, p. e2200554, Apr. 2023, doi: 10.1002/ardp.202200554.

[18] Huang, B. Ou, and L. Prior, "The chemistry behind antioxidant capacity assays," *J. Agric. Food Chem.*, vol. 53, no. 6, pp. 1841–1856, 2005, doi: 10.1021/jf030723c.

[19] T. Bakır and J. B. Lawag, "Preparation, characterization, antioxidant properties of novel Schiff bases including 5-chloroisatin thiocarbohydrazone," *Res. Chem. Intermed.*, vol. 46, pp. 2541–2557, 2020, doi: 10.1007/s11164-020-04105-y.

[20] N. Frankel and A. S. Meyer, "The problems of using one-dimensional methods to evaluate multifunctional food and biological antioxidants," *J. Sci. Food Agric.*, vol. 80, pp. 19–25, 2000.

[21] W. Brand-Williams, M. E. Cuvelier, and C. Berset, "Use of a free radical method to evaluate antioxidant activity," *LWT - Food Sci. Technol.*, vol. 28, no. 1, pp. 25–30, 1995.

[22] Q. ul-Ain, M. T. Muhammad, K. M. Khan, and M. I. Choudhary, "Estimation of in-vitro free radical scavenging and cytotoxic activities of thiocarbohydrazones derivatives," *arXiv*, pp. 1–18, 2023, doi: 10.48550/arXiv.2310.00939.

[23] C. Peyrot et al., "Bifunctional compounds targeting both D2 and non-α7 nACh receptors: Design, synthesis and pharmacological characterization," *Eur. J. Med. Chem.*, vol. 101, pp. 442–452, 2015.

[24] B. Bakti and M. A. Martoprawiro, "Computational study of the effect of structure on antioxidant activity and drug score of coumarin derivatives," *Walisongo J. Chem.*, vol. 7, no. 2, pp. 181–192, 2024, doi: 10.21580/wjc.v7i2.23327.

[25] P. Rajan et al., "Synthesis and evaluation of caffeic acid amides as antioxidants," *Bioorg. Med. Chem. Lett.*, vol. 11, pp. 215–217, 2001.

[26] R. Gudipati, R. N. R. Anreddy, and S. Manda, "Synthesis, anticancer and antioxidant activities of some novel N-(benzo[d]oxazol-2-yl)-2-(7- or 5-substituted-2-oxoindolin-3-ylidene) hydrazinecarboxamide derivatives," *J. Enzyme Inhib. Med. Chem.*, vol. 26, no. 6, pp. 813–818, 2011, doi: 10.3109/14756366.2011.556630.

[27] Studer, "A 'Renaissance' in radical trifluoromethylation," *Angew. Chem. Int. Ed.*, vol. 51, no. 36, pp. 8950–8958, Sep. 2012, doi: 10.1002/anie.201202624.

[28] A. Rice-Evans, N. J. Miller, and G. Paganga, "Structure-antioxidant activity relationships of flavonoids and phenolic acids," *Free Radic. Biol. Med.*, vol. 20, no. 7, pp. 933–956, 1996, doi: 10.1016/0891-5849(95)02227-9.

BİTLİS EREN ÜNİVERSİTESİ
FEN BİLİMLERİ DERGİSİ

ISSN: 2147-3129 / e-ISSN: 2147-3188

Article Type	: Research Article	**Year**	: 2025
Received	: May 29, 2025	**Volume**	: 14
Revised	: September 17, 2025	**Issue**	: 3
Accepted	: September 20, 2025	**Pages**	: 1718-1735
DOI	: 10.17798/bitlisfen.1707347		

DESIGN AND MANUFACTURING OF SHAKING TABLE FROM SCRAP/USED PARTS

Ersan KIRAR [1,*], Muhammed Şerif YOLUK [2], Cihan AYHANCI [3]

[1] *Harran University, Department of Machinery and Metal Technologies, Şanlıurfa, Türkiye*

[2] *Harran University, Department of Construction Technologies, Şanlıurfa, Türkiye*

[3] *Harran University, Department of Electrical and Energy Technologies, Şanlıurfa, Türkiye*

**** Corresponding Author:*** *ekirar@harran.edu.tr*

ABSTRACT

Structures are exposed to different loadings throughout their lifespan. One of these loadings is the vibration loading caused by earthquakes. Examining the effects of these loading conditions on structures is very important in terms of structural safety. Examining the vibration characteristics of structures using a shaking table is frequently preferred. It has been determined from the literature review that shaking tables can be designed and used as one, two or three axes. However, no study has been found that produces one axes shaking tables using scrap/used parts. Therefore, in the study, a low-budget and environmentally friendly shaking table was designed and produced using scrap/used parts.

Keywords: Earthquake, Shaking table, Scrap/used parts.

1 INTRODUCTION

Earthquakes are sudden vibrations caused by fractures in the earth's crust, and the main reasons for past structural fractures have usually been engineering defects or inadequate inspection. In order to reduce earthquake risk, it is of great importance to determine the earthquake resistance of building materials and subunits in advance [1].

Due to their dynamic nature, earthquakes are generally the greatest threat that structures face throughout their service life. This dynamic force can affect the structure in many different

ways. It would be correct to evaluate characteristic parameters such as the height, geometry and load-bearing system of the structure and the effects of the earthquake together. Carrying out the structural design by considering these dynamic threats plays an important role in ensuring that the structure meets the expected service standard [2].

Shaking tables are one of the methods used to investigate the effects of dynamic earthquake loads on structures. Therefore, when the boundary conditions are correctly adapted in shaking tables, important information can be obtained about the behavior of structures during earthquakes. Additionally, full-scale structures can be tested on this table [2,3,4].

In the literature review, a limited number of studies on shaking table design and manufacturing were found. When these studies are examined; Durgun et al. (2013) [5], examined the dynamic characteristic changes of the structure by applying forces at different frequencies to the structure and recording free vibrations. Birdal et al. (2015) [6], performed dynamic experiments using a 1/3 scaled reinforced concrete model of a prototype structure. As a result of the experiment, they determined that the damage to the structure generally occurred at the nodes due to the shear effect. Bayhan et al. (2013) [7], present the numerical analysis results of the shaking table experiments conducted in the "blind guess" competition at the 15th World Conference on Earthquake Engineering. It was stated that the analytical results successfully followed the displacement motion measured in consecutive experiments, but there was a 20-35% error margin in high-intensity experiments. Ağcakoca (2019) [8], tested a scaled 30 floor shear wall building model on the shaking table in order to examine the behavior of the structure under earthquake load. The finite element analysis results of the structure were compared with the experimental results and it was determined that the finite element model provided a sufficient approach for the examined structure. Şahin et al. (2017) [4], carried out vibration tests on the shaking table on a scale model of a real 6 floor reinforced concrete structure in order to determine the seismic capacity of the structures. Künkcü et al. (2023) [9], applied Multi-Criteria Decision Making methods for the selection of the shaking table test model. The ranking results of the applied methods were compared and it was shown that these methods are frequently used in similar studies in the literature. Kan et al. (2025) [10], conducted a review study on the adjustment of the scale and seismic vibration wave input that should be taken into consideration when using the shaking table in testing samples. Çelik et al. (2013) [11], introduced the low-cost unidirectional shaking table with electric motor, designed and manufactured at Pamukkale University. They stated that they obtained acceleration values up to 600 cm/s² and speed values up to 30 cm/s with the shaking table. Tayfur et al. (2020) [2],

developed a two-axis shaking table as an alternative to existing high-cost shaking tables within the scope of the study. They determined that the produced device can simulate the desired earthquake data with 0.05 mm precision. Torun et al. (2009) [3], designed and manufactured a two-axis shaking table that can visually produce the L-wave oscillation motion in order to experimentally examine the dynamic behavior of structures under the effect of earthquakes.

As a result of the literature review, it was seen that the majority of the studies on the shaking table were used for testing the samples. However, it was determined that a small number of studies were on the design and manufacturing of the shaking table. In addition, no study was found on the design and production of shaking tables using scrap or used parts. For this reason, scrap/ used parts were used in the study for the design and production of the shaking table. Considering the scrap/used parts provided, the mechanical design was first created in a computer environment with solid modeling. The dynamic examination of the most optimum mechanical design was carried out and its suitability for application was checked. The production and assembly of the parts belonging to the clarified mechanical design were carried out. The electrical infrastructure was created for the movement of the table in the mechanical design according to the earthquake vibration data. The final shaking table obtained was examined dynamically and its suitability was determined. As a result of the study, a low-cost single axis shaking table was designed and produced using scrap/used parts and a different perspective was presented to the literature. In addition, the study has originality because there is no environmentally friendly shaking table obtained by using scrap/used parts in the literature.

2 MATERIAL AND METHODS

2.1 Material

2.1.1 Parts Used in the Design

- Main chassis: A main chassis consisting of L-shaped profiles (50x50x6 mm^3) obtained from scrap was used in the design and manufacturing of the shaking table. As the scrap main chassis was already durable and rigid, it was directly employed in the design without modifications (Figure 1). The cost of creating a main chassis from scratch was eliminated with the scrap main chassis used.



Figure 1. Scrap main chassis

-Table: Since the shaking table used was supplied together with the main chassis obtained from scrap, it was used directly in the table design. Since the used table was suitable for the designed shaking table sample dimensions, it was used directly without any extra processing (Figure 2). The dimensions of the table used are 500x500x6 mm^3.

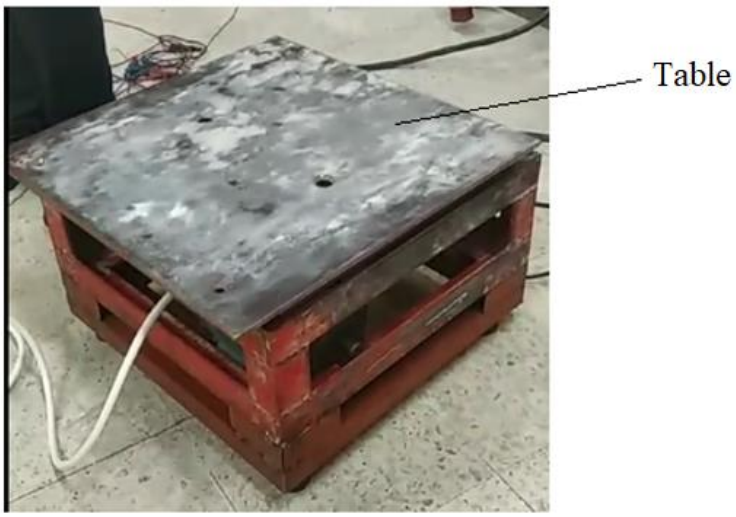


Figure 2. Scrap table

- Induction motor: The induction motor is the most widely used type of electric motor in industry, powered by alternating current (AC). It is called “asynchronous” (non-synchronous) because its main characteristic is that the rotor speed lags behind the rotating speed of the stator field. The basic principle of operation of asynchronous motors is based on electromagnetic induction [12]. It was ensured that the induction motor used was powerful enough to move the table with the sample on it. For this reason, a 1.5 kW induction motor was preferred (Figure 3). The motor was also supplied from a scrap dealer. The deficiencies on the motor were completed and used in the design.



Figure 3. Induction motor obtained from scrap

- Sled: In order to reduce the cost in the shaking table design, a vehicle seat sled suitable for the working conditions was used. While custom-made or ready-made sleds could normally be used for the design, they were not used in this design. A used vehicle seat sled was obtained and incorporated into the design (Figure 4). In addition, the suitability of the used sled for the sample load to be carried (Maximum load 100 kg) was determined by considering the working conditions in the normal vehicle. The design cost was reduced in this part with the used ready-made sled.



Figure 4. Vehicle seat sled preferred in design

- Variable frequency drive: Variable frequency drive, also known as variable speed drive, is an electronic device used to control the rotational speed and torque of alternating current motors by varying the frequency and voltage of the supplied power [13]. A variable frequency drive (VFD) converts a constant frequency alternating current supply into direct current using a rectifier, then uses power electronic switches to produce an alternating current output with adjustable frequency and voltage [14]. By controlling the frequency, the motor speed is precisely regulated, which is not possible with direct grid connection [15]. Used in many applications, VFDs are also important for soft-start motors, reducing inrush currents and

shocks [16]. In the study, a variable frequency drive was used to change the speed of the electric motor rotating at a fixed speed (Figure 5). In this way, the linear movement of the table was obtained at the desired speed.



Figure 5. Used variable frequency drive

- Tie rod: An arm and a disc were used in the design to convert the circular motion coming out of the motor into the linear motion of the table. A vehicle tie rod with a circular profile of sufficient strength was used in the design to move the loaded table linearly (Figure 6). Since the tie rod used has sufficient strength considering where it is used in the vehicle, it was interpreted that it would not cause any problems in terms of strength in the design. In addition, the preferred cantilever tie rod piece was used for the shaking table because its shape and dimensions were suitable.



Figure 6. Tie rod removed from the vehicle

- Tie rod and main chassis connection rod: This part is a part obtained by welding scrap parts (Figure 7). With this part, the tie rod and main chassis connection is provided and the circular motion of the motor is converted to linear and transferred by the mechanism.



Figure 7. Tie rod and main chassis connecting rod

- Square profiles: Extra square profiles were added under the main chassis to create a more aesthetic design by placing the engine and mechanisms inside the main chassis used. The height of the design was increased by 80 mm with the new profiles added. Scrap square profiles of 40x40x2 mm^3 were used for ground elevation (Figure 8).

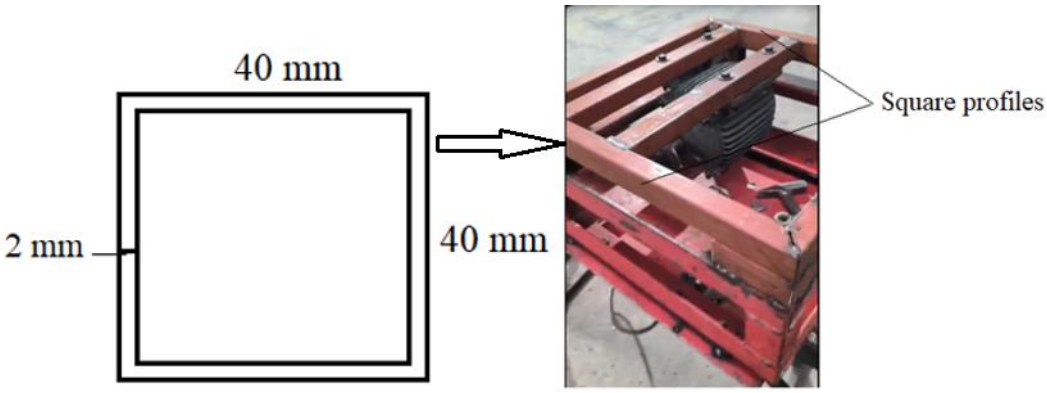


Figure 8. Square profiles

- Disk at the motor end: A 95 mm diameter and 10 mm thick disk was used to convert the circular motion coming out of the motor into linear motion and was mounted to the motor end with a wedge channel in the mechanism (Figure 9). The motor motion was transferred to the table by moving the arm with the disk used. The design cost and recycling were contributed by providing the circular disk used from scrap.



Figure 9. Scrap disc used and its assembled form

2.2 Method

2.1.1 Shaking Table Design

For the design of the shaking table, preliminary work was carried out using solid modelling in a computer environment, taking into account the parts obtained from scrap/used. The shaking table was solid modelled by taking into account the dimensions and geometries of the parts used (Figure 10).

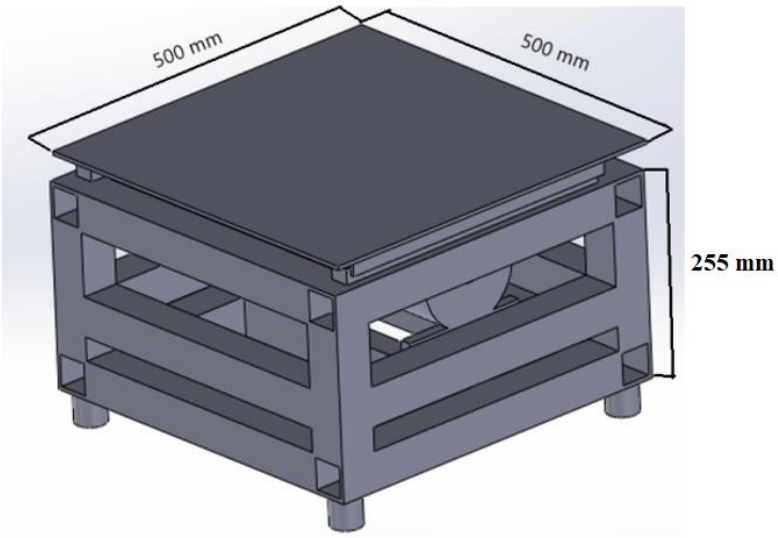


Figure 10. Solid modeled shaking table design

The linear movement limit of the table (±25 mm) was determined. In order to obtain the determined linear movement, the mechanism frequently preferred in the literature [3] was used to convert the circular movement coming from the electric motor into linear movement in Figure 10. In the mechanism used, the circular movement obtained from the motor was converted to linear by a wedge on the motor shaft and a disc and jointed arm welded from a point (to limit the axial movement on the shaft) (Figure 11).



Figure 11. Mechanism used to convert circular motion into linear motion

2.2.2 Shaking Table Manufacturing, Assembly and Painting

The scrap/used parts provided were revised in order to make them suitable for use in the design at the first stage. The drilling operations in Figure 12 were performed for the assembly of the sled to be used on the main chassis. The vehicle seat sled used was divided into two and revised for assembly on the main chassis. The locking mechanism on the seat sled was cancelled and the sled was easily used on the shaking table. The tie rod was adjusted to be suitable for assembly. The connection pole to which the tie rod would be mounted was formed by welding the scrap parts to the main chassis. The strength of the structure was increased by placing triangular supports on the edges of the connection pole (Figure 12). Since there was not enough volume under the main chassis for the engine and movement mechanisms, an addition was made by welding scrap square profiles underneath. Afterwards, the electric motor was mounted on the added square profiles with bolts. The table used on the shaking table was mounted on the sled without any revision process by welding (bolt) connections (Figure 12).

Table 1. Joining methods between parts used in the design

Parts	Joining method
Main chassis-additional profiles	Welded joint
Main chassis-sled	Mechanical (Bolt) joint
Sled-table	Welded joint
Electric motor-Main chassis	Mechanical (Bolt) joint
Electric motor-disc	Wedge and welded joint
Disc-arm (Tie rod)	Mechanical (Pin) joint

According to the obtained data, the parts used in the design were combined. The methods of combining the parts are presented in Table 1. As a result of combining the parts, the mechanical processes of the shaking table were completed. The shaking table parts, whose mechanical processes were completed, were cleaned by grinding (Figure 12). The cleaned shaking table parts were painted in anthracite color with spray paint as seen in Figure 12.



Figure 12. Revision stages, assembly and painting of shaking table

2.2.3 Shaking Table Electrical Installation

In the mechanically designed shaking table, the linear movement of the table was provided by the 1.5 kW electric motor (Figure 13). A variable frequency drive was used to adjust the table speed. Thanks to the inverter and electric motor used, the table could be moved at the desired speed and dynamic examination of the samples on the table could be performed.

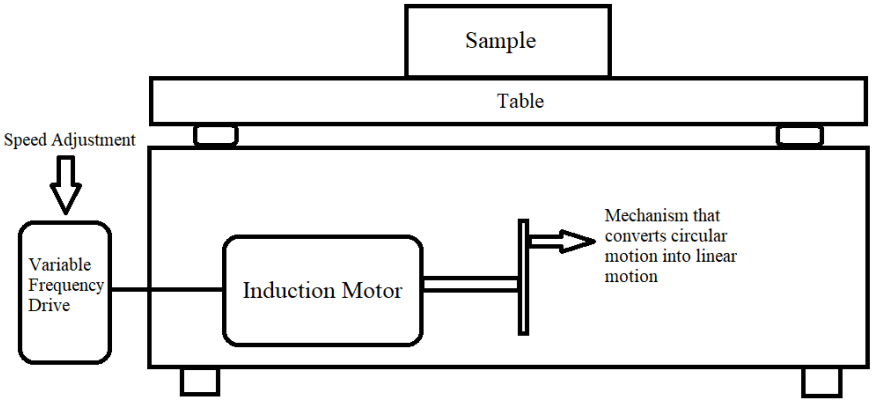


Figure 13. Electrical installation used in shaking table design

In the study, it was assumed that the table had a fixed single axis speed during operation. Therefore, the table speed could be adjusted to the desired fixed speed by adjusting the frequency of the speed variable frequency drive obtained from the motor. Within the scope of the study, the speed adjustment equations for the inverter system were also presented between Equations 1-6. With the help of the presented equations, the table could be adjusted to the desired speed by adjusting the frequency in the variable frequency drive.

Stator and rotor voltage equations study the electrical behavior of stator and rotor circuits. They are usually written in a rotating reference frame [17,18].

$$V_s = R_s I_s + \frac{d\psi_s}{dt} \tag{1}$$

$$0 = R_r I_r + \frac{d\psi_r}{dt} + j\omega_r \psi_r \tag{2}$$

In this equation, V_s is the stator voltage, I_s and I_r are the stator and rotor currents, R_s and R_r are the stator and rotor resistances, ψ_s and ψ_r are the stator and rotor magnetic fluxes, and ω_r is the rotor angular speed [17,18].

Magnetic flux equations determine the relationship between stator and rotor currents and magnetic fluxes [17,18].

$$\psi_s = L_s I_s + L_m I_r \tag{3}$$

$$\psi_r = L_m I_s + L_r I_r \tag{4}$$

In this equation; L_s, L_r are the stator and rotor inductances and L_m is the mutual inductance [17,18].

The mechanical equation of motion relates the angular velocity change of the rotor to the electromagnetic torque T_e, the load torque T_L and the frictional effect. J is the inertial moment and B is the coefficient of friction [17,18].

$$J\frac{d\omega_r}{dt} = T_e - T_L - B\omega_r \tag{5}$$

Slip (s) is defined as the ratio of the difference between the synchronous speed ω_s and the rotor speed ω_r [17,18].

$$s = \frac{\omega_s - \omega_r}{\omega_s} \tag{6}$$

3 RESULTS AND DISCUSSION

3.1 Review Of Shaking Table Design

The majority of the shaking table seen in Figure 14 is made of scrap/used parts. With the design in Figure 14 where the scrap/used parts used can work in harmony, a shaking table with a size of 500x500 mm^2 and a maximum sample carrying capacity of 100 kg was obtained. In the obtained design, the outcome was an environmentally friendly and low-cost design by revising and reusing the scrap/used parts. All parts of the obtained design were painted in anthracite color at the final stage. In addition, yellow lines were added to the table and the mechanism at the end of the motor was painted in yellow to provide visuality.



Figure 14. Final painted version of the shaking table

3.2 Dynamic Investigation of Shaking Table

The shaking table is designed with a ±25 mm linear working limit. Figure 15b shows the zero position of the design. Figure 15a shows the -25 mm movement limit of the table. Figure 15c shows the +25 mm movement limit of the table.

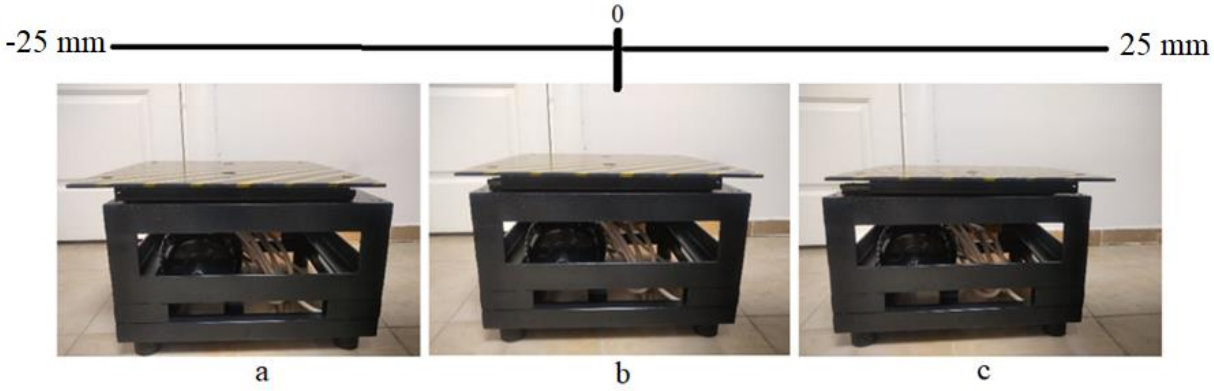


Figure 15. Linear movement limits of the shaking table

The table displacement/disc rotation angle graph is presented in Figure 16. When Figure 16 is examined, it is determined that dynamic examination of the samples can be performed by moving the table between +25 and -25 mm.

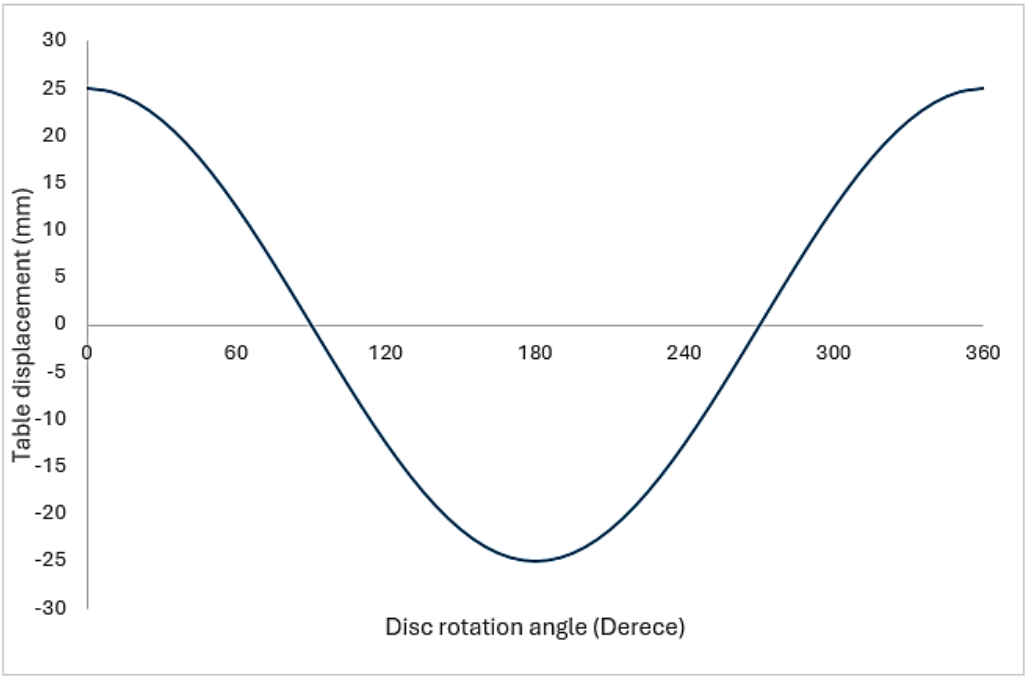


Figure 16. Table displacement/disc rotation angle graph

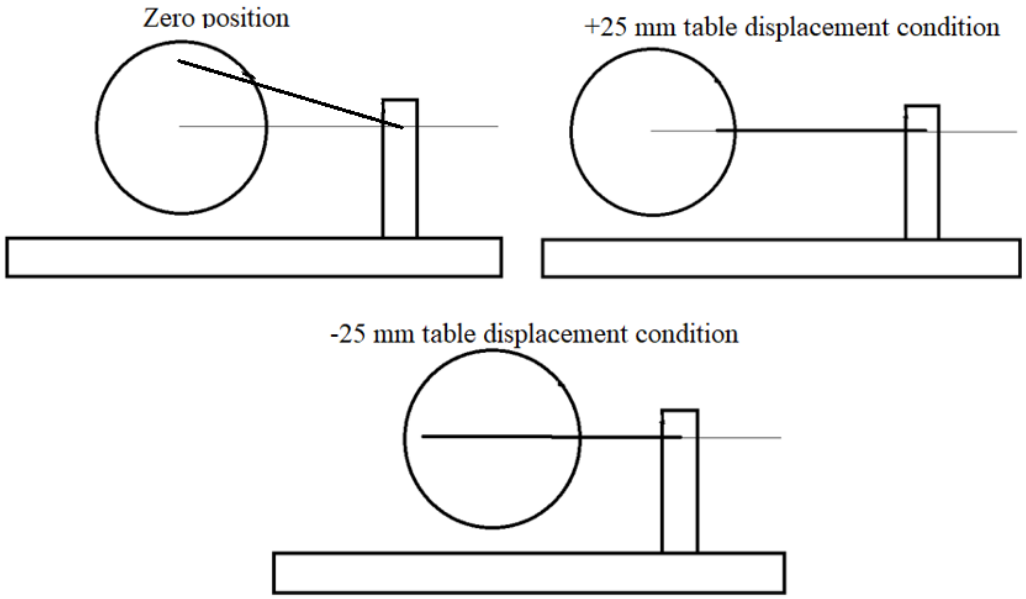


Figure 17. Mechanism shape according to table position

The mechanism shapes at the maximum, minimum and zero positions of the table are presented in Figure 17. In order to determine the table speed during the movement of the mechanism, the visual for the dynamic examination in Figure 18 was prepared and the motion equation in Equation 7 was created. With Equation 7, the speeds of the tie rod and table can be found by placing the motor speed at the desired disk angle into the equation. Simplifying assumptions were used in the derivation of Equation 7. The assumptions used are;

• Because the mechanism used has two axes of motion, the third axis is not included in the equation.

• Due to the sufficient lubrication of the moving parts in the mechanism, the effect of friction is considered to be minimal, so it is neglected.

• Due to the low inertial resistance of the disc and arm used, the table's inertia effects on the velocity equation are considered to be minimal, so the inertia effects of the parts are neglected.

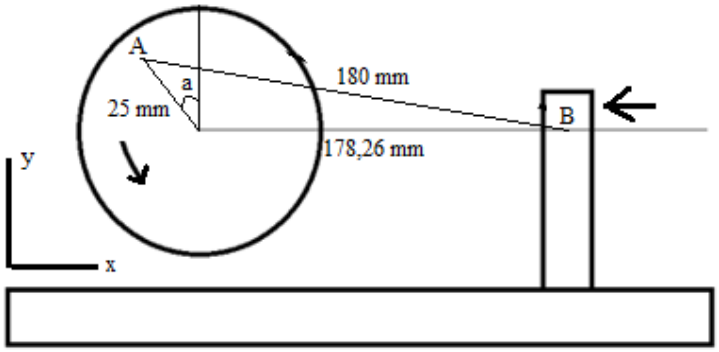


Figure 18. Dynamic motion equations of the table

$$-V_B = W_d k(-25cos(a)i + 25sin(a)j) + W_{tr} k((178{,}26 + 2525cos(a))i - 25sin(a)j) \quad (7)$$

3.3 Cost Analysis of Shaking Table

Table 2 presents the manufacturing costs and comparison of the shaking table from scrap material and new parts. While making cost analysis as a new part, raw material and processing costs were taken into consideration for a part that needs to be processed (Main chassis, Table, Connecting rod, Connecting rod and main chassis connection pole, Disc at motor end). If there is no need for any processing for the part used in production (Electric motor, Inverter, Sled, Square profiles), the procurement cost was used.

For the shaking table, mostly scrap/used parts were used to contribute to recycling. By evaluating the scrap/used parts for redesign, both a contribution to nature was made through recycling and a low-cost design was obtained. Table 2 presents the cost of the design obtained from scrap/used parts and the cost schedule of the design obtained from zero parts.

As a result of the study, a shaking table with a very low cost compared to its peers in the literature [2,3] and an environmentally friendly shaking table was obtained. According to the data obtained, it was determined that 85.15% savings were achieved in the design by using mostly scrap/used parts.

Table 2. Cost comparison of design for scrap/used and new part usage cases

	Cost analysis in case of using scrap/used parts (TL)	**Cost analysis in case of using new parts (TL)**
Main chassis	1000	15000
Table	500	5000
Electric motor	1000	7000
Sled	250	5000
Inverter	4000	4000
Connecting rod	50	2000
Connecting rod and main chassis connection pole	400	3000
Square profiles	500	3000
Disc at motor end	250	3000
Assembly cost	1000	10000
Painting and grinding	1000	10000
Total cost	9950	67000

4 CONCLUSION

In the study, scrap/used parts were revised again and used in the shaking table design. In the design phase, solid modeling study was carried out by considering the geometry and dimensions of the scrap/used parts. The manufacturing phase of the design determined with solid modeling was started. The scrap/used parts were revised as determined and the parts were assembled. After the mechanical processes were completed, the electrical processes were carried out and the movement of the table was provided. When the data obtained as a result of the study was examined;

• Dynamic examination confirmed that the shaking table design using scrap/used parts was suitable.

• It was determined that the table had a movement limit of 25 mm.

• The maximum safe sample carrying capacity was 100 kg was determined.

• The shaking table can be moved at the desired speed with the variable frequency drive used.

• It was ensured that the table speed could be obtained with the dynamic motion equation of the table depending on the motor speed and the angular position of the disk.

• 85.15% cost savings were achieved with the use of scrap/used parts compared to the design using new parts.

• It has been determined that recycling of scrap/used parts contributes to nature.

Acknowledgements

We would like to thank Ahmet ÖNCEL, İrfan ŞİT, Muhammed Ali COLBAN from the Mechanical Program students and Osman TOĞUN, Abdulkadir YETİM, İzzettin TAŞ from the Construction Program students who contributed to the study phase.

Conflict of Interest Statement

There is no conflict of interest between the authors.

Statement of Research and Publication Ethics

The study is complied with research and publication ethics.

Artificial Intelligence (AI) Contribution Statement

This manuscript was entirely written, edited, analyzed, and prepared without the assistance of any artificial intelligence (AI) tools. All content, including text, data analysis, and figures, was solely generated by the authors.

Contributions of the Authors

Conceptualization E.K., M.Ş.Y. and C.A.; methodology E.K., M.Ş.Y. and C.A.; investigation E.K. and M.Ş.Y.; writing—original draft preparation E.K., M.Ş.Y. and C.A.; All authors have read and agreed to the published version of the manuscript.

REFERENCE

[1] T. Özbıyık, "Sismik analiz simülatörlerinde hidrolik sistemlerin yeri", *VIII. Ulusal Hidrolik Pnömatik Kongresi Bildiriler Kitabı*, Makina Mühendisleri Odası Yayın No: 678, s. 123-145.2017.

[2] B. Tayfur, E. Uslu, Ö. Can, A. Cihan and E. Öztekin, "2 Eksenli Sarsma Tablası Tasarımı ve İmalatı", *Bayburt Üniversitesi Fen Bilimleri Dergisi*, 3(2), 131-137. 2020.

[3] A. Torun and M. Çunkaş, "İki eksende salınım yapan sarsma tablası tasarımı ve gerçekleştirilmesi", *Afyon Kocatepe Üniversitesi Fen ve Mühendislik Bilimleri Dergisi*, 9(2), 85-96. 2009.

[4] Ö. Şahin, N. Çağlar and E. Çelebi, "Küçük Ölçekli sarsma tablası test modelleri için uygun ölçeklendirme katsayısının araştırılması", *In 5th International Symposium on Innovative Technologies in Engineering and Science*, pp. 7-16. 2017.

[5] Y. G. Durgun, M. Aktaş and M. Kutanis, "Sarsma tablasına yerleştirilmiş 3 katlı hasarlı ve hasarsız çelik yapı modelinin dinamik karakteristiklerinin belirlenmesi", *2. Türkiye Deprem Mühendisliği ve Sismoloji Konferansı*, 25-27 Eylül, MKÜ, Hatay. 2013.

[6] F. Birdal, F. Altun and A. K. Tanrıkulu, "Sarsma tablası deney sonuçlarına göre dinamik karakteristiklerin belirlenmesi, ölçekli betonarme bir yapının nonlineer dinamik ve statik analizlerinin karşılaştırılması". *Sekizinci Ulusal Deprem Mühendisliği Konferansı*, 11-14 Mayıs, İstanbul. 2015.

[7] B. Bayhan and G. Özdemir, "Betonarme binaların sismik tepkisinin tahmininde ne ölçüde başarılıyız": Sarsma Tablası Simülasyonları, *2. Türkiye Deprem Mühendisliği ve Sismoloji Konferansı*, 25-27 Eylül, Hatay.2013.

[8] E. Ağcakoca, "Yüksek katlı yapının sarsma tablası üzerinde deprem performansının incelenmesi", *ALKÜ Fen Bilimleri Dergisi*, 1(3), 132-143. 2019.

[9] H. Künkcü, O. Aytekin and H. Kuşan, "Sarsma tablası test modelinin çok kriterli karar verme yöntemleri ile seçilmesi: bir uygulama", *Eskişehir Osmangazi Üniversitesi Mühendislik ve Mimarlık Fakültesi Dergisi*, 31(2), 620-629. 2023.

[10] Y. Kan, X. Rong and J. Zhang, "Shaking table test research on novel frame structures:a review", *Buildings* 15, 1368. 2025.

[11] S. B. Çelik, H. Kumsar and Ö. Aydan, "Mekanik bir sarsma masasıyla elde edilebilen hareket parametreleri ve bir uygulama", *Pamukkale Üniversitesi Mühendislik Bilimleri Dergisi*, 19(5), 224-230. 2013.

[12] M. B. de F. Sartori, "Asynchronous motors" *Elsevier eBooks*, pp. 280–298.2023. https://doi.org/10.1016/b978-0-12-821204-2.00003-9.

[13] N. Sawalhi," Improved order tracking in vibration data utilizing variable frequency drive signature", *Sensors (Basel, Switzerland)*, 25(3), 815. 2025.

[14] S. Nadweh, O. Khaddam, G. Hayek, B. Atieh and H. H. Alhelou, "Time response enhancement for variable speed drive systems by using five-level cascade four quadrant chopper in dc-link", *Heliyon*, 6(8). 2020.

[15] Y. Verma, B. Mazumdar and P. Ghosh," Dataset on the electrical energy consumption and its conservation in the cement manufacturing industry", *Data in brief*, 28, 104967. 2020.

[16] Y. Sapkota, S. Devkota, V. Borra, P. Cortes, S. Itapu and F. Li, "Harmonic content analysis of a soft starting variable frequency motor drive based on FPGA", *IEEE 3rd International Conference on Sustainable Energy and Future Electric Transportation*, pp.1-5.2023.

[17] A. Karakaya, "Asenkron motorun modellenmesi ve modern denetim yöntemleri ile hız analizi", *Karaelmas Fen ve Mühendislik Dergisi*, 7(2), 497-502. 2017.

[18] K. Kayışlı and H. Güldemir, "Asenkron motorun kayma mod algılayıcısız hız kontrolü". *Bitlis Eren Üniversitesi Fen Bilimleri Dergisi*, 1(2), 92-106. 2004.

BİTLİS EREN ÜNİVERSİTESİ
FEN BİLİMLERİ DERGİSİ

ISSN: 2147-3129 / e-ISSN: 2147-3188

Article Type : Research Article
Received : June 4, 2025
Revised : July 26, 2025
Accepted : September 8, 2025
DOI : 10.17798/bitlisfen.1713149

Year : 2025
Volume : 14
Issue : 3
Pages : 1736-1758

THE EFFECT OF WASTE GLASS POWDER ON THE MECHANICAL AND PERMEABILITY PROPERTIES OF ROLLER-COMPACTED CONCRETE

Zeynep ALGIN [1,*], Delil DEMİR [1]

[1] *Harran University, Civil Engineering Department, Şanlıurfa, Türkiye*

**** Corresponding Author:*** *zyilmaz@harran.edu.tr*

ABSTRACT

In the context of endeavours to mitigate the global environmental impact of the construction industry, the utilization of pozzolanic additives derived from waste materials has emerged as a pivotal area of research, particularly in the pursuit of sustainable materials. The present study investigates the use of ground waste glass powder (WGP) as a binder material in roller-compacted concrete (RCC), whilst also examining the effects of different curing regimes on the mechanical performance of RCC. Within the experimental programme, four main mixture groups were designed by replacing CEM I 52.5 N type cement with WGP at ratios of 0%, 10%, 20%, and 30%. The production process was conducted for each group at five distinct water contents. The optimum water content was determined on the basis of the maximum dry density. The consistency of the fresh mixtures was determined using the modified Vebe test. The mechanical and permeability performance of the samples that had been cured for 28 days was evaluated using a range of testing methods, including compressive strength, flexural strength, water absorption, and sorptivity tests. Furthermore, chemical curing, membrane and wet burlap methods were employed on specimens produced with a 10% WGP replacement rate, and the impact of the curing method was examined. The findings indicate that a 10% replacement of WGP results in optimal performance with regard to both compressive and flexural strength. Conversely, the incorporation of 20% WGP has been demonstrated to enhance permeability properties. The highest strength values were obtained from RCC samples cured wet burlap. The findings of this study demonstrate that WGP can be regarded as an effective binder with a low carbon footprint, and that it offers contributions to RCC in terms of both environmental sustainability and technical performance.

Keywords: Roller-compacted concrete, Waste glass powder, Optimum water content, Curing methods.

1 INTRODUCTION

In the contemporary context, sustainable construction practices are acquiring mounting significance due to a range of factors, including the imperative to curtail environmental degradation, conserve natural resources, and enhance waste management. In this context, the research of new materials aimed at reducing environmental impacts in cement-based materials and the reuse of industrial waste has become a fundamental focus in both academic and applied studies in the field of construction materials. The production of cement, the most widely used binder in the construction industry, is directly linked to high energy consumption and carbon emissions. In particular, it has been reported that Portland cement production accounts for approximately 7% of global carbon dioxide (CO_2) emissions [1-3]. This has prompted research into reducing cement consumption or replacing it with environmentally friendly alternative materials. Consequently, the development of environmentally sensitive, durable, and economically viable binding systems is imperative for achieving sustainability goals in the field of concrete technology. In this context, new-generation concretes produced using alternative materials that can partially or completely replace Portland cement contribute to both reducing carbon emissions and utilising industrial waste.

Waste glass powder (WGP) is regarded as a prospective pozzolanic material that can be integrated into cement matrices due to its elevated silica (SiO_2) content and amorphous structure. This material, which is obtained by grinding waste glass, can be used as a partial substitute for cement in the production of concrete. It has been demonstrated that finely ground glass dust reacts with calcium hydroxide ($Ca(OH)_2$) released during cement hydration, thereby promoting the formation of secondary C-S-H phases [4-6]. The reactivity of amorphous silica in glass powder plays a pivotal role in this process, and the resulting secondary phases increase the amount of C–S–H gel, thereby enhancing the mechanical strength and permeability resistance of concrete [5-6]. Furthermore, the fine-grained structure of WGP has been demonstrated to fill the voids in the concrete's microstructure, thereby reducing permeability and enhancing durability [7]. The utilisation of WGP as a pozzolanic additive in concrete production has been demonstrated to reduce the consumption of natural resources and contribute to a reduction in the carbon footprint [8].

The impact of WGP on conventional concrete has been extensively examined in numerous studies in the extant literature. Uzun et al. (2018) [9] reported that replacing 0–20% of cement with WGP reduces workability but increases compressive strength. This phenomenon

is attributed to the increased water demand resulting from the high specific surface area of glass powder and its micro-filling effect. In the study conducted by Aliabdo et al. (2016) [10], the production of concrete with target compressive strengths of 33 MPa and 45 MPa was achieved through the incorporation of 5–20% WGP replacement [10]. This outcome serves to demonstrate the efficacy of the method in achieving high compressive strengths at low replacement ratios. Orhan and Esen (2017) [11] stated that the pozzolanic activity of WGP is approximately 80%, and that it complies with Turkish standards. The optimum outcomes in terms of tensile strength were achieved with a 10% WGP replacement. In a recent study, Muhedin and Ibrahim (2023) [12] observed an increase in compressive strength of 32% at seven days and 14% at 28 days with a 5% WGP replacement. However, as the replacement ratio increased, the strength increases remained limited or decreased. Ibrahim (2021) [13] reported an increase in compressive strength of 7.5% and a further increase in tensile strength of 13.15% with a 5% WGP replacement, but a decrease in strength was observed after a 15% replacement ratio. Sakale et al. (2016) [14] reported that the optimal substitution ratio is 20%, at which flexural and tensile strength reach their highest values, but mechanical strength decreases at ratios above 20%. It was also noted that elevated substitution ratios have a detrimental effect on workability. In their study, Mahmoud et al. (2019) [15] examined the impact of partial replacement of cement with 10–25% WGP, observing substantial increases in compressive strength at replacement ratios of 15–20%. The highest observed strength was recorded at a 20% replacement ratio, which resulted in a 53% increase. Conversely, a decrease in strength was observed at a 25% replacement ratio.

Roller compacted concrete (RCC) is a type of concrete characterised by a low water-to-cement ratio and dry consistency, with placement and compaction typically carried out using vibrating rollers. Its primary applications include large-scale infrastructure projects such as roads, dams, and airports [16]. Although it shares similar components with traditional concrete, RCC offers cost-effectiveness due to its ability to be applied without formwork, its lack of reinforcement requirements, and its rapid placement [17-19]. However, due to its low water-to-cement ratio, RCC's performance is highly sensitive to curing conditions. The large surface area and rapid production increase moisture loss in fresh concrete, which negatively affects hydration and strength development [20-22]. Therefore, curing conditions are as critical as mix design in RCC production.

In recent years, there has been an increase in the utilisation of alternative binders in the production of RCC. This approach is significant in terms of both reducing environmental impact

and offering cost advantages. Pozzolanic additives, such as fly ash, granulated blast furnace slag, and silica fume, have been extensively researched [23-28]. Conversely, alternative pozzolans, such as glass powder, have been the focus of only a limited number of studies. The extant literature pertaining to the effects of WGP on RCC is relatively limited, with existing studies primarily focusing on strength development. For instance, Faubert et al. (2013) [29] reported that RCC mixtures produced with 10–25% WGP replacement achieved the highest compressive and flexural strengths at 91 days at a 20% replacement ratio. Omran et al. (2017) [30] observed that RCC containing 20% WGP demonstrated compressive and flexural strengths that were 5% and 15% higher, respectively, at 91 days. Furthermore, SEM analyses revealed a more dense microstructure.

The efficacy of curing methods is a critical factor in the development of mechanical strength, particularly in RCC mixtures with low water-to-cement ratios. As outlined in the ASTM C171 [31] and ASTM C309 [32] standards, the implementation of curing methods must be executed in a manner that ensures moisture retention, thereby facilitating continuous hydration in RCC. In the study conducted by Keleş (2019) [22], the application of chemical curing, membrane, and wet burlap methods with delays ranging from 0 to 60 minutes was investigated, and it was demonstrated that the optimal results were obtained with water curing, while wet burlap emerged as an economical and feasible alternative.

The objective of this study is to systematically evaluate the effects of WGP content and different curing methods on the fresh and hardened properties of RCC. RCC mixtures were produced with varying optimum water contents for various WGP replacement ratios. The fresh concrete properties were evaluated using the modified Vebe test, while the hardened concrete properties were assessed through compressive strength, flexural strength, water absorption, and sorptivity tests. Furthermore, three distinct curing methodologies (chemical, membrane, and wet burlap) were employed on mixtures comprising 10% WGP, and their impact on mechanical performance was evaluated.

This study makes significant contributions to the literature in terms of both the utilization of environmental waste in construction materials and the optimization of the performance of alternative binding material. The partial replacement of cement with WGP in RCC mixtures not only reduces cement consumption and contributes to lowering carbon emissions but also enables the use of more sustainable materials in the construction industry. Furthermore, the study emphasizes that curing conditions represent a critical technical parameter that must be carefully selected in RCC applications, by highlighting the significant

effects of different curing methods on mechanical strength development. In this regard, the study makes a significant contribution to the objectives of sustainable material development and to engineering requirements related to application safety and performance.

2 MATERIAL AND METHOD

2.1 Materials

In experimental studies, Portland cement of type CEM I 52.5 N, with a specific gravity of 3.16 g/cm³, a Blaine specific surface area of 3123 cm²/g, and compliant with the EN 197-1 (2011) [33] standard, was used as the binding material. The chemical analysis results for the cement are presented in Table 1.

Table 1. Chemical composition of Portland cement

CaO	SiO_2	Al_2O_3	Fe_2O_3	MgO	SO_3	K_2O	Na_2O
62.94	19.03	5.13	3.04	1.62	2.66	0.65	0.14

The mechanical and durability performance of RCC is directly influenced by fundamental parameters, including aggregate type and granulometry. In particular, aggregate size, gradation range, and mix design play a decisive role in the compactness, workability, and final density of the mixture in RCC mixtures. The ACI 211.3R-02 (2009) [34] guideline specifies the maximum particle size recommended for road-type RCC applications, along with the lower and upper limit gradation curves to achieve optimal granulometry. In this study, marble dust and basalt aggregate with a maximum particle size of 19 mm were utilized, in accordance with the aforementioned guideline. The particle size distribution ratios of each aggregate are presented in Table 2, while the specific gravity values and water absorption capacity are shown in Table 3. As demonstrated in Figure 1, the gradation curve obtained for the aggregate mixture is observed to fall within the recommended limit gradation curves by ACI 211.3R-02 (2009) [34], thereby meeting the optimal granulometry conditions. This finding suggests that the prepared aggregates are adequate for supporting the formation of a compact structure and meet the strength and durability criteria targeted for RCC mixtures.

Table 2. Results of aggregate sieve analysis

Sieve size (mm)	Marble dust	Basalt Aggregate		
		0.075-4.75 mm	2.36-12.5 mm	4.75-19 mm
25	100	100	100	100
19	100	100	100	100
12.5	100	100	100	39.24
9.5	100	100	87.87	1.18
4.75	100	99.70	15.79	0.22
2.36	99.61	76.85	1.49	0.22
1.18	96.60	57.74	1.21	0.22
0.6	84.20	42.94	1.21	0.22
0.3	54.70	29.59	1.21	0.22
0.15	34.57	18.36	1.21	0.22
0.075	21.97	11.96	1.21	0.22

Table 3. Physical properties of aggregates used

Aggregate		Specific gravity	Water absorption (%)
Basalt aggregate	4.75-19 mm	2.76	1.47
	2.36-12.5 mm	2.70	2.83
	0.075-4.75 mm	2.65	2.51
Marble dust		2.66	7.36

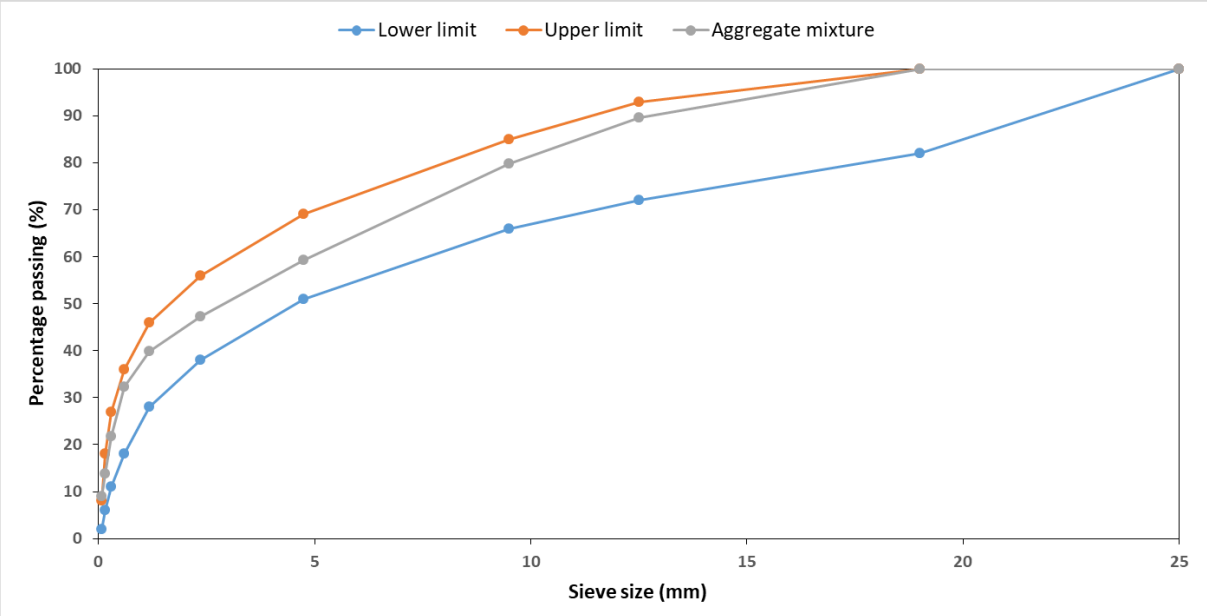


Figure 1. Gradation curve of the aggregate mixture and the limit curves recommended in the ACI guideline

In this experimental study, WGP shown in Figure 2 with a specific gravity of 2.58 g/cm³ and water absorption ratio of 0.02% was used. The WGP used in this study was obtained from Akcihan Glass Industry and Trade Ltd. The particle size distribution percentages of WGP are presented in Figure 3, and its chemical composition is given in Table 4.

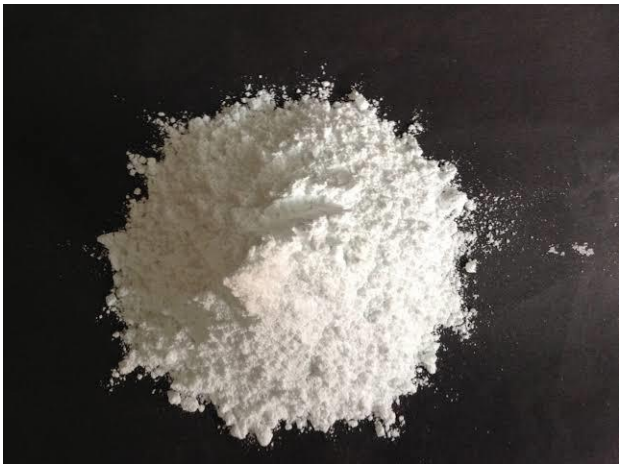


Figure 2. Photograph of WGP used

Table 4. Chemical composition of WGP

SiO_2	Fe_2O_3	CaO	Al_2O_3	MgO	Na_2O	LOI
69.42	0.4	8.27	1.09	4.25	12.31	16.18

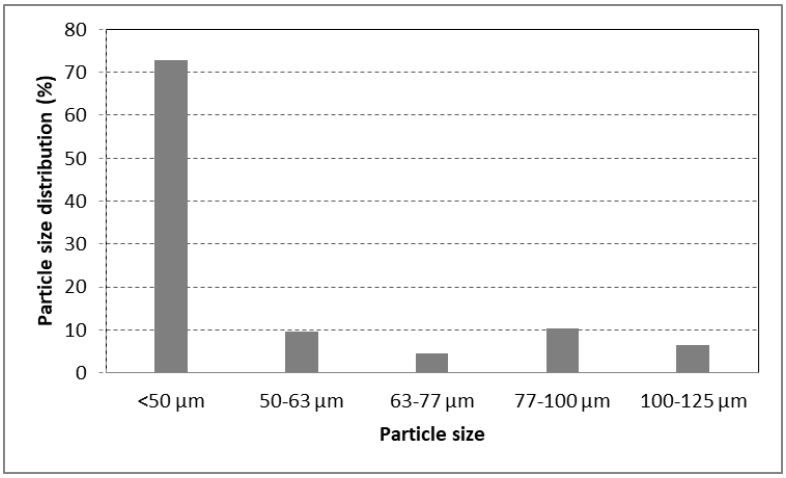


Figure 3. Particles distribution percentage of WGP

For this study, a paraffin-based curing chemical that complies with ASTM C309 (2017) [32] was used in the curing process. The physical properties of this chemical are presented in Table 5.

Table 5. Physical properties of paraffin-based curing chemical

Parameter	Value
Density	0.95-1.00 kg/lt
Colour	White
Consistency	Liquid
Appearance of the final film layer	opaque layer
Consumption	0.15-0.2 kg/m^2

In the process of wet burlap curing, jute fabric that complies with the ASTM C171 (2016) [31] standard was utilised. The material exhibits a surface density of 230 g/m² and a porosity of approximately 2 mm. Furthermore, a 1.5 mm-thick black plastic cover, which complies with the ASTM C171 [31] standard, was utilised as a membrane coating material in the curing process.

2.2 Detail of Mixes and Preparation

In this study, RCC mixtures with varying binder compositions were prepared by replacing cement with WGP at ratios of 0%, 10%, 20%, and 30% by weight. In the initial phase of the experimental programme, the objective was to ascertain the optimal water content for each WGP replacement ratio. In all mixtures, the binder content was maintained at a constant 14% of the total dry aggregate weight. A total of 20 mixtures were designed by testing five different water contents for each WGP level.

The optimum water content was determined based on the principle of maximum density within the framework of the relationship between wet and dry density. For the purpose of this study, each mixture was placed in cylindrical moulds measuring 150×300 mm in three layers. Each layer was then compacted using a vibrating rammer in accordance with the ASTM C1435 (2014) [35] standard (see Figure 4). The total weight of the fresh concrete placed in the mould was measured, and the wet unit volume weights (γ_{wet}) were calculated using Equation 1. Subsequently, random samples were obtained from each layer of the RCC samples extracted from the mould, and their mass (m_{wet}) was determined. The samples were then dried in an oven at 105 ± 5 °C for a period of 24 hours, after which their dry weights (m_{dry}) were determined. The water contents and dry densities of the specimens were calculated using Equation 2 and Equation 3, respectively. Following the creation of point distribution graphs utilizing the water content values corresponding to the dry density obtained, a second-degree polynomial trend line was derived through the implementation of the least squares method. The optimum water contents corresponding to the maximum dry density were identified for each RCC mixture.

$$\gamma_{wet} = \frac{m}{v} \tag{1}$$

$$w = \frac{(m_{wet} - m_{dry})}{m_{dry}} x100 \tag{2}$$

$$\gamma_{dry} = \frac{\gamma_{wet}}{1 + w} \tag{3}$$



Figure 4. Stages of determining the optimum water content of RCC mixtures

The RCC mixture ratios utilized in this study were determined in accordance with the ACI 211.3R-02 [34] guideline, which encompasses the mixture principles advocated for concrete with zero slump values. Following the determination of the optimal water content for each WGP replacement ratio (0%, 10%, 20%, and 30%), four distinct RCC mixtures were produced. The material quantities utilized in the prepared RCC mixtures are presented in Table 6.

Table 6: Quantities of materials used in 1 m³ of RCC mixtures

Mix ID	Cement (kg)	Aggregate		WGP (kg)	Water (kg)
		0-4.75 mm (kg)	4.75-16 mm (kg)		
%0 WGP	276.7	1086.9	889.3	0.00	162.6
%10 WGP	247.8	1081.5	884.9	27.5	164.8
%20 WGP	218.3	1072.1	877.2	54.6	170.0
%30 WGP	189.5	1063.4	870.1	81.2	174.6

As demonstrated in Figure 5, the RCC samples were produced by compaction using vibrating hammer in accordance with the ASTM C1435 (2014) [35] standard. During the production process, fresh concrete mixtures were placed in moulds in three stages, with compaction applied for approximately 20 seconds for each stage. Subsequent to the completion of the compaction process, the samples were left in the moulds for a period of 24 hours, after which they were removed from the moulds and subjected to water curing until the day of testing.



Figure 5. Production of RCC samples

2.3 Testing

The present study employed the modified Vebe test to ascertain the consistency of the RCC mixtures produced. Water absorption, sorptivity, compressive strength, and flexural strength tests were conducted to ascertain the properties of hardened concrete.

In order to ascertain the consistency of RCC mixtures, a modified-Vebe test was conducted in accordance with the ASTM C1170 (2014) [36] standard. In this test, 12.5 kilograms of fresh RCC mixture was loosely placed in the cylindrical chamber of the Vebe device, and a standard load of 22.7 kilograms was applied on top. The stopwatch was initiated when the load came into contact with the mixture, and the device was activated to compress the mixture. The stopwatch was halted when a continuous and distinct ring formed between the surface of the plate exposed to the load and the surface of the test device mould. The measured time was recorded as the modified-Vebe time for the mixture and used as the basis for evaluating the mixture's consistency.

The sorptivity test was conducted on RCC samples measuring 100x100x100 mm in accordance with the ASTM C1585 (2013) [37] standard. The samples were dried in an oven at a temperature of 105 ± 5 °C until they reached a constant mass. The lateral surfaces of the samples were coated with a waterproof adhesive membrane measuring approximately 2–3 cm in width, thereby ensuring that only the inferior surfaces were in contact with water. Subsequent to the membrane application, the dry weight of each sample was measured. The samples were positioned within a capillary water apparatus, characterized by a constant water level, such that only their bottom surfaces were in contact with water. At predetermined time intervals, the samples were retrieved, the excess water on their surfaces was dried using a towel, and they were weighed again. Consequently, the water absorption quantities of the samples were determined as a function of time. The water absorption quantities were calculated by dividing the water absorption quantities by the base area of the sample in contact with water. A graph was then plotted using these values and the square root of the corresponding time intervals. The slope of the best fit line obtained from this graph was defined as the sorption coefficient for each sample. The experiment was conducted on three samples for each mixture, and the sorptivity coefficient was calculated by taking the average.

The water absorption test was conducted in accordance with the ASTM C642 (2013) [38] standard, utilizing RCC samples measuring 100×100×100 mm. The samples were initially dried in an oven at a temperature of 105 ± 5 °C until a constant mass was achieved. Thereafter, the dry masses obtained in this state were recorded. Subsequent to the drying process, the samples were immersed in water for a period of 24 hours, with the objective of achieving a state of saturated surface dry. Subsequently, the residual water present on the surfaces of the samples was removed, and the samples were weighed. The weights obtained from this measurement were recorded as saturated surface dry mass. The water absorption ratio was calculated for each sample, and the arithmetic average of the results obtained from three samples for each mixture was taken.

The flexural strength was conducted in accordance with the ASTM C293 (2016) [39] standard, employing prismatic RCC specimens with dimensions of 100×100×400 mm. The test was conducted based on the three-point loading principle, and three specimens were tested for each mixture. The arithmetic means of the obtained results were calculated.

The compressive strength test was conducted in accordance with the ASTM C39 (2012) [40] standard, on RCC specimens with dimensions of 100×100x100 mm. Three samples were prepared for each mixture and loaded under uniaxial load until failure to determine the

compressive strength. The mean value of the three measurements obtained for each mixture was accepted as the compressive strength of the corresponding mixture.

The workflow diagram, which summarises the stages of the research conducted within the scope of the study, is presented in Figure 6.

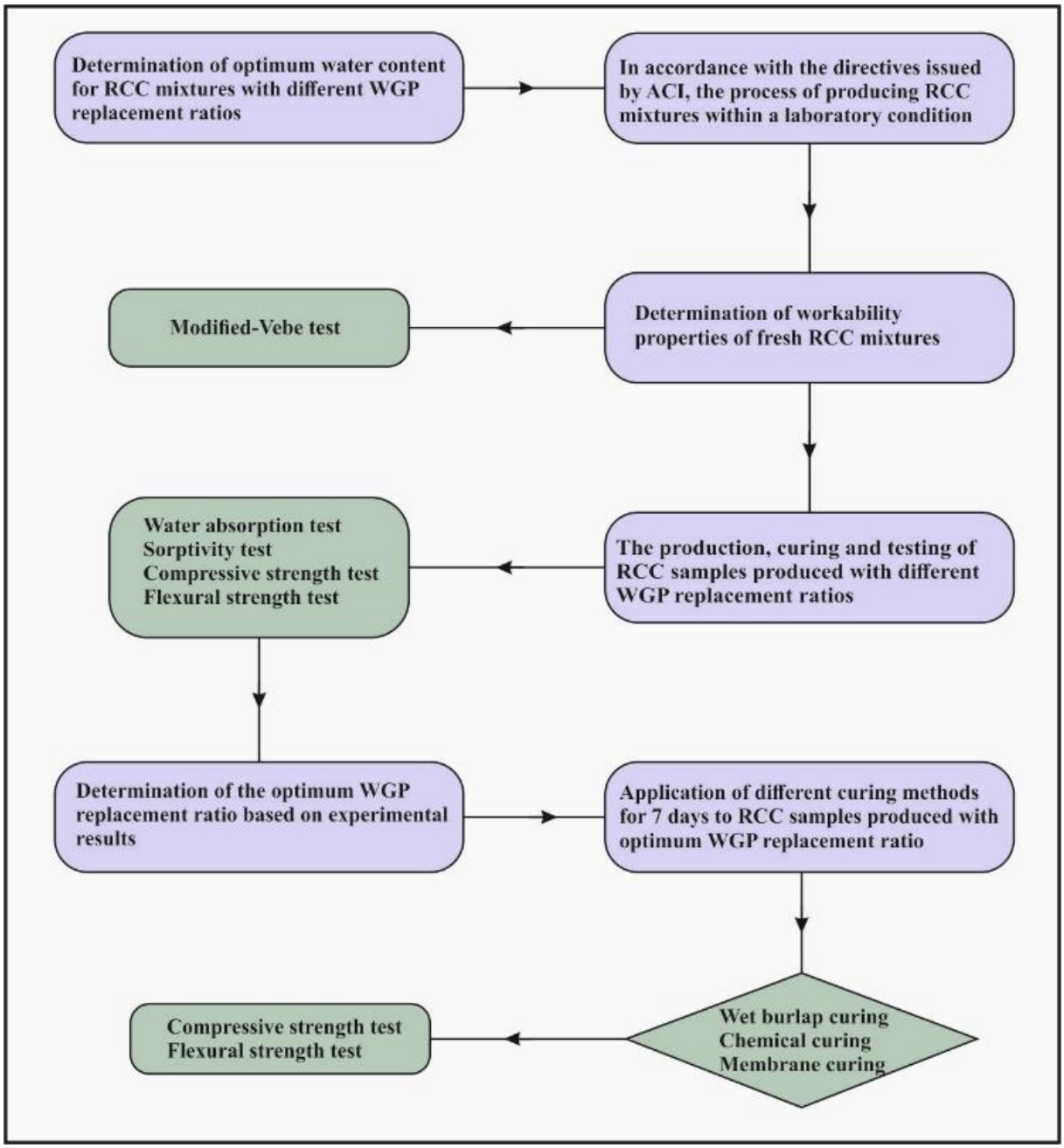


Figure 6. Workflow diagram

3 RESULTS AND DISCUSSION

3.1 Optimum Water Content and Dry Density

Figure 7 shows the relationship between the water content and dry density of RCC mixtures prepared by replacing WGP at different ratios. Experimental studies conducted for each mixture revealed that the optimum water content values corresponding to the maximum dry density for mixtures containing 0%, 10%, 20%, and 30% WGP were 8.23%, 8.38%, 8.72%, and 9.03%, respectively. The results clearly demonstrate that the optimum water requirement of the mixture increases gradually with the increase in the WGP replacement ratio. This phenomenon can be explained by WGP having the finer particle size and higher specific surface area compared to cement. Furthermore, the maximum dry density results corresponding to the optimum water content values obtained for each WGP replacement ratio are also shown in Figure 7. The dry density values thus determined for mixtures containing 0%, 10%, 20%, and 30% WGP were measured as 2291 kg/m³, 2272 kg/m³, 2244 kg/m³, and 2230 kg/m³, respectively. The findings indicate a decreasing trend in the density values of the mixtures as the WGP content increases. This phenomenon can be attributed to the lower specific gravity of WGP in comparison to cement, resulting in a reduction in the total mass per unit volume of the mixture.

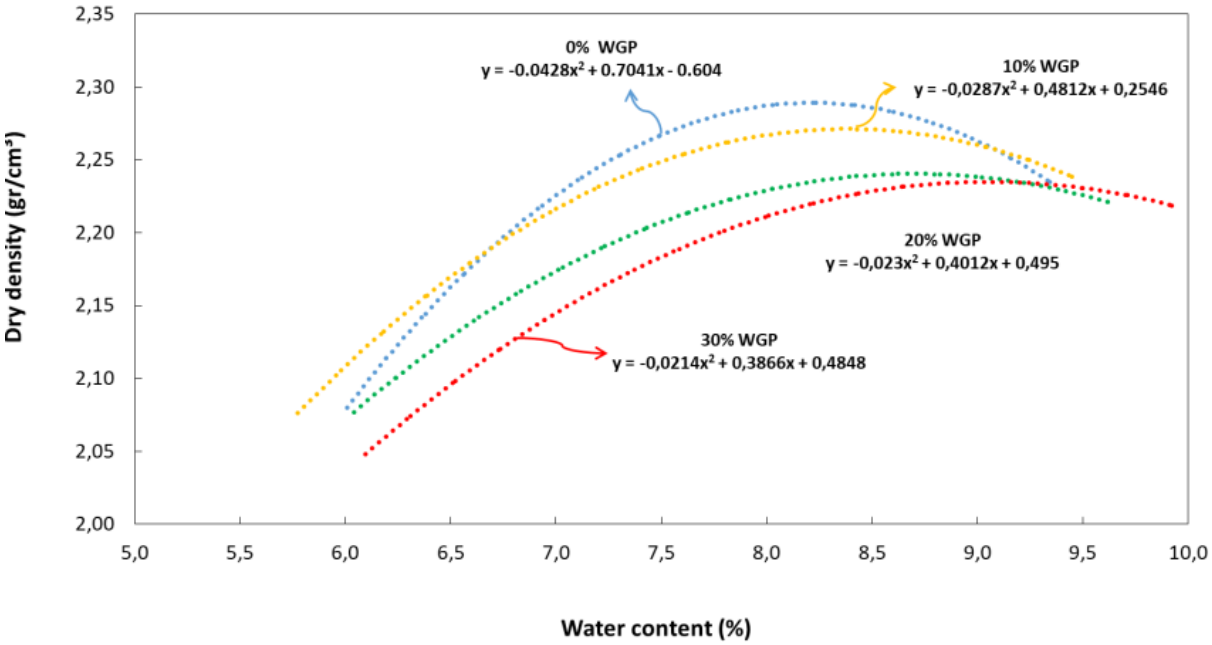


Figure 7. Relationship between water content and dry density of RCC mixtures

3.2 Modified-Vebe Time

In this study, the consistency of RCC mixtures was determined using a modified Vebe test apparatus in accordance with the ASTM C1170 (2014) [36] standard. The Vebe times obtained for mixtures containing 0%, 10%, 20%, and 30% RCC, prepared using the optimum water content, were measured as 34, 35, 37, and 40 seconds, respectively. The results indicate that the Vebe time increases with an increase in the RCC replacement ratio. According to ACI 325.10R (2001) [41] standard, the recommended suitable Vebe time range for RCC mixtures is specified as 30 to 40 seconds. Within this scope, it was determined that all Vebe time values obtained in the study fall within the aforementioned range and thus meet the RCC production criteria. Similarly, in the literature, it is stated that the replacement of cement with WGP in both conventional concrete and RCC increases the water requirement of the mixture and negatively affects workability [9-11].

3.3 Sorptivity

Figure 8 presents the sorptivity coefficients obtained for RCC mixtures with different WGP replacement ratios. The sorptivity coefficients determined for mixtures containing 0%, 10%, 20%, and 30% WGP were measured as 0.0585, 0.0584, 0.0567, and 0.0965 mm/min$^{1/2}$, respectively. These results indicate that the use of WGP at low concentrations positively affects the capillary water absorption of RCC. When compared to the control sample, the sorptivity coefficients of mixtures with 10% and 20% WGP replacement ratios were found to be 0.2% and 3.1% lower, respectively. This improvement is attributed to the fine structure of glass powder, which fills the porous matrix regions and restricts the capillary pore network. However, the sorptivity coefficient of the mixture produced with a 30% WGP replacement ratio showed a 65% increase compared to the control sample. This significant increase can be attributed to the mixture having a higher optimal water content and water/binder ratio.

In line with previous studies, this research found that using glass powder decreases the sorptivity value of concrete, especially at low ratios. A study conducted by Du and Tan (2017) [42] found that using glass powder in concrete significantly improves its sorptivity capacity. Concrete prepared with a 15% glass powder replacement exhibited the highest sorptivity resistance, with only 9% water absorption compared to the reference concrete. This improvement was attributed to the refinement of the pore structure in the cement paste, the reduction of pore connections and densification of the microstructure in the transition zone. Meanwhile, Schwarz et al. (2008) [43] reported that concrete containing 10% glass powder

exhibited lower sorptivity after 14 days, though this effect was reversed after 90 days, with higher sorptivity observed compared to the reference concrete. Matos and Sousa-Coutinho (2012) [44] found that there was no significant change in sorptivity in mixtures containing 10% or 20% glass powder.

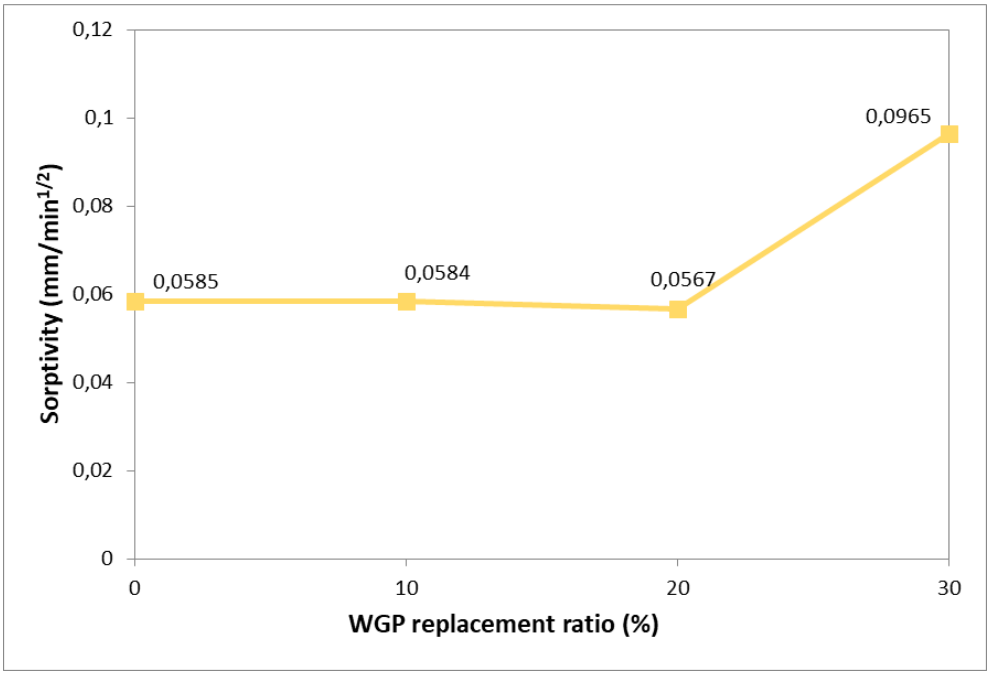


Figure 8. Sorptivity coefficients of RCC samples with different WGP ratios

3.4 Water Absorption Ratio

Figure 9 shows the change in water absorption values of RCC mixtures depending on WGP replacement ratios. The water absorption values measured in RCC samples with 0%, 10%, 20%, and 30% WGP content were determined as 3.72%, 3.67%, 3.61%, and 3.87%, respectively. The results obtained indicate that the use of WGP at low replacement ratios improves the permeability properties of concrete. Compared to the control mixture, the water absorption ratios of mixtures containing 10% and 20% WGP were found to be 1.4% and 3% lower, respectively. This can be explained by the micro-filling effect of glass powder, which partially fills capillary voids and reduces the concrete's permeability to water. However, when the WGP replacement ratio was increased to 30%, the water absorption ratio increased by 4.04% compared to the control mixture.

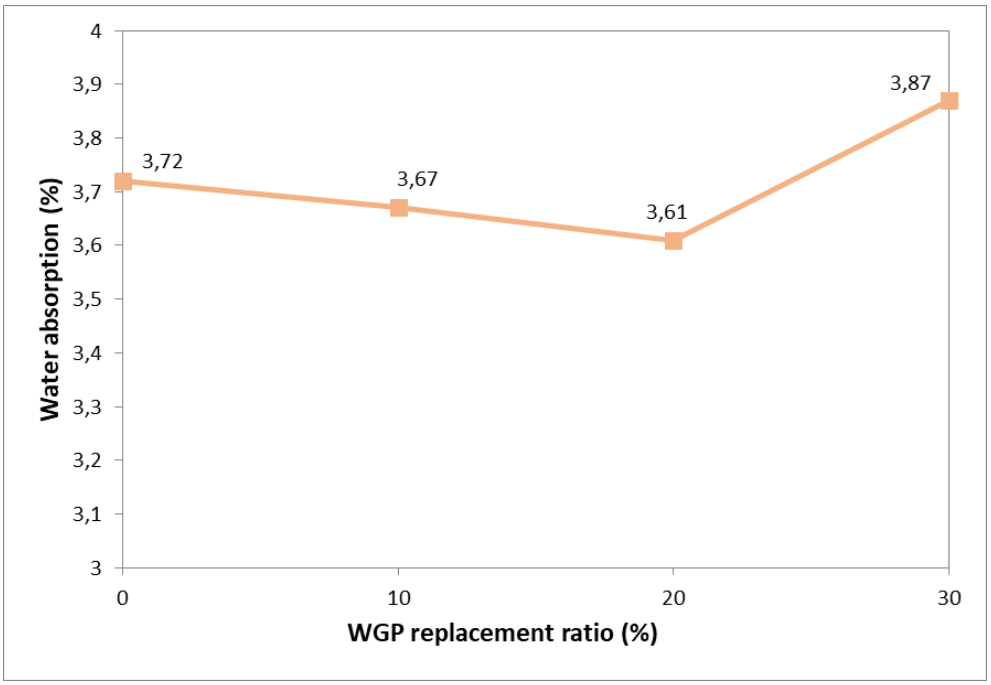


Figure 9. Water absorption ratios of RCC samples with different WGP ratios

The enhancement of concrete permeability properties through the utilization of WGP, up to a specific ratio, is predominantly associated with the chemical composition and the size of the material's particles. Fine-grained WGP reacts with calcium hydroxide ($Ca(OH)_2$) released during cement hydration, forming secondary calcium silicate hydrate (C-S-H) gels. These gels contribute to the formation of a denser and more impermeable structure by filling voids in the concrete matrix. Furthermore, the physical filling effect and fine structure of WGP increase the microstructural integrity in the ITZ region between the cement paste and aggregate, and reduce the void ratio in this region. Consequently, regions of weakness, which play an instrumental role in permeability, are fortified, thereby restricting capillary water movement. Omran et al. (2017) [7] also reported that finely ground glass powder reduces permeability due to both its pozzolanic reactivity and microstructural improvement effect.

3.5 Compressive and Flexural Strength

Figure 10 presents the 28-day compressive and flexural strength values of RCC mixtures produced using the optimum water content, depending on different WGP replacement ratios. According to the results obtained, the highest compressive and flexural strength values were achieved in mixtures containing 10% WGP. The 28-day flexural strength values of RCC mixtures with WGP replacement ratios of 0% (control), 10%, 20%, and 30% were 7.28, 7.41, 5.69, and 4.94 MPa, respectively; while the compressive strength values were determined as 55.98, 58.65, 50.30, and 36.00 MPa, respectively. Compared to the control mixture, a 10%

WGP replacement resulted in a 1.79% increase in flexural strength and a 4.77% increase in compressive strength. Conversely, increasing the WGP replacement ratio to 20% and 30% resulted in significant decreases in both flexural and compressive strength values. The decrease in flexural strength was determined to be 21.85% and 32.15% compared to the control mixture, while the compressive strength decrease occurred at levels of 10.15% and 35.70%. These results indicate that the use of WGP at low ratios improves the strength properties of RCC, but this effect decreases and even becomes negative as the replacement ratio increases. This improving effect is attributed to the pozzolanic reaction capacity of ground glass powder, which is associated with its high amorphous silica content. WGP reacts with calcium hydroxide ($Ca(OH)_2$), which is formed as a result of cement hydration and is weak in terms of strength, to form secondary C–S–H gel phases. This mechanism contributes to the densification of the matrix's internal structure and improves the ITZ region between the cement paste and aggregate, thereby limiting crack propagation.

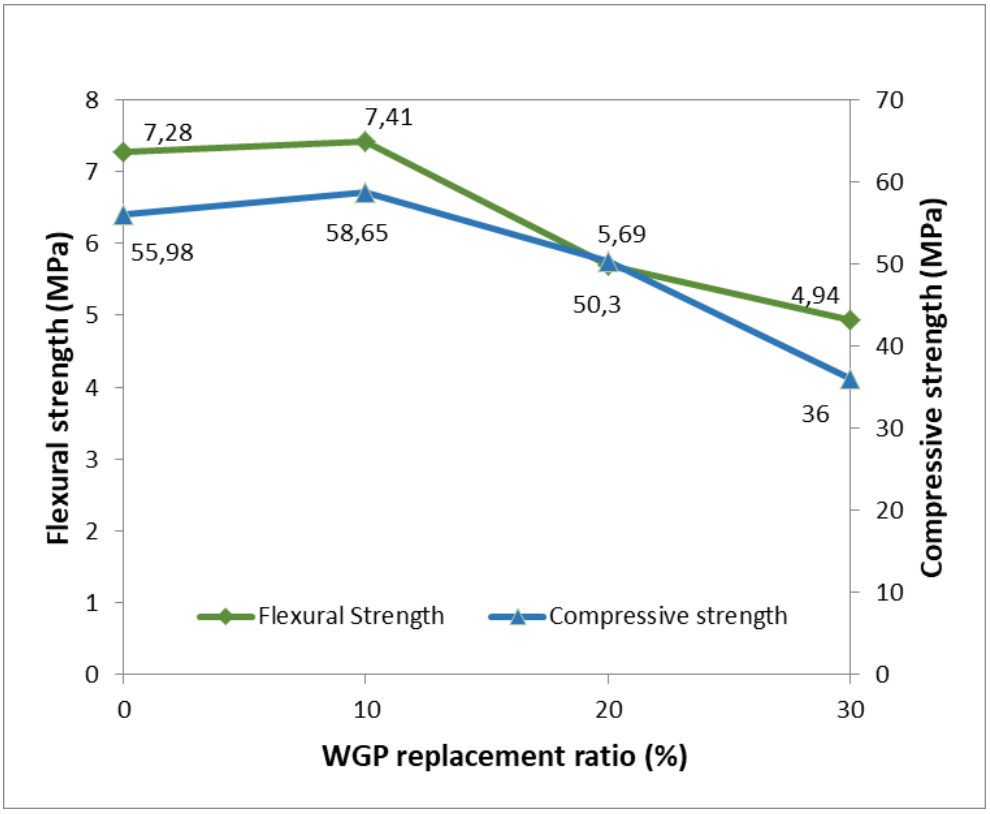


Figure 10. Compressive and flexural strength test results of RCC samples with different WGP ratios

The flexural and compressive strength results obtained are consistent with some studies in the literature. In this study, it was determined that a 10% WGP replacement ratio provides the best performance in terms of both compressive and flexural strength. Similarly, studies conducted on conventional concrete and RCC have reported that the use of low WGP ratios (especially 10%) improves mechanical performance, but strength decreases when the replacement ratio exceeds 20%. Indeed, in the study conducted by Omran et al. (2017) [30], it was observed that the flexural strength of RCC mixtures containing 20% WGP decreased after 28 days; this finding aligns with the low flexural strength values observed in the current study for WGP ratios of 20% and 30%.

Similarly, studies conducted by Shao et al. (2000) [45] and Elaqra et al. (2019) [46] have also indicated that the use of WGP at a 30% ratio negatively affects the flexural strength of conventional concrete. However, some studies have reported that the optimal replacement ratio for WGP is 20% [9,10,29, 47-49]. However, other studies have shown that a replacement ratio of 10% yields more effective results in terms of both compressive and flexural strength [11,50,51]. These differences can be attributed to various factors such as the type of binder used, aggregate characteristics, mixture ratios, particle size distribution, and curing conditions.

3.6 The Effect of Curing Methods on Compressive and Flexural Strength

To evaluate the effects of different curing methods on the mechanical performance of RCC, RCC samples containing 10% WGP were produced. The produced samples were subjected to three different curing methods—burlap, membrane, and chemical curing—for the first 7 days. Following the curing process, the samples were stored in a laboratory environment until they reached 28 days of age and were then subjected to compressive and flexural strength tests. The relevant mechanical strength results are presented in Figure 11. The highest flexural and compressive strength values were obtained in the samples cured with wet burlap. As shown in Figure 11, the flexural strength of RCC samples cured with wet burlap, chemical curing, and membrane curing methods at 28 days was determined to be 6.15 MPa, 5.68 MPa, and 5.61 MPa, respectively. These values correspond to 83%, 77%, and 76% of the characteristic flexural strength of the sample cured under standard conditions with the same composition, which is 7.41 MPa. A similar trend was observed in the compressive strength results. The 28-day compressive strength of the samples treated with wet burlap, chemical curing, and membrane curing was determined to be 55.62 MPa, 51.82 MPa, and 50.57 MPa, respectively. These values represent 95%, 89%, and 86% of the 28-day characteristic compressive strength of the sample with the same composition.

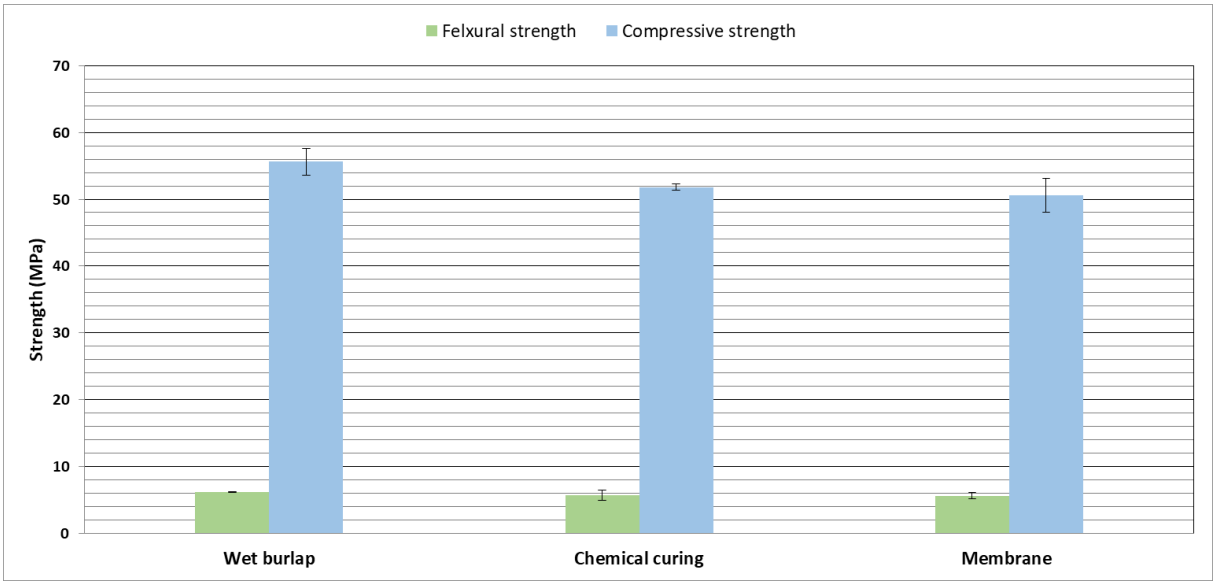


Figure 11. Compressive and flexural strength results of RCC samples under different curing conditions

4 CONCLUSION AND SUGGESTIONS

As a consequence of the experimental studies undertaken in this investigation, the effects of varying ratios of WGP replacement on the fresh and hardened concrete properties of RCC were evaluated, and the findings are summarized below.

- The optimal water content values of RCC mixtures containing different ratios of WGP were found to increase with an increase in the WGP content.

- When compared to the control mixture, it was determined that the maximum dry density value decreased with an increase in the WGP replacement ratio in RCC mixtures containing WGP.

- The modified Vebe time of RCC mixtures increased with increasing WGP replacement ratio. According to ACI 325.10R, the suitable Vebe time range for RCC is 30 to 40 seconds, and it was determined that the Vebe times of all RCC mixtures produced in this study were within the standard range.

- As the WGP replacement ratio increased up to 20%, the sorptivity coefficient and water absorption ratio decreased. However, it was observed that the sorptivity coefficient and water absorption ratio of RCC samples produced at a 30% WGP replacement ratio were higher than those of the control sample.

- The best results in terms of compressive and flexural strength were obtained from RCC samples with a 10% WGP replacement ratio.

- It was determined that the curing method is a decisive parameter affecting the mechanical performance of RCC, and that the curing application performed with wet burlap, in particular, significantly contributes to the development of compressive and flexural strength by more effectively supporting the hydration process.
- From an environmental perspective, the use of WGP as a cement substitute facilitates the recycling of waste glass while reducing cement usage and, consequently, contributing to the reduction of CO_2 emissions from cement production. In this regard, WGP emerges as one of the sustainable and environmentally friendly binding materials alternatives.
- In this study, WGP obtained from a single source was used. In subsequent research, the impact of material diversity should be examined by utilising diverse categories of glass waste.
- All experiments were conducted within a controlled laboratory environment. In order to evaluate the role of environmental effects on performance, it is recommended that future studies be conducted on field applications.
- The present study concentrated on the partial replacement of cement with WGP. In future studies, the synergistic effects of combinations of WGP with other pozzolanic materials, such as fly ash, silica fume, and blast furnace slag, should be investigated.
- Further studies are required to evaluate the long-term durability performance of the materials. It is imperative that these studies comprehensively address resistance to environmental effects such as freeze-thaw, sulphate attack and wetting-drying cycles.

Conflict of Interest Statement

There is no conflict of interest between the authors.

Statement of Research and Publication Ethics

The study is complied with research and publication ethics.

Artificial Intelligence (AI) Contribution Statement

Artificial intelligence-supported language editing tools were employed to improve the clarity and coherence of the final manuscript.

Contributions of the Authors

First author: Conceptualization, Methodology, Validation, Investigation, Writing—review and editing. Second author: Formal analysis, Investigation, Data curation, Writing—original draft preparation, Visualization.

REFERENCES

[1] G. Habert, S. A. Miller, V. M. John, J. L. Provis, A. R. Favier, A. Horvath, and K. L. Scrivener, "Environmental impacts and decarbonization strategies in the cement and concrete industries," *Nat. Rev. Earth Environ.*, vol. 1, no. 11, pp. 559–573, Nov. 2020.

[2] L. McDonald, F. Glasser, and M. Imbabi, "A new, carbon-negative precipitated calcium carbonate admixture (PCC-A) for low carbon Portland cements," *Materials*, vol. 12, no. 4, p. 554, Feb. 2019.

[3] F. A. Khan, K. Shahzada, Q. S. Ullah, M. Fahim, S. W. Khan, and Y. I. Badrashi, "Development of environment friendly concrete through partial addition of waste glass powder (WGP) as cement replacement," *Civil Eng. J.*, vol. 6, no. 12, pp. 2332–2343, Dec. 2020.

[4] M. A. Mansour, M. H. B. Ismail, I. Latif, A. F. Alshalif, A. Milad, and W. A. Al Bargi, "A systematic review of the concrete durability incorporating recycled glass," *Sustainability*, vol. 15, no. 4, p. 3568, Feb. 2023.

[5] C. Shi, Y. Wu, C. Riefler, and H. Wang, "Characteristics and pozzolanic reactivity of glass powders," *Cem. Concr. Res.*, vol. 35, no. 5, pp. 987–993, May 2005.

[6] Ş. Erdoğdu and Ş. Kurbettçi, "Chemical and mineral admixtures in terms of their effectiveness on concrete performance," *Turkish Eng. News*, vol. 426, no. 4, pp. 115–120, 2003 [in Turkish].

[7] A. F. Omran, D. Etienne, D. Harbec, and A. Tagnit-Hamou, "Long-term performance of glass-powder concrete in large-scale field applications," *Constr. Build. Mater.*, vol. 135, pp. 43–58, Mar. 2017.

[8] S. Khan, R. Patel, and V. Gupta, "Roles of waste glass and the effect of process parameters on the properties of sustainable cement and geopolymer concrete—A state-of-the-art review," *Polymers*, vol. 13, no. 22, p. 3935, Nov. 2021.

[9] M. Uzun, M. T. Çöğürcü, and Ü. S. Keskin, "The effect of waste glass powder on the compressive strength of concrete," *Beykent Univ. J. Eng. Sci.*, vol. 11, no. 2, pp. 42–51, n.d. [in Turkish].

[10] A. A. Aliabdo, M. Abd Elmoaty, and A. Y. Aboshama, "Utilization of waste glass powder in the production of cement and concrete," *Constr. Build. Mater.*, vol. 124, pp. 866–877, Oct. 2016.

[11] E. Orhan and E. Yüksel, "Determination of pozzolanic activity and splitting tensile strength of concrete incorporating ground waste glass powder," *J. New World Sci. Acad.*, vol. 12, no. 2, pp. 108–116, 2017 [in Turkish].

[12] D. A. Muhedin and R. K. Ibrahim, "Effect of waste glass powder as partial replacement of cement and sand in concrete," *Case Stud. Constr. Mater.*, vol. 19, p. e02512, Mar. 2023.

[13] K. I. M. Ibrahim, "Recycled waste glass powder as a partial replacement of cement in concrete containing silica fume and fly ash," *Case Stud. Constr. Mater.*, vol. 15, p. e00630, Jan. 2021.

[14] R. Sakale, S. Jain, and S. Singh, "Experimental investigation on strength of glass powder replacement by cement in concrete with different dosages," *Int. J. Sci. Technol. Eng.*, vol. 2, no. 8, p. 13, 2016.

[15] A. S. Mahmoud, M. M. Yassen, and S. M. Hama, "Effect of glass powder as partial replacement of cement on concrete strength and stress-strain relationship," in *Proc. 2019 12th Int. Conf. Develop. eSystems Eng. (DeSE)*, Kazan, Russia, 2019, pp. 109–114.

[16] D. Harrington, F. Abdo, W. Adaska, C. V. Hazaree, H. Ceylan, and F. Bektas, *Guide for Roller-Compacted Concrete Pavements*. Ames, IA, USA: Inst. Transp., Iowa State Univ., 2010.

[17] A. Gür, Y. Abut, and İ. Ö. Yaman, "Kent içi yollarda silindirle sıkıştırılmış beton yol uygulamaları: Kocaeli örneği," in *Proc. Karayolu 4. Ulusal Kongresi ve Sergisi*, 2019, pp. 217–226 [in Turkish].

[18] E. Şengün, M. A. Aykutlu, and O. Yaman, "State of the art review of roller compacted concrete pavements—Part I: Properties and mixture proportions," *Cem. Concr. World*, vol. 22, no. 130, pp. 93–114, 2017.

[19] F. Vahedifar, M. Nili, and C. L. Meehan, "Assessing the effects of supplementary cementitious materials on the performance of low-cement roller compacted concrete pavement," *Constr. Build. Mater.*, vol. 24, no. 12, pp. 2528–2535, Dec. 2010.

[20] ACI Committee 308, *Guide to Curing Concrete (ACI 308-01)*. Farmington Hills, MI, USA: Amer. Concr. Inst., 2008.

[21] A. Nanni, "Curing of roller compacted concrete: Strength development," *J. Transp. Eng.*, vol. 114, no. 6, pp. 684–694, 1988.

[22] Ö. F. Keleş, "Investigation of the type and application time of curing in roller-compacted concrete pavements," M.S. thesis, Dept. Civ. Eng., Karadeniz Tech. Univ., Trabzon, Turkey, 2019 [in Turkish].

[23] A. Kumar, N. Bheel, I. Ahmad, S. H. Rizvi, R. Kumar, and A. A. Jhatial, "Effect of silica fume and fly ash as cementitious material on hardened properties and embodied carbon of roller compacted concrete," *Environ. Sci. Pollut. Res.*, vol. 29, no. 1, pp. 1210–1222, Jan. 2022.

[24] Z. Abed, H. Ahmed, and W. Khalil, "Optimization of silica fume and slag in roller compacted concrete by Taguchi method," *Eng. Technol. J.*, vol. 41, no. 6, pp. 724–733, 2023.

[25] C. Cao, W. Sun, and H. Qin, "Analysis on strength and fly ash effect of roller-compacted concrete with high volume fly ash," *Cem. Concr. Res.*, vol. 30, no. 1, pp. 71–75, Jan. 2000.

[26] S. H. Bayqra, A. Mardani-Aghabaglou, and K. Ramyar, "Physical and mechanical properties of high volume fly ash roller compacted concrete pavement (A laboratory and case study)," *Constr. Build. Mater.*, vol. 314, pt. B, p. 125664, Apr. 2022.

[27] R. B. A. V. Kumar and G. Ramakrishna, "Performance evaluation of sustainable materials in roller compacted concrete pavements: A state-of-the-art review," *J. Build. Pathol. Rehabil.*, vol. 7, p. 78, Dec. 2022.

[28] A. Aghaeipour and M. Madhkhan, "Effect of ground granulated blast furnace slag (GGBFS) on RCCP durability," *Constr. Build. Mater.*, vol. 141, pp. 533–541, Jun. 2017.

[29] J. P. Faubert, R. Gagné, A. Yahia, and B. Fournier, "Valorisation de particules fines dans les bétons compactés au rouleau et les bétons moulés à sec," M.S. thesis, Univ. Sherbrooke, Sherbrooke, QC, Canada, 2013.

[30] A. Omran, D. Harbec, A. Tagnit-Hamou, and R. Gagné, "Production of roller-compacted concrete using glass powder: Field study," *Constr. Build. Mater.*, vol. 133, pp. 450–458, Feb. 2017.

[31] ASTM C171-16, *Standard Specification for Sheet Materials for Curing Concrete*. West Conshohocken, PA, USA: ASTM Int., 2016.

[32] ASTM C309-17, *Standard Specification for Liquid Membrane-Forming Compounds for Curing Concrete*. West Conshohocken, PA, USA: ASTM Int., 2017.

[33] EN 197-1, *Cement – Part 1: Composition, Specifications and Conformity Criteria for Common Cements*. Brussels, Belgium: Eur. Comm. Stand., 2011.

[34] ACI Committee 211, *Guide for Selecting Proportions for No Slump Concrete (ACI 211.3R-02)*. Farmington Hills, MI, USA: Amer. Concr. Inst., 2009.

[35] ASTM C1435-14, *Standard Practice for Molding Roller-Compacted Concrete in Cylinder Molds Using a Vibrating Hammer*. West Conshohocken, PA, USA: ASTM Int., 2014.

[36] ASTM C1170-14, *Standard Test Method for Determining Consistency and Density of Roller-Compacted Concrete Using a Vibrating Table*. West Conshohocken, PA, USA: ASTM Int., 2014.

[37] ASTM C1585-13, *Standard Test Method for Measurement of Rate of Absorption of Water by Hydraulic-Cement Concretes*. West Conshohocken, PA, USA: ASTM Int., 2013.

[38] ASTM C642-13, *Standard Test Method for Density, Absorption, and Voids in Hardened Concrete*. West Conshohocken, PA, USA: ASTM Int., 2013.

[39] ASTM C293-16, *Standard Test Method for Flexural Strength of Concrete (Using Simple Beam With Center-Point Loading)*. West Conshohocken, PA, USA: ASTM Int., 2016.

[40] ASTM C39-12, *Standard Test Method for Compressive Strength of Cylindrical Concrete Specimens*. West Conshohocken, PA, USA: ASTM Int., 2012.

[41] ACI Committee 325, *ACI 325.10R-01: Report on Roller-Compacted Concrete Pavements*. Farmington Hills, MI, USA: Amer. Concr. Inst., 2001.

[42] H. Du and K. H. Tan, "Properties of high volume glass powder concrete," *Cem. Concr. Compos.*, vol. 75, pp. 22–29, Feb. 2017.

[43] N. Schwarz, H. Cam, and N. Neithalath, "Influence of a fine glass powder on the durability characteristics of concrete and its comparison to fly ash," *Cem. Concr. Compos.*, vol. 30, no. 6, pp. 486–496, Jul. 2008.

[44] A. M. Matos and J. Sousa-Coutinho, "Durability of mortar using waste glass powder as cement replacement," *Constr. Build. Mater.*, vol. 36, pp. 205–215, Nov. 2012.

[45] Y. Shao, T. Lefort, S. Moras, and D. Rodriguez, "Studies on concrete containing ground waste glass," *Cem. Concr. Res.*, vol. 30, no. 1, pp. 91–100, Jan. 2000.

[46] H. A. Elaqra, M. A. Abou Haloub, and R. N. Rustom, "Effect of new mixing method of glass powder as cement replacement on mechanical behavior of concrete," *Constr. Build. Mater.*, vol. 203, pp. 75–82, Apr. 2019.

[47] J. S. Dali and S. N. Tande, "Performance of concrete containing mineral admixtures subjected to high temperature," in *Proc. 37th Conf. Our World Concr. Struct.*, Singapore, Aug. 2012.

[48] G. Vasudevan and S. G. K. Pillay, "Performance of using waste glass powder in concrete as replacement of cement," *Amer. J. Eng. Res.*, vol. 2, no. 12, pp. 175–181, 2013.

[49] S. M. Chikhalikar and S. N. Tande, "An experimental investigation on characteristics properties of fibre reinforced concrete containing waste glass powder as pozzolana," in *Proc. 37th Conf. Our World Concr. Struct.*, Singapore, Aug. 2012.

[50] D. M. Patil and K. K. Sangle, "Experimental investigation of waste glass powder as partial replacement of cement in concrete," *Int. J. Adv. Technol. Civ. Eng.*, vol. 2, no. 1, 2013.

[51] R. Vandhiyan, K. Ramkumar, and R. Ramya, "Experimental study on replacement of cement by glass powder," *Int. J. Eng. Res. Technol.*, vol. 2, no. 5, 2013.

BİTLİS EREN ÜNİVERSİTESİ
FEN BİLİMLERİ DERGİSİ

ISSN: 2147-3129 / e-ISSN: 2147-3188

Article Type : Research Article
Received : June 4, 2025
Revised : September 5, 2025
Accepted : October 7, 2025
DOI : 10.17798/bitlisfen.1714462

Year : 2025
Volume : 14
Issue : 3
Pages : 1759-1771

EFFECT OF BUILD ORIENTATION AND HEAT TREATMENT ON SHEAR STRENGTH OF ADDITIVELY MANUFACTURED Ti6Al4V ALLOY

Gürkan KAYA [1], **Yusuf POLAT** [1, 2, *]

[1] *Erzurum Technical University, Mechanical Engineering Department, Erzurum, Türkiye*

[2] *Erzurum Technical University, High Technology Application and Research Center, Erzurum, Türkiye*

**** Corresponding Author:*** *yusuf.polat@erzurum.edu.tr*

ABSTRACT

This study investigates the effects of build orientation and heat treatment on the transverse shear properties of additively manufactured Ti6Al4V alloy produced by laser powder bed fusion (LPBF). Specimens were fabricated in three different build orientations (0°, 45°, and 90°) and subjected to heat treatment at 900 °C under argon gas atmosphere. Transverse shear strength was evaluated using the short beam shear test method. The results revealed that build orientation significantly affects both shear strength and ductility of materials. Compared to the 0° reference, the 45° and 90° samples showed an approximately 43% increase in shear strength, along with 56% and 103% increases in displacement, respectively. Heat treatment further enhanced the ductility, especially for the 45° oriented specimen, which exhibited the highest displacement and a 26% increase in shear strength compared with reference 0° sample. However, heat treatment slightly reduced the strength of the 45° and 90° specimens relative to their untreated counterparts. Fractographic analysis confirmed quasi-brittle failure with the presence of dimples, indicating enhanced ductility post-heat treatment. These findings provide novel insight into optimizing process parameters and post-processing strategies to improve the shear performance of LPBF Ti6Al4V components for critical structural applications.

Keywords: Laser powder bed fusion, Ti6Al4V alloy, Shear strength, Build orientation, Heat treatment, Fracture behavior.

1 INTRODUCTION

Additive manufacturing is an advanced manufacturing technology which is able to produce parts for high technology applications like biomedical [1], [2], [3], aerospace [4], [5],

and automotive [6], [7] in one step. The one step production technique is based on layer by layer construction of 3D designed models [8]. By these means, additive manufacturing allows the manufacturer to produce complex geometries with limited waste [9]. This unconventional and innovative manufacturing method is categorized to seven methods according to ASTM F2792-12 standard as powder bed fusion (PBF), sheet lamination, direct energy deposition, material extrusion, binder jetting, material jetting, and vat photopolymerization [10]. Among others, PBF is one of the most popular and utilized additive manufacturing technique [11], and it is most adaptable technique to produce 3D parts from various materials [12], [13].

Powder bed-based additive manufacturing by laser melting is of significance within the variety of other techniques [14]. The laser powder bed fusion (L-PBF) technology is based on melting powders which could be alloy or mixed powder by using laser source. This technique provides opportunities for production of various materials and components with almost near net geometry, flexibility in design, low production time [15], [16]. The CoCrFeMnNi alloy [17], CoCrMoW alloy [18], 316L stainless steel [19], Ti6Al4V alloy [16] are some common materials to be used for L-PBF method.

Ti6Al4V alloy is widely used in the aerospace and biomedical industries due to its advantageous properties, including a low coefficient of thermal expansion, biocompatibility, high strength-to-weight ratio, superior corrosion resistance, and greater strength compared to stainless steels [20]. As the most commonly used α+β titanium alloy, Ti6Al4V contains approximately 15% β phase, and its microstructure can be easily tailored through appropriate heat treatments. While the α phase is dominant at room temperature, the alloy transforms into a single β phase at around 995 °C [21]. Aluminum acts as an α-phase stabilizer enhancing strength, whereas vanadium stabilizes the β phase, improving ductility at room temperature and enabling a balanced combination of mechanical properties. The extra-low interstitial (ELI) grade of Ti6Al4V offers even higher fracture toughness and excellent damage tolerance, making it especially suitable for critical applications [22].

Several studies in the literature have emphasized that build orientation plays a crucial role in determining the anisotropic mechanical behavior of LPBF-fabricated Ti6Al4V components. Vrancken et al. [23] showed that anisotropy in LPBF-produced Ti6Al4V is strongly linked to build orientation and solidification behavior. Zhang et al. [24] further highlighted how tensile and shear properties vary significantly with orientation, with distinct fracture mechanisms observed across different build directions. More recently, Singh et al. [25] presented a comprehensive study demonstrating that build orientation directly affects tensile

strength, hardness, residual stress, and fracture mechanisms of Ti6Al4V alloys fabricated by L-PBF. Likewise, Yang et al. [26] systematically investigated multiple build orientations (0°, 30°, 45°, 60°, 90°) and reported orientation-dependent variations in microstructure and mechanical behavior, with the 45° samples showing the lowest tensile strength and ductility due to β-phase evolution and stair-step effects.

The heat-treated titanium alloy Ti6Al4V has been studied by researchers extensively. The studies were focused on effect of heat treatment on phase morphology [21], [27], kinetics model of heat treatment [28], [29], high temperature effect on alpha fraction [30], change in mechanical performance [31], [32], and so on. However, among other mechanical properties, there are no study on transverse shear strength of LPBF titanium alloy. The short beam shear method is suitable for the shear strength measurement of additively manufactured parts. Although L-PBF has many advantages for the production of complex parts to be used high tech applications, it also has drawbacks like poor ductility. The microstructure of parts produces by LPBF are affected by high cooling rate for highly dense part production requirements which yields poor ductility [23], [33].

Despite the extensive research on the tensile, compressive, and fatigue behavior of additively manufactured Ti6Al4V alloys, the transverse shear response of these materials has remained largely unexplored. Shear properties are critical for many load-bearing applications, where components are subjected to complex multiaxial stresses rather than uniaxial loading alone. In particular, the anisotropic nature of LPBF processed Ti6Al4V makes shear performance highly sensitive to build orientation and post-processing conditions, yet this aspect has not been systematically addressed in the literature. The present study bridges this knowledge gap by providing a comprehensive assessment of the shear strength and ductility of Ti6Al4V fabricated under different build orientations, with and without heat treatment.

2 MATERIALS AND METHODS

2.1 Materials

In this study, Ti6Al4V-ELI powder (General Electric, MA, USA), commercially available and produced via gas atomization, was utilized. Figure 1 presents the scanning electron microscope (SEM) image of the Ti6Al4V-ELI alloy powder used in this research. The powder particles were observed to have a predominantly spherical morphology, exhibit a uniform size distribution, and show no signs of agglomeration.

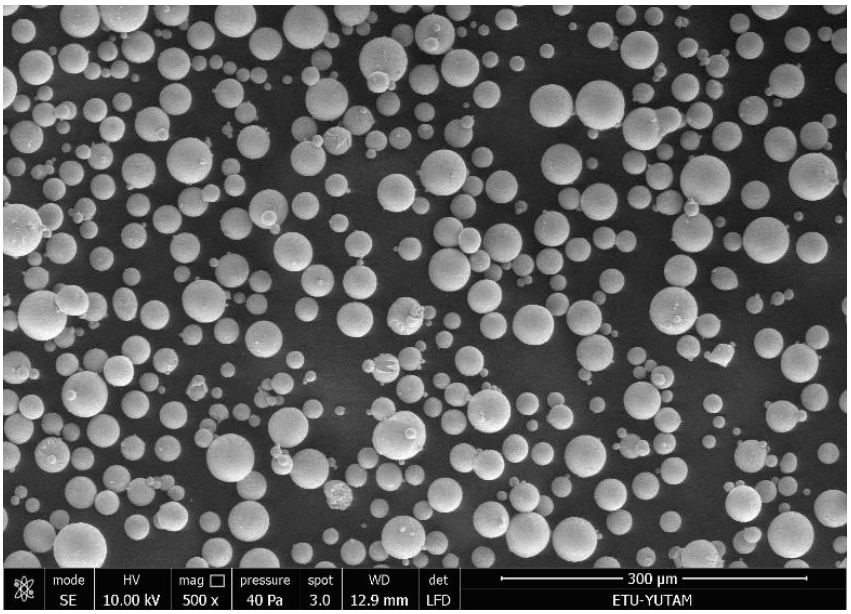


Figure 1. SEM image of Ti6Al4V-ELI powder.

2.2 Laser Powder Bed Fusion Technique

Additive manufacturing was carried out using a Concept Laser MLab-R LPBF system (max. 100 W), employing a bidirectional scanning strategy and operating in continuous laser mode. LPBF production process parameters was given in Table 1. To prevent oxidation, the entire fabrication process took place within an Argon (Ar) gas-shielded atmosphere. The specimens with 5 x 12 x 35 mm prismatic dimensions were produced by L-PBF method for short beam shear testing. Three different orientation angles (0°, 45° and 90°) were used during LPBF production. The schematic view of the samples on the build platform and post-production images are shown in Figure 2.

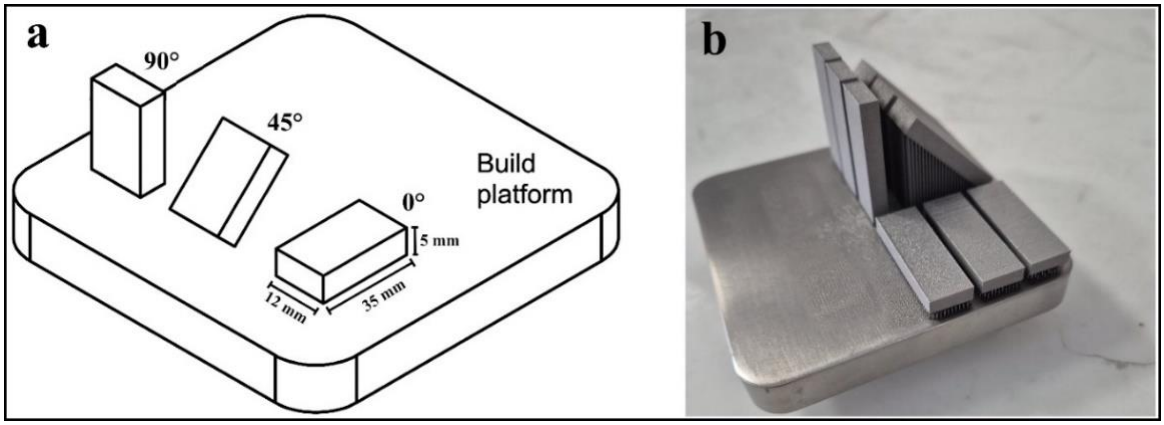


Figure 2. (a) Schematic view and (b) produced samples on the build platform.

Table 1. LPBF production parameters [16].

LPBF Process Parameters	Values
Laser power	80 W
Scanning speed	1125 mm/s
Layer thickness	25 µm
Hatch distance	45 µm

2.3 Heat Treatment

Samples fabricated using the LPBF technique were subjected to heat treatment. To minimize oxidation caused by exposure to the surrounding atmosphere, experiments were conducted in an Argon gas-controlled environment. The heat treatment was performed at 900 °C (HT900), within the temperature range between Tα and the Tβ (β transus temperature of 995 °C) [34]. Heat treatment procedure was conducted in a Protherm Furnace brand, atmosphere-controlled heat treatment system.

2.4 Transverse Shear Strength Test

The transverse shear strength test was conducted by using a short beam with 27 mm span length, and 5 mm x 12 mm cross section as seen in Figure 3. A 3-point bending test apparatus were used with a 1 mm/min crosshead speed. The diameter for supporting pins was selected as 3 mm, and the diameter of pin for force application was selected as 6 mm. An Instron 5900 universal static test device was used to apply the force to materials. The experimental setup of the test system is shown in Figure 3.

The shear strength was calculated by using transverse shear formula as given in following equation;

$$\tau = \frac{V.Q}{I.t}$$

In which V is the shear force, Q is the $(\bar{y}'.A')$, where A' is the area of the top (or bottom) part of the cross section, above (or below) the section plane where thickness t is measured, and $\bar{y}'$ is the distance from the neutral axis to the centroid of A'. For rectangular cross section the formula becomes as follows;

$$\tau = 0.75\frac{P}{b.h}$$

where P is the maximum force, b is width, and h is the thickness.

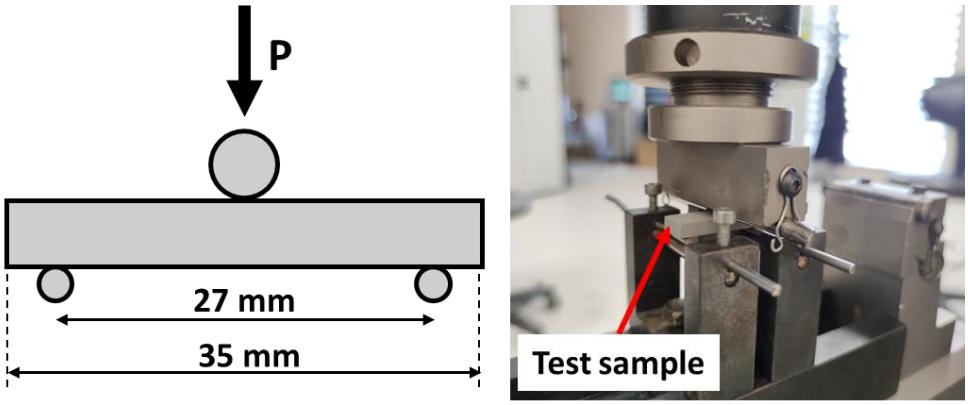


Figure 3. Schematic illustration for transverse shear test (left), and experimental setup (right).

3 RESULTS AND DISCUSSION

3.1 Post-process Analysis

The applied post-processing heat treatment at 900 °C (HT900), conducted between the α-transus and β-transus temperatures, had a clear influence on the microstructural evolution and mechanical performance of the LPBF-fabricated Ti6Al4V specimens. This treatment promoted the partial decomposition of the acicular α′ martensitic structure into an α+β lamellar morphology, which is consistent with previous reports [23], [31], [34]. As a result, the heat-treated samples generally exhibited improved ductility and defect tolerance, particularly evident in the 45° orientation, which showed the highest displacement (+36.2% compared to the as-built condition) and a 26% increase in shear strength relative to the 0° reference. Nevertheless, a slight reduction in ultimate strength was observed for the 45° and 90° orientations after heat treatment, which agrees with earlier studies indicating that lamellar α+β transformation enhances plasticity at the expense of strength [23], [32]. Fractography results further supported these findings, revealing a transition from quasi-brittle fracture surfaces in the as-built state to more ductile dimpled morphologies after heat treatment. These observations confirm that the applied post-processing heat treatment is an essential factor in tailoring the balance between strength and ductility in LPBF-produced Ti6Al4V components.

3.2 Transverse Shear Strength Test Results

The shear test was conducted to both untreated and heat-treated samples. The effect of build orientation and heat treatment were discussed. Simonelli et al. [35] investigated the influence of build orientation on the mechanical behavior of Ti6Al4V alloy fabricated by SLM,

demonstrating that the alignment of prior β grain boundaries relative to the applied axial load governed both the fracture mechanism and crack propagation. Figure 4 shows the shear stress – displacement curves for reference (0° build orientation), 45°, and 90° oriented samples during production. The results showed that the transverse shear strength for 45° and 90° samples are increased to nearly same values which is nearly 210 MPa. The displacement at maximum load is 1.463 mm for reference sample. The displacement of samples was increased with build orientation around 2.281 mm for 45°, while it is 2.964 mm for 90°. Table 2 summarized the force, displacement, and shear stress values of all samples, and it compares the improvements of heat-treatment for each orientation. The build orientation effect enhanced the shear strength nearly 43% for both angles. However, the improvement in displacement is different for 45° and 90° build orientations, which are 56% and 103%, respectively. The influence of build orientation on tensile and shear behavior is highly complex, as the mechanical response of additively manufactured materials is strongly governed by their microstructure and the distribution of internal defects [36]. In the case of Ti6Al4V fabricated in the horizontal direction, the content of fine needle-like α′ martensite is increased due to the elevated cooling rate during the selective laser melting process [37]. Moreover, the dimples observed in the horizontal specimen appear slightly larger and shallower compared to those in the vertical specimen, suggesting reduced ductility in the horizontally built sample [24].

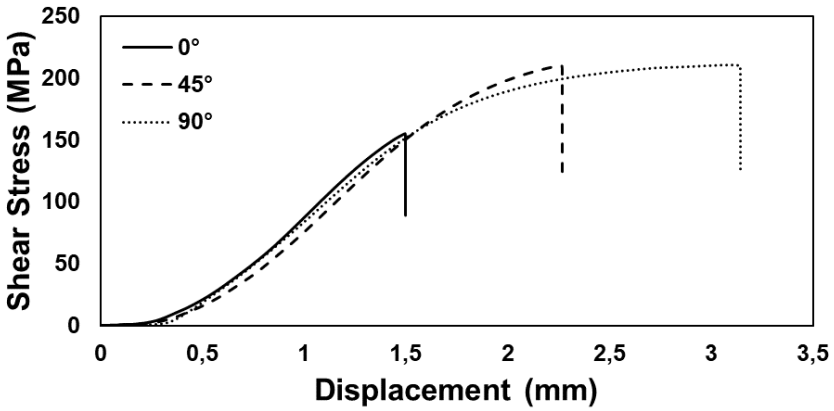


Figure 4. Shear stress – Displacement curves for untreated Ti6Al4V alloys.

The results in Figure 4 showed that the 90° build orientation enhanced the ductility of material more than 45°. In addition to build orientation, heat-treatment was applied to Ti6Al4V alloys to enhance their ductility. The effect of temperature improved the both shear strength and displacement of reference sample by nearly 15% and 48%, respectively. After heat-treatment, the displacement of 45° sample (HT_45°) increased to 3.108 mm (36.2% more than untreated sample, and maximum obtained) from 2.281 mm. However, the heat treatment did not change the displacement of 90° sample significantly.

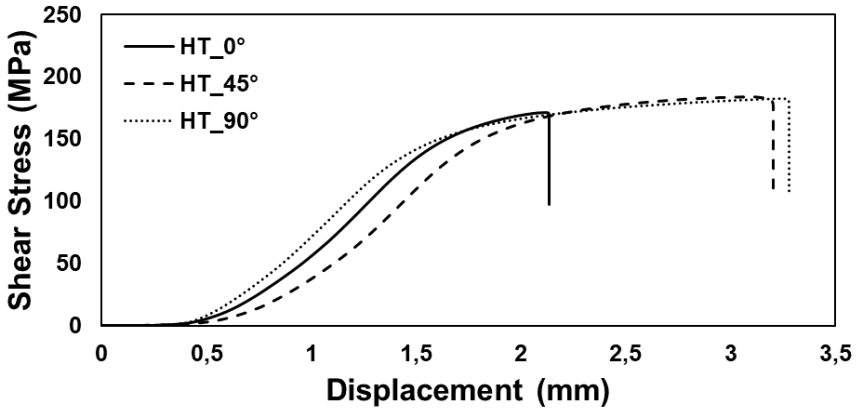


Figure 5. Shear stress – Displacement curves for heat-treated Ti6Al4V alloys.

The Figure 5 shows the Shear stress – displacement curve for heat-treated samples. The results showed that shear strength of reference sample is increased to 169 MPa, while it is decreased for oriented samples when compared with their oriented versions. The ratio of decrease is in shear strength nearly 12% for 45° orientated sample and 17% for 90° orientated sample. However, the strength values are higher than reference sample. Overall, the HT_45° sample with highest ductility and 26% increment in strength (compared with reference 0° sample) is the best sample for engineering applications. Sabban et al. [38] also found similar results that heat treatment is increasing the ductility of both vertically and horizontally build additively manufactured Ti6Al4V alloy. The lessening of defects like unmelted particles during production and porosity is expected to result in a further enhancement of ductility following heat treatment [38], [39].

Table 2. Force-Displacement-Shear strength values.

Sample code	Force (kN)	Displacement at max. force (mm)	Improvement in displacement (%)	Shear strength (MPa)	Improvement in shear strength (%)
0°	11.74±0.91	1.463±0.048	-	146.7±11.39	-
HT_0°	13.55±0.14	2.165±0.109	+47.9	169.4±1.69	+15.5
45°	16.81±0.04	2.281±0.032	-	210.2±0.47	-
HT_45°	14.81±0.12	3.108±0.065	+36.2	185.1±1.50	-11.9
90°	16.82±0.02	2.964±0.179	-	210.2±0.25	-
HT_90°	14.16±0.65	2.878±0.525	-2.9	176.9±8.10	-15.8

3.3 Fractography Analysis

SEM images of the fracture surfaces of untreated and heat-treated samples after the shear test are presented in Figure 6. The left column of the figure (Figure 6a-c) shows the fracture surfaces of untreated samples, and the right column (Figure 6d-f) shows the fracture

surfaces of heat-treated samples. In the horizontally build (0°) sample, the loading direction is perpendicular to the building direction, while in the vertically build (90°) sample, it is parallel to the building direction. In the sample produced at a 45° angle, the loading direction is at an angle to the building direction.

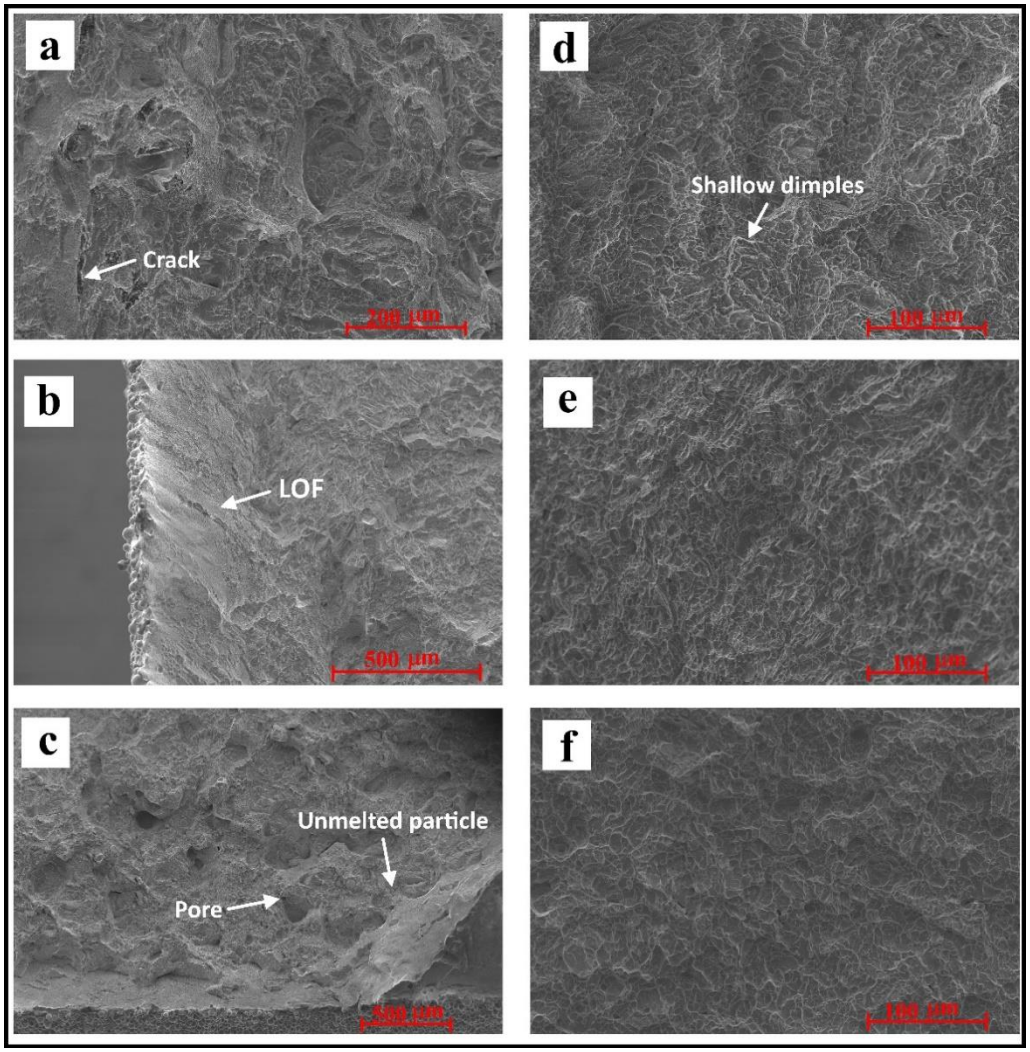


Figure 6. SEM images of fracture surfaces of shear samples, (a) 0°, (b) 45°, (c) 90°, (d) HT_0°, (e) HT_45° and (f) HT_90°.

Upon examination of the fracture surfaces of the specimens following shear tests, it was generally observed that the failure mode corresponded to a quasi-brittle fracture. Materials containing pores, lack of fusion (LOF), and microcracks due to the manufacturing process can exhibit such quasi-brittle behavior (Figure 6a-c). The defects are randomly distributed in the material. In this context, this type of fracture is expected in materials produced by LPBF. A shallow dimples structure, which is a typical indicator of ductile fracture, was observed across a large portion of the cross-sectional area (Figure 6d–f). The dimples observed in the vertically fabricated (90°) specimen are somewhat narrower and deeper compared to those in the

horizontally fabricated (0°) one, indicating that the vertical specimen has undergone more intense plastic deformation. Consequently, this indicates that the elongation at failure of the vertically build specimen is higher [24].

Due to the fracture characteristics of the samples under shear, the overall fracture morphology is relatively flat, and pit-free regions resulting from the friction of the fracture surfaces are observed in the edge regions (Figure 6b). In addition, it is seen that in the specimen build at a 45° angle, the LOF defect extends angularly along the shear loading direction, which is caused by the friction between the two fracture surfaces.

4 CONCLUSION

In this study, the influence of build orientation and post-process heat-treatment on the transverse shear properties of Ti6Al4V alloy fabricated via LPBF was systematically investigated. The main conclusions are as follows:

- Compared to the horizontally build (0°) samples, both 45° and 90° orientations enhanced the transverse shear strength by approximately 43%. The most significant improvement in ductility was observed in the 90° oriented sample with a 103% increase in displacement at maximum force.
- Post-process heat treatment at 900 °C under an inert atmosphere led to an increase in ductility across most build orientations. Notably, the HT_45° sample exhibited the highest displacement (3.108 mm), corresponding to a 112% improvement in ductility and a 26% increase in shear strength over the reference sample. However, heat treatment slightly reduced the strength of the 45° and 90° samples compared to their untreated counterparts.
- SEM analysis revealed a transition from quasi-brittle fracture surfaces in untreated samples to more ductile features (dimples) after heat treatment, confirming the improvement in ductility. The LOF defects and microstructural features induced by LPBF were responsible for the fracture behavior, which varied with orientation and heat treatment.
- HT_45° sample offers the most balanced mechanical performance, with improved strength and ductility, making it the most promising candidate for applications requiring resistance to shear loading.

Overall, this study provides a novel and comprehensive understanding of the shear performance of LPBF Ti6Al4V, emphasizing the critical role of build orientation and heat treatment. The outcomes can guide the development of optimized design and processing strategies for high-performance components in aerospace, biomedical, and structural applications.

Conflict of Interest Statement

There is no conflict of interest between the authors.

Statement of Research and Publication Ethics

The study is complied with research and publication ethics.

Artificial Intelligence (AI) Contribution Statement

This manuscript was entirely written, edited, analyzed, and prepared without the assistance of any artificial intelligence (AI) tools. All content, including text, data analysis, and figures, was solely generated by the authors.

Contributions of the Authors

G. Kaya and Y. Polat designed the conceptualization of the study, and contributed similar effort to writing of the manuscript. G. Kaya performed the production of test samples, and Y. Polat performed the shear strength tests. Discussion on the results were written by both authors.

REFERENCES

[1] G. Liu *et al.*, 'Development of Bioimplants with 2D, 3D, and 4D Additive Manufacturing Materials', *Engineering*, vol. 6, no. 11, pp. 1232–1243, Nov. 2020, doi: 10.1016/j.eng.2020.04.015.

[2] X. Wang *et al.*, 'Topological design and additive manufacturing of porous metals for bone scaffolds and orthopaedic implants: A review', *Biomaterials*, vol. 83, pp. 127–141, Mar. 2016, doi: 10.1016/j.biomaterials.2016.01.012.

[3] E. Alabort, D. Barba, and R. C. Reed, 'Design of metallic bone by additive manufacturing', *Scripta Materialia*, vol. 164, pp. 110–114, Apr. 2019, doi: 10.1016/j.scriptamat.2019.01.022.

[4] V. Madhavadas *et al.*, 'A review on metal additive manufacturing for intricately shaped aerospace components', *CIRP Journal of Manufacturing Science and Technology*, vol. 39, pp. 18–36, Nov. 2022, doi: 10.1016/j.cirpj.2022.07.005.

[5] V. Mohanavel, K. S. Ashraff Ali, K. Ranganathan, J. Allen Jeffrey, M. M. Ravikumar, and S. Rajkumar, 'The roles and applications of additive manufacturing in the aerospace and automobile sector', *Materials Today: Proceedings*, vol. 47, pp. 405–409, Jan. 2021, doi: 10.1016/j.matpr.2021.04.596.

[6] V. Juechter, M. M. Franke, T. Merenda, A. Stich, C. Körner, and R. F. Singer, 'Additive manufacturing of Ti-45Al-4Nb-C by selective electron beam melting for automotive applications', *Additive Manufacturing*, vol. 22, pp. 118–126, Aug. 2018, doi: 10.1016/j.addma.2018.05.008.

[7] M. S. Muhammad, L. Kerbache, and A. Elomri, 'Potential of additive manufacturing for upstream automotive supply chains', *Supply Chain Forum: An International Journal*, vol. 23, no. 1, pp. 1–19, Jan. 2022, doi: 10.1080/16258312.2021.1973872.

[8] F. A. Talebi *et al.*, 'Spreadability of powders for additive manufacturing: A critical review of metrics and characterisation methods', *Particuology*, vol. 93, pp. 211–234, Oct. 2024, doi: 10.1016/j.partic.2024.06.013.

[9] L. Jin *et al.*, 'Big data, machine learning, and digital twin assisted additive manufacturing: A review', *Materials & Design*, vol. 244, p. 113086, Aug. 2024, doi: 10.1016/j.matdes.2024.113086.

[10] I. Astm, 'ASTM F2792-10: standard terminology for additive manufacturing technologies', *ASTM International*, 2010.

[11] D. Sarkar, A. Kapil, and A. Sharma, 'Advances in computational modeling for laser powder bed fusion additive manufacturing: A comprehensive review of finite element techniques and strategies', *Additive Manufacturing*, vol. 85, p. 104157, Apr. 2024, doi: 10.1016/j.addma.2024.104157.

[12] T. DebRoy *et al.*, 'Additive manufacturing of metallic components – Process, structure and properties', *Progress in Materials Science*, vol. 92, pp. 112–224, Mar. 2018, doi: 10.1016/j.pmatsci.2017.10.001.

[13] S. Chowdhury *et al.*, 'Laser powder bed fusion: a state-of-the-art review of the technology, materials, properties & defects, and numerical modelling', *Journal of Materials Research and Technology*, vol. 20, pp. 2109–2172, 2022.

[14] J.-P. Kruth, G. Levy, F. Klocke, and T. H. C. Childs, 'Consolidation phenomena in laser and powder-bed based layered manufacturing', *CIRP Annals*, vol. 56, no. 2, pp. 730–759, Jan. 2007, doi: 10.1016/j.cirp.2007.10.004.

[15] W. Abd-Elaziem *et al.*, 'On the current research progress of metallic materials fabricated by laser powder bed fusion process: a review', *Journal of Materials Research and Technology*, vol. 20, pp. 681–707, Sept. 2022, doi: 10.1016/j.jmrt.2022.07.085.

[16] G. Kaya *et al.*, 'Effects of process parameters on selective laser melting of Ti6Al4V-ELI alloy and parameter optimization via response surface method', *Materials Science and Engineering: A*, vol. 885, p. 145581, Oct. 2023, doi: 10.1016/j.msea.2023.145581.

[17] C. Bulut, F. Yıldız, T. Varol, G. Kaya, and T. O. Ergüder, 'Effects of Selective Laser Melting Process Parameters on Structural, Mechanical, Tribological and Corrosion Properties of CoCrFeMnNi High Entropy Alloy', *Met. Mater. Int.*, vol. 30, no. 11, pp. 2982–3004, Nov. 2024, doi: 10.1007/s12540-024-01694-w.

[18] T. Varol, H. C. Aksa, F. Yıldız, S. B. Akçay, G. Kaya, and M. Beder, 'Influence of post processing on the mechanical properties and wear behavior of selective laser melted Co-Cr-Mo-W alloys', *Tribology International*, vol. 192, p. 109336, Apr. 2024, doi: 10.1016/j.triboint.2024.109336.

[19] G. Kaya, U. Köklü, T. O. Ergüder, F. Cengiz, and F. Yıldız, 'Effects of build orientation and hatch spacing on high-speed milling behavior of L-PBF 316L stainless steel', *Materials Testing*, vol. 65, no. 10, pp. 1571–1581, Oct. 2023, doi: 10.1515/mt-2023-0210.

[20] J. Zhao, H. Liu, Y. Zhou, Y. Chen, and J. Gong, 'Effect of relative density on the compressive properties of Ti6Al4V diamond lattice structures with shells', *Mechanics of Advanced Materials and Structures*, vol. 29, no. 22, pp. 3301–3315, Aug. 2022, doi: 10.1080/15376494.2021.1893418.

[21] T. Ahmed and H. J. Rack, 'Phase transformations during cooling in α + β titanium alloys', *Materials Science and Engineering: A*, vol. 243, no. 1–2, pp. 206–211, 1998, doi: 10.1016/s0921-5093(97)00802-2.

[22] A. A. Antonysamy, *Microstructure, texture and mechanical property evolution during additive manufacturing of Ti6Al4V alloy for aerospace applications*. The University of Manchester (United Kingdom), 2012. Accessed: May 02, 2025. [Online]. Available: https://search.proquest.com/openview/6d22965546ce3092918e9ad2280b68fc/1?pq-origsite=gscholar&cbl=51922

[23] B. Vrancken, L. Thijs, J.-P. Kruth, and J. Van Humbeeck, 'Heat treatment of Ti6Al4V produced by Selective Laser Melting: Microstructure and mechanical properties', *Journal of Alloys and Compounds*, vol. 541, pp. 177–185, Nov. 2012, doi: 10.1016/j.jallcom.2012.07.022.

[24] H. Zhang, T. Gao, C. Xu, L. Zhao, H. Song, and G. Huang, 'Study on the Tensile and Shear Behaviors of Selective Laser Melting Manufactured Ti6Al4V', *Met. Mater. Int.*, vol. 29, no. 10, pp. 2852–2864, Oct. 2023, doi: 10.1007/s12540-023-01433-7.

[25] P. K. Singh, S. Kumar, P. K. Jain, and U. S. Dixit, 'Effect of Build Orientation on Metallurgical and Mechanical Properties of Additively Manufactured Ti-6Al-4V Alloy', *J. of Materi Eng and Perform*, vol. 33, no. 7, pp. 3476–3493, Apr. 2024, doi: 10.1007/s11665-023-08218-4.

[26] X. Yang *et al.*, 'Multi-build orientation effects on microstructural evolution and mechanical behavior of truly as-built selective laser melting Ti6Al4V alloys', *Journal of Materials Research and Technology*, vol. 30, pp. 3967–3976, May 2024, doi: 10.1016/j.jmrt.2024.04.031.

[27] I. Katzarov, S. Malinov, and W. Sha, 'Finite element modeling of the morphology of β to α phase transformation in Ti-6Al-4V alloy', *Metall Mater Trans A*, vol. 33, no. 4, pp. 1027–1040, Apr. 2002, doi: 10.1007/s11661-002-0204-4.

[28] N. Stefansson, S. L. Semiatin, and D. Eylon, 'The kinetics of static globularization of Ti-6Al-4V', *Metall Mater Trans A*, vol. 33, no. 11, pp. 3527–3534, Nov. 2002, doi: 10.1007/s11661-002-0340-x.

[29] S. Malinov, Z. Guo, W. Sha, and A. Wilson, 'Differential scanning calorimetry study and computer modeling of β ⇒ α phase transformation in a Ti-6Al-4V alloy', *Metall Mater Trans A*, vol. 32, no. 4, pp. 879–887, Apr. 2001, doi: 10.1007/s11661-001-0345-x.

[30] R. Pederson, O. Babushkin, F. Skystedt, and R. Warren, 'Use of high temperature X-ray diffractometry to study phase transitions and thermal expansion properties in Ti-6Al-4V', *Materials Science and Technology*, vol. 19, no. 11, pp. 1533–1538, 2003, doi: 10.1179/026708303225008013.

[31] M.-T. Tsai *et al.*, 'Heat-treatment effects on mechanical properties and microstructure evolution of Ti-6Al-4V alloy fabricated by laser powder bed fusion', *Journal of Alloys and Compounds*, vol. 816, p. 152615, Mar. 2020, doi: 10.1016/j.jallcom.2019.152615.

[32] S. A. Etesami, B. Fotovvati, and E. Asadi, 'Heat treatment of Ti-6Al-4V alloy manufactured by laser-based powder-bed fusion: Process, microstructures, and mechanical properties correlations', *Journal of Alloys and Compounds*, vol. 895, p. 162618, 2022.

[33] L. Thijs, F. Verhaeghe, T. Craeghs, J. V. Humbeeck, and J.-P. Kruth, 'A study of the microstructural evolution during selective laser melting of Ti–6Al–4V', *Acta Materialia*, vol. 58, no. 9, pp. 3303–3312, May 2010, doi: 10.1016/j.actamat.2010.02.004.

[34] X. Yan *et al.*, 'Effect of heat treatment on the phase transformation and mechanical properties of Ti6Al4V fabricated by selective laser melting', *Journal of Alloys and Compounds*, vol. 764, pp. 1056–1071, Oct. 2018, doi: 10.1016/j.jallcom.2018.06.076.

[35] M. Simonelli, Y. Y. Tse, and C. Tuck, 'Effect of the build orientation on the mechanical properties and fracture modes of SLM Ti–6Al–4V', *Materials Science and Engineering: A*, vol. 616, pp. 1–11, Oct. 2014, doi: 10.1016/j.msea.2014.07.086.

[36] J. M. Jeon *et al.*, 'Effects of microstructure and internal defects on mechanical anisotropy and asymmetry of selective laser-melted 316L austenitic stainless steel', *Materials Science and Engineering: A*, vol. 763, p. 138152, Aug. 2019, doi: 10.1016/j.msea.2019.138152.

[37] Z. Xie, Y. Dai, X. Ou, S. Ni, and M. Song, 'Effects of selective laser melting build orientations on the microstructure and tensile performance of Ti–6Al–4V alloy', *Materials Science and Engineering: A*, vol. 776, p. 139001, Mar. 2020, doi: 10.1016/j.msea.2020.139001.

[38] R. Sabban, S. Bahl, K. Chatterjee, and S. Suwas, 'Globularization using heat treatment in additively manufactured Ti-6Al-4V for high strength and toughness', *Acta Materialia*, vol. 162, pp. 239–254, Jan. 2019, doi: 10.1016/j.actamat.2018.09.064.

[39] C. Wang, Y. Lei, and C. Li, 'Achieving an Excellent Strength and Ductility Balance in Additive Manufactured Ti-6Al-4V Alloy through Multi-Step High-to-Low-Temperature Heat Treatment', *Materials*, vol. 16, no. 21, p. 6947, Jan. 2023, doi: 10.3390/ma16216947.

BİTLİS EREN ÜNİVERSİTESİ
FEN BİLİMLERİ DERGİSİ

ISSN: 2147-3129 / e-ISSN: 2147-3188

Article Type : Research Article
Received : June 5, 2025
Revised : July 14, 2025
Accepted : July 30, 2025
DOI : 10.17798/bitlisfen.1714876

Year : 2025
Volume : 14
Issue : 3
Pages : 1772-1786

CORRELATED SKU ASSIGNMENT IN WAREHOUSES USING THE JOINT DEMAND PROBABILITY DISTRIBUTION: A METAHEURISTIC ALGORITHM APPROACH

Bayram DÜNDAR [1]

[1] *Bartın University, Department of Computer Engineering, Bartın, Türkiye, bdundar@bartin.edu.tr*

ABSTRACT

In warehouse management, picking orders from storage locations quickly and in the shortest time has become even more important with the development of e-commerce. Thus, efficiently assigning affined products to storage locations within the warehouses is crucial in reducing operational costs and preserving product quality. In this study, a Mixed-Integer Linear Programming model (MILP) is developed to minimize in-warehouse picking distances. Based on demand data, inter-product relationships are analyzed, and correlation coefficients are estimated for product pairs with a high tendency to be ordered together. These correlation values are then integrated into the objective function to optimize storage location decisions. To obtain faster and near-optimal solutions from the MILP model on large-scale data sets, a genetic algorithm (GA)-based approach has been developed. A set of computational experiments conducted on medium and large-scale instances compares the performance of the proposed GA approach with the Random-Based Correlated Skus Assignment Model (RBC-SAM). The GA approach under different scenarios shows an improvement of up to 22%.

Keywords: SKUs assignment problem, Demand correlation, Genetic algorithm, Mathematical modeling.

1 INTRODUCTION

With the rapid development of e-commerce and international supply chains today, warehouse management has become one of the most critical stages of the supply chain. Stocking products within a specific plan provides significant convenience in placing and picking products after the order. A Stock Keeping Unit, or SKU, is the smallest physical unit of a product to facilitate tracking in warehouse management [2]. Optimal assignment of SKUs

allows warehouse management to offer significant cost advantages to businesses in terms of both time and distance during the process of picking orders from storage locations. As stated in the study by [2], the order-picking process consists of several key sub-activities, including traveling, searching, and extracting. Among these, traveling accounts for approximately 55\% of the total order-picking time, making it the most time-consuming activity. Therefore, warehouse management systems should primarily focus on reducing traveling time to expedite the fulfillment of any given order. Moreover, since traveling is a labor-intensive activity, it constitutes one of the most significant cost components in warehouse operations. To the end, optimizing the traveling activity is crucial for enhancing warehouse efficiency and reducing operational costs.

Effectively managing space and time is among the most critical elements in warehouse operations. An analysis of customer orders often reveals meaningful relationships between certain SKUs. In other words, strong correlations can be observed between specific SKU pairs. This strategy aims to optimize both time and space efficiency by leveraging the inherent relationships between frequently co-ordered items. In the literature, this problem is generally known as the SKU assignment problem. There are various studies addressing the SKUs assignment problem. For example, [6] examined the assignment of SKUs to areas in area-based carton collection distribution centers (DCs) where they decide which products to collect. In their study, a simulated annealing-based heuristic approach was used due to the large-scale nature of the problem. There are also some studies addressing the storage assignment problem within the framework of the Quadratic Assignment Problem (QAP). In this study, the problem of allocating related SKUs to storage locations is addressed. Some SKUs are frequently ordered together; therefore, the relationship between such SKUs should be taken into account when assigning them to available storage locations. Placing related SKUs close together could reduce the total picking distance and, therefore, the total cost of warehouse operations. This highlights the importance of considering proximity relationships between SKUs. In this study, unlike the approaches in the literature, the correlation value between two SKUs is calculated using the 'joint distribution' methodology. Furthermore, since the correlated SKU assignment problem exhibits a combinatorial structure, a genetic algorithm (GA) based metaheuristic approach is proposed.

The remaining sections of this study are planned as follows: In the second section, the literature on modeling and solution approaches for the correlated SKU assignment problem is reviewed. In the third section, the modeling details of the SKU assignment problem are

presented, and the details of the Genetic Algorithm (GA) based solution approach used are given. The developed GA approach is subjected to computational tests under various scenarios in the fourth section. The last section presents a general evaluation and a brief summary of the study.

2 LITERATURE REVIEW

This section reviews studies in the literature that focus on the assignment of correlated SKUs to storage locations. Particular attention has been paid to how these problems are modeled and which solution methods are employed.

Bottani et al. [3] solved a class-based assignment problem in warehouses using a genetic algorithm. However, their work did not take into account the correlation between products. Xiao and Zheng [13] utilized the product bill of materials to estimate demand correlation among the SKUs in the storage assignment problem. The authors proposed heuristic algorithms to solve the mathematical model. Wisittipanich and Kasemset [12] presented a mixed-integer linear programming (MILP) model for the storage location assignment problem and proposed two metaheuristic algorithms to solve large-scale instances. Li et al. [9] used data mining techniques for the dynamic storage allocation problem to calculate the "affinity" values of the products, and based on these values, they used a greedy genetic algorithm to assign the products to achieve the maximum possible total relatedness value. Zhang et al. [14] took into account the pattern of correlation of demand between products to assign items to storage areas in warehouses. The developed model was solved using simulated annealing and a heuristic algorithm. Ansari et al. [1] proposed a gravity model including a clustering method in order to optimize the SKUs assignment to storage locations. Kim et al. [7] took into account the heuristic algorithms when assigning the affined SKUs to storage locations. Squires et al. [11] has developed a genetic algorithm-based solution for the scheduling problem of medical treatment processes.

Lee et al. [8] proposed a bi-objective optimization model for the correlated assignment problem, taking into account traffic congestion in warehouses. The proposed model aims to improve the efficiency of the picking process. It was validated through a case study using data collected from an actual warehouse. The simulation results demonstrated significant improvements in travel time and delays. Mirzaei et al. [10] proposed a mixed integer model for the distribution center of personal care products by considering the correlation between the products. The aim of this model is to minimize the travel time of robots by assigning products

to optimal storage locations. Gabellini et al. [4] proposed a genetic algorithm and a machine learning-based model to address a batch assignment problem in warehouses, with the aim of predicting the pick-up time of orders. Dündar [15] developed a robust counterpart of the correlated SKUs assignment model and solved it with a commercial solver. In that study, a limited number of SKUs could be assigned within an efficient computational time.

Islam et al. [5] have conducted a comprehensive literature review on the correlated assignment problem. The vast majority of studies in the literature aim to minimize travel time and distance within the warehouse. To this end, optimal or near-optimal solutions to large-scale problems have been proposed, usually using various heuristic and metaheuristic algorithms. However, no study has been found that specifically addresses the correlation between two SKUs using the marginal distribution method. The summary of reviewed studies is provided in Table 1.

Table 1 The summary of reviewed studies

Authors	Developed model	Solution method
Bottani et all.(2012)	Class based assignment problem	Genetic Algorithm
Xiao and Zheng (2012)	Bill of material based correlation assignment model	Heuristic Algorithm
Wisittipanich and Kasemset (2015)	Mixed integer programming model	Metaheuristic algorithms
Li et al. (2016)	Data mining technique based dynamic storage allocation problem	Greedy genetic algorithm
Zhang et al. (2019)	The storage location assignment problem	Simulated annealing and a heuristic algorithm
Ansari et al. (2020)	A gravity model based clustering method	A simulation model approach
Kim et al. (2020)	Storage location assignment model	Heuristic Algorithm
Lee et al. (2020)	A bi-objective optimization model	Multi-objective evolutionary algorithms
Mirzaei et al. (2022)	Correlated dispersed storage assignment model	Heuristic Algorithm
Gabellini et al. (2024)	A batch assignment problem	Genetic Algorithm and a machine learning-based approach
Dündar (2025)	Correlated SKUs assignment model with uncertainty	Gurobi solver

3 PROBLEM FORMULATIONS

A mixed-integer linear programming (MILP) model is proposed for assigning correlated SKUs to storage racks. The proposed model aims to minimize the total picking time in warehouses. The objective function depends on the correlation between each pair of SKUs, the distance between the racks to which they are assigned, and the associated decision variables. Let i and j represent the SKUs from the set I, and let t and r represent the stock locations from the set $\aleph$. δ_{tr} represents the distance between stock location t and stock location r. y_{ijtr} is a binary decision variable; if SKU i and SKU j are assigned to stock locations t and r, respectively, y_{ijtr} takes the value of 1. Otherwise, it takes the value of 0. Additionally, Q_i is a random variable representing the demand quantity for product i within a specific period. The details of sets, indices, parameters, and decision variables are provided in Table 2.

Table 2: The description of notations in the mathematical model

Sets and Indices	**Description**
$\aleph$	Set of SKUs
I	Set of stock locations
i, j	Represents SKUs in a set of $\aleph$
t, r	Denotes the stock locations in the set of I
Parameters	
δ_{tr}	Distance between the stock locations t and r
Q_i	Random variable for the number of SKUs ordered
Decision variables	
y_{ijtr}	If SKU i and SKU j are assigned to stock locations t and r, respectively, y_{ijtr} takes the value of 1, otherwise 0
z_{it}	A binary variable used in linearization that enforces the binary nature of y_{ijtr}. If SKU i is assigned to stock location t, the value of 1 is taken; otherwise, 0

The following assumptions were used in the correlated SKUs assignment problem. First, only one SKU is assigned to a single storage location. Second, there are as many available storage locations as SKUs to be assigned. The number of storage locations to which the SKUs will be assigned is fixed. Finally, the storage locations to which the SKUs will be assigned are large enough to accommodate large quantities of SKUs.

$$\min \sum_{\{(i,j)\in I|i<j\}} \sum_{t,r\in \aleph} \frac{\mathbb{E}[Q_iQ_j] - \mathbb{E}[Q_i]\mathbb{E}[Q_j]}{\sqrt{(\mathbb{E}[Q_i^2]\mathbb{E}[Q_i]^2)(\mathbb{E}[Q_j^2]\mathbb{E}[Q_j]^2)}}\ \delta_{tr} y_{ijtr} \tag{1}$$

The division operation in the objective function calculates the correlation value between SKUs. The expected value expressions used here are calculated with the help of marginal distributions obtained from the Q random variables. Assume that the joint probability distribution of two SKUs, i and j, is estimated based on the demand pattern. In this case, the marginal distributions for each SKU, denoted as $P(Q_i)$ and $P(Q_j)$, are obtained as follows:

$$P(Q_i = q_i) = \sum_{q_j} P_{(Q_i,Q_j)}\left(Q_i = q_i, Q_j = q_j\right) \tag{2}$$

In the objective function, $\mathbb{E}[Q_i]$ represents the expected value of SKU i (Q_i), which is calculated as $\mathbb{E}[Q_i] = \sum_q q\, P(Q = q)$. The term $\mathbb{E}[Q_iQ_j]$ denotes the expected value of the product of SKUs i and j, as given in the following equation $\mathbb{E}[Q_iQ_j] = \sum_{q_iq_j} P_{(Q_i,Q_j)}\left(Q_i = q_i, Q_j = q_j\right)$. The terms in the objective function denominator represent the product of the standard deviations of SKU i and SKU j. The objective function is subject to the following constraints. In the constraint (3), $SKU\ i$ can only be assigned to one storage location.

$$\sum_{k\in \aleph} z_{it} = 1, \qquad \forall t \in I \tag{3}$$

The constraint (4) stipulates that each storage location t can be assigned to only one $SKU\ i$.

$$\sum_{i\in I} z_{it} = 1, \qquad \forall t \in \aleph \tag{4}$$

The following constraints ensure that the variable y_{ijtr} takes binary values, i.e., either 0 or 1, within the linearized objective function. Similarly, z_{ij} is defined as a binary variable, $z_{it} \in \{0,1\}$, that enforces the binary nature of y_{ijtr}.

$$y_{ijtr} \le z_{it}, \qquad \forall i,j \in I|i<j, \qquad \forall t,r \in \aleph \tag{5}$$

$$y_{ijtr} \le z_{jr}, \qquad \forall i,j \in I|i<j, \qquad \forall t,r \in \aleph \tag{6}$$

$$z_{it} + z_{jr} - 1 \le y_{ijtr}, \qquad \forall i,j \in I|i<j, \qquad \forall t,r \in \aleph \tag{7}$$

3.1 Genetic Algorithm Approach

The SKU assignment problem is inherently combinatorial and falls into the class of NP-hard problems. In solving large-scale versions of such problems, as widely emphasized in the literature, it is possible to reach optimal or near-optimal solutions within reasonable times through genetic algorithm (GA) based approaches. In this study, the solution of the correlation-based SKU assignment model is obtained using the genetic algorithm framework. The basic steps of the proposed genetic algorithm approach are outlined in Algorithm 1. In the following subsections, detailed explanations of the functions and procedures of the genetic algorithm are provided.

3.1.1 Chromosome Structure

The chromosome structure consists of genes equal in number to the SKUs and storage locations. Each gene in the chromosome represents an assigned SKU. In this context, a permutation-based encoding method is employed. The number of potential chromosomes corresponds to the total number of permutations of the SKUs.

3.1.2 Evaluation Function

This function is used to evaluate the extent to which each chromosome in the population, that is, the potential solution, is suitable according to the objective function. The evaluation function aims to minimize the product of the correlation between SKUs and the distance between the locations to which these SKUs are assigned.

Algorithm 1 Genetic algorithm

[H] **Input:** $\mathcal{C}$, $|\mathcal{I}|$, φ, ξ, number of generation(n),$\mathcal{S}$

```
function EvaluationFunc(C)
    return obj
end function
function Crossover(f_candidate,s_candidate,|I|,S)
    Crossover procedure
    return best candidate solution
end function
function Mutation(chromozom)
    Mutation procedure
    return mutated chromozom
end function
function Selection(C)
    return parent 1, parent 2
end function
function CandidateSolution(C)
    Mutation
    Selection
    Immigration
    return New candidate solution
end function
function GeneticAlgorithm(C, |I|, φ, ξ, n, S)
    for i in range(n):
        if New candidate solution ≤ incumbent solution then
            incumbent solution = New candidate solution
end function
return Assigned SKUs
```

3.1.3 Selection Procedure

This function contains the procedures that define how any two solutions are obtained in order to generate new candidate solutions from the population. In this study, within the scope of the selection procedure, two candidate solutions are randomly selected from the existing population.

3.1.4 Crossover Procedure

The crossover procedure defines the rules by which a new solution is produced from the two selected parent chromosomes. In this method, the genes on both chromosomes are compared based on the index. If the genes in the same index are different, the value of the gene on the first chromosome is determined by the index it is located on the second chromosome. Then, the relevant gene on the first chromosome is replaced with the corresponding value on the second chromosome. As a result of these operations, the first candidate solution is obtained. Similarly, similar changes are made on the second chromosome, and an alternative candidate solution is produced.

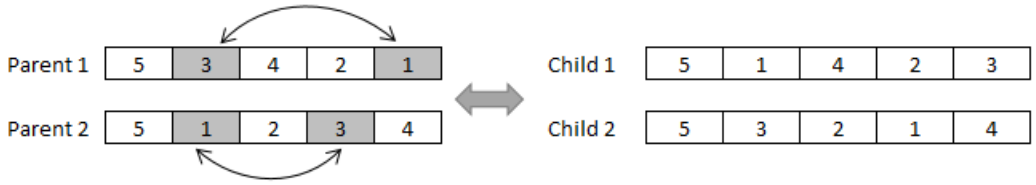


Figure 1. Illustration of the crossover procedure for generating new candidate solution

3.1.5 Mutation

It is the process of exchanging two randomly selected genes on a chromosome with each other in order to increase genetic diversity. This mutation process is performed on the new candidate solution obtained as a result of the crossover process. Whether or not the mutation will be applied is decided according to whether a randomly generated number in the range [0,1] is smaller than the predefined mutation rate ξ.

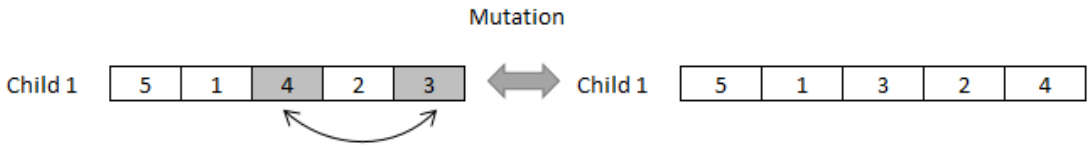


Figure 2. Mutation procedure for generating more diverse candidate solutions

3.1.6 Generation of A New Candidate Solution

A new candidate solution is generated on the basis of the crossover and mutation procedures previously explained. The steps related to this process are presented in detail in Algorithm 2. The predefined chromosome set C, the number of SKUs (|I|) to be assigned, the crossover rate (φ), the mutation rate (ξ) and the set S, which includes the correlation values between SKUs, are used as input parameters. If the two candidate solutions determined as a result of the selection procedure are identical, two different individuals from the chromosome set C are selected again. As stated in the third line of the algorithm, if a randomly generated number in the range [0,1] is smaller than the crossover rate (φ), the crossover procedure is applied. Similarly, as stated in the eighth line, if a random number generated in the range [0,1] is smaller than the mutation rate (ξ), the mutation procedure is activated. This mechanism increases genetic diversity, resulting in a more diverse candidate solution.

Algorithm 2 A function of generating a candidate solution

Input: $\mathcal{C}$, $|\mathcal{I}|$, φ, ξ
Output: A new candidate solution
Select *f_candidate* and *s_canditate* from $\mathcal{C}$ using *Selection* procedure **while** *f_candidate.Sequence* = *s_candidate.Sequence* **do**
  Select *f_candidate* and *s_candidate* again from $\mathcal{C}$
if *random.random()* $\leq \varphi$ **then**
  Candidate solution ← `crossover procedure`
else
  Candidate solution ← copy of *f_candidate* ()
if *random.random()* $\leq \xi$ **then**
  Candidate solution ← `mutation procedure`
return Candidate solution

4 COMPUTATIONAL RESULTS

In order to test the GA model, an artificial distance data set was created with a distance of 4 meters between storage locations. The correlation data expressing the relationship between SKUs is also created artificially. As aforementioned in the objective function of the MILP model, the correlation is calculated based on the context of the marginal distribution of demand for SKUs. Identifying the most suitable combination of these parameters ensures that the algorithm converges on the optimal solution quickly and accurately. In this context, the GA model developed is evaluated through a series of experimental tests on a data set consisting of 15 SKUs and 15 storage locations, with the aim of determining the optimal parameter settings. As shown in Figure 3, four different crossover rate values, 0.50, 0.75, 0.90, and 0.99, are tested. As a result of the analyses, the crossover rate of 0.99 led to the fastest convergence to the optimal solution. In this study, we assume that the number of SKUs to be assigned and the number of stock locations are equal to each other. If the number of products to be assigned is less than the number of available storage locations, a routine assignment is performed. Conversely, if the number of products to be assigned is greater than the number of available storage locations, a routine assignment is performed by grouping products according to the number of storage locations, taking into account the correlation value between products.

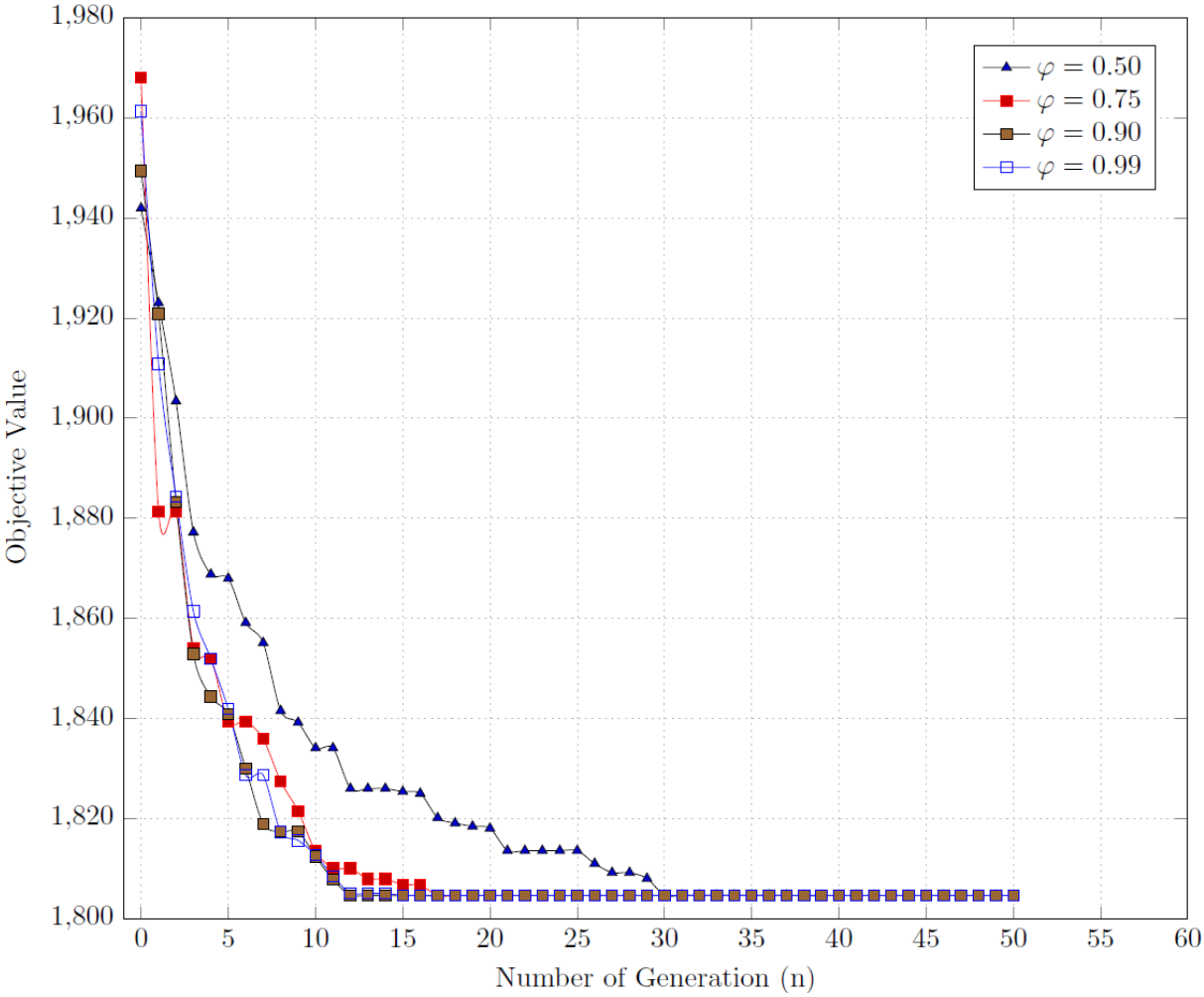


Figure 3. The convergence of objective value for various crossover rates

One of the key parameters that enhances the diversity of candidate optimum solutions in the GA model is the mutation rate. In this context, in order to evaluate the effect of the mutation rate, the GA algorithm was tested for four different values, 0.25, 0.50, 0.75, and 0.90, as shown in Figure 4. The experimental test remarked that the mutation rate of 0.5 led to the fastest convergence to the optimal or near-optimal solution.

The GA model was tested for different immigration probabilities, 0.04, 0.05, 0.50, and 0.90, as shown in Figure 5. According to the experimental results, the immigration probability of 0.05 is identified as the most appropriate optimum rate that provides the optimal solution.

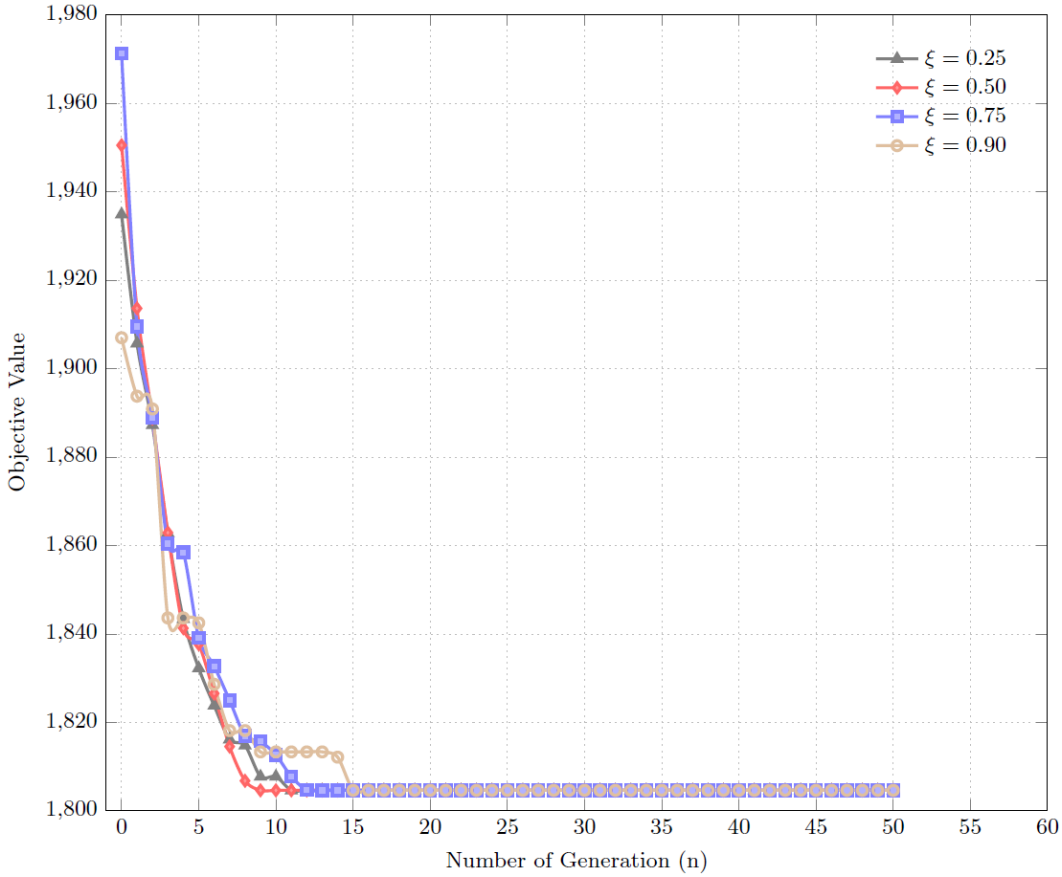


Figure 4. The convergence of objective value for various mutation rates

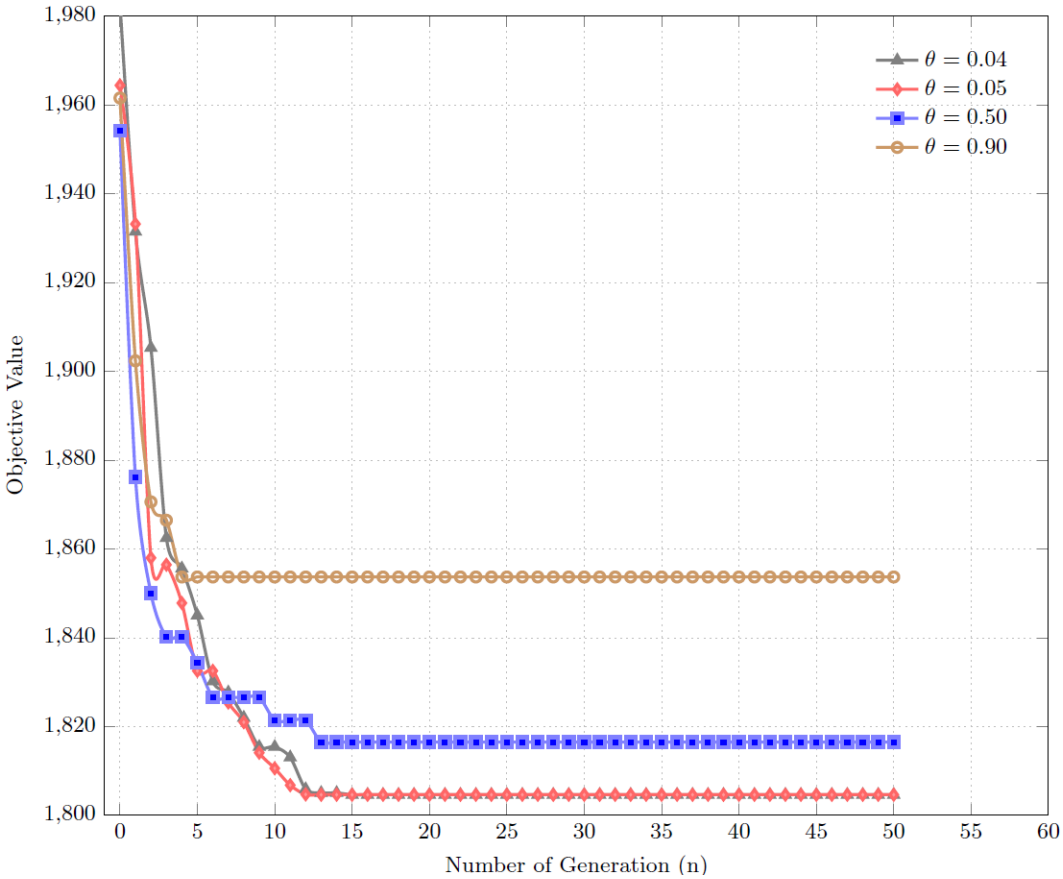


Figure 5. The convergence of the objective value for various immigration rates

As seen in Table 3, the GA model was tested for a range of scenarios that start with 15 SKUs and storage locations and increase to 100 SKUs, according to the GA parameters specified previously. Each scenario was run 50 times, and the best, average, and worst objective function values obtained in each run were recorded. For example, in the assignment scenario with 15 SKUs, the objective function value was the same in all runs and was measured as 1825.7. The average CPU time was only 1.9 seconds, which shows that the GA model can produce a high-quality and consistent solution in a short time. When the number of SKUs was increased to 20, the best objective function value was obtained as 4554.4, and the deviation between the best and worst results was only 0.48 %. Notice that in the case of assigning 50 SKUs, as can be estimated from Table 3, the 1.27 % deviation occurred compared to the best solution. The average CPU time per run increased to 67.68 seconds. When the GA model was run to assign 100 SKUs, there was a difference of approximately 1.05% between the best and worst solutions obtained. With an average CPU time of 768.92 seconds, the GA model provided a valid solution for 100 correlated SKUs.

Table 3. Computational performance of the GA

# of runs	# of SKUs	Objective function value			Avg. CPU Time (sec)
		Best	Average	Worst	
50	15	1825.7	1825.7	1825.7	1.9
	20	4554.4	4558.7	4576.3	4.6
	30	14542.3	14542.8	14544.1	15.3
	40	35948.2	35968.0	36012.7	36.3
	50	72277.0	72452.7	73195.0	67.7
	70	207742.4	208842.0	211304.9	295.2
	90	449931.5	452993.6	457804.2	599.8
	100	622699.0	626176.3	629223.9	768.9

Within the framework of the parameters mentioned above, the GA model was tested for different numbers of SKUs and storage location scenarios in terms of both computation time and optimal solution quality. In this framework, a comparison was made between randomly assigned SKUs and GA based SKU assignment.

As seen in Table 4, the GA-based assignment model and the RBC-SAM were compared. In other words, the effect of an assignment made without considering the correlation relationship between SKUs on the objective function in terms of minimizing the total picking distance was examined. According to the results in Table 4, in the scenario where 15 SKUs were assigned, the GA-based model produced a 22.65% better solution in terms of the objective

function value than the RBC-SAM. When the number of SKUs increased to 40, the GA model performed 20.24% better than the RBC-SAM model. In the scenario where 100 SKUs were assigned, the GA model produced an 8.83% better result compared to the RBC-SAM model in terms of the objective function value. Hence, reducing the total picking distance in warehouse management plays an important role in terms of requiring less labor in operational activities within the warehouse, reducing internal traffic density, maintaining product quality and generally reducing total operational costs.

Table 4. Comparison of objective values between the GA Model and RBC-SAM

# of SKUs	GA Model	GA Std. deviation	RBC-SAM	% of Difference
15	1,8250.7	0	2,239.14	22.65
20	4,554.4	7.42	5,392.47	18.40
30	14,542.3	7.50	17,051.83	17.26
40	35,948.2	16.24	43,223.76	20.24
50	72,277.0	344.91	81,824.62	13.21
70	207,742.4	827.75	230,417.04	10.91
90	449,931.5	1948.49	493,591.99	9.70
100	622,699.0	2165.45	677,688.26	8.83

5 CONCLUSION AND SUGGESTIONS

This study considers the problem of assigning correlated SKUs to the storage location. The correlation between SKUs is estimated by using the joint probability distribution function. In preliminary computational tests conducted with commercial solvers, especially in cases where the problem reaches large instances, namely, more than 13 SKUs, it became intractable to provide a solution. The Genetic Algorithm (GA) based approach is proposed to solve medium and large instances of SKUs. The GA model was tested on up to 100 SKUs with an artificial data set under various scenarios. The proposed algorithm was able to provide optimal solutions for small-scale problems in a shorter time. However, as the instances of the SKUs increased, it was not possible to test whether the solution found by the model was optimal or not, but it still produced high-quality solutions in a very short time. The GA-based assignment method provided 8.8% to 22.6% more efficient solutions in terms of total distance compared to the Random-Based Correlated SKUs Assignment Model (RBC-SAM). For future work, one could apply the robust counterpart of the correlated assignment model to larger-scale problems. An algorithm could be proposed that would enable this problem to be solved efficiently.

Statement of Research and Publication Ethics

The study is complied with research and publication ethics.

Artificial Intelligence (AI) Contribution Statement

The author used AI-based tools, ChatGP and Grammarly to assist with language editing of the manuscript. All revisions were reviewed and approved by the author.

REFERENCES

[1] M. Ansari and J. S. Smith, "Gravity clustering: A correlated storage location assignment problem approach," in *Proc. 2020 Winter Simulation Conf. (WSC)*, 2020, pp. 1288–1299.

[2] J. J. Bartholdi and S. T. Hackman, *Warehouse & Distribution Science: Release 0.96*. Atlanta, GA: The Supply Chain and Logistics Institute, 2014. [Online]. Available: https://www.warehouse-science.com

[3] E. Bottani, M. Cecconi, G. Vignali, and R. Montanari, "Optimisation of storage allocation in order picking operations through a genetic algorithm," *Int. J. Logist. Res. Appl.*, vol. 15, no. 2, pp. 127–146, 2012.

[4] M. Gabellini, F. Calabrese, A. Regattieri, D. Loske, and M. Klumpp, "A hybrid approach integrating genetic algorithm and machine learning to solve the order picking batch assignment problem considering learning and fatigue of pickers," *Comput. Ind. Eng.*, vol. 191, p. 110175, 2024.

[5] S. Islam and K. Uddin, "Correlated storage assignment approach in warehouses: A systematic literature review," *J. Ind. Eng. Manag.*, vol. 16, no. 2, pp. 294–318, 2023.

[6] B. S. Kim and J. S. Smith, "Slotting methodology using correlated improvement for a zone-based carton picking distribution system," *Comput. Ind. Eng.*, vol. 62, no. 1, pp. 286–295, 2012.

[7] J. Kim, F. Méndez, and J. Jimenez, "Storage location assignment heuristics based on slot selection and frequent itemset grouping for large distribution centers," *IEEE Access*, vol. 8, pp. 189025–189035, 2020.

[8] G. Lee, S. H. Chung, and S. W. Yoon, "Two-stage storage assignment to minimize travel time and congestion for warehouse order picking operations," *Comput. Ind. Eng.*, vol. 139, p. 106129, 2020.

[9] J. Li, M. Moghaddam, and S. Y. Nof, "Dynamic storage assignment with product affinity and ABC classification—A case study," *Int. J. Adv. Manuf. Technol.*, vol. 84, pp. 2179–2194, 2016.

[10] M. Mirzaei, N. Zaerpour, and R. B. de Koster, "How to benefit from order data: Correlated dispersed storage assignment in robotic warehouses," *Int. J. Prod. Res.*, vol. 60, no. 2, pp. 549–568, 2022.

[11] M. Squires, X. Tao, S. Elangovan, R. Gururajan, X. Zhou, and U. R. Acharya, "A novel genetic algorithm based system for the scheduling of medical treatments," *Expert Syst. Appl.*, vol. 195, p. 116464, 2022.

[12] W. Wisittipanich and C. Kasemset, "Metaheuristics for warehouse storage location assignment problems," *Chiang Mai Univ. J. Nat. Sci.*, vol. 14, no. 4, pp. 361–377, 2015.

[13] J. Xiao and L. Zheng, "Correlated storage assignment to minimize zone visits for BOM picking," *Int. J. Adv. Manuf. Technol.*, vol. 61, pp. 797–807, 2012.

[14] R.-Q. Zhang, M. Wang, and X. Pan, "New model of the storage location assignment problem considering demand correlation pattern," *Comput. Ind. Eng.*, vol. 129, pp. 210–219, 2019.

[15] B. Dündar, "A robust optimization approach to address correlation uncertainty in stock-keeping unit assignment in warehouses," *Alphanumeric J.*, vol. 13, no. 1, pp. 1–12, 2025.

BİTLİS EREN ÜNİVERSİTESİ
FEN BİLİMLERİ DERGİSİ

ISSN: 2147-3129 / e-ISSN: 2147-3188

Article Type : Research Article
Received : June 8, 2025
Revised : July 21, 2025
Accepted : July 30, 2025
DOI : 10.17798/bitlisfen.1715597

Year : 2025
Volume : 14
Issue : 3
Pages : 1787-1801

TOWARD A SAFER AND GREENER FUTURE: RELIABLE AQUEOUS AMMONIUM-ION BATTERIES WITH $LiMnO_2$ CATHODES

Dilara OZGENÇ [1], Melisa UÇAN [1], **Burak TEKİN [1,*]**

[1] *Ondokuz Mayıs University, Chemical Engineering Department, Samsun, Türkiye*

**** Corresponding Author:*** *burak.tekin@omu.edu.tr*

ABSTRACT

Ammonium-ion-based energy storage systems have gained attention as a sustainable alternative for efficient charge storage. In this study, $LiMnO_2$ is explored for the first time as a cathode material in an aqueous ammonium-ion battery using a 2M $(NH_4)_2SO_4$ electrolyte. XRD analysis confirms the formation of phase-pure, highly crystalline orthorhombic $LiMnO_2$, while SEM imaging reveals a nanorod morphology that enhances ion transport. Cyclic voltammetry identifies two distinct charge storage mechanisms: NH_4^+ insertion/extraction and surface-controlled redox reactions, with oxidation peaks at 0.89 V and 0.72 V vs. Ag/AgCl and reduction peaks at 0.53 V and 0.28 V vs. Ag/AgCl. Galvanostatic charge-discharge testing demonstrates an initial discharge capacity of ~60 mAh/g at 1C, stabilizing at ~50 mAh/g after the second cycle and maintaining excellent capacity retention over 130 cycles. The stable electrochemical performance suggests that $LiMnO_2$ undergoes minimal structural degradation, while the mildly acidic $(NH_4)_2SO_4$ electrolyte effectively mitigates Mn dissolution. Electrochemical impedance spectroscopy reveals a moderate increase in charge transfer resistance (Rct) from 135 Ω to ~200 Ω after cycling, indicating stable interfacial kinetics. The successful demonstration of $LiMnO_2$ as a hosting material in an aqueous ammonium-ion battery highlights its potential for next-generation energy storage applications.

Keywords: Aqueous ammonium ion batteries, Lithium manganese oxide, Ammonium-ion intercalation, Electrochemical performance, Energy storage materials.

1 INTRODUCTION

With the increasing global demand for sustainable and high-performance energy storage solutions, researchers have explored a wide range of battery technologies beyond conventional lithium-ion systems [1]. Among these emerging alternatives, aqueous ammonium-ion batteries (AAIBs) have garnered significant attention due to their potential advantages in terms of safety, cost-effectiveness, and environmental sustainability. Unlike lithium-ion batteries, which rely on expensive and sometimes geopolitically constrained metal resources such as lithium and cobalt, AAIBs make use of abundant ammonium ions (NH_4^+) as charge carriers [2]. The utilization of an aqueous electrolyte further enhances their appeal by offering intrinsic non-flammability, higher ionic conductivity, and simplified battery assembly compared to non-aqueous counterparts [3-6]. Furthermore, AAIBs operate under mild pH conditions, which reduces corrosion-related degradation and extends battery lifespan. Given these advantages, AAIBs represent a promising candidate for next-generation, sustainable energy storage applications [7, 8].

The fundamental working principle of aqueous ammonium-ion batteries revolves around the reversible insertion and extraction of NH_4^+ ions in suitable electrode materials [9]. The unique properties of the NH_4^+ ion, including its small size, high mobility, and hydrogen-bonding capability, play a crucial role in the electrochemical behavior of the battery (Figure 1) [10]. However, these properties also introduce certain challenges, such as the stability of the NH_4^+ intercalation process and the structural integrity of electrode materials during prolonged cycling [7]. To address these concerns, researchers have explored various cathode and anode materials, including transition metal oxides [10], Prussian blue analogies [11], and Organic polymer materials [12], which exhibit compatibility with NH_4^+ ion insertion and extraction. Additionally, hybrid nanostructured electrodes have been proposed to enhance ion diffusion kinetics and improve overall electrochemical performance. The choice of electrolyte composition is another critical aspect influencing the performance of AAIBs, as factors such as pH, ionic strength, and solubility limits can significantly affect battery efficiency and longevity [13].

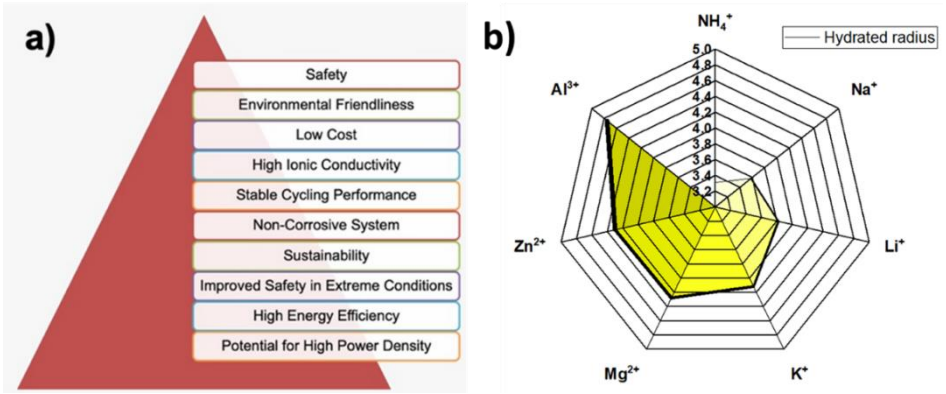


Figure 1. a) Advantages of aqueous ammonium-ion batteries and b) Comparison of atomic radii of different cation carriers.

In recent years, advancements in materials science and electrochemical engineering have led to substantial progress in the development of AAIBs. Novel electrode materials with enhanced electrochemical stability and optimized structural frameworks have been designed to accommodate the unique characteristics of NH_4^+ ions. Additionally, innovations in electrolyte formulation, including the incorporation of stabilizing additives and buffering agents, have contributed to improved cycle life and energy density [14]. Despite these advancements, several challenges remain, particularly in achieving higher voltage windows, minimizing side reactions, and mitigating capacity fading over extended cycling. In-depth studies on electrode-electrolyte interfaces have revealed that solvation effects and hydrogen bonding interactions significantly influence the mobility and reversibility of NH_4^+ ions. Addressing these challenges requires a comprehensive understanding of the fundamental ion transport mechanisms, electrode-electrolyte interactions, and the role of solvation effects in AAIBs [15].

The potential applications of aqueous ammonium-ion batteries span a broad range of energy storage needs, including grid-scale energy storage, backup power systems, and portable electronics. Their inherent advantages, such as low toxicity and ease of disposal, align well with the growing emphasis on green energy solutions. Furthermore, the compatibility of AAIBs with renewable energy sources, such as solar and wind power, highlights their potential role in facilitating a more sustainable and resilient energy infrastructure. Ongoing research in operando characterization techniques, such as in-situ spectroscopy and electrochemical impedance spectroscopy, has provided deeper insights into the dynamic behavior of NH_4^+ ions during charge-discharge cycles, aiding in the rational design of next-generation AAIBs [16-18]. Future research efforts should focus on overcoming existing technical limitations through advanced material design, in-depth mechanistic studies, and system-level optimization. By addressing these aspects, AAIBs could emerge as a viable and scalable energy storage solution,

complementing or even surpassing existing battery technologies in specific applications. The continued exploration of aqueous ammonium-ion batteries is not only of scientific interest but also holds the promise of contributing to a cleaner and more sustainable energy landscape [19].

In this study, we synthesized $LiMnO_2$ cathode material via a solid-state method and characterized its structural and electrochemical properties for ammonium-ion battery applications. The synthesized material was analyzed using X-ray diffraction (XRD) to confirm phase purity and scanning electron microscopy (SEM) to examine morphology. Electrochemical performance was evaluated through cyclic voltammetry (CV), galvanostatic charge-discharge (GCD), and electrochemical impedance spectroscopy (EIS) in an aqueous $(NH_4)_2SO_4$ electrolyte. The study investigated the redox behavior, charge storage mechanism, rate capability, and long-term cycling stability of $LiMnO_2$. The findings provide insights into the feasibility of ammonium-ion intercalation in $LiMnO_2$ and highlight the material's potential as a cathode for next-generation aqueous rechargeable batteries.

2 MATERIALS AND METHODS

The synthesis of $LiMnO_2$ via the solid-state reaction method was carried out through a multi-step process to ensure phase purity and homogeneity (Figure 2). High-purity $MnCO_3$ (≥99%) and $LiOH·H_2O$ (≥98%) were first precisely weighed in a Li:Mn molar ratio of 1:1.05**,** with the slight lithium excess compensating for potential volatilization losses during high-temperature treatment. The precursors were thoroughly mixed and ground in an agate mortar and pestle for 30–60 minutes to achieve a uniform mixture. To enhance reactivity, the mixed powder underwent hydrothermal pre-treatment in a Teflon-lined autoclave at 120°C for 24 hours, promoting better precursor interaction. The resulting product was then calcined in a muffle furnace at 400°C for 12 hours (5°C/min heating rate) under static air to facilitate the solid-state reaction and crystallization of $LiMnO_2$. To remove impurities such as unreacted manganese oxides or lithium residues, the calcined material was stirred in 5 M HCl for 48 hours, followed by filtration and repeated washing with deionized water until neutral pH (~7) was achieved. The purified product was finally dried at 80°C for 12 hours to obtain the desired $LiMnO_2$ powder. For a purely solid-state approach without hydrothermal treatment, the mixture can alternatively be calcined at 600–800°C for 24 hours with intermediate grindings**.** This detailed procedure ensures the production of high-quality $LiMnO_2$ suitable for battery applications, with adjustments possible for targeting specific polymorphs like layered or orthorhombic structures.

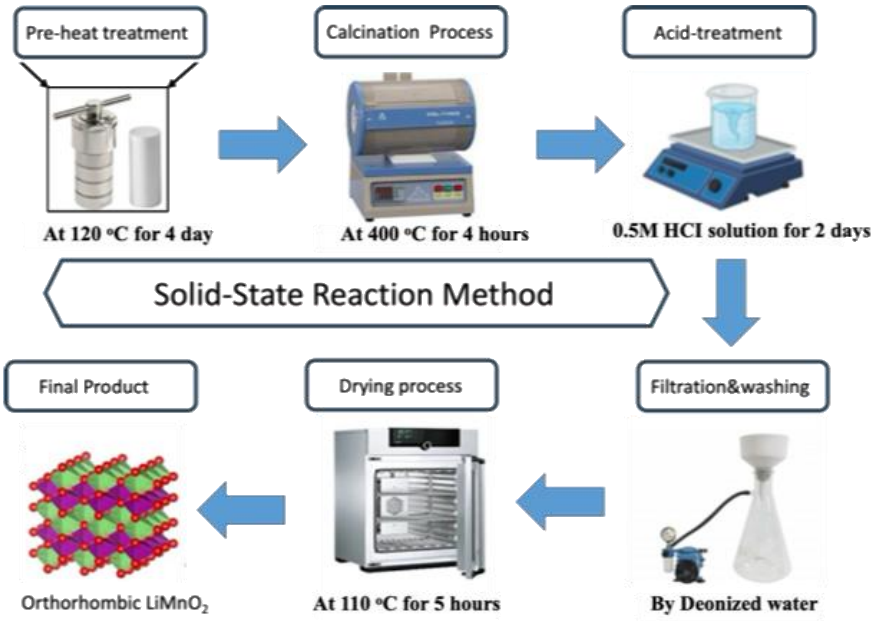


Figure 2. Schematic representation of the solid-state reaction synthesis process for $LiMnO_2$.

Following the synthesis of electroactive host materials ($LiMnO_2$), electrode slurries were separately prepared by homogenously mixing the active material, carbon black, and polyvinylidene fluoride (PVDF) in an 80:10:10 weight ratio. In this composition, carbon black functions as a conductive agent to enhance electron transport, while PVDF serves as a binder to improve electrode integrity and adhesion. The mixture was subsequently dispersed in N-methyl-2-pyrrolidone (NMP) as the solvent, ensuring uniform distribution of all components. The resulting slurry was continuously stirred on a magnetic stirrer overnight to achieve thorough homogenization, thereby optimizing the electrochemical performance and mechanical stability of the electrode. The electrode slurries were then cast using a doctor blade with a thickness of 1 mm onto a graphite plate, which served as the current collector. Subsequently, the coated electrodes were dried in an oven at 70°C to remove residual solvent and ensure proper adhesion of the active material to the current collector.

The battery configuration was assembled using a three-electrode glass beaker cell. The dried electrode slurries, previously cast onto graphite plates, were employed as the working electrode. A graphite rod was used as the auxiliary (counter) electrode to facilitate charge transfer, while an Ag/AgCl electrode served as the reference electrode to provide a stable reference potential. The electrodes were immersed in an aqueous electrolyte solution, ensuring proper ionic conductivity and electrochemical interaction. This setup enabled precise electrochemical measurements and characterization of the electrode materials.

The electrochemical performance of the $LiMnO_2$ cathode was investigated through several electrochemical techniques. Cyclic voltammetry (CV) tests were conducted in an aqueous $(NH_4)_2SO_4$ electrolyte within the voltage range of 0 V to 1.2 V vs. Ag/AgCl at room temperature. The CV was performed with a scan rate of 3 mV/s to assess the oxidation and reduction processes of the material. Each CV experiment was performed for 100 cycles to ensure reproducibility and assess electrochemical stability. Galvanostatic charge-discharge (GCD) tests were carried out within the same voltage window (0 V to 1.2 V vs. Ag/AgCl) using current densities ranging from 1C to 10C, where 1C corresponds to 148 mA/g, to evaluate the capacity, cycling stability, and rate performance of the cathode. Additionally, electrochemical impedance spectroscopy (EIS) was performed in the frequency range from 100,000 Hz to 0.1 Hz to analyze the charge transfer resistance and ion diffusion behavior with an applied AC amplitude of **10 mV**. All electrochemical measurements were conducted using an Admiral Instrument Squid Stat Plus Potentiostat. In this study, the active mass loading was between 0.002 and 0.003 g, and the surface area of the active material was approximately 0.75 cm^2, ensuring consistency and reliability in the electrochemical evaluations.

The structural properties of the synthesized $LiMnO_2$ cathode were analyzed using X-ray diffraction (XRD). The crystal structure and phase purity of the synthesized $LiMnO_2$ were examined using X-ray diffraction (XRD) analysis. The measurements were conducted on a Bruker D8 Advance X-ray diffractometer equipped with a Cu Kα radiation source ($\lambda = 1.5406$ Å), operating at 40 kV and 40 mA. The diffraction patterns were recorded in the 2θ range of 10°–80°with a step size of 0.02° and a scan speed of 1°/min.

3 RESULTS AND DISCUSSIONS

The XRD pattern of $LiMnO_2$, as shown in Figure 3a, reveals well-defined diffraction peaks, indicating a highly crystalline structure. The observed peaks correspond well with the standard JCPDS card 35-749 of orthorhombic $LiMnO_2$, confirming the successful phase formation without significant impurities. The most intense peak around $2\theta = \sim40°$ suggests a preferred orientation, which may be related to the synthesis conditions and the structural anisotropy of the material [20]. The absence of additional peaks from secondary phases, such as Mn_2O_3 or Mn_3O_4, indicates the phase purity of the synthesized sample [21]. Additionally, the sharpness of the peaks suggests a relatively large crystallite size and the peak broadening at lower angles may be attributed to micro-strain effects, which could impact the electrochemical properties of $LiMnO_2$ by influencing cation diffusion pathways [22]. The SEM images of

pristine $LiMnO_2$ synthesized via hydrothermal methods reveal a nanostructured, porous morphology with secondary agglomerates composed of fine primary particles (Figure 3b). The particle surfaces appear rough and loosely packed, with interconnected porous regions that are typical of hydrothermally synthesized oxides. This microstructure is advantageous for electrochemical applications, as it promotes electrolyte infiltration and shortens the ion charger diffusion paths. The particle sizes range from sub-micron to nanoscale, with no evidence of severe agglomeration or sintering. The uniform distribution and relatively homogeneous texture suggest controlled nucleation and growth during the hydrothermal process. Overall, the SEM analysis confirms that hydrothermal synthesis yields $LiMnO_2$ with a favorable porous architecture and nanoscale features, which could enhance the electrochemical kinetics and cycling stability in amonium-ion battery applications.

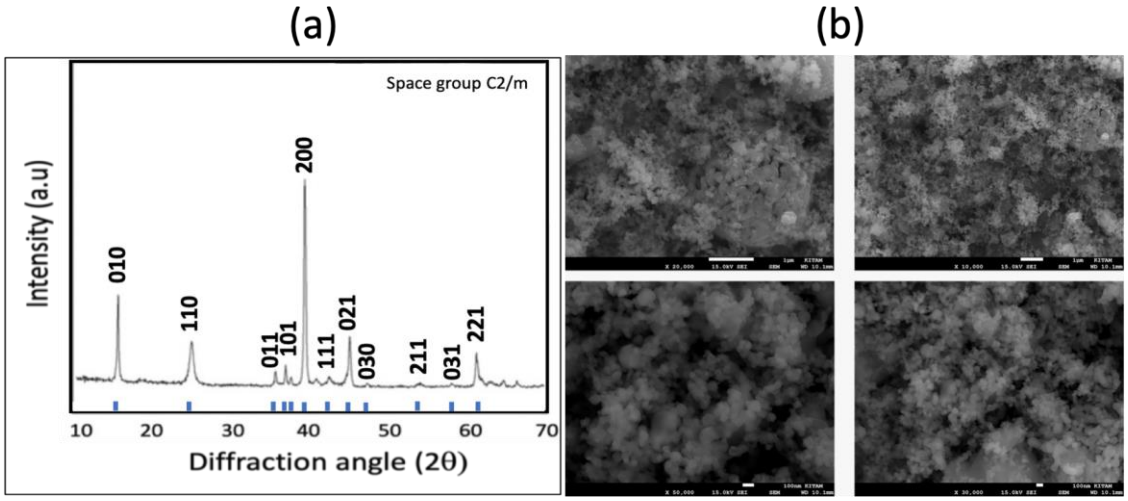


Figure 3. a) XRD pattern of orthorhombic $LiMnO_2$ showing well-defined diffraction peaks corresponding to the C2/m space group, confirming phase purity and crystallinity. b) SEM images of pristine $LiMnO_2$ synthesized via hydrothermal method.

The cyclic voltammetry (CV) curves of $LiMnO_2$ in 0.5 M $(NH_4)_2SO_4$ electrolyte exhibit two distinct electrochemical mechanisms. In Figure 4(a), which represents the electrochemical ion-exchange process, the oxidation peak appears at approximately 0.82 V vs. Ag/AgCl, while the reduction peak is observed at 0.41 V vs. Ag/AgCl. The interaction between ammonium ions and the host material following the Li-extraction process occurs through hydrogen bonding between the oxygen atoms of the host and the hydrogen atoms of the ammonium ions. This interaction is schematically illustrated in Figure 4c. The second cycle in Figure 4b exhibits an increase in current, suggesting structural activation and improved ion accessibility facilitated by NH_4^+ insertion/extraction. This contrasts with the initial decline observed in Figure 4a (Li^+-based process), highlighting the distinct redox kinetics of NH_4^+ compared to Li^+. The divergence

underscores the role of NH_4^+ in enhancing electrochemical activity after the first cycle, possibly due to reduced kinetic barriers or optimized host structure rearrangement. The shape of the CV curve suggests a process influenced by ion diffusion and insertion, typically seen in battery-type materials [23, 24]. In Figure 4(b), corresponding to the NH_4^+-based redox process, broader redox peaks are observed, indicating a more complex charge storage mechanism. The oxidation peaks occur at 0.89 V and 0.72 V vs. Ag/AgCl, while the reduction peaks appear at 0.53 V and 0.28 V vs. Ag/AgCl, suggesting multi-step redox transitions involving NH_4^+ interactions with the electrode [25, 26]. The broader nature of the peaks and their relatively higher currents suggest a pseudocapacitive contribution, where NH_4^+ ions participate not just in insertion/extraction but also in surface-controlled redox reactions [27]. The differences between Figures 4(a) and 4(b) highlight the dual role of NH_4^+ in the system—acting as a charge carrier in an ion-exchange mechanism in Figure 4(a) and actively participating in redox reactions in Figure 4(b)—which significantly affects the electrochemical performance of the $LiMnO_2$ electrode in ammonium-based electrolytes.

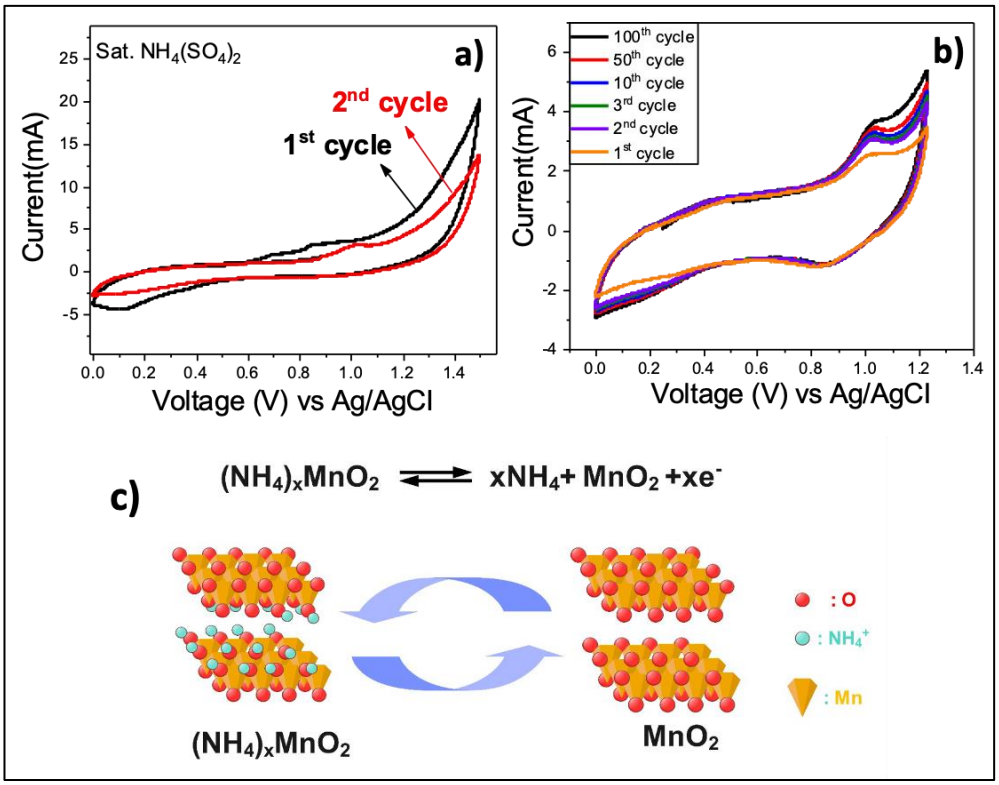


Figure 4. a) Electrochemical phase change from $LiMnO_2$ to $(NH_4)_xMnO_2$ by cyclic voltammetry analysis, and b) cyclic voltammogram of $(NH_4)_xMnO_2$ phase in saturated aqueous $(NH_4)_2SO_4$ electrolyte, and c) schematically representation of ammonium intercalation into the active host material.

The galvanostatic charge-discharge (GCD) curves at different C-rates (1C, 2C, 4C, 8C, and 10C) demonstrate the electrochemical performance of the electrode under varying current densities. At lower C-rates (1C and 2C), where 1C corresponds to a current rate that discharges the battery in one hour (for $LiMnO_2$, 1C is typically 148 mA/g, based on its theoretical capacity of approximately 148 mAh/g), the charge-discharge curves exhibit well-defined voltage plateaus, indicating efficient redox reactions and higher capacity due to slower ion diffusion and more complete electrochemical processes. However, as the C-rate increases to 4C, 8C, and 10C, the charge-discharge times shorten significantly, and the voltage plateaus become less distinct, suggesting increased polarization and kinetic limitations [28]. The observed capacity fading at higher C-rates indicates that the charge storage mechanism is affected by ion transport resistance, possibly due to NH_4^+ diffusion barriers within the electrode structure. Despite this, if the electrode retains reasonable capacity at 10C, it implies good rate performance and fast charge transfer dynamics, making it suitable for high-power applications. The steep decline in capacity at higher C-rates suggests that further optimization, such as improving electrode conductivity or modifying the material structure, could enhance rate capability. Overall, the GCD analysis confirms that while the electrode material can sustain charge-discharge cycles over a wide range of C-rates, its electrochemical performance is limited by ion transport kinetics and internal resistance at higher current densities [29-31].

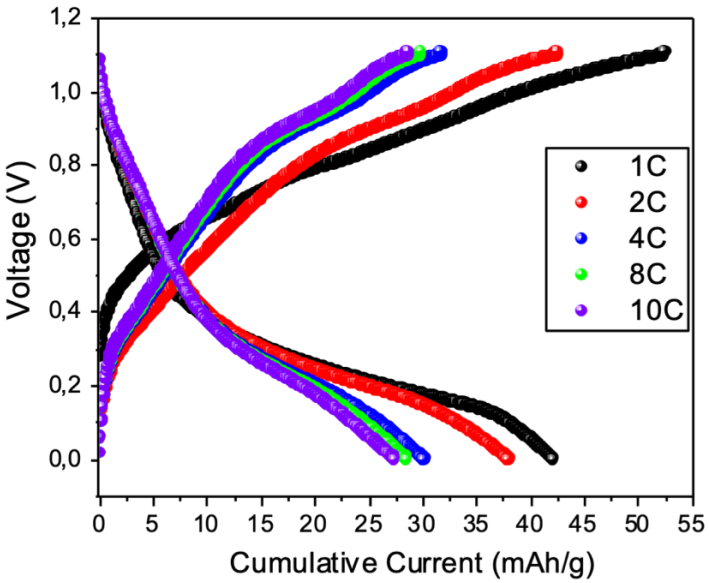


Figure 5. Electrochemical Performance of $(NH_4)_xMnO_2$ at different Current densities.

Figure 6a shows the discharge capacity of $LiMnO_2$ in a 2M $(NH_4)_2SO_4$ electrolyte at a 1C rate over 130 cycles. The electrode delivers an initial capacity of ~60 mAh/g, which drops slightly to ~50 mAh/g by the second cycle and then remains remarkably stable for the remaining

cycles, demonstrating excellent long-term cycling stability. This behavior suggests that the electrode undergoes minimal structural degradation or active material loss after the initial cycles. The mild acidic nature of $(NH_4)_2SO_4$ does not appear to cause significant Mn dissolution, unlike in stronger acidic environments. The stable capacity retention indicates that $LiMnO_2$ exhibits pseudocapacitive-like behavior, where surface-dominated charge storage mechanisms help maintain performance over extended cycling. The absence of severe capacity fade implies that the electrolyte-electrode interface remains relatively stable, possibly due to the formation of a passivating layer that prevents further side reactions. This makes $LiMnO_2$ in $(NH_4)_2SO_4$ a promising candidate for applications requiring long cycle life, though further optimization could improve the initial capacity loss. Figures 6b and 6c provide complementary electrochemical impedance spectroscopy (EIS) data, revealing interfacial and transport changes before and after cycling. The fresh electrode (Figure 6c) exhibits a small high-frequency semicircle, indicative of moderate charge-transfer resistance (R_{ct}), and a linear Warburg tail, reflecting efficient ion diffusion [15, 32, 33]. After cycling, the enlarged semicircle (Figure 6b) signals increased R_{ct} due to passivating SEI (solid electrolyte interphase) growth or Mn dissolution products, while the steeper Warburg slope suggests hindered Li^+ diffusion from pore clogging or particle cracking. The zoomed-in Nyquist plot (Figure 6c) further highlights a rise in ohmic resistance (R_Ω), likely from electrode delamination or electrolyte depletion. Together, these trends explain the capacity fade in Figure 6a: interfacial degradation exacerbates kinetic limitations, creating a feedback loop that accelerates performance loss.

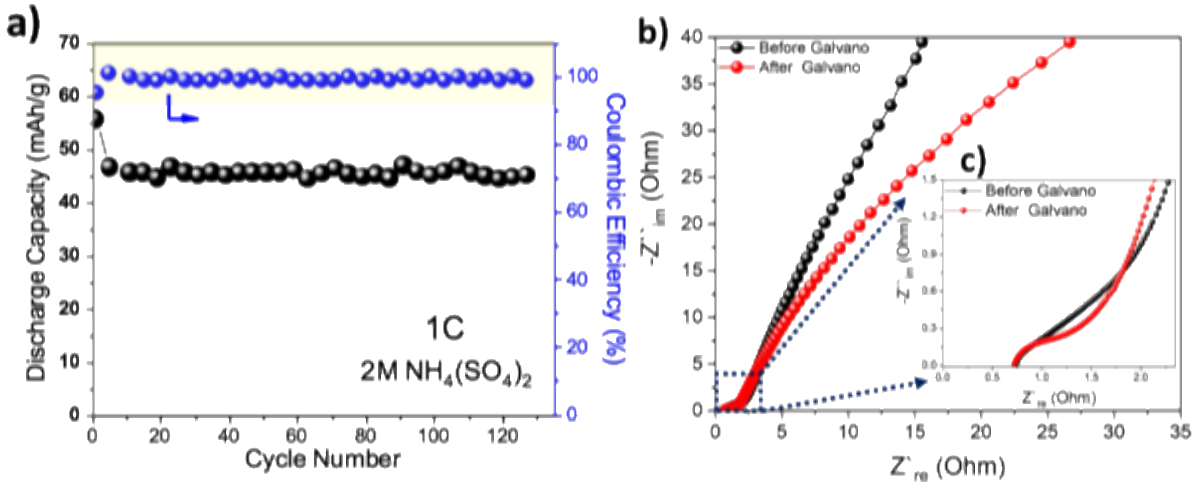


Figure 6. a) Discharge capacity (mAh/g) of $LiMnO_2$ in 2M $(NH_4)_2SO_4$ electrolyte at a 1C rate over 120 cycles. b) Nyquist plots of $LiMnO_2$ before and after galvanostatic charge-discharge testing, with c) showing a zoomed-in view of the high-frequency region.

The fitted equivalent circuit parameters from Figure 6b provide quantitative insights into the electrochemical behavior of the $LiMnO_2$ system. The impedance spectra were fitted using a hierarchical equivalent circuit model accounting for all interfacial processes (Figure 7). This model intentionally separates the passive surface layer effects ($R_{sh}||CPE_{sh}$) from the electrode processes ($Rct||CPE_t+W$) to reflect their distinct physical origins – ionic transport through surface films versus Faradaic reactions at the electrode interface. The series resistance ($R_s = 4.8 \pm 0.2\ \Omega$), representing bulk electrolyte and contact resistances, was determined from the high-frequency real-axis intercept. A surface film branch ($R_{sh} = 15 \pm 2\ \Omega$ || $CPE_{sh} = 5.2\times10^{-6}$ $F\cdot s^{n-1}$, $n = 0.92\pm0.03$) was included to model the high-frequency semicircle (10^4-10^2 Hz), where R_{sh} quantifies ion conduction resistance through surface layers (e.g., SEI) and CPE_{sh} captures their capacitive properties, which differ fundamentally from the electrode's charge-transfer behavior. The dominant charge-transfer resistance ($R_{ct} = 135 \pm 5\ \Omega$), derived from the mid-frequency semicircle diameter (10^2-10^0 Hz), reflects the kinetic barrier for Faradaic reactions, while its associated double-layer CPE_t (1.2×10^{-5} $F\cdot s^{n-1}$,$n= 0.88\pm0.02$) accounts for electrode surface heterogeneity. The Warburg coefficient ($\sigma = 92 \pm 3\ \Omega\cdot s^{-0.5}$), extracted from the low-frequency linear slope (10^0-10^{-2} Hz), characterizes solid-state diffusion limitations. This circuit topology is specifically chosen because passive surface layers (e.g., native oxides) lack the Faradaic charge-transfer and diffusion elements required to describe active electrode processes. These parameters collectively demonstrate that while the interfacial charge transfer presents the dominant resistance, the system maintains reasonable ionic conductivity and surface properties for electrochemical processes. The relatively large R_{ct} value compared to R_s highlights that charge-transfer kinetics rather than ohmic losses constitute the primary limitation in this system [34, 35].

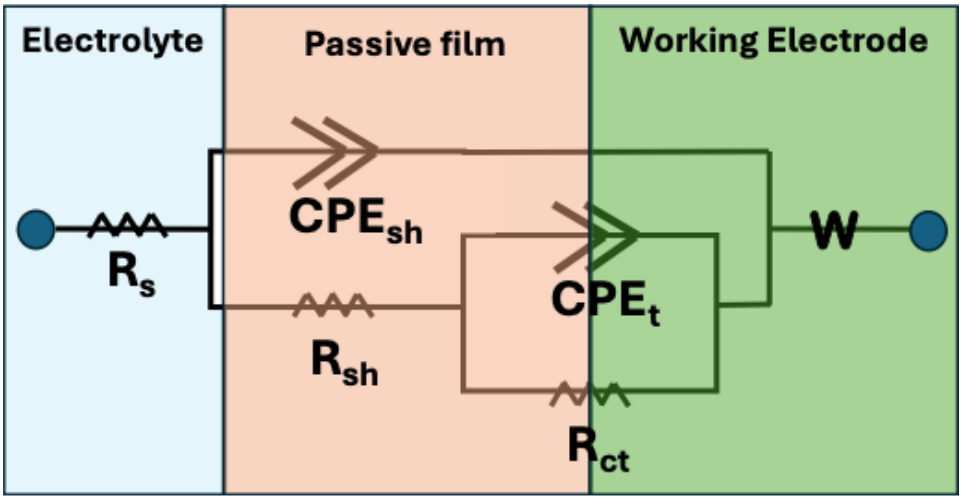


Figure 7. Equivalent Circuit for Nyquist plot of $LiMnO_2$ upon the Galvanostatic charge-discharge measurement at 2M $(NH_4)_2SO_4$ at 1C.

4 CONCLUSION

This study presents a comprehensive investigation of $LiMnO_2$ as a novel cathode material for ammonium-ion-based energy storage systems, marking its first application as a host electrode in this context. Structural and morphological characterization via XRD and SEM confirmed the successful synthesis of phase-pure, highly crystalline orthorhombic $LiMnO_2$ with a nanostructured, porous morphology composed of interconnected secondary agglomerates. The absence of secondary phases and sharp XRD diffraction peaks indicate high crystallinity, while the SEM analysis reveals a favorable porous architecture with rough, loosely packed particles ranging from sub-micron to nanoscale dimensions. This unique microstructure enhances electrolyte infiltration and shortens ion diffusion paths, contributing to improved electrochemical kinetics.

Electrochemical analyses provided valuable insights into the charge storage mechanisms and performance limitations of $LiMnO_2$ in $(NH_4)_2SO_4$ electrolyte. Cyclic voltammetry results revealed two distinct electrochemical behaviors: an ion-exchange process facilitating NH_4^+ insertion/extraction and a redox-dominated process contributing to charge storage through surface-controlled reactions. The oxidation peaks at 0.89 V and 0.72 V vs. Ag/AgCl and reduction peaks at 0.53 V and 0.28 V vs. Ag/AgCl confirm the involvement of multi-step redox transitions. The galvanostatic charge-discharge tests demonstrated that the electrode delivers an initial discharge capacity of ~60 mAh/g at a 1C rate, and experiences high-capacity retention over 130 cycles. At higher C-rates (4C, 8C, and 10C), the voltage plateaus become less distinct due to increased polarization and kinetic limitations, with a notable capacity decline.

Long-term cycling performance in 2M $(NH_4)_2SO_4$ electrolyte demonstrated excellent stability, with the discharge capacity stabilizing at ~50 mAh/g after the second cycle and maintaining this value over 130 cycles. This remarkable capacity retention suggests minimal structural degradation and effective suppression of Mn dissolution in the mildly acidic electrolyte environment. Electrochemical impedance spectroscopy showed only a moderate increase in charge transfer resistance (Rct) from 135 Ω to ~200 Ω after prolonged cycling, indicating relatively stable interfacial kinetics. The fitted equivalent circuit analysis revealed that while some interfacial changes occurred during cycling, the system maintained favorable charge-transfer characteristics that supported the observed long-term stability. These findings highlight the robust electrochemical behavior of $LiMnO_2$ in $(NH_4)_2SO_4$ electrolyte, with the

stable capacity retention suggesting dominant pseudocapacitive charge storage mechanisms that are less susceptible to the structural degradation typically observed in bulk intercalation processes.

The results demonstrate that $LiMnO_2$ effectively functions as a stable host material for ammonium-ion storage, exhibiting remarkable cycling stability with a retained capacity of ~50 mAh/g over 130 cycles in $(NH_4)_2SO_4$ electrolyte. This performance, coupled with its pseudocapacitive charge storage behavior, positions $LiMnO_2$ as a promising cathode candidate for next-generation ammonium-ion batteries. The minimal capacity fade and moderate interfacial resistance growth confirm its structural resilience against Mn dissolution and phase degradation in mildly acidic electrolytes—a critical advantage for sustainable energy storage systems. To further advance this technology, future research should focus on optimizing $LiMnO_2$'s host properties through nanostructuring or composite design to enhance NH_4^+ diffusion kinetics while maintaining its inherent stability. Additionally, exploring concentrated or hybrid electrolytes could unlock higher capacities without compromising cyclability. This work establishes $LiMnO_2$ as a viable host framework for ammonium-ion batteries and provides a foundation for developing high-performance, low-cost energy storage alternatives to lithium-based systems.

Acknowledgements

The authors gratefully acknowledge the financial support provided by Ondokuz Mayıs University Scientific Research Projects Coordination Unit (OMU BAP) under project number [Project no: 5202]. This support was instrumental in conducting the research and acquiring the necessary materials and equipment.

Conflict of Interest Statement

There is no conflict of interest between the authors.

Statement of Research and Publication Ethics

The study is complied with research and publication ethics.

Artificial Intelligence (AI) Contribution Statement

This manuscript was entirely written, edited, analyzed, and prepared without the assistance of any artificial intelligence (AI) tools. All content, including text, data analysis, and figures, was solely generated by the authors.

Contributions of the Authors

Burak Tekin, as the corresponding author, led the study's conception and design, performed electrochemical measurements, created the graphs, interpreted the results, and wrote and edited the manuscript. Melisa Ucan and Dilara Ozgenc conducted the material characterization and contributed to the electrochemical testing.

REFERENCES

[1] M. D. Ahmed and K. M. Maraz, "Revolutionizing energy storage: Overcoming challenges and unleashing the potential of next generation Lithium-ion battery technology," *Materials Engineering Research,* vol. 5, no. 1, pp. 265-278, 2023.

[2] A. Kulkarni, C. Padwal, J. MacLeod, P. Sonar, T. Kim, and D. Dubal, "Toward Safe and Reliable Aqueous Ammonium Ion Energy Storage Systems," *Advanced Energy Materials,* vol. 14, no. 31, p. 2400702, 2024.

[3] R. Demir-Cakan, M. R. Palacin, and L. Croguennec, "Rechargeable aqueous electrolyte batteries: from univalent to multivalent cation chemistry," *Journal of Materials Chemistry A,* vol. 7, no. 36, pp. 20519-20539, 2019.

[4] B. Tekin, "Nafion-protected Na3V2 (PO4) 3 electrodes for aqueous zinc-ion batteries: A breakthrough in dissolution resistance and electrochemical enhancement," *Materials Science and Engineering: B,* vol. 307, p. 117534, 2024.

[5] B. Tekin, S. Sevinc, M. Morcrette, and R. Demir-Cakan, "A new sodium-based aqueous rechargeable battery system: the special case of Na0. 44MnO2/dissolved sodium polysulfide," *Energy Technology,* vol. 5, no. 12, pp. 2182-2188, 2017.

[6] J. Huang, Z. Guo, Y. Ma, D. Bin, Y. Wang, and Y. Xia, "Recent progress of rechargeable batteries using mild aqueous electrolytes," *Small Methods,* vol. 3, no. 1, p. 1800272, 2019.

[7] X. Wu, Y. Qi, J. J. Hong, Z. Li, A. S. Hernandez, and X. Ji, "Rocking-chair ammonium-ion battery: a highly reversible aqueous energy storage system," *Angewandte Chemie International Edition,* vol. 56, no. 42, pp. 13026-13030, 2017.

[8] Y. Yao *et al.*, "Electrochemical synthesis of ammonia from nitrogen under mild conditions: current status and challenges," *Electrochemical Energy Reviews,* vol. 3, pp. 239-270, 2020.

[9] D. Chao *et al.*, "Roadmap for advanced aqueous batteries: From design of materials to applications," *Science advances,* vol. 6, no. 21, p. eaba4098, 2020.

[10] S. Dong *et al.*, "Ultra-fast NH4+ storage: strong H bonding between NH4+ and bi-layered V2O5," *Chem,* vol. 5, no. 6, pp. 1537-1551, 2019.

[11] C. Li *et al.*, "Achieving a high-performance Prussian blue analogue cathode with an ultra-stable redox reaction for ammonium ion storage," *Nanoscale Horizons,* vol. 4, no. 4, pp. 991-998, 2019.

[12] Y. Zhang *et al.*, "A novel aqueous ammonium dual-ion battery based on organic polymers," *Journal of Materials Chemistry A,* vol. 7, no. 18, pp. 11314-11320, 2019.

[13] X. Wu *et al.*, "NH4+ topotactic insertion in berlin green: an exceptionally long-cycling cathode in aqueous ammonium-ion batteries," *ACS Applied Energy Materials,* vol. 1, no. 7, pp. 3077-3083, 2018.

[14] W. Zheng *et al.*, "Advanced ammonium salt materials for electrochemical energy storage: Recent progress and future perspectives," *Chemical Engineering Journal,* vol. 454, p. 140194, 2023.

[15] Y. Sun *et al.*, "Ammonium-ion energy storage devices for real-life deployment: storage mechanism, electrode design and system integration," *Energy & Environmental Science,* vol. 16, no. 12, pp. 5568-5604, 2023.

[16] R. Yuan, H. Jiao, H. Zhu, D. Fang, and S. Jiao, "In situ characterization techniques and methodologies for high-temperature electrochemistry," *Chem,* vol. 9, no. 9, pp. 2481-2508, 2023.

[17] G. N. P. F. Franklin, "Operando studies by SECM, ECD, and EQCM of materials for electrochemical energy storage," Université Paul Sabatier-Toulouse III, 2023.

[18] G. Gourdin and V. Doan-Nguyen, "In situ, operando characterization of materials for electrochemical devices," *Cell Reports Physical Science,* vol. 2, no. 12, 2021.

[19] Z. Zhao *et al.*, "A 2.75 V ammonium-based dual-ion battery," *Angewandte Chemie International Edition,* vol. 61, no. 51, p. e202212941, 2022.

[20] X. Tu and K. Shu, "X-ray diffraction study on phase transition of orthorhombic LiMnO2 in electrochemical conversions," *Journal of Solid State Electrochemistry,* vol. 12, no. 3, pp. 245-249, 2008.

[21] S.-h. Wu and M.-t. Yu, "Preparation and characterization of o-LiMnO2 cathode materials," *Journal of Power Sources,* vol. 165, no. 2, pp. 660-665, 2007.

[22] M. A. Kebede, "An investigation of the lattice parameter and micro-strain behaviour of LiMn2O4 coated with LiMn1. 5Ni0. 5O4 to attain high-rate capability and cycling stability," *Journal of Energy Storage,* vol. 72, p. 108602, 2023.

[23] C. Costentin, "Cyclic voltammetry to study dynamics of ion insertion in porous materials," *Advanced Energy and Sustainability Research,* vol. 5, no. 5, p. 2300242, 2024.

[24] J. Heinze, "Cyclic voltammetry—"electrochemical spectroscopy". New analytical methods (25)," *Angewandte Chemie International Edition in English,* vol. 23, no. 11, pp. 831-847, 1984.

[25] F. Marken, A. Neudeck, and A. M. Bond, "Cyclic voltammetry," *Electroanalytical methods: guide to experiments and applications,* pp. 57-106, 2010.

[26] P. T. Kissinger and W. R. Heineman, "Cyclic voltammetry," *Journal of chemical education,* vol. 60, no. 9, p. 702, 1983.

[27] W. Pholauyphon, P. Charoen-Amornkitt, T. Suzuki, and S. Tsushima, "Perspectives on accurately analyzing cyclic voltammograms for surface-and diffusion-controlled contributions," *Electrochemistry Communications,* vol. 159, p. 107654, 2024.

[28] X. Zhang *et al.*, "Unlocking High-Performance Ammonium-Ion Batteries: Activation of In-Layer Channels for Enhanced Ion Storage and Migration," *Advanced Materials,* vol. 35, no. 40, p. 2304209, 2023.

[29] W. F. Wu *et al.*, "A High-Rate and Ultrastable Ammonium Ion-Air Battery Enabled by the Synergy of ORR and NH4+ Storage," *Advanced Materials,* p. 2415476.

[30] G. Yüksek and A. Alkaya, "Effect of the Depth of Discharge and C-Rate on Battery Degradation and Cycle Life," in *2023 14th International Conference on Electrical and Electronics Engineering (ELECO)*, 2023: IEEE, pp. 1-5.

[31] R. Zheng *et al.*, "Ammonium ion batteries: material, electrochemistry and strategy," *Angewandte Chemie,* vol. 135, no. 23, p. e202301629, 2023.

[32] H. J. Watson and M. N. Frolick, "Determining information requirements for an EIS," *MIS quarterly,* pp. 255-269, 1993.

[33] Z. Bao *et al.*, "An acetate electrolyte for enhanced pseudocapacitve capacity in aqueous ammonium ion batteries," *Nature Communications,* vol. 15, no. 1, p. 1934, 2024.

[34] J. Wu, "Understanding the electric double-layer structure, capacitance, and charging dynamics," *Chemical Reviews,* vol. 122, no. 12, pp. 10821-10859, 2022.

[35] D. M. Adams *et al.*, "Charge transfer on the nanoscale: current status," *The Journal of Physical Chemistry B,* vol. 107, no. 28, pp. 6668-6697, 2003.

BİTLİS EREN ÜNİVERSİTESİ
FEN BİLİMLERİ DERGİSİ

ISSN: 2147-3129 / e-ISSN: 2147-3188

Article Type : Research Article
Received : June 13, 2025
Revised : August 17, 2025
Accepted : August 18, 2025
DOI : 10.17798/bitlisfen.1718523

Year : 2025
Volume : 14
Issue : 3
Pages : 1802-1821

ARCHITECTURAL FEATURES AND CONSERVATION ISSUES OF ADJACENT PUBLIC FOUNTAINS AND BUILT-IN FOUNTAINS (ABDESTLİK) IN THE PROVINCE OF BİTLİS

Enes ARKAN [1,*], Mine TOPÇUBAŞI [2]

[1] *Bitlis Eren University, Department of Architecture, Bitlis, Türkiye*

[2] *Gebze Technical University, Department of Architecture, Kocaeli, Türkiye*

**** Corresponding Author:*** *earkan@beu.edu.tr*

ABSTRACT

Located in Eastern Anatolia, Bitlis is among Türkiye's provinces with the highest precipitation. Heavy snowfall and prolonged snow cover enhance groundwater recharge, supporting a stable water supply. Historically a frontier settlement, Bitlis preserves a rich heritage of water structures -baths, bridges, and fountains- reflecting the legacy of past civilizations. In the city center of Bitlis, 22 fountains are registered as immovable cultural assets by the Van Regional Board for the Conservation of Cultural Heritage. Additionally, there are adjacent or built-in fountains located within registered structures that have not been individually registered. These fountains, which once added comfort and value to the buildings they were part of, have now become a source of various structural problems. Over time, fountains in neglected buildings deteriorate, while at the same time, water-related damage from the fountains accelerates the decay of the structures. In addition to the 4 independent registered fountains adjacent the structure, 8 adjacent and 5 built-in the registered building fountains will be evaluated within the scope of this study. The characteristics of these fountains in Bitlis will be examined, and a typological comparison will be conducted. The conservation issues arising from the abandonment of buildings and the impact of conservation issues on the abandonment process will be evaluated through observational analysis. The findings obtained will serve as a basis for future conservation efforts aimed at preserving these fountains.

Keywords: Bitlis, Adjacent public fountains, Built-in fountains (abdestlik), Conservation issues.

1 INTRODUCTION

Water is a fundamental element of human life and has played a decisive role in the development of civilizations throughout history. In this context, fountains have stood out not only as functional structures but also as architectural elements with aesthetic, symbolic, and social dimensions. This tradition of water-related architecture in Anatolia is rooted in a deep belief system that extends from pre-Islamic periods to the Ottoman (Islamic) era. The indispensable role of water in sustaining life has made fountains one of the essential components of architectural history [1], [2].

Fountains historically served not only as sources of water supply but also fulfilled a significant social function as gathering spaces where people came together and fostered social interactions [3]. Water structures built for charitable purposes during the Seljuk and Ottoman periods played a formative role in shaping architectural tradition. As water is considered sacred in Islamic belief, constructing fountains in Anatolia was regarded as both a religious and social responsibility [4].

Historical fountains located in traditional urban centers are categorized based on their location and typology. They are generally examined under groups such as square fountains, street fountains, and those adjacent to architectural buildings [5]. Square fountains were positioned at central locations to ensure easy access to water. In addition, various other types exist, such as fountains adjacent to or integrated into mosques and residential buildings [6].

Cultural heritage and sustainability are two complementary concepts that are increasingly being addressed in a more integrated manner within contemporary sustainable development discourse. Cultural heritage contributes to social identity, a sense of belonging, and historical continuity, while also promoting sustainable living practices through construction techniques in harmony with nature and the use of local materials [7], [8]. The preservation and functional revitalization of this heritage help reduce resource consumption and support local economic dynamics [9]. Developing integrated and balanced management approaches for the conservation and sustainable use of cultural heritage is critically important for a future aligned with sustainable development goals [10].

In this context, historical fountains, which form an inseparable part of the urban landscape, represent a unique type of cultural heritage with both functional and cultural values. Constructed in various periods, fountains have played significant roles in public spaces as elements reflecting urban identity, water culture, and aesthetic sensibilities. Serving religious,

social, and aesthetic functions, fountains have contributed to shaping urban memory [11]. However, today, factors such as climate change, urban transformation, and neglect threaten the preservation of these structures [12]. The conservation of fountains serves not only to protect their physical structures but also to sustain water culture, local identity, and collective memory [13]. International literature highlights the need to develop documentation, conservation, and sustainable use approaches for such water structures. In this regard, interdisciplinary conservation strategies that integrate cultural heritage management, water management, and community participation are of critical importance for ensuring the sustainable transmission of water heritage elements such as fountains to future generations [14], [15].

The conservation of water heritage buildings, including historic fountains, requires approaches that go beyond the preservation of their physical fabric to address the ecological, social, and governance contexts in which they operate. The International Council on Monuments and Sites (ICOMOS) emphasizes that safeguarding such structures entails maintaining their historical functionality and cultural relevance, which often involves the integration of traditional knowledge with contemporary water management practices [16]. As discussed in Adaptive Strategies for Water Heritage, conservation strategies must be adaptive, acknowledging the impacts of climate change, urban expansion, and water scarcity while ensuring that heritage structures continue to serve communities in meaningful ways [17]. The United Nations Educational, Scientific and Cultural Organization (UNESCO) further stresses that protecting these assets contributes to sustainable development goals by fostering resilience, promoting community participation, and sustaining the cultural narratives that link people to their water resources [18].

With its high altitude, the province of Bitlis is among the regions in Türkiye that receive the highest amount of precipitation. Due to its snowfall-dominated climate regime, it possesses rich potential in terms of underground water resources. The historical fountains located in the city center have long served to meet the public's water needs and stand out as significant components of the urban identity. [19], based on archival sources, reveal that more than 300 fountains once existed in the city center of Bitlis, emphasizing that water architecture constituted a significant component of the city's vernacular architectural fabric. The arched, finely cut stone fountain structures observed in present-day Bitlis were constructed between the 17th and 19th centuries [20].

In the early 1970s, significant urban planning and infrastructure activities were carried out in the city center, including the development along the Bitlis Stream and its branches, as

well as the construction of the main arterial road known as the NATO Road [21]. [22] notes that during this period, water began to be supplied directly to homes through the municipal water network. As a consequence, a number of fountains were demolished, while the majority of the remaining ones were neglected and fell into disrepair.

According to the data from the Van Regional Board for the Conservation of Cultural Heritage (VKVKBK), there are currently 22 fountains in the city center of Bitlis that are officially registered and serve public purposes. Among the independently registered fountains, four that are attached to buildings and used for public purposes will be examined. As part of the field study, eight fountains that are either adjacent to or built-in registered structures and used for public purposes will be examined. In addition, five fountain niches (*abdestlik*) located in registered traditional houses -supplied by a cistern or the municipal water network and used under private ownership- will also be studied. The architectural characteristics of these 17 historical fountains, which represent the region's water heritage, will be analyzed and their conservation issues evaluated.

2 MATERIAL AND METHOD

The main materials of this study consist of fountains located either adjacent to or built-in (*abdestlik*) registered cultural heritage structures-both public and private use-in the city center of Bitlis (Figure 1). Based on data provided by the VKVKBK, these fountains were identified within listed buildings, examined on-site, and their locations were mapped. During the on-site investigation, structural features and deterioration types were documented through visual inspection and photographic recording. In the subsequent office phase, the recorded structural characteristics and damage were classified, and conservation proposals were developed accordingly (Figure 2).

Fountains that are adjacent to or built into traditional houses are listed with their cadastral block and parcel information, while those located in public spaces and known by specific names are presented in the tables under their respective names. All fountains were identified with a reference number (Ref. No.) to ensure a systematic classification. This numbering was carried out using the initial letter of the word "Fountain," assigning codes from F1 to F17. Through this method, consistency in the comparisons made within the scope of the study and the traceability of the analyses were ensured.

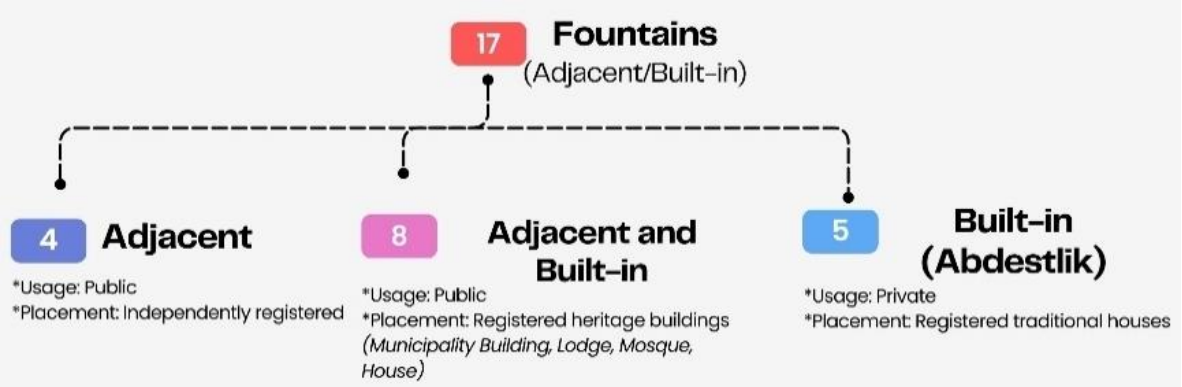


Figure 1. Fountain types to be examined within the scope of the study.

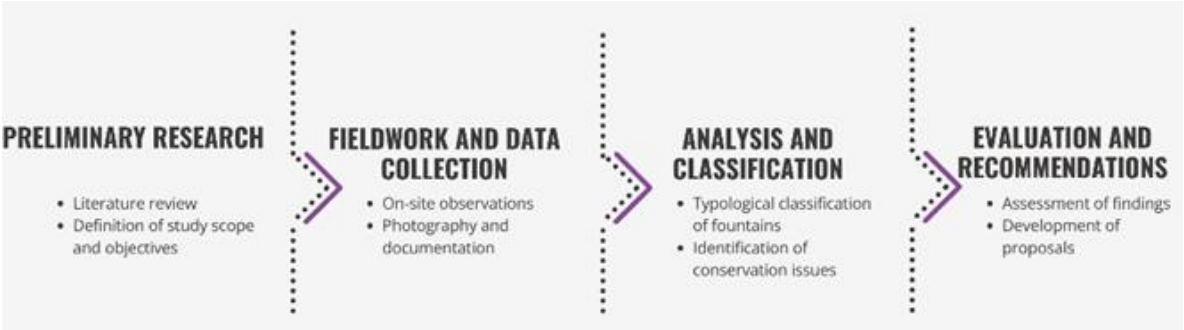


Figure 2. Flowchart of the study.

3 GENERAL CHARACTERISTICS OF THE FOUNTAINS: ADJACENT PUBLIC FOUNTAINS AND BUILT-IN FOUNTAINS IN THE PROVINCE OF BITLIS

Fountain architecture, as a significant field reflecting the social and cultural value of water, has evolved throughout history in various stylistic forms. In Anatolia, fountains incorporated both functional and aesthetic innovations during the Seljuk and Ottoman periods. These structures should continue to be preserved today as both historical and cultural heritage assets. Considering the fountains in Bitlis as well, the architectural elements typically found in an ideal fountain design include the eaves, *iwan, arch, faucet, through (basin), tank, inner arch, drainage channel, inscription, cup niche, niche, and platform* [6], [20].

The elements found in fountain architecture possess both functional and aesthetic qualities. The eaves, located at the upper part of the fountain, are projecting covers typically made of wood or stone, designed to protect both the user and the structure from rain. The *iwan* is a semi-open space that protects both the fountain and the user from environmental conditions, typically found in fountains with minimal or no eaves. The *arch*, visible on the façade of the fountain or the *iwan*, is usually constructed in a pointed or semi-circular form. In fountains

featuring an *iwan*, the arch often mirrors the shape of the *iwan's* vault. It is also stepped in design, serving a decorative function in addition to its structural role.

The primary water elements in fountain architecture are of great importance for maintaining the functionality of the structure. The *faucet* is the outlet through which water flows in fountains, typically made of bronze or brass; however, as most of them have been damaged over time, they are now often seen only as voids carved into the stone. The water flowing from the *faucet* is collected in the *through* (basin), a rectangular-shaped section located at the lower part of the structure. The *tank*, which supplies water to the fountain, is typically a concealed reservoir situated at the rear or beneath the structure. The opening that allows access to this reservoir for cleaning and maintenance purposes is referred to as the *inner arch*. In addition, the *drainage channel* serves to direct excess water into the surrounding drainage system, thereby preventing water accumulation around the fountain and ensuring its safe discharge.

Among the elements that stand out for their aesthetic and social significance are inscriptions and architectural niches. The *inscription*, typically located above the faucet, is a written panel that identifies the structure, often including the name of the patron, the date of construction, and religious invocations or poetry. The small-sized *cup niches*, intended for drinking purposes, are specially designed recesses positioned on either side of the faucet, where cups or vessels were traditionally placed. The larger and deeper *niches*, compared to cup niches, are located on the lateral surfaces of the fountain and serve more general purposes, such as placing various objects. Another element reflecting the social dimension of fountain architecture is the *platforms*, which are elevated sections positioned on either side of the *iwan* niche. These platforms could be used for placing water jugs or for sitting and resting. Collectively, these features demonstrate that fountains function not only as sources of water but also as spaces for social interaction and rest.

These architectural elements constitute both the aesthetic composition and the functional integrity that ensures user comfort in fountain design. The architectural components of a typical neighborhood fountain are illustrated schematically in Figure 3.

As a result of the field studies conducted in the city center, the urban distribution of a total of 17 historical fountains -either adjacent to registered buildings or built-in them- has been visualized on a map prepared with consideration of their spatial characteristics (Figure 4).

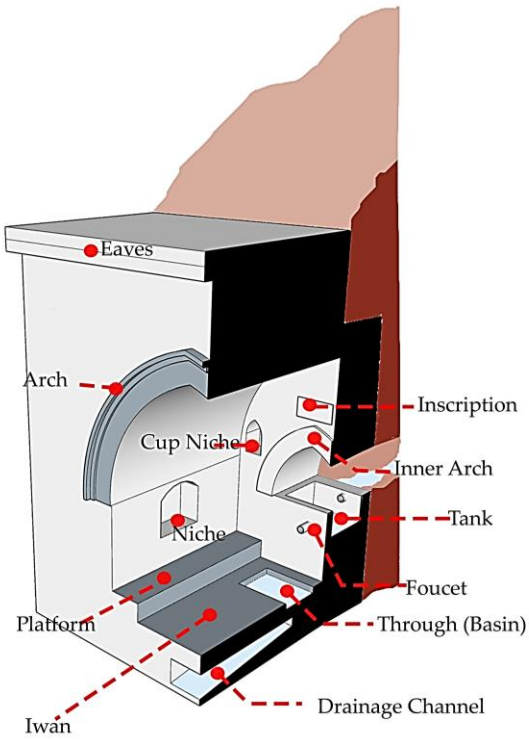


Figure 3. Schematic representation of a typical neighborhood fountain.

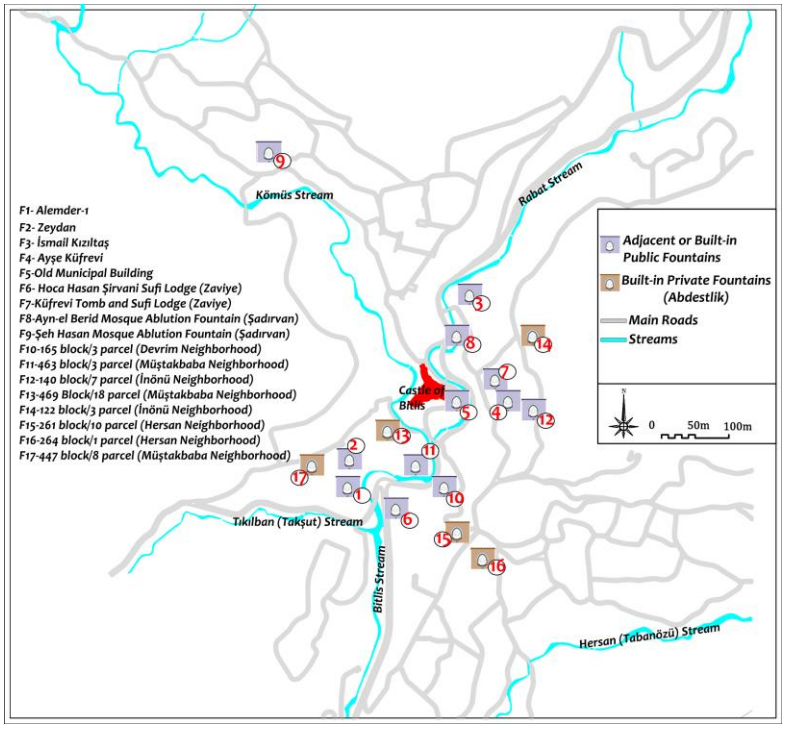


Figure 4. Location of adjacent public fountains and built-in fountains in the province of Bitlis

3.1 Adjacent or Built-In Public Fountains and Their Architectural Features in the Province of Bitlis

In the city center, there are 12 fountains adjacent to buildings that are classified as immovable cultural heritage assets and are in public use. Of these, 4 have been registered as independent structures (F1–F4), while 8 are integrated within registered buildings (F5–F12). The general characteristics and locations of these fountains are presented in Table 1.

Table 1. General characteristics of adjacent and built-in public fountains in Bitlis

Ref. No.	Fountain	Neighborhood	Type	Placement	Construction Date	Vault Type of Iwan/Fountain
F1	Alemder-1	Müştakbaba	Public	House		Pointed Vault
F2	Zeydan	Müştakbaba	Public	House	1667	Pointed Vault
F3	İsmail Kızıltaş	Gazibey	Public	Tandoor House	--	Barrel Vault
F4	Ayşe Küfrevi	İnönü	Public	House	--	Barrel Vault
F5	Old Municipal Building	Gazibey	Public	Municipality Building	1898	Segmental Arch
F6	Hoca Hasan Şirvani Sufi Lodge (Zaviye)	Hersan	Public	Lodge	1823	Barrel Vault
F7	Küfrevi Tomb and Sufi Lodge (Zaviye)	İnönü	Public	Lodge	1898	Pointed Vault
F8	Ayn-el Berid Mosque Ablution Fountain (Şadırvan)	Gazibey	Public	Mosque	1664	Barrel Vault
F9	Şeyh Hasan Mosque Ablution Fountain (Şadırvan)	Gazibey	Public	Mosque	1725	--
F10	165 block/3 parcel	Devrim	Public	House	1845	Barrel Vault
F11	463 block/3 parcel	Müştakbaba	Public	House	--	Pointed Arch
F12	140 block/7 parcel	İnönü	Public	House	--	Barrel Vault

In terms of location, these fountains are situated on, adjacent to, or within the structural walls of buildings. Although some are found within privately owned traditional houses, they have retained their function as public fountains (Figure 5). While the oldest examples date back to the second half of the 17th century, the majority were constructed in the second half of the 19th century. Those with an iwan are typically covered with a barrel or pointed vault.

According to the names listed in the official records obtained from the VKVBK, the independently registered fountains F1–F4 are identified as Alemdar-1 (F1), Zeydan (F2), İsmail Kızıltaş (F3), and Ayşe Küfrevi (F4). Fountains F1, F2, and F4 are adjacent to traditional houses, while F3 is attached to a *tandır* (traditional oven) house (Figure 6).

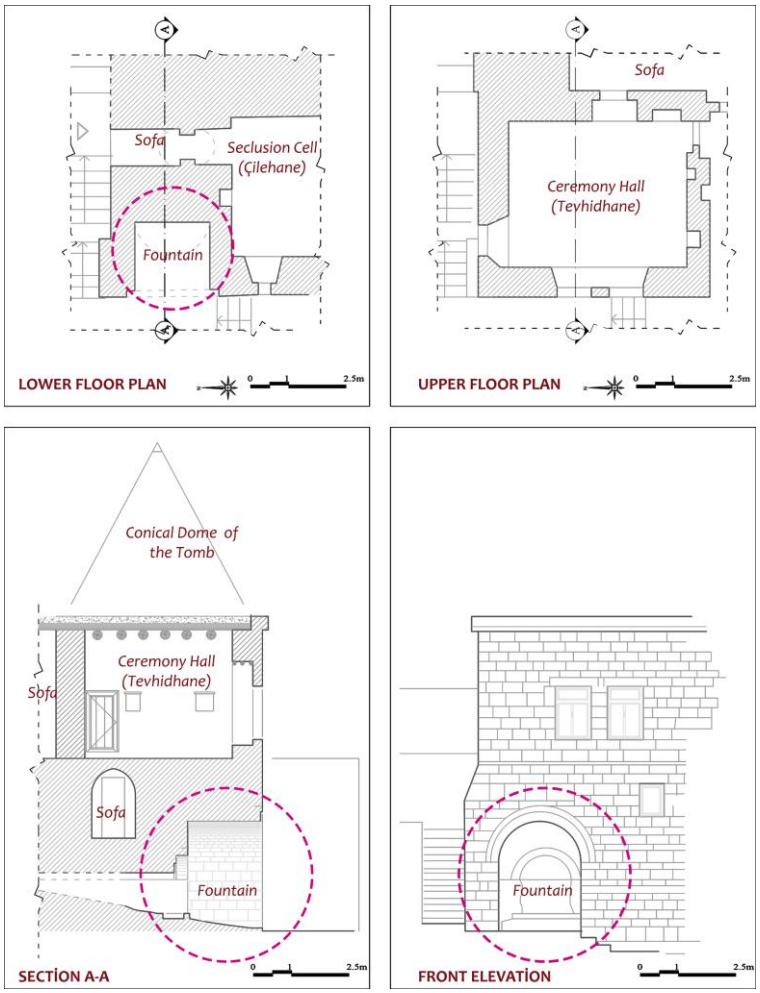


Figure 5. Architectural drawings of Fountain F6 attached to the Hoca Hasan Şirvani Sufi Lodge (Zaviye).



Figure 6. Independently registered fountains adjacent to buildings (F1–F4)

Of the eight fountains that are adjacent to or built into registered buildings and used for public purposes, F5 is in an administrative building; F6 and F7 are associated with a zaviye (Sufi lodge); F8 and F9 are part of mosque complexes; and F10 to F12 are located within traditional houses (Figure 7).



Figure 7. Adjacent or built-in fountains within registered buildings (F5–F12)

There are two fountains with inscriptions. In F2, the inscription is located above the water tank, contrary to the typical layout. Dated 1667, this fountain is located beneath an unregistered traditional house. The inscription of F11 is illegible, as it was damaged during the Russian occupation in 1916. Since the fountains were constructed as integral parts of the buildings in which they are located, the dates inscribed on those buildings are considered to reflect the construction dates of the fountains as well (Figure 8).

Although F5 and F11 are open to the exterior, they do not feature an *iwan* niche. F5 is set within a segmental-arched niche, while F11 is housed within a pointed-arched one. The fountains F8 and F9, which function as *şadırvans* (ablution fountains), exhibit different structural configurations: F8 is located within a space covered by a barrel vault, whereas the area containing F9 currently survives as an enclosed space with a reinforced concrete roof.

Relieving arches were added to the *iwans* of F2, F3, and F6 for both structural reinforcement and decorative purposes.



Figure 8. Inscriptions of F2 and F11

F2 and F3 feature open-arch designs. All the examined fountains are equipped with water tanks. Seki (platforms) are present in fountains F3 and F17. Cup niches or recessed spaces for placing drinking vessels are found in fountains F16 and F17.

In F8 (Şeyh Hasan Mosque) and F9 (Ayn-el Berid Mosque), water from a natural spring is conveyed through pipes routed between the seating areas, enabling these fountains to function as *şadırvans* (ablution fountains). F5, located beneath the staircase of the former municipal building, is connected to the city's municipal water supply network. F8, F9, and F12 are built-in fountains that serve public purposes.

3.2 Private Built-In Fountains (*Abdestlik*) and Their Architectural Features in the Province of Bitlis

In traditional houses, there are water niches located on the sofa (interior hall), commonly referred to as abdestlik. These niches typically feature a scalloped or shell-shaped motif at the top and are positioned at basin height. The original niches include a stone basin. As illustrated in the example of fountain F16, they are generally located near the entrance and are functionally connected to service areas (Table 2; Figure 9).

The traditional houses containing built-in fountains dated to the late 19th century. Compared to other traditional dwellings, these privately used houses are relatively larger, and the fountains were constructed to supply water for domestic use.

Table 2. General characteristics of private built-in (abdestlik) fountains in Bitlis.

Ref. No.	Fountain	Neighborhood	Type	Placement	Construction Date	Arch Type of Fountain
F13	469 block/18 parcel	Müştakbaba	Private	House	1898	non-structural decorative niche heads
F14	122 block/3 parcel	İnönü	Private	House	1908	non-structural decorative niche heads
F15	261 block/10 parcel	Hersan	Private	House	1893	non-structural decorative niche heads
F16	264 block/1 parcel	Hersan	Private	House	1889	non-structural decorative niche heads
F17	447 block/8 parcel	Müştakbaba	Private	House	1900	non-structural decorative niche heads

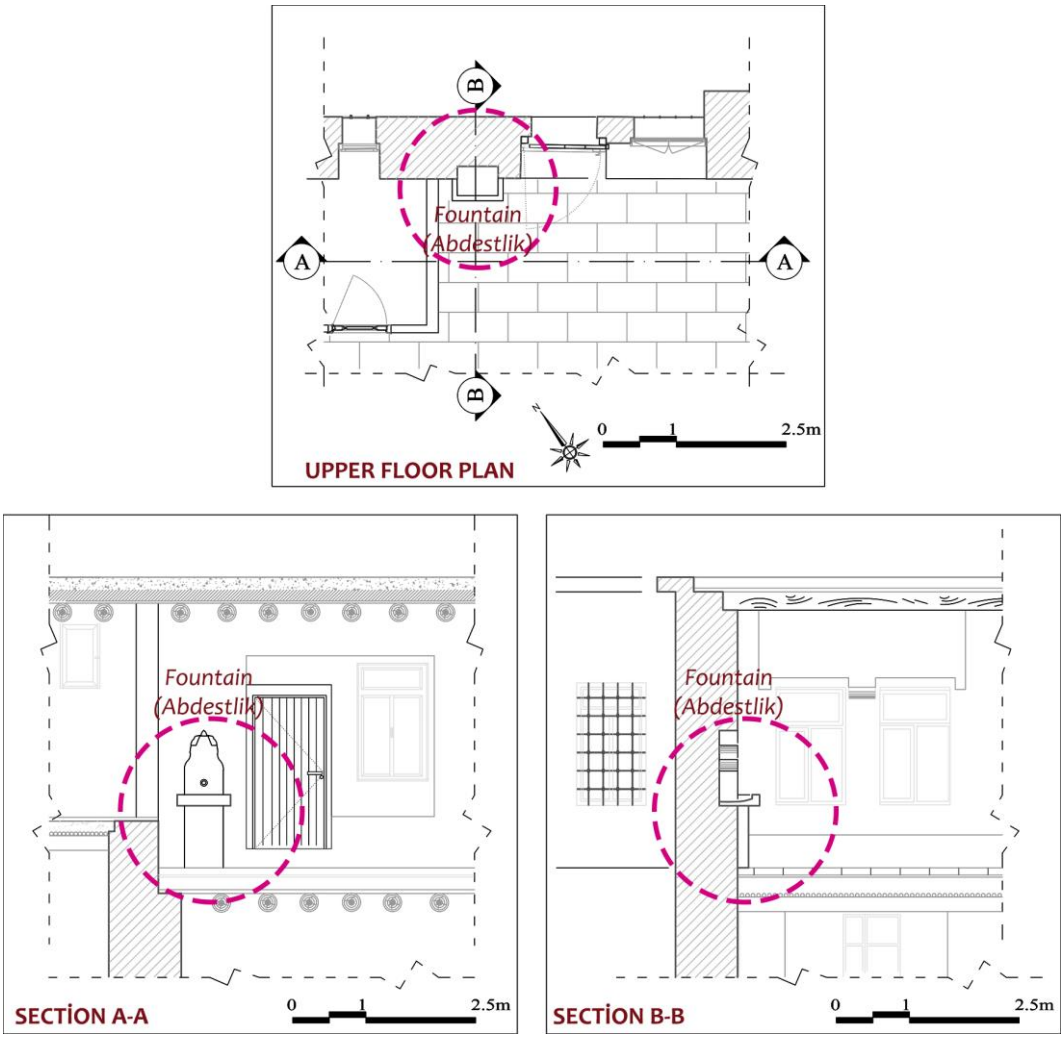


Figure 9. Architectural drawings of built-in (abdestlik) fountain F15 located on the sofa of a tradi-tional house (Hersan Neighborhood, block 261, parcel 10).

Among the built-in fountains identified within the scope of the study, examples F14 and F16 are still in use. These fountains are supplied by the municipal water network. In F16, a ceramic sink has been installed in front of the *abdestlik* niche (Figure 10).



Figure 10. Built-in (abdestlik) fountains in private use

4 CONSERVATION ISSUES AND TYPES OF DETERIORATION

The conservation of heritage assets faces persistent challenges such as insufficient funding, inadequate maintenance practices, and a lack of coordination among stakeholders [23],[24]. The institution responsible for the maintenance and repair of fountains used for public purposes in Bitlis is the Bitlis Municipality. These structures are not provided with adequate funding for their conservation, nor are regular maintenance and repairs carried out. In the case of public fountains that are adjacent to or built into buildings, the involvement of different institutions responsible for the preservation of the associated structures further complicates coordination efforts. Moreover, since the residents of traditional houses typically have low-income levels, conservation efforts are generally limited to basic and periodic maintenance of the dwellings.

Legal constraints and urban development pressures further complicate interventions, often leading to delays or the loss of historical integrity [25]. In the province, zoning and construction activities carried out particularly since the 1970s have resulted in the destruction of a significant portion of the cultural heritage. Today, activities conducted within the scope of

urban conservation are rapidly transforming the historic environment. Environmental factors exacerbate the challenges faced by heritage structures, highlighting the need for comprehensive, adaptable, and interdisciplinary conservation strategies [26].

The factors causing deterioration in immovable cultural assets can be evaluated as internal and external. Location and construction characteristics constitute the internal causes of damage, while natural, biological, and human-induced factors represent the external causes [27],[28]. Examples of deterioration observed in the examined fountains are presented in Figure 11, and the types of damage identified for each fountain category are listed in Table 3.

Table 3. Types of Deterioration Observed in the Fountains

Ref. No.	Type	Placement	Vegetation	Algae Formation	Surface Pollution	Joint Loss	Surface and Material Loss	Abandonment and Neglect	Inappropriate Intervention	Vandalism
F1	Public	House	-	-	-	-	-	✓	-	-
F2	Public	House	✓	✓	✓	-	-	✓	-	✓
F3	Public	Tandoor House	✓	✓	✓	✓	✓	✓	✓	-
F4	Public	House	-	-	✓	✓	-	-	-	-
F5	Public	Municipality Building	-	-	✓	-	-	-	✓	-
F6	Public	Lodge	✓	-	-	-	-	✓	-	-
F7	Public	Lodge	-	✓		✓	-	-	✓	-
F8	Public	Mosque	-	-	-	-	-	-	✓	-
F9	Public	Mosque	-	-	-	-	-	-	✓	-
F10	Public	House	✓	✓		✓	✓	-	-	-
F11	Public	House	-		✓		✓	✓	-	✓
F12	Public	House	-	✓	✓	✓	✓	✓	-	-
F13	Private	House	-		✓	✓		✓	-	-
F14	Private	House	-	-	-	-	-	✓	✓	-
F15	Private	House	-	-	-	-	-	-	✓	-
F16	Private	House	-	-	-	-	-	-	✓	-
F17	Private	House	-	-	-	-	-	-	-	-

The snowy and precipitation-prone climate of Bitlis, particularly during the spring and summer months, creates favorable conditions for the uncontrolled growth of vegetation on fountain surfaces. This condition clogs the capillary pores within the stone material, resulting in both aesthetic and physical deterioration. During the field study, vegetation growth was identified on fountains F2, F3, F6, and F10. Notably, the vegetation covering the entire surface of fountain F3 poses a significant threat to both the structural and visual integrity of the fountain.

Algae formation is a result of continuous water flow or leakage on stone surfaces, contributing to biological deterioration over time. This process is particularly accelerated in Bitlis stone, which has high water absorption properties, when exposed to prolonged moisture. Algae accumulation was observed on both publicly accessible fountains such as F2, F3, F7, F10, and F12. In the case of fountain F3, extensive algae layers covering both the inner chamber and the front surfaces obscure the structure's original appearance

In the urban environment, external factors such as vehicular traffic, air pollution, and lack of maintenance lead to surface soiling and darkening on the fountains. This condition particularly reduces legibility in areas containing inscriptions and diminishes their aesthetic value. Surface pollution was identified on fountains F2, F3, F4, F5, F11, F12, and F13. In the case of fountain F5, surface soiling caused by vehicle traffic is especially severe.

Due to freeze–thaw cycles, mortar joints gradually become dislodged or completely lost over time. This condition reduces the bonding between the stone units and weakens the overall structural integrity. Joint loss was observed in fountains F3, F4, F7, F10, F12, and F13. In fountain F3, the joints between the stone blocks were found to be largely missing and, in some areas, filled with plant roots.

Surface and material loss occurs in the form of cracking, fragmentation, and texture deterioration in the stone, resulting from natural weathering over time, inappropriate interventions, or vandalism. This type of damage directly affects both the architectural integrity and the feasibility of future conservation efforts of the structure. Material loss was identified in fountains F2, F10, F11, F13, and F12. In particular, fractures and spalling were notably observed in the arched section of the reservoir area in fountain F3.

Due to the provision of water directly to buildings via the municipal supply system, many fountains have lost their original function over time, leading to abandonment and the absence of regular maintenance. This situation has contributed to both physical deterioration and a sense of insecurity within the historic environment. Neglect and abandonment were commonly observed in fountains F1, F2, F3, F6, F11, F12, F13, and F14. Fountains F2 and F3, having become non-functional, have suffered both physical and visual degradation, as their iwan, reservoir, and niche interiors have been filled with garbage and various types of waste.

Inappropriate interventions on the fountains often compromise their historical character and result in further damage rather than repair. In cases where original architectural elements are missing, restorations carried out with contemporary and incompatible materials undermine the integrity of the cultural heritage. Interventions involving the use of incompatible modern materials were observed in fountains F2, F5, F7, F8, F9, F14, F15, and F16, compromising the authenticity and material coherence of the structures.

Vandalism, classified among human-induced damages, typically occurs in structures that have been neglected or left without supervision. In particular, illicit treasure hunting and misuse by substance abusers cause direct physical damage to the structures. Fountains F2 and F11 have been subjected to such acts. During the Russian occupation, the inscription and ornamental elements of fountain F11 were deliberately defaced.

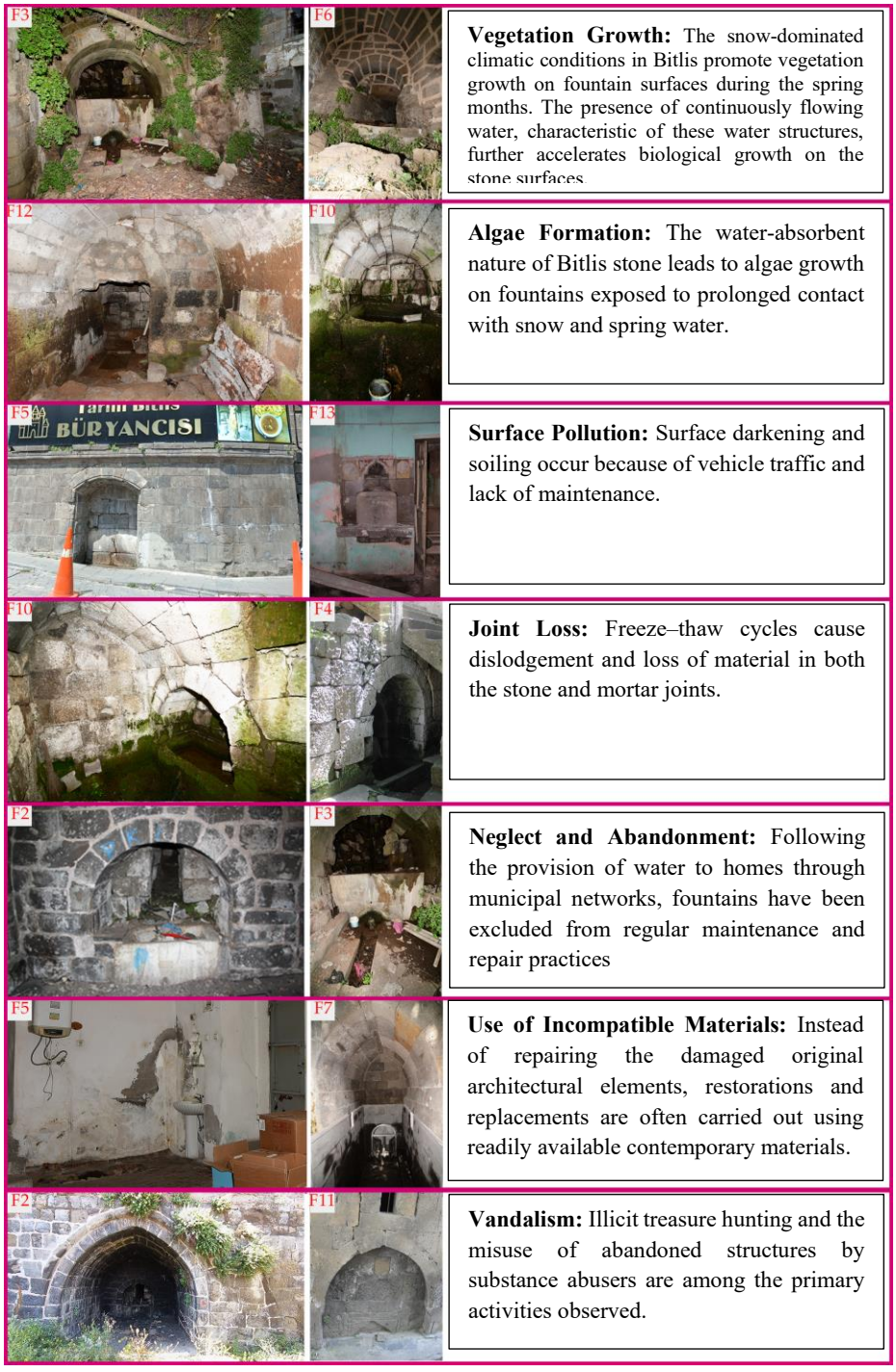


Figure 11. Deterioration conditions observed in the fountains

Historic fountains, integral to urban water heritage, deteriorate due to environmental exposure and human activity. International guidelines stress that such structures require targeted documentation, preventive conservation, and sustainable management to address vulnerabilities like biological colonization, stone decay, vandalism, and mechanical damage [29]. Preservation should strengthen original features and use compatible materials [4], while combining passive and active measures -such as climate-responsive maintenance, controlled water flow, and physical protection- to reduce risks [30]. Community awareness and stakeholder engagement remain essential for their long-term preservation [18]. These principles directly inform the conservation proposals presented in Table 4. [27],28],[29], [30],[31].

Table 4. Conservation proposals for observed types of deterioration in the fountains

Deterioration Type	Affected Fountains (F-No.)	Conservation Proposal
Vegetation Growth	F2, F3, F6, F10	Remove vegetation mechanically (roots out of stone pores); apply low-toxicity biocides under specialist supervision; adjust drainage to prevent moisture accumulation; implement seasonal monitoring and maintenance plan.
Algae Formation	F2, F3, F7, F10, F12	Clean using low-pressure water and soft brushes; eliminate leaks or constant damp conditions; improve drainage for quicker drying.
Surface Pollution	F2, F3, F4, F5, F11, F12, F13	Use test panels to identify least invasive cleaning methods; apply reversible poultices or gels; install landscaping or physical barriers to reduce traffic-related soiling.
Joint Loss	F3, F4, F7, F10, F12, F13	Repoint joints with lime-based mortar compatible with original material; enhance runoff to reduce freeze-thaw damage; document interventions meticulously.
Surface and Material Loss	F2, F10, F11, F12,	Apply consolidation treatments; replace lost stones with compatible materials; use breathable protective coatings.
Neglect / Abandonment	F1, F2, F3, F6, F11, F12, F13, F14	Reintegrate fountains into public life with adaptive reuse; establish regular maintenance protocols; improve lighting/security; engage community stewardship.
Inappropriate Intervention	F3, F5, F7, F8, F9, F14, F15, F16	Remove incompatible additions; use compatible, distinguishable, and reversible repair techniques; adhere to conservation standards.
Vandalism	F2, F11	Implement passive surveillance, lighting, and cameras; initiate community watch; ensure prompt repairs to discourage recurrence.

5 RESULTS

Historic fountains hold a significant place in the architectural heritage of civilizations, not only due to the need for water access but also for their aesthetic and social functions. The province of Bitlis, with its climatic conditions and rich cultural background, possesses a strong tradition of water-related architectural structures. Within the scope of this study, 17 fountains located in the city center were examined; some of these are neighborhood fountains used for public purposes (F1–F12), while others are called *abdestlik* fountains (F13–F17) situated within the interiors of traditional houses.

Field studies revealed that the majority of the fountains are no longer in use, have been abandoned, and lack regular maintenance and repair. In particular, the wide-spread expansion of the municipal water network has led to the loss of function of many fountains, making their preservation more difficult. It was observed that fountains still in active use and regularly maintained exhibit significantly fewer signs of deterioration.

In this context, the following conclusions were drawn:

- The primary reason for the inability to preserve the fountains is the loss of function. The exclusion of unused fountains from maintenance processes accelerates their physical deterioration.
- Water-induced deterioration is the most prevalent type of damage. Bitlis's snow-dominated climate and frequent freeze–thaw cycles contribute to the rapid degradation of building materials.
- Most of the built-in fountains remain in usable condition. Their connection to the municipal water network and their relatively sheltered locations have contributed to their preservation.
- The responsibilities of public institutions must be clearly defined, and issues of inter-agency coordination should be resolved. Neighborhood fountains attached to buildings and designated for public use should be preserved through regular maintenance, repair, and lighting interventions carried out by the Bitlis Municipality.
- Conservation efforts must be holistic. Fountains should be preserved in conjunction with the structures to which they are attached, as treating them separately leads to a chain of neglect.
- Adaptive reuse should be proposed within the framework of urban design. Fountains should be integrated as elements of urban furniture and reintroduced into con-temporary urban life by establishing meaningful connections with the historic environment.

Furthermore, in cases where fountains are supplied by natural spring sources, their connection with urban drainage systems should be regularly monitored and controlled from a public health perspective. Built-in *abdestlik* fountains, on the other hand, should be brought back into contemporary use with careful preservation of their original architectural features.

Acknowledgements

This article is based on the doctoral dissertation entitled “Bitlis İli Taşınmaz Kültür Varlıklarının Koruma ve Kullanma Dengesi Kriterlerinin Belirlenmesine Yönelik Bir Yöntem Önerisi” (Gebze Technical University, 2025).

Conflict of Interest Statement

There is no conflict of interest between the authors.

Statement of Research and Publication Ethics

The study is complied with research and publication ethics.

Artificial Intelligence (AI) Contribution Statement

This manuscript was entirely written, edited, analyzed, and prepared without the assistance of any artificial intelligence (AI) tools. All content, including text, data analysis, and figures, was solely generated by the authors.

Contributions of the Authors

Conceptualization, E.A. and M.T.; methodology, E.A.; writing—original draft preparation, E.A. and M.T.; investigation, E.A.; All authors have read and agreed to the published version of the manuscript.

REFERENCES

[1] İ. Oymak, “Anadolu'da su kültünün izleri,” *Fırat Üniversitesi İlahiyat Fakültesi Dergisi*, vol. 15, no. 1, 2010.

[2] T. Acar, “Uşak merkez köylerinde yer alan çeşmelerin tipolojisi üzerine bir değerlendirme,” *Sanat Tarihi Dergisi*, vol. 27, no. 1, pp. 163–179, 2018.

[3] İ. Aktürk, “Trabzon’da Osmanlı Dönemi yapılan tarihî çeşmelerin mimari özelliklerinin incelenmesi ve korumaya yönelik değerlendirilmesi,” *Külliyat, Osmanlı Araştırmaları Dergisi*, vol. 14, pp. 137–151, Aug. 2021.

[4] S. Çetintaş, “Türklerde su, çeşme, sebil,” *Güzel Sanatlar Dergisi*, vol. 5, pp. 125–147, 1944.

[5] F. Koçyiğit, “Osmanlı mimarisinde meydan çeşmeleri,” *Akdeniz Sanat*, vol. 13, pp. 339–354, 2019.

[6] S. Eyice, “Çeşme,” in *TDV İslam Ansiklopedisi*, vol. 8, pp. 277–287, TDV İslâm Araştırmaları Merkezi, 1993.

[7] E. M. Okba and M. E. Embaby, “Sustainability and heritage buildings,” *Int. J. Eng. Res. Technol.*, vol. 2, pp. 1682–1690, 2013.

[8] R. Harrison, *Heritage: Critical Approaches*. London: Routledge, 2012.

[9] S. Mazzetto, "Heritage conservation and reuses to promote sustainable growth," *Mater. Today: Proc.*, vol. 85, pp. 100–103, 2023.

[10] S. Elyasi and R. Yamaçlı, "Architectural sustainability with cultural heritage values," *Cultural Heritage and Science*, vol. 4, no. 2, pp. 55–61, 2023.

[11] B. Shilling and P. Stephenson, Eds., *Fountains and Water Culture in Byzantium*. Cambridge: Cambridge Univ. Press, 2016.

[12] S. Yeler and G. Yeler, "Kırklareli tarihi çeşmelerinin kültürel miras olarak değerlendirilmesi," *Kent Akademisi*, vol. 14, no. 2, pp. 315–334, 2021, doi: 10.35674/kent.884584.

[13] V. de Freitas, M. Ramazanova, R. E. Cortés, and P. P. Leite, "Water conservation in the urban landscape through heritage and capacity building: The case of Guimarães, Portugal," in *Capacity Building Through Heritage Tourism*. Apple Academic Press, 2021, pp. 1–29.

[14] J. Douet, *The Water Industry as World Heritage*. TICCIH Thematic Study, 2018.

[15] N. Novakovic, I. F. Yorke, and N. Micovic, "Reconstruction, restoration and presentation of the XVI century fountain at the Belgrade fortress," *Multidiscip. Rev.*, vol. 7, 2024.

[16] ICOMOS, *Statement of Significance for Water as Cultural Heritage*. ICOMOS International Scientific Committee on Water, 2021.

[17] C. Hein, H. van Schaik, D. Six, T. Mager, J. C. A. Kolen, M. Ertsen, S. Nijhuis, and G. Verschuure-Stuip, "Foreword," in *Adaptive Strategies for Water Heritage: Past, Present and Future*. Cham, Switzerland: Springer, 2020.

[18] UNESCO, *The United Nations World Water Development Report 2021: Valuing Water*. Paris: UNESCO, 2021.

[19] Ş. Öztürk and V. E. Belli, "Tarihi Bitlis Çeşmeleri," in *II. Uluslararası Ahlat–Avrasya Bilim, Kültür ve Sanat Sempozyumu*, Bitlis, Türkiye, 2013, pp. 177–200.

[20] Ş. Öztürk, "Bitlis Tarihi Hatun Çeşmesi koruma çalışmaları hakkında bir araştırma," *Amisos*, vol. 7, no. 13, pp. 420–430, 2022, doi: 10.48122/amisos.1166730.

[21] Bitlis Valiliği, *Bitlis 1973 İl Yıllığı*. Ankara: Çam Matbaası, 1974.

[22] Ş. Öztürk, "An example of Bitlis historical fountains: Sokakbaşı Fountain," in *III. Int. Architecture Symp. "Built Environment Practices and Actors"*, Diyarbakır, Türkiye, 2023, pp. 211–220.

[23] N. Z. M. Azizi, A. A. Razak, M. A. M. Din, and N. M. Nasir, "Recurring issues in historic building conservation," *Procedia - Social Behav. Sci.*, vol. 222, pp. 587–595, 2016, doi: 10.1016/j.sbspro.2016.05.217.

[24] M. I. Adegoriola, J. H. K. Lai, E. H. K. Yung, and E. H. W. Chan, "Development of a significant index model for assessing heritage building maintenance management challenges," *Eng. Constr. Archit. Manag.*, vol. 31, no. 8, pp. 3398–3428, 2024, doi: 10.1108/ECAM-05-2022-0457.

[25] M. Shan, Y. F. Chen, Z. Zhai, and J. Du, "Investigating the critical issues in the conservation of heritage building: The case of China," *J. Build. Eng.*, vol. 51, p. 104319, 2022, doi: 10.1016/j.jobe.2022.104319.

[26] Z. Cao, L. Huang, Y. Mao, M. Mustafa, and M. H. M. Isa, "Navigating complexity in sustainable conservation: A multi-criteria decision making of architectural heritage in urbanizing China," *J. Build. Eng.*, vol. 102, p. 111906, 2025, doi: 10.1016/j.jobe.2025.111906.

[27] Z. Ahunbay, *Kültür Mirasını Koruma İlke ve Teknikleri*. İstanbul: Yapı Endüstri Merkezi Yayınları, 2019.

[28] L. Zakar and K. K. Eyüpgiller, *Mimari Restorasyon Koruma Teknik ve Yöntemleri*. İstanbul: Ömür Matbaacılık, 2015.

[29] C. Hein et al., *Adaptive Strategies for Water Heritage: Past, Present and Future*. Cham: Springer, 2020.

[30] ICOMOS-ISCS, *Illustrated Glossary on Stone Deterioration Patterns*. Paris: ICOMOS, 2008.

[31] B. Feilden and J. Jokilehto, *Management Guidelines for World Cultural Heritage Sites*. Rome: ICCROM, 1998.

BİTLİS EREN ÜNİVERSİTESİ
FEN BİLİMLERİ DERGİSİ

ISSN: 2147-3129 / e-ISSN: 2147-3188

Article Type	: Research Article	**Year**	: 2025
Received	: June 19, 2025	**Volume**	: 14
Revised	: September 10, 2025	**Issue**	: 3
Accepted	: September 26, 2025	**Pages**	: 1823-1848
DOI	: 10.17798/bitlisfen.1723313		

THE COHESIVE AND FATIGUE DAMAGE MECHANICS OF CEMENT-STABILIZED SOIL COMPOSITES USING NEW GENERATION SUSTAINABLE CEMENT

Nazife ERARSLAN [1]

[1] *İzmir Demokrasi University, Civil Engineering Department, İzmir, Türkiye, nazife.dogan@idu.edu.tr*

ABSTRACT

In this study, fracture toughness (KIc) and cohesive fracture properties of sandy-clay soils stabilized with low (%2) and high (%10) cement under static and cyclic loading using semicircular (SCB) specimens were investigated by experimental and numerical analysis. Higher KIc values were obtained with samples containing high amounts of cement compared to soils containing low amounts of cement. A significant decrease in KIc value was also observed under cyclic loading compared to monotonic loading test results. Load-crack opening displacement (COD) plots obtained by cyclic loading experiments showed high plastic deformation accumulation before final fracture. Beside these, cohesive and stable critical crack length and the initiation of unstable crack propagation were determined using nonlinear simulations and cohesive fracture analyses of the FRANC2D program. Thus, combined evaluation of the findings from both experimental and numerical studies in this research could lead to improved design strategies for stabilized soil composites by strengthening a comprehensive understanding of fracture mechanics alongside empirical data.

Keywords: Cement-stabilized soil, SCB testing and soil, Fracture toughness and stabilized soil, Cohesive crack analysis and soil.

1 INTRODUCTION

Soil stabilization is an essential process in the field of geotechnical engineering, which involves modifying the physical properties of soil to enhance its load-bearing strength, stability, and durability. One of the most effective methods of soil stabilization is the use of cement, which has been widely used in various civil engineering projects, including road construction, building foundations, and embankment construction. There are different mechanical and

chemical methods for the stabilization of soils [1], [2]. Cement, fly-ash, lime, chlorite, bitumen, molasses, lignin, and some chemical agents are among the widely used materials for chemical stabilization of the soils and soft geomaterials. The required percentage of cement that should be added and combined with the soil may depend on the engineering and mechanical properties of the given soil material as well as the type of construction project. The effectiveness of cement stabilization depends on several factors, including the type of soil, cement content, water-cement ratio, and compaction methods. The type of soil being stabilized plays a crucial role in determining the required amount of cement and the optimal water-cement ratio. For instance, soils with high clay content may require more cement and a higher water-cement ratio compared to soils with low clay content. Accordingly, more cement should be added to those soils having higher amounts of plasticity. Soil mechanics and geo-technique researchers often explore the methods and process to decrease the plasticity, compressibility and permeability indexes of the soil in which such activities can finally result in increasing the soil strength and its load bearing capacity [3]. On the other hand, using fly ash in soil stabilization has a positive effect on reducing the plasticity index and improving the soil strength. The type of soil, plasticity, amount of cement or additive, mixing and compaction methods, water content ratios, curing conditions, grain sizes and distribution of additives in the soil structure are some of the major parameters affecting the performance of soil stabilization process in the resultant soil materials (as a kind of randomly distributed heterogeneous composite). Based on the determination of the load-carrying and strength properties of the soil, approximately 80–90% of the properties affecting the stabilized soil would be under control for the field applications. This confirms that the parameters of such building materials could not be evaluated only based on the compressive strength and the other parameters such as tensile, shear, bending strengths and also toughness and cracking resistance indexes (which are as effective as compressive strength) should also be considered in all stability analyses.

Soil materials stabilized with cement may dominantly behave as elastic-plastic materials under static loading [4], [5], [6], [7]. In determination of the ultimate load carrying capacity (ULCC) and designing real projects with such materials, the uniaxial-compressive-strength (UCS) data are usually utilized. However, such reinforced soils are subjected to repetitive loads as they are often used in highways and road foundations, airports, and rail transportation systems (Figure 1). The fatigue properties of any composite road material such as stabilized base and aggregate base materials are very important when considering the application of cyclic loads from vehicles on road pavements, foundations, and bituminous foundations, but little

work has been found on the fatigue characterization of the cement stabilized soils [8], [9]. It is well-known that indirect/induced tensile and shear stresses/deformations are developed in the upper layers of a pavement system through the wheel loads of passing vehicles and such stresses can finally transfer towards the subbase soil-like materials [10], [11], [12], [13]. Since the cement-stabilized soil (CSS) material is commonly used in compacted subbase part of the road and pavement structures, it is very vital to evaluate its fracture (crack resistance) and induced fatigue crack growth behavior and fatigue life under real complex deformations and loads. However, the fatigue effect on many of the building materials (such as metals, ceramics, concrete, rock, asphalt and soil) that can reduce the ultimate strength up to 35% is a matter that has been demonstrated by several researchers for many years [14], [15]. International standards for testing the strength of cement-stabilized materials have not been developed as in other construction and industrial materials. For this reason, testing methods, which are used for materials with quasi-brittle behavior, have been utilized in the literature for the testing of geomaterials in recent years [16], [17], [18], [19]. For example, a semi-circular bend configuration suggested in ASTM D8044-16 for fracture testing of bituminous asphalt materials, seems to be a relatively suitable method for testing CSS materials as well [17],[18], [20], [21], [22].

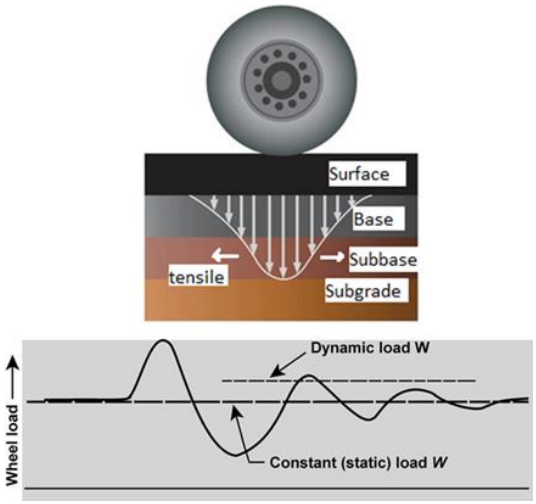


Figure 1. Static and cyclic stress distribution in stabilized soil under a cyclic wheel loading

This research focused on analyzing the crack propagation mechanisms in cement-stabilized soils subjected to monotonic tensile (Mode I) and cyclic loading. Understanding fracture mechanics modes mode I (tensile), mode II (shear) and mode III (tearing) are essential for engineers and researchers to predict and prevent failure in critical components and structures, ultimately ensuring the safety and reliability of engineering systems and reducing the risk of catastrophic failures. There are no widely accepted and well-known international test

procedures to determine the static and cyclic crack resistance characteristic of soils and soft geomaterials under pure modes I, II, III and general combined mode I/II or I/III fracture modes and their failure and damage mechanisms. Due to quasi-brittle behavior of the soil-cement composite mixtures the fracture mechanics discipline has widely been used for understanding the crack growth and failure behavior of soils and soft geomaterials [23], [24], [25], [26]. Dealing with the determination of fracture and cracking behavior indexes in quasi-brittle geomaterials a number of specimens in the shape of edge cracked beam and loaded by three or four point bend loading [27], [28], [29] edge cracked discs or semi-discs subjected to compressive, bending and tensile loads [30], [31], [32], [33], [34], [35] circumferential cracked cylinders loaded by tensile or torsional loads, center cracked hollow discs subjected to diametral tension or compression have been proposed for conducting the fracture mechanics experiments in geomaterials and construction materials [17], [18], [30], [36]. Among the available methods, the semicircular bending (SCB) specimen with either straight through thickness crack or chevron notch shown in Fig. 2 is among the simple and advantageous methods for conducting fracture toughness and fracture toughness experiments on different construction and building materials including rocks mortars, asphalt concrete, polymer concrete and cementitious concrete [10], [38], [39]. The SCB method has also been used by many geo-technique and soil mechanics researchers for investigating the cracking resistance of soft geomaterials such as clay, soil and cement-soils. For example, Wang et al. [28] utilized the SCB geometry with straight vertical edge notch to determine opening mode fracture toughness (K_{Ic}) of the compacted clay material. They investigated the influence of some geometrical and physical parameters such as the crack length, thickness of the SCB and density of the soil at dry condition and with moisture content. Zhang et al., [21] also investigated the fracture toughness of mine tailing soils using the SCB sample with straight crack under combined tensile-in-plane shear deformations. In another work, the fracture toughness of Opalinus clay was determined by Valente et al. [41] using the notched SCB specimens. Olivares-Rodríguez et al. [40] did research on characterizing the influence of suction on mode I fracture response of undisturbed Guadalquivir blue marl using SCB specimen geometry and concluded that the K_{Ic} value (mode I fracture toughness) increases linearly by increasing the suction. The effect of water content and dry density of compacted bentonite clay on its fracture toughness value was also studied experimentally by Qiao et al. [42] using the SCB specimen. However, these research regarding the fracture resistance study of soil materials using the SCB sample have been done using the straight crack under only monotonic loading.

This study aims to understand the static and fatigue failure mechanisms of soil composite materials stabilized with different cement ratios under static and cyclic loads and to contribute to the design and research of soil stabilization materials against failure. This research emphasizes the SCB-chevron method as a reliable and efficient technique for fracture toughness assessment, providing crucial data for performance-based design of cement-stabilized soil applications under various loading conditions. The understanding of fracture mechanics in cement-stabilized geomaterials is critical for ensuring the long-term integrity and performance of civil infrastructure, ranging from road bases and retaining structures to geotechnical barriers. By incorporating cyclic loading, this study addresses a significant limitation in existing literature by exploring the time-dependent degradation mechanisms and the fatigue life of cement-stabilized soils. The comparison of static and fatigue fracture behavior is paramount for moving beyond empirical design approaches towards more mechanistic and reliable service life predictions for cement-stabilized geomaterials. Thus, while fatigue is recognized as an issue, a systematic, mechanics-based quantification of fatigue fracture toughness in these specific geomaterials, coupled with sophisticated modeling, has been absent. This study bridges this gap by providing both empirical data and a theoretical framework for understanding and predicting fatigue-induced fractures.

2 RESEARCH METHODOLOGY AND MATERIALS

2.1 Preparation of the mode I fracture toughness test specimen

Fracture toughness (KIc) refers to the capacity to resist crack propagation or failure when unstable crack propagation begins when a material is subjected to tensile stress. Geomaterials are elasoplastic materials, and it is not easy to create a sharp internal crack in a specimen with SCB geometry, and the blunt chevron notching technique is used to prepare and simulate the actual crack in these materials [8], [43], [44], [45]. Such method has been implemented successfully for rocks and rigid geomaterials, however, its utilization for the some geomaterials such as soils or clay has rarely been investigated in literature. Hence, the SCB sample with chevron notch (CN) shown in Figure 2 was used for conducting the fracture toughness and fatigue cracking tests on the soil materials. The FDZ in front of the CN tip is investigated and modelled using experimental theoretical or numerical models such as the cohesive zone model.

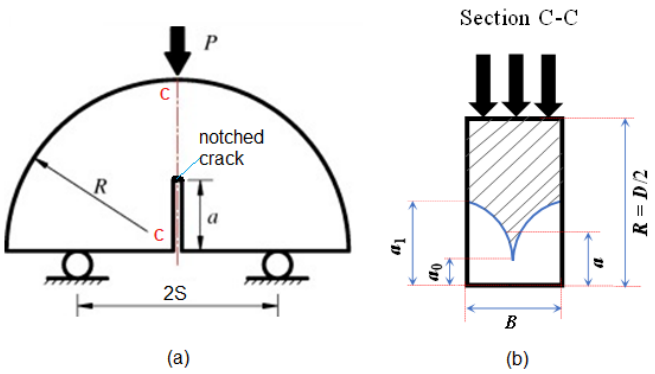


Figure 2. (a) Basic geometrical parameters and (b) CC cross-sectional view of CN-SCB specimen

The stress intensity factor (SIF) value or K_I for mode I condition in the SCB specimen is calculated as:

$$K_I = \frac{P\sqrt{\pi a}}{DB} Y_I \tag{1}$$

where D is the diameter of semi-disc (D=2R) and Y_I is the dimensionless SIF corresponding to mode I that is related to the dimensionless crack length a/D or a/R and loading span ratio s/D. B is also the thickness of the semi-disc. There are some analytical and numerical solutions for calculating Y_I for the SCB specimen with either straight or chevron notch for a wide range of crack lengths and loading spans. For example, the following relation has been proposed for determining Y_I value in the SCB under mode I loading condition:

$$Y_I = 4.47 + 7.4\frac{a}{R} - 106\left(\frac{a}{R}\right)^2 + 433.3\left(\frac{a}{R}\right)^3 \tag{1}$$

2.2 Properties and preparation of cement-stabilized specimens

Well-graded soils and clays with low plasticity are the most suitable soil types for stabilization with cement. On the other hand, clays that contain more sodium or hydrogen are more common in nature and more suitable for stabilization with lime. The soil material analyzed in this study was obtained from a project site previously stabilized with cement by Turkey Highways. In order to determine the engineering properties of the soil specimens, some physical characterization tests including specific gravity, sieve analysis, and standard proctor were carried out.

For the preparation and production of test specimens in this research, sandy soil containing clay was used as the substrate and low (2%) and high (10%) cement was added for

the stabilization process. Based on extensive research, field experience, and various international standards, the typical range for cement content in cement-stabilized soil generally falls between 2% and 15% by dry weight of the soil. The determination of the optimal cement content is not a universal constant but rather a project-specific parameter influenced by a multifaceted factor. However, this study aims to examine ductile fracture behavior with the lowest cement content of 2% and a more brittle fracture mechanism with a high cement content of 10%. Therefore, cement contents of 2% and 10% were selected for this study. As a result of sieve analyses, the soil material was classified as SC according to the Unified Soil Classification System (USCS). The nomenclature of the samples was done in two ways to analyze the results of the analyses: 'SC-L' class represents the soil stabilized with low (2%) cement and "SC-H" represents the samples with high (10%) cement. The sieve analysis results and engineering properties of the soils of current research are provided in Table 1.

Table 1 Soil material constitution

	Specimen constitution
Soil	SC
Sieve analysis	73% passing #4 sieve
	38% passing #200 sieve
Stabilizer contents	%2, %10
Liquid limit	33%
Plastic limit	21%
Plasticity index	12%
Dry unit weight	18.2 kN/m3
Optimum moisture content	20% kN/m3

The cement was CEM II/A-S 42.5 R type and was supplied from the OYAK Çimento A.Ş (Turkey). Chemical composition of the cement is given in Table 2. The components of cement are 80% < Clinker < 94% and 6% < Blast Furnace Slag < 20%.

Table 2 Chemical composition and specific gravity (SG) of the utilized cement for soil stabilization: CEM II/A-S 42.5 R

SO_3	**Na_2O**	**K_2O**	**CL´**	**Na(eq)**	**Sp. Grav. (SG)**
%2,77	%0,37	%1,28	%0,0141	%1.21	3,11 g/cm^3

The soil was mixed with cement at the rate of 2% and 10% by weight of the dry soil and then placed in a 103 mm diameter mould (Figure3). In order to resemble the field stabilisation to the laboratory sample, the soil-cement composite material was placed in the mould in 3 layers or steps, and 25 blows were applied for each layer with a 2.7 kg hammer dropped from a height

of 36 cm. The prepared samples were tightly covered in plastic bags and stored at room temperature for testing after 28 days. The cement-stabilized soil samples were first cut into 40 mm thick discs, and then these discs were cut in half to prepare the SCB geometry (Figure 3). The radius or length of the inner and outer chevron-notch, a_0 and a_1 were 11 and 26 mm, respectively. A circular sawblade coated with the synthetic diamond grains was used to cut the sample and create the chevron-notch (CN). In some studies in the literature, SCB sample geometry and sample preparation have been used in cement-stabilized soil studies [20], [21], [57], [58].

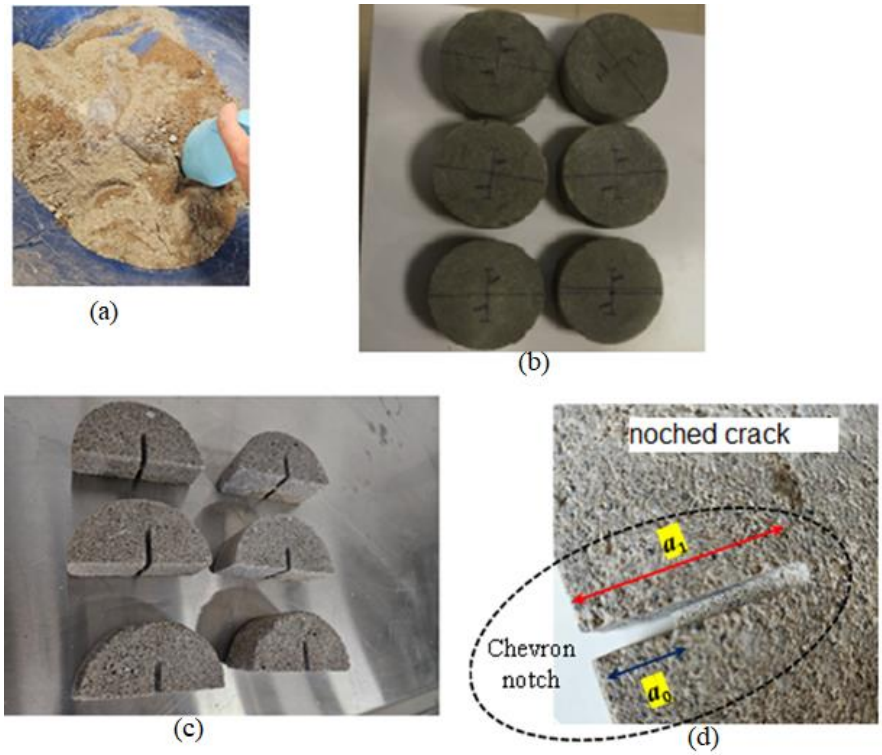


Figure 3. (a) Preparation of the cement-stabilized SCB specimens (b) prepared disc specimens (c) prepared SCB specimens with notch cracks and (d) notch crack parameters

In the fracture toughness tests, three-point loading was applied on the SCB specimens by placing the samples into the machine that the upper loading roller was precisely in the middle of the specimen and that the two lower supporting rollers were placed symmetrically under the SCB specimen. The first series of experiments with the SCB specimens were conducted under static loading conditions, and the rate of loading was equal to 0.025 mm/min. The load versus crack opening displacement (COD) data were recorded for each static test performed on the stabilized soils. Once the failure loads of the static tests were obtained, the amplitude values for the cyclic loading tests would be determined for the cyclic fracture toughness tests. The loading frequency was kept constant in cyclic loading tests at 1 Hz. In cyclic loading tests, the amplitude

of loading was selected to be 30% of the static failure load of each soil group, and sinusoidal-type cyclic loading experiments were carried out at a constant amplitude. The amplitude is most meaningfully defined as a percentage of the material's monotonic strength or deviatoric stress at failure. The choice of 30% is not arbitrary; it is a representative value for many operational, service-level loading conditions. For instance, the cyclic damage induced by traffic on a subgrade may often fall within this range [58], [59], [60]. For both static and cyclic tests, the SCB samples were loaded by placing the semi-discs on two lower cylindrical supports in equal distances from the crack plane. The support distance ratio (*s/D*) between the two cylindrical supports were considered equal to 0.4 for all experiments.

3 RESULTS AND DISCUSSION

In this research, experimental and numerical analyses were used to analyze the crack propagation and cohesive damage properties of cement-stabilized soil specimens under static and cyclic loading. The findings revealed significant differences in the fracture toughness of the materials depending on the cement content under Mode I loading conditions and provided valuable information on crack propagation behavior. The study also contributed to a comprehensive understanding of crack propagation mechanisms by investigating the influence of various factors such as material microstructure and loading type on the fracture behavior of the materials.

Figure 4 shows some load-COD graphs for specimens tested under static loading, which was the first test series. Figure 4 a and b show the load-COD graphs of SC soil specimens containing 10% cement, while Figure 4c and d show the load-COD graphs of specimens containing 2% cement. The graphs show that the failure load, Pmax, increases with increasing cement content and behaves predominantly as a linear and elastic material up to this value. An important finding here is an instability in the loading-COD behavior of the specimens containing 2% cement at the beginning of the test (Figures 4c-d). This is due to the cohesive displacements of the soil grains in the specimens due to the lower cement content. A small non-linearity is observed in the loading curves typically at 85% of the peak or maximum load and this behavior can be attributed to the saturation of the FDZ around the crack tip by nucleated microcracks before the main fracture. An effective tensile softening deformation was obtained in the post-peak damage zone after Pmax and such behavior in the damaged zone in cement stabilized soils is due to the formation and growth of localized inclined shear cracks and longitudinal tensile cracks. However, the semi-friable nature of cement soils and the cohesion

between soil grains cause a non-linear load-displacement reduction, which results in softening rather than a brittle-type fracture and a sudden reduction of the load carried by the soil material. The mode I critical stress intensity factor (which can be considered as a fracture toughness value) for the tested soil materials, peak fracture loads obtained from mode I fracture tests were calculated by Equation 1. The load and fracture toughness values of SCB specimens obtained as a result of static and dynamic loading are given in Table 3.

In both static and cyclic fracture toughness tests, significantly different KIc values were obtained between static loading and cyclic loading. Similar to literature, higher strength and fracture resistance values were obtained for well-graded granular soils compared to sand-clay mix soils [46], [47], [48]. The highest KIc value was obtained with SC-H soil samples. In fact, the experimental results showed that the fracture toughness and resistance to cracking of the material is increased by increasing the cement content in both classes of stabilized soil materials. Depending on the soil type and cement content, the fracture toughness value typically varied between 0.12 and 0.16 MPa.m$^{0.5}$. The reduction in fracture toughness of SC-L specimens under cyclic loads is 15%, while this value is 25% for SC-H specimens. This outcome is in agreement with the fracture toughness of different stabilized soil materials reported in the literature [44], [48].

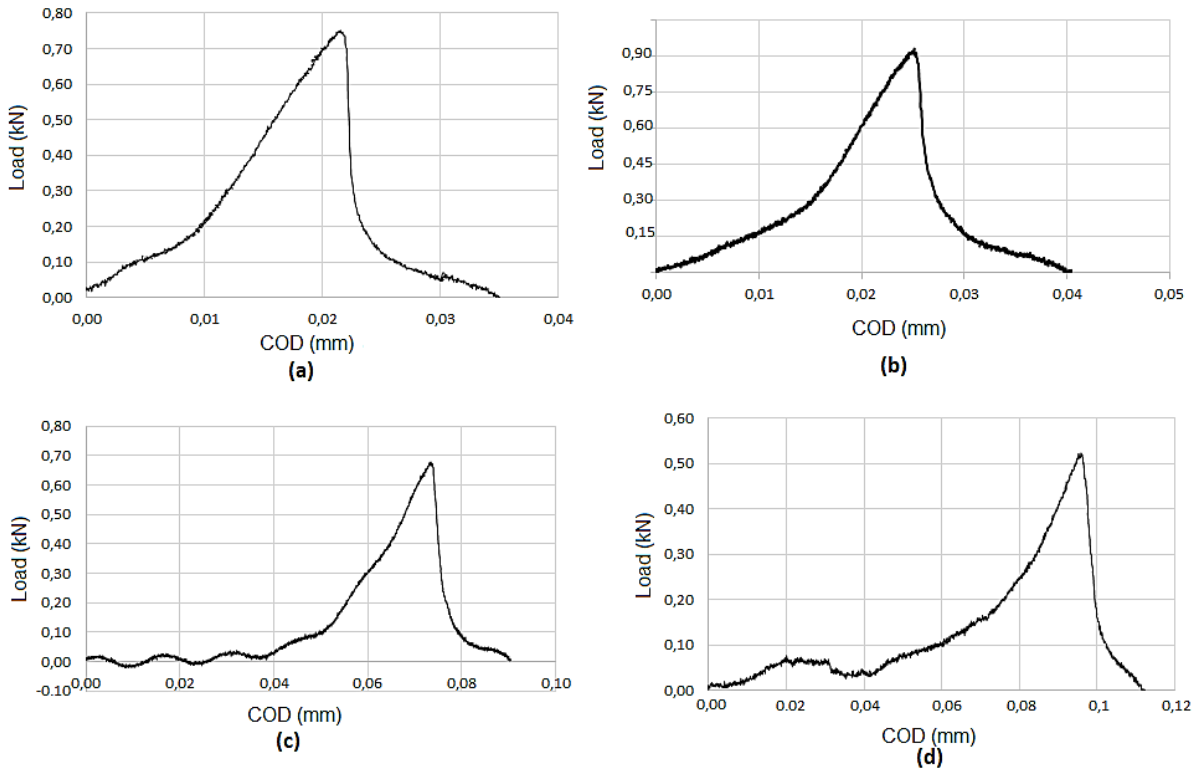


Figure 4. Examples of load versus COD graphs obtained for the SCB samples under static loading, (a-b) with 2% cement and (c-d) 10% cement

Table 3 The details of SCB geometry made of stabilized soil-cement and the fracture toughness results under static and cyclic loading conditions

Soil type	D (mm)	B (mm)	Failure load (P_{cr}) (N)	K_{Ic} MPa$\sqrt{m}$
Static loading test results (avr. of three replicates)				
SC-L	103	41	471	0.16
SC-H	103,5	40,5	698	0.34
Cyclic loading test results (avr. of three replicates)				
SCC-L	103	41	382	0.10
SCC-H	103,5	40,5	501	0.22

A direct comparison between the experimental and numerical K_IC values is presented in Figure 5. The agreement between the two sets of values is remarkably good across all variations of cement content. The percentage difference between the experimental mean and numerical values ranged from -4.62% to 4.17%, with an average absolute difference of approximately 3.36%. These differences are well within acceptable limits for engineering applications and often fall within the experimental scatter.

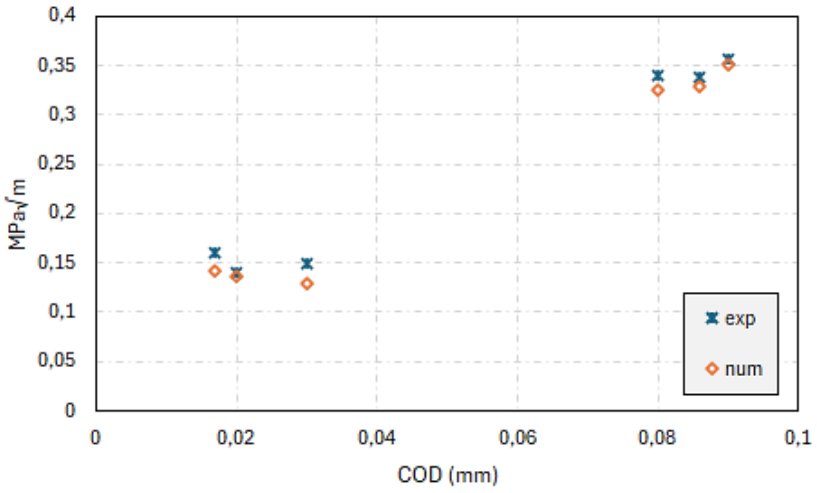


Figure 5. Mode I fracture toughness comparison between experimental and numerical analysis findings

Besides the static test results, some new and unique fracture toughness data were obtained for the first time under cyclic loading for the cement-stabilized soil specimens. A significant decrease (up to 25%) in the value of K_{Ic} values of both WGCG and SCFG samples (that were stabilized with low and high content of the cement) under cyclic loading was found compared to the values obtained with the static tests (Table 3). Although in general addition of cement increased the cracking resistance of the stabilized soils, it was shown that, when the WGCG and SCFG soils were tested under cyclic loads, the effect of cement ratio was not as

effective as in static loading tests. On the other hand, well-graded coarse grain granular soils were accepted as suitable class of soils for stabilization with the cement, and the greatest fracture and cracking resistance values were achieved for the WGCG samples for both cyclic and monotonic loads compared to the sandy clay stabilized with cement. This finding that is in agreement with the available published works, would be related to intergranular crack growth between the soil grains and matrix part [90], [91], [92].

To further investigate the influence and role of mix type and loading type on the cracking resistance of the tested soils, Figure 6 compares the 'fracture toughness ratio'-FTR, defined as (KIc (cyclic) / KIc (monotonic)) for the different soil mixtures of the present investigation. From this figure, it can be concluded that SC specimens stabilized with 10% cement are more sensitive to cyclic loading than specimens containing 2% cement. The reduction in fracture toughness of SC-L specimens under cyclic loads is 15%, while this value is 25% for SC-H specimens. According to the results, increasing the cement content from 2% to 10% did not influence improving the performance of the mix against cyclic loading and fatigue cracking. This finding would be explained by the fact that some fatigue damage studies of composite materials under cyclic loads in the literature are due to fracture between grain and matrix [49], [50], [51], [52].

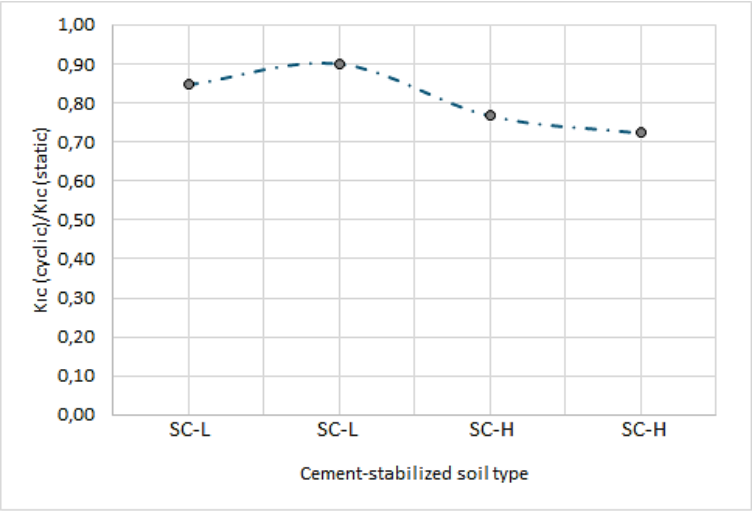


Figure 6. Fracture toughness ratios obtained from both cyclic and static loads

Some of the tested soils are shown in Figure 7. In all stabilized soil SC specimens examined in both static and cyclic loading tests, it was observed that fracture initiated first at the notch end due to the larger crack opening width at the chevron crack tip. It was observed that the main crack causing failure propagated along the axis of the chevron crack and grew towards the loading point, as expected under mode I loading.



Figure 7. Fracture propagation leading to failure at opening (mode I) load condition

Cement-stabilized soil is increasingly recognized for its enhanced performance under cyclic loading conditions, particularly in pavement construction. Since cement stabilized soils are used in road foundations, they are subjected to repetitive traffic loads at each vehicle passage. In this study, successful cyclic loading experiments at a frequency of 1 Hz were performed to simulate such repetitive loading. Fatigue micro fractures, cohesive fractures, and plastic strain are interrelated phenomena that significantly impact the structural integrity of cohesive materials under cyclic loading. Micro-plastic fatigue damage mechanisms play a crucial role in understanding the instability in cohesive materials subjected to repeated stress. When the stabilized soil is subjected to cyclic loading, stable cracks occur first until the final macro-unstable crack propagation begins. As cyclic loading increases during the development of fatigue crack growth, a zone called the fracture process zone 'FDZ' develops at the crack tip. The process zone associated with fatigue fractures is characterized by the accumulation of microfractures, which ultimately lead to catastrophic macrofracture events. As the fatigue load decreases during unloading, the branching cracks change direction, and the crack tip folds inwards. This stage continues with each loading cycle and leads to the formation of additional micro-cracks in region in front of the propagating macro-crack. This mechanism is explained by the accumulation of plastic deformation shown in the COD versus number of cycle (N) plots (Figure 7). Fig.7 shows that the high amount of plastic deformation accumulation indicates the formation of FDZ in front of the notch and the development of cohesive and stable cracks leading to eventual unstable macrocrack propagation. In SC specimens stabilized with low and high cement percentage (2% and 10%, respectively), it was observed that all displacements occurring in front of the notch were in the opening mode but with high plastic deformation accumulation. When Figure 8 is analyzed, it is seen that the plastic deformation that causes opening at the crack tip in SC specimens with 2% cement percentage causes closing at the crack tip afterwards. These results are quite impressive and interesting. Because the principal stress in composite materials under mode I loading conditions is tensile stress and crack surface plain opening is expected, however the reason for the closing tendency of the chevron crack in SC specimens will give qualified information about the strength of these materials. This outcome

introduces a novel fatigue damage model that distinguishes between macro-elastic and plastic components, enhancing predictive capabilities for material behavior by analyzing ductile fatigue fracture by simplifying elastic-plastic behavior under cyclic loads.

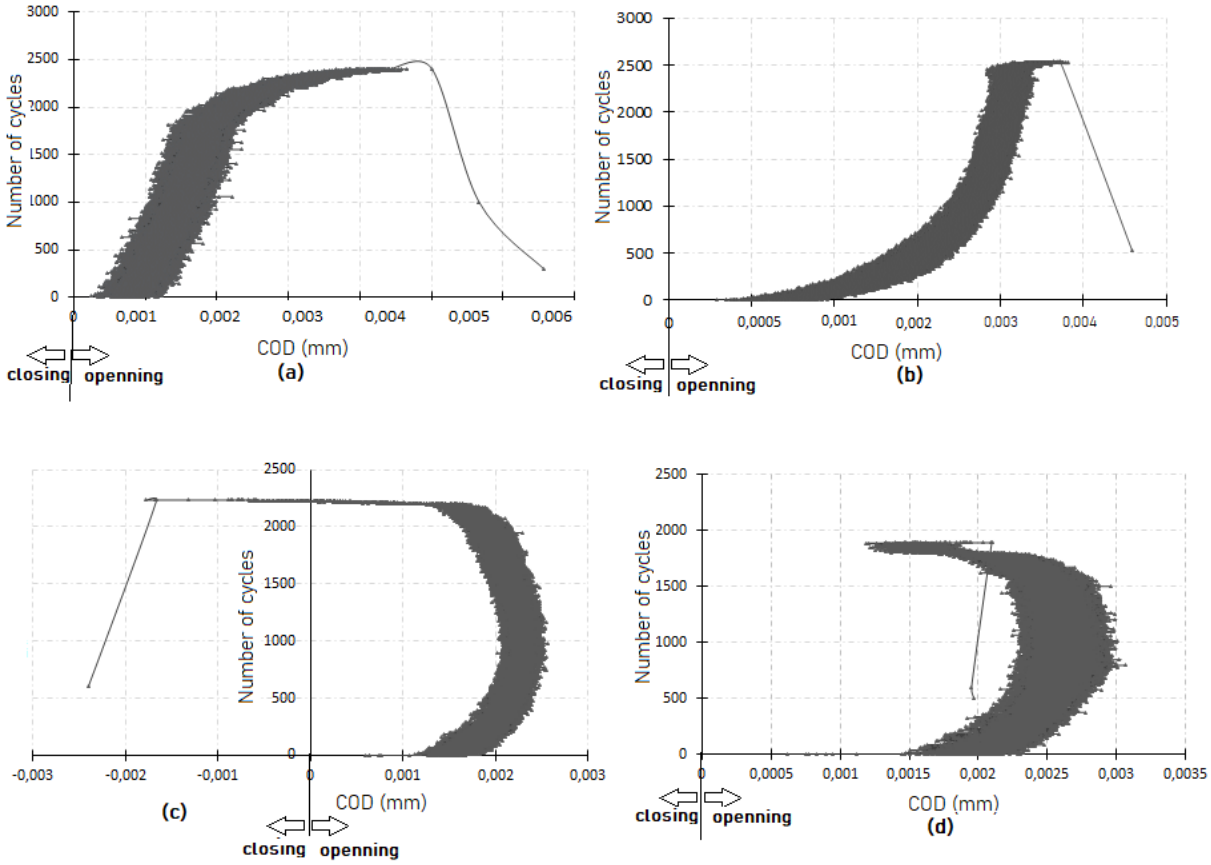


Figure 8. Mode I Cyclic loading test results of the (a) SC-L (b) SC-L (c) SC-H and (d) SC-H SCB specimens

One of purposes of this study was to utilize the fracture mechanics principles in the analysis of fracture in the cement-stabilized soil and to explain the cohesive fracturing and fatigue damage characteristics. Cohesive fracturing in composite materials, such as soils, occurs when the intergranular fracture process reveals that the "weakest bond" is either in the matrix or at the interface between soil grains and matrix. It is known that numerical analyses are useful for such micromechanical fracturing analyses. The second series of analyses in this study were numerical analyses to explain the results obtained from static and dynamic loading experiments and to understand the damage mechanisms. Numerical modelling programs are widely used in this field since the initiation and subsequent propagation tendencies of microcracks under micro-scale stresses in cement stabilized soil specimens and the behavior of the crush zone are partially explained by experiments. Numerical analyses were performed using Fracture Analysis Code (FRANC2D), which performs discrete crack propagation analysis, linear elastic

and elastoplastic. Maximum Tangential Stress (MTS) criterion, one of the most used crack propagation theories in fracture mechanics, was used for stress and crack propagation analyses with FRANC2D. The sample geometry and parameters were modelled using a CASCA mesh generator program before performing stress and crack analyses with FRANC2D. FRANC2D, developed at the Cornell Fracture Group, is a specialized, interactive graphical software designed explicitly for the simulation of crack propagation in two-dimensional, planar bodies [60]. Its primary strength lies in its automated local remeshing capabilities, which allow for the efficient and accurate modeling of a growing crack without requiring a complete re-discretization of the entire domain for each step of propagation. The two-dimensional stress state is 'plain stress' which is assumed to be for thin plates where the out-of-plane stress is negligible. The material is free to contract or expand in the thickness direction. The fundamental properties required to define stress-strain relationship are the Young's Modulus, Poisson's Ratio and fracture toughness values. These values are 1 GPa, 0,22 and the experimentally obtained KIc values respectively. When a crack is inserted, the software automatically generates a "rosette" of triangular, six-noded, quadratic elements around the tip. This seemingly simple modification to the isoparametric element formulation forces the element's shape functions to reproduce the desired strain singularity, thereby dramatically improving the accuracy of the near-tip stress field and, consequently, the stress intensity factor (SIF) calculation. The loading in simulations was applied as a three-point bending test configuration and the compressive force was applied as homogeneously distributed loading throughout the 2 mm contact area. The points where the sub-roller supports were located were fixed in both directions (x, horizontal direction, and y, vertical direction). Nodes along an edge are constrained in the direction normal to the edge but are free to move tangentially.

Before performing crack analyses with FRANC2D, initial numerical analyses were performed to obtain the stress distribution around the chevron crack tip in SCB specimens (Figure 9). Based on the primary analysis, it was observed that the FDZ was located at the center of the notch tip, in agreement with the predictions of the MTS criterion (Figure 9). In addition, while pure tensile stresses are expected under mode I fracture loading according to the MTS criterion, shear stress was found to be present at the tip of the chevron crack in regard of low compared to the tensile stress magnitude (Figures 9b and d).

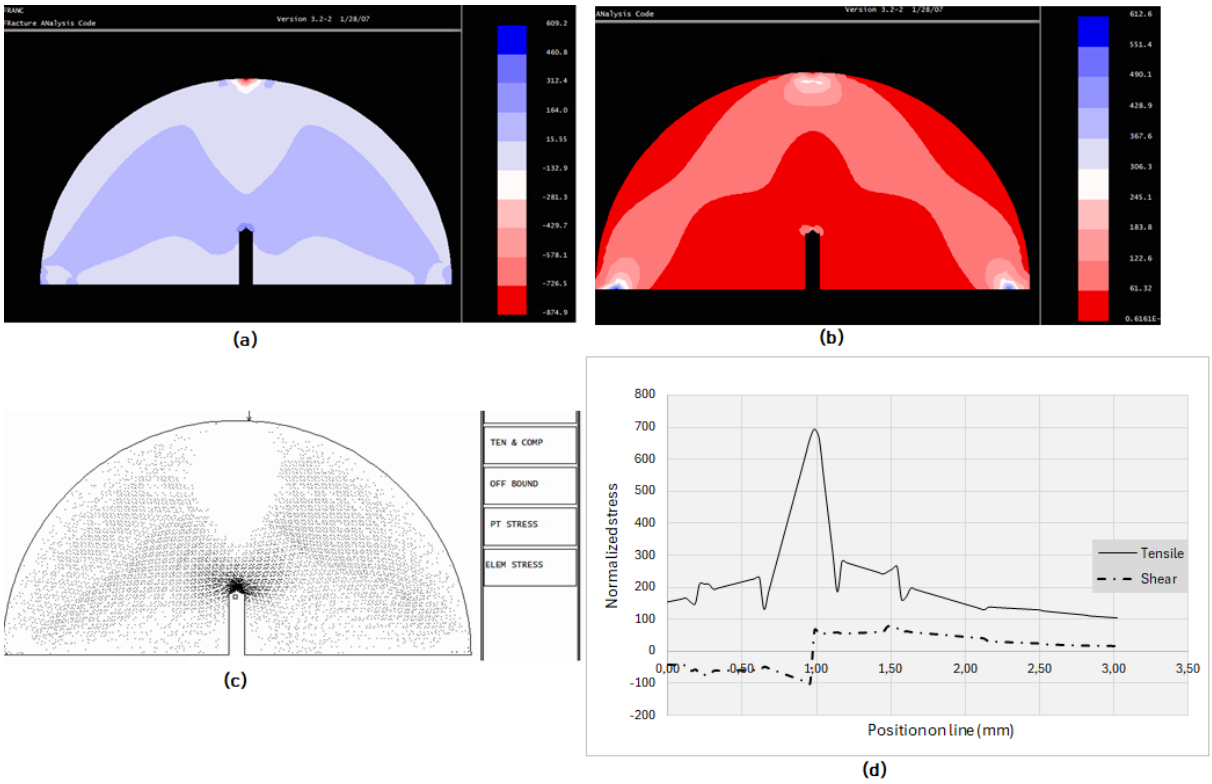


Figure 9. Stress distribution analysis using FRANC2D (a) max. principal stress (tensile) distribution, (b) shear stress distribution (c) Dash-like representation of tensile stress distribution and (d) Graphical representation of stress distribution results

One of the notable advantages of FRANC2D, in comparison to other numerical analysis programs, is that during the crack analysis, the generated mesh at the tip of growing crack is deleted at each increment. Afterwards, the FRANC2D generates automatically a new mesh according to the new stress state at the crack tip for each increment of crack growth to finally capture the whole fracture path (Figure 10a and 10b). The mode I fracture obtained in the experiments was successfully modelled with this feature of the program (Figure 10c).

Research has shown that the formation and propagation of stable cracks in the FDZ region continues in the material under loading until ultimate failure when crack growth becomes unstable [21], [52], [53]. In order to investigate this damage mechanism and fracture process, load-COD curves were analyzed in this study. The first notch-crack progresses critically when it reaches the critical crack length (ac). The initial crack growth in front of the notch is followed by the formation and growth of a stable crack, which also forms the FDZ zone. These stable cracks come together with increasing load to form unstable cracks that cause fracture. Therefore, the maximum load is used as the critical fracture load, while the minimum value of the stress intensity factor (SIF) corresponding to this value is used to determine the mode I fracture toughness. The normalized stress intensity factors (K_{nd}) were determined along the

crack axis (a_c = a/R) using the relative load-COD readings of specimens SC-L and SC-H and plotted as shown in Figure 11. Unstable crack propagation is expected to start at the minimum of Knd, which is equal to a_c = 0.24-0.27 for SC-L and 0.31-0.37 for SC-H specimens (Figure 10). Unstable crack growth occurs at the minimum value of SIF and the critical stable crack length (ac) is 14-15 mm for SC-L soil specimens and 17-20 mm for SC-H specimens.

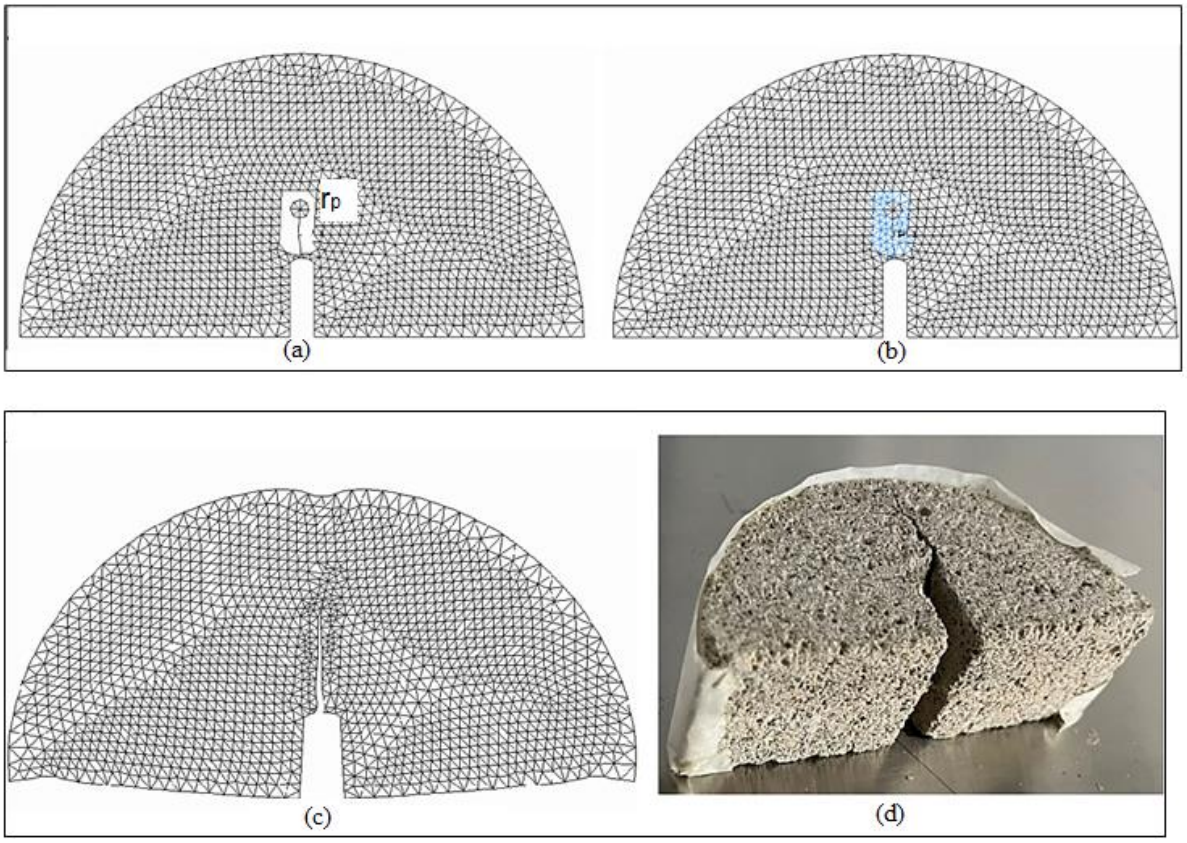


Figure 10. (a) Deleted mesh and (b) re-generated mesh at the tip of stress induced crack propagation provided by FRANC2D simulations (c) fracture path simulation and its comparison with the fracture trajectory observed with the tested SCB specimens

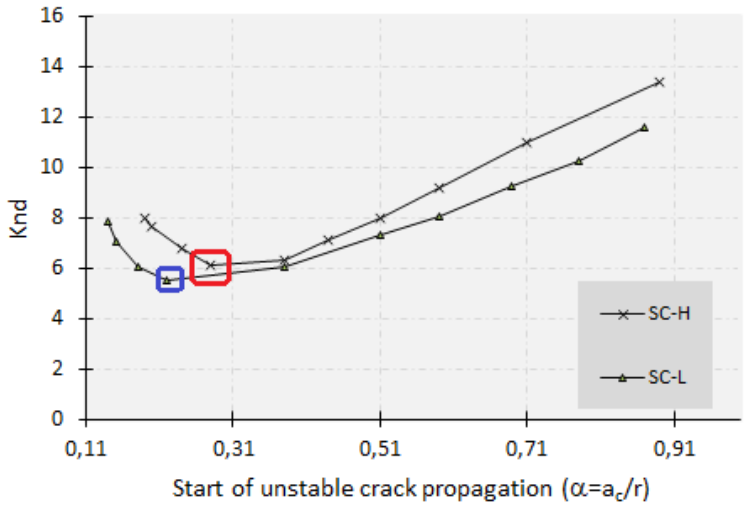


Figure 11. The normalized stress intensity factor (Knd) versus α for the investigated CN-SCB specimens

The second series of analyses were performed to analyze the cohesive crack characteristics after determination of the stress and SIF values with FRANC2D. The critical crack length, a_c, is between a_0 and a_1. Therefore, it is possible to perform cohesive fracture analyses with FRANC2D in order to verify the correlation between the theory, experimental and numerical findings. The linear elastic fracture mechanics modeling was used to determine the values of critical SIF (i.e., SIF_{min}) via the Critical-Crack-Threshold analyses. However, non-linear modeling was used for cohesive crack simulation in the current study. The cohesive zone or CZM model is a common method for numerically modeling of cohesive fracturing. The dynamic relaxation and non-linear solution method utilized in the FRANC2D program is able to consider the non-linear process zone and strain-softening in front of the crack tip. In the FRANC2D simulations for analyzing the cohesive fracturing in the tested SCB samples, the Q-Non-linear (Q/NL) type element (non-linear interface element) was employed to consider the non-linear softening phenomenon induced by the strain localization of the fictitious fracture zone (Figure 12). The cohesive crack growth takes place when the maximum tangential stress value at the crack tip is exceeded from a critical value. The calculated non-linear stress with the Q-NL elements is then utilized to determine the next cohesive crack growth orientation with a determined crack length using the FRANC2D.

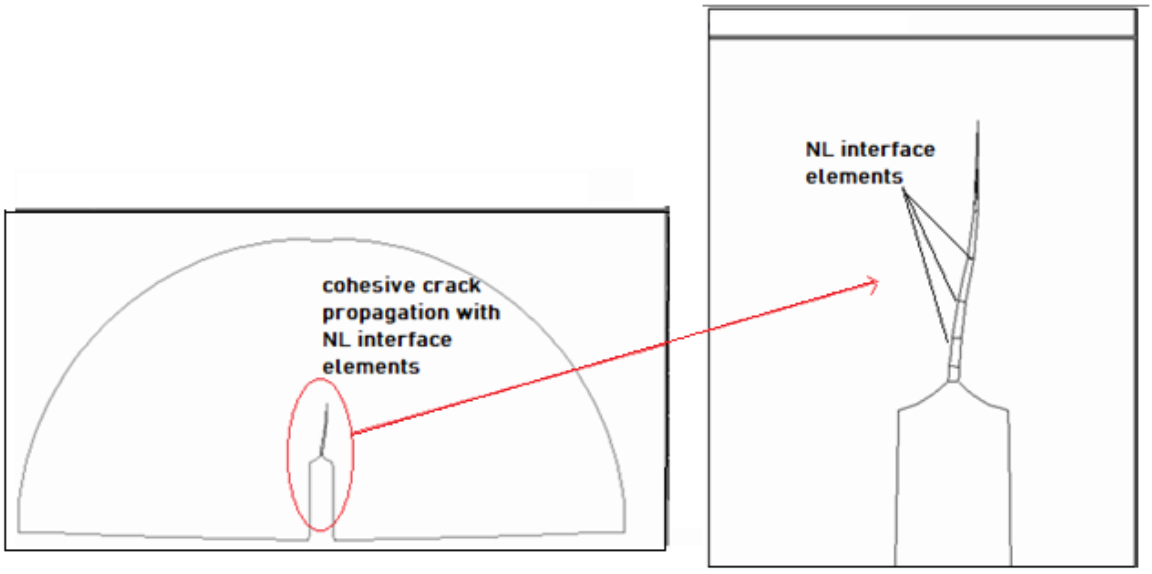


Figure 12. Cohesive crack growth modeling of SCB specimens with FRANC2D using Q-NL interface elements

The nonlinear cohesive crack analysis are a feature of the FRANC2D program that is not available in any other program that can perform nonlinear analyses After the cohesive crack analyses performed with FRANC2D, further analyses were performed to analyze the stable cohesive crack lengths for SC-L and SC-H specimens and the sliding relationships between the

crack surfaces in NL-coupled elements and are shown in Figure 12. The results of the slip surface at each increment of the growing stable cohesive crack were obtained using one of the FRANC2Dcohesive analysis options. When the graph given in Figure13 is analyzed, it is understood that the first stable crack growth at the end of the chevron crack with load increase is in pure tensile state with zero sliding in NL-couples interface elements. With increasing load, cohesive stable crack length could be determined until the value where sliding starts between NL-couple elements and unstable crack growth (failure) occurs. Accordingly, the cohesive stable crack length was found to be 13-15 mm for SC-L specimens with higher sliding values and 15 mm for SC-H specimens in accordance with the ac values shown in Figure 13.

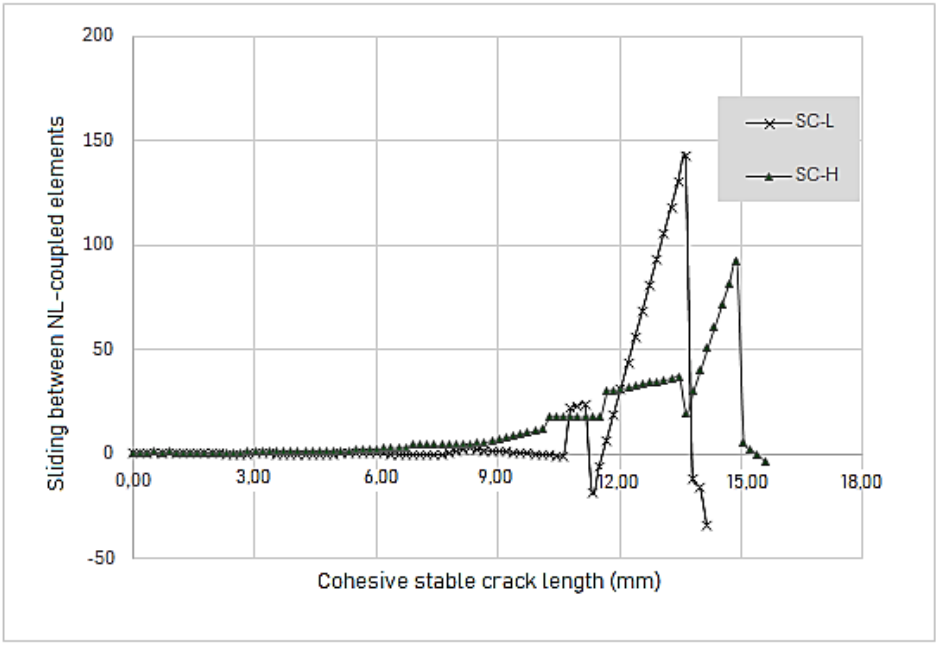


Figure 13. Crack faces sliding with relative cohesive crack lengths

It was determined that the FDZ developed in front of the notch tip first before the final unstable fracture under loading in the SCB samples obtained with different cement contents and that stable crack propagation developed within this zone. For geomaterials and composite materials, this damage or fracture process zone is formed by the formation and coalescence of microcracks in front of the notch tip and it is expected that rapid and unstable fracture will occur after this zone is completely saturated by microcracks. Some theoretically based fracture models such as maximum normal or principal stress criterion have been proposed to estimate the size of the FDZ zone or critical distance (rc) in geomaterials [54], [55], [56]. The use of cohesive cracks in understanding the damage mechanisms of cement-stabilized soil is pivotal for enhancing its structural integrity. In recent studies, cohesive zone modeling (CZM) has been employed to predict fatigue crack growth behavior in chemically stabilized soils. Zhang and

Zhou [21] demonstrated that by integrating monotonic fracture tests with CZM, researchers could accurately forecast the initiation and propagation of cracks under various loading conditions. This predictive capability is essential for assessing the long-term durability of cement-stabilized structures. According to such models, the length of the critical distance in front of the crack tip can be determined by the values of mode I fracture toughness (KIc) and tensile strength (σt) of the cracked component through the following formula:

$$r_c = \frac{1}{2\pi}\left(\frac{K_{Ic}}{\sigma_t}\right)^2 \tag{1}$$

The critical FDZ values of both groups of SC specimens tested are shown in Table 4. According to this Table, the size of the critical distance for the tested soil classes ranges from 3 to 6 mm. This range is within the limit of $1 < r_c < 5$ mm for clay and soil materials as reported in some studies in the literature [54], [55], [56]. Assuming that after such a critical distance (i.e. the fracture and damage process is fully developed and saturated with microcracks), unstable fast propagating fracture occurs, the value of the critical crack length ac is determined by adding the size rc to the initial chevron notch length (a_0). The ac values thus determined are shown in Table 4. It can be observed that the calculated values of ac are in agreement with the unstable crack length (a_c) previously determined using the cohesive zone model with the FRANC2D analysis.

Table 4 Critical FDZ size (rc) and stress-induced crack lengths

Soil type	r_c(mm)	a_c (mm)
SC-L	4.4	14.5
SC-H	4.94	15.94

In conclusion, the use of fracture mechanics models with this study to enhance in understanding the damage mechanisms of cement-stabilized soil for enhancing its structural integrity. Although this study does not explicitly focus on cohesive crack models, it lays a foundation for understanding the complexities depending on the determination of amount of cement in regard to the grain size and type of soil involved in soil stabilization processes. By correlating these findings with fracture mechanics approaches, engineers can develop more resilient materials capable of withstanding various cement content, grain sizes and mechanical loads. Therefore, integrating findings from both experimental and numerical studies could lead to improved design strategies for stabilized soil composites by leveraging a comprehensive understanding of fracture mechanics alongside empirical data.

4 CONCLUSIONS

In this study, chevron-notched semicircular flexural (CN-SCB) specimens were tested under both static (monotonic) and cyclic loading to determine the mode I fracture toughness (KIc) values of soil mixtures stabilized with different cement ratios, and the failure mechanisms of SCB specimens tested under both static and cyclic loads were investigated using both experimental and numerical analyses. The effect of two different amounts of cement-stabilizer (low 2% and high 10%) on the mode I fracture behavior of two different soil classes (SC-L and SC-H) depending on the loading type (monotonic or cyclic) was investigated. The static fracture toughness range for the investigated soil material varied from 0.16 to 0.35 MPa.m$^{0.5}$. In general, this increase is due to increasing the cement content and increasing the size of the soil grain. However, there was a noticeable reduction of about 25% in the measured static fracture toughness of both 'SC-L' and 'SC-H' soil classes when subjected to cyclic loading conditions compared to the monotonic loading condition. However, further analyses and experimental results showed that, indeed, increasing the cement content caused a decrease in the crack resistance performance of the soil against cyclic loads compared to the specimens containing less cement content. This is due to the increased quasi-brittle behavior of the soil with higher cement content and easier formation of intergranular cracks between the cement and soil grains, which are responsible for the fatigue mechanism.

The load-COD graphs obtained from cyclic loading tests revealed that a high plastic deformation accumulated in the soil sample before the final fracture. This indicates that a fracture process zone was formed in front of the crack tip and then a stable and stable cohesive crack surface was formed before the unstable fracture stage. The graphs of crack opening displacement (COD) versus the number of cycles (N) in the fatigue tests revealed that COD values, which are related to damage accumulation in the SCB specimens, decreased with increasing cement content and were higher in soil classes with low cement content. On the other hand, another impressive result is that the plastic deformation that caused the crack tip to open in the SC samples with 2% cement percentage later caused the crack tip to close. These results are quite impressive and interesting. Because under mode I loading conditions, the main stress in the composite materials is the tensile stress and the chevron crack is expected to open, but the reason for the closure tendency of the chevron crack in the SC samples will provide qualified information about the strength and cohesive strength of these materials.

In the study, cohesive fracture analysis with FRANC2D fracture mechanics program was used to estimate the size of the fracture process zone (critical distance) and the onset and length of stable cohesive crack initiation. The critical stable crack length (ac) is found as 14-15 mm for SC-L soil specimens and 17-20 mm for the SC-H specimens. The cohesive stable crack length is also determined using sliding values between the NL-couple elements to confirm the non-linear numerical analysis with FRANC2D. Accordingly, the cohesive stable crack length was found to be 13-15 mm for SC-L specimens with higher sliding values and 15 mm for SC-H specimens. Moreover, the size of the FDZ, which is responsible damage zone of the nucleation of stable fatigue cracks, was found for both soil classes between 3 to 6 mm.

Acknowledgements

This research article was published within the TÜBİTAK 1001 program and project number 124M468. The author would like to thank TÜBİTAK for this support.

Conflict of Interest Statement

There is no conflict of interest between the authors.

Statement of Research and Publication Ethics

The study is complied with research and publication ethics.

Artificial Intelligence (AI) Contribution Statement

This manuscript was entirely written, edited, analyzed, and prepared without the assistance of any artificial intelligence (AI) tools. All content, including text, data analysis, and figures, was solely generated by the authors.

REFERENCES

[1] A.A. Fondjo, E. R., Theron, Ray P. “Stabilization of expansive soils using mechanical and chemical methods: a comprehensive review”. *Civ. Eng. Arch.,* vol. 9, pp. 1295-1308. 2021.

[2] U. Zada, J. Arshad, M. Iqbal, S.M Eldin, A. Meshal, R.B Souhila, A. Sultan. “Recent advances in expansive soil stabilization using admixtures: current challenges and opportunities”, *Case Studies in Constr. Mater.,* vol. 18, e01985, 2023.

[3] N. Koukouzas, P. Tyrologou, P. Koutsovitis, D. Karapanos, and C. Karkalis, “Soil stabilization.” *Handbook of Fly Ash*, pp. 475-500, 2022, doi: 10.1016/b978-0-12-817686-3.00004-9.

[4] E. Güneri, "Zeolit-Bentonit Karışımlarının Farklı Sıcaklıklar Altında Sıkışma İndisinin Hesaplanmasında Ampirik ve Deneysel Yöntemlerin Karşılaştırılması." *Fırat Üniversitesi Mühendislik Bilimleri Dergisi*, vol. 36, no. 2, pp. 765-773, 2024, doi: 10.35234/fumbd.1445113.

[5] E. Güneri, Determination of the Hydraulic Conductivity Behavior of Seaweed Added Zeolite-Bentonite Mixtures in the Presence of Temperature with Empirical Relationships. Çukurova University *Eng. Sci. J.*, vol.39(3), pp.617-623, 2024.

[6] B. Xia, L. Zeng, F. Ji, M., Xie, Z., Hong. "Plasticity role in strength behavior of cement-phosphogypsum stabilized soils"*, J. Rock Mech. Geotech. Eng*., vol. 14(6), pp. 1977-1988, 2022

[7] Z. Yin, P. Wang, and S. Dai, "Microstructures and micromechanics of geomaterials," *J. Zhejiang Univ. Sci. A*, vol. 24, pp. 299–302, 2023, doi: 10.1631/jzus.A2300MMG.

[8] D. R. Biswal, U. C. Sahoo, and S. R. Dash, "Fatigue Characteristics of Cement-Stabilized Granular Lateritic Soils," *Journal of Transportation Engineering, Part B: Pavements*, vol. 146, no. 1, 2019.

[9] D. K. Paul and C. T. Gnanendran, "Characterization of lightly stabilized granular base materials using monotonic and cyclic load flexural testing," J. Mater. Civ. Eng., vol. 28, no. 1, p. 04015074, 2016.

[10] M. R. M. Aliha, H. Ziari, B. Mojaradi, and M. J. Sarbijan, "Heterogeneity effects on mixed-mode I/II stress intensity factors and fracture path of laboratory asphalt mixtures in the shape of SCB specimen," *Fatigue & Fract. Eng. Mate. & Struct.*, vol. 43, no. 3, pp. 586–604, 2020, doi: 10.

[11] N. Erarslan, Investigation of the tensile-shear failure of asphalt concrete base (ACB) construction materials using a non-linear cohesive crack model and critical crack threshold analysis, *Const. and Build. Mater.*, vol. 364, p. 129901, 2023.

[12] N. Mashaan, M. Karim, F. Khodary, N. Saboo, and A. Milad, Bituminous Pavement Reinforcement with Fiber: A Review. *CivilEng*, vol. 2, no. 3, pp. 599-611, 2021, doi: 10.3390/civileng2030033.

[13] H. Ziari, M. R. M. Aliha, E. S. Fard, and M. J. Sarbijan, "Mixed mode I+II fracture parameters and cracking trajectory of heterogeneous multilayer pavement structure containing reflective crack." *Fatigue & Fracture of Engineering Materials & Structures*, vol. 45, no. 10, pp. 2958-2977, 2022, doi: 10.1111/ffe.13796.

[14] N. Erarslan, D.J.Williams, "Mechanism of rock fatigue damage in terms of fracturing modes". *Int. J. Fatigue,* vol. 43, pp. 76-89, 2012.

[15] F. Bjørheim, S. C. Siriwardane, and D. Pavlou, "A review of fatigue damage detection and measurement techniques." *International Journal of Fatigue*, vol. 154, p. 106556, 2022, doi: 10.1016/j.ijfatigue.2021.106556.

[16] M. Aliha, H. reza Karimi, and M. Abedi, "The role of mix design and short glass fiber content on mode-I cracking characteristics of polymer concrete." *Construction and Building Materials*, vol. 317, p. 126139, 2022, doi: 10.1016/j.conbuildmat.2021.126139.

[17] X. Chen, J. Yuan, Q. Dong, and X. Zhao, "Meso-scale cracking behavior of Cement Treated Base material." *Construction and Building Materials*, vol. 239, p. 117823, 2020, doi: 10.1016/j.conbuildmat.2019.117823.

[18] C.-H. Chen, C.-S. Chen, and J.-H. Wu, "Fracture toughness analysis on cracked ring disks of anisotropic rock." *Rock Mechanics and Rock Engineering*, vol. 41, no. 4, pp. 539-562, 2007, doi: 10.1007/s00603-007-0152-9.

[19] N. Erarslan, "Analysing mixed mode (I–II) fracturing of concrete discs including chevron and straight-through notch cracks." *International Journal of Solids and Structures*, vol. 167, pp. 79-92, 2019, doi: 10.1016/j.ijsolstr.2019.03.005.

[20] M. Aliha, P. Jafari Haghighatpour, and A. Tavana, "Application of asymmetric semi-circular bend test for determining mixed mode I + II fracture toughness of compacted soil material." *Engineering Fracture Mechanics*, vol. 262, p. 108268, 2022, doi: 10.1016/j.engfracmech.2022.108268.

[21] J.-Z. Zhang and X.-P. Zhou, "Fracture process zone (FPZ) in quasi-brittle materials: Review and new insights from flawed granite subjected to uniaxial stress." *Engineering Fracture Mechanics*, vol. 274, p. 108795, 2022, doi: 10.1016/j.engfracmech.2022.108795.

[22] QB. Zhang, , K Liu, G.Wu, J. Zhao, Dynamic Deformation, Damage, and Fracture in Geomaterials. In: Voyiadjis, G.Z. (eds) Handbook of Damage Mechanics . Springer, Cham, (2022). https://doi.org/10.1007/978-3-030-60242-0_73

[23] W. W. Crockford and D. N. Little, "Tensile Fracture and Fatigue of Cement-Stabilized Soil." *Journal of Transportation Engineering*, vol. 113, no. 5, pp. 520-537, 1987, doi: 10.1061/(asce)0733-947x(1987)113:5(520).

[24] J. Davies, "Fracture characteristics of cement-stabilized soils." *Journal of Materials Science*, vol. 26, no. 15, pp. 4095-4103, 1991, doi: 10.1007/bf00553494.

[25] K. Sobhan and B. M. Das, "Durability of Soil–Cements against Fatigue Fracture." *Journal of Materials in Civil Engineering*, vol. 19, no. 1, pp. 26-32, 2007, doi: 10.1061/(asce)0899-1561(2007)19:1(26).

[26] H. Takahashi, S. Omori, H. Asada, H. Fukawa, Y. Gotoh, and Y. Morikawa, "Mechanical Properties of Cement-Treated Soil Mixed with Cellulose Nanofibre." Applied Sciences, vol. 11, no. 14, p. 6425, 2021, doi: 10.3390/app11146425.

[27] S. A. Saed, H. R. Karimi, S. M. Rad, M. Aliha, X. Shi, and P. J. Haghighatpour, "Full range I/II fracture behavior of asphalt mixtures containing RAP and rejuvenating agent using two different 3-point bend type configurations." Construction and Building Materials, vol. 314, p. 125590, 2022, doi: 10.1016/j.conbuildmat.2021.125590.

[28] J. Wang, S. Huang, W. Guo, Z. Qiu, and K. Kang, "Experimental study on fracture toughness of a compacted clay using semi-circular bend specimen." *Engineering Fracture Mechanics*, vol. 224, p. 106814, 2020, doi: 10.1016/j.engfracmech.2019.106814.

[29] J.- ping Zuo, H.- ping Xie, F. Dai, and Y. Ju, "Three-point bending test investigation of the fracture behavior of siltstone after thermal treatment." International Journal of Rock Mechanics and Mining Sciences, vol. 70, pp. 133-143, 2014, doi: 10.1016/j.ijrmms.2014.04.005.

[30] M. R. Mohammad Aliha, H. Ghesmati Kucheki, and M. M. Asadi, "On the use of different diametral compression cracked disc shape specimens for introducing mode III deformation." *Fatigue & Fracture of Engineering Materials & Structures*, vol. 44, no. 11, pp. 3135-3151, 2021, doi: 10.1111/ffe.13570.

[31] A. Bahmani and S. Nemati, "Fracture resistance of railway ballast rock under tensile and tear loads." Engineering Solid Mechanics, vol. 9, no. 3, pp. 271-280, 2021, doi: 10.5267/j.esm.2021.3.003.

[32] J. He, L. Liu, H. Yang, and M. Aliha, "Using two and three-parameter Weibull statistical model for predicting the loading rate effect on low-temperature fracture toughness of asphalt concrete with the ENDB specimen." *Theoretical and Applied Fracture Mechanics*, vol. 121, p. 103471, 2022, doi: 10.1016/j.tafmec.2022.103471.

[33] R. Raeisi, F. Rezaie, and M. R. M. Aliha, "Mixed mode I/II and I/III fracture toughness investigation for preplaced aggregate concrete mixtures: Experimental study and theoretical prediction." *Fatigue & Fracture of Engineering Materials & Structures*, vol. 47, no. 8, pp. 2873-2887, 2024, doi: 10.1111/ffe.14328.

[34] X. Gu, T. Cheng, F. Zhang, and M. R. M. Aliha, "Experimental and theoretical framework for illustrating the dependency of fracture toughness with tensile, bending, and compression loading in asphaltic samples." Fatigue & Fracture of Engineering Materials & Structures, vol. 46, no. 9, pp. 3321-3341, 2023, doi: 10.1111/ffe.14077.

[35] S. R. Mousavi, M. Ghasemi, and M. Dehghani, "Investigating the fracture toughness of the self compacting concrete using ENDB samples by changing the aggregate size and percent of steel fiber." *Engineering Solid Mechanics*, vol. 12, no. 1, pp. 17-26, 2024, doi: 10.5267/j.esm.2023.7.006.

[36] H. reza Karimi, E. Khedri, M. Aliha, and A. Mousavi, "A comprehensive study on ring shape specimens under compressive and tensile loadings for covering the full range of I+II fracture modes of gypsum material." International Journal of Rock Mechanics and Mining Sciences, vol. 160, p. 105265, 2022, doi: 10.1016/j.ijrmms.2022.105265.

[37] S. Fuan, M. Ke, L. Kanghe, L. Kun, and M. Aliha, "Influence of specimen geometry on mode I fracture toughness of asphalt concrete." Construction and Building Materials, vol. 276, p. 122181, 2021, doi: 10.1016/j.conbuildmat.2020.122181.

[38] N. S. Karamzadeh, M. R. M. Aliha, and H. R. Karimi, "Investigation of the effect of components on tensile strength and mode-I fracture toughness of polymer concrete." *Arabian Journal of Geosciences*, vol. 15, no. 13, 2022, doi: 10.1007/s12517-022-10466-y.

[39] M. D. Kuruppu and K. P. Chong, "Fracture toughness testing of brittle materials using semi-circular bend (SCB) specimen." *Engineering Fracture Mechanics*, vol. 91, pp. 133-150, 2012, doi: 10.1016/j.engfracmech.2012.01.013.

[40] P. Olivares-Rodríguez, M. Aranda, M. Vázquez-Boza, P. Durand, and J. Reinoso, "Experimental characterization of Mode I fracture toughness of the undisturbed Guadalquivir Blue Marl: Effect of suction." *Theoretical and Applied Fracture Mechanics*, vol. 128, p. 104113, 2023, doi: 10.1016/j.tafmec.2023.104113.

[41] S. Valente, C. Fidelibus, S. Loew, M. Cravero, G. Iabichino, and F. Barpi, "Analysis of Fracture Mechanics Tests on Opalinus Clay." *Rock Mechanics and Rock Engineering*, 2012, doi: 10.1007/s00603-012-0225-2.

[42] L. Qiao, J. Liu, X. Li, Q. Li, and J. Xie, "Experimental study on mode I fracture characteristics of compacted bentonite clay." *Engineering Fracture Mechanics*, vol. 285, p. 109294, 2023, doi: 10.1016/j.engfracmech.2023.109294.

[43] P. Miarka, L. Pan, V. Bílek, S. Seitl, and H. Cifuentés, "Influence of the chevron notch type on the values of fracture energy evaluated on alkali-activated concrete." *Engineering Fracture Mechanics*, vol. 236, p. 107209, 2020, doi: 10.1016/j.engfracmech.2020.107209.

[44] M.-D. Wei, F. Dai, N.-W. Xu, Y. Liu, and T. Zhao, "A novel chevron notched short rod bend method for measuring the mode I fracture toughness of rocks." *Engineering Fracture Mechanics*, vol. 190, pp. 1-15, 2018, doi: 10.1016/j.engfracmech.2017.11.041.

[45] M. Fakhri, F. Yousefian, E. Amoosoltani, M. R. M. Aliha, and F. Berto, "Combined effects of recycled crumb rubber and silica fume on mechanical properties and mode I fracture toughness of self-compacting concrete." *Fatigue & Fracture of Engineering Materials & Structures*, vol. 44, no. 10, pp. 2659-2673, 2021, doi: 10.1111/ffe.13521.

[46] B.Das. Principles of foundation engineering. Ed. Hilda Gowans, Cengage Learning, USA, 2007.

[47] M. Rezaeian, P. M. V. Ferreira, and A. Ekinci, "Mechanical behaviour of a compacted well-graded granular material with and without cement." Soils and Foundations, vol. 59, no. 3, pp. 687-698, 2019, doi: 10.1016/j.sandf.2019.02.006.

[48] S. Song, C. Lv, J. Du, and J. Wang, "Correlation analysis between fracture toughness and tensile strength of cement soil based on notched semi-circle bend specimen." *Journal of Adhesion Science and Technology*, vol. 38, no. 16, pp. 3047-3062, 2024, doi: 10.1080/01694243.2024.2327723.

[49] B. Beriha and U. C. Sahoo, "Fatigue behaviour of cement stabilized materials using dissipated energy." International Journal of Pavement Research and Technology, vol. 13, no. 4, pp. 434-441, 2020, doi: 10.1007/s42947-020-0274-y.

[50] D. R. Biswal, U. C. Sahoo, and S. R. Dash, "Fatigue Characteristics of Cement-Stabilized Granular Lateritic Soils." *Journal of Transportation Engineering, Part B: Pavements*, vol. 146, no. 1, p. 04019038, 2020, doi: 10.1061/jpeodx.0000147.

[51] M. Preteseille and T. Lenoir, "Mechanical Fatigue of a Stabilized/Treated Soil Tested with Uniaxial and Biaxial Flexural Tests." *Transportation Research Procedia*, vol. 14, pp. 1923-1929, 2016, doi: 10.1016/j.trpro.2016.05.159.

[52] N. Erarslan, "Feasibility Study of an ASTM Standard in Determining the Mixed-Mode I-II Fracture Toughness of Asphalt Concrete Materials." *Advances in Civil Engineering Materials*, vol. 12, no. 1, pp. 218-236, 2023, doi: 10.1520/acem20220107.

[53] M. H. Anders, S. E. Laubach, and C. H. Scholz, "Microfractures: A review." Journal of Structural Geology, vol. 69, pp. 377-394, 2014, doi: 10.1016/j.jsg.2014.05.011.

[54] E. Melese, H. Baaj, and S. Tighe, "Fatigue behaviour of reclaimed pavement materials treated with cementitious binders." *Construction and Building Materials*, vol. 249, p. 118565, 2020, doi: 10.1016/j.conbuildmat.2020.118565.

[55] R. A. Schmidt. *A microcrack model and its significance to hydraulic fracturing and fracture toughness testing.* In ARMA US rock mechanics/Geomechanics symposium (pp. ARMA-80), ARMA1980

[56] K. Fang and L. Cui, “Experimental investigation of evolutive mode-I and mode-II fracture behavior of fiber-reinforced cemented paste backfill: Effect of curing temperature and curing time.” *Frontiers of Structural and Civil Engineering*, vol. 17, no. 2, pp. 256-270, 2023, doi: 10.1007/s11709-022-0924-z.

[57] J. Zhang, D. N. Little, J. Grajales, T. You, Y.-R. Kim. Use of Semicircular Bending Test and Cohesive Zone Modeling to Evaluate Fracture Resistance of Stabilized Soils. Transportation Research Record, 2657(1), 67-77, 2019 https://doi.org/10.3141/2657-08

[58] N. Erarslan, and M. Aliha. Fracture and Damage Analysis of Cement-Stabilized Fine and Coarse Grain Soils Under Static and Cyclic Loading Using Chevron-Notched SCB Specimen. Fatigue Fract Eng Mater Struct, 48: 2708-2724, 2025, https://doi.org/10.1111/ffe.14598

[59] H. Qi, X. Zhang, J. Liu, T. Zhang, G. Lv, L. Cui, Xie, Q. Study on Deformation Characteristics of Low-Highway Subgrade under Traffic Load. *Appl. Sci.* **2022**, *12*, 3406. https://doi.org/10.3390/app12073406

[60] L. An, X. Zhao, D. Li, L. Yang, P. Li, L. Guo, Wang, L. Cyclic and Post-Cyclic Behaviors of Stabilized Sand-Containing Soft Soil in Coastal Areas. Sustainability 2022, 14, 15017. https://doi.org/10.3390/su142215017

[61] P. A., Wawrzynek, A. R. Ingraffea, Interactive finite element analysis of fracture processes: An integrated approach. Theoretical and Applied Fracture Mechanics, 8(2), 137–150, 1987.

BİTLİS EREN ÜNİVERSİTESİ
FEN BİLİMLERİ DERGİSİ

ISSN: 2147-3129 / e-ISSN: 2147-3188

Article Type	: Research Article	**Year**	: 2025
Received	: June 30, 2025	**Volume**	: 14
Revised	: September 22, 2025	**Issue**	: 3
Accepted	: September 22, 2025	**Pages**	: 1849-1865
DOI	: 10.17798/bitlisfen.1731042		

DEVULCANIZATION AND CHARACTERIZATION OF GROUND TIRE RUBBER WITH MICROWAVE METHOD

İlker ERZİNCANLI [1,*], Fazliye KARABÖRK [2]

[1] *Aksaray University, Machinery and Metal Technologies Department, Aksaray, Türkiye*

[2] *Aksaray University, Mechanical Engineering Department, Aksaray, Türkiye*

**** Corresponding Author:*** *ilkererzincanli@aksaray.edu.tr*

ABSTRACT

The increase in transportation vehicles worldwide has also led to an increase in the production of tires, which are an important part of the vehicle and are used in these vehicles. Industrially, vehicle tires are produced through a process called vulcanization and acquire their high elasticity in this way. However, the sulfur crosslinks formed by the vulcanization process make it very difficult to recycle tire rubber. In the evaluation of vehicle tires that become waste after their service life is completed, direct evaluation, use as an energy source and pyrolysis are used in recycling methods. However, none of these methods aim to recycle tire rubber as a material, that is, to turn it into a re-moldable rubber. In recent years, studies have stated that devulcanization, that is, the breaking of crosslinks, is possible with thermal, mechanical and chemical effects.

In this study, ground tire rubber was devulcanized by the microwave method. The aim of this study is to examine the effectiveness of the process by characterizing the ground tire rubber exposed to different microwave durations. For this purpose, the characterization of devulcanized rubber was carried out by soluble fractions, crosslink densities, FTIR analyses and SEM imaging.

Keywords: Rubber, Vulcanization, Waste vehicle tires, Microwave devulcanization, Recycling.

1 INTRODUCTION

The increasing usage rate of vehicles leads to an increase in tire production and therefore waste tires. Approximately 2.47 billion tires were sold globally in 2023 [1].

Natural and synthetic rubbers are used as the main material in tire production. As in other rubber products, the high elastic properties expected from vehicle tires are obtained due to the sulfur crosslinks formed in the rubber with the vulcanization process. Vulcanization can be defined as the formation of a three-dimensional crosslinked network structure between rubber macromolecules with the help of sulfur, activators, accelerators and other additives as a curing agent and with the effect of heat (Figure 1) [2], [3]. However, these crosslinks prevent rubber-based products from being melted and recycled or remolded by being transformed into another way after their service life has ended [4], [5].

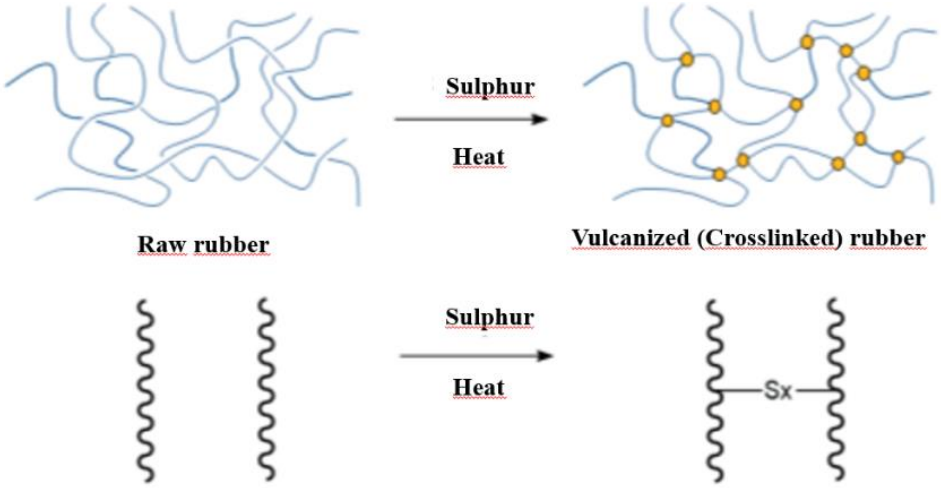


Figure 1. Sulphur crosslinks in vulcanized rubber [3].

Disposal of end-of-life tires is both an environmental and economic problem all over the world. Leaving waste tires in nature in an unorganized manner causes fires, insect reproduction, and environmental pollution with chemicals leaking from their structure [6]-[8]. In recent years, increasing environmental sensitivity and the search for efficient use of raw material resources have led to legal regulations all over the world. In this context, the Waste Tire Regulation was published in Turkey in 2006 and the processes were defined for the collection and evaluation of waste tires [9].

There are various methods currently applied all over the world for the evaluation and recovery of waste tires. These include using granulated tire rubber as a ground covering in parks, burning it as an energy source in factories, or separating it into various raw materials through the pyrolysis method [10]-[12]. However, since the amount of waste is very large, the recovery of waste rubber products as a reusable rubber material should be the basis. This is possible with devulcanization, which is the reverse of vulcanization. In devulcanization, it is

aimed to break the sulfur crosslinks formed by vulcanization without damaging the polymer main chain structure, thus making the waste rubber remoldable (revulcanization). It is seen that devulcanization is a subject on which many studies have been conducted and is still being worked on intensively. There are methods developed and studied on devulcanization such as chemical, mechano-chemical, thermomechanical, ultrasonic, microwave and biological devulcanization. [13]-[16]. Among these methods, microwave and ultrasonic devulcanization stand out in terms of their potential to be used on an industrial scale and the quality of the devulcanized rubber obtained, provided that the process parameters are controlled [12],]17].

In the microwave technique, the energy required to break down the C-S and S-S bonds in vulcanized rubber is provided by using microwave energy at a certain frequency and level. For the microwave technique to be applied, there must be polar components in the structure. Heating is provided by dipole rotation under the influence of microwave energy. Rubber materials are essentially apolar, but heating occurs due to the polar structure of the carbon black in their structure [18].

In this study, an experimental study was carried out for the recycling of waste vehicle tires, which is very important in terms of both environmental effects and raw material recovery by microwave devulcanization method. To determine the properties of devulcanized rubber obtained from devulcanized waste vehicle tires and to demonstrate the effectiveness of devulcanization, it was aimed to determine the parameters where high rates of devulcanization were obtained by soluble fractions, crosslink densities, SEM and FTIR analyses.

2 MATERIAL AND METHOD

The study was carried out in the form of supply of ground tire rubber, characterization of the powder, microwave devulcanization studies and characterization of devulcanized rubber.

2.1 Supply and Characterization of Ground Tire Rubber

In the study, ground tire rubber (GTR) in the size range of 0-1 mm, produced by mechanically shredding waste truck tire at room temperature, supplied by Unsal Rubber Co. Ltd (Adana, Turkey)., was used. Powder size measurement, thermogravimetric analysis (TGA), Fourier transform infrared spectroscopy (FTIR), scanning electron microscope (SEM) analyses were performed to characterize the untreated powder.

2.1.1 Particle Size Measurement

The size measurement of the rubber powder was made by sieve analysis method according to ASTM D 5644-01. This analysis was made by vibratory sieve shaker in Aksaray University Civil Engineering Laboratory. For size measurement, 100 g sample was passed through vibrating sieve for 10 minutes and the obtained results are given in Figure 2. According to the sieve analysis results, it is seen that the particle size of ground tire rubber is mostly in the range of 0.45-1 mm and 0.25-0.45 mm.

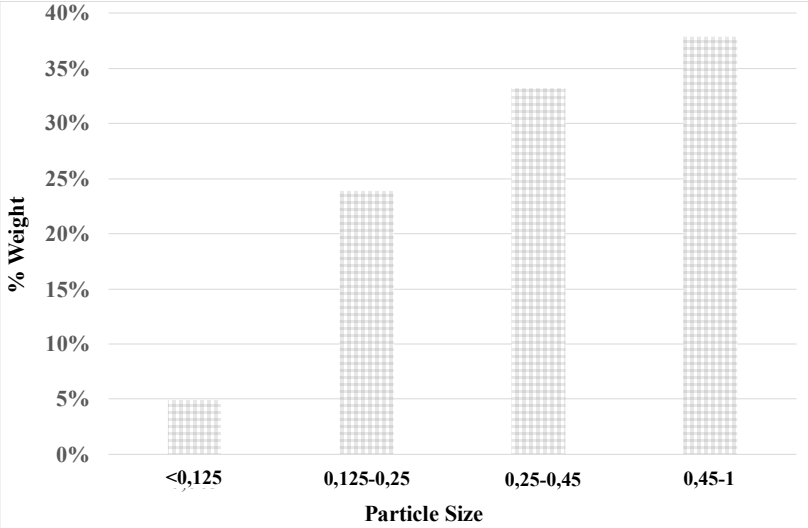


Figure 2. Particle size distribution of ground tire rubber.

In the studies, it has been stated that the small sample size has a positive effect on increasing the homogeneity of devulcanization and that better mechanical properties are obtained after revulcanization [5], [19]-[23].

2.1.2 SEM Imaging

SEM images of the ground tire rubber used have been given in Figure 3. It is seen that it consists of particles of varying sizes and has a rough surface structure. This shows that it was obtained through mechanical disintegration at room temperature.

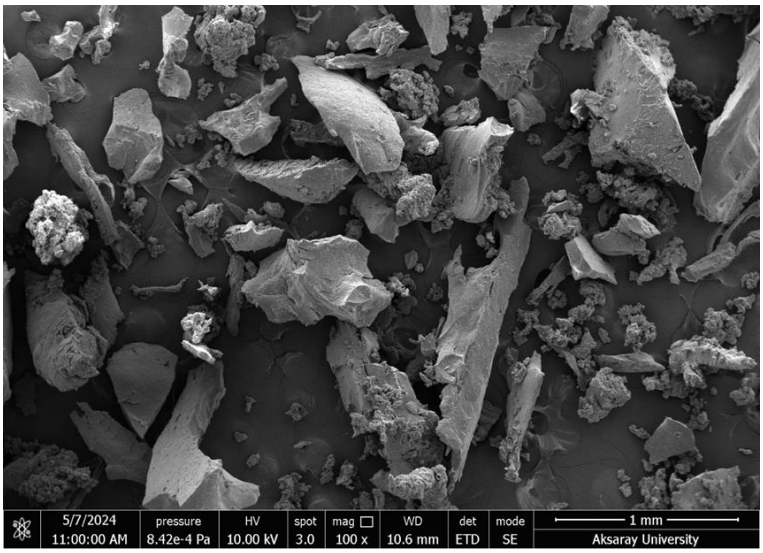


Figure 3. SEM image of used ground tire rubber.

2.1.3 Thermogravimetric Analysis

With TGA, the change in the mass of a material is measured depending on temperature or time. As a result of the chemical reaction caused by temperature, the material decomposes and a gradual change in its mass occurs. As a result of this change, both the thermal behavior of the material is characterized and an idea about the material composition is obtained. In the study, thermogravimetric analysis of ground tire rubber was performed in accordance with the ASTM E1131 standard, by heating approximately 10 mg of the sample in the Aksaray University Central Research Laboratory (ASUBTAM) at a heating rate of 10 °C/min in a nitrogen atmosphere to a temperature of 800 °C.

The TGA/DTG curves of ground tire rubber are given in Figure 4. The peak at 382.6 °C indicates the presence of polymer in GTR and its decomposition temperature. According to the results obtained from the TGA analysis, it is seen that the first mass loss starts around 165 °C, and between 165–300 °C, the mass decreases due to the decomposition of oils and other non-polymeric additives added to the rubber material as process facilitators. This mass loss was determined to be approximately %9.3. The mass loss accelerated between 300–500 °C due to the decomposition of polymeric phases in rubber. It is seen that the curve becomes horizontal where the mass loss decreases above 500 °C. In the TGA curve, it is seen that the GTR composition consists of %54.2 polymer and %35.8 carbon black and the non-decomposed part (consisting of ash and other inorganic additives).

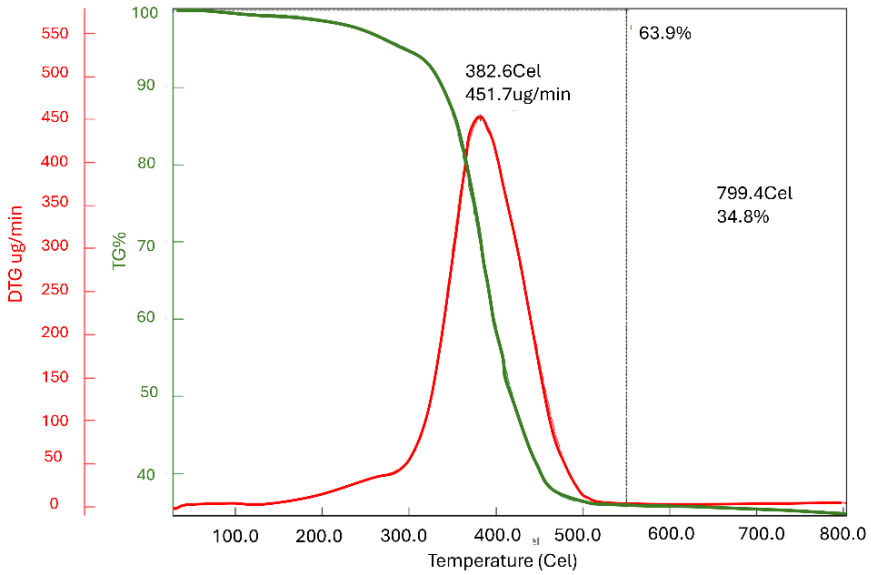


Figure 4. TGA analysis of used ground tire rubber.

In this study, TGA analysis of ground tire rubber was performed not only to characterize the material but also to determine the appropriate temperature and time for microwave devulcanization. The composition of the ground tire rubber used as a result of the interpretation of the TGA curves is given in Table 1.

Table 1. Composition of GTR (%wt).

Sample	Process oil, humidity and other additives %	Rubber %	Carbon black and ash %
GTR	9.7	54.2	36.1

2.2 Microwave Devulcanization

For the devulcanization process, a Samsung brand household type microwave oven operating in the 300-800 W power range has been used (Figure 5). The material was placed in a 1000 ml glass container inside the oven.



Figure 5. Microwave oven.

Studies have shown that the sample should be mixed in the oven to ensure homogeneous heating and to prevent hot spots [24]-[26]. For this purpose, a stainless-steel apparatus was fixed to the oven ceiling and the sample was mixed while the oven tray was rotating (6 rpm).

A 100 g sample has been used for microwave devulcanization. To determine which temperature was reached at which time for the oven, the samples were heated at 800 W microwave power for 4 to 7.5 minutes. Sample temperatures were measured with a probe surface thermometer immediately after the process. The change in temperature depending on time is shown in Figure 6. The results of TGA analysis were used when determining the appropriate time and temperature for devulcanization. Since the aim of devulcanization is to break only the crosslinks without damaging the polymer chains of the rubber, the temperature was kept below 300 °C, which is the temperature at which the rubber begins to decompose.

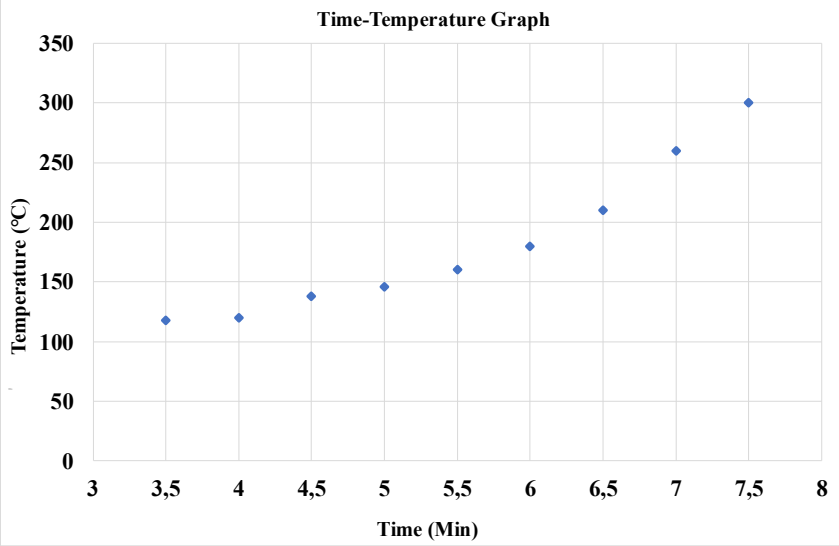


Figure 6. Microwave heating-time graph.

2.3 Characterization of Devulcanized Rubber

2.3.1 Determination of Soluble Fraction

Typically, a vulcanized rubber material contains a large amount of insoluble fraction (gel fraction) that is insoluble in any solvent and a small amount of soluble fraction (sol fraction) that can be dissolved and removed from the structure. These fractions can be determined by extracting the rubber in a suitable solvent. In this study, the soluble fractions of both devulcanized and unvulcanized ground tire rubber were measured using the Soxhlet extraction apparatus shown in Figure 7 according to the ASTM D 297 standard. Toluene has been used as the solvent. The sample amount was approximately 2 g, and the extraction time was 24 hours.

After extraction, the sample was dried in a 70 °C oven for 24 hours. The following equation was used to calculate the soluble fraction of the sample.

$$\%\, Soluble\ Fraction = \frac{W_i - W}{W_i}\ x100 \quad (1)$$

In this equation;

W: weight of dried sample after extraction (g)

Wi: weight of sample before extraction (g)



Figure 7. Soxhlet extraction apparatus.

2.3.2 Crosslink density measurement

With vulcanization, crosslinking occurs, which transforms the linear molecular chain structure of the rubber into a network structure. The degree of crosslinking within the network structure of the rubber molecular chains can be characterized by the crosslink density [27]. The Flory-Rehner equilibrium volume swelling equation is used to calculate the crosslink density of vulcanized rubbers. With this calculation method, the amount of solvent absorbed by the vulcanized rubber is evaluated and the crosslink density is calculated. The low penetration of the solvent into the rubber and the swelling of the rubber mean that the crosslink density is high [28]-[30].

In this study, for the calculation of the crosslink density of the devulcanized and undevulcanized samples, 0.2 g of the sample was inflated by waiting in 10 ml of toluene at room temperature for 72 hours and then removed from the toluene and the excess solvent was

immediately removed and its weight was measured. Afterwards, the sample was dried for 24 hours and its weight was measured again. Crosslink density is calculated from the Flory-Rehner equation, which was developed by considering the Kraus correction factor with filled rubber, with the following equation [31], [32];

$$\rho_c = \frac{1}{2Vs} \frac{\ln(1 - v_r) + v_r + X(v_r)^2}{v_r^{\frac{1}{3}} - \frac{v_r}{2}} \quad (2)$$

In this equation:

ρ_c: Crosslink density (mol/m^3)

V_s: Molar volume of toluene (1.069 x 10^{-4} m^3/mol)

v_r: Volumetric ratio of rubber in the swollen sample (calculations were made by considering the Kraus correction factor)

X: Rubber-toluene interaction parameter (0.3795 for ground tire rubber-toluene) [31].

After finding the crosslink density of the samples, the degree of devulcanization for each sample was calculated with the following equation:

$$\%Devulcanization = \left[1 - \frac{vf}{vi}\right] \quad (3)$$

In this equation;

v_f : Crosslink density of devulcanized rubber

v_i : Crosslink density of ground tire rubber.

2.3.3 Fourier Transform Infrared Spectrophotometer Analysis

To see the chemical modifications after devulcanization, FTIR analyses of devulcanized and undevulcanized samples were performed in accordance with ASTM D 3677 standard using Perkin Elmer FTIR analyzer at Erciyes University Technological Research and Application Center (TAUM). Infrared spectra of the samples were recorded in the range of 450–4000 cm-1 with 4 cm-1 resolution.

3 RESULTS AND DISCUSSION

3.1 Soluble Fraction of Microwave Devulcanized Samples

Soxhlet extraction is a good method for measuring the effectiveness of the devulcanization process. The increase in the soluble fraction in devulcanized rubber indicates that the sulfur crosslinks are broken and devulcanization has occurred [33].

The soluble fractions of ground tire rubber devulcanized at different temperatures are given in Table 2. While the soluble fraction of ground tire rubber is %6.15, it is seen that the soluble fractions increase with the increase in temperature because of microwave devulcanization, and the highest increase is obtained at 240 °C. It was observed that the soluble fraction decreased when the temperature increased to 270 °C. This situation can be explained by the production of free radicals by breaking the bonds and the re-crosslinking of some of the produced macro radicals after the breaking of these bonds. [34], [35].

In the literature review, soluble fraction in microwave devulcanization studies were reported as %14-31 depending on time by Garcia et al. [36], %19.8-21.2 between 190-210 °C by Simon et al. [37], %13.23 to %25.85 for 3-5 min by Musidin [38], %18.2 for 200 °C by De Sousa [33], %26.2 for 220 °C by Molanorouzi and Mohaved [39] and %19.05 to %25.1 depending on time. It is seen that the results obtained from this study are compatible with literature.

Table 2. Soluble fraction depending on temperature.

Sample	Soluble fraction (%)
GTR	%6,15
150±10	%10,08
180±10	%15,44
210±10	%20,89
240±10	%28,40
270±10	%22,08

3.2 Crosslink Densities of Microwave Devulcanized Samples

Crosslink densities were calculated by applying swelling tests to devulcanized and non-devulcanized samples at different temperatures. The calculated crosslink density values are given in Table 3. It is observed that the crosslink density values of devulcanized samples decrease compared to the non-devulcanized sample up to 210 °C and devulcanization occurs. It is observed that the broken crosslinks tend to reconnect with increasing temperature.

Table 3. Crosslink densities.

Sample	Temperature (°C)	Crosslink density (mol/dm^3)	Devulcanization rate (%)
GTR		0,260	-
MD180	180±10	0,221	%15,08
MD210	210±10	0,157	%39,62
MD240	240±10	0,179	%31,30
MD270	270±10	0,393	-

**Sample names are coded with md representing microwave devulcanization and numbers representing temperature.*

In the literature, it is seen that the devulcanization rates in microwave devulcanization studies are given as %40, %35 and %43 by Rajendran [40], %42 by Khavarnia and Mohaved [41], %42.5 by Molanorouzi and Mohaved [39], between %12.16 to %29.43 by Vahdatbin and Jamshidi [42], and %28 by Shabani and Jamshidi [43]. It is seen that the results obtained are consistent with the literature.

Since the crosslinks are broken by the effect of heat during devulcanization, the crosslink density decreases. The increase in the soluble fraction in the extraction of devulcanized rubber is also an indicator of the decrease in crosslink density.

3.3 FTIR Analysis of Microwave Devulcanized Samples

The spectra of the untreated sample and the MD210 sample with the lowest crosslink density obtained by FTIR analysis are given in Figure 8-a.

To see the changes in functional groups after devulcanization in detail, the 1700-900 cm-1 region of the spectrum is given in Figure 8-b. The peaks formed at 1370 cm-1 and indicated the presence of methyl groups characterize natural rubber. Similarly, the peaks formed at 700 cm-1 characterize SBR rubber [44]-[46]. The preservation of both peaks after devulcanization shows that there is no regeneration, i.e. breakage in the main chain structure. The preservation of the peak formed at 1500 cm-1 and characterizing the C=C bond again shows that the polymer main chain structure is preserved. The deepening of the C-O and S=O peaks seen at 1000-1100 cm-1 is a situation that characterizes oxidative decomposition that may occur in the event of thermal devulcanization and was also observed here [47]. The decrease in the peak characterizing carbon black at 1020 cm-1 also occurred for a similar reason [48]. The peak formed at 1538 cm-1 indicates the –C=O peak in the presence of Zn stearate in rubber recipes and the weakening of the peak is an indication of the decrease in crosslink density [49], [50].

The 900-400 cm-1 region of the spectrum is given in Figure 8-c. The most important indicator showing that devulcanization has occurred is the weakening observed in the S-S peaks formed at 460 and 550 cm-1 [38], [45], [50]-[54].

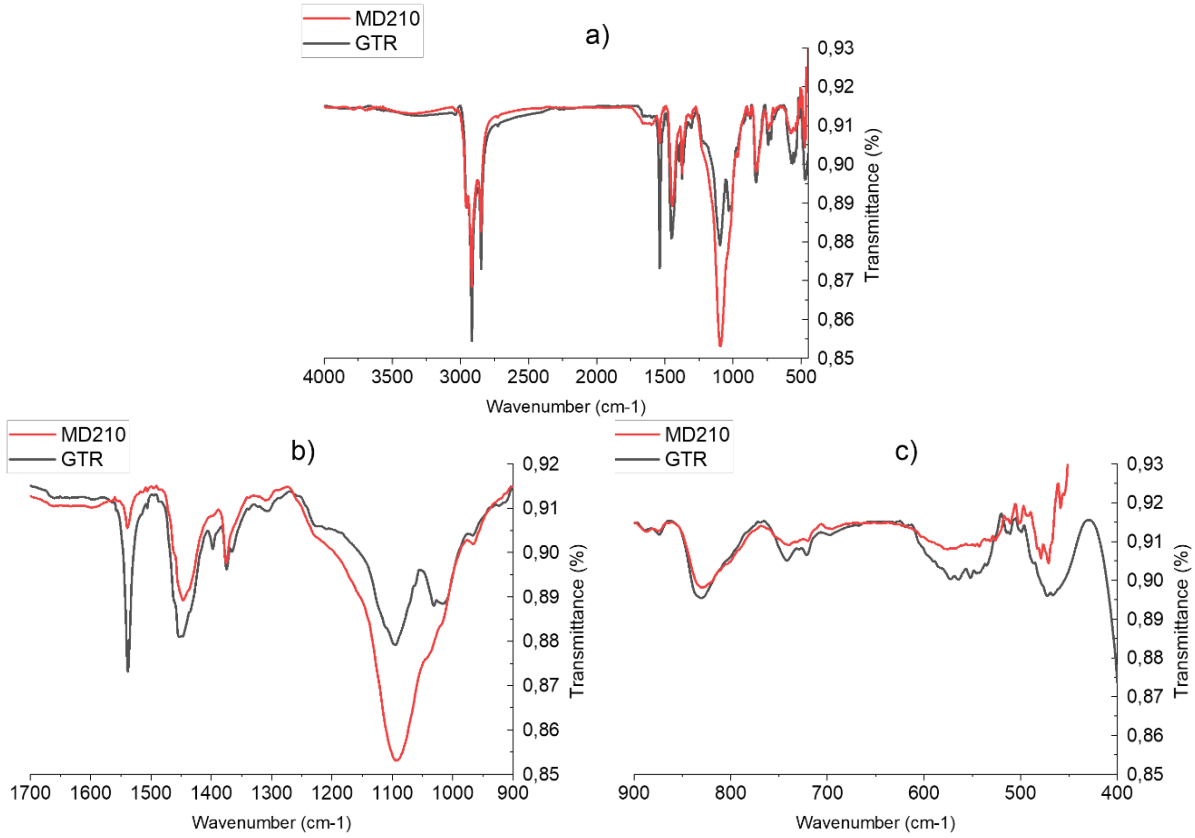


Figure 8. a) FTIR spectra of ground tire rubber and devulcanized sample; b) Spectra of ground tire rubber and devulcanized sample in the range of 1700-900 cm-1; c) Spectra of ground tire rubber and devulcanized sample in the range of 900-400 cm-1.

3.4 SEM Imaging of Microwave Devulcanized Samples

The SEM image of devulcanized ground tire rubber is shown in Figure 9. When compared with the structure of the ground tire rubber given in Figure 3, it was observed that the surface roughness of the devulcanized rubber increased. It has been stated in some studies that this situation is an indication of devulcanization [10], [48], [52], [55].

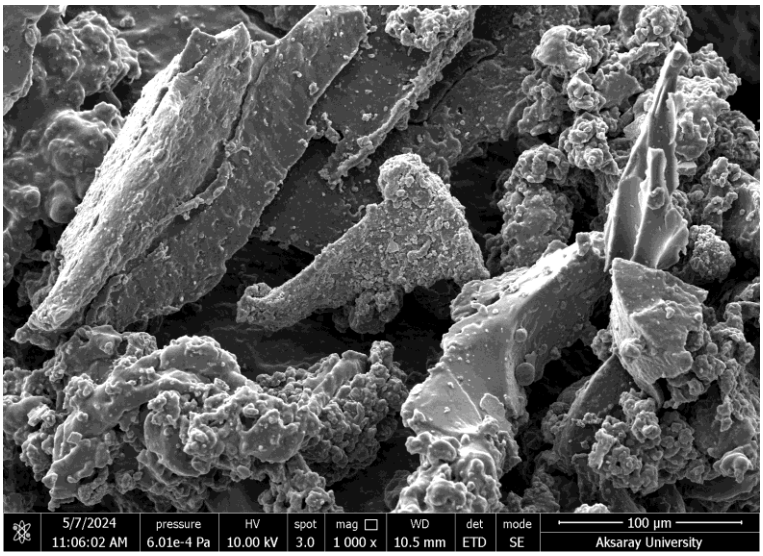


Figure 9. SEM image of devulcanized rubber.

4 CONCLUSION AND SUGGESTIONS

In this study, ground tire rubber with a particle size of less than 1 mm obtained by shredding waste tires at room temperature was subjected to microwave devulcanization. The results obtained because of the study are listed below:

- The soluble fractions obtained by extraction of devulcanized rubber changed depending on the devulcanization time and temperature. While the soluble fraction, which is an important parameter in terms of revealing the effectiveness of devulcanization, was %6.15 in ground tire rubber, this rate increased to %28.40 in the sample devulcanized at 240 °C.
- In the measurement of the crosslink densities of devulcanized rubber, it was observed that the crosslink density values in the samples devulcanized at 210 and 240 °C decreased significantly compared to the ground tire rubber and the devulcanization rate increased in these samples.
- The results obtained from the FTIR analysis performed after devulcanization revealed that the main polymer chain structure was not damaged and the sulfur crosslinks were broken as targeted.
- All the results obtained revealed that microwave treatment at appropriate temperatures is a suitable process for the devulcanization of waste tires.

Acknowledgements

This research was supported by Aksaray University Scientific Research Projects Coordination. (Project No: 2024-004).

Conflict of Interest Statement

There is no conflict of interest between the authors.

Statement of Research and Publication Ethics

The study is complied with research and publication ethics.

Artificial Intelligence (AI) Contribution Statement

This manuscript was entirely written, edited, analyzed, and prepared without the assistance of any artificial intelligence (AI) tools. All content, including text, data analysis, and figures, was solely generated by the authors.

Contributions of the Authors

Conceptualization İ.E. and F.K., Methodology İ.E. and F.K., Writing İ.E. Review and editing F.K. Supervision F.K. All authors have read and agreed to the published version of the manuscript.

REFERENCES

[1] *Smithers.com. [Online]. Available: https://www.smithers.com/resources/2023/november/infographic-overview-of-the-global-tires-market. [Accessed: 21-Jun-2025].*

[2] C. B. B. Luna, E. M. Araújo, D. D. Siqueira, D. D. de S. Morais, E. A. dos S. Filho, and M. V. L. Fook, "Incorporation of a recycled rubber compound from the shoe industry in polystyrene: Effect of SBS compatibilizer content," *J. Elastomers Plast.*, vol. 52, no. 1, pp. 3–28, 2020.

[3] R. Ghosh, *Design of a Devulcanization Process for Tire Material in a Twin Screw Extruder. Doktora Tezi*, vol. 87. The Netherlands, 2021.

[4] B. Adhikari, "Reclamation and recycling of waste rubber," *Prog. Polym. Sci.*, vol. 25, no. 7, pp. 909–948, 2000.

[5] A. Yehia, M. A. Mull, M. N. Ismail, Y. A. Hefny, and E. M. Abdel-Bary, "Effect of chemically modified waste rubber powder as a filler in natural rubber vulcanizates," *J. Appl. Polym. Sci.*, vol. 93, no. 1, pp. 30–36, 2004.

[6] J. Fiksel, B. R. Bakshi, A. Baral, E. Guerra, and B. DeQuervain, "Comparative life cycle assessment of beneficial applications for scrap tires," *Clean Technol. Environ. Policy*, vol. 13, no. 1, pp. 19–35, 2011.

[7] Abdel-Hakim, E. H. Awad, and K. F. El-Nemr, "Evaluation of composites based on virgin rubber/devulcanized rubber reinforced with chemically and radiation activated polyurethane scrap for possible applications," *Polym. Eng. Sci.*, vol. 64, no. 7, pp. 3059–3072, 2024.

[8] H. Chittella, L. W. Yoon, S. Ramarad, and Z.-W. Lai, "Rubber waste management: A review on methods, mechanism, and prospects," *Polym. Degrad. Stab.*, vol. 194, no. 109761, p. 109761, 2021.

[9] "Regulation on Control of End-of-Life Tires." *Ministry of Environment, Urbanisation and Climate Change*, Ankara, 2006.

[10] M. M. Phiri, M. J. Phiri, K. Formela, and S. P. Hlangothi, "Chemical surface etching methods for ground tire rubber as sustainable approach for environmentally-friendly composites development–a review," *Compos. B Eng.*, vol. 204, no. 108429, p. 108429, 2021.

[11] L. Bockstal, T. Berchem, Q. Schmetz, and A. Richel, "Devulcanisation and reclaiming of tires and rubber by physical and chemical processes: A review," *J. Clean. Prod.*, vol. 236, no. 117574, p. 117574, 2019.

[12] Dorigato, D. Rigotti, and G. Fredi, "Recent advances in the devulcanization technologies of industrially relevant sulfur-vulcanized elastomers," *Adv. Ind. Eng. Polym. Res.*, vol. 6, no. 3, pp. 288–309, 2023.

[13] R. Saputra, R. Walvekar, M. Khalid, C. T. Ratnam, N. M. Mubarak, and S. Dharaskar, "Devulcanisation of ground rubber tyre by novel ternary deep eutectic solvents," *J. Mol. Liq.*, vol. 306, no. 112913, p. 112913, 2020.

[14] E. Markl and M. Lackner, "Devulcanization technologies for recycling of tire-derived rubber: A review," *Materials (Basel)*, vol. 13, no. 5, p. 1246, 2020.

[15] R. Wintersteller, E. Markl, and M. Lackner, "Feedstock recycling of rubber – A review on devulcanization technologies," *Preprints*, 2020.

[16] L. Asaro, M. Gratton, S. Seghar, and N. Aït Hocine, "Recycling of rubber wastes by devulcanization," *Resour. Conserv. Recycl.*, vol. 133, pp. 250–262, 2018.

[17] L. Fontana, "Present Status of Desulfurization Technology," *Centerplastics Enterprise Ltd*, pp. 1–25, 2011.

[18] B. Kılıç, S. Akpınar, and B. Karaağaç, "Devulkanizasyon," *Kauçuk (Kauçuk Derneği)*, vol. 58, pp. 72–75, 2016.

[19] H. van Hoek, J. Noordermeer, G. Heideman, A. Blume, and W. Dierkes, "Best practice for DE-vulcanization of waste passenger car tire rubber granulate using 2-2'-dibenzamidodiphenyldisulfide as DE-vulcanization agent in a twin-screw extruder," *Polymers (Basel)*, vol. 13, no. 7, p. 1139, 2021.

[20] S. H. Lee, Z. X. Zhang, D. Xu, D. Chung, G. J. Oh, and J. K. Kim, "Dynamic reaction involving surface modified waste ground rubber tire powder/polypropylene," *Polym. Eng. Sci.*, vol. 49, no. 1, pp. 168–176, 2009.

[21] E. Bilgili, H. Arastoopour, and B. Bernstein, "Pulverization of rubber granulates using the solid-state shear extrusion process: Part II, Powder characterization," *Powder Technol.*, vol. 115, 2001.

[22] K. Naskar, S. K. De, A. K. Bhowmick, P. K. Pramanik, and R. Mukhopadhyay, "Characterization of ground rubber tire and its effect on natural rubber compound," *Rubber Chem. Technol.*, vol. 73, no. 5, pp. 902–911, 2000.

[23] T. Weber, A. Zanchet, R. N. Brandalise, J. S. Crespo, and R. C. R. Nunes, "Grinding and characterization of scrap rubbers powders," *J. Elastomers Plast.*, vol. 40, no. 2, pp. 147–159, 2008.

[24] K. Formela, A. Hejna, L. Zedler, X. Colom, and J. Canavate, "Microwave treatment in waste rubber recycling – recent advances and limitations," *Express Polym. Lett.*, vol. 13, no. 6, pp. 565–588, 2019.

[25] T. Zhang, L. Asaro, M. Gratton, and N. Aït Hocine, "An overview on waste rubber recycling by microwave devulcanization," *J. Environ. Manage.*, vol. 353, no. 120122, p. 120122, 2024.

[26] D. Á. Simon, D. Pirityi, P. Tamás-Bényei, and T. Bárány, "Microwave devulcanization of ground tire rubber and applicability in SBR compounds," *J. Appl. Polym. Sci.*, vol. 137, no. 6, 2020.

[27] C. Zhou, Y. Huang, Y. Zheng, and Z. Hua, "Hydrogen permeation behavior of rubber sealing materials for hydrogen infrastructure: Recent advances and perspectives," *Int. J. Hydrogen Energy*, vol. 59, pp. 742–754, 2024.

[28] X. Colom, M. Marín, M. R. Saeb, K. Formela, and J. Cañavate, "Recycling devulcanized EPDM to improve engineering properties of SBR rubber compounds," *Resour. Conserv. Recycl. Adv.*, vol. 23, no. 200227, p. 200227, 2024.

[29] D. De and D. De, "Processing and material characteristics of a reclaimed ground rubber tire reinforced styrene butadiene rubber," *Mater. Sci. Appl.*, vol. 02, no. 05, pp. 486–495, 2011.

[30] X. Colom, F. Carrillo-Navarrete, M. R. Saeb, M. Marin, K. Formela, and J. Cañavate, "Evaluation and rationale of the performance of several elastomeric composites incorporating devulcanized EPDM," *Polym. Test.*, vol. 121, no. 107976, p. 107976, 2023.

[31] D. De, A. Das, D. De, B. Dey, S. C. Debnath, and B. C. Roy, "Reclaiming of ground rubber tire (GRT) by a novel reclaiming agent," *Eur. Polym. J.*, vol. 42, no. 4, pp. 917–927, 2006.

[32] X. Sun, *The Devulcanization of Unfilled and Carbon Black Filled Isoprene Rubber Vulcanizates by High Power Ultrasound. Doktora Tezi*, University of Akron, USA, 2007.

[33] D. Sousa, *Polyethylene blends reinforced with nanometric fillers and tire waste devulcanized by microwaves*, France, 2018.

[34] M. Sabzekar, M. P. Chenar, S. M. Mortazavi, M. Kariminejad, S. Asadi, and G. Zohuri, "Influence of process variables on chemical devulcanization of sulfur-cured natural rubber," *Polym. Degrad. Stab.*, vol. 118, pp. 88–95, 2015.

[35] E. Broman, *Devulcanization and reuse of peroxide cured EPDM rubber for a greener world*, Karlskrona, Sweden, 2021.

[36] P. S. Garcia, F. D. B. de Sousa, J. A. de Lima, S. A. Cruz, and C. H. Scuracchio, "Devulcanization of ground tire rubber: Physical and chemical changes after different microwave exposure times," *Express Polym. Lett.*, vol. 9, no. 11, pp. 1015–1026, 2015.

[37] D. Á. Simon, D. Z. Pirityi, and T. Bárány, "Devulcanization of ground tire rubber: microwave and thermomechanical approaches," *Sci. Rep.*, vol. 10, no. 1, p. 16587, 2020.

[38] F. B. Musidin, *Microwave devulcanization of ground tyre rubber (GTR), MSc Thesis*, Barcelona, 2015.

[39] M. Molanorouzi and S. O. Mohaved, "Reclaiming waste tire rubber by an irradiation technique," *Polym. Degrad. Stab.*, vol. 128, pp. 115–125, 2016.

[40] V. K. Rajendran, *Process-Design For Devulcanization of Whole Truck Tire Rubber. PhD Thesis*, The Netherlands, 2016.

[41] M. Khavarnia and S. O. Movahed, "Butyl rubber reclamation by combined microwave radiation and chemical reagents," *J. Appl. Polym. Sci.*, vol. 133, no. 17, 2016.

[42] M. Vahdatbin and M. Jamshidi, "Using chemical agent in microwave assisted devulcanization of NR/SBR blends: An effective recycling method," *Resour. Conserv. Recycl.*, vol. 179, no. 106045, p. 106045, 2022.

[43] M. Shabani and M. Jamshidi, "Recycling NR/SBR waste using probe sonication as a new devulcanizing method; study on influencing parameters," *RSC Adv.*, vol. 12, no. 40, pp. 26264–26276, 2022.

[44] Ł. Zedler et al., "Preliminary investigation on auto-thermal extrusion of ground tire rubber," *Materials (Basel)*, vol. 12, no. 13, p. 2090, 2019.

[45] R. Barbosa and J. D. Ambrósio, "Devulcanization of natural rubber compounds by extrusion using thermoplastics and characterization of revulcanized compounds," *J. Polym. Res.*, vol. 26, no. 7, 2019.

[46] S. K. Ghosh et al., "Silane functionalization of sodium montmorillonite and halloysite (HNT) nanoclays by 'grafting to' method to improve physico-mechanical and barrier properties of LLDPE/clay nanocomposites," *Polym. Bull. (Berl.)*, vol. 80, no. 4, pp. 4307–4335, 2023.

[47] R. Pérez-Campos, J. Fayos-Fernández, and J. Monzó-Cabrera, "Real-time monitoring of ground-tire rubber microwave devulcanization with thermal and electrochemical sensors," *Measurement (Lond.)*, vol. 223, no. 113781, p. 113781, 2023.

[48] X. Colom, A. Faliq, K. Formela, and J. Cañavate, "FTIR spectroscopic and thermogravimetric characterization of ground tyre rubber devulcanized by microwave treatment," *Polym. Test.*, vol. 52, pp. 200–208, 2016.

[49] R. Saputra, R. Walvekar, M. Khalid, N. M. Mubarak, and M. Sillanpää, "Current progress in waste tire rubber devulcanization," *Chemosphere*, vol. 265, no. 129033, p. 129033, 2021.

[50] S. Rooj, G. C. Basak, P. K. Maji, and A. K. Bhowmick, "New route for devulcanization of natural rubber and the properties of devulcanized rubber," *J. Polym. Environ.*, vol. 19, no. 2, pp. 382–390, 2011.

[51] S. Azarabtin et al., "Effect of different devulcanization agents on the mechano-chemical devulcanization process of waste tires," *Mater. Today Commun.*, vol. 33, no. 104416, p. 104416, 2022.

[52] X. Zhang, P. Saha, L. Cao, H. Li, and J. Kim, "Devulcanization of waste rubber powder using thiobisphenols as novel reclaiming agent," *Waste Manag.*, vol. 78, pp. 980–991, 2018.

[53] Mangili, M. Oliveri, M. Anzano, E. Collina, D. Pitea, and M. Lasagni, "Full factorial experimental design to study the devulcanization of ground tire rubber in supercritical carbon dioxide," *J. Supercrit. Fluids*, vol. 92, pp. 249–256, 2014.

[54] S. Paul et al., "Optimization of scrap tire devulcanization process using Taguchi and DEAR method in a supercritical fluid extraction pilot scale setup," *Chem. Eng. Process.*, vol. 198, no. 109738, p. 109738, 2024.

[55] H. Ramezani et al., "Green and sustainable devulcanization of ground tire rubber using choline chloride–urea deep eutectic solvent," *RSC Sustainability*, vol. 2, no. 8, pp. 2295–2311, 2024.

BİTLİS EREN ÜNİVERSİTESİ
FEN BİLİMLERİ DERGİSİ

ISSN: 2147-3129 / e-ISSN: 2147-3188

Article Type	: Research Article	**Year**	: 2025
Received	: July 6, 2025	**Volume**	: 14
Revised	: September 16, 2025	**Issue**	: 3
Accepted	: September 20, 2025	**Pages**	: 1866-1890
DOI	: 10.17798/bitlisfen.1736282		

EFFECT OF RUBBER AND STEEL FİBERS OBTAINED FROM WASTE TIRES ON MECHANICAL AND PHYSICAL PROPERTIES OF CONCRETE: AN EXPERIMENTAL STUDY

Ersin AYHAN [1,*], Murat DOĞRUYOL [2]

[1] *Siirt University, Department of Civil Technology, Siirt, Türkiye*

[2] *Siirt University, Civil Engineering Department, Siirt, Türkiye*

**** Corresponding Author:*** *ersinayhan@siirt.edu.tr*

ABSTRACT

This study investigated the incorporation of rubber particles and steel fibers, derived from end-of-life vehicle tires, into concrete as partial replacements for fine aggregates, with the goal of enhancing sustainability in construction materials. Twelve concrete mixtures containing varying proportions of rubber (5%, 10%, and 15%) and steel fibers (0.4% and 0.8%) were prepared. The mechanical and physical properties of these mixtures were evaluated through compressive and flexural strength tests, ultrasonic pulse velocity measurements, water absorption analyses, and scanning electron microscopy. The results showed that while rubber significantly reduced compressive strength and increased porosity, it improved flexibility at low contents. In contrast, steel fibers increased density and flexural strength, and counteracted the negative effects of rubber by reducing internal voids and inhibiting crack propagation. The combined use of rubber and steel fibers yielded a complementary improvement in both mechanical performance and durability. These findings confirm the technical feasibility of incorporating waste tire materials into concrete and underscore their relevance in sustainable construction practices.

Keywords: Waste tires, Crumb rubber, Waste recycle tire steel fibers, Rubberized steel fiber concrete, Mechanical properties, Sustainability.

1 INTRODUCTION

Nowadays, with the increasing awareness of sustainable development and environmental protection, the recycling and reuse of industrial waste have received significant importance [1–4]. Environmental issues and the limited availability of natural areas are

increasing this trend. Trends in the use of industrial waste as a construction material in concrete have increased, especially due to the energy crisis that emerged in 1970 and environmental issues [5]. Especially in the automotive sector, vehicle tires, after completing their lifespan, become waste in large quantities, and the disposal of this waste leads to serious environmental problems. The decomposition of waste tires in nature can take hundreds of years, and during this process, they can cause soil, water, and air pollution. Therefore, in recent years, efforts to recycle waste tires for use in various fields have received momentum [6]. In the process of recycling waste tires, rubber and steel fibers are separated from the tires and can be used in various industrial applications. The use of waste tires does not have a positive effect on the compressive strength of concrete [7,8]. However, it is understood from many studies that waste tire rubbers and steel fibers contribute to the ductile behavior of concrete [9–12].

The use of these materials as aggregates in concrete mixtures provides both environmental benefits and the potential to improve the mechanical and physical properties of concrete. The addition of rubber particles to the concrete mix can increase the crack resistance of the concrete, enhance its impact resistance, and improve its thermal properties [13,14]. Similarly, the addition of steel fibers to concrete can enhance the tensile strength and toughness of the concrete, contributing to the increased durability of structures [15,16].

The use of waste rubber and steel in concrete as a replacement for traditional fine and coarse aggregates has been the subject of extensive research in recent years. The primary goal of these studies is to offer an environmentally sustainable alternative for the millions of discarded tires accumulating worldwide [6,17,18]. Therefore, adopting this approach can reduce the consumption of natural aggregates while significantly mitigating the environmental problems associated with burning or landfilling scrap tires [19].

Waste tire rubber (crumb rubber) has been used as a replacement for fine aggregate at a rate of 0-20%. As a result of the analysis of compressive strength, flexural strength, abrasion resistance, microstructure, and water permeability on concrete samples, it was determined that waste tire rubber could be used as a replacement for fine aggregate up to 7.5% without causing significant strength loss [18].

In the study conducted by Sengül (2016) [20], the use of waste steel fibers recovered from scrap tires and production steel fibers in concrete mixtures was examined. According to the study's results, both waste and production steel fibers were found to negatively affect the workability of concrete. It has been observed that production steel fibers reduce the compressive

strength of concrete by approximately 10%, whereas the compressive strengths of mixtures containing waste steel fibers remained at levels similar to the reference mixture. Additionally, it has been determined that the values of flexural strength and splitting tensile strength increase when using waste steel fibers recovered from scrap tires compared to plain concrete. However, no statistically significant difference has been found between the mechanical properties of production steel fibers and waste steel fibers.

The main aim of this study is to experimentally investigate the effects of rubber and steel fibers, recovered from end-of-life vehicle tires using mechanical methods, on the mechanical and physical properties of concrete when used as a fine aggregate substitute in concrete mixtures. In this context, concrete mixtures containing rubber and steel fiber additives in different proportions were prepared, and a comprehensive evaluation was conducted based on parameters such as compressive strength, flexural strength, water absorption rate, unit weight, and ultrasonic pulse velocity (UPV). Additionally, it is aimed to observe the changes in the internal structure of the concrete through scanning electron microscope (SEM) analysis. The study aims to contribute to both the improvement of concrete performance and the re-evaluation of waste tires as construction materials, thereby establishing a scientific foundation for the development of sustainable building technologies.

Toughness and ductility are widely recognized as key parameters in evaluating the post-cracking performance of fiber-reinforced concretes, as they provide valuable insights into energy absorption and deformation capacity [21–24]. While these values are not directly calculated in the present study, their importance is acknowledged, and they are suggested as essential aspects for future investigations.

2 MATERIAL AND METHOD

2.1 Material

The separation of rubber and steel fibers from vehicle tires is a process carried out using mechanical methods. Figure 1 [25], schematically shows the mechanical separation of rubber and steel fibers during the recycling process of waste tires. The process begins with the collection of scrap tires. Then, these tires are broken down into small pieces in machines called tire shredders. During the shredding process, the steel wires and rubber components inside the tires are revealed. The steel wires are separated from the rubber using the magnetic separation method. As a result of this process, steel wire and rubber are obtained separately. Rubber

particles are then classified according to their size using methods such as screening or air classification. At this stage, the rubber particles are generally processed to have a particle diameter in the range of 2-4 mm. Steel wires, on the other hand, are converted into finer steel fibers through the heel wire drawing process. These fibers are prepared for use as reinforcement in construction materials such as concrete. The mechanical separation process reduces the environmental impact of waste tires while allowing the recovered rubber and steel fibers to be used in industrial applications.

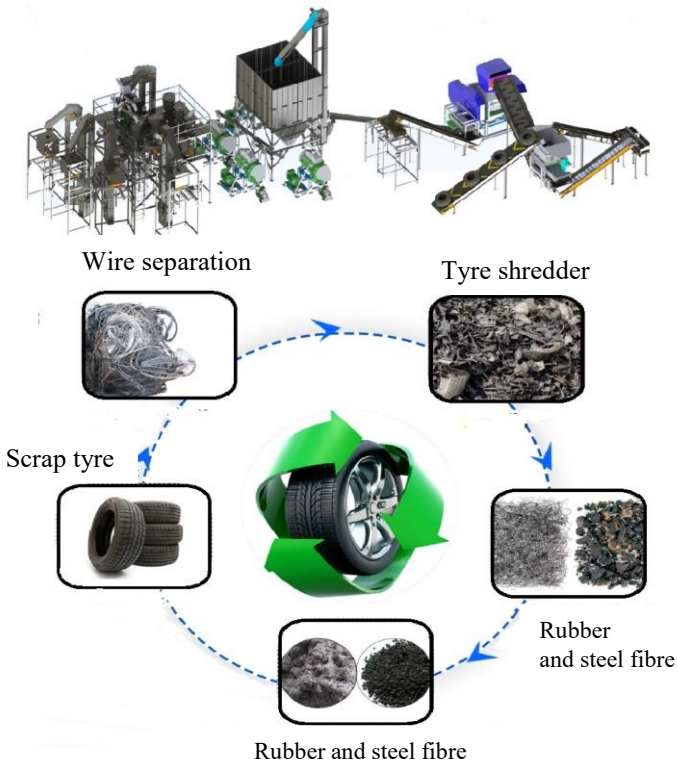


Figure 1. The process of separating rubber and steel fibers from waste tires using mechanical methods [25]

The waste rubber and steel fiber materials used in this experimental study were obtained from the Yakupoğulları Recycling Facility located in the Mardin Organized Industrial Zone [26] (Figure 2). The facility in question produces rubber for areas such as children's playgrounds, walking paths, and artificial turf fields; rubber powder for the production of wheels, shoe soles, vehicle mats, and conveyor belts; and waste steel fibers for use as raw materials in iron and steel factories. This facility contributes substantially to sustainable material production through recycling processes. The diameters of the steel fibers (Figure 3a) separated from heavy vehicle waste tires using mechanical methods were determined through measurements made with an electronic caliper. The analytical results revealed two distinct groups of steel fibers with differing diameters. Due to variations induced by mechanical fragmentation processes, fiber lengths were

reported as measurement ranges. The fineness values of the fibers were calculated by the ratio of their lengths to their diameters. Type 1 has a diameter of 0.11 mm and Type 2 has a diameter of 0.29 mm, with Type 1 having a length of 25-55 mm and a fineness of 227-500, while Type 2 has a length of 35-50 mm and a fineness of 120-172 (Table 2). After being separated by mechanical methods, the rubber crumbs (Figure 3b) were sieved and found to have a particle diameter in the range of 2−4 mm (Table 3). These findings provide important data for the characterization of the geometric properties of rubber crumbs and steel fibers obtained from waste tires.

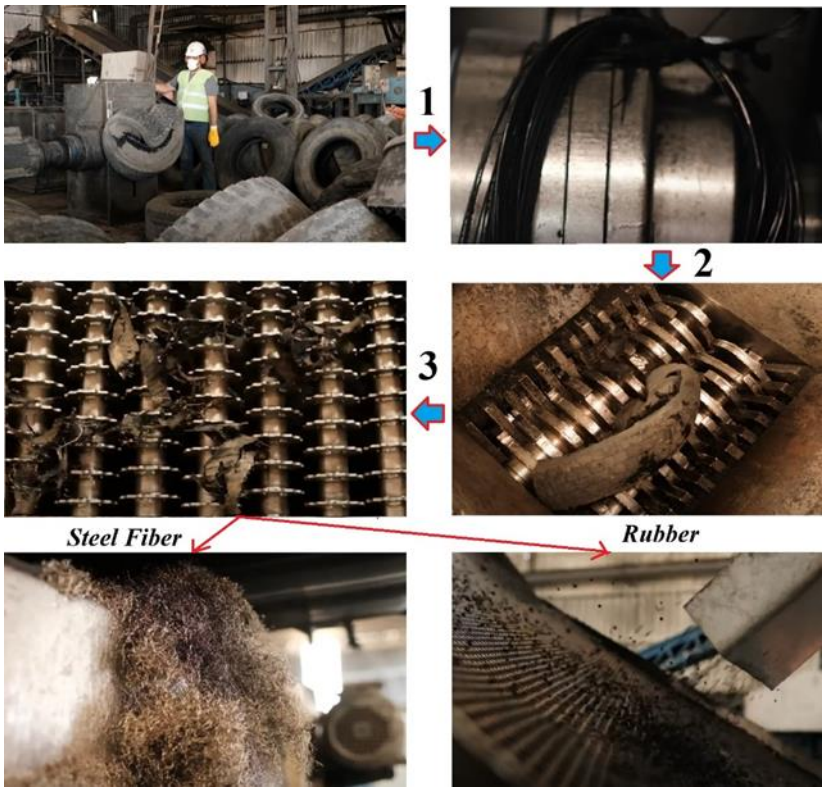


Figure 2. Production process of waste steel fiber and rubber [26]

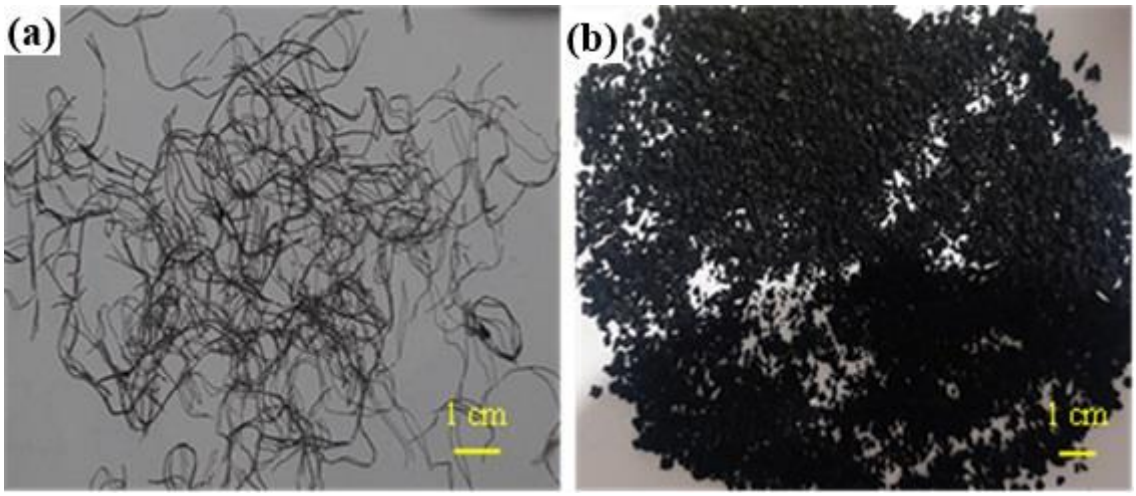


Figure 3. Waste tire rubber and steel fiber utilized in the experimental study.

2.1.1 Cement

In the experimental study, CEM I 42.5 N type Portland cement was utilized. The physical and chemical properties of the cement are offered in Table 1.

2.1.2 Aggregate

Natural aggregates were utilized in three size fractions: 0-4 mm (fine), 4-11.2 mm (medium), and 11.2-22.4 mm (coarse). The measured densities were 2.62 g/cm^3 for fine aggregate (sand), 2.69 g/cm^3 for medium aggregate, and 2.72 g/cm^3 for coarse aggregate. The sieve analysis of the natural aggregate utilized in the experiment is given in Figure 4.

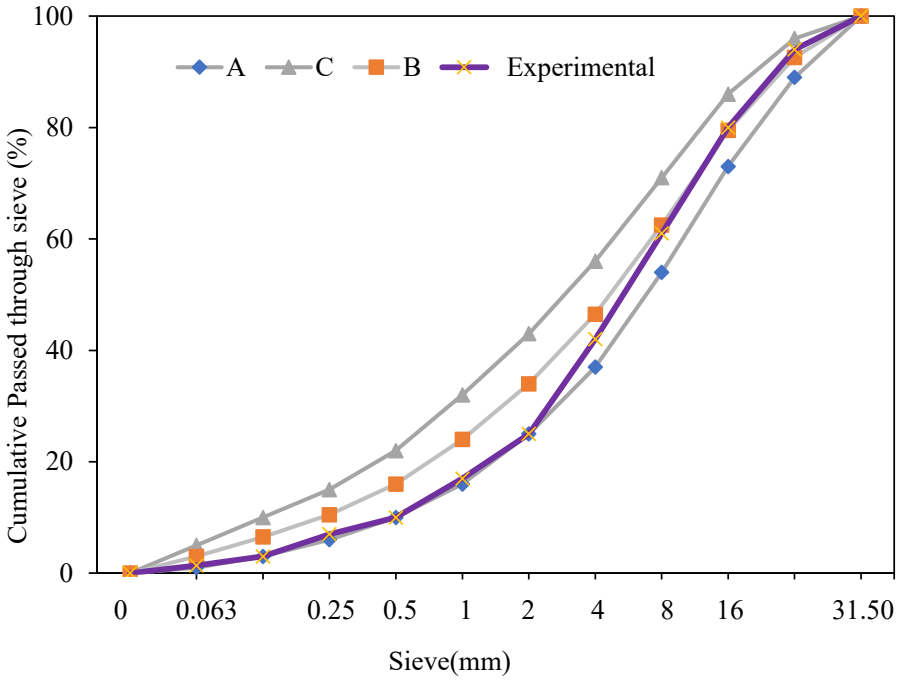


Figure 4. Aggregate gradation.

2.1.3 Waste Tire Product

The diameters of steel fibers extracted from heavy-vehicle waste tires via mechanical processing were measured using an electronic caliper. The results revealed two distinct groups of fibers with different diameters. Due to differences in length caused by mechanical breakage, fiber lengths are presented as a range. The aspect ratio (length-to-diameter ratio) was calculated to determine fiber fineness. Table 2 summarizes the physical properties of the steel fibers. As a result of sieve analysis of rubber crumbs obtained from waste tires after mechanical shredding, it has been determined that they have a diameter range of 2−4 mm. The physical properties of the rubber are offered in Table 3.

Table 1. The properties of cement

SiO_2	Al_2O_3	Fe_2O_3	CaO	MgO	SO_3	Na_2O	K_2O	LOI*	Blaine (m^2/kg)	Specific gravity (g/cm^3)
21.12	4.62	3.80	62.94	2.73	2.20	0.02	0.35	2.22	338	3.10

LOI = Loss on ignition*

Table 2. Characteristics of steel fiber [6]

Steel fiber	Diameter (mm)	Length (mm)	Slenderness	Weight ratio
Type I	0.11	25-55	227-500	61%
Type II	0.29	35-50	120-172	39%

Table 3. The properties of rubber

Diameter range	Fineness module	Specific gravity (g/cm^3)
2-4 mm	2.17	0.95

2.1.4 Superplasticizer

Superplasticizer The Chryso Delta Superplasticizer additive contributed to concrete strength by reducing the water/cement ratio. The dosage was set at 6 kg/m^3 of concrete.

The weight ratio given in Table 2 is provided as the percentage by weight of the waste steel fibers in the mixture, as the fibers are a blend of different sizes and diameters. The weight ratio is the percentage distribution by weight of the components that make up a mixture relative to the total weight of the mixture. It is a proportion used in designing the mixture, not a calculated property of the components. The fineness modulus (Table 3) is a calculated parameter that expresses the average particle size of the rubber granules used in the study as a numerical value, replacing the aggregate.

2.2 Method

The experiments were conducted in the Structural Laboratory of Siirt University using testing instruments and equipment calibrated by TÜRKAK (Figure 5).

To improve the mechanical properties of concrete and contribute to the recycling of waste tires, which are an environmental issue and prohibited from storage by the European Union [27,28], fine aggregate in concrete mixtures has been partially replaced with rubber

crumbs and steel fibers. In this context, rubber crumbs were used as a partial replacement for fine aggregate in volumes of 5%, 10%, and 15% (the acceptable replacement rate is up to 25% [29]), and steel fibers were used in volumes of 0.4% and 0.8% (the optimum steel fiber replacement rate is 0.56% − 0.64% [16]). These substitution ratios aim to both enhance the performance of concrete and evaluate waste tires by adopting a sustainable approach. The concrete mix design values and details are presented in Table 5. This study demonstrates that the use of environmentally friendly materials in concrete technology is possible and that waste management and building materials performance can be optimized to obtain them.

In the process of preparing the concrete mix, first, coarse aggregates, sand, and cement were placed into the mixer. These materials were mixed homogeneously in the mixer for three minutes before adding the superplasticizer and water. Then, water and superplasticizer were added, followed by steel fibers and rubber, and the mixer was run for an additional two minutes. As a result of this process, a homogeneous fresh concrete was obtained, particularly with the steel fibers evenly distributed.

Mechanical Analysis Concrete mixtures produced in accordance with the TS EN 206-1 [30] standard was poured into cylindrical molds sized 150 × 300 mm and beam molds sized 150 × 150 × 600 mm (Figure 6). The samples were removed from the molds after 24 h and cured for 28 days under conditions of 20 ± 5 °C temperature and 97 ± 2% humidity. This process provided standard curing conditions for the development of the mechanical properties of the concrete. Based on the experimental results, 12 different designs were prepared, and the average of the results obtained from analyses conducted on 3 samples for each design was taken.

The compressive strength tests of cylindrical concrete specimens with dimensions of 150 × 300 mm were carried out in accordance with the requirements of both the TS EN 12390-3 and the ASTM C39/C39M, ensuring the reliability and international comparability of the results.

The flexural strength test was performed on a 3-point bending test setup. The flexural strength test was performed on the beam specimens using the device in accordance with, TS EN 12390–5[31], ASTM C 78 [32] , and the flexural strength was calculated using the following equation (1):

$$\sigma_f = \frac{3 \times (F \times l)}{2 \times (b \times h^2)} \quad (1)$$

where σ_f is the flexural strength (MPa), F is the failure load (N), l is the span length (mm), b is the specimen width (mm), and h is the specimen height (mm).

2.2.1 Ultrasonic Experiment

Ultrasonic tests were conducted using the Proceq brand ultrasonic pulse velocity (UPV) measurement device (Pundit Lab) in accordance with the EN 12504-4 [33], ASTM C 597-02 [26], and ISO 1920-7:2004 standards to determine the sound transmission velocities. The ultrasonic tests, on the other hand, were conducted according to ASTM C597-02 [34], and the average value of three readings was calculated.

2.2.2 Water Absorption

Water absorption was measured on 28-day cured specimens following oven-drying at 105°C for 24 h to constant mass. Then, the samples were placed in a water-filled tank and left for 24 hours to determine the saturated dry surface weight. The water absorption of the concrete samples was measured according to equation (2) in accordance with the TS 3624 [35] standard.

$$Water\ absorption\ (\%) = \frac{W_s - W_d}{W_d} \tag{2}$$

$W_s = water - saturated\ weight\ (kg)$

$W_d = dry\ weight (kg)$

2.2.3 Scanning Electron Microscope (SEM) Analysis

Prior to SEM imaging, sample surfaces were sputter-coated with gold (Au) to ensure conductivity. The specimens were then placed in the SEM chamber for examination. Microstructural characterization was performed using a Hitachi SU3500 scanning electron microscope to analyze surface morphology.



Figure 5. The Siirt University Building Materials Laboratory, Where Experimental Studies Are Conducted

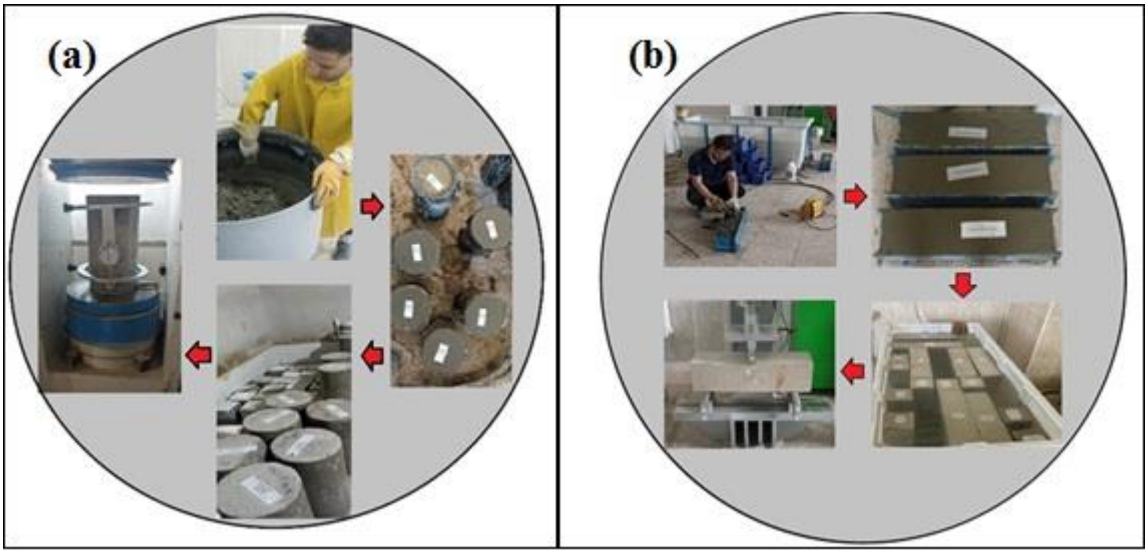


Figure 6. Processes for compressive strength (a) and flexural (b) tests

Table 4. Concrete mix codes (%)

Materials	Mix ID											
	PL	K5C0	K10C0	K15C0	K5C4	K10C4	K15C4	K5C8	K10C8	K15C8	K0C4	K0C8
Rubber	0	5	10	15	5	10	15	5	10	15	0	0
Steel Fiber	0	0	0	0	0.4	0.4	0.4	0.8	0.8	0.8	0.4	0.8

Table 5. 1 m^3 concrete mix ratios (kg)

Mix ID	Cement	Corse Aggregate	Fine Aggregate			Water	Chemical additive
			Sand	Rubber	Steel Fiber		
PL	350	1026.33	813.75	0	0	175	6.0
K5C0	350	1026.33	773.06	13.51	0	175	6.0
K10C0	350	1026.33	732.37	27.02	0	175	6.0
K15C0	350	1026.33	691.69	40.53	0	175	6.0
K5C4	350	1026.33	762.58	13.51	28.36	175	6.0
K10C4	350	1026.33	721.89	27.02	28.36	175	6.0
K15C4	350	1026.33	681.21	40.53	28.36	175	6.0
K5C8	350	1026.33	752.10	13.51	56.72	175	6.0
K10C8	350	1026.33	711.41	27.02	56.72	175	6.0
K15C8	350	1026.33	670.73	40.53	56.72	175	6.0
K0C4	350	1026.33	803.27	0	28.36	175	6.0
K0C8	350	1026.33	792.79	0	56.72	175	6.0

3 RESULTS AND DISCUSSION

3.1 Water Absorption

The water absorption rate of concrete is a critical parameter in terms of durability and service life [36]. According to Figure 7, the measured water absorption rate for the reference concrete sample (PL) was determined to be 4.44%. In the rubber-modified concrete samples (K5C0, K10C0, K15C0), the water absorption rates were measured as 4.48%, 4.80%, and 5.45%, respectively. These results indicate that the rubber additive enhances the water absorption rate of the concrete [13]. The formation of voids within the concrete matrix by rubber has been considered the primary reason for this enhance in water absorption rate [18].

In concrete samples with steel fiber additives (K0C4, K0C8), the water absorption rates were measured as 2.60% and 2.33%, respectively. The results demonstrate that incorporating steel fibers reduces concrete's water absorption while enhancing its tensile strength. The fibers act as crack-arresting components, restricting crack propagation and promoting a denser microstructure. This situation causes water to penetrate less into the concrete and reduces the water absorption rate [37]. However, in cases where steel fibers are not evenly distributed, voids can form within the concrete, which can increase the water absorption rate [38]. The combined use of rubber and steel fibers in concrete has been effective in reducing the voids caused by rubber and has ensured that the water absorption rate remains below the PL value. This situation

can be explained by the steel fibers filling the voids created by the rubber within the concrete matrix, resulting in a denser and more homogeneous structure. To reduce the water absorption rate of rubber-modified concrete, the use of steel fibers, which facilitate better compatibility of rubber with the concrete matrix, provides a significant advantage in improving the physical and mechanical properties of the concrete. This approach can be considered an effective strategy, especially for enhancing the durability and water permeability performance of rubber-modified concrete.

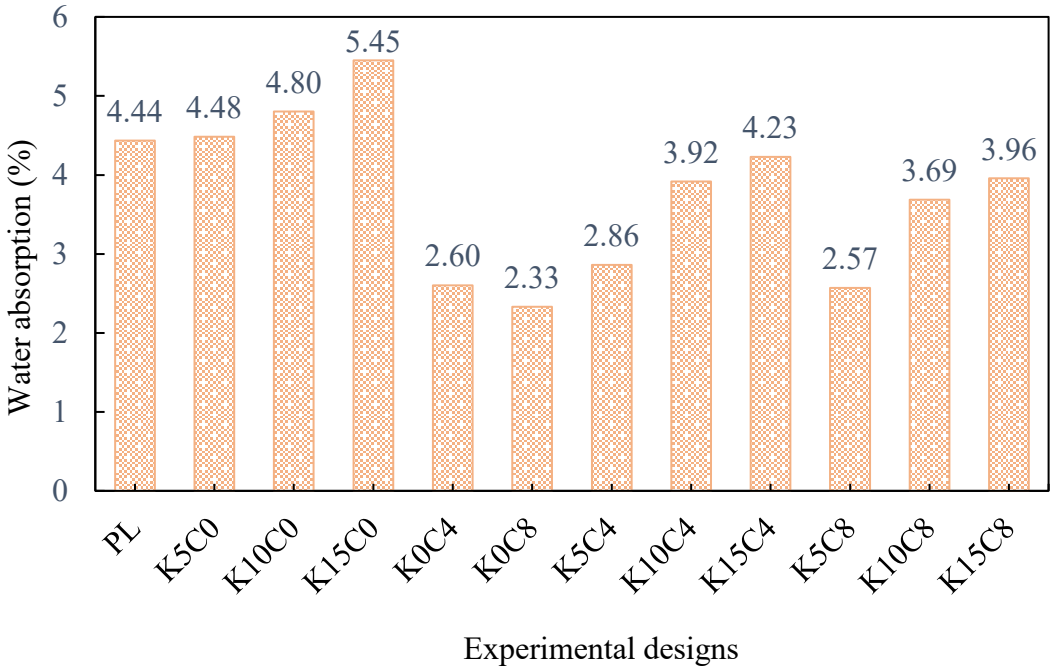


Figure 7. Water absorption

3.2 Unit Volume Weight

The density of a substance is defined as the mass per unit volume. All samples were measured by dividing their masses by the mold dimensions (150 mm × 300 mm) after curing at room temperature for 28 days. As the rubber fiber ratio increased, it was observed that the unit volume weight decreased. According to Figure 8, the density of the PL mixture was 2371.08 kg/m^3, while in the K15C0 mixture, this value decreased to 2289.55 kg/m^3. This situation indicates that rubber fibers reduce the density of the material [13,39]. On the other hand, the addition of steel fibers has increased the unit volume weight. For example, in the K0C8 mixture, the density was measured as 2406.84 kg/m^3. It has been determined that steel fibers increase the density of the material. It is a finding noted by Harshavardhan and Bala Murugan that the

density of concrete increases with the addition of aggregates or reinforcement fibers with higher specific gravity [40].

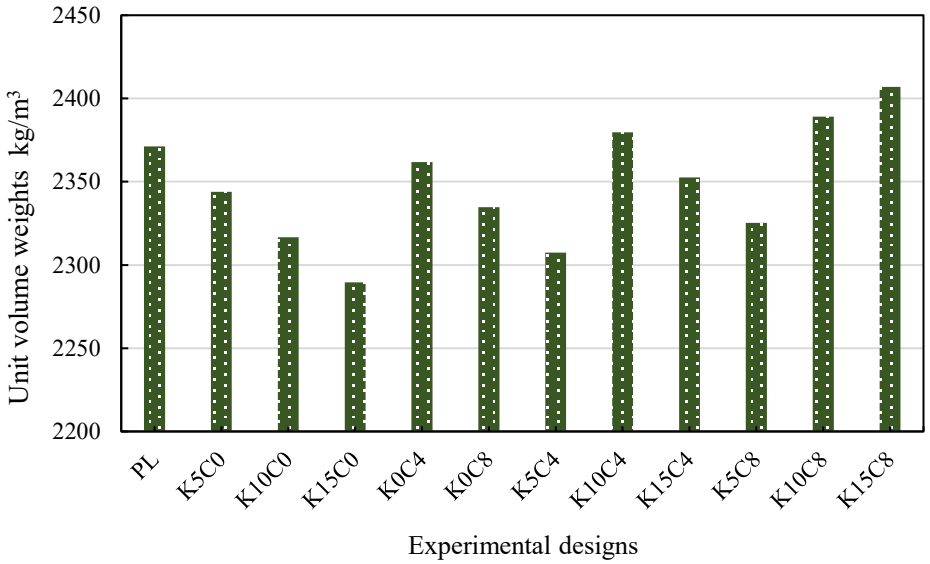


Figure 8. Unit volume weights

3.3 Ultrasonic Pulse Velocity

UPV is an important parameter that provides information about the internal structure, density, and homogeneity of concrete. UPV values depend on factors such as voids, cracks, and density in the internal structure of the concrete. UPV values are used to evaluate the quality of concrete. Table 6 shows the UPV values of the concrete samples and the concrete quality classification based on the BIS 13311-92-Part-I [41] standard according to these values. As long as the UPV values are in the range of 3660 m/s to 4580 m/s, the samples can be categorized as being in good condition, which means they are free from large voids or cracks that could affect the structural reliability of the concrete [42]. Figure 9 presents a schematic simulation illustrating the bridging effect of rubber aggregates and steel fibers. Observations indicate that crumb rubber particles inhibit the propagation of micro-cracks within the cement matrix, while their elastic properties enhance energy absorption [43]. Especially at high crack propagation levels, steel fibers effectively bridged the cracks, and this effect continued until the moment of fracture. The SEM observations presented in Figure 10 clearly reveal the effect of the material's characteristics on the void structure, and these findings are consistent with the results of UPV analysis and water absorption analysis. It has been determined that the addition of rubber crumbs, in particular, causes the formation of voids and microcracks within the material. However, it has been observed that the use of steel fibers plays an important role in reducing

these cracks and improving the mechanical properties of the material. These results highlight the effectiveness of steel fibers in optimizing the performance of composite materials and reveal that they are an important parameter to consider in material design. This finding is also supported by Rambo et al. (2014) [44], who examined the effect of fiber hybridization on the fracture behavior of concrete. In the study, it was demonstrated that the combination of rubber aggregate and steel fibers improved the energy absorption by increasing the crack resistance of the concrete, thereby enhancing the toughness of the concrete. These findings demonstrate that incorporating both rubber aggregates and steel fibers in concrete can substantially improve its mechanical performance [45].

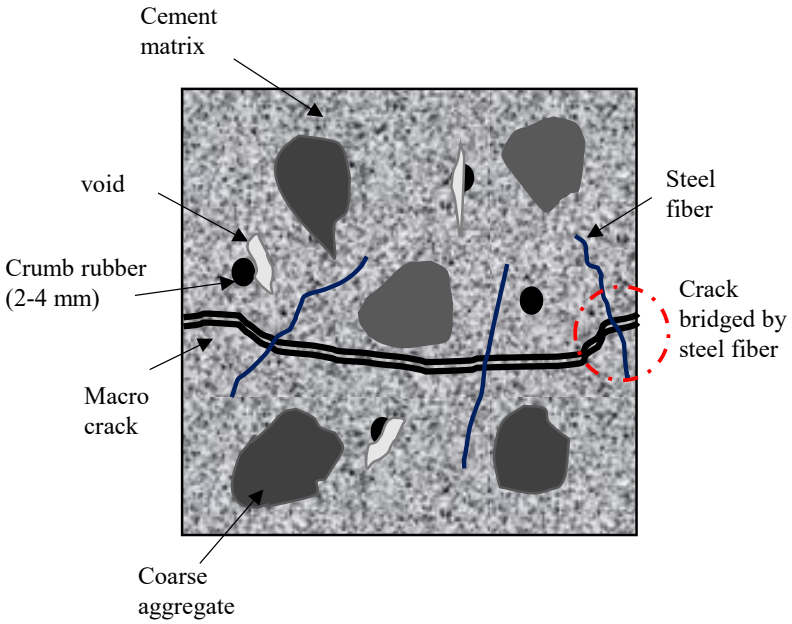


Figure 9. The effect of rubber and steel fibers on crack characterization in a concrete matrix [44]

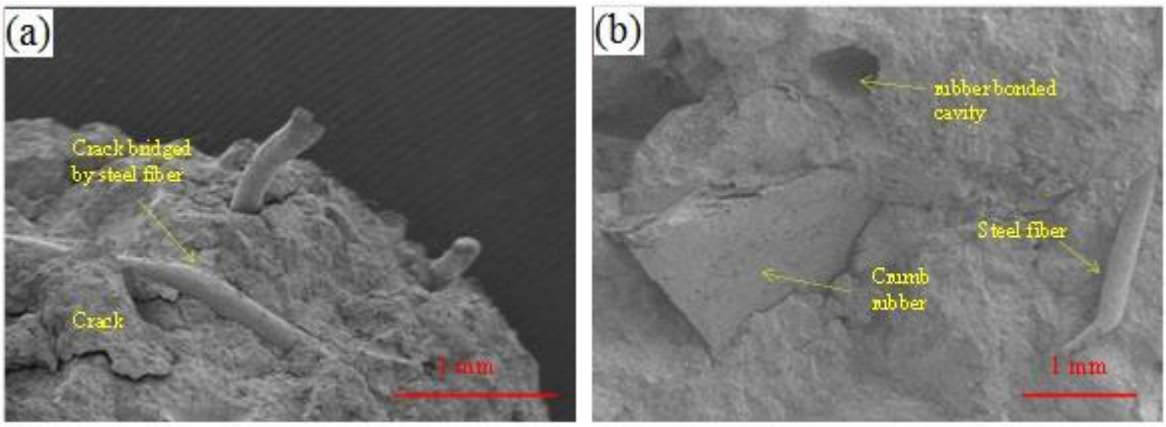


Figure 10. SEM image of the behavior of steel fibers (a) and rubber (b) in a concrete matrix

According to Table 6, the reference PL concrete without rubber and steel fibers has the highest UPV value (4667 m/s) and is of excellent quality class. This indicates that the concrete has a dense and homogeneous structure [46,47]. However, as the rubber content increases, the UPV values decrease [29]. This indicates that rubber reduces the density of concrete and creates voids in the internal structure [48]. However, even with a rubber content of up to 15%, the concrete still remains in a good quality class. Increasing the crumb rubber content to a limit of 25% keeps the alters in the mechanical properties of the rubberized concrete mix within an acceptable range [29]. The addition of steel fibers has maintained UPV values and improved the quality of the concrete [6,45]. Especially the mixtures containing only steel fibers (K0C4 and K0C8) have placed in the excellent quality class.

Table 6. Ultrasonic pulse velocity (UPV) and concrete quality classification.

Mix ID	UPV (m/s)	Concrete quality classification according to the BIS 13311-92-Part-I standard [33].	
		UPV (m/s)	Concrete quality classification
PL	4667	> 4500	Excellent
K5C0	4542	3500-4500	Good
K10C0	4340	3000-3500	Medium
K15C0	3832	< 3000	Doubtful
K5C4	4550		
K10C4	3910		
K15C4	3670		
K5C8	4515		
K10C8	4163		
K15C8	4050		
K0C4	4641[8]		
K0C8	4588[8]		

3.4 Mechanical Properties

The mechanical analysis results of the concrete were obtained in accordance with TS EN 206-1. The results are presented in Table 7.

According to Table 7, the measured compressive strength value for PL has been determined to be 53.22 MPa. In the rubber-modified concrete samples (K5C0, K10C0, K15C0), the compressive strength values were reduced by 16%, 23%, and 41%, respectively. These results indicate that the rubber additive significantly reduces the compressive strength of concrete [49]. The voids created by rubber within the concrete matrix and the weak bond between the aggregate and the cement matrix can be considered the main reasons for this

decrease in compressive strength [50]. In concrete samples with steel fiber additives (K0C4, K0C8), the compressive strength values were reduced by 29% and 18%, respectively. In the literature, different results have been reported regarding the effect of steel fiber addition on the compressive strength of concrete. Some studies have reported that the addition of steel fibers causes an increase in compressive strength [51–53], while other studies have stated that steel fibers have no significant effect on compressive strength [15,54]. However, some researchers have suggested that it would be beneficial to conduct more studies on steel fiber-reinforced concrete to achieve more definitive results [55,56].

Steel fibers play an important role in controlling crack formation in concrete. When concrete begins to crack under load, steel fibers prevent the propagation of these cracks, thereby increasing the strength of the concrete. This is particularly a critical factor for flexural strength [57]. Steel fibers increase the energy dissipation capacity of concrete. This makes the concrete more durable under sudden loads or impact and improves its flexural strength [12,16]. The flexural strength of the PL mix was measured at 6.76 MPa. The designs K0C4 and K0C8, which include steel fiber addition, improved the flexural strength by 5.3% and 16.4% respectively compared to PL. However, when rubber was added to the concrete mix, it was observed that more voids and pores formed within the concrete structure. Rubber particles do not fully bond with the concrete matrix, resulting in a decrease in the density of the concrete and an increase in its porosity. This situation negatively affects the flexural strength of the concrete [58,59]. In rubber-added concretes, the K5C0 mixture improved the flexural strength by 16.6% compared to PL, while the K10C0 and K15C0 mixtures decreased it by 13.5% and 23.8%, respectively. These results indicate that rubber increases the flexibility of concrete, but significantly reduces its strength at high ratios. The addition of steel fibers partially compensates for the negative effect of rubber on flexural strength. Especially the K5C8 and K10C8 mixtures with high steel fiber content significantly increase the flexural strength, thereby balancing this negative effect.

Although experimental compressive and flexural strength results were obtained for the 12 different mix designs given in Table 7, the 3D surface graphs in Figure 11 were generated on a 16-point grid. This approach was adopted not to add supplementary data or predictions, but to provide a smoother and more continuous graphical representation of the experimental results. By using this arrangement, the trends between the measured points were visualized more clearly, thereby facilitating a better interpretation of the effects of the WS and WR variables on the mechanical performance.

Table 7. Mechanical results (28-day)

Mix ID	Compressive strength	σ*	Flexural strength	σ
	MPa		MPa	
PL	53.22	1.32	6.76	0.10
K5C0	45.94	3.36	7.88	0.15
K10C0	43.27	2.29	5.85	0.12
K15C0	37.86	3.28	5.15	0.12
K5C4	40.43	1.98	7.40	0.15
K10C4	34.66	1.93	6.53	0.10
K15C4	33.18	1.61	6.47	0.10
K5C8	38.42	2.00	7.98	0.32
K10C8	36.01	2.68	7.75	0.20
K15C8	34.92	1.97	5.94	0.19
K0C4	41.17[8]	1.86	7.12[8]	0.16
K0C8	44.96[8]	2.59	7.87[8]	0.32

σ* =Standard deviation

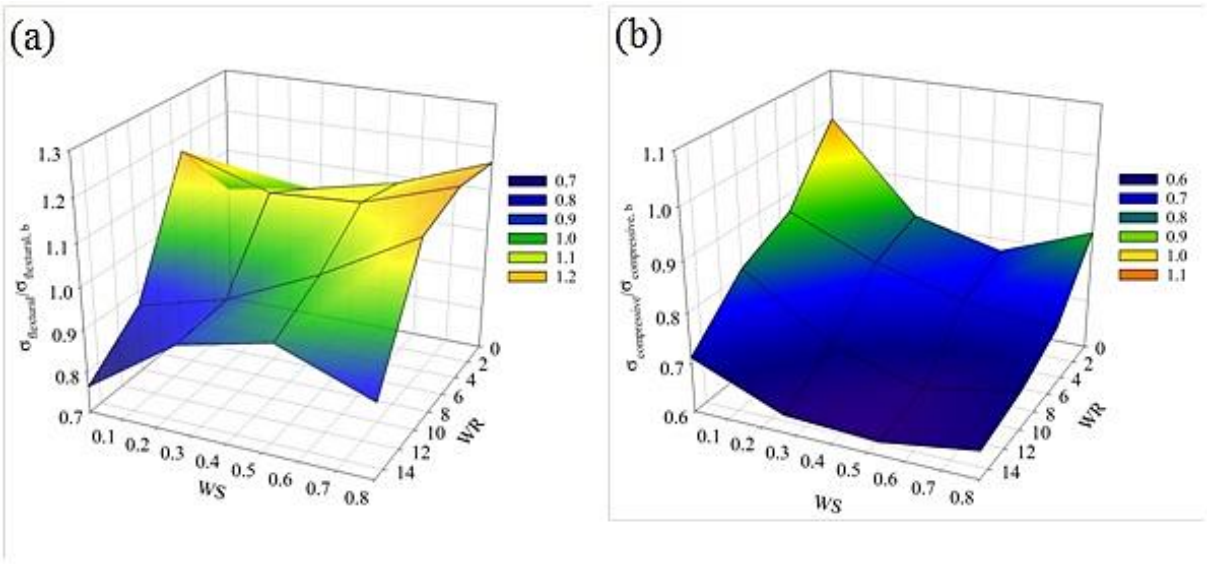


Figure 11. According to concrete mixtures, (a) Flexural strength; (b) Effect on compressive strength, (WS: steel fiber; WR: rubber).

3.5 UPV-Compressive Strength Relationship

According to Figure 12, there is a general positive correlation between UPV and compressive strength [60]. As the UPV value increases, the compressive strength also tends to increase. However, this relationship is not exactly linear, and deviations are observed in some cases. PL has the highest correlation between UPV and compressive strength with R^2= 0.97. Rubber concretes, on the other hand, are the designs with the weakest correlation. Rubber

reduces the density of concrete, lowers its elastic modulus, and increases crack formation [29,45].

These factors directly affect the relationship between UPV and compressive strength, causing the correlation to weaken. Rubber and steel fiber combinations perform better, especially as the steel fiber ratio increases. This shows that steel fibers compensate for the negative effects of rubber. The presence of steel fibers plays an important role in maintaining the relationship between UPV and compressive strength, especially in concrete where rubber is used as a substitute. Therefore, combinations of rubber and steel fibers should be carefully balanced to optimize the performance of concrete.

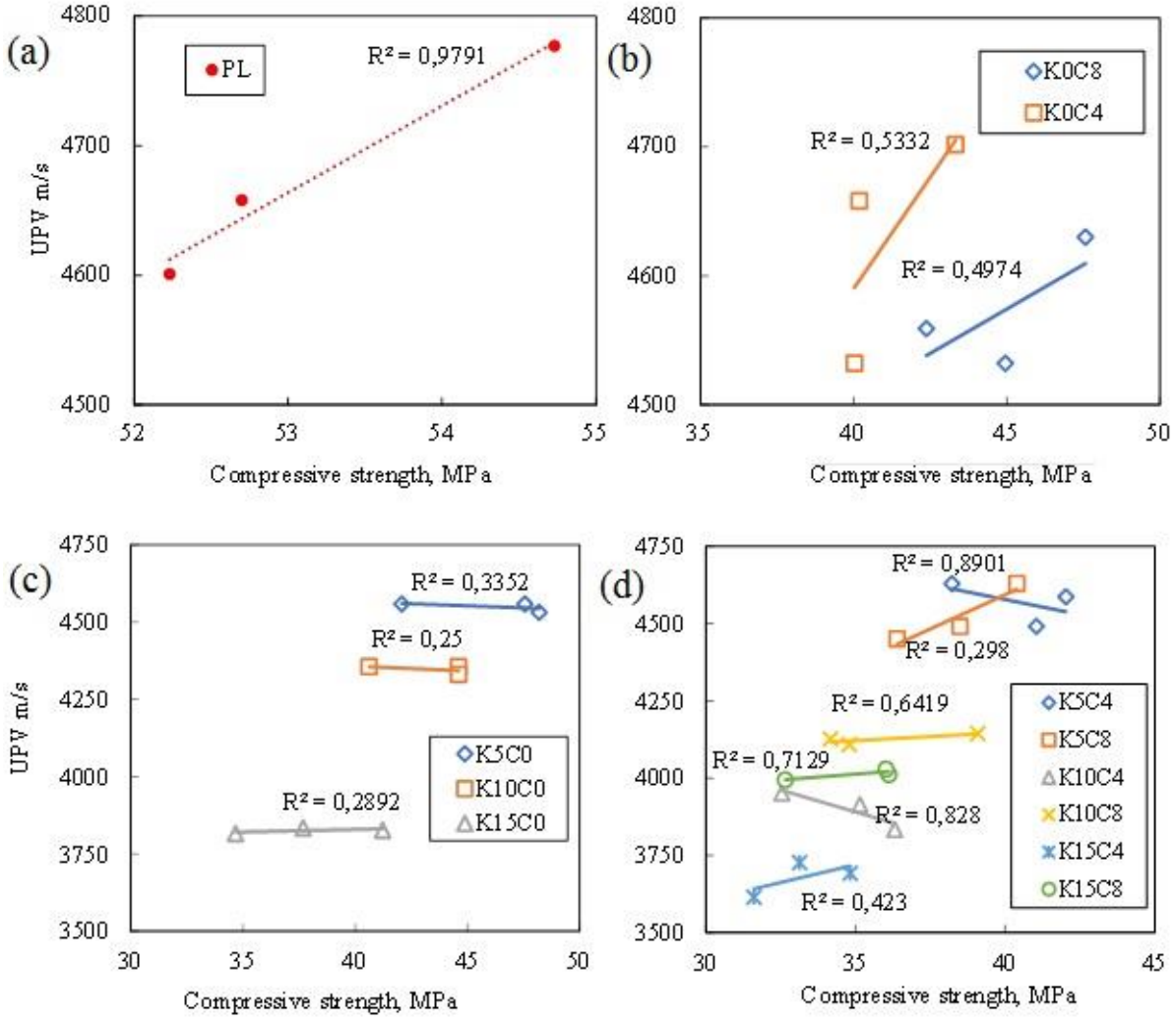


Figure 12. (a) Observation (PL) (b) steel fiber (c) rubber (d) the relationship between UPV-compressive strength of samples using steel fiber and rubber together

Researchers have conducted various experimental studies to evaluate the performance of concrete reinforced with recycled materials. Gül and Naseer (2019) [61] prepared concrete

mixtures containing recycled rubber and steel fibers and conducted compression and flexural tests. In their studies, it was found that the addition of rubber reduces the compressive strength of concrete, while steel fibers increase its flexural strength. However, unit weight, ultrasonic UPV, water absorption, and (SEM analyzes were not evaluated in this study. Rahim et al. (2024) [62] conducted a study on the use of rubber and steel fibers in concrete and found that steel fibers significantly contribute to crack resistance. Additionally, it has been observed that the combined use of rubber and steel fiber yields acceptable optimal results that contribute to sustainability. However, the fact that waste tire steel fiber was used in the current study while industrial steel fiber was used in the previous study constitutes a significant difference. In the current study, SEM analyzes were performed. Fu et al. (2018)[63] investigated the effects of rubber and steel fiber on concrete performance. The studies concluded that using rubber alone reduces compressive strength, while adding steel fibers increases tensile strength, and using both materials together improves ductile behavior. While industrial steel fiber and waste tire rubber were used in the example study, the fact that UPV experiments and SEM analyzes were conducted in the current study constitutes a methodological difference. Liu and colleagues (2020) [64] investigated the effect of adding steel fibers to rubberized concrete. It has been observed that the addition of rubber causes a decrease in compressive and tensile strength, while steel fibers increase bending and tensile strength and positively contribute to crack resistance. In the current study, the use of UPV analysis and waste tire steel fibers differs from the previous study, as the previous study used steel fibers with standard properties. Gao et al. (2022) [65]investigated the effect of recycled rubber particles and steel fibers on the compressive toughness of concrete. It has been found that using rubber alone reduces compressive strength, while adding steel fibers partially compensates for this decrease. In the case study, industrial-type steel fibers were used, and SEM and UPV tests were not performed. Luo et al. (2020) [66]added steel fibers to improve the mechanical properties and freeze-thaw resistance of rubber-modified concrete. It has been determined that steel fibers contribute particularly to bending strength and toughness, and that bending strength is more prominent than compressive strength in cold weather conditions. In the current study, rubber granules and waste tire steel are used, while in the reference study, rubber powder and standard steel fibers were used. Additionally, an UPV test was performed in the current study. Finally, Yan et al. (2024) [67] experimentally investigated the effect of rubber particles obtained from waste tires and recycled spiral steel fibers on the mechanical properties and toughness of concrete. It has been found that the use of waste tires causes a loss in mechanical properties, but both materials positively contribute to the toughness properties, and the spiral fibers increase the bending and

compressive strength. While the example study used spiral steel fibers, the current study used waste tire steel and rubber; additionally, UPV and SEM analyzes were performed. The use of waste materials, especially waste tires, in concrete mixtures stands out as a more environmentally friendly practice. In literature reviews, the complete data on the comprehensive experiments included in the current study, which combine both rubber and steel fiber-reinforced concrete derived from waste vehicle tires, is not available in one place. In conclusion, the fact that all the steel fibers and rubber used are derived from waste tires, the number and scope of the experiments conducted, and the concrete contents differ from many similar studies in the literature, making an independent contribution to the field.

4 CONCLUSIONS AND RECOMENDATION

This study experimentally investigated the influence of waste tire-derived rubber aggregates and steel fibers on the mechanical and physical properties of concrete. The results demonstrate that incorporating these recycled materials offers substantial technical benefits while simultaneously addressing environmental concerns. The key findings can be summarized as follows:

The measured compressive strength for the reference concrete (PL) was 53.22 MPa, while in the rubber-modified concretes with 5%, 10%, and 15% rubber, this value decreased by 16%, 23%, and 41%, respectively. This decrease is due to the voids created by rubber within the concrete matrix and the weak bond between the aggregate and the cement matrix. The contribution of rubber to mechanical properties improved the flexural strength of the K5C0 sample by 16.6%. However, as the rubber content increased, it decreased by 13.5% and 23.8% for K10C0 and K15C0, respectively.

The designs K0C4 and K0C8, which include steel fiber addition, improved the flexural strength by 5.3% and 16.4% respectively compared to PL. This shows that steel fibers increase the tensile strength of concrete, limiting the expansion of cracks.

The combined use of rubber and steel fibers has been considered an effective strategy for improving the mechanical properties of concrete. Especially the K5C8 and K10C8 mixtures have significantly increased the flexural strength, balancing the negative effects of rubber.

The measured unit weight of PL is 2371.08 kg/m^3, while in rubber concrete K15C0, this value has been reduced to 2289.55 kg/m^3, a decrease of 3%. This decrease is due to the low density of rubber and the voids it creates within the concrete matrix. It shows that rubber can

be utilized in the production of lightweight concrete. On the other hand, it increased the unit volume weight by 1.5% in K0C8 with steel fibers. This situation can be explained by the high density of the steel fibers and their ability to make the concrete matrix more compact.

The water absorption rate for PL was 4.44%, while it increased to 5.45% in rubber concrete K15C0. In steel fiber-reinforced K0C8, the water absorption rate has decreased to 2.33%. This situation indicates that the steel fibers increase the density of the concrete, causing less water to penetrate within the concrete.

UPV values have decreased as the rubber content increased. However, the 0.4% and 0.8% steel fiber replacements have maintained the UPV values and improved the quality of the concrete. This shows that steel fibers maintain the internal structural integrity of concrete and serve as an effective additive against void formation.

Conflict of Interest Statement

There is no conflict of interest between the authors.

Statement of Research and Publication Ethics

The study is complied with research and publication ethics.

Artificial Intelligence (AI) Contribution Statement

This manuscript was entirely written, edited, analyzed, and prepared without the assistance of any artificial intelligence (AI) tools. All content, including text, data analysis, and figures, was solely generated by the authors.

Contributions of the Authors

First Author contributed to experimental work, investigation, data analysis, interpretation, and writing. Second Author contributed to study design, visualization, interpretation, and writing.

REFERENCES

[1] Karaşin and M. Doğruyol, "An experimental study on strength and durability for utilization of fly ash in concrete mix," *Adv. Mater. Sci. Eng.*, vol. 2014, 2014, doi: 10.1155/2014/417514.

[2] Karasin, M. Hadzima-Nyarko, E. Işık, M. Doğruyol, I. B. Karasin, and S. Czarnecki, "The effect of basalt aggregates and mineral admixtures on the mechanical properties of concrete exposed to sulphate attacks," *Materials*, vol. 15, 2022, doi: 10.3390/ma15041581.

[3] F. Z. Çiçek, R. Pekgökgöz, S. B. Kazanasmaz, A. Sarıışık, and F. Avcil, "Effect of fly ash and metakaolin substituted forms on structural properties in light mortar with pumice aggregate," *Bitlis Eren Univ. J. Sci.*, vol. 13, pp. 709–722, 2024, doi: 10.17798/bitlisfen.1479126.

[4] M. Doğruyol and M. Durmaz, "The effect of pistachio vera shell ash (PSA) on concrete performance," *Bitlis Eren Univ. J. Sci.*, 2025, doi: 10.17798/bitlisfen.1602440.

[5] E. Güneyisi, M. Gesoğlu, Z. Algın, and H. Yazıcı, "Effect of surface treatment methods on the properties of self-compacting concrete with recycled aggregates," *Constr. Build. Mater.*, vol. 64, pp. 172–183, 2014, doi: 10.1016/j.conbuildmat.2014.04.090.

[6] M. Doğruyol, E. Ayhan, and A. Karaşin, "Effect of waste steel fiber use on concrete behavior at high temperature," *Case Stud. Constr. Mater.*, vol. 20, 2024, doi: 10.1016/j.cscm.2024.e03051.

[7] F. Liu, G. Chen, L. Li, and Y. Guo, "Study of impact performance of rubber reinforced concrete," *Constr. Build. Mater.*, vol. 36, pp. 604–616, 2012, doi: 10.1016/j.conbuildmat.2012.06.014.

[8] E. Ayhan, M. Doğruyol, F. Kıpçak, and A. Karaşin, "Atık taşıt lastik çelik lifinin beton davranışına etkisi," *DUJE*, 2024, doi: 10.24012/dumf.1468070.

[9] Siddika, Md. A. Al Mamun, R. Alyousef, Y. H. M. Amran, F. Aslani, and H. Alabduljabbar, "Properties and utilizations of waste tire rubber in concrete: A review," *Constr. Build. Mater.*, vol. 224, pp. 711–731, 2019, doi: 10.1016/j.conbuildmat.2019.07.108.

[10] N. N. Gerges, C. A. Issa, and S. A. Fawaz, "Rubber concrete: Mechanical and dynamical properties," *Case Stud. Constr. Mater.*, vol. 9, p. e00184, 2018, doi: 10.1016/j.cscm.2018.e00184.

[11] O. Atahan and A. Ö. Yücel, "Crumb rubber in concrete: Static and dynamic evaluation," *Constr. Build. Mater.*, vol. 36, pp. 617–622, 2012, doi: 10.1016/j.conbuildmat.2012.04.068.

[12] F. Köksal, A. Ilki, and M. A. Tasdemir, "Optimum mix design of steel-fibre-reinforced concrete plates," *Arab J. Sci. Eng.*, vol. 38, pp. 2971–2983, 2013, doi: 10.1007/s13369-012-0468-y.

[13] M. T. Lakhiar et al., "Thermal and mechanical properties of concrete incorporating silica fume and waste rubber powder," *Polymers (Basel)*, vol. 14, no. 4858, 2022, doi: 10.3390/polym14224858.

[14] C. Bu, D. Zhu, L. Liu, X. Lu, Y. Sun, L. Yu, Y. OuYang, X. Cao, F. Wang, "Research progress on rubber concrete properties: A review," *J. Rubber Res.*, vol. 25, pp. 105–125, 2022, doi: 10.1007/s42464-022-00161-8.

[15] M. Yalçin, C. Taşdemir, and M. A. Taşdemir, "Çelik lif donatılı betonların performans sınıflarının belirlenmesi," *İTÜ Dergisi*, vol. 8, no. 6, 2011.

[16] F. Bayramov, A. Ilki, C. Taşdemir, M. A. Taşdemir, and M. Yerlikaya, "An optimum design for steel fiber reinforced concretes under cyclic loading," in *Proc. 5th Int. Conf. Fracture Mech. Concrete Struct.*, 2004, pp. 1121–1128.

[17] F. Pelisser, N. Zavarise, T. A. Longo, and A. M. Bernardin, "Concrete made with recycled tire rubber: Effect of alkaline activation and silica fume addition," *J. Clean. Prod.*, vol. 19, pp. 757–763, 2011, doi: 10.1016/j.jclepro.2010.11.014.

[18] S. Thomas, R. C. Gupta, P. Kalla, and L. Cseteneyi, "Strength, abrasion and permeation characteristics of cement concrete containing discarded rubber fine aggregates," *Constr. Build. Mater.*, vol. 59, pp. 204–212, 2014, doi: 10.1016/j.conbuildmat.2014.01.074.

[19] S. Elbialy, W. Ibrahim, S. Mahmoud, N. M. Ayash, and H. Mamdouh, "Mechanical characteristics and structural performance of rubberized concrete: Experimental and analytical analysis," *Case Stud. Constr. Mater.*, vol. 21, p. e03727, 2024, doi: 10.1016/j.cscm.2024.e03727.

[20] O. Sengul, "Mechanical behavior of concretes containing waste steel fibers recovered from scrap tires," *Constr. Build. Mater.*, vol. 122, pp. 649–658, 2016, doi: 10.1016/j.conbuildmat.2016.06.113.

[21] F. Köksal, K. S. Rao, Z. Babayev, and M. Kaya, "Effect of steel fibres on flexural toughness of concrete and RC beams," *Arab J. Sci. Eng.*, vol. 47, pp. 4375–4384, 2022, doi: 10.1007/s13369-021-06113-5.

[22] H. T. Wang and L. C. Wang, "Experimental study on static and dynamic mechanical properties of steel fiber reinforced lightweight aggregate concrete," *Constr. Build. Mater.*, vol. 38, pp. 1146–1151, 2013, doi: 10.1016/j.conbuildmat.2012.09.016.

[23] W. Abbass, M. I. Khan, and S. Mourad, "Evaluation of mechanical properties of steel fiber reinforced concrete with different strengths of concrete," *Constr. Build. Mater.*, vol. 168, pp. 556–569, 2018, doi: 10.1016/j.conbuildmat.2018.02.164.

[24] R. V. Balendran, F. P. Zhou, A. Nadeem, and A. Y. T. Leung, "Influence of steel fibres on strength and ductility of normal and lightweight high strength concrete," *Build. Environ.*, vol. 37, pp. 1361–1367, 2002, doi: 10.1016/S0360-1323(01)00109-3.

[25] "Lastik geri dönüşüm tesisi," Yıldız Endüstri, Accessed: Jun. 20, 2024. [Online]. Available: https://www.yildizendustri.com.tr/?page_id=7671

[26] "Yakupoğulları geri dönüşüm," Accessed: Apr. 10, 2023. [Online]. Available: https://yakupogullari.com.tr/

[27] B. S. Mohammed, K. M. Anwar Hossain, J. T. Eng Swee, G. Wong, and M. Abdullahi, "Properties of crumb rubber hollow concrete block," *J. Clean. Prod.*, vol. 23, pp. 57–67, 2012, doi: 10.1016/j.jclepro.2011.10.035.

[28] A. Benazzouk, O. Douzane, K. Mezreb, B. Laidoudi, and M. Quéneudec, "Thermal conductivity of cement composites containing rubber waste particles: Experimental study and modelling," *Constr. Build. Mater.*, vol. 22, pp. 573–579, 2008, doi: 10.1016/j.conbuildmat.2006.11.011.

[29] Marie, "Zones of weakness of rubberized concrete behavior using the UPV," *J. Clean. Prod.*, vol. 116, pp. 217–222, 2016, doi: 10.1016/j.jclepro.2015.12.096.

[30] TS EN 206+A2, *Beton - Özellik, performans, imalat ve uygunluk*, 2021.

[31] TS EN 12390-5, *Testing hardened concrete – Part 5: Flexural strength of specimens of hardened concrete*, 2010.

[32] ASTM C78-09, *Standard test method for flexural strength of concrete (using simple beam with third-point loading)*, 2010.

[33] EN 12504-4, *Testing concrete – Part 4: Determination of ultrasonic pulse velocity*, British Standards Institution, 2004.

[34] ASTM C597-02, *Pulse velocity through concrete*, ASTM International, West Conshohocken, PA, USA, 2003.

[35] TS 3624, *Sertleşmiş betonda özgül ağırlık, su emme ve boşluk oranı tayin metodu*, n.d.

[36] Y. T. Erdoğan, *Materials of Construction*. Ankara: M.E.T.U. Press, 2002.

[37] N. Ganesan, R. Abraham, and S. D. Raj, "Durability characteristics of steel fibre reinforced geopolymer concrete," *Constr. Build. Mater.*, vol. 93, pp. 471–476, 2015, doi: 10.1016/j.conbuildmat.2015.06.014.

[38] M. A. Faris et al., "Comparison of hook and straight steel fibers addition on Malaysian fly ash-based geopolymer concrete on the slump, density, water absorption and mechanical properties," *Materials*, vol. 14, no. 1310, 2021, doi: 10.3390/ma14051310.

[39] R. Khaloo, M. Dehestani, and P. Rahmatabadi, "Mechanical properties of concrete containing a high volume of tire–rubber particles," *Waste Manag.*, vol. 28, pp. 2472–2482, 2008, doi: 10.1016/j.wasman.2008.01.015.

[40] C. Harshavardhan and S. BalaMurugan, "Study on high-density concrete reinforced with steel fiber at elevated temperatures," *ARPN J. Eng. Appl. Sci.*, vol. 11, pp. 11415–11420, 2016.

[41] IS 13311, *Non-destructive testing of concrete methods of test, Part 1*, Bureau of Indian Standards, Manak Bhavan, New Delhi, India, 1992.

[42] V. M. Malhotra, *Testing hardened concrete: Nondestructive methods*. Ottawa, Canada: CRC Press, 1976.

[43] Afshinnia and A. Poursaee, "The potential of ground clay brick to mitigate alkali–silica reaction in mortar prepared with highly reactive aggregate," *Constr. Build. Mater.*, vol. 95, pp. 164–170, 2015, doi: 10.1016/j.conbuildmat.2015.07.155.

[44] D. A. S. Rambo, F. de A. Silva, and R. D. T. Filho, "Effect of steel fiber hybridization on the fracture behavior of self-consolidating concretes," *Cem. Concr. Compos.*, vol. 54, pp. 100–109, 2014, doi: 10.1016/j.cemconcomp.2014.02.004.

[45] A. T. Noaman, B. H. Abu Bakar, and H. M. Akil, "Investigation on the mechanical properties of rubberized steel fiber concrete," *Eng. Struct. Technol.*, vol. 9, no. 2, pp. 79–92, 2017, doi: 10.3846/2029882x.2017.1309301.

[46] M. Doğruyol, "Characterisation of acrylic copolymer treated concretes and concretes of reinforced concrete buildings collapsed in the 6 February 2023 Mw = 7.8 Kahramanmaraş (Türkiye) earthquake," *Eng. Fail. Anal.*, vol. 161, 2024, doi: 10.1016/j.engfailanal.2024.108249.

[47] M. Doğruyol, A. Gönül, and M. Başboğa, "Comparative analysis of cement-based and historic gypsum-based mortars for historical restoration: Implications on mechanical and thermal compatibility," *J. Build. Eng.*, vol. 109, p. 112982, 2025, doi: 10.1016/j.jobe.2025.112982.

[48] N. Segre and I. Joekes, "Use of tire rubber particles as addition to cement paste," *Cem. Concr. Res.*, vol. 30, no. 9, pp. 1421–1425, 2000, doi: 10.1016/S0008-8846(00)00373-2.

[49] Liu, Q. Guan, L. Zhang, C. Liu, X. Chen, and X. Cai, "Evaluation of the compressive-strength reducing behavior of concrete containing rubber aggregate," *Cleaner Mater.*, vol. 4, p. 100057, 2022, doi: 10.1016/j.clema.2022.100057.

[50] Y.-F. Wu, S. M. S. Kazmi, M. J. Munir, Y. Zhou, and F. Xing, "Effect of compression casting method on the compressive strength, elastic modulus and microstructure of rubber concrete," *J. Clean. Prod.*, vol. 264, p. 121746, 2020, doi: 10.1016/j.jclepro.2020.121746.

[51] Y. Li and Y. Li, "Experimental study on performance of rubber particle and steel fiber composite toughening concrete," *Constr. Build. Mater.*, vol. 146, pp. 267–275, 2017, doi: 10.1016/j.conbuildmat.2017.04.100.

[52] M. V. Mohod, "Performance of steel fiber reinforced concrete," *Int. J. Eng. Sci.*, vol. 1, no. 12, pp. 1–4, 2012.

[53] W. Abbass, M. I. Khan, and S. Mourad, "Evaluation of mechanical properties of steel fiber reinforced concrete with different strengths of concrete," *Constr. Build. Mater.*, vol. 168, pp. 556–569, 2018, doi: 10.1016/j.conbuildmat.2018.02.164.

[54] C. G. Papakonstantinou and M. J. Tobolski, "Use of waste tire steel beads in Portland cement concrete," *Cem. Concr. Res.*, vol. 36, no. 9, pp. 1686–1691, 2006, doi: 10.1016/j.cemconres.2006.05.015.

[55] K. M. Liew and A. Akbar, "The recent progress of recycled steel fiber reinforced concrete," *Constr. Build. Mater.*, vol. 232, p. 117232, 2020, doi: 10.1016/j.conbuildmat.2019.117232.

[56] S.-C. Lee, J.-H. Oh, and J.-Y. Cho, "Compressive behavior of fiber-reinforced concrete with end-hooked steel fibers," *Materials*, vol. 8, no. 4, pp. 1442–1458, 2015, doi: 10.3390/ma8041442.

[57] A. Alsaif, L. Koutas, S. A. Bernal, M. Guadagnini, and K. Pilakoutas, "Mechanical performance of steel fibre reinforced rubberised concrete for flexible concrete pavements," *Constr. Build. Mater.*, vol. 172, pp. 533–543, 2018, doi: 10.1016/j.conbuildmat.2018.04.010.

[58] M. Akgül, O. Doğan, and S. Etli, "Investigation of mechanical properties of granulated waste rubber aggregates substituted self-compacting concrete mortar produced with different cement," *Uluslararası Mühendislik Araştırma ve Geliştirme Dergisi*, vol. 12, no. 3, pp. 787–798, 2020, doi: 10.29137/umagd.734614.

[59] Köksal M., A., "Atık lastiklerden çıkan kauçuk ve tellerin beton üretiminde kullanılması," Ph.D. dissertation, Necmettin Erbakan University, Konya, Türkiye, 2024.

[60] Q. A. Yousif, I. Bedirhanoglu, M. E. Aydin, and Z. Zebari, "The effect of age on the compressive strength of concrete by using ultrasonic pulse velocity," in *Interdependence between Structural Engineering and Construction Management*, F. Ozevin, Ed. 2019.

[61] S. Gul and S. Naseer, "Concrete containing recycled rubber steel fiber," *Procedia Struct. Integr.*, vol. 18, pp. 101–107, 2019, doi: 10.1016/j.prostr.2019.08.144.

[62] M. Abdul Rahim, S. N. A. Ramli, S. Salehuddin, N. Mohamad Ibrahim, A. Ayob, and N. L. Rahim, "The mechanical properties of crumb rubber steel fiber concrete (CRSFC)," *J. Teknol.*, vol. 86, pp. 69–75, 2024, doi: 10.11113/jurnalteknologi.v86.20951.

[63] C. Fu, H. Ye, K. Wang, K. Zhu, and C. He, "Evolution of mechanical properties of steel fiber-reinforced rubberized concrete (FR-RC)," *Compos. B Eng.*, vol. 160, pp. 158–166, 2019, doi: 10.1016/j.compositesb.2018.10.045.

[64] R. Liu, H. Li, Q. Jiang, and X. Meng, "Experimental investigation on flexural properties of directional steel fiber reinforced rubberized concrete," *Structures*, vol. 27, pp. 1660–1669, 2020, doi: 10.1016/j.istruc.2020.08.007.

[65] Y. Gao et al., "Experimental investigation on static compressive toughness of steel fiber rubber concrete," *Rev. Adv. Mater. Sci.*, vol. 61, no. 1, pp. 576–586, 2022, doi: 10.1515/rams-2022-0260.

[66] T. Luo, C. Zhang, C. Sun, X. Zheng, Y. Ji, and X. Yuan, "Experimental investigation on the freeze–thaw resistance of steel fibers reinforced rubber concrete," *Materials*, vol. 13, no. 5, p. 1260, 2020, doi: 10.3390/ma13051260.

[67] J. Yan, Y. Gao, M. Tang, N. Ding, Q. Xu, M. Peng, and H. Zhao, "Experimental study on the mechanical properties of recycled spiral steel fiber-reinforced rubber concrete," *Buildings*, vol. 14, no. 4, p. 897, 2024, doi: 10.3390/buildings14040897.

BİTLİS EREN ÜNİVERSİTESİ
FEN BİLİMLERİ DERGİSİ

ISSN: 2147-3129 / e-ISSN: 2147-3188

Article Type : Research Article
Received : July 8, 2025
Revised : September 30, 2025
Accepted : September 30, 2025
DOI : 10.17798/bitlisfen.1737223

Year : 2025
Volume : 14
Issue : 3
Pages : 1891-1920

ASSESSMENT OF ERGONOMIC RISK FACTORS FOR SUSTAINABLE AGRICULTURAL PRACTICES BASED ON PICTURE FUZZY LODECI-ARTASI APPROACH

Veysel TATAR [1]

[1] *Artvin Çoruh University, Department of Maritime and Port Management, Artvin, Türkiye, ytatar@artvin.edu.tr*

ABSTRACT

The implementation of proactive risk management from an occupational health and safety (OHS) perspective is of paramount importance in ensuring sustainable production and enhancing work efficiency among employees. This paper aims to develop an innovative occupational health and safety risk assessment (OHSRA) model for workers exposed to ergonomic risks during agricultural harvesting operations. The approach to achieving this objective is through the implementation and validation of two innovative methodologies: the LOgarithmic DEcomposition Of Criteria Importance (LODECI) and Alternative Ranking Technique based on Adaptive Standardized Intervals (ARTASI) methods. This study utilized an integrated approach, incorporating LODECI's weighting method and ARTASI's prioritization technique, based on picture fuzzy sets which employs Fine-Kinney risk parameters, to prioritize ergonomic risk factors affecting work-related musculoskeletal disorders (WMSDs). The validation of the proposed model is conducted through a sensitivity and comparative analysis. The research findings indicated that the five most significant hazards in harvesting operations are ERH_{11} (Land of harvesting area), ERH_2 (Repetitive motion), ERH_4 (Standing for a long time), ERH_{12} (Work stress) and ERH_9 (Unsuitable climatic conditions), respectively. In finally concluding the paper, discussion is provided of potential future research directions.

Keywords: ARTASI, Ergonomic risk assessment, LODECI, Picture fuzzy sets, Sustainable agriculture, Work-related musculoskeletal disorders.

ABBREVIATIONS AND NOMENCLATURE

ARTASI	Alternative Ranking Technique based on Adaptive Standardized Intervals	$\widetilde{\Re}$	Initial decision risk matrix
LODECI	LOgarithmic DEcomposition Of Criteria Importance	$\mathbb{D}_{ij}$	Decomposition value
PFS	Picture fuzzy sets	$\mathbb{L}_j$	Logarithmic decomposition value
WMSDs	Work-related musculoskeletal disorders	$\mathbb{V}_{ij}^{+}$	The degree of usefulness of the ideal value
FST	Fuzzy Set Theory	$\mathbb{V}_{ij}^{-}$	The degree of usefulness of the anti-ideal value
OHSRA	Occupational Health and Safety Risk Assessment	P_i^{+}	The aggregate degree of utility for the ideal value
PFWA	Picture Fuzzy Weighted Averaging	P_i^{-}	The aggregate degree of utility for the anti-ideal value
IFS	Intuitionistic Fuzzy Sets	$\mathbb{F}_i$	The final utility functions value
OHS	Occupational Health and Safety	P	Probability
MCDM	Multi-Criteria Decision-Making	E	Exposure
PFNs	Picture fuzzy numbers	C	Consequence

1 INTRODUCTION

The OHSRA process is a proactive approach aimed at safeguarding workers' health and safety by preventing work-related accidents and occupational diseases caused by hazards in the workplace. The identification and evaluation of the major work-related hazards for the implementation of preventive measures constitutes a critical activity within the framework of the OHSRA [1]. The standard risk management process is comprised of four major phases: (i) the hazard determination, (ii) the classification of risk, (iii) the risk control measures implementation, and (iv) the regular review and monitoring of the implementation of the control measures [2].

Globally, musculoskeletal disorders impact a reported 1.71 billion people [3]. The prevalence of musculoskeletal pain in the world's working population is between 50% and 80% [4]. The aetiology of WMSDs is multifactorial, involving biomechanical, socio-demographic, managerial, and psychosocial risk aspects [5]. WMSDs are associated with a number of ergonomic risk factors, including non-neutral body postures, vibration, repetitive movements and heavy physical exertion [6]. The frequent occurrence of WMSDs has a significant impact on workers' productivity [7].

The prevalence of occupational hazards inherent in agricultural activities underscores the necessity for a comprehensive examination of their occupational health and safety implications for agricultural workers. Biomechanical and physical factors, such as noise and vibration from the equipment they use in their daily work, expose agricultural workers to the

risk of WMSDs [8]. The repetitive nature of the work involved in the harvesting process is liable to induce fatigue in muscles, joints and nerves, and to cause WMSDs [9]. WMSDs are a category of occupational injury that may develop over time and are prevalent among agricultural workers [10]. The three main hazard factors for WMSDs in agriculture have been identified as: lifting and carrying heavy loads (more than 50 lb); continuous or repeated whole-body bending (stooping); and high levels of repetitive manual activity (e.g. clipping, cutting) [11, 12]. Furthermore, awkward postures, vibration-generating tools or equipment, cold working environments and locations of pressure are identified as ergonomic risk factors [13]. The literature's emphasis on the correlation between low job satisfaction and neck and back pain in agricultural workers, thereby suggesting the potential significance of psychosocial variables in the aetiology of musculoskeletal issues [14].

Conventionally, methodologies for conducting ergonomic risk assessments are based on observational techniques for the evaluation of workers' body posture [15]. Rapid Entire Body Assessment (REBA) [16, 17], Rapid Upper Limb Assessment (RULA) [18, 19], Ovako Working Posture Analysing System [20], Quick Exposure Check (QEC) [21], Occupational Repetitive Action (OCRA) [22], Loading on the upper body assessment (LUBA) [23].

The capacity of conventional methodologies for the assessment of ergonomic risks to address the multifaceted nature of risk factors which contribute to the occurrence of WMSDs in the field of agriculture is limited. These risk factors are complex and uncertain in nature and encompass physical, biomechanical, environmental, organizational, psychosocial, and demographic factors. A comprehensive assessment is required to fully determine their impact. In recent years, fuzzy multi-criteria decision-making (MCDM) studies have been conducted in the field of ergonomic risk assessment [24, 25, 26, 27]. The utilization of MCDM methodologies is recognized as a highly effective approach in scenarios where the decision-making process is characterised by a high degree of uncertainty. This research adopted the MCDM approach for the development of an innovative decision support model (DSM) within the scope of ergonomic risk assessment. In this study, Picture fuzzy sets (PFS) introduced by Cuong and Kreinovich [28] as an extension of intuitionistic fuzzy sets (IFS) [29] due to their advantages in expert evaluations.

Hazard analysis, when considered as a part of the risk assessment process, can be interpreted as a group decision-making procedure [30]. The Fine-Kinney technique is a quantitatively based methodology for the analysis of hazards [31]. In the original version of the Fine–Kinney methodology, the computation of risk value (RV) is achieved through the

utilization of the following formula: $RV = P \times E \times C$, where P, E, and C represent probability, exposure, and consequence, respectively [32]. Nevertheless, the conventional Fine-Kinney technique is subject to limitations in practical application [30, 33, 34]: The first limitation pertains to the equal importance attributed to the effects represented by the risk parameters P, E, and C. However, it is important to note that these parameters may be evaluated differently in real-life scenarios. Secondly, defining the values of P, E and C with crisp numbers can cause significant challenges in practical application. Thirdly, the capacity to comprehensively address the various categories of uncertainty inherent in the information presented in the risk assessment provided by the expert is insufficient.

The present study proposes an MCDM approach, integrating PFS to develop a dynamic model for providing decision support in the context of risk assessment in relation to ergonomic factors. To address the shortcomings of the traditional Fine-Kinney approach concerning the expression of data pertaining to uncertain risk assessment, the utilization of PFS has been proposed in order to facilitate the description of such uncertainties. In the context of the MCDM framework, the utilization of PFS-LODECI-ARTASI, a hybrid model, is proposed for the purpose of evaluating the ergonomic risk priority. The LOgarithmic DEcomposition Of Criteria Importance (LODECI) [35] theoretical framework, which is based on PFS, is utilized to calculate weights for risk parameters P, E and C. The Alternative Ranking Technique based on Adaptive Standardized Intervals (ARTASI) [36] method is utilized in combination with PFS for the purpose of ranking hazards. Therefore, this study aims to provide a robust decision-support framework for related to ergonomic risk assessment by proposing a Fine-Kinney-based PFS-LODECI-ARTASI hybrid model.

The objective of this research is to devise a hybrid MCDM approach to prioritize hazards due to ergonomic risk factors that may affect WMSDs in harvesting operations carried out by agricultural workers. Whilst preceding studies in the relevant literature have, as a general rule, addressed the ergonomic risk assessment process by means of observational and statistical techniques, the present study aims to develop this research by using recently established techniques and emphasising the benefits of these techniques. The main focal point of this study is the introduction of a hybrid model for the ergonomic risk assessment framework, distinguished by the construction an algorithm that is specifically designed to this hybrid model. PFS are utilized in this hybrid model, along with Picture Fuzzy Weighted Averaging (PFWA) aggregation operator. The LODECI method is the preferred option for Fine-Kinney risk parameter weighting due to the efficiency with which it overcomes the instability that can be

present in alternative methods of criterion weighting. In the context of hazard ranking, the ARTASI approach is preferred due to its two-step standardization procedure, which has been demonstrated to yield more effective results. The combination of these three methodological approaches with PFS results in the development of the Fine-Kinney-based PFS-LODECI-ARTASI (FK-PFLODAR) approach.

This paper makes significant contributions to the extant knowledge base on the following topics:

(i) *Construction of a Pioneering Ergonomic Risk Assessment Framework*: The paper proposes a pioneering ergonomic risk assessment framework, the FK-PFLODAR approach, for the ergonomic risk assessment process. The model integrates picture fuzzy sets, PFWA aggregation operations, Fine-Kinney, LODECI, and ARTASI methods, providing a new methodology within the existing literature.

(ii) *Harmonized Weighting of Criteria*: The LODECI approach is selected on the basis of its ability to stabilize situations that may be unstable in alternative approaches, thus rendering it an optimal choice for weighting risk parameters in the proposed model. This contributes to enhancing the model's robustness.

(iii) *Flexibly Designed Alternate Rating System*: The ARTASI approach in hazard ranking enables the extension of levels of uncertainty in the assessments of experts, thereby facilitating the development of more adaptable and flexible resolutions in the ergonomic risk assessment procedure.

1.1 The impetus of the study

Risk management is a process that involves evaluating the potential hazards and their associated risks, while also assessing the efficacy of preventive measures in order to determine the degree of acceptability of the risks [37]. The processing of information obtained from experts' experience and knowledge during the risk assessment process is a complex cognitive task [38]. As previously discussed, to overcome the limitations of the Fine-Kinney model and address uncertain information in risk assessment more comprehensively, a hybrid framework combining picture fuzzy modeling is proposed. Despite the study's primary orientation towards application and the lack of a conventional hypothesis testing framework, it is underpinned by a fundamental research question: The fundamental research question guiding this study is as follows: "Can integrating picture fuzzy MCDM methods into the Fine-Kinney process enhance

the effectiveness, reliability, and adaptability of risk assessment practices in agricultural harvesting fields?" The exploration of this subject is of significance to both the advancement of academic knowledge and the practical endeavours aimed at enhancing safety in agricultural workplaces. The investigation provides valuable insights into the systematic integration of uncertainty into risk management methodologies.

1.2 The architecture of the study

This research is articulated into seven sections. Section 2 provides a comprehensive survey of the related literature. Section 3 presents a comprehensive overview of the methodological framework, within which detailed descriptions of PFS are provided. The FK-PFLODAR model is formulated in this section, including a detailed explanation of all the steps, and an algorithm is presented. In Section 4, a case study is conducted and information regarding the case study is provided. Thereafter, the implementation of the FK-PFLODAR model is demonstrated. Section 5 presents the validation results of the sensitivity analysis and comparative analysis. Section 6 of the paper discusses the managerial implications of the proposed risk assessment model, and the limitations of the research, and provides directions for future research. Finally, Section 7 concludes the paper.

2 LITERATURE SURVEY

2.1 Researchs on Ergonomic Risk Assessment

Non-ergonomic working conditions have been highlighted as a significant problem for employees in terms of occupational health and safety. The pervasiveness of musculoskeletal disorders (MSDs) within working environments constitutes a substantial problem [39]. In a multitude of developed countries, a considerable proportion of upper extremity and low back pain cases are attributable to identified risk factors, including physical exertion, repetitive motions, and prolonged exposure to awkward body postures [40]. In view of the significant economic and social costs of work-related musculoskeletal disorders (WMSDs), it is essential to identify the contributors to these injuries so that efficacious preventative measures can be formulated and executed [41]. Consequently, a plethora of WMSD exposure and risk assessment methodologies have been formulated.

Law et al. [42] employed the Rapid Entire Body Assessment (REBA) method to evaluate the potential for WMSDs in the healthcare sector during patient transfers. Ipaki et al.

[43] applied the Quick Exposure Check (QEC) method for the evaluation of physical and virtual prototype in the workstation design process. Cimino et al. [44] proposed a risk assessment framework that combines ergonomic methods with the Analytic Hierarchy Process (AHP) for lashing and unlashing operations at container terminals. De-Benavides-Jiménez et al. [45] utilized the Ovako Working Posture Analysing System (OWAS) and Rapid Upper Limb Assessment (RULA) methodologies due to the risk of WMSDs that agricultural workers are susceptible to as a consequence of forceful postures and repetitive motions.

2.2 PFS

The OHSRA can be considered as a subject within the MCDM paradigm, characterized by a fuzzy and complex framework, a consequence of factors such as uncertainty and inaccuracy in the evaluative processes of decision makers with regard to criteria and alternatives. It can thus be concluded that a fuzzy occupational risk assessment is a rational instrument for addressing uncertainty and imprecision in traditional occupational risk assessment approaches. Since Zadeh's pioneering work in 1965 [46], fuzzy set theory (FST) has been instrumental in resolving decision-making challenges in uncertain situations. Within the framework of Zadeh's FST, the degree of membership of each element of a fuzzy set is characterised by a membership function, which is delineated as a value ranging from 0 to 1. Subsequently, a plethora of extensions of fuzzy sets are discussed, with the purpose of dealing with uncertain information in real-life problems. Atanassov [29] proposed the intuitionistic fuzzy sets approach. IFSs have been applied to deal with the limitations of the fuzzy set by characterizing uncertainty in terms of degrees of membership, non-membership and hesitancy. In 2013, Cuong and Kreinovich [28] presented a proposal for a PFS that extended the IFS. The PFS is characterised by four distinct membership functions: positive membership, neutral membership, negative membership, and a refusal function. It is evident that the PFS provides a more comprehensive and meticulous account of information in comparison to the IFS. Consequently, numerous MCDM methodologies grounded in picture fuzzy sets have been devised to address decision-making challenges in contexts characterised by ambiguity and complexity: picture fuzzy Weighted Aggregated Sum Product Assessment (WASPAS) [47], picture fuzzy Measurement of Alternative and Ranking According to the Compromise Solution (MARCOS) [48], picture fuzzy Combined Compromise Solution (CoCoSo) [49], etc.

2.3 OHSRA Approaches Modelled on the Fine-Kinney Methodology

The assessment of occupational risks and the establishment of task priorities are of the utmost importance in the context of OHS management and the proactive prevention of potential hazards [34]. The Fine-Kinney model proposed by Kinney and Wiruth [50], provides a quantitative and comprehensive tool for the rating and control of risk within the OHSRA process. The assessment of risks is based on a combination of empirical observation and expert judgment in applying this model. This results in the risk assessment process being more complex, given that it inherently involves uncertain information. Consequently, to address the aforementioned limitations and uncertainties in evaluation, the researchers incorporated fuzzy sets into their proposed Fine-Kinney-based models. Gul et al. [51] used triangular fuzzy numbers (TrFNs) to represent the decision-makers' uncertainty regarding risk assessment. Ilbahar et al. [52] employed Pythagorean fuzzy set (PyFS) to address uncertainty and imprecision in the evaluation of occupational risks. Tang et al. [53] utilized interval-type 2 fuzzy set (IT2FS) to formulate uncertain risk values from various decision-makers. Seker [54] used interval-valued intuitionistic fuzzy set (IVIFS) to address uncertainty within the context of risk evaluation. Wang et al. [33] constructed a model based on Fermatean fuzzy set (FFS) with a view to processing uncertainty in risk assessment information provided by decision-makers with higher efficiency. Chen et al. [55] employed spherical fuzzy set (SFS) to manage the risk data provided by experts.

Within the framework of an OHS risk management strategy, it is critical for the decision-making procedure to consider multiple factors in order to ensure a comprehensive and effective evaluation of the situation. Risk prioritization is widely acknowledged as an MCDM problem. Therefore, in the OHSRA process, researchers implemented MCDM approaches with Fine-Kinney model. Wang et al. [30] developed a novel Fine-Kinney-based approach to risk evaluation, extending the MULTIMOORA (Multiple Multi-Objective Optimization by Ration Analysis) technique to determine the risk priority of hazards. Wang et al. [56] developed an interval 2-tuple linguistic ORESTE method-based risk priority computation model to improve the effectiveness of the Fine-Kinney procedure. Wang et al. [33] proposed a model for the assessment of occupational risk that is a hybrid model based on Fine–Kinney approach. The model utilizes an extended MARCOS (Measurement of Alternatives and Ranking to Compromise Solution) methodology. Chen et al. [55] proposed an approach to risk assessment that utilized an improved MABAC (Multi-Attributive Border Approximation Area Comparison) technique applied based on the Fine-Kinney framework.

2.4 Research Gaps

According to the above discussion, existing ergonomic risk assessment methods comprise processes based on observational techniques. The utilization of observational methods is inherently associated with the necessity for time-consuming and costly risk assessment procedures. Nonetheless, conventional observational ergonomic risk assessment methodologies predominantly concentrate on the analysis of workers' posture or movements. In addition to the acknowledged role physical factors, psychosocial factors and individual factors have been identified as contributing factors in the occurrence of WMSDs. In this context, there is a literature gap for ergonomic risk assessment that incorporates quantitatively and qualitatively determined factors in the risk decision-making process. Consequently, the most significant gap in the extant literature pertains to the absence of a holistic approach in ergonomic risk assessment frameworks.

In comparison to other industries, there has been a limited implementation of research on OHS risk assessment practices for the agricultural sector. Within the field of agricultural operations, the prevalence of WMSDs among workers is a salient issue, yet numerous studies have conspicuously failed to adequately address this salient issue. Therefore, this study highlights the literature gap in the need to develop preventive policies and increase these options for the affected agricultural workforce in relation to ergonomic issues.

Within the framework of conventional Fine-Kinney risk evaluation methodologies, the outcomes of risk scoring results may not always be rational due to the incapacity of decision makers to address uncertainty in their assessment. In this context, the capacity of PFSs to articulate uncertainty more comprehensively is advantageous for OHSRA.

In consideration of the aforementioned motivations, the paper posits a model of a hybrid picture fuzzy-based MCDM approach on the basis of Fine-Kinney that takes into account the uncertainties in decision-makers' judgments and can be an alternative to occupational ergonomic risk assessment tools.

In this research, the MCDM approach is adopted to construct an enhanced occupational risk assessment. Furthermore, due to their linguistic underpinnings, fuzzy sets are considered more suitable for utilization in expert evaluations. The OHSRA process is characterized by a substantial number of uncertain variables, which renders PFS a rational instrument with which to adequately represent DMs' fuzzy preferences. The weighting of risk parameters is enhanced by extending the LODECI method using PFS. The innovative PFS-LODECI approach offers

the distinct advantage of computing the levels of stability of the risk parameter weights derived during the parameter weighted process. The ARTASI method is employed in combination via PFS for the purpose of ranking hazards. The proposed PFS-ARTASI approach is advantageous in that it offers a two-step standadization option derived from absolute maximum and minimum values. Therefore, this study proposes the utilization of the FK-PFLODAR approach to provide DSM for the problem of ergonomic risk assessment on the basis of MCDM.

3 METHODOLOGY

3.1 Preliminaries of PFS

PFS, an extension of IFS introduced by Cuong and Kreinovich [28], are widely utilized to address uncertainty in real-world problems. The following section provides a definition of PFS, along with a description of the relevant operations [28, 57, 58]:

Definition I: A PFS $\tilde{\mathfrak{P}}$ on a universe U is given by;

$$\tilde{\mathfrak{P}} = \left\{\left(u, a_{\tilde{\mathfrak{P}}}(u), b_{\tilde{\mathfrak{P}}}(u), c_{\tilde{\mathfrak{P}}}(u)\right) | u \in U\right\} \tag{1}$$

where $a_{\tilde{\mathfrak{P}}}(u), b_{\tilde{\mathfrak{P}}}(u), c_{\tilde{\mathfrak{P}}}(u)$: $U \rightarrow [0,1]$ is positive membership, neutral membership, and negative membership in the set $\tilde{\mathfrak{P}}$ respectively, with $0 \leq a_{\tilde{\mathfrak{P}}}(u) + b_{\tilde{\mathfrak{P}}}(u) + c_{\tilde{\mathfrak{P}}}(u) \leq 1, \forall u \in U$.

For the set $\tilde{\mathfrak{P}}$, $\lambda_{\tilde{\mathfrak{P}}}(u) = 1 - (a_{\tilde{\mathfrak{P}}}(u) + b_{\tilde{\mathfrak{P}}}(u) + c_{\tilde{\mathfrak{P}}}(u))$ is referred as the refusal function in $\tilde{\mathfrak{P}}$.

Definition II: Mathematical operations for single-valued picture fuzzy sets are defined as follows [59];

$$\tilde{\mathfrak{P}}_1 \oplus \tilde{\mathfrak{P}}_2 = \left\{a_{\tilde{\mathfrak{P}}_1} + a_{\tilde{\mathfrak{P}}_2} - a_{\tilde{\mathfrak{P}}_1} a_{\tilde{\mathfrak{P}}_2}, b_{\tilde{\mathfrak{P}}_1} b_{\tilde{\mathfrak{P}}_2}, c_{\tilde{\mathfrak{P}}_1} c_{\tilde{\mathfrak{P}}_2}\right\} \tag{2}$$

$$\tilde{\mathfrak{P}}_1 \otimes \tilde{\mathfrak{P}}_2 = \left\{a_{\tilde{\mathfrak{P}}_1} a_{\tilde{\mathfrak{P}}_2}, b_{\tilde{\mathfrak{P}}_1} + b_{\tilde{\mathfrak{P}}_2} - b_{\tilde{\mathfrak{P}}_1} b_{\tilde{\mathfrak{P}}_2}, c_{\tilde{\mathfrak{P}}_1} + c_{\tilde{\mathfrak{P}}_2} - c_{\tilde{\mathfrak{P}}_1} c_{\tilde{\mathfrak{P}}_2}\right\} \tag{3}$$

$$\mathfrak{w}.\tilde{\mathfrak{P}}_1 = \left\{\left(1 - \left(1 - a_{\tilde{\mathfrak{P}}_1}\right)^{\mathfrak{w}}\right), b_{\tilde{\mathfrak{P}}_1}^{\mathfrak{w}}, c_{\tilde{\mathfrak{P}}_1}^{\mathfrak{w}}\right\} \quad \text{for } \mathfrak{w} > 0 \tag{4}$$

$$\tilde{\mathfrak{P}}_1{}^{\mathfrak{w}} = \left\{a_{\tilde{\mathfrak{P}}_1}^{\mathfrak{w}}, \left(1 - \left(1 - b_{\tilde{\mathfrak{P}}_1}\right)^{\mathfrak{w}}\right), \left(1 - \left(1 - c_{\tilde{\mathfrak{P}}_1}\right)^{\mathfrak{w}}\right)\right\} \quad \text{for } \mathfrak{w} > 0 \tag{5}$$

Definition III: The score function, denoted as $\mathbb{Sc}(\tilde{\mathfrak{P}})$, can be calculated as follows [57];

$$\mathbb{Sc}(\tilde{\mathfrak{P}}) = \mathfrak{a} - \mathfrak{c} + 1 + \frac{e^{\mathfrak{a}-\mathfrak{b}-\mathfrak{c}}}{1+\lambda}, \quad \mathbb{Sc}(\tilde{\mathfrak{P}}) \in [e^{-1}, 2+e] \tag{6}$$

Definition IV: Picture Fuzzy Weighted Averaging (PFWA) aggregation operator. Concurrently, the relevant weight vector $w = (w_1, w_2, \ldots, w_n); w_j \in [0,1]; \sum_{j=1}^{n} w_j = 1$, is defined as follows [59];

$$\mathrm{PFWA}_w = \left\{ 1 - \prod_{j=1}^{n} (1 - \mathfrak{a}_{\tilde{\mathfrak{P}}_j})^{w_j}, \prod_{j=1}^{n} \mathfrak{b}_{\tilde{\mathfrak{P}}_j}^{w_j}, \prod_{j=1}^{n} \mathfrak{c}_{\tilde{\mathfrak{P}}_j}^{w_j} \right\} \tag{7}$$

3.2 A Proposed Hybrid Ergonomic Risk Assessment Methodological Framework

This framework is comprised of two main phases. The first phase of this methodology details the utilization of PFS-LODECI for the weighting of Fine-Kinney risk parameters. In the subsequent phase, the procedures for ranking potential hazards related to WMSDs are performed utilizing PFS-ARTASI. Figure 1 provides a visualisation of the methodological framework underpinning the developed ergonomic risk assessment framework.

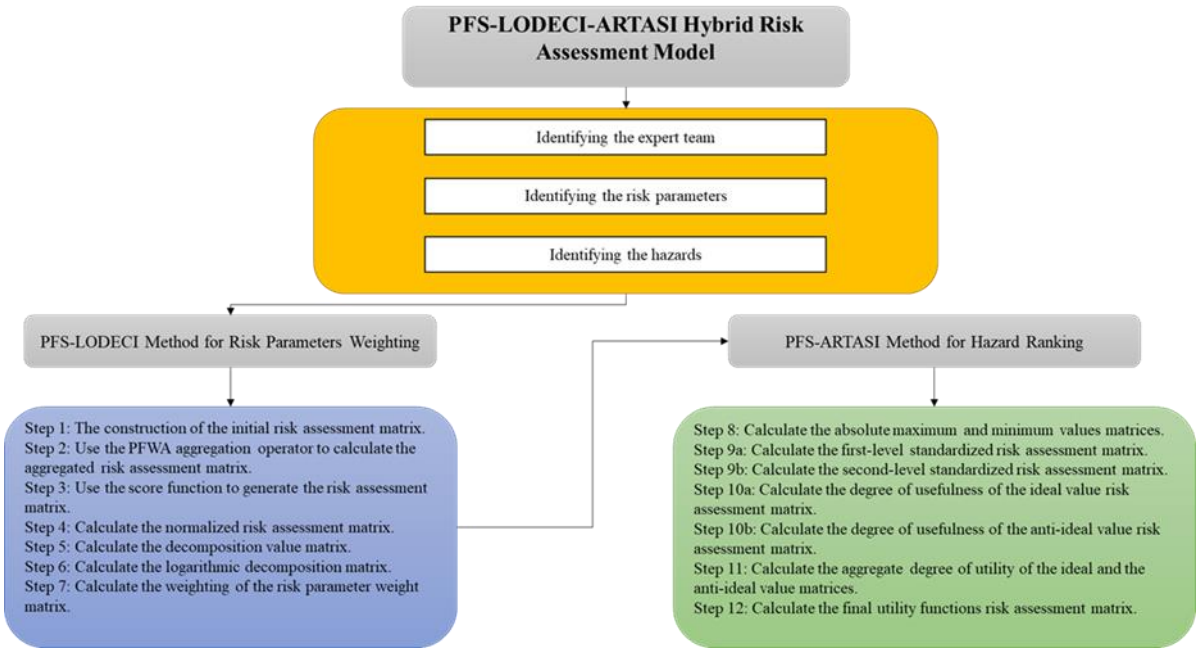


Figure 1. The flowchart of the methodological framework.

The problem of ergonomic risk assessment with picture fuzzy risk information is addressed by the FK-PFLODAR approach. Let $(ERH_i) = \{ERH_1, ERH_2, \dots, ERH_m\}(i = 1,2,\dots,m)$ be ergonomic hazards and n risk parameters $(RP_j) = \{RP_1, RP_2, \dots, RP_n\}(j = 1,2,\dots,n)$, and experts $(\mathbb{E}_k) = \{\mathbb{E}_1, \mathbb{E}_2, \dots, \mathbb{E}_q\}(k = 1,2,\dots,q)$ for the ergonomic risk assessment problem.

Phase 1. PFS-LODECI

The determination of the weighting of risk parameters by utilization of the PFS-LODECI method:

Step 1: The expert $(\mathbb{E}_k)$ evaluation of each ergonomic hazard (ERH_i) is conducted with reference to the linguistic terms (LTs) shown in Table 1, concerning each risk parameter (RP_j). Following the evaluation process, the LTs are converted into the matching PFSs, as outlined in Table 1, thereby establishing the initial risk assessment matrix $\left[\widetilde{\Re}_{ij}^{(\mathbb{E}_k)}\right]_{mxn}$ where $\widetilde{\mathfrak{P}}_{\widetilde{\Re}_{ij}^{(\mathbb{E}_k)}} = \left(\mathfrak{a}_{\widetilde{\mathfrak{P}}_{\widetilde{\Re}_{ij}^{(\mathbb{E}_k)}}}(u), \mathfrak{b}_{\widetilde{\mathfrak{P}}_{\widetilde{\Re}_{ij}^{(\mathbb{E}_k)}}}(u), \mathfrak{c}_{\widetilde{\mathfrak{P}}_{\widetilde{\Re}_{ij}^{(\mathbb{E}_k)}}}(u)\right)(i = 1,2,\dots,m; j = 1,2,\dots,n; k = 1,2,\dots,q)$

The initial decision risk matrix $\widetilde{\Re} = \left[\widetilde{\Re}_{ij}^{(\mathbb{E}_k)}\right]_{mxn}$ for each expert k by using picture fuzzy numbers (PFNs).

$$\widetilde{\Re} = \left[\widetilde{\Re}_{ij}^{(\mathbb{E}_k)}\right]_{mxn} = \begin{matrix} \\ ERH_1 \\ \vdots \\ ERH_m \end{matrix} \begin{matrix} RP_1 & \cdots & RP_n \end{matrix} \begin{bmatrix} \Phi_{11}^k & \cdots & \Phi_{11}^k \\ \vdots & \vdots & \vdots \\ \Phi_{m1}^k & \cdots & \Phi_{mn}^k \end{bmatrix} \tag{8}$$

where, $\Phi_{ij}^k = \widetilde{\mathfrak{P}}\left(\mathfrak{a}_{\Phi_{ij}^k}, \mathfrak{b}_{\Phi_{ij}^k}, \mathfrak{c}_{\Phi_{ij}^k}\right)$ refers the degree of positive membership, the neutral membership, and the negative membership of ergonomic hazards ERH_i regard to criterion RP_j (Fine-Kinney risk parameter; P, E, C) $(i = 1,2,\dots,m \text{ and } j = 1,2,\dots,n)$.

Step 2. The aggregated risk assessment matrix $\widetilde{\Re} = \left[\widetilde{\Re}_{ij}\right]_{mxn}$ is derived through the utilization of the PFWA aggregation operator, as detailed in Eq. (9). In Eq. (9), the weight vector of the expert is denoted as $\mathcal{w}_k = (\mathcal{w}_1, \mathcal{w}_2, \dots, \mathcal{w}_q)$, for $\mathcal{w}_k \epsilon [0,1]$ and $\sum_{k=1}^{q} \mathcal{w}_k = 1$.

$$\begin{aligned} \text{PFWA}\left(\widetilde{\Re}^{(\mathbb{E}_1)}, \widetilde{\Re}^{(\mathbb{E}_2)}, \dots, \widetilde{\Re}^{(\mathbb{E}_q)}\right) &= \oplus_{k=1}^{q} \mathcal{w}_k \widetilde{\Re}^{(q)} \\ &= \left\{1 - \prod_{k=1}^{q}\left(1 - \mathfrak{a}_{\widetilde{\Re}^{(k)}}(u)\right)^{\mathcal{w}_k}, \prod_{k=1}^{q}\left(\mathfrak{b}_{\widetilde{\Re}^{(k)}}(u)\right)^{\mathcal{w}_k}, \prod_{k=1}^{q}\left(\mathfrak{c}_{\widetilde{\Re}^{(k)}}(u)\right)^{\mathcal{w}_k}\right\} \end{aligned} \tag{9}$$

Table 1. Linguistic terms used in the assessment of risk parameters and hazards (Mao et al. [58]).

Linguistic terms	Picture fuzzy numbers		
	a	**b**	**c**
Extremely high (EH)	0.90	0.00	0.10
Very high (VH)	0.80	0.10	0.10
High (H)	0.70	0.10	0.10
Medium high (MH)	0.60	0.20	0.20
Medium (M)	0.50	0.20	0.20
Medium low (ML)	0.40	0.20	0.30
Low (L)	0.30	0.30	0.30
Very low (VL)	0.20	0.30	0.50
Extremely low (EL)	0.10	0.30	0.60

Step 3. The utilization of the score function $\left(\mathbb{Sc}\left(\widetilde{\Re}_{ij}\right)\right)$ as defined in Eq. (10) enables the calculation of the crisp values, and the subsequent generation of a crisp risk assessment matrix $\left(\mathfrak{D} = \left[\mathfrak{D}_{ij}\right]_{mxn}\right)$.

$$\mathbb{Sc}\left(\widetilde{\Re}_{ij}\right) = \mathfrak{a}_{\widetilde{\Re}_{ij}} - \mathfrak{c}_{\widetilde{\Re}_{ij}} + 1 + \frac{e^{\mathfrak{a}_{\widetilde{\Re}_{ij}} - \mathfrak{b}_{\widetilde{\Re}_{ij}} - \mathfrak{c}_{\widetilde{\Re}_{ij}}}}{1 + \lambda_{\widetilde{\Re}_{ij}}}, \quad \mathbb{Sc}\left(\widetilde{\Re}_{ij}\right) \in [e^{-1}, 2 + e], \quad for\ (i = 1,2, \dots, m; j = 1,2, \dots, n) \tag{10}$$

Step 4. The calculation of the normalized risk assessment matrix $\left(\mathbb{N} = \left[\mathbb{N}_{ij}\right]_{mxn}\right)$ is achieved through the utilization of Eq. (11).

$$\mathbb{N}_{ij} = \begin{pmatrix} \frac{\mathfrak{D}_{ij}}{\mathfrak{D}_j^{max}}\ i\ fj \in benefit\ criteria \\ \frac{\mathfrak{D}_j^{min}}{\mathfrak{D}_{ij}}\ i\ fj \in cost\ criteria \end{pmatrix} for\ (i = 1,2, \dots, m; j = 1,2, \dots, n) \tag{11}$$

Step 5. The calculation of the decomposition value matrix $\left(\mathbb{D} = \left[\mathbb{D}_{ij}\right]_{mxn}\right)$ use Eq. (12).

$$\mathbb{D}_{ij} = max\left\{\left|\mathbb{N}_{ij} - \mathbb{N}_{rj}\right|\right\} for\ r \neq i\ and\ \times\ (r = 1,2, \dots, m; i = 1, \dots, m; j = 1, \dots, n) \tag{12}$$

Step 6. The calculation of the logarithmic decomposition matrix $\left(\mathbb{L} = \left[\mathbb{L}_j\right]_n\right)$ use Eq. (13).

$$\mathbb{L}_j = \ln\left(1 + \frac{\sum_{i=1}^{m} \mathbb{D}_{ij}}{m}\right) \tag{13}$$

Step 7. The determination of the risk parameter weight matrix $\left(\mathbb{W} = [\mathbb{W}_j]_n\right)$ is achieved through the utilization of Eq. (14).

$$\mathbb{W}_j = \frac{\mathbb{L}_j}{\sum_{j=1}^{n} \mathbb{L}_j} \; for \; (j = 1,2,\dots,n) \tag{14}$$

Phase 2. PFS-ARTASI

The calculation of the ranking of ergonomic hazards is achieved through the utilization of the PFS-ARTASI method:

Step 8. The crisp risk assessment matrix $\left(\mathfrak{D} = [\mathfrak{D}_{ij}]_{mxn}\right)$, calculated in accordance with the procedures delineated under Step 3, provides an initial risk assessment matrix relating to the PFS-ARTASI methodology. The crisp risk assessment matrix employed in order to calculate the absolute maximum values matrix$\left(\mathfrak{D}^{max} = [\mathfrak{D}_j^{max}]_n\right)$ and the absolute minimum values matrix $\left(\mathfrak{D}^{min} = [\mathfrak{D}_j^{min}]_n\right)$, as depicted the formulae provided in Eqs. (15) and (16), respectively.

$$\mathfrak{D}_j^{max} = \max_{1\le i\le m} \mathfrak{D}_{ij} + \left\{\max_{1\le i\le m} \mathfrak{D}_{ij}\right\}^{1/m} \; for \; (i = 1,2,\dots,m; j = 1,2,\dots,n) \tag{15}$$

$$\mathfrak{D}_j^{min} = \min_{1\le i\le m} \mathfrak{D}_{ij} - \left\{\min_{1\le i\le m} \mathfrak{D}_{ij}\right\}^{1/m} \; for \; (i = 1,2,\dots,m; j = 1,2,\dots,n) \tag{16}$$

Step 9. The subsequent step involves implementing the standardized risk assessment matrix via two sub-steps.

Step 9a. The first-level standardized risk assessment matrix $[\mathfrak{F}_{ij}]_{mxn}$ is computed utilizing Eq. (17).

$$\mathfrak{F}_{ij} = \frac{\mathcal{B}^u - \mathcal{B}^l}{\mathfrak{D}_j^{max} - \mathfrak{D}_j^{min}} \mathfrak{D}_{ij} + \frac{\mathfrak{D}_j^{max}.\mathcal{B}^l - \mathfrak{D}_j^{min}.\mathcal{B}^u}{\mathfrak{D}_j^{max} - \mathfrak{D}_j^{min}} \; for \; (i = 1,2,\dots,m; j = 1,2,\dots,n) \tag{17}$$

In the context of the aforementioned parameters, the absolute maximum value $\left(\mathfrak{D}_j^{max}\right)$ and the absolute minimum values $\left(\mathfrak{D}_j^{min}\right)$ are represented, while $\mathcal{B}^u$ and $\mathcal{B}^l$ denote the upper and lower limits of the standardized interval, respectively. $\left(\mathfrak{D}_{ij}\right)$ represents initial risk assessment matrix value. Additionally, the values in the standardized $[\mathcal{B}^l, \mathcal{B}^u]$ values are equivalent to $[1,\ 100]$ [36].

Step 9b. The second-level standardized risk assessment matrix $\left[\mathfrak{Q}_{ij}\right]_{mxn}$ is computed utilizing Eq. (18).

$$\mathfrak{Q}_{ij} = \begin{pmatrix} \left(\mathfrak{Q}_{ij}\right) = \left(-\mathfrak{F}_{ij} + \underset{1\le i\le m}{max}\,\mathfrak{F}_{ij} + \underset{1\le i\le m}{min}\,\mathfrak{F}_{ij}\right); if\mathrm{j} \in cost\ criteria \\ \left(\mathfrak{Q}_{ij}\right) = \left(\mathfrak{F}_{ij}\right);\ if j \in benefit\ criteria \end{pmatrix} \tag{18}$$

Step 10. This step involves the calculation of the degree of usefulness of the hazards for the ideal and anti-ideal values through the employment of two sub-steps.

Step 10a. The degree of usefulness of the ideal value risk assessment matrix $\mathbb{V}^{+} = \left[\mathbb{V}_{ij}^{+}\right]_{mxn}$ is determined by the implementation of Eq. (19).

$$\mathbb{V}_{ij}^{+} = \left(\frac{\mathfrak{Q}_{ij}}{\underset{1\le i\le m}{max}\,\mathfrak{Q}_{ij}}\,\mathbb{W}_j\,\mathcal{B}^{u}\right) for\ (i = 1,2,\dots,m; j = 1,2,\dots,n) \tag{19}$$

where $\mathcal{B}^{u} = 100$ and $\mathbb{W}_j$ are criterion weights.

Step 10b. The degree of usefulness of the anti-ideal value risk assessment matrix $\mathbb{V}^{-} = \left[\mathbb{V}_{ij}^{-}\right]_{mxn}$ is determined by the implementation of Eq. (20).

$$\mathbb{V}_{ij}^{-} = -\mathfrak{U}_{ij} + \underset{1\le i\le m}{max}\,\mathfrak{U}_{ij} + \underset{1\le i\le m}{min}\,\mathfrak{U}_{ij}\ for\ (i = 1,2,\dots,m; j = 1,2,\dots,n) \tag{20}$$

where $\mathfrak{U}_{ij}$ is the degree of usefulness. $\mathfrak{U}_{ij}$ derived from Eq. (21).

$$\mathfrak{U}_{ij} = \left(\left(\frac{\underset{1\le i\le m}{min}\,\mathfrak{Q}_{ij}}{\mathfrak{Q}_{ij}}\,\mathbb{W}_j\,\mathcal{B}^{u}\right)\right) for\ (i = 1,2,\dots,m; j = 1,2,\dots,n) \tag{21}$$

where $\mathcal{B}^{u} = 100$ and $\mathbb{W}_j$ are criterion weights.

Step 11. To calculate the aggregate degree of utility of the hazards for the ideal value matrix ($\mathrm{P}^{+} = [\mathrm{P}_i^{+}]_m$) and anti-ideal value matrix ($\mathrm{P}^{-} = [\mathrm{P}_i^{-}]_m$), the application of of Eqs. (22) and (23) is utilized, respectively.

$$\mathrm{P}_i^{+} = \sum_{j=1}^{n} \mathbb{V}_{ij}^{+}\ for\ (i = 1,2,\dots,m; j = 1,2,\dots,n) \tag{22}$$

$$\mathrm{P}_i^{-} = \sum_{j=1}^{n} \mathbb{V}_{ij}^{-}\ for\ (i = 1,2,\dots,m; j = 1,2,\dots,n) \tag{23}$$

Step 12. The final utility functions risk assessment matrix $\mathbb{F} = [\mathbb{F}_i]_m$ is determined through the utilization of the equation provided in Eq. (24). Subsequently, the highest value of the final utility functions risk assessment matrix represents the most significant hazard.

$$\mathbb{F}_i = \{P_i^+ + P_i^-\}\left\{\theta\, f(P_i^+)^\beta + (1-\theta).f(P_i^-)^\beta\right\}^{1/\beta};\ \theta \in [0,1];\ \beta \in [1,+\infty] \quad (24)$$

where $f(P_i^+)$ and $f(P_i^-)$ denote additive functions and calculated as $f(P_i^+) = \frac{P_i^+}{P_i^+ + P_i^-}$ and $f(P_i^-) = \frac{P_i^-}{P_i^+ + P_i^-}$, respectively.

4 CASE STUDY

The focus of this section is to apply the proposed risk assessment methodology for ergonomic hazards affecting workers during the harvesting of tea in the Eastern Black Sea region of Türkiye. Firstly, a group of three experts $\{\mathbb{E}_1, \mathbb{E}_2, \mathbb{E}_3\}$ with differing backgrounds is selected for the purpose of establishing the risk evaluation team, with the aim of addressing the risk assessment problem regarding the potential hazards utilizing the proposed framework. The weights of experts with different levels of experience are as follows: "$(\omega_1 = 0.4), (\omega_2 = 0.4), (\omega_3 = 0.2)$". Detailed information regarding the experts is given in Table 2. The Fine-Kinney risk parameters (RPs)—probability (P), exposure (E), and consequence (C)—are used within this case study to evaluate the hazards in order to provide a thorough and systematic evaluation. Each of the three risk parameters is regarded as a benefit criterion [60]. A comprehensive literature review and consultation of experts has identified thirteen potential ergonomic hazards (see Table 3). The aforementioned potential ergonomic hazards are denoted as $ERH = \{ERH_1, ERH_2, \ldots, ERH_{13}\}$.

Table 2. Information about the experts.

No	Area of expertise	Experience (year)	Academic degrees
$\mathbb{E}_1$	OHS specialist	15	Ph.D.
$\mathbb{E}_2$	Academician	20	Ph.D.
$\mathbb{E}_3$	OHS specialist	10	Master Degree

Table 3. The potential ergonomic hazards of the tea harvesting process.

No	The potential hazards	Description
ERH_1	Work posture	The manifestation of symptoms within the musculoskeletal system is characterised by the presence of fatigue and inflammation in muscular and articular tissues.
ERH_2	Repetitive motion	Musculoskeletal symptoms include tendinitis, tenosynovitis and carpal tunnel syndrome.
ERH_3	Exerting excessive force	Musculoskeletal symptoms lead to added stress on the postural muscles and other affected tissues.
ERH_4	Standing for a long time	The presence of musculoskeletal symptoms, characterised by muscular fatigue.
ERH_5	Using unsuitable tools and equipment	Symptoms affecting the muscles and joints, including fatigue and inflammation.
ERH_6	Weight	Symptoms affecting the muscles and skeleton in the lower extremity.
ERH_7	Height	Symptoms affecting the muscles and tendons in the upper extremity.
ERH_8	Experience	Musculoskeletal symptoms.
ERH_9	Unsuitable climatic conditions	Musculoskeletal symptoms.
ERH_{10}	Vibration	Symptoms related to the muscles and tendons; damage to the upper limbs.
ERH_{11}	Land of harvesting area	Symptoms and injuries affecting the muscles and skeleton.
ERH_{12}	Work stress	Musculoskeletal symptoms.
ERH_{13}	Organizational factor	Musculoskeletal symptoms.

Step 1. In this risk assessment process, each potential hazard is evaluated in regard to the RPs. The evaluation information derived from the experts using the LTs provided in Table 1 is displayed in Table 4.

Table 4. The linguistic terms based evaluations of potential hazards provided by experts.

$\mathbb{E}_1$	P	E	C	$\mathbb{E}_2$	P	E	C	$\mathbb{E}_3$	P	E	C
ERH_1	VH	H	M	ERH_1	VH	H	M	ERH_1	VH	H	M
ERH_2	EH	EH	MH	ERH_2	EH	EH	MH	ERH_2	EH	VH	M
ERH_3	H	ML	M	ERH_3	MH	L	M	ERH_3	H	L	M
ERH_4	EH	VH	M	ERH_4	EH	VH	MH	ERH_4	EH	VH	MH
ERH_5	ML	L	M	ERH_5	L	L	M	ERH_5	ML	L	M
ERH_6	M	M	M	ERH_6	ML	ML	M	ERH_6	M	M	MH
ERH_7	M	M	M	ERH_7	M	M	M	ERH_7	MH	M	MH
ERH_8	MH	M	M	ERH_8	M	M	M	ERH_8	MH	M	M
ERH_9	VH	ML	MH	ERH_9	H	VH	MH	ERH_9	VH	VH	M
ERH_{10}	VL	L	M	ERH_{10}	VL	L	M	ERH_{10}	VL	L	M
ERH_{11}	EH	H	H	ERH_{11}	EH	EH	H	ERH_{11}	EH	VH	VH
ERH_{12}	EH	EH	M	ERH_{12}	H	MH	M	ERH_{12}	M	M	MH
ERH_{13}	M	M	M	ERH_{13}	M	M	MH	ERH_{13}	M	M	M

Step 2. The PFWA aggregation operator, as described in Eq. (9), is utilized to compute the aggregated risk assessment matrix. The aggregated risk assessment matrix is shown in Table 5.

Table 5. The aggregated risk assessment matrix.

	P			E			C		
ERH_1	0.80	0.10	0.10	0.70	0.10	0.10	0.50	0.20	0.20
ERH_2	0.90	0.00	0.10	0.89	0.00	0.10	0.58	0.20	0.20
ERH_3	0.66	0.13	0.13	0.34	0.26	0.30	0.50	0.20	0.20
ERH_4	0.90	0.00	0.10	0.80	0.10	0.10	0.56	0.20	0.20
ERH_5	0.36	0.24	0.30	0.30	0.30	0.30	0.50	0.20	0.20
ERH_6	0.46	0.20	0.24	0.46	0.20	0.24	0.52	0.20	0.20
ERH_7	0.52	0.20	0.20	0.50	0.20	0.20	0.52	0.20	0.20
ERH_8	0.56	0.20	0.20	0.50	0.20	0.20	0.50	0.20	0.20
ERH_9	0.76	0.10	0.10	0.69	0.13	0.16	0.58	0.20	0.20
ERH_{10}	0.20	0.30	0.50	0.30	0.30	0.30	0.50	0.20	0.20
ERH_{11}	0.90	0.00	0.10	0.82	0.00	0.10	0.72	0.10	0.10
ERH_{12}	0.79	0.00	0.11	0.76	0.00	0.15	0.52	0.20	0.20
ERH_{13}	0.50	0.20	0.20	0.50	0.20	0.20	0.54	0.20	0.20

Step 3. The calculation of $\left[\mathfrak{D}_{ij}\right]_{mxn}$ is achieved through the utilization of the score function presented in Eq. (10). The matrix $\left[\mathfrak{D}_{ij}\right]_{mxn}$ is displayed in Table 6.

Table 6. The crisp risk assessment matrix.

	P	E	C
ERH_1	3.5221	3.0988	2.3047
ERH_2	4.0255	3.9457	2.5595
ERH_3	2.9215	1.7743	2.3047
ERH_4	4.0255	3.5221	2.4969
ERH_5	1.8242	1.6735	2.3047
ERH_6	2.1587	2.1587	2.3695
ERH_7	2.3695	2.3047	2.3695
ERH_8	2.4969	2.3047	2.3047
ERH_9	3.3640	2.9960	2.5595
ERH_{10}	1.2488	1.6735	2.3047
ERH_{11}	4.0255	3.6304	3.1909
ERH_{12}	3.4506	3.2957	2.3695
ERH_{13}	2.3047	2.3047	2.4336

The weights of RPs, as obtained by applying the Eqs. (11), (12), (13), and (14) in Steps 4, 5, 6 and 7, respectively, are presented in Table 7.

Table 7. The weights of the RPs.

$\mathbb{W}$	**P**	**E**	**C**
$\mathbb{W}_j$	0.394	0.355	0.251

After determining the weight of the RPs, the PFS-ARTASI steps are employed. As outlined in Step 8, Eqs. (15) and (16) are utilized to calculate the $\mathfrak{D}_j^{max}$ and the $\mathfrak{D}_j^{min}$, respectively. The matrices are provided in Table 8.

Table 8. The absolute maximum and minimum values.

$\mathfrak{D}$	P	E	C
$\mathfrak{D}_j^{max}$	5.1386	5.0571	4.2843
$\mathfrak{D}_j^{min}$	0.2316	0.6331	1.2384

The $\mathbb{F}_i$ value of potential hazards for the ideal value risk assessment matrix are computed ($(\theta = 0.5)$ and $(\beta = 1)$) by applying the following steps of the PFS-ARTASI methodology: 9, 10, 11 and 12. The matrix $[\mathbb{F}_i]_m$ is given in Table 9. The maximum value of this matrix is indicative of the most serious potential hazard.

Table 9. $\mathbb{F}_i$ values and rankings of potential hazards.

Hazards	$\mathbb{F}_i$	Rank
$\boldsymbol{ERH_1}$	78.9707	6
$\boldsymbol{ERH_2}$	92.7671	2
$\boldsymbol{ERH_3}$	58.9329	11
$\boldsymbol{ERH_4}$	88.8070	3
$\boldsymbol{ERH_5}$	46.1399	12
$\boldsymbol{ERH_6}$	59.1833	10
$\boldsymbol{ERH_7}$	63.1046	9
$\boldsymbol{ERH_8}$	63.1777	8
$\boldsymbol{ERH_9}$	80.9522	5
$\boldsymbol{ERH_{10}}$	36.2905	13
$\boldsymbol{ERH_{11}}$	97.7368	1
$\boldsymbol{ERH_{12}}$	81.1756	4
$\boldsymbol{ERH_{13}}$	63.5039	7

5 VALIDATION OF RESULTS

5.1 Sensitivity analysis

The proposed framework employs the Fine–Kinney parameters to signify the impact of the relationship between the data on risk rating and the results of hazard ranking. To investigate the effect of parameter value changes on the ultimate risk ranking, a sensitivity analysis was conducted by applying different values to these risk parameters. Therefore, the weight vectors of the Fine–Kinney parameters were changed. Given the three parameters inherent to the Fine–Kinney method, a total of six combinations were established in the context of this case study. In order to evaluate the robustness of the proposed model, five different weight scenarios (SC1, SC2, SC3, SC4, SC5) were constructed in addition to the original weight scenario (OSC), as displayed in Table 10. The effect of changes in the parameters on the hazard ranking was analyzed. The risk priority ranking of hazards from the sensitivity analysis is illustrated in Figure 2.

Table 10. The Fine–Kinney risk parameter weights for the chosen scenarios.

Scenario	Fine–Kinney parameter weight value		
	P	E	C
OSC	0.394	0.355	0.251
SC1	0.355	0.394	0.251
SC2	0.394	0.251	0.355
SC3	0.251	0.394	0.355
SC4	0.251	0.355	0.394
SC5	0.355	0.251	0.394

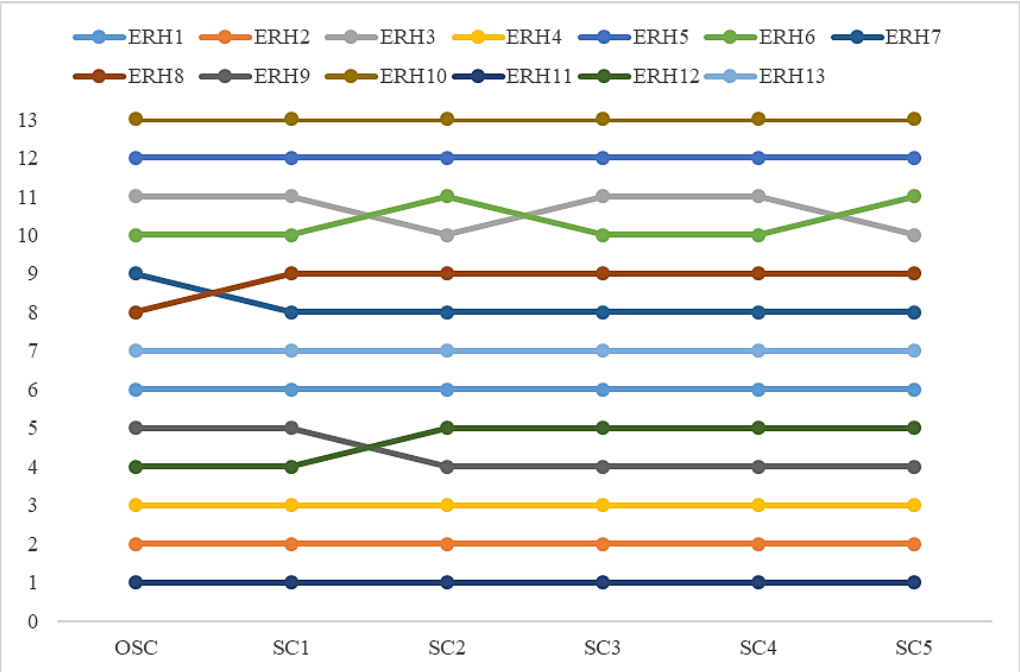


Figure 2. The results of sensitivity analysis.

As demonstrated in Figure 2, the final risk priority ranking results for hazards indicate that changes executed to the weight vector of the model's parameters have a negligible effect on the risk prioritization ranking. From Figure 2, there is a high correlation between the ranking results of hazards in different scenarios, and moreover, the ranking of critical hazards ($ERH_{11}, ERH_2, ERH_4, ERH_{12}$) remains consistent. The results of the conducted sensitivity analysis provide an indication of both the reliability and the applicability of the ranking results derived from the application of the established methodology.

5.2 Comparative analysis

A comparison with Fine-Kinney-based several conventional MCDM techniques, such as WASPAS, CoCoSo, EDAS, CODAS, and ARAS, has been conducted to illustrate the viability of the FK-PFLODAR model. The final hazard rankings from each of the above-mentioned methodologies are presented in Table 11. To provide a more lucid depiction delineated illustration of the results of the comparison study, the ranking order of each potential hazard as ascertained by alternative Fine-Kinney-based modelling approaches is also illustrated in Figure 3. Thereafter, the Spearman's rank correlation coefficients (SCC) for the results of the ranking obtained by the aforementioned employed approaches were calculated, as illustrated in the final row of Table 11.

Table 11. The result of the comparative analysis with conventional MCDM techniques.

	Based on Fine-Kinney					
	The proposed model	**PF-WASPAS**	**PF-CoCoSo**	**PF-EDAS**	**PF-CODAS**	**PF-ARAS**
	Ranking order					
ERH_1	6	5	5	5	5	5
ERH_2	2	2	2	2	2	2
ERH_3	11	10	10	10	8	10
ERH_4	3	3	3	3	3	3
ERH_5	12	12	12	12	12	12
ERH_6	10	11	11	11	11	11
ERH_7	9	8	8	8	9	8
ERH_8	8	7	7	7	7	7
ERH_9	5	6	6	6	6	6
ERH_{10}	13	13	13	13	13	13
ERH_{11}	1	1	1	1	1	1
ERH_{12}	4	4	4	4	4	4
ERH_{13}	7	9	9	9	10	9
SCC	1.00	0.97	0.97	0.97	0.94	0.97

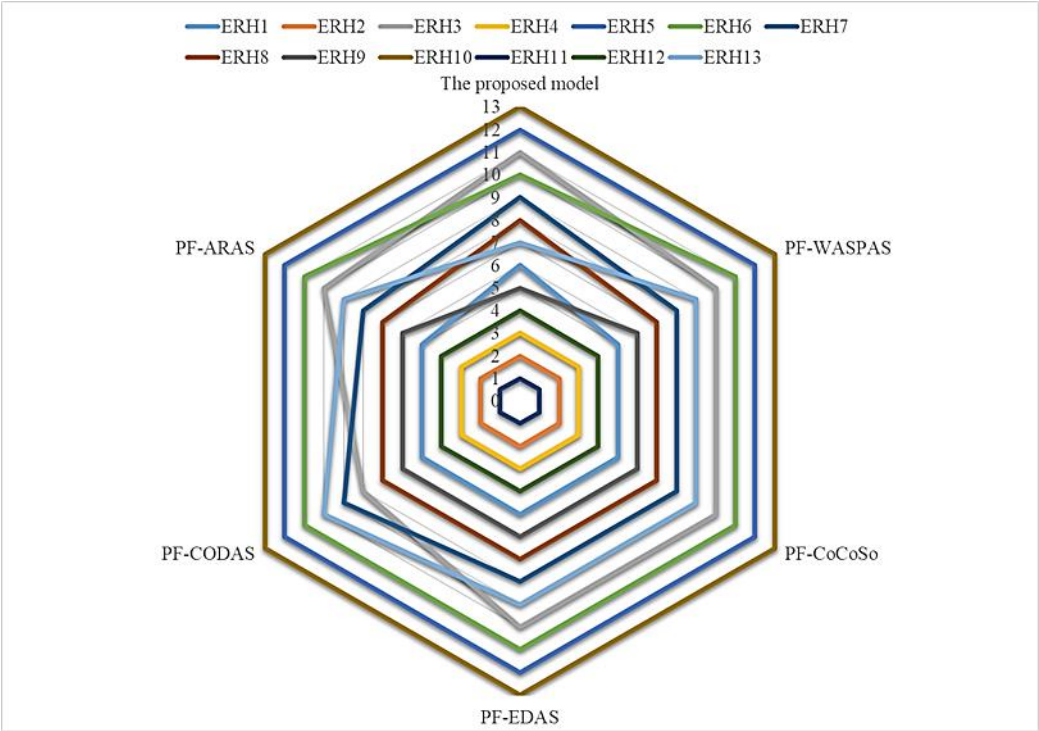


Figure 3. The presentation of the comparative analysis in graphical form.

The application of the WASPAS, CoCoSo, EDAS, CODAS, and ARAS methodologies yielded results that exhibited a strong correlation with the ARTASI approach.

6 DISCUSSION

6.1 Managerial Implications

The present model has been developed with the objective of facilitating a more exhaustive comprehension of the correlation between ergonomic risk factors and WMSDs. It is posited that this may engender beneficial insights with regard to the control of WMSD risk factors among agricultural workers in the operational field. Thus, a robust risk assessment model will empower authorities and stakeholders to act with greater alacrity and efficacy in response to significant potential occupational hazards. The developed FK-PFLODAR hybrid model, integrating PFS and advanced aggregation operator, provides useful practical information and managerial implications:

(i) Pioneering OHSRA Model: The conceptualization of the FK-PFLODAR hybrid model represents a significant innovation in the field of occupational risk assessment, providing a pioneering model for experts and practitioners engaged in ergonomic risk assessment. This

pioneering approach transcends traditional methodologies to the field, incorporating recent advancements with a view to enhancing the OHSRA process.

(ii) Importance Evaluation of Amplified Risk Parameters: The employment of the LODECI method for risk parameters weighting provides a robust and reliable assessment of the relative importance of different criteria. This approach enables managers to make informed decisions by taking into account the sophisticated significance of each criterion.

(iii) Adaptable Option for Ranking: The ARTASI technique enables those tasked with decision-making processes to consider the inevitable uncertainties that arise during expert assessments. This adaptability in the ordering of alternatives allows the model to accommodate varying degrees of precision and divergent perceptions.

(iv) Reliability of Decisions and Resistance to Falsification: The integration of sensitivity analysis strategies within the validation process, in conjunction with their comparative evaluation against extant methodologies, ensures the resilience of the proposed model. These analyses constitute a framework for determining the model's efficaciousness. This insight facilitates the selection of the optimal decision support instrument in accordance with management requirements.

In conclusion, the FK-PFLODAR OHSRA framework, as posited in this paper, constitutes a sophisticated and pioneering instrument for practitioners intending to circumvent the complexity inherent in ergonomic risk assessment, thereby encouraging more systematic and strategic OHSRA processes.

6.2 Limitations and future directions

The aforementioned OHSRA model is subject to several limitations that could be the focus of future research. First, the OHSRA is a multifaceted decisional process that necessitates the involvement of a variety of experts. Given the heterogeneity of experts' backgrounds in terms of demographics, specialisms and professional experience, it is to be considered that opinions are frequently expressed that are both divergent and contradictory. This finding has the potential to have a significant impact on the classification of occupational hazards in terms of risk. Consequently, it is advised that a strategy be formulated for the mitigation of professional differences among experts associated with the OHSRA. Second, the proposed model determines risk priority based on only three parameters. Nevertheless, it is crucial to consider that various parameters, for example cost, can exert a substantial influence on the risk

assessment process and its outcomes. Therefore, the integration of supplementary risk variables as additional dimensions within the Fine-Kinney approach may signify a viable direction for subsequent research endeavours. Finally, efficacy of the aforementioned model is dependent upon the incorporation of expert judgement in the assessment of risk variables and the delineation of hazard rankings. The inevitable subjectivity of expert evaluations may result in the presence of cognitive bias, and the robustness of the model's inferences may be contingent on the expertise and heterogeneity of the expert team engaged. In conclusion, the FK-PFLODAR model has been demonstrated to provide a robust OHS risk assessment tool; however, it is imperative to emphasise the limitations of the model, which are derived from the subjective evaluations of experts. It is suggested that future research efforts endeavours concentrate on incorporating Artificial Intelligence (AI) components to validate and improve model performance, with the aim of achieving a higher rate of accurate outcomes.

7 CONCLUSION

This study addressed the necessity to develop a DSM within the scope of ergonomic risk assessment, with a specific focus on prioritizing ergonomic risk factors affecting WMSDs among agricultural workers in terms of sustainable agriculture. Human factors/ergonomics possesses the capacity to contribute to processes that aim to combine both the human and financial dimensions in order to achieve sustainability, by optimizing the employees' performance and well-being [61].

The conventional Fine-Kinney model has been employed as a successful methodology in addressing the issue of occupational risk analysis. However, it is significant to emphasise that the model does possess some inherent limitations with regard to its capacity to manage uncertainty in expert judgements and the modelling of risk prioritization. Ergonomic risk factors are a major cause of WMSDs, which are known to have a significant impact on employee health and safety. The aim of ergonomic risk assessments, which are conducted to identify and evaluate the discrepancy between requirements of the workplace and the physical abilities of the workforce, is to prevent WMSDs [62]. This study proposes a hybrid ergonomic risk assessment model as a means to achieve the stated objective. This model integrates Fine-Kinney-based LODECI-ARTASI methods based on PFSs.

A total of 13 potential ergonomic hazards were identified in this study. The results demonstrate that the five most significant ergonomic hazards are ERH_{11} (Land of harvesting area), ERH_2 (Repetitive motion), ERH_4 (Standing for a long time), ERH_{12} (Work stress) and

ERH_9 (Unsuitable climatic conditions), respectively. The findings of the study demonstrate that ERH_{11} is the most significant potential hazard, necessitating the implementation of preventive and protective measures to ensure the health and safety of workers. The geography of the Eastern Black Sea region of tea plantations, characterized by slope, constitutes a significant hazard factor contributing to the prevalence of WMSDs. This is attributable to the physical demands of the work, which require workers to assume awkward postures during tea harvesting, resulting in potential musculoskeletal discomfort and injury. It is also important to note that ERH_{12} (Work stress) has been ranked among the most significant hazards. In the literature, psychosocial factors such as role conflict, low job control, job dissatisfaction and job insecurity are discussed as having an impact on WMSDs [63, 64]. The suggestion that psychological factors may be more influential on WMSDs than other factors is discussed in the literature [6]. A decline in the productivity of workers is likely to result in a corresponding decrease in the output of the agricultural sector of a nation, which, in turn, will have an impact on that country's GDP [7]. In order to manage the risk of WMSDs more effectively, it is essential that OHSRA practices address work-related psychosocial hazards [65]. In conclusion, this study provides beneficial implications for OHS professionals, decision-makers and practitioners in the control and prevention of ergonomic risks in the agricultural sector.

The proposed framework is acknowledged to have certain limitations, which are posited to be conducive to the suggestion of future directions. Firstly, it is important to note that only three risk parameters are included during the process of risk assessment. However, other factors such as cost or time might need to be taken into account in the event of more complicated risk assessment problems. Secondly, the proposed model was applied in agricultural studies. In such cases, its application can be diversified into various industries. Finally, the evaluation was conducted in accordance with the framework of three expert opinions in the current study. In future studies, the establishment oflarger decisional groups has the capacity to augment the efficacy of the model.

Acknowledgements

This article is derived from Veysel TATAR’s Ph.D.’s Dissertation at Istanbul Ticaret University, Industrial Engineering Doctorate’s Program. The author would like to express his gratitude to late doctoral thesis advisor, Prof. Dr. Osman YAZICIOĞLU, for his valuable contributions.

Conflict of Interest Statement

There is no conflict of interest between the authors.

Statement of Research and Publication Ethics

The study is complied with research and publication ethics.

Artificial Intelligence (AI) Contribution Statement

This manuscript was entirely written, edited, analyzed, and prepared without the assistance of any artificial intelligence (AI) tools. All content, including text, data analysis, and figures, was solely generated by the authors.

REFERENCES

[1] Q.-Y. Chen, H.-C. Liu, J.-H. Wang, and H. Shi, "New model for occupational health and safety risk assessment based on Fermatean fuzzy linguistic sets and CoCoSo approach," *Applied Soft Computing*, vol. 126, p. 109262, Sep. 2022, doi: 10.1016/j.asoc.2022.109262.

[2] M. Gul and M. F. Ak, "A comparative outline for quantifying risk ratings in occupational health and safety risk assessment," *Journal of Cleaner Production*, vol. 196, pp. 653–664, Sep. 2018, doi: 10.1016/j.jclepro.2018.06.106.

[3] World Health Organization (WHO), "Musculoskeletal health," Jul. 14, 2022. Accessed: Jul. 7, 2025. [Online]. Available: https://www.who.int/news-room/fact-sheets/detail/musculoskeletal-conditions

[4] D. S. F. de Souza, J. M. N. da Silva, J. V. de O. Santos, M. S. B. Alcântara, and M. G. L. Torres, "Influence of risk factors associated with musculoskeletal disorders on an inner population of northeastern Brazil," *International Journal of Industrial Ergonomics*, vol. 86, p. 103198, Nov. 2021, doi: 10.1016/j.ergon.2021.103198.

[5] J. M. N. da Silva, L. G. M. Bispo, W. K. dos S. Leite, E. M. de A. Vieira, A. H. S. Lisboa, and R. de S. Teixeira, "Assessing the link between occupational risk factors, work-related musculoskeletal disorders and quality of work life: An analysis using PLS-SEM," *International Journal of Industrial Ergonomics*, vol. 104, p. 103658, Nov. 2024, doi: 10.1016/j.ergon.2024.103658.

[6] B. Zhang, X. Yin, J. Li, and R. Tong, "Incorporating ergonomic and psychosocial stressors: A comprehensive model for assessing miners' work-related musculoskeletal disorders," *Safety Science*, vol. 176, p. 106564, Aug. 2024, doi: 10.1016/j.ssci.2024.106564.

[7] K. A. Akbar, P. Try, P. Viwattanakulvanid, and K. Kallawicha, "Work-related musculoskeletal disorders among farmers in the Southeast Asia region: A systematic review," *Safety and Health at Work*, vol. 14, no. 3, pp. 243–249, Sep. 2023, doi: 10.1016/j.shaw.2023.05.001.

[8] T.-H.-Y. Nguyen, M. Bertin, J. Bodin, N. Fouquet, N. Bonvallot, and Y. Roquelaure, "Multiple exposures and coexposures to occupational hazards among agricultural workers: A systematic review of observational studies," *Safety and Health at Work*, vol. 9, no. 3, pp. 239–248, Sep. 2018, doi: 10.1016/j.shaw.2018.04.002.

[9] S. Mohamaddan et al., "Investigation of oil palm harvesting tools design and technique on work-related musculoskeletal disorders of the upper body," *International Journal of Industrial Ergonomics*, vol. 86, p. 103226, Nov. 2021, doi: 10.1016/j.ergon.2021.103226.

[10] A. Thetkathuek, P. Meepradit, and T. Sa-ngiamsak, "A cross-sectional study of musculoskeletal symptoms and risk factors in Cambodian fruit farm workers in Eastern Region, Thailand," *Safety and Health at Work*, vol. 9, no. 2, pp. 192–202, Jun. 2018, doi: 10.1016/j.shaw.2017.06.009.

[11] F. A. Fathallah, "Musculoskeletal disorders in labor-intensive agriculture," *Applied Ergonomics*, vol. 41, no. 6, pp. 738–743, Oct. 2010, doi: 10.1016/j.apergo.2010.03.003.

[12] D. Kee and R. Haslam, "Prevalence of work-related musculoskeletal disorders in agriculture workers in Korea and preventative interventions," *Work*, vol. 64, no. 4, pp. 763–775, Dec. 2019, doi: 10.3233/WOR-193038.

[13] S. R. Kirkhorn, G. Earle-Richardson, and R. J. Banks, "Ergonomic risks and musculoskeletal disorders in production agriculture: Recommendations for effective research to practice," *Journal of Agromedicine*, vol. 15, no. 3, pp. 281–299, Jul. 2010, doi: 10.1080/1059924x.2010.488618.

[14] A. Dianat, D. Afshari, N. Sarmasti, M. S. Sangdeh, and R. Azaddel, "Work posture, working conditions and musculoskeletal outcomes in agricultural workers," *International Journal of Industrial Ergonomics*, vol. 77, p. 102941, May 2020, doi: 10.1016/j.ergon.2020.102941.

[15] A. Mazloumi and B. Kouhnavard, "Investigation of observational techniques ergonomic risk assessment of work-related musculoskeletal disorders among farmers—A systematic review," *Journal of Agromedicine*, vol. 30, no. 3, pp. 616–639, Jan. 2025, doi: 10.1080/1059924x.2024.2436447.

[16] M. J. J. Law et al., "REBA assessment of patient transfer work using sliding board and motorized patient transfer device," *International Journal of Industrial Ergonomics*, vol. 90, p. 103322, Jul. 2022, doi: 10.1016/j.ergon.2022.103322.

[17] N. R. Kodle, S. P. Bhosle, and V. B. Pansare, "Ergonomic risk assessment of tasks performed by workers in granite and marble units using ergonomics tool's REBA," *Materials Today: Proceedings*, vol. 72, pp. 1903–1916, 2023, doi: 10.1016/j.matpr.2022.10.153.

[18] C. K. Brazil, T. A. Pottorff, M. Miller, and M. J. Rys, "Using the Rapid Upper Limb Assessment to examine the effect of the new Hotel Housekeeping California Standard," *Applied Ergonomics*, vol. 106, p. 103868, Jan. 2023, doi: 10.1016/j.apergo.2022.103868.

[19] S. De-Benavides-Jiménez, M. Gómez-Galán, J.-C. Rubio-Romero, M. Díaz-Pérez, and Á.-J. Callejón-Ferre, "Physical load assessment of greenhouse cucumber farmers using OWAS and RULA methods," *Safety Science*, vol. 187, p. 106838, Jul. 2025, doi: 10.1016/j.ssci.2025.106838.

[20] C. Brandl, A. Mertens, and C. M. Schlick, "Effect of sampling interval on the reliability of ergonomic analysis using the Ovako working posture analysing system (OWAS)," *International Journal of Industrial Ergonomics*, vol. 57, pp. 68–73, Jan. 2017, doi: 10.1016/j.ergon.2016.11.013.

[21] S. Oliv, E. Gustafsson, A. N. Baloch, M. Hagberg, and H. Sandén, "The Quick Exposure Check (QEC)—Inter-rater reliability in total score and individual items," *Applied Ergonomics*, vol. 76, pp. 32–37, Apr. 2019, doi: 10.1016/j.apergo.2018.11.005.

[22] L. Tiacci and M. Mimmi, "Integrating ergonomic risks evaluation through OCRA index and balancing/sequencing decisions for mixed model stochastic asynchronous assembly lines," *Omega*, vol. 78, pp. 112–138, Jul. 2018, doi: 10.1016/j.omega.2017.08.011.

[23] D. Kee and W. Karwowski, "LUBA: An assessment technique for postural loading on the upper body based on joint motion discomfort and maximum holding time," *Applied Ergonomics*, vol. 32, no. 4, pp. 357–366, Aug. 2001, doi: 10.1016/S0003-6870(01)00006-0.

[24] K. Koppiahraj, S. Bathrinath, and S. Saravanasankar, "A fuzzy VIKOR approach for selection of ergonomic assessment method," *Materials Today: Proceedings*, vol. 45, pp. 640–645, 2021, doi: 10.1016/j.matpr.2020.02.725.

[25] B. Rathore, A. K. Pundir, R. Iqbal, and R. Gupta, "Development of fuzzy based ergonomic-value stream mapping (E-VSM) tool: A case study in Indian glass artware industry," *Production Planning & Control*, vol. 34, no. 16, pp. 1618–1638, Feb. 2022, doi: 10.1080/09537287.2022.2035447.

[26] A. Ramaswamy Govindan and X. Li, "Fuzzy logic-based decision support system for automating ergonomics risk assessments," *International Journal of Industrial Ergonomics*, vol. 96, p. 103459, Jul. 2023, doi: 10.1016/j.ergon.2023.103459.

[27] C. Zhao, Q. Q. Li, C. Harris Adamson, and A. Nemati, "A fuzzy logic approach to improve the sensitivity of the rapid entire body assessment method," *International Journal of Occupational Safety and Ergonomics*, vol. 31, no. 2, pp. 419–430, Jan. 2025, doi: 10.1080/10803548.2024.2445980.

[28] B. C. Cuong and V. Kreinovich, "Picture fuzzy sets—A new concept for computational intelligence problems," in *Proc. 2013 World Congress on Information and Communication Technologies (WICT)*,

Dec. 2013, pp. 1–6. Accessed: Jul. 7, 2025. [Online]. Available: https://doi.org/10.1109/WICT.2013.7113099

[29] K. T. Atanassov, "Intuitionistic fuzzy sets," *Fuzzy Sets and Systems*, vol. 20, no. 1, pp. 87–96, Aug. 1986, doi: 10.1016/S0165-0114(86)80034-3.

[30] W. Wang, X. Liu, and Y. Qin, "A fuzzy Fine-Kinney-based risk evaluation approach with extended MULTIMOORA method based on Choquet integral," *Computers & Industrial Engineering*, vol. 125, pp. 111–123, Nov. 2018, doi: 10.1016/j.cie.2018.08.019.

[31] M. Gul, B. Guven, and A. F. Guneri, "A new Fine-Kinney-based risk assessment framework using FAHP-FVIKOR incorporation," *Journal of Loss Prevention in the Process Industries*, vol. 53, pp. 3–16, May 2018, doi: 10.1016/j.jlp.2017.08.014.

[32] M. Gul, S. Mete, F. Serin, and E. Celik, *Fine–Kinney-Based Fuzzy Multi-criteria Occupational Risk Assessment: Approaches, Case Studies and Python Applications*. Springer Nature, 2021a.

[33] W. Wang, X. Han, W. Ding, Q. Wu, X. Chen, and M. Deveci, "A Fermatean fuzzy Fine–Kinney for occupational risk evaluation using extensible MARCOS with prospect theory," *Engineering Applications of Artificial Intelligence*, vol. 117, p. 105518, Jan. 2023, doi: 10.1016/j.engappai.2022.105518.

[34] Y. Wang, W. Wang, M. Deveci, and X. Yu, "An integrated interval-valued spherical fuzzy Choquet integral based decision making model for prioritizing risk in Fine-Kinney," *Engineering Applications of Artificial Intelligence*, vol. 127, p. 107437, Jan. 2024, doi: 10.1016/j.engappai.2023.107437.

[35] O. Pala, "Assessment of the social progress on European Union by logarithmic decomposition of criteria importance," *Expert Systems with Applications*, vol. 238, p. 121846, Mar. 2024, doi: 10.1016/j.eswa.2023.121846.

[36] D. Pamucar, V. Simic, Ö. F. Görçün, and H. Küçükönder, "Selection of the best Big Data platform using COBRAC-ARTASI methodology with adaptive standardized intervals," *Expert Systems with Applications*, vol. 239, p. 122312, Apr. 2024, doi: 10.1016/j.eswa.2023.122312.

[37] M. Gul and E. Celik, "Fuzzy rule-based Fine–Kinney risk assessment approach for rail transportation systems," *Human and Ecological Risk Assessment: An International Journal*, vol. 24, no. 7, pp. 1786–1812, Jan. 2018, doi: 10.1080/10807039.2017.1422975.

[38] A. Karasan, E. Ilbahar, S. Cebi, and C. Kahraman, "A new risk assessment approach: Safety and Critical Effect Analysis (SCEA) and its extension with Pythagorean fuzzy sets," *Safety Science*, vol. 108, pp. 173–187, May 2018, doi: 10.1016/j.ssci.2018.04.031.

[39] M.-È. Chiasson, D. Imbeau, J. Major, K. Aubry, and A. Delisle, "Influence of musculoskeletal pain on workers' ergonomic risk-factor assessments," *Applied Ergonomics*, vol. 49, pp. 1–7, Jan. 2015, doi: 10.1016/j.apergo.2014.12.011.

[40] M. MassirisFernández, J. Á. Fernández, J. M. Bajo, and C. A. Delrieux, "Ergonomic risk assessment based on computer vision and machine learning," *Computers & Industrial Engineering*, vol. 149, p. 106816, Sep. 2020, doi: 10.1016/j.cie.2020.106816.

[41] M. J. Jorgensen, A. Martinez, and N. A. Hakansson, "Comparison of multi-task ergonomic assessment methods for risk of upper extremity and low back musculoskeletal disorders," *Applied Ergonomics*, vol. 119, p. 104313, May 2024, doi: 10.1016/j.apergo.2024.104313.

[42] M. J. J. Law et al., "REBA assessment of patient transfer work using sliding board and motorized patient transfer device," *International Journal of Industrial Ergonomics*, vol. 90, p. 103322, Jun. 2022, doi: 10.1016/j.ergon.2022.103322.

[43] B. Ipaki, J. F. M. Molenbroek, Z. Merrikhpour, and S. A. Faregh, "Applying the quick exposure check in the workstation design process, physical and virtual prototype assessment," *Work*, vol. 76, no. 2, pp. 569–586, Mar. 2023, doi: 10.3233/WOR-220503.

[44] A. Cimino, M. G. Gnoni, F. Longo, and L. Nicoletti, "A risk assessment framework based on ergonomic methods and AHP for prioritizing interventions to prevent container terminal operator's musculoskeletal disorders," *Safety Science*, vol. 159, p. 106017, Mar. 2023, doi: 10.1016/j.ssci.2022.106017.

[45] S. De-Benavides-Jiménez, M. Gómez-Galán, J.-C. Rubio-Romero, M. Díaz-Pérez, and Á.-J. Callejón-Ferre, "Physical load assessment of greenhouse cucumber farmers using OWAS and RULA methods," *Safety Science*, vol. 187, p. 106838, Mar. 2025, doi: 10.1016/j.ssci.2025.106838.

[46] L. A. Zadeh, "Fuzzy sets," *Information and Control*, vol. 8, no. 3, pp. 338–353, Jun. 1965, doi: 10.1016/S0019-9958(65)90241-X.

[47] V. Simić, D. Lazarević, and M. Dobrodolac, "Picture fuzzy WASPAS method for selecting last-mile delivery mode: A case study of Belgrade," *European Transport Research Review*, vol. 13, no. 1, Jul. 2021, doi: 10.1186/s12544-021-00501-6.

[48] V. Tatar and B. Ayvaz, "Assessment of environmental performance of ports utilizing an integrated LBWA–MARCOS decision-making approach based on picture fuzzy sets," in *Lecture Notes in Networks and Systems*. Cham: Springer Nature Switzerland, 2024, pp. 622–629. Accessed: Jul. 7, 2025. [Online]. Available: https://doi.org/10.1007/978-3-031-70018-7_69

[49] A. Tarafdar, A. Shaikh, M. N. Ali, and A. Haldar, "An integrated fuzzy decision-making framework for autonomous mobile robot selection: Balancing subjective and objective measures with fuzzy TOPSIS and picture fuzzy CoCoSo approach," *Journal of the Operational Research Society*, pp. 1–27, Apr. 2025, doi: 10.1080/01605682.2025.2486705.

[50] G. F. Kinney and A. D. Wiruth, *Practical Risk Analysis for Safety Management*. 1976.

[51] M. Gul, E. Celik, and E. Akyuz, "A hybrid risk-based approach for maritime applications: The case of ballast tank maintenance," *Human and Ecological Risk Assessment: An International Journal*, vol. 23, no. 6, pp. 1389–1403, Jul. 2017, doi: 10.1080/10807039.2017.1317204.

[52] E. Ilbahar, A. Karaşan, S. Cebi, and C. Kahraman, "A novel approach to risk assessment for occupational health and safety using Pythagorean fuzzy AHP & fuzzy inference system," *Safety Science*, vol. 103, pp. 124–136, Mar. 2018, doi: 10.1016/j.ssci.2017.10.025.

[53] J. Tang, X. Liu, and W. Wang, "A hybrid risk prioritization method based on generalized TODIM and BWM for Fine-Kinney under interval type-2 fuzzy environment," *Human and Ecological Risk Assessment: An International Journal*, vol. 27, no. 4, pp. 954–979, Jul. 2020, doi: 10.1080/10807039.2020.1789840.

[54] S. Seker, "A novel risk assessment approach using a hybrid method based on Fine–Kinney and extended MCDM methods under interval-valued intuitionistic fuzzy environment," *International Journal of Information Technology & Decision Making*, vol. 21, no. 05, pp. 1591–1616, May 2022, doi: 10.1142/S0219622022500250.

[55] Y. Chen, X. Yu, and Z. Yang, "A fuzzy decision support system for risk prioritization in Fine-Kinney-based occupational risk analysis," *Journal of Soft Computing and Decision Analytics*, vol. 3, no. 1, pp. 1–17, 2025, doi: 10.31181/jscda31202545.

[56] W. Wang, L. Ding, X. Liu, and S. Liu, "An interval 2-tuple linguistic Fine-Kinney model for risk analysis based on extended ORESTE method with cumulative prospect theory," *Information Fusion*, vol. 78, pp. 40–56, Feb. 2022, doi: 10.1016/j.inffus.2021.09.008.

[57] X. Peng and Z. Luo, "Decision-making model for China's stock market bubble warning: The CoCoSo with picture fuzzy information," *Artificial Intelligence Review*, vol. 54, no. 8, pp. 5675–5697, Jan. 2021, doi: 10.1007/s10462-021-09954-6.

[58] Q. Mao, J. Fan, and Y. Gao, "An investment framework for hydro-wind-photovoltaic-hydrogen hybrid power system based on the improved picture fuzzy regret-PROMETHEE model," *International Journal of Hydrogen Energy*, vol. 106, pp. 565–585, Mar. 2025, doi: 10.1016/j.ijhydene.2025.01.505.

[59] E. Haktanır and C. Kahraman, "A novel picture fuzzy CRITIC & REGIME methodology: Wearable health technology application," *Engineering Applications of Artificial Intelligence*, vol. 113, p. 104942, May 2022, doi: 10.1016/j.engappai.2022.104942.

[60] M. Gul, S. Mete, F. Serin, and E. Celik, "Fine–Kinney-based occupational risk assessment using intuitionistic fuzzy TODIM," in *Studies in Fuzziness and Soft Computing*. Cham: Springer International Publishing, 2021b, pp. 69–89. Accessed: Jul. 7, 2025. [Online]. Available: https://doi.org/10.1007/978-3-030-52148-6_5

[61] J. Dul et al., "A strategy for human factors/ergonomics: Developing the discipline and profession," *Ergonomics*, vol. 55, no. 4, pp. 377–395, Feb. 2012, doi: 10.1080/00140139.2012.661087.

[62] M. MassirisFernández, J. Á. Fernández, J. M. Bajo, and C. A. Delrieux, "Ergonomic risk assessment based on computer vision and machine learning," *Computers & Industrial Engineering*, vol. 149, p. 106816, Nov. 2020, doi: 10.1016/j.cie.2020.106816.

[63] E. M. Eatough, J. D. Way, and C.-H. Chang, "Understanding the link between psychosocial work stressors and work-related musculoskeletal complaints," *Applied Ergonomics*, vol. 43, no. 3, pp. 554–563, May 2012, doi: 10.1016/j.apergo.2011.08.009.

[64] H.-C. Liu, Y. Cheng, and J.-J. Ho, "Associations of ergonomic and psychosocial work hazards with musculoskeletal disorders of specific body parts: A study of general employees in Taiwan," *International Journal of Industrial Ergonomics*, vol. 76, p. 102935, Mar. 2020, doi: 10.1016/j.ergon.2020.102935.

[65] J. Oakman, W. Macdonald, and N. Kinsman, "Barriers to more effective prevention of work-related musculoskeletal and mental health disorders," *Applied Ergonomics*, vol. 75, pp. 184–192, Feb. 2019, doi: 10.1016/j.apergo.2018.10.007.

BİTLİS EREN ÜNİVERSİTESİ
FEN BİLİMLERİ DERGİSİ

ISSN: 2147-3129 / e-ISSN: 2147-3188

Article Type	: Research Article	**Year**	: 2025
Received	: July 9, 2025	**Volume**	: 14
Revised	: September 17, 2025	**Issue**	: 3
Accepted	: September 19, 2025	**Pages**	: 1921-1941
DOI	: 10.17798/bitlisfen.1738850		

INVESTIGATION OF PHYSICAL, MECHANICAL, AND DRILLING MACHINABILITY PROPERTIES OF NANOPARTICLES REINFORCED CARBON/GLASS FIBER HYBRID COMPOSITES

Alper GUNOZ [1, *], Umut Ozgur OZALTAY [1]

[1] *Mersin University, Mechanical Engineering Department, Mersin, Türkiye*

**** Corresponding Author:*** *alpergunoz@mersin.edu.tr*

ABSTRACT

This study aims to investigate the effects of nanoparticle reinforcement, fiber hybridization, and stacking sequences on the mechanical properties and drilling machinability of composite materials. For this purpose, 12-layered polymer composite plates reinforced with graphene nanoplatelets (GnPs) and boron nitride nanoparticles (BNNPs) were produced using the vacuum bagging method. Carbon fiber (CF), glass fiber (GF), and hybrid fiber (HF) with different stacking sequences were used as reinforcements. The samples were subjected to density and hardness measurements, as well as conventional drilling tests. Drilling operations were carried out on a CNC vertical machining center using Ø6.5 mm drills with point angles of 90°, 110°, and 130°, at a constant spindle speed (1000 rpm) and three different feed rates (200, 600, and 1000 mm/min). The results demonstrated that the neat CF specimen exhibited the highest hardness, whereas the incorporation of nanoparticles reduced hardness, with BNNP-reinforced specimens showing the greatest reduction of about 15%. Drilling machinability was significantly enhanced, as evidenced by the reduction in delamination, and the optimum hole diameter (Ø6.48 mm) was achieved in the GF-based composite reinforced with BNNPs using a 130° drill point angle and a feed rate of 200 mm/min. The effects of GnPs and BNNPs on the drilling machinability of fiber-reinforced composites have been investigated only to a limited extent in the literature, and this study provides new insights. These findings may contribute to improving the quality and efficiency of drilling processes in the aerospace and automotive industries.

Keywords: Hybrid composite material, Nanoparticles, Drilling machinability, Graphene nanoplatelets (GnPs), Boron nitride nanoparticles (BNNPs).

1 INTRODUCTION

Fiber-reinforced polymer matrix composites are widely used in various engineering applications—particularly in the aerospace, automotive, marine, and defense industries—due to their superior properties such as high specific strength, low density, corrosion resistance, and design flexibility [1]. However, despite these advantages, they still exhibit certain limitations, primarily stemming from the brittle nature of the matrix phase, which results in low toughness and poor impact resistance [2, 3]. To overcome these mechanical drawbacks, numerous studies have recently focused on enhancing the performance of composite materials by incorporating various nanoparticles into the matrix phase [4-7]. Nanostructures such as graphene nanoplatelets (GnPs) and hexagonal boron nitride nanoparticles (BNNPs) have demonstrated promising effects on the composite structure due to their high surface area and excellent mechanical properties when added to the matrix [8, 9]. According to the literature, such nanoparticle reinforcements contribute to matrix toughening, thereby increasing the ductility of the overall composite system [10, 11].

Enhancing the mechanical performance of composite materials can be effectively achieved not only by toughening the matrix phase but also by hybridizing the reinforcing elements and optimizing the stacking sequence in hybrid structures [12, 13]. For instance, in CF/GF hybrid composites, CFs contribute high strength and stiffness, whereas GF enhance the overall toughness of the material due to their relatively ductile behavior. Furthermore, a well-designed stacking sequence of the fibers in the hybrid structure can help confine damage under external loading and provide better control over fracture mechanisms [14].

Composite materials undergo various machining processes during their service life, both for dimensional shaping and joining purposes. Among these, drilling is the most common machining operation. Drilling is a complex mechanical process involving the interaction of multi-component cutting forces [15, 16]. The primary challenge encountered during drilling of composite materials is the deformation occurring at the hole entry and exit regions. Such deformations compromise the structural integrity of the composite and significantly reduce its mechanical strength [17]. Therefore, numerous studies have focused on improving hole quality and minimizing damage formation by investigating various parameters. Karaca [15] examined the effects of drill point angle and feed rate on hole deformation in GF reinforced epoxy composites and reported that increases in both parameters lead to increased deformation. Rajamurugan et al. [18] reported that feed rate and drill diameter are the primary factors affecting deformation, while spindle speed has a limited impact. Sunny et al. [19], demonstrated that high spindle speeds combined with low feed rates reduce delamination and burr formation,

with feed rate having a more dominant influence on such damages. Additionally, studies in the literature have reported measurements and analyses of burr size and have focused on deburring techniques [20-22]. Tsao et al. [23] successfully reduced deformation by applying mechanical support at the hole exit. Anaç et al. [24] investigated the mechanical properties and drilling-induced damages of GF epoxy composites produced by different manufacturing methods; they found that hand lay-up samples exhibited higher tensile strength, while the least delamination occurred in samples produced by 3D printing. Unal [25] studied the effects of drill point angle and process parameters on thrust force and temperature during drilling of GF reinforced composites. The findings revealed that feed rate predominantly affects thrust force, whereas point angle has a stronger influence on temperature. Vankanti et al. [26] explored the effects of cutting speed, feed rate, point angle, and cutting edge width on thrust force during drilling of GF composites, highlighting feed rate as the most influential parameter. Gemi et al. [27] examined the influence of different drill geometries and process parameters on damage formation in GF reinforced composite pipes, demonstrating that drill type and feed rate directly affect hole quality.

Several studies have investigated the effects of nanoparticle reinforcement, hybridization, and stacking sequences on the mechanical properties and drilling machinability of composites. Singh and Kumar [28] demonstrated that the addition of multi-walled carbon nanotubes (MWCNTs) reduces delamination and surface roughness in GF epoxy composites. Similarly, Heidary et al. [29] reported that MWCNTs significantly contribute to the reduction of delamination and thrust force in GF epoxy composites. Sathish and Varadhan [30] found that the incorporation of MWCNTs and nano-SiO_2 considerably decreases delamination in basalt fiber (BF)/GF hybrid composites. Erhan et al. [31] highlighted the importance of stacking sequences on mechanical behavior and hole quality in BF reinforced composite pipes. Patel et al. [32] investigated the effect of stacking sequences on the drilling machinability of BF/GF hybrid composites and reported that stacking sequences significantly influences the results. Gemi et al. [33] experimentally examined the mechanical properties and machinability of filament-wound CF/GF fiber hybrid composites with various stacking sequences. Their results indicated that placing a CF layer between two GF layers yields better mechanical performance and machinability characteristics.

A review of the literature indicates that most investigations on drilling of FRP composites have focused on machining parameters such as feed rate, spindle speed, drill diameter, and drill type in order to improve hole quality. Although some studies have explored the role of nanoparticle additives, such as MWCNTs, and the effect of stacking sequences,

research on the influence of GnPs and BNNPs remains scarce. In particular, no comprehensive study has simultaneously addressed how these reinforcements, in combination with hybridization and stacking sequences, affect drilling-induced damages. Moreover, the correlation between such modifications and the fundamental physical and mechanical properties of the composites has not yet been systematically investigated. Therefore, this study aims to fill this gap by experimentally examining the combined effects of drill point angle, feed rate, GnPs and BNNPs reinforcement, hybridization, and stacking sequences on drilling machinability, while also evaluating density and hardness as key material properties. This integrated approach provides new insights into tailoring both the performance and machinability of advanced hybrid composites.

2 MATERIAL AND METHOD

2.1 Materials

In the present study, a diglycidyl ether of bisphenol A (DGEBA)-based epoxy laminating resin (MGS® L285) and its corresponding hardener (MGS® H285), both manufactured by Hexion, were utilized. The reinforcing materials consisted of CF fabric (245 g·m^{-2}, twill weave) and GF fabric (300 g·m^{-2}, twill weave), procured from Dost Kimya (Istanbul, Turkey). Detailed technical properties of the epoxy resin and hardener system are presented in Table 1. In this study, GnPs (Purity:99.9%, Size: 3 nm, Specific Surface Area: 800 m^2·g^{-1}, Diameter: 1.5 µm) and BNNPs (Purity: 99.85+%, Size: 65-75 nm, Hexagonal) supplied by Nanografi Nanotechnology AS (Ankara, Turkey) were incorporated into the epoxy resin.

Table 1. Material properties of the epoxy system used in nanocomposite manufacturing

Property	Epoxy Matrix (L285)	Hardener (H285)
Density	1.18 – 1.23 g·cm^{-3}	0.94 – 0.97 g·cm^{-3}
Viscosity (25 °C)	600 - 900 mPa·s	50 - 100 mPa·s
Gel time	2 - 3 h at 20 - 25 °C; 45-60 min at 40 - 45 °C	
Mixing ratios	100:40 ± 2 (by weight); 100:50 ± 2 (by volume)	

2.2 Composite Fabrication

12-layered CF, GF, and CF/GF epoxy composites, both with and without nanoparticle reinforcements, were fabricated using the vacuum bagging method. The composite manufacturing process is illustrated in Figure 1. For the reinforced samples, the ratios of GnPs (0.25 wt.%) and BNNPs (0.5 wt.%) were selected based on previous studies reported in the

literature [9, 34-37] to ensure effective reinforcement while minimizing agglomeration and processing difficulties. After the nanoparticles were incorporated into the epoxy, the mixture was mechanically stirred for 5 minutes, followed by ultrasonic stirring for 15 minutes using a probe with a diameter of Ø13 mm to ensure uniform dispersion. The ultrasonic device had a nominal power of 200 W and operated at a frequency of 20 kHz. The mixing was performed at 85% amplitude in a pulsed mode with a cycle of 2 s on and 3 s off to limit temperature rise. Temperature was monitored and controlled via a thermocouple built into the device. Subsequently, the hardener was added to the reinforced epoxy and mixed mechanically for an additional 5 minutes to achieve homogeneity. The curing process involved a pre-curing stage at 70 °C for 1 hour, followed by a post-curing stage at 100 °C for 3 hours in an autoclave oven, with heating and cooling rates of approximately 1.5 °C/min.

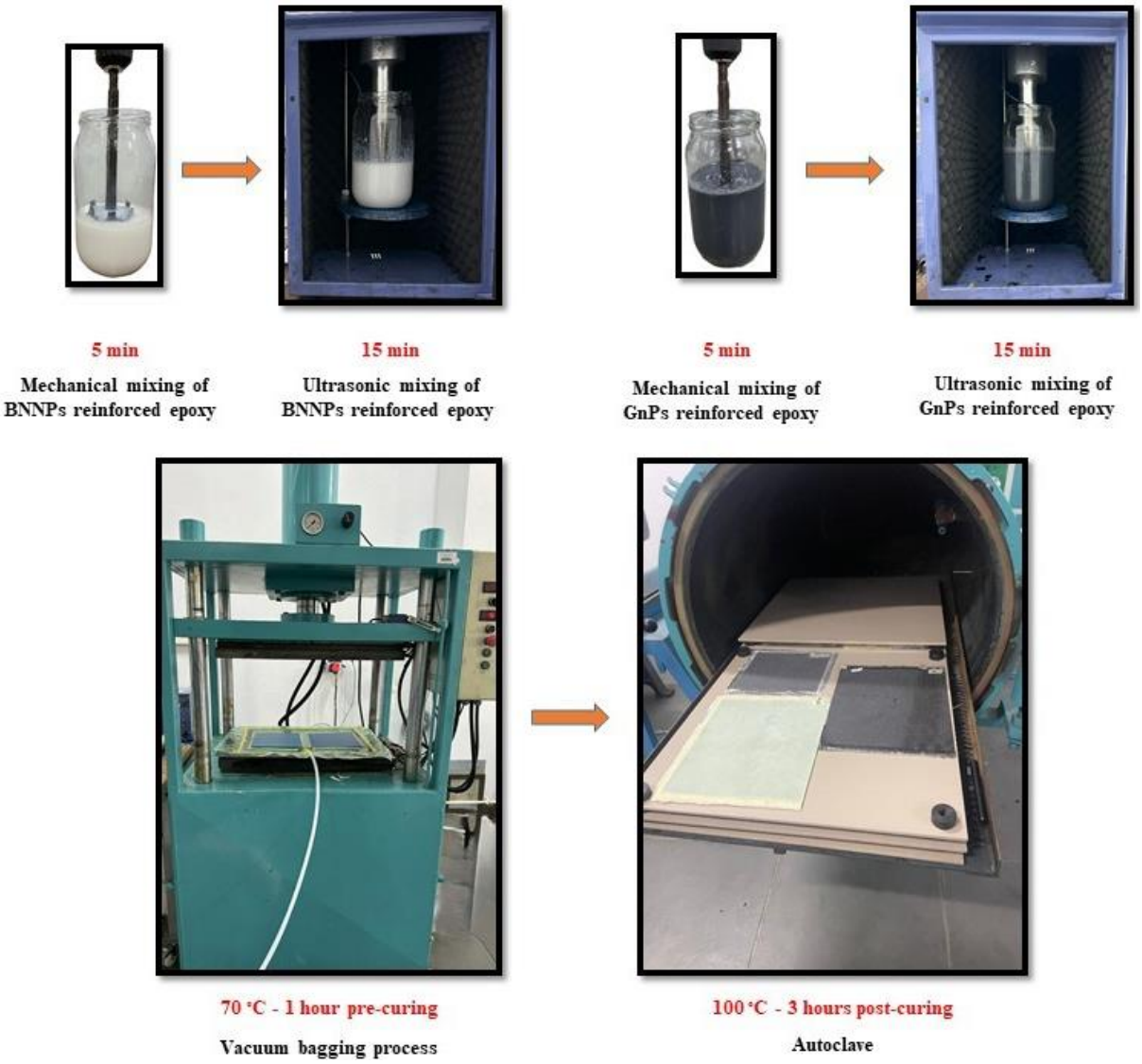


Figure 1. Production process of the composite specimens.

Figure 2 schematically illustrates the stacking sequences of the composite specimens produced in this study. Figures 2a and 2b represent 12-layer composites reinforced solely with CF and GF, respectively. Figures 2c, 2d, and 2e show the HF configurations, labeled as HF1, HF2, and HF3 according to their stacking sequences. The specimens shown in Figures 2f–2j correspond to those in Figures 2a–2e, respectively, with the addition of GnPs into the matrix. Similarly, Figures 2k–2o represent the BNNPs modified versions of the same composites. Figures 2p–2t depict hybrid nanocomposites in which both GnPs and BNNPs were incorporated into the matrix. In total, 20 different composite configurations were fabricated for this study.

The naming of composite specimens begins with the type of reinforcement: “N” denotes neat specimens, “G” indicates GnPs-reinforced, “B” represents BNNPs-reinforced, and “G-B” refers to specimens reinforced with both GnPs and BNNPs. This is followed by the fiber type: “CF” for carbon fiber, “GF” for glass fiber, and “HF1,” “HF2,” and “HF3” for three different stacking sequences of hybrid fibers. For instance, the designation “G-B-CF” refers to a carbon fiber epoxy composite specimen reinforced with both GnPs and BNNPs. A summary of the sample coding and contents is provided in Table 2 to facilitate comparison of the different composite configurations.

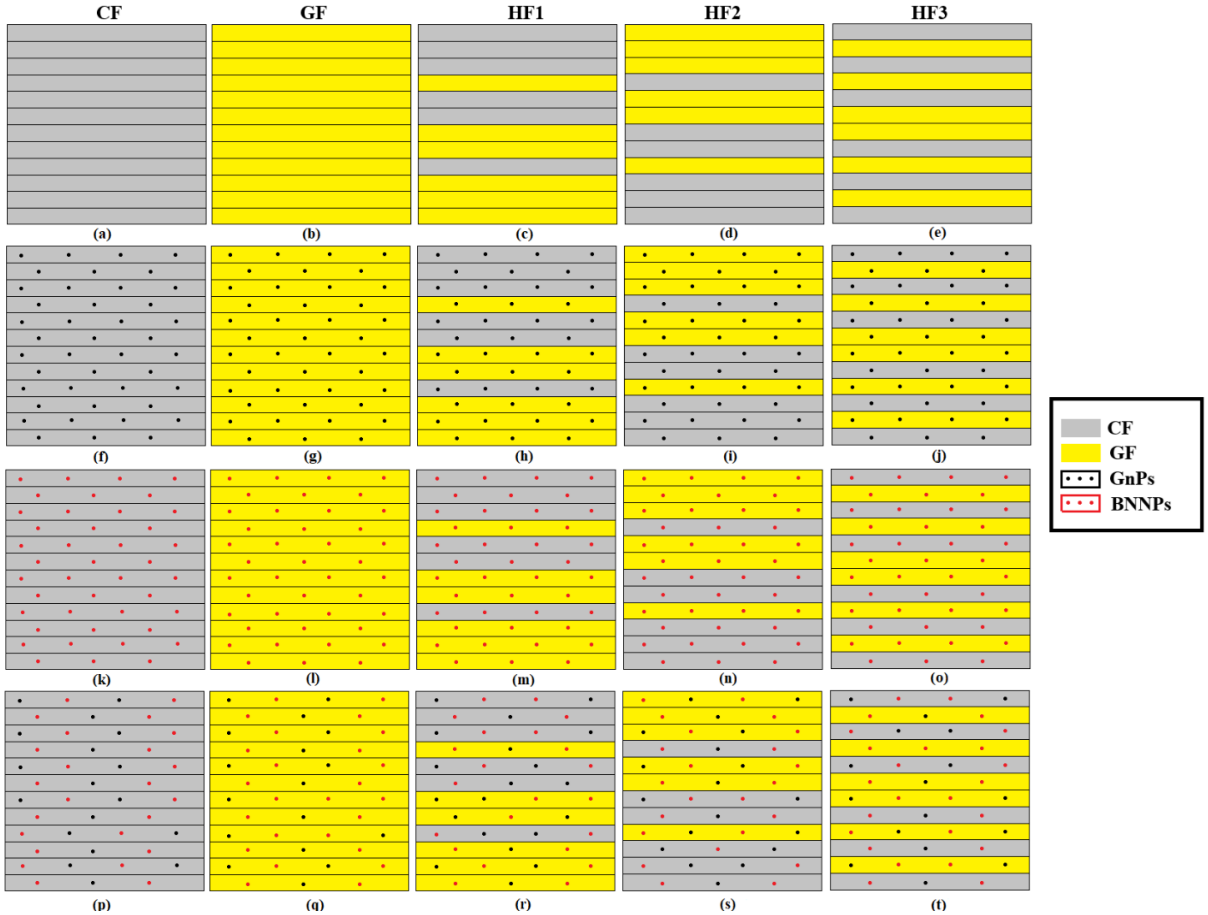


Figure 2. Schematic illustration of the stacking sequences of the composite specimens.

Table 2. Nomenclature of produced composite materials

Sample Code	Sample Content	Stacking Sequence of Layers
N-CF	Neat carbon fiber epoxy composite	$[CF_{12}]$
N-GF	Neat glass fiber epoxy composite	$[GF_{12}]$
N-HF1	Neat hybrid fiber epoxy composite 1	$[CF_3, GF, CF_2, GF_2, CF, GF_3]$
N-HF2	Neat hybrid fiber epoxy composite 2	$[GF_3, CF, GF_2, CF_2, GF, CF_3]$
N-HF3	Neat hybrid fiber epoxy composite 3	$[CF, GF, CF, GF, CF, GF]_s$
G-CF	GnPs reinforced carbon fiber epoxy composite	$[CF_{12}]$+GnPs
G-GF	GnPs reinforced glass fiber epoxy composite	$[GF_{12}]$+GnPs
G-HF1	GnPs reinforced hybrid fiber epoxy composite 1	$[CF_3, GF, CF_2, GF_2, CF, GF_3]$+GnPs
G-HF2	GnPs reinforced hybrid fiber epoxy composite 2	$[GF_3, CF, GF_2, CF_2, GF, CF_3]$+GnPs
G-HF3	GnPs reinforced hybrid fiber epoxy composite 3	$[CF, GF, CF, GF, CF, GF]_s$+GnPs
B-CF	BNNPs reinforced carbon fiber epoxy composite	$[CF_{12}]$+BNNPs
B-GF	BNNPs reinforced glass fiber epoxy composite	$[GF_{12}]$+BNNPs
B-HF1	BNNPs reinforced hybrid fiber epoxy composite 1	$[CF_3, GF, CF_2, GF_2, CF, GF_3]$+BNNPs
B-HF2	BNNPs reinforced hybrid fiber epoxy composite 2	$[GF_3, CF, GF_2, CF_2, GF, CF_3]$+BNNPs
B-HF3	BNNPs reinforced hybrid fiber epoxy composite 3	$[CF, GF, CF, GF, CF, GF]_s$+BNNPs
G-B-CF	GnPs and BNNPs reinforced carbon fiber epoxy composite	$[CF_{12}]$+GnPs+BNNPs
G-B-GF	GnPs and BNNPs reinforced glass fiber epoxy composite	$[GF_{12}]$+GnPs+BNNPs
G-B-HF1	GnPs and BNNPs reinforced hybrid fiber epoxy composite 1	$[CF_3, GF, CF_2, GF_2, CF, GF_3]$+GnPs+BNNPs
G-B-HF2	GnPs and BNNPs reinforced hybrid fiber epoxy composite 2	$[GF_3, CF, GF_2, CF_2, GF, CF_3]$+GnPs+BNNPs
G-B-HF3	GnPs and BNNPs reinforced hybrid fiber epoxy composite 3	$[CF, GF, CF, GF, CF, GF]_s$+GnPs+BNNPs

2.3 Density Measurement

The density of the composite specimens was determined based on Archimedes' principle, in accordance with ASTM D792 [38]. Test specimens were cut into 75 mm × 75 mm squares with a thickness of approximately 3 mm. Although the standard allows for specimens of different shapes and sizes, care was taken to ensure smooth edges and flat surfaces to avoid errors due to compressive stress or frictional heating during cutting. Prior to testing, the surfaces of the specimens were cleaned with compressed air to remove dust and debris, and all specimens were conditioned at 23 ± 2 °C and 50 ± 5% relative humidity for 48 h.

Each specimen was first weighed in air (W_{air}) using an analytical balance (DESIS NHB model, Turkey) with a precision of 0.001 g, and then immersed in distilled water at 23 ± 2 °C (ρ_{water}=0.997 g·cm^{-3}) and weighed again (W_{water}), as shown in Figures 3(a) and 3(b). Figure 3(a) illustrates weighing the dry specimen, while Figure 3(b) shows the specimen suspended in water. Two measurements were performed for each specimen, and the arithmetic average was calculated. The density (ρ) was calculated using Equation (1).

$$\rho = \frac{W_{air}}{W_{air} - W_{water}} \rho_{water} \tag{1}$$

All test conditions, including water temperature and measurement procedure, were in accordance with ASTM D792 [38]. Care was taken to ensure the specimen was fully immersed

without contact with the vessel walls. The final reported density values represent the average of all measured specimens for each composite configuration.



(a) **(b)**

Figure 3. Weighing of composite specimens on a precision balance: (a) dry and (b) wet.

2.4 Hardness Measurement

The hardness of the composite specimens was measured using a Rockwell hardness device (Digirock-RB model, BMS Bulut brand, Turkey), as shown in Figure 4. Test specimens were cut and prepared according to ASTM D785 [39]. Test specimens were cut into 75 mm × 75 mm squares with a thickness of approximately 3 mm. Although the standard specifies a minimum thickness of 6 mm, ASTM D785 allows the use of thinner specimens if it has been verified that the hardness values are not affected by the supporting surface and that no imprint appears beneath the specimen during testing. The surfaces of the composite specimens were cleaned with compressed air to remove dust and debris. Prior to testing, all specimens were conditioned at 23 ± 2 °C and 50 ± 5% relative humidity for 48 h.

The measurements were carried out using the Rockwell L scale, which is widely preferred for polymer-based materials. According to this method, a steel ball indenter with a diameter of 6.35 mm was used, applying a minor load of 10 kg and a major load of 60 kg. All tests were conducted at room temperature. Each specimen was placed on a flat and rigid surface, and the indenter was pressed into the material. Hardness values (HRL) were recorded 10 seconds after stable contact was achieved. For each specimen, measurements were taken at six

different locations, and the arithmetic average values were calculated. The Rockwell hardness tester was calibrated according to the standard procedure using appropriate test blocks before measurements to ensure accuracy.



Figure 4. Rockwell hardness test setup for composite specimens (L scale, 6.35 mm steel ball, 10 kg minor load, 60 kg major load)

2.5 Drilling Processes

The drilling operations were performed on composite specimens fixed to a Topper TMV 850A CNC vertical machining center using a vise. High-speed steel (HSS) drill bits with a diameter of Ø6.5 mm and point angles of 90°, 110°, and 130° were employed. Since no official standard exists for drilling-induced damages in polymer composites, the test procedure was adapted from previous studies [40, 41]. The drilling was carried out without pecking or coolant, directly plunging into the material. The spindle speed was kept constant at 1000 rpm, while the feed rates were set at 200, 600, and 1000 mm/min. The spindle speed and feed rates were chosen based on previous studies [42, 43] on polymer composite drilling to represent typical ranges used in similar materials.

The composite specimens were securely clamped on the CNC machine using custom aluminum fixtures, which acted as support plates beneath the specimens. These fixtures prevented deflection of the composite panels during drilling, ensuring consistent hole quality [44]. The aluminum support plates had a thickness of 10 mm and were machined flat to guarantee uniform contact with the specimen surface. Figure 5 shows the composite specimens mounted on the CNC machine and the drill bit point angles used.

Each drilling condition (combination of feed rate and point angle) was repeated on three specimens to ensure reproducibility. Multiple holes were drilled on each specimen, with a minimum spacing of 15 mm to prevent interaction effects. All procedures were performed at room temperature, and the specimens were conditioned under controlled laboratory conditions prior to testing.

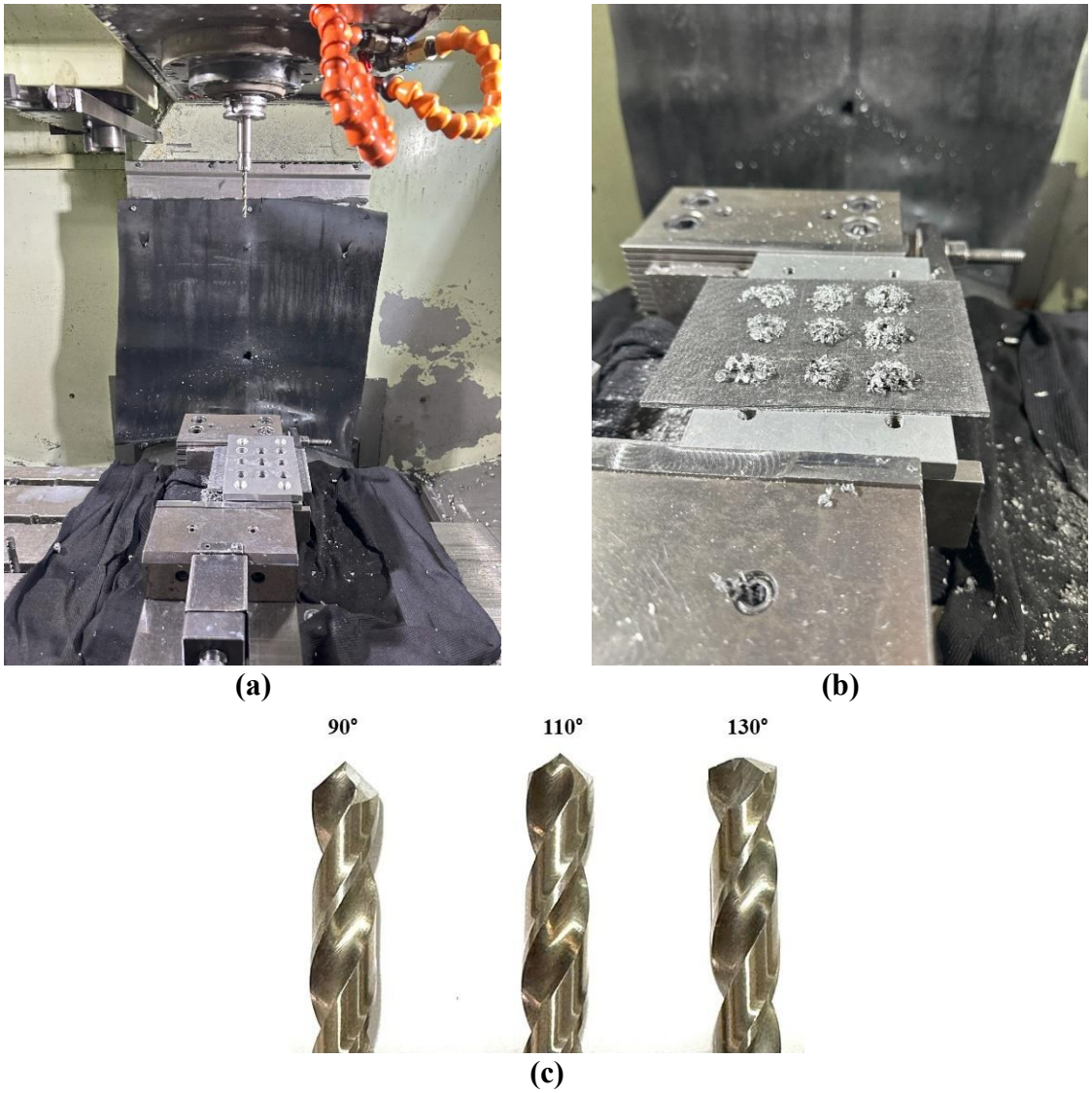


Figure 5. (a) Composite specimen before drilling, (b) composite specimen after drilling, and (c) drill bits with different point angles.

3 RESULTS AND DISCUSSION

3.1 Density Measurement Results

Figure 6 presents the density values of neat and nanoparticle-reinforced composite specimens. Among the neat samples, N-CF, N-GF, N-HF1, N-HF2, and N-HF3 exhibited approximate densities of 1.29, 1.65, 1.59, 1.59, and 1.53 g·cm^{-3}, respectively. In this group, the highest density was recorded for the N-GF sample, while the lowest was observed in the N-CF specimen. The lowest density in N-CF can be attributed to the relatively lower areal weight of CF compared to GF (245 g·m^{-2} for CF vs. 300 g·m^{-2} for GF) and possible void formation during the manufacturing process [45]. The densities of the hybrid-reinforced samples fell between these two extremes.

Upon the addition of nanoparticles (GnPs and/or BNNPs), a general trend of increasing density was observed. This increase can be attributed not only to the higher intrinsic densities of the nanoparticles but also to their good dispersion within the epoxy matrix, which reduces porosity and fills interstitial spaces, as well as the enhanced fiber–matrix interface bonding due to nanoparticle reinforcement. This increase can be attributed not only to the higher intrinsic densities of the nanoparticles but also to their good dispersion within the epoxy matrix, which reduces porosity and fills interstitial spaces, as well as the enhanced fiber–matrix interface bonding due to nanoparticle reinforcement. The highest density values were obtained in the samples reinforced with both GnPs and BNNPs. Among all specimens, the highest density—1.83 g·cm^{-3}—was measured for the G-B-GF sample. These observations are consistent with previous studies reporting that well-dispersed nanoparticles improve packing and reduce void content in polymer composites [46, 47].

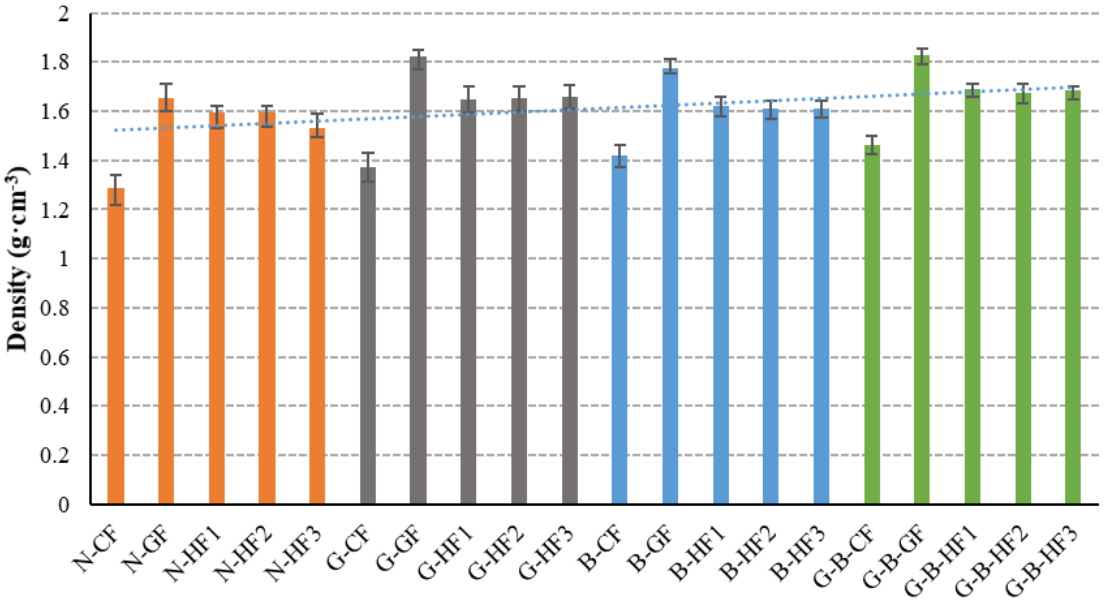


Figure 6. Average density values of the composite specimens.

3.2 Hardness Measurement Results

Figure 7 shows the Rockwell hardness (HRL) values of the neat and nanoparticle-reinforced composite specimens. The average hardness values of the neat specimens N-CF, N-GF, N-HF1, N-HF2, and N-HF3 were measured as 114.95, 88.65, 94.47, 93.53, and 96.68 HRL, respectively. The highest hardness was observed in the N-CF specimen, while the lowest hardness was recorded for the N-GF specimen. This difference is attributed to the more ductile nature of the GF-based composite compared to the CF-based composite. The hardness values of the hybrid-reinforced neat specimens fall between these two extremes.

The incorporation of GnPs and/or BNNPs nanoparticles into the composite structure resulted in a general decrease in hardness, indicating that nanoparticle reinforcement enhances the matrix toughness and improves the composite's ductility [10]. The reduction in hardness can be seen as a positive effect in terms of enhancing toughness-related properties such as impact absorption capacity. Additionally, the differences in hardness between GF- and CF-based composites may not only result from variations in ductility but can also be influenced by other factors, such as the fiber elastic modulus, fiber volume fraction, and fiber/matrix adhesion [48].

Furthermore, BNNPs reinforcement was found to cause a more significant increase in ductility compared to GnPs. Consequently, the lowest hardness values were measured in the BNNPs-containing specimens. Among all samples, the lowest average hardness was found in the B-GF specimen, with a value of 75.35 HRL.

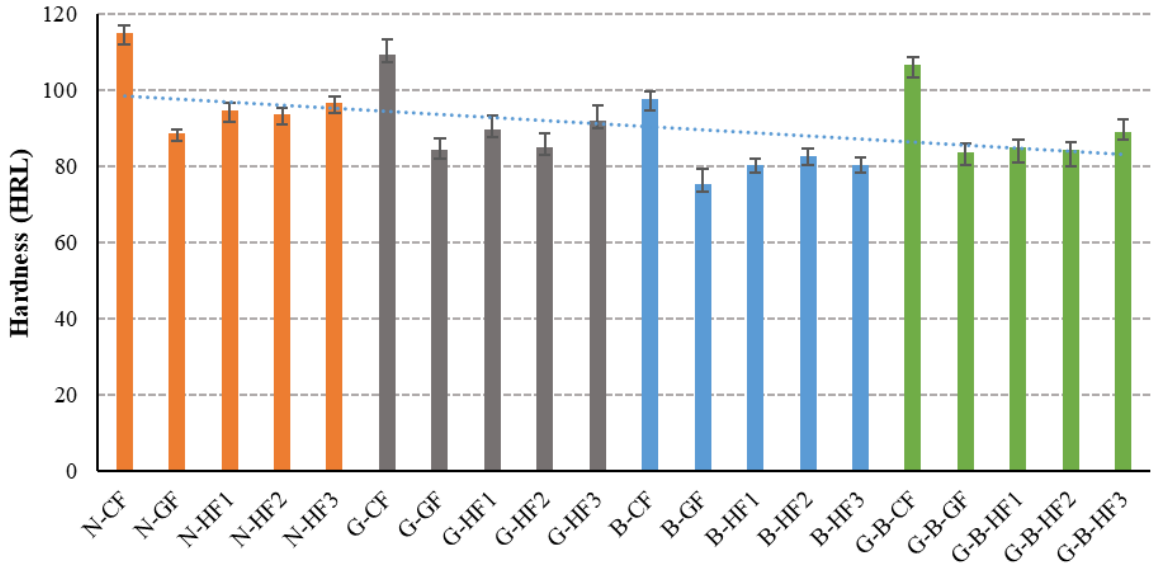


Figure 7. Average hardness values of the composite specimens.

3.3 Drilling Machinability Results

The measured hole diameters as a result of drilling are presented in Table 3. According to Table 3, the hole diameters obtained under all drilling conditions were smaller than the nominal drill diameter. The closest hole diameter to the nominal value (Ø6.48 mm) was measured in the B-GF specimen drilled using a 130° point angle and a feed rate of 200 mm/min. It was observed that increasing the feed rate at a constant point angle resulted in smaller hole diameters, whereas increasing the point angle at a constant feed rate led to larger hole diameters. Feed rate is a critical parameter affecting thrust force, exit delamination, and hole diameter in drilling operations [49]. Notably, a strong linear relationship exists between feed rate and thrust force; as the feed rate increases, the thrust force applied by the tool to the material also increases [50]. According to the literature, thrust force is considered the most influential factor in the formation of delamination. Therefore, reducing the feed rate lowers the thrust force and helps minimize both entrance and exit delamination [51]. On the other hand, higher feed rates may cause excessive heat generation due to friction around the hole, which can locally degrade the polymer matrix and reduce the overall hole quality [52]. It is also important to note that the decrease in hole diameter with increasing feed rate is accompanied by an increase in the delamination factor, which represents the extent of interlaminar separation around the drilled hole. In other words, while higher feed rates tend to produce smaller hole diameters, they also promote more severe damage in terms of delamination [53].

Moreover, under the same point angle and feed rate conditions, larger hole diameters were observed in the nanoparticle-reinforced composites. The observed decrease in hardness due to nanoparticle reinforcement also correlates with the improved drilling machinability, as a more ductile matrix accommodates cutting forces better, reducing delamination and promoting more uniform hole diameters. This can be attributed to the ability of GnPs and BNNPs to make the matrix phase more ductile, thereby facilitating the interaction between the tool and the material. The more ductile matrix structure contributed to more stable cutting conditions during drilling, resulting in improved machinability to some extent. Similar trends have been reported in previous studies. Kaybal et al. [54] demonstrated that the incorporation of BNNPs reduced the delamination factor of CF/epoxy composites, attributing this improvement to the enhanced shear and bending resistance imparted by the BNNPs. Thakur and Singh [55] investigated the effect of different loadings of GnPs on the drilling machinability of GF/epoxy composites, reporting the lowest delamination factor for specimens containing 0.25 wt.% GnPs. This improvement was ascribed to the increased interlaminar bonding strength provided by the

GnPs. Furthermore, Thakur et al. [56] reported that the addition of GnPs formed a bridging network, delayed crack propagation, and improved the fiber–matrix interfacial strength, thereby enhancing the bearing strength and reducing drilling-induced damage in both CF and GF composites. Additionally, due to the relatively more brittle nature of CF compared to GF, crack propagation was more pronounced in CF-based composites.

Table 3. Hole diameters (mm) obtained in composite materials at different point angles and feed rates

Material	Point Angles (°)- Feed Rates (mm/min)								
	90°			110°			130°		
	200	600	1000	200	600	1000	200	600	1000
N-CF	6.24	6.22	6.20	6.26	6.24	6.22	6.32	6.30	6.26
N-GF	6.34	6.30	6.28	6.36	6.32	6.30	6.38	6.34	6.32
N-HF1	6.28	6.26	6.22	6.30	6.28	6.24	6.32	6.30	6.28
N-HF2	6.30	6.24	6.20	6.32	6.26	6.22	6.38	6.28	6.26
N-HF3	6.28	6.26	6.22	6.34	6.30	6.26	6.36	6.30	6.28
G-CF	6.28	6.26	6.24	6.30	6.28	6.26	6.40	6.38	6.28
G-GF	6.36	6.32	6.30	6.38	6.36	6.34	6.40	6.38	6.36
G-HF1	6.32	6.28	6.24	6.36	6.30	6.26	6.38	6.32	6.30
G-HF2	6.34	6.28	6.26	6.44	6.30	6.28	6.46	6.32	6.30
G-HF3	6.30	6.28	6.24	6.40	6.32	6.28	6.42	6.32	6.30
B-CF	6.40	6.28	6.26	6.42	6.38	6.32	6.44	6.40	6.36
B-GF	6.44	6.34	6.32	6.46	6.36	6.34	6.48	6.38	6.36
B-HF1	6.40	6.34	6.26	6.42	6.36	6.28	6.44	6.38	6.30
B-HF2	6.38	6.32	6.22	6.40	6.34	6.26	6.46	6.36	6.30
B-HF3	6.42	6.30	6.24	6.44	6.32	6.28	6.46	6.34	6.30
G-B-CF	6.38	6.34	6.32	6.40	6.36	6.34	6.42	6.38	6.36
G-B-GF	6.40	6.36	6.30	6.42	6.38	6.36	6.44	6.40	6.38
G-B-HF1	6.38	6.34	6.24	6.40	6.36	6.28	6.42	6.38	6.30
G-B-HF2	6.36	6.32	6.30	6.38	6.34	6.32	6.40	6.36	6.34
G-B-HF3	6.36	6.30	6.26	6.38	6.36	6.32	6.40	6.38	6.34

The surface images of the drilled holes obtained from composite specimens under various point angles and feed rates are presented in Figure 8. Examination of Figure 8 reveals that delamination and burr formation increased with increasing feed rate, which is consistent with trends reported in the literature [42]. Davim and Reis [57, 58] stated that delamination tends to increase with cutting parameters such as feed rate and spindle speed. Since the spindle speed was kept constant in this study, the observed increase in delamination and burr formation is directly associated with the increased feed rate.

The most pronounced delamination and burr formation occurred at a point angle of 130° and a feed rate of 1000 mm/min. In contrast, the least burr formation was observed at a feed rate of 200 mm/min. This behavior can be attributed to the lower mechanical loads and thermal effects induced on the material at lower feed rates.

When evaluating the neat and reinforced specimens within their respective groups, it was observed that GF-based composites (N-GF, G-GF, B-GF, G-B-GF) exhibited less delamination and burr formation. This can be explained by the more ductile nature of GF-based specimens, which allows them to better withstand cutting forces and thus exhibit superior machinability. The enhanced ductility helps absorb cutting-induced stresses more effectively, thereby contributing to improved surface integrity.

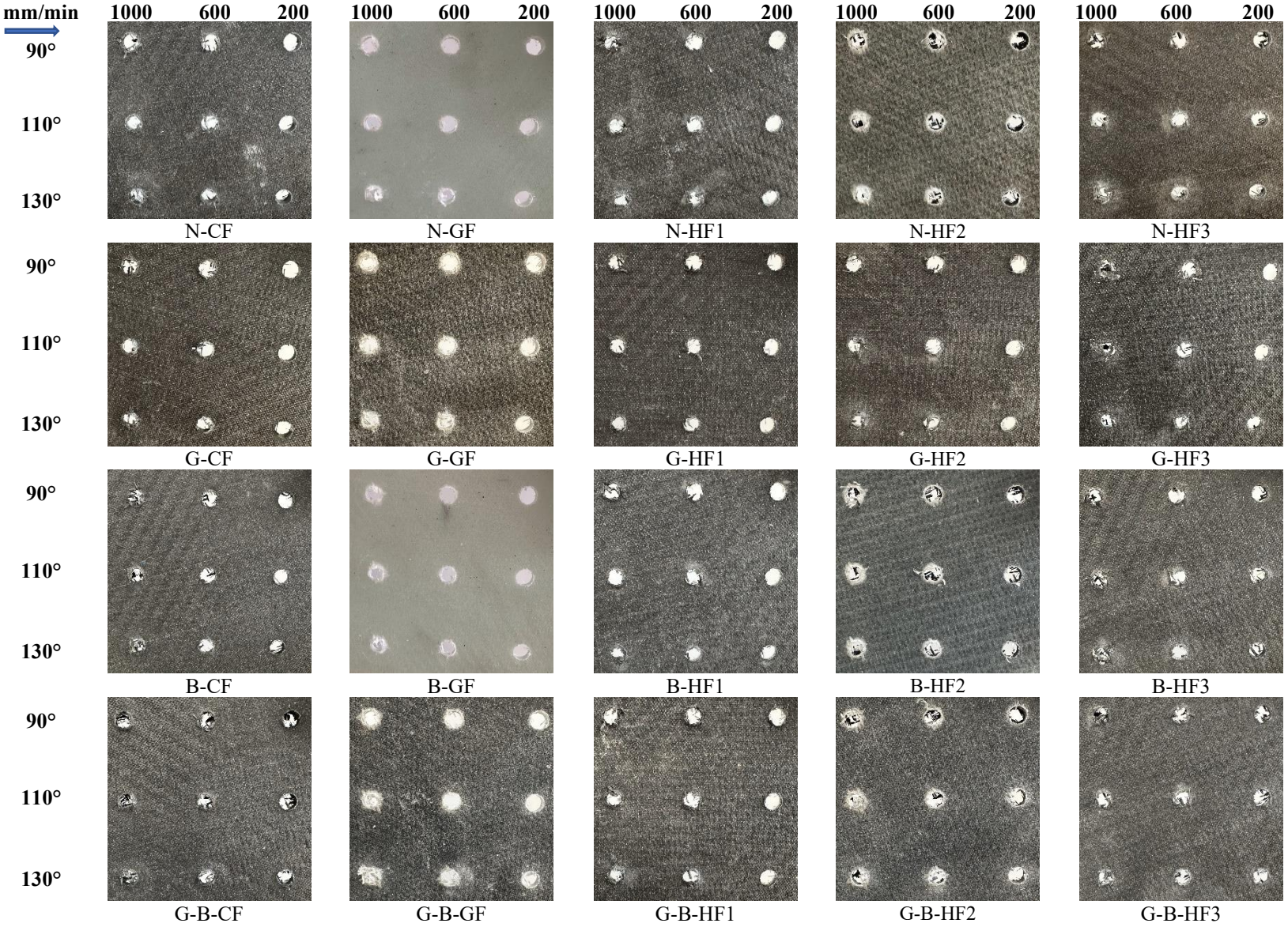


Figure 8. Post-drilling images of the holes in composite materials under different drill point angles and feed rates.

4 CONCLUSION AND SUGGESTIONS

In this study, the effects of reinforcing epoxy-based composite materials—comprising CF, GF, and HF with different stacking sequences—with GnPs and BNNPs on density, hardness, and machinability were investigated. The main findings are summarized below:

- Density measurements revealed that the incorporation of GnPs and/or BNNPs increased the overall density of the composites. The lowest density was recorded for the neat CF specimen (N-CF) at 1.29 $g \cdot cm^{-3}$, while the highest density was observed in the G-B-GF specimen, which contained both GnPs and BNNPs, at 1.83 $g \cdot cm^{-3}$. This increase was attributed to the high specific gravity of the nanoparticles and their distribution within the matrix.
- Hardness tests indicated that the addition of nanoparticles reduced the hardness due to increased ductility of the material, with BNNP-reinforced specimens showing the greatest reduction of about 15%. This decrease in hardness also correlates with the improved drilling machinability, as a more ductile matrix accommodates cutting forces better, resulting in reduced delamination and more uniform hole diameters. The highest hardness value was 114.95 HRL for the N-CF specimen, whereas the lowest value was 75.35 HRL for the B-GF specimen. It was observed that BNNPs led to a more significant increase in ductility compared to GnPs, which in turn caused a greater reduction in hardness.
- Machinability evaluations were conducted based on hole diameter, burr formation, and delamination behavior. In all conditions, the hole diameters obtained from drilling were smaller than the nominal drill diameter. The incorporation of nanoparticles improved the machinability by enhancing the ductility of the composite structure, allowing for larger hole diameters. The optimum hole diameter (Ø6.48 mm) was achieved in the B-GF specimen drilled at 130° point angle and 200 mm/min feed rate.
- Delamination and burr formation increased with higher feed rates. The most significant damage was observed when drilling was performed using a 130° drill at a feed rate of 1000 mm/min, while the minimum burr formation occurred at a feed rate of 200 mm/min. GF–based specimens (N-GF, G-GF, B-GF, G-B-GF) exhibited less delamination and burr formation compared to other specimens, which was attributed to the enhanced ductility provided by the GF reinforcement. This ductile behavior helped absorb cutting forces more effectively, thereby preserving surface integrity.

In conclusion, the addition of GnPs and BNNPs resulted in increased density, reduced hardness, and significant improvements in machinability. Among all the samples, the GF–based composites reinforced with nanoparticles demonstrated superior performance in terms of machinability. Future studies may focus on investigating the effects of different types and concentrations of nanoparticles on the drilling behavior of natural fiber composites under various environmental and thermal aging conditions.

Acknowledgements

This study was performed using some of the materials produced during the Master's thesis project of Umut Ozgur OZALTAY, supervised by Alper GUNOZ at the Institute of Science, Mersin University. The study was supported by the Mersin University Scientific Research Projects Unit under project number 2023-2-TP2-4988.

Conflict of Interest Statement

There is no conflict of interest between the authors.

Statement of Research and Publication Ethics

The study is complied with research and publication ethics.

Artificial Intelligence (AI) Contribution Statement

During the preparation of this manuscript, the authors used artificial intelligence (ChatGPT) to improve the clarity and readability of the English text. All outputs were carefully reviewed and edited by the authors, who take full responsibility for the content of this publication.

Contributions of the Authors

Alper GUNOZ: investigation; methodology; data curation; formal analysis; validation; supervision; writing – review and editing.

Umut Ozgur OZALTAY: investigation; resources; visualization; roles/writing – original draft.

REFERENCES

[1] L. Urtekin, D. Gunes, F. Yılan, and M. Çanlı, "The effect of layers on the unidirectional carbon fibers of the reinforced polyester resin matrix composite material," *Gazi Üniversitesi Fen Bilimleri Dergisi Part C: Tasarım ve Teknoloji,* vol. 10, no. 3, pp. 495-503, 2022.

[2] M. R. Zakaria, M. H. A. Kudus, H. M. Akil, and M. Z. M. Thirmizir, "Comparative study of graphene nanoparticle and multiwall carbon nanotube filled epoxy nanocomposites based on mechanical, thermal and dielectric properties," *Composites Part B: Engineering,* vol. 119, pp. 57-66, 2017.

[3] İ. Bozkurt, "Numerical investigation of the effects of impactor geometry on impact behavior of sandwich structures," *Bitlis Eren Üniversitesi Fen Bilimleri Dergisi,* vol. 13, no. 3, pp. 750-771, 2024.

[4] A. Gunoz and M. Kara, "Damage behavior of functionally graded kevlar/carbon epoxy nanocomposites reinforced with polyamide 6.6 nanofiber and MWCNTs subjected to low-velocity impact," *International Journal of Damage Mechanics,* p. 10567895241305324, 2024.

[5] A. Gunoz and M. Kara, "Mechanical behavior of the polyamide 6.6 nanofiber and MWCNT-reinforced hybrid nanocomposites," *Polymer Composites,* vol. 45, no. 5, pp. 4693-4708, 2024.

[6] H. Ulus, T. Üstün, Ö. S. Şahin, S. E. Karabulut, V. Eskizeybek, and A. Avcı, "Low-velocity impact behavior of carbon fiber/epoxy multiscale hybrid nanocomposites reinforced with multiwalled carbon nanotubes and boron nitride nanoplates," *Journal of Composite Materials,* vol. 50, no. 6, pp. 761-770, 2016.

[7] H. B. Kaybal, H. Ulus, O. Demir, Ö. S. Şahin, and A. Avcı, "Effects of alumina nanoparticles on dynamic impact responses of carbon fiber reinforced epoxy matrix nanocomposites," *Engineering Science and Technology, an International Journal,* vol. 21, no. 3, pp. 399-407, 2018.

[8] D. Lee *et al.*, "Enhanced mechanical properties of epoxy nanocomposites by mixing noncovalently functionalized boron nitride nanoflakes," *Small,* vol. 9, no. 15, pp. 2602-2610, 2013.

[9] H. Ulus, T. Üstün, V. Eskizeybek, Ö. S. Şahin, A. Avcı, and M. Ekrem, "Boron nitride-MWCNT/epoxy hybrid nanocomposites: Preparation and mechanical properties," *Applied Surface Science,* vol. 318, pp. 37-42, 2014.

[10] H. Sepetcioglu *et al.*, "Improved mechanical properties of graphene-modified basalt fibre–epoxy composites," *Nanotechnology Reviews,* vol. 13, no. 1, p. 20240052, 2024.

[11] Ç. Uzay and M. S. Kamer, "Effect of Silane-Coated SiO2 Nanoparticles on the Hardness Values of Glass FRP Composites," *Bitlis Eren Üniversitesi Fen Bilimleri Dergisi,* vol. 11, no. 3, pp. 751-758, 2022.

[12] Z. A. Oğuz, "UV aging effect on buckling properties of nanoclay particulated intraply hybrid composites," *Physica Scripta,* vol. 100, no. 2, p. 025916, 2025.

[13] H. Geçmez and H. A. Deveci, "Optimization Of Hybrid Composite Laminates With Various Materials Using GA/GPSA Hybrid Algorithm for Maximum Dimensional Stability," *Bitlis Eren Üniversitesi Fen Bilimleri Dergisi,* vol. 13, no. 1, pp. 107-133, 2024.

[14] K. Nagaraja, G. Rajeshkumar, M. Sanjay, and S. Siengchin, "Influence of stacking sequence and halloysite addition on the fracture toughness and low-velocity impact strength of carbon/glass fiber reinforced hybrid composites," *Polymer Composites,* vol. 45, no. 1, pp. 328-337, 2024.

[15] F. Karaca, "Cam elyaf takviyeli plastik kompozitlerde delme parametrelerinin deformasyon faktörüne etkisinin araştırılması," *Fırat Üniversitesi Mühendislik Bilimleri Dergisi,* vol. 28, no. 2, pp. 23-27, 2016.

[16] G. Başar, Y. Fedai, and H. K. Akın, "Kompozit malzemelerin delme işleminde itme kuvvetinin taguchi metodu ile optimizasyonu ve regresyon analizi ile tahmini," *Çukurova Üniversitesi Mühendislik-Mimarlık Fakültesi Dergisi,* vol. 35, no. 4, pp. 969-982, 2020.

[17] H. Ho-Cheng and C. Dharan, "Delamination during drilling in composite laminates," *Journal of Manufacturing Science and Engineering,* vol. 112, no. 3, pp. 236-239, 1990.

[18] T. Rajamurugan, K. Shanmugam, and K. Palanikumar, "Analysis of delamination in drilling glass fiber reinforced polyester composites," *Materials & Design,* vol. 45, pp. 80-87, 2013.

[19] T. Sunny, J. Babu, and J. Philip, "Experimental studies on effect of process parameters on delamination in drilling GFRP composites using Taguchi method," *Procedia Materials Science,* vol. 6, pp. 1131-1142, 2014.

[20] J. Matuszak and K. Zaleski, "Edge states after wire brushing of magnesium alloys," *Aircraft Engineering and Aerospace Technology: An International Journal,* vol. 86, no. 4, pp. 328-335, 2014.

[21] J. Matuszak and K. Zaleski, "Analysis of deburring effectiveness and surface layer properties around edges of workpieces made of 7075 aluminium alloy," *Aircraft Engineering and Aerospace Technology,* vol. 90, no. 3, pp. 515-523, 2018.

[22] J. Matuszak, M. Kłonica, and I. Zagórski, "Measurements of forces and selected surface layer properties of AW-7075 aluminum alloy used in the aviation industry after abrasive machining," *Materials,* vol. 12, no. 22, p. 3707, 2019.

[23] C. Tsao, H. Hocheng, and Y. Chen, "Delamination reduction in drilling composite materials by active backup force," *CIRP annals,* vol. 61, no. 1, pp. 91-94, 2012.

[24] N. Anaç *et al.*, "Cam fiber takviyeli plastik malzemelerin delaminasyon durumunun incelenmesi," *Mühendislik Bilimleri ve Tasarım Dergisi,* vol. 13, no. 1, pp. 234-249, 2025.

[25] E. Unal, "Temperature and thrust force analysis on drilling of glass fiber reinforced plastics," *Thermal Science,* vol. 23, no. 1, pp. 347-352, 2019.

[26] V. K. Vankanti and V. Ganta, "Optimization of process parameters in drilling of GFRP composite using Taguchi method," *Journal of Materials Research and Technology,* vol. 3, no. 1, pp. 35-41, 2014.

[27] L. Gemi, S. Morkavuk, U. Köklü, and D. S. Gemi, "An experimental study on the effects of various drill types on drilling performance of GFRP composite pipes and damage formation," *Composites Part B: Engineering,* vol. 172, pp. 186-194, 2019.

[28] K. K. Singh and D. Kumar, "Experimental investigation and modelling of drilling on multi-wall carbon nanotube–embedded epoxy/glass fabric polymeric nanocomposites," *Proceedings of the Institution of Mechanical Engineers, Part B: Journal of Engineering Manufacture,* vol. 232, no. 11, pp. 1943-1959, 2018.

[29] H. Heidary, N. Z. Karimi, and G. Minak, "Investigation on delamination and flexural properties in drilling of carbon nanotube/polymer composites," *Composite Structures,* vol. 201, pp. 112-120, 2018.

[30] T. Sathish and B. Varadhan, "Enhancing drilling performance in hybrid Basalt/E-Glass fiber epoxy modified with MWCNTs+ SiO2 nanocomposites," *The International Journal of Advanced Manufacturing Technology,* vol. 136, no. 1, pp. 315-328, 2025.

[31] F. Erhan, L. Gemi, Ş. Yazman, S. Morkavuk, and U. Köklü, "A comprehensive investigation into the influence of variation in the stacking sequence on the mechanical behaviour and drilling machinability of basalt fiber-reinforced composite tubes," *Composites Part B: Engineering,* vol. 299, p. 112405, 2025.

[32] N. Patel, K. Patel, V. Chaudhary, and P. Gohil, "Investigations on drilling of hybrid basalt/glass polyester composites," *Australian Journal of Mechanical Engineering,* vol. 20, no. 4, pp. 1154-1163, 2022.

[33] L. Gemi, U. Köklü, Ş. Yazman, and S. Morkavuk, "The effects of stacking sequence on drilling machinability of filament wound hybrid composite pipes: Part-1 mechanical characterization and drilling tests," *Composites Part B: Engineering,* vol. 186, p. 107787, 2020.

[34] H. Sepetcioglu, A. Gunoz, and M. Kara, "Effect of hydrothermal ageing on the mechanical behaviour of graphene nanoplatelets reinforced basalt fibre epoxy composite pipes," *Polymers and Polymer Composites,* vol. 29, no. 9_suppl, pp. S166-S177, 2021.

[35] K. A. Zarasvand and H. Golestanian, "Investigating the effects of number and distribution of GNP layers on graphene reinforced polymer properties: Physical, numerical and micromechanical methods," *Composites Science and Technology,* vol. 139, pp. 117-126, 2017.

[36] J. Naveen, M. Jawaid, E. S. Zainudin, M. Thariq Hameed Sultan, and R. Yahaya, "Improved mechanical and moisture-resistant properties of woven hybrid epoxy composites by graphene nanoplatelets (GNP)," *Materials,* vol. 12, no. 8, p. 1249, 2019.

[37] T. Üstün *et al.*, "Evaluating the effectiveness of nanofillers in filament wound carbon/epoxy multiscale composite pipes," *Composites Part B: Engineering,* vol. 96, pp. 1-6, 2016.

[38] *ASTM D792-20: Standard test methods for density and specific gravity (relative density) of plastics by displacement*, ASTM, West Conshohocken, PA, USA, 2013.

[39] *ASTM D785-08: Standard Test Method for Rockwell Hardness of Plastics and Electrical Insulating Materials*, ASTM, West Conshohocken, PA, USA, 2015.

[40] M. A. Doğan, Ş. Yazman, L. Gemi, M. Yildiz, and A. Yapici, "A review on drilling of FML stacks with conventional and unconventional processing methods under different conditions," *Composite Structures,* vol. 297, p. 115913, 2022.

[41] Ş. Yazman, L. Gemi, S. Morkavuk, and U. Köklü, "Investigation of the effect of symmetrical hybrid stacking on drilling machinability of unidirectional CFRP, GFRP and hybrid composites: Drilling tests and damage analysis," *Composites Part A: Applied Science and Manufacturing,* vol. 187, p. 108486, 2024.

[42] F. Ceritbinmez and A. Yapıcı, "Kompozit malzemelerin delinmesinde matkap nokta açısının ve ÇCKNT'lerin etkisi," *Academic Perspective Procedia,* vol. 3, no. 1, pp. 180-188, 2020.

[43] G. Franz, P. Vantomme, and M. H. Hassan, "A review on drilling of multilayer fiber-reinforced polymer composites and aluminum stacks: optimization of strategies for improving the drilling performance of aerospace assemblies," *Fibers,* vol. 10, no. 9, p. 78, 2022.

[44] D. Liu, Y. Tang, and W. Cong, "A review of mechanical drilling for composite laminates," *Composite Structures,* vol. 94, no. 4, pp. 1265-1279, 2012.

[45] M. Mehdikhani, L. Gorbatikh, I. Verpoest, and S. V. Lomov, "Voids in fiber-reinforced polymer composites: A review on their formation, characteristics, and effects on mechanical performance," *Journal of Composite Materials,* vol. 53, no. 12, pp. 1579-1669, 2019.

[46] P. Govindaraj *et al.*, "Distribution states of graphene in polymer nanocomposites: A review," *Composites Part B: Engineering,* vol. 226, p. 109353, 2021.

[47] M. Owais, J. Zhao, A. Imani, G. Wang, H. Zhang, and Z. Zhang, "Synergetic effect of hybrid fillers of boron nitride, graphene nanoplatelets, and short carbon fibers for enhanced thermal conductivity and electrical resistivity of epoxy nanocomposites," *Composites Part A: Applied Science and Manufacturing,* vol. 117, pp. 11-22, 2019.

[48] X. Jiang, M. Gao, J. Zhu, H. Ji, and F. Lang, "Studying the interfacial properties of carbon/glass hybrid composites via the nanoindentation method," *Polymers,* vol. 14, no. 14, p. 2897, 2022.

[49] A. Caggiano, "Machining of fibre reinforced plastic composite materials," *Materials,* vol. 11, no. 3, p. 442, 2018.

[50] J. P. Davim, *Machinability of fibre-reinforced plastics*. Walter de Gruyter, 2015.

[51] M. T. H. Sultan, A. I. Azmi, M. S. Abd Majid, M. R. M. Jamir, and N. Saba, *Machining and Machinability of Fiber Reinforced Polymer Composites*. Springer, 2020.

[52] A. P. Mouritz, *Introduction to aerospace materials*. Elsevier, 2012.

[53] F. Shi, Y. Yang, N. Sun, Z. Du, C. Zhang, and D. Zhao, "Research on Damage Caused by Carbon-Fiber-Reinforced Polymer Robotic Drilling Based on Digital Image Correlation and Industrial Computed Tomography," *Machines,* vol. 12, no. 1, p. 22, 2023.

[54] H. B. Kaybal, A. Unuvar, Y. Kaynak, and A. Avcı, "Evaluation of boron nitride nanoparticles on delamination in drilling carbon fiber epoxy nanocomposite materials," *Journal of Composite Materials,* vol. 54, no. 2, pp. 215-227, 2020.

[55] R. K. Thakur and K. K. Singh, "Evaluation of drilling characteristics to explore the effect of graphene nanoplatelets on glass fiber reinforced polymer composite," *Measurement,* vol. 219, p. 113233, 2023.

[56] R. K. Thakur, K. K. Singh, and P. Rawat, "Evaluation of graphene nanoplatelets addition and machining methods on the hole quality and bearing strength of glass and carbon fibre reinforced epoxy laminates," *Journal of Manufacturing Processes,* vol. 115, pp. 137-155, 2024.

[57] J. P. Davim and P. Reis, "Drilling carbon fiber reinforced plastics manufactured by autoclave—experimental and statistical study," *Materials & design,* vol. 24, no. 5, pp. 315-324, 2003.

[58] J. P. Davim, P. Reis, and C. C. António, "Experimental study of drilling glass fiber reinforced plastics (GFRP) manufactured by hand lay-up," *Composites Science and Technology,* vol. 64, no. 2, pp. 289-297, 2004.

BİTLİS EREN ÜNİVERSİTESİ
FEN BİLİMLERİ DERGİSİ

ISSN: 2147-3129 / e-ISSN: 2147-3188

Article Type : Research Article
Received : July 12, 2025
Revised : September 15, 2025
Accepted : September 17, 2025
DOI : 10.17798/bitlisfen.1740843

Year : 2025
Volume : 14
Issue : 3
Pages : 1942-1960

CLOSE BINARY OPEN CLUSTER SYSTEMS: A *GAIA* DR3 PERSPECTIVE ON ALESSI 36 AND COLLINDER 135

Hülya Karagöz [1], Deniz Cennet Çınar [1], Seval Taşdemir [1], **Remziye Canbay [2, *]**

[1] *İstanbul University, Programme of Astronomy and Space Sciences, İstanbul, Türkiye*

[2] *İstanbul University, Department of Astronomy and Space Sciences, İstanbul, Türkiye*

**** Corresponding Author:*** *remziye.canbay@istanbul.edu.tr*

ABSTRACT

In this study, we examined the nearby open clusters (OCs) Alessi 36 and Collinder 135. Their spatial proximity was assessed using photometric and astrometric data from *Gaia* DR3. Likely member stars were identified based on a membership probability threshold ($P \geq 0.5$), yielding 230 members for Alessi 36 and 342 members for Collinder 135. The mean proper-motion components ($\mu_\alpha \cos\delta$, μ_δ) were determined as (-9.681±0.072, 7.021±0.081) mas yr^{-1} for Alessi 36 and (-10.061±0.083, 6.256±0.095) mas yr^{-1} for Collinder 135, the parallax-based distances (d_ϖ) were found to be 278±7 and 299±11 pc, while their estimated ages (t) were 39±5 and 36±5 Myr for Alessi 36 and Collinder 135, respectively. The Galactic orbital analysis of Alessi 36 and Collinder 135 reveals nearly circular orbits with low eccentricities and minor fluctuations in their apogalactic and perigalactic distances. The maximum heights they attain above the Galactic plane are 0.035±0.001 for Alessi 36 and 0.074±0.003 kpc for Collinder 135, respectively, supporting their classification as part of the young stellar disc population.

Keywords: Alessi 36, Collinder 135, Binary open clusters, Open clusters, Galaxy: disc.

1 INTRODUCTION

Star formation occurs over a wide range of spatial and temporal scales, giving rise to both gravitationally bound clusters and more diffuse stellar associations. These structures often exhibit hierarchical organization, reflecting the underlying physical processes that govern star formation and early cluster evolution [1-5]. Among these stellar systems, open clusters (OCs) arise from the fragmentation and gravitational collapse of dense regions within giant molecular

clouds (GMCs). While some OCs may form in relative isolation, accumulating stars from their neighborhood, others appear to form as part of larger stellar complexes, commonly referred to as primordial groups. Observational studies provide compelling evidence that OCs forming in close proximity often share common kinematic properties, suggesting a common origin. Analyzing spatial and kinematic relationships among young OCs enhances our understanding of hierarchical star formation processes in the Milky Way and improves our knowledge of their long-term dynamical evolution.

The launch of ESA's *Gaia* mission has revolutionized the field of precision astrometry, allowing the study of Galactic clusters with unprecedented accuracy, and facilitating the discovery of previously unknown OCs [6, 7]. The release of *Gaia* Data Release 3 (*Gaia* DR3) on 13 June 2022 marks a major milestone in this effort, providing positional and photometric measurements for about 1.8 billion sources, along with trigonometric parallax (ϖ), proper motion components ($\mu_\alpha \cos\delta$, μ_δ), and *BP-RP* colours for nearly 1.5 billion sources [6].

The substantial improvements in astrometric precision, especially in PMs, compared to *Gaia* DR2 have opened new avenues for revisiting the OC population and refining its fundamental properties. The new findings show that some open clusters are close to each other and may have gravitational interactions [15-19]. These systems, known as close binary open clusters (CBOCs), provide unique opportunities to study the interaction between clusters and their surrounding Galactic environment. The study of CBOCs provides key insights into cluster dynamics, their interactions, and the role of the Galactic gravitational field in establishing their long-term stability.

Based on the analysis of [20], this study provides an in-depth investigation of the binary open cluster Collinder 135 and Alessi 36 through a comprehensive astrometric, astrophysical, and dynamic orbit analysis. While previous work has suggested possible gravitational interaction between these clusters, our study improves their characterization by using high-precision astrometric measurements and advanced orbital modelling techniques. By thoroughly examining their kinematics, structural properties, and orbits, we aim to determine whether they form a physically bound binary open cluster system or merely exhibit a random alignment. This refined analysis will advance our understanding of the dynamical evolution of pair open clusters in the Galactic field by elucidating the physical mechanisms that govern their formation, mutual interactions, and long-term stability.

Table 1. Summary of literature studies for Alessi 36 and Collinder 135

$E(B-V)$ (mag)	d (pc)	[Fe/H] (dex)	t (Myr)	$\mu_\alpha \cos\delta$ (mas yr^{-1})	μ_δ (mas yr^{-1})	v_r (km s^{-1})	References
Alessi 36							
0.032	276	---	32	-9.703±0.199	6.982±0.216	---	[07]
0.045±0.020	275 ±1	---	16±9	-9.669±0.016	7.046±0.089	14.54±1.82	[08]
---	---	---	40	---	---	---	[10]
---	273±2	---	---	14.2	-7.4	11.6	[11]
---	---	---	---	-10.25±0.05	-5.98±0.05	16.7±1.5	[12]
Collinder 135							
0.003	292	---	26	-9.975±0.445	6.157±0.350	---	[07]
0.034±0.01	295±1	---	30±23	-10.077±0.019	6.23±0.017	13.16±1.14	[08]
---	---	---	40	---	---	---	[10]
---	294±2	---	---	13.6	-6.9	6.6	[11]
---	---	---	---	-9.92±0.05	-6.47±0.06	17.4±1.3	[12]
0.058±0.02	307±8	0.111±0.058	50±6	-9.977±0.491	6.211±0.453	16.513±2.254	[13]
0.07±0.01	310±8	0.10±0.002	38±2	---	---	2.87±0.17	[12]
---	---	---	---	-9.280±0.027	5.57±0.22	---	[13]
-0.06	630	---	---	---	---	---	[14]

Collinder 135 and Alessi 36 have been the subject of various studies aimed at determining their key astrophysical properties, including color excess, proper motion components, ages, metallicities, and distances. These clusters provide an ideal environment for studying their dynamics, with potential interactions influencing their evolution. A summary of these studies and their results is given in Table 1.

The remaining sections of this paper are structured as follows: Section 2 describes the data sources and selection criteria used in this study. Section 3 outlines the methodology used to derive the fundamental astrometric, astrophysical, and kinematical parameters of the clusters and presents the results. Section 4, provides a comprehensive summary of the study, consolidating the main conclusions drawn from our analysis.

2 DATA

The photometric and astrometric investigation of Collinder 135 and Alessi 36 was conducted using data obtained from the *Gaia* DR3 catalogue [8]. *Gaia* DR3 provides high-precision astrometric, photometric, and radial velocity measurements for over 1.8 billion sources, including trigonometric parallax (ϖ), proper motion components ($\mu_\alpha \cos\delta$, μ_δ), and integrated G, G_{BP}, and G_{RP} magnitudes for approximately 1.5 billion stars. Additionally, *Gaia* DR3 includes radial velocities for ~33 million bright stars ($G \leq 14$ mag) and astrophysical parameters such as effective temperature, extinction, and metallicity for millions of sources.

These two OCs are located in a relatively sparse region of the Milky Way, providing valuable opportunities for detailed observational studies [21]. Collinder 135 is located at α = $07^h17^m26^s.9$ and δ = -37°02′38″ (J2000.0), with Galactic coordinates of l = 248°.9884 and b = -11°.2010, while Alessi 36 is located at α = $07^h07^m08^s.6$ and δ = -37°43′44″ (J2000.0), corresponding to Galactic coordinates of l = 248°.7423 and b = -13°.3458.

To ensure a comprehensive examination, all stars within a 90′ radius from the center of each cluster were included in the study. As a result, a total of 300707 stars and 215885 stars in the magnitude range $6 < G$ (mag) ≤ 23 were identified for Collinder 135 and Alessi 36, respectively. These datasets form the basis for the subsequent membership analysis and derivation of the clusters' fundamental parameters.

3 METHODS AND RESULTS

3.1 Cluster Membership Determination: UPMASK

The UPMASK (Unsupervised Photometric Membership Assignment in Stellar Clusters) program [22], was used to calculate the membership probabilities of stars in the Alessi 36 and Collinder 135 regions. This program utilizes the k-means clustering algorithm, which groups parameters with similar characteristics within a dataset and assigns the most appropriate probability values. The k-means values are user-defined and can vary between 6 and 30, depending on the cluster morphology, to provide the optimal solution. The algorithm works by dividing the data into a set number of clusters (k), assigning each point to the nearest cluster center, and updating the centers iteratively until the best grouping is achieved.

Following the UPMASK [22] guidelines, we explored $k \in (6,30)$ in the five-dimensional space used for membership (position and astrometry). For each k we computed three diagnostics: (i) the mean silhouette coefficient in the ($\mu_\alpha \cos\delta$, μ_δ, ϖ) subspace as an internal validity metric; (ii) a surface-density contrast between members and surrounding field within the cluster half-number radius as a compactness proxy; and (iii) a stability score defined as the Jaccard index between member lists obtained at adjacent k values. The solutions become stable for $k \gtrsim 20$ derived bulk parameters (mean proper motions, mean parallax, distances) vary within their 1σ uncertainties across this regime, while the intersecting fraction of members between neighboring k values exceeds 0.90 for both clusters. We therefore adopt k=27, which provides near-maximal silhouette and stability without over-fragmenting the data.

A membership probability threshold of $P \geq 0.5$ was adopted. This value is commonly used in UPMASK-based studies and provides a reliable separation of cluster members from field stars [7, 8]. To test sensitivity, we also examined thresholds of $P \geq 0.3$ and $P \geq 0.7$. The former led to noticeably higher field-star contamination, while the latter removed genuine members even in the cluster center. The adopted $P \geq 0.5$ criterion therefore represents the most balanced and literature-consistent choice. Consequently, the number of highly probable members was found to be 230 for Alessi 36 and 342 for Collinder 135.

3.2 Astrometric Parameters

To analyze the distribution of stars with high membership probability ($P \geq 0.5$) in the proper motion space relative to field stars and to determine the mean proper motion components, vector point diagrams (VPDs) were constructed for the Alessi 36 and Collinder 135 clusters (Figure 1; right panel). Additionally, the sky-projected vectorial motions of these stars in equatorial coordinates were examined. The results of this analysis are presented in Figure 1 (left panel), which shows the VPDs and the equatorial coordinate distributions for both clusters, clearly distinguishing high-probability members and field stars. In this figure, stars with membership probabilities $P \geq 0.5$ and those with $0 < P < 0.5$ are represented by colored and grey circular symbols, respectively. The analysis indicates that Alessi 36 and Collinder 135 are significantly influenced by field stars.

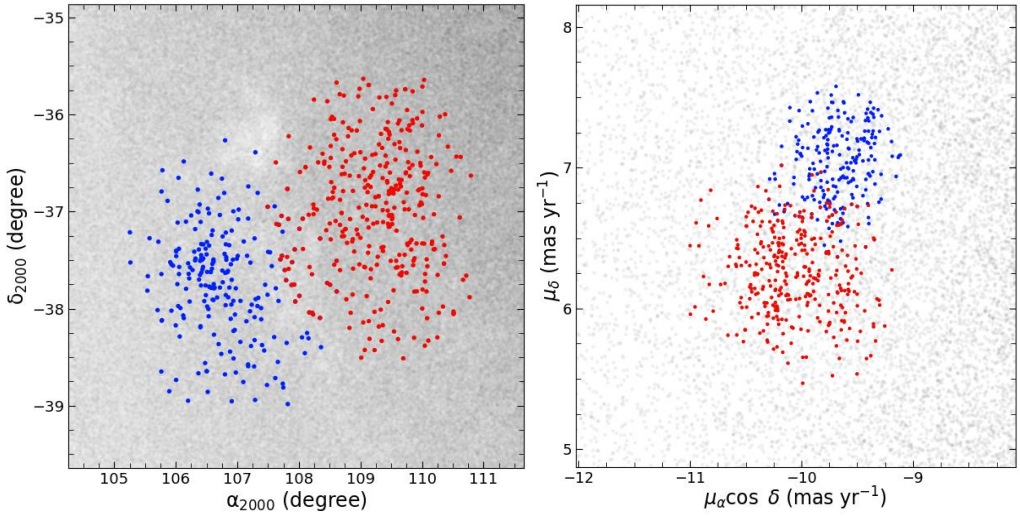


Figure 1. The image of Alessi 36 (blue dots) and Collinder 135 (red dots) distributed on the equatorial coordinate plane (left panel). VPD of the most likely member stars belong to the open clusters (right panel). The background grey points represent field stars.

A detailed examination of the high-probability cluster members ($P \geq 0.5$) reveals that Alessi 36 and Collinder 135 show a significantly higher stellar density near their centers compared to their outskirts, indicating a dense central stellar distribution, and they appear as a

binary system in the sky. The mean proper motion components ($\langle \mu_\alpha \cos\delta, \mu_\delta \rangle$) for these clusters were determined by calculating the median values of parameters with $P \geq 0.5$. The resulting values for Alessi 36 and Collinder 135 are (-9.703±0.004, 6.982±0.004) and (-9.975±0.006, 6.157±0.007) mas yr^{-1}, respectively (see Table 2).

Furthermore, the mean trigonometric parallaxes ($\langle \varpi \rangle$) of both clusters were computed. Histograms of the trigonometric parallax measurements for stars with membership probability $P \geq 0.5$ were generated, and a Gaussian function was fitted to the distribution. To ensure data reliability, we imposed a relative parallax error constraint of $\sigma_\varpi/\varpi \leq 0.2$. The mean parallaxes of Alessi 36 and Collinder 135 were thus determined as 3.601 and 3.348 mas, respectively. These values were then converted to heliocentric distances using the relation d (pc) = 1000 / ϖ (mas), yielding distances of 278±7 and 299±11 pc for Alessi 36 and Collinder 135, respectively.

We note that direct inversion of parallaxes can introduce biases (e.g., Lutz-Kelker effect) for distant stars with large relative uncertainties. However, for the nearby clusters studied here (around 300 pc) and with the applied condition $\sigma_\varpi/\varpi \leq 0.2$, such biases are negligible and the results are robust [41, 43]. Moreover, the obtained distances are consistent with those derived from isochrone fitting (Section 3.3), further supporting the reliability of this approach. While Bayesian distance estimates (e.g., [42]) could serve as an alternative, we adopted the direct method here for its simplicity and consistency under our selection criteria.

As illustrated in Figure 2, the trigonometric parallax histograms of Alessi 36 and Collinder 135 are presented together with the Gaussian function (black line), which has been fitted to the distributions. The astrometric parameters derived for both clusters are summarized in Table 2.

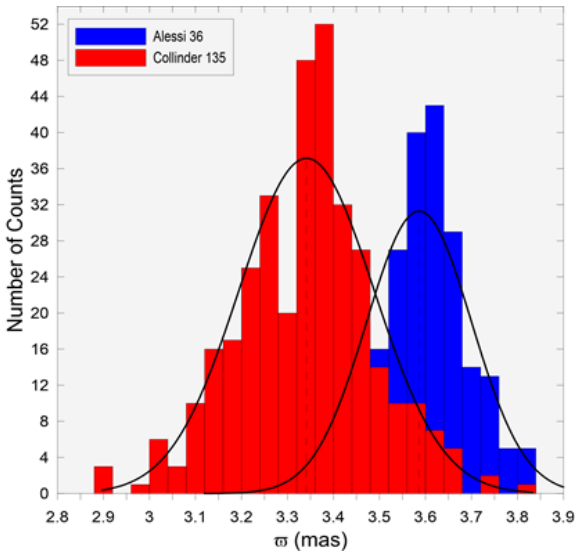


Figure 2. The figure displays the trigonometric parallax histograms based on Gaia DR3 data, with black dashed lines indicating the median of the Gaussian fits to the parallax distributions of Alessi 36 (blue bars) and Collinder 135 (red bars).

3.3 Fundamental Astrophysical Parameters

The interstellar reddening of open clusters is of critical importance in providing insights into the extent of dust extinction affecting their observed photometric properties [18, 26, 28]. Utilizing data from the *Gaia* mission, the reddening values for Alessi 36 and Collinder 135 were determined using the color excess in the *Gaia* photometric bands, specifically $E(G_{BP}\text{-}G_{RP})$ value. For Alessi 36, the derived reddening value is $E(G_{BP}\text{-}G_{RP}) = 0.104\pm0.027$ mag, indicating a moderate level of extinction within its Galactic environment. In contrast, Collinder 135 exhibits a lower reddening value of $E(G_{BP}\text{-}G_{RP}) = 0.065\pm0.022$ mag, consistent with its location in a region with relatively low interstellar dust content. These findings suggest that although both clusters experience some degree of interstellar extinction, the effect is more pronounced in Alessi 36 compared to Collinder 135. Despite their close proximity on the sky, the differing reddening values likely reflect variations in dust distribution or differences in their distances.

The reddening values of Alessi 36 and Collinder 135 were derived by fitting PARSEC isochrones to the observed *Gaia* DR3 color-magnitude diagrams (CMDs), with the color excess determined in the *Gaia* photometric system as $E(G_{BP}\text{-}G_{RP})$ and shown in Figure 3. For Alessi 36, the derived value is $E(G_{BP}\text{-}G_{RP}) = 0.104\pm0.027$ mag, while for Collinder 135 it is $E(G_{BP}\text{-}G_{RP}) = 0.065\pm0.022$ mag. Converting to the *UBV* system using the relation $E(G_{BP}\text{-}G_{RP}) = 1.41 \times E(B\text{-}V)$, we obtained $E(B\text{-}V) = 0.074\pm0.019$ mag and $E(B\text{-}V) = 0.046\pm0.016$ mag, respectively. These results are consistent with earlier estimates reported in the literature [23, 27, 29, 30], which place the reddening of both clusters in the range $E(B\text{-}V) \approx 0.03\text{-}0.07$ mag. The agreement confirms that our derived reddening values are robust and reliable for subsequent distance and age determinations.

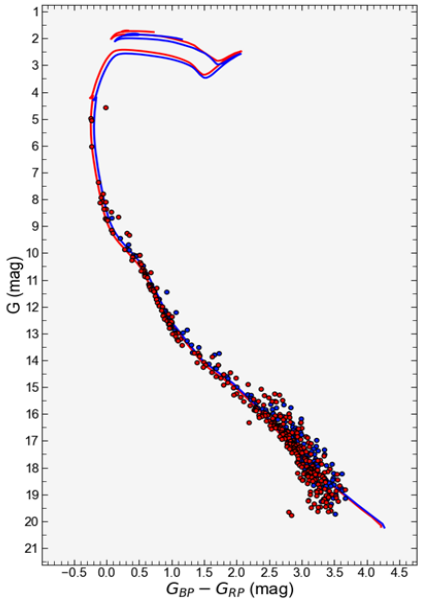


Figure 3. Color-magnitude diagram of the OCs of clusters Collinder 135 (red) and Alessi 36 (blue).

The determination of metallicity in open clusters is of importance for the purposes of understanding their chemical composition, formation environment, and evolutionary status. In instances where spectroscopic data is not available, photometric methods emerge as a reliable approach for estimating the metal abundance of stellar populations by using color indices and empirical calibrations. Photometric metallicity values for Alessi 36 and Collinder 135 have been derived based on *Gaia* observations and calibrated photometric relations. To select isochrones for determining age and distance modulus, [Fe/H] of each open cluster was converted into the mass fraction z. This conversion used formulas adapted from Bovy[1] based on the PARSEC [45] models. The process involves calculating an intermediate value z_x and then obtaining z, with the solar metallicity fixed at $z_\odot$=0.0152:

$$z_x = 10^{\left[\frac{Fe}{H}\right]+\log\left(\frac{z_\odot}{1-0.248-2.78\times z_\odot}\right)}, \qquad z = \frac{z_x(1-0.2485)}{1+2.78\times z_x} \tag{1}$$

Applying this to Alessi 36 and Collinder 135 yielded mass fractions of 0.0152 and 0.01195, respectively. The results indicate that both clusters exhibit metallicities close to the solar value, consistent with their locations in the Galactic disk. The estimated metallicity values are [Fe/H] = 0.00±0.05 and -0.01±0.04 dex, respectively. Nonetheless, our result for Collinder 135 is consistent with the spectroscopic value reported by [12], and both clusters fall within the typical metallicity range of young open clusters in the solar neighbourhood. The conclusion that Alessi 36 has a metallicity close to solar is thus supported by the photometric calibrations and indirectly by the agreement with spectroscopic findings for Collinder 135.

A comparative analysis with other open clusters of similar age and location suggests that Alessi 36 and Collinder 135 share chemical properties typical of intermediate-age clusters in the solar neighbourhood. Determining the distance and age of open clusters is essential for understanding their evolutionary status, formation environment, and role in the Galactic structure. Utilizing *Gaia*'s high-precision astrometric data, the distances of Alessi 36 and Collinder 135 were estimated as 279±7 and 296±6 pc, respectively. These values indicate that both clusters are relatively nearby and situated within the Galactic disk, making them valuable objects for studying stellar evolution and kinematics in the solar neighborhood. The distances quoted here are the isochrone-based values ($d_{\rm iso}$), adopted as our fiducial distances. They are fully consistent within 1σ with the parallax-based distances (d_{ϖ}) reported in Section 3.2. The small present-day |Z| (-64 and -57 pc) and low $Z_{\rm max}$ (35 and 74 pc) further indicate membership

[1] https://github.com/jobovy/isodist/blob/master/isodist/Isochrone.py

in the young thin disc, in line with the concentration of young open clusters toward the Galactic plane reported in previous *Gaia* studies [7,21].

The ages of the clusters were estimated through isochrone fitting of *Gaia* DR3 photometry using PARSEC models, yielding 39 ± 5 Myr for Alessi 36 and 36 ± 5 Myr for Collinder 135. These values indicate that both systems are relatively young, consistent with literature estimates for nearby open clusters of similar type. At such ages, which are shorter than typical two-body relaxation times for clusters of comparable size, significant mass segregation or tidal disruption is not expected to have occurred yet. This supports the interpretation that both clusters are still in an early stage of their dynamical evolution. Their nearly coeval ages further suggest that they may have formed under comparable Galactic conditions or within similar star-forming environments, in line with previous studies of young disc clusters.

3.4 Kinematic and Galactic Orbit Analyses

The kinematical properties of open clusters are of crucial significance in providing insights into their dynamical evolution, Galactic motion, and possible origin within the Milky Way [24]. Utilizing data from the *Gaia* astrometric and radial velocity surveys, the kinematic parameters of Alessi 36 and Collinder 135 were obtained. Orbital integrations were then carried out using the *Galpy* package [40], adopting the MilkyWayPotential model consisting of a Miyamoto-Nagai disk, a Hernquist bulge, and an NFW halo. This axisymmetric potential is widely applied in open cluster studies and provides a realistic description of the solar neighbourhood dynamics. The orbits were integrated backward for 3 Gyr with a timestep of 1.5 Myr using a fourth-order Runge-Kutta scheme. Initial conditions were set using *Gaia* DR3 astrometry (positions, parallaxes, proper motions) and *Gaia* radial velocities. This approach ensures consistency with previous *Gaia*-based orbital analyses of young open clusters.

This encompassed their Galactic positions (X, Y, Z), radial velocity, Galactocentric distance (R_{gc}), and velocity components relative to the Local Standard of Rest (U, V, W)$_{LSR}$. Systemic radial velocities were computed as inverse-variance weighted means of *Gaia* RVS measurements for probable members ($P \geq 0.5$) with iterative 3σ clipping. For Alessi 36, 55 stars yielded v_r = 15.58±0.42 km s^{-1}, while 12 stars gave v_r = 15.62±1.11 km s^{-1} for Collinder 135. Heliocentric Galactic Cartesian coordinates were derived from (l, b, d) using the standard transformations, yielding (X, Y, Z) ≈ (-98, -253, -64) pc for Alessi 36 and (-104, -271, -57) pc for Collinder 135 (see Table 2). Galactocentric radii were calculated assuming R_0 = 8.0 kpc,

giving R_{gc} = 8.10 and 8.11 kpc, respectively, showing that both clusters lie at essentially the same Galactocentric distance. A right-handed coordinate system was adopted, with *U* directed toward the Galactic center, *V* along the direction of Galactic rotation, and *W* toward the North Galactic Pole. Velocities were corrected to the Local Standard of Rest using $(U, V, W)_{\odot}$ = (8.5, 13.38, 6.49) km s^{-1} [44]. The results, summarized in Table 2, show $(U, V, W)_{LSR}$ = (-12.39±0.63, 14.05±0.34, 0.06 ± 0.21) km s^{-1} for Alessi 36 and (-9.13±0.76, 6.53±0.95, -5.22±0.31) km s^{-1} for Collinder 135.

The current positions of the clusters are marked with filled circles in Figure 4, whereas their birth positions are indicated by filled triangles. The motion directions of Collinder 135 and Alessi 36 are represented by red and blue arrows, respectively. Furthermore, the clusters' orbits, including uncertainties in the input parameters, are depicted in orange dotted lines. The triangles correspond to the lower and upper error margins for the clusters' birth locations, respectively (middle panels). The similarity of these values suggests that the clusters may have formed under similar initial conditions or may have originated from the same star forming region. The Galactic positions (*X*, *Y*, *Z*) and Galactocentric distances (R_{gc}) further confirm this hypothesis, demonstrating that both clusters are situated at comparable distances from the Galactic center.

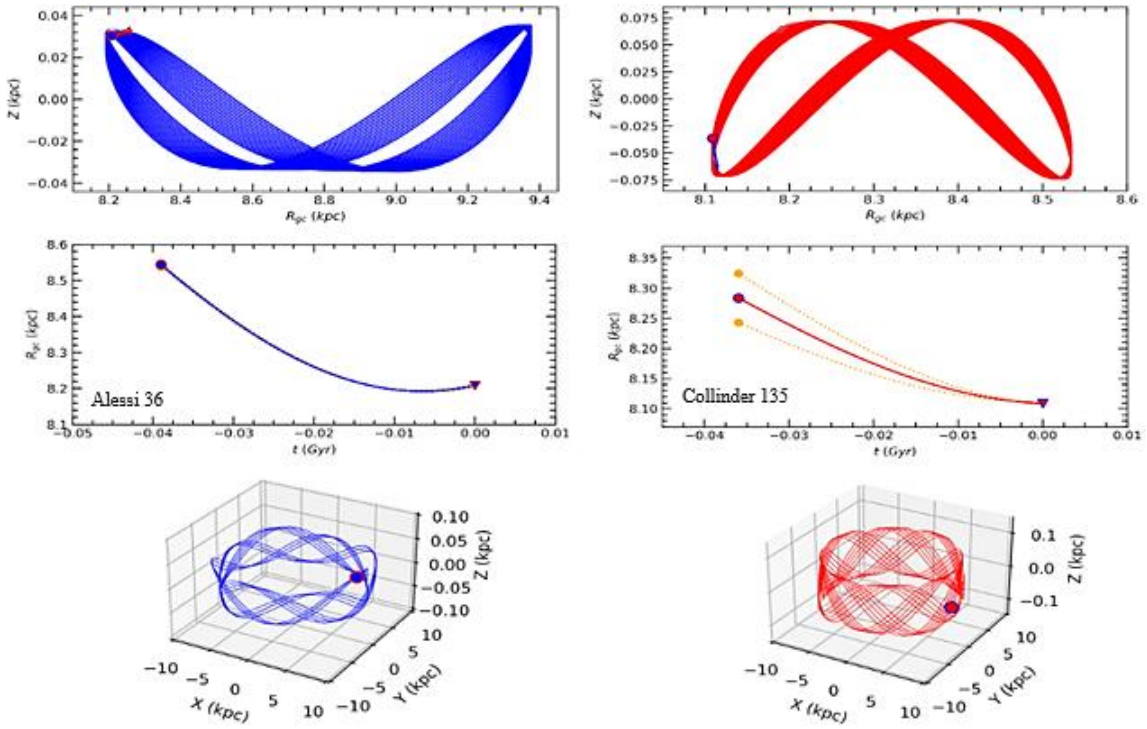


Figure 4. The Galactic trajectories and birth radii of the Collinder 135 (red) and Alessi 36 (blue) clusters are illustrated across two separate panels. Upper panels show the Z × Rgc plane, the middle panels present the Rgc × t, the circles represent the birthplaces and the triangles represent the current locations of the clusters, respectively. The bottom panels visualize the X × Y × Z plane.

The velocity components relative to the Local Standard of Rest $(U, V, W)_{LSR}$ provide additional insight into the orbital motion of the clusters (see also [27, 31, 32]). These parameters are essential for understanding the clusters' trajectories within the Milky Way and their interactions with the Galactic potential. These modest velocities, together with the low orbital eccentricities ($e < 0.07$) and small vertical excursions ($Z_{max} < 0.08$ kpc), are typical of young thin-disc open clusters (e.g., [7, 21]) and confirm that both systems follow stable, nearly circular orbits within the Galactic disk, without evidence for recent strong gravitational perturbations or external interactions.

4 DISCUSSION

In this study, we conducted a close binary cluster analysis of Alessi 36 and Collinder 135 via *Gaia* DR3 data for photometric, astrometric, and kinematic evaluations. In the following subsections we discuss the results of our analyses.

4.1 Astrometric Parameters

Based on membership probabilities $P \geq 0.5$, the most probable member stars of both clusters were identified by using the machine learning k-means method. These stars formed the basis for deriving key astrophysical parameters and Galactic orbital characteristics. The age, distance, and reddening of the clusters were simultaneously determined using *Gaia*-based CMDs. Using the vector point diagram (VPD) of most probable member stars, the mean proper-motion components $\mu_\alpha \cos\delta$, μ_δ were estimated for Alessi 36 and Collinder 135 as (-9.681±0.072, 7.021±0.081) and (-10.06±0.083, 6.256±0.095) mas, respectively. The mean trigonometric parallaxes, $<\varpi>$, obtained from Gaussian fits to parallax histograms constructed from the most likely stars are 3.601±0.086 and 3.348±0.129 mas for Alessi 36 and Collinder 135, respectively. [8] present the largest all-sky search for open clusters using *Gaia* DR3, identifying 7,167 clusters with their astrometric, photometric, and kinematic parameters. As can be seen from Table 1, the proper motion components and trigonometric parallax values obtained from this study are in good agreement with the results presented by [8].

4.2 Fundamental Astrophysical Parameters

The main sequence fitting method is a fundamental technique for determining cluster parameters such as distance, age, and extinction by comparing observed CMD with theoretical isochrones [7, 12, 17, 23, 26]. However, estimation of these parameters is often affected by

degeneracies, since different combinations of parameters can produce similar fits, making precise determination challenging. In order to minimize this degeneracy, the trigonometric parallax distance and the metallicity value obtained from spectral observations in the literature were fixed in this stage. The color excess for both clusters was derived for Alessi 36 and Collinder 135, as $E(G_{BP}\text{-}G_{RP})$ = 0.104±0.027, $E(G_{BP}\text{-}G_{RP})$ = 0.065±0.022 mag, respectively. Using the relation $E(G_{BP}\text{-}G_{RP}) = 1.41\times E(B\text{-}V)$ [33, 34], the UBV-system color excesses were obtained as $E(B\text{-}V)$ = 0.074±0.019 mag for Alessi 36 and $E(B\text{-}V)$ = 0.046±0.016 mag for Collinder 135.

For Alessi 36, our derived distance (279±7 pc) and age (39±5 Myr) are in good agreement with the recent study by [36] who reported a distance of 281 ± 9 pc and an age of 41 ± 6 Myr based on *Gaia* DR3 data. The proper motion components we obtained also overlap within uncertainties with their values, supporting the robustness of our membership determination. For Collinder 135, our results are broadly consistent with those of [37] and [38], who both reported distances near 300 pc and ages around 35-40 Myr. More recent determinations by [39] and [36] also provide similar results, with ages of ~36-38 Myr and distances close to 295-300 pc. The minor discrepancies in membership numbers and mean proper motions likely reflect differences in the adopted membership probability thresholds and astrometric filtering criteria. Overall, these comparisons confirm that our analysis is consistent with previous literature while providing refined estimates of the clusters' physical and kinematical properties.

4.3 Kinematic Analyses

Radial velocity measurements have an important place in performing kinematic analyses. In this study, radial velocity values measured with *Gaia*'s radial velocity spectrometer (RVS) were used in kinematic analyses. When compared with other studies in the literature, it is seen that these measurement results are compatible with each other. [21] constructed a comprehensive radial velocity catalogue with *Gaia* DR2 data, giving radial velocity values for Alessi 36 and Collinder 135, respectively, as 16.80±0.67 and 16.87±0.23 km s^{-1}. Our measurements, 15.58±0.42 km s^{-1} for Alessi 36 and 15.62±1.11 km s^{-1} for Collinder 135, are slightly lower but remain broadly consistent within uncertainties (see Table 2).

Galactic orbit analyses were conducted for both clusters. Using precisely determined ages, their orbits were traced backward in time to identify their birthplaces within the Galaxy, revealing that they originated in different regions. Alessi 36 is located at 8544 pc, while

Collinder 135 is at 8284 pc (Figure 3). A review of the literature shows that [20] classified these clusters as pairs in their binary cluster catalogue. However, our kinematic analysis confirms that although they are binary clusters, they did not form simultaneously. Galactic orbit analysis revealed that both clusters follow low eccentricity nearly circular orbits within the young thin-disc population of the Milky Way [33, 34, 35].

Table 2. The fundamental parameters of Alessi 36 and Collinder 135 open clusters have been derived in this study and confronted with values available in the literature.

Parameters	This Study		Hunt and Reffert (2024)	
	Alessi 36	**Collinder 135**	**Alessi 36**	**Collinder 135**
$(\alpha)_{J2000}$ (Sexagesimal)	07 07 08.65	07 17 26.89	07 06 15.64	07 17 37.34
$(\delta)_{J2000}$ (Sexagesimal)	-37 43 44.5	-37 02 38.5	-37 35 45.49	-36 55 15.26
$(l, b)_{J2000}$ (Decimal)	248.742, -13.345	248.989, -11.201	248.544, -13.451	248.890, -11.11627
Members ($P \geq 0.5$)	230	342	198	209
$\mu_\alpha \cos\delta$ (mas yr^{-1})	-9.681±0.072	-10.061±0.083	-9.669±0.016	-10.078±0.019
μ_δ (mas yr^{-1})	7.021±0.081	6.256±0.095	7.046±0.018	6.230±0.017
ϖ (mas)	3.601±0.086	3.348±0.129	3.598±0.066	3.330±0.080
d_{ϖ} (pc)	278±7	299±11	278±5	300±7
$E(G_{BP}$-$G_{RP})$ (mag)	0.104±0.027	0.065±0.022	0.06±0.01	0.076±0.01
A_G (mag)	0.194±0.05	0.121±0.04	0.119±0.01	0.141±0.01
$E(B$-$V)$ (mag)	0.074±0.019	0.046±0.016	0.046±0.01	0.034±0.01
[Fe/H] (dex)	0.00±0.05	-0.011±0.040*	---	----
μ_G (mag)	7.425±0.051	7.474±0.047	7.221±0.002	7.337±0.10
d_{iso} (pc)	279±7	296±6	275±1	295±1
Age (Myr)	39±5	36±5	28±7	29±6
(X, Y, Z) (pc)	(-98, -253, -64)	(-104, -271, -57)	(-98, -249, -42)	(-104, -270, -35)
v_r (km s^{-1})	15.58±0.42 (N=55)	15.62±1.11 (N=12)	16.80±0.67**	16.87±0.23**
R_{gc} (kpc)	8.10	8.11	---	---
U_{LSR} (km s^{-1})	-12.39±0.63	-9.13±0.76	---	---
V_{LSR} (km s^{-1})	14.05±0.34	6.53±0.95	---	---
W_{LSR} (km s^{-1})	0.06±0.21	-5.22±0.31	---	---
S_{LSR} (km s^{-1})	18.73±0.75	12.38±1.26	---	---
Z_{max} (kpc)	0.035±0.001	0.074±0.003	---	---
R_a (kpc)	9.377±0.015	8.534±0.073	---	---
R_p (kpc)	8.192±0.002	8.108±0.004	---	---
e	0.067±0.001	0.026±0.005	---	---
Birthplace (pc)	8544	8284	---	---
P_{orb} (Myr)	248±1	233±1	---	---

(*: [12], **: [21])

The estimated birth radii of the clusters indicates that they originated beyond the solar neighborhood, with Alessi 36 at 8544 pc and Collinder 135 at 8284 pc. [20] conducted a multidimensional analysis of candidate binary systems, incorporating coordinates, trigonometric parallax, proper motion components, and color-magnitude diagrams to assess their potential physical interactions. Based on this comprehensive evaluation, the candidate systems were classified into three categories: genetic pairs (B), which share a common origin, similar age, distance, and kinematics; tidal capture or resonant trapping pairs (C), which exhibit common kinematics but may differ in age, indicating dynamic interaction without a common

origin; and optical pairs (O), which appear close in the sky but are not physically associated. Although our candidate system initially appeared to resemble a genetic pair due to its similar distance, kinematics, and age, tracing the clusters' orbits back in time revealed that they originated from different locations. This finding suggests that the system does not fully match with any of the established categories, highlighting the need for a new classification to describe such cases.

5 CONCLUSION

In this study, we performed a comprehensive astrometric, photometric, and kinematic characterization of the nearby open cluster pair Alessi 36 and Collinder 135, based on the high-precision *Gaia* DR3 dataset. Through a methodologically integrated approach combining with machine learning technique, color-magnitude diagram (CMD) fitting, and Galactic orbital modeling, we obtained the most probable cluster members and inferred their fundamental astrophysical and dynamical properties.

The astrometric parameters of both clusters such as proper motion components and trigonometric parallaxes were determined using the k-means clustering algorithm, focusing on stars with membership probabilities $P \geq 0.5$. The derived mean parallaxes and proper motions were found to be in excellent agreement with previous large-scale *Gaia*-based cluster catalogs, such as [8]. The CMD based isochrone fitting, performed under constraints from *Gaia* parallaxes and spectroscopic metallicity values, yielded distance estimates of ~279 pc and ~296 pc for Alessi 36 and Collinder 135, respectively, along with nearly solar metallicities. Both clusters exhibit moderate but different reddening values, indicating slightly different interstellar environments despite their spatial proximity.

The kinematic analysis utilized *Gaia* radial velocities, confirming systemic velocities around 15.6 - 15.7 km s^{-1} for both clusters, consistent with previous spectroscopic studies. Combined with 3D astrometric parameters, we computed the full space motions and Galactic orbits of both clusters. These orbits suggest that the clusters are members of the young thin disc population, with low eccentricities and small vertical deviations ($Z_{max} < 0.08$ kpc), typical for dynamically cold systems in the solar neighborhood.

A backward integration of their Galactic orbits revealed that, although the clusters are presently co-moving and exhibit similar spatial and kinematic characteristics, they originated from distinct Galactic radii approximately 8.5 kpc for Alessi 36 and 8.3 kpc for Collinder 135.

This spatial separation at birth, coupled with their slight age difference (~3 Myr), rules out the possibility of a common formation event. Consequently, while these clusters may appear as a binary cluster in projection and kinematics, our results indicate that they are not a genetic pair in the strictest sense.

This finding provides an important case study in the classification of close binary open clusters (CBOCs). It highlights the limitations of conventional binary cluster classification schemes namely genetic (B), tidal resonant (C), and optical (O) by introducing an example that defies full categorization. The Alessi 36 Collinder 135 pair likely represents a dynamically coupled system without a shared origin, possibly formed via resonant trapping or convergent motion in the Galactic disc.

Although the present analysis provides significant insights into the nature and origin of Alessi 36 and Collinder 135, several points remain open for further investigation. While this work relies on *Gaia* DR3 radial velocities and previously published metallicities, high-resolution spectroscopic observations are needed to refine chemical abundance patterns (e.g., α-elements, s- and r-process elements) of individual member stars. Such chemical tagging could offer crucial constraints on the clusters' birth environments and further confirm their non-genetic origin.

As young clusters, Alessi 36 and Collinder 135 present ideal laboratories to study stellar rotation and magnetic activity. Cross-matching with large photometric surveys (e.g., TESS, ZTF) may reveal periodicities associated with stellar rotation, enabling gyrochronological age estimates as independent checks of the isochronal ages. The presence and distribution of binary systems within the clusters could impact both their internal dynamics and apparent CMD morphology. Future astrometric and spectroscopic monitoring could identify unresolved binaries and constrain the binary fraction, mass segregation, and dynamical evolution state of each cluster.

The orbital integrations in this study were based on static Galactic potential models. Incorporating time-varying or bar-spiral-interacting potentials in N-body simulations could offer a more realistic picture of the clusters' migration history and potential capture scenarios. This may also clarify whether the clusters became a binary system after birth or were temporarily trapped in a co-moving configuration due to disc perturbations.

In conclusion, this study illustrates the potential of *Gaia* DR3 data not only for accurately characterizing individual open clusters but also for uncovering complex dynamical

relationships among them. The findings underscore the importance of multidimensional analyses in the study of star cluster evolution and Galactic structure and pave the way for future refinements in cluster classification and formation theory.

Acknowledgements

This study was supported by the Scientific and Technological Research Council of Turkey (TÜBİTAK) 122F109. We also utilised NASA's Astrophysics Data System, along with the VizieR and Simbad databases operated by CDS in Strasbourg, France. Additionally, our study incorporated data from the European Space Agency's (ESA) *Gaia* mission, processed by the *Gaia* Data Processing and Analysis Consortium (DPAC), which is supported by national institutions, particularly those participating in the *Gaia* Multilateral Agreement.

Conflict of Interest Statement

There is no conflict of interest between the authors.

Statement of Research and Publication Ethics

The study is complied with research and publication ethics.

Artificial Intelligence (AI) Contribution Statement

This manuscript was entirely written, edited, analyzed, and prepared without the assistance of any artificial intelligence (AI) tools. All content, including text, data analysis, and figures, was solely generated by the authors.

Contributions of the Authors

The conception and design of the study were undertaken by H. Karagöz, D. C. Çınar, S. Taşdemir, and R. Canbay. Data acquisition was carried out by H. Karagöz, D. C. Çınar, and S. Taşdemir, whereas data analysis and interpretation were primarily conducted by D. C. Çınar, S. Taşdemir, and R. Canbay. The initial drafting of the manuscript was prepared by H. Karagöz, D. C. Çınar, S. Taşdemir, and R. Canbay, while the critical revision of the text was undertaken by D. C. Çınar, S. Taşdemir, and R. Canbay. Final approval of the version to be published, along with full accountability for all aspects of the work, was provided by all authors. Technical and material support were contributed by D. C. Çınar, S. Taşdemir, and R. Canbay, and the overall supervision of the study was ensured by H. Karagöz, D. C. Çınar, S. Taşdemir, and R. Canbay.

REFERENCES

[1] W. E. Harris and R. E. Pudritz, Supergiant molecular clouds and the formation of globular cluster systems, *Astrophys. J.*, vol. 429, p. 177, 1994.

[2] E. D. Friel, The old open clusters of the milky way, *Annu. Rev. Astron. Astrophys.*, vol. 33, no. 1, pp. 381-414, 1995.

[3] B. G. Elmegreen, M. Kaufman, C. Struck, D. M. Elmegreen, E. Brinks, M. Thomasson, M. Klarić, Z. Levay, J. English, L. M. Frattare, H. E. Bond, C. A. Christian, F. Hamilton, K. Noll, Erratum: Hubble space telescope observations of the interacting galaxies NGC 2207 and IC 2163, *Astron. J.*, vol. 120, no. 6, pp. 3371-3371, 2000.

[4] C. J. Lada and E. A. Lada, Embedded clusters in molecular clouds, *Annu. Rev. Astron. Astrophys.*, vol. 41, no. 1, pp. 57-115, 2003.

[5] G. Carraro and E. Costa, Photometry of the five marginally studied open clusters Collinder 74, Berkeley 27, Haffner 8, NGC 2509, and VdB-Hagen 4, *Astron. Astrophys.*, vol. 464, no. 2, pp. 573-580, 2007.

[6] Gaia Collaboration, Gaia data release 3. Summary of the contents and survey properties, *Astronomy and Astrophysics*, vol. 674, id.A1, pp 22 , 2023.

[7] T. Cantat-Gaudin and F. Anders, Clusters and mirages: cataloguing stellar aggregates in the Milky Way, *Astron. Astrophys.*, vol. 633, p. A99, 2020.

[8] E. L. Hunt and S. Reffert, Improving the open cluster census: III. Using cluster masses, radii, and dynamics to create a cleaned open cluster catalogue, *Astron. Astrophys.*, vol. 686, p. A42, 2024.

[9] X. Pang, S. Liao, J. Li, Z. Yan, M. Jian, M. B. N. Kouwenhoven, S.Y. Tang, and Y. Wang, The present-day mass function of star clusters in the solar neighborhood, *Astrophys. J.*, vol. 966, no. 2, p. 169, 2024.

[10] M. Žerjal, N. Lodieu, A. Pérez-Garrido, J. Olivares, V. J. S. Béjar, and E. L. Martín, Young nearby open clusters and their luminosity functions, *Astronomy and Astrophysics*, vol. 678, id. A75, 26 pp, 2023.

[11] D. A. Kovaleva, M. Ishchenko, E. Postnikova, P. Berczik, A. E. Piskunov, N. V. Kharchenko, E. Polyachenko, S. Reffert, K. Sysoliatina, and A. Just, Collinder 135 and UBC 7: A physical pair of open clusters, *Astron. Astrophys*, vol. 642, p. L4, 2020.

[12] W. S. Dias, H. Monteiro, A. Moitinho, J. R. D. Lépine, G. Carraro, E. Paunzen, B. Alessi, and L. Villela, Updated parameters of 1743 open clusters based on Gaia DR2, *Mon. Not. R. Astron. Soc.*, vol. 504, no. 1, pp. 356-371, 2021.

[13] T. Cantat-Gaudin, C. Jordi, A. Vallenari, A. Bragaglia, L. Balaguer-Núñez, C. Soubiran, D. Bossini, A. Moitinho, A. Castro-Ginard, A. Krone-Martins, L. Casamiquela, R. Sordo, and R. Carrera, A Gaia DR2 view of the open cluster population in the Milky Way, *Astron. Astrophys.*, vol. 618, p. A93, 2018.

[14] J. J. Claria and S. O. Kepler, Wide- and narrow-band photometry of stars in a field around Collinder 135, *Publ. Astron. Soc. Pac.*, vol. 92, p. 501, 1980.

[15] F. Song, A. Esamdin, Q. Hu, and M. Zhang, Binary open clusters in the Gaia data, *Astron. Astrophys*, vol. 666, p. A75, 2022.

[16] Z. Li and Z. Zhu, A catalog of newly discovered close binary open clusters in the Milky Way from Gaia DR3*, Astronomy and Astrophysics*, vol. 700, id. A280, 12 pp, 2024.

[17] A. A. Haroon, W. H. Elsanhoury, A. S. Saad, and E. A. Elkholy, Deep investigation of a pair of open clusters NGC 7031 and NGC 7086 utilizing Gaia DR3, *Contrib. Astron. Obs. Skaln. Pleso*, vol. 54, no. 3, 2024.

[18] A. Yousef-Alzahrani, A. A. Haroon, W. H. Elsanhoruy, and D. C. Çınar, An in-depth analysis of photometric and kinematic characteristics of SAI 16, SAI 81 and SAI 86 open clusters utilizing Gaia, *Journal of Astrophysics and Astronomy*, Volume 46, Issue 2, id.58, 2025.

[19] S. Taşdemir and D. C. Çınar, A detailed analysis of close binary OCs, *Contributions of the Astronomical Observatory Skalnaté Pleso*, vol. 55, no. 3, p. 506-511, 2025.

[20] T. Palma, V. Coenda, G. Baume, and C. Feinstein, Binary and grouped open clusters: A new catalogue, *Astron. Astrophys.*, vol. 693, p. A218, 2025.

[21] Y. Tarricq, C. Soubiran, L. Casamiquela, T. Cantat-Gaudin, L. Chemin, F. Anders, T. Antoja, M. Romero-Gómez, F. Figueras, C. Jordi, A. Bragaglia, L. Balaguer-Núñez, R. Carrera, A. Castro-Ginard, A. Moitinho, P. Ramos, and D. Bossini, 3D kinematics and age distribution of the open cluster population, *Astron. Astrophys*., p. A19, 2021.

[22] A. Krone-Martins and A. Moitinho, UPMASK: unsupervised photometric membership assignment in stellar clusters, *Astron. Astrophys*., vol. 561, p. A57, 2014.

[23] A. Yousef-Alzahrani, A. A. Haroon, W. H. Elsanhoruy, and D. C. Çınar, Enhancing SED-based astrometric, photometric, and kinematic studies of SAI 72 and SAI 75 Using Gaia, *Journal of Astrophysics and Astronomy*, vol. 46, Issue 2, id.50, 2025.

[24] G. Yücel, R. Canbay, and V. Bakış, The fundamental parameters and evolutionary status of V454 aurigae, *Physics and Astronomy Reports*, vol. 2, no. 1, pp. 18-28, 2024.

[25] C. Soubiran, G. Jasniewicz, L. Chemin, C. Zurbach, N. Brouillet, P. Panuzzo, P. Sartoretti, D. Katz, J. -F. Le Campion, O. Marchal, D. Hestroffer, F. Thévenin, F. Crifo, S. Udry, M. Cropper, G. Seabroke, Y. Viala, K. Benson, R. Blomme, A. Jean-Antoine, H. Huckle, M. Smith, S. G. Baker, Y. Damerdji, C. Dolding, Y. Frémat, E. Gosset, A. Guerrier, L. P. Guy, R. Haigron, K. Janßen, G. Plum, C. Fabre, Y. Lasne, F. Pailler, C. Panem, F. Riclet, F. Royer, G. Tauran, T. Zwitter, A. Gueguen, and C. Turon, Gaia Data Release 2: The catalogue of radial velocity standard stars, *Astronomy and Astrophysics*, vol. 616, p. 8, 2018.

[26] D. Dursun, S. Taşdemir, S. Koç, and S. Iyer, SED analysis of the old open cluster NGC 188, *Physics and Astronomy Reports*, vol. 2, no. 1, pp. 1-17, 2024.

[27] T. Yontan and R. Canbay, Comprehensive analysis of the open cluster Collinder 74, *Physics and Astronomy Reports*, Vol 1, No. 2, p. 65, 2023.

[28] S. Tasdemir and T. Yontan, Analysis of the young open cluster Trumpler 2 using Gaia DR3 data, *Physics and Astronomy Reports*, Vol. 1, No. 1, pp. 1-10, 2023.

[29] W. H. Elsanhoury, A. A. Haroon, E. A. Elkholy, and D. C. Çınar, Deeply comprehensive astrometric, photometric, and kinematic studies of the three OCSN open clusters with Gaia DR3, *Journal of Astrophysics and Astronomy*, Volume 46, Issue 1, id.21, 2024.

[30] S. Taşdemir, D. Çınar, R. Canbay, S. Taştan, W. Elsanhoury, and A. Haroon, Comprehensive analysis of middle-aged open cluster NGC 6793 in vulpecula via Gaia DR3 data, *Physics and Astronomy Reports*, vol. 3, no. 1, pp. 1-12, 2025.

[31] A. Haroon, W. Elsanhoury, E. Elkholy, A. N. Saad, and D. C. Çınar, Study of open star clusters using the Gaia DR3: I- poorly studied King 2 and King 5, *Physica Scripta*, vol. 100, Issue 5, id.055006, 18 pp., 2025.

[32] T. Yontan, H. Çakmak, S. Bilir, T. Banks, M. Raúl, R. Canbay, S. Koç, S. Taşdemir, H. Erçay, B. Tanık Oztürk, D. C. Çınar, A Study of the NGC 1193 and NGC 1798 Open Clusters Using CCD UBV Photometric and Gaia EDR3 Data, *Rev. Mex. Astron. Astrofis*., vol. 58, no. 2, pp. 333-353, 2022.

[33] R. Canbay, S. Bilir, A. Özdönmez, and T. Ak, Galactic Model Parameters and Spatial Density of Cataclysmic Variables in the Gaia Era: New Constraints on Population Models, *The Astronomical Journal*, vol. 165, Issue 4, id.163, pp 16, 2023.

[34] R. Canbay, T. Ak, S. Bilir, F. Soydugan, and Z. Eker, Kinematics of Cataclysmic Variables in the Solar Neighborhood in the Gaia Era, *The Astronomical Journal*, vol. 169, Issue 2, id.87, pp 18, 2025.

[35] D. C. Çınar, S. Bilir, T. Şahin, and O. Plevne, Tracing the Galactic Origins of Selected Four G-type Stars in the Solar Neighborhood, *The Astronomical Journal*, vol. 170, Issue 1, id.13, pp 26, 2025.

[36] L. Cavallo, L. Spina, G. Carraro, L. Magrini, E. Poggio, T. Cantat-Gaudin, M. Pasquato, S. Lucatello, S. Ortolani, J. Schiappacasse-Ulloa, Parameter Estimation for Open Clusters using an Artificial Neural Network with a QuadTree-based Feature Extractor, *The Astronomical Journal*, vol. 167, Issue 1, id.12, 18 pp., 2024.

[37] N. V. Kharchenko, A. E. Piskunov, S. Röser, E. Schilbach, and R.-D. Scholz, Global survey of star clusters in the Milky Way. II. The catalogue of basic parameters, *Astron. Astrophys*., vol. 543, p. A156, 2012.

[38] V. P. Loktin and M. E. Popova, Updated version of the homogeneous catalog of open cluster parameters, *Astrophys. Bull*., vol. 72, pp. 257-265, 2017.

[39] Z. He, K. Wang, Y. Luo, J. Li, X. Liu, Q. Jiang, A Blind All-sky Search for Star Clusters in Gaia EDR3: 886 Clusters within 1.2 kpc of the Sun, *The Astrophysical Journal Supplement Series*., vol. 262, id.7, 16 pp, 2022.

[40] J. Bovy, galpy: A python Library for Galactic Dynamics, *The Astrophysical Journal Supplement Series*, vol. 216, Issue 2, article id. 29, 27 pp, 2015.

[41] C. A. L. Bailer-Jones, Estimating Distances from Parallaxes, *Publications of the Astronomical Society of the Pacific*, vol. 127, Issue 956, pp. 994, 2015.

[42] C. A. L. Bailer-Jones, J. Rybizki, M. Fouesneau, M. Demleitner, R. Andrae, Estimating Distances from Parallaxes. V. Geometric and Photogeometric Distances to 1.47 Billion Stars in Gaia Early Data Release 3*, The Astronomical Journal*, vol. 161, Issue 3, id.147, 24 pp, 2021.

[43] X. Luri, A. G. A. Brown, L. M. Sarro, F. Arenou, C. A. L. Bailer-Jones,; A. Castro-Ginard, J. de Bruijne, T. Prusti, C. Babusiaux, H. E. Delgado, Gaia Data Release 2. Using Gaia parallaxes, *Astronomy and Astrophysics*, vol. 616, id.A9, 19 pp., 2018.

[44] B. Coşkunoglu, S. Ak, S. Bilir, S. Karaali, E. Yaz, G. Gilmore, G. M. Seabroke, O. Bienayme, J. Bland-Hawthorn, R. Campbell, K. C. Freeman, B. Gibson, E. K. Grebel, U. Munari, J. F. Navarro, Q. A. Parker, A. Siebert, A. Siviero, M. Steinmetz, F. G. Watson, R. F. G. Wyse and T. Zwitter, Local stellar kinematics from RAVE data I. Local standard of rest, *Monthly Notices of the Royal Astronomical Society*, vol. 412, Issue 2, pp. 1237-1245, 2011.

[45] A. Bressan, P. Marigo, L. Girardi, B. Salasnich, C. Dal Cero, S. Rubele, A. Nanni, PARSEC: stellar tracks and isochrones with the PAdova and TRieste Stellar Evolution Code, *Monthly Notices of the Royal Astronomical Society*, vol. 427, Issue 1, pp. 127-145, 2012.

BİTLİS EREN ÜNİVERSİTESİ
FEN BİLİMLERİ DERGİSİ

ISSN: 2147-3129 / e-ISSN: 2147-3188

Article Type	: Research Article	**Year**	: 2025
Received	: July 17, 2025	**Volume**	: 14
Revised	: September 11, 2025	**Issue**	: 3
Accepted	: September 27, 2025	**Pages**	: 1961-1979
DOI	: 10.17798/bitlisfen.1745184		

EXPERIMENTAL AND NUMERICAL MODAL ANALYSIS OF A SPHERICAL NOMEX HONEYCOMB CORE SANDWICH PLATE

Osman YİĞİD [1], **Murat ŞEN** [2,*]

[1] *Bitlis Eren University, Mechanical Engineering Department, Bitlis, Türkiye*

[2] *Fırat University, Mechanical Engineering Department, Elazığ, Türkiye*

**** Corresponding Author:*** msen@firat.edu.tr

ABSTRACT

This study investigated the dynamic properties of a spherical sandwich composite structure made of carbon fiber face sheets and a Nomex honeycomb core. The structure was produced using the hand lay-up method. The results from Experimental Modal Analysis (EMA) and the numerical model created in ANSYS showed high consistency. The natural frequency difference was only 0.73% for the second mode, with the largest discrepancy of 6.5% was observed in the first mode. These differences are thought to be related to structural variations from the manufacturing process, such as resin distribution, carbon fiber fabric stacking, and air voids and experimental challenges such as double hit errors, measurement resolutions related to force sensors, accelerometer and environmental noise. The vibration damping capability of the sandwich structure was investigated. Some modes exhibited high damping, while others had relatively lower values. The highest and the lowest damping ratios were obtained as 0.83% for the third mode and 0.23% for the fourth mode. A numerical equivalent model of the structure was created in ANSYS to determine its natural frequencies and vibration modes, confirming its effectiveness in modeling complex structures.

Keywords: Spherical sandwich plate, Modal analysis, Equivalent model, Experimental modal analysis, Mode shape, Damping.

1 INTRODUCTION

Honeycomb sandwich structures are widely used in many engineering fields due to their lightweight nature, low mass density, high energy absorption, and excellent vibration and sound insulation properties. They are particularly effective in aerospace, automotive, marine, and

spacecraft applications where dynamic effects are frequently observed. These structures are generally fabricated by bonding thin metal or composite face sheets to a thin-walled honeycomb core layer, typically using adhesives. Aluminum is a commonly used core material. Additionally, Nomex honeycomb cores are preferred for the significant weight reduction they offer. Thanks to their low density, Nomex honeycomb structures reduce the mass of the systems they are used in, thereby increasing energy efficiency. Their superior mechanical properties also enhance structural integrity in their applications. Furthermore, they are effectively utilized in vibration and sound insulation applications.

Researchers have been intensely focused on determining the mechanical and dynamic characteristics of these structures over the past few decades [1-4]. These studies aim to identify the mechanical and dynamic properties of honeycomb sandwich structures. Ejaz et al. [5] investigated the flexural and impact responses of sandwich panels with a Nomex honeycomb core and hybrid fiber-reinforced composite skins (carbon, glass, and Kevlar). They examined the effects of laminate thickness and the content percentages of carbon, glass, and Kevlar on the strength, ductility, and energy absorption capabilities of the panels. In reference [6], the authors investigated the properties of a sandwich structure composed of a Nomex-Aramid honeycomb core and carbon fiber face sheets, along with the effect of the core's characteristics on the overall structural strength. Using numerical simulations with the finite element method, they conducted three-point bending, tensile, compression, and torsional tests. The study also compared the influence of the core material's geometry and type on the sandwich structure's strength. In their study, Chen and Fan [7] investigated the fabrication and mechanical behavior of sandwich structures created with flexible honeycomb cores. These honeycombs gain their flexibility from the removal of specific node points, and they aimed to produce structures that can conform to complex surfaces, such as spherical ones, without the need for wrinkles or cutting. Their work demonstrated that the flexible honeycomb structure possesses both a high deformation capacity and a strong load-bearing ability.

Although the complex core geometry of such structures complicates analytical approaches, researchers are actively working on effective methods in this area [8–10]. Analytical solutions for globally curved plates and sandwich structures are more complex. Van Do and Lee [11] developed a numerical model based on isogeometric analysis coupled with a higher-order shear deformation shell theory to perform static and dynamic analyses of composite curved panels. They determined the equivalent modulus of elasticity for the panels using the Halpin-Tsai model. Additionally, they employed a modified rule of mixtures to

ascertain the poisson ratio and equivalent mass density. Qu et al. [12] presented a variational formulation that utilizes the first-order shear deformation theory and a multi-segment partitioning technique. The study investigated the free, steady-state, and transient vibrations of cross-ply and angle-ply laminated cylindrical, conical, and spherical shells under varying material, geometric, and boundary conditions. The proposed formulation allows for the use of any linearly independent and complete polynomial and enables the analysis of most linear vibration problems with arbitrary boundary conditions and dynamic loads. Ref. [13], presents a novel model for the buckling analysis of partially spherical and partially cylindrical honeycomb sandwich shells under external pressure. In the developed model, the influence of the hemispherical shell on the cylindrical shell is treated as elastic support with specific rigidity. Tang and Dai [14] investigated the dynamic behavior of a carbon fiber reinforced polymer spherical shell panel under hygrothermal effects. They derived the necessary equations using nonlinear static stability analysis and solved these equations using the Galerkin method. In another study, Kiani [15], utilized the first-order shear deformation shell theory and Sanders kinematics for the free vibration analysis of carbon nanotube-reinforced composite spherical panels. Sayyad and Ghugal [16], on the other hand, presented a novel higher-order shell theory independent of the shear stress function, which combines existing classical and higher-order shear deformation theories for the free vibration analysis of sandwich spherical shells. Guo et al. [17] utilized the spectral-Tchebyshev technique to perform dynamic analyses of combined structures composed of conical, cylindrical, and spherical shells. They employed artificial spring elements to connect the sub-components forming the combined structure.

Numerical methods are also employed in the dynamic analysis of honeycomb sandwich structures. Performing mechanical and dynamic analyses of these structures using numerical models is a considerably challenging and time-consuming process. Consequently, equivalent model approaches have been developed to streamline numerical modeling efforts. In equivalent model approaches, models are created by determining the equivalent mechanical properties of the honeycomb core structure or the sandwich structure containing the honeycomb core. Analyses conducted on these simplified models allow for the mechanical and dynamic properties of the structure to be obtained more quickly and easily. Gibson and Ashby [18] developed an equivalent theory to model the orthotropic honeycomb layer of a honeycomb structure. This theory provides formulas to find equivalent values for moduli of elasticity and shear moduli in three directions, an equivalent density and suggested Poisson's ratios. These material properties can then be used to model a simplified orthotropic honeycomb layer for

numerical analysis. Xia et al. [19] investigated the performance and consistency of various equivalent methods for modeling honeycomb sandwich structures. In this study, an isotropic equivalent model was developed for a sandwich plate consisting of two face sheets and a core structure. These approaches have also been utilized in other studies for analysis, and the obtained results were compared with those from actual sandwich structures to investigate the performance of the equivalent approach [20, 21].

Experimental approaches offer significant advantages for determining the dynamic behavior of complex structures, such as sandwich composite structures. In this context, the Experimental Modal Analysis (EMA) method provides considerable convenience. With EMA, dynamic properties like natural frequencies, mode shapes, and damping ratios of complex structures can be determined through vibration measurements taken directly on the structure [22-24]. Al-Khazraji et al. [25] conducted a comparative experimental study on the dynamic behavior (natural frequency and damping) of four different sandwich composite structures. These structures were fabricated using carbon fiber, glass fiber, and foam, and their properties were analyzed using Experimental Modal Analysis (EMA). Aborehab et al. [26] verified their equivalent numerical model of a honeycomb sandwich structure using Experimental Modal Analysis (EMA). Elangovan and Rajamohan [27] aimed to determine the effectiveness of numerical models they developed for structures with various honeycomb core configurations. They did this by using EMA to validate the governing equations, which were derived and solved numerically using Higher Order Shear Deformation Theory. They investigated the frequency and loss factor behaviors for different boundary conditions, face sheet taper angles, and plate aspect ratios.

In this study, the dynamic performance of a spherical Nomex honeycomb-cored composite sandwich plate was investigated using EMA under free boundary conditions. It's a known challenge to conduct EMA on spherical sandwich structures due to their complex geometries. While research on these types of structures often focuses on determining mechanical properties, like through three-point bending tests, the investigation of their dynamic behavior (especially with EMA) is limited in the literature. Therefore, our work fills a significant gap in this field. Using EMA, we determined the natural frequencies, damping ratios, and vibration mode shapes for the first five vibration modes of the structure in detail. Furthermore, we created numerical models of the produced sandwich structure in ANSYS using equivalent model approaches. The results from these analyses are presented and compared with our experimental findings. This comparison serves to validate the reliability of our developed

numerical model and contributes to a better understanding of the dynamic behavior of spherical sandwich structures.

2 MATERIAL AND METHOD

This section sequentially details the manufacturing of the Nomex sandwich composite spherical plate, the stages of EMA finally creation and analysis of the sandwich structure's equivalent model using the ANSYS software package.

2.1 Production of Nomex Honeycomb Core Composite Sandwich Spherical Plate

The face sheets of the spherical sandwich plate analyzed in this study were manufactured using the hand lay-up method with 200 g/m² 3k plain carbon fiber fabrics. Initially, a spherical mold was prepared. Mold release wax and peel ply were applied to this mold. Subsequently, carbon fiber fabrics cut to appropriate dimensions were laid sequentially in four layers onto the mold and impregnated with resin using a brush. Following this, a Nomex honeycomb core layer was placed on top of these four carbon fiber layers. For the outer layer, four more layers of carbon fiber fabric were similarly laid and impregnated with resin. Finally, the spherical structure was tensioned at its edges to ensure a tight fit onto the mold. The sandwich structure prepared in this manner was left to cure for one day, after which it was removed from the mold along with the peel ply, resulting in a rigid structure (Figures 1-2).

The numbers on the spherical sandwich structure shown in Figure 2-b represent the measurement coordinates prepared for EMA. The geometric dimensions of the prepared spherical sandwich-layered structure are given in Figure 3.

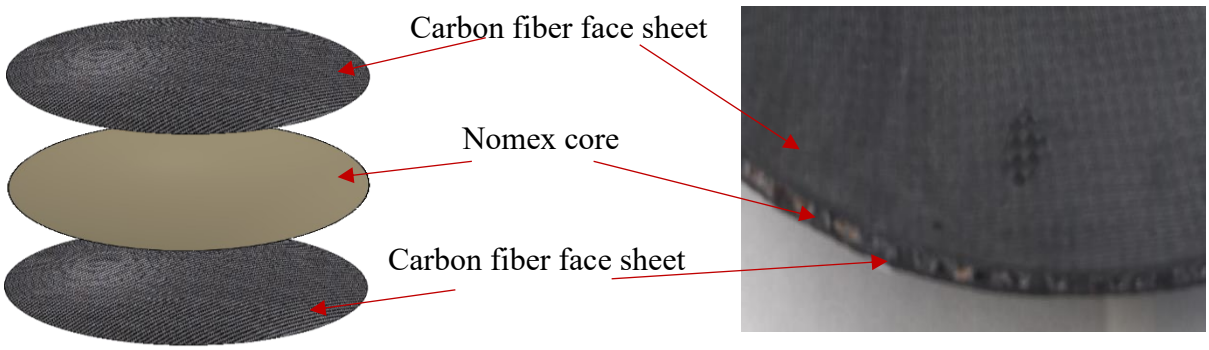
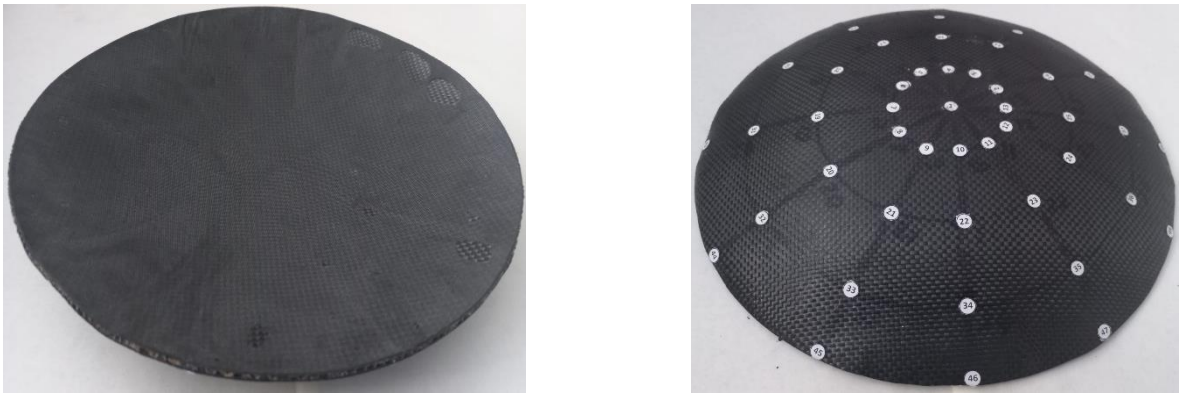


Figure 1. Sandwich structure layers



a) b)

Figure 2. The produced spherical sandwich structure: a) bottom view, b) top view

The numbers on the spherical sandwich structure shown in Figure 2-b represent the measurement coordinates prepared for EMA. The geometric dimensions of the prepared spherical sandwich-layered structure are given in Figure 3.

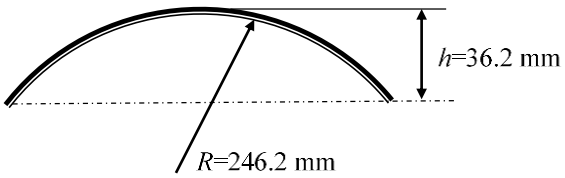


Figure 3. Geometric properties of the inner layer

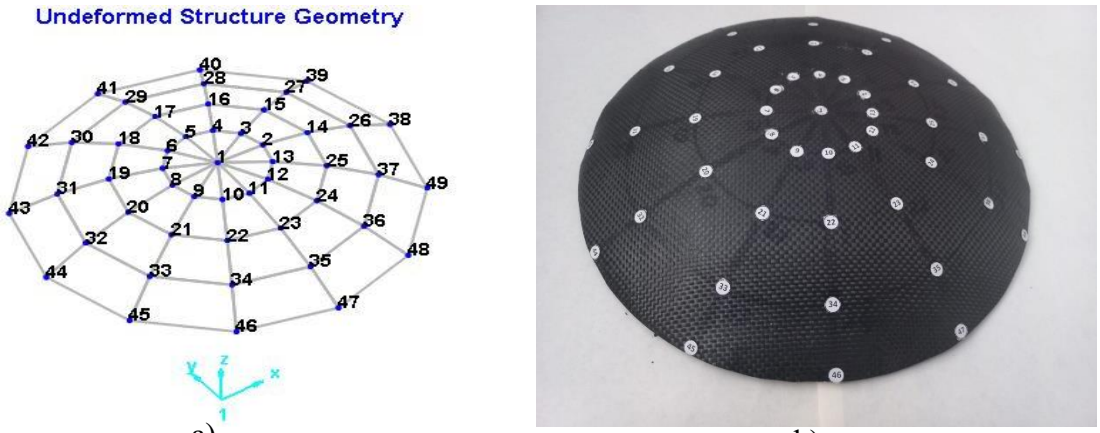
2.2 Experimental Modal Analysis (EMA)

The EMA studies of the prepared spherical sandwich structure were conducted at the Vibration Laboratory of Fırat University's Mechanical Engineering Department. The aim of this work was to determine the dynamic characteristics of the spherical sandwich composite structure, which consists of a Nomex core and carbon fiber face sheet, including its natural frequencies, damping ratios, and vibration mode shapes.

In EMA, the system is excited at predetermined coordinates on the structure under test, and the system's responses to this excitation force are measured. This process yields Frequency Response Functions (FRFs), which describe the relationship between the force input and the acceleration, velocity, or displacement output of the system. These obtained FRFs can be used for various purposes, including determining the structure's dynamic properties such as natural frequencies, anti-resonance frequencies, damping ratios, and vibration mode shapes, as well as for model validation and updating. Experimentally obtaining the complete set of FRFs is a very time-consuming and arduous process. Furthermore, acquiring the entire FRF matrix may not always be possible, depending on the structure's shape and boundary conditions. In practice,

experimental modal analysis typically involves measuring only a single row or column of the FRF matrix. Since dynamic properties like natural frequency and damping, which are desired from test results, are typical characteristics of a system, a single row or column of the FRFs matrix is sufficient for their determination. To excite the system, tools such as shakers or modal hammers can be utilized. When exciting with a shaker, the shaker is typically fixed at a predetermined coordinate on the system, and the system is excited from this point. In response, the system's outputs are measured from all other coordinates using a displacement transducer, velocity transducer, or accelerometer. This method yields the column vector of the FRFs matrix. Conversely, when exciting with a modal hammer, the system's responses are measured at a single point while excitation is applied from all other coordinates using the modal hammer. This method yields the row vector of the FRFs matrix.

In this study, a Kistler modal hammer (Model: 9724A200) was used to excite the test structure during the EMA procedures. The structure's responses to these excitation forces were measured using a single-axis DYTRAN ICP type accelerometer (Model: 3097A2). This process yielded accelerance-type FRFs for the structure. For the EMA, response and excitation coordinates were first defined on the test structure. Due to the spherical shape of the structure, these response and excitation coordinates were symmetrically distributed in a circumferential arrangement as in Figure 4.



a) b)

Figure 4. Coordinate planning a) on the numerical model, b) on the test piece

As shown in Figure 4, the spherical shape was symmetrically divided into 48 segments, creating a total of 49 coordinate points. To ensure free boundary conditions, the test structure was placed on a soft sponge material. The accelerometer was attached to coordinate number 36 on the test structure using wax (Figure 5). The structure was then excited sequentially from coordinates 1 to 49, with three impacts at each point, using a modal hammer. In modal hammer

excitation, applying the excitation forces to the same point requires striking that exact location with the hammer. One of the biggest challenges in modal testing is the difficulty of hitting the exact same spot, and another is the occasional occurrence of double hits. By averaging the three impacts, attempts were made to minimize potential errors arising from these issues.

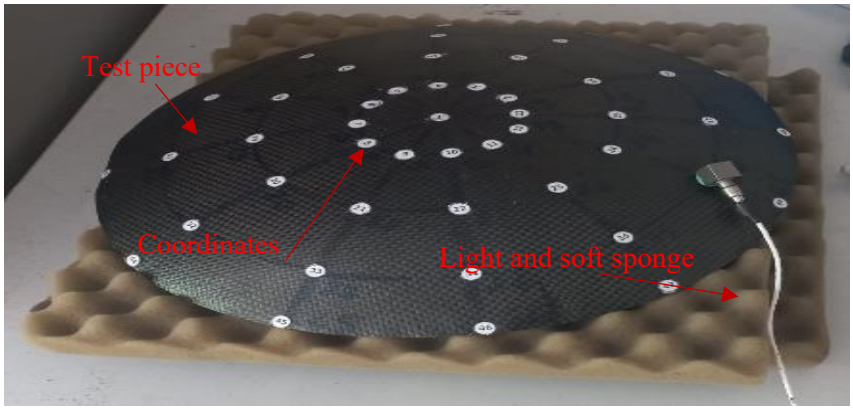


Figure 5. Test piece on the light and soft sponge

Excitation and response data were collected using an OROS vibration analyzer (Model: OR36). FFT transformations were performed, and modal analysis was conducted using NVGate and OROS Modal software. A visual representation of the EMA test setup is shown in Figure 6.

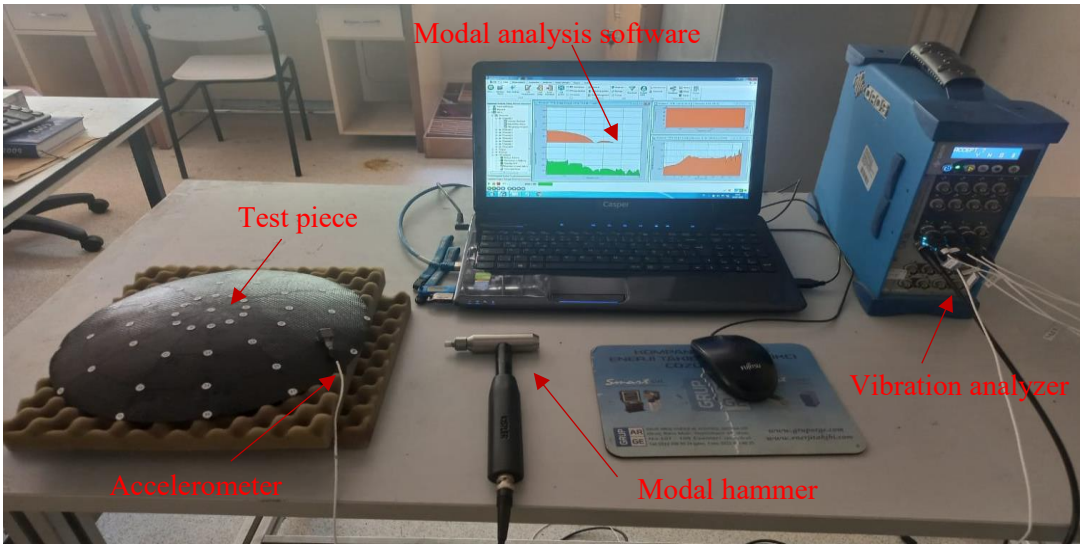
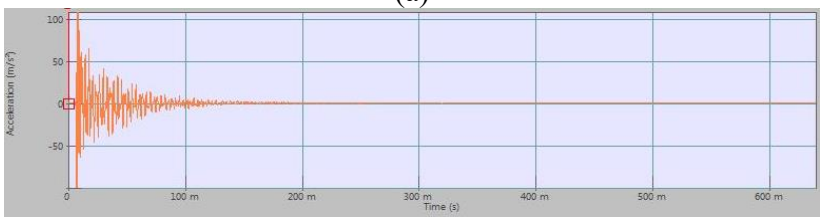


Figure 6. EMA test setup

Prior to conducting the modal test, calibration tests, reciprocity tests, and linearity tests were performed. Furthermore, it was observed that the acceleration response to the applied excitations returned to zero within the defined measurement period, thus eliminating the need for any windowing function. A sample of the time-domain test data acquired from the force and accelerometer is shown in Figure 7. The measurement parameters used in the experiments are provided in Table 1.



(a)



(b)

Figure 7. Time signal of the (a) force and (b) accelerometer

Figure 7-b illustrates that the acceleration response diminishes towards zero within the measurement period. Consequently, no windowing function was employed, thereby preventing any additional damping effects.

Table 1. Measurement parameters used for modal testing

Parameter	Value
Frequency bandwidth	0-1500 Hz
Frequency resolution	468.750 mHz
Sampling	3200
Measurement time	0.6 s
Windowing (response/impulse)	(uniform/uniform)

A total of 49 FRFs were obtained for the 49 measurement coordinates. Some of these FRFs are presented in Figure 8 and the stabilization chart of the modal indicator function is given with Figure 9.

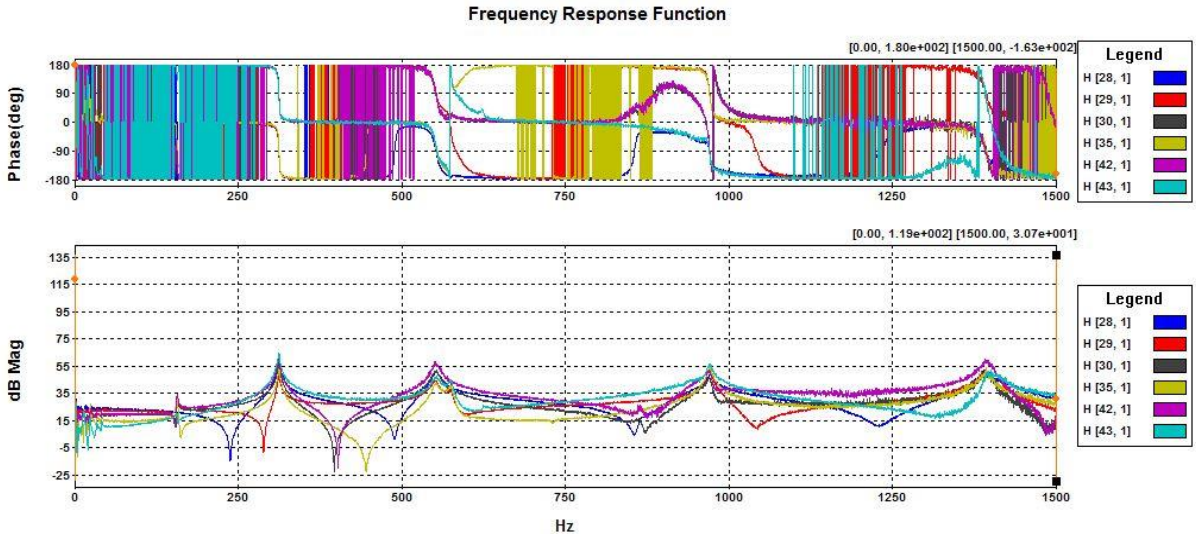


Figure 7. Some of the calculated FRFs

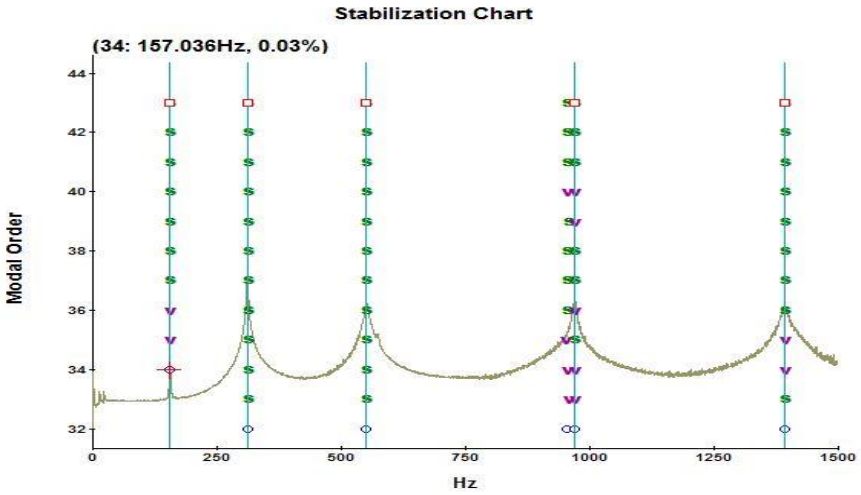
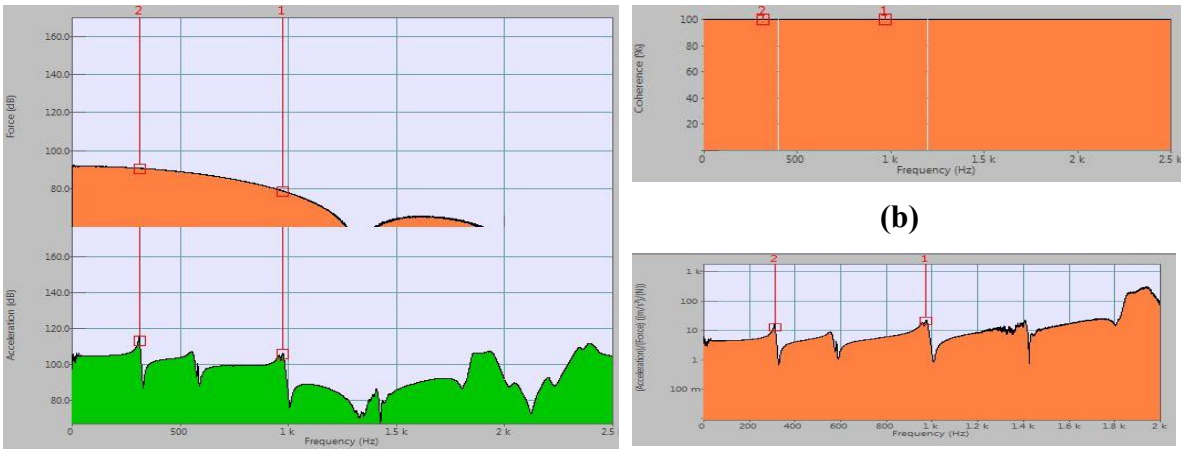


Figure 8. Stabilization chart of the modal indicator function

Figure 8 displays the amplitude-frequency and phase angle-frequency graphs of the FRFs in dB. The peaks in the amplitude graph indicate the structure's natural frequencies, or in other words, its resonance frequencies. Conversely, the troughs represent anti-resonance frequencies.

Since resonance frequencies are global properties of mechanical systems, they are visible in all FRFs unless they fall within a nodal region. However, anti-resonance frequencies are local properties of mechanical systems, meaning they may appear in some FRFs while being absent in others. This phenomenon is clearly illustrated in Figure 8. The frequency domain representations of force-acceleration responses for a single measurement, along with the coherence graph and the appearance of an FRF, are also depicted in Figure 10.



(a) **(b)** **(c)**

Figure 9. Frequency-domain (a) force-acceleration responses, (b) coherence, (c) FRF graph for a single measurement

The damping ratios (ζ) for the natural frequencies were determined and checked using the Half-power Bandwidth Method. This was achieved by analyzing the half-power points of the peaks in the frequency spectrum, as shown in Figure 11 and calculated with Equation 1 [28].

$$\zeta = \frac{\omega_2 - \omega_1}{2\omega_n} \tag{1}$$

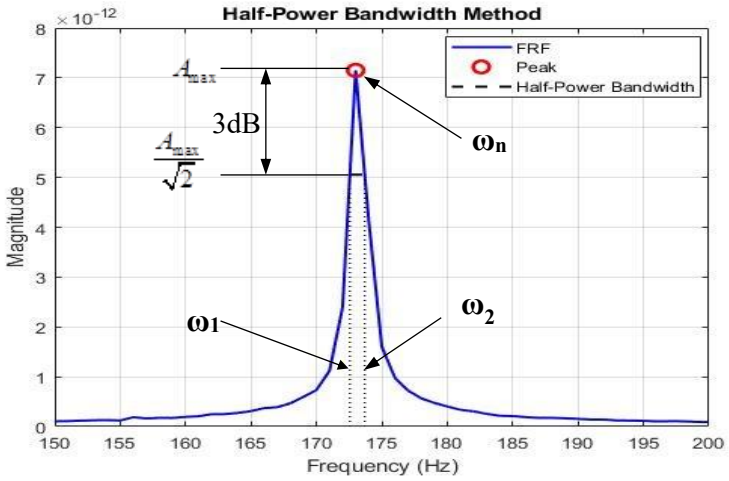


Figure 10. Half-power Bandwidth Method for finding damping ratios [29]

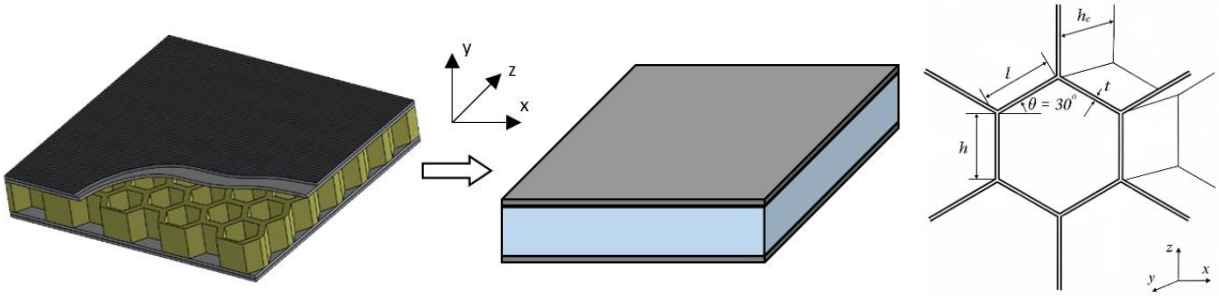
The vibration mode shapes were compared for different experiments via MAC (Modal Assurance Criterion). MAC can be calculated using Equation 2 given below.

$$\mathrm{MAC} = \frac{\left|\{\phi_A\}_i^T \{\phi_B\}_j\right|^2}{\left(\{\phi_B\}_j^T \{\phi_B\}_j\right)\left(\{\phi_A\}_i^T \{\phi_A\}_i\right)} \tag{2}$$

In Equation 2, ϕ_A and ϕ_B are the mode shape vectors to be compared. The subscripts i and j represent the relevant mode. The value approaches 1 as the two mode shape vectors become more linearly dependent and approaches 0 as they become more linearly independent.

2.3 FE Modelling Using Equivalent Approach

The development and numerical analysis of FE models for honeycomb structures and sandwich structures incorporating honeycomb cores are highly complex, time-consuming and often impractical. Therefore, several equivalent modeling approaches have been proposed to simplify this process. One such approach, the Equivalent Theory developed by Gibson [18], has proven to be highly effective for this purpose. In this equivalent approach, the orthotropic honeycomb cell structure is modeled as a uniform equivalent plate (Figure 12), which is then used in subsequent analyses.



(a) **(b)** **(c)**

Figure 11. Gibson's approach (a) real model, (b) equivalent model, (c) geometry of the cell

Investigated structure is a hemispherical dome honeycomb sandwich plate shown in Figure 3. The plate has total thickness of 3.8 mm. Composite plate consists of two carbon fiber facing sheets, material properties is given in Table 2, each of thickness 1 mm and a nomex honeycomb core of 1.8 mm thickness. The utilized honeycomb core is a regular hexagon core (l=h,θ=30°) with the geometric properties, density and material specifications listed in Table 3.

Table 2. Material properties of facing sheets

Parameter	Value
E_{xf}=E_{zf} (GPa)	65
E_{yf} (GPa)	6
G_{xy} =G_{yz} (GPa)	3
G_{xz} (GPa)	9
v_{xy} =v_{yz}	0.15
v_{xz}	0.40
ρ_f (kg/m^3)	1500

Table 3. Material and geometric properties of core honeycomb structure

Parameter	Value
E_c (GPa)	6
G_c (GPa)	3.5
l=h (mm)	1.8
h_c (mm)	1.8
t_c (mm)	0.1
θ (˚)	30
vc	0.33
ρ_c (kg/m^3)	29

Where subscript f represents carbon fiber face sheet and subscript c represents Nomex core material. E is the modulus of elasticity, ρ density, v Poisson's ratio, G shear modulus, l cell wall length, θ cell angle, t cell wall thickness and h_c is the cell height.

In the present study, the honeycomb core structure was idealized as an equivalent continuum model, and the equivalent in-plane and out-of-plane material properties were determined using the formulations given below [18, 30]. Calculated equivalent material properties of the Nomex honeycomb core are given in Table 4.

$$\rho_{eq} = \left(\frac{t}{l}\right)\frac{\left(\frac{h}{l}+2\right)}{2\cos\theta\left(\frac{h}{l}+\sin\theta\right)}\rho_c \tag{3}$$

$$E_x = \left(\frac{t}{l}\right)^3 \frac{\cos\theta}{\left(\frac{h}{l}+\sin\theta\right)\sin^2\theta}E_c \tag{4}$$

$$E_z = \left(\frac{t}{l}\right)^3 \frac{\left(\frac{h}{l}+\sin\theta\right)}{\cos^3\theta}E_c \tag{5}$$

$$\nu_{xz} = \frac{\cos^2\theta}{\left(\frac{h}{l}+\sin\theta\right)\sin\theta} \tag{6}$$

$$\nu_{yz} = \frac{\left(\frac{h}{l}+\sin\theta\right)\sin\theta}{\cos^2\theta} \tag{7}$$

$$G_{xz} = \left(\frac{t}{l}\right)^3 \frac{\left(\frac{h}{l}+\sin\theta\right)}{\left(\frac{h}{l}\right)^2\left(1+2\left(\frac{h}{l}\right)\right)\cos\theta}E_c \tag{8}$$

$$E_y = \left(\frac{t}{l}\right)\frac{\left(\frac{h}{l}+1\right)\cos\theta}{\left(\sin\theta+\frac{h}{l}\right)\cos\theta}E_c \tag{9}$$

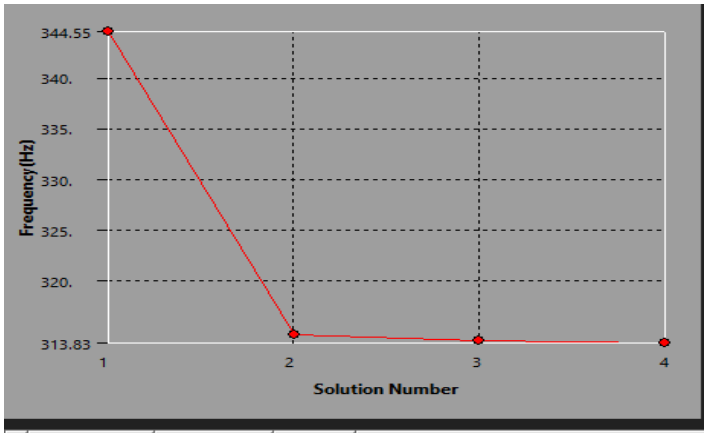
$$G_{xy} = \left(\frac{t}{l}\right)\frac{\cos\theta}{\left(\frac{h}{l}+\sin\theta\right)}G_c \tag{10}$$

$$G_{yz} = \left(\frac{t}{l}\right)\left[\frac{\left(\frac{h}{l}+\sin\theta\right)}{\left(1+\frac{h}{l}\right)\cos\theta}+0.787\frac{\left(\frac{h}{l}+\sin^2\theta\right)}{\left(\frac{h}{l}+\sin\theta\right)\cos\theta}\left(\frac{l}{h_c}\right)\right]G_c \tag{11}$$

Table 4. Equivalent material properties of the honeycomb core

Parameter	Value
E_{xc}=E_{zc} (MPa)	2.38
E_{yc} (GPa)	0.51
G_{xy} (GPa)	0.11
G_{yz} (GPa)	0.32
G_{xz} (MPa)	1.43
ν_{xy} =ν_{yz}	0
ν_{xz}	1
P_c (kg/m^3)	1.86

For the FE analysis, a spherical composite plate consisting of three layers was modeled in SolidWorks and transferred to ANSYS for modal analysis. The convergence analysis was performed with the allowable change criterion set to 0.1%. The results obtained from the iterative process are summarized in Figure 13, so the composite structure was meshed with 43023 elements and has 66502 nodes. The entire volume was modeled using solid finite elements (SOLID187). It was assumed that the layers were perfectly bonded, and the adhesive interface between them was neglected. The structure was modeled with free boundary conditions on all edges, and modal analysis was performed. The first five natural frequencies within the measurement range were obtained.



	Frequency(Hz)	Change (%)	Nodes	Elements
1	344.55		9739	5760
2	314.61	-9.0846	66502	43023
3	314.04	-0.18005	476640	328193
4	313.83	-6.6097e-002	3552334	2545374

Figure 12. Mesh convergence study for mesh selection from ANSYS

3 RESULTS AND DISCUSSION

The natural frequencies and the damping ratios of the EMA and those obtained from the ANSYS numerical modal analysis are presented in Table 5, comparatively.

Table 5. Comparison of the natural frequencies and damping ratios of the composite structure

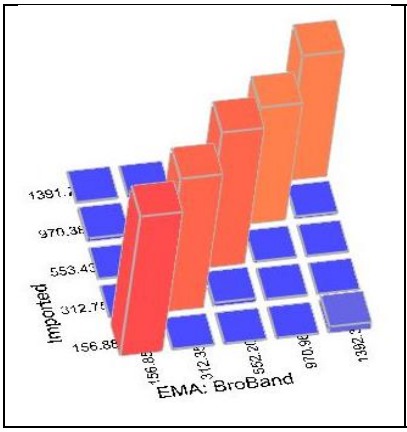
Modes	Experimental		FEM	% Difference
	Frequency (Hz)	Damping Ratio (%)	Frequency (Hz)	
1	156.8	0.24	167.7	-6.50
2	312.3	0.40	314.6	-0.73
3	552.2	0.83	559.3	-1.27
4	970.9	0.23	950.1	2.14
5	1392.3	0.33	1348.7	3.23

In Table 5, the first six natural frequencies for the free vibration of the spherical composite plate, determined both experimentally and numerically, are presented along with their percentage differences. The finite element results are based on a composite structure with mechanical and physical properties calculated using the equivalent model approach.

The experimental results for the first three natural frequencies were found to be lower than the corresponding numerical values. Conversely, this trend was reversed for the fourth and fifth natural frequencies. Based on the calculated percentage differences, the equivalent model approach provided results with a reasonable degree of accuracy. This outcome is expected for a spherical honeycomb sandwich structure, as the results can be influenced by numerous factors throughout the manufacturing and testing processes. For instance, the manual layup process inevitably leads to variations in the surface and volumetric distribution of carbon fiber fabric and epoxy. Also, geometric tolerances, transducer mass loading effects, imperfect free boundaries have great effects. Additionally, forming the Nomex honeycomb structure into a spherical shape causes unavoidable cell contractions and external edge shrinkages, all of which significantly influence the dynamic behavior of the structure and cause nonlinearity.

An analysis of the damping ratios revealed that some modes exhibited high damping, while others had relatively lower values. The third mode showed the highest damping ratio, at 0.83%.

To validate the accuracy of the experimental data, the mode shapes of the first five vibration modes were investigated. MAC values were calculated, plotted, and analyzed, as shown in Figure 14.



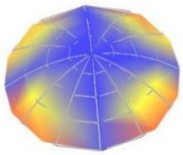
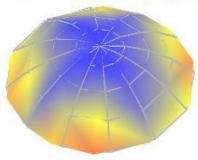
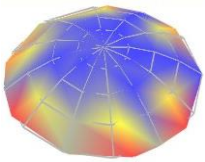
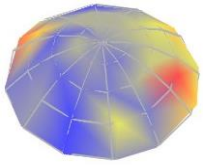
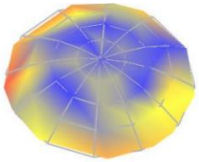
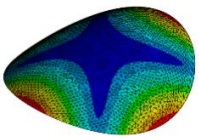
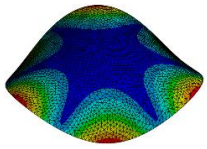
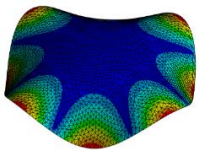
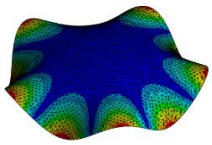
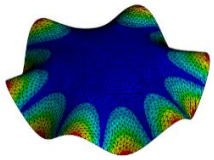
Modes		1	2	3	4	5
		156.85	312.35	552.20	970.90	1392.30
1	156.88	98.7	0.3	0.1	1.8	0.4
2	312.75	0.3	94.4	1.6	0.2	0.3
3	553.43	0.1	2.1	96.2	0.1	0.1
4	970.38	0.2	0.6	0.4	89.8	0.1
5	1391.20	4.2	0.3	0.2	1.2	88.5

Figure 13. MAC comparison for different experimental studies

In Figure 14, a graph is shown presenting the natural frequencies obtained from two different EMA applications for the first five vibration modes, along with the MAC values comparing the corresponding mode shape vectors. The high MAC values confirm that the mode shapes were captured with a high level of accuracy (all MAC values are greater than 80).

The experimental and the numerical mode shapes corresponding to the first five natural frequencies are presented in Table 6.

Table 6. Experimental and numerical mode shapes of the structure for the first 5 modes

Modes	1	2	3	4	5
Experimental					
Numerical					

An examination of the vibration mode shapes in Table 6 reveals no significant differences between the experimental and numerical results. The clarity of the experimentally obtained mode shapes, however, is negatively impacted by several factors, including the inherent difficulty of measuring a spherical shape, double-hit errors, regional fabric fiber buildups during composite production, edge stresses, Nomex core cell stresses, challenges in establishing free boundary conditions, and irregularities in epoxy resin distribution.

4 CONCLUSION AND SUGGESTIONS

This study aimed to determine the dynamic properties of a spherical sandwich structure composed of carbon fiber face sheets and a Nomex honeycomb core. The inner and outer layers each consisted of four layers of carbon fiber fabric, and the spherical sandwich structure was manufactured using the hand lay-up method. The natural frequencies, vibration mode shapes, and vibration damping ratios of this structure were obtained through EMA.

Subsequently, the equivalent mechanical and physical properties of the same structure were calculated using the equivalent model approach proposed by Gibson. Utilizing these calculated equivalent parameters, a numerical equivalent model of the structure was created in

ANSYS software, and a numerical modal analysis was performed. This yielded numerical natural frequency values and vibration mode shapes of the structure.

The analysis results obtained from EMA and the numerical equivalent model approach were compared. It can be stated that the experimental and numerical results were found to be highly consistent. Notably, the smallest difference in natural frequencies was obtained for the second mode as -0.73 percent. The largest discrepancy was observed in the first mode, at 6.5 percent. The percentage differences for all modes are smaller than 8-10% which is ideal for many applications for equivalent models. The larger difference in the natural frequency of the first mode, compared to others, is believed to be related to the material structure, including resin distribution, fabric stacking, and air voids, which are inherent to the manufacturing process of the fabricated sandwich structure and the experimental challenges i.e. double hit errors, measurement resolutions related to force sensor and accelerometer and environmental noise.

Furthermore, the vibration damping capability of the sandwich structure was observed. Some modes exhibited high damping, while others had relatively lower values. The highest and the lowest damping ratios were obtained as 0.83% for the third mode and 0.23 for the fourth mode.

Future work should focus on optimizing the manufacturing process to reduce material defects and improve the consistency of experimental results. Advanced numerical models that account for the detailed micro-structure of the composite are needed to further reduce the discrepancies between experimental and numerical data. A comprehensive parametric study is recommended to evaluate the effects of different material combinations and geometric parameters on the dynamic properties of spherical sandwich structures. Detailed investigation into the damping mechanisms is necessary to fully understand the exceptional damping capabilities of this type of structure.

Conflict of Interest Statement

There is no conflict of interest between the authors.

Statement of Research and Publication Ethics

The study is complied with research and publication ethics.

Artificial Intelligence (AI) Contribution Statement

This manuscript was entirely written, edited, analyzed, and prepared without the assistance of any artificial intelligence (AI) tools. All content, including text, data analysis, and figures, was solely generated by the authors.

Contributions of the Authors

Murat ŞEN: Performed the experiment, collected the data, methodology, analyses, writing original draft, interpretation. Osman YİĞİD: Conceptualization, formal analysis, validation, software, writing—review and editing, interpretation.

REFERENCES

[1] Pach, J., Wroblewski, R., Muszynski, B. Comparative Analysis of Sandwich Composites with Balsa, Rohacell, and Nomex Cores for Aerospace Applications, Materials, 2025, 18, 1126.

[2] Sahib, M.M., Kovács, G. Using Artificial Neural Networks to Predict the Bending Behavior of Composite Sandwich Structures, Polymers 2025, 17, 337.

[3] Çelik, M., Güden, M., Sarıkaya, M., Tasdemirci¸ A., Genç, C., Ersoy, K., Serin, O. The impact response of a Nomex® honeycomb core/E-glass/epoxy composite sandwich structure to increasing velocities: Experimental and numerical analysis, Composite Structures 320 (2023) 117205.

[4] Sadiq, S.E., Bakhy, S.H., Jweeg, M.J. Optimum Vibration Characteristics for Honey Comb Sandwich Panel Used in Aircraft Structure, Journal of Engineering Science and Technology, Vol. 16, No. 2 (2021) 1463 – 1479.

[5] Ejaz, H., Khalid, S., Saeed, M.B., Nadeem, A. Flexural and impact response of sandwich panels with Nomex honeycomb core and hybrid fiber composite skins, Journal of Sandwich Structures & Materials, 2025, Vol. 27(1) 32–50.

[6] Naufal, A.M., Prabowo, A.R., Muttaqie, T., Hidayat, A., Purwono J., Adiputra, R., Akbar, H.I., Smaradhana, D.F. Characterization of sandwich materials – Nomex-Aramid carbon fiber performances under mechanical loadings: Nonlinear FE and convergence studies, Reviews on Advanced Materials Science 2024; 63: 20230177.

[7] Chen, X., Fan, H. Flexible forming mechanism of curved sandwich shell with flexible honeycombs and twill carbon fiber fabrics, Composite Structures 354 (2025) 118779.

[8] Tran, T.T., Pham, Q.H., Nguyen-Thoi, T., Tran, T. Van (2020). Dynamic Analysis of Sandwich Auxetic Honeycomb Plates Subjected to Moving Oscillator Load on Elastic Foundation, *Advances in Materials Science and Engineering*, 2020.

[9] Bai, Z., Chen, C., Yang, X., Zhong, Y., Liu, R. (2023). Dynamic Characteristics and Effective Stiffness Properties of Sandwich Panels with Hierarchical Hexagonal Honeycomb, *Materials*, 16(17).

[10] Saraswathy, B., Mangal, L., Kumar, R.R. (2012). Analytical Approach for Modal Characteristics of Honeycomb Sandwich Beams with Multiple Debond, *Journal of Sandwich Structures and Materials*, 14(1).

[11] Van Do, V.N., Lee, C.H. (2020). Static Bending and Free Vibration Analysis of Multilayered Composite Cylindrical and Spherical Panels Reinforced with Graphene Platelets by Using Isogeometric Analysis Method, *Engineering Structures*, 215.

[12] Qu, Y., Long, X., Wu, S., Meng, G. (2013). A Unified Formulation for Vibration Analysis of Composite Laminated Shells of Revolution Including Shear Deformation and Rotary Inertia, *Composite Structures*, 98.

[13] Liu, J., Yu, B., Zhou, Y., Zhang, Y., Duan, M. (2021). The Buckling of Spherical-Cylindrical Composite Shells by External Pressure, *Composite Structures*, 265.

[14] Tang, H., Dai, H.L. (2021). Nonlinear Vibration Analysis of CFRP Spherical Shell Panel under Hygrothermal Effects, *Composite Structures*, 274.

[15] Kiani, Y. (2017). Free Vibration of FG-CNT Reinforced Composite Spherical Shell Panels Using Gram-Schmidt Shape Functions, *Composite Structures*, 159.

[16] Sayyad, A.S., Ghugal, Y.M. (2019). Static and Free Vibration Analysis of Laminated Composite and Sandwich Spherical Shells Using a Generalized Higher-Order Shell Theory, *Composite Structures*, 219.

[17] Guo, C., Liu, T., Bin, Q., Wang, Q., Wang, A. (2022). Free Vibration Analysis of Coupled Structures of Laminated Composite Conical, Cylindrical and Spherical Shells Based on the Spectral-Tchebychev Technique, *Composite Structures*, 281.

[18] Gibson, L.J., Ashby, M.F. (2014). *Cellular Solids: Structure and Properties*, 2nd ed., Cambridge University Press, Cambridge.

[19] Xia, L.-J., Jin, X.-D., Wang, Y.-B. (2001). The Equivalent Analysis of Honeycomb Sandwich Plates for Satellite Structure, *J Shanghai Jiao Tong Univ*, 37(7), ss. 999–1001.

[20] Boudjemai, A., Bouanane, M.H., Mankour, Amri, R., Salem, H., Chouchaoui, B. (2012). MDA of Hexagonal Honeycomb Plates Used for Space Applications, *International Journal of Mechanical and Mechatronics Engineering*, 6(6), ss. 1061–1069.

[21] Boudjemai, A., Amri, R., Mankour, A., Salem, H., Bouanane, M.H., Boutchicha, D. (2012). Modal Analysis and Testing of Hexagonal Honeycomb Plates Used for Satellite Structural Design, *Materials and Design*, 35.

[22] Wang, Y., Zhang, Z., Xue, X., Zhang, L. Free vibration analysis of composite sandwich panels with hierarchical honeycomb sandwich core, Thin–Walled Structures, 145 (2019) 106425.

[23] Zhang, Z., Han, B., Zhang, Q., Jin, F. Free vibration analysis of sandwich beams with honeycomb-corrugation hybrid cores, Composite Structures 171, (2017) 335–344.

[24] Zhou, Y., Liu, A., Xu, Y., Guo, Y., Yi, X., Jia, Y. Frequency-dependent orthotropic damping properties of Nomex honeycomb composites, Thin–Walled Structures 160 (2021) 107372.

[25] Al-Khazraji, M.S., Bakhy, S.H., Jweeg, M.J. Modal Analysis of Specific Composite Sandwich Structures, Engineering and Technology Journal 41(01) (2023) 13- 22.

[26] Aborehab, A., Kamel, M., Nemnem, A.F., Kassem, M. Experimental modal testing of a honeycomb sandwich plate, IOP Conf. Series: Materials Science and Engineering 973 (2020) 012034.

[27] Elangovan, H., Rajamohan, V. Dynamic characterization of tapered composite sandwich plate with honeycomb core: Numerical and experimental investigations, Thin-Walled Structures 178 (2022) 109515.

[28] Treszkai, M.F., Vehovszky, B., Feszty, D. Damping determination by the half power bandwidth method for a rectangular flat plate with bitumen damping layer application. J. Vibroeng. 2021, 23, 1267–1277.

[29] Yildiz, Y.O., Sen, M., Yigid, O., Huseyinoglu, M., Kara, S.E. Vibration Analysis of Variable-Thickness Multi-Layered Graphene Sheets, Appl. Sci. 2025, 15, 9200.

[30] Sun, W.Q., Cheng, W. (2017). Finite Element Model Updating of Honeycomb Sandwich Plates Using a Response Surface Model and Global Optimization Technique, *Structural and Multidisciplinary Optimization*, 55(1).

BİTLİS EREN ÜNİVERSİTESİ
FEN BİLİMLERİ DERGİSİ

ISSN: 2147-3129 / e-ISSN: 2147-3188

Article Type : Research Article
Received : June 18, 2025
Revised : September 11, 2025
Accepted : September 26, 2025
DOI : 10.17798/bitlisfen.1745357

Year : 2025
Volume : 14
Issue : 3
Pages : 1980-1995

INVESTIGATING EARTHQUAKE SOURCE SCALING LAWS IN THE AKHISAR SEISMIC ZONE

Alper DEMİRCİ [1]

[1] *Çanakkale Onsekiz Mart University, Geophysical Engineering Department, Çanakkale, Türkiye, alperdemirci@comu.edu.tr*

ABSTRACT

Spectral earthquake source parameters like corner frequency, fmax, stress drop and source radius are important parameters in terms of an earthquake's source properties. In this study, the source parameters of 40 local earthquakes (3.5≤M≤5.0) were calculated using Matlab-based codes. From 2011 to 2017 a database belonging to broadband earthquake stations for earthquakes occured near the location of the 12 September 2016 Akhisar (Manisa) earthquake was created from the Kandilli Observatory and Earthquake Research Institute seismic station network. Displacement and acceleration spectra including P and SH waves were analysed with a Brune ω^{-2} source model. A total of 40 earthquakes had 1097 waveforms investigated and parameters belonging to each earthquake were manually calculated. For each source parameter, mean values were calculated according to the number of seismic stations used for each earthquake. Observational spectra had damping effect removed using the Qs quality factor previously determined for the region. Seismic moment values obtained for the earthquakes varied from 0.19×10^{15} and 36.19×10^{15} Nm ($3.5 \leq Mw \leq 5$) with corner frequency values from 1.01 Hz to 5.07 Hz for P phase and 0.69 Hz to 2.63 Hz for SH phase. Additionally, calculations for SH phase in a circular fracture area varied from 0.72 km^2 to 11.12 km^2, with analyses of P phase calculated from 0.4 km^2 to 9.42 km^2. Noting the two phase calculations, the stress drop of the sources appeared to vary from 0.02 Mpa to 1.37 Mpa. In conclusion, these source parameters calculated at local scale revealed empirical relation functions with great importance to represent the region and as input for other scientific studies and were compared with results obtained from other similar studies in the literature.

Keywords: Corner frequency, Seismic Moment, Source Radius, Spectral Source Parameters, Stress Drop

1 INTRODUCTION

Earthquake source parameters and the relation functions between these parameters have great importance in revealing the kinematic and dynamic properties of the earthquake source. These parameters are commonly used in scaling relationship calculations for seismic risk analyses [1,2,3,4,5,6]. As understood from the Gutenberg-Richter scale [7], large earthquakes at global or local scale occur more rarely than moderate or low energy earthquakes. It is possible to research source functions for previously occurring large earthquakes by digitizing old analog earthquake records and analysing them. This situation brings with it many technical problems. As a result, small and moderate degree seismic events form the basis of the most important data source to identify relative uncertainties in both large and small events, to estimate the effect of large events and for seismic risk studies. As a result, increasing technological developments in recent years in seismic source theory make it possible to reveal the physical characteristics of a source reliably by calculation of parameters like seismic moment, stress drop and source radius considering the spectral characteristics of object waves for all micro and macro scale seismic events (e.g. [8]). Scientific studies on this topic by earth scientists increase every day. For example, when an earthquake occurs, a certain amount of stress energy is released and a sudden stress drop forms. The value of this stress drop ($\Delta\sigma$) is a parameter that should be calculated on a regional basis as it contains effects of the earthquake source at local scale. Thus, scaling the relationship between this and a variety of similar source parameters provides important clues to understand the source process. The relationship between corner frequency (fc) and seismic moment (M_0) especially has been researched by many researchers. Aki [9] revealed that theoretically for large earthquakes the two parameters should have $M_0 \sim fC^{-3}$ relationship. Lio [10] revealed that for relatively lower seismic moment values ($M_0 < 10^{15}$ Nm), this relationship was around $M_0 \sim fC^{-4}$ and stated that the incompatibility of scaling relationships between large and small earthquakes was due to differences in the rupture process. Apart from these parameters, scaling relationships provide important contributions to calculating low error rates for parameters like stress drop and source radius which are necessary to be able to identify the effects of possible strong ground motion in a region, in other words for modelling. According to variable tectonism and faulting character, these relationships have their own specific variable form for each region. As a result, using regional earthquake databases instead of current global correlations to reveal the regional scaling correlations and the rapid identification of these parameters and their use as an input for earthquake risk studies becomes very important. Additionally, this study is the first to examine the Akhisar Fault, not just due to using spectral

source parameters for earthquake data occurring on this fault, but because no detailed seismologic and seismotectonic study has been completed in this area.

The equations forming the basis and contributing to development of these types of studies were first determined by Brune [11]. Brune recommended a model to calculate source parameters using displacement amplitude spectra in close and distant areas as a function of the physical parameters of the source. Abercrombie and Leary [12] are researchers who provided significant contributions to the field of source parameter studies in recent times for a variety of locations on earth. Sharma and Wason [13] calculated the spectral source parameters for the Himalayas and surrounding regions.

In this study spectral analyses were completed using data from B.U. Kandilli Observatory and Earthquake Research Institute (KOERI) Regional Earthquake-Tsunami Monitoring and Evaluation Center [14] belonging to the 12.09.2016 Akhisar earthquake and events occurring before and after the earthquake around the epicenter area and obtained source parameters. These source parameters were correlated with each other in terms of representing the regional seismicity and the regional empirical relation functions were determined.

2 TECTONIC SETTINGS OF THE STUDY AREA

The study area was determined as 38.50 – 39.20 North latitude and 27.50 – 28.20 East longitude. This area is located within the Aegean Graben system (Figure 1). The Aegean Graben system represents one of the most active systems globally in terms of seismic activity showing the rapid expansion. The topic of this study, based on earthquakes occurring in the Akhisar Basin located within this active tectonism, is a 5.1 magnitude earthquake occurring on 12.09. 2016 at 11.26 at the intersection of 3 fault zones of the NNW-SSE oriented Soma-Kırkağaç Fault Zone, the 40 km long NNE-SSE right lateral strike-slip Akhisar-Sındırgı Fault Zone and the 35-40 km long NW-SE oriented Akhisar-Akselendi-Gölmarmara Fault Zone [15]. The distribution of aftershocks occurring after this earthquake continued and formed a NNW-SSE lineation. Koçyiğit et al. [16] in studies investigating the Akşehir Fault Zone stated the important fault zones in the region formed five separate regions from southeast to northwest with faults locking and making movement difficult and as a result forming a geometry that caused energy accumulation. One of these locking regions was stated to be around the Akhisar Fault Zone located west of Sındırgı. Kartal et al. [15] dealt with the tectonism in the region locally and obtained focal mechanism solutions showing left-lateral strike slip faulting and determined that the occurring earthquakes were due to rupture between two normal faults with opposite dips (Akselendi and Akhisar Faults).

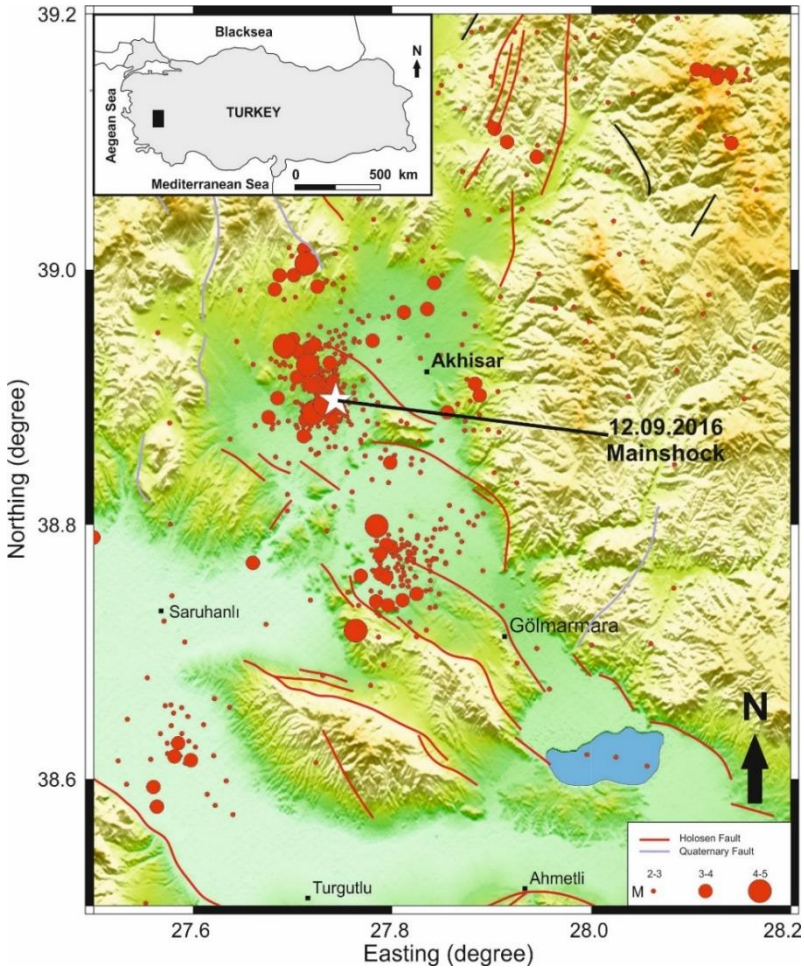


Figure 1. Active faults [17] and earthquakes occurred (M>2) in the study area between 2011 and 2017.

3 MATERIAL AND METHOD

Observational displacement spectrum (u) is stated below.

$$U(w)=S(w)*G(w)*R(w)*I(w) \quad (1)$$

In the equation S(w) is the source spectrum, G(w) includes the geometric distribution, wave propagation pattern and damping effects. R(w) comprises the local ground amplification at the measurement station while I(w) represents the instrument response spectrum of the measurement station.

In this study with the aim of obtaining the source spectrum, firstly raw data from broadband earthquake stations operated by KOERI had the instrument effect removal processes completed using the pole-zero data for the relevant station. In the next stage, a rotation process was applied to horizontal components with the aim of obtaining the SH wave phase. For the P wave phase vertical components were used. Brune's [11] source model showed clear slope variations at larger frequency than the corner frequency values. With the aim of preventing this,

changes formed at high frequency especially acceleration and displacement spectra had the 2nd degree low-pass Butterworth filter applied as recommended by Boore [18]. The theoretical acceleration and displacement source spectra as determined by Brune [11] are given in equations 2 and 3, respectively.

$$A(R,f) = \frac{C\omega^2\Omega_0}{1 + (\frac{f}{f_c})^2} \tag{2}$$

$$D(R,f) = \frac{C\Omega_0}{1+(\frac{f}{f_c})^2} \tag{3}$$

In earthquake source models in the acceleration spectrum, the increase is fixed for a certain frequency interval until the corner frequency value, with transition to decreasing trend at different frequency values defined by Hanks [19]. This frequency value is named fmax. There are different opinions about this source of this value. Hanks [19] and Anderson and Hough [20] state this value is affected by local ground conditions, while Papageorgiou and Aki [21,22] and Yokai and Irikura [23] associated the fmax value with the source effect [24].

Especially in acceleration spectra, the frequency values equivalent to sharp slope changes like fc and fmax become clearer and their distinctiveness is more obvious. As a result, on the obtained acceleration spectra, the fc value was chosen as the frequency value where the spectrum amplitude increases suddenly, while the fmax value is the frequency value where the curve begins to fall again after continuing at stable level for a while. In light of this information, the fc, fmax and Ω0 (low frequency displacement spectral level) were manually determined on the acceleration spectrum (Figure 2).

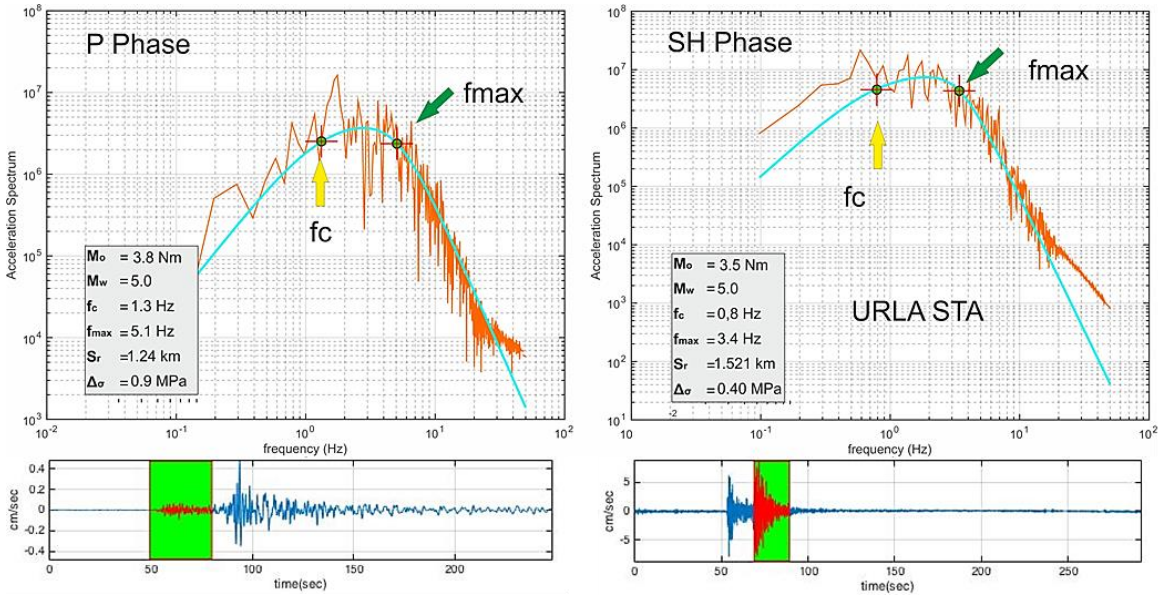


Figure 2. Two different phase spectral curves using URLA station data. Corner frequencies and calculated source parameters. (M_o will be multiplied by 10^{16})

In the next stage the previously calculated frequency-linked damping quality factor (Qsh) calculated for the region including the study area by Kurtulmuş and Akyol [25] was used with $Qsh=113.45f^{0,47}$ equation for distant stations (120-200 km) and $Qsh=60.97f^{1,42}$ equation for close stations (10-70 km). In this stage of spectral analysis, P wave phase Qp=2,25Qs assumption was applied (e.g., [26]). Using the chosen fc, fmax and Ω0 spectral parameters, the spectral curves belonging to the Brune source model calculated in equations 2 and 3 were overlaid with the observational spectra. Using the synthetic model determined with the trial and error method and representing lowest error of the observational curve, the source parameters like seismic moment, stress drop and source radius were obtained with the aid of the following equations.

$$M_0 = \frac{4\pi\rho\beta^3 R\Omega_0}{R_{\theta\varphi}S_a} \tag{4}$$

In the equation, M_0 is seismic moment, ρ is mean density value, β is mean shear wave velocity around the source, R is the distance from the hypocenter, $R_{\theta\varphi}$, is mean propagation pattern value and S_a represents the free surface ground amplification factor. After obtaining the seismic moment, the moment magnitude value (Mw) may be calculated with the aid of empirical equations developed by Hanks and Kanamori [27].

$$M_w = 0.66.log\, M_0 + 10.7 \tag{5}$$

The source radius (Sr) and stress drop (Δσ) parameters were calculated from equations 6 and 7.

$$S_r = \frac{K\beta}{2\pi f_c} \tag{6}$$

$$\Delta\sigma = \frac{7M_0}{16{s_r}^3} \tag{7}$$

The K constant used in source radius calculations was taken as 2.34 for calculations with the SH wave phase and as 1.92 for calculations with the P wave phase [28].

When the equations above are investigated, it may be said the obtained and calculated spectral source parameters have a linear and/or inverse correlation with each other. However, as the source radius and seismic moment are completely independent parameters it is important to correlate these two parameters, especially, with a range of regression analyses.

With the aim of minimizing the probable errors for 40 different earthquakes with moment magnitudes ranging between 3.5 and 5.0 occurred in the study area, the above calculations were completed using the mean results obtained for stations with high signal/noise

ratio taking note of azimuthal distribution. Due to the high data quality belonging to the main shock on 12.09.2016 and it being recorded at distant stations, this earthquake was analysed using SH phase data from 19 stations and P phase data from 21 stations. The stations used for main shock analysis and the spectral curves belonging to the SH wave phase are shown in Figure 3.

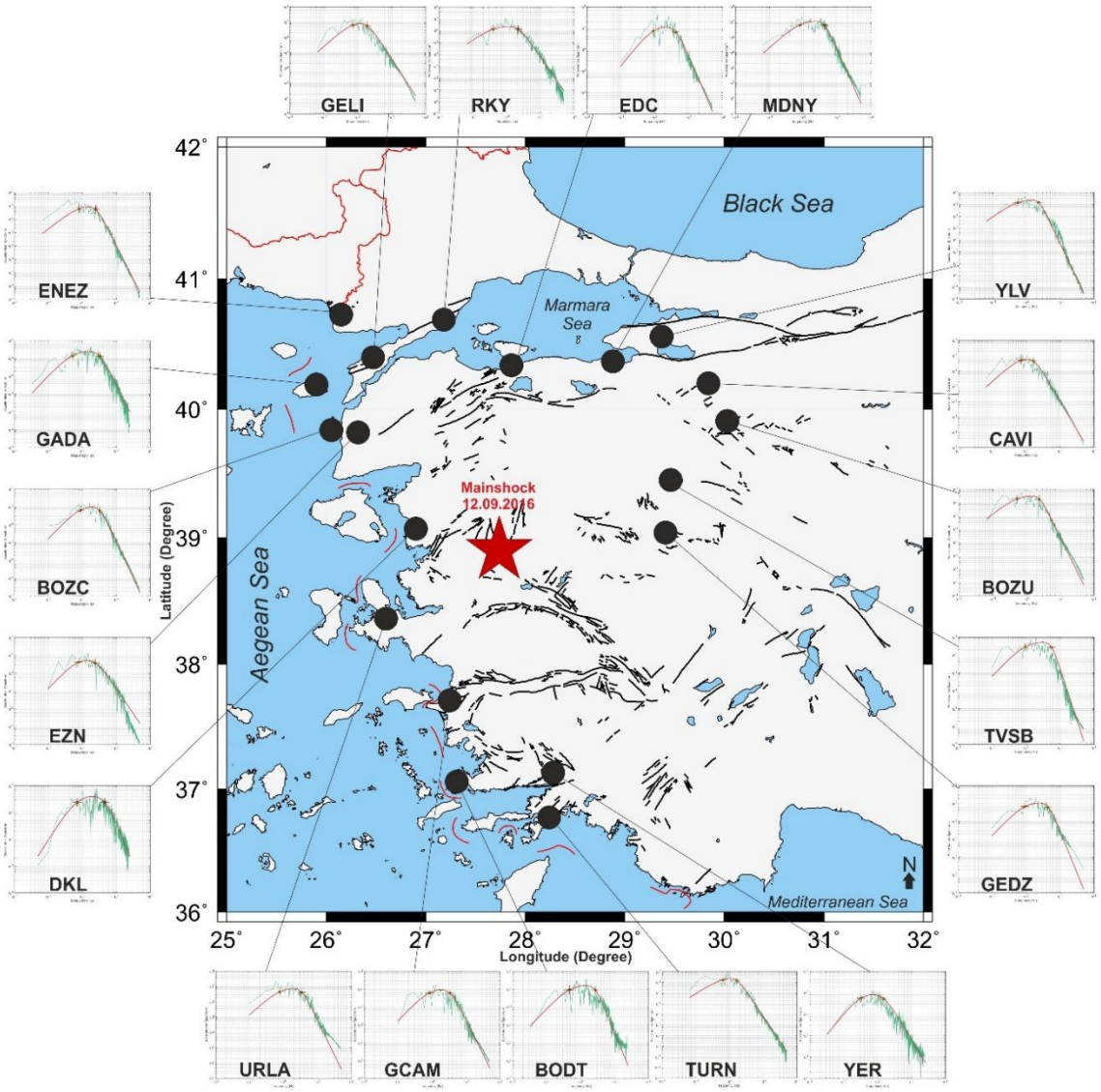


Figure 3. Stations used in spectral source analysis and observed SH wave phase spectra at these stations for 12.09.2016 earthquake

4 RESULTS AND DISCUSSIONS

The character of earthquake spectra and especially the scaling of this character with earthquake magnitude has great importance for engineering-based strong and weak motion simulation studies. With this aim in the scope of the study, the spectral source parameters belonging to 40 local earthquakes with magnitudes from 3.5 to 5.0 occurred near Akhisar (Western Anatolia) were separately calculated for the SH and P wave phases. It is an

unavoidable reality that the obtained results contain a certain amount of error due to the heterogeneity of the fault zone and the 1-D crustal model used in calculations. As a result, in the study, data from more than one station was used for each earthquake and the results obtained from the stations were taken as mean for each parameter in an attempt to reduce possible errors to a minimum. After completing the necessary corrections (damping response, instrument response, etc.), the obtained source spectrum curves were overlain with the Brune ω^{-2} source model with the aim of calculating parameters reflecting the source character (stress drop, corner frequency, seismic moment and source radius). The obtained source parameters for two different wave phases are given in Table 1 and Table 2.

Table 1. Spectral source parameters obtained using SH phase

Date	Tıme (UTM)	Lat	Long	Depth (km)	Mw	M_0 ($x10^{15}$Nm)	Fc (Hz)	Fmax (Hz)	Sd (Mpa)	Sr (m)	RA (km^2)	Nsta
06.10.2011	22:47:05	39.09	28.36	15.8	4.6	8.87	1.17	5.88	0.44	1055	3.50	5
04.08.2011	09:15:51	38.88	27.70	4.7	3.5	0.23	2.48	4.48	0.09	481	0.73	4
25.08.2011	10:45:27	38.96	27.60	8.6	3.8	0.64	1.86	5.35	0.11	649	1.32	7
08.02.2012	19:57:26	39.23	27.84	8.9	4.2	2.37	1.20	3.78	0.12	1010	3.20	8
03.08.2012	10:18:20	38.70	28.03	7.4	4.6	10.15	0.99	3.17	0.29	1240	4.83	11
04.08.2012	02:23:50	38.68	28.05	8.9	4.2	1.99	1.26	3.79	0.13	1010	3.20	6
04.08.2012	02:30:28	38.69	28.06	6.2	3.6	0.33	2.35	6.48	0.12	512	0.82	4
07.08.2012	23:17:37	38.70	28.06	9.7	4.1	1.80	1.30	3.84	0.10	918	2.65	6
07.08.2012	23:57:37	38.69	28.06	10.6	4.1	1.53	0.97	3.81	0.04	1258	4.97	9
25.08.2012	07:24:46	38.66	27.97	4.5	3.9	0.91	1.28	4.19	0.05	936	2.75	6
17.03.2013	14:03:04	39.28	27.84	8	3.9	0.69	1.37	3.93	0.05	895	2.52	7
24.05.2013	05:18:57	38.89	27.68	14	3.9	0.83	1.40	5.34	0.06	861	2.33	7
10.06.2013	16:36:03	39.01	27.86	6.8	3.5	0.24	1.72	3.93	0.03	701	1.54	5
25.06.2013	04:00:40	39.33	27.89	12.7	3.5	0.24	2.00	7.55	0.06	609	1.17	5
21.08.2013	14:54:18	38.71	27.93	9.4	3.7	0.37	1.85	6.18	0.06	648	1.32	5
12.11.2013	21:04:06	39.09	28.35	6.8	3.7	0.45	2.10	9.18	0.11	568	1.01	4
10.01.2014	21:33:13	38.81	27.81	12.4	3.7	0.36	1.69	4.36	0.05	719	1.62	7
02.06.2014	15:05:24	38.85	28.08	6.7	3.5	0.24	2.63	6.78	0.13	490	0.75	6
02.12.2015	15:52:44	39.15	28.14	14	3.8	0.51	2.14	7.19	0.17	583	1.07	9
13.12.2015	08:16:58	39.18	27.80	9.8	3.6	0.30	1.90	4.56	0.06	635	1.27	7
20.01.2016	06:07:44	39.10	27.91	7.7	3.6	0.33	1.45	5.46	0.03	860	2.32	8
03.07.2016	18:05:43	38.78	27.79	12.3	4.1	1.65	1.17	3.93	0.07	1042	3.41	7
12.09.2016	08:26:04	38.90	27.74	14	5.0	34.35	0.69	2.98	0.36	1882	11.13	19
12.09.2016	09:29:37	38.89	27.73	13.1	4.6	8.59	0.92	3.78	0.34	1338	5.62	7
15.09.2016	08:15:42	38.91	27.72	12.4	3.8	0.56	1.64	4.47	0.07	768	1.85	8
16.09.2016	07:23:23	38.88	27.68	6.1	3.6	0.27	1.61	3.70	0.03	762	1.82	6
17.09.2016	12:53:33	38.90	27.73	10.8	3.8	0.70	1.55	3.93	0.09	805	2.04	5
18.09.2016	22:48:24	38.90	27.68	8.4	3.7	0.39	1.72	4.85	0.06	717	1.62	6
19.09.2016	06:25:50	38.89	27.73	12.6	3.5	0.19	1.63	5.33	0.03	755	1.79	5
21.09.2016	14:56:51	38.91	27.72	7.7	3.7	0.38	1.46	4.65	0.04	865	2.35	8
22.09.2016	21:30:05	39.00	27.69	7.7	3.8	0.58	1.41	4.08	0.05	864	2.35	7
25.09.2016	20:51:20	38.90	27.73	12.7	4.0	1.01	1.37	4.36	0.08	898	2.53	6
09.10.2016	06:21:00	39.00	27.71	11.7	4.0	1.19	1.21	4.20	0.06	1002	3.15	9
15.10.2016	02:49:15	38.93	27.72	11.3	4.3	2.94	1.29	3.92	0.20	965	2.93	8
15.10.2016	02:51:03	38.94	27.69	6.3	4.4	4.27	1.13	3.53	0.17	1079	3.66	8
15.10.2016	03:02:28	38.92	27.70	8.3	3.7	0.43	1.52	4.69	0.04	793	1.98	5
15.10.2016	04:52:09	38.95	27.70	6.5	3.7	0.42	1.19	4.84	0.02	1038	3.38	6
15.10.2016	05:03:24	38.93	27.71	7.1	3.6	0.37	1.41	5.94	0.03	921	2.66	8
15.10.2016	22:23:23	38.94	27.70	8.2	3.7	0.46	1.22	4.69	0.02	995	3.11	8
15.10.2016	22:35:29	38.94	27.69	7.6	3.8	0.50	1.32	5.13	0.04	1001	3.15	7

Table 2. Spectral source parameters obtained using P phase

Date	Tıme (UTM)	Lat	Long	Depth (km)	Mw	M_0 ($x10^{15}$Nm)	Fc (Hz)	Fmax (Hz)	Sd (Mpa)	Sr (m)	RA (km^2)	Nsta
06.10.2011	22:47:05	39.09	28.36	15.8	4.6	9.60	2.04	6.46	1.37	1005	3.17	7
04.08.2011	09:15:51	38.88	27.70	4.7	3.8	0.83	2.94	5.30	0.15	726	1.66	3
25.08.2011	10:45:27	38.96	27.60	8.6	3.8	0.52	2.41	6.78	0.10	698	1.53	8
08.02.2012	19:57:26	39.23	27.84	8.9	4.2	2.15	2.57	5.48	0.42	671	1.41	6
03.08.2012	10:18:20	38.70	28.03	7.4	4.6	10.54	1.70	5.02	0.70	942	2.79	8
04.08.2012	02:23:50	38.68	28.05	8.9	4.2	2.12	2.04	5.86	0.96	974	2.98	8
04.08.2012	02:30:28	38.69	28.06	6.2	3.7	0.41	3.53	10.53	0.20	489	0.75	4
07.08.2012	23:17:37	38.70	28.06	9.7	3.9	0.94	1.82	4.07	0.09	1066	3.57	5
07.08.2012	23:57:37	38.69	28.06	10.6	4.1	1.79	3.10	6.73	1.09	614	1.18	6
25.08.2012	07:24:46	38.66	27.97	4.5	3.9	0.81	3.33	6.76	0.48	582	1.06	5
17.03.2013	14:03:04	39.28	27.84	8	3.8	0.59	2.29	8.24	0.12	765	1.84	7
24.05.2013	05:18:57	38.89	27.68	14	3.9	0.94	1.62	5.46	0.05	985	3.05	6
10.06.2013	16:36:03	39.01	27.86	6.8	3.5	0.35	2.90	6.36	0.09	603	1.14	6
25.06.2013	04:00:40	39.33	27.89	12.7	3.7	0.37	3.25	8.22	0.12	539	0.91	6
21.08.2013	14:54:18	38.71	27.93	9.4	3.7	0.41	4.05	6.82	0.35	434	0.59	6
12.11.2013	21:04:06	39.09	28.35	6.8	3.8	0.48	5.07	9.47	0.79	359	0.40	4
10.01.2014	21:33:13	38.81	27.81	12.4	3.7	0.44	2.72	5.22	0.09	627	1.24	7
02.06.2014	15:05:24	38.85	28.08	6.7	3.5	0.21	4.82	8.35	0.24	370	0.43	4
02.12.2015	15:52:44	39.15	28.14	14	3.8	0.63	3.10	6.38	0.22	551	0.95	7
13.12.2015	08:16:58	39.18	27.80	9.8	3.6	0.32	4.70	9.46	0.48	405	0.52	5
20.01.2016	06:07:44	39.10	27.91	7.7	3.6	0.31	3.76	8.88	0.17	459	0.66	4
03.07.2016	18:05:43	38.78	27.79	12.3	4.1	1.60	2.29	6.28	0.27	776	1.89	7
12.09.2016	08:26:04	38.90	27.74	14	5.0	36.19	1.01	4.58	0.45	1732	9.42	21
12.09.2016	09:29:37	38.89	27.73	13.1	4.6	8.25	1.11	4.51	0.27	1648	8.53	9
15.09.2016	08:15:42	38.91	27.72	12.4	3.8	0.65	2.82	5.44	0.15	587	1.08	7
16.09.2016	07:23:23	38.88	27.68	6.1	3.6	0.27	2.86	6.25	0.07	582	1.06	5
17.09.2016	12:53:33	38.90	27.73	10.8	3.9	0.85	2.19	4.93	0.10	765	1.84	4
18.09.2016	22:48:24	38.90	27.68	8.4	3.7	0.43	3.14	5.72	0.13	527	0.87	5
19.09.2016	06:25:50	38.89	27.73	12.6	3.6	0.28	3.61	7.63	0.13	472	0.70	5
21.09.2016	14:56:51	38.91	27.72	7.7	3.7	0.43	2.90	6.91	0.12	584	1.07	6
22.09.2016	21:30:05	39.00	27.69	7.7	3.9	0.81	2.35	5.28	0.11	716	1.61	7
25.09.2016	20:51:20	38.90	27.73	12.7	4.0	1.23	2.38	6.79	0.18	710	1.58	6
09.10.2016	06:21:00	39.00	27.71	11.7	4.1	1.55	1.84	6.63	0.11	960	2.90	9
15.10.2016	02:49:15	38.93	27.72	11.3	4.3	3.09	2.09	5.80	0.32	825	2.14	6
15.10.2016	02:51:03	38.94	27.69	6.3	4.5	6.65	1.67	5.05	0.35	1108	3.86	7
15.10.2016	03:02:28	38.92	27.70	8.3	3.8	0.63	2.86	6.67	0.16	588	1.09	7
15.10.2016	04:52:09	38.95	27.70	6.5	3.7	0.44	2.65	6.71	0.09	649	1.32	6
15.10.2016	05:03:24	38.93	27.71	7.1	3.7	0.51	3.02	7.67	0.14	552	0.96	8
15.10.2016	22:23:23	38.94	27.70	8.2	3.9	0.81	2.71	6.81	0.17	618	1.20	7
15.10.2016	22:35:29	38.94	27.69	7.6	3.8	0.61	2.45	7.04	0.11	690	1.50	6

Accordingly, for the earthquakes included in the study;

- Seismic moment values; for SH phase are between 0.23 - 34.35 ($x10^{15}$ Nm)
  for P phase are between 0.21 - 36.19 ($x10^{15}$ Nm)
- Corner frequency values; for SH phase are between 0.69 - 2.63 Hz
  for P phase are between 1.01-5.07 Hz
- Stress drop values; for SH phase are between 0.03 - 0.44 Mpa
  for P phase are between 0.09-1.37 Mpa
- Source radius values; for SH phase are between 481 - 1882 m
  for P phase are between 370 -1732 m

In light of the obtained results, all results obtained from two different phases were compared and the relations between these parameters were revealed using exponential and logarithmic regression analyses. The controversial parameter of fmax value was associated with seismic moment together with corner frequency value and it was observed that both frequency values displayed variation with close slope values (Figure 4). In terms of enlightening the debate, it may be said the fmax parameter includes similar source effects to the fc parameter.

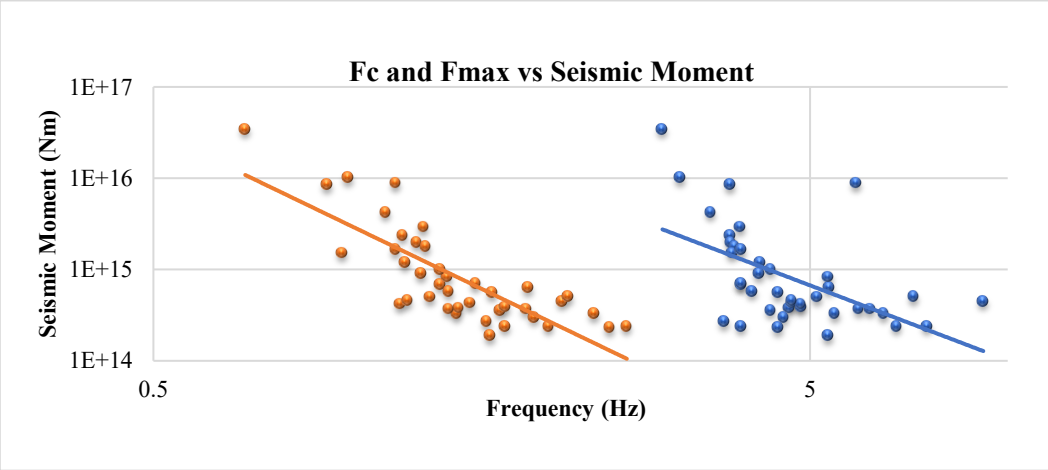


Figure 4. Variation in seismic moment of corner frequency and Fmax parameters

Firstly, the corner frequency (f_c) parameter has been dealt with by many researchers in different regions. Gusev et al. [29] stated the ratio obtained for corner frequency calculated from the P phase and S phase Fc (P) / Fc (S) should be about 1.4 for earthquakes in the shallow crust. This ratio was calculated as 1.5 by Lin et al. [30] and as 1.52 by Convertito et al. [31], while Ambeh and Fairhead [32] emphasized that this ratio may vary according to the geometry of the source model used. They observed this Fc(P) / Fc (S) ratio varied over a broad interval like 1.4±0.7 for different models, and stated this ratio approached 1 in linear source models especially (Haskell, etc.). Ambeh and Fairhead [32] revealed that in circular models this ratio should be close to the ratios of P and S wave velocities used in the crustal model. The corner frequency ratio obtained as a result of this study was calculated as 1.7 in accordance with the crustal model used [33] (Table 3).

Table 3. Crustal velocity model used in the study [33]

Depth (Km)	Vp (km/s)	Vs (km/s)	Vp / Vs
0.0	4.50	2.60	1.73
5.40	5.91	3.10	1.90
31.6	7.80	4.50	1.73
89.2	8.30	4.80	1.73

Additionally, corner frequency is associated with seismic moment in many studies (Table 4). Especially for the related function containing a range of information in terms of determining the type of source, Aki [9] revealed that theoretically these two parameters should have $M_0 \sim fC^{-3}$ correlation for large earthquakes. Lio [10] revealed that at relatively lower seismic moment values ($M_0 < 10^{15}$ Nm) this relationship is around $M_0 \sim fC^{-4}$ and stated the incompliance in scaling relationships between large and small earthquakes is due to differences in the rupture processes. In this study the correlation between the seismic moment and corner frequency was calculated as $Mo.fc^{3.46} = 3.10^{15}$ N-m/sec for the SH phase and as $Mo.fc^{2.7} = 10^{16}$ N-m/sec for the P phase.

Table 4. Related functions for different regions in the literature (seismic moment- corner frequency)

Ref.	Studied Region	Scaling Function
Watanabe et al. [34]	Kanto Basin (Japan)	$Mo.fc^3 = (2.5\text{-}3.0).10^{16}$ N-m/sec
Dutta et al [35]	South-Central Alaska	$Mo.fc^3 = 2.09.10^{16}$ N-m/sec
Kumar et al. [36]	Himalayan Region (India)	$Mo.fc^3 = 1.7.10^{16}$ N-m/sec
Kumar [37]	Garhwal Himalaya (India)	$Mo.fc^3 = 3.10^{16}$ N-m/sec
Borkar et al. [38]	Kumaun Himalaya (India)	$Mo.fc^{2.7} = 5.10^{16}$ N-m/sec
Yoo et al. [39]	Korean Peninsula	$Mo.fc^{3.54} = 10^{16}$ N-m/sec
Present Study	Akhisar Region (Western Türkiye)	$Mo.fc^{3.46} = 3.10^{15}$ N-m/sec (SH Phase)
Present Study	Akhisar Region (Western Türkiye)	$Mo.fc^{2.7} = 10^{16}$ N-m/sec (P Phase)

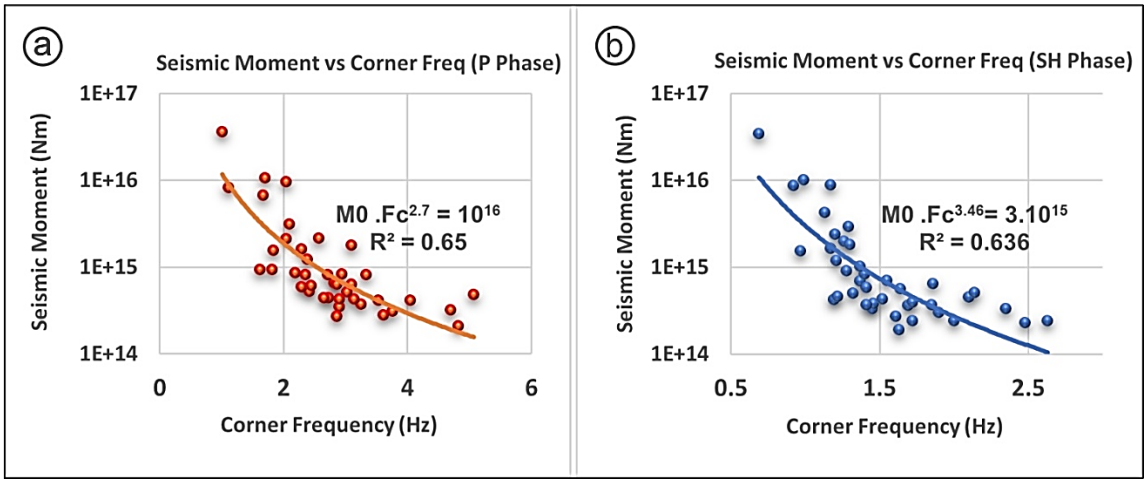


Figure 5. Graphs of relationship between seismic moment and corner frequencies a) P phase, b) SH phase

Similarly, another relation function mentioned in many studies is between the seismic moment and source radius parameters (Table 5). As seen in Figure 6, the relation function between these two parameters was calculated as $Log(M_0)= 3.36.log(r) + 5.06$ with regression coefficient of 0.63. The similarity with crustal model and with the scaling function ($Log(M_0)=3.38.log (r) + 4.79$) obtained for northwest Greece by Stavroulopoulou et al. [40] noted in Table 5 for areas close to the study area is one of the clear indicators that these types of functions represent regional character.

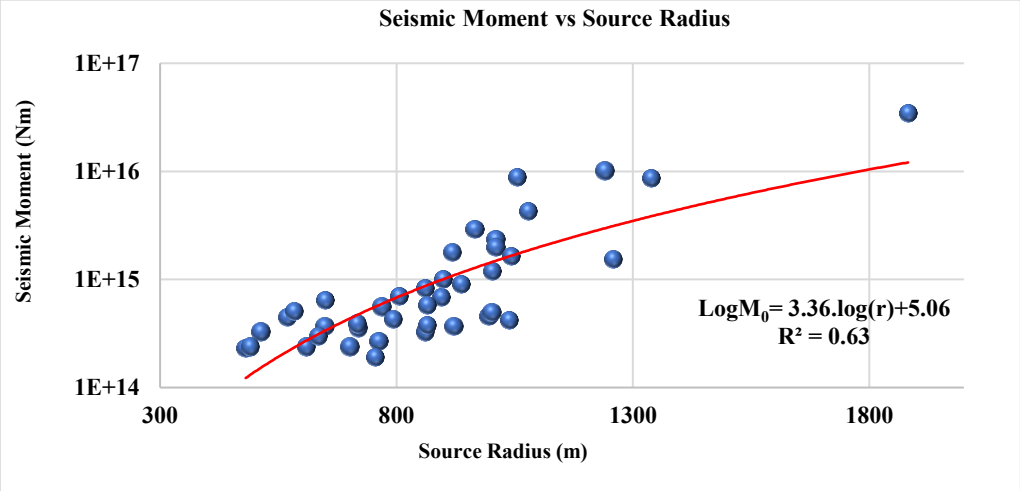


Figure 6. Graph of correlation between seismic moment and source radius

Table 5. Related functions for different regions in the literature (seismic moment and source radius)

Ref.	Studied Region	Scaling Function
Dobrynina [41]	Baikal Rift (Northern Eurasia)	$Log(M_0)\pm0.90= 8.85.log(r) + 15.16$
Sule and Weber [42]	Central Pannonian basin (Hungary)	$Log(M_0)= 4.76.log (r) + 1.62\pm2.05$
Sanoujam [43]	Manipur (India)	$Log(M_0)= 1.56.r + 13.68$
Popescu et al. [44]	Vrancea (Romania)	$Log(M_0) = 2.87\pm0.03.log(r) + 7.41\pm0.3$
Stavroulopoulou et al [40]	Epirus (Northwestern Greece)	$Log(M_0)= 3.38.log (r) + 4.79$
Mohamed [45]	Kalabsha (Egypt)	$Log(M_0) = 0.7\pm0.04.log(r) + 11.06\pm0.5$
Present Study	Akhisar Region (Western Türkiye)	$Log(M_0)= 3.36.log(r)+5.06$

It is noteworthy that the relation function between the stress drop and seismic moment ($Log (M_o)= 1.16.log (\Delta\sigma) + 16.22$) is more similar to the results obtained by Stavroulopoulou et al. [40] ($Log (M_0)= 1.11.log (\Delta\sigma) + 11.7$) compared to other studies (Table 6). As shown on Figure 6 and 7, as in studies comparing variations in stress drop and source radius linked to seismic moment, this only includes results from the SH phase.

Table 6. Related functions for different regions in the literature (seismic moment and stress drop)

Ref.	Studied Region	Scaling Function
Dobrynina [41]	Baikal Rift (Northern Eurasia)	$Log(M_0)\pm0.30= 1.26.log(\Delta\sigma) + 15.3$
Garcia-Garcia et al. [46]	Southern Spain	$Log(M_0)=1.1\pm0.17.log(\Delta\sigma)+19.47\pm0.09$
Radulian and Popa [47]	Vrancea (Romania)	$Log(M_0)= 3.7. log(\Delta\sigma) + 20.48$
Stavroulopoulou et al [40]	Epirus (Northwestern Greece)	$Log(M_0)= 1.11.log (\Delta\sigma) + 11.7$
Mohammed [45]	Kalabsha (Egypt)	$Log(M_0) = 0.44\pm0.19.log(\Delta\sigma) + 12.23\pm0.5$
Present Study	Akhisar Region (Western Türkiye)	$Log(M_0)= 1.16.log(\Delta\sigma) + 16.22$

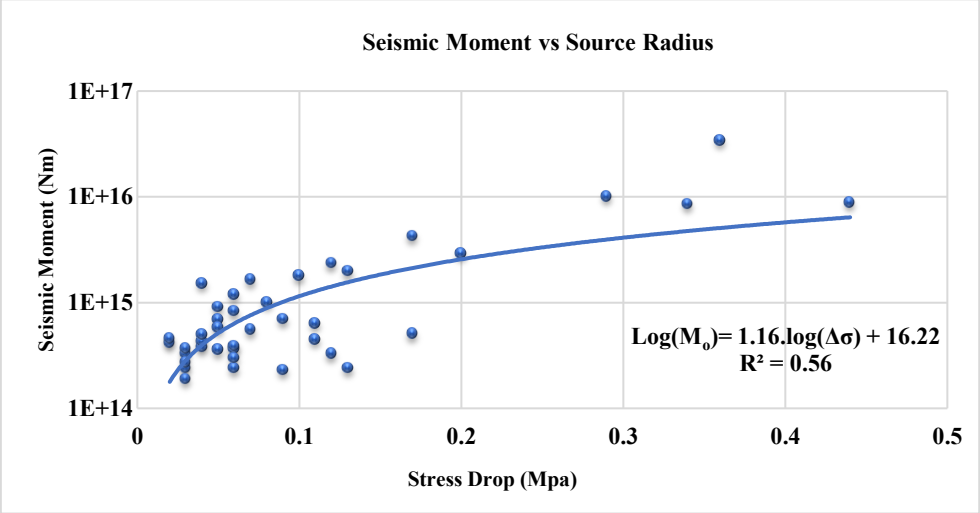


Figure 7. Graph of correlation between seismic moment and stress drop

5 CONCLUSIONS

The relation functions obtained in this study using small and moderate magnitude earthquake data from the region are an important reference in terms of being able to calculate the effects of possible large earthquakes in the region and close surroundings. The absence of prior comprehensive studies in this region highlights the significance of the derived scaling relationships, which may serve as essential input parameters for earthquake simulations, stress modeling, and other seismological applications in adjacent areas. Furthermore, this research closes a major gap by investigating the first detailed seismic source analysis for the Akhisar Basin. The resulting regional empirical relationship functions are vital inputs for assessing seismic hazards, ground motion simulations, and modeling future earthquake scenarios in Western Anatolia. Subsequent studies might expand the approach to include higher-magnitude events, fault-specific segmentation, and wider spatial data to test the scaling laws' generalizability. The established methodology is also applicable to similar intraplate regions lacking robust source characterization.

Acknowledgments

Analyses are performed by using modified form of Matlab –based EQK-SRC-PARA codes [24] and some figures were created with the Generic Mapping Tools of Wessel and Smith [48].

Statement of Research and Publication Ethics

The study is complied with research and publication ethics.

Artificial Intelligence (AI) Contribution Statement

This manuscript was entirely written, edited, analyzed, and prepared without the assistance of any artificial intelligence (AI) tools. All content, including text, data analysis, and figures, was solely generated by the author.

REFERENCES

[1] T. C. Hanks and M. Wyss, "Use of body-wave spectra in determination of seismic-source parameters," *Bull. Seismol. Soc. Amer.*, vol. 62, no. 2, pp. 561–589, Apr. 1972.

[2] T. C. Hanks and W. Thatcher, "Graphical representation of seismic source parameters," *J. Geophys. Res.*, vol. 77, no. 23, pp. 4393–4405, Dec. 1972.

[3] R. E. Abercrombie, "Earthquake source scaling relationships from 1 to 5 ML using seismograms recorded at 2.5 km depth," *J. Geophys. Res. Solid Earth*, vol. 100, no. B12, pp. 24015–24036, Dec. 1995.

[4] N. Akyol and Ö. Karagöz, "Empirical attenuation relationships for Western Anatolia, Turkey," *Turkish Journal of Earth Sciences*, vol. 18, no. 3, pp. 351–382, 2009.

[5] Demirci, T. Bekler, İ. B. Karaşin, and E. Işık, "Karlıova (Bingöl) üçlü birleşim noktasında spektral kaynak parametreleri," in *Proc. 1st Int. Multidisciplinary Studies Congr.*, Dec. 28–29, 2018.

[6] E. Gök, "Source parameters and scaling relations of local earthquakes from a strong motion network in Izmir, Western Turkey," *Pure Appl. Geophys.*, vol. 176, no. 8, pp. 3391–3409, 2019.

[7] B. Gutenberg and C. F. Richter, "Frequency of earthquakes in California," *Bull. Seismol. Soc. Amer.*, vol. 34, no. 4, pp. 185–188, Oct. 1944.

[8] H. Kanamori, "Importance of historical seismograms for geophysical research," in *Historical Seismograms and Earthquakes of the World*, W. H. K. Lee, H. Meyers, and K. Shimazaki, Eds. San Diego, CA, USA: Academic Press, 1988.

[9] K. Aki, "Scaling law of seismic spectrum," *J. Geophys. Res.*, vol. 72, no. 4, pp. 1217–1231, Feb. 1967.

[10] Y. Iio, "Scaling relation between earthquake size and duration of faulting for shallow earthquakes in seismic moment between 10^{10} and 10^{25} dyne/cm," *J. Phys. Earth*, vol. 34, pp. 127–169, 1986.

[11] J. N. Brune, "Tectonic stress and the spectra of seismic shear waves from earthquakes," *J. Geophys. Res.*, vol. 75, no. 26, pp. 4997–5009, Sep. 1970.

[12] R. E. Abercrombie and P. Leary, "Source parameters of small earthquakes recorded at 2.5 km depth, Cajon Pass, southern California: Implications for earthquake scaling," *Geophys. Res. Lett.*, vol. 20, no. 14, pp. 1511–1514, Jul. 1993.

[13] M. L. Sharma and H. R. Wason, "Occurrence of low stress drop earthquakes in the Garhwal Himalayan region," *Phys. Earth Planet. Interiors*, vol. 85, no. 3–4, pp. 265–272, 1994.

[14] KOERI Earthquake Catalog, Boğaziçi Univ., Kandilli Observatory and Earthquake Research Institute, National Earthquake Monitoring Center. [Online]. Available: http://www.koeri.boun.edu.tr/sismo/2/data-request/

[15] R. F. Kartal, R. Demirtaş, F. T. Kadirioğlu, and S. Zünbül, "12 Eylül 2016 Akhisar-Manisa depremleri (Mw=4.6, Mw=4.5)," in *Proc. 20th Active Tectonic Research Group Workshop*, Denizli, Türkiye, Oct. 13–15, 2016, p. 10. (in Turkish)

[16] Koçyiğit, E. Bozkurt, N. Kaymakcı, and F. Şaroğlu, "3 Şubat 2002 Afyon Çay depreminin kaynağı ve ağır hasarının nedenleri: Akşehir Fay Zonu," *Jeolojik Ön Rapor*, Ortadoğu Teknik Üniversitesi, Ankara, Türkiye, 2002, 19 pp. (in Turkish)

[17] Ö. Emre, T. Y. Duman, S. Özalp, H. Elmacı, Ş. Olgun, and F. Şaroğlu, *Açıklamalı Türkiye Diri Fay Haritası*. Ankara, Türkiye: Maden Tetkik ve Arama Genel Müdürlüğü, 2013.

[18] D. M. Boore, "Stochastic simulation of high-frequency ground motions based on seismological models of the radiated spectra," *Bull. Seismol. Soc. Amer.*, vol. 73, no. 6, pp. 1865–1894, Dec. 1983.

[19] T. C. Hanks, "fmax," *Bull. Seismol. Soc. Amer.*, vol. 72, no. 6, pp. 1869–1879, Dec. 1982.

[20] J. G. Anderson and S. E. Hough, "A model for the shape of the Fourier amplitude spectrum of acceleration at high frequencies," *Bull. Seismol. Soc. Amer.*, vol. 74, no. 5, pp. 1969–1993, Oct. 1984.

[21] S. Papageorgiou and K. Aki, "A specific barrier model for the quantitative description of inhomogeneous faulting and the prediction of strong ground motion – Part I: Description of the model," *Bull. Seismol. Soc. Amer.*, vol. 73, no. 3, pp. 693–722, Jun. 1983.

[22] S. Papageorgiou and K. Aki, "A specific barrier model for the quantitative description of inhomogeneous faulting and the prediction of strong ground motion – Part II: Applications of the model," *Bull. Seismol. Soc. Amer.*, vol. 73, no. 4, pp. 953–978, Aug. 1983.

[23] T. Yokai and K. Irikura, "Meaning of source-controlled fmax in empirical Green's function technique based on a T^2-scaling law," *Annu. Disas. Prev. Res. Inst., Kyoto Univ.*, vol. 34, no. B-1, 1991.

[24] Kumar, A. Kumar, H. Mittal, A. Kumar, and R. Bhardwaj, "Software to estimate earthquake spectral and source parameters," *Int. J. Geosci.*, vol. 3, pp. 1142–1149, 2012.

[25] T. Ö. Kurtulmuş and N. Akyol, "Crustal attenuation characteristics in western Türkiye," *Geophys. J. Int.*, vol. 195, no. 2, pp. 1384–1394, 2013.

[26] D. Gajewski, R. Stangl, K. Fuchs, and K. Sandmeier, "A new constraint on the composition of the topmost continental mantle: Anomalously different depth increases of P and S velocity," *Geophys. J. Int.*, vol. 103, pp. 497–507, 1990.

[27] T. C. Hanks and H. Kanamori, "A moment magnitude scale," *J. Geophys. Res.*, vol. 84, no. B5, pp. 2348–2350, May 1979.

[28] K. Sivaram, D. Kumar, and S. S. Teotia, "Source parameters and scaling relations for small earthquakes in Kumaon Himalaya, India," *J. Seismol.*, vol. 17, no. 3, pp. 579–592, 2013.

[29] Gusev, M. Radulian, M. Rizescu, and G. F. Panza, "Source scaling of intermediate-depth Vrancea earthquakes," *Geophys. J. Int.*, vol. 151, no. 3, pp. 879–889, 2002.

[30] Lin, T. Satsukawa, M. Wang, A. Z. Mohammadi, R. Fueta, and F. Nakajima, "Coseismic rupturing stopped by Aso volcano during the 2016 Mw 7.1 Kumamoto earthquakes," *Science*, vol. 354, no. 6314, pp. 869–875, Nov. 2016.

[31] V. Convertito, A. Zollo, N. Sharma, A. Orefice, and A. Emolo, "Earthquake source parameters and scaling relationships at The Geysers geothermal field, California," in *Proc. AGIS Workshop Induced Seismicity*, Davos, Switzerland, Mar. 10–30, 2015.

[32] W. B. Ambeh and J. D. Fairhead, "Spectral characteristics and source parameters of micro earthquakes from the Mt Cameroon volcanic region, West Africa," *Geophys. J. Int.*, vol. 106, no. 2, pp. 229–237, 1991.

[33] D. Kalafat, C. Gürbüz, and S. B. Üçer, "Batı Türkiye'de kabuk ve üst manto yapısının araştırılması," *Deprem Araştırma Bülteni*, vol. 59, pp. 43–64, 1987. (in Turkish)

[34] K. Watanabe, H. Sato, S. Kinoshita, and M. Ohtake, "Source characteristics of small to moderate earthquakes in the Kanto region, Japan: Application of a new definition of the S-wave time window length," *Bull. Seismol. Soc. Amer.*, vol. 86, no. 5, pp. 1284–1291, Oct. 1996.

[35] U. Dutta, N. Biswas, A. Martirosyan, A. Papageorgiou, and S. Kinoshita, "Estimation of earthquake source parameters and site response in Anchorage, Alaska, from the strong motion network data using generalized inversion method," *Phys. Earth Planet. Interiors*, vol. 137, pp. 13–29, 2003.

[36] D. Kumar, V. Sriram, I. Sarkar, and S. S. Teotia, "An estimate of a scaling law of seismic spectrum for earthquakes in Himalaya," *Indian Minerals*, vol. 61, no. 3–4, pp. 83–92, 2008.

[37] Kumar, "Study of earthquake source parameters using micro-earthquakes and strong motion data," Ph.D. dissertation, Indian Inst. Technol., Roorkee, India, 2011.

[38] Y. Borkar, A. Kumar, and S. C. Gupta, "Source parameters and scaling relation for local earthquakes in the Garhwal and Kumaun Himalaya, India," *Int. J. Adv. Seismol.*, vol. 1, no. 1, pp. 1–15, 2013.

[39] S. H. Yoo, J. R. Rhie, H. Choi, and K. Mayeda, "Coda-derived source parameters of earthquakes and their scaling relationships in the Korean Peninsula," *Bull. Seismol. Soc. Amer.*, vol. 101, no. 5, pp. 2388–2398, Oct. 2011.

[40] O. Stavroulopoulou, E. Sokos, and G. A. Tselentis, "S-wave spectral analysis and estimation of spectral parameters in Northwestern Greece," *Bull. Geol. Soc. Greece*, vol. 50, pp. 1232–1240, 2016.

[41] A. Dobrynina, "Source parameters of the earthquakes of the Baikal rift system," *Izv., Phys. Solid Earth*, vol. 45, no. 12, pp. 1093–1109, 2009.

[42] Süle and Z. Wéber, "Earthquake source parameters and scaling relationships in Hungary (central Pannonian basin)," *J. Seismol.*, vol. 17, no. 2, pp. 507–521, 2013.

[43] M. Sanoujam, "Seismotectonic studies in Manipur," Ph.D. dissertation, Manipur Univ., Manipur, India, 2002.

[44] E. Popescu, A. O. Placinta, F. Borleasnu, and M. Radulian, "Repeated earthquakes in the Vrancea subcrustal source and source scaling," *IOP Conf. Ser.: Earth Environ. Sci.*, vol. 95, p. 032005, 2017.

[45] H. H. Mohamed, "Determination of basic physical source parameters and scaling relations for Kalabsha earthquakes, Aswan, Egypt," *Acta Geodyn. Geomater.*, vol. 1, no. 2, pp. 201–212, 2004.

[46] J. M. García-García, M. D. Romacho, and A. Jiménez, "The corner frequencies, stress drops and apparent stresses of microearthquakes in the Betic region (Southern Spain)," *Física de la Tierra*, vol. 14, pp. 161–182, 2002.

[47] M. Radulian and M. Popa, "Scaling of source parameters for Vrancea (Romania) intermediate depth earthquakes," *Tectonophysics*, vol. 261, pp. 67–81, 1996.

[48] P. Wessel and W. H. F. Smith, "New version of generic mapping tools released," *EOS Trans. Amer. Geophys. Union*, vol. 76, p. 329, 1995.

BİTLİS EREN ÜNİVERSİTESİ
FEN BİLİMLERİ DERGİSİ

ISSN: 2147-3129 / e-ISSN: 2147-3188

Article Type	: Research Article	**Year**	: 2025
Received	: August 23, 2025	**Volume**	: 14
Revised	: September 21, 2025	**Issue**	: 3
Accepted	: September 24, 2025	**Pages**	: 1996-2007
DOI	: 10.17798/bitlisfen.1771205		

DESIGN AND IMPLEMENTATION OF LOGIC AND GATES IN INTERNET OF THINGS (IOT) BASED SYSTEMS

Emine Canan GÜNAY DEMİREL [1]

[1] *Çanakkale Onsekiz Mart University, Electric and Energy Department, Çanakkale, Türkiye,*
ecanan@comu.edu.tr

ABSTRACT

In this study, a web-based "AND gate experiment platform" was designed using the ESP8266-based nodemcu, a popular component of the Internet of Things (IOT) and a key component of automation systems over the Internet and networks in recent years. The two-input AND gate is selected as one of the fundamental gates in digital electronics. This web-based platform, which provides interactive simulations and visual demonstrations of the AND gate's operation in classroom or laboratory environments, particularly in physics, electrical and electronics, and computer science departments, allows multiple users to connect to the nodemcu and practice simultaneously. Since the nodemcu is used in this study, the software connects the nodemcu to the local network via a modem and receives a fixed IP address. This allows each user connected to the IP address to individually simulate the operation of the AND gate through their web browser. Furthermore, by adjusting the modem settings, each user accessing the IP address over the internet can individually simulate the operation of the AND gate in their own web browser. The input and output values on the platform will be those of the last user performing the operation. This makes the platform also suitable for distance learning.

Keywords: AND gate, nodemcu, 74574, ESP8266, IOT, Shift register.

1 INTRODUCTION

Today, it is crucial to test the theoretical knowledge taught in electronics-related vocational education experimentally in a classroom or laboratory environment [1-3]. Because concepts such as electronics, computers, and the internet are intertwined in many professional fields, experimental applications of these concepts have also been conducted in the education

of related fields [4],[5]. Naturally, owing to the wide student population, the understanding levels of different educational fields will vary for various reasons. Therefore, the subject should be approached in its simplest form and the most effective and cost-effective techniques used today [6].

Logic gates are the fundamental elements of digital systems with one or more inputs and a single output. Without this, data transmission, processing and storage are difficult. The operating principles of logic gates are implemented in various devices, even though they may not be aware of them owing to technological advancements. These electronic circuits, which have input, output, processing, and recording capabilities compatible with binary number systems, are used in almost every field of daily life, especially in industry, military, space technologies, communications and similar fields. Examples of these circuits include computers, clocks, televisions, telephones, medical devices, and all types of electronic automation and control circuits, particularly those using microprocessors and microcontrollers [7].

There are seven basic logic gates, NAND and NOR gates are known as universal gates. These logic gates are AND, OR, XOR, NOT, XNOR, NOR and NAND gates. Logic gates have inputs in a binary format, and all have at least to inputs, except for the NOT gate. Only the NOT gate had one input and one output. Similarly, the outputs of all logic gates are in a binary format and have a single output. The truth tables provide all possible input and output values according to the characteristics of the relevant gate. In the table, "0" indicates a low logic level and "1" indicates a high logic level [8-12].

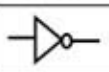
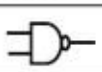
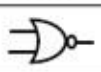
Gate Name		NOT		AND	OR	NAND	NOR	XOR	XNOR
Gate Symbol									
Inputs		Boolean Expression Outputs							
A	B	$\overline{A}$	$\overline{B}$	A·B	A+B	$\overline{A \cdot B}$	$\overline{A + B}$	A⊕B	$\overline{A \oplus B}$
0	0	1	1	0	0	1	1	0	1
0	1	1	0	0	1	1	0	1	0
1	0	0	1	0	1	1	0	1	0
1	1	0	0	1	1	0	0	0	1

Figure 1. Logic Gates, Their Symbols and Truth Demonstrations.

Figure 1 summarizes logic gates, their symbols, and truth demonstrations [13].

Ease of internet access and advancements in hardware and software technologies have enabled the development and proliferation of web-based applications. The advantages of web-based applications include remote access, free use via a web server without time or location

restrictions, multiple simultaneous connections, ability to handle many desired operations with software and the lack of additional hardware requirements for applications to run. Therefore, they can be used as alternatives for educational applications [14].

A microcontroller can be defined as a programmable computer that contains a central processing unit (CPU), random access memory (RAM), a specific type of memory (ROM/PROM/EPROM/EEPROM), and input/output (I/O) ports on a single integrated circuit. The impact of microcontrollers on our lives is significant and cannot be ignored. Unlike general-purpose computers, microcontrollers are specialized in performing specific tasks and are designed to run only a single application [15]. Therefore, they can emulate (or act like) various logic devices depending on the program loaded, paving the way for new designs [16]. There are many types of microcontrollers. The ESP8266 microcontroller stands out with its Wi-Fi feature and can be used as a web server. Data can be transferred to the internet via a web page using the ESP8266 module, and data from the internet can be received from the ESP8266 module. This allows all real-time information to be shared online in the applications where the module is used. This also means that the input and output pins can be controlled over the web [17].

In this study, the Nodemcu V3 ESP12-e development board, based on the ESP8266 microcontroller, was used to develop the AND gate Experiment Set. Owing to its structural features, it can connect to the internet, operate as a web server by obtaining an IP address on the network, and its inputs and outputs can be easily controlled using software. It is a low-cost, easy-to-access development board. Despite its versatility, the number of physical inputs and outputs that can be used was limited. Various techniques are used to increase the number of input and output ports on microcontrollers. One of these is the use of shift registers to increase input/output capacity [18]. Therefore, the 74574 integrated circuit, serial input and parallel output registers can be used to display the input and output values of the AND gate.

Because the main stages in the development of microcontroller systems are the hardware and software stages, the materials and methods used are reviewed under two main headings in the remainder of this article. First, the circuit was constructed using nodemcu and other electronic components. Then, the software and its operation, including a flow diagram, will be discussed, and the construction of the "Logic Gate Experiment Set" circuit will be explained. The constructed circuit was then run, and the results were examined.

Recognizing that the primary stages in the development of microcontroller systems involve both hardware and software components, the subsequent sections of this article will explore the materials and methods employed within these two main categories. Initially, the circuit will be assembled using nodemcu in conjunction with other electronic components.

Following this, the software and its functionality, including a flow diagram, will be analyzed, and the construction of the "Logic Gate Experiment Set" circuit will be elucidated. After assembly, the circuit was operated, and the results were thoroughly examined.

2 MATERIAL AND METHODS

2.1 Logic AND Gate Experiment Set Hardware

Logic gates are used according to the design for operating digital electronic circuits. These gates are usually encased in plastic or epoxy sheaths and manufactured as integrated circuits. The truth table of an example 7408 integrated circuit containing four two-input and gates is shown in Figure 1. A and B represent the inputs, and C represents the output. Pin 14, designated as VCC, represents the supply voltage (5V), and pin 7, designated as GND, represents ground (chassis). Logic circuits are operated using a binary number system. A logic "0" indicates no input current or voltage, while a logic "1" indicates that it is present. In these 78 series integrated circuits, a logic "0" represents 0 volts and a logic "1" represents 5 volts. In other words, if an LED diode is connected to the output through a resistor, the LED diode is off at logic "0" and on logic "1." Examining the truth table, the output is definitely "0" when any input is 0, and the output is "1" when all inputs are 1. And this rule is the same no matter how many entrances there are [1].

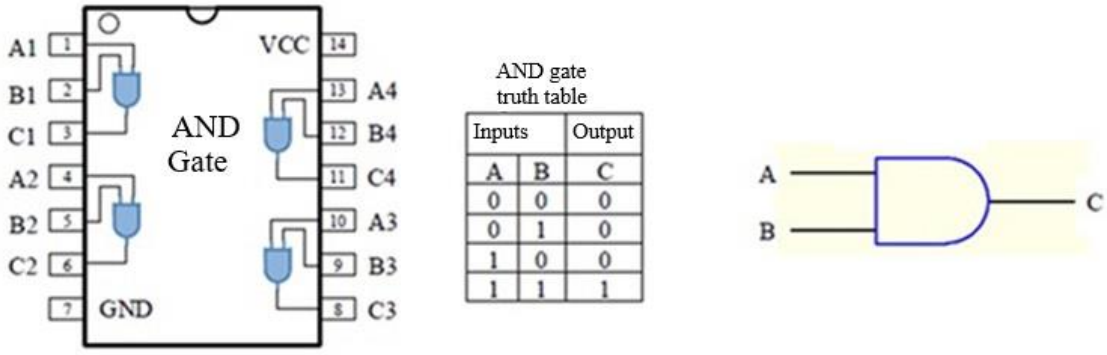


Figure 2. AND Gate Schematic Representation, Truth Table and Symbol [1].

In the circuit, a nodemcu microcontroller was used to simulate the operation of the AND gate, whereas a 74HC574 integrated circuit, resistors and LED diodes were used to create the shift register. A laptop connected to a local network was used to monitor the system's operation. Alternatively, a device with a web browser, such as a tablet, phone or computer could be used.

Figure 3 shows the circuit diagram drawn using Proteus. While 11 pins of the nodemcu can be used as input/output, only six of them can be used safely owing to special circumstances. Using others requires a more complex circuit structure and software. Therefore, if we want to use a nodemcu directly as a gate, we can have at most two 2-input and 1-output gates. To achieve this, we used a 74574 integrated circuit containing eight D-type flip-flops and two shift registers. Considering the physical usability of the circuit and the experimental set with eight gates in the design, the number of inputs was determined to be 8 x 2 = 16, and the number of outputs was determined to be 8 x 1 = 8. In this case, two 74HC574 ICs were used as inputs and one 74574 IC was used for outputs, creating an 8-bit shift register. Both registers are designed as serial and inputs. Pin D1 of the nodemcu was used as the data input of the 16-bit shift register representing the inputs, and pin D2 was used as the clock pin to shift the input data. Similarly, pin D5 of the nodemcu was used as the data input of the 8-bit shift register representing the outputs, and pin D6 was used as the clock pin to shift the output data. Thus, the input data are loaded into the registers with a 16-bit clock pulse, and output data are loaded into the registers with an 8-bit clock pulse. The input and output values were displayed using LEDs connected to the outputs of each register. In the experimental set, the AND gate symbols were drawn, and LEDs representing the input and output values were connected to the inputs of the symbols to show the outputs based on the input values. When the AND gate is checked against the truth table, the results are obtained as if the gate is present even though the elements constituting the gate are physically absent. Figure 4 shows that the appearances in the software and experimental set are identical. Although the LED diodes at the output of the AND gates in the experimental set appear to be reverse-connected visually, because the AND gates are hypothetical, the diode terminals are hidden below the symbols and are not visible. As in the circuit diagram, the (-) terminals of all diodes are connected to the chassis.

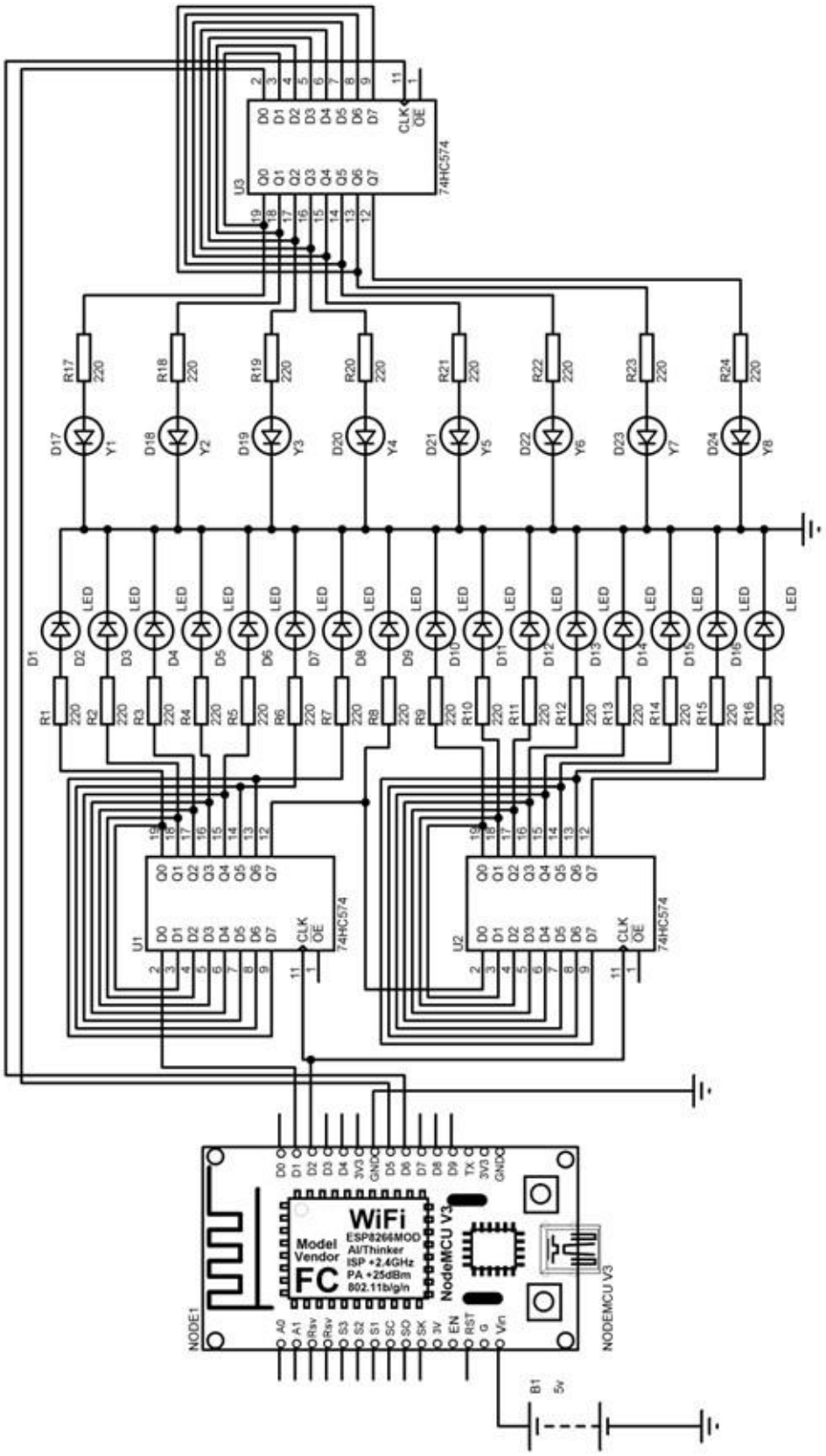


Figure 3. AND Gate Experiment Set circuit diagram.

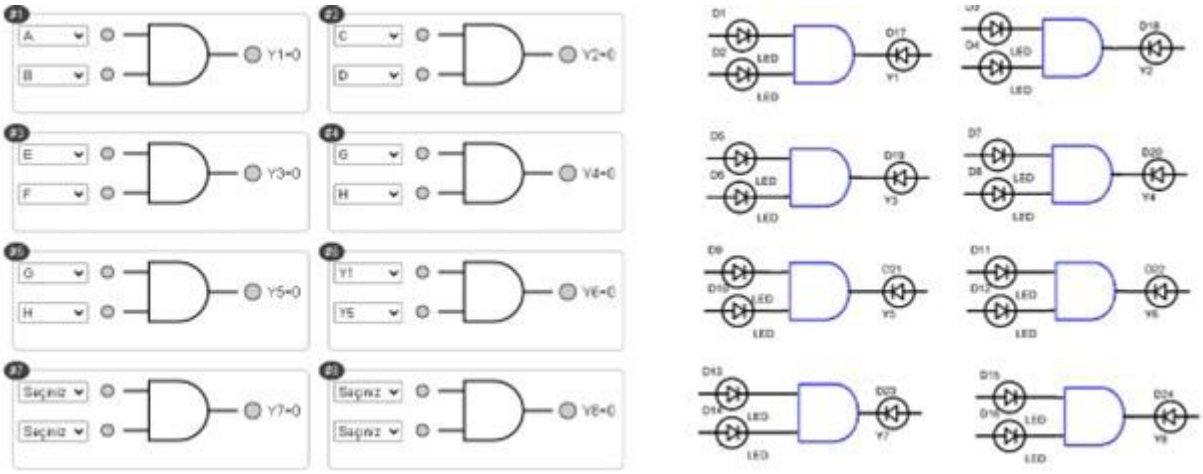


Figure 4. The view in the software and the view on the experimental set.

Although the implemented circuit has 8 gates, it can simulate gates represented by 100s using the same logic. After designing and drawing the circuit using Proteus, it was installed on two breadboards. Nodemcu was installed on the first breadboard, and a 16-bit register representing the inputs and an 8-bit register representing the outputs, made with 74HC574, was installed on the second breadboard to create the circuit.

2.2 Logic AND Gate Experiment Set Software

The software is an integral part of the microcontroller. Regardless of the hardware circuit design, coding in the appropriate language and loading it onto the microcontroller are essential for the microcontroller to perform the desired operations. Because nodemcu is an ESP8266-based microcontroller, the primary programming language was Lua. However, the Arduino programming language was used because it has a broader scope and supports nodemcu programming with customizations. Arduino is a user-friendly, open-source electronic prototyping platform. Offering microcontroller-based hardware and easy-to-program software, Arduino is used in a wide range of applications, from education to industrial applications [19].

The Arduino compiler was downloaded from the relevant website and installed on a Windows computer. The libraries necessary for nodemcu's operation were installed and configured. Nodemcu was connected to the computer via a micro USB cable, and the compiled version of the program was ready to be loaded. After all the settings were completed, the program was written and loaded onto the microcontroller. Figure 5 shows a flowchart of the written program.

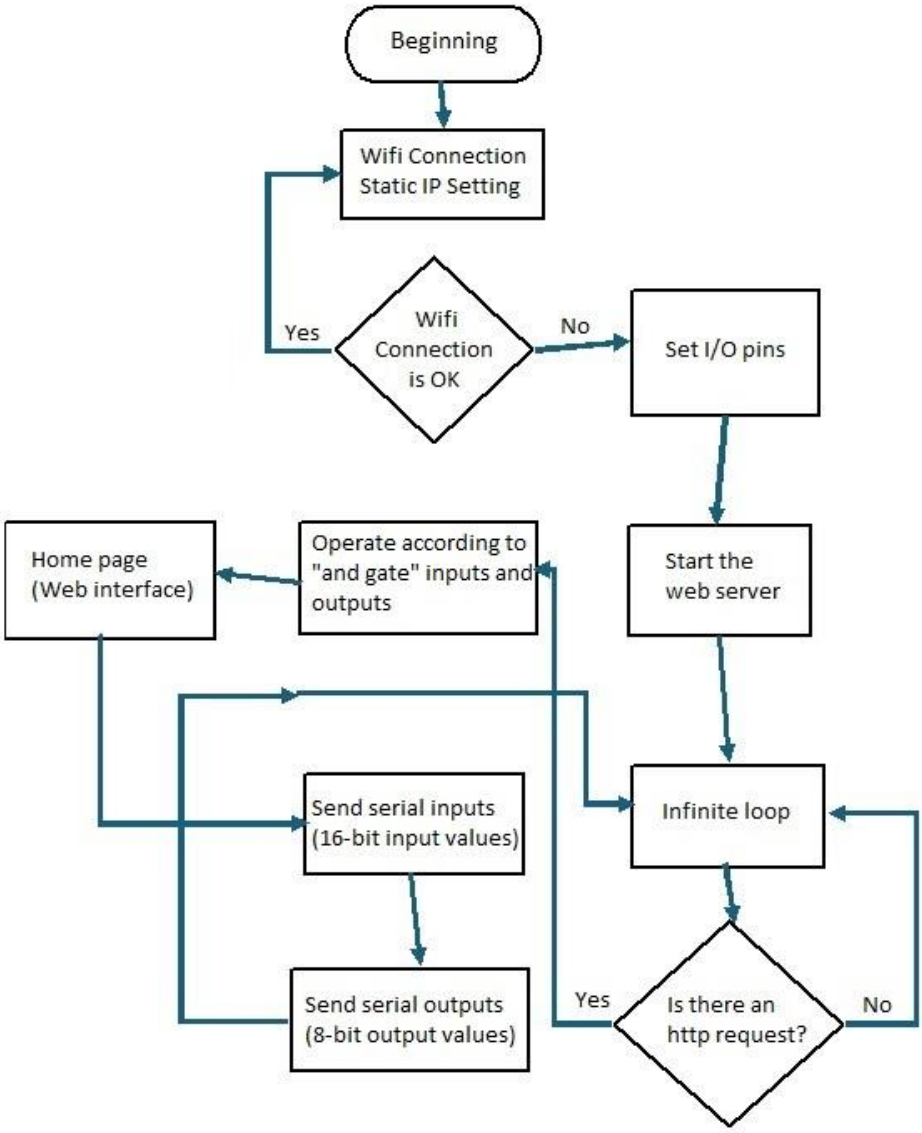


Figure 5. Flow chart of the program loaded into the microcontroller.

3 RESULTS AND DISCUSSION

"Select" and the LEDs at the input and output of all ports in the test set are off. The desired input variable was selected from the relevant DropDown box. If desired, the input variables displayed in the list and selected can be increased or decreased from the menu on the left side. The output variables were fixed, as shown on the screen. The output variables are optional in the DropDown box. By clicking on the input variables, a value of 0 can be changed to 1, and a value of 1 to 0. The Y output variables take values based on the output of the AND gate and cannot be changed otherwise. When the inputs of the gate symbols on the screen are selected and the input values are selected, the LED at the symbol's input turns gray if 0 and red if 1. When the AND gate operates according to the truth table, the output turns gray if 0 and red

if 1. Each time an operation is performed on the browser screen, a request is sent simultaneously to the web page (Figure 6). To display the gate input and output values on the test set, nodemcu sends the 16-bit input values first, followed by the 8-bit output values.

Thus, the AND gate operations observed on the screen were also visible on the test set. All users connected to the network could connect to the test set and conduct individual experiments on the browser. The final user's values were displayed on the test set.

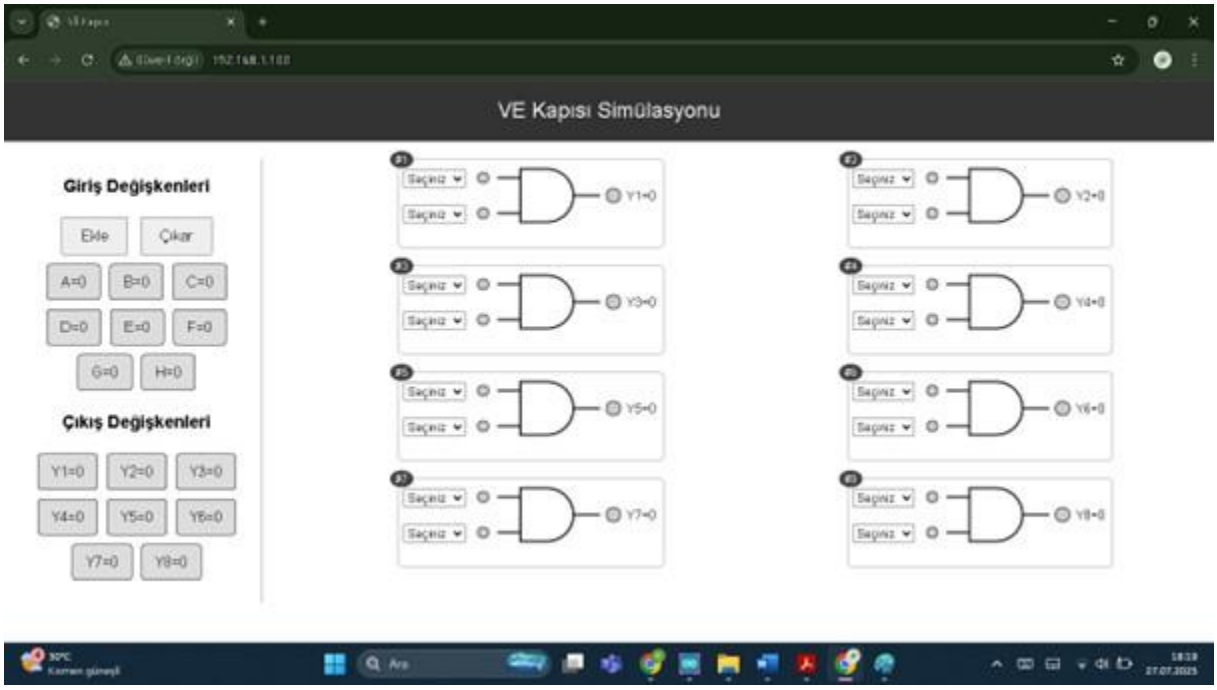


Figure 6. Web page screenshot.

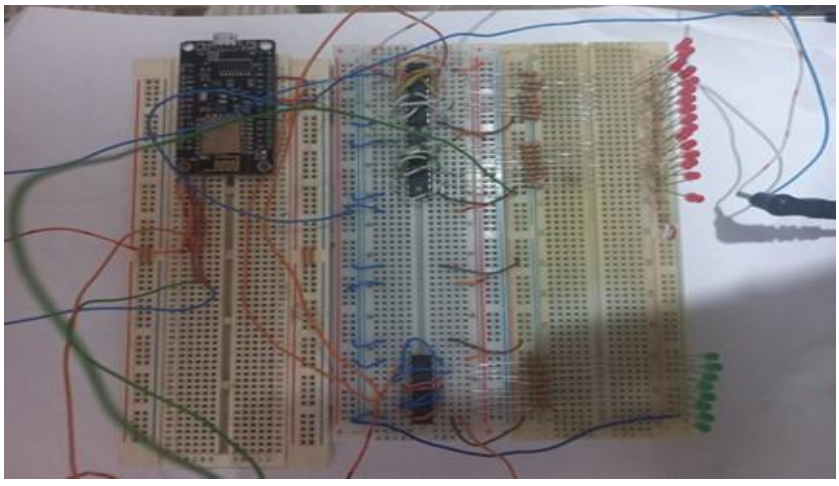


Figure 7. Circuit built on breadboard.

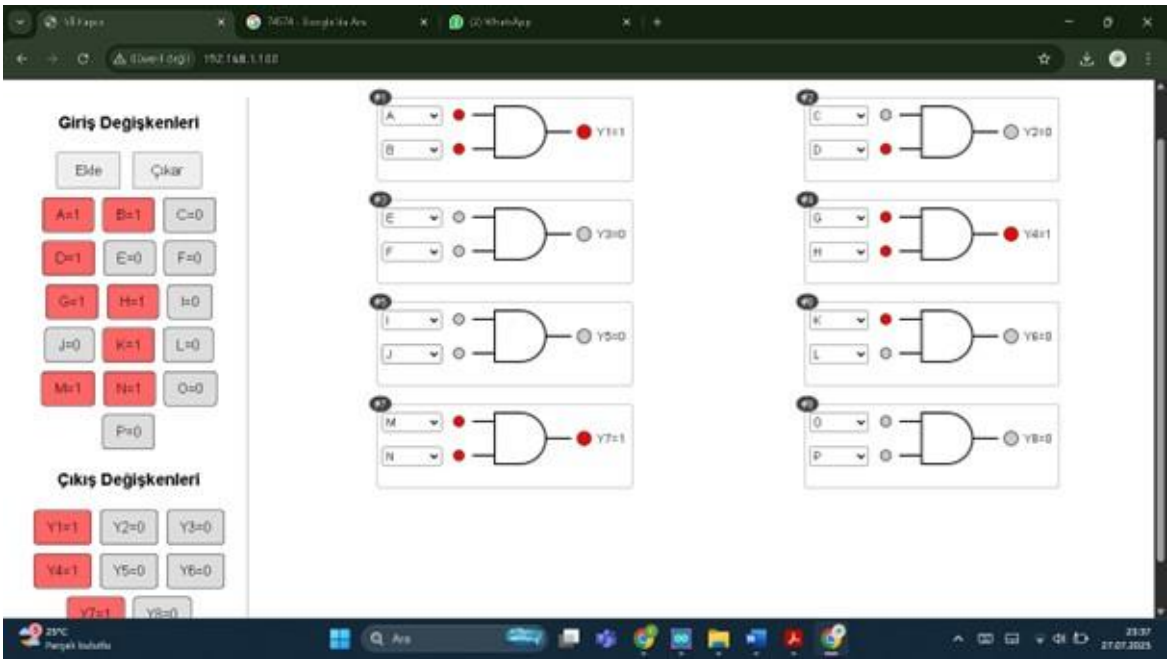


Figure 8. Values of the outputs depending on the inputs on the web page.

4 CONCLUSION

The circuit was built and tested on a breadboard. In the tests, the circuit functioned as intended. The values displayed on the web page were found to be identical on the test set. Figure 7 shows the circuit built on the breadboard, and Figure 8 shows the output values depending on the inputs on the web page as examples. As can be seen, the buttons for the input and output variables are gray when logic is 0 and red when logic is 1.

Logic gates are a crucial concept in digital electronics education. Therefore, as in every field of electronics, understanding the operation of these gates requires hands-on experience in a laboratory setting. The sheer variety of experimental materials, especially in crowded classrooms and environments, leads to time loss, cost loss, malfunctions and other problems. Considering that there are only seven logic gates, and each can have more than two inputs, it's clear how confusing it can be for beginners. In this circuit we designed using nodemcu, we simulated 20 two-input gates and their corresponding gates on the web page and demonstrated them on the experimental set. When a smart board is connected to nodemcu in a classroom, the input and output values for 20 gates can be selected and modified on the web page, which can be demonstrated on the experimental set. Students can also connect to nodemcu with their own mobile phones and simulate the operation independently. With further design, it's possible to significantly increase the number of gates and implement other gate designs. In addition, because nodes can communicate with each other via Wi-Fi, it is possible to design a dynamic

circuit by adding a different port to each node and establishing a wireless connection. We believe that our circuit can be used to develop new teaching techniques in digital electronics laboratories in physics, electrical, electronics, and computer science departments.

Statement of Research and Publication Ethics

The study is complied with research and publication ethics.

Artificial Intelligence (AI) Contribution Statement

This manuscript was entirely written, edited, analyzed, and prepared without the assistance of any artificial intelligence (AI) tools. All content, including text, data analysis, and figures, was solely generated by the authors.

REFERENCES

[1] S. Çınar, "Integrated Test Circuit Design for Logic Circuit Laboratories," *Gazi University Journal of Science Part C Design and Technology,* vol. 7, pp. 165-174, 2019, doi: 10.29109/gujsc.449163.

[2] C. S. Lee, J. H. Su, K. E. Lin, J. H. Chang and G. H. Lin, "A project-based laboratory for learning embedded system design with industry support," *IEEE Transactions on Education*, vol. *53*, pp. 173-181, 2009,

[3] L. A. Ajao, J. Agajo, J. G. Kolo, M. A. Adegboye and Y. Yusuf, "Learning of embedded system design, simulation and implementation: a technical approach,"*American Journal of Embedded Systems and Applications*, *vol*. 3, pp. 35-42, 2016, doi: 10.11648/j.ajesa.20150303.12.

[4] K. Krismadinata, I. Husnaini, A. Asnil, R. Lapisa, and H.S. Mulya, "Development of Digital Electronics Lab Kit for Vocational Education," *5th Vocational Education International Conference (VEIC-5 2023),* Atlantis Press, 2024, doi: 10.2991/978-2-38476-198-2_144.

[5] W.G. Ecton and S.M. Dougherty, "Heterogeneity in high school career and technical education outcomes,"*Educational Evaluation and Policy Analysis,* vol. 45, pp. 157-181, 2023, doi: 10.26300/4jwf-wb39.

[6] N. Goyibova., N. Muslimov, G. Sabirova, N. Kadirova, and B. Samatova, "Differentiation approach in education: Tailoring instruction for diverse learner needs," *MethodsX,* vol. 14, pp. 103163, 2025, doi:10.1016/j.mex.2025.103163.

[7] Y. Raghuvanshi, "Modelling Logic Gates in Python," *International Journal for Multidisciplinary Research*, vol. 4, 2022, doi: 10.36948/ijfmr.2022.v04i05.043.

[8] P. Dumka, "Building Logic Gate Circuits in Python," *Mathematics and Computer Science: Contemporary Developments*, vol. 5, pp. 104-115, 2024, doi: 10.9734/bpi/mcscd/v5/2500.

[9] R. L. Boylestad, " Electronic devices and circuit theory," *Pearson Education India*, 2009

[10] K. W. Martin, "Digital integrated circuit design, " *No Title*, 2000.

[11] B. Borowik, M. Karpinskyy, V. Lahno and O. Petrov, " Basic logical functions and gates. Logic Design.In" *Theory of Digital Automata*, vol. 63, pp. 51–73, 2013, doi:10.1007/978-94-007-5228-3_6

[12] V. S. Popov, ,"Equivalence of logical operations and other operations in Python programming language," In *2023 5th International Youth Conference on Radio Electronics, Electrical and Power Engineering (REEPE)*, IEEE, Moscow, Russian Federation, March vol. 5, pp. 1-6, 2023, doi: 10.1109/REEPE57272.2023.10086928.

[13] R.T. Rasheed, and S.K.C. Olajumoke," The Use of Truth Table, Logical Reasoning and Logic Gate in Teaching and Learning Process", *International Journal of Latest Technology in Engineering, Management & Applied Science*, vol. 13, pp. 1-12, 2024, doi: 10.51583/IJLTEMAS.2024.130601.

[14] S. Sazak, "PHP Tabanly Application Development Method for Logic Circuits Course," *Technological Applied Sciences*, vol. 6, pp. 24-29, 2011, S. Sazak, "PHP Tabanly Application Development Method for Logic Circuits Course," *Technological Applied Sciences*, vol. 6, pp. 24-29, 2011, doi: 10.12739/10.12739.

[15] A. Hussain, M. Hammad, K. Hafeez, and T. Zainab, "Programming a microcontroller," *Int. J. Comput. Appl.,* vol. 155, pp. 21-26, 2016, doi: 10.5120/ijca2016912310.

[16] G.O. Uzedhe, H.C. Inyiama, C.C. Udeze, and E.S. Mbonu, "Microcontroller Based Real-Time Emulator for Logic Gate and Structured Logic Devices," *International Journal of Science and Technology,* vol. 2, pp. 639-647, 2013.

[17] F. Başçiftçi, and K.A. Gündüz, "A Research on Internet of Things Compatible Microcontrollers," *Selçuk University Journal of Social and Technical Research*, vol.18, pp.66-76, 2019.

[18] R.K. Mishra, M. Pitale, and G. Singh, "Expanding I/O Pins of Microcontroller by Cascading Shift Registers," *In TENCON 2024-2024 IEEE Region 10 Conference (TENCON)*, pp. 1105-1108, 2024, doi: 10.1109/TENCON61640.2024.10902701.

[19] “Arduino Genu ino” [Online]. Available at: https://www.arduino.cc. [Accessed: 26-Jul-2025].